Woodhead Publishing Series in Electronic and Optical Materials

# Single Crystals of Electronic Materials

## Growth and Properties

Edited by Roberto Fornari

WP
WOODHEAD PUBLISHING

# Single Crystals of Electronic Materials

## Related titles

*Handbook of Thin Film Deposition*
(ISBN: 9781437778731)
*Epitaxial Growth of Complex Metal Oxides*
(ISBN: 9781782422457)
*Handbook of Crystal Growth: Thin Films and Epitaxy*
(ISBN: 9780444633040)
*Bulk Crystal Growth*
(ISBN: 9780444633033)

Woodhead Publishing Series in Electronic and Optical Materials

# Single Crystals of Electronic Materials

## Growth and Properties

*Edited by*

***Roberto Fornari***

ELSEVIER
WP
WOODHEAD PUBLISHING
An imprint of Elsevier

Woodhead Publishing is an imprint of Elsevier
The Officers' Mess Business Centre, Royston Road, Duxford, CB22 4QH, United Kingdom
50 Hampshire Street, 5th Floor, Cambridge, MA 02139, United States
The Boulevard, Langford Lane, Kidlington, OX5 1GB, United Kingdom

Copyright © 2019 Elsevier Ltd. All rights reserved.

No part of this publication may be reproduced or transmitted in any form or by any means, electronic or mechanical, including photocopying, recording, or any information storage and retrieval system, without permission in writing from the publisher. Details on how to seek permission, further information about the Publisher's permissions policies and our arrangements with organizations such as the Copyright Clearance Center and the Copyright Licensing Agency, can be found at our website: www.elsevier.com/permissions.

This book and the individual contributions contained in it are protected under copyright by the Publisher (other than as may be noted herein).

**Notices**
Knowledge and best practice in this field are constantly changing. As new research and experience broaden our understanding, changes in research methods, professional practices, or medical treatment may become necessary.

Practitioners and researchers must always rely on their own experience and knowledge in evaluating and using any information, methods, compounds, or experiments described herein. In using such information or methods they should be mindful of their own safety and the safety of others, including parties for whom they have a professional responsibility.

To the fullest extent of the law, neither the Publisher nor the authors, contributors, or editors, assume any liability for any injury and/or damage to persons or property as a matter of products liability, negligence or otherwise, or from any use or operation of any methods, products, instructions, or ideas contained in the material herein.

**Library of Congress Cataloging-in-Publication Data**
A catalog record for this book is available from the Library of Congress

**British Library Cataloguing-in-Publication Data**
A catalogue record for this book is available from the British Library

ISBN: 978-0-08-102096-8 (print)
ISBN: 978-0-08-102097-5 (online)

For information on all Woodhead Publishing publications visit our website at https://www.elsevier.com/books-and-journals

ELSEVIER
Book Aid International
Working together to grow libraries in developing countries
www.elsevier.com • www.bookaid.org

*Publisher:* Matthew Deans
*Acquisition Editor:* Kayla Dos Santos
*Editorial Project Manager:* Gabriela Capille
*Production Project Manager:* Swapna Srinivasan
*Cover Designer:* Victoria Pearson

Typeset by TNQ Technologies

# Contents

**List of contributors** **xi**

1 **Electronic materials and crystal growth** **1**
*Roberto Fornari*

2 **Silicon single crystals** **5**
*Joel K. Kearns*
2.1 Introduction **5**
2.2 Applications and requirements of silicon crystalline material **8**
2.3 Thermodynamic properties and definition of suitable growth technologies **14**
2.4 Schematics of growth methods for silicon **25**
2.5 Description of up-to-date growth technologies/processes **30**
2.6 Tailoring crystal properties via growth parameters **35**
2.7 Benefits of computer modeling **36**
2.8 Doping issues and reduction of defect density **36**
2.9 State-of-the-art of the material **41**
2.10 New trends and future developments **43**
2.11 Summary **52**
References **52**
Further reading **56**

3 **Solar silicon** **57**
*C.W. Lan*
3.1 Introduction **57**
3.2 The CZ method **63**
3.3 The DS method **71**
3.4 Conclusions and future perspectives **81**
List of abbreviations and acronyms **82**
Acknowledgments **83**
References **83**

**4 Germanium crystals** **89**

*Ichiro Yonenaga*

4.1 Introduction **89**

4.2 Basic properties **89**

4.3 Material preparation **96**

4.4 Ge crystal growth **97**

4.5 Growth-related phenomena **103**

4.6 Structural defects **110**

4.7 Applications **119**

4.8 Concluding remarks **121**

References **121**

**5 Silicon carbide** **129**

*Didier Chaussende and Noboru Ohtani*

5.1 Applications of silicon carbide and materials requirements **129**

5.2 Thermodynamic properties and suitable growth technologies **131**

5.3 Description of SiC bulk growth methods **134**

5.4 Tailoring of crystal properties via growth parameters **139**

5.5 Benefits of computer modeling **143**

5.6 Doping issues and reduction of defect density **147**

5.7 State of the art of SiC material **164**

5.8 New trends and future developments **167**

References **169**

**6 III Arsenide** **181**

*Christiane Frank-Rotsch, Natasha Dropka and Peter Rotsch*

6.1 Introduction **181**

6.2 Comparison of properties **182**

6.3 Applications and availability **194**

6.4 Requirements for the substrate **196**

6.5 Growth of GaAs crystals **202**

6.6 Wafer and sample preparation **227**

Nomenclature for Chapter 6.5.3 **229**

Greek symbols **229**

Subscripts **230**

References **230**

**7 Indium phosphide** **241**

*David F. Bliss and Roberto Fornari*

7.1 Applications and requirements of indium phosphide **241**

7.2 Thermodynamic properties and definition of suitable growth technologies **242**

7.3 Schematics for synthesis and crystal growth apparatus **246**

7.4 Benefits of computer modeling **250**

7.5 Tailoring crystal properties via growth technology **252**

7.6 Doping issues and reduction of defect density **257**
7.7 New trends and future developments **267**
References **268**

**8 Cadmium telluride and cadmium zinc telluride 273**
*Andrea Zappettini*
8.1 Applications and requirements **273**
8.2 Thermodynamic properties and definition of suitable growth technologies **274**
8.3 Synthesis of the polycrystalline material **278**
8.4 Description of up-to-date growth technologies/processes **280**
8.5 Benefits of computer modeling **288**
8.6 Postgrowth thermal treatments **289**
8.7 State of the art of CdTe and CdZnTe crystals **292**
8.8 New trends and future developments **293**
References **294**

**9 II sulfides and II selenides: growth, properties, and modern applications 303**
*Nazar O. Kovalenko, Sergei V. Naydenov, Igor M. Pritula and Sergiy N. Galkin*
9.1 Introduction **303**
9.2 Zinc sulfide: classical phosphor and new compositions **304**
9.3 Zinc−selenide compounds: scintillation properties and crystal growth **307**
9.4 Multi-energy radiography based on $A_2B_6$ scintillators for security and medical applications **312**
9.5 II selenides with metal dopants: laser applications and improved growth **318**
References **325**

**10 Diamond 331**
*Hideaki Yamada*
10.1 Introduction **331**
10.2 Growth technologies for artificial diamond **332**
10.3 Promotion of predominant crystal surfaces via growth parameters **338**
10.4 Benefits of computer modeling **338**
10.5 Issues in large-size wafer production **343**
10.6 Doping **344**
10.7 Processing techniques **345**
10.8 New trends and future developments in the growth technique and applications **346**
References **347**
Further Reading **350**

11 **Gallium nitride** **351**
*Siddha Pimputkar*
11.1 Overview of applications **351**
11.2 Single crystal growth technologies **354**
11.3 Ammonothermal method **357**
11.4 Na-flux method **369**
11.5 Hydride vapor phase epitaxy **380**
References **388**

12 **Growth of AlN and GaN crystals by sublimation** **401**
*E.N. Mokhov and A.A. Wolfson*
12.1 Introduction **401**
12.2 Methods of AlN and GaN bulk crystal growth **401**
12.3 Goals of the present review **402**
12.4 The sublimation sandwich method (SSM) **402**
Acknowledgments **439**
References **439**
Further Reading **445**

13 **Aluminum oxide** **447**
*Leonid Lytvynov*
13.1 Introduction **447**
13.2 Growth methods **447**
13.3 Properties **454**
13.4 Applications **472**
References **483**

14 **Gallium oxide** **487**
*Vladimir I. Nikolaev, Sergey I. Stepanov, Alexey E. Romanov and Vladislav E. Bougrov*
14.1 Introduction **487**
14.2 Applications and requirements of a given crystalline material **487**
14.3 Thermodynamic properties and definition of suitable growth technologies **498**
14.4 Schematics of adapted growth methods **500**
14.5 Description of up-to-date growth technologies/processes **505**
14.6 Tailoring of crystal properties via growth parameters **511**
14.7 Doping issues and reduction of defect density **513**
14.8 State-of-the-art of the material **515**
14.9 New trends and future developments **515**
References **517**

15 **Indium oxide: $In_2O_3$** **523**
*Takahiro Nagata*
15.1 Introduction **523**
15.2 Crystal growth **524**

15.3 Tailoring of crystal properties **529**
15.4 Theoretical knowledge on $In_2O_3$ **533**
15.5 Doping issues and reduction of defect density **536**
15.6 Summary **539**
References **540**

**16 Preparation, properties and electronic structure of $SnO_2$ 547**
*Karsten Henkel, Jörg Haeberle, Klaus Müller, Christoph Janowitz and Dieter Schmeißer*
16.1 Introduction **547**
16.2 Basic properties, crystal growth, and thin film deposition **547**
16.3 Photoelectron spectroscopy of $SnO_2$ **552**
16.4 pDOS and intrinsic electronic defects **558**
16.5 Electronic energy diagram **561**
16.6 Summary **568**
Acknowledgments **568**
References **568**

**Index 573**

This page intentionally left blank

# List of Contributors

**David F. Bliss** United States Air Force Research Laboratory, Retired, MA, United States

**Vladislav E. Bougrov** ITMO University, St. Petersburg, Russia

**Didier Chaussende** Univ. Grenoble Alpes, CNRS, Grenoble INP, SIMAP, Grenoble, France

**Natasha Dropka** Leibniz Institute for Crystal Growth, Berlin, Germany

**Roberto Fornari** University of Parma, Parma, Italy

**Christiane Frank-Rotsch** Leibniz Institute for Crystal Growth, Berlin, Germany

**Sergiy N. Galkin** Institute of Scintillation Materials, Kharkiv, Ukraine

**Jörg Haeberle** BTU Cottbus-Senftenberg, Cottbus, Germany

**Karsten Henkel** BTU Cottbus-Senftenberg, Cottbus, Germany

**Christoph Janowitz** Humboldt-Universität zu Berlin, Berlin, Germany

**Joel K. Kearns** NASA John H. Glenn Research Center at Lewis Field, Cleveland, OH, United States

**Nazar O. Kovalenko** Institute of Single Crystals, Kharkiv, Ukraine; V.N. Karazin Kharkiv National University, Kharkiv, Ukraine

**C.W. Lan** National Taiwan University, Taipei, People's Republic of China

**Leonid Lytvynov** Institute for Single Crystals of NASU, Kharkiv, Ukraine

**E.N. Mokhov** Ioffe Physical-Technical Institute of the Russian Academy of Sciences, St. Petersburg, Russia

**Klaus Müller** BTU Cottbus-Senftenberg, Cottbus, Germany

**Takahiro Nagata** National Institute for Materials Science, Tsukuba, Japan

**Sergei V. Naydenov** Institute of Single Crystals, Kharkiv, Ukraine

**Vladimir I. Nikolaev** ITMO University, St. Petersburg, Russia; Ioffe Institute, St. Petersburg, Russia

**Noboru Ohtani** Kwansei Gakuin University, Sanda, Japan

**Siddha Pimputkar** Lehigh University, Bethlehem, PA, United States

**Igor M. Pritula** Institute of Single Crystals, Kharkiv, Ukraine

**Alexey E. Romanov** ITMO University, St. Petersburg, Russia; Ioffe Institute, St. Petersburg, Russia

**Peter Rotsch** OSA Opto light GmbH, Berlin, Germany

**Dieter Schmeißer** BTU Cottbus-Senftenberg, Cottbus, Germany

**Sergey I. Stepanov** Perfect Crystals LLC, St. Petersburg, Russia

**A.A. Wolfson** Ioffe Physical-Technical Institute of the Russian Academy of Sciences, St. Petersburg, Russia

**Hideaki Yamada** National Institute of Advanced Industrial Science and Technology, Ikeda, Japan

**Ichiro Yonenaga** Tohoku University, Sendai, Japan

**Andrea Zappettini** IMEM-CNR, Parma, Italy

# Electronic materials and crystal growth

# 1

*Roberto Fornari*
University of Parma, Parma, Italy

Crystal growth is a scientific discipline that has made terrific progress over the past three decades. Among the different classes of crystalline materials developed and commercially produced, semiconductors are certainly very important. Many extraordinary new technological advances have been achieved thanks to microelectronic, optoelectronic, and optical devices based on artificial semiconducting crystals. Let us consider wide-bandgap nitride semiconductors, for example: blue, green, and white light-emitting diodes and ultraviolet (UV) detectors and emitters are already available, and great steps have been made toward reliable high-power lasers in the visible range. Bulk single crystals of GaN and AlN are absolutely necessary to make the fabrication of high-power lasers possible. However, the development of these single crystals is much slower that the corresponding development of epitaxial structures owing to the extreme thermodynamic properties of the nitride semiconductors, which make single crystal growth very complicated.

Generally, the growth of bulk crystalline materials remains one of the most challenging technical tasks of materials science. Beside issues related to thermodynamics and kinetics, the crystal growth process is closely connected to a variety of physical phenomena, such as momentum, heat and mass transport, heat radiation of participating media, phase transitions, capillarity, anisotropy of physical properties, etc. To prepare bulk crystals of high quality, i.e., with low defect density and uniform characteristics, an understanding of these phenomena and their coupling with growth mechanisms and the associated defect formation becomes crucial. Due to the typical high-temperature environment of the crystal growth systems, experimental investigation and in-situ observations are quite difficult; thus in view of this difficulty and cost reduction, the experimental work must be supported by computer modeling. Very accurate and reliable codes have been specifically developed for different crystal growth methods and classes of materials. Nowadays, it would be impossible to grow high-quality semiconductor single crystals without computer simulation to identify the growth parameters and computer control of the growth process; indeed, the process complexity and the elevated number of parameters to be controlled would make any manual process irreproducible.

The most exciting discoveries of recent years in the field of solid-state physics and electronics are based on the ability to grow thin layers and nanostructures with exceptional control of size and composition. This ability has led to the discovery of artificial size-linked materials properties, which in turn has paved the way to entirely new generations of devices and components and stimulated extensive research in the

**Single Crystals of Electronic Materials.** https://doi.org/10.1016/B978-0-08-102096-8.00001-X
Copyright © 2019 Elsevier Ltd. All rights reserved.

area of epitaxial technologies. As a side effect, there has been a certain drop of interest in bulk crystal growth. A quick survey of the scientific literature shows that the number of papers on nanostructures and quantum heterostructures is booming, in comparison to a more or less steady number of publications on single crystals.

However, there are very good reasons for not considering bulk crystals as commodities and for pushing forward crystal growth technology. First of all, in many advanced applications single crystals are themselves active components and not simple "substrates." This is true, for instance, in silicon solar cells, where the generation of photocarriers occurs up to tens of micrometers from the surface; in radiation and particle detectors (CdTe, CdZnTe, Ge) to obtain efficient conversion of the radiation to be detected; and in piezoelectric sensors and actuators to have sufficiently high signals and/or displacements. Furthermore, in many cases advancements in epitaxial technology were made possible by the availability of substrates with excellent quality as well as good thermal and structural matching to epilayers. The growth of single crystals of electronic materials should thus be regarded as the key factor underlying many innovations.

Looking at today's crystal growth, one can clearly identify two major challenges. The first is to improve and scale up the growth processes of established materials to achieve cost-effective single crystals of superior quality. This applies, for instance, to traditional semiconductors, such as silicon, germanium, GaAs, InP, and CdTe. The demand for larger crystals with improved uniformity and low defect density has stimulated a remarkable development of traditional growth equipment and processes to meet the new commercial and technological demands. After the first metal crystals pulled from the melt by Jan Czochralski in 1915 and crystallized within a crucible by Percy Bridgman in 1925, many generations of Czochralski and Bridgman furnaces for bulk semiconductors followed over the decades. The addition of external fields, predominantly electromagnetic fields, to standard machines became increasingly popular in melt growth as an efficient tool to suppress the undesired effects of melt convection.

The second challenge involves the need to grow single crystals of materials with extreme thermodynamic properties, in particular very high melting temperatures or high dissociation pressures at the melting point. The technical advancement of the crystal growth machinery today allows the achievement of extremely high temperature and compensating pressures. New models of autoclaves and crucible-free melt growth systems are now commercially available. This has opened the way to exploratory research on single crystal growth of materials which, given their almost prohibitive phase diagrams, were previously available only as ceramics or tiny crystallites. As examples of such electronic materials, the reader can find in this book SiC, GaN, AlN, and diamond grown from either the vapor phase or high-pressure high-temperature solutions. It is thanks to the availability of such advanced materials that new devices for power electronics and UV optoelectronics have been developed in recent years.

This book updates the body of information on properties and crystal growth of well-established electronic materials (silicon and III—V, II—VI, and IV—VI semiconductors). In addition it provides an overview of emerging bulk semiconductors, particularly wide-bandgap oxides such as $In_2O_3$, $Ga_2O_3$, and $Al_2O_3$, nitrides (AlN and GaN), and diamond. It is a complete but focused overview of the state of the art in preparation of bulk semiconductors, conceived for professional crystal growers, university teachers, and PhD students approaching the fascinating world of electronic crystals and their properties, growth, and applications.

I wish to thank all the authors for their valuable contributions and the Elsevier staff for their support at all stages of book editing.

This page intentionally left blank

# Silicon single crystals

# 2

*Joel K. Kearns*
NASA John H. Glenn Research Center at Lewis Field, Cleveland, OH, United States

## 2.1 Introduction

Single crystal silicon is unique. It is both the foundation of the global microelectronics-based economy and a model material. Although the word “technology” today is associated with the internet, wireless devices, social media, software coding, and “apps,” all these are enabled by dislocation-free single crystal silicon. The reference to software companies as being a cultural part of “Silicon Valley” acknowledges this foundation. The single crystal growth methods, and resulting silicon structure, properties, and defects are extremely well studied and documented in the literature [1−6]. However, single crystal silicon is today still an active subject of intensive study, and continues to be developed and improved for both optimized crystal performance in devices and reduced cost.

Silicon exists at room temperature as a diamond cubic, covalently bonded crystal [7]. Each silicon atom is covalently bonded to four other silicon atoms, in low coordination number packing. The silicon atoms are tetrahedrally coordinated due to $sp^3$ orbitals. Silicon acts as an insulator at room temperature, but can be made conducting by substitution of small amounts of electronic impurities. The electronic impurities, once ionized, provide electrons in the conduction band or holes in the valence band of the silicon’s indirect forbidden gap. The concentration of charge carriers sets the bulk electrical resistivity of the silicon, and important transistor electrical characteristics such as current−voltage behavior and blocking voltage [8]. Silicon’s relatively large indirect bandgap of 1.10 eV means that it can be used as an extrinsic semiconductor at operating temperatures up to 200°C, and provides lower reverse currents for p−n junctions than competing materials such a germanium [8]. Silicon’s electronic properties are adequate for semiconductor transistor operation (i.e., acceptable indirect bandgap, carrier mobilities, minority carrier lifetimes, etc.) but it has several other advantages compared to other semiconducting materials that allow it to sustain a commanding position in a highly competitive field. It is abundant in nature, the second most common element on Earth, and bound in silicates. Silicon exhibits a very thermally and chemically stable native oxide ($SiO_2$), allowing barriers to be established between adjacent regions of transistors or between transistors and the environment. Over decades, the declining cost and increasing volume of purified polycrystalline silicon (polysilicon), which is used as the starting material for single crystal growth allowed greater control and less variation of silicon crystal bulk properties. Polysilicon is now produced in great volumes and exhibits up to eleven nines measured purity of metals and heavy elements. Purified silicon has a relatively large thermal conductivity,

**Single Crystals of Electronic Materials.** https://doi.org/10.1016/B978-0-08-102096-8.00002-1
Copyright © 2019 United States Government as represented by the Administrator of the National Aeronautics and Space Administration.
Published by Elsevier Ltd. All Rights Reserved.

supporting large thermal gradients, and fast solidification and cooling rates. The structural, chemical, and electronic properties of single crystal silicon have been revealed by more than 65 years of competitive research and development carried out by governments and industry worldwide.

For the growth of large single crystals, silicon is one of the few materials systems that can be grown threading dislocation free (DF) relatively simply and repeatedly. Although dislocation-free crystals are extremely difficult to grow in most materials systems, dislocation generation is not favorable due to the increase in Gibbs free energy in the crystal, and no equilibrium number of dislocations can be calculated. However, most materials do not exhibit the thermophysical properties that allow dislocations to be reduced during growth, and avoid nucleation of new dislocations. Eliminating dislocations in silicon enabled the avoidance of polycrystalline breakdown due to dislocation multiplication in an initially single crystal, as crystal diameter, crystal length, growth rate, and cooling rate were increased. The diamond cubic lattice can be modeled as two interpenetrating face-centered cubic (FCC) lattices. If dislocations are present, their motion occurs in the 12 slip systems for FCC, along the close-packed {111} planes in the <110> directions. In slices cut from dislocated silicon crystals, preferential etching reveals slip lines.

Single crystal diameters were progressively increased from the initial 10 mm diameters of the early 1950s to the 300 mm diameter standard of 2018 [9–12]. Growing bulk crystals dislocation free also allows the nucleation and growth of specific bulk microdefects in the silicon that provide either device advantages (e.g., gettering of metal impurities) or disadvantages (e.g., vacancy-agglomerate voids, the so-called "crystal-originated particles" which interfere with small-scale features in transistors). Silicon's starting purity and controllable net generation and agglomeration of native point defects during solidification made it a repeatable model material for physics study. The international standard of the "kilogram" in the International System of Units' Avogadro project has proposed that a new standard be developed based on a round sphere of dislocation-free single crystal silicon.

There are several unusual aspects of silicon that presented challenges for developing the technology to grow single crystals. Silicon has a higher melting point (1683 K) than germanium and the III–V and melt-grown II–VI compounds. The higher melting point aggravates the high chemical reactivity between molten silicon and any container. The only melt container material that has been developed is fused (amorphous) silica, $SiO_2$, the native oxide. Certain impurities (carbon and metals) have very small equilibrium distribution coefficients, which can be somewhat advantageous from the point of view of fractional crystallization purification, but the electronic impurities' segregation coefficients do lead to appreciable macrosegregation and microsegregation that vary wafer-to-wafer electrical properties within a crystal. However, several substitutional impurities are available with very small energy gaps between gap energy level and the conduction (or valance) band, leading to high ionization percentages at room temperature [13].

Single crystal dislocation-free silicon is used for more than 90% of semiconductor devices [14]. For devices that demand a direct bandgap (i.e., optoelectronics) or very large bandgap, other semiconductors are used. Silicon is also used for about 90% of all

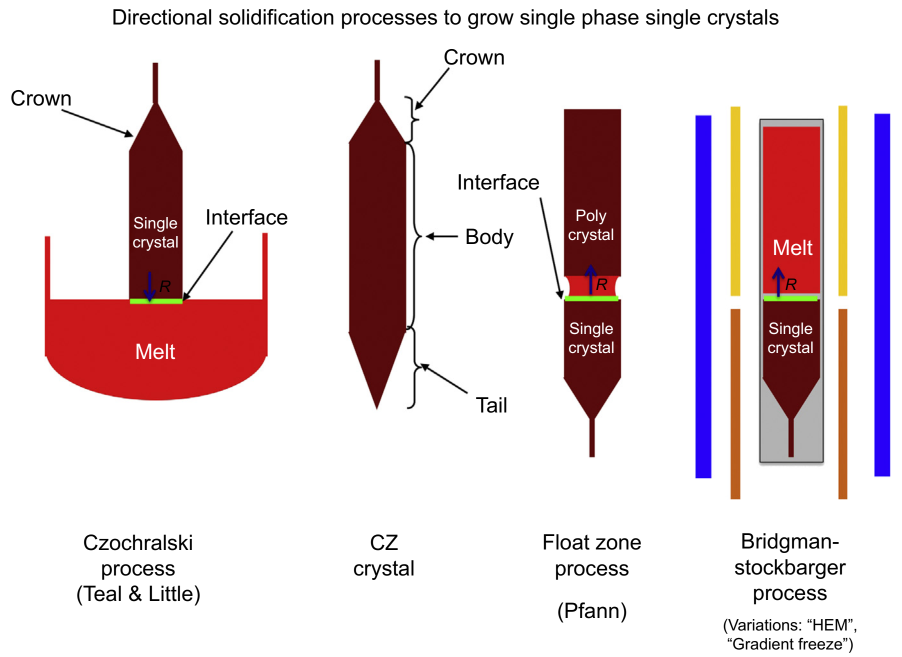
Directional solidification processes to grow single phase single crystals
Crown
Single crystal
Interface
R
Melt
Czochralski process (Teal & Little)
Crown
Interface
Body
Tail
CZ crystal
Poly crystal
R
Single crystal
Float zone process
(Pfann)
Melt
R
Single crystal
Bridgman-stockbarger process
(Variations: "HEM", "Gradient freeze")

**Figure 2.1** Silicon single crystal growth processes.

photovoltaic cell material (solar cells), and single crystal silicon is roughly half of all silicon used for solar cells. In solar cells, single crystal silicon is called "mono" silicon (for "monocrystalline") [15,16].

Single crystal silicon for semiconductor devices is grown dislocation free by the Czochralski (Cz) and floating zone (FZ) techniques (see Fig. 2.1) [1,9,17–19]. "Mono" solar silicon is grown by the Cz method, traditionally from less chemically pure polysilicon than that used for semiconductors. The Cz method for growing silicon was developed by Teal and Buehler [20–22]. The FZ method was developed by Theuerer [23] and Emeis [24] as a modification of the zone refining work of Pfann [17,18]. A new single crystal silicon growth process under development for lower-cost "mono" solar cells is a dislocated single grain called "mono$^2$," "quasimono," or "mono-like-multi" (MLM) [25]. The "quasimono" silicon is directionally solidified in a crucible using a modified seeded heat-exchange method (HEM) technique. Single crystal seeds are made from discarded Cz material (or recycled HEM single crystal MLM material). The most recent new process to produce single crystal (dislocated) silicon for photovoltaics, without a melt container, is neogrowth silicon (NGS) [26]. FZ silicon is grown without the traditional feedstock rod, but depositing granular polysilicon during crystal growth is being examined as a lower-cost FZ method for mono solar cells [27,28]. But today the only method for growing dislocation-free single crystal silicon in very large volumes is Cz.

Cz growth of dislocation-free single crystal silicon continues to progress in different directions for different end wafer markets. Semiconductor silicon is focused on crystal

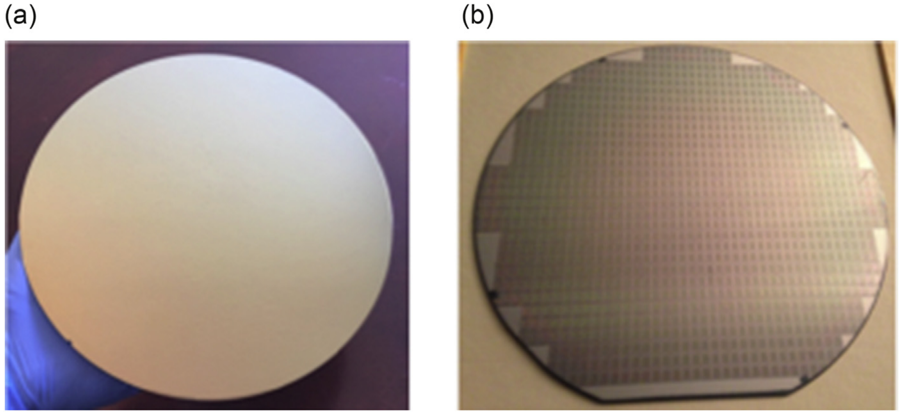

**Figure 2.2** Silicon wafers: (a) finished polished wafer, (b) computer chips in wafer.

diameters up to 450 mm (and potentially 675 mm), while maintaining desired bulk microdefect attributes and reducing costs. Solar single crystal silicon is focused on reducing cost while improving bulk properties for photovoltaic conversion efficiency, such as minority carrier lifetime. Crystals for optical and mechanical applications are increasing in diameter even as silicon directionally solidified in a crucible offers an alternative.

For semiconductor devices, the crystals are sawed into round, flat disks called "wafers" for later device processing [10]. Fig. 2.2(a) shows a polished wafer ready for device manufacturing, and Fig. 2.2(b) is the finished wafer with many copies of the same "chip" made in rows and columns on the wafer. Dislocation-free silicon crystals are used as the starting materials for several different types of semiconductor silicon wafers: polished wafers, substrates for epitaxial wafers, "perfect" (microdefect engineered) polished wafers, surface-annealed wafers, and buried-layer wafers, including silicon on insulators.

The scale-up of size of dislocation-free silicon crystals from the 1950s to today is a key enabler of "Moore's law," which predicted that the cost of transistors would decrease and the number of transistors per device would increase at a regular pace [13]. The increase of wafer size and improvement of wafer physical quality contributed greatly to this trend, as did the complementary decrease of transistor feature size and increase of numbers of transistors in a single semiconductor device. The increase of silicon single crystal diameter and length is an unusual success story of a manufacturing process scale-up, and it occurs on a dislocation-free single crystal.

## 2.2 Applications and requirements of silicon crystalline material

The function of the device for which the silicon wafer serves as starting material defines the specific properties the silicon must possess and the phase transformation processing required. The devices are manufactured by different industries, notably those that produce semiconductor devices and solar photovoltaic cells. Single crystal silicon is also used for optical windows (transparent at particular infrared wavelengths) and sputtering targets for materials deposition tools, and these are also different end user communities with different needs for material properties. The semiconductor community develops public, precompetitive roadmaps for silicon quality advancement as part of the front-end materials of the International Technology Roadmap for Semiconductors [29]. The photovoltaic community has defined a similar International Technology Roadmap for Photovoltaics [30].

Silicon wafers are the fundamental building material for semiconducting devices, and semiconducting devices are the foundational components of virtually all electronic goods, including computers, telecommunications products, and consumer electronics. Silicon wafers are produced in various standard diameters (of nominally 4—12 inches) and serve as the substrate material on which the great majority of semiconductor devices or "chips" are fabricated. The dislocation-free silicon crystals are routinely grown to diameters of 300 mm and lengths of up to 3 m. Crystals of 200 mm diameter have been grown to 3.5 and 4 m length for solar cells. Fig. 2.3 shows a 200 mm diameter dislocation-free single crystal of silicon after growth.

The crystals must be free from edge, screw, and mixed dislocations throughout their entirety [12,31]. Advanced memory and processor devices are made on 300 mm diameter silicon. Power control, analog, and discrete semiconductors are often made using previous-generation feature sizes and manufacturing equipment, so they use 200 and 150 mm diameter silicon wafers. For the great majority of semiconductor devices, including solar cells, the single crystals, which are sliced into the round substrates, must be of <100> crystallographic orientation (normal to the wafer surface) and dislocation free. If dislocations are generated during silicon crystal growth itself, the affected sections of the crystal are unusable for device processing. If any

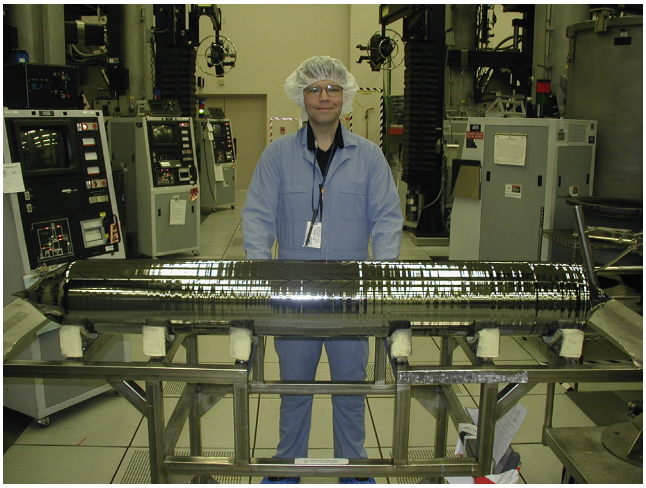

**Figure 2.3** 200 mm diameter crystal.

threading dislocations are already present in the growing silicon crystal, the high strain during fast crystal cooling leads to dislocation multiplication and eventually polycrystalline growth. During polycrystalline growth, twins can also develop. Dislocations act as impurity concentration sites during both crystal growth and later device processing, and lead to electrical shorts and deficient electrical performance, so any material with dislocations is not usable and is scrapped.

Wafers are cut from the crystal with (100) orientation normal to the flat wafer surface, so the crystal must be grown with the long body in the (100) direction. This surface orientation exhibits fewer "dangling" bonds, providing lower interface states and lower oxide fixed charge for gate oxides in complementary metal oxide semiconductor (CMOS) or BiCMOS (bipolar interface CMOS) device types [10]. In the fabrication of metal oxide semiconductor (MOS) integrated circuits, the crystal orientation is important because of orientation effects on electrical charge density arising from surface states and carrier mobility. The charged surface states density is important with regard to MOS devices, since it directly affects the threshold voltage. MOS, CMOS, and BiCMOS devices are historically made on the (100) wafer (crystal) surface to get the desired low oxide charge, making it easier to target the required MOS threshold voltage ($V_T$) [11,13].

The semiconductor integrated circuit device market was estimated to reach $419 billion value in 2017, up more than 20% from 2016 [32]. This is dependent on an approximately $10 billion worldwide production of single crystal silicon wafers [14]. The main demand is for dynamic random access memories. Demand was also great for analog, flash memory, and logic devices. Ostensibly still following Moore's law, device manufacturers initially introduced a new process every 18 months, to lower the cost per transistor. At each node (design feature size), process cost and complexity increase, so now the time to develop at new node fully has increased from 18 months to up to 36 months. In 2018 device foundries are expected to manufacture products with 7—10 nm transistor critical feature sizes. As feature sizes are decreased, device makers seek smaller bulk defect sizes, their absence, and more uniformity within wafer properties. All this makes demands on crystal properties.

Typical semiconductor device property specifications are translated into crystal property specifications such as:

- crystallographic orientation;
- electrical resistivity maximum and minimum;
- resistivity radial variation maximum value (from wafer center to edge);
- interstitial oxygen concentration target value and variation;
- interstitial oxygen radial variation maximum value;
- harmful bulk metals concentration maximum value;
- no oxidation-induced stacking faults (OISFs);
- no slip, and etch pit density of zero (no threading dislocations);
- concentration of desired bulk microdefects (after device process thermal cycle) (for metals gettering);
- number, size, and size distribution of "light point defects" (on wafer surface, contributed from bulk crystal);
- minority carrier lifetime minimum value (under specified surface passivation and charge injection conditions).

The wafer seller must prove by test “qualification” that its wafers demonstrate adequate device function when devices are made in the customer’s manufacturing line. This requires a relatively large number of wafers (hundreds, at least) so that statistics can be developed for thousands or tens of thousands of devices. If the average device yield is lower than expected or devices do not function as expected, wafer and crystal properties may need to be adjusted and the qualification process repeated.

The values of silicon crystal properties for different types of semiconductor devices are distinct for each type of device. The largest volume is for digital and logic products, such as CMOS devices. These are approximately 75% of the semiconductor device market. They include central processing units, dynamic and static memories, application-specific integrated circuits, and charge-coupled devices. Typical wafer properties are:

- 300 mm diameter;
- <100> crystallographic orientation;
- lightly boron-doped polished wafer, or heavily boron-doped substrate for a lightly boron-doped epitaxy-grown layer (note: epitaxial layers can also be made on lightly doped substrates, and polished wafers can be based on lightly phosphorous-doped wafers, although this is not common);
- carbon less than 0.1 ppma;
- oxygen at a specified value, usually low (less than 12 ppma), +/−2 ppma;
- OISF density;
- crystal-originated particle maximum size and density;
- critical surface metals maximum concentration (Fe, Cu, Ni, Co, K, Mn, Ca, Na);
- variation of resistivity (dopant concentration) and oxygen concentration across the crystal diameter is specified to not exceed a particular percentage;
- microdefect-“free” polished wafer, with or without bulk precipitation profiling for impurity gettering;
- surface region annealed with argon, hydrogen, or ammonia gas after slicing, to remove crystal-originated particles in the near-surface region;
- special silicon on insulator internal layer.

Analog and discrete products are the next largest market. These include power MOS field-effect transistors, linear, analog, rectifiers/diodes, bipolar junction transistors, and insulated-gate bipolar transistors (IGBTs). A wide range of wafer properties are needed, depending on the particular device type and design:

- crystallographic orientation (defined by crystal seed during pulling): $\langle 100\rangle$, $\langle 111\rangle$, $\langle 110\rangle$;
- diameter: 125, 150, 200, and 300 mm;
- usually crystal is heavily doped n-type to serve as substrate for a lightly doped n-type epitaxial layer (but IGBTs are made on lightly doped p-type substrate);
- crystal n-type dopant can be phosphorous, arsenic, or antimony;
- carbon less than 0.1 ppma;
- oxygen between a specified minimum and maximum value (usually between 10 and 18 ppma).

Mechanical products include very different applications such as microelectronic mechanical systems (MEMS), ink-jet printer cartridge ink sprayers, and optical windows or sputtering targets. These are all grown by the Cz technique. MEMS and ink-jet devices can have stringent chemical and electrical requirements similar to CMOS, while the main specifications for targets and windows may only be size and chemical purity. Some of these are made on very heavily boron-doped crystals at diameters even larger than those use for CMOS semiconductors: from 375 mm to over 400 mm diameter. Because there is no large supply of crystal pullers with charge sizes large enough to grow long-aspect-ratio 400–450 mm diameter crystals, growing very large-diameter crystals using batch Cz leads to relatively short crystal length.

Unlike the semiconductor field, there is no drive to increase the diameter of wafers greatly for solar cells, as solar cells are a "whole wafer" single device built to an industry-standard size. The simplest solar cell is one p–n junction, which is used to collect the charge carriers generated by insolation. In this case the size is not a diameter, as the wafers are roughly square in plan area. The wafer size characteristic is measured from straight edge to straight edge of the square, as shown for two sizes of cell in Fig. 2.4. The square wafers are cut from round cross-section crystals pulled by the Cz method, as shown in Fig. 2.5. Fig. 2.5 shows a finished cell on the same size of crystal used as starting material to make the square wafer. Over time a standard was developed for wafer shape which is a compromise between the solar panel makers' desire for a completely square wafer and the cost premium to grow a crystal with large enough diameter that a completely square wafer could be cut form it. The result is a "pseudosquare" (PS) wafer with flat sides and rounded corners, as shown in Fig. 2.4. The round corners indicate the diameter of the crystal that was used to make the wafer. Over time, mono wafers have increased in size from 100 mm to 125 mm to 156 mm PS; 156 mm PS is a roughly equivalent size to the 156 mm full square multicrystalline solar wafer grown by the gradient freeze technique.

The standard solar cell is build with a p-type base region, which means the crystal used to make the wafer must be p-type. It is almost always doped with boron.

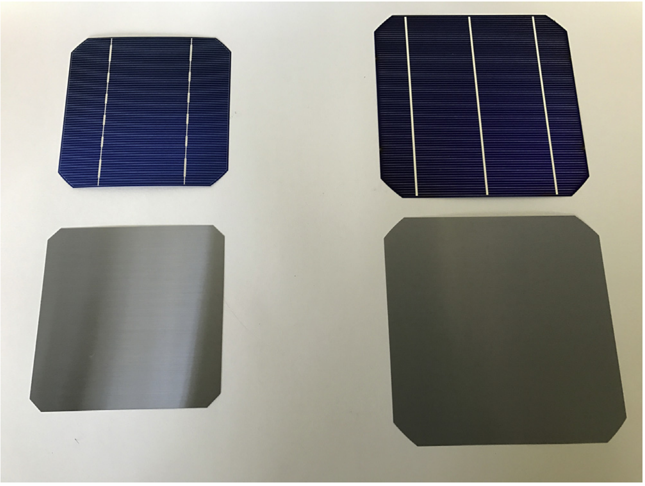

**Figure 2.4** Solar cells on solar wafers, 125 and 156 mm.

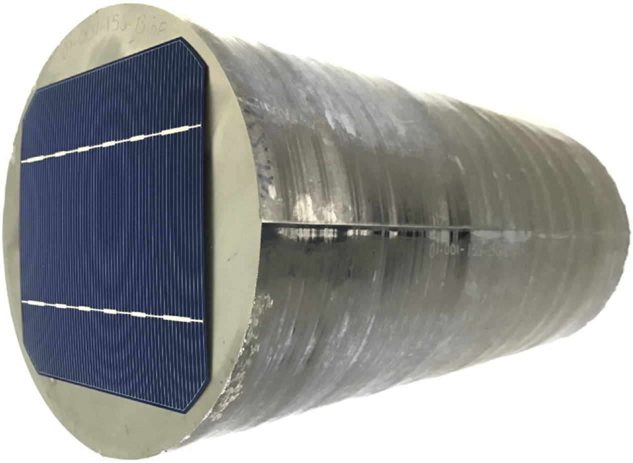

**Figure 2.5** 125 mm pseudosquare cell on cut 7 inch diameter Cz crystal.

Some advanced cell designs in large-scale production use n-type wafers, so the crystals are instead doped with phosphorous. Compensation (substantial amounts of both n- and p-type dopants in the same crystal) is not permitted.

156 mm PS requires a roughly 205 mm diameter crystal be pulled. Depending on how sharp the corners are to be, the crystal diameter may need to be larger. In some cases manufacturers pay a premium to grow an even larger (approximately 225 mm diameter) crystal to produce a true "full square" mono wafer. Whether this cost is justified depends on the value of producing power from the full corners' area compared to the cost of growing a larger crystal. This may not be obvious until one evaluates the entire solar panel, composed of many solar cells.

Standard "mono" silicon crystal properties for solar cells are:

- p-type (doped almost always with boron, but sometimes gallium);
- pulled by the Cz technique;
- crystal orientation (100) (enables lower reflectivity caustic etch texturing);
- resistivity of crystal between 0.5 and 3 Ω-cm;
- nominal wafer thickness sliced from crystal must be 160−190 um;
- interstitial oxygen less than 10−18 ppma;
- substitutional carbon less than 1 ppma
- no secondary phases;
- free of threading dislocations;
- lifetime greater than 10 μs on block form, measured by Sinton;
- passivated lifetime greater than 150 μs (on slice);
- light-induced degradation less than 3% over 1 year of use;
- resulting photovoltaic conversion efficiency in aluminum back surface field standard solar cell greater than 19.5%.

A recent big difference between semiconductor device production and solar photovoltaic production is production volume. As recently as the late 2000s, solar production was a small fraction of the volume of single crystal silicon made for semiconductor devices. In 2018 those fractions are reversed, and the great majority of single silicon crystals being pulled are made for use in solar cells. Many process design complexities originally designed for semiconductor wafer devices (e.g., Oi target) are not needed for solar cell crystal, so the process directions are simplified. Conversely, Cz processes developed for solar silicon often cannot produce properties acceptable for semiconductor devices.

## 2.3 Thermodynamic properties and definition of suitable growth technologies

The phase transformation used to convert polycrystalline silicon to single crystal silicon is solidification. The thermophysical properties of the crystal and melt have been intensively investigated [5]. The Cz pulling technique is shown at laboratory scale in Fig. 2.6. Cz pulling is a normal freezing solidification process, where the solute is incorporated in the crystal according to the Gulliver−Scheil expression, with an effective segregation coefficient ($k_{eff}$) close in value to the equilibrium segregation coefficient ($k_0$) [9,33,34]. Because the amount of dopant in even "heavily doped" crystals is $<0.1\%$ atomic, global heat transfer calculations model this plane front solidification process as a unary component phase transformation. The alpha phase is silicon plus dopant (or for particular studies silicon plus carbon or silicon plus oxygen). Ternary or quaternary phase diagrams often do not need to be consulted for bulk single crystal growth.

The temperature gradients in the melt or crystal (in the thermal diffusion boundary layer) can be estimated in one dimension from the conservation of heat flux at the interface:

$$K_S G_s = K_L G_L + L\rho R$$

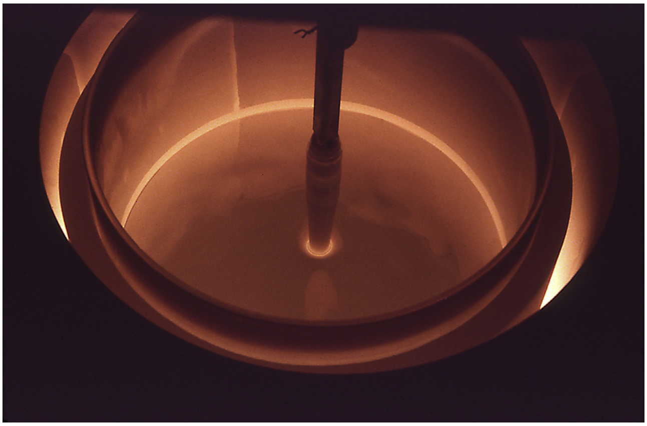

**Figure 2.6** Research-scale Cz silicon pulling, through diameter window.

Here $K$ is thermal conductivity, $L$ is latent heat of fusion, $\rho$ is crystal density, and $R$ is solidification (growth) rate. The subscripts $S$ and $L$ refer to solid (crystal) and liquid (melt). The values of $K_S$, $K_L$, $L$, and $\rho$ are known from thermophysical property measurements on silicon. The value of $R$ is defined by the process conditions and is readily measureable during growth. $G_S$ and $G_L$ are also defined by process conditions, and can be calculated from a global heat transfer numerical model (or measured in experiments). As crystal diameter is increased, attainable $G_S$ values decrease. The maximum growth rate is obtained when $G_L$ is zero, although a zero gradient in the melt would promote unacceptable dendritic growth even with no impurities, and the diameter could not be controlled.

$$R_{\max} = \frac{(K_S G_S)}{L\rho}$$

In practice, to maintain dislocation-free growth the maximum growth rate is less than this value even for small melt temperature gradients. Small melt temperature gradients require more aggressive diameter-control seed lift adjustments, increasing the probability of great variations in local undercooling. As $R$ is increased, more latent heat is liberated and the crystal–melt interface becomes more concave. Nonlinear temperature gradients at the crystal periphery increase in magnitude, and for small-diameter crystals the stresses produced can nucleate dislocations [9,35,36].

In Cz the crystal is growing over the melt, so the temperature gradients are destabilizing with respect to gravity [9]. Depending on the dopant species, the solutal gradients at the interface can be either stabilizing or destabilizing. The opposite conditions hold for FZ. In Cz the crystal–melt interface is slightly concave, but in FZ the interface can be extremely curved concave [19,37].

The Cz melt meniscus attached to the crystal is defined not just by geometry and local melt flow but also by the melt–vapor surface energy (surface tension), the value of which is heavily dependent on local melt oxygen concentration [38–44]. The silicon melt partially wets the silicon crystal [39]. The molten zone in FZ growth is partially supported by a Lorentz force from the radio-frequency induction-heating coil, which maintains the silicon temperature above the melting point [19]. The melt surface tension also helps to support and contain the molten zone in FZ growth from spilling over the growing crystal or breaking contact with the polysilicon feed rod [19,37].

The segregation coefficients for the most-used dopants in silicon range from 0.023 (antimony) to 0.8 (boron) [12,45,46]. The dopants gallium and indium, with much smaller segregation coefficients, are rarely used, and only for photovoltaic material. Carbon (one of the two most prevalent light unwanted impurities, the other being oxygen) has a segregation coefficient of 0.007 [1]. For small segregation coefficients, melt concentration scales inversely with volume of melt. In general, when a segregation coefficient is less than unity, the decrease in the amount of solute is less than the decrease in volume of melt as solidification proceeds. Melt concentration increases with crystal growth. Variations in buoyancy-driven convection produce small-scale compositional variation, chemical striations, or bands, as shown in Fig. 2.7.

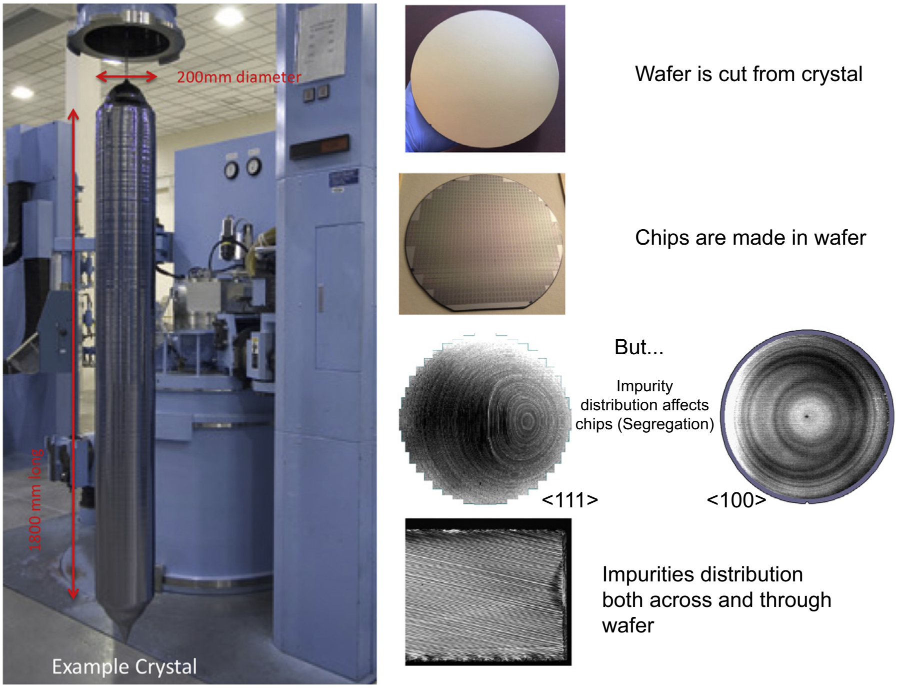
200mm diameter
1800 mm long
Example Crystal
Wafer is cut from crystal
Chips are made in wafer
But...
Impurity distribution affects chips (Segregation)
<111>
<100>
Impurities distribution both across and through wafer

**Figure 2.7** 200 mm diameter crystals showing microsegregation on wafers.

In FZ growth dopant can be added by gas flow to the molten zone during growth or as a pellet in the initial stage of growth, or the crystal can be grown undoped. After growth, small-diameter crystals can undergo neutron transmutation doping, where a small percentage of silicon is converted to phosphorus [19,37]. This can only produce n-type material.

In Cz growth, oxygen is introduced into the melt from crucible dissolution [11,35]. Approximately 99% of oxygen evaporates from the melt in the compound silicon monoxide, so phase equilibria do not predict segregation of oxygen in silicon [11,47,48]. Carbon does not evaporate from the melt once introduced.

The starting polysilicon used to form the initial melt is produced by chemical vapor deposition, to purity greater than eleven nines, from metals and heavy elements. A photograph of a large piece of "chunk" polysilicon is shown in Fig. 2.8. An electrically active dopant (e.g., boron) is deliberately added to the melt before crystal growth commences, at a concentration to provide the desired crystal resistivity during normal freezing. Oxygen and carbon are unwanted impurities introduced during the Cz growth process. The fused silica crucible, which contains the silicon melt, is slowly dissolved by the melt, and the graphite insulation and heater parts dissociate in the hot argon growth environment. Oxygen evaporates from the melt in the form of SiO, and only about 1% of the melt oxygen is incorporated into the crystal. Any carbon dissolved into the melt does not evaporate and is incorporated into the crystal by normal freezing.

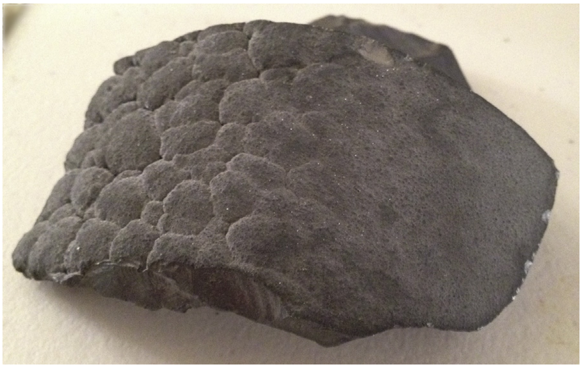

**Figure 2.8** CVD-grown polysilicon chucks grown by Siemens process.

Dislocation-free silicon exhibits pronounced "habit lines" or "flats" at equally spaced locations on the periphery of the crystal exterior [12,49,50]. This is shown in a crystal crown during growth in Fig. 2.9, and in bodies of two different orientation crystals in Fig. 2.10. These habit lines are generated by vicinal flat {111} facets at the crystal—melt—vapor three-phase boundary.

An explanation of why dislocation-free silicon exhibits these particular morphological characteristics is provided by the Jackson alpha factor [51,52]:

$$\alpha = \frac{\eta}{Z}\frac{L}{kT_M}$$

where $\alpha$ is the "alpha factor," $\eta$ is the number of nearest neighbor sites adjacent to an atom in the plane of the interface, Z is the total number of nearest neighbors of an atom in the crystal, L is the latent heat of fusion, k is the Boltzmann constant, and $T_M$ is the melting temperature of the material.

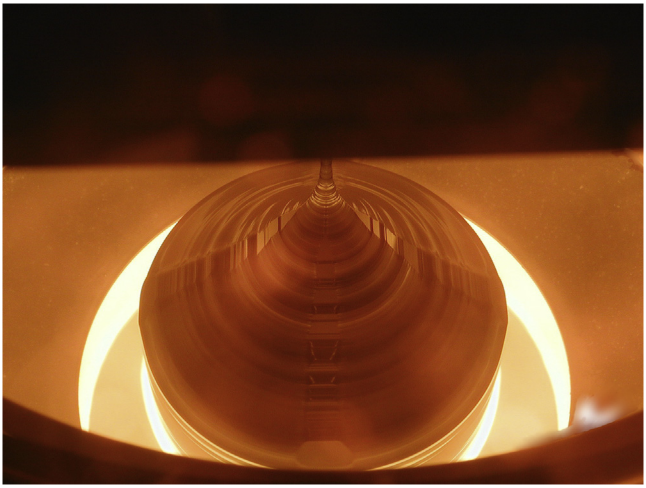

**Figure 2.9** Cz pulling of "crown" showing facets.

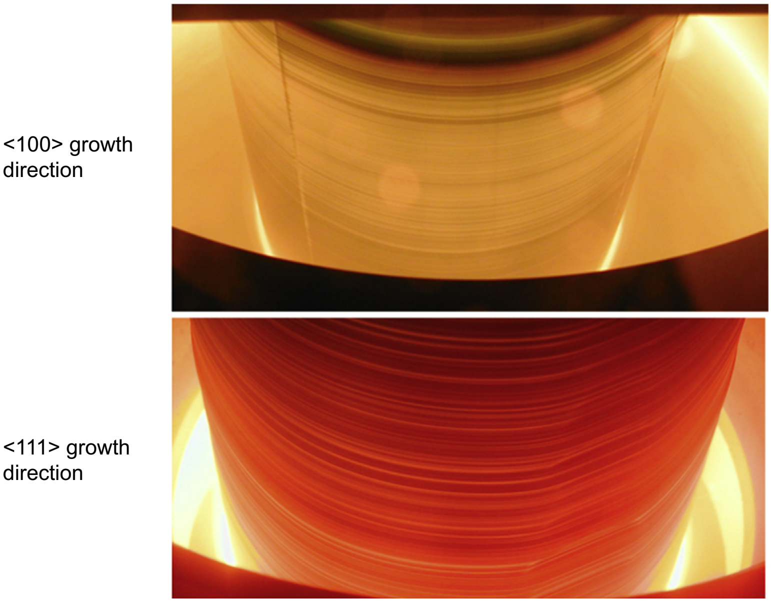

**Figure 2.10** Habit lines at periphery of two different orientation crystals.

For $\alpha$ less than 2, the lowest energy of the interface occurs when the interface is rough (half covered with adatoms); if $\alpha$ is greater than 2, the interface has only a few adatoms or missing atoms at lowest energy. Silicon exhibits $\alpha > 2$ for only the $\{111\}$ directions, and has $\alpha < 2$ for all other orientations [52].

When grown dislocation free, the $\{111\}$ planes that intersect the three-phase boundary grow by two-dimensional (2D) nucleation (birth and spread of layers) and require a substantial ($\sim$3.7 K) undercooling to grow [53]. Growth on all other orientations, such as the $\{100\}$ direction, require undercooling of less than 0.01 K on those "rough" interfaces. In the temperature gradients provided in the puller, the successive growths of these "layer source planes" as the crystal grows downward and is pulled upward provide visible habit lines down the exterior of the crystal. In the crown, these $\{111\}$ facets can be a centimeter or more in width, while in the body of the crystal they are usually less than $\sim$1.5 mm wide. The habit lines (manifestations of the facets) are thought to arise from either crystallographic dependency of the crystal—melt—vapor equilibrium contact angle [6,54] made visible because of the large facet size, or due to the terrace—kink—ledge model of spreading 2D layers lifting the three-phase boundary at the facet location [3,49].

If dislocations are generated anywhere in the crystal for whatever reason, the dislocations multiply by climb and glide due to the relatively high crystal cooling rates during pulling. Dislocations eventually intersect the $\{111\}$ facets, and suddenly 2D nucleation is no longer required to generate new layers. The layers now grow by screw or edge dislocation propagation at relatively low undercooling. The facet size collapses to a much smaller size, commensurate with the undercooling, and the habit

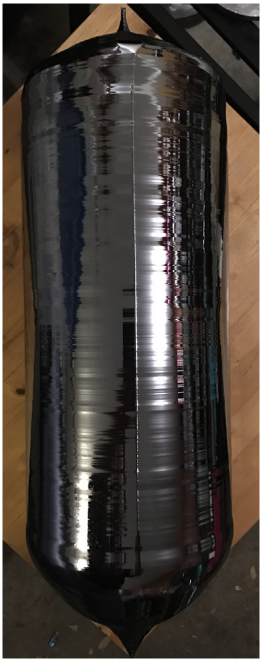

**Figure 2.11** 200 mm <100> crystal terminated due to habit line collapse (dislocations).

lines are no longer macroscopically visible to the crystal production operator. The loss of the habit lines is an indication of the loss of the dislocation-free state. Fig. 2.11 shows a 200 mm diameter, <100> growth direction dislocation free crystal of silicon, which grew for approximately 1000 mm length before some event led to dislocation nucleation and collapse of the four equidistant habit lines at the crystal surface. After that event, crystal growth was terminated by growing a short tail to avoid thermal shock and minimize further dislocation multiplication.

Fig. 2.12 shows a close view of one collapsed habit line. At the point the habit line collapsed, there is a slight reduction in the crystal diameter. Fig. 2.13 shows a 30X optical image of the habit line collapse. There are no unusual structure features at the region of collapse; the facet was just greatly reduced in size due to no longer requiring 2D nucleation to propagate.

Fig. 2.14 shows a scanning electron microscope image of a similar habit line collapse for a 150 mm diameter, <100> orientation but heavily arsenic-doped silicon crystal. There are again no unusual structural features other than termination of the habit line. A similar sample was measured by high-resolution laser confocal microscopy in Fig. 2.15 to verify the surface topology and measure the ridge height reduction.

Although the repeatable, reliable growth of dislocation-free silicon provides large-size crystals with outstanding electrical properties, dislocation nucleation is still one of the largest yield losses in practical production. It increases batch process time and cost of production. The problem is aggressively managed rather than solved. Manufacturers measure “attempt rate” (number of repeated seedings, Dash necks, and melt-backs)

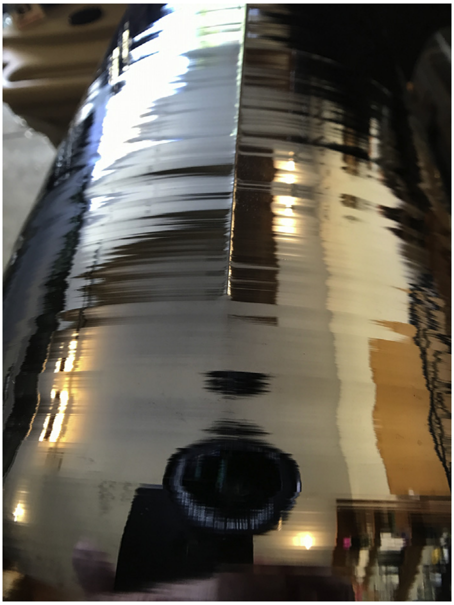

**Figure 2.12** Habit line collapse location of Fig. 2.11.

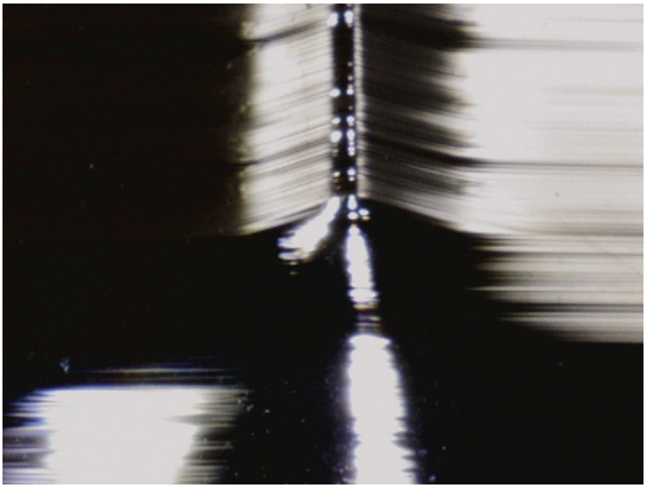

**Figure 2.13** Zoomed image of habit line collapse.

before the final crystal is grown. Dislocation nucleation early in growth leads to melting back the previously grown good material and restarting with a new seed. As more melt-backs are done, the crucible is repeatedly heated, thinning the crucible wall from higher dissolution rates at high temperatures, and using up time until the crucible may not longer be able to hold the melt and the run must be terminated. Dislocation nucleation late in body growth or in tail growth leads to scrapping of

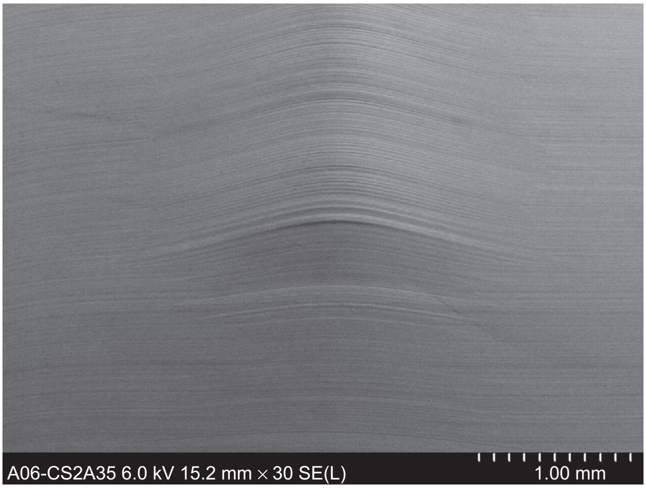
A06-CS2A35 6.0 kV 15.2 mm × 30 SE(L)
1.00 mm

**Figure 2.14** SEM of habit line collapse in heavily arsenic doped crystal.

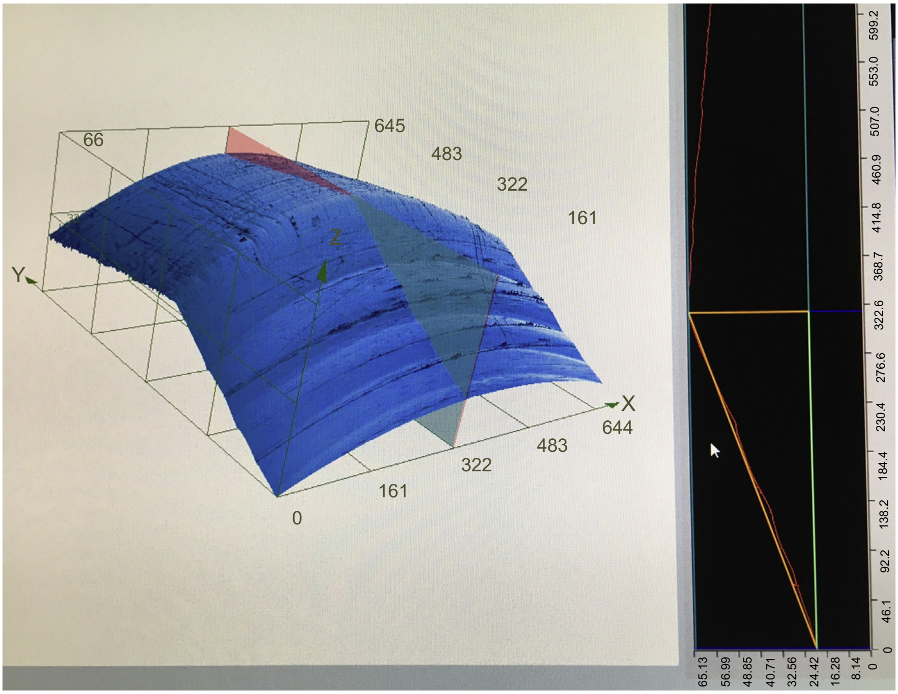

**Figure 2.15** LCM elevation map of habit line collapse.

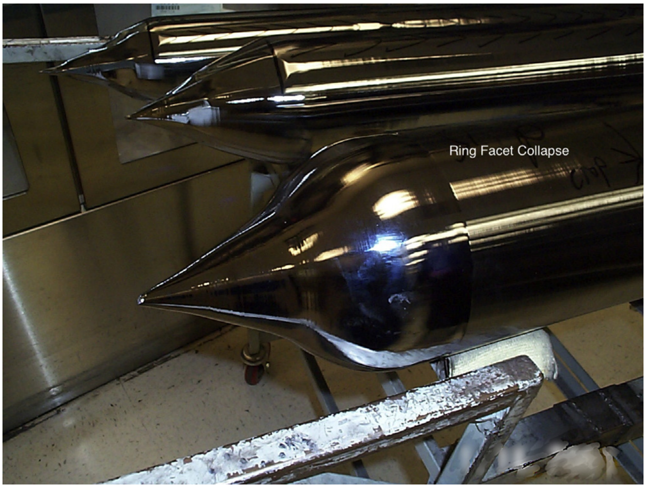

**Figure 2.16** Ring facet collapse at tail of <111> orientation crystal.

now slipped but previously dislocation-free material, up to one diameter equivalent length from the point the habit lines disappeared. Fig. 2.16 shows <111> orientation crystals for bipolar junction transistors. The collapse of the {111} "ring facet" at the crystal–melt periphery is shown as the diameter decrease. One diameter of previously grown length is now slipped, and must be scrapped from that ingot.

A batch Cz process with a calculated maximum yield of 82% may only in practice yield 65%–75% in repeated production, due to dislocation nucleation occurring sporadically in crown, body, or tail. That loss may be in capital equipment utilization, increased operator time, scrapped silicon, finished crystal cost per kilogram pulled, or all of these.

A single crystal of silicon grown by the Cz technique has several different sections, as shown in Fig. 2.17.

- Seed: determines crystallographic orientation. Seeds are cut from previously grown dislocation-free crystals. The seeds are cut to provide the desired crystallographic orientation to within fractions of a degree of arc.
- Dash neck: removes the dislocations generated by thermal shock when seed is dipped into the melt. The neck diameter, length, growth rate, and cooling rate are determined by individual industrial manufacturers.
- Crown, top, shoulder, and taper: transitions from thin neck to required diameter for wafers.
- Body: the part of the crystal actually used for wafers, the right circular cylinder of dislocation-free silicon grown at the target diameter to give the correct wafer diameter.
- Endcone, tail, or bottom: gradual taper prevents thermal shock-back into the body when the crystal is decanted from the hot melt.

The geometry of FZ-grown single crystal silicon is similar, but the seed is at the bottom and the tail is grown at the top, as the crystal grows from bottom to top as the molten zone is moved up [19,37].

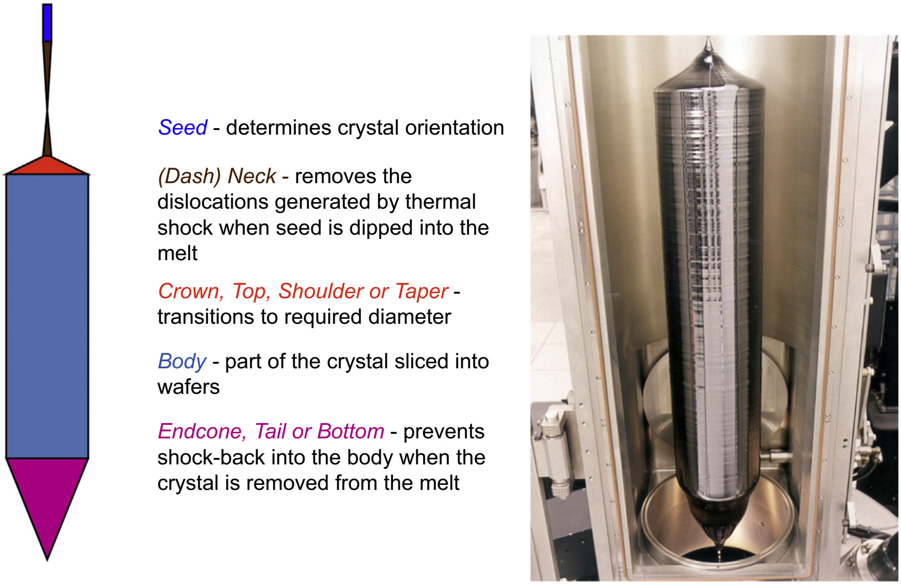

*Seed* - determines crystal orientation

*(Dash) Neck* - removes the dislocations generated by thermal shock when seed is dipped into the melt

*Crown, Top, Shoulder or Taper* - transitions to required diameter

*Body* - part of the crystal sliced into wafers

*Endcone, Tail or Bottom* - prevents shock-back into the body when the crystal is removed from the melt

**Figure 2.17** As-grown silicon crystal shape and purpose.

The Cz process is now carried out using many computer-controlled steps, without operator intervention or manual control [11,55]. Since the phase boundary does not contact the container during solidification, there is ample opportunity for slight variations in crystal geometry as the crystal grows. This makes the crystal growth process somewhat empirical as well as based on process control theory.

Interstitial oxygen (Oi) at some concentration is an unavoidable impurity during Cz pulling of silicon. The effect of oxygen on devices can be either good or bad [3,4,36,46–48,56,57].

Positive effects:

- Oi will produce “dislocation locking” (impurity hardening) in the wafer, improving resistance to plastic deformation and slip during later high temperature semiconductor device processing [48];
- precipitation of supersaturated Oi into $SiO_2$ inclusions (bulk microdefects (BMDs)) in the wafer provide internal gettering sites that attract and sink metal impurities away from the active device region [46].

Negative effects are as follows.

- Oxygen can provide a small concentration of donors (electron charge carriers) which contribute to or subtract from the net resistivity provided by deliberately substituted ionized electronic impurities [31,46]. Oi atoms are electrically inactive in silicon. Oi can agglomerate into a series of larger oxygen clusters, $O_N$. These oxygen clusters (for N from two to eight) are electrically active, acting as double donors, called “thermal donors” (TDs). Their energy is 50–150 meV below the conduction band. The TDs form in the temperature range 350–500°C as the crystal cools after solidification, with a peak generation rate at about 450°C. TDs dissociate back into Oi with brief heat treatment above 550°C. That wafer level step is performed for semiconductor devices, but not for solar cells. The initial TD concentration depends on oxygen concentration and crystal cooling conditions. The locations of higher oxygen concentration, usually the start or end of the crystal body, provide the most TDs. The effect is measureable only in lightly doped material, but that type of material is used for advanced logic devices. For a heavily doped crystal, the number of dopant charge carriers is many orders of magnitude larger than the TD concentration, so TDs are not noticed.

- BMDs in the active device region near the wafer surface can degrade device performance and yield. In "vertical" devices such as power and high-voltage transistors, the active device region may encompass the whole wafer thickness, so a complete lack of BMDs is desired. However, that means there is no gettering action.
- Excessive precipitation (a high density of large BMDs) consumes Oi and generates dislocations, increasing the plastic deformation/slip in device processing.
- BMDs near the surface can nucleate into OISFs during oxidation device processing [6].
- In solar cells, BMDs act as charge recombination centers, which reduce minority carrier lifetime and diffusion length. Charge carriers must travel across the wafer thickness for collection, so they can be captured by BMDs [56,57].
- In p-type solar cells, B—O complexes form which lead to "light-induced degradation" that reduces photovoltaic conversion efficiency [58].

Oxygen precipitation in silicon has been extensively studied [6,48,50,59]. When the oxygen concentration, Oi, sufficiently exceeds the oxygen solubility, $C_{ox}(T)$, in silicon (Si) at a given temperature, oxygen precipitation can begin:

$$2Si + 2Oi \rightarrow SiO_2 + I$$

where I is a silicon self-interstitial.

The initial oxygen precipitate nucleation rate is controlled by point defects, especially vacancies (VO and $VO_2$) in lightly doped silicon. Since the volume per O atom in $SiO_2$ is greater than volume per Oi in silicon ($V_{SiO_2} \sim 2.25\ V_{Si}$), the growth of an oxygen precipitate is accompanied by a compressive strain in the silicon matrix. The strain is relieved by silicon interstitial emission or vacancy absorption. If Oi falls below $C_{ox}(T)$, this reaction will be reversed and precipitate dissolution will begin. The rate of growth (or dissolution) depends on the rate at which oxygen atoms can diffuse from the silicon bulk matrix to the precipitate (or vice versa). The precipitate growth/dislocation is diffusion limited.

After growing to a sufficient size, oxygen precipitates become heterogeneous nucleation sites (BMDs) for metal contaminants to precipitate out on, "gettering" the metals in the area away from the device region. Precipitates in the device region would disrupt device operation, so one needs a "denuded zone" near the surface of the wafer (the device region) where BMDs do not form. Historically, this led to the design of silicon crystals with defined Oi concentrations and wafer thermal treatments during device processing, first to remove Oi from the wafer surface region, then to precipitate BMDs in the bulk of the wafer. This required somewhat complex wafer thermal treatment steps, which were a potential source for additional metal contamination. Fig. 2.18 shows a BMD in a cleaved surface in a wafer after heat treatment, surrounded by stacking faults.

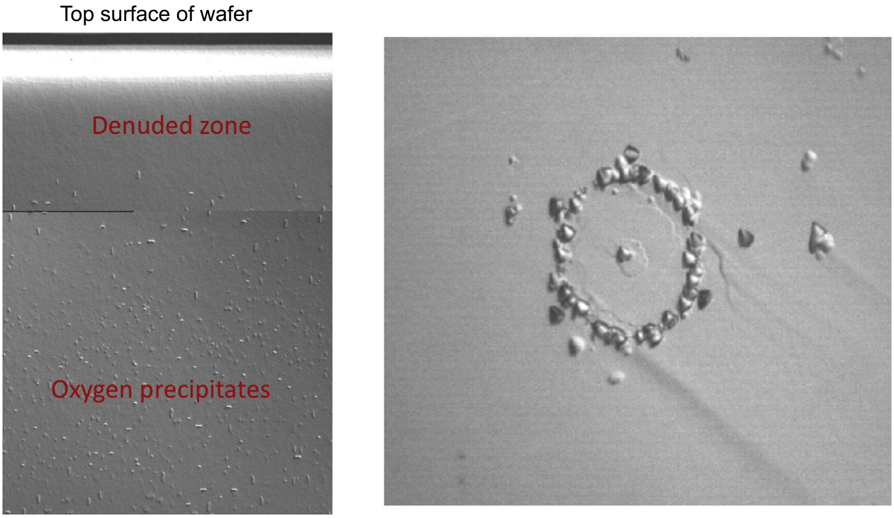

Optical photomicrograph of a post-processed wafer bevel surface after Wright etched for 2 min. Bevel angle: 5° 43’. Magnification: 200X.

Optical photomicrograph of oxygen precipitate ($SiO_2$) surrounded by stacking faults. Magnification: 1000X.

**Figure 2.18** Oxygen precipitate surrounded by stacking faults.

The need to provide oxygen at defined concentrations throughout the crystal length (so devices made on wafers sliced from different crystal sections exhibit the same gettering efficiency, strength, or microdefect distribution) led to a wide variety of Cz process recipes and equipment modifications [31,50,60,61]. Crucible temperature, melt convection (due to buoyancy, crucible and crystal rotation rates), melt surface areas, and pull rates were combined with argon flow rates and pressure profiles during a run to drive oxygen concentration to a desired value and minimize its variation along the crystal length. Magnets can be used to modify melt convective flow and affect crucible dissolution rate, and various magnet strengths (100—1000 Gauss) and field geometries (axial, transverse, cusp, or saddle) have been incorporated in high-volume production [2,11,35,55]. While these increase cost and may increase the probability of dislocation nucleation and scrap, they minimize growth of crystals with out-of-specification (OOS) oxygen, which cannot be sold as wafers. However, even with this attention, normal run-to-run variations of crucible as-built dimensions, charge mass, aging of furnace thermal components, etc. still result in run-to-run variation of crystal oxygen and periodic anomalous oxygen distributions.

## 2.4 Schematics of growth methods for silicon

For dislocation-free single crystal silicon growth, the Cz and FZ methods have developed to mature technologies over the last 65 years [6,9,37]. For both methods, the cost for the feedstock material was a dominant cost driver until the early 2010s, despite the dramatic reduction of polysilicon prices since that year. This is particularly true for FZ, where approximately 50% of the production cost is for the defined shape polysilicon feed “rods.” These are more expensive to produce than the chunk, chip, or granular polysilicon used to fill the crucible for Cz. As a consequence, the FZ method is economically less attractive than Cz. FZ-grown crystals are used only for applications requiring very low oxygen or carbon, or high resistivities (where oxygen TDs’ presence could shift resistivity). Applications are high-power regulation devices. FZ is not used for solar cell production, although the very low oxygen content of FZ crystals enables higher cell photovoltaic efficiencies and avoids light-induced degradation. The FZ wafer cost is much higher than that of a Cz-produced wafer.

The largest-diameter FZ crystals are grown to 200 mm. Larger diameters would require both larger melted zones to be suspended by Lorentz force and larger starting polycrystalline feed rods, neither of which have been demonstrated. The limit for the Cz process has not been reliably estimated, even based on the strength of the small-diameter Dash neck that suspends the crystal during growth. Various techniques were developed to suspend crystals whose mass would generate stress which exceeds the strength of the Dash neck, although these have not been needed in most 300 mm diameter crystal production [62]. Cz crystals are grown in production at 300 mm for semiconductor wafers, and up to 400 mm for mechanical parts. Crystal growth processes have been demonstrated for pilot 450 mm semiconductor wafers [63,64], although the date to transition to 450 mm production has been repeatedly delayed.

The Cz technique and resulting crystals are shown schematically in Fig. 2.19. The crystal is pulled up vertically above the melt, so the crystal grows downward at solidification rate $R$. The crystal and melt are rotated, usually in opposite directions,

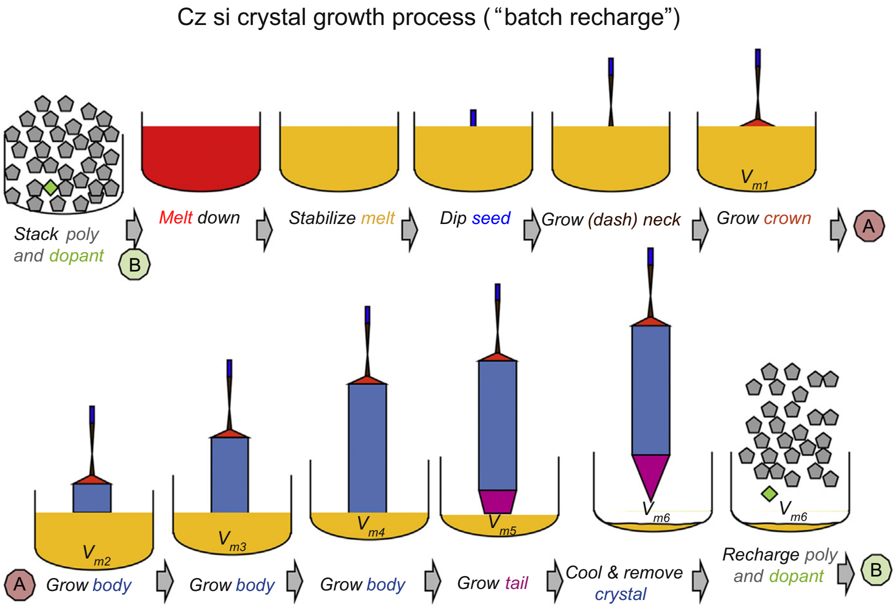
Cz si crystal growth process (“batch recharge”)
Stack poly and dopant
B
Melt down
Stabilize melt
Dip seed
Grow (dash) neck
Grow crown
$V_{m1}$
A
A
$V_{m2}$
Grow body
$V_{m3}$
Grow body
$V_{m4}$
Grow body
$V_{m5}$
Grow tail
$V_{m6}$
Cool & remove crystal
$V_{m6}$
Recharge poly and dopant
B

**Figure 2.19** Cz process steps.

during growth. Rotation of the crucible mixes the melt in a more regular manner by forced convection, and homogenizes temperature variations at the hot crucible wall from the nearby resistance heater. Rotation of the seed uses the crystal to mix the melt, leading to axisymmetric crystal axial temperature gradients and cooling, and uses the crystal—melt interface to emulate a rotating disk, leading to a low radial variation in the solute boundary layer at the interface. That enables smaller values of resistivity radial gradient during crystal pulling. The desirable ratios of rotation speeds can be developed by numerical simulation or empirically.

The Cz method provides several advantages for silicon single crystal growth.

- The cooling crystal and crystal—melt interface do not contact a container, so container interactions do not lead to local chemical or structural defects.
- Crystal orientation is defined by a standard consumable seed, which can be precut to a variety of different orientations using the same puller interface, such as <100>, <111>, <110>, <211>, and others.
- Control of diameter is independent of any container. The diameter can be controlled by manipulation of temperature gradients and pull rate and rotation rates, or by weighing the mass of the growing crystal.
- The crystal surface is observed during growth so obvious structural defects can be detected during growth.
- The crystal habit lines are visible to trained operators and provide a clear indication of the dislocation-free state.
- It is possible to detect, remelt, and restart a "bad" (i.e., dislocated, twinned, polycrystalline, or wrong diameter) growth run, using the same original batch of melted polysilicon.
- There is good radial chemical composition control due to crystal rotation acting to minimize radial boundary layer variation at the crystal—melt interface.
- The process is scalable (3—450 mm diameters, up to meters in crystal length). Often a puller designed for one charge size, crystal diameter, and crystal length can be converted to grow larger crystals by converting consumables such as graphite insulation and crucibles.
- Relatively fast dislocation-free growth rates are attainable (e.g., $\sim 3 \times 10^{-3}$ cm/s), which can allow complementary high cooling rates. High growth rates can be used to reduce conversion cost, but can bias microdefect distribution to unwanted states.

There are some unique aspects to silicon growth by the Cz technique.

Pure silicon's melting temperature is approximately 1683 K. The high temperature demands robust insulation materials and in general accelerates degradation of materials over crystal growth times. The only crucible chemically compatible for these long times is fused silica (amorphous $SiO_2$). The only insulation and resistance heater material is high-purity graphite. The graphite can oxidize at high temperatures if exposed to SiO, and CO or $CO_2$ can be put into the argon gas flow. If CO or $CO_2$ contacts the melt surface, carbon will dope the melt and will not evaporate.

SiO evaporates from the melt. $P_{vapor}$ at 1683 K is approximately 12 mbar [65]. The reaction proceeds continuously during the growth of a crystal, because the silicon monoxide produced is volatile at 1683 K even at the argon gas pressures used (approximately 100 torr). The fused silica crucible reacts with the melt and the monoxide evaporates from the melt:

$$Si + SiO_2 = 2 \cdot SiO$$

The density of solid silicon is less than that of liquid silicon. Solid silicon is packed less efficiently than liquid silicon in the fused silica crucible, leading to silicon being stacked high in the crucible until the silicon chunks melt. Higher regions of the crucible have a lower temperature, so sharp pieces of solid silicon chunk can stick into the softening crucible walls at high temperature, finally falling into the melt and splashing silicon. If splashed silicon freezes on puller parts (or colder parts of the higher crucible wall), these become nucleation sites for $SiO_2$ particles condensing from the SiO evaporating from the melt. If the $SiO_2$ particle falls back into the melt, contacts the crystal, and is engulfed, a new grain can form, or dislocations will nucleate from stress concentration due to different coefficients of thermal expansion between silicon and $SiO_2$.

Because the density of solid silicon is less than that of liquid silicon, the growing crystal floats on the melt. It is possible that a chunk of polysilicon at the bottom of the crucible will not melt completely (due to unusual excessive cooling at the bowl bottom) and stick to the crucible after the melt is established, hidden. After melt stabilization or even the start of crystal pulling, the solid polysilicon may lose adherence to the crucible and quickly float to the surface of the melt due to buoyancy. Such “floaters” will hit and dislocate the growing crystal.

The shape of the fused silica crucible is based on historical experimental work and numerical simulation [35]. The bottom shape affects both convective flow pattern and also transmitted infrared radiation to the crystal from the susceptor holding the crucible, through the melt. For a given crucible diameter, the maximum melt depth can be predicted, which minimizes buoyancy-driven turbulent convection, allowing a melt surface that is quiescent enough to grow a dislocation-free crystal at the three-phase boundary. This can limit the melt depth (and length of crystal grown from a melt volume), but can be improved by application of magnetic fields or customized heater geometries (shaped heaters, and bottom heaters in addition to standard side heaters).

Since the semiconductor field evolved to use round cross-section wafers, the crystals must be grown as right circular cylinders.

Progress in developing the Cz and FZ techniques for single crystal silicon followed distinct, somewhat time-sequential phases, as both device and material knowledge and performance increased.

1. Reliably growing single crystals (which contained dislocations and sometimes twin boundaries), scaling up the diameter and length of crystals. The focus here was on increasing “free yield (%),” which is the ratio of mass single crystal pulled to mass of polysilicon used.
2. Adding electronic impurities at specific concentrations to provide desired resistivity values. Early work focused on macrosegregation calculations, and pioneered use of solidification rate programmed profiles to encourage quasiconstant axial resistivity along a great percentage of the crystal length.
3. Dash [66–68] identified a robust method to eliminate threading dislocations. He also developed the theoretical rationale to allow its customized use and advancement. This allowed greater diameter increases and growth rate increases without polycrystalline breakdown. Later it was realized that eliminating dislocations reduced metal precipitation and improved device function, but only after transistor fabrication moved away from alloyed junctions to junctions made by vapor diffusion, oxidation, and ion implantation. The presence of dislocations aided fabrication of alloy junctions [12].

4. TDs were identified and a method to eliminate them was established.
5. Early computer simulations were made for heat and mass transfer, to predict in greater detail the effect of crystal growth process parameters on resulting crystal defect and chemical distribution. This continued to mature to today's three-dimensional transient simulations of heat and mass transfer in crystal and convecting melt.
6. Microsegregation and growth rate studies showed that chemical striations and banding were caused by bulk melt convection leading to periodical heat and mass transfer changes. Here the striations can be of oxygen, carbon, dopant, or defects.
7. The cause of large-scale voids in the crystals was established and controls generated. It was found that dislocation-free crystals could contain macroscopic voids, termed "argon holes," "air pockets," or "pin holes" depending on the method of discovery and suspected cause. Large voids would be revealed as concave hemispheres on sliced wafers surfaces. Small voids (less than 300 μm diameter) could be hidden within the thickness of the sliced wafer, but revealed in device processing such as oxidation. It was found that particular charge meltdown processes in Cz pullers could cause a substantial risk of incorporation of bubbles into the melt. The melting of polysilicon could trap argon gas in pockets at the crucible surface. The polysilicon surface roughness can trap argon between the solid polysilicon and the crucible (see Fig. 2.20). Bubbles in the melt could gradually rise to the melt surface (or crystal−melt interface), but if they do not travel to the crystal they may be eliminated over time after meltdown completion. This outgassing of bubbles can be accelerated by setting appropriate conditions during the stabilization period between completion of meltdown and start of crystal growth. When feeding polysilicon while pulling a crystal (continuous Cz or CCz), particular conditions are needed to avoid bubble generation and incorporation. The rough surface of polysilicon can trap argon gas at meltdown, forming bubbles. It is also possible that gas trapped in the crucible during its manufacture can be liberated as the crucible surface either dissolves away or transforms under high temperature from fused silica to crystabolite.
8. Control of interstitial oxygen concentration, and its precipitation and diffusion out of surface layers to create wafer "denuded zones."
9. Minimization of carbon concentration, by avoiding having hot carbon furnace parts contribute CO to the argon gas stream before it is swept over the melt.

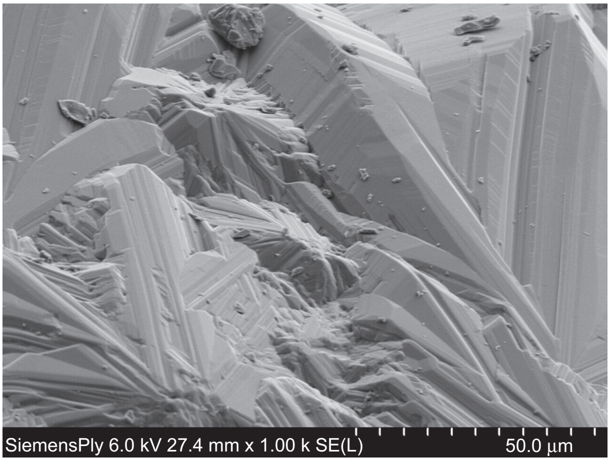

**Figure 2.20** CVD polysilicon surface features.

10. Reduction of metal concentration, either in the starting polysilicon or from metal parts in the puller. Certain metal species already in the crystal, such as iron, copper, or nickel, could diffuse under device processing conditions and kill the device function. Sources in pullers were reduced, although the pullers still used metal and alloy parts (such as seed holders). In some cases metals were found to have been transported to the melt by the argon gas stream, similar to carbon transport, and steps were taken to eliminate that. In other cases internal gettering was required to pull any metals unavoidably grown into the crystal away from the device region at the wafer surface.
11. The eliminate of dislocations, reduction of metals, carbon, and oxygen, and resulting observations of "new" defects led to studies of how thermodynamic point defects are generated, associate with other species, and condense to BMDs.
12. Some of the earliest defects detected and eliminated through crystal growth process modifications were nuclei for OISFs on wafers, and self-interstitial defects called "swirl" because of the pattern made on the wafer surface, similar to Centro symmetric striation patterns.
13. $SiO_2$ BMDs outside the device region were established as being desired for metals gettering, but within the device region these were destructive to device function.
14. The various defects generated by the generation of point defects (vacancies and interstitials), their association with chemical impurities (oxygen, carbon, metals, dopants), and condensation and agglomeration during crystal cooling in temperature gradients were named based on the method of detection or sequential discovery [6]. These were investigated widely for both effect on device performance and correlation to crystal growth conditions. A-, B-, and D-defects were identified, as well as flow pattern defects (FPDs). Light point defects (LPDs) were seen to scatter light at polished wafer surfaces, but could not be removed by cleaning; some of these were later found to be D-defects, or imaged in a different manner as laser-scattering tomography defects (LSTDs). Extremely small octahedral voids (below 150 nm diameter, and not "argon holes") were discovered on polished wafers and designated "crystal-originated particles" (COPs) [69]. Imaged by atomic force microscopes, these were later identified as similar to or the same defects as shown by LPDs, FPDs, and LSTDs: the result of vacancies condensing to macroscopic octahedral voids instead of collapsed disks (intrinsic stacking faults). Large dislocation loops (LDLs) were identified on Cz crystals grown at low growth rates; these could be "stretched" under high stress to form threading dislocations after crystal growth, rendering the material unusable for devices. LDLs were eventually explained as interstitial agglomerates. It was found that particular defects, combined with strain, could be used to engineer desired bulk properties.

## 2.5 Description of up-to-date growth technologies/processes

The Cz puller for silicon is widely described in the literature [31,35,60]. Key elements of the puller are Fig. 2.21:

- cable, which holds the seed in a seed "chuck," rotates the seed, and pulls the seed up to drive crystal growth in the axial temperature gradient;
- silicon seed;
- fused (amorphous) $SiO_2$ crucible, standard or synthetic inner surface, bubble-free thickness specified; the crucible softens at the melt temperature, and if not supported can tear or collapse, spilling the melt;

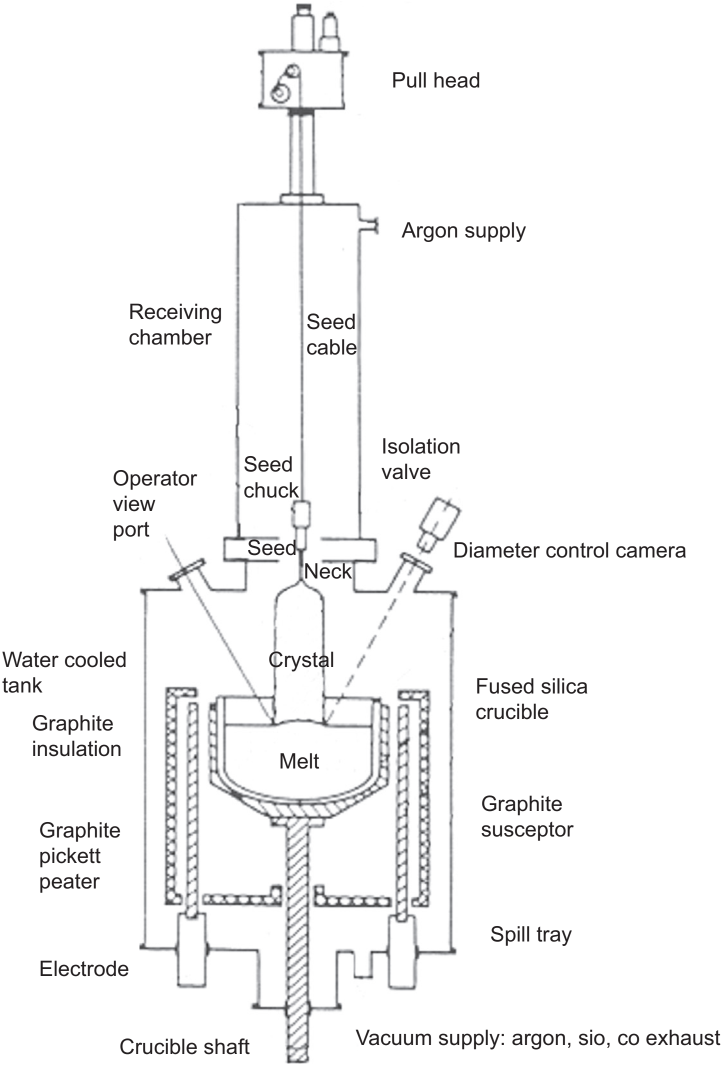
Pull head
Argon supply
Receiving chamber
Seed cable
Isolation valve
Seed chuck
Operator view port
Seed
Diameter control camera
Neck
Water cooled tank
Crystal
Fused silica crucible
Graphite insulation
Melt
Graphite susceptor
Graphite pickett peater
Spill tray
Electrode
Crucible shaft
Vacuum supply: argon, sio, co exhaust

**Figure 2.21** Notional puller cross-section, open hot zone type.

- graphite “susceptor” or “cup,” which provides structural support and quasiaxisymmetric heat to the crucible;
- graphite resistance heater;
- crucible rotation and lift, which rotates the crucible and lifts it to keep the melt level at the same height in the temperature field as the crystal is grown and melt is consumed.

Figs. 2.19 and 2.22 show illustrations and photographs, through the puller diameter control window, of key sequential steps to grow the single crystal of silicon. Solid polysilicon is melted in the quartz crucible. If the dopant is p-type, boron was added at the time the polysilicon was stacked in the crucible. The crucible is rotated

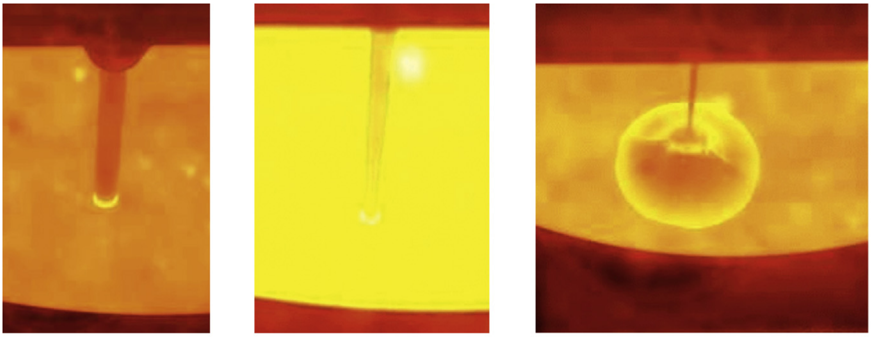

Dip seed Grow neck Grow crown

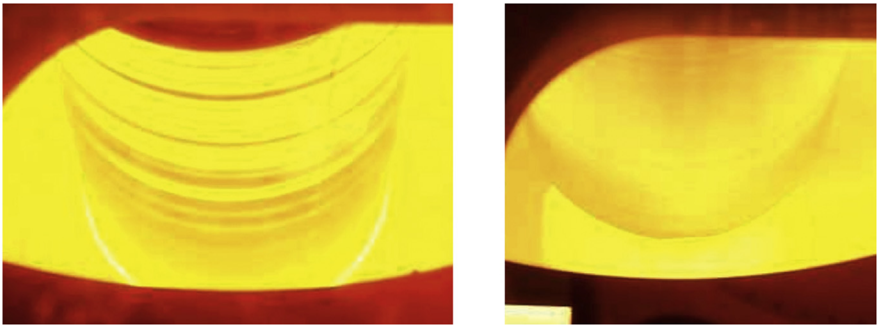

Grow body Grow tail

**Figure 2.22** Important growth phase, photographed through diameter window.

to mix the melt. After the melt temperature is stable, if instead the dopant is n-type, arsenic (for example) is sublimated over the melt surface, where it diffuses into the melt to dope it. A dislocation-free single crystal silicon seed of the correct (<100>) orientation is rotated in the opposite direction to the crucible and dipped into the melt, where a few millimeters of length are melted away and the molten silicon wets the seed. The seed is slowly withdrawn, growing a long thin neck, which eliminates any dislocations from the seed itself or the thermal shock of the seed contacting the melt. Once a dislocation-free state is confirmed by observing the habit lines on the surface, the neck diameter is increased by slowing the seed withdrawal rate and reducing the melt temperature. The crystal is grown at the target diameter until a predetermined length is reached or the melt mass reduces to a desired target mass. At that point the tail is grown, so that when the crystal detaches from the hot melt there is only a small area of contact and any dislocation generated by the thermal shock is restricted to the tail region, not the round cross-section crystal body.

If a crystal is dislocated during the later stages of body growth, the growth is completed and the defective regions discarded after characterization. If the crystal dislocates early in growth, it is possible to melt the entire crystal back, reforming the melt. Growth can be started again from that melt, with a new seed and Dash neck. The number of melt-back and regrowth attempts while the crucible is hot is limited, based on impurity incorporation and crucible and furnace deterioration during processing. Also, if the dopant evaporates from the melt, the melt may need to be redoped after melting back the crystal, which can result in overdoping or underdoping the crystal compared to the desired resistivity target. Arsenic, antimony, and phosphorus will evaporate from the hot melt surface, with the rate of evaporation a function of the melt dopant concentration, so heavily doped melts evaporate faster. Indium and gallium will also evaporate from melts. After growth, crystals are inspected for slip and other line and planar defects, and defective areas are removed by scrapping the material. Once a dislocation appears during growth, the high cooling strains in the already-grown dislocation-free crystal sections will cause climb and glide of dislocations backward into the crystal, eliminating up to one diameter length of previously dislocation-free material. This greatly reduces the free yield and increases cost per unit produced from that lot.

Crystal diameter during solidification is measured using a camera or diode-scanning optical sensor, which measures the position of the "bright ring" of light at the crystal—melt three-phase boundary [55]. The bright ring is the reflection of the hot melt, crystal, and crucible wall at the smooth, curved meniscus at the three-phase boundary. The crystal diameter is unstable. To control the diameter, the bright ring location is measured and the seed lift cable speed increased or decreased. Increasing the seed lift stretches the meniscus and slopes it from the crystal side toward the crystal centerline. Decreasing the seed lift reduces the meniscus height and slopes it from the crystal side away from the crystal centerline. Since the contact angle between the silicon crystal and silicon melt is a material defined value, this decreases or increases the crystal diameter. However, there is a limit to the amount the meniscus can be pulled or pushed, so the melt heater is also adjusted to heat or cool the melt to influence the meniscus angle. The action of the seed lift is very fast compared to the ability to heat or cool the large silicon melt, so the seed lift controls on a fast inner control loop compared to the large, lagging melt heater control loop. The melt temperature is read by an optical pyrometer, which measures in "set points" on a dimensionless scale rather than converting to temperature.

Typical steps to grow the silicon crystal are as follows [55,61].

**Before growth**

- Puller cleaning, graphite setup, machine calibration.
- Polysilicon charge stacking (or recharge operation).

**Crystal growth**

- Meltdown at $T > 1683$ K in flowing argon at low pressure (760 torr to 20 torr, depending on process design).
- Melt held at stable temperature to ensure melting and ejection of bubbles (which may be captured later and cause voids in crystal).
- Seed crystal dipped until it begins to melt.
- Good meniscus contact established between seed and melt.
- Seed withdrawn from melt so neck is formed by gradually reducing diameter. <111> requires small neck diameter; <100> requires an even thinner neck. Argon flows to carry off silicon monoxide and carbon monoxide. If not removed, the oxides may condense, fall into the melt, and become particles that disturb dislocation-free growth.

- After confirmation of dislocation-free state, the neck is gradually grown out to crown diameter by decreasing pulling rate and/or melt temperature.
- The crown is transitioned to the body by increasing the pulling rate.
- The cylindrical body is grown by controlling pulling rate and melt temperature while compensating for the dropping melt level. The crucible is raised as melt level drops, so the sequentially grown length of crystal sees the same thermal environment. The pulling rate is generally reduced towards the tail end of the crystal.
- Before the crucible is completely emptied of melt, the crystal diameter is reduced gradually to form a “tail” to minimize the thermal shock of removal from the melt.
- At a small target diameter, the tail can be separated from melt without slip back.

### After growth

- Controlled cooling down to removal temperature.
- Crystal and process data removed and evaluated.
- Recharge crucible for next crystal, or remove used crucible and “pot scrap” silicon, and clean and calibrate puller for next run.

The crystal puller design has evolved to grow larger crystals, faster, with defined microdefect concentration and fewer required manual operations. Key design modifications over time are outlined below.

Seed cable versus shafts: seeds were originally mounted on nonrotating wires, then on rotating shafts made from manufacturing drill presses. As pullers increased in size, long customized shafts were made; the rod would be extended to great heights as a long crystal was pulled up, needing a high ceiling. As crystals became still longer, rods transitioned to cables. The cables are wound on barrels. Certain rotation frequencies must be avoided to preclude resonance and crystal swinging, but growth processes are designed to avoid those regions.

Low-pressure versus high-pressure argon: originally crystals were grown at close to atmospheric pressure, in a helium, hydrogen, or argon atmosphere. Purified argon became the standard clean inert gas to carry away SiO, and lower pressures were used to discourage SiO condensations and as part of oxygen control. As pressure was reduced, collimating tubes, which directed cooling gas flow around the growing crystal, were eliminated.

Open hot zone versus radiation shield surrounding crystal: if there is no radiation shield between the growing crystal and the crucible, the growing crystal views a different crucible wall height as the crystal is grown longer, changing crystal axial temperature gradients. The power delivered to the crucible changes as melt is consumed, changing the crucible temperature. The radial and axial temperature gradients are also driven by the crystal view of the crucible, top of the hot zone, and water-cooled tank top. Adding a metal or graphite sleeve (radiation shield, or cone) immediately above the melt surface into which the crystal is pulled provides a defined and steady cooler body next to the growing crystal, regardless of crystal length or melt depth. This provides more quasisteady axial and radial temperature gradients to generate desired conditions for microdefect formation, or to maximize the solidification rate. The radiation shield also provides a relatively small gap between the shield and the crystal surface and melt surface for the argon gas to flow through, leading to both more efficient silicon monoxide removal and enhanced cooling at the meniscus.

Isolation gate/pull chamber: the crystal is pulled up into a separate chamber as it grows. Once the tail is separated from the melt, the crystal is pulled completely up into the "pull chamber" and a closing valve isolates the pull chamber from the growth chamber. The pull chamber can be vented to the atmosphere to remove the crystal and cool it. If the crucible is maintained hot and uncracked, additional polysilicon can be fed from the pull chamber into the crucible, another seed provided on the pull cable, and another crystal pulled from the same crucible.

Addition of chuck, chip, or granular polysilicon feeder: instead of feeding more polysilicon using the pull chamber between crystals, a dedicated feeder or dispenser can be mounted on the growth tank to dispense small-size polysilicon into the crucible. This can be used to "top off" the crucible after meltdown to maximum melt volume, or to replenish the melt between successive runs using the same hot crucible. The polysilicon used is small chip, dendritic, or fluidized-bed reactor granules.

Use of magnet: an axial, transverse, cusp, or saddle magnet can be mounted around the hot zone outside the tank. Depending on the field strength and shape, a magnetic field can be used to reduce or increase oxygen concentration, reduce buoyancy-driven convection in the melt, reduce magnitude or change periodicity of chemical striations, and reduce melt surface temperature and physical position fluctuations to provide stable dislocation-free growth conditions.

Diameter control methods: the crystal diameter was originally measured by adjusting the heater power manually. This later evolved to adjustment of crystal pull rate, crystal and crucible rotation rate, and heater power. Initial attempts to control diameter by measuring crystal mass or melt mass were not successful, due to the crystal—melt density difference and meniscus contact surface tension. The diameter is measured by imaging the bright ring defined by the curved meniscus reflecting the hot crucible walls, or by videocamera imaging of the crystal and the bright ring.

Computer process control: pullers were converted from primarily manual control to closed-loop body manual control, and then to closed-loop microprocessor control for all steps from seeding to tailing. Groups of pullers can be monitored, and have growth instructions updated, from central monitoring stations. The operators primarily address between-run cleaning, charge stacking, puller calibration, and start-up and checking diameter and correct sensor operation.

## 2.6 Tailoring crystal properties via growth parameters

To provide their semiconducting properties, silicon single crystals are pulled with defined low concentrations of deliberately added electronic impurities. The wafer resistivity is generated by precisely doping the silicon melt before crystal growth—with boron in the cases described above. The crystal is grown from the doped melt using a seed to define the crystallographic orientation. The Dash necking technique prevents any dislocations present in the seed, or generated by the thermal shock of dipping the seed into the melt, from propagating into the new crystal. The crystal growing on the seed is reduced to a small diameter and grown at a high rate, which eventually results in a dislocation-free crystal that can then be increased to the desired wafer diameter.

The chemical, structural, and electrical properties grown into the crystal are carried into the wafers/substrate, and can affect any epitaxial layer grown on the wafer.

Resistivity of silicon is a function of dopant concentration. Gulliver–Scheil solutions using Burton Prim and Slichter estimates for the $k_{eff}$, with appropriate estimates for the boundary layer thickness, give reasonable predictions for dopant incorporation in the crystal [70]. The predicted and actual macrosegregation down the axial crystal centerline are shown in Fig. 2.23. Resistivity is measured nondestructively by a four-point probe, and is an inverse function of dopant concentration. The US National Bureau of Standards established reference measurements for boron and phosphorus in silicon, and resistivity for arsenic and antimony is estimated from the phosphorus expression [71]. Fig. 2.23 shows that for n-type resistivity of approximately 0.003 Ω-cm, dopant concentration of approximately $2 \times 10^{19}$ atoms/cm$^3$ is required.

## 2.7 Benefits of computer modeling

Global heat and mass transfer simulations are widely used in industry to design crystal growth processes and equipment, and diagnose source of unusual crystal properties, if observed. The simulations are used to reduce the probability of dislocation nucleation, increase pull speed, adjust cooling rate, and determine desirable growth conditions (and their control limits) to provide desired microdefect distributions. Simulations were pioneered by government laboratories and universities, and matured by companies into commercially available software or simulation services. Simulations are commonly performed for:

- crystal diameter scale-up
- crystal length scale-up
- hot zone design
- crystal thermal history
- growth rate maximization
- avoiding SiO deposition
- macrosegregation of dopant, oxide, carbon, or melts
- microsegregation of dopant, oxide, carbon, or metals
- designing argon gas flow path (and local cooling) in puller
- transport of oxygen from crucible to crystal
- microdefect nucleation and growth.

The greatest attention recently has been paid to microdefect nucleation and growth.

## 2.8 Doping issues and reduction of defect density

Doping of silicon is straightforward in either Cz or FZ methods. The n-type dopants will evaporate from the melt during growth; if growth is restarted, additional dopant may need to be added [46]. Gallium and indium also evaporate, but are used only experimentally for solar cells to avoid light-induced degradation in a p-type cell.

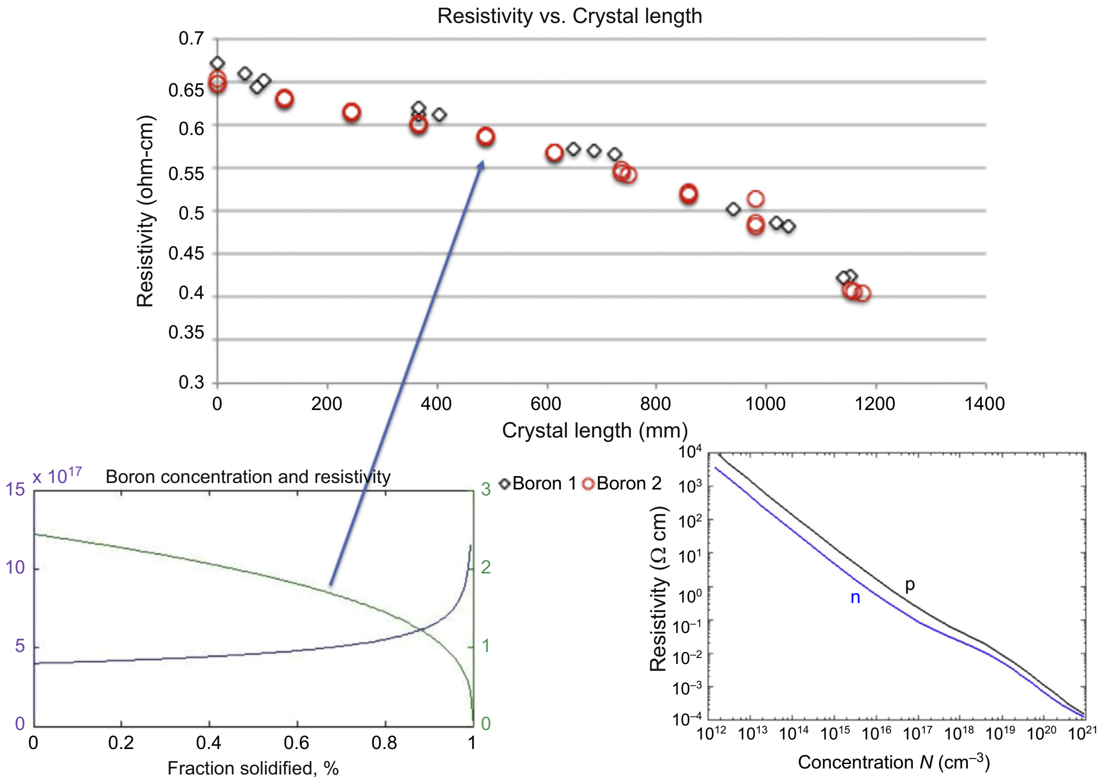

**Figure 2.23** Crystal resistivity and dopant concentration axial distribution.

Dislocations are avoided, and any material with dislocations is scrapped. Heavy doping with some n-type impurities can increase incidence of growth twinning. Twin material is scrapped, because of wrong orientation, the presence of the twin boundary, and strain, which will lead to dislocation nucleation. Obviously single crystals have no grain boundaries, but modern material has no lineage defects either.

The most commonly observed native defects are as follows [6].

A-defects, or large dislocation loops, form from interstitial agglomerates. Typical densities, if not avoided, are below $\sim 1 \times 10^4$ $cm^3$.

D-defects, or "COPs," are very small vacancy agglomerates. They are smaller than 100 nm diameter and are not small "argon holes." Typical densities, if not avoided, are $10^5-10^6$ $cm^3$.

The "P-band" is one term for the lower precipitation region in radial vicinity of the vacancy/interstitial boundary in the crystal. This is the location of an OISF "ring" in oxidized wafers, so this region contains the nuclei for those stacking fault defects. After oxidation, the oxygen precipitate density is approximately $10^6-10^8$ /$cm^3$.

A-defects (LDLs) are device killers, and whole-wafer A-defect silicon is not used for devices. D-defects (COPs) can substantially degrade devices [72]. At a minimum, the presence of COPs strongly influences the number of total light-scattering events measured on a polished wafer, and interferes with accurate particle or in-line defect density measurements during device fabrication. In device fabrication, COPs intersecting the wafer cut surface will lead to low field-gate oxide failure [73,74]. The gate oxide integrity yield is sensitive to COP area density on the wafer surface [75,76]. Device or trench isolation can be compromised, and there is evidence that this defect increases junction leakage in transistors. The presence of the COP "pit" at the wafer surface can interfere with construction of small-feature-size elements of transistors.

Careful control of point defect concentrations and dynamics can grow a dislocation-free and "COP-free" bulk silicon crystal [77,78]. Alternatively, the near-surface region of a silicon wafer can be made "COP free" by depositing an epitaxial layer on the surface or conducting a high-temperature anneal in argon, hydrogen, or ammonia. In theory the epitaxial layer covers defects on the wafer surface, but types of defects can propagate into the epitaxial layer or lead to different defects in the epitaxial layer than in the polished wafer substrate.

Dislocation-free single crystal silicon is unusual in that it can deliberately be grown vacancy-rich or interstitial-rich, depending on the growth conditions chosen, particularly axial temperature gradient and growth rate. After studies of the different defects (e.g., A-defects, D-defects) by many different workers [78–80], Voronkov identified that one critical parameter determined which point-defect type predominates in the grown silicon crystal [77,79]. The figure of merit is V/G, where V is the growth rate and G is the axial temperature gradient at crystal/melt interface. Voronkov and other workers found an experimental value of $(V/G)_{critical} = 0.16 \pm 0.04$ $mm^2$/min K for lightly doped p-type silicon [6,81]. They developed a theory to predict whether vacancy- or interstitial-agglomerated defects would occur, depending on growth conditions [81]. At that critical value there were neither agglomerated vacancy defects nor agglomerated interstitial defects of any type. To set up a growing process to produce such material means great control over solidification rate (which is normally varied for diameter control), axial temperature gradients, and in particular the radial variations of axial temperature gradients. The $(V/G)_{critical}$ value also depends on coexisting chemical impurities (concentrations of dopant, oxygen, carbon) and designing a crystal with no agglomerated vacancy impurities implies no vacancies available to assist in $SiO_2$ precipitation for gettering. Designing a robust industrial process to produce such “perfect” silicon repeatedly is challenging engineering, but has been successfully done for crystal diameters of 150, 200, and 300 mm by several silicon manufacturers. The understanding also allowed improvements to growing process conditions to, for example, reduce the density of OISF nuclei and avoid formation of LDLs.

In general, axial temperature gradients are not the same from the crystal centerline to the crystal periphery, and they can vary monotonically across the radius. Since the growth rate is constant across the radius for a time-invariant crystal—melt interface shape, the actual (V/G) is different at different crystal radius positions. This means that the type of agglomerated point defect varies from the crystal centerline to the wafer edge. The crystal can be vacancy defect rich at the center, show a “ring” of OISF nuclei at a particular radius, and be interstitial rich at the wafer periphery. To produce a low COP wafer across the whole wafer area to provide high device yield, one must minimize and control the radial variation of axial temperature gradients within strict limits.

Fig. 2.24 schematically shows the variation of (V/G) versus radial position. A horizontal slice through the crystal could contain different regions of vacancy- or interstitial-originated defects. Fig. 2.25 shows light scattering and etching images from slices taken from crystals grown at different (V/G) values. The center of

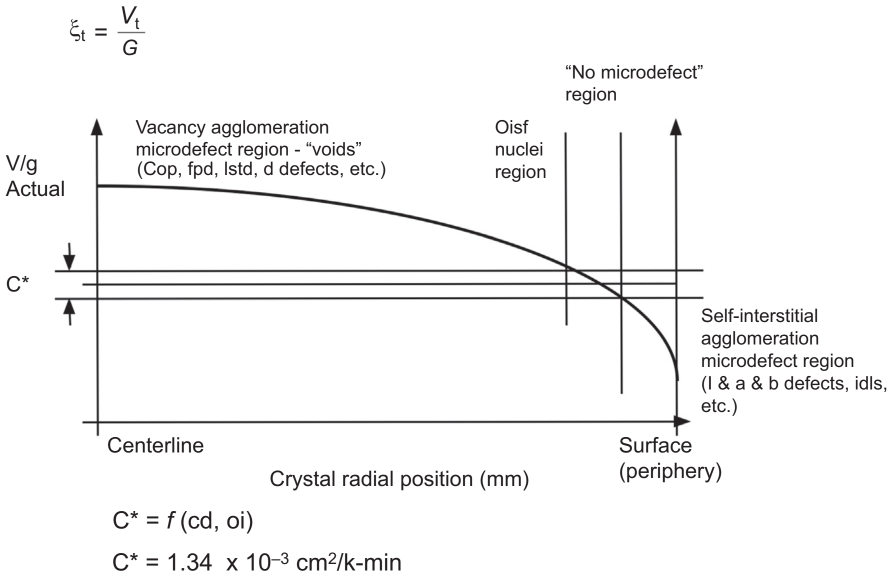

**Figure 2.24** V/G variation with crystal radius.

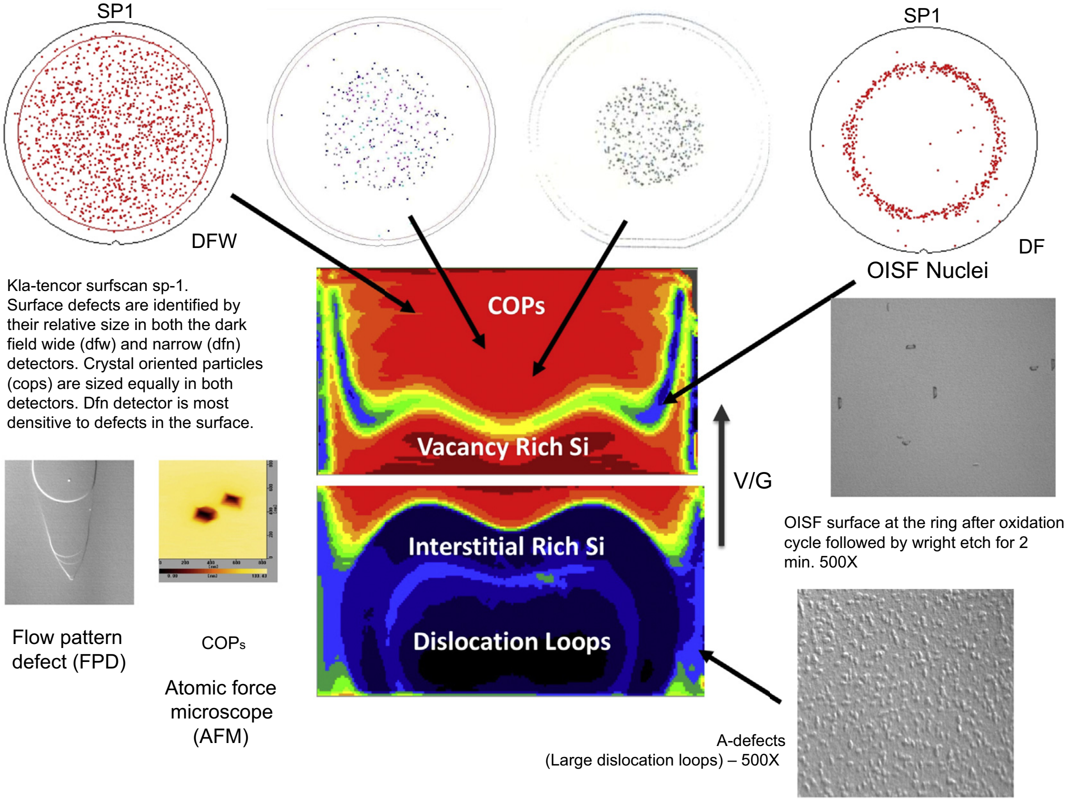
SP1
DFW
SP1
DF
OISF Nuclei
COPs
Vacancy Rich Si
V/G
Interstitial Rich Si
Dislocation Loops
Flow pattern defect (FPD)
COPs
Atomic force microscope (AFM)
A-defects
(Large dislocation loops) – 500X

Kla-tencor surfscan sp-1. Surface defects are identified by their relative size in both the dark field wide (dfw) and narrow (dfn) detectors. Crystal oriented particles (cops) are sized equally in both detectors. Dfn detector is most densitive to defects in the surface.

OISF surface at the ring after oxidation cycle followed by wright etch for 2 min. 500X

**Figure 2.25** Variation of point-defect-originated regions with growth rate [87].
Adapted from H. Furuya, K. Harada and J-G. Park, Defect reduction and improved gettering in CZ single-crystal silicon, Solid State Technology, (2001), (Pennwell).

Fig. 2.25 show lifetime measurements along a cross-section of a crystal which was grown by varying the growth rate from large to small while keeping axial temperature gradient near constant. At high growth rate, vacancy-originated defects (COPs) dominate and can be seen in a light scattering of polished wafer cut from such crystals. At lower growth rates the OISF nuclei are present, and lead to a "ring" of OISFs after wafer heat treatment. At very low growth rates, wafers cut from the crystal are full of LDLs and are unusable for devices.

Photovoltaic material has different defect concerns. The silicon crystals contain oxygen that comes from the quartz crucible used in the Cz process, and oxygen concentration is correlated to affect efficiency of a solar cell adversely. Oxygen can also precipitate in the crystal, providing surfaces for recombination [40,41]. The process of oxygen precipitation is part of the overall defect dynamics in Cz crystals. As stated earlier, various other microdefects exist in Cz crystals (e.g., COPs) but are not electrically active or dense enough to degrade over the lifetime. The crystal growth process and oxygen incorporation and precipitation depend on the temperature field in the crystal and the entire crystal puller. Segregation rejects metal impurities, but as metals increase, lifetime decreases. Recycling "wings" (which are slabbed off the right circular cylinder crystal to make pseudosquare cross-section cells) is economically important.

Sunlight is absorbed primarily in the first few microns of depth of the silicon wafer, generating electron—hole pairs. Impurities or structural defects in silicon are sites where electrons and holes recombine, reducing photocurrent.

If the emitter is on the front (illuminated side) of the wafer, the electrons have a short path to the conducting layer and impurities in the bulk silicon have limited influence. That is the geometry of the traditional standard solar cell. Bulk impurities will still influence electron—hole pairs generated by long-wavelength infrared photons that are absorbed deeper in the silicon wafer. If the emitter is on the rear of the wafer, the charge carriers must travel the entire thickness of the wafer (approximately 200 μm) and are susceptible to recombination at impurities or oxygen precipitates. Impurities and precipitates have a greater impact when emitters are on the rear of the cell. This geometry is being developed for next-generation, higher-efficiency solar cells. To realize that efficiency, bulk properties of silicon may need to be optimized.

## 2.9 State-of-the-art of the material

The Cz method of crystal pulling is used to produce large amounts of dislocation-free silicon economically for semiconductor device and photovoltaic conversion applications. Crystal production costs depend to a great extent on the yield of crystal properties compared to a specification of acceptable values, and the costs of materials, in particular the fused silica crucible, graphite heater, insulation and susceptor, and polysilicon. The conventional Cz method is a batch process, in that a crystal is pulled from a single crucible charge; the crucible is used once and is discarded after use. To increase yield per crystal growth operation and reduce unit crystal growth cost, strategies such as larger starting charge sizes and pulling several crystals sequentially from a single crucible after "recharging" the melt with additional polysilicon have been employed in high-volume, large-scale production. The melt is replenished prior to pulling each crystal; during each pull the crystal is frozen from a fixed initial volume melt. However, a disadvantage of recharging the melt is that unwanted impurities can build up in the residual melt between recharges, due to solute partitioning.

Because of the strong effect of polysilicon material cost on crystal cost, one focus of the development work for both Cz and FZ methods has been to increase crystal yield. Poor yield will increase crystal cost and can totally offset savings from reduced cost of starting materials (such as crucible or graphite insulation) or extreme engineering efforts to, for example, increase growth rates. Crystal yield directly affects crystal conversion cost per gram (fixed and variable cost), capital equipment utilization, and process turnaround time.

Some crystal yield losses in the Cz or FZ process are expected and "designed in": the seed incrementally melts down in length from repeated use, and is eventually consumed and requires replacement. Necks, crowns, and tails must be either scrapped or recycled (as "remelt"). Depending on wafer specification, remelt may be usable to offset new polysilicon in a future crystal growth run, or may only be usable for certain low-technology products or downrated to sell to a different business. The remaining frozen melt left in the fractured crucible ("pot scrap") is sold for scrap—at one time, this was a source of low-cost multicrystalline solar cell feedstock.

The crystal is grown slightly over the desired diameter so that it can be ground down to the correct wafer diameter. The ground-away material, known as "swarf," can be sold as metallurgical silicon feed. Slices are taken from particular positions along the crystal axial length to measure resistivity, oxygen, carbon, and other specified properties. These are "losses," but are kept for a time as a record of the crystal properties.

There are a large number of potential yield losses to design out or which require extreme efforts to control. Nucleation of dislocations on a crystal which cannot be completely melted back and restarted for some reason (for example, hot time in run) means that further pulling is not worth the time and cost, and previously grown dislocation-free material must be cut away and scrapped after the crystal is removed and cooled. Although there are standard rules on removal length of body (for example, one diameter of axial loss for <100> orientation when dislocations appear), the actual amount to remove must be set by progressive cropping and testing until the point is reached where no slip is visible on the remaining crystal body. The actual extent of slipback will depend on growth process conditions (cooling rates) and how extensive and traumatic was the cause of the initial dislocation nucleation.

It is possible that the crystal will be grown underdiameter (a diameter too small to make the desired-size wafer) and any length below the minimum diameter would be scrapped and contribute to yield loss. Mistaken overdiameter (too large a diameter), which would lead to excessive losses in grinding to a desired diameter, would have less of an impact.

The most disruptive yield losses come from the measured property being OOS, where sections of the dislocation-free crystal which visibly appear acceptable do not meet allowable specification values. Each property must be measured, and the extent of any OOS determined so that acceptable material can be saved from the crystal.

Examples of material properties which are checked are resistivity, resistivity radial gradient, Oi, oxygen radial variation, microdefects: V/I boundary (radial boundary in crystal cross-section between interstitial defects and vacancy defects, OISF “ring”, COP density/size distribution, LDL presence, BMD density, minority carrier lifetime, and metal impurity concentration (e.g., of iron).

In addition to loss of material from a particular crystal which does not meet specification, the appearance of OOS can indicate faults in the crystal growth equipment, consumable quality, or instability in crystal growth process parameters. Diagnosing the OOS root cause can lead to process changes. Comparing actual yield over many runs to “prime specification” of maximum theoretical yield for that process will point to crystal growth process improvements requiring attention.

The epitaxial layer optimized substrate is has been proposed as a low-cost dislocation-free silicon substrate for epitaxial layers [59,61]. The idea is to reduce the number of specified properties as far as possible for the substrate to save cost, as long as a high-quality thin epitaxial layer can be grown on the substrate to serve as the actual device region. Early visions of using “solar-grade mono” dislocation-free single crystal silicon as an epitaxial substrate for semiconductor devices did not bear fruit, as more studies were done showing which bulk defects in the silicon crystal could affect the quality of the epitaxial layer. In addition to epitaxial defects growing due to substrate surface defects (such as revealed argon holes) or carbon concentration in the bulk diffusing upwards into the epitaxial layer, any device failures investigated would reopen an evaluation of properties of the substrate as a potential root cause.

## 2.10 New trends and future developments

The eventual diameter scale-up of semiconductor device silicon to 450 mm diameter is the clearest future direction [64]. Application of true CCz (continuous, melt-replenished Cz method) for both solar mono production and heavily doped semiconductor device substrates will probably be realized. In addition, the great demand for lower-cost but high-efficiency solar cells is leading to exploration of alternate growth techniques aiming to produce either low-cost dislocation-free material or single crystal but dislocated silicon.

One strategy to provide quasisteady state heat and mass transfer conditions during pulling, and produce multiple crystals during a single operation, is to add polysilicon and dopant continuously during the crystal growth itself. In doing so, the melt can be maintained at a near-constant volume and the chemical species maintained at a quasisteady-state concentration in the melt during growth of the crystal. CCz has long been envisioned to increase crystal quality while reducing crystal growth cost, and is only recently entering production for solar silicon [82]. Macroscopic crystal axial impurity variation is inherent in the Cz “batch” growth process due to macrosegregation phenomena during normal freezing conditions. By continuously controlling charging of both polysilicon and dopant via CCz, the resistivity dictated by dopant macrosegregation can be directly controlled.

Many bulk chemical inhomogeneities in crystals grown by the conventional Cz method are a direct result of nonsteady mass transport due to the melt volume change during crystal growth. The CCz method can be used to reduce the production cost of crystals as well as to grow crystals under quasisteady and heat and mass transport conditions, leading to quasisteady structural and chemical defect distributions. For example, to affect the oxygen incorporated into a growing silicon crystal, the ratio of the area of the crucible-to-melt interface to the area of the silicon-melt to argon-free surface can be kept near constant during the crystal growth, so the mass transport of oxygen atoms from the melt to the melt–crystal interface and melt–gas interface can be made quasisteady. A disadvantage of the CCz method could be, similar to the multiple crystal recharge method, the impurity build-up in the residual melt. However, the CCz process can be designed to lead to a much slower build-up of impurities than sequential melt replenishment. It has been shown that a lower impurity build-up, and greater axial uniformity of impurities incorporated, can be achieved by the CCz method when compared to either the conventional or sequential multiple crystal growth Cz methods.

The CCz method of crystal pulling has been developed by at least three manufacturers. The method can be used economically to produce crystals with either low or high resistivity values. There are several benefits of the CCz approach for single crystal silicon production, in particular as crystal diameters are increased. Metered dopant and polysilicon introduction during crystal growth allows more uniform axial resistivity than batch Cz, resulting in improved crystal manufacturing yield. The oxygen concentration can be decoupled from crucible size and crystal diameter, and relatively low oxygen concentrations are obtained over long crystal lengths without the use of a magnet to change the melt flow conditions. The crystal length is determined by "height of building" (length of pull chamber) instead of crucible size. This allows longer crystals to be made in a run without increasing the size and cost of the consumables or the production equipment. The continuous supply of polysilicon during body growth allows shortening of the sequential charge–melt–stabilize–grow–remove cycle for crystals.

The advantages of CCz processes are listed below.

- Many long-body crystals are made from each CCz run, which lowers conversion cost.
- A continuous supply of fresh polysilicon during body growth saves power compared to the charge–melt–stabilize–grow–remove cycle of batch Cz.
- Metered dopant/polysilicon introduction during crystal growth for "uniform" axial resistivity for both p-type and n-type. Crystal manufacturing yield is increased, particularly for dopants with $k_0 << 1$. This not only benefits phosphorus for n-type solar cells, but also allows a reasonable cost for use of gallium or indium dopants as a p-type alternative to boron.
- "Wings" cropped from crystal also exhibit uniform axial composition, simplifying recycle/remelt operations in n-type materials flows.
- Crystal resistivity can be maintained under the constitutional supercooling threshold (for heavily doped crystal substrates or highly doped melts with small $k_0$).
- Constant melt height maintains targeted bulk crystal growth heat and mass transfer conditions.
- One can design the gradual build-up of unwanted impurities (i.e., carbon, metals) by geometry and size of the meltdown versus growing volumes.
- Oi concentration is decoupled from crucible size and crystal diameter.

- Crystal body pull speed can be maximized.
- Ability to generate quasisteady state of bulk microdefects.
- Maximum ingot length is determined by "height of building" (or puller), not crucible/hot zone size.

In batch or batch-recharge Cz, rejected impurities build up in diminishing melt volume. The lifetime decreases from the seed to tail of each crystal. Recharging at the completion of one crystal pull dilutes the impurity, but not to the original low melt concentration. As more crystals are pulled, the average metal concentration increases. In CCz, rejected impurities are concentrated in the growth melt volume. There can be a designed level of concentration enrichment set by choice of growth melt volume and incoming concentration.

Constitutional supercooling is a problem for heavily doped crystals, or crystals grown from heavily doped melts. The threshold for its occurrence is dopant specific, but in general doping must be over $1 \times 10^{18}$ atoms/cm$^3$. For very heavily doped silicon for power control substrates, onset of constitution supercooling will lead to a corrugated crystal—melt interface, which eventually traps and enriches solute and nucleate dislocations, as shown in Figs. 2.26 and 2.27. The crystal habit lines collapse. However, since the lowest axial temperature gradients and highest solute concentrations are at the crystal centerline, this can occur before the periphery of the crystal is affected. Fig. 2.28 shows two heavily doped crystals that generated not only dislocations but also new grains because of constitutional supercooling. Crystal 1 showed habit line collapse, and the crystal was decanted from the melt to reveal the interface. The "cells" shaped like pyramids (bounded by {111} planes) are clearly visible. Crystal 2 completed growth and dislocated at the end of the tail. After the tail was sliced off and crystal evaluation was begun, it was found that constitutional supercooling had begun at the centerline and generated a central domain of not only dislocations but also new grains. There was substantial yield loss from cropping back both multigrain and slipped material. Precluding constitutional supercooling by adjusting melt dopant concentration continuously during growth to avoid the constitutional supercooling G/V threshold would lead to substantial yield increases for such crystals.

If there are such advantages to CCz, why has it not already been widely adopted? There is much effort involved in developing a high-yield, high-volume production process. One must grow the crystal and feed the polysilicon and dopant simultaneously, leading to process equipment and process control complexity. Usually separate growth volumes and meltdown volumes are established in the crucible, with boundaries between them. The crucible cost for CCz is in general higher than for Cz, because of the need to have separate feed and pull zones.

The polysilicon can be fed as a solid, or first melted and fed as a liquid, but in either case must not disturb the growing crystal nearby. Temperature fields must be set up both to melt (and keep liquid) the silicon feed and also grow a dislocation-free crystal. The mass of polysilicon added must just balance that withdrawn as single crystal, or else the melt level and local temperature in both regions can change.

Hot run times can be long. There will be a desire to grow many long crystals during each run, to minimize cost/mass from one silica crucible (and any other consumable parts).

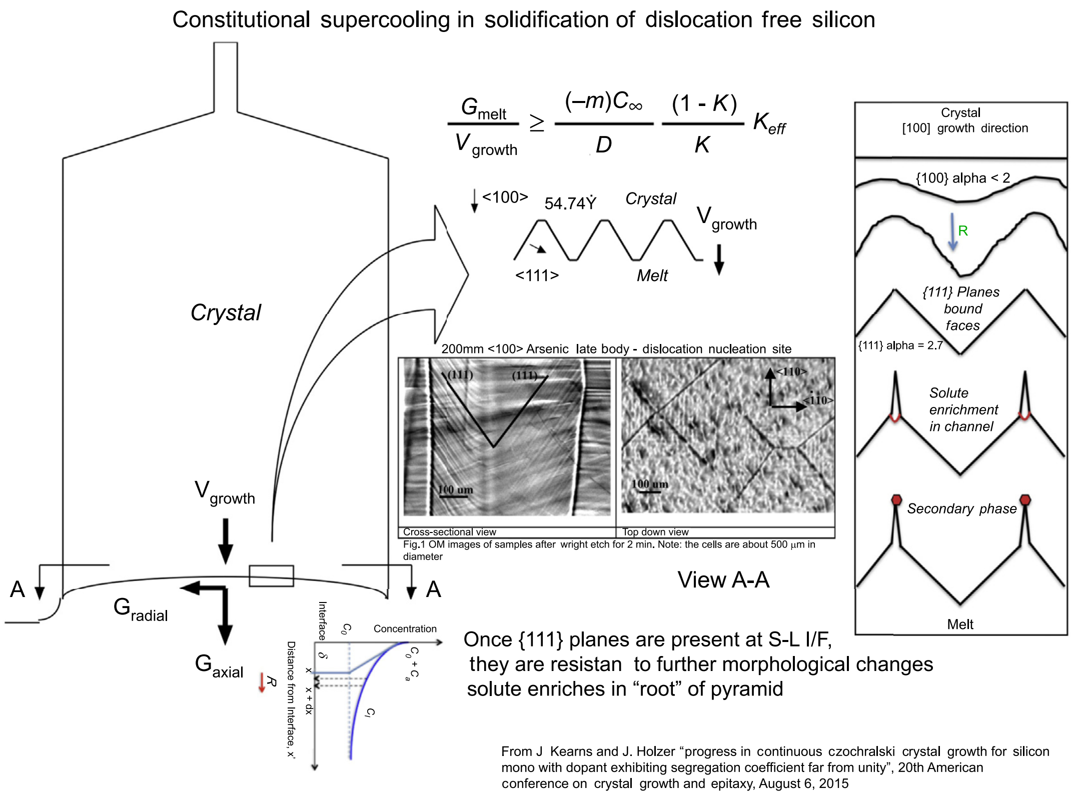
Constitutional supercooling in solidification of dislocation free silicon
Crystal
V growth
A
A
G radial
G axial
R
Interface
Distance from Interface, x'
Concentration
$C_0$
$C_0 + C_a$
$C_l$
δ
x
x + dx
<100>
54.74Ẏ
Crystal
V growth
<111>
Melt
200mm <100> Arsenic late body - dislocation nucleation site
(111)
(111)
100 um
<110>
<110>
100 um
Cross-sectional view
Top down view
Fig.1 OM images of samples after wright etch for 2 min. Note: the cells are about 500 μm in diameter
View A-A
Crystal
[100] growth direction
{100} alpha < 2
R
{111} Planes bound faces
{111} alpha = 2.7
Solute enrichment in channel
Secondary phase
Melt

$$\frac{G_{melt}}{V_{growth}} \geq \frac{(-m)C_\infty}{D}\,\frac{(1-K)}{K}\,K_{eff}$$

Once {111} planes are present at S-L I/F,
they are resistan to further morphological changes
solute enriches in “root” of pyramid

From J Kearns and J. Holzer “progress in continuous czochralski crystal growth for silicon mono with dopant exhibiting segregation coefficient far from unity”, 20th American conference on crystal growth and epitaxy, August 6, 2015

**Figure 2.26** Model of Constitutional Supercooling in Silicon Cz Growth.

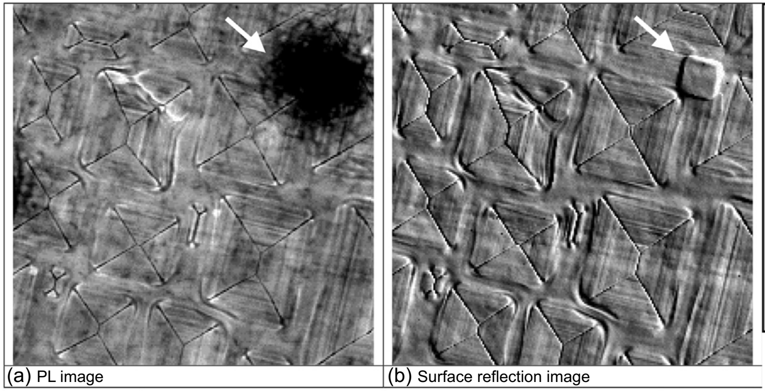

(a) PL image (b) Surface reflection image

Dislocation nucleation in body of initially DF silicon during CZ crystal growth of Sb <100> 200mm diameter due to sb-induced crystal-melt interface morphological instability: resistivity ~ 0.008 ohm-cm.

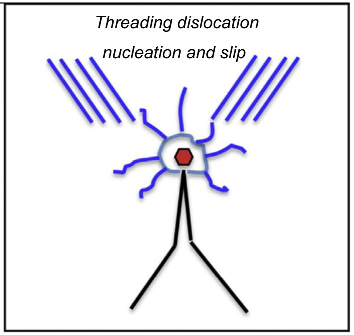

From J. Kearns and J. holzer “progress in continuous czochralski crystal growth for silicon mono with dopant exhibiting segregation coefficient far from unity”, 20th american conference on crystal growth and epitaxy, August 6, 2015.

Dislocation nucleation in body of initially DF silicon during CZ crystal growth of as <100> 150mm diameter due to as-induced crystal-melt interface morphological instability: resistivity ~ 0.0025 ohm-cm.

From S. Rouvimov, J. Kearns, v. Todt, B. Orschel, H. Siriwardane, A. Buczkowski, R. Kuytt, I. Shul’ pina and G. Rozgonyi, solid state phenomena vols 95-96 (2004) 17-22.

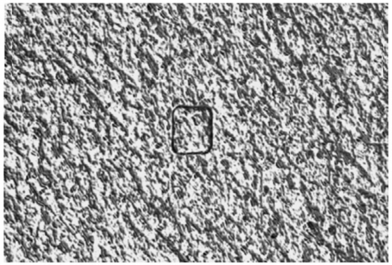

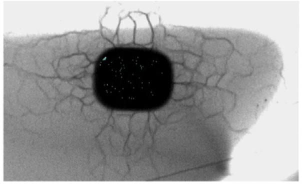

Dislocations generated around small domain of higher arsenic content. 250 $\mu$m x 400 $\mu$m.

**Figure 2.27** Nucleation of Dislocations from Constitutional Supercooling.

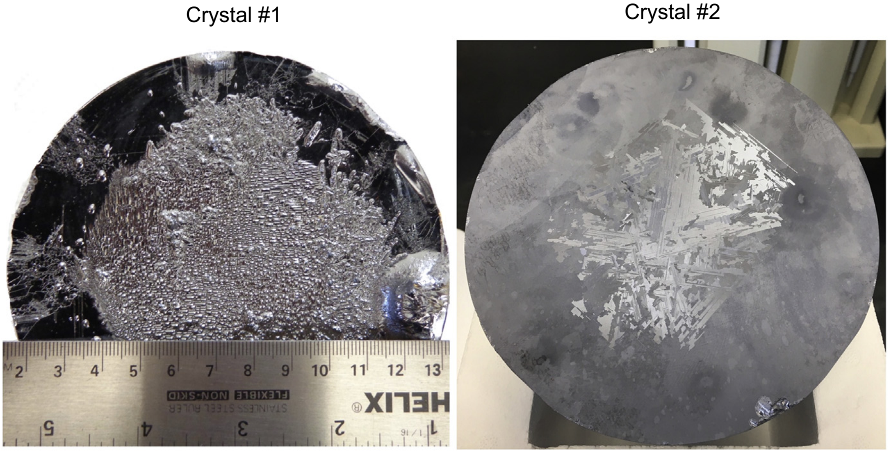

Crystal #1

Crystal #2

Decanted crystal-melt interface after constitutional super-cooling but before loss of {111} facets on crystal exterior. Cells are ~ 1 mm x 1 mm.

Cross-section of crystal after constitutional super-cooling but before loss of {111} facets on crystal exterior - periphery of crystal single and dislocation-free, but interior has grains and twins. KOH etched after slicing.

**Figure 2.28** Cells and grains from constitutional supercooling.

Many crystals will lead to many hot hours during a single sealed run. Temperature and thermal cycles will wear on hot zone parts, potentially shortening their life and giving the potential for particles to detach from them and reduce yield. Extended hot time of crucibles could lead to recrystallization of particles from the crucible and loss of dislocation-free growth. It is only after decades of development of longer-life crucibles and hot zone graphite parts for large-diameter, batch-recharge Cz that such parts for CCz are feasible.

Since melt is fed to maintain a constant melt volume as crystal is grown, there is no ability to melt-back a short crystal which dislocates. The crystal must be withdrawn and the yield loss taken, then a new crystal started. But for a multicrystal run which converts many kilograms, the loss of the slipped body may be a very small fraction of the polysilicon used.

The chemical composition performance (“flat” axial macrosegregation) was beneficial to, but not essential for, semiconductor wafer properties, so the initial drive for CCz was to increase quality radically (property uniformity) and also reduce cost. Predictable wafer-to-wafer resistivity variation from Cz, due to Gulliver−Scheil behavior, is acceptable for semiconductor devices. CMOS devices were based on p-type (boron) substrates, and macrosegregation from $k_0 \sim 0.8$ was acceptable.

To implement CCz one needs a large supply of good-purity “flowable” polysilicon source material. The polysilicon must be of small size, have a high area-to-volume ratio for fast melting, and not have large shape-aspect ratios, which could clog feed equipment tubes. Equipment (dimensional and materials choices) and process (heat and mass transfer choices) in the crystal growth approach are critical. If the approach is overly complex or not robust, poor crystal yield and associated costs will wipe out

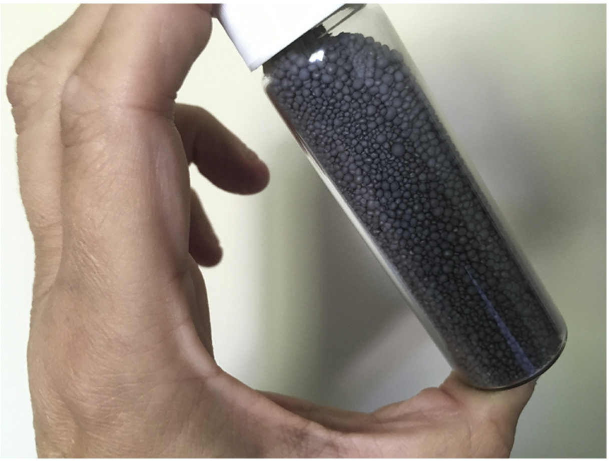

**Figure 2.29** Granular polysilicon produced by fluidized-bed reactors. This type of feed material may be conveniently employed in CCz process.

theoretical conversion cost advantage and limit the quantity produced. Small, granular polysilicon beads, produced by fluidized-bed chemical reactors, produce suitable-size flowable material, as shown in Fig. 2.29.

There are challenges to implementing a CCz process successfully, and issues seen in earlier development discouraged continued improvement or adoption until the early 2010s. In 1996 Shin-Etsu studied small voids seen in early CCz silicon crystals [83]. The crystals were grown using dehydrogenated granular polysilicon ($<10$ ppma hydrogen) as feed material. Granular polysilicon is grown by fluidized bed reaction, with silicon—hydrogen or silicon—chlorine precursors. The workers found many small pits on chemically polished wafers made from the crystals, with diameters up to 15 μm. The pits were observed only in the part of a CCz crystal grown by feeding granular polysilicon, and never observed in conventional Cz crystals, even when granular polysilicon was used for the initial charge or for recharging between pulls. They attempted to measure hydrogen in the crystal by FTIR or hydrogen gas in the puller using a quadrupole mass spectrometer but were not successful. They concluded that the pits are cavities formed during crystal growth by the hydrogen released during granular polysilicon melting. The also reported on "melt splashing" during the delivery of polygranules into the melt, caused by hydrogen liberation as the granules contacted the hot melt. Both fluidized bed reactor gas concentration and granular polysilicon meltdown procedures had to be improved in the 2010s so that CCz could avoid such microvoid defects.

Although the recent interest in CCz has involved producing lightly doped silicon crystals for 156 mm PS solar cells, the process can also be applied to heavily doped substrates for power semiconductor devices, to avoid constitutional supercooling-driven dislocation nucleation during growth of such substrates. A larger-diameter scale-up of CCz may allow production of 300 mm high-resistivity wafers for high-voltage power devices, removing the current 200 mm diameter size limit for those devices, which are made on FZ crystal. Further scale-up of CCz may be the key process enabler for 450 mm diameter (and eventually 675 mm diameter) wafer scale-up: 450 mm diameter dislocation-free silicon crystals have been demonstrated, but to reduce crystal cost to near that of 300 mm diameter the crystal lengths should be much longer than the diameter. That implies extremely large crucibles for large starting melts, hotter crucible wall temperatures, and additional heat wear on graphite in larger hot zones. CCz may provide the method to use smaller-size crucibles and still grow extremely long 450 mm diameter single crystals.

Some are seeking to reduce the high cost of the FZ process by avoiding the use of expensive polysilicon feed rods and enables the FZ method to grow dislocation-free crystals with inexpensive granular polysilicon [27,28]. The polysilicon granules are supplied through a funnel on to the surface of a rotating silicon plate, where they are melted by an induction coil. The melt flows through a round opening in the center of the silicon plate to form a melt pool on top of a growing dislocation-free crystal, begun by standard FZ necking. The use of silicon granules both significantly lowers the cost of the feedstock material and minimizes the feedstock losses in case of dislocation nucleation during growth. The granule supply and the process can be stopped at any time without the consequence of making unusable polysilicon feed rods. Although FZ is limited to crystals of 200 mm diameter, if the costs were reduced these might be used to produce very low oxygen (high lifetime) 156 mm PS cell wafers.

Since multicrystalline silicon, grown by gradient freeze, has a much lower conversion cost than Cz growth, there have been repeated efforts to develop a seeded single crystal gradient freeze process [84,85]. The mono$^2$, quasimono, and MLM processes have been developed to grow a very large single grain of defined orientation over most of the volume of the HEM crucible [25]. The desired attribute for solar cells is that the wafers have <100> orientation, so that wafer surface caustic etching will generate pyramidal {111} planes on the wafer surface. These "textures" act to improve light trapping and avoid light reflection, which would reduce charge carriers and photovoltaic efficiency. Eliminating dislocations, while beneficial, is secondary if the dislocation density is low enough, and cooling rates low enough, that existing dislocations do not interact and generate new grains. The standard multicrystalline gradient freeze processes for solar ingot grow charge sizes from 550 kg (a square of $5 \times 5$, 156 mm full square bricks) to 1650 kg (a square of $8 \times 8$, 156 mm full square bricks). Silicon interaction with the crucible sidewalls will generate new grains, and the goal is to minimize the depth of that occurrence and maximize the interior of the single crystal volume. Some implementations have been generated to, for example, have the middle $3 \times 3$ of the $5 \times 5$ bricks be of one orientation, or the interior $6 \times 6$ of the $8 \times 8$, or to grow a pattern of $7 \times 7$ bricks. Barriers to acceptance have been variable single crystal yields, higher than expected costs, and a noticeably broader distribution of solar cell performance properties (open circuit voltage, short circuit current, fill factor) compared to either multicrystalline ingots or Cz crystals. Like multicrystalline silicon, MLM is saturated with nitrogen, from the crucible wall-coating material, so the crystal includes $Si_3N_4$ inclusions and is not single phase. The Oi is substantially lower than that of Cz material, while carbon concentration can be two orders of magnitude larger. Minority carrier lifetime is very low compared to Cz, and one cause is metal contamination from the multigrain ceramic $SiO_2$ crucible used to contain the melt and ingot.

A very recent development, NGS, grows single crystal ingots by melting granules and solidifying them on single orientation seeds (from either Cz crystals or prior NGS ingots) with no crucible contact [26,86]. Because there is no container connect, the approach promises low oxygen and carbon, and single crystal orientation throughout the ingot. Since there is no Dash neck to remove dislocations, the ingots produced are single crystal but not dislocation free. The process can be scaled up to produce ingots equivalent to a 450 mm diameter Cz crystal. Four "bricks" of 156 mm full square area can be cut from such an ingot. The process is in early development, but has already demonstrated the desired crystal properties. Much like CCz, dopant as polysilicon is added, so dopants with small segregation coefficients (e.g., gallium) can be grown with low axial macrosegregation.

The mechanical silicon parts manufacturers are watching the semiconductor and solar communities to see which advanced processes may be adapted to their unique needs. For example, both MLM and NGS are being considered to supply single crystals for large-size optical windows and sputtering targets.

Semiconductor and photovoltaic community precompetitive roadmaps indicate what problems will need to be solved by new crystal growth processes to give crystals with required properties. For semiconductors, 450 mm diameter has been discussed. Besides conversion cost and volume production, key questions are whether temperature gradient and growth rates can be established to provide the same bulk microdefect nucleation and growth conditions now expected for 300 mm and smaller-diameter silicon; 200 and 300 mm crystals will be used for many decades. As transistor critical dimensions shrink to less than 5 nm, there will be new restrictions on maximum COP size and number in those crystals, and perhaps also impurity striations across the wafer. Chemical striations and bands can lead to variations in etching and polishing uniformity across the wafer radius. Similarly, restrictions on critical metals concentrations may be tightened. If the larger-diameter 450 mm crystal cannot provide the expected COP, OISF, or BMD distributions, there may be a migration away from polished wafers to epitaxial wafers. Regardless, the crystals will still need to be dislocation free.

For photovoltaics, the drive to improve crystal and wafer contributions to decreasing cost, increasing photovoltaic conversion efficiency, and decreasing the "dollars per watt peak" figure of merit will only increase. Both the crystal conversion cost and polysilicon cost will be aggressively attacked to produce a dislocation-free crystal that currently does not need to exhibit all the properties of semiconductor wafers (like BMDs). At the same time, photovoltaic efficiency will be improved by changes to both solar cell geometry and architecture and crystal quality. The MCLT variation from crystal to crystal and within crystals for advanced cell architectures will both need to be tightened, and the average value increased. Changing to n-type cells may generate a new focus to eliminate oxygen-related recombination centers [56]. Competitors to Cz, such as FZ using FBR polysilicon, quasimono, and NGS (and others) will continue to be evaluated. If benefits are seen, the solar market could shift rapidly away from Cz to one of these new processes.

## 2.11 Summary

Silicon single crystals are designed for specific applications, and the crystal design can be as important as the device design to the success of the application. Photovoltaics today use the greatest volume of single crystal silicon grown, but silicon for semiconductors is the purest and "most structurally and chemically perfect" material made by man.

The vast majority of research and development work in modern Cz silicon growth for the semiconductor device industry was aimed at controlling oxygen, native point defects, and the interactions between them. The wafer must exhibit properties such as the desired doping level and type, desired crystal orientation, freedom from deleterious agglomerated interstitial defects such as dislocation loops, and control of agglomerated vacancies (COPs) so as to not cause issues in devices. An early improvement was to design the growth processes to provide desired oxygen precipitation behavior for internal gettering of unwanted metal impurities.

A separate area of R&D is to reduce crystal resistivity further for discrete devices while simultaneously improving gettering.

CCz offers a broad range of oxygen capabilities and an exceptionally flat resistivity profile along crystal axial location, and after decades of development it is a realistic choice for future dislocation-free growth processes. Semiconductor scale up to 450 mm diameter is likely, but the date is uncertain and will be driven more by wafer manufacturing readiness than crystal growth readiness.

Solar silicon is focused on reducing conversion cost, increasing photovoltaic efficiency (improving whole-wafer and wafer-to-wafer MCLT), and improving capital equipment utilization. As cell architectures change, so may the required crystal properties. Solar is not focused on diameter scale-up, as the solar cell size is an industry standard.

There is a great incentive to develop new or modified growth techniques to produce silicon with improved cost per watt peak photovoltaic performance, which can be realized by increasing Wp or reducing cost, or both. These approaches could be "mono-like" cast silicon, NGS, or FZ grown by feeding granular polysilicon.

This chapter is written in the author's personal capacity, and the views expressed do not represent the views of the United States Government.

## References

[1] G. Harbecke, M. Schultz, Semiconductor Silicon, Springer-Verlag, Berlin, 1981.
[2] R. Fornari, C. Paorici (Eds.), Theoretical and Technological Aspects of Crystal Growth, Trans Tech Publications, Switzerland, 1998.
[3] W. Tiller, The Science of Crystallization: Microscopic Interface Phenomena, Cambridge University Press, Cambridge, 1991 (Facets, angle).
[4] W. Tiller, The Science of Crystallization: Macroscopic Phenomena and Defect Generation, Cambridge University Press, Cambridge, 1992 (defects).

[5] Properties of Silicon, EMIS Dataviews Series No. 4, INSPEC, the Institution of Electrical Engineers, Unwin Brothers, Surrey, UK, 1988.

[6] V. Voronkov, B. Dai, M. Kulkarni, Fundamentals and engineering of the Czochralski growth of semiconductor silicon crystals, in: P. Bhattacharya, R. Fornari, H. Kamimura (Eds.), Comprehensive Semiconductor Science and Technology, Volume 3, Elsevier, Amsterdam, 2011, pp. 81−169.

[7] F. Bloss, Crystallography and Crystal Chemistry, Holt, Rinehart and Winston, New York, 1971.

[8] N. Hannay, Recent advances in silicon, in: F. Biondi, D. Van Nostrand (Eds.), Transistor Technology, Volume II, 1958, pp. 2−36. Princeton.

[9] J. Brice, Crystal Growth Processes, Blackie, Halsted Press, Glasgow, 1986 (Cz).

[10] S.M. Sze, VLSI Technology, second ed., McGraw Hill, New York, 1988 (Silicon, Devices).

[11] F. Shimura, Semiconductor Silicon Crystal Technology, Academic Press, San Diego, 1989 (Cz silicon).

[12] T. Abe, Crystal fabrication, in: N. Einspruch, H. Huff (Eds.), VLSI Electronics Microstructure Science, Volume 12, Silicon Materials, Academic Press, 1985 (dislocations, history).

[13] S.M. Sze, Physics of Semiconductor Devices, second ed., Wiley, 1981 (Silicon, devices).

[14] SEMI Silicon Manufacturers Group, Press Release, February 10, 2018.

[15] Fraunhofer Institute for Solar Energy Systems, Photovoltaics Report, February 26, 2018.

[16] F. Colville, Mono and Multi Production 50:50 in 2018, but Mono Is the Future, PVTECH, Photovoltaics International, May 9 , 2017.

[17] W. Pfann, J. Metals 4 (1952) 747.

[18] W. Pfann, Zone Melting, Wiley, New York, 1958.

[19] W. Dietze, W. Keller, A. Mühlbauer, Float-zone grown silicon, in: J. Grabmaier (Ed.), Crystals (Growth, Properties, and Applications), vol. 5, Springer, Berlin, Heidelberg, 1981.

[20] G. Teal, E. Buehler, Phys. Rev. 87 (1952) 190.

[21] G. Teal, IEEE Trans. Electron. Devices Ed-23 (7) (1976) 621−639.

[22] W.R. Runyon, Silicon Semiconductor Technology, McGraw-Hill, NY, 1965.

[23] H.C. Theuerer, US Patent 3,060,123 (October 23, 1962).

[24] R. Emeis, Z. Naturforsch 9a (1954) 67.

[25] N. Stoddard, B. Wu, I. Witting, M. Wagener, Y. Park, G.A. Rozgonyi, R.F. Clark, Casting single crystal silicon: novel defect profiles from BP Solar's Mono$^2$ ™ wafers, Solid State Phenom. 131 (2008) 1−8 (MLM).

[26] N. Stoddard, W. Von Ammon, Apparatus and Method for the Production of Ingots, U.S. patent 9,315,917, 2016 (NGS).

[27] W. von Ammon, Phys. Status Solidi A 211 (11) (2014) 2461−2470 (FZ).

[28] W. von Ammon, US patent application US 2003/0145781A1.

[29] See http://www.itrs2.net/ and https://www.semiconductors.org/main/2015_international_technology_roadmap_for_semiconductors_itrs/.

[30] See http://www.itrpv.net/.

[31] W. Zulehner, Czochralski growth of silicon, in: G. Harbeke, M. Schultz (Eds.), Semiconductor Silicon, Materials Science and Technology, Springer Verlag, Berlin, 1989 (Cz silicon).

[32] Garter Research Inc., Press Release "Gartner Says Worldwide Semiconductor Revenue Forecast to Grow 7.5 Percent in 2018", January 15, 2018. Stamford, Connecticut.

[33] R. Rhodes, Imperfections and Active Centres in Semiconductors, Pergamon Press, New York, 1964 (Silicon).

[34] R. Laudise, The Growth of Single Crystals, Prentice-Hall, Englewood Cliffs, NJ, 1970 (Growth processes).

[35] J. Wilkes, The growth of single crystal silicon, in: “Proceedings of the International Summer School on Crystal Growth”, Palm Springs, CA, 1992.

[36] W. Lin, D. Hill, Large-diameter Czochralski silicon crystal growth for VLSI, in: D.C. Gupta (Ed.), Silicon Processing, STP-804, ASTM, Baltimore, 1983 (Cz).

[37] W. Keller, A. Muhlbauer, Floating zone silicon, in: W.R. Wilcox (Ed.), Preparation and Properties of Solid State Materials Volume 5, Marcel Dekker, New York, 1981.

[38] W. Bardsley, F. Frank, G. Green, D.T.J. Hurle, J. Cryst. Growth 23 (1973) 341−344 (Meniscus).

[39] T. Surek, B. Chalmers, J. Cryst. Growth 29 (1975) 1−11 (contact angle).

[40] B.J. Keene, Surf. Interface Anal. 10 (1987) 367−383 (Surface energy).

[41] K. Mukai, Z. Yuan, Mater. Trans. Jpn Inst. Metals 41 (2) (2000) 331−337 (Surface energy).

[42] Z. Yuan, K. Mukai, W. Huang, J. Colloid Interface Sci. 249 (2002) 471−475 (Surface energy).

[43] N. Eustathopoulos, B. Drevet, J. Cryst. Growth 371 (2013) 77−83 (Si surface tension).

[44] Z. Yuan, K. Mukai, W. Huang, Langmuir 18 (2002) 2054−2062 (Si surface tension).

[45] F.A. Trumbore, Bell Syst. Tech. J. 39 (1960) 205−233 (solubility).

[46] W. Zulehner, D. Huber, Czochralski-grown silicon, in: H.C. Freyhardt (Ed.), Crystals: Growth, Properties and Applications 8, Springer-Verlag, Berlin, 1982 (Cz silicon).

[47] W. Lin, K.E. Benson, Annu. Rev. Mater. Sci. 17 (1987) 273−298 (Cz).

[48] A. Murgai, W. Patrick, J. Combronde, J. Felix, IBM J. Res. Dev. 6 (5) (1982) 546−552 (Oi).

[49] W. Tiller, Some unresolved theoretical problems in crystal growth Part II: consequences of properly accounting for surface creation, in: R. Trivedi, J. Sekhar, J. Mazumdar (Eds.), Crystal Properties and Preparation Vol. 22−25, Trans Tech Publications, Switzerland, 1990 (Facet).

[50] W. O’Mara, Silicon materials technology, in: G.E. McGuire (Ed.), Semiconductor Materials and Process Technology Handbook, Noyes Publications, Park Ridge, NJ, 1988, pp. 8−45.

[51] K. Jackson, Interface structures, in: R. Doremus, B. Roberts, D. Turnbull (Eds.), Growth and Perfection of Crystals, John Wiley and Sons, New York, 1958 (2D nucleation).

[52] K. Jackson, Kinetic Processes: Crystal Growth, Diffusion and Phase Transformations in Materials, Wiley-VCH, Weinheim, 2010 (2D nucleation).

[53] V. Voronkov, Sov. Phys. Crystallogr. 17 (5) (1973) 807−813 (Undercooling, facets).

[54] V. Voronkov, Sov. Phys. Crystallogr. 23 (1978) 249−256.

[55] D.T.J. Hurle, Crystal Pulling from the Melt, Springer-Verlag, Berlin, 1993 (Cz).

[56] P. Cousins, Proceedings of the 2010 35th IEEE Photovoltaic Specialists Conference, vol. 5, 2010, p. 275 (Oi).

[57] M. Binns, J. Kearns, E. Good, ECS Trans. 60 (1) (2014) 1233−1238 (Oi).

[58] J. Schmidt, K. Bothe, Phys. Rev. B 69 (2004) 024107.

[59] D. Elwell, Prog. Cryst. Growth Charact. 4 (1981) 297−316 (EOS).

[60] W. Zulehner, Mater. Sci. Eng. B73 (2000) 7−15 (Cz pulling).

[61] W. O’Mara, R. Herring, L. Hunt (Eds.), Handbook of Semiconductor Silicon Technology, Noyes Publications, Ridge Park, New Jersey, 1990 (Cz, Si).

[62] W. von Ammon, E. Dornberger, P. Hansson, J. Cryst. Growth 198/199 (1999) 390−398 (Large scale bulk properties).

[63] Y. Shiraishi, K. Takano, J. Matsubara, T. Iida, N. Takase, N. Machida, M. Kuramoto, H. Yamagishi, J. Cryst. Growth 229 (2001) 17−21 (400mm).

[64] Z. Lu, S. Kimbel, J. Cryst. Growth 318 (2011) 193−195 (450mm).

[65] G. Kubaschewski, T. Chart, J. Chem. Thermodyn. 6 (1974) 467 (SiO monoxide).

[66] W. Dash, J. Appl. Phys. 29 (1958) 736.

[67] W. Dash, The growth of silicon crystals free from dislocations, in: R. Doremus, B. Roberts, D. Turnbull (Eds.), Growth and Perfection of Crystals, John Wiley and Sons, New York, 1958.

[68] W. Dash, J. Appl. Phys. 30 (4) (1959) 459−474.

[69] J. Ryuta, E. Morita, T. Tanaka, Y. Shimanuki, Jpn. J. Appl. Phys. 29 (3B) (1990) L1497 (COPs).

[70] J. Burton, W. Slichter, The distribution of solute elements: steady state growth, Princeton, in: H. Bridgers, J. Scaff, J. Shive, D. Van Nostrand (Eds.), Transitor Technology, Volume 1, 1958, pp. 71−106 (Solute).

[71] W. Thurber, R. Mattis, Y. Liu, J. Filliben, NBS Special Publication 400-64, “The Relationship between Resistivity and Dopant Density for Phosphorous- and Boron-Doped Silicon”, 1981.

[72] H. Kubota, H. Nagano, J. Sugamoto, H. Matsushita, M. Momose, S. Nitta, S. Samata, N. Tsuchiya, High Purity Silicon VI: Proceedings of the Sixth International Symposium, Volumes 2000−2017, The Electrochemical Society, 2000 (VG).

[73] E. Dornberger, D. Temmler, W. von Ammon, J. Electrochem. Soc. 149 (4) (2002) G226−G231 (VG).

[74] J. Park, G. Lee, J. Park, S. Chon, 99-1, in: Proceedings of ECS Conference on Defects in Silicon III, Electrochemical Society, 1999, pp. 324−341 (VG).

[75] M. Itsumi, M. Maeda, J. Appl. Phys. 84 (1998) 1241.

[76] M. Itsumi, H. Akiya, T. Ueki, J. Appl. Phys. 78 (1995) 5894.

[77] Falster, Voronkov, in: Proceedings of the First International School on Crystal Growth Technology, 1998 (VG).

[78] T. Sinnoa, E. Dornberger, W. von Ammon, R. Brown, F. Dupret, Mater. Sci. Eng. 28 (2000) 149−198 (VG).

[79] V.V. Voronkov, R. Falster, J. Appl. Phys. 86 (1999) 5975 (VG).

[80] V.V. Voronkov, R. Falster, J. Cryst. Growth 226 (2001) 192 (VG).

[81] V. Voronkov, R. Falster, J. Appl. Phys. 87 (9) (2000) 4126−4129 (VG).

[82] J. Kearns, J. Holzer, Progress in continuous Czochralski crystal growth for silicon mono with dopant exhibiting segregation coefficient far from unity, in: Presentation at the 20th American Conference on Crystal Growth and Epitaxy, August 6, 2015 (CCz).

[83] E. Iino, K. Takano, M. Kimura, H. Yamagishi, Mater. Sci. Eng. B36 (1996) 146 (SEH CCz voids).

[84] N. Stoddard, R. Sidhu, J. Creager, S. Dey, B. Kinsey, L. Maisano, C. Phillips, R. Clark, J. Zahler, X. Xie, T. Wu, Q. Jiang, Evaluating BP Solar’s Mono$^2$ ™ material: lifetime and cell electrical data, in: 2009 34th IEEE Photovoltaic Specialists Conference (PVSC), Philadelphia, PA, 2009, pp. 1163−1168 (MLM).

[85] N. Stoddard, B. Gründig-Wendrock, A. Krause, D. Oriwol, M. Bertoni, T. Naerland, I. Witting, L. Sylla, J. Cryst. Growth 452 (2016) 272−275 (MLM).

[86] N. Stoddard, J. Russell, E. Hixson, H. She, W. Chester, A. Krause, F. Wolny, M. Bertoni, T.U. Nærland, L. Sylla, W. von Ammon, NeoGrowth Silicon: a new high purity, low-oxygen crystal growth technique for photovoltaic substrates, Prog. Photovolt. Res. Appl. (2018), https://doi.org/10.1002/pip.2984 (NGS).

[87] H. Furuya, K. Harada, J-G. Park, in: Defect reduction and improved gettering in CZ single-crystal silicon, Solid State Technology, 2001 (Pennwell).

# Further reading

[1] K. Bachmann, The Materials Science of Microelectronics, VCH Publishers, New York, 1995 (Facets, pulling).

[2] J.P. Kalejs, B. Chalmers, J. Cryst. Growth 79 (1986) 487−492 (Carbon).

[3] J. Ryuta, E. Morita, T. Tanaka, Y. Shimanuki, Part 2, Jpn. J. Appl. Phys. 31 (11) (1992) L293 (COPs).

[4] A. Chernov, Modern Crystallography III: Crystal Growth, Springer-Verlag, Berlin, 1984 (Cz etc).

[5] V.I. Voronkov, Sov. Phys. Crystallogr. 19 (1975) 573 (Surface angle).

[6] D.T.J. Hurle, P. Rudolf, J. Cryst. Growth 264 (2004) 550−564 (Defects).

# Solar silicon

# 3

*C.W. Lan*
National Taiwan University, Taipei, People's Republic of China

## 3.1 Introduction

Photovoltaics (PV) is a technology for converting sunlight into electricity. Although PV technology has been researched and developed for over 60 years, the growth of the solar market was initially slow; however, the pace has increased in recent years due to various incentive programs, particularly in Japan and Europe, and latterly mainland China. As compared with 740 MW of PV modules installed in 2003, more than 77 GW of modules were installed in 2016 and the accumulated installation capacity was over 320 GW [1,2]. Among these, 93% were made from crystalline silicon (c-Si), and approximately one-fourth (20 GW) were made from monocrystalline silicon (mono-Si) grown by the Czochralski (CZ) method, which is the method used for producing silicon for the semiconductor industry. The remainder, nearly 70 GW, were made from multicrystalline silicon (mc-Si) grown by directional solidification (DS) or casting. Interestingly, before 2010 the market shares of mono-Si and mc-Si were comparable, and in fact mono-Si was dominant in the early years. But with the emergence of high-performance (HP) mc-Si in 2011 [3–5], giving high yield, excellent uniformity, and low cost, DS-grown mc-Si has become the mainstream in the solar market, and its market share increased rapidly. However, the wafer price has dropped more than 10 times in the past 10 years [1,2], so finding ways to decrease production cost without sacrificing material quality remains the major challenge for crystal growers. Moreover, due to the low cost and high throughput of the DS method, DS-grown mono-like (ML) silicon became a promising product and was introduced to the market by BP Solar in 2007 [6,7]. In principle, if the defect concentration is sufficiently low, ML silicon could have nearly the material quality of CZ-grown silicon while having the low cost of the DS technology. Nevertheless, there are still some challenges, such as poor growth yield and uniformity, and these need to be conquered before ML silicon can take a share of the PV market. The floating-zone (FZ) method can also be used to grow solar silicon. However, for PV applications the need for low-cost wafers has been a big obstacle for FZ-grown silicon [1]; thus FZ technology is disappearing in the PV industry. Moreover, because pyramid texturing by alkaline chemical etching is used in mono-Si solar cell processing, all solar silicon has crystallographic orientation (100). In addition, the majority of solar cells use p-type wafers for historical reasons, mainly B and some Ga doped, and the resistivity level is around 1–3 Ω-cm. Nevertheless, the main reason for the use of mono-SI was that in the early days for space applications demonstrated by Bell Laboratory, the p-type Si substrate was less sensitive to degradation caused by exposure to cosmic rays. N-type wafers,

**Single Crystals of Electronic Materials.** https://doi.org/10.1016/B978-0-08-102096-8.00003-3
Copyright © 2019 Elsevier Ltd. All rights reserved.

doped with P, could also be used, but they are mainly used for high-efficiency solar cells. In this chapter we focus on discussion of CZ-grown and DS-grown mono-Si. The development of HP mc-Si is introduced for comparison.

Fig. 3.1(a) and (b) show photographs of silicon crystal growth by the FZ and CZ methods, respectively. Due to the high production cost, very few companies use the FZ method to produce solar silicon; but Topsil Semiconductor Materials A/S is one of the few putting a special effort into cost reduction to produce FZ solar silicon (PV-FZ). Through the design of multiple high-frequency induction coils, it was able to increase the pulling rate (up to one order or at least three times higher than CZ) and reduce the power consumption significantly [8]. PV-FZ was introduced to the market in 2002, but was mainly used for 6 in. pseudosquare (128 × 128 $mm^2$) solar cells. Because there is no crucible used in the FZ method, the oxygen content of FZ silicon could be as low as 1 or 2 ppma. Low-oxygen wafers are particularly suitable

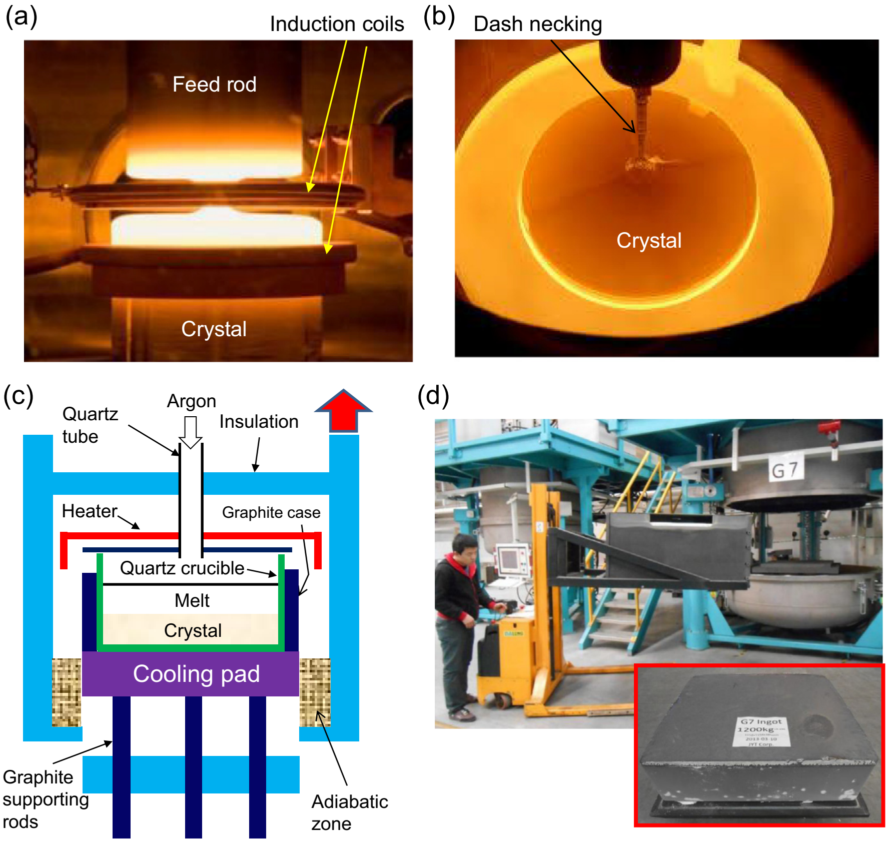
(a)
Induction coils
Feed rod
Crystal
(b)
Dash necking
Crystal
(c)
Quartz tube
Argon
Insulation
Heater
Graphite case
Quartz crucible
Melt
Crystal
Cooling pad
Graphite supporting rods
Adiabatic zone
(d)
G7
G7 ingot
1200kg

**Figure 3.1** (a) Floating-zone silicon growth; (b) Czochralski silicon growth; (c) schematic of silicon ingot growth by directional solidification; (d) photograph of a Gen 7 DS station; the inset photo is an ingot after growth (1151 mm × 1151 mm × 389 mm).
Courtesy of JYT Co C.W. Lan, C.F. Yang, A. Lan, M. Yang, A. Yu, H.P. Hsu, B. Hsu, C. Hsu, Engineering silicon crystals for photovoltaics, CrystEngComm 18 (2016) 1474−1485.

for high-efficiency solar cells because the light-reduced degradation (LID) caused by the B−O pairs is greatly reduced [9]. On the other hand, because there is not enough oxygen to strengthen the ingot, nitrogen doping is often necessary. The comparison of the FZ method with other growth methods for solar silicon is summarized in Table 3.1. As shown, due to the high thermal gradient, the pulling speed of FZ is the highest among all the methods, but the power consumption is the highest as well; more skillful operation is also needed. Although the consumables for FZ are less, the feed rod for FZ is costly. Dold et al. [10,11] proposed a new feed rod obtained from a fast-pulled CZ ingot, and the technology seems to be promising for PV applications. Unfortunately, in recent years, as the oversupply of solar silicon has slashed the wafer price dramatically, FZ material is disappearing from the PV market due to its higher production cost [1].

The CZ growth of solar silicon shown in Fig. 3.1(b) is pretty much the same as the method used in semiconductors, but the puller is often a low-cost machine without any fancy design. The hot-zone materials are also not as good as those used for semiconductor-grade Si production. The growth sequences, including the melting, dash necking, crown, shoulder, body, tail, and cooling down, are about the same as for semiconductor silicon. For ease of texturing during solar cell production using alkaline etching, the growth of mono-Si is in (100) orientation only. Fortunately, this direction is the easiest to grow. As shown in Fig. 3.1(b), there are four growth habit lines for this orientation. In addition, for solar silicon the production cost needs to be low, especially the electricity cost. For example, for semiconductor applications the

**Table 3.1** **Comparison of different growth methods for solar silicon**

| **Characteristics** | **FZ** | **Cz** | **DS (ML)** |
|---|---|---|---|
| Growth speed (mm/h) | 180−300 | 60−120 | 5−15 |
| Dislocation free | Yes | Yes | No ($10^4$ $cm^{-2}$) |
| Crucible material | No | Quartz | $Si_3N_4$ coated quartz |
| Consumable cost | Low | High | Low |
| PPH | High | Low | Very high |
| Axial resistivity uniformity | Low | High | High |
| Oxygen content (ppma) | 1−2 | 5−20 | <6 |
| Carbon content (ppma) | 0.1−0.2 | 2 | 6 |
| Metallic impurity content (ppma) | Low | High | Very high |
| Bulk minority lifetime (μs) | 1000−3000 | ∼100 | <100 |
| Production size (mm) | 100−150 | 150−200+ | 1000 |
| Operation skill | High | Less | Easy |
| Polysilicon feed | Crack-free rod | Chunk | Chunk |
| Seed size (mm × mm) | <10 × 10 | <10 × 20 | 156 × 156 |

power consumption for 8 in. silicon is usually in the order of 40 kW/kg; for solar silicon production, 20 kW/kg or even less is common, but this power consumption is still much higher than that used in the DS method (less than 10 kW/kg). Moreover, the pressure used in CZ is about 60 mtorr, the same as that used for semiconductor silicon. Because of the use of a quartz crucible, the oxygen content of a CZ solar ingot is usually slightly higher than 10 ppma. If a magnetic field is used, an oxygen level of several ppma is feasible. Again, due to the high oxygen content in CZ-grown silicon, the LID due to the B—O pairs is profound in solar cells. The standard size for mono-Si in industry is 8 in. or 200 mm. After slicing, the 156 mm × 156 mm wafers still have round corners, i.e., they are pseudosquare in shape. Recently a slightly bigger size, the so-called M1 or M2 size (156.75 mm × 156.75 mm), is becoming the mainstream in the PV industry as more power can be generated per solar cell. A normal CZ puller used for a solar ingot has a charge weight around 180 kg; the crystal pulled is more than 2 m in length. Although the bigger pullers could increase the throughput, the pullers also cost more. An alternative to increase the throughput and reduce the cost is to grow a few ingots from one crucible by using a charge feeder; in fact, continuous pulling of 10 crystals has been reported [12]. The continuous CZ (CCZ) method with double crucibles has also been used, especially for n-type silicon [13,14].

A schematic of the DS method is shown in Fig. 3.1(c) [15]. The DS technology for mc-Si has been developed for more than 30 years [3,16]. Nowadays the normal silicon charge per run for a Gen 6 furnace used in production is around 800—900 kg; a Gen 6 ingot could be cut into 6 × 6 bricks for wafer slicing (156 mm × 156 mm in size for standard solar cells). In 2006 the normal size was only Gen 4 with a charge of 270 kg. The hot zones for different generations are similar. Nevertheless, as the crucible dimension becomes bigger, a top heater becomes essential. The photograph shown in Fig. 3.1(d) is a Gen 7 DS station during loading, and the inset photo is a 1.2 ton ingot after crystal growth. In 2012 Gen 8 growth with a charge of 1.65 tons was demonstrated by MEMC Co. [17] The dimensions and normal throughputs for different generations of the DS furnace are summarized in Table 3.2 [5]. The DS growth of solar silicon also uses a quartz crucible. However, because the growing crystal is in contact with the crucible during its growth, to prevent sticking the crucible requires $Si_3N_4$ coating. As a result, to avoid the decomposition of $Si_3N_4$, the growth ambient pressure is higher than that in CZ, being about 0.5 atm, again in the argon environment; the growth pressure in CZ is about 60 mtorr.

As compared with the FZ and CZ methods, the production cost of a solar ingot by DS is the lowest, as shown in Table 3.1. This is due to its high throughput and low power consumption; the labor cost is also the lowest. However, the major product available in the market is still mc-Si, and the market share of ML silicon is small [1]. The challenges in growing ML silicon using DS are discussed below. In addition, due to the less pure quartz crucible and $Si_3N_4$ coating, as compared to the crucible used in CZ, the impurity contents in DS-grown solar silicon are normally higher [3]. Table 3.3 shows the typical impurity levels in the materials used in DS solar silicon [3]. Due to the higher impurity levels, the polysilicon feedstock in DS, which is normally called solar grade (SOG) silicon, is usually not as pure as the material used in CZ. As a result, the efficiency of solar cells made from DS-grown silicon is also lower.

Table 3.2 **The generations of DS technology and their dimensions and throughput [4]**

| | G5 | G5+ | G6 | G7 | G8 |
|---|---|---|---|---|---|
| Silicon charge (kg) | 450 | 600 | 800 | 1200 | 2000 |
| Ingot dimension (mm × mm × mm) | 840 × 840 × 275 | 840 × 840 × 360 | 995 × 995 × 350 | 1151 × 1151 × 390 | 1340 × 1340 × 500 |
| No. of blocks | 5 × 5 | 5 × 5 | 6 × 6 | 7 × 7 | 8 × 8 |
| Estimated yield (%) by removing red zone | 68 | 71 | 73 | 75 | 77 |
| Cycle/mon | 12 | 11 | 9.5 | 9 | 8 |
| Wafer no. | 14,300 | 17,000 | 27,000 | 43,000 | 69,000 |
| Annual output (MW) | 8.4 | 9.2 | 12.6 | 19 | 22 |

**Table 3.3** Impurity concentrations in crucible, $Si_3N_4$, and SOG silicon [3] expressed in ppma

| Element | Crucible | High-purity crucible | $Si_3N_4$ | High-purity $Si_3N_4$ | SOG Si |
|---|---|---|---|---|---|
| B | | | | $<10$ | $<0.05$ |
| P | | | | $<6$ | $<0.1$ |
| Al | $<1500$ | $<160$ | $<34$ | $<21$ | $<0.05$ |
| Fe | $<100$ | $<5$ | $<30$ | $<15$ | $<0.05$ |
| Ca | $<89$ | | $<1$ | | – |
| Ti | $<110$ | $<2$ | $<25$ | $<1$ | – |
| Ni | $<1$ | $<0.2$ | $<1$ | $<1$ | $<0.01$ |
| Mn | $<2$ | $<0.2$ | $<0.2$ | $<0.2$ | |
| O | | | $<16$ | $<1$ | $<5$ |
| C | | | | | $<5$ |

For ML silicon, solar cell efficiency is about 0.2%–0.5% lower than that using CZ wafers; currently the average efficiency for a p-type CZ mono-Si solar cell is around 20.5% using a screen-printing aluminum back surface field (BSF) structure [1].

Fig. 3.2 shows the PV value chain from polysilicon to solar cell modules. As discussed, the wafer shape is pseudosquare if produced from CZ or FZ mono-Si, and the solar cell has the same shape. Some space near solar cell corners in the solar module cannot be occupied, and this slightly affects the solar module efficiency. On the other hand, the surface texture of mono-Si by alkaline solution makes it easy to get a pyramid structure, as shown in Fig. 3.3(a). Due to the relatively slow etching rate in the

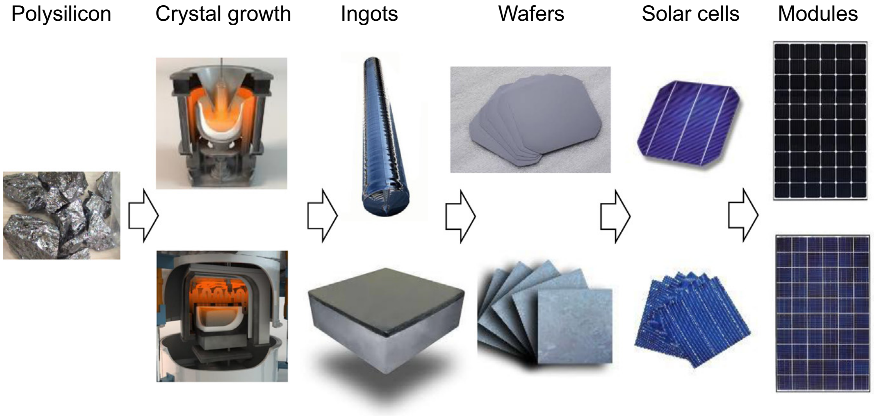

**Figure 3.2** The value chain of PVs from polysilicon to solar modules.

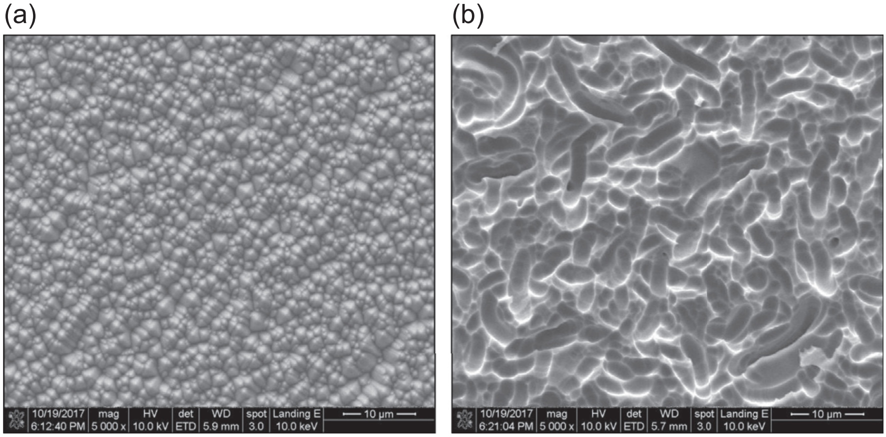

**Figure 3.3** (a) Alkaline texture morphology of monocrystalline silicon wafer; (b) acid texture morphology of multicrystalline silicon wafer.

(111) crystallographic planes, the anisotropic alkaline etching leads to the pyramid texture morphology having a low surface reflectivity for solar cells. On the other hand, for mc-Si the isotropic acid etching gives a worm-like morphology, as shown in Fig. 3.3(b), and the reflectivity is relatively higher, even after antireflection coating. The difference in the surface reflectivity contributes around 0.3% to solar cell efficiency. Thus if ML silicon is used, alkaline texturing can also be used, and solar cell performance could be better than for mc-Si. However, as compared to solar cells made from CZ wafers, the inferior material quality of DS-grown ML silicon results in solar cells with slightly lower efficiency. Nevertheless, because of the use of nitride-coated quartz crucibles, DS-grown silicon also has a low oxygen content, usually less than 6 ppma, which is located at the bottom ingot. Hence the LID of the solar cells is usually smaller than that when using CZ wafers.

In the following sections a detailed discussion on the CZ and DS growth methods for mono-Si is presented; DS-grown mc-Si is introduced for comparison. For the CZ method, the hot-zone design is particularly important to increase the pulling rate and reduce power consumption, as well as to enhance the lifetime of hot-zone components by argon flow control. For the DS method, we give a short review of mc-Si and the newly emerged HP mc-Si. The issues in the growth of ML silicon, especially defects from the seed joints, are discussed in detail. Section 3.4 is devoted to conclusions and perspectives.

## 3.2 The CZ method

The CZ method is the major process for growing mono-Si ingots. For PV, the annual production for c-Si solar cells was more than 76 GW in 2016 [1,2], in which about 20 GW were made from CZ-grown mono-Si. Of the mono-Si wafers, about 80%

were used for p-type BSF or PERC (passivated emitter rear contact) solar cells and the rest were used for n-type back contact or heterojunction (HIT) solar cells. The average cell efficiency during production is about 20.5% for BSF and 21.5% for PERC mono-Si solar cells. A record cell efficiency of 26.63% was recently achieved by Kaneka Co. for a back-contact HIT solar cell. The diameter of the pseudosquare wafers is 200, and 210 mm will soon become the mainstream in industry. For CZ growth, the ingot mass was around 180 kg; this will soon be 200 kg. Driven by CCZ technology, the ingot mass of mono-Si is expected to double within the next 10 years [1]. Currently, the cut wafer thickness, mainly sliced by diamond wire, is about 180 μm, and wafer price in 2016 was around 80 US cent/pc. Due to rapid cost reduction along the entire value chain, the R&D effort in CZ solar silicon is also focused on cost reduction. In the following sections we discuss a few directions for cost reduction, as well as some ideas for improving the material quality.

### 3.2.1 Hot-zone design

Most hot-zone designs for CZ growth are focused on cost reduction. An efficient hot zone is designed for high pulling speeds or high production per hour (PPH, kg/h) and low power consumption. A reduction of the consumables, such as argon and graphite components (mainly the heater and the crucible susceptor), is also important. Computer simulation has been a useful tool in hot-zone design and simulation, and several commercial computer packages, such as CGSim [18,19], are available. The calculated results are reliable if the thermal properties of used materials and the hot-zone geometry are known with reasonable accuracy.

As an example, we take a hot-zone design project in Sino-American Silicon Products Inc. (SAS) for discussion [20,21]. Although the data is a bit out of date, the general ideas are the same as for modern hot-zone design. In this project, 5.5 in. N-type solar silicon was pulled from Kayex CG6000 pullers, and then shipped to Sanyo (now Parasonics) for making HIT solar cells. The pullers were originally used for the growth of semiconductor silicon products. The major hot-zone components, the argon flow (right) and the thermal fields, are shown in Fig. 3.4(a) [20]. The hot-zone components were divided into six major components: (1) radiation shield (or cone); (2) top-side insulation; (3) additional side insulation; (4) bottom insulation; (5) top-wall insulation; and (6) argon venting. The default hot zone from Kayex did not include the cone and the top-wall insulation. The space for the bottom and side-wall insulation was still large. Both molybdenum (Mo) and graphite with coating were considered for the cone material. The main purpose of the cone is to block the thermal radiation from the melt toward the crystal, so the crystal can be rapidly cooled. The increase of the axial thermal gradient of the crystal also allows a further increase in pulling speed without excessive deformation of the growth interface. Fig. 3.4(b) shows photographs of both cones. The lifetime of both cones was long, but the Mo cone was more robust and could be cleaned easily by sand blast. In practice, the graphite cone can also be cleaned by high-temperature baking. Deposits with different thermal expansion coefficients fall off easily during baking.

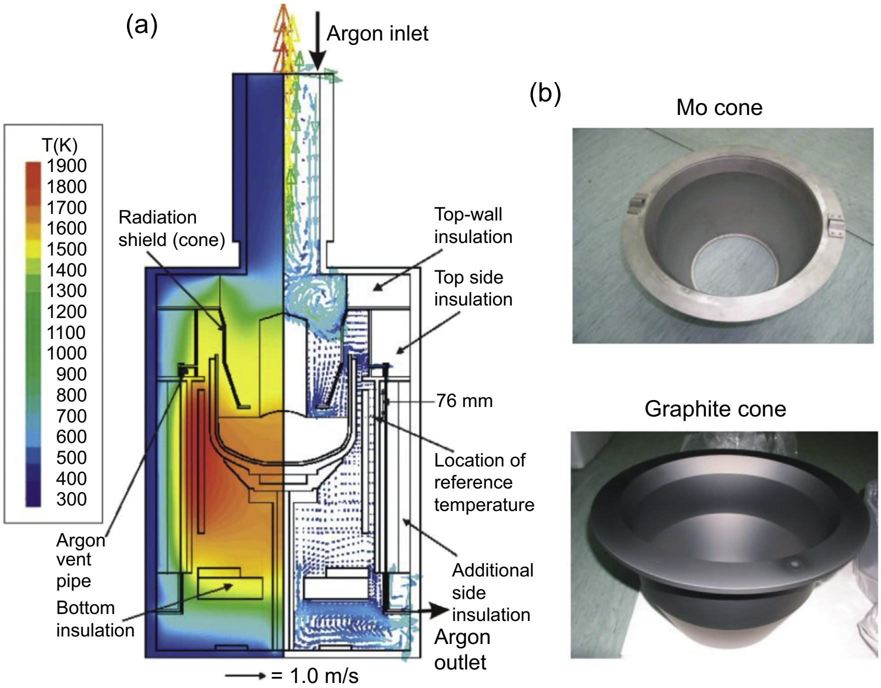
(a)
Argon inlet
T(K)
1900
1800
1700
1600
1500
1400
1300
1200
1100
1000
900
800
700
600
500
400
300
Radiation shield (cone)
Top-wall insulation
Top side insulation
76 mm
Location of reference temperature
Additional side insulation
Argon outlet
Argon vent pipe
Bottom insulation
= 1.0 m/s
(b)
Mo cone
Graphite cone

**Figure 3.4** (a) Typical hot zone and the simulated temperature (left) and flow fields for Cz silicon growth; (b) thermal shields (*cone*) made from molybdenum (top) and graphite. The crystal diameter is 5.5 inch [20].

### 3.2.2 Power consumption and pulling rate

The power and growth rate histories without and with the Mo cone are shown in Fig. 3.5. At the beginning, with the Mo cone the dipping power was reduced by more than 25 kW. This power remained till the end of the growth. The initial pulling rate after seeding was very high, up to 120 mm/h, and this was necessary for better diameter control. At this stage, due to the large cooling from the crystal shoulder, a high growth speed was inevitable. As the growth proceeded, the rate was reduced gradually to enhance growth stability. Near the end, a slower growth rate was used for tailing; without this speed reduction there was a higher risk of a sudden detachment of the crystal from the melt, which could cause thermal-shock damage to the bulk crystal. With the Mo cone, the average growth speed was slightly increased from 45 to 60 mm/h. With further hot-zone improvement, a body growth speed of 80 mm/h was achieved [21]. The calculated interface concavity in the original hot zone was 9.9 mm; however, with the Mo cone the interface concavity was reduced to 5.1 mm. In other words, there was still some room to increase the pulling speed for the Mo cone. Good agreement on power consumption was obtained, as shown in Fig. 3.5.

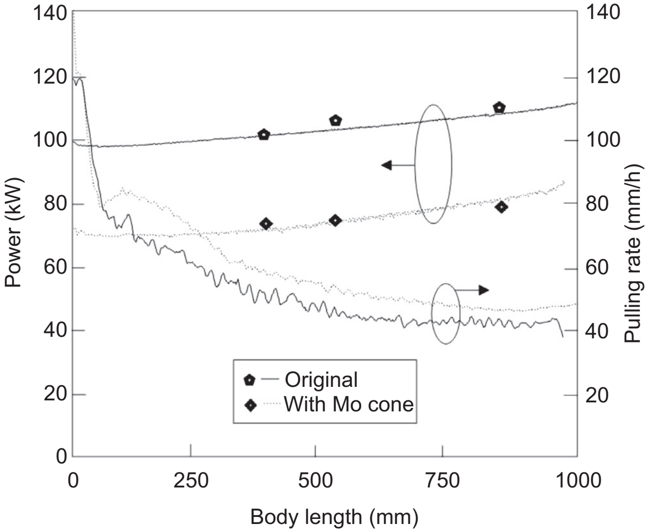

**Figure 3.5** The effect of a molybdenum cone on the power consumption and pulling rate [20].

Further improvement can be made to achieve lower power consumption, higher growth rate, or lower interface concavity. However, these factors are hard to optimize in parallel and normally a compromise has to be sought. Three additional types of insulation were also considered. The simplest, without much influence on the growth conditions, is additional side insulation. However, the improvement in the power consumption was quite modest: only about 2 kW on average. Bottom insulation was considered as well, and an additional 8 kW could be saved. The power consumption could be further reduced to 64 kW with a SiC-coated graphite cone and additional side and graphite-felt bottom insulation. In this case the growth speed of the main body section was about 75 mm/h, but the interface concavity also increased. At the end of the project in 2004, the power used for main body growth was lower than 55 kW, while the growth speed for the body increased to 80 mm/h [21]. Moreover, after the redundant electrode bases were removed, an additional 5—10 kW could be saved. Finally, a power consumption of 50 kW or slightly lower was achieved.

Through this hot-zone design, the maximum total saving per kg of silicon (kWh/kg) was more than 58%, which was comparable to the SSI/NEEA design [12]. Interestingly, if we allowed a faster growth speed (about 80 mm/h was feasible) toward the crystal end in the modified hot-zone designs, the growth time could be reduced substantially beside the lower power usage. Then an additional 5% of power could be cut, and the total power saving per kg ingot could be more than 60%. Furthermore, the use of a Pyrolytic carbon-coated graphite cone, which has better reflectivity, gave a better performance than the SiC-coated cone. Recently active cooling, such as a water-cooled tube or spiral [22] around the ingot, has also been adopted. Due to the large thermal gradient in the growing crystal, the pulling speed could be greatly enhanced; a main body pulling speed of more than 100 mm/h would be feasible.

### 3.2.3 Argon consumption and graphite degradation

During silicon growth, oxygen is dissolved from the crucible into the melt forming silicon monoxide (SiO). Carrying SiO away from the melt by argon flow is very important in practice. SiO easily reacts with graphite components at high temperature, forming SiC and CO; the former reduces the component lifetime, while the latter increases the carbon content in the growing crystal. On the other hand, too much deposition of SiO particles on the cooler surfaces, such as the chamber wall, crucible inner wall, and ingot surface, could cause problems when the particles fall into the melt. The structure integrity is lost, i.e., dislocations are generated if the particles are incorporated in the growing crystal. In this case the growth needs to be restarted, and the PPH or growth yield is significantly affected. The argon flow rate and path are important in avoiding this catastrophe. Furthermore, with the cone it was observed that argon flow consumption could be significantly reduced. The major reason was that the flow space between the cone and the melt was small and the argon flow across the melt surface became faster. Accordingly, the removal of SiO from the melt surface was more effective. Indeed, when the cone was used the argon flow rate could be reduced from 60 to 15 slpm. This corresponded to the specific argon usage of 27 cf/kg of Si; the original was 93 cf/kg. The argon flow path is shown by the vector field on the right-hand side of Fig. 3.4(a). With the cone, near the melt surface no flow circulation was found, which minimized the possibility of falling SiO particles. Moreover, with the top-wall insulation or a composite cone, SiO deposition was further reduced due to the increase of temperature there.

Beside the argon consumption, the original argon flow path had to go through the graphite heater and SiO reacted with the graphite, forming silicon carbide. This deteriorated the heater and shortened its lifetime; the graphite susceptor suffered the same degradation. By redirecting argon to the pipes embedded inside the side insulation, we found that the heater and susceptor lifetimes could be significantly extended. Over the project period, heater lifetime was increased to 4600 h from the original lifetime of 3000 h. The susceptor lifetime was increased to 1500 h, which was almost double the original (880 h). Fig. 3.6 shows photographs of the heater before (Fig. 3.6(a)) and after (Fig. 3.6(b)) the venting pipes were installed. As shown, when argon was

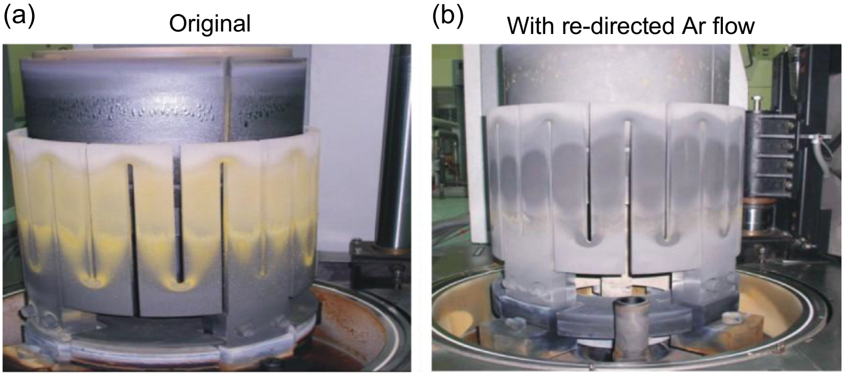

**Figure 3.6** SiO deposition on the heater: (a) without redirected argon flow; (b) with redirected argon flow [20].

redirected to the venting pipes in the side wall, the deposition of SiO on the heater was significantly reduced after crystal growth. Nowadays such venting pipes for argon flow are widely adopted, e.g., in the Kayex KX170 pullers.

Moreover, using software to design and modify the hot zone for solar silicon is very common. With the advance of computing power, in addition to the flow and temperature fields detailed chemical reactions, including SiO and CO, can be considered. The simulated deposition of SiO on the cone and the heater by CGSim was in good agreement with the experimental observations [20].

### 3.2.4 Multiple charges

The PPH for 6–8″ diameter ingot growth is usually below 2 kg/h. The easiest way to increase PPH in practice is to increase the charge size. A typical charge for a CZ puller, such as the Kayex 6000 for 6–8″ ingot growth, is less than 100 kg. Nowadays the normal charge for solar ingot growth has increased to 180–200 kg. Multiple charges are also an effective way to increase PPH. In other words, after a crystal is pulled out and removed, without cooling down, new feedstock can be fed from a feeder. In SSI, with the feeder the PPH for 6″ diameter ingots has been pushed to 1.7 kg/h [12], and 10 crystals can be grown from the same silica crucible. A similar design has also been adopted for semiconductor applications. Fig. 3.7 shows a typical Kayex 150 puller with the installation of the feeder and the recharge tank. PVA TePla pullers have a similar feeder design. Typically, the feeder requires granular or small-chunk polysilicon. This kind of multiple charges can save time for cooling down and thus improve PPH. Meanwhile, since several crystals can be pulled out from one crucible, the crucible cost per kilogram of silicon is greatly reduced. Typically, five crystals

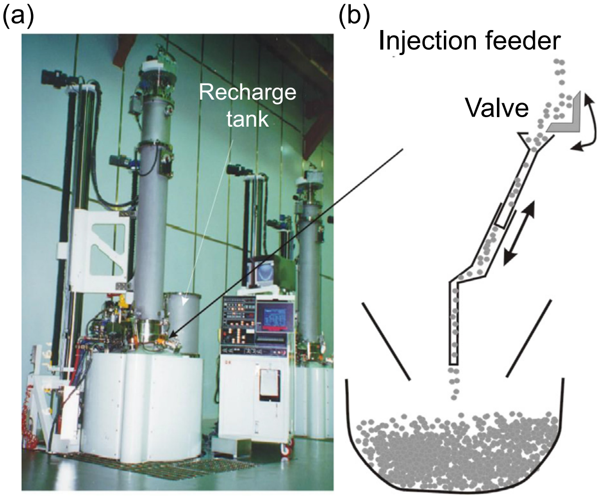

**Figure 3.7** (a) Czochralski silicon puller with recharge tank; (b) schematic of injection feeder [21].

(150 kg each) can be grown from a 22″ diameter crucible for semiconductor applications. If such a puller is used for a solar ingot, a PPH up to 4−5 kg/h can be anticipated.

For semiconductor applications the problems of using multiple charges are metal contamination during recharge and the impurity accumulation in the crucible. The former problem can be resolved by careful design of the feeder and the materials used. However, for impurity accumulation one has to use high-purity granular polysilicon. Fortunately, for solar silicon both problems are greatly relieved because of the lesser purity requirement. The improvement of PPH further reduces the specific energy consumption (kWh/kg). In SSI, with multiple charges the overall specific energy saving was over 51% [12]. In SAS, before the project the electricity consumption was 59.1 kWh/kg; after hot-zone optimization and using multiple charges the electricity consumption was reduced to only 17.4 kWh/kg for 5.5″ diameter ingots. For 8 in. silicon this figure is even lower due to high PPH. In the past few years the electricity consumption in CZ silicon has been greatly reduced, and for the growth of 200 mm solar ingot, 20 kWh/kg is quite common.

### 3.2.5 Coated crucible

The quartz crucible is a major cost in solar silicon production, and unfortunately no cheap crucibles are available for PV applications. The production of a quartz crucible is quite tedious, and a multiple-layer design is necessary. The outer layer of the quartz crucible often need to be less dense, the so-called bubble layer, to make the crucible a good insulator, while the inner layer has to be prepared with a denser and stronger amorphous structure. During crystal growth at high temperature, the devitrification of silica forms crystobalite. This often detaches from the crucible surface and causes dislocations in the growing crystal. For multiple charges the situation is even worse, due to the long operation time, and a special coating on the inner crucible surface is necessary. Typically, a dense barium silicate coated layer is used, as reported in one patent [23]. In this GE patent barium oxide is used as a good devitrification promoter that helps to form a uniform crystobalite layer on the crucible inner surface during crystal growth; hence the particle generation is reduced. Adding Ba or Sr before or during melting down is also useful to form a devitrification layer on the inner surface of the crucible.

### 3.2.6 The continuous CZ method

In addition to multiple charges, the CCZ method has been developed for high PPH production, as illustrated in Fig. 3.8(a) [24]. The CCZ method is particularly useful for n-type silicon. Because the segregation of phosphorus is small (0.35), the use of continuous charging effectively reduces the segregation. In principle, it is also suitable for Ga-doped silicon. However, the lifetime of the crucible, the accumulation of the impurities, and the buildup of SiO remain the key challenges for CCZ technology. Fig. 3.8(b) shows the minority lifetime from five ingots continuously pulled from a CCZ puller [14]. As shown, the average lifetime decreased with the ingot numbers. Although the resistivity uniformity was reasonably good, ranging from 5 to 6 Ω-cm,

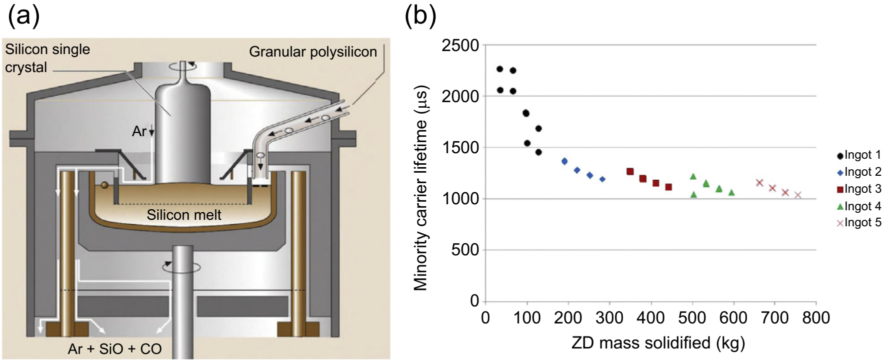

**Figure 3.8** (a) Schematic of CCZ silicon growth [24]; (b) minority-carrier lifetime zero-dislocation (ZD) ingots [14].

both the oxygen and carbon contents increased with the ingot numbers. Thus hot-zone design is quite important in CCZ to mitigate these issues. The reduction of SiO buildup through flow control is crucial to reduce SiO particles that cause structure loss. Wang et al. [13] also developed a shallow two-crucible CCZ with three heaters. Because of the shallow melt used, the turbulent flow can be suppressed.

Due to the high demand for low-cost n-type solar silicon for high-efficiency solar cells, the development of CCZ technology has been accelerated in recent years. Solaicx designed CCZ equipment optimized for solar silicon, and this was acquired by SunEdison Solar in 2010. According to the patent application by SunEdison Solar, the axial resistivity variation of the CCZ-grown ingot was within 10% [25]. In 2016 GCL-Poly Energy purchased SunEdison Solar's assets and continued to improve the technology. To realize continuous feeding, it has used 1—5 mm or broken polycrystalline ships for continuous charge. Between three and six ingots, each 3500—4500 mm long, can be pulled from one quartz crucible.

### 3.2.7 Quality improvement

Crystal quality is directly related to solar cell efficiency, thus it is crucial to the overall PV cost. One of the major indicators for the solar cell performance of a wafer is the minority-carrier lifetime. The control of oxygen and carbon contents has been found important to improve the minority-carrier lifetime, especially for n-type silicon [26]. Oxygen precipitates usually reduce the minority-carrier lifetime by the introduction of high strain fields [27,28]. On the other hand, carbon and its complex act as the nuclei for oxygen precipitation, and they are harmful as well [26]. Transition metals are also detrimental (e.g., Macdonald and Geerligs [29]). The oxygen content in the grown crystal is affected by many factors. However, the crucible temperature is believed to be important. With a lower crucible temperature, the oxygen dissolution into the melt is less. Based on hot-zone simulation [20], it was observed that the crucible temperature in contact with the melt decreases with the decreasing power consumption.

Thus an energy-saving design is favorable for reaching a lower oxygen content. However, the oxygen content in the CZ-grown ingot is usually greater than 10 ppma, and this would have sufficient number of B—O pairs for p-type ingots and the LID would be quite significant [9].

In addition to oxygen and carbon, transition metals and types A and B swirls have negative effects on the minority-carrier lifetime [30]. Thus controlling the growth at a high $V/G$ ratio, where $V$ is the growth rate and $G$ the thermal gradient, for getting a vacancy-rich ingot [31,32] is helpful. Yet near the crystal shoulder, due to the higher cooling rate there, getting vacancy rich is difficult unless an exceptionally high pulling rate is used. Accordingly, the oxidation-induced stacking-fault ring (OISF ring), which a visible boundary roughly separating the vacancy-rich (inside) and the selfinterstitial-rich (outside) regions, is often observed in solar ingots near the shoulder. The minority-carrier lifetime is also shorter there. Again, through enhanced growth speed using a high-performance hot zone, most of the grown ingot can be vacancy rich, and the portion of interstitial rich is significantly reduced [32,33]. On the other hand, there is always a trade-off for the growth rate. The cooling rate, i.e., $VG$, is proportional to the pulling rate, and the minority-carrier lifetime often decreases with the increasing cooling rate [30]. Hence using an optimal $V/G$ for growth is necessary for crystal quality [21,32].

In recent years, to reduce the LID due to B—O pairs, gallium doping has been considered for p-type silicon [34]. However, the severe segregation for this impurity greatly reduces the growth yield of the ingot. To enhance the mechanical strength of the wafers and reduce the occurrence of breakage during slicing and solar cell processing, as well as LID, germanium doping has also been considered [35,36]. Nitrogen doping is useful to increase the mechanical strength of silicon [36,37]. A nice review of impurity engineering in CZ silicon can be found in Yu et al. [38]. Using a magnetic field (the so-called magnetic CZ or MCZ) to reduce the melt convection and crucible dissolution in low-oxygen (~5 ppma) solar silicon is also possible, but at the expense of higher production costs. A detailed discussion of MCZ and a review of CZ technology can be found in the literature [11,39].

## 3.3 The DS method

The DS or casting method is a low-cost and high-throughput method for growing solar silicon, mainly mc-Si [3,15]. As compared to the CZ method, the energy consumption for DS is very low (<10 kWh/kg). The DS station used in industry is highly automated, so the required labor cost is also very low; normally a process engineer can take care of 5—10 growth stations. As a result, during the PV boom period in the past 10 years significant investment has been made in this technology, especially in China and Taiwan. The size of the furnace also increased rapidly during this period to reduce costs. Nowadays a normal silicon charge per run for a Gen 6 furnace used in production is around 800—900 kg. The growth cycle is about 3 days, or 9—10 cycles per month, as shown in Table 3.2. Normally the ingot yield after removing the red zone, the area near the crucible wall and top surface with a low lifetime, is more than 70%, so the weight of the 36 bricks is about 584 kg. About 27,000 wafers can be sliced from the bricks, i.e., 46 wafers/kg Si with a thickness of 190 μ, by using slurry-based wire (SW) sawing. The wire thickness for SW slicing is 120 μ and size of the SiC grit is 12 μ. This could lead to a kerf loss of more than 40%. If diamond wire (DW) slicing is adopted, more than 33,000 wafers could be obtained per ingot as the kerf loss is greatly reduced thanks to a smaller wire thickness (about 70 μm). Currently, the market share of DW slicing is about 80% for mono-Si and 50% for mc-Si. In 2017 the faster adoption of DW slicing for mono-Si significantly eroded the mc-Si market because of the much lower slicing cost and higher wafer throughput. It is expected that the DW share for mc-Si will pick up very quickly in 2018.

### 3.3.1 HP mc-Si

In this section we briefly introduce the HP mc-Si, which was introduced in 2011 and soon became the mainstream in the PV market. Although DS has been a mature technology for many years [3,15], due to the higher concentration of structure defects and impurities the ingot quality of mc-Si has been much inferior to the dislocation-free mono-Si grown by the CZ method. Therefore, to mimic the CZ-grown mono-Si, over the past 30–40 years tremendous effort has been focused on the growth of large grains with fewer grain boundaries (GBs). Even with fewer GBs, electrically inactive GBs, especially the Σ3 twin boundaries, are preferred. Among these efforts, the ML [6,7] and dendritic casting techniques [40–42] are the most typical. Due to the limited size of the mono-Si seeds from the CZ ingot, the splitting seeds are usually necessary in the DS growth of ML ingots, as illustrated in Fig. 3.9(a). The seed orientation is usually (100), again for the sake of alkaline etching surface texturing during solar cell production. Instead of using seeds, the dendritic casting technique makes use of the characteristic growth habit of silicon, having facetted dendrites at high undercooling to initiate a dendritic layer, as illustrated in Fig. 3.9(b). Because the lateral dendritic growth at high undercooling (>10 K) is in the <110> direction, the crystal grains follow the <112> growth direction. Both approaches are effective in the growth of large grains with fewer GBs, and the GBs in dendritic casting are mainly Σ3. By using

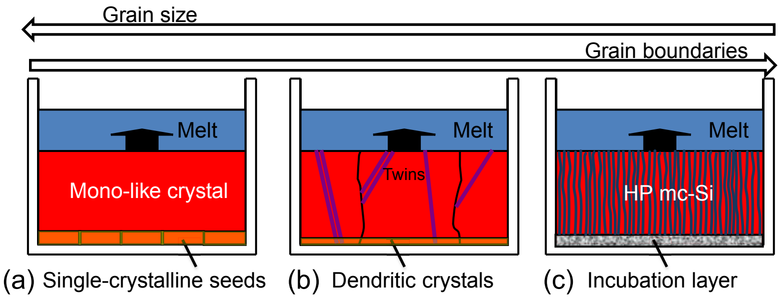

**Figure 3.9** Schematic of different DS technologies: (a) ML casting using splitting seeds; (b) dendritic casting; (c) HP mc-Si.

the dendritic casting method [43], the grown ingot can have up to 80% of Σ3 GBs and low defects, exhibiting a very high minority-carrier lifetime in small ingots. Even in industry-scale wafers, the twinning area had relatively low defect density and high minority-carrier lifetime [44].

Although high-quality ingots have been demonstrated for both ML and dendritic casting techniques, the multiplication and propagation of dislocation clusters due to thermal stress are still very difficult to control during crystal growth, especially for industrial-scale production. As a result, the solar cells fabricated from the wafers grown by both techniques have a very wide distribution in conversion efficiency, and the low-efficiency tail in the distribution causes significant yield loss in cell production. During the development of the dendritic casting method, Yang et al. [4] found that occasionally small grains could be induced by controlling the undercooling, and surprisingly the ingot grown from small grains turned out to have much better uniformity. The defect multiplication and propagation were significantly mitigated. To implement small-grain growth, they later used silicon particles ranging from 2 to 5 mm as seeds for mass production. Smaller particles could also be used, but the material could be easily contaminated due the larger specific surface area. They named the seed layer for small grains the incubation [4] or nucleation promotion layer [45], as illustrated in Fig. 3.9(c), and the relevant growth of such small-grain ingots was called the HP mc-Si method. The use of nucleation agents was also found helpful [45]. However, using silicon particles was found to be very robust in mass production in terms of ingot quality, but the melting stage required more care to keep a flat melting interface. As the red zone (the low-lifetime area created by impurity diffusion from the crucible and the contaminated seeds) above the seed layer was found to be proportional to the remaining thickness of the seed, the remaining seed layer needed to be thin as well. Because of the small randomly oriented seeds, in the HP mc-Si wafers the percentage of noncoherent or random GBs was unprecedentedly high, more than 70%. However, beside the improved ingot quality and minority-carrier lifetime, the solar cell performance was significantly improved, and especially the efficiency spread was very narrow.

The results of HP mc-Si were first presented in the Fifth International Workshop on Crystal Growth Technology in June 2011 [44,46], and later in the Fifth International Workshop on Crystalline Silicon Solar Cells held in Boston, MA, in November 2011 [47]. More detailed disclosure was given at later conferences [48,49]; detailed discussion can be found elsewhere [4,5]. The patent for such grain structures in the ingot and the wafer was filed in 2011 and granted in 2014 [45]; both silicon and nonsilicon particle seeds were used for ingot growth of HP mc-Si in the illustrated examples. After this finding, different approaches for getting such a grain structure have been explored [50−54].

Fig. 3.10(a) shows the comparison of HP and conventional mc-Si. The lifetime mappings of both ingots are shown in Fig. 3.10(a), where the HP mc-Si ingot was grown from small silicon particles [4,49,50]. It is apparent that the minority-carrier lifetime of HP mc-Si was very uniform, and the low-lifetime areas due to dislocation clusters were significantly reduced. Fig. 3.10(b) shows the grain structures of the wafers at the bottom and top portions of the ingots. As shown for HP mc-Si, the grains

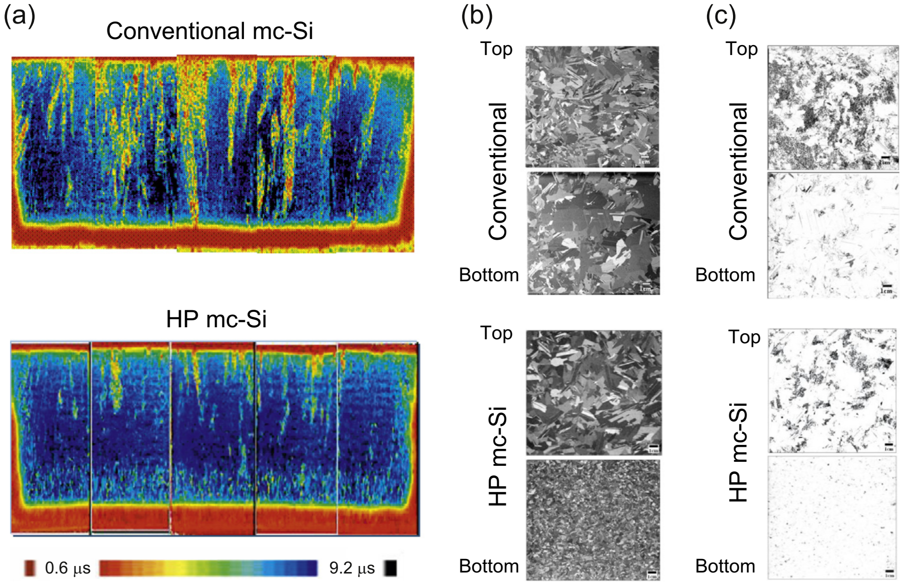

**Figure 3.10** Comparison of (a) ingot lifetime mapping, (b) grains and (c) EPD mapping at ingot bottom and top for conventional (top) and HP mc-Si; the ingot width in (a) is 780 mm and wafer size in (b) and (c) is 156 mm × 156 mm [15].

near the bottom part of the ingot were small and uniform, whereas the grains were large but nonuniform in conventional mc-Si. In general, the grain size increased with the increasing ingot height for both growths, but sometimes the grain size decreased in conventional mc-Si due to the nucleation of new grains from grits, subgrains, or twins [44,50]. More importantly, as shown by the etch pit density (EPD) mappings in Fig. 3.10(c), the high-EPD areas in HP mc-Si were much less and were confined within the small grains. Because of the columnar grain growth in HP mc-Si, the propagation of dislocation clusters from the bottom to the top was easily blocked by the random GBs [55]. Furthermore, because the defected grains tended to be softer, due to the plastic deformation assisted by the dislocations, they were easily overgrown by others [4,5,48−50,55]; and the large number of random GBs seems to quite effective in relaxing the thermal stress, presumably due to the sliding nature of the amorphous layer at the GBs [4,5,38−50,55].

In addition to the use of silicon particles for seeding, the use of a nucleation agent for getting small grains can be helpful [52−54]. A few nucleation coatings have been considered, including silica, silicon nitride, and their mixtures with silicon particles [53], and some have been adopted in production. Using a nucleation agent significantly reduced the red zone thickness. As a result, the growth yield was increased. On the other hand, as compared with silicon seeding, the initial percentage of non$\Sigma$ or random GBs ($\sim$50%) of the ingot was found to be lower when using a silica nucleation agent. Interestingly, Kupka et al. [56] also observed that although small grains could be initiated from SiC particles, the fraction of $\Sigma 3$ GBs was not low. On the contrary, the silica nucleation layer gave grain structures closer to HP mc-Si, i.e., small grains with a high fraction of random GBs. The silica particles used previously were presumed to be in the β-cristobalite phase during nucleation. Increasing temperature gradients was found to facilitate getting smaller grains by nucleation control; however, the fraction of Σ3 GBs depended on the coatings. The quality and thus the solar cell performance of the ingot grown from the nucleation agent were usually found to be slightly inferior to that of ingots grown from the silicon particles. This indicated that the amount of "random GBs" would be more crucial for stress relaxation and thus defect reduction, instead of just the small grains. This observation was consistent with recent experiments by Reimann et al. [57] showing that the longer length of random GBs from the seeds led to smaller EPD in the grown ingot.

### 3.3.2 ML silicon

Besides the development of mc-Si, many companies paid attention to the ML technique after the Mono2 wafers of BP Solar appeared on the market in 2006 [7]. In 2011 a few companies announced the success of ML silicon production; examples are the U-grade wafers from SAS, Virtus wafers from Renasolar, S2 wafers from GCL, Maple wafers from JA Solar, etc. SAS also branded the <110> ML wafers the E-wafers, and these were found to have better lifetime uniformity in ingot production, even though the texturing in the solar cell processing was more complicated. Although the ML technology attracted much attention in 2006, it stayed on the market for only a short time [58]. After HP mc-Si emerged in late 2011 [3−5], ML wafers pretty much disappeared from the market after 2012.

In the early days of DS growth, seeded growth was considered [16], but the ingot quality was not as good as expected. Seeded growth for DS silicon was forgotten for a long time and rediscovered only in 2006 when a research group at BP Solar reported the growth of large DS-grown mono-Si ingots by using splitting seeds, the so-called ML or quasimono method [6,7]. BP Solar branded its ML wafers Mono2 in early 2006. However, the ML wafers did not receive much attention until 2011 due to the sluggish development of the dendritic casting technique. Unfortunately, the ML technology itself was not that easy. Its major drawbacks are nucleation from the crucible wall; seed cost; and uncontrolled defect generation and multiplication, especially from the seed gaps.

#### 3.3.2.1 Nucleation from the crucible wall

Grain formation from the crucible wall is a well-known problem in the growth of single crystals. Through the control of the convex growth interface via hot-zone design [59−63], nowadays 90% of the ingot can remain almost monocrystalline. For example, Fig. 3.11 shows an infrared scan of two ML ingots from different hot zones using partition blocks [61]. If the growth interface was concave near the crucible wall, new grains from the crucible wall could be easily induced, as shown in Fig. 3.11(a). In contrast, as shown in Fig. 3.11(b), a convex growth front significantly reduced grain formation from the crucible wall. Recently, Kutsukake et al. [64,65] arranged the

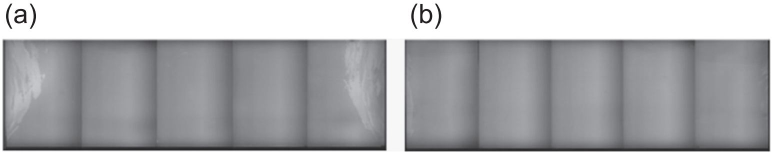

**Figure 3.11** Infrared scan of central bricks: (a) Case 2; (b) Case 3 partition block [61].

orientation of the extra seeds to have the {310} Σ5 GB as the functional GB within the central seeds, which could block the inward growth of the grains from the crucible wall. Wu et al. [66] and Lan et al. [67] used a 20° tilt GB, which also effectively blocked the grains and the defects from the crucible wall when the growth front was convex.

Recently, Trempa et al. [68] reported a systematic study to understand the new grain formation from the crucible wall and the junction of split seeds. They used seeds with orientation varied between ⟨100⟩, ⟨111⟩, and ⟨110⟩; in some cases, split seeds were considered. They showed that the nucleation at the crystal periphery as well as the gap between the split seeds depend on the seed orientation. The typical <100> direction turned out to be the most difficult one to grow an ML ingot. The twin nucleation at the {111} facets was used to explain the formation of misoriented grains, as illustrated in Fig. 3.12(a) [68]. As shown in the figure, as the undercooling ΔT at the edge is high enough for nucleation, the layer L, which could be oriented or misoriented, grows until it reaches the melt/solid interface. The process is repeated until the undercooling is not enough for nucleation. This growth mode, the so-called Frank—van der Merwe growth [69], is quite rapid compared to the normal growth rate of the facet. The twin orientation is {221}, consistent with the calculations by Wilhelm [70] for first-order twinning on {111}. Fig. 3.12(b) is an example of new grain formation from the crucible wall for growth from a {100} seed. It turns out that the growth in the {111} direction is more prone to have twin grains from the crucible wall. In conclusion, the control of a convex interface with lower undercooling at the crucible wall is crucial in minimizing twinning.

### 3.3.2.2 Seed cost

The seeds for ML silicon growth are from CZ mono-Si, thus the cost of the seeds is not trivial. The cost issue could be mitigated by better control of the interface shape and back melting, so the seed thickness could be greatly reduced to 1—3 cm. In addition, if the seeds can be recycled a couple of times without affecting the ingot quality too much, the cost can be further reduced. Thus the reduction of the red zone and the damage inside the seeds is important for seed recycling. For ML growth, the red zone is caused by the diffusion of metallic impurities from the melt during melting, the impurities being mainly from the crucible [71]. Hence a purer crucible and coating, as well as careful seeding, are important in reusing the seeds.

Miyamura et al. [72] proposed an idea of using a small seed (20 cm in diameter) for growing a bigger ingot (50 cm in diameter). With careful control of the growth front and the thermal environment, they were able to grow an ingot with a very low dislocation density of $10^4$ $cm^{-2}$. The carbon content was also suppressed with an effective argon flow. This would be a good direction for future ML development.

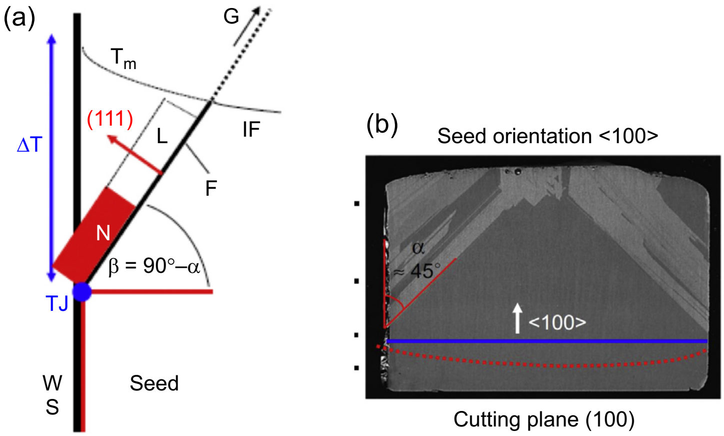

**Figure 3.12** (a) Sketch of a seed edge near the crucible wall W or another seed crystal S with a {111} facet plane (*bold line* F) oriented at an angle to the horizontal x direction. $T_J$ is the position of the triple junction of melt—seed—crucible wall or melt—seed—seed. A two-dimensional nucleus N is formed at the lower edge of the {111} facet where the supercooling DT is maximum (at $T_J$). The size of the nucleus N is blown up in the figure to aid legibility. The nucleus N grows in the direction of the arrow G, thus completing the layer L until it reaches the melting-point isotherm $T_m$ (*dotted line*). The melting-point isotherm $T_m$ is identical to the interface IF, where the original seed grows with a facetted interface. (b) Scan image revealing the <100> grain orientation of the vertical cut at {100}.
Both figure and photograph are reproduced from M. Trempa, C. Reimann, J. Friedrich, G. Mueller, D. Oriwol, Mono-crystalline growth in directional solidification of silicon with different orientation and splitting of seed crystals, J. Cryst. Growth 351 (2012) 131—140, with permission of Elsevier.

### *3.3.2.3 Defect formation*

The defect formation issue is much more troublesome in the ML technology. Although some ideas have been proposed in the patent literature to overcome the problems using different seeding concepts, the control of dislocation multiplication is still difficult. Jouini et al. [73] reported some nice results for n-type ML ingots. Fig. 3.13(a) shows the arrangement of the (100) seeds in their G5 experiment. As shown, in addition to the central 5 × 5 seeds, there are extra seeds near the edges which can be used to accommodate the red zone or the grains nucleated from the crucible wall. The appearance of the grown crystal is shown in Fig. 3.13(b): the seed print could be clearly seen from the top surface due to the use of tilted GBs [66]. Moreover, if the seeds were not properly arranged, defects could be induced easily from the seed joints, as shown on the left of Fig. 3.13(c). Again, they could multiply upward easily. However, for the nondislocated GBs, as seen in the right figure, no defect propagation was observed. Nevertheless, dislocation clusters could be generated near the upper part of the ingot due to the accumulation of thermal stress. As shown in Fig. 3.13(c), the bottom red zone was rather thick. The best part of the ingot, near the middle height, was used for solar cells, and the cell efficiency was more than 21.5% [73]. Again, due to the higher density of

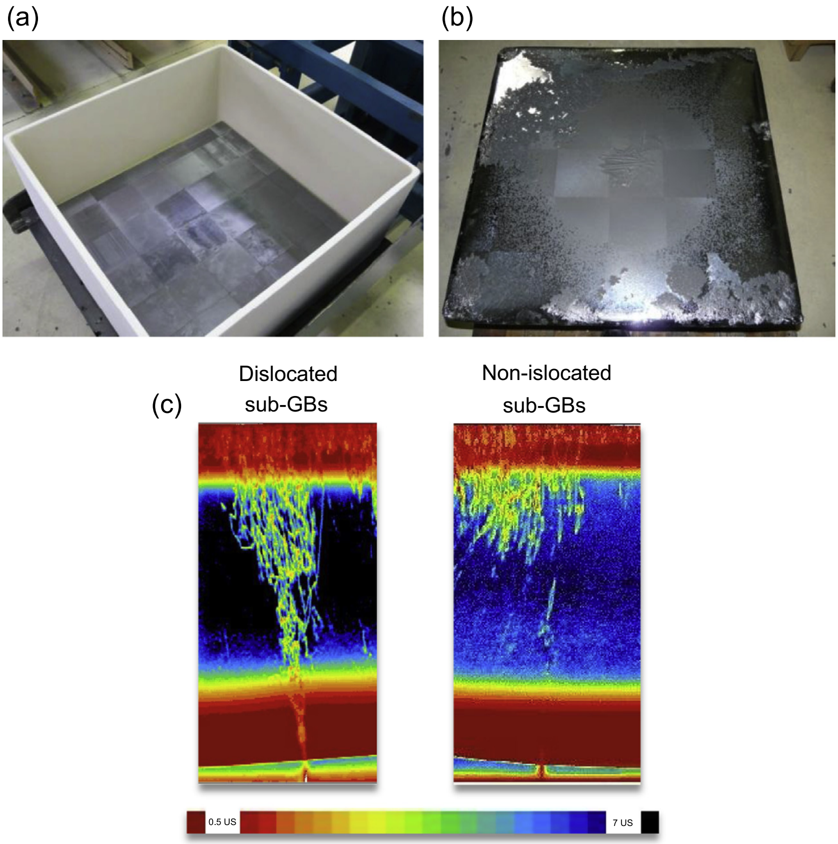

**Figure 3.13** (a) Arrangement of (100) seeds (5 × 5) at the bottom of the crucible; (b) grown ML ingot; (c) two different lifetime mappings of the block from the dislocated subgrain boundaries (left) and nondislocated subgrain boundaries originated from the junction of the seeds. Both photographs and figures are from A. Jouini, F. Jay, V. Amaral, E. Pihan, Y. Veschetti, in: The 7th International Conference on Crystalline Silicon Solar Cells, Fukuoka, Japan, October 22−25, 2013, 2013, with permission of Dr. A. Jouini.

metallic impurities from the crucible and coating, gettering becomes necessary for ML silicon before or during solar cell processing.

The dislocations generated from the seed joints and their multiplications under thermal stress remain the key issues in mass production [74]. Recently, the dislocation generation from the seed joints has been mitigated significantly by special seed arrangements using low-symmetry random GBs [66,67,75−78], i.e., by introducing a tilting angle between seed plates. Trempa et al. [75] considered different types of GBs, and concluded that the nonperfect highly symmetrical GBs can cause GB splitting and dislocation generation, while the low-symmetry GBs can keep their singular structure with consequent lesser dislocation formation at the seed junctions. Hu et al. [76] further purposely introduced random GBs by twisting the angle between the

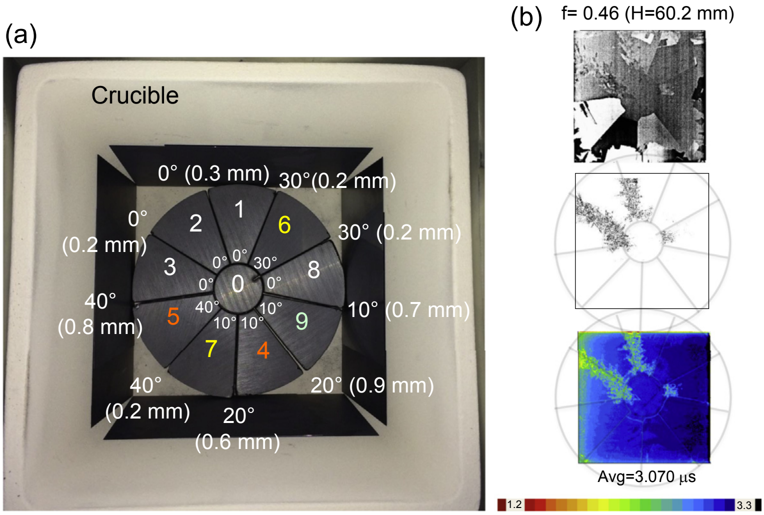

**Figure 3.14** (a) Seed arrangements; (b) grains (top), EPD, and minority-carrier lifetime of the wafer at f = 0.46 [66].

adjacent (100)-oriented seeds by 10°—45°. In the G5 ingot grown from these seeds, the dislocations generated at the seed joints were significantly reduced. By combining the concepts of small- and large-angle GBs and the functional grain GBs, Takahashi et al. [77] proposed a novel seed manipulation for an artificially controlled defect technique (SMART). Their results were promising for reducing defects generated from the seed junctions. However, for better texturing the growth of an (100) ML ingot is preferred for industry. Although the work by Hu et al. [76] was promising, the details were not disclosed and the optimum tilt angle was not discussed. The use of large rotation angles (from 30° to 60°) for the splitting (100) seeds was reported in a Chinese patent application [78], but this patent was never granted.

Wu et al. [66] designed an interesting experiment to study the seed arrangement with different tilt angles. As shown on the left-hand side of Fig. 3.14(a), a 200 mm diameter (20 mm in thickness) (100) seed was cut first by a high-pressure water jet evenly into nine sector pieces, but leaving a circle seed (45 mm in diameter) at the center; the nine sector pieces were numbered counterclockwise from 1 to 9. When the seeds were placed into the crucible, some sector pieces were rearranged, e.g., seed 5 was moved to the original position of seed 4, as shown on the left. As a result, different tilt angles between two adjacent seeds could be obtained, as indicated in Fig. 3.14(a). Trijunctions of three seeds with different tilt angles along the rim of the inner circle seeds could also be obtained. Different seed gaps from 0.2 to 0.9 mm were considered, as seen in Fig. 3.14(a). Different tilt angles between the center circle seed (seed 0) and the sector seeds were also included. Moreover, an overcut of the center seed was considered as well, which was located at the junction of seeds 0, 6, and 8. After growth, the wafers at the fraction of solidification (f) of 0.46 were examined, as shown in Fig. 3.14(b). The clear grain structures after KOH etching showed that the grains

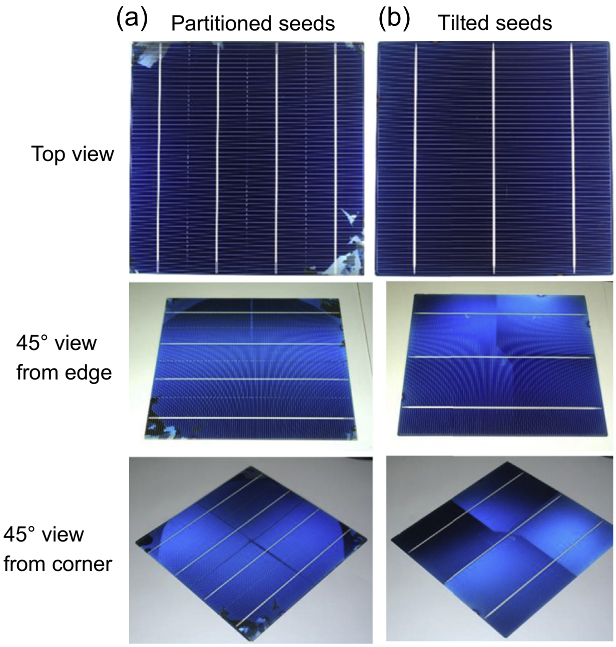

**Figure 3.15** Appearances at different view angles of solar cells made from (a) partitioned seeds; (b) tilted seeds [67].

near the center were all in (100) direction; some grains were introduced from the crucible wall. From the EPD mapping in Fig. 3.14(b), it is interesting that dislocations and subgrains were easily induced at the boundaries with the 0° tilt angle. No significant defects were observed for the boundaries of nonzero tilt angles. As a result, the low lifetime areas were located near the boundaries with 0° tilt angle. These results were similar to the ones reported by Hu et al. [76]. However, when these ML wafers were used for solar cells, color mismatch was found from the side view for the solar cell. This might be an issue in production. Recently, Lan et al. [67] proposed a partition approach that used partition plate seeds to generate the tilt boundaries between the (100) seeds. With this approach, in addition to the ease of seed preparation, the color mismatch was mitigated significantly. A comparison of the appearance of solar cells made from ML wafers using partition seeds and tilted seeds is shown in Fig. 3.15. With the partition seeds, seen in Fig. 3.15(a), the color mismatch area was significantly reduced, while the color mismatch was still present in case of the tilt seeds (Fig. 3.15(b)).

### 3.3.2.4 Codoping and gettering

For B-doped silicon, the resistivity distribution of the ingot is fairly uniform due to the large segregation coefficient ($k = 0.8$). However, for Ga-doped or P-doped silicon, the resistivity variation is much larger due to segregation. To reduce the resistivity gradient, codoping is often used. For example, for P-doped silicon Ga was used for codoping, and this increased the growth yield significantly. Moreover, Ge doping

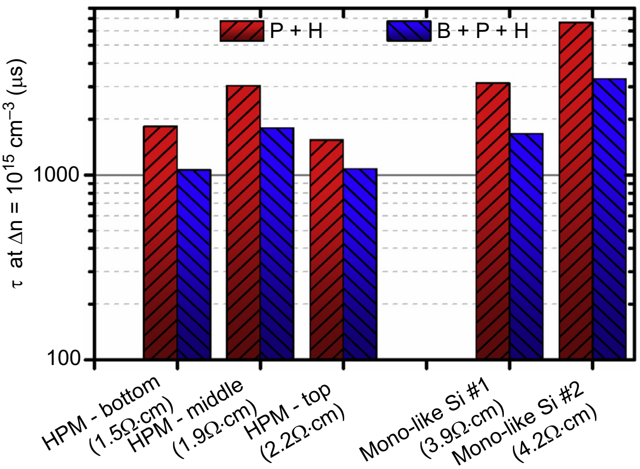

**Figure 3.16** Lifetimes of wafers from n-type HP mc-Si and ML Si ingots, after phosphorus diffusion and hydrogenation, with and without a priori boron diffusion. Lifetime values were measured at an excess carrier density of $1 \times 10^{15}$ cm$^{-3}$ [79].

can also be used to increase the mechanical strength of the material, which could reduce the dislocation density and the breakage rate during wafer slicing and solar cell processing. The LID of the solar cells could be reduced as well. For ML silicon, n-type (P) doping is frequently used to reduce LID and increase wafer lifetime. However, gettering is crucial to enhance the lifetime. Fig. 3.16 shows a comparison of HP mc-Si and ML silicon wafers after P or/and B gettering and hydrogen passivation [79]. As seen, a long lifetime (up to 6.6 ms) can be obtained after phosphorus gettering and hydrogen passivation, without B diffusion. Hydrogen passivation was more effective in HP mc-Si. Boron diffusion seemed to have a negative effect on the lifetime, although for n-type solar cells this step is inevitable.

## 3.4 Conclusions and future perspectives

In this chapter several growth methods of solar silicon are presented and discussed. As the demand for solar silicon for PV continues to increase, its market size has grown much bigger than that of semiconductor silicon. In 2017 alone the installation of silicon solar panels was expected to be near 100 GW; the equivalent weight of the crystal is more than 300,000 tons. This large demand has made solar silicon the biggest commodity in the crystal growth industry. The market share of mono-Si was only 30% in 2016, but it will continue to increase due to the quicker progress of the related solar cell technology as compared with HP mc-Si. According to the roadmap prediction, the market share of mono-Si in 2027 will be greater than 60% [1]. However, following the historical trend that the price of solar cells has to decrease continuously, the production of solar silicon has to face the same challenge of cost reduction. Hot-zone design has been found extremely useful in this aspect. Beside the faster growth rate and lower power consumption, the cost of consumables, such as argon and graphite components, can be significant reduced. Crystal quality can also be improved by reducing the oxygen and carbon contents, and by the vacancy-rich growth at higher growth rates. However, hot-zone improvements have reached a limit, so using a bigger charge size and multiple or continuous charges are inevitable for production. This includes better design of the feeder to reduce contamination and better preparation of small-chunk or granular silicon. In addition, a long-lifetime silica crucible or a valid substitute is required; a reusable crucible is preferred. The CCZ technology is a good choice to meet future requirements; but its success greatly relies on better hot-zone design and the materials used, especially the long-lifetime crucibles. DS growth of ML silicon is also potentially applicable for PV because it supplies materials of good quality and low cost, featuring high PPH and low power consumption. However, there are several challenges ahead for this material, such as defect control and seed cost issues. As the issue of defect formation from the seed joints has been resolved through the seed arrangement, defect control during ingot growth may be improved through better hot-zone design. Moreover, using recycled and smaller seeds will be one good option to reduce seed cost. Unfortunately, the progress of ML technology over the past 10 years has been slow, and an innovative crystal growth technology for solar silicon is still necessary to meet the future PV demand.

## List of abbreviations and acronyms

| | |
|---|---|
| **BSF** | Back surface field |
| **c-Si** | Crystalline silicon |
| **CCZ** | Continuous Czochralski |
| **CZ** | Czochralski |
| **DS** | Directional solidification |
| **DW** | Diamond wire |
| **EPD** | Etch pit density |
| **FZ** | Floating zone |
| **GBs** | Grain boundaries |
| **HIT** | Heterojunction with intrinsic thin layer |
| **HP** | High-performance |
| **LID** | Light-induced degradation |
| **mc-Si** | Multicrystalline Si |
| **MCZ** | Magnetic Czochralski |
| **ML** | Mono-like |
| **Mo** | molybdenum |
| **mono-Si** | Monocrystalline silicon |
| **PERC** | Passivated emitter and rear contact |
| **PPH** | Production per hour |
| **PV** | Photovoltaics |
| **PV-FZ** | FZ solar silicon |
| **SiO** | silicon monoxide |
| **SOG** | Solar grade |
| **SW** | Slurry-based wire |

## Acknowledgments

I am grateful for the generous support from the Ministry of Science and Technology (MOST) of Taiwan. The continuous support from SAS and Global Wafer is highly appreciated.

## References

[1] International Technology Roadmap for Photovoltaic (ITRPV) Results 2016, Including Maturity Report, eighth ed., September 2017.
[2] Photovoltaics Report, Fraunhofer Institute for Solar Energy Systems, ISE, Freiburg, Germany, July 12, 2015, www.ise.fraunhofer.de.
[3] C.W. Lan, C. Chuck, K. Nakajima, Multicrystalline silicon crystal growth for photovoltaic applications, in: P. Rudolph (Ed.), Handbook of Crystal Growth 2A: Bulk Crystal Growth: Basic Techniques, second ed., 2015, p. 373. North-Holland, Amsterdam.
[4] Y.M. Yang, A. Yu, B. Hsu, W.C. Hsu, A. Yang, C.W. Lan, Development of high-performance multicrystalline silicon for photovoltaic industry, Prog. Photovolt. Res. Appl. 23 (2015) 340−351.
[5] C.W. Lan, A. Lan, C.F. Yang, H.P. Hsu, M. Yang, A. Yu, B. Hsu, W.C. Hsu, A. Yang, The emergence of high-performance multi-crystalline silicon in photovoltaics, J. Cryst. Growth 468 (2017) 17−23.
[6] N. Stoddard, BP Corp., Patent Application, WO 2007/084936 A2.
[7] N. Stoddard, B. Wu, I. Witting, M. Wagener, Y. Park, G. Rozgonyi, R. Clark, Casting single crystal silicon: novel defect profiles from BP Solar′s Mono 2 wafers, Solid State Phenom. 1 (2008) 131−133.
[8] J. Vedde, T. Clausen, L. Jensen, Floating-zone silicon for high volume production of solar cells, in: Proceeding in the 3rd World Conference on Photovoltaic Energy Conversion, Osaka, Japan May 11−18, 2003.
[9] J. Schmidt, K. Bothe, Structure and transformation of metastable boron and oxygen related defect center in crystalline silicon, Phys. Rev. B 69 (2004) 024107.
[10] P. Dold, F. Zobel, R. Kunert, K. Lauer, B. Michl, Low oxygen, high life-time wafers produced by a modified Float Zone process (pp-FZ), in: 29th EU PVSEC Conference, Amsterdam, The Netherlands, 2014.
[11] P. Dold, Chapter one - Silicon crystallization technologies, Semiconduct. Semimet. 92 (2015) 1−61.
[12] B. Fickett, G. Mihalik, Multiple batch recharging for industrial CZ silicon growth, J. Cryst. Growth 225 (2001) 580−585.
[13] C. Wang, H. Zhang, T.H. Wang, T.F. Ciszek, A continuous Czochralski silicon crystal growth system, J. Cryst. Growth 250 (2003) 209−214.
[14] H. Xu, Characterization of n-type mono-crystalline silicon ingots produced by continuous Czochralski (Cz) technology, Energy Procedia 77 (2015) 658−664.
[15] C.W. Lan, C.F. Yang, A. Lan, M. Yang, A. Yu, H.P. Hsu, B. Hsu, C. Hsu, Engineering silicon crystals for photovoltaics, CrystEngComm 18 (2016) 1474−1485.
[16] C.P. Khattak, F. Schmid, Growth of silicon ingots by HEM for photovoltaic applications, in: C.P. Khattak, K.V. Ravi (Eds.), Silicon Processing for Photovoltaics II, Elsevier Science Publishers, 1987, pp. 153−183.
[17] J. Chen, A.J. Deshpande, G. Shi, L. Wen, M. Seacrist, J. Kearns, Key issues in crystalline silicon manufacturing technology for photovoltaics, in: China PV Technology International Conference (CPTIC), 2012. Shanghai.

[18] http://www.str-soft.com/products/CGSim/.

[19] A.N. Vorob'ev, A.P. Sidko, V.V. Kalaev, Advanced chemical model for analysis of Cz and DS Si-crystal growth, J. Cryst. Growth 386 (2014) 226−234.

[20] L.Y. Huang, P.C. Lee, C.K. Hsieh, W.C. Hsu, C.W. Lan, On the hot-zone design of Czochralski silicon growth for photovoltaic applications, J. Cryst. Growth 261 (2004) 433−443.

[21] C.W. Lan, C.K. Hsieh, W.C. Hsu, in: K. Nakajima, N. Usami (Eds.), Crystal growth for Solar Cells, Springer Verlag, Berlin, Heidelberg, 2009, p. 25.

[22] http://www.pvatepla.com/en/products/crystal-growing-systems/pva/cz—equipment/active-crystal-cooling.

[23] R.L. Hansen, L.E. Drafall, R.M. McCutchan, J.D. Holder, L.A. Allen, R.D. Shelley, Surface-Treated Crucibles for Improved Zero Dislocation Performance, US Patent No. 5,976,247, November 1999.

[24] F. Shimura, Single-crystal silicon: growth and properties, in: S. Kasap, P. Capper (Eds.), Springer Handbook of Electronic and Photonic Materials, Springer, 2017, p. 293.

[25] J.P. DeLuca, F.S. Delk, B.K. Johnson, W.L. Luter, N.D. Middendorf, D.S. Williams, N.P. Ostrom, J.N. Highfill, Silicon Single Crystal Doped with Gallium, Indium, or Aluminum US2012/0056135 A1, 2012.

[26] S. Zhang, M. Juel, E.J. Ovrelid, G. Tranell, Investigating the effect of carbon on oxygen behavior in n-type Czochralski silicon for PV application, J. Cryst. Growth 411 (2015) 63−70.

[27] J.D. Murphy, R.E. McGuire, K. Bothe, V.V. Voronkov, R.J. Falster, Minority carrier lifetime in silicon photovoltaics: the effect of oxygen precipitation, Sol. Energy Mater. Sol. Cells 120 (2014) 402−411.

[28] M. Yonemura, K. Sueoka, K. Kamei, Analysis of local lattice strain around oxygen precipitates in silicon crystals using CBED technique, Appl. Surf. Sci. 130−132 (1998) 208−213.

[29] D. Macdonald, L.J. Geerligs, Recombination activity of interstitial iron and other transition metal point defects in p- and n-type crystalline silicon, Appl. Phys. Lett. 85 (2004) 4061−4063.

[30] T.F. Ciszek, T.H. Wang, Silicon defect and impurity studies using float-zone crystal growth as a tool, J. Cryst. Growth 237−239 (2002) 1685−1691.

[31] V.V. Voronkov, The mechanism of swirl defects formation in silicon, J. Cryst. Growth 59 (1982) 625−643.

[32] L.I. Huang, P.C. Lee, C.K. Hsieh, W.C. Hsu, C.W. Lan, Simulation of boron effects on OISF-ring dynamics for Czochralski silicon growth: a comparative study, J. Cryst. Growth 266 (2004) 132−139.

[33] W. Su, Z. Ran, J. Lu, C. Di, X. Cheng, Numerical and experimental studies on the Black Periphery Wafer in CZ Si growth, J. Cryst. Growth 388 (2014) 42−47.

[34] V. Meemongkolkiat, K. Nakayashiki, A. Rohatgi, G. Crabtree, J. Nickerson, T.L. Jester, Resistivity and lifetime variation along commercially grown Ga- and B-Doped Czochralski Si ingots and its effect on light-induced degradation and performance of solar cells, Prog. Photovolt. Res. Appl. 14 (2006) 125−134.

[35] M. Arivanandhan, R. Gotoh, T. Watahiki, K. Fujiwara, Y. Hayakawa, S. Uda, M. Konagai, The impact of Ge codoping on the enhancement of photovoltaic characteristics of B- doped Czochralski grown Si crystal, J. Appl. Phys. 111 (2012) 043707.

[36] P. Wang, X. Yu, P. Chen, X. Li, D. Yang, X. Chen, Z. Huang, Germanium-doped Czochralski silicon for photovoltaic applications, Sol. Energy Mater. Sol. Cells 95 (2011) 2466−2470.

[37] V. Orlova, H. Richter, A. Fischer, J. Reif, T. Mueller, R. Wahlich, Mechanical properties of nitrogen-doped CZ silicon crystals, Mater. Sci. Semicond. Process. 5 (2003) 403−407.

[38] X. Yu, J. Chen, X. Ma, D. Yang, Impurity engineering of Czochralski silicon, Mater. Sci. Eng. R 74 (2013) 1−33.

[39] K. Kakimoto, Czochralski silicon single crystals for semiconductor and solar cell applications (Chapter 8), in: G. Dhanaraj, K. Byrappa, V. Prasad, M. Dudley (Eds.), Springer Handbook of Crystal Growth, Springer, 2010.

[40] K. Fujiwara, W. Pan, K. Sawada, M. Tokairin, N. Usami, Y. Nose, A. Nomura, T. Shishido, K. Nakajima, Directional growth method to obtain high quality polycrystalline silicon from its melt, J. Cryst. Growth 292 (2006) 282−285.

[41] K. Nakajima, K. Kutsukake, K. Fujiwara, N. Usami, S.I. Yamasaki, High efficiency solar cells using small size ingots with 30 cm by controlling the distribution and orientation of dendrite crystals grown along the bottom of the ingots, in: Proceedings of the 35th IEEE Photovoltaic Specialists Conference, USA, June 2010, pp. 817−819.

[42] K. Nakajima, K. Kutsukake, K. Fujiwara, N. Usami, S. Ono, I. Yamasaki, in: Proceedings of the 25th European Photovoltaic Solar Energy Conference and Exhibition (25th EU PVSEC), The 5th World Conference on Photovoltaic Energy Conversion (WCPEC-5), Spain, September 2010.

[43] K.M. Yeh, C.K. Hseih, W.C. Hsu, C.W. Lan, High-quality multi-crystalline silicon growth for solar cells by grain-controlled directional solidification, Prog. Photovolt. Res. Appl. 18 (2010) 265−271.

[44] C.W. Lan, Grain control in directional solidification of photovoltaic silicon, in: Presented at 5th International Workshop on Crystal Growth Technology, Berlin, Germany, June 2011.

[45] C.W. Lan, W.H. Yu, Y.M. Yang, H.S. Chou, C.L. Hsu, W.C. Hsu, Crystalline Silicon Ingot and Silicon Wafer Therefrom, ROC Patent TWI452185B.

[46] C.W. Lan, W.C. Lan, T.F. Li, A. Yu, Y.M. Yang, C. Hsu, B. Hsu, A. Yang, Grain control in directional solidification of photovoltaic silicon, J. Cryst. Growth 360 (2013) 68−75.

[47] C.W. Lan, Grain control in directional solidification of photovoltaic silicon, in: Presented at 5th International Workshop on Crystalline Silicon Solar Cells, Boston, USA, November 2011.

[48] C.W. Lan, W.C. Lan, T.F. Li, A. Yu, Y.M. Yang, C. Hsu, B. Hsu, A. Yang, From A+ to A+++, on the development of high-quality multi-crystalline silicon crystal growth technology for photovoltaic industry, in: 22nd Workshop on Crystalline Silicon Solar Cells & Modules: Materials and Processes, Vail USA, July 2012.

[49] C.W. Lan, Y.M. Yang, A. Yu, B. Hsu, A. Yang, in: Presented at the 27th European Photovoltaic Solar Energy Conference (27th EU PVSEC), Frankfurt Germany, September 2012.

[50] Y.T. Wong, C. Hsu, C.W. Lan, Development of grain structures of multi-crystalline silicon from randomly orientated seeds in directional solidification, J. Cryst. Growth 387 (2014) 59−64.

[51] D. Zhu, L. Ming, M. Huang, Z. Zhang, X. Huang, Seed-assisted growth of high-quality multi-crystalline silicon in directional solidification, J. Cryst. Growth 386 (2014) 52−56.

[52] Y.T. Wong, C.T. Hsieh, A. Lan, C. Hsu, C.W. Lan, The effect of silica nucleation layers on grain control of multi-crystalline silicon in directional solidification, J. Cryst. Growth 404 (2014) 59−64.

[53] C.W. Lan, Y.M. Yang, A. Yu, Y.C. Wu, B. Hsu, W.C. Hsu, A. Yang, Recent progress of crystal growth technology for multi-crystalline silicon solar ingot, Solid State Phenom. 242 (2016) 21−29.

[54] H. Zhang, D. You, C. Huang, Y. Wu, Y. Xu, P. Wu, Growth of multicrystalline silicon ingot with both enhanced quality and yield through quartz seeded method, J. Cryst. Growth 435 (2016) 91−97.

[55] G. Stokkan, Y. Hu, O. Mjos, M. Juel, Study of evolution of dislocation clusters in high performance multicrystalline silicon, Sol. Energy Mater. Sol. Cells 130 (2014) 679−685.

[56] I. Kupka, C. Reimann, T. Lehmann, D. Oriwol, F. Kropfgans, J. Friedrich, Influence of different nucleation layers on the initial grain structure of multi-crystalline silicon ingots, J. Cryst. Growth 465 (2017) 18−26.

[57] C. Reimann, M. Trempa, T. Lehmann, K. Rosshirt, J. Stenzenberger, J. Friedrich, K. Hesse, E. Dornberger, Influence of different seed materials on multi crystalline silicon ingot properties, J. Cryst. Growth 434 (2016) 88−95.

[58] PV Mag. (September 2012) 94−99.

[59] W. Ma, G. Zhong, L. Sun, Q. Yu, X. Huang, L. Liu, Influence of an insulation partition on a seeded directional solidification process for quasi-single crystalline silicon ingot for high-efficiency solar cells, Sol. Energy Mater. Sol. Cells 100 (2012) 231−238.

[60] Q. Yu, L. Liu, W. Ma, G. Zhong, X. Huang, Local design of the hot-zone in an industrial seeded directional solidification furnace for quasi-single crystalline silicon ingots, J. Cryst. Growth 358 (2012) 5−11.

[61] C. Ding, M. Huang, G. Zhong, L. Liu, X. Huang, Movable partition designed for the seed-assisted silicon ingot casting in directional solidification process, Cryst. Res. Technol. 49 (2014) 405−413.

[62] X. Qi, W. Zhao, L. Liu, Y. Yang, G. Zhong, X. Huang, Optimization via simulation of a seeded directional solidification process for quasi-single crystalline silicon ingots by insulation partition design, J. Cryst. Growth 398 (2014) 5−12.

[63] L. Liu, Q. Yu, X. Qi, W. Zhao, G. Zhong, Controlling solidification front shape and thermal stress in growing quasi-single-crystal silicon ingots: process design for seeded directional solidification, Appl. Therm. Eng. 91 (2015) 225−233.

[64] K. Kutsukake, N. Usami, Y. Ohno, Y. Tokumoto, I. Yonenaga, Control of grain boundary propagation in mono-like Si: utilization of functional grain boundaries, Appl. Phys. Express 6 (2013) 025505-1−025505-3.

[65] K. Kutsukake, N. Usami, Y. Ohno, Y. Tokumoto, I. Yonenaga, Mono-Like silicon growth using functional grain boundaries to limit area of multicrystalline grains, IEEE J. Photovolt. 4 (2014) 84−87.

[66] Y.C. Wu, A. Lan, C.F. Yang, C.W. Hsu, C.M. Lu, A. Yang, C.W. Lan, Effect of seed arrangements on the quality of n-type mono-like silicon grown by directional solidification, Cryst. Growth Design 16 (2016) 6641−6647.

[67] C.Y. Lan, Y.C. Wu, A. Lan, C.F. Yang, C. Hsu, C.M. Lu, A. Yang, C.W. Lan, Control of ingot quality and solar cell appearance of cast mono-like silicon by using seed partitions, J. Cryst. Growth 475 (2017) 136−143.

[68] M. Trempa, C. Reimann, J. Friedrich, G. Mueller, D. Oriwol, Mono-crystalline growth in directional solidification of silicon with different orientation and splitting of seed crystals, J. Cryst. Growth 351 (2012) 131−140.

[69] F.C. Frank, J.H. van der Merwe, Proc. R. Soc. Lond. A 198 (1949) 125 (1949) 205 and A 200.

[70] F. Wilhelm, The orientation of high-order growth twins in diamond-type crystals, J. Appl. Cryst. 4 (1971) 521−523.

[71] B. Gao, S. Nakano, K. Kakimoto, Influence of back-diffusion of iron impurity on lifetime distribution near the seed-crystal interface in seed cast-grown monocrystalline silicon by numerical modeling, Cryst. Growth Design 12 (2012) 522−525.

[72] Y. Miyamura, H. Harada, K. Jiptner, J. Chen, R.R. Prakash, S. Nakano, B. Gao, K. Kakimoto, T. Sekiguchi, Crystal growth of 50 cm square mono-like Si by directional solidification and its characterization, J. Cryst. Growth 401 (2014) 133−136.

[73] A. Jouini, F. Jay, V. Amaral, E. Pihan, Y. Veschetti, in: The 7th International Conference on Crystalline Silicon Solar Cells, Fukuoka, Japan, October 22−25, 2013, 2013.

[74] I. Guerrero1, V. Parra, T. Carballo, A. Black, M. Miranda, D. Cancillo, B. Moralejo, J. Jimenez, J. Lelievre, C. del Cañizo, About the origin of low wafer performance and crystal defect generation on seed-cast growth of industrial mono-like silicon ingots, Prog. Photovolt. Res. Appl. 22 (2014) 923−932.

[75] M. Trempa, C. Reimann, J. Friedrich, G. Müller, A. Krause, L. Sylla, T. Richter, Influence of grain boundaries intentionally induced between seed plates on the defect generation in quasi-mono-crystalline silicon ingots, Cryt. Res. Technol. 50 (2015) 124−132.

[76] D. Hu, S. Yuan, L. He, H. Chen, Y. Wan, X. Yu, D. Yang, Higher quality mono-like cast silicon with induced grain boundaries, Sol. Energy Mater. Sol. Cells 140 (2015) 121−125.

[77] I. Takahashi, S. Joonwichien, T. Iwata, N. Usami, Effects of grain boundary structure controlled by artificially designed seeds on dislocation generation, Appl. Phys. Express 8 (2015) 105501.

[78] C. Lee, Y. Ma, Production Method of Solar Energy Level Polysilicon Ingot with Crystalline Grains Arranged Regularly, CN102392300 A.

[79] S.P. Phang, H.C. Sio, C.F. Yang, C.W. Lan, Y.M. Yang, A. Yu, B. Hsu, C. Hsu, D. Macdonald, N-type high-performance multicrystalline and mono-like silicon wafers with lifetimes above 2 ms, Jpn. J. Appl. Phys. 56 (2017) 08MB10.

This page intentionally left blank

# Germanium crystals

# 4

*Ichiro Yonenaga*
Tohoku University, Sendai, Japan

## 4.1 Introduction

Germanium (Ge) is the material used in the first transistor invented by Bardeen, Brattain, and Shockley at Bell Laboratories in 1947, a historical landmark in the semiconductor world. With this as a trigger, the semiconductor industry started. Silicon (Si) of the same group IV was soon preferred to Ge for its practical superiorities and intrinsic properties; Si became the main material in the industry, and has taken the lead in the miniaturization and large-scale integration of modern electronic devices. Ge crystals were used in the limited fields of $\gamma$-ray detectors and infrared optics plus in the basic research community; indeed, some reference books of the period omitted descriptions and data on Ge. After a long period of disinterest, since the 1990s Ge has again become the focus of keen interest for its applications in ultrafast electronic devices and its favorable basic properties of intrinsic carrier mobility. A number of groups around the world have renewed development of Ge as a material for mainstream semiconductors. Belgian research groups and companies in particular have promoted growth of large-sized crystals and electronic device fabrication [1,2]. Fig. 4.1(a) shows a dislocation-free Ge crystal of 300 mm in diameter made by Umicore Electro-Optic Materials. As seen in Fig. 4.1(b), Ge wafer size expanded very rapidly to 300 mm in diameter, comparable to an Si wafer [3]. As seen in Table 4.1, current applications of Ge crystals can be divided into three categories: infrared optics, radiology, and electronics. Ge is also used widely as a chemical for polymerization catalysts of high-quality polyethylene terephthalates (PETs) and dopants of optical fibers.

To clarify and understand the current knowledge on Ge crystals, this chapter reviews the most relevant aspects of these crystals and related alloys comprehensively: the basic properties, material preparation, crystal growth, growth-related problems, structural defects, and applications with recent achievements. The chapter elucidates the intrinsic characteristics of Ge in comparison with those of Si. Finally, future prospects are discussed in the concluding remarks.

## 4.2 Basic properties

Ge is a typical group IV semiconductor, sometimes called “Brother Silicon, Sister Germanium” in the history of semiconductor science and technology [4]. Table 4.2 shows some basic properties of Ge in comparison with those of Si [5]. Ge has a diamond cubic structure, and its lattice parameter is larger by 4% than that of Si.

**Single Crystals of Electronic Materials.** https://doi.org/10.1016/B978-0-08-102096-8.00004-5
Copyright © 2019 Elsevier Ltd. All rights reserved.

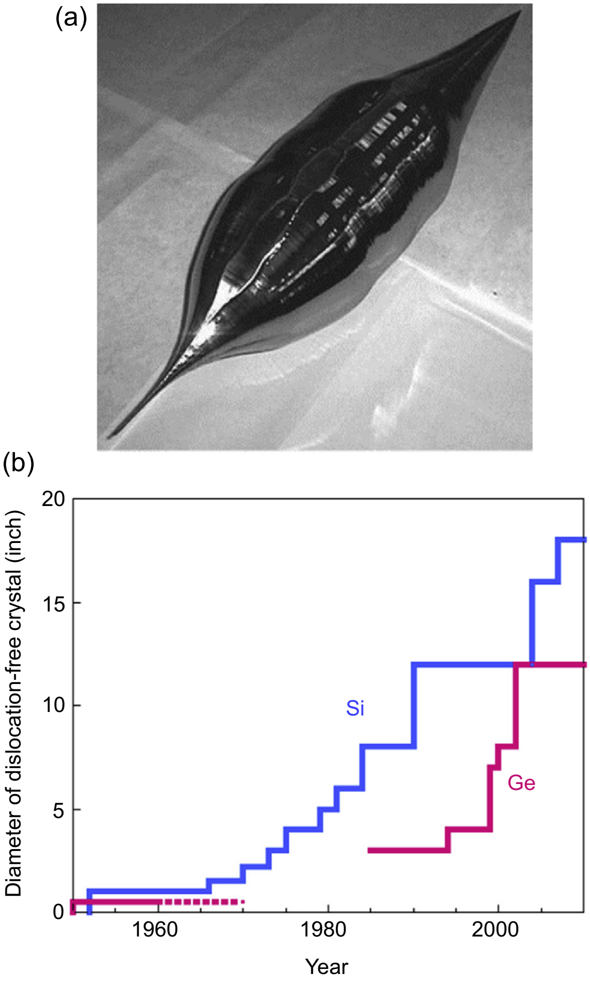

**Figure 4.1** (a) Dislocation-free Ge crystal of 300 mm in diameter grown by Umicore Electro-Optic Materials (EOM); (b) Increase of Ge crystal size in diameter with year, in comparison to Si. Reprinted from B. Depuydt, Growth of germanium single crystals, in: K.H.J. Buschow, R.W. Cahn, M.C. Flemings, B. Ilschner, E.J. Kramer, S. Mahajan (Eds.), The Encyclopedia of Materials: Science and Technology, Elsevier, 2001, 3507–3517, Copyright 2001, with permission from Elsevier.

Fig. 4.2 shows the energy-band structure of Ge [6]. The position of the lowest energy of the conduction band is $L_6$ along the $<111>$ axis, shifted from $\Gamma_8$ of the highest energy of the valence band, showing that Ge is an indirect transition type. The energy separation between $L_6$ and $\Gamma_8$ is 0.66 eV at room temperature (RT) and is called the bandgap. The bandgap energy $E_g$ of Ge is given as a function of temperature $T$ by

$$E_g = 0.7437 - 4.774 \times 10^{-4} T^2 / (T + 235) \tag{4.1}$$

### Table 4.1 Applications of Ge crystals

| | **Infrared optics** | **Electronics** | **Radiology** |
|---|---|---|---|
| Main products | Lenses, windows | CMOS, substrates | $\gamma$-ray detectors |
| Mechanism | Transmission 1.85−15 μm | High carrier mobility | Photoelectric effect |
| Purity of raw material | Optics grade $\sim 10^{13}$ cm$^{-3}$ | Electronics grade $\sim 10^{13}$ cm$^{-3}$ | Ultrahigh purity $<10^{11}$ cm$^{-3}$ |
| Carrier concentration | $4 \times 10^{13}$−$1 \times 10^{15}$ cm$^{-3}$ | Intentional doping | $10^{9}$−$2 \times 10^{10}$ cm$^{-3}$ |
| Defects | Single (desired) | Single | Single |
| Dislocation density | | Free | $10^{2}$−$10^{4}$ cm$^{-2}$ |
| Harmful defects | Low angle grain boundary, mosaicity | Dislocations | $V_2H$, C, $SiO_2$ grain boundary |
| Remarks | Low residual stress, flat growth interface | | |
| Current max. weight/ diameter (approximately) | 300 kg/350 mm | 35 kg/350 mm | 10 kg/100 mm |

### Table 4.2 Basic properties of Ge and Si

| | **Ge** | **Si** |
|---|---|---|
| Atomic weight: $M$ | 32 | 14 |
| Atomic radius: $r$ nm | 0.123 | 0.117 |
| Lattice constant: $a$ nm | 0.56575 | 0.5431 |
| Density: $\rho$ g/cm$^3$ | 5.33 | 2.33 |
| Atomic number in a unit volume: $N$ cm$^{-3}$ | $4.42 \times 10^{22}$ | $5 \times 10^{22}$ |
| Bandgap (@0K/@RT): $E_g$ eV | 0.74/0.66 | 1.17/1.12 |
| Intrinsic carrier density (@RT): $n_i$ cm$^{-3}$ | $2.5 \times 10^{13}$ | $1.45 \times 10^{13}$ |
| Effective mass (electron rest mass $m_0 = 0.91095 \times 10^{-27}$ g) | | |
| (Electron) density of state $m_{de}/m_0$ | 0.19 | 0.36 |
| longitudinal $m_{le}/m_0$, transversal $m_{he}/m_0$ | 1.64, 0.082 | 0.98, 0.19 |
| (Hole) density of state $m_{dh}/m_0$ | 0.34 | 0.81 |
| light $m_{lh}/m_0$, heavy $m_{hh}/m_0$ | 0.044, 0.28 | 0.16, 0.49 |

*Continued*

## Table 4.2 Continued

| | Ge | Si |
|---|---|---|
| Mobility (electron): $\mu_e$ cm$^2$/V s | 3900 | 1500 |
| (Hole): $\mu_h$ cm$^2$/V s | 1900 | 450 |
| Dielectric constant: $\varepsilon$ | 16.0 | 11.9 |
| Refractivity: $n$ | 4.01 | 3.42 |
| Elastic constant (@RT): $C_{11}$ GPa | 129 | 166 |
| $C_{12}$ GPa | 48.3 | 64.0 |
| $C_{44}$ GPa | 67.1 | 79.6 |
| Shear modulus: $G$ GPa | 48.9 | 60.5 |
| Strength (@$T_M$/@(2/3)$T_M$): $\tau$ GPa | 0.3/25 | 1.0/40 |
| Surface energy (111): $\gamma$ erg/cm$^2$ | 1060 | 1230 |
| Linear thermal expansion (@RT/@$T_M$): $\alpha$ K$^{-1}$ | $5.9 \times 10^{-6}$/ $\sim 9 \times 10^{-6}$ | $2.6 \times 10^{-6}$/ $4.4 \times 10^{-6}$ |
| Thermal conductivity (@RT/@$T_M$): $\kappa$ W/m K | 58/24 | 157/31 |
| Gibbs standard free energy of dioxide formation (@$T_M$): $\Delta G$ kJ/mol | 3.41 | 6.80 |

Data based on S.M. Sze, Physics of Semiconductor Devices, second ed., Wiley-Interscience Publication, 1981. (In the current version published in 2007, some descriptions and data on Ge have been removed.)

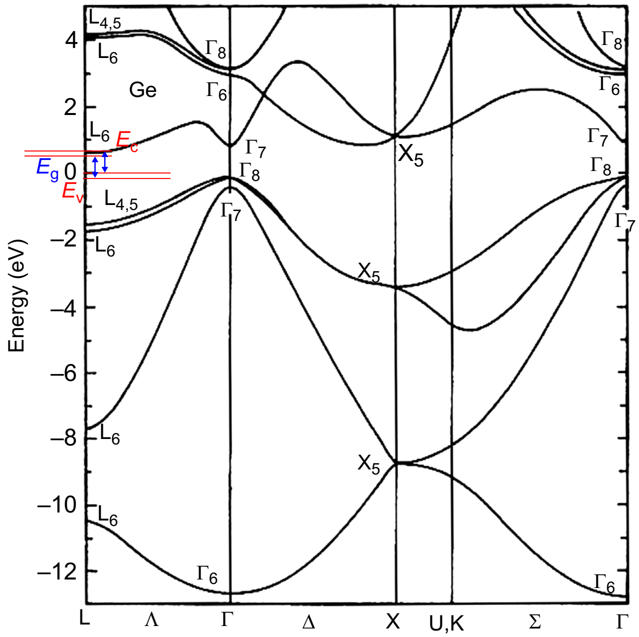

**Figure 4.2** Band structure for Ge evaluated theoretically [6]. $E_c$ is the bottom of the conduction band, $E_v$ is the top of the valence band, and $E_g$ is the bandgap.
Modified from J.R. Chelikowsky, M.L. Cohen, Nonlocal pseudopotential calculations for the electronic structure of eleven diamond and zinc-blende semiconductors, Phys. Rev. B 14 (1976) 556−582, Copyright 1976, with permission from American Physical Society.

The energy separation between $\Gamma_8$ of the valence band and $\Gamma_7$ of the conduction band for direct transition is 0.8 eV, very close to $E_g$, which is an important feature in the optical absorption of Ge.

The intrinsic carrier density $n_i$ depends on the temperature $T$ as

$$n_i = 4.9 \times 10^{15} \left( m_{de} m_{dh} / m_0^2 \right)^{3/4} T^{3/2} \exp\left( - E_g / 2k_B T \right) \tag{4.2}$$

where $m_0$ is the electron rest mass and $m_{de}$ and $m_{dh}$ are the density of state effective mass for electrons in the conduction band and holes in the valence band, respectively [7]; $k_B$ is the Boltzmann constant. In Ge with a small $E_g$, $n_i$ is $2.4 \times 10^{13}$ $\mathrm{cm}^{-3}$ at RT and exceeds carrier density designed by impurity doping at temperatures higher than around 100°C, which limits the availability of Ge as a semiconductor device. At the valence band top $\Gamma_8$, heavy-hole (hh) and light-hole (lh) bands are degenerate, while in the conduction band the electrons conduct two effective masses: $m_{el}$ is longitudinal along the symmetry axis of the ellipsoid <111> at $L_6$ and $m_{et}$ is transversal within the plane normal to the symmetry axis. Application of strain lifts the degeneracy of the hh and lh bands at the valence band top $\Gamma_8$ point, which is useful for strained devices.

The mobility of electron $\mu_e$ and hole $\mu_h$ is 3900 and 1900 $\mathrm{cm}^2/\mathrm{Vs}$ in Ge at RT, faster than in Si by 2.5 and 4 times, respectively. Mainly due to phonons scattering against them, the mobility decreases with temperature [5] as

$$\mu_e = 4.9 \times 10^7 T^{-1.66}, \mu_h = 1.05 \times 10^9 T^{-2.33}. \tag{4.3}$$

Donor and acceptor impurities induce energy levels in the bandgap, as shown in Table 4.3 [5,8−12], where a donor level is given from the bottom of the conduction band $E_c$ and an acceptor from the top of the valence band $E_v$. By scattering due to such ionized impurities, carrier mobility decreases with impurity concentration.

The elastic constants $C_{11}$, $C_{12}$, and $C_{44}$ of Ge and Si, measured by the resonance method, decrease gradually with increasing temperature, as shown in Fig. 4.3 [13,14]. The shear modulus $G$ is 48.9 GPa at RT.

The photoelectric effect is the emission of electrically charged particles in a material in response to electromagnetic radiation with energy higher than the threshold, which is the direct photo-to-current conversion. Fig. 4.4 shows the experimental absorption coefficients near and above the fundamental absorption edge for Ge at 77K and RT alongside those for Si and gallium arsenide (GaAs) [5,15,16]. Ge shows a steep absorption edge in spite of an indirect semiconductor. This feature is based on the direct-transition gap 0.8 eV at the valence band top $\Gamma_8$ to $\Gamma_7$, close to $E_g$, which is the physical reason why Ge is applied in the field of infrared and far infrared detectors and devices.

As seen in Table 4.2, the density of Ge is higher than that of Si by a factor of around 2.3. The thermal conductivity of Ge is 58 $\mathrm{W/cm^2\,K}$, lower than that of Si in the practical temperature range up to the melting point $T_M$, which induces large temperature gradients in axial and radial directions. The Gibbs standard free energy of germanium dioxide ($GeO_2$) is 3.41 kJ/mol at $T_M$, comparable to that of $H_2O$, which means that $GeO_2$ is unstable [17]. These intrinsic features are closely related to the disadvantages of Ge in preparation and application of its crystals.

**Table 4.3** **Energy level, maximum solubility, and segregation coefficient of main impurities doped into Ge; segregation coefficients of main impurities doped into Si are also shown**

| Impurity | Electric type | Energy level $E_c-$, $E_v+$ | Max. solubility (cm$^{-3}$@ $T$[°C]) | Segregation coefficient | Max. solubility (cm$^{-3}$@ $T$[°C]) | Segregation coefficient |
|---|---|---|---|---|---|---|
| Ge | | | | | Si | |
| P | d | −0.013 | $2.0 \times 10^{20}$@ 560 | 0.08 | $1.3 \times 10^{21}$@ 1200 | 0.35 |
| As | d | −0.014 | $7.0 \times 10^{19}$@ 800 | 0.02−0.04 [12] | $1.8 \times 10^{21}$@ 1150 | 0.3 |
| Sb | d | −0.010 | $1.2 \times 10^{19}$@ 800 | 0.003 | $7.0 \times 10^{19}$@ 1325 | 0.023 |
| Te | d | −0.093 | $7.0 \times 10^{18}$@ 850 | 0.000001 | | |
| Li | d | −0.010 | $7.5 \times 10^{18}$@ 825 | 0.002−0.01 | $6.5 \times 10^{19}$@ 1200 | 0.01 |
| Bi | d | −0.013 | $6.0 \times 10^{16}$@ 850 | 0.000045 | $8.0 \times 10^{17}$ | 0.0007 |
| B | a | +0.011 | $1.0 \times 10^{18}$ | 6.2 [11] | $1.0 \times 10^{22}$@ 1410 | 0.8 |
| Al | a | +0.011 | $4.3 \times 10^{20}$@ 750 | 0.073 | $5.0 \times 10^{20}$@ 1030 | 0.002 |
| Ga | a | +0.011 | $5.0 \times 10^{20}$@ 650 | 0.087 [12] | $4.0 \times 10^{19}$@ 1250 | 0.008 |
| In | a | +0.012 | $4.0 \times 10^{18}$@ 800 | 0.001 | $2.0 \times 10^{18}$ | 0.0004 |
| Tl | a | +0.013 | $9.0 \times 10^{18}$@ 910 | 0.00004 | $8.8 \times 10^{17}$ | 0.00017 |
| Cd | a | +0.160 | $2.5 \times 10^{18}$@ 825 | ∼0.00001 | | 0.000001 |
| H | | | $8 \times 10^{14}$ [10] | | $7.0 \times 10^{15}$@ 1410 | |
| C | | | $2.5 \times 10^{14}$ | | $3.0 \times 10^{17}$@ 1410 | 0.07 |
| O | | | $1.0 \times 10^{18}$ | 0.11, 1.0−1.4 | $3.0 \times 10^{18}$@ 1410 | 1.4 |
| Sn | | | $5 \times 10^{20}$@ 400 | 0.02 [12] | $6.0 \times 10^{19}$@ 1100 | 0.016 |
| Si | | | Complete mixing | 5.5 | – | – |

Notes: d and a mean donor and acceptor, respectively.
+ and − means above the valence band and below the conduction band, respectively.
Data based on S.M. Sze, Physics of Semiconductor Devices, second ed., Wiley-Interscience Publication, 1981 (in the current version published in 2007, some descriptions and data on Ge have been removed); A. Trumbore, Solid solubilities of impurity elements in germanium and silicon, Bell Syst. Tech. J. 39 (1960) 205−233; M. Schulz, H. Weiss (Eds.), Comprehensive Data Book: Landolt-Börnstein Group III, Vol. 17c, Technology of Si, Ge and SiC, Springer-Verlag, 1984.

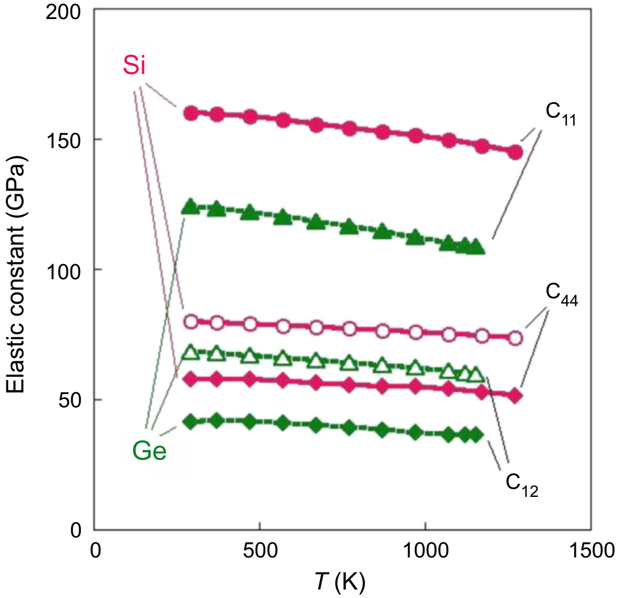

**Figure 4.3** Temperature dependences of elastic constants $C_{11}$, $C_{12}$, and $C_{44}$ of Ge and Si, measured by the resonance method [13,14].

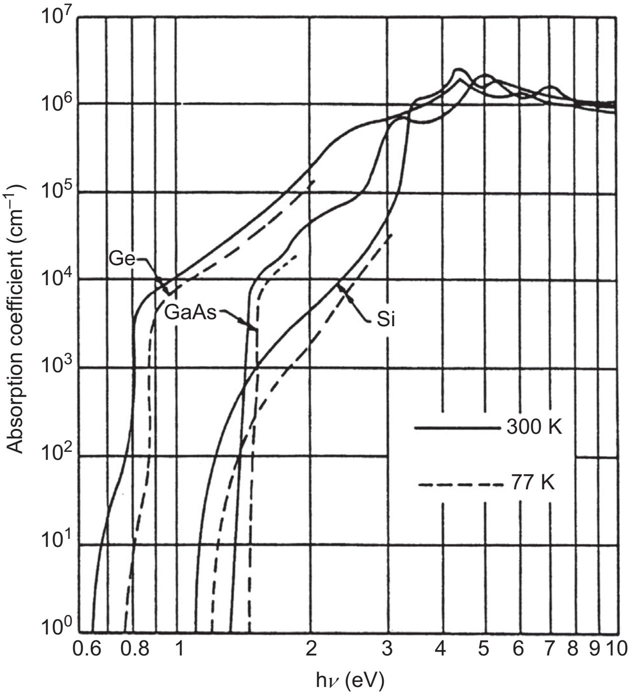

**Figure 4.4** Absorption spectra near and above the fundamental absorption edge for single-crystal Ge, Si, and GaAs at 77K and RT [5,15,16].
Reprinted from S.M. Sze, Physics of Semiconductor Devices, second ed., Wiley-Interscience Publication, 1981. Copyright 1981, with permission from Wiley-Interscience Publications.

## 4.3 Material preparation

Ge is a minor constituent at the low concentration of around 0.00065% in the earth's crust and is included in some metallic ores and minerals, such as germanite ($Cu_{26}Fe_4Ge_4S_{32}$), renierite [$(Cu, Zn)_{11}(Ge, As)_2Fe_4S_{16}$], and argyrodite [$(Cu, Ag)_8GeS_6$]. Ge for industrial use is produced as a by-product in zinc, lead, and copper refining plants and is in some cases recovered from coal ash. Recently, recycling of Ge products is being developed.

Fig. 4.5 shows a flowchart of extraction, production, and reclamation of Ge. First, Ge ores, or minerals such as germanite and renierite containing around 5−10% Ge, are leached by sulfuric acid and solvent extracted; this is condensed to 50% Ge crude. Then the Ge crudes are chlorinated and fractionally distilled to high-purity germanium tetrachloride ($GeCl_4$). $GeCl_4$ is hydrolyzed, filtrated, and dried to produce a white powder of $GeO_2$ of various grades. Finally, the $GeO_2$ powder, put in a graphite boat, is reduced at a temperature of 650−675°C in an atmosphere of flowing hydrogen gas, melted at an elevated temperature, and then solidified to a polycrystalline Ge ingot with a high purity of around $10^{14}$ $cm^{-3}$. Depending on applications, the reduction of the $GeO_2$ is handled with special care to avoid synthesis of the intermediate volatile product germanium oxide (GeO).

The polycrystalline Ge ingots are purified through zone refining (Pfann's method) according to the principle of segregation of impurities at the liquid−solid interface, since most impurities, except Boron (B) and Si, in Ge have a segregation coefficient

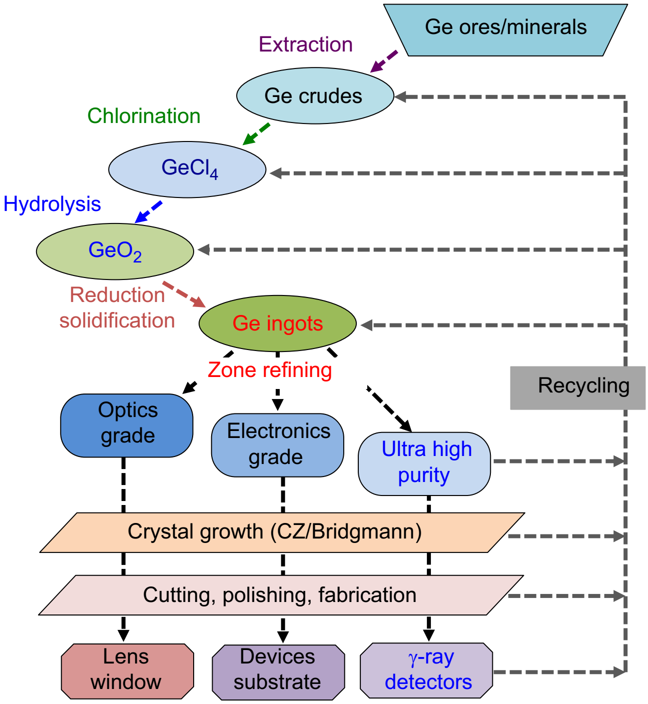
Ge ores/minerals
Extraction
Ge crudes
Chlorination
GeCl4
Hydrolysis
GeO2
Reduction solidification
Ge ingots
Zone refining
Recycling
Optics grade
Electronics grade
Ultra high purity
Crystal growth (CZ/Bridgmann)
Cutting, polishing, fabrication
Lens window
Devices substrate
γ-ray detectors

**Figure 4.5** Flowchart of extraction, production, and reclamation of Ge.

**Table 4.4 Solutions for chemical polishing and preferential etchants for defect detection for Ge**

| Composition | Conditions |
|---|---|
| $HNO_3$:HF = 3−5:1 | Chemical polishing, RT−30°C |
| $HNO_3$:HF:$CH_3COOH$:$Br_2$ = 5:3:3:0.2 | Chemical polishing, RT−70°C |
| $HNO_3$:HF:$CH_3COOH$ = 5:3:3 | Chemical polishing,<br>preferential etchants for dislocations<br>RT |
| 8 g $K_2Fe(CN)_6$, 12 g KOH, 100 mL $H_2O$ | Preferential etchants for dislocations<br>(111), (100) surface<br>RT |

much smaller than 1. Table 4.3 shows the segregation coefficient and solubility limits of typical impurities in Ge and Si. Such impurities are swept out to the tail side of the ingot during controlled directional solidification of the molten phase. Ge ingots are zone refined several times to an impurity content level below $10^{13}$ $cm^{-3}$, and are used in crystal growth for electronic and optical applications. For the crystal growth of Ge for $\gamma$-ray detectors, an additional zone-refining process is conducted using a single crystal seed to avoid segregation of residual impurities on grain boundaries. The impurity concentration in these single crystalline Ge ingots is lower than $10^{11}$ $cm^{-3}$. Recently, Yang et al. proposed the optimal system and conditions of zone refining, including the quartz tube, container, length ratio of molten zone to ingot, and so forth, for high-purity ingots [18].

Table 4.4 shows typical solutions for chemical polishing and preferential etchants for defect detection in Ge.

## 4.4 Ge crystal growth

Ge single crystals can be grown by the Czochralski (CZ) or Bridgman methods. The latter includes the horizontal Bridgman (HB), vertical Bridgman (VB), and vertical gradient freeze (VGF) methods. Ge single crystals cannot be grown by the floating-zone (FZ) method because of the small ratio of the melt surface tension to the density where a floating zone exceeds 10 mm in diameter cannot be stable. An FZ growth trial of 15 mm diameter was conducted in a microgravity environment aboard the FOTO spacecraft [19]. Table 4.5 shows the physical properties of Ge melt in comparison with those of Si melt [8,20,21].

### *4.4.1 Bridgman growth*

Cressell and Powell [22] reviewed HB growth of Ge conducted in the 1950s. Though work on Bridgman growth of Ge was limited for a long time, the VGF method has

**Table 4.5** **Physical properties of Ge and Si melts**

| | | Ge | Si |
|---|---|---|---|
| Melting temperature, $T_M$ (°C) | | 937 | 1414 |
| Density of melt (g/cm$^3$) | | 5.51 | 2.53 |
| Emissivity | | 0.2 | 0.55 |
| Vapor pressure at $T_M$ (Pa) | | 0.0001 | 0.03 |
| Thermal conductivity (W/m K) at $T_M$ | | 71 | 67 |
| Thermal volume expansion (K$^{-1}$) | | $1.1 \times 10^{-4}$ | $1.44 \times 10^{-4}$ |
| Kinematic viscosity (cm$^2$/s) | | $1.35 \times 10^{-3}$ | $3.5 \times 10^{-3}$ |
| Latent heat of fusion (kJ/mol) | | 33.9 | 50.7 |
| Specific heat (W/g K) at $T_M$ (melt) | | 3.79 | 1.037 |
| Surface energy (J/m$^2$) at $T_M$ | | 0.60–0.62 | 0.72–0.88 |
| Thermal diffusivity (cm$^2$/s) | | 0.175 | 0.13 |
| Prandtl number | | 0.008 | 0.027 |
| Schmidt number | | 22 | 12 |
| Diffusion coefficient of impurities (cm$^2$/s) | Pure | $6 \times 10^{-5}$ [20] | $3.0 \times 10^{-4}$ [20] |
| | B | $1.4 \times 10^{-4}$ | $1.8 \times 10^{-4}$ |
| | Ga | $2.8 \times 10^{-5}$ [21] | $3.6 \times 10^{-4}$ |
| | As | $8.9 \times 10^{-5}$ | $2.5 \times 10^{-4}$ |
| | Sb | $2.5 \times 10^{-4}$ [21] | $1.1 \times 10^{-4}$ |

Data based on S.M. Sze, Physics of Semiconductor Devices, second ed., Wiley-Interscience Publication, 1981. (In the current version published in 2007, some descriptions and data on Ge have been removed).

again attracted attention recently to reduce the density of grown-in dislocations. Essentially VGF imposes low axial and radial thermal gradients on the growing crystals, which is effective to reduce thermal stress. In addition, Azoulay and Gafni adopted a graphite crucible lined with soft graphite felt to suppress dislocation generation from the crucible wall [23]. Langheinrich et al. reported VGF growth of Ge with a diameter of up to 75 mm where an inert gas or vapor pressure was induced to give no contact with the crucible, as seen in Fig. 4.6 [24].

### 4.4.2 *Czochralski growth*

Started by Teal and Little at Bell Laboratories in the 1950s [25], at present Ge single crystals are grown up to 30 cm in diameter by the CZ method. Umicore succeeded in growing dislocation-free crystals of this size, as noted in Section 4.1, though even now

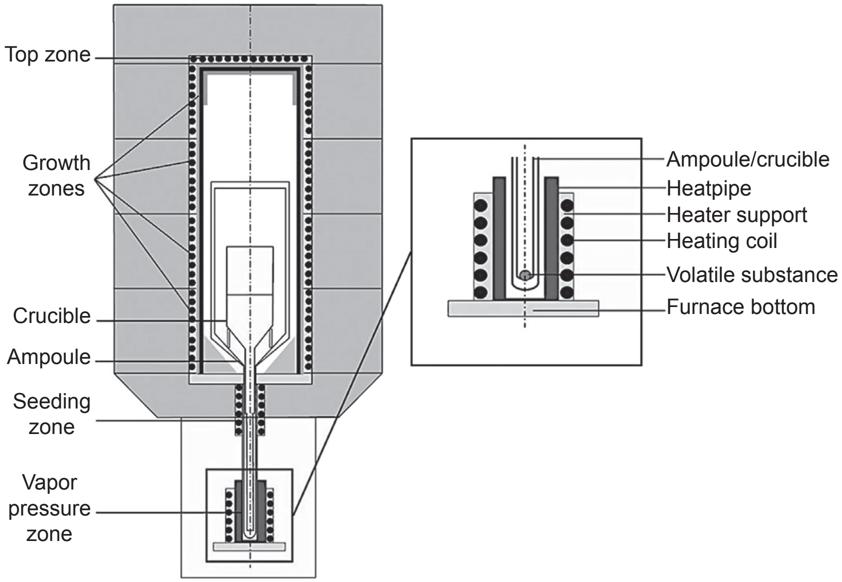

**Figure 4.6** VGF furnace with the crucible in an enclosed ampoule and the vapor pressure zone for growth with no contact with the crucible (enlarged) [24].
Reprinted from D. Langheinrich, O. Pätzold, L. Raabe, M. Stelter, VGF growth of germanium single crystals without crucible contact, J. Cryst. Growth 312 (2010) 2291−2296, Copyright 2010, with permission from Elsevier.

it is not technologically easy to grow dislocation-free Ge crystals on a commercial basis. Here we briefly review some basic features of the CZ method for Ge growth.

A general CZ Si puller can be used for Ge crystal growth for its low melting point, its relatively low vapor pressure at the melting point, its low toxicity level, and its low interaction with crucible materials of graphite or quartz. Usually automatic control of growing crystals is achieved by using a weight-sensing system or camera monitoring of the meniscus. However, the melting point of Ge (937°C) is much lower than that of Si (1414°C) and also the emissivity of Ge (0.2) is smaller than that of Si (0.55). Owing to them, the meniscus ring of Ge is rather darker than that of Si. Thus a camera monitoring system finds it difficult to detect variations in the meniscus ring and can be used only in the limited case that the growing crystal is round in shape with a uniform meniscus ring.

Crucibles are prepared from graphite of isostatically pressed quality (or nuclear reactor grade) or quartz. The crucible is set into a susceptor made of high-quality graphite during crystal growth.

A picket-fence-type resistance heater fabricated from electro-graphite provides three-phase alternating current or direct current. The growth chamber can be used in vacuum or in an ambient inert gas such as Ar or $H_2$, but pulling under vacuum should be avoided for large-diameter crystals since the amount of latent heat of fusion is not easy to remove from the grown Ge crystal due to its low thermal conduction.

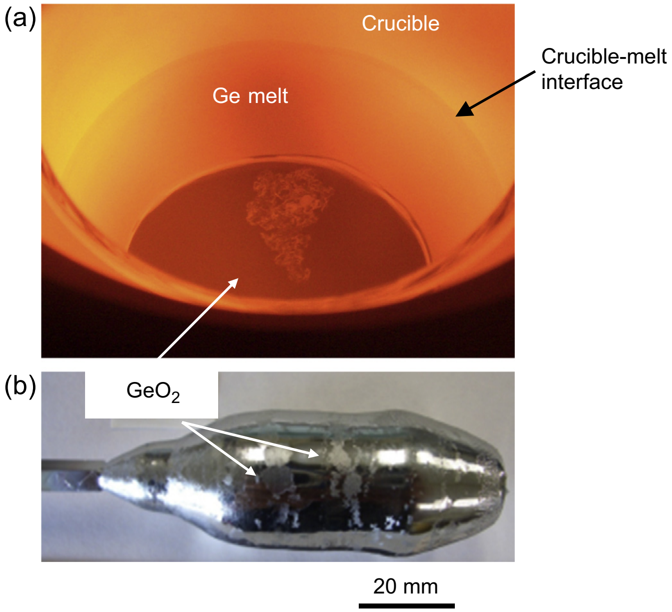

**Figure 4.7** (a) $GeO_2$ floating on the melt surface in a crucible; (b) grown Ge boule with $GeO_2$.

The conductivity of Ge crystals increases from 24 to 58 W/m K at the melting point and RT, respectively, which is rather gradual in comparison to Si crystals. For growth of ultra high pure Ge crystals a radio frequency (RF) induction heating system is used; in this case the ambient inert gas should be $H_2$.

During CZ Ge crystal growth some particles appear and float on the Ge melt surface in a silica crucible, as shown in Fig. 4.7(a), and attach to the growing crystal surface (Fig. 4.7(b)), which eventually results in generation of dislocations and penetration into the crystal. Since the particles are thought to be $GeO_2$, the melting point of which is 1115°C [26], higher than that of Ge (937°C), these particles cannot be removed completely during the growth process. They are formed in the melt, originating in a thin oxide layer on the surface of charged Ge raw material, air leakage of the chamber, or residual moisture in the growth furnace. Generation of $GeO_2$ particles can be effectively suppressed by partial or full coverage of the melt surface with liquid boron oxide ($B_2O_3$) glass [27].

## 4.4.3 Dislocation-free crystal growth

### 4.4.3.1 Seeding

For single crystal growth, a seed, usually a cylindrical or rectangular bar typically $5 \times 5 \times 50\ \mathrm{mm}^3$ in size, is prepared from a single crystal of Ge, the axis being along the crystallographic orientation of the crystal to be designed for the purpose. A seed should be prepared from a crystal free from dislocations or at least with a low density of dislocations. The seed is slowly taken to the melt surface and its tip is dipped into the melt, avoiding thermal shock, to develop a meniscus around the dipped seed. Interestingly, an Si seed can be used to grow a crystal from a pure Ge melt [28]. Of course, the grown crystal becomes a dilute SiGe alloy, less than ~1 atomic %, due to Si segregating from the melted Si seed.

#### 4.4.3.2 Dash necking

Dislocations generate easily in the seed due to the thermal stress induced by the thermal shock during the dipping process. For topological reasons no dislocation can terminate inside a crystal, so such dislocations propagate into the growing crystal and multiply there through movement under the thermo-elastic stress applied in the environment of crystal growth. In Ge with a diamond structure, dislocations have (a/2) [110]-type Burgers vector and move on the {111} planes in the <110> direction. In Ge grown in a <100> or <111> direction, all the (111) slip planes are oblique against the growth axis except the (111) perpendicular to the growth axis. Thus etch pits of the dislocations on the wafer perpendicular to the growth axis of <100> and <111> directions exhibit distributions of typically octagonal and hexagonal patterns, respectively.

Dislocations act as a harmful trap of carriers, so dislocation-free crystals are desirable. As described above, dislocations move on {111} planes inclined against the growth axis and can reach to the crystal surface and leave the crystal if the crystal is small and thin. Indeed, after dipping and starting crystal growth, if the crystal diameter is decreased to about 2–4 mm for any length longer than a few tenths of millimeters, the crystal becomes dislocation-free. This is so-called Dash necking, originated by Dash in 1959 [29], and is a standard method widely adopted in crystal growth.

Fig. 4.8 shows an X-ray topographic image of a Dash-necked part of an undoped Ge crystal. Dislocations propagated from the seed, escaped from the thin neck, and then were free in the crystal (Fig. 4.8b) [30].

The fact that the melting point $T_M$ of Ge is lower than that of Si by around 500°C is an important advantage for crystal growth, since the thermal condition for Ge crystal growth is easier to establish in comparison with that for Si. However, the growth of dislocation-free Ge crystals, especially of a large diameter, is difficult, essentially due to its physical properties, shown in Table 4.2. First, the thermal conductivity of Ge is lower than that of Si, which means that thermo-elastic stress is more significantly induced by temperature inhomogeneity inside the crystal. Second, dislocations, once generated, move and multiply more easily in Ge than in Si. This means Ge is weaker than Si. Third, the density of Ge is much higher than that of Si, by a factor of around 2.3. Thus a Ge thin neck processed by Dash necking should withstand the heavier weight of the crystal body in spite of the seed being weaker than Si.

#### 4.4.3.3 New CZ method

To overcome the above-mentioned difficulties, Moskovskih et al. developed a low temperature gradient (LTG) CZ method. By adopting a temperature gradient at a level

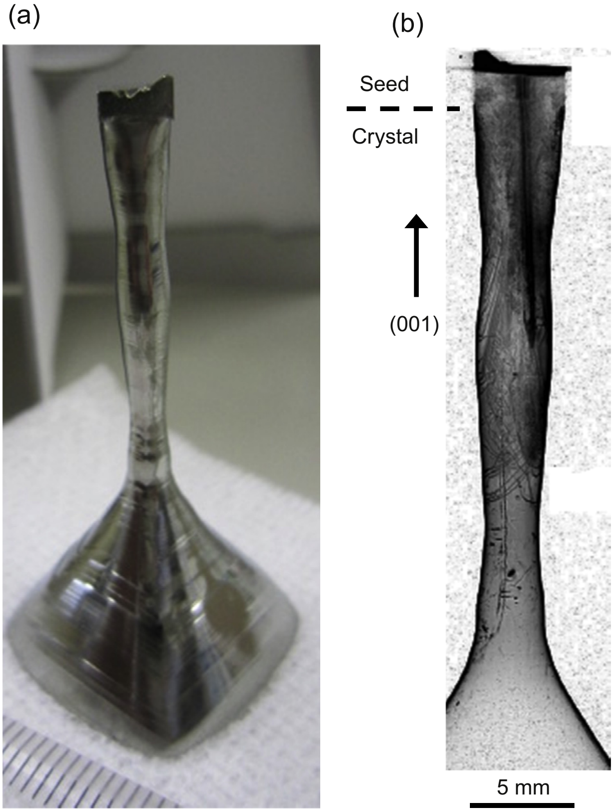

**Figure 4.8** (a) Dash-necked part of an undoped Ge crystal; (b) X-ray topographic image of the neck part [30].

lower than around 1 K/cm as shown in Fig. 4.9, they suppressed axial and radial thermo-elastic stresses and succeeded in growing Ge crystals of 45−48 mm in diameter with a dislocation density of $10^2$ $cm^{-2}$ without Dash necking, pointing to a possibility of dislocation-free crystal growth in future [31,32].

Taishi et al. reported growth of oxygen (O)-enriched Ge crystals of 25 mm in diameter with an extremely low density of grown-in dislocations or almost free from them [33]. The crystals were grown from a Ge melt covered with liquid $B_2O_3$ glass with the addition of $GeO_2$ powder in a silica crucible. Maximum concentration of O in the Ge was $5.5 \times 10^{17}$ $cm^{-3}$, two orders of magnitude higher than O in a conventionally grown Ge crystal. O atoms dissolved from $GeO_2$ powder are incorporated effectively into Ge crystals without evaporating from the $B_2O_3$-covered melt surface, and possibly suppress dislocation generation and multiplication through their mutual interaction (described later).

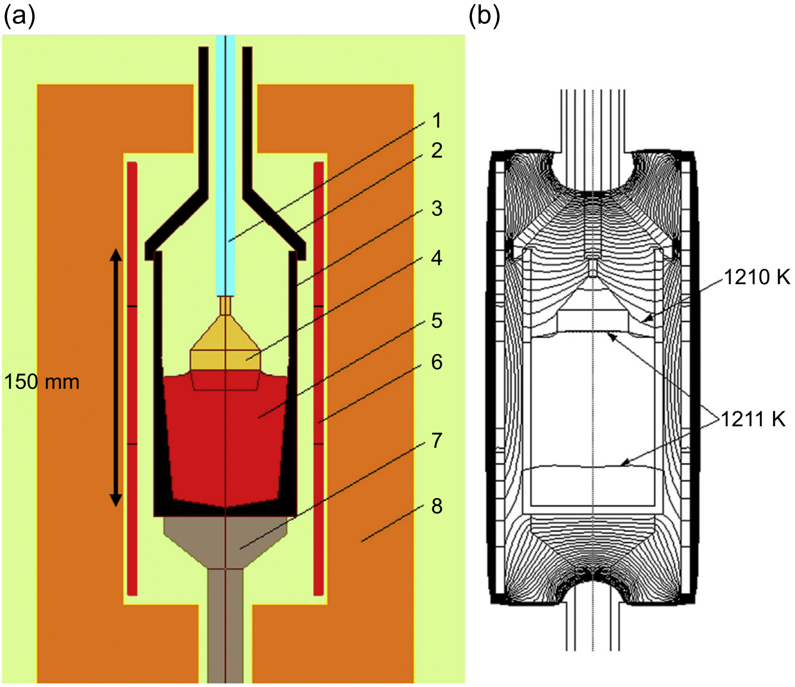

**Figure 4.9** (a) Illustration of low thermal gradient CZ furnace. (1) Crystal holder, (2) graphite cove, (3) graphite crucible, (4) crystal, (5) melt, (6) three-band heater, (7) pedestal, and (8) shield. (b) Temperature distribution during Ge crystal growth [31].
Reprinted from V.A. Moskovskih, P.V. Kasimkin, V.N. Shlegel, Y.V. Vasiliev, V.A. Gridchin, O.I. Podkopaev, The low thermal gradient CZ technique as a way of growing of dislocation-free germanium crystals, J. Cryst. Growth 401 (2014) 767–771, Copyright 2014, with permission from Elsevier.

## 4.5 Growth-related phenomena

### *4.5.1 Periphery facets*

It is known that flat areas develop on the sides of a CZ-grown Ge boule, as seen in Fig. 4.10(a), more clearly than in Si. The flat area consists of mirror-like (111) faces, developed layer by layer and typically observed in the corn part of a grown crystal, as seen in Fig. 4.10(b). This is periphery facet formation, associated with anisotropy of the surface energy. A facet is usually the most densely packed crystallographic plane with the smallest surface energy; that is (111) in Ge. As seen in Table 4.2, the free energy is 1.23 $\mathrm{Jm}^{-2}$ for a (111) face of Si. In contrast, the free energy is 1.06 $\mathrm{Jm}^{-2}$ for a (111) face of Ge. The free energy is 1.30 $\mathrm{Jm}^{-2}$ for a (110) face. These figures are considerably lower than those for other faces [34]. Thus growth is fast along the densely packed (111) planes while slow in the perpendicular direction, leading to

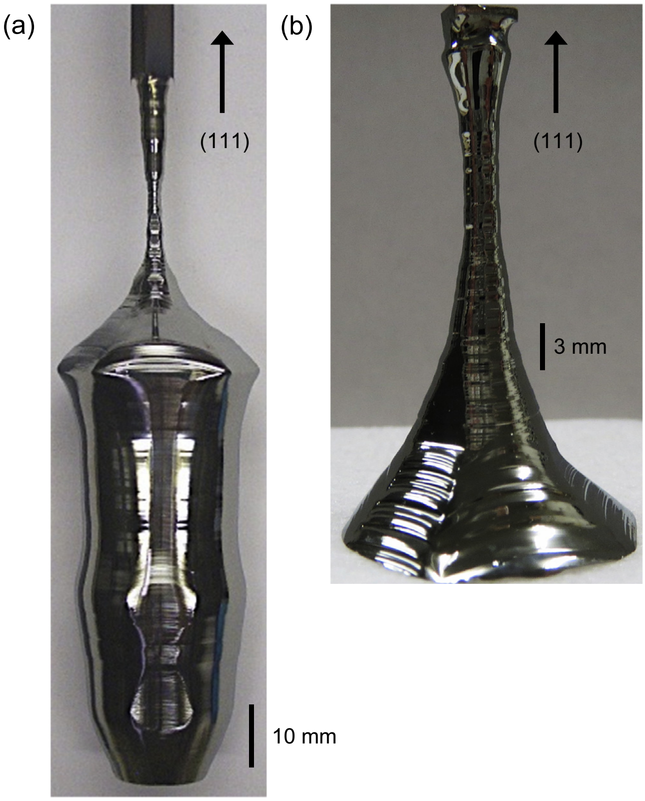

**Figure 4.10** (a) Periphery facets developed on the side of a CZ Ge crystal grown along a [111] direction; (b) mirror-like (111) faces developed layer by layer in the corn part of a CZ Ge crystal.

the appearance of step-like growth of the (111) face, as seen in Fig. 4.11. Also, the steps consist of {111} faces inclined to the (111).

Usually the cross-section of a Ge crystal is almost circular in shape due to rotation during growth, while the crystal loses its shape under an effect of the inclined facets, leading to the above-mentioned flat areas on the outside of the crystals. Thermodynamically the crystal tends to be bordered by (111) flats and/or facets. Thus a <100> pulling crystal tends to be square and a <111> crystal is triangular, as seen in Figs. 4.8(a) and 4.10(b).

The (111) faces are inclined to the isotherm of the melt/crystal interface of the growing crystal, and are undercooled compared to the rough (nonfacet) portions of the interface. Thus more impurities segregate into these facet regions than to the nonfacet portions inside the crystal, especially in Ge, where almost all the impurities have a segregation coefficient much lower than 1.

Formation of growth twins is a typical phenomenon in indium phosphide (InP) [35,36] but not observed frequently in Ge under a conventional growth system and

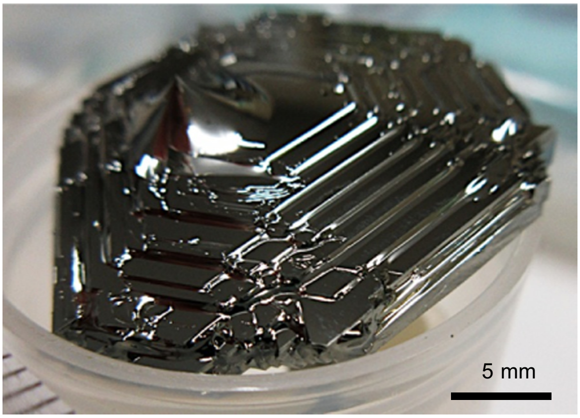

**Figure 4.11** Step-growth morphology observed at the bottom of a CZ Ge boule doped with Si at a concentration of $5 \times 10^{19}$ cm$^{-3}$.

conditions, since the stacking fault energy [37] of Ge is much larger than that of InP [38]. However, some twins start from the $\{111\}$ periphery facets during the shoulder part of growth of crystals, especially those doped with impurities, at the three-phase boundary in conditions of high temperature and growth-rate fluctuations [39,40].

### 4.5.2 Segregation

When Ge is undoped, it is not hard to grow a dislocation-free crystal or a low dislocation-density crystal, mainly due to the low temperature needed for growth. In contrast, growth of doped crystals is not easy because of the small segregation coefficient and low solubility of dopants, shown in Table 4.3.

For device applications, Ge crystals require doping with a specific impurity to give the desired electrical carrier concentration of up to $10^{18}$ cm$^{-3}$. Usually gallium (Ga) and indium (In) (group III) are used for p-type crystals, while antimony (Sb) and arsenide (As) (group V) are used for n-type crystals. Fig. 4.12(a) shows a CZ Ge boule doped with Ga in the top-part concentration of $4 \times 10^{19}$ cm$^{-3}$, grown by a pulling velocity of 10 mm/h [12]. The boule changes to polycrystalline at the arrowed position. Fig. 4.13 shows the variation of Ga concentration plotted against the solidification ratio in a Ge crystal [12]. The impurity concentration was determined by Hall effect measurements at RT under an assumption that almost all the impurity atoms are supposed to be ionized as suppliers of carriers in the concentration range. In the same figure, results for B-, As-, and tin (Sn)-doped Ge are superimposed. The concentration of the electrically neutral impurity (Sn) was determined by wavelength dispersive X-ray (WDX) spectroscopy. The variations of the impurity concentration were analyzed using

$$C_s(g) = k_{\mathrm{eff}} C_0 (1-g)^{k_{\mathrm{eff}}-1} = C_s(0)(1-g)^{k_{\mathrm{eff}}-1} \tag{4.4}$$

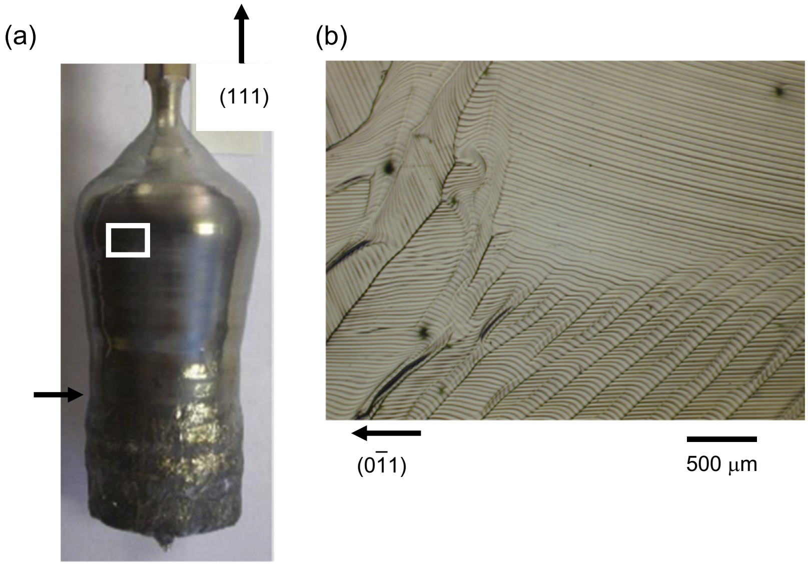

**Figure 4.12** (a) A CZ Ge boule doped with Ga in the top-part concentration of $4 \times 10^{19}$ cm$^{-3}$ which was grown by a pulling velocity of 10 mm/h along the [111]. Polycrystallized at the arrowed position. (b) Appearance of fluctuations from regular growth striations observed in the *squared area* in (a) [12].

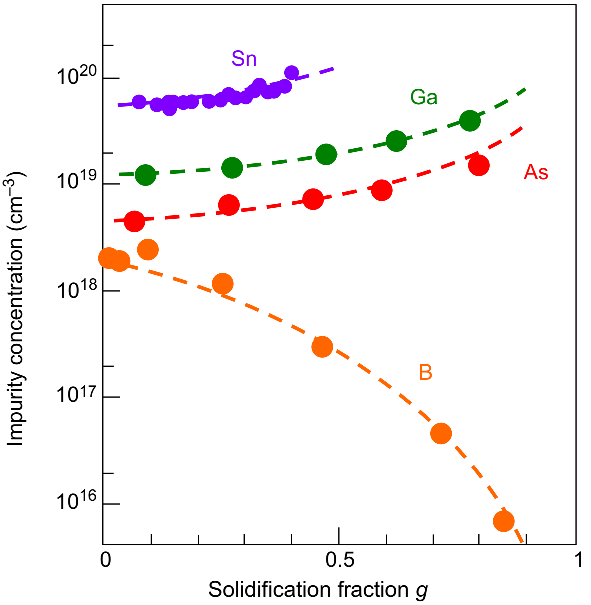

**Figure 4.13** Variation of concentrations of Ga, As, B, and Sn plotted against the solidification fraction *g* in Ge crystals [12].

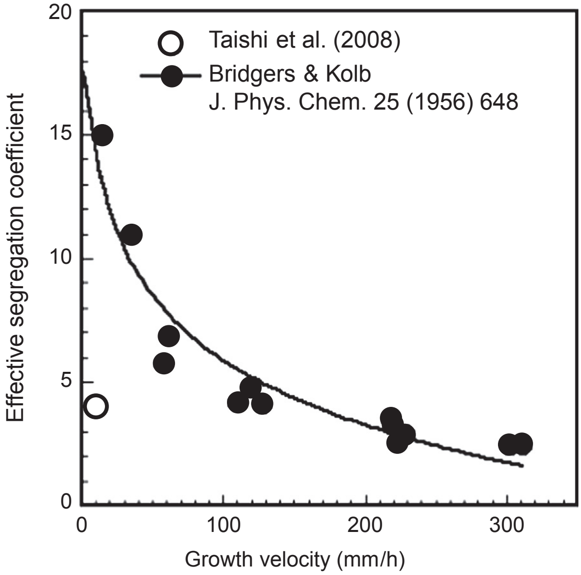

**Figure 4.14** Reduction of effective segregation coefficient of B in Ge with an increase of the growth velocity [11].
Modified from T. Taishi, Y. Murao, Y. Ohno, I. Yonenaga, Segregation of boron in germanium crystal, J. Cryst. Growth 311 (2008) 59–61, Copyright 2008, with permission from Elsevier.

where $C_s(g)$ is the impurity concentration in the grown Ge with a solidification fraction $g$ and an effective segregation coefficient of $k_{\text{eff}}$ according to the Pfann relation of the complete mixing of a melt [41]. We can obtain an effective segregation coefficient of impurity in Ge crystals without precious knowledge of the initial dopant concentration $C_0$ in the melt. As seen in Fig. 4.14 [11], the effective segregation coefficient $k_{\text{eff}}$ decreases with increasing growth velocity $v$

$$k_{\text{eff}} = k_0 \Big/ [k_0 + (1 - k_0)\exp(-vd/D)], d = 1.61(\nu/\omega_s)^{1/2}\text{Sc}^{-1/3} \tag{4.5}$$

where $k_0$ is the equilibrium segregation coefficient, $d$ is the diffusion layer thickness, and $D$ is the dopant diffusivity in the Ge melt [42]. The diffusion layer thickness is given with $\nu$ the kinematic viscosity of the melt, $\omega_s$ the crystal rotation rate, and Sc the Schmidt number ($=\nu/D$).

In the Ge crystals shown in Fig. 4.13, $k_0$ of Ga, B, As, and Sn was evaluated to be 0.087, 5–6, 0.04, and 0.02, respectively [11,12]. The pulling velocity for the crystals was 4–10 mm/h, which is rather slow, and it can be thought that the $k_{\text{eff}}$ obtained from the relation between dopant concentration and solidification ratio is almost equal to the $k_0$.

As seen in Table 4.3, donor impurities in Ge have a smaller segregation coefficient by an order of magnitude than in Si, while acceptor impurities in Ge are larger by an order of magnitude than in Si. The large segregation coefficient of B in Ge is unique.

A segregation coefficient of an impurity into crystal is supposed to be governed by the bonding energy and strain energy [43]. The fact that B segregates more easily in Ge crystal than in Si crystal despite the increase of strain energy due to the large size misfit seems to show a neccessity to include some electronic effect in the segregation mechanism.

## *4.5.3 Interface instabilities*

### *4.5.3.1 Striations*

Since almost all the dopants in Ge, except B, have a segregation coefficient less than 1, a solute-rich boundary layer is formed ahead of the growth interface during crystal growth. The layer may posses a temperature lower than the liquidus temperature given by thermodynamic equilibrium under conditions of a fast growth velocity, a low temperature gradient, or a high concentration of solutes in the melt: this is microsegregation and constitutional supercooling. The supercooling is the result of the higher diffusivity of heat than that of solute in Ge. This is described as $\mathrm{Pr} < \mathrm{Sc}$, where Pr is the Prandtl number $\mathrm{Pr} = \nu/\kappa$ with $\kappa$ the thermal diffusivity. In a region of constitutional supercooling, deviations of flatness of the growth interface lead to growth instability and formation of a cellular structure in the crystal. Fig. 4.12(b) shows an appearance of fluctuations from regular growth striations, observed in a Ga-doped Ge boule. The instability appeared at the concentration of $5 \times 10^{19}\ \mathrm{cm}^{-3}$. In a similar concentration region, some plate-like precipitates were observed in heavily As- or Sn-doped Ge. These crystals polycrystallized. In this situation we cannot adopt the relation in Eq. (4.4) for analyzing the segregation process.

### *4.5.3.2 X-ray topographic observations*

Fig. 4.15(a) shows an X-ray topographic image of a longitudinal cross-section of Si-rich $\mathrm{Ge}_{1-x}\mathrm{Si}_x$ alloy (where $x$ indicates the mole fraction of Si) [44]. The composition of the boule starts at $x_0 = 0.89$ and gradually decreases to 0.82 up to the tail along the growth axis according to the segregation $k = 0.51$ of Ge in the GeSi. Externally, the boule was known to be single crystalline along the [001] direction. However, we can find many interesting features inside the boule with respect to crystal growth. A high density of grown-in dislocations ($10^3$–$10^5\ \mathrm{cm}^{-2}$) generated at the seed–crystal interface expands in the whole section. The growth interface can be recognized as growth striations developed homogeneously from the seed–crystal interface up to the tail, except in the regions starting at $S$ and $T$. In these regions the growth interface is strongly disturbed and many vertical white lines are present. The disturbed region $S$ ends soon, with some defects that remain as white linear images. In contrast, the disturbed region $T$ expands in size and finally occupies almost the entire crystal at the tail. Indeed, an outer view of the tail shows fourfold configurations of factory-roof arrays formed by pairs of $\{111\}$ facet planes as seen in Fig. 4.15(e).

These features correspond well to optical micrographic observations of regions $S_1$, $S_2$, and $T$ in Figs. 4.15(b)–(d), respectively. In these regions the striations become unstable, just wavy lines parallel to the traces of (111) planes, showing the occurrence of

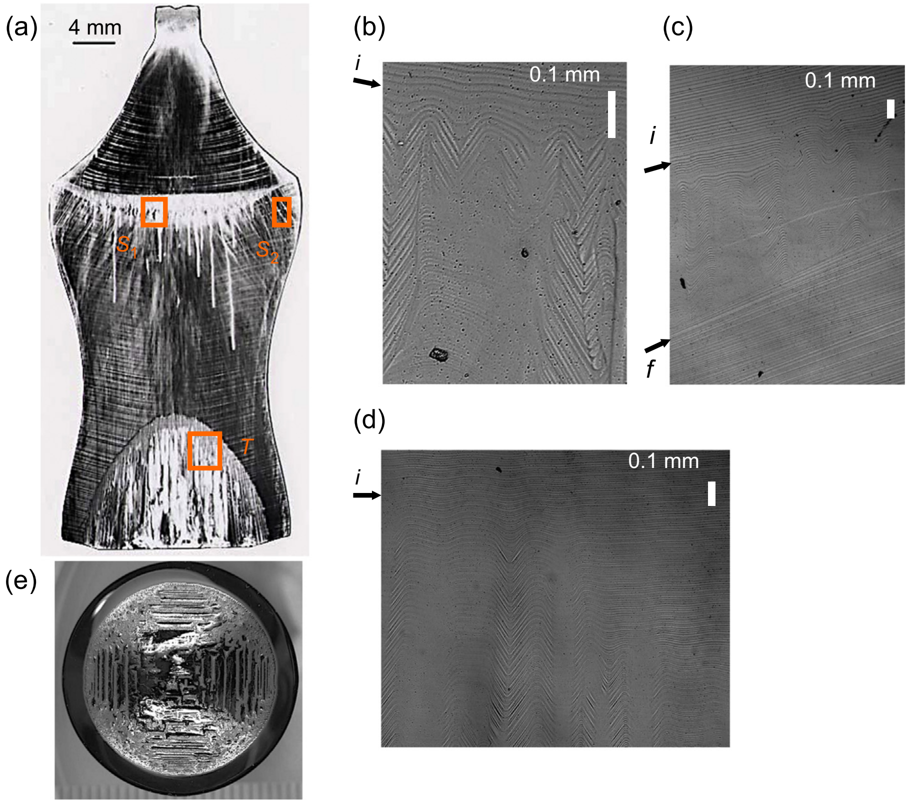

**Figure 4.15** (a) X-ray topographic image of the grown Si-rich GeSi alloy. Image of the sample plate parallel to the pulling axis. (b), (c), and (d) Striation patterns observed in the areas $S_1$, $S_2$, and $T$, respectively, shown in (a). *Arrows* labeled by *i* and *f* show initiation and disappearance of cellular growth, respectively. (e) Outer view of the bottom of the SiGe boule [44]. Reprinted from I. Yonenaga, T. Taishi, Y. Ohno, Y. Tokumoto, Cellular structures in Czochralski-grown SiGe bulk crystal, J. Cryst. Growth 312 (2010) 1065−1068, Copyright 2010, with permission from Elsevier.

a typical cellular growth. As seen in Fig. 4.15(c), the cellular structure in the periphery region $S_2$ was ended by remelting due to some increase of melt temperature during the growth, and homogeneous growth restarted with regular striations. The cellular structure in the region starting at position $T$ continued toward the crystal tail.

The observed occurrence and development of cellular structures starting at positions $S_1$, $S_2$, and $T$ are explained by constitutional supercooling. The cellular structure appears and disappears in the following ways. First, the cellular structure generation at $S_1$ and $S_2$ may be attributed to a variation in the effective growth velocity at a certain stage. In the growth stage, the melt temperature was intentionally reduced to expand the shoulder part of the crystal, which led to enhancement of the effective growth velocity. As a result, the growth velocity exceeded the critical growth velocity at that time. The effective growth velocity was then reduced by heating the melt/crystal.

Meanwhile, the development of the cellular structure at $T$ can be understood as follows. The Si composition of the growing alloy decreases gradually and the effective pulling rate simultaneously increases with the progress of growth. Thus the Si fraction and the local growth velocity at the growth interface at $T$ may exceed the critical relation of the growth velocity, resulting in the initiation of cellular growth. That is fatal to further growth if the effective pulling rate is not reduced.

### 4.5.3.3 Critical concentration and velocity in constitutional supercooling

In the growth of heavily impurity-doped Ge crystals an unstable growth interface and further polycrystallization were observed, and are explained by microsegregation and constitutional supercooling [45]. The critical concentration $C_s$ for the initiation of polycrystallization caused by the constitutional supercooling can be estimated as a function of growth rate $v$ by the following equation:

$$C_s = G_l D k_0^2 \Big/ \nabla T_l v (1 - k_0), \tag{4.6}$$

where $G_l$ is the temperature gradient in the melt of the melt/crystal interface and $\nabla T_l$ is the slope of liquidus where the constitutional supercooling occurs in the Ge-solute phase diagram. In the present CZ growth system, $C_s$ is evaluated to be $5 \times 10^{19}$, $1.4 \times 10^{19}$, and $3.4 \times 10^{16}\ \mathrm{cm}^{-3}$ for Ga-, As-, and Sb-doped Ge, respectively, which is somewhat lower than their solubility limits. Similarly, the critical growth velocity $v_c$ for the start-up of polycrystallization caused by constitutional supercooling can be estimated as a function of the composition $x$ for GeSi alloys.

## 4.6 Structural defects

Atomic-scale defects critically affect the quality of crystals and their device functionalities and degradations. Here, native (intrinsic) point defects and dislocations are reviewed briefly.

### 4.6.1 Native point defects

In a dislocation-free CZ Si or FZ Si, grown-in microdefects such as voids and dislocation loops or bundles are detected, mainly dependent on the pulling rate. The defects originate in intrinsic point defects (vacancies or self-interstitials) incorporated during crystal growth. At the crystal/melt interface, the vacancies and self-interstitial atoms at equilibrium concentrations are taken into the crystal and become supersaturated with decreasing temperature as the crystal is growing. Such excess point defects aggregate into clusters through diffusion. Clarification and control of their formation mechanism were major issues until recently. Nowadays, Voronkov's criteria that a vacancy

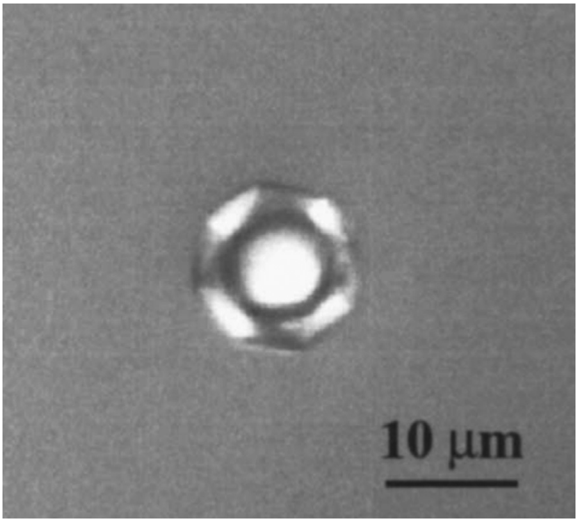

**Figure 4.16** Optical micrographs of a large crystallographic pit observed on polished CZ Ge wafers [46].
Reprinted from S. Hens, J. Vanhellemont, D. Poelman, P. Clauws, I. Romandic, F. Holsteyns, J. Van Steenbergen, Experimental and theoretical evidence for vacancy-clustering-induced large voids in Czochralski-grown germanium crystals, Appl. Phys. Lett. 87 (2005) 061915, Copyright 2005, with permission from American Institute of Physics.

generates in Si pulled with a ratio of velocity over axial temperature gradient larger than a critical value while a self-interstitial atom lower than the value is well known.

In Ge the situation is very different: there are only vacancy-based microdefects in CZ-grown Ge crystals. Fig. 4.16 shows a surface pit corresponding to so-called crystal-originated particles (COPs) in Ge [46]. In comparison to Si, the density is lower and the size is much larger, typically around one order of magnitude, which may hamper the quality of the electronic grade and the gate oxide integrity of transistors. The pit is a truncated octahedral void formed by aggregation of vacancies. From the results we can suppose that vacancies preferentially generate in Ge in comparison with self-interstitial atoms. Indeed, various research groups measured thermal equilibrium concentrations of vacancy experimentally in Ge. The concentration $C_{\mathrm{V}}^{*}$ is given by

$$C_{\mathrm{V}}^{*} = C_0(\mathrm{V})\exp\left(-E_{\mathrm{V}}^{\mathrm{F}}/k_{\mathrm{B}}T\right) \tag{4.7}$$

where $T$ is the temperature. The preexponential factor $C_0(\mathrm{V})$ and activation energy for formation $E_{\mathrm{V}}^{\mathrm{F}}$ reported by various groups is given in Table 4.6 [47–63]. The formation energy evaluated is in the range 1.8–2.3 eV and the concentration is typically around $10^{15}$ cm$^{-3}$ at the melting point. In addition, the migration energy of a vacancy is reported to be 0.42–1.0 eV [55,56]. Here the vacancies are revealed to be in the single negative charge state with a $D_2$ or $D_{2\mathrm{d}}$ structure due to Jahn–Teller distortion. To date there are no experimental reports on the formation of the self-interstitial in Ge.

**Table 4.6** **Experimentally determined formation energy $E_v^F$ and preexponential factor $C_0$(V) of a negatively charged vacancy in Ge; its migration energy and the formation energy of a neutral vacancy and self-interstitial atom are estimated by *ab initio* calculations**

| Experiments | | | *Ab initio* | | |
|---|---|---|---|---|---|
| $E^F$ ($V^-$) | $C_0$ ($V^-$) | $E^M$ ($V^-$) | $E^F$ ($V^0$) | $E^F$ ($I^0$) | References |
| 2.01 eV | 6.8 | | | | [47] |
| 2.26 | 10 | | | | [48] |
| 1.79 | 1.3 | | | | [49] |
| 1.9 | 4.16 | | | | [50] |
| 2.0 | 1.0 | | | | [51] |
| 1.9 | 162 | | | | [52] |
| 1.9 | 6.75 | | | | [53] |
| 2.09 | – | | | | [54] |
| 1.98 | 5 | | | | [55] |
| | | 0.42 eV | | | [56] |
| | | 1.0 | | | [57] |
| | | | 1.93 eV | 2.3 eV | [58] |
| | | | 2.56 | 3.5 | [59] |
| | | | 2.6 | – | [60] |
| | | | 2.33 | 3.17 | [61] |
| | | | 2.87 | 3.61 | [62] |
| | | | 2.32 | – | [63] |

These experimental results are supported by *ab initio* calculations reported by the groups shown in Table 4.6. Fig. 4.17 shows the formation energies of a vacancy and a self-interstitial atom in Ge plotted against the Fermi energy level of Ge [64]. Though their formation energies vary with an increase of the Fermi energy from p-type to n-type, it is found that the formation energy of a vacancy is far less than that of a self-interstitial atom in the whole energy range. Probably the feature of preferential formation of vacancies is attributed to the covalent bonding being weaker in Ge than in Si.

The self-diffusion coefficient in Ge is reported to be

$$D^{SD} = 13.6 \exp(-3.09\ \mathrm{eV}/k_B T)\mathrm{cm}^2/\mathrm{s} \tag{4.8}$$

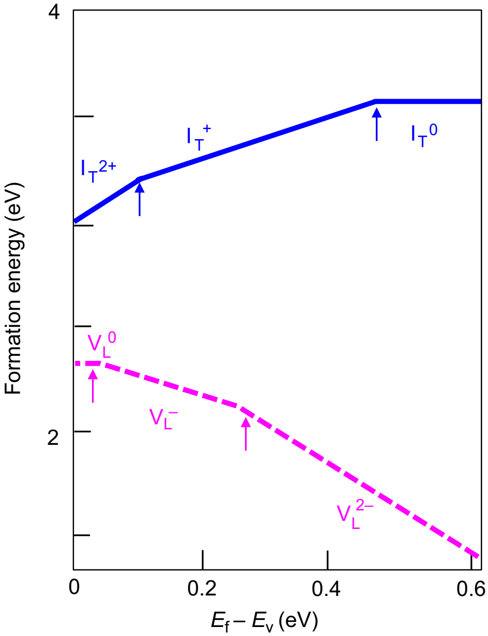

**Figure 4.17** Formation energies of a vacancy (V) and a self-interstitial atom (I) in Ge plotted against the Fermi energy level of Ge evaluated by *ab initio* calculations [64]. Here, $I_T$ means that the self-interstitial atom occupies a tetrahedral lattice site. The superscripts show the charge state of the point defect as double negative (2−), negative (−), neutral (0), positive (+), and double positive (2+).

This figure was newly drawn using original data of J. Vanhellemont, P. Śpiewak, K. Sueoka, I. Romandic, On intrinsic point defect cluster formation during Czochralski crystal growth, Phys. Status Solidi (c) 6 (2009) 1906−1911 under permission and courtesy of Professor K. Sueoka.

as seen in Fig. 4.18 [65−69]. The process described by a single activation energy is known to be mediated only by vacancies, since the activation energy of self-diffusion is equal to the sum of the formation and migration energies. In the figure, diffusion coefficients of various impurities in Ge are also shown as a function of temperature. The diffusion of the n-type impurities clearly exceeds the diffusion of the p-type ones and self-diffusion, while the diffusion of B impurity is very slow. Here, in n-type Ge the formation energy of a vacancy is smaller than in intrinsic and p-type Ge, as seen in Fig. 4.17. Probably, n-type impurities diffuse under an association with vacancies. In addition, in B-doped Ge formation of vacancies may be suppressed due to the induction of an elastic energy originating in the large size misfit of B−Ge. It may be noted that the character of B helps to make a sharp diffused region toward a gate insulator in the metal oxide semiconductor field-effect transistor (MOSFET) channel [70]. Diffusivities of neutral impurities of Si and Sn are almost comparable to self-diffusion [67,68]. O diffuses much faster than other impurities [69].

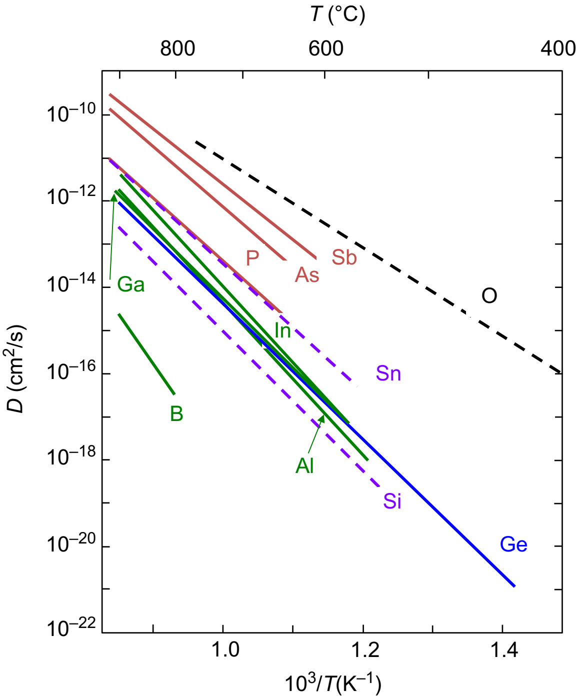

**Figure 4.18** Diffusion coefficients of n-type dopants (P, As, Sb), p-type dopants (B, Al, Ga, In), and neutral impurities (Si, Sn, O) in Ge compared with Ge self-diffusion [65–69].
Some data superimposed on the original illustration of E. Hüger, U. Tietze, D. Lott, H. Bracht, D. Bougeard, E.E. Haller, H. Schmidt, Self-diffusion in germanium isotope multilayers at low temperatures, Appl. Phys. Lett. 93 (2008) 162104 under permission of the author and American Institute of Physics.

The preexponential factor $D_0$ and activation energy for formation $E^M$ of various impurities are given in Table 4.7 [8,10,65–69,71].

### 4.6.2 Oxygen donors

O concentration is less than $10^{16}$ cm$^{-3}$ in CZ Ge crystals, while as noted in Section 4.4.3 the concentration can be enriched up to $10^{18}$ cm$^{-3}$ in Ge by growing in an O-rich atmosphere [72,73] or from a melt doped with $GeO_2$ [30]. O atoms are interstitially dissolved ($O_i$), occupying a bond-centered position, and behave as a Ge–$O_i$–Ge quasimolecule, leading to local vibration at 855 cm$^{-1}$ due to the $\nu_3$ antisymmetric stretching mode [74]. O atoms precipitate and form electrically active clusters at temperatures of 300–450°C; these are typically known as thermal double donors (TDDs), just the same as those in Si crystals. A TDD develops from an $O_i$-pair to a pair of atomic chains consisting of 16–19 $O_i$s [75], as illustrated in Fig. 4.19. This finding in Ge strongly addresses elucidation of the defect formation mechanism developed in Si [76].

**Table 4.7** **Diffusion coefficient; the preexponential factor and activation energy of various impurities in Ge, including self-diffusion, reported by experimental research [8,10,65–69,71]**

| | Diffusivity | | |
|---|---|---|---|
| **Impurity** | **$D_0$ ($cm^2/s$)** | **Q (eV)** | **References** |
| Ge | 13.6 | 3.09 | Self-diffusion [65] |
| Ge | $2.54 \times 10^1$ | 3.13 | Self-diffusion [71] |
| P | 9.1 | 2.85 | [66] |
| As | 32 | 2.71 | [66] |
| Sb | 16.7 | 2.55 | [66] |
| Te | 2.0 | 2.82 | [8] |
| B | $1.97 \times 10^5$ | 4.65 | [66] |
| Al | $1 \times 10^3$ | 3.45 | [66] |
| Ga | $8 \times 10^1$ | 3.21 | [66] |
| In | $5.123 \times 10^3$ | 3.51 | [66] |
| H | $2.7 \times 10^{-3}$ | 0.38 | [10] |
| C | – | – | |
| O | 0.40 | 2.08 | [69] |
| Sn | $1.5 \times 10^1$ | 2.90 | [68] |
| Si | 42 | 3.32 | [67] |

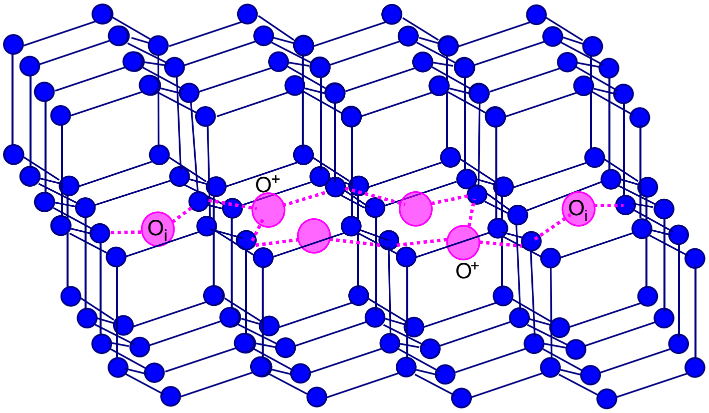

**Figure 4.19** Model of a thermal double donor in Ge. ● (navy) and ● (peach) show Ge and O atoms, respectively.

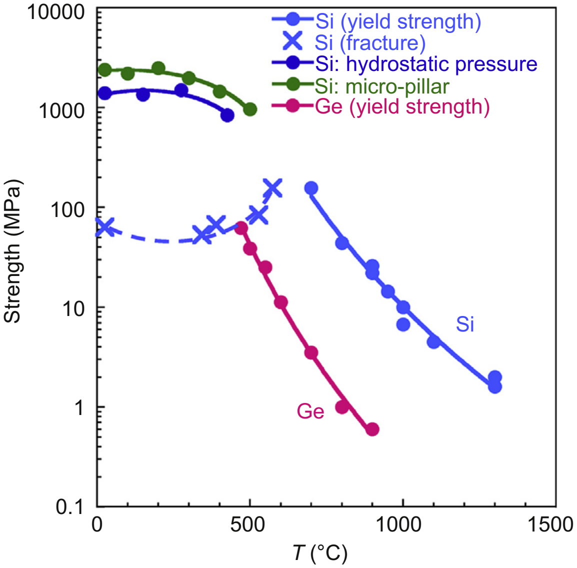

**Figure 4.20** Strength of Ge and Si as a function of temperature. Symbols of solid circles and crosses show yield and fracture strength, respectively. ● (red): conventional test of Ge [77], ● and × (blue): conventional test of Si [78,79], ● (navy): under a hydrostatic pressure of 5 GPa [80], ● (green): compression test of micron-scaled pillars [81].

### 4.6.3 Dislocations

Ge is thermomechanically weaker than Si in the practical temperature range. This lower mechanical strength combined with the more than two times heavier density of Ge than of Si leads to significant issues in suppressing dislocation generation and plastic deformation during crystal growth and wafer/device processing. Fig. 4.20 shows the yield and fracture strength of Ge and Si plotted against the temperature for deformation [77—81]. Generally, in a standard atmosphere semiconductors are ductile at elevated temperatures and are brittle, with cleavage along the (111) plane, at temperatures lower than (2/3)$T_M$. With decreasing temperature the yield strength increases, and after showing a maximum decreases to be almost constant, which is known as ductile-to-brittle (brittle-to-ductile) transition. The fracture depends strongly on the test mode, surface treatment, sample size, atmosphere, and so forth. The strength of Si increases up to 2.5 GPa under a hydrostatic pressure or with a micropillar shape. Brittleness (fracture) is characterized by a stress-intensity factor $K_{IC}$ that is 0.7 MPa m$^{1/2}$ for Si, as shown in Table 4.8 [77,82—85]. In contrast, such knowledge on Ge is currently limited, as seen in Fig. 4.20. The yield strength of Ge is much lower than that of Si, with similar temperature dependence. The yield stress $\sigma_y$ of Ge in the ductile (plastic deformation) temperature range is described as a function of temperature $T$ and strain rate $\dot{\varepsilon}$ by the following empirical equation [84,86,87]:

$$\tau_y = A\dot{\varepsilon}^{1/n}\exp\left(U/k_BT\right) \tag{4.9}$$

**Table 4.8** **Magnitudes of $K_{IC}$ for fracture, $n$ and $U$ for yield strength, and $m$ and $Q$ for 60° dislocation velocity in Ge plus data for Si [77,82–85]**

| | | Ge | Si |
|---|---|---|---|
| Stress-intensity factor | $K_{IC}$ | 0.6 [82] | 0.7 [82] |
| Yield strength | $n$ | 2.8 [83] | 2.4 [84] |
| | $U$ (eV) | 0.77 [77] | 1.25 [84] |
| Dislocation velocity | $m$ | 1.7 [85] | ~1.0 [84] |
| | $Q$ (eV) | 1.65 [85] | 2.3–2.4 [84] |

where $A$, $n$, and $U$ are constants. $n$ and $Q$ are obtained experimentally to be 3.1 and 0.77 eV, respectively [77,83]. Though a ductile-to-brittle transition is not clear, we can expect similar fractures of Ge at low temperature ranges. $K_{IC}$ for Ge is known to be 0.6 MPa $m^{1/2}$. Here it may be noted that there is a universal relationship in the temperature dependences of the yield strength $\tau_y$ of plasticity of Ge with that of Si when $\tau_y$ and the temperature $T$ are scaled respectively by the shear modulus $G$ and $Gb^3/k_B$, with $b$ being the magnitude of the Burger's vector and $k_B$ [87,88].

Plastic deformation of a crystal takes place through the generation, motion, and multiplication of dislocations in the crystal under physical/chemical stimulation such as stress and chemical reaction. The processes are controlled by the dynamic properties of dislocations. Fig. 4.21 shows the velocities of an isolated 60° dislocation in Ge and Si in a wide temperature range up to their melting points [85,89–94]. It is well known that dislocations move faster in Ge than in Si. The dislocation velocity $v$ in Ge and Si is expressed by the following empirical equation as a function of applied shear stress $\tau$ and temperature $T$:

$$v = v_0(\tau/\tau_0)^m \exp(-Q/k_B T), \tag{4.10}$$

where $\tau_0 = 1$ MPa and $v_0$, $m$, and $Q$ are constants. The stress exponent $m$ and activation energy $Q$ for a dislocation motion of 60° are shown in Table 4.8 [85].

Various impurities affect dislocation motion in semiconductors. Fig. 4.22 shows the velocities of 60° dislocations in impurity-doped Ge crystals under a stress of 15 MPa plotted against the reciprocal temperature [89]. Dislocations moved faster in As-doped Ge and slower in Ga-doped than in undoped Ge, while neutral-impurity O had no effect against the dislocation velocity in motion. Dislocation velocities can be expressed by Eq. (4.10). The feature of dislocation velocity enhancement/retardation is understood in terms of an electronic property of dislocation that an acceptor level may be associated with dislocations in the conductive Ge. Moreover, it has been clarified that the Ga and O impurities effectively suppress dislocation nucleation, while the As impurity does not. Dislocations in Ga- and O-doped Ge are supposed to be locked by the complexes formed through impurity interaction and segregation. The locking

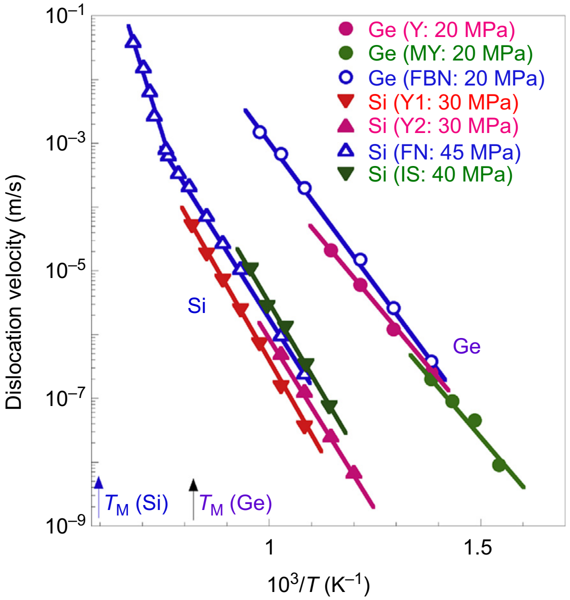

**Figure 4.21** Velocities of 60° dislocations as a function of temperature. In Ge: Y [85], MY [89], FBN [90]. In Si: Y1 [91], Y2: [92], FN [93], IS [94]. Numerals show the stress applied in the research. $T_M$(Ge) and $T_M$(Si) mean the melting points of Ge and Si, respectively.

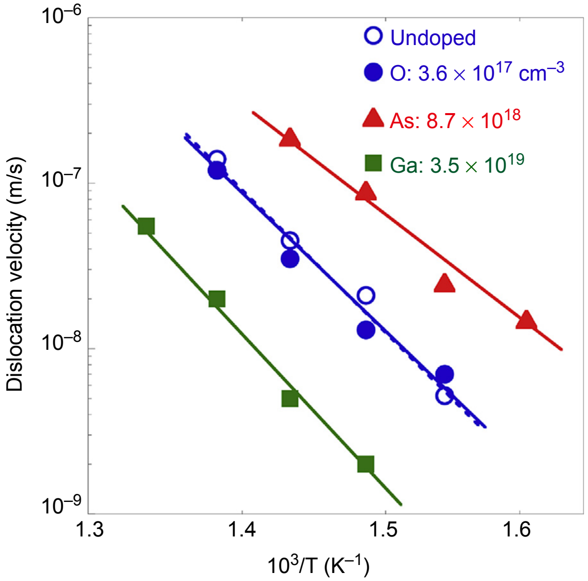

**Figure 4.22** Temperature dependence of velocities of 60° dislocations in undoped Ge crystals and doped with Ga, As, and O. The applied shear stress was 15 MPa. Numerals show the concentration of impurities [89].

Reprinted from Y. Murao, T. Taishi, Y. Tokumoto, Y. Ohno, I. Yonenaga, Impurity effects on the generation and velocity of dislocations in Ge, J. Appl. Phys. 109 (2011) 113502, Copyright 2011, with permission from American Institute of Physics.

effect of O in Si is well known and widely applied in crystal growth and device fabrication [95]; hence this result of O in Ge opens the possibility of crystal strengthening and also dislocation-free crystal growth by O doping.

## 4.7 Applications

### 4.7.1 Ge crystals for infrared optics

Ge is optically transmittable in a range from 1.85 to 15 μm, and is a noble material in infrared and far-infrared optical components, e.g., lenses, windows, etc., in a range of 8−12 μm wavelength. In addition, the free carrier absorption in the range can be minimized by n-type doping in concentrations between $4 \times 10^{13}$ and $1 \times 10^{15}$ $\mathrm{cm}^{-3}$. At present single crystals in large diameters over 350 mm are grown for these purposes. This requires high refractivity of the index $n = 4$ with a homogeneity of less than $\Delta n < 10^{-4}$ and a low birefringence of less than 1 μm/cm. Lenses need crystals with low mosaicity and a small number of low-angle grain boundaries, and for windows low residual stress inside the crystals is necessary. To decrease thermal stresses, the melt/crystal interface should be kept as flat as possible during the growth, corresponding with an almost vanishing radial temperature gradient [96].

Ge can be used as an avalanche photodiode (APD) for 1.3−1.5 μm infrared; and by doping with Au or Cu deep-level impurities it can be used for a high-sensitive and highly responsive detector for infrared and far infrared up to 40 μm.

### 4.7.2 Ge crystals for radiation detection

Ge is one of the most important materials for γ-ray detection due to its intrinsic characteristics of high atomic number, high density, and high carrier mobility. For this purpose, Ge crystals should be highly pure with an electrically active impurity in the limited concentration range of $10^9$−$2 \times 10^{10}$ $\mathrm{cm}^{-3}$. Ge crystals are grown from the melt in a fused silica crucible using an RF heating system under a high-purity $H_2$ gas atmosphere for several reasons. Crystals using a graphite crucible and/or carbon heater contain C, including its clusters, in a concentration of $10^{14}$ $\mathrm{cm}^{-3}$ [97,98]. Crystals grown in a vacuum contain Cu atoms that lead to carrier-trapping centers. Crystals grown from a silica crucible under an inert gas have $SiO_2$ precipitates; thus $H_2$ gas should be used. In addition, under an $H_2$ gas atmosphere, crystals should be dislocated since a dislocation-free high-purity Ge crystal grown in this atmosphere has a deep-level center at $E_V + 0.072$ eV in a concentration of about $10^{11}$ $\mathrm{cm}^{-3}$ [99,100]. Haller et al. identified that the center is a divacancy hydrogen complex ($V_2H$) [101]. Since dislocations absorb vacancies, crystals for γ-ray detectors are recommended to have dislocations uniformly distributed at a density of $10^2$−$10^4$ $\mathrm{cm}^{-2}$. Wang et al. grew high-purity Ge crystals of 9 cm diameter with dislocations of 2000−7000 $\mathrm{cm}^{-2}$ for a highly sensitive detector of dark matter and neutrinoless double-beta decay experiments [102,103]. The crystals were grown in an underground facility to reduce background cosmic ray exposure.

### 4.7.3 Ge crystals for electronics and photonics

Ge single crystals are widely used in current nano-electronics and photonics. Downscaling of complementary metal oxide semiconductor (CMOS) devices, facing the physical limitations of Si, addresses development of three-dimensional integrated structures such as tri-gate transistors [104] and alteration of high-mobility channel materials. Ge is a favorable material for channels, sources, and drains in MOSFETs, since the electron and hole in Ge move faster than in Si by two and four times, respectively. To obtain high mobility of long and short channels in n- and p-MOSFET, various gate stacks using polycrystalline Ge thin-film deposition and lamp annealing [105], ultrathin $SiO_2/GeO_2$ bilayer passivation [106], compressively strained Ge [107,108], GeSi and GeSn alloys, and so forth have been studied. Gupta et al. reported a fabrication of 7 nm FinFET CMOS using a strain engineering approach [109].

For further performance enhancement of CMOS devices, especially to overcome the current intrinsic leakage of Ge due to the small bandgap, thin-film Ge-on-insulator (GeOI) substrates are adopted in three-dimensional MOSFETs analogous to Si on insulator (SOI) [110–113]. Recently, Sarkar et al. developed band-to-band tunnel field-effect transistors (TFETs), where a strain-free hetero-structure is built using highly doped Ge as the source and atomically thin molybdenum disulfide as the channel, and showed a low power-supply voltage of only 0.1 V [114].

Dislocation-free Ge is applied in advanced solar cells for power generator in satellites. Ge is used as a substrate for epitaxial growth of GaAs compounds due to its small lattice mismatch. For example, the mismatch of GaAs on Ge is only $\Delta a/a \sim 0.12\%$. Indeed, triple-junction solar cells of InGaP/InGaAs/Ge for Mars exploration rovers achieved efficiency higher than 30% for satellites [115].

### 4.7.4 GeSi and GeSn

$Ge_{1-x}Si_x$ (or $Si_xGe_{1-x}$) alloy is a complete solid-solution semiconductor with a diamond cubic structure. The lattice parameters of the two elements differ by 4%, and those of the solid solution closely follow Vegard's law from 0.564 (pure Ge) to 0.534 nm (pure Si), while the bandgap ($E_g$) changes from 0.66 (Ge) to 1.12 eV (Si) according to composition. GeSi thin films grown on crystalline substrates can address various functionalities of the Ge-related devices discussed above. In contrast, bulk GeSi crystals offer potential to bandgap and lattice parameter engineering. GeSi alloy is an important material in thermoelectrics because of its low thermal conductivity and high Seebeck coefficient at elevated temperatures of ~1000°C; it was successfully used as a power generator in the deep-space probes of Voyager, Galileo, Cassini-Huygens, and so on. Lattice parameter variations of up to 4% are obtained by changing the composition, and this may enable fabrication of tunable monochromators for thermal neutron, X-ray, and focusing systems. Variation of the bandgap energy of the alloy, corresponding to the wavelength range of about 1–1.5 μm, is useful for direct and indirect photodetectors. Some details are given in the literature [116–118].

The solubility limit of Sn into Ge is at most $5.5 \times 10^{20}\ \mathrm{cm^{-3}}$, though epitaxial-grown $Ge_{1-x}Sn_x$ (where $x$ indicates the mole fraction of Sn) expands Ge-based bandgap and lattice parameter engineering used in far-infrared detection, introduction of compressively strained channels, etc. Especially, GeSn shows a crossover from indirect to direct transition semiconductors at an Sn content of about 8%, which provides new applications in infrared optoelectronics made with group IV semiconductors [119,120].

## 4.8 Concluding remarks

This chapter reviews the current knowledge of growth, basic properties, and applications of Ge crystals. Ge crystals have been well developed and refined, and stand comparable with Si with respect to crystalline quality, size, and defect density or freedom from dislocations. The disadvantage of low strength indicated previously can be overcome by O impurity doping. Unfortunately, even now the applications of Ge are rather limited, especially for nano-electronics as channel material, layer, dot, and so forth. That is, Ge remains symbiotic or parasitic with state-of-the-art Si devices. This might be a way to provide novel engineering technology for the strain and energy band control for Si nano-electronics. In addition, combined with its high absorption coefficient in the infrared wavelength range, Ge is a candidate for integration platforms of electronics and photonics as one-chip devices. Indeed, high-performance photodetectors using Ge dots on Si have been fabricated [121]. Nevertheless, it should be emphasized that peculiar applications of Ge, unaccomplished by Si, should be explored, which requires clarification and full utilization of the latent faculties of Ge. Some unique properties have been reported, like superconductivity in Ga-doped Ge [122,123] and spin accumulation/communication in p-tye Ge [124], opening new avenues in the semiconductor field. Basic research on Ge should also be addressed diversely. As seen in this review, some data on physical properties, especially for crystal growth, remains as reported in the 1950s and should be updated promptly. Basic research on Ge not only promotes further elucidation of potential but also can lead to comprehensive and synergic understanding of physical properties and mechanisms in semiconductor materials, including Si.

## References

[1] B. Depuydt, Growth of germanium single crystals, in: K.H.J. Buschow, R.W. Cahn, M.C. Flemings, B. Ilschner, E.J. Kramer, S. Mahajan (Eds.), The Encyclopedia of Materials: Science and Technology, Elsevier, 2001, pp. 3507−3517.

[2] C. Claeys, E. Simoen (Eds.), Comprehensive Book: Germanium-Based Technologies, Elsevier, 2007.

[3] G. Raskin, I. Romandic, L. Wouters, D. Hellin, I. Teerlinck, M. Meuris, P. Mijlemans, Germanium substrates for micro-electronic applications up to 300 mm diameter, in: Abstracts of “Symposium B: High-Mobility Group-IV Materials and Devices” of the 2004 MRS Spring Meeting at San Francisco, 12−16 Apr. 2004, p. 48.

[4] J. Vanhellemont, E. Simoen, Brother silicon, sister germanium, J. Electrochem. Soc. 154 (2007) H572−H583.

[5] S.M. Sze, Physics of Semiconductor Devices, second ed., Wiley-Interscience Publication, 1981. In the current version published in 2007, some description and data on Ge have been removed.

[6] J.R. Chelikowsky, M.L. Cohen, Nonlocal pseudopotential calculations for the electronic structure of eleven diamond and zinc-blende semiconductors, Phys. Rev. B 14 (1976) 556−582.

[7] C.D. Thurmond, The standard thermodynamic function of the formation of electrons and holes in Ge, Si, GaAs and GaP, J. Electrochem. Soc. 122 (1975) 1133−1141.

[8] A. Trumbore, Solid solubilities of impurity elements in germanium and silicon, Bell Syst. Tech. J. 39 (1960) 205−233.

[9] M. Schulz, H. Weiss (Eds.), Comprehensive Data Book: Landolt-Börnstein Group III, Vol. 17c, Technology of Si, Ge and SiC, Springer-Verlag, 1984.

[10] R.C. Frank, J.E. Thomas Jr., The diffusion of hydrogen in single-crystal germanium, J. Phys. Chem. Solids 16 (1960) 144−151.

[11] T. Taishi, Y. Murao, Y. Ohno, I. Yonenaga, Segregation of boron in germanium crystal, J. Cryst. Growth 311 (2008) 59−61.

[12] T. Taishi, Y. Murao, K. Inoue, Y. Ohno, I. Yonenaga (Unpublished work).

[13] Y.A. Burenko, S.P. Nikanorov, A.V. Stepanov, Elastic properties of germanium, Soviet Phys. Solid State 12 (1971) 1940−1942.

[14] S.P. Nikanorov, Y.A. Burenko, A.V. Stepanov, Elastic properties of silicon, Soviet Phys. Solid State 13 (1972) 2516−2518.

[15] W.C. Dash, R. Newman, Intrinsic optical absorption in single-crystal germanium and silicon at 77°K and 300°K, Phys. Rev. 99 (1955) 1151−1155.

[16] D.E. Hill, Infrared transmission and fluorescence of doped gallium arsenide, Phys. Rev. 133 (1964) A866−A872.

[17] I. Barin, Thermochemical Data of Pure Substances, Parts I and II, VCH, Weinheim, 1989.

[18] G. Yang, J. Govani, H. Mei, Y. Guan, G.-J. Wang, M.-L. Huang, D.-M. Mei, Investigation of influential factors on the purification of zone-refined germanium ingot, Cryst. Res. Technol. 49 (2014) 269−275.

[19] I.A. Prokhorov, B.G. Zakharov, A.S. Senchenkov, A.V. Egorov, D. Camel, P. Tison, Structural features of Ge(Ga) single crystals grown by the floating zone method in microgravity, J. Cryst. Growth 310 (2008) 4701−4707.

[20] L. Helmers, J. Schilz, G. Bäihr, W.A. Kaysser, Macrosegregation during Bridgman growth of $Ge_{1-x}Si_x$ mixed crystals, J. Cryst. Growth 154 (1995) 60−67.

[21] J.P. Garandet, Estimation of liquid phase diffusion coefficients of gallium and antimony in germanium from segregation data in crystal growth experiments, J. Cryst. Growth 310 (2008) 3268−3273.

[22] I.G. Cressell, J.A. Powell, The production of high-quality germanium single crystals, in: A.F. Gibson, R.E. Burgess, P. Aigrain (Eds.), Progress in Semiconductors, vol. 2, John Wiley &Sons, Inc., New York, 1957, p. 137.

[23] M. Azoulay, G. Gafni, Seeded growth in a soft lined crucible: application to phosphorus doped optical germanium single crystals, J. Cryst. Growth 79 (1986) 326−330.

[24] D. Langheinrich, O. Pätzold, L. Raabe, M. Stelter, VGF growth of germanium single crystals without crucible contact, J. Cryst. Growth 312 (2010) 2291−2296.

[25] G.K. Teal, J.B. Little, Growth of germanium single crystals, Phys. Rev. 72 (1950) 647.

[26] H. Okamoto, in: T.B. Massalski (Ed.), Binary Alloy Phase Diagram II, American Society for Metals, OH, 1996, p. 358.

[27] T. Taishi, Y. Ohno, I. Yonenaga, Reduction of grown-in dislocation density in Ge Czochralski-grown from the $B_2O_3$-partially-covered melt, J. Cryst. Growth 311 (2009) 4615−4618.

[28] I. Yonenaga, Y. Murakami, Segregation during the seeding process in the Czochralski growth of GeSi alloys, J. Cryst. Growth 191 (1998) 399−404.

[29] W.C. Dash, Growth of silicon crystals free from dislocations, J. Appl. Phys. 30 (1959) 459−474.

[30] S. Iida, T. Furukawa, K. Kajiwara, S. Kawado, T. Taishi, I. Yonenaga, To be submitted to J. Cryst. Growth.

[31] V.A. Moskovskih, P.V. Kasimkin, V.N. Shlegel, Y.V. Vasiliev, V.A. Gridchin, O.I. Podkopaev, The low thermal gradient CZ technique as a way of growing of dislocation-free germanium crystals, J. Cryst. Growth 401 (2014) 767−771.

[32] E.M. Trukhanova, K.B. Fritzler, A.P. Vasilenko, A.V. Kolesnikov, P.V. Kasimkin, V.A. Moskovskih, Dislocation structure of Ge crystals grown by low thermal gradient Czochralski technique, J. Cryst. Growth 468 (2017) 457−461.

[33] T. Taishi, H. Ise, Y. Murao, T. Osawa, M. Suezawa, Y. Tokumoto, Y. Ohno, K. Hoshikawa, I. Yonenaga, Czochralski-growth of germanium crystals containing high concentrations of oxygen impurities, J. Cryst. Growth 312 (2010) 2783−2787.

[34] R.C. Jaccodine, Surface energy of germanium and silicon, J. Electrochem. Soc. 110 (1963) 524−527.

[35] D.T.J. Hurle, A mechanism for twin formation during Czochralski and encapsulated vertical Bridgman growth of III-V compound semiconductors, J. Cryst. Growth 147 (1995) 239−250.

[36] H. Chung, M. Dudley, D.J. Larson Jr., D.T.J. Hurle, D.F. Bliss, V. Prasad, The mechanism of growth-twin formation in zincblende crystals: new insights from a study of magnetic liquid encapsulated Czochralski-grown InP single crystals, J. Cryst. Growth 187 (1998) 9−17.

[37] I. Yonenaga, S.-H. Lim, D. Shindo, Dislocation dissociation and stacking-fault energies in $Ge_{1-x}Si_x$ alloys, Philos. Mag. Lett. 80 (2000) 193−197.

[38] S. Takeuchi, K. Suzuki, Stacking fault energies of tetrahedrally coordinated crystals, Phys. Status Solidi (a) 171 (1999) 99−103.

[39] E. Billig, Growth twins in crystals of low-co-ordination number, J. Inst. Met 83 (1954−1955) 53−56.

[40] V.V. Voronkov, Processes at the boundary of a crystallization front, Soviet Phys. Crystallogr. 19 (1975) 573−577.

[41] W.G. Pfann, Principles of zone-melting, J. Met 4 (1952) 747−753.

[42] J.A. Burton, R.C. Prim, W.P. Slitcher, The distribution of solute in crystals grown from the melt, J. Chem. Phys. 21 (1953) 1987−1991.

[43] K. Weiser, Theoretical calculation of distribution coefficients of impurities in germanium and silicon, heats of solid solution, J. Phys. Chem. Solids 7 (1958) 118−126.

[44] I. Yonenaga, T. Taishi, Y. Ohno, Y. Tokumoto, Cellular structures in Czochralski-grown SiGe bulk crystal, J. Cryst. Growth 312 (2010) 1065−1068.

[45] W.A. Tiller, K.A. Jackson, J.W. Rutter, B. Chalmers, The redistribution of solute atoms during the solidification of metals, Acta Metall. 1 (1953) 428−437.

[46] S. Hens, J. Vanhellemont, D. Poelman, P. Clauws, I. Romandic, F. Holsteyns, J. Van Steenbergen, Experimental and theoretical evidence for vacancy-clustering-induced large voids in Czochralski-grown germanium crystals, Appl. Phys. Lett. 87 (2005) 061915.

[47] S. Mayburg, Vacancies and interstitials in heat treated germanium, Phys. Rev. 95 (1954) 38−43.

[48] R.A. Logan, Thermally induced acceptors in germanium, Phys. Rev. 101 (1956) 1455−1459.

[49] A.G. Tweet, Precipitation of Cu in Ge, Phys. Rev. 106 (1957) 221−224.

[50] A. Hiraki, Experimental determination of diffusion and formation energies of thermal vacancies in germanium, J. Phys. Soc. Jpn. 21 (1966) 34−41.

[51] A.D. Belyaev, L.I. Datsenko, S.S. Malogolovets, Investigation of quenching defects in dislocationless germanium, Ukr. Fiz. Zh. (in Russian) 12 (1967) 655−660.

[52] S. Samuelsson, Quenching experiments on n-type germanium, Ark. Fys. (Sweden) 35 (1967) 321−327.

[53] L.F. Konorova, Thermal defects in germanium, Soviet Phys. Solid State 10 (1969) 2233−2234.

[54] A. Giese, N.A. Stolwijk, H. Bracht, Double-hump diffusion profiles of copper and nickel in germanium wafers yielding vacancy-related information, Appl. Phys. Lett. 77 (2000) 642−644.

[55] J. Vanhellemont, P. Śpiewak, K. Sueoka, On the solubility and diffusivity of the intrinsic point defects in germanium, J. Appl. Phys. 101 (2007) 036103.

[56] R.E. Wahn, Investigations of oxygen-defect interactions between 25 and 700°K in irradiated germanium, Phys. Rev. 140 (1965) A690−A698.

[57] D. Shaw, Self- and impurity diffusion in Ge and Si, Phys. Status Solidi (b) 72 (1975) 11−39.

[58] J.R. Antonio, R. de Silva, J. Baierle, E. Motta, A. Fazzio, Native defects in germanium, Physica B 302−303 (2001) 364−368.

[59] K. Sueoka, J. Vanhellemont, Ab initio studies of intrinsic point defects, interstitial oxygen and vacancy or oxygen clustering in germanium crystals, Mater. Sci. Semicond. Process. 9 (2006) 494−497.

[60] H.M. Pinto, J. Coutinho, V.J.B. Torres, S. Öberg, P.R. Briddon, Formation energy and migration barrier of a Ge vacancy from ab initio studies, Mater. Sci. Semicond. Process. 9 (2006) 498−502.

[61] P. Śpiewak, J. Vanhellemont, K. Sueoka, K.J. Kurzydlowski, I. Romandic, Ab-initio simulation of self-interstitial in germanium, Mater. Sci. Semicond. Process. 11 (2008) 328−331.

[62] P. Śpiewak, J. Vanhellemont, K.J. Kurzydłowski, Improved calculation of vacancy properties in Ge using the Heyd-Scuseria-Ernzerh of range-separated hybrid functional, J. Appl. Phys. 110 (2011) 063534.

[63] Sholihun, F. Ishii, M. Saito, First-principles calculations of multivacancies in germanium, Jpn. J. Appl. Phys. 55 (2016) 011301.

[64] J. Vanhellemont, P. Śpiewak, K. Sueoka, I. Romandic, On intrinsic point defect cluster formation during Czochralski crystal growth, Phys. Status Solidi (c) 6 (2009) 1906−1911.

[65] E. Hüger, U. Tietze, D. Lott, H. Bracht, D. Bougeard, E.E. Haller, H. Schmidt, Self-diffusion in germanium isotope multilayers at low temperatures, Appl. Phys. Lett. 93 (2008) 162104.

[66] A. Chroneos, H. Bracht, Diffusion of n-type dopants in germanium, Appl. Phys. Rev. 1 (2014) 011301.

[67] H.H. Silvestri, H. Bracht, J.L. Hansen, A.N. Larsen, E.E. Haller, Diffusion of silicon in crystalline germanium, Semicond. Sci. Technol. 21 (2006) 758−762.

[68] I. Riihimäki, A. Virtanen, S. Rinta-Anttila, P. Pusa, J. Räisänen, The ISOLDE Collaboration, Vacancy-impurity complexes and diffusion of Ga and Sn in intrinsic and p-doped germanium, Appl. Phys. Lett. 91 (2007) 091922.

[69] J.W. Corbett, R.S. McDonald, G.D. Watkins, The configuration and diffusion of isolated oxygen in silicon and germanium, J. Phys. Chem. Solids 25 (1964) 873−879.

[70] D.A. Antoniadis, J.E. Chung, Physics and technology of ultra short channel MOSFET devices, in: IEDM Technical Digest, 1991, pp. 21−24.

[71] M. Werner, H. Mehrer, H.D. Hochheimer, Effect of hydrostatic pressure, temperature, and doping on self-diffusion in germanium, Phys. Rev. B 32 (1985) 3930−3937.

[72] C.S. Fuller, W. Kaiser, C.D. Thurmond, Donor equilibria in the germanium-oxygen system, J. Phys. Chem. Solids 17 (1961) 301−307.

[73] V.V. Litvinov, L.I. Murin, V.P. Markevich, A.R. Peaker, J.L. Lindström, Oxygen loss and thermal double donor formation in germanium, Mater. Sci. Semicond. Process. 9 (2006) 619−624.

[74] P. Clauws, Oxygen related defects in germanium, Mater. Sci. Eng. B 36 (1996) 213−220.

[75] K. Inoue, T. Taishi, Y. Tokumoto, Y. Murao, K. Kutsukake, Y. Ohno, M. Suezawa, I. Yonenaga, Interstitial oxygen behavior for thermal double donor formation in germanium: infrared absorption studies, J. Appl. Phys. 113 (2013) 073501.

[76] R. Jones, J. Coutinho, S. Öberg, P.R. Briddon, Thermal double donors in Si and Ge, Physica B 308−310 (2001) 8−12.

[77] I. Yonenaga, K. Sumino, Mechanical strength of GeSi alloy, J. Appl. Phys. 80 (1996) 3244−3247.

[78] W.D. Sylwestrowicz, Mechanical properties of single crystals of silicon, Philos. Mag. 7 (1962) 1825−1845.

[79] I. Yonenaga, Strength of Si crystals, Recent Res. Dev. ElectroChem. 1 (1998) 161−176.

[80] J. Rabier, L. Pizzagalli, J.L. Demenet, Dislocations in silicon at high stress, in: J.P. Hirth, L. Kubin (Eds.), Dislocations in Solids, vol. 16, Elsevier, Amsterdam, 2010, pp. 47−108.

[81] S. Korte, J.S. Barnard, R.J. Stearn, W.J. Clegg, Deformation of silicon − insights from micro compression testing at 25−500°C, Int. J. Plast. 27 (2011) 1853−1866.

[82] W.W. Gerberich, W.M. Mook, C.B. Carter, R. Ballarini, A crack extension force correlation for hard materials, Int. J. Fract. 148 (2007) 109−114.

[83] K. Kojima, K. Sumino, Strain-rate and temperature dependence of mechanical behaviour in germanium crystals, Cryst. Lattice Defects 2 (1971) 147−158.

[84] I. Yonenaga, An overview of plasticity of Si crystals governed by dislocation motion, Eng. Fract. Mech. 147 (2015) 468−479.

[85] I. Yonenaga, Dislocation dynamics in SiGe alloys, J. Phys. Conf. Ser. 471 (2013) 012002.

[86] I. Yonenaga, K. Sumino, Dislocation dynamics in the plastic deformation of silicon crystals I. Experiments, Phys. Status Solidi (a) 50 (1978) 685−693.

[87] I. Yonenaga, Hardness, yield strength, and dislocation velocity in elemental and compound semiconductors, Mater. Trans. 46 (2005) 1979−1985.

[88] H.O.K. Kirchner, T. Suzuki, Plastic homology of tetrabonded crystals, Acta Mater. 46 (1998) 305−311.

[89] Y. Murao, T. Taishi, Y. Tokumoto, Y. Ohno, I. Yonenaga, Impurity effects on the generation and velocity of dislocations in Ge, J. Appl. Phys. 109 (2011) 113502.

[90] B.Y. Farber, I.E. Bondarenko, V.I. Nikitenko, High-temperature mobility of isolated dislocations in germanium single crystals, Soviet Phys. Solid State 23 (1981) 285−286.

[91] I. Yonenaga, Dislocation-impurity interaction in Si, Mater. Sci. Eng. B 124−125 (2005) 293−296.

[92] I. Yonenaga (Unpublished work).

[93] B.Y. Farber, V.I. Nikitenko, Change of dislocation mobility characteristics in silicon single crystals at elevated temperatures, Phys. Status Solidi (a) 73 (1982) K141−K144.

[94] M. Imai, K. Sumino, In situ X-ray topographic study of the dislocation mobility in high-purity and impurity-doped silicon crystals, Philos. Mag. A 47 (1983) 599−621.

[95] K. Sumino, I. Yonenaga, Oxygen effect on mechanical properties, in: F. Shimura (Ed.), Semiconductors and Semimetals, vol. 42, Academic Press, New York, 1994, pp. 449−511.

[96] B. Depuydt, P. Boone, P. Union, P. Muys, D. Vyncke, C. Goessens, Interferometrical characterization of stress birefringence in germanium, SPIE Proc. 3098 (1997) 559−565.

[97] E.E. Haller, W.L. Hansen, P. Luke, R. McMurray, Carbon in high-purity germanium, IEEE Trans. Nucl. Sci. 29 (1982) 745−750.

[98] L. Hoffman, J.C. Bach, B. Bech Nielsen, P. Leary, R. Jones, S. Öberg, Substitutional carbon in germanium, Phys. Rev. B 55 (1997) 11167−11173.

[99] R.N. Hall, T.J. Soltys, High-purity germanium for detector fabrication, IEEE Trans. Nucl. Sci. 18 (1971) 160−165.

[100] W.L. Hansen, E.E. Haller, High-purity germanium-observations on the nature of acceptors, IEEE Trans. Nucl. Sci. 19 (1) (1972) 260−264.

[101] E.E. Haller, G.S. Hubbard, W.L. Hansen, A. Seeger, Divacancy-hydrogen complexes in dislocation-free high-purity germanium, Inst. Phys. Conf. Ser. 31 (1977) 309−318.

[102] G.-J. Wang, Y.-C. Sun, G. Yang, W.-C. Xiang, Y. Guan, D.-M. Mei, C. Keller, Y.-D. Chan, Development of large size high-purity germanium crystal growth, J. Cryst. Growth 352 (2012) 27−30.

[103] G.-J. Wang, Y. Guan, H. Mei, D.-M. Mei, G. Yang, J. Govani, M. Khizar, Dislocation density control in high-purity germanium crystal growth, J. Cryst. Growth 393 (2014) 54−58.

[104] Intel. https://www.intel.com/content/www/us/en/silicon-innovations/standards-22nm-3d-tri-gate-transistors.

[105] K. Usuda, Y. Kamata, Y. Kamimuta, T. Mori, M. Koike, T. Tezuka, High-performance poly-Ge short-channel metal-oxide-semiconductor field-effect transistors formed on $SiO_2$ layer by flash lamp annealing, Appl. Phys. Express 7 (2014) 056501.

[106] K. Yamamoto, R. Ueno, T. Yamanaka, K. Hirayama, H. Yang, D. Wang, H. Nakashima, High-performance Ge metal-oxide−semiconductor field-effect transistors with a gate stack fabricated by ultrathin $SiO_2/GeO_2$ bilayer passivation, Appl. Phys. Express 4 (2011) 051301.

[107] S. Takagi, T. Tezuka, T. Irisawa, S. Nakaharai, K. Usuda, N. Sugiyama, M. Shichijo, R. Nakane, S. Sugahara, Device structures and carrier transport properties of advanced CMOS using high mobility channels, Solid State Electron. 51 (2007) 526−536.

[108] D.P. Brunco, B. De Jaeger, G. Eneman, J. Mitard, G. Hellings, A. Satta, V. Terzieva, L. Souriau, F.E. Leys, G. Pourtois, M. Houssa, G. Winderickx, E. Vrancken, S. Sioncke, K. Opsomer, G. Nicholas, M. Caymax, A. Stesmans, J. Van Steenbergen, P.W. Mertens, M. Meuris, M.M. Heyns, Germanium MOSFET devices: advances in materials understanding, process development, and electrical performance, J. Electrochem. Soc. 155 (2008) H552−H561.

[109] S. Gupta, V. Moroz, L. Smith, Q. Lu, K.C. Saraswat, 7-nm FinFET CMOS design enabled by stress engineering using Si, Ge, and Sn, IEEE Trans. Electron Devices 61 (2014) 1222−1230.

[110] C.J. Tracy, P. Fejes, N. David Theodore, P. Maniar, E. Johnson, A.J. Lamm, A.M. Paler, I.J. Malik, P. Ong, Germanium-on-insulator substrates by wafer bonding, J. Elecron. Mater. 33 (2004) 886−892.

[111] C. Deguet, L. Sanchez, T. Akatsu, F. Allibert, J. Dechamp, F. Madeira, F. Mazen, A. Tauzin, V. Loup, C. Richtarch, D. Mercier, T. Signamarcheix, F. Letertre, B. Depuydt, N. Kernevez, Fabrication and characterization of 200 mm germanium-on-insulator (GeOI) substrates made from bulk germanium, Electron. Lett. 42 (2006) 415−417.

[112] T. Akatsu, C. Deguet, L. Sanchez, F. Allibert, D. Rouchon, T. Signamarcheix, C. Richtarch, A. Boussagol, V. Loup, F. Mazen, J.-M. Hartmann, T. Campidelli, L. Clavelier, F. Letertre, N. Kernevez, C. Mazure, Germanium-on-insulator (GeOI) substrates − a novel engineered substrate for future high performance devices, Mater. Sci. Semicond. Process. 9 (2006) 444−448.

[113] M. Vinet, C. Le Royer, P. Batude, J.-F. Damlencourt, J.-M. Hartmann, L. Hutin, K. Rmanjek, A. Pouydebasque, O. Thomas, Germanium on insulator and 3D architectures opportunities for integration, Int. J. Nanotechnol. 7 (2010) 304−319.

[114] D. Sarkar, X.-J. Xie, W. Liu, W. Cao, J.-H. Kang, Y.-J. Gong, S. Kraemer, P.M. Ajayan, K. Banerjee, A subthermal tunnel field-effect transistor with an atomically thin channel, Nature 526 (2015) 91−95.

[115] Umicore. http://eom.umicore.com/en/germanium-solutions/markets/multi-junction-solar-cells/s.

[116] E. Kasper, K. Lyutovich (Eds.), Comprehensive Book: Properties of Silicon Germanium and SiGe: Carbon, INSPEC, 2000.

[117] I. Yonenaga, Growth and characterization of silicon-germanium alloys, in: G. Kissinger, S. Pizzini (Eds.), Silicon, Germanium, and Their Alloys, CRC Press, 2015, pp. 23−60.

[118] I. Yonenaga, $Si_xGe_{1-x}$ bulk crystals, in: S. Hashmi (Ed.), Reference Module in Materials Science and Materials Engineering, Elsevier, Oxford, 2016, p. 03687, http://doi.org.10.101013/B978-0-12-803581-8.03687-0.

[119] S. Zaima, O. Nakatsuka, N. Taoka, M. Kurosawa, W. Takeuchi, M. Sakashita, Growth and applications of GeSn-related group-IV semiconductor materials, Sci. Technol. Adv. Mater. 16 (2015) 043502.

[120] S. Wirths, D. Buca, S. Mantl, Si-Ge-Sn alloys: from growth to applications, Prog. Cryst. Growth Charact. Mater. 62 (2016) 1−39.

[121] J. Michel, J.-F. Liu, L.C. Kimerling, High-performance Ge-on-Si photodetectors, Nature Photo 4 (2010) 527−534.

[122] T. Herrmannsdörfer, V. Heera, O. Ignatchik, M. Uhlarz, A. Mücklich, M. Posselt, H. Reuther, B. Schmidt, K.-H. Heinig, W. Skorupa, M. Voelskow, C. Wündisch, R. Skrotzki, M. Helm, J. Wosnitza, Superconducting state in a gallium-doped germanium layer at low temperatures, Phys. Rev. Lett. 102 (2009) 217003.

[123] S. Lebègue, Electronic structure of superconducting gallium-doped germanium from ab-initio calculations, Phys. Status Solidi RRL 3 (2009) 224−227.

[124] S. Iba, H. Saito, A. Spiesser, S. Watanabe, R. Jansen, S. Yuasa, K. Ando, Spin accumulation and spin lifetime in p-type germanium at room temperature, Appl. Phys. Express 5 (2012) 053004.

This page intentionally left blank

# Silicon carbide

# 5

*Didier Chaussende*[1,a], *Noboru Ohtani*[2]
[1]Univ. Grenoble Alpes, CNRS, Grenoble INP, SIMAP, Grenoble, France;
[2]Kwansei Gakuin University, Sanda, Japan

## 5.1 Applications of silicon carbide and materials requirements

Energy saving is one of the most critical problems of this century. In this context, improving the efficiency of electricity usage is of the highest importance, since electricity can be produced through nearly any energy generation process (e.g., steam, coal, solar arrays) and can travel vast distances without losing much energy. Regardless of the means by which electrical power is generated, power conditioning and conversion are required before using electricity for specific purposes. Thus the efficiencies of power conditioning and conversion are of paramount importance for energy saving.

In general, efficiency is mainly limited by the performance of semiconductor devices used in power conditioning and conversion systems. Silicon (Si) is currently the most commonly used semiconductor for power devices. Si is abundant, and large high-quality single crystals can be produced at an economical cost, which makes it dominant in the electronics industry, including power devices. The performance of Si power-switching devices has been significantly improved in the last 3 decades through the development of power metal oxide semiconductor field-effect transistors (MOSFETs) and insulated gate bipolar transistors (IGBTs) [1,2]. However, in recent years this prominent material has faced limitation in certain application fields because of its intrinsic material properties; one of these fields is high blocking voltage (>600 V) power device applications. Now that Si power device technology is relatively mature, it is not easy to achieve innovative breakthroughs in power semiconductor devices using this material, and thus there are high hopes for the emergence of novel power semiconductor materials, such as silicon carbide (SiC) and gallium nitride (GaN).

The technological potential of SiC for power devices stems from its outstanding combination of physical and electronic properties [3]. The large bandgap (roughly three times that of Si) enables device operation at increased temperatures (873 K for transistors) and low-leakage currents. SiC can withstand high electric fields before breakdown, 10 times greater than Si, and also high current densities. The large electron saturation drift velocity enables SiC to generate high power at high frequencies. SiC has excellent thermal conductivity, greater than copper at room temperature, which

---

[a] Institute of Engineering Univ. Grenoble Alpes

**Single Crystals of Electronic Materials.** https://doi.org/10.1016/B978-0-08-102096-8.00005-7
Copyright © 2019 Elsevier Ltd. All rights reserved.

makes it suitable for high-power operation. Its strong chemical stability is a prominent advantage for sensors intended to operate in severe environments, for example in the aerospace and automotive industries.

These superior material properties have long been recognized, and SiC research was intensively pursued in the United States and Europe during the 1960s and 1970s. However, around 1973 many institutes halted research when they failed to grow SiC in large single crystals. In 1978 Tairov and Tsvetkov made a major step in the development of SiC, with the use of a physical vapor transport (PVT) growth technique, the so-called "modified-Lely method," for SiC bulk crystal growth [4], and this breakthrough led to the possibility of growing large single crystalline SiC. In the last decade SiC bulk crystal growth technology has achieved significant progress and enabled the growth of large high-quality SiC crystals. The availability of large-diameter SiC single crystal substrates has resulted in rapid progress in SiC thin-film epitaxy and device fabrication, and the application of SiC to electronic and optoelectronic semiconductor devices is fast reaching its real potential.

The first commercial SiC power devices were Schottky barrier diodes, released by Infineon Technologies, Germany, in 2001. Today more than 20 device manufacturers produce SiC Schottky barrier-based diodes with a breakdown voltage higher than 600 V. SiC power MOSFETs are also available in the market, but they still have problems related to manufacturing costs and reliability, and these problems largely stem from the SiC crystals used for device manufacturing. Thus low-cost manufacturing of large-size, high-quality SiC crystals is required to enable SiC power devices to penetrate into the market further and enhance their adaptation to a wide range of power electronic systems.

Increasing the crystal diameter is crucial for reducing the cost of SiC power devices through economies of scale and use of leading-edge Si device fabrication lines; so far, diameter enlargement of SiC crystals up to 200 mm has been successfully demonstrated [5]. However, crystal quality tends to fall as the diameter becomes larger, because of the lack of an established methodology for expanding the single crystal area without crystal quality degradation. The difficulty in growing high-quality single crystals rapidly increases as the crystal diameter increases, and various technological problems become apparent in the course of diameter enlargement. Over the last decade numerical simulation and other process optimization techniques have been applied to SiC single crystal growth. Particularly numerical simulation of the crystal growth process has proved to be an essential tool for optimizing growth, since in-situ monitoring during growth is extremely difficult due to the extremely high growth temperature of SiC (more than 2273 K).

Another important requirement for SiC crystal growth is low densities of crystallographic defects, particularly extended defects such as dislocations and stacking faults. In the last 2 decades significant progress in defect reduction has been made, and now low-defect-density SiC substrates are commercially available for manufacturing SiC power devices. The total dislocation density in commercially available 100 mm diameter 4H−SiC substrates was reduced from more than 10,000 to a few thousands per square centimeter, and an even lower dislocation density was achieved for R&D substrates. This level of crystal quality appears enough for SiC SBD manufacturing but is still to be improved to fulfill the demand for high-yield manufacturing of SiC power MOSFETs. Thus the reduction of extended defects in SiC crystals remains a most crucial issue for its growth technology.

The last issue to be addressed in SiC crystal growth is the control of the doping and electrical resistivity in SiC crystals. From the perspective of substrates, very different electrical properties are required for the fabrication of high-performance SiC devices. SiC has several advantages over other wide-bandgap semiconductor materials, such as GaN, gallium oxide ($Ga_2O_3$), and diamond. In SiC, ambipolar doping, i.e., both *n*- and *p*-type doping are possible, and a wide range of resistivity from $10^{-3}$ to more than $10^{10}\,\Omega\,\mathrm{cm}$ can be achieved by selecting appropriate dopants. For power device applications of SiC crystals, the goal is to obtain a sufficiently low uniform electrical resistivity to prevent unnecessary substrate resistance negatively impacting the device performance as well as to achieve extremely low ohmic contact resistances. The most common dopants for *n*- and *p*-type materials are nitrogen (N) and aluminum (Al) for SiC crystals, which can be introduced up to a concentration range of $10^{20}\,\mathrm{cm}^{-3}$. Nevertheless, there are still some issues to be addressed for doping in SiC crystals, and much research effort is still devoted to solving these problems.

This chapter reviews technological advances in SiC bulk crystal growth technology and discusses its current status. The key issues in the field are discussed, to achieve SiC bulk crystals of large diameter and increased length with well-defined structural and electrical properties. The chapter deals with several crucial technological aspects related to SiC bulk crystal growth, including fundamentals such as thermodynamics and kinetics, and practical issues such as diameter enlargement, defect reduction, and doping. All these aspects are combined to provide a comprehensive picture of the current status of SiC bulk crystal growth technology.

## 5.2 Thermodynamic properties and suitable growth technologies

**The Si–C binary phase diagram.** The main features of the Si–C binary phase diagram were described long ago, with SiC being the only stable compound of the diagram (Fig. 5.1). Some discrepancies can be found in the literature, especially in the determination of the invariant transformations and the description of the SiC liquidus. For example, a first assessment of the Si–C phase diagram was proposed by Olesinski et al. in 1984 [6], based on experimental data measured by Dollof [7]. This diagram clearly overestimates the carbon (C) solubility in liquid Si and gives a peritectic decomposition of SiC at 2820 K, i.e., more than 280° below the currently accepted value. A review of the literature shows that the reported data is closely linked to its determination methods. An accurate and precise determination of the Si–C binary diagram is still pending, because of specific experimental difficulties related to the implementation of extremely high temperature measurements. This has been pointed out by several critical reviews of the available experimental data [8,9].

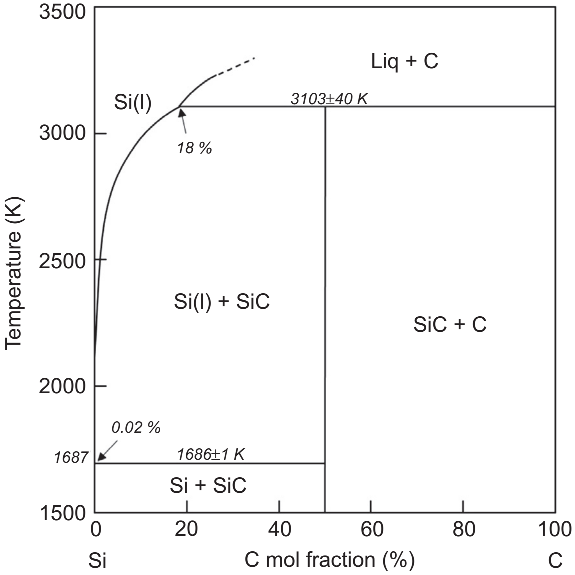

**Figure 5.1** Si–C binary phase diagram at a pressure of $10^5$ Pa.
Adapted from G. Honstein, C. Chatillon, F. Baillet, Thermodynamic approach to the vaporization and growth phenomena of SiC ceramics. I. SiC and SiC-$SiO_2$ mixtures under neutral conditions, J. Eur. Ceram. Soc. 32 (5) (2012) 1117–1135, Copyright 2011, with permission from Elsevier.

More recent experimental determinations converge toward a much lower C solubility in liquid silicon (0.02 mol%), close to the eutectic point (1686 K) [10,11], and a peritectic temperature of about 3100 K with C mole fraction in the liquid phase equal to ≈18% [12]. It is worth noting that the diagram proposed in 1959 by Scace and Slack [13] was almost correct, especially for the high-temperature side. A dissolution enthalpy of $(247 \pm 12) \times 10^3$ J/mol can thus describe the solubility curve of C in liquid Si at high temperature.

From a crystal growth point of view, the peritectic decomposition of SiC at about 3100 K prevents the use of classical growth processes, such as growth from a stoichiometric melt. To get a stoichiometric melt, a temperature of about 3500 K and pressure in the range of $10^9$ Pa would be necessary, as predicted by the calculations [14]. Below or close to atmospheric pressure, the diagram suggests two different approaches: (1) growth from a silicon-based saturated solution, and (2) growth from the vapor phase. If the pressure is low enough, Si(l) gets metastable and SiC can be vaporized, starting typically above 2100 K. Note that for both cases any bulk growth process would require high temperatures.

**Description of the vapor phase.** SiC vaporization was first described by Drowart et al. [15] and further refined by Rocabois et al. [16] using high-temperature Knudsen effusion cells coupled with mass spectrometry. Despite the large number of species identified, only three (Si(g), $Si_2C$(g) and $SiC_2$(g)) are necessary to describe accurately the behavior of the vapor phase in equilibrium with the solid. The equilibrium partial pressures of each gaseous components have been calculated as a function of temperature for both sides of the phase diagram SiC−C(s) and SiC−Si(l) [12,17] and for different polytypes [18]. It is worth noting that the choice of the thermodynamic database used for the process modeling can have an important impact on the results. Indeed, some discrepancies in the absolute values are obtained, such as a factor of two for the growth rates and three for the Si/C ratios [19]. However, the trends regarding growth rate calculation, crystal shape, and Si/C ratio in the gas phase are correctly described and none of the databases would bring about unacceptable errors from the process development point of view.

An important point for SiC vaporization is that the noncongruency of the vapor is associated with graphitization of the SiC source materials. This graphitization adds a kinetic barrier for the vaporization, which can be considered by the use of evaporation coefficients. Rocabois et al. [16] determined them using a multiple Knudsen cells geometry. They found the same evaporation coefficients for the three main gaseous species, equal to $(5 \pm 2) \times 10^{-3}$ at 2150 K. This must be used for the calculation of the vapor fluxes, using the Hertz−Knudsen equation.

**Polytypism.** The polytypic nature of SiC, i.e., that the crystal structure exhibits a number of different one-dimensional ordering sequences without any variation in stoichiometry, has been known and investigated for many years. Though well described (see for instance [20,21]), its origin is still controversial. The polytypism in SiC crystals is not only a relevant issue for their industrial applications but also a topic of great scientific interest, since this material property brings about a marked distinction between SiC and others materials. The SiC polytypes can be represented by various periodic hexagonal Si−C double-layer structures along the *c* axis. Fig. 5.2 shows commonly observed polytypes in the bulk crystal growth of SiC, where large and small circles represent Si and C atoms, respectively [22]. The structure (3C, 6H, 4H, and 15R) of SiC is expressed by a figure indicating the number of (double) layers in the unit cell, followed by a letter recording the symmetry of the lattice (C: cubic, H: hexagonal, R: rhombohedral). Another way of representing the polytypes is by "*ABC*" notation. The order or sequence of the hexagonal double layers in the stack, either the (0001) basal plane of a hexagonal structure or the (111) plane of a cubic structure, is referred to by fixing one layer as an *A* layer and all other layers with atoms in positions identical thereto as *A* layers also. Layers of atoms in other positions in the stack are referred to as *B*, *C* layers. For example, 3C is represented as *ABC* by this notation, 6H as *ABCACB*, and 4H as *ABCB*. The only cubic polytype (3C−SiC) is denoted by β−SiC, while the hexagonal and rhombohedral polytypes are collectively referred to as α−SiC. More than 250 different polytypes of SiC are usually claimed, even if only a few dozen have been effectively reported, and many physical and electronic properties of SiC vary depending on the polytype (e.g., bandgap energy [23−25]).

The difference of the formation enthalpy between the polytypes is very narrow [26], and usually considered as much smaller than the measurement errors. Theoretical works have faced strong difficulties in estimating the total energy difference between the polytypes [27]. Here lies the huge challenge of SiC bulk crystal growth: the stabilization of one and only one polytype among the possible structures in a process operated under extreme temperature conditions.

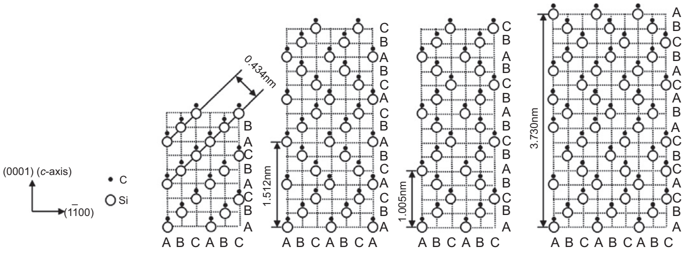

| | 3C-SiC | 6H-SiC | 4H-SiC | 15R-SiC |
|---|---|---|---|---|
| ABC notation | ABC | ABCACB | ABCB | ABCACBCABACABCB |
| Zhdanov notation | $(\infty)$ | (33) | (22) | $(32)_3$ |
| Häag notation | + + + | + + + − − − | + + − − | + + − − − |
| Hexagonality (D) | 0% | 33% | 50% | 40% |

**Figure 5.2** Schematic diagram of the stacking sequences in SiC polytypes commonly observed in bulk crystal growth of SiC, where *large and small circles* represent Si and C atoms, respectively.
Modified from Y.M. Tairov, V.F. Tsvetkov, Group IV materials (mainly SiC), in: J.I. Pankove (Ed.), Electroluminescence, Springer, Berlin, 1977, pp. 31–61, Copyright 1977, with permission from Springer.

## 5.3 Description of SiC bulk growth methods

**Seeded sublimation process.** In 1978 Tairov and Tsvetkov introduced the so-called modified Lely method, often referred to as either the PVT or seeded sublimation technique [4]. The basic idea was to localize the growth on a slightly cooler seed, thus avoiding widespread spontaneous nucleation on the inner graphite walls of the growth cavity. By applying a temperature difference between a SiC source powder (higher temperature) and a SiC seed substrate (lower temperature), the sublimation–condensation process can be controlled. A schematic drawing of the process is presented in Fig. 5.3. Growth is carried out in a quasiclosed high-density graphite crucible, with the main challenge being to control temperature distribution (heat transfer) and gas species concentration fields (mass transfer). Using proper graphite insulation, it is quite easy-to-operate process at temperatures of typically 2573 K with radio frequency (RF) induction heating. The process can be described as having three elementary steps: noncongruent vaporization of the SiC source powder; mass transfer between the source and the seed; and crystallization from the Si– and C–containing gas species on the seed. The temperature gradient between the source and the seed is in the range of a few tens of K/cm (typically 10–50 K/cm). High-purity Ar or He is used as ambient gas, usually in a 133 Pa to 6650 Pa pressure range. Seeded sublimation is currently the standard industrial process and a dozen companies in the United States, Japan, China, Russia,

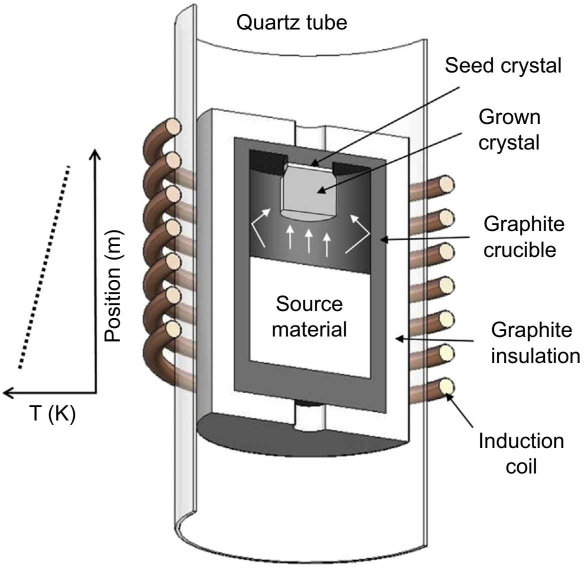

**Figure 5.3** Schematic description of the seeded sublimation growth process. (a) Schematic view of the sublimation reactor concept, which is the current "state-of-the-art" industrial growth technique for SiC bulk single crystals; (b) schematic temperature profile along the symmetry axis of the crucible. Typical growth conditions are 2573 K and 1330 Pa of argon.

Korea, Sweden, and Germany produce SiC wafers with it. There is a huge literature available on sublimation growth and several groups have contributed considerably to its development, mainly since the early 1990s [26,28–38].

**High-temperature chemical vapor deposition (HTCVD).** Although the PVT technique dominates today's SiC wafer production, HTCVD, first introduced by Kordina et al. [39], has become important [40–43]. The HTCVD growth system is based on a vertical reactor geometry, where the precursors like $SiH_4$ and $C_2H_4$, diluted in a carrier gas, are fed upward through a heating zone to the seed crystal holder (Fig. 5.4(b)). The main advantages of this technique are the continuous supply of the source material, which could allow the growth of long ingots; direct control of the C/Si ratio; and the perfect control of doping, from high-purity semi–insulating crystals to *n*-type or *p*-type doped crystals. The particular chemistry of the HTCVD process requires a separated inlet for Si– and C–containing precursors to avoid prereaction, and an adapted temperature distribution. The aim is to control the formation of a "SiC clusters cloud" by homogeneous nucleation which could act as a "virtual SiC solid source" for the sublimation step [40].

**Halide chemical vapor deposition (H-CVD).** This method is a transposition to high temperature of the classic chemical vapor deposition (CVD) of SiC developed for thin and thick layer deposition (Fig. 5.4(c)). Chlorinated precursors are used to avoid homogeneous nucleation in the gas phase close to the seed surface. This process is a pure CVD technique, which is not true of the HTCVD method discussed above.

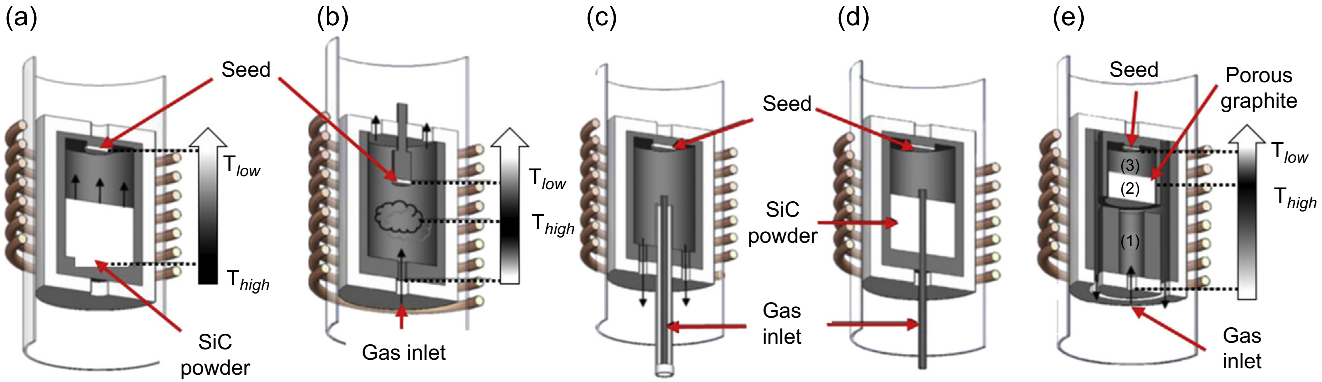
(a)
Seed
$T_{low}$
$T_{high}$
SiC powder
(b)
$T_{low}$
$T_{high}$
Gas inlet
(c)
Seed
SiC powder
Gas inlet
(d)
(e)
Seed
Porous graphite
(3)
(2)
(1)
$T_{low}$
$T_{high}$
Gas inlet

**Figure 5.4** Overview of the SiC bulk growth vapor phase processes. (a) PVT (see details in Fig. 5.3); (b) HTCVD process concept; (c) H-CVD process; (d) modified PVT (M-PVT) reactor concept; (e) continuous feed PVT (CF-PVT) reactor concept. *Large arrows* schematically indicate the temperature profile along the symmetry axis of the crucible, black being the hot area and white the cold. Note the temperature distribution specificities for the different vapor phase processes.

The first results from this process were very promising regarding growth rates, intrinsic crystal purity, and *n*-type doping [44–46], but no development of the process has been reported since then.

**Modified PVT (M-PVT).** In the case of the M-PVT setup an additional gas pipe is used to fine-tune the gas phase composition in a conventional PVT reactor [47] (Fig. 5.4(d)). Silane and propane may be added to adjust the C/Si ratio in the growth cell. Of technically higher importance is the possibility of continuously feed doping gases into the system to improve doping homogeneity; i.e., axial as well as radial dopant distribution. For example, very high *p*-type doping using Al vapor and *n*-type doping using phosphine gas have been achieved in bulk SiC material. Again, no further developments have been reported.

**Continuous feed PVT (CF-PVT).** Basically, CF-PVT has the intrinsic advantage of combining the maturity of PVT for single crystal growth and HTCVD for continuous feeding of the high-purity polycrystalline SiC source (Fig. 5.4(e)) [48]. The process is composed of three different reaction zones: the feeding zone, in which the polycrystalline SiC source is formed from gaseous precursors diluted in a carrier gas; the transfer zone, consisting of highly porous graphite foams which support the CVD deposit and allow SiC transfer to the sublimation area; and the sublimation zone for the growth of the single crystal, this latter area having a similar design as in PVT crucibles. Due to the high porosity of the "transfer zone," close to 95%, the PVT zone is partially open. Consequently, the precursor concentration in the feeding zone effectively acts as an additional parameter for simple and precise control of the supersaturation close to the crystal surface, keeping pressure and thermal environment constant [49,50]. Using in-situ X-ray imaging, the concept of "continuous" growth could be demonstrated [51]. However, this two-in-one process appeared to be very difficult to optimize, and no further developments were reported. Nevertheless, it is worth noting that with the specific supersaturation control achievable with CF-PVT, it was the only process to demonstrate the growth of a few millimeters thick "bulk" 3C–SiC single crystals [52,53].

**Top-seeded solution growth.** Growth from high-temperature solutions usually leads to lower dislocation density than other methods [54]. This is related to the lower supersaturation level required for the growth, as compared to vapor phase processes. As an obvious choice, solution growth was tentatively applied to SiC more than 60 years ago; but despite many attempts (see, for instance [55]), it is only recently that major achievements have been reported, with the real demonstration of bulk single crystals. The current configuration is based on the geometry presented in Fig. 5.5, which implemented Czochralski-type crystal growth pullers. A high-density graphite crucible, thermally insulated with graphite felt, is heated by induction. The graphite crucible usually acts both as the container for the Si-based solvent and as the C source for the process, in the sense that it is continuously dissolved. The process is composed of three different elementary steps: dissolution of the C at the crucible–liquid interface; transport of the solute from the dissolution area to the crystallization area; and crystallization of SiC on the seed, the latter being stuck on a graphite shaft. Translation and rotation movements of both the crystal and the crucible can usually be applied. The temperature range is slightly lower than in PVT (typically 2273–2373 K), as

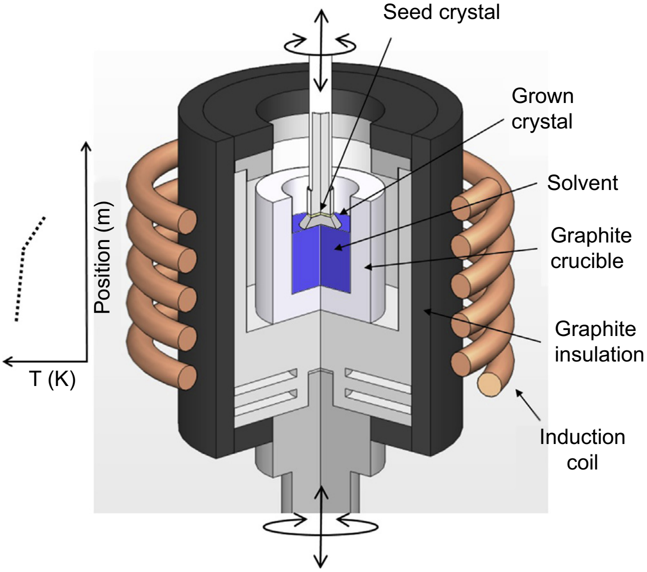

**Figure 5.5** Description of the top-seeded solution growth process. (a) Schematic view of the TSSG reactor concept; (b) schematic temperature profile along the symmetry axis of the crucible. Typical growth conditions are 2273 K and $10^5$ Pa of argon.
Modified from J. Lefebure, et al., Modeling of the growth rate during top seeded solution growth of SiC using pure silicon as a solvent, Cryst. Growth Des. 12 (2) (2012) 909–913, Copyright 2011, with permission from American Chemical Society.

are the temperature gradients. The working atmosphere is high-purity Ar or He above atmospheric pressure to reduce the vaporization rate of liquid Si.

In pure Si the growth rate is extremely slow [56], and not really compatible with a bulk crystal growth process. This is due to the very low C solubility in a reasonable temperature range. To increase the growth rate, two different strategies have been investigated.

1. Improvement of the C solubility. In pure Si this can be achieved by a significant increase of the temperature, up to 2473–2575 K. Due to the high vaporization flux of Si(l), this requires operating at high Ar overpressure, typically in the $1{-}2 \times 10^7$ Pa range [57]. However, fast growth regimes were found to be difficult to stabilize, particularly due to the complex and unstable C feeding from the graphite crucible [58]. Much easier is the use of a proper solvent, i.e., a Si-based alloy, to increase the C solubility in a more "realistic" temperature and pressure range. Many metal additives have been investigated [59–65], the best being Fe, Cr, and Ti [66,67]. In particular, Cr–Al–Si-based alloys gave the best published results in terms of growth rate (up to 2 mm/h) [68,69], control of the interface shape (meniscus) [67], and stability of the growth front (smoothness of the liquid–SiC interface) [70]. Contamination of the crystals from the solvent is still unknown; obviously, depending on the application; this could be problematic.
2. Improvement of the C transport between the dissolution area and the crystallization area. Unlike the growth from the vapor phase at reduced pressure, the use of a liquid solution

makes the system much more complex in terms of fluid dynamics. Besides diffusion, several different convective mechanisms, like buoyancy, forced convection, electromagnetic convection, and thermocapillary convection (Marangoni), contribute to the global convection pattern [71]. Though more complex, this constitutes an advantage as these convective mechanisms can be controlled almost independently. For example, electromagnetic convection can be tuned by selecting the proper induction frequency [72], or by adding other electromagnetic fields [73,74]. Forced convection can be controlled by specific crucible design and adapted movements of the crystal and/or the crucible [75]. Accelerated crucible rotation technique has also proven its efficiency in increasing the growth rate [76].

## 5.4 Tailoring of crystal properties via growth parameters

Control of crystal properties is crucial for successful industrial applications of SiC crystals. Among them, crystal diameter, polytype, and crystallographic defect density in SiC crystals are parameters of paramount importance to implement reliable low-cost SiC semiconductor devices. In this section we focus on the crystal diameter enlargement and polytype control in SiC bulk crystal growth. The control of crystallographic defects in SiC crystals is treated in Section 5.6.

The availability of large-diameter SiC wafers is crucial for reducing the cost of SiC devices through economies of scale and the use of depreciated Si or GaAs device fabrication lines. In this respect, much effort has been made over the last decade, leading to the recent fabrication of fully single crystal wafers with diameters of up to 200 mm. Fig. 5.6 shows a photograph of a 200 mm diameter 4H—SiC wafer fabricated by Cree Inc. in the United States [5]. The crystal quality generally degrades as the crystal diameter increases, due to the lack of an established methodology for expanding the diameter of high-quality SiC crystals without degrading the crystal quality. It becomes increasingly difficult to grow high-quality SiC crystals as the crystal diameter increases, and various technological problems have become apparent in the diameter enlargement process.

Most problems related to crystal diameter enlargement originate from large temperature gradients during the growth process of large-diameter SiC crystals. Large thermoelastic stresses are imposed on the grown crystals when the temperature difference between the center and the edge of the crystal is large during the crystal growth process. Numerical simulation of the temperature distribution in grown crystals showed that the temperature difference is relatively small in growth of crystals with a small diameter, e.g., 50.8 mm diameter [77]. However, this difference will be as high as 50—60 K if the diameter is increased to 150 mm. Such a large temperature difference is expected to impose large thermoelastic stresses on the grown crystal and often results in cracks in the crystal [78]. As the crystal diameter is increased, cracks parallel to the growth direction often occur at the edge of SiC boules, implying that a large thermoelastic stress in the tangential direction at the boule edge is placed on the grown crystal. This cracking problem considerably hinders growth of large-diameter (>100 mm) SiC crystals and is a serious issue for their development.

CREE
200 mm Wafer

**Figure 5.6** Photograph of a 200 mm diameter 4H−SiC wafer.
After A.R. Powell, et al., Bulk growth of large area SiC crystals, Mater. Sci. Forum (2016) 5−10.

The large temperature difference present in large-diameter SiC crystals gives rise to another problem, namely a relatively high concentration of basal plane dislocations (BPDs) introduced into the crystals. The larger the diameter of SiC crystals, the higher the density of BPDs. This is due to a larger temperature gradient caused by the enhanced inhomogeneous heating of SiC crystals during the growth of larger-diameter SiC crystals. BPDs are one of the most detrimental defects in SiC devices [3], and thus they need to be eliminated from SiC crystals. The basal plane slip system ($\{0001\}<11\bar{2}0>$) is the primary slip system observed in hexagonal SiC crystals, and thus the glides and multiplication of BPDs are relatively easily activated in 4H−SiC crystals. Particularly, at high temperatures the critical resolved shear stress for the basal plane glides in 4H−SiC crystals is significantly lowered, and thus the problem is more serious for high-temperature PVT growth processes.

To solve these problems, a high degree of control of both the transient and continuous thermal profiles during crystal growth is required. However, experimental optimization of such growth parameters usually takes much effort and is time-consuming. Consequently, results of numerical simulation of the temperature profile inside the crucible are used. This approach has allowed a successful diameter enlargement of up to 200 mm without cracks, and the grown 200 mm diameter 4H−SiC crystals show a relatively low density of BPDs.

In solution growth of SiC, diameter enlargement has also been pursued over the last decade, and growth of 90 mm diameter 4H−SiC crystals was successfully demonstrated [75]. In solution growth of SiC crystals, the top-seeded solution growth (TSSG) method is almost always employed for large-diameter crystal growth. The TSSG method has long suffered from parasitic deposition of polycrystalline SiC on the peripheral regions of the seed crystal when it is dipped in the solution

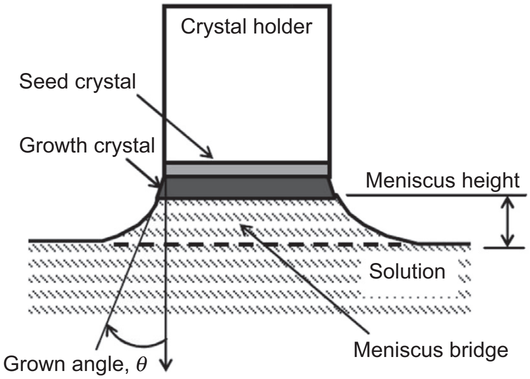

**Figure 5.7** Schematic figure of the meniscus-controlled growth technique, where a meniscus bridge is formed between the grown SiC crystal and the Si or Si alloy melt.
After H. Daikoku, et al., Top-seeded solution growth of 4H-SiC bulk crystal using Si-Cr based melt, Mater. Sci. Forum (2012) 61−64.

(C in the Si(l) or Si-based liquid alloys). The parasitic deposition not only hampers the crystal diameter enlargement but also largely degrades the crystalline quality of grown crystals. To address these problems, a group at Toyota Motor Corporation in Japan proposed a novel seeding technique called "meniscus-controlled" growth, where a meniscus bridge is formed between the grown SiC crystal and the melt, as shown in Fig. 5.7 [67]: the seed crystal was dipped in the solution and then slightly pulled upward from the solution surface to adjust the meniscus height and angle. This technique successfully suppresses the parasitic deposition of polycrystalline SiC and achieved successful crystal diameter enlargement in solution growth of SiC. In this technique, the degree of the enlargement is adjusted by controlling the meniscus angle; the angle can be controlled from −22 degrees (diameter shrinkage) to 61 degrees (enlargement). Prevention of the parasitic deposition also allows prolonged solution growth, resulting in 4H−SiC crystals of more than 10 mm in length.

Another important crystal property in SiC crystal growth is given by the possibility of growing different SiC polytypes. Owing to its high merit for device applications (e.g., large bandgap, high electron mobility, and approximately isotropic nature of electron mobility), the 4H polytype has gained more attention than other polytypes. Experimentally, however, establishing crystal growth conditions for 4H−SiC has been more difficult than for other polytypes, such as 3C− and 6H−SiC. The polytype of SiC crystals is thought to be determined by the interplay between the thermodynamics (energetics) and kinetics of crystal growth. The well-known kinetics determining the grown polytype of SiC crystals is the spiral growth mechanism, in which the ledge extending from the emergence point of a screw dislocation at the growing crystal surface acts as a source of the stacking information of SiC polytypes, kinetically forcing the grown crystal to inherit the polytype of the underlying crystal via the step flow mechanism.

A large body of literature already exists on the theories for the cause of SiC polytypism [79−81]. However, many aspects of the polytype formation during SiC bulk crystal growth remain unclear. The formation of various SiC polytypes has been discussed from the perspectives of thermodynamics [79,80] and kinetics [79,81] of SiC crystal growth. The occurrence of the short-periodic polytypes of SiC (e.g., 3C, 6H, 4H, and 15R) is mainly affected by thermodynamics such as the formation enthalpy of SiC polytypes and the vapor phase composition, while the long-periodic structures of SiC are assumed to be stabilized by growth kinetics such as spiral growth due to screw dislocations [81].

As for the thermodynamical nature of SiC polytype, there are well-known results obtained by Knippenberg based on the spontaneous nucleation of SiC crystals from the vapor phase (Fig. 5.8). He investigated the statistical polytype occurrence in a Lely furnace, and indicated that the 4H polytype is an equilibrium phase in a lower and narrower temperature range than 6H [82]. The 15R polytype is often observed in the bulk crystal growth of SiC but would be a metastable polytype in the temperature range of PVT and solution growth of SiC bulk crystals, since large crystals of the 15R polytype are only stable in a very narrow temperature range around 2723 K, whereas the 3C polytype is metastable over all temperatures (Fig. 5.8).

Under crystal growth conditions, where the growth rates are of the order of several hundred μm to 1 mm/h, the relative influence of thermodynamic and kinetic effects on polytype stability may not be obvious [35]. It should, however, be noted that the temperature dependence of the 4H versus 6H polytype occurrence similar to that observed by Knippenberg (Fig. 5.8) has been reported in PVT growth [34]. As reported by several groups [26,83], the gas phase stoichiometry also plays an important role in SiC crystal growth. Higher C/Si ratios favor the formation of the 4H polytype. This has been related to a higher relative concentration of Si versus

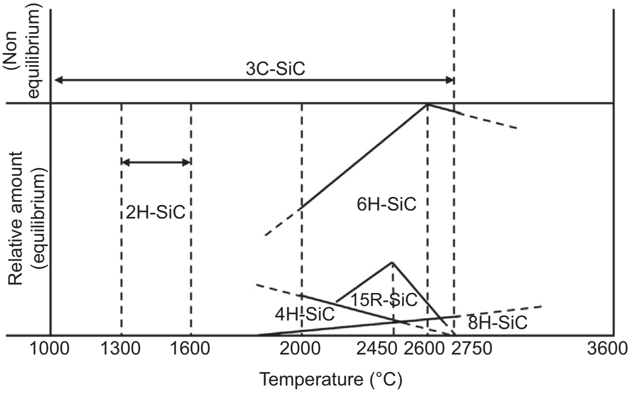

**Figure 5.8** Relationship between SiC crystal structure and the temperature at which each polytype occurs. The relative amounts of different hexagonal and rhombohedral structures of SiC are shown.

After W.F. Knippenberg, Growth phenomena in silicon carbide, Philips Res. Rep. 18 (3) (1963) 161−274.

**Table 5.1** **Formation on a seed crystal of different polytypes and surface polarities**

| | **Seed crystal** | **Grown crystal** |
|---|---|---|
| Polytype | Surface polarity | Dominant polytype |
| 6H | (000$\bar{1}$)C | 4H, 6H |
| | (0001)Si | 6H (often 15R mixed) |
| 4H | (000$\bar{1}$)C | 4H |
| | (0001)Si | 6H (often 15R mixed) |

C vacancies in the structures with increased hexagonality [26]. The addition of some impurities (e.g., Sc [84], Ce [85]) in the source material also favors 4H–SiC formation. They are characterized by low solubility ($\sim 10^{16}$ cm$^{-3}$) in SiC and are assumed to work as "surfactants" which change the surface energetics of the nuclei. By contrast, N, which also stabilizes the 4H polytype [36,86], is highly incorporated in SiC crystals ($>10^{20}$ cm$^{-3}$). A number of N impurities injected into the growth zone increases the C/Si ratio on the growing surface and stabilizes more hexagonal polytypes, i.e., 4H–SiC.

As first pointed out by Stein et al. [31], the surface polarity of the seed crystal largely affects the polytype formation. Table 5.1 summarizes the seed surface polarity effect on polytype formation during PVT growth of SiC [87]. The 6H, 4H, and 15R polytypes occur on the (000$\bar{1}$)C surface, while the 6H and 15R polytypes are grown on the (0001)Si surface, regardless of the polytype of the seed crystal. The 4H polytype never occurs on the (0001)Si surface even when a seed crystal of the 4H polytype is used. In contrast, the 4H polytype is preferentially grown on a 4H–SiC(000$\bar{1}$)C seed crystal [36], and thus the use of this 1seed crystal gives a great advantage for obtaining a single polytypic 4H–SiC crystal. These surface polarity effects were explained by the sp$^2$ hybridized bonds on the C-terminated (000$\bar{1}$)C surface [88], or, as more recently reported, by an interplay between the surface energy difference [(0001)Si versus (000$\bar{1}$)C] and the difference in formation enthalpy of the 4H and 6H polytypes [31].

## 5.5 Benefits of computer modeling

As a general rule for bulk crystal growth processes, the results in terms of size, structural quality, doping, and homogeneity of the crystals are directly related to the degree of control over the process. Thus precise and accurate monitoring of the physico-chemical parameters and their distribution in the reactor is of primary importance. SiC bulk growth processes are usually considered as "black boxes," because the experiments are carried out in quasiclosed graphite crucibles at extremely high temperatures, typically in the 2300–2800 K range. By "black box" is meant that there is no direct access to the internal process parameters without disturbing the system. The question is thus how to link the controllable parameters (coil current and frequency, temperature of the external surface of the crucible, pressure, geometry) to the observable parameters after the experiments (growth rate, defects density, shape, doping level, and homogeneity). The experimental approach alone has not been sufficient to develop such processes. In the last 15 years major improvements have been achieved due to the parallel development of modeling and simulation tools. A macroscopic approach linked with experiments and characterization has allowed researchers to open the black box of the process step by step and gain insight into the intricate mixture of phenomena. A global approach involving experimentation, characterization, and modeling is a noteworthy achievement in the history of SiC, as there are not many examples in the literature in which so complete an approach has been implemented in such extreme experimental conditions. A useful model should be able to predict quantitatively how these phenomena influence the crystal growth process. The results of modeling are usually twofold. Firstly, it gives an insight into what is actually happening in the system, in the sense that it constitutes a "characterization" or "visualization" of the process. Secondly, once a high enough maturity level is reached, modeling can be used as a "design tool" for optimization and development of the process.

After the pioneering work of Hofmann et al. [89] and Pons et al. [90], several groups have tackled the development of the computer code models, with the aim of either improving some specific aspect of the simulation or getting a global coupled multiphysics model. Today, heat and mass transfer calculations can be considered as state of the art [91,92]. Different approaches have been implemented for the chemical reactions, especially at the solid–vapor interfaces [93–98]. These models require a certain degree of connection with thermodynamics. A model for predicting the dislocation density has also been developed based on the thermal stress calculations [99], while the most recent achievement is the implementation of the Alexander–Haasen (AH) model to describe the dynamics of plastic deformation in SiC, where the effects of the cooling time on the final dislocation density, residual stress, and stacking faults can be studied [100].

Very importantly, a reliable database for electrical and thermal materials properties as well as chemical reactions, e.g., heterogeneous reactions of the SiC gas species with the graphite wall, is mandatory to achieve reliable modeling results. Basically, the accuracy of the physical, chemical, and thermodynamical parameters predecides whether the simulation can be considered as quantitative or if it provides more of a qualitative trend.

Temperature field calculations are carried out taking into account heat transfer by conduction (solid parts of the growth setup and liquid phase), convection (fluids), and radiation, the latter being the dominant process at elevated growth temperatures of $T > 2273$ K. A proper treatment of heat transfer must also consider the latent heat for both SiC sublimation at the source and SiC crystallization at the seed. Due to the low growth rates, the heat produced at the crystallization front is usually neglected; but with the recent development of high-growth-rate processes (>1 mm/h) [68,101], this has to be considered. Also, convection, which is often neglected in PVT [90,91] because of the low pressure of the ambient gas, must be seriously considered in TSSG [71]. Temperature distribution is the minimum required for fast initial development of SiC bulk growth processes, and has become easier with the use of commercial turnkey software packages. However, for process upscaling an optimization of the calculation of the temperature distribution is critical, as it directly impacts the stress generation and evolution in the bulk crystals. An accurate and precise description of the temperature gradients (both axial and radial) is difficult because SiC is semitransparent at growth temperature. The absorption of radiation is not constant, as it is linked to the doping level of the crystal and the temperature. The overall temperature field is slightly affected by the semitransparency, while the local effect on the crystal and its vicinity is significant [102,103]. Thermal stress plays a significant role in the dislocation density distribution. It can cause multiplication of dislocations when the resolved shear stress on a primary slip system exceeds the "critical resolved shear stress." As a first approximation, the shear stress can therefore be used as an indicator of dislocation density in the crystal [104,105].

While most research has been conducted in the quasistationary state, it is also important to investigate transient phenomena in the crucible. This is especially important when one wants to describe the behavior of the growth setup during heating and cooling stages, or if geometry evolves with time, such as the coil position with respect to the crucible. This was mainly investigated by Klein et al. [103,106]. They showed, for instance, that the heating of the SiC source powder can be significantly delayed in comparison with the heating of the bulk of the growth apparatus. Such an effect becomes obviously more prominent if a larger powder charge is used, and less prominent if the powder has a higher thermal conductivity. For the configuration they studied, a time lag of up to 1.5 h between the heating of the powder surface and its interior was assessed [107]. Even more important is the link between heating and cooling stages and the development of stress and extended defects in the final crystal [100,108]. The AH model has been used to describe the plastic deformation of 4H–SiC single crystals. In the high-temperature region (above 1273 K), the activation of the C–core partial dislocations is implemented, and in the low-temperature conditions (below 1273 K), the Si–core partial dislocations are modeled. The time evolution of the dislocation density can thus be evaluated, and the effects of the cooling time on the final dislocation density, residual stress, and stacking faults can be examined [100]. A proper power control has been demonstrated to reduce the resulting basal plane dislocation density effectively [109].

To go one step further, mass transfer must be included and strongly coupled with heat transfers in the growth processes. The mass transport from the charge to the seed and the growth kinetics determine the growth rate and crystal shape. The driving force for vapor transport is the partial pressure difference of the various SiC gas species (in particular Si, $Si_2C$, and $SiC_2$) between source and seed. From an experimental point of view, the growth rate is a strong function of growth temperature, temperature gradient, inert gas pressure, the distance between charge and seed, etc., which ultimately establish the partial pressures of the mentioned SiC gas species. For numerical simulation, the Stefan flow caused by the phase change of the SiC powder and crystal needs to be taken into account. To relate the growth rate to the supersaturation, the Hertz–Knudsen equation is generally used. It is now well established that control of the local flux of species (i.e., the supersaturation) in the vicinity of the crystal and the crystal/vapor interface is one of the key issues to get a high-quality homogeneous crystal. This can be done by using a "screen" or "guide" at the periphery of the growth front which allows the growth of self-standing single crystals, free of polycrystalline inclusions [110]. Such a guide also governs the crystal enlargement. Regarding such development, the correlation between numerical modeling and experiments was well demonstrated by Nishizawa et al. in the picture in Fig. 5.9 [111].

For solution growth, the main difficulty in simulating mass transfer is the correct description of the convection pattern that governs the solute (C) transport from the dissolution zone to the crystallization zone. In pure Si, four main contributions must be considered: buoyancy convection, forced convection, Marangoni convection, and electromagnetic convection. This complexity is a major difficulty, as it can easily give rise to process instability, but it can also be an advantage, considering that

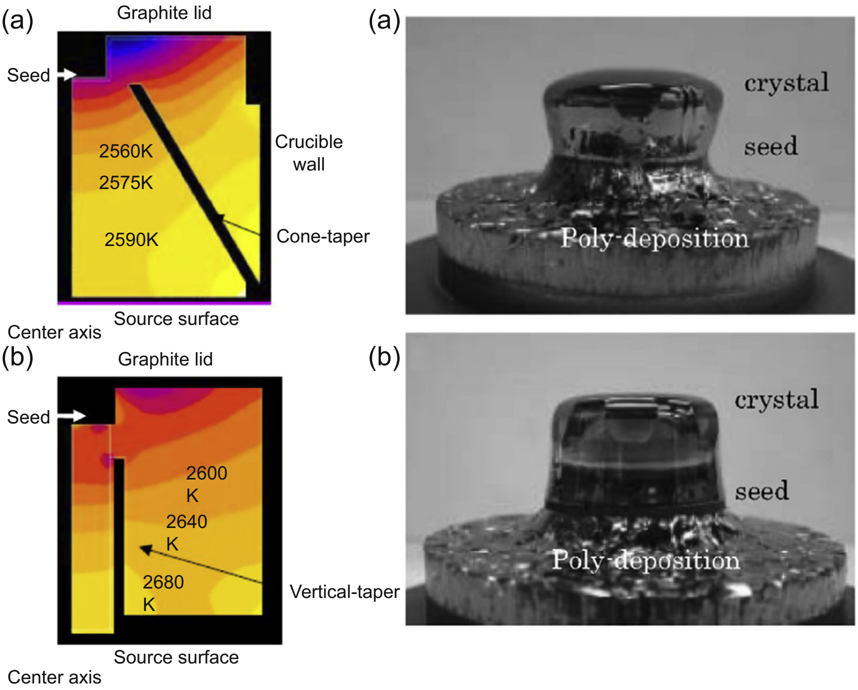
(a)
Graphite lid
Seed
2560K
2575K
2590K
Crucible wall
Cone-taper
Source surface
Center axis
(b)
Graphite lid
Seed
2600 K
2640 K
2680 K
Vertical-taper
Source surface
Center axis
(a)
crystal
seed
Poly-deposition
(b)
crystal
seed
Poly-deposition

**Figure 5.9** Illustration of the use of a "guide" or "screen" for the single crystal growth of SiC by PVT. Left: temperature distribution inside the growth cavity with two different guide shapes, (a) cone-shaped guide, and (b) vertical guide. Right: camera picture of the corresponding crystals. It is shown by proper design of an inner "guide" that a polycrystal-free single crystalline SiC ingot could be obtained. Such an approach opened the way to large-diameter, high-quality crystals. Adapted from S.-i. Nishizawa, T. Kato, K. Arai, Effect of heat transfer on macroscopic and microscopic crystal quality in silicon carbide sublimation growth, J. Cryst. Growth 303 (1) (2007) 342–344, Copyright 2007, with permission from Elsevier.

some of these convection mechanisms can be controlled externally to enhance the carbon transport [71–73], as mentioned in Section 5.3. Here again, numerical simulation is the only tool that allows opening the black box of the process. Solutal convections can be neglected because of the very low C solubility in pure Si. This might be not the case for other solvents with much higher carbon solubility, typically higher than 10 at%, such as in Cr–Si alloys. The growth rate is simply computed from the C flux arriving at the crystal surface. A perfect agreement is found with pure Si as solvent [56]. However, the complexity of the convection patterns brought some limitations in upscaling the TSSG process by only considering two-dimensional (2D) axial geometry. A correct description would require a full three-dimensional geometry, which drastically increases the computation time.

## 5.6 Doping issues and reduction of defect density

As described in Section 5.1, SiC has a great advantage over the other wide bandgap semiconductor materials with respect to the doping and resistivity control; ambipolar doping is possible, and a wide range of resistivity control is achieved for both *p*- and *n*-type doping. N, which substitutes at the C sites in SiC crystals, is the most important shallow donor impurity for SiC, and it can be easily introduced into the crystal during PVT growth using a controlled N gas flow. Several groups have used optimized growth conditions to fabricate 4H–SiC substrates with ultralow resistivities of $1-3 \times 10^{-3}\ \Omega$ cm [35,112].

The N-doping kinetics in the PVT growth of SiC are discussed in terms of the polytype of grown crystals [113–115], crystal growth direction [87,114], N partial pressure in the source gas [114–116], and growth temperature [112,115]. The surface polarity and crystal growth direction have a significant influence on the incorporation kinetics of donor and acceptor dopants. Fig. 5.10 shows the dependence of the impurity incorporation on the seed surface orientation during PVT growth of 6H– and 4H–SiC crystals [114]. N donors are preferentially incorporated on the $(000\bar{1})$ C surface, whereas acceptor atoms such as boron (B) and Al show preferential incorporation on the (0001)Si surface. Impurity incorporation on nonpolar surfaces such as $(1\bar{1}00)$ and $(11\bar{2}0)$ is intermediate between those on the $(000\bar{1})$C and (0001)Si surfaces. The easiness of N donor incorporation follows this plane sequence: (0001) Si < $(11\bar{2}0)$ < $(1\bar{1}00)$ < $(000\bar{1})$C. For B acceptors the sequence changes, and B atoms are preferentially incorporated in the order (0001)Si < $(1\bar{1}00)$ < $(11\bar{2}0)$ < $(000\bar{1})$C. Among the nonpolar surfaces, $(1\bar{1}00)$ appears to be the most advantageous for impurity incorporation [87] due to its surface structure, which has more dangling bonds per unit area compared to $(11\bar{2}0)$ [117].

In the impurity incorporation mechanism, the polytype dependence of impurity incorporation on the surfaces perpendicular to {0001} is of great interest, since the difference in the stacking sequence fully appears at the growing surface. However, no polytype dependence of N and B incorporation between 4H– and 6H–SiC was observed for growth on the $(1\bar{1}00)$ and $(11\bar{2}0)$ surfaces [114]. This result is supported

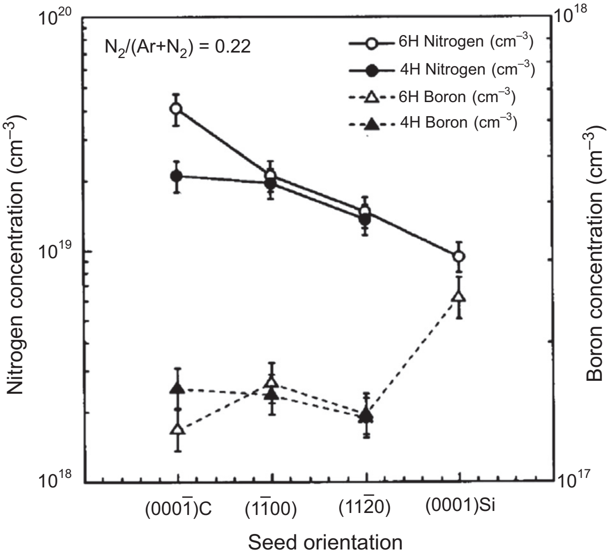

**Figure 5.10** Dependence of the impurity incorporation on the seed surface orientation during PVT growth of 6H— and 4H—SiC crystals.

Reprinted from N. Ohtani, et al., Impurity incorporation kinetics during modified-Lely growth of SiC, J. Appl. Phys. 83 (8) (1998) 4487—4490, Copyright 1998, with the permission of AIP Publishing.

by the fact that impurity atoms are uniformly incorporated into different lattice sites (cubic and hexagonal sites) of SiC crystals. For impurity incorporation on the $(000\bar{1})$C growing surface, the effect of the polytype of grown crystals is still under debate. Ohtani et al. reported that 6H—SiC incorporated more N and less B than 4H—SiC [114]; however, the opposite dependence was reported by Tsavdaris et al. [118]. Further studies are needed to clarify the existence and origin of the polytype dependence of impurity incorporation.

It is well known that N incorporation is enhanced on the {0001} facet of SiC crystals. The {0001} facet develops at the growth front of SiC boules during bulk crystal growth, accompanying nonfacetted regions outside the facet. The facet is a flat plane covered with surface steps emanating from growth spirals located at the facet center. It is generally thought that Burton—Cabrera—Frank-type growth kinetics governs growth on the {0001} facet of SiC boules and results in stable, polytype-preserving growth. Rost et al. reported the enhancement ratio of N incorporation on the $(000\bar{1})$C facet of 4H—SiC boules compared with that on the nonfacetted regions [115]. In unintentionally doped boules ([N] ~ $10^{17}$ $cm^{-3}$), this ratio of incorporation between the $(000\bar{1})$C facet and the nonfacetted regions is close to a factor of 2. Upon intentional doping, it rapidly decreases with doping to a factor of 1.2 at N concentrations of more than $10^{19}$ $cm^{-3}$: at more than 15% addition of N gas in the growth ambient, the N concentration in the crystal part grown on the $(000\bar{1})$C facet ([N] > $10^{19}$ $cm^{-3}$) is approximately 20% higher than that in the crystal part grown on the nonfacetted regions. The mechanism of the higher incorporation is still unclear, but would be related to the difference in the step structure between the facet and the nonfacetted regions.

The temperature dependence of N incorporation is another important issue for doping control. It was revealed that N incorporation is enhanced at low growth temperatures for PVT growth of SiC crystals; the lower the growth temperature, the more N is incorporated in the grown crystals [112,115]. The temperature dependence of N incorporation is explained through the understanding of the N adsorption/desorption kinetics on the SiC {0001} surface. The N adsorption on the {0001} surface is well described by a Langmuir isotherm type equation [114,118]. The observed Langmuir isotherm type dependence of N incorporation implies that the adsorption/desorption kinetics on the {0001} surfaces during PVT growth is virtually in thermal equilibrium. At such "quasiequilibrium" the rate of adsorption of N atoms on the growing surface virtually equals the rate of desorption, and the number of N atoms incorporated in the grown crystals is negligibly small compared with those impinging to and desorbed from the growing surface. This assumption is well supported by the fact that the N doping concentration is hardly influenced by the growth rate of 0.41−1.1 mm/h, which is typical for PVT growth of SiC [113], implying that the N incorporation is not kinetically limited, and at each N partial pressure an equilibrium surface coverage of adsorbed N is always established during growth. These results imply that the amount of N incorporated into the grown crystal is determined by the amount of N adsorbed on the growing {0001} surface. For this reason N incorporation is enhanced at low temperatures, where the amount of N adsorbed on the growing {0001} surface is controlled by the adsorption/desorption kinetics on the surface, and the lower the growth temperature, the longer the desorption lifetime. The activation energy for desorption derived from the temperature dependence of N incorporation is $150-220 \times 10^3$ J/mol [118], which well agrees with a theoretical estimation of the twofold adsorption energy of $N_2$ molecules on the $(000\overline{1})$C surface ($144 \times 10^3$ J/mol) [119] and lends support to the desorption-limited kinetics model for temperature-dependent N incorporation in SiC crystals.

N doping during solution growth of SiC crystals is also easily achieved by adding N gas in the growth atmosphere (usually helium) during solution growth. A mixed gas of helium and N at atmospheric pressure was used for N doping during TSSG of 4H−SiC using a Si−Ti solvent at 2213 K, in which the N content in the atmosphere was varied from 0.17 to 0.5 vol% [120]. Under these optimized growth conditions, 4H−SiC crystals with an N concentration of $1.1 \times 10^{20}$ $cm^{-3}$ and an electrical resistivity of $3 \times 10^{-3}$ $\Omega$ cm were grown. The N incorporation kinetics during solution growth is still not well understood, but the dissolution of $N_2$ gas into the Si or Si−Ti solvent was reported to limit the incorporation kinetics of N in the TSSG 4H−SiC crystals [120].

Low-resistivity *p*-type SiC crystals are required to fabricate bipolar-type SiC devices. Particularly, these crystals are essential for fabricating *n*-channel SiC IGBTs; however, low-resistivity *p*-type crystals are very hard to obtain and still not commercially available. Early investigations employed high-purity metallic Al as a precursor state for Al doping. During the PVT growth of *p*-type SiC crystals, Al acceptors are supplied to the growing surface through the evaporation of metallic Al. A major drawback of this procedure is the quick exhaustion of Al source materials, resulting in significantly inhomogeneous doping along the growth direction [121,122]. Furthermore, it was pointed out that a high initial Al concentration in the gas phase of PVT growth resulting from high vapor pressure of metallic Al causes a high density of crystallographic defects in the initial part of the grown crystal [121].

To solve these problems, Eto et al. employed a two-zone PVT growth reactor to control the sublimation of the SiC source and dopant materials almost independently [123]. They also used an Al compound with relatively low vapor pressure, i.e., $Al_4C_3$, as an Al-bearing dopant material. Fig. 5.11 shows a schematic diagram of the two-zone PVT growth system for the codoping of N donors and Al acceptors [124]. Two coaxially located induction coils allow independent control of the temperatures of the source and dopant ($Al_4C_3$) materials. By optimizing the growth conditions, especially the temperature difference between the source and dopant materials, they achieved uniformly doped *p*-type 4H—SiC crystals with a hole concentration higher than $1 \times 10^{20}$ $cm^{-3}$, which is among the highest hole concentrations ever reported for PVT-grown SiC crystals. However, heavy Al doping destabilizes the 4H polytype, and the grown *p*-type crystals always contain 6H polytype inclusions even when a 4H—SiC seed crystal is used. Eto et al. proposed a way to mitigate this problem by codoping of N donors into Al-doped *p*-type 4H—SiC crystals. The codoping of

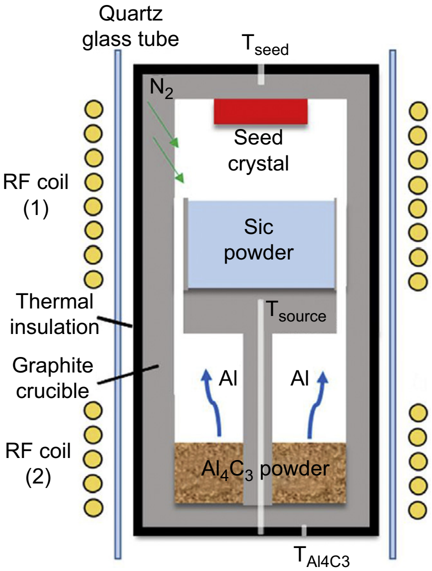

**Figure 5.11** Schematic diagram of the two-zone PVT growth system for codoping of nitrogen donors and aluminum acceptors.
After K. Eto, et al., Growth of P-type 4H—SiC single crystals by physical vapor transport using aluminum and nitrogen co-doping, J. Cryst. Growth 470 (2017) 154—158, Copyright 2017, with permission from Elsevier.

N donors stabilizes the 4H polytype, and under the optimized doping conditions *p*-type 4H—SiC crystals with a hole concentration of $4 \times 10^{19}$ $\mathrm{cm}^{-3}$ and an electrical resistivity of less than $9 \times 10^{-2}$ Ω cm were obtained [124].

Further, lower-resistivity *p*-type 4H—SiC crystals were also obtained by the solution growth method. The addition of Al has advantages in growing high-quality SiC crystals by this method: Al addition to the Si solvent has been reported to suppress step bunching on the growing surface during the solution growth of SiC crystals [70]. Step bunching is one of the major problems in the solution growth of SiC; it results in the formation of giant macrosteps of heights greater than several micrometers, and often causes solvent inclusions in the grown crystals. Heavy Al doping during solution growth of SiC crystals was reported by Shirai et al. [125]. They grew heavily Al-doped *p*-type bulk 4H—SiC crystals on a 4H—SiC $(000\overline{1})$C seed crystal by the solution growth method using a Si—Cr—Al solvent at 2000°C, where the Al content in the solvent varied from 0 to 20 at%. They were successful in obtaining low-resistivity ($35 \times 10^{-3}$ Ω cm) *p*-type 4H—SiC crystals, which demonstrated the advantage of the solution method for growing *p*-type SiC crystals.

For vertical-type power devices, SiC substrate crystals with electrical resistivities as low as a few $\times\ 10^{-3}$ Ω cm are required to minimize the parasitic resistance due to substrates. However, SiC substrates with such low resistivities are still not commercially available even though *n*-type 4H—SiC crystals with ultralow resistivities of $1-3 \times 10^{-3}$ Ω cm can be obtained, as described earlier in this chapter. This unavailability stems from the structural instability of heavily N-doped 4H—SiC crystals during high-temperature treatments. It was reported that these crystals undergo structural changes during oxidation or Ar annealing at temperatures exceeding 1373 K [126,127]. The structural changes have been attributed to a 4H to 3C polytype transformation that is induced by the formation and expansion of double-layer Shockley-type stacking faults (DSSFs) during the high-temperature treatments [126—128]. Fig. 5.12 shows a high-resolution transmission electron microscopy (HRTEM) image of a DSSF observed in a heavily N-doped 4H—SiC crystal; schematic diagrams of the stacking sequences of perfect 4H—SiC crystal and crystals with a single Shockley stacking fault (SSSF) and a DSSF are also shown [129]. The driving force for the fault expansion is the so-called quantum well action (QWA) mechanism, in which electrons in heavily N-doped 4H—SiC entering stacking-fault-induced quantum wells lower the system energy [130—132]. The 4H to 3C polytypic transformation not only influences the electrical properties of the substrate crystals [115,117], but also severely degrades their geometrical parameters such as substrate flatness [116]. This problem is discussed later in this chapter.

From the viewpoint of industrial applications of SiC crystals, another major requirement for crystal growth is the reduction of crystallographic defects. The manufacturing of SiC electronic devices started around the year 2000 and steadily expanded in the semiconductor device market; however, the crystals still contain a variety of crystallographic defects and this largely hinders further penetration of SiC devices into the market. The defects include micropipes (hollow tubes) [133,134], dislocations [135—140], and subgrain boundaries [135,136,141]; they are all observed in SiC crystals grown by the PVT method. Table 5.2 summarizes

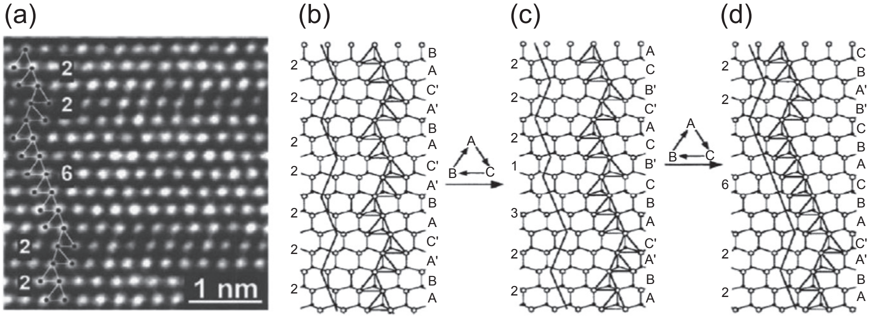

**Figure 5.12** (a) HRTEM image of a DSSF observed in a heavily nitrogen-doped 4H−SiC crystal. Schematic diagrams of (b) perfect 4H−SiC, (c) crystal sheared once at the seventh layer from bottom (SSSF), and (d) structure shown in (c) sheared again at the eighth layer from bottom (DSSF).
Reprinted from M. Skowronski, S. Ha, Degradation of hexagonal silicon-carbide-based bipolar devices, J. Appl. Phys. 99 (1) (2006), Copyright 2006, with the permission of AIP Publishing.

**Table 5.2** **Extended defects commonly observed in SiC bulk crystals**

| **Dislocation type** | **Line direction** | **Slip plane** | **Burgers vector** |
|---|---|---|---|
| Micropipes | <0001> | – | n times *c*-lattice parameter (n$\geq$2: 6H, n$\geq$3: 4H) |
| 1*c* or 2*c* closed-core Screw dislocations (TSDs) | <0001> | – | c-lattice parameter (6H); 1 or 2 times c-lattice parameter (4H) |
| Threading edge dislocations (TEDs) | <0001> | (11$^{-}$00) | $\frac{1}{3}$<11$\bar{2}$0> |
| Basal plane dislocations (BPDs) | In the (0001) plane preferentially along <11$\bar{2}$0> | (0001) | $\frac{1}{3}$<11$\bar{2}$0> |
| Basal plane stacking faults (Frank type) | $\frac{1}{n}$<0001> (n = 4 for 4H and n = 6 for 6H) | | |
| Basal plane stacking faults (Shockley type) | $\frac{1}{3}$<11$^{-}$00> | | |

the types of extended defects commonly observed in SiC bulk crystals. Dislocations in SiC crystals are classified into two groups depending on their propagation directions. One is threading dislocations propagating along the crystal growth direction, and the other is dislocations lying in the (0001) basal plane, which are referred to as BPDs. The former type of dislocations are further classified into screw and edge-type threading dislocations depending on their Burgers vectors. They are known as threading screw dislocations (TSDs) and threading edge dislocations (TEDs), respectively. Basal plane stacking faults are also commonly observed extended defects in SiC crystals, since the formation energies for basal plane stacking faults in hexagonal SiC crystals are fairly small compared with those in other semiconductor materials [142,143].

Among these extended defects, micropipes, which penetrate the entire crystal along the growth direction as hollow tubes, are most harmful to SiC devices, since they are replicated in the epitaxial layers and become a fatal defect from the viewpoint of fabrication and yield of working devices [144]. Micropipes are a type of TSD and have a hollow tube at the dislocation core extending along the *c* axis. They are also called "superscrew dislocations," since they have a huge Burgers vector parallel to the *c* axis. As described in Table 5.2, the size of their Burgers vector ranges from several to more than 10 times the *c*-lattice constant, and the minimum size of their Burgers vector is assumed to be three times the *c*-lattice constant for 4H$-$SiC, which gives rise to the critical stress at the dislocation core to stabilize the hollow core [145].

In the early days of the development of SiC crystals, micropipes were a most serious concern among the crystallographic defects, and much effort was devoted to eradicating them from SiC crystals. The causes of micropipes are categorized into three groups: thermodynamic, kinetic, and technological [138]. The thermodynamic causes include thermoelastic stresses due to nonuniform heating, while the kinetic causes are related to the nucleation process and growth surface morphology. In all cases one must also consider the technological aspects, such as seed surface preparation and contamination of the growth system. An important aspect of micropipes is that while they develop during growth, simultaneous processes also occur which reduce their density, such as dissociation, coalescence, recombination, and transformation [140]. These processes are largely controlled by growth kinetics rather than equilibrium thermodynamics, and many are believed to be surface-mediated processes [146]. In principle, a dislocation with a Burgers vector $\boldsymbol{b} = \mathrm{n}\boldsymbol{c}$ ($\boldsymbol{c}$: smallest translation vector) is energetically unfavorable compared to the distribution of n elementary dislocations with a Burgers vector $\boldsymbol{c}$. The fact that micropipes appear stable and propagate in the crystal implies that a large kinetic energy barrier exists to nucleate a dislocation in SiC crystals adjacent to micropipes.

Over the last 2 decades the PVT growth technique has made considerable advances, and in the course of these advances a methodological approach to eliminating micropipes from SiC crystals has been established. Consequently, large-diameter ($>$100 mm) 4H$-$SiC substrates with an extremely low micropipe density (less than one per square centimeter or even zero) are commercially available [139], and thus micropipes are no longer focus defects in SiC crystal growth.

Although not as detrimental to SiC devices as micropipes, dislocations in SiC crystals have been reported to degrade several characteristics of SiC devices. Among the dislocations in SiC crystals, TSDs and BPDs are of the most serious concern since they have a significant negative impact on the performance of SiC power devices.

A well-known effect of dislocations in SiC crystals is the forward bias degradation of SiC bipolar diodes due to BPDs [147]. The electron−hole recombination during bipolar device operation induces the expansion of Shockley stacking faults, which are nucleated from BPDs in the SiC epitaxial layer. This phenomenon can be understood in terms of the electronically driven glide of Si−core partial dislocations in 4H−SiC epitaxial layers [148]. BPDs in 4H−SiC epitaxial layers are usually dissociated into Si−core and C−core partial dislocations, and under the forward bias operation (electron−hole injection), recombination-enhanced dislocation glide preferentially occurs for the Si−core partial dislocations.

Basal plane stacking faults act not only as an efficient recombination center but also as a potential barrier for electron transport, and as a result the on-resistance of SiC bipolar devices gradually increases with the forward bias operation. This is fatal for SiC bipolar devices and also for some types of SiC unipolar devices. It has recently been demonstrated that the same phenomenon happens in certain types of SiC unipolar devices where bipolar injection can occur during device operation [149,150].

On the other hand, TSDs negatively affect the blocking capabilities of SiC power devices. They cause a leakage current when the devices are reversely biased. The mechanism that leads to the enhanced leakage currents is yet to be clarified, but when the TSD density exceeds a critical value it brings about a large reverse leakage current to SiC power devices [151]. TSDs have long been recognized as pure screw dislocations having a Burgers vector along the $c$ axis. However, recent results of X-ray topography and HRTEM revealed that a certain amount (more than one-third of the total) of TSDs have a Burgers vector component parallel to $[11\bar{2}0]$ or $[1\bar{1}00]$ in addition to that parallel to the $c$ axis [152−155]. They are often referred to as $c + a$ or $c + m$ TSDs. Similar conclusions came from birefringence microscopy investigations [156]. It was suggested that the $c + a$ or $c + m$ TSDs more negatively impact SiC devices than pure $c$ TSDs; however, there is still no conclusive experimental result. TSDs are also often converted to or cause a variety of extended defects in SiC crystal during CVD and PVT growth, such as carrots [157,158] and stacking fault complexes [159].

Both TSDs and BPDs are detrimental to the gate oxide reliability of SiC MOSFETs. They have been shown to trigger the dielectric breakdown of the gate oxide and significantly impair the long-term reliability of SiC MOSFETs, and thus the reduction of their density is crucial for the implementation of SiC power MOSFETs [160]. The mechanism of their negative impact is still not well understood, but surface-mediated effects are likely to be involved in this phenomenon [161−164].

After the work by Wahab et al. [151], reduction of TSDs in 4H−SiC crystals was pursued over the two subsequent decades. In the course of this effort, several important aspects of TSDs were revealed, particularly their formation and propagation behavior. A major cause of TSDs is foreign polytype inclusions during crystal growth [140]. Different polytypes possess different stacking sequences along the $c$ axis and thus cause a disregistry in the atomic bonding when they have a nonbasal plane interface. This disregistry and associated large localized strains are relaxed by the formation of TSDs at the interface. TSDs are also formed by foreign particle or secondary phase inclusions during growth. Dudley et al. tried to explain the nucleation of screw dislocations during SiC bulk growth by considering the lateral growth over foreign particles or secondary-phase precipitates on the growing surface [165]. When the particles or precipitates on the surface are overgrown, the growth fronts may coalesce with misalignment under the influence of small stresses. To accommodate this misalignment, screw dislocations of opposite signs are created, with Burgers vector magnitudes equal to the magnitude of the misalignment. Their model is based on the observation of TSDs often originating at secondary-phase inclusions in PVT-grown SiC crystals.

Another major source of TSDs is the nonoptimal growth initiation of a bulk crystal growth process. Takahashi et al. reported, using X-ray topography, that whereas a relatively large portion of dislocations existing in PVT-grown crystals are inherited from the seed crystal, an additional high density of threading dislocations extending along the <0001> growth direction are introduced at the initial stage of crystal growth [139]. Defect formation at the initial stage of PVT growth of SiC was examined by Sanchez et al. using transmission electron microscopy, atomic force microscopy, X-ray topography, and defect selective etching [166]. They observed the formation of basal plane stacking faults at the initial stage of growth, with densities showing a good correlation with the threading dislocation density. TSDs tended to form in pairs with opposite Burgers vectors, and these results bear out the pair-generation model of screw dislocations by Dudley et al. [165]. Sanchez et al. also showed pair generation of edge dislocations at the stacking faults nucleated at the initial stage of growth [166]. If partial dislocations encompassing the stacking faults were of a Shockley type, the resulting threading dislocations would have an edge character. Frank-type partial dislocations would result in screw-type threading dislocations. The stacking-fault formation was attributed to nucleation of 2D islands on the surface of seed crystals, and the density of threading dislocations markedly decreased as the growth rate decreased as well as at growth on the off-oriented seed crystal.

N enrichment near the grown crystal/seed interface is another major cause of dislocation formation during the early stage of PVT growth of SiC crystals [167,168]. Ohtani et al. revealed a convex basal plane bending toward the growth direction near the grown crystal/seed interface, and attributed it to N enrichment due to the incorporation of residual N during the early stage of crystal growth [168]. The N enrichment causes not only a smaller lattice parameter of the grown layer but also a smaller coefficient of thermal expansion [169]; thus the misfit between the seed and grown crystal is significantly enhanced at high temperatures like PVT growth temperature (approximately 2673 K). The smaller lattice constant of the grown layer during the initial stage of high-temperature PVT growth gives rise to misfit dislocations near the grown crystal/seed interface, which have an extra half plane pointing toward the growth direction and result in the convex basal plane bending toward the growth direction. Many of the misfit dislocations formed during the initial stage of growth are converted to threading dislocations propagating along the growth direction [167].

Regarding the propagation behavior of TSDs, Powell et al. reported a relevant experimental result that TSD density in 4H−SiC crystals is significantly reduced

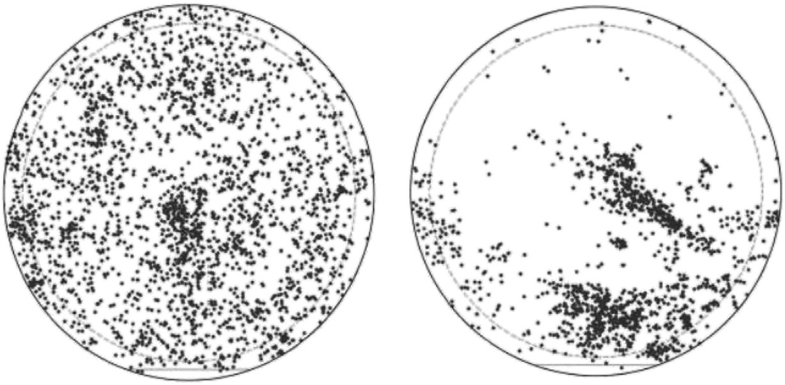

**Figure 5.13** Maps of etch pits associated to TSDs in 30 mm diameter 4H−SiC wafers showing a significant redistribution and a 30% reduction of the etch pit density between the seed wafer (left) and the last wafer sliced from the grown crystal (right).
After A. Ellison, et al., SiC crystal growth by HTCVD, Mater. Sci. Forum (2004) 9−14.

during PVT growth [170]. They measured the TSD density along the growth direction and found a significant decrease in TSD density in 4H−SiC crystals from the bottom of the crystal (near the seed crystal region) to the top of grown crystals (near the growth front region). Other groups reported similar results: Ellison et al. found that substantial reduction and redistribution of TSDs occurs during high-temperature CVD growth of SiC bulk crystals [42]. Fig. 5.13 shows maps of etch pits associated with TSDs in 30 mm diameter 4H−SiC substrates showing a significant redistribution and a 30% reduction of the etch pits density between the seed wafer (left) and the last wafer sliced from the grown crystal (right) [42]. The mechanism of this reduction and redistribution of TSDs during bulk crystal growth is not well understood, but recent X-ray topographic investigations of the propagation behavior of TSDs revealed that TSDs are often transformed into basal plane defects (Frank-type stacking faults) and then turn back to TSDs during crystal growth [171−173]. Fig. 5.14 shows an example of X-ray topographic observation of the TSD propagation in 4H−SiC crystals, where a synchrotron X-ray transmission topograph ($\boldsymbol{g} = 0004$) of a vertically sliced 4H−SiC crystal is shown [172]. In the figure, dark lines approximately extending along the *c* axis correspond to TSDs. The figure shows that TSDs exhibit a complex propagating behavior, and quite often deflect into the basal plane direction and turn back to the *c*-axis direction. Such a meandering process of TSDs greatly activates their moving, transformation, and recombination, and leads to a significant reduction and redistribution of TSDs during bulk crystal growth of SiC.

As described above, TSDs arise mainly due to instabilities, such as foreign polytype and secondary-phase inclusions, during growth. Thus a fairly stable growth process combined with dislocation moving, transformation, and recombination is required to decrease the TSD density. Under optimized growth conditions, a steady reduction in TSD density has been achieved over the last decade. Nowadays, SiC crystals with a TSD density lower than a few hundreds per square centimeter are manufactured.

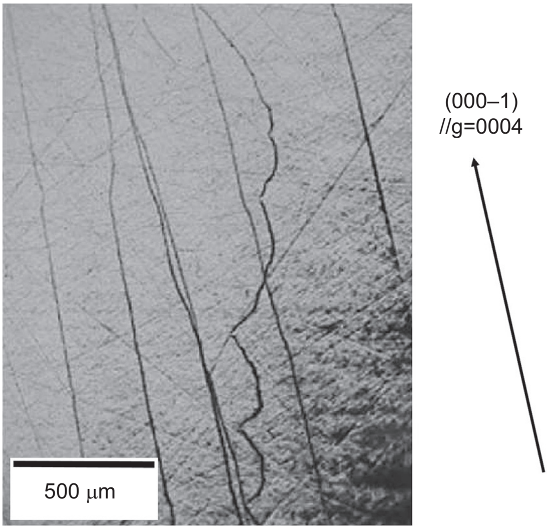

**Figure 5.14** Synchrotron transmission X-ray topograph of 4H−SiC crystal with g = 0004. Dark lines in the figure are TSDs with a Burgers vector component parallel to <0001>. After M. Katsuno, et al., Complex behavior of threading dislocations observed in PVT-grown 4H-SiC single crystals, Mater. Sci. Forum (2012) 355−358.

In terms of the reduction of TSD density, solution growth of SiC crystals has a great advantage over the PVT growth process. During solution growth, all or most TSDs are converted to Frank-type basal plane stacking faults [154,174,175]. When solution growth is conducted on a PVT-grown 4H−SiC seed crystal, which contains a high density (more than several hundred per square centimeter) of TSDs, 4H−SiC crystals with an almost zero TSD density can be grown. Fig. 5.15 shows reflection synchrotron X-ray topography images ($\boldsymbol{g} = 11\bar{2}8$) of the same area of the (0001) surface of a 4H−SiC crystal before and after solution growth [154]. Dashed triangles indicate substrate TEDs that directly propagated to the layer grown by the solution method. White circles in Fig. 5.15(a) indicate TSDs existing in the seed crystal, while those in Fig. 5.15(b) indicate the original positions of TSDs before solution growth. As seen in the figure, all the dotted contrast images associated with TSDs are converted to the teardrop-shaped contrast images associated with Frank-type basal plane stacking faults extending toward the crystal surface. The conversion from TSDs to Frank-type basal plane stacking faults has also been reported for CVD growth of 4H−SiC [176]; however, its occurrence probability is very low, whereas the conversion almost always occurs during solution growth of SiC. The observed difference in the conversion behavior of TSDs between solution growth and CVD processes is likely to stem from the difference in their surface morphology during growth. During solution growth, macrosteps evolve on the growing surface, and this macrostep formation would significantly enhance the conversion probability [174,175], although the mechanism governing this phenomenon is still to be clarified.

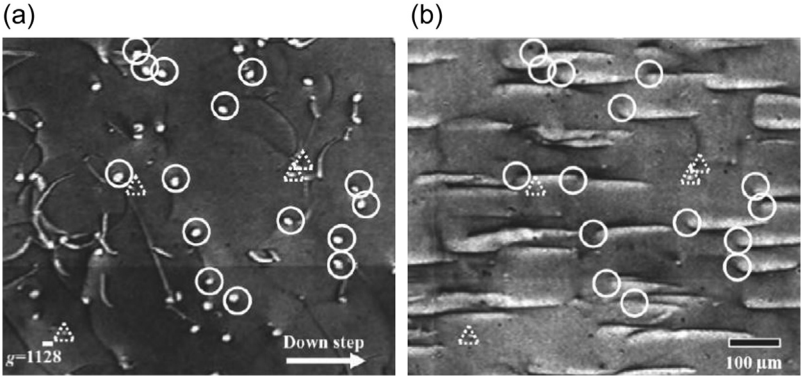

**Figure 5.15** Synchrotron reflection X-ray topography images ($\boldsymbol{g} = 11\bar{2}8$) of the (0001) surface of a 4H–SiC crystal; the images show the same area (a) before and (b) after solution growth. Dashed triangles indicate TEDs that directly propagated from the seed crystal to the layer grown by solution growth. The white circles in (a) indicate TSDs in the seed crystal, while the white circles in (b) show the original positions of TSDs before solution growth.
Reprinted from S. Hamada, et al., Dislocation conversion in 4H-SiC crystals grown by metastable solvent epitaxy, ECS J. Solid State Sci. Technol. 2 (8) (2013) N3092–N3097, Copyright 2013, with permission from The Electrochemical Society.

Another way to reduce the TSD density in SiC crystals significantly is to use the growth perpendicular to the *c* axis, i.e., crystal growth in the $[1\bar{1}00]$ and $[11\bar{2}0]$ directions. The growth kinetics and defect formation are significantly different between the growth parallel and the growth perpendicular to the *c* axis [117,134]. The growth in the directions perpendicular to the *c* axis completely suppresses the formation of threading dislocations extending along the *c* axis, including micropipes. The only remaining defect in the grown crystals is basal plane defects such as BPDs and stacking faults. They propagate in the crystals along the growth direction, i.e., $[1\bar{1}00]$ or $[11\bar{2}0]$. In the crystals, BPDs having the same Burgers vector are often aligned along the *c* axis, which gives rise to a corrugated structure of the (0001) basal plane in the crystals.

Based on these characteristics of the growth perpendicular to the *c* axis, Nakamura and coworkers proposed the so-called "repeated *a*-face (RAF)" growth process in 2004 [177]. Fig. 5.16 illustrates the procedure of RAF growth and how it can eradicate dislocations from the grown crystals. The RAF growth process comprises alternately conducted crystal growths in the $[1\bar{1}00]$ and $[11\bar{2}0]$ directions, followed by a growth in the $[000\bar{1}]$ direction. The growths in the $[1\bar{1}00]$ and $[11\bar{2}0]$ directions are alternately conducted several times; in this repetition of crystal growth, the grown crystal is used as the seed crystal for the subsequent crystal growth toward the direction perpendicular to that in the previous growth process. After the alternate $[1\bar{1}00]$ and $[11\bar{2}0]$ growths, the densities of BPDs and basal plane defects causing TSDs at the final *c*-axis growth process are reduced. Actually, the defects in the seed crystal used for each growth lie almost parallel to the growth surface, and thus the subsequent crystal growth process does not inherit defects from the seed crystal [178].

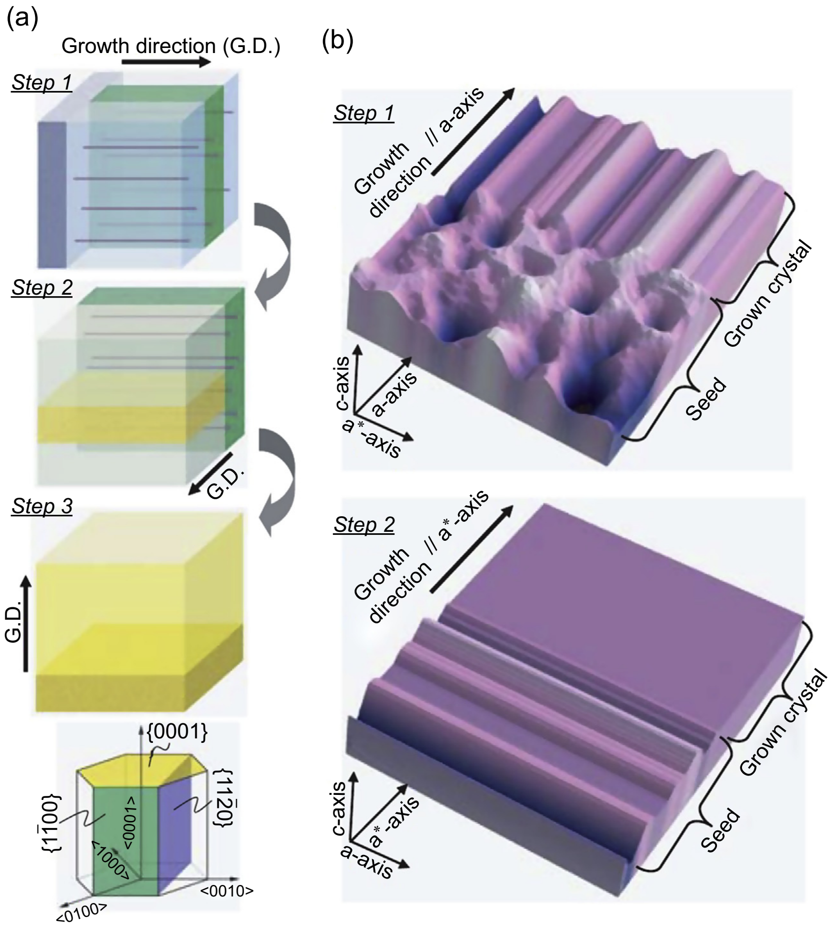
(a)
Growth direction (G.D.)
Step 1
Step 2
G.D.
Step 3
G.D.
{0001}
{1$\bar{1}$00}
{11$\bar{2}$0}
<0001>
<1000>
<0010>
<0100>
(b)
Step 1
Growth direction // a-axis
Grown crystal
Seed
c-axis
a-axis
a*-axis
Step 2
Growth direction // a*-axis
Grown crystal
Seed
c-axis
a*-axis
a-axis

**Figure 5.16** (a) Schematic illustrations of the RAF growth process. The growth sequences are as follows. Step 1: the first *a*-face growth (the seed and grown crystals are shown as dark and light blues, respectively). Step 2: the second *a*-face (i.e., *m*-face) growth perpendicular to the first *a*-face growth (the seed crystal is sliced from the first *a*-face grown crystal, and the seed and grown crystals are shown as dark and light greens, respectively). Step 3: the *c*-face growth on a (0001) seed crystal with an off-axis angle of several degrees. The seed crystal is sliced from the second *a*-face grown crystal, and the seed and grown crystals are shown as dark and light yellows, respectively. At the bottom of (a) are shown the major crystallographic axes and lattice planes in hexagonal SiC crystals. Dislocations characteristics of the *a*-face and *m*-face growth are shown by purple lines. (b) Top-side view, showing the corrugated {0001} lattice plane of the seed and grown crystals after Steps 1 and 2.

Reprinted from D. Nakamura, et al., Ultrahigh-quality silicon carbide single crystals, Nature 430 (7003) (2004) 1009−1012, Copyright 2004, by permission from Macmillan Publishers Ltd, Nature.

Employing the RAF growth process, a significant reduction of the TSD density in 4H—SiC crystals was achieved by a group at Denso Corporation in Japan [178]. The dislocation density was largely dependent on the number of repetitions of the growths in $[11\overline{2}0]$ and $[1\overline{1}00]$; with a total of seven $[11\overline{2}0]$ and $[1\overline{1}00]$ growths, they obtained a one inch diameter 4H—SiC crystal with a TSD density of 1.3 $\text{cm}^{-2}$, which is the lowest TSD density ever reported.

As mentioned earlier in this section, BPDs are another critical defect in SiC crystals. BPDs are primarily caused by the thermoelastic stresses during bulk crystal growth processes. Thus a reduction of the thermoelastic stresses is crucial for obtaining SiC crystals with a low BPD density. In this respect, numerical modeling of the SiC bulk crystal growth process provides a good solution to this problem [78,104,179—181]; details of numerical simulations for SiC crystal growth are provided in Section 5.5 of this chapter. The results of numerical simulation for thermoelastic stresses imposed on the grown crystals during and at the cooling stage of growth are well correlated with the experimental observations of BPD distribution in the crystals, and thus the numerical modeling of the SiC crystal growth process provides valuable information for crystal growers to improve their processes.

Another important aspect of BPDs is their interaction with threading dislocations. When BPDs glide in SiC crystals, they encounter a forest of TSDs and interact with them, which gives rise to superjogs in BPDs because TSDs have a relatively large Burgers vector parallel to the *c* axis. The superjogs are sessile and act as a pivot point to rotate BPDs around TSDs. This leads to the well-known Frank—Read-type dislocation multiplication, resulting in enhanced BPD densities in SiC crystals [182,183]. Fig. 5.17 shows the correlation between the

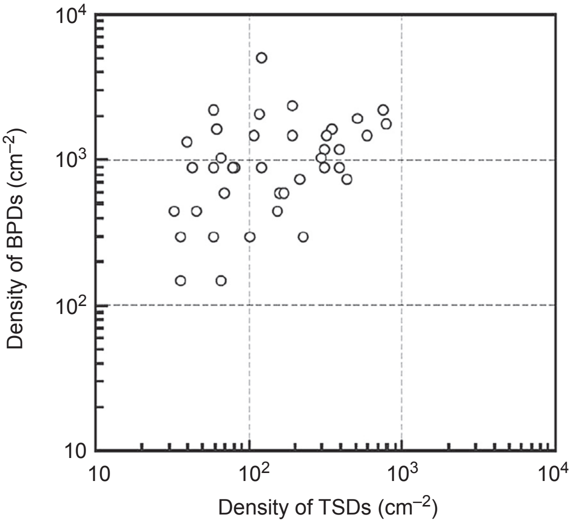

**Figure 5.17** Correlation between the BPD and TSD densities in PVT-grown 4H—SiC crystals. After N. Ohtani, et al., Analysis of basal plane bending and basal plane dislocations in 4H-SiC single crystals, Jpn. J. Appl. Phys. 48 (6) (2009), Copyright 2009, with the permission of The Japan Society of Applied Physics.

BPD and TSD densities in PVT-grown 4H−SiC crystals. The measurements of TSD and BPD densities were conducted on more than 30 surface areas from a couple of 4H−SiC substrates by counting the etch pits caused by TSDs and BPDs. As the figure shows, there is a positive correlation between the densities of BPDs and TSDs [184], which means that SiC crystals which contain more TSDs generally exhibit a larger density of BPDs. This correlation is indicative of the relevance of the reduction of TSDs to reduce the BPD density.

Similarly, TEDs are also a source of BPDs and play an active role in their multiplication. It was found that TEDs were converted to BPDs and vice versa through a cross-slip mechanism during crystal growth; the mechanism of the conversion is yet to be clarified, but it is likely to be kinetically driven. The glide of TEDs (prismatic slip) also takes place in the grown crystals under the large thermoelastic stresses imposed on the crystals during the growth and/or cooling process [185]. In a prismatic slip, TEDs are forced to glide on the $\{1\bar{1}00\}$ prismatic plane, leaving two segments of BPDs with roughly screw orientation in their wakes. The abovementioned conversion and prismatic slip processes of TEDs bring about BPD segments terminated at both ends with sessile TEDs, and thus lead to the Frank−Read-type dislocation multiplication through the rotation of BPDs around the TED portion of the dislocations. As we have seen, the interaction and conversion of BPDs to other types of dislocations play an important role in the multiplication of BPDs, and thus further investigation of dislocation interaction and conversion processes is needed to grow SiC crystals with a lower BPD density.

Finally, we describe the spontaneous formation of stacking faults in heavily N-doped 4H−SiC crystals. As described earlier in this section, heavily N-doped 4H−SiC crystals suffer structural changes during high-temperature treatments exceeding 1273 K. The structural changes have been attributed to a 4H to 3C polytypic transformation that is induced by the formation and expansion of DSSFs during the high temperature annealing (see Fig. 5.12). This spontaneous formation of basal plane stacking faults is driven by the QWA effect, in which electrons within heavily N-doped 4H−SiC enter stacking-fault-induced quantum wells, giving rise to lower system energy.

Recently a couple of new findings have been reported regarding DSSF formation in heavily N-doped 4H−SiC crystals. Straubinger et al. reported an anisotropic increase in bulk resistivity of 4H−SiC crystals by annealing at 1423 K, and that the resistivity increase can be partially recovered (reduced) by additional annealing at even higher temperatures (2073 K) [186]. Fig. 5.18 illustrates the results of their annealing experiments of heavily N-doped 4H−SiC crystals. They examined axially sliced N-doped 4H−SiC crystals along the growth direction and conducted eddy current resistivity measurements and defect selective etching of the crystals using molten KOH. They revealed that the resistivity increase was due to the stacking fault formation; upon resistivity recovery, the stacking faults were healed (shrunk). Annealing-induced shrinkage of stacking faults has also been reported for SSSFs formed in 4H−SiC *p-i-n* diodes during forward-bias operation [187−189], where SSSF growth in the diodes was reversed via low-temperature (483−873 K) annealing. Similar to that observed in heavily N-doped material, the shrinkage of SSSFs was associated with resistivity recovery [189].

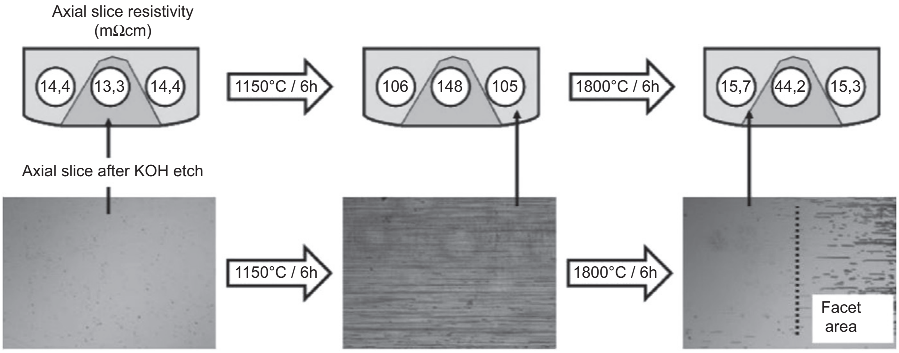

**Figure 5.18** Top: changes in resistivity (mΩcm) of heavily nitrogen-doped 4H−SiC crystal when the as-grown crystal (left) was annealed at 1423 K (center) and further annealed at 2073 K (right). The resistivity was measured in an axially sliced wafer from the crystal which contained a crystal portion grown under the $(000\overline{1})$ facet (indicated by a slightly darker color in the schematic figure). Bottom: stacking faults in the crystal revealed by molten KOH etching on the axially sliced wafer as a function of annealing conditions.
After T. Straubinger, et al., Increase of SiC substrate resistance induced by annealing, Mater. Sci. Forum (2010) 223−226.

Another finding on DSSF formation in heavily N-doped 4H−SiC crystals is the effect of codoping of Al acceptors to heavily N-doped 4H−SiC crystals. Kojima et al. grew 4H−SiC epitaxial films by CVD [190]; the films were doped with N or Al and excess N that maintained the films as *n*-type. They observed DSSF formation in the films solely doped with N ($N_d > 8 \times 10^{19}\text{cm}^{-3}$) during CVD growth and found that the codoping of Al acceptors tends to reduce the density of DSSFs in heavily N-doped 4H−SiC crystals when the Al/N doping ratio $\left(N_a/N_d\right)$ reached 10%. As the $N_a/N_d$ ratio increased the DSSF density in heavily N-doped 4H−SiC was further reduced, and DSSFs were almost fully suppressed when the $N_a/N_d$ ratio exceeded 40%. Such a codoping effect of Al acceptors was also confirmed for PVT-grown 4H−SiC crystals [191]. It was revealed that codoping of B acceptors also suppresses the DSSF formation in heavily N-doped 4H−SiC crystals, suggesting that the effect is electronically driven rather than chemically induced [192].

Taniguchi et al. clarified the relevant physics behind the stacking formation in heavily N-doped 4H−SiC crystals [193] and were successful in explaining all the experimental results described above. In their theoretical investigation of the stacking-fault formation they discussed several important physical and electronic parameters which influence the stability of Shockley-type basal plane stacking faults in 4H−SiC crystals. Fig. 5.19 shows the results of their calculation of the temperature dependence of the electronic energy gain associated with the introduction of a DSSF in highly N-doped ($3.5 \times 10^{19}$ cm$^{-3}$) 4H−SiC crystals, considering the carrier distribution in the depletion regions adjacent to the DSSF (nondepletion layer approximation). For comparison, the result with the depletion layer approximation (dashed line), in which the carrier distribution in the depletion regions is ignored, is also plotted.

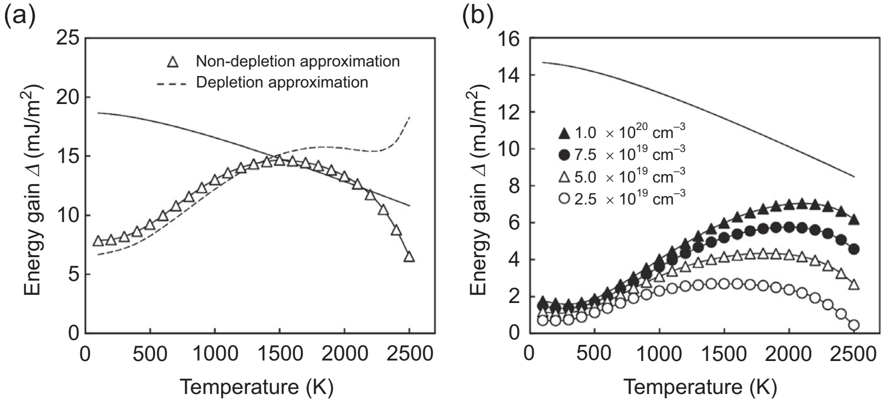

**Figure 5.19** (a) Temperature dependence of the electronic energy gain due to DSSF formation calculated by Taniguchi et al. for heavily nitrogen-doped 4H−SiC crystals with a nitrogen concentration of $3.5 \times 10^{19}$ cm$^{-3}$ based on both the nondepletion layer approximation (open triangles) and the depletion layer approximation (dashed line). (b) Temperature dependence of energy gain for SSSFs based on the nondepletion layer approximation at nitrogen concentrations from $2.5 \times 10^{19}$ to $1.0 \times 10^{20}$ cm$^{-3}$. The solid lines in (a) and (b) represent the temperature-dependent structural formation energy of DSSFs and SSSFs in 4H−SiC, respectively.

Reprinted from C. Taniguchi, et al., Theoretical investigation of the formation of basal plane stacking faults in heavily nitrogen-doped 4H-SiC crystals, J. Appl. Phys. 119 (14) (2016), Copyright 2016, with the permission of AIP Publishing.

The figure shows that the electronic energy gain decreases at high temperatures and becomes less than the structural formation energy of a DSSF (solid line in Fig. 5.19(a)) even at an N concentration of $3.5 \times 10^{19}$ cm$^{-3}$. The reduction of the electronic energy gain is noticeable at high temperatures, while in the temperature range of 1400−2100 K the electronic energy gain still exceeds the structural formation energy. This is in good agreement with the experimental results by Straubinger et al. [186]. Fig. 5.19(b) shows the results of calculating the electronic energy gain for introduction of an SSSF into heavily N-doped 4H−SiC crystals as a function of temperature, where the solid line represents the temperature-dependent structural formation energy of an SSSF in 4H−SiC. As shown in the figure, the electronic energy gain by the introduction of an SSSF never exceeds the structural formation energy over the entire temperature range, even at an N concentration of $1.0 \times 10^{20}$ cm$^{-3}$. This is consistent with the experimental results.

An essential physics governing this phenomenon is the dimensionality of electrons residing in bulk crystal and stacking faults. The difference in the dimensionality of the two systems gives rise to the high-temperature stability of basal plane stacking faults in 4H−SiC crystals through the difference in the density of states between bulk crystal and stacking fault (which acts as quantum well). The density of states in a bulk crystal shows a square root energy dependence, whereas the density of states for electrons trapped in a stacking fault is constant with energy, since they are confined in a quantum well (stacking fault) and form a 2D electron gas. At low temperatures the effective density of states is larger for the stacking fault, and thus the total energy of conduction-band electrons is larger in the system with stacking faults. By contrast, at high temperatures the effective density of states in a bulk crystal is larger, and thus the total energy of conduction-band electrons is larger in the system without stacking faults. This is the reason why DSSFs are stabilized at high temperatures in heavily N-doped 4H−SiC crystals.

## 5.7 State of the art of SiC material

The PVT growth process developed by Tairov and Tsvetkov [4] paved the way to growing large SiC single crystals. After this pioneering work, many research laboratories started projects in this field and much effort has been devoted to the enlargement and quality improvement of SiC crystals. The diameter of SiC crystals reached 200 mm in 2015, and currently 4H−SiC single crystal substrates up to 150 mm in diameter are commercially available. Fig. 5.20 shows the development of larger-diameter SiC wafers in comparison with those of Si and GaAs crystals, where the

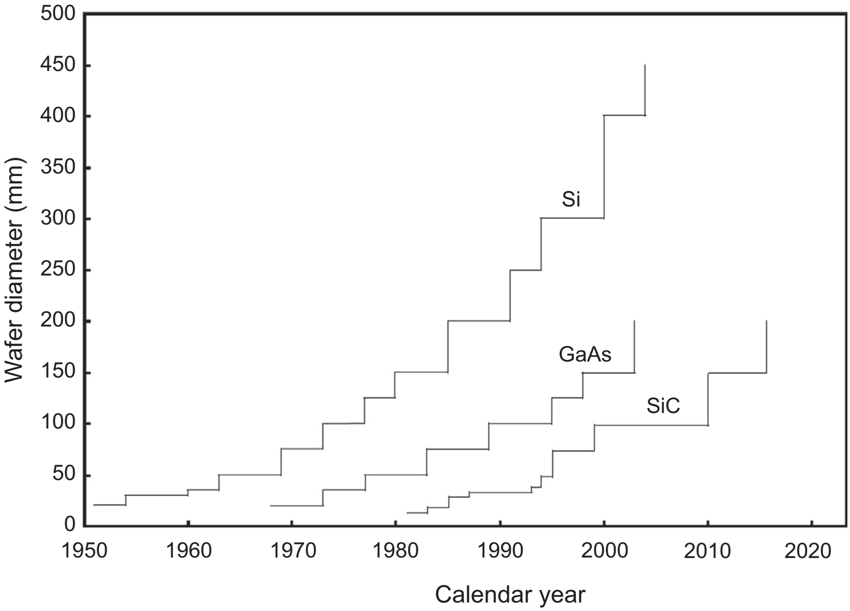

**Figure 5.20** Increase in wafer diameter as a function of time demonstrated in R&D for Si, GaAs, and SiC.
Modified from G.K. Teal, J.B. Little, Growth of germanium single crystals, Phys. Rev. 78 (5) (1950) 647−647; J.B. Mullin, et al., Liquid encapsulation crystal pulling at high pressures, J. Cryst. Growth 3−4 (1968) 281−285; M.G. Spencer, J. Palmour, C. Carter, Substrate and epitaxial issues for SiC power devices, IEEE Trans. Electron. Dev. 49 (5) (2002) 940−945.

Table 5.3 **Dislocation densities in commercially available 4H−SiC wafers and the best-quality R&D wafers**

| Type | Negative impact on devices | Density (commercial wafers) | Density (R&D wafers) |
|---|---|---|---|
| TSD | Blocking voltage, gate oxide reliability, epitaxial defects | 100−1000/cm$^2$ (sub) | 1−100/cm$^2$ (sub) |
| TED | Minority carrier lifetime | 3000−10,000/cm$^2$ (sub) | 100−1000/cm$^2$ (sub) |
| BPD | On resistance, gate oxide reliability | 200−2000/cm$^2$ (sub)[a]<br>0.1−10/cm$^2$ (epi)[a] | ~0/cm$^2$ (epi)[a] |

[a] Estimated on the 4 degree off-oriented (0001) surface.

increase in wafer diameter as a function of time was demonstrated in R&D for Si, GaAs, and SiC [194−196]. It should be noted in the figure that the wafer diameter increase demonstrated in SiC has been steadily implemented and slightly accelerated in recent years, compared to that of Si or GaAs wafers, resulting in wafer diameter enlargement from 100 to 200 mm over a decade.

The crystal quality of SiC crystals has also been much improved over the last 2 - decades. Table 5.3 summarized the current status of the dislocation densities in commercially available 4H−SiC wafers as well as the densities in the best-quality R&D wafers. Among the dislocations in SiC crystals, TSDs and BPDs are of the greatest concern, and thus their densities must be reduced below a certain level that secures reliable operation of SiC devices. The TSD density in the R&D best wafers ranges from a few to a hundred per square centimeter, and the lowest TSD density ever reported is 1.3 cm$^{-2}$. The typical TSD density in commercially available 4H−SiC wafers is much larger, and ranges from a few hundred to a thousand per square centimeter.

As shown in the table, BPD density is largely different between bare wafers (substrates) and epitaxial wafers (substrates with an epitaxial layer). This is because of the conversion from BPDs to TEDs during the CVD process, which significantly reduces the BPD density in the epilayer. This conversion phenomenon from BPDs to TEDs during the CVD process was first reported by Ha et al. [197] and then investigated by many authors [198−202]. Ha et al. found the conversion occurred close to the epilayer/substrate interface, and interpreted it as a result of the image force in the epilayers between flowing growth steps and BPDs. Fig. 5.21 shows the result of analysis of defect selective etching for the BPD to TED conversion during CVD growth of 4H−SiC crystals [197]. Fig. 5.21(a) and (b) show a micrograph of dislocation etch pits on the surface of a low-doped $n$-type epilayer and on the surface of the underlying $n^+$ substrate, respectively. The rounded hexagonal etch pits were due to TEDs in the epilayer (Fig. 5.21(a)), whereas the oval-shaped etch pits were caused by BPDs existing in the substrate (Fig. 5.21(b)). The relationship between the etch pit morphologies and dislocation characters is schematically illustrated in Fig. 5.21(c), where the

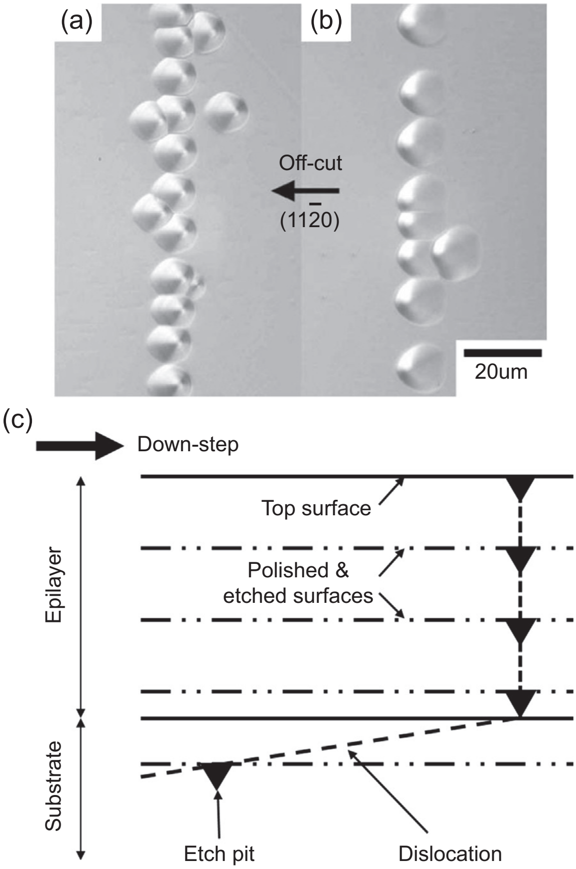

**Figure 5.21** Dislocation etch pits revealed by molten KOH etching: (a) on the surface of a 10 μm thick low-doped *n*-type epilayer; (b) on the surface of the underlying $n^+$ substrate, 10 μm below the epilayer/substrate interface; (c) schematic of the dislocation propagation in the BPD-to-TED conversion process during CVD growth, where changes in the etch pit morphology are also illustrated.

Reprinted from S. Ha, et al., Dislocation conversion in 4H silicon carbide epitaxy, J. Cryst. Growth 244 (3–4) (2002) 257–266, Copyright 2002, with the permission of Elsevier.

dislocation propagation behavior before and after the BPD-to-TED conversion at the epilayer/substrate interface is schematically illustrated. The probability of the conversion depends on the BPD propagation direction [200], Burgers vector [199], C/Si ratio of the source gas [198], surface polarity [201] and off-angle [202] of the substrate, and growth rate [124]. By optimizing these growth conditions almost 100% conversion probability has been achieved, resulting in nearly BPD-free 4H–SiC epitaxial wafers, as indicated in Table 5.3.

The acceptable dislocation density for SiC devices to operate properly is still unclear. However, the current dislocation density in commercially available 100 mm diameter 4H−SiC epitaxial wafers appears to be sufficiently low to enable commercial production of SiC devices. Nevertheless, further reduction of the dislocation density is required to obtain reliable SiC devices with much higher production yields and for further penetration of SiC devices into the market.

## 5.8 New trends and future developments

There have been many different approaches to growth of bulk SiC, but in most cases they were abandoned; this was the case, for instance, for H-CVD, M-PVT, and CF PVT. Other processes, for example HTCVD and TSSG, are still at the R&D stage. Only the PVT process has reached the industrial production stage, so it is clearly far more advanced than all the others. Nevertheless, the very recent achievements for HTCVD and TSSG processes should make them serious considerations in the future, as they exhibit the highest potential.

**Towards a high-rate continuous process**. The main limitation of the PVT process is related to its batch nature. For example, geometrical parameters such as polycrystalline powder properties and ingot dimensions evolve during growth. Even if there are only slight changes in temperature and species distributions, these modifications within the crucible can lead to drastic changes in growth behavior. Thus it is a challenge to maintain the thermal and chemical conditions required for the controlled growth of a long ingot at a high rate and without defects. Second, ingot purity is dependent on the purity of the SiC powder, which is very difficult to control accurately. The high-temperature gas-source method (or HTCVD) was recently reconsidered by Denso. High growth rates exceeding 9 mm/h were achieved at a seed temperature of 2823 K [101,203]. Interestingly, at such a high rate, i.e., with a highly concentrated gas phase, the growth front shows very similar behavior to that in solution growth. For example, it exhibits similar morphological evolution, with the formation of macrostep bunching, causing doping fluctuation and voids in the grown crystal. The growth of highly N-doped 4H−SiC crystals with a stable, smooth growth front at a growth rate of 3 mm/h has been achieved, keeping the same density of TSDs as present in the seed crystal.

**Towards ultimate-quality crystals.** After the publication of the RAF method, which sounded like a breakthrough in the development of bulk growth of high-quality SiC crystals, it appeared to be convenient to focus efforts on stress management during the PVT growth process. This has been, and still is, critical for accessing large-diameter wafers. Yet SiC bulk growth process control is difficult, and high-quality crystals, though demonstrated, cannot be obtained on a routine basis. Although rarely discussed, the early stage of growth on the seed substrate (the so-called seeding stage) is really crucial because it affects the quality of the whole ingot. This seeding stage is often associated with local distortions of the crystal and the creation of dislocations [167,168]. Proper in-situ surface preparation can help improve the growth [204]. Kato et al. demonstrated that an etch-back step prior to the growth could significantly reduce the dislocation and micropipe densities [205]. Preventing the parasitic formation of SiC polycrystals around the single crystalline ingot is another important issue. The solution consists in having perfect local control of the gaseous species concentration field, i.e., flux of species, all along the growth interface and for the entire growth duration. This can be achieved in different ways. First, proper design of the growth cavity is necessary, using for instance a "thermal screen" or "guide tube" [110,111,206]. A second possibility is the use of a TaC crucible or coating [207,208] that locally modifies the thermal environment and gas-phase composition, and probably reduces the parasitic SiC nucleation frequency on it.

Tremendous progress has been recently reported in the development of the TSSG process. The main difficulty is to keep a stable growth front to ensure no macrostep formation, usually associated with solvent inclusion and crystal degradation [209]. This is due to the strong interactions between the growth front (step movements) and the fluid movement close to the growing surface [210]. By coupling the concepts of "meniscus control" and "concave interface" growth, the difficult problem of interface stability is about to be solved. In addition, the solution growth process intrinsically offers the possibility to reduce extended defect density. Demonstrated long ago for closing micropipes [211,212], TSSG also benefits from a very efficient defect conversion mechanism [174,213–215]. Whatever the growth process, a long-term stable growth front is absolutely necessary for the growth of high-quality crystals. The control of the interface morphology/geometry is thus of primary importance at different scales. At nanometer scale it must be smooth, as the formation of large on-axis terraces is always subject to 2D nucleation of foreign polytypes [209]. At a more macroscopic scale, the shape of the interface directly affects the generation and propagation of defects [216].

**Towards comprehensive insight into the process chemistry.** Even for an industrial process such as PVT, some aspects are still far from being described or understood. For example, the following questions are still open. How can one describe correctly the heterogeneous reactions for the sublimation of the powder, for the crystallization on the substrate, and for the interaction with the graphite crucible? In particular, is there a specific reaction path between the different species ($Si_2C$, $SiC_2$, and Si) and the SiC surface? Is there a link between chemistry and polytypism? The link between the Si/C ratio in the solid and the percentage of hexagonality for a given polytype was proposed quite a long time ago [26]. As an intuitive consequence, the stoichiometry of the fluid (gas or liquid) should play a role in favoring one or the other polytype. As a rule, Si-rich conditions increase the probability of getting 3C–SiC (hexagonality close to zero), and C-rich conditions are more suitable for stabilizing polytypes with higher hexagonality such as 4H–SiC [217]. From a process point of view, the 2D classical nucleation theory has been coupled with mass transfer [218,219]. At a given supersaturation, calculations were able to locate where a foreign polytype could occur. Despite all approximations, this approach was even able to predict the polytype, in fairly good agreement with experiments [216]. Another computation approach proposed by Ariyawong et al. [220] consists of describing SiC as a solid solution in a coupled thermodynamic and mass-transport model. The computation of both Si and C activities in the SiC crystal, between the SiC–C and SiC–Si two-phase equilibria, allows first the assessment of the SiC crystal chemistry and second the linking of SiC–C and SiC–Si chemistry with the growth process parameters. It was demonstrated that depending on temperature, pressure, and temperature gradient, the activities of Si and C in the crystals can be calculated and tuned. It was found, for instance, that increasing the axial temperature gradient in the PVT process produced a SiC crystal with a higher Si activity (and a lower C activity). Such a computational approach, though not yet mature, could pave the way for linking the process conditions to the polytypism. By extension, the same treatment could be also applied to any growth processes (TSSG, HTCVD, or even CVD for epilayer growth) and to any point defects, as well as to dopants.

Finally, the strong development of computational methods would be beneficial to faster development of SiC bulk growth process. An illustration of this tendency, which is general in material sciences, is given by the recent use of a genetic algorithm for the optimization of the PVT process [221].

## References

[1] D.A. Grant, J. Gowar, Power MOSFETs: Theory and Applications, Wiley-Interscience, New York, 1989.

[2] B.J. Baliga, Fundamentals of Power Semiconductor Devices, Springer Science & Business Media, Berlin, 2010.

[3] T. Kimoto, J.A. Cooper, Fundamentals of Silicon Carbide Technology: Growth, Characterization, Devices and Applications, John Wiley & Sons, Singapore, 2014.

[4] Y.M. Tairov, V.F. Tsvetkov, Investigation of growth processes of ingots of silicon carbide single crystals, J. Cryst. Growth 43 (2) (1978) 209−212.

[5] A.R. Powell, et al., Bulk growth of large area SiC crystals, Mater. Sci. Forum 858 (2016) 5−10.

[6] R.W. Olesinski, G.J. Abbaschian, The C−Si (Carbon−Silicon) system, Bull. Alloy Phase Diagr. 5 (5) (1984) 486−489.

[7] R.T. Dolloff, Research Study to Determine the Phase Equilibrium Relations of Selected Metal Carbides at High Temperatures, 1960.

[8] F. Durand, J.C. Duby, Carbon solubility in solid and liquid silicon − a review with reference to eutectic equilibrium, J. Phase Equilb. 20 (1) (1999) 61−63.

[9] J. Gröbner, H.L. Lukas, F. Aldinger, Thermodynamic calculation of the ternary system Al-Si-C, Calphad 20 (2) (1996) 247−254.

[10] H. Dalaker, M. Tangstad, Time and temperature dependence of the solubility of carbon in liquid silicon equilibrated with silicon carbide and its dependence on boron levels, Mater. Trans. 50 (5) (2009) 1152−1156.

[11] H. Kleykamp, G. Schumacher, The constitution of the silicon-carbon system (English), Ber. Bunsen-Gesellschaft 97 (6) (1993) 799−805.

[12] G. Honstein, C. Chatillon, F. Baillet, Thermodynamic approach to the vaporization and growth phenomena of SiC ceramics. I. SiC and SiC-$SiO_2$ mixtures under neutral conditions, J. Eur. Ceram. Soc. 32 (5) (2012) 1117−1135.

[13] R.I. Scace, G.A. Slack, Solubility of carbon in silicon and germanium, J. Chem. Phys. 30 (6) (1959) 1551−1555.

[14] R.C. Glass, et al., SiC-seeded crystal growth, MRS Bull. 22 (3) (2013) 30−35.

[15] J. Drowart, G. De Maria, M.G. Inghram, Thermodynamic study of SiC utilizing a mass spectrometer, J. Chem. Phys. 29 (5) (1958) 1015−1021.

[16] P. Rocabois, C. Chatillon, C. Bernard, Thermodynamics of the Si-C system. I. mass spectrometric studies of the condensed phases at high temperature, High Temp. High Press. 27−28 (1) (1995) 3−23.

[17] S.Y. Karpov, Y.N. Makarov, M.S. Ramm, Simulation of sublimation growth of SiC single crystals, Phys. Status Solidi B 202 (1) (1997) 201−220.

[18] S.K. Lilov, Thermodynamic analysis of phase transformations at the dissociative evaporation of silicon carbide polytypes, Diam. Relat. Mater. 4 (12) (1995) 1331−1334.

[19] K. Ariyawong, et al., Comparison of thermodynamic databases for the modeling of SiC growth by PVT, Materials Science Forum 778-780 (2014) 35−38.

[20] A. Baronnet, Some aspects of polytypism in crystals, Prog. Cryst. Growth Char. 1 (2) (1978) 151−211.

[21] G.C. Trigunayat, A survey of the phenomenon of polytypism in crystals, Solid State Ionics 48 (1−2) (1991) 3−70.

[22] Y.M. Tairov, V.F. Tsvetkov, Group IV materials (mainly SiC), in: J.I. Pankove (Ed.), Electroluminescence, Springer, Berlin, 1977, pp. 31−61.

[23] C. Haberstroh, R. Helbig, R.A. Stein, Some new features of the photoluminescence of SiC(6H), SiC(4H), and SiC(15R), J. Appl. Phys. 76 (1) (1994) 509−513.

[24] W.R.L. Lambrecht, et al., Electronic band structure of SiC polytypes: a discussion of theory and experiment, Phys. Status Solidi B 202 (1) (1997) 5−33.

[25] F. Bechstedt, et al., Polytypism and properties of silicon carbide, Phys. Status Solidi B Basic Res. 202 (1) (1997) 35−62.

[26] Y.M. Tairov, V.F. Tsvetkov, Progress in controlling the growth of polytypic crystals, Prog. Cryst. Growth Char. 7 (1−4) (1983) 111−162.

[27] S. Limpijumnong, W.R.L. Lambrecht, Total energy differences between SiC polytypes revisited, Phys. Rev. B 57 (19) (1998) 12017−12022.

[28] Y.M. Tairov, V.F. Tsvetkov, General principles of growing large-size single crystals of various silicon carbide polytypes, J. Cryst. Growth 52 (1981) 146−150.

[29] G. Ziegler, et al., Single-crystal growth of SiC substrate materials for blue-light emitting diodes, IEEE Trans. Electron. Dev. 30 (4) (1983) 277−281.

[30] D.L. Barrett, et al., SiC boule growth by sublimation vapor transport, J. Cryst. Growth 109 (1−4) (1991) 17−23.

[31] R.A. Stein, P. Lanig, S. Leibenzeder, Influence of surface energy on the growth of 6H- and 4H-SiC polytypes by sublimation, Mater. Sci. Eng. B 11 (1−4) (1992) 69−71.

[32] D.L. Barrett, et al., Growth of large SiC single crystals, J. Cryst. Growth 128 (1−4) (1993) 358−362.

[33] V.D. Heydemann, et al., Growth of 6H and 4H silicon carbide single crystals by the modified Lely process utilizing a dual-seed crystal method, Appl. Phys. Lett. 69 (24) (1996) 3728−3730.

[34] G. Augustine, et al., Physical vapor transport growth and properties of SiC monocrystals of 4H polytype, Phys. Status Solidi B 202 (1) (1997) 137−148.

[35] R.C. Glass, et al., SiC seeded crystal growth, Phys. Status Solidi B 202 (1) (1997) 149−162.

[36] N. Ohtani, et al., Development of large single-crystal SiC substrates, Electron. Commun. Jpn. II Electron. 81 (6) (1998) 8−19.

[37] I. Garcon, et al., Study of SiC single-crystal sublimation growth conditions, Mater. Sci. Eng. B 29 (1) (1995) 90−93.

[38] R. Yakimova, et al., Seeded sublimation growth of 6H and 4H−SiC crystals, Mater. Sci. Eng. B 61 (1999) 54−57.

[39] O. Kordina, et al., High temperature chemical vapor deposition of SiC, Appl. Phys. Lett. 69 (10) (1996) 1456−1458.

[40] O. Kordina, et al., Growth of SiC by “Hot-Wall” CVD and HTCVD, Phys. Status Solidi B 202 (1) (1997) 321−334.

[41] A. Ellison, et al., HTCVD growth of semi-insulating 4H-SiC crystals with low defect density, in: MRS Online Proceedings Library Archive, 2000, p. 640.

[42] A. Ellison, et al., SiC crystal growth by HTCVD, Mater. Sci. Forum 457-460 (2004) 9−14.

[43] A. Ellison, et al., High temperature CVD growth of SiC, Mater. Sci. Eng. B 61−62 (1999) 113−120.

[44] M. Fanton, et al., Growth of nitrogen-doped SiC boules by halide chemical vapor deposition, J. Cryst. Growth 287 (2) (2006) 359−362.

[45] M.A. Fanton, et al., Thermodynamic equilibrium limitations on the growth of SiC by halide chemical vapor deposition, J. Appl. Phys. 101 (1) (2007) 014903.

[46] S. Nigam, et al., Growth kinetics study in halide chemical vapor deposition of SiC, J. Cryst. Growth 284 (1−2) (2005) 112−122.

[47] P. Wellmann, et al., SiC single crystal growth by a modified physical vapor transport technique, J. Cryst. Growth 275 (1) (2005) e555−e560.

[48] D. Chaussende, et al., Continuous feed physical vapor transport: toward high purity and long boule growth of SiC, J. Electrochem. Soc. 150 (10) (2003) G653−G657.

[49] D. Chaussende, et al., Thermodynamic aspects of the growth of SiC single crystals using the CF-PVT process, Chem. Vapor Depos. 12 (8−9) (2006) 541−548.

[50] D. Chaussende, et al., Control of the supersaturation in the CF-PVT process for the growth of silicon carbide crystals: research and applications, Cryst. Growth Des. 5 (4) (2005) 1539−1544.

[51] D. Chaussende, et al., In-situ observation of mass transfer in the CF-PVT growth process by X-ray imaging, Materials Science Forum 527-529 (2006) 63−66.

[52] D. Chaussende, et al., Prospects for 3C-SiC bulk crystal growth, J. Cryst. Growth 310 (5) (2008) 976−981.

[53] G.L. Sun, et al., Improvements of the continuous feed-physical vapor transport technique (CF-PVT) for the seeded growth of 3C-SiC crystals, Mater. Sci. Forum 645-648 (2010) 63−66.

[54] D. Elwell, H.J. Scheel, Crystal Growth from High-temperature Solutions, Academic Press, London, 1975.

[55] D. Chaussende, P.J. Wellmann, M. Pons, Status of SiC bulk growth processes, J. Phys. Appl. Phys. 40 (20) (2007) 6150−6158.

[56] J. Lefebure, et al., Modeling of the growth rate during top seeded solution growth of SiC using pure silicon as a solvent, Cryst. Growth Des. 12 (2) (2012) 909−913.

[57] D.H. Hofmann, M.H. Muller, Prospects of the use of liquid phase techniques for the growth of bulk silicon carbide crystals, Mater. Sci. Eng. B 61−62 (1999) 29−39.

[58] B.M. Epelbaum, et al., Top-seeded solution growth of bulk SiC: search for fast growth regimes, Mater. Sci. Forum 338-342 (2000) 107−110.

[59] S. Kawanishi, et al., Solution growth behavior of SiC by a temperature difference method using Fe−Si solvent, J. Cryst. Growth 381 (2013) 121−126.

[60] S. Maruyama, et al., High-throughput screening of Si-Ni flux for SiC solution growth using a high-temperature laser microscope observation and secondary ion mass spectroscopy depth profiling, ACS Comb. Sci. 15 (6) (2013) 287−290.

[61] Y. Yonezawa, et al., Screening of metal flux for SiC solution growth by a thin-film combinatorial method, Sci. Technol. Adv. Mater. 12 (5) (2011).

[62] L.B. Griffiths, A.I. Mlavsky, Growth of alpha-SiC single crystals from chromium solution, J. Electrochem. Soc. 111 (7) (1964) 805−810.

[63] Y.M. Tairov, et al., Liquid phase epitaxy of SiC in the system Si Tb SiC by temperature gradient zone melting (I). Investigation of solubilities in the system Si Tb SiC, Cryst. Res. Technol. 21 (12) (1986) 1503−1507.

[64] M. Syväjärvi, et al., Liquid phase epitaxial growth of SiC, J. Cryst. Growth 197 (1−2) (1999) 147−154.

[65] P.W. Pellegrini, J.M. Feldman, Liquid phase epitaxial growth of SiC from transition-metal silicide solvents, J. Cryst. Growth 27 (1974) 320−324.

[66] T. Narumi, et al., Thermodynamic evaluation of the C−Cr−Si, C−Ti−Si, and C−Fe−Si systems for rapid solution growth of SiC, J. Cryst. Growth 408 (2014) 25−31.

[67] H. Daikoku, et al., Top-seeded solution growth of 4H−SiC bulk crystal using Si-Cr based melt, Mater. Sci. Forum 717-720 (2012) 61−64.

[68] M. Kado, et al., High-Speed growth of 4H-sic single crystal using Si−Cr based melt, Mater. Sci. Forum 740-742 (2013) 73−76.

[69] T. Mitani, et al., Growth rate and surface morphology of 4H−SiC crystals grown from Si−Cr−C and Si−Cr−Al−C solutions under various temperature gradient conditions, J. Cryst. Growth 401 (2014) 681−685.

[70] T. Mitani, et al., Effect of aluminum addition on the surface step morphology of 4H-SiC grown from Si-Cr-C solution, J. Cryst. Growth 423 (2015) 45−49.

[71] F. Mercier, et al., Coupled heat transfer and fluid dynamics modeling of high-temperature SiC solution growth, J. Cryst. Growth 312 (2) (2010) 155−163.

[72] K. Ariyawong, J.M. Dedulle, D. Chaussende, Electromagnetic enhancement of carbon transport in SiC solution growth process: a numerical modeling approach, Mater. Sci. Forum 778-780 (2014) 71−74.

[73] F. Mercier, S-i Nishizawa, Comparative numerical study of the effects of rotating and traveling magnetic fields on the carbon transport in the solution growth of SiC crystals, J. Cryst. Growth 362 (2013) 99−102.

[74] F. Mercier, S-i Nishizawa, Solution growth of SiC from silicon melts: influence of the alternative magnetic field on fluid dynamics, J. Cryst. Growth 318 (1) (2011) 385−388.

[75] K. Kusunoki, et al., Top-seeded solution growth of three-inch-diameter 4H−SiC using convection control technique, J. Cryst. Growth 395 (2014) 68−73.

[76] K. Kusunoki, et al., Solution growth of SiC crystal with high growth rate using accelerated crucible rotation technique, Mater. Sci. Forum 527-529 (2006) 119−122.

[77] M. Selder, et al., Numerical simulation of global heat transfer in reactors for SiC bulk crystal growth by physical vapor transport, Mater. Sci. Eng. B 61-62 (1999) 93−97.

[78] M. Nakabayashi, et al., Growth of crack-free 100mm-diameter 4H-SiC crystals with low micropipe densities, Mater. Sci. Forum 600-603 (2009) 3−6.

[79] G.R. Fisher, P. Barnes, Towards a unified view of polytypism in silicon carbide, Philos. Mag. B Phys. Condens. Matter Stat. Mech. Electron. Opt. Magn. Prop. 61 (2) (1990) 217−236.

[80] V. Heine, C. Cheng, R.J. Needs, The preference of silicon carbide for growth in the metastable cubic form, J. Am. Ceram. Soc. 74 (10) (1991) 2630−2633.

[81] F.C. Frank, The growth of carborundum - dislocations and polytypism, Philos. Mag. 42 (332) (1951) 1014−1021.

[82] W.F. Knippenberg, Growth phenomena in silicon carbide, Philips Res. Rep. 18 (3) (1963) 161−274.

[83] A. Ellison, Silicon carbide growth by high temperature CVD techniques, in: Linköping Studies in Science and Technology, Linköping University, 1999.

[84] Y.A. Vodakov, et al., Impurity influence on silicon carbide polytypism, Sov. Tech. Phys. Lett. 5 (1979) 147−149.

[85] K. Racka, et al., Growth of SiC by PVT method with different sources for doping by a cerium impurity, $CeO_2$or $CeSi_2$, J. Cryst. Growth 401 (2014) 677−680.

[86] H.J. Rost, et al., Polytype stability in nitrogen-doped PVT−grown 2″−4H−SiC crystals, J. Cryst. Growth 275 (1−2) (2005) e451−e454.

[87] J. Takahashi, N. Ohtani, M. Kanaya, Influence of the seed face polarity on the sublimation growth of α−SiC, Jpn. J. Appl. Phys. Part 1 34 (9A) (1995) 4694−4698.

[88] Y.A. Vodakov, et al., Effect of crystallographic orientation on the polytype stabilization and transformation of silicon carbide, Phys. Status Solidi A 51 (1) (1979) 209−215.

[89] D. Hofmann, et al., On the sublimation growth of SiC bulk crystals: development of a numerical process model, J. Cryst. Growth 146 (1−4) (1995) 214−219.

[90] M. Pons, et al., Thermodynamic heat transfer and mass transport modeling of the sublimation growth of silicon carbide crystals, J. Electrochem. Soc. 143 (11) (1996) 3727−3735.

[91] Q.S. Chen, et al., 7-Silicon carbide crystals — Part II: process physics and modeling A2-Byrappa, Kullaiah, in: T. Ohachi, et al. (Eds.), Crystal Growth Technology, William Andrew Publishing, Norwich, NY, 2003, pp. 233−269.

[92] X.J. Chen, et al., Optimization of the design of a crucible for a SiC sublimation growth system using a global model, J. Cryst. Growth 310 (7−9) (2008) 1810−1814.

[93] K. Kakimoto, et al., Thermodynamic analysis of SiC polytype growth by physical vapor transport method, J. Cryst. Growth 324 (1) (2011) 78−81.

[94] A.S. Segal, et al., Transport phenomena in sublimation growth of SiC bulk crystals, Mater. Sci. Eng. B 61-62 (1999) 40−43.

[95] Q.S. Chen, et al., Kinetics and modeling of sublimation growth of silicon carbide bulk crystal, J. Cryst. Growth 224 (1−2) (2001) 101−110.

[96] Ö. Danielsson, U. Forsberg, E. Janzén, Predicted nitrogen doping concentrations in silicon carbide epitaxial layers grown by hot-wall chemical vapor deposition, J. Cryst. Growth 250 (3−4) (2003) 471−478.

[97] S.Y. Karpov, Y.N. Makarov, M.S. Ramm, Analytical model of silicon carbide growth under free-molecular transport conditions, J. Cryst. Growth 169 (3) (1996) 491−495.

[98] S.I. Nishizawa, M. Pons, Growth and doping modeling of SiC-CVD in a horizontal hot-wall reactor, Chem. Vapor Depos. 12 (8−9) (2006) 516−522.

[99] S.G. Müller, et al., The status of SiC bulk growth from an industrial point of view, J. Cryst. Growth 211 (1) (2000) 325−332.

[100] B. Gao, K. Kakimoto, Dislocation-density-based modeling of the plastic behavior of 4H−SiC single crystals using the Alexander−Haasen model, J. Cryst. Growth 386 (2014) 215−219.

[101] Y. Tokuda, et al., Stable and high-speed SiC bulk growth without dendrites by the HTCVD method, J. Cryst. Growth 448 (2016) 29−35.

[102] B. Gao, K. Kakimoto, Effect of the inclusion of transparency on the thermal field and interface shape in long-term sublimation growth of SiC crystals (<special issue> Opening up a new world of crystal growth on SiC), J. Jpn. Assoc. Cryst. Growth 40 (1) (2013) 20−24.

[103] O. Klein, et al., Radiation- and convection-driven transient heat transfer during sublimation growth of silicon carbide single crystals, J. Cryst. Growth 222 (4) (2001) 832−851.

[104] M. Selder, et al., Global modeling of the SiC sublimation growth process: prediction of thermoelastic stress and control of growth conditions, J. Cryst. Growth 226 (4) (2001) 501−510.

[105] M.V. Bogdanov, et al., Advances in modeling of wide-bandgap bulk crystal growth, Cryst. Res. Technol. 38 (3−5) (2003) 237−249.

[106] O. Klein, P. Philip, Transient numerical investigation of induction heating during sublimation growth of silicon carbide single crystals, J. Cryst. Growth 247 (1−2) (2003) 219−235.

[107] O. Klein, P. Philip, Transient temperature phenomena during sublimation growth of silicon carbide single crystals, J. Cryst. Growth 249 (3−4) (2003) 514−522.

[108] B. Gao, K. Kakimoto, Three-dimensional modeling of basal plane dislocations in 4H-SiC single crystals grown by the physical vapor transport method, Cryst. Growth Des. 14 (3) (2014) 1272−1278.

[109] B. Gao, K. Kakimoto, Optimization of power control in the reduction of basal plane dislocations during PVT growth of 4H−SiC single crystals, J. Cryst. Growth 392 (2014) 92−97.

[110] M. Pons, R. Madar, T. Billon, Principles and limitations of numerical simulation of SiC boule growth by sublimation, in: W.J. Choyke, H. Matsunami, G. Pensl (Eds.), Silicon Carbide: Recent Major Advances, Springer Berlin Heidelberg, Berlin, Heidelberg, 2004, pp. 121−135.

[111] S-i. Nishizawa, T. Kato, K. Arai, Effect of heat transfer on macroscopic and microscopic crystal quality in silicon carbide sublimation growth, J. Cryst. Growth 303 (1) (2007) 342−344.

[112] N. Ohtani, et al., Investigation of heavily nitrogen-doped $n^+$ 4H−SiC crystals grown by physical vapor transport, J. Cryst. Growth 311 (6) (2009) 1475−1481.

[113] K. Onoue, et al., Nitrogen incorporation kinetics during the sublimation growth of 6H and 4H SiC, Jpn. J. Appl. Phys. Part 1 35 (4A) (1996) 2240−2243.

[114] N. Ohtani, et al., Impurity incorporation kinetics during modified-Lely growth of SiC, J. Appl. Phys. 83 (8) (1998) 4487−4490.

[115] H.J. Rost, D. Schulz, D. Siche, High nitrogen doping during bulk growth of SiC, in: W.J. Choyke, H. Matsunami, G. Pensl (Eds.), Silicon Carbide, Springer Berlin Heidelberg, 2004, pp. 163−178.

[116] H.J. Rost, et al., Influence of nitrogen doping on the properties of 4H−SiC single crystals grown by physical vapor transport, J. Cryst. Growth 257 (1−2) (2003) 75−83.

[117] J. Takahashi, et al., Sublimation growth of 6H− and 4H−SiC single crystals in the $[1\bar{1}00]$ and $[11\bar{2}0]$ directions, J. Cryst. Growth 181 (3) (1997) 229−240.

[118] N. Tsavdaris, et al., Nitrogen incorporation during seeded sublimation growth of 4H-SiC and 6H-SiC, Mater. Sci. Forum 821-823 (2015) 60−63.

[119] J. Olander, K.M.E. Larsson, Adsorption of N-containing species onto SiC(0001) surfaces: a theoretical study, Phys. Rev. B 67 (11) (2003) 115306.

[120] K. Kusunoki, et al., Nitrogen doping of 4H-SiC by the top-seeded solution growth technique using Si-Ti solvent, J. Cryst. Growth 392 (2014) 60−65.

[121] V.P. Rastegaev, et al., Features of SiC single-crystals grown in vacuum using the LETI method, Mater. Sci. Eng. B 61-62 (1999) 77−81.

[122] T.L. Straubinger, et al., Aluminum p-type doping of silicon carbide crystals using a modified physical vapor transport growth method, J. Cryst. Growth 240 (1−2) (2002) 117−123.

[123] K. Eto, et al., Growth study of p-type 4H-SiC with using aluminum and nitrogen co-doping by 2-zone heating sublimation method, Mater. Sci. Forum 821-823 (2015) 47−50.

[124] K. Eto, et al., Growth of P-type 4H−SiC single crystals by physical vapor transport using aluminum and nitrogen co-doping, J. Cryst. Growth 470 (2017) 154−158.

[125] T. Shirai, et al., Solution growth of p-type 4H-SiC bulk crystals with low resistivity, in: Mater. Sci. Forum 778-780, 2014, pp. 75−78.

[126] R.S. Okojie, et al., Observation of 4H-SiC to 3C-SiC polytypic transformation during oxidation, Appl. Phys. Lett. 79 (19) (2001) 3056−3058.

[127] J.Q. Liu, et al., Structural instability of 4H-SiC polytype induced by n-type doping, Appl. Phys. Lett. 80 (12) (2002) 2111−2113.

[128] T.A. Kuhr, et al., Spontaneous formation of stacking faults in highly doped 4H-SiC during annealing, J. Appl. Phys. 92 (10) (2002) 5863−5871.

[129] M. Skowronski, S. Ha, Degradation of hexagonal silicon-carbide-based bipolar devices, J. Appl. Phys. 99 (1) (2006).

[130] M.S. Miao, S. Limpijumnong, W.R.L. Lambrecht, Stacking fault band structure in 4H-SiC and its impact on electronic devices, Appl. Phys. Lett. 79 (26) (2001) 4360−4362.

[131] W.R.L. Lambrecht, M.S. Miao, Electronic driving force for stacking fault expansion in 4H SiC, Phys. Rev. B 73 (15) (2006).

[132] M.S. Miao, W.R.L. Lambrecht, Electronic structure of 3C inclusions in 4H SiC, J. Appl. Phys. 101 (10) (2007).

[133] K. Koga, et al., Growth and characterization of 6H-SiC bulk crystals by the sublimation method, in: Amorphous and Crystalline Silicon Carbide IV, Springer, 1992, pp. 96−100.

[134] J. Takahashi, M. Kanaya, Y. Fujiwara, Sublimation growth of SiC single crystalline ingots on faces perpendicular to the (0001) basal plane, J. Cryst. Growth 135 (1−2) (1994) 61−70.

[135] R.C. Glass, et al., Structural macro-defects in 6H-SiC wafers, J. Cryst. Growth 132 (3−4) (1993) 504−512.

[136] M. Tuominen, et al., Crystalline imperfections in 4H SiC grown with a seeded Lely method, J. Cryst. Growth 144 (3−4) (1994) 267−276.

[137] M. Dudley, et al., White-beam synchrotron topographic studies of defects in 6H−SiC single crystals, J. Phys. Appl. Phys. 28 (4) (1995) A63−A68.

[138] V.F. Tsvetkov, et al., Recent progress in SiC crystal growth, in: S. Nakashima, et al. (Eds.), Silicon Carbide and Related Materials 1995, IOP Publishing Ltd, Bristol, 1996, pp. 17−22.

[139] J. Takahashi, N. Ohtani, M. Kanaya, Structural defects in α−SiC single crystals grown by the modified-Lely method, J. Cryst. Growth 167 (3−4) (1996) 596−606.

[140] N. Ohtani, et al., Defect formation during sublimation bulk crystal growth of silicon carbide, in: MRS Online Proceedings Library Archive, vol. 510, 1998, p. 37.

[141] M. Katsuno, et al., Structural properties of subgrain boundaries in bulk SiC crystals, J. Cryst. Growth 216 (1) (2000) 256−262.

[142] M.H. Hong, A.V. Samant, P. Pirouz, Stacking fault energy of 6H-SiC and 4H-SiC single crystals, Philos. Mag. A 80 (4) (2000) 919−935.

[143] H. Iwata, et al., Theoretical calculation of stacking fault energies in silicon carbide, Mater. Sci. Forum 389-393 (2002) 439−442.

[144] P.G. Neudeck, J.A. Powell, Performance limiting micropipe defects in silicon carbide wafers, IEEE Electron. Device Lett. 15 (2) (1994) 63−65.

[145] F.C. Frank, Capillary equilibria of dislocated crystals, Acta Crystallogr. 4 (6) (1951) 497−501.

[146] N. Ohtani, et al., Surface step model for micropipe formation in SiC, J. Cryst. Growth 226 (2−3) (2001) 254−260.

[147] J.P. Bergman, et al., Crystal defects as source of anomalous forward voltage increase of 4H-SiC diodes, Mater. Sci. Forum 353-356 (2001) 299−302.

[148] O. Ueda, S.J. Pearton, Materials and Reliability Handbook for Semiconductor Optical and Electron Devices, Springer Science & Business Media, 2012.

[149] A. Agarwal, et al., A new degradation mechanism in high-voltage SiC power MOSFETs, IEEE Electron. Device Lett. 28 (7) (2007) 587−589.

[150] V. Veliadis, et al., Degradation and full recovery in high-voltage implanted-gate SiC JFETs subjected to bipolar current stress, IEEE Electron. Device Lett. 33 (7) (2012) 952−954.

[151] Q. Wahab, et al., Influence of epitaxial growth and substrate-induced defects on the breakdown of 4H-SiC Schottky diodes, Appl. Phys. Lett. 76 (19) (2000) 2725−2727.

[152] F. Wu, et al., Synchrotron X-ray topography studies of the propagation and post-growth mutual interaction of threading growth dislocations with C-component of burgers vector in PVT-grown 4H-SiC, Mater. Sci. Forum 717-720 (2012) 343−346.

[153] Y. Sugawara, et al., Transmission electron microscopy analysis of a threading dislocation with $c + a$ burgers vector in 4H-SiC, Appl. Phys. Express 5 (8) (2012).

[154] S. Hamada, et al., Dislocation conversion in 4H-SiC crystals grown by metastable solvent epitaxy, ECS J. Solid State Sci. Technol. 2 (8) (2013) N3092−N3097.

[155] S. Onda, et al., Transmission electron microscope study of a threading dislocation with and its effect on leakage in a 4H-SiC MOSFET, Philos. Mag. Lett. 93 (8) (2013) 439−447.

[156] L.T.M. Hoa, T. Ouisse, D. Chaussende, Critical assessment of birefringence imaging of dislocations in 6H silicon carbide, J. Cryst. Growth 354 (1) (2012) 202−207.

[157] M. Benamara, et al., Structure of the carrot defect in 4H-SiC epitaxial layers, Appl. Phys. Lett. 86 (2) (2005) 021905.

[158] T. Aigo, et al., Formation of epitaxial defects by threading screw dislocations with a morphological feature at the surface of 4° off-axis 4H-SiC substrates, Mater. Sci. Forum 740-742 (2013) 629−632.

[159] M. Dudley, et al., Stacking faults created by the combined deflection of threading dislocations of Burgers vector c and $c+a$ during the physical vapor transport growth of 4H-SiC, Appl. Phys. Lett. 98 (23) (2011).

[160] J. Senzaki, et al., Effects of dislocations on reliability of thermal oxides grown on n-type 4H-SiC wafer, Mater. Sci. Forum 483-485 (2005) 661−664.

[161] T. Katsuno, et al., Analysis of surface morphology at leakage current sources of 4H-SiC Schottky barrier diodes, Appl. Phys. Lett. 98 (22) (2011) 222111.

[162] H. Fujiwara, et al., Relationship between threading dislocation and leakage current in 4H-SiC diodes, Appl. Phys. Lett. 100 (24) (2012) 242102.

[163] J. Senzaki, et al., Challenges of high-performance and high-reliability in SiC MOS structures, Mater. Sci. Forum 717-720 (2012) 703−708.

[164] A. Bandoh, et al., Step-bunching dependence of the lifetime of MOS capacitors on 4° off-axis si-face 4H-SiC epitaxial wafers, Mater. Sci. Forum 778-780 (2014) 611−614.

[165] M. Dudley, et al., The mechanism of micropipe nucleation at inclusions in silicon carbide, Appl. Phys. Lett. 75 (6) (1999) 784−786.

[166] E.K. Sanchez, et al., Nucleation of threading dislocations in sublimation grown silicon carbide, J. Appl. Phys. 91 (3) (2002) 1143−1148.

[167] C. Ohshige, et al., Defect formation during the initial stage of physical vapor transport growth of 4H-SiC in the $[11\bar{2}0]$ direction, J. Cryst. Growth 408 (2014) 1−6.

[168] N. Ohtani, et al., Structural investigation of the seeding process for physical vapor transport growth of 4H-SiC single crystals, J. Cryst. Growth 386 (2014) 9−15.

[169] S. Sasaki, J. Suda, T. Kimoto, Doping-induced lattice mismatch and misorientation in 4H-SiC crystals, Mater. Sci. Forum 717-720 (2012) 481−484.

[170] A.R. Powell, et al., Large diameter 4H-SiC substrates for commercial power applications, Mater. Sci. Forum 457-460 (2004) 41−46.

[171] D. Nakamura, et al., Topographic study of dislocation structure in hexagonal SiC single crystals with low dislocation density, J. Cryst. Growth 304 (1) (2007) 57−63.

[172] M. Katsuno, et al., Complex behavior of threading dislocations observed in PVT-grown 4H-SiC single crystals, Mater. Sci. Forum 717-720 (2012) 355−358.

[173] H.H. Wang, et al., Study of v and y shape frank-type stacking faults formation in 4H-SiC Epilayer, Mater. Sci. Forum 778-780 (2014) 332−337.

[174] Y. Yamamoto, et al., High-efficiency conversion of threading screw dislocations in 4H−SiC by solution growth, Appl. Phys. Express 5 (11) (2012) 115501.

[175] T. Ujihara, et al., Conversion mechanism of threading screw dislocation during SiC solution growth, Mater. Sci. Forum 717-720 (2012) 351−354.

[176] H. Tsuchida, I. Kamata, M. Nagano, Formation of basal plane Frank-type faults in 4H-SiC epitaxial growth, J. Cryst. Growth 310 (4) (2008) 757−765.

[177] D. Nakamura, et al., Ultrahigh-quality silicon carbide single crystals, Nature 430 (7003) (2004) 1009−1012.

[178] Y. Urakami, et al., TSD reduction by RAF (repeated A-face) growth method, Mater. Sci. Forum 717-720 (2012) 9−12.

[179] D. Hobgood, et al., Status of large diameter SiC crystal growth for electronic and optical applications, Mater. Sci. Forum 338-342 (2000) 3−8.

[180] R.H. Ma, et al., Thermal system design and dislocation reduction for growth of wide band gap crystals, J. Cryst. Growth 258 (3−4) (2003) 318−330.

[181] R.H. Ma, et al., Integrated process modeling and experimental validation of silicon carbide sublimation growth, J. Cryst. Growth 252 (4) (2003) 523−537.

[182] N. Ohtani, et al., Behavior of basal plane dislocations in hexagonal silicon carbide single crystals grown by physical vapor transport, Jpn. J. Appl. Phys. Part 1 45 (3 A) (2006) 1738−1742.

[183] Y. Chen, et al., Multiplication of basal plane dislocations via interaction with c-axis threading dislocations in 4H-SiC, Mater. Res. Soc. Symp. Proc. 911 (2006) 151−156.

[184] N. Ohtani, et al., Analysis of basal plane bending and basal plane dislocations in 4H-SiC single crystals, Jpn. J. Appl. Phys. 48 (6) (2009) 065503.

[185] J. Guo, et al., Prismatic slip in PVT-grown 4H−SiC crystals, J. Electron. Mater. 46 (4) (2017) 2040−2044.

[186] T. Straubinger, et al., Increase of SiC substrate resistance induced by annealing, Mater. Sci. Forum 645-648 (2010) 223−226.

[187] T. Miyanagi, et al., Annealing effects on single Shockley faults in 4H-SiC, Appl. Phys. Lett. 89 (6) (2006) 062104.

[188] J.D. Caldwell, et al., Thermal annealing and propagation of Shockley stacking faults in 4H-SiC PiN diodes, J. Electron. Mater. 36 (4) (2007) 318−323.

[189] J.D. Caldwell, et al., Reversal of forward voltage drift in 4H-SiC p-i-n diodes via low temperature annealing, Appl. Phys. Lett. 90 (14) (2007) 143519.

[190] K. Kojima, et al., Reducing stacking faults in highly doped n-type 4H-SiC crystal, Mater. Sci. Forum 679-680 (2011) 8−11.

[191] H. Suo, et al., Bulk growth of low resistivity n-type 4H-SiC using co-doping, Mater. Sci. Forum 897 (2017) 3−6.

[192] H. Suo, et al., Difference of double Shockley-type stacking faults expansion in highly nitrogen-doped and nitrogen-boron co-doped n-type 4H-SiC crystals, J. Cryst. Growth 468 (2017) 879−882.

[193] C. Taniguchi, et al., Theoretical investigation of the formation of basal plane stacking faults in heavily nitrogen-doped 4H-SiC crystals, J. Appl. Phys. 119 (14) (2016) 145704.

[194] G.K. Teal, J.B. Little, Growth of germanium single crystals, Phys. Rev. 78 (5) (1950) 647−647.

[195] J.B. Mullin, et al., Liquid encapsulation crystal pulling at high pressures, J. Cryst. Growth 3−4 (1968) 281−285.

[196] M.G. Spencer, J. Palmour, C. Carter, Substrate and epitaxial issues for SiC power devices, IEEE Trans. Electron. Dev. 49 (5) (2002) 940−945.

[197] S. Ha, et al., Dislocation conversion in 4H silicon carbide epitaxy, J. Cryst. Growth 244 (3−4) (2002) 257−266.

[198] T. Ohno, et al., Influence of growth conditions on basal plane dislocation in 4H-SiC epitaxial layer, J. Cryst. Growth 271 (1−2) (2004) 1−7.

[199] T. Ohno, et al., Direct observation of dislocations propagated from 4H-SiC substrate to epitaxial layer by X-ray topography, J. Cryst. Growth 260 (1−2) (2004) 209−216.

[200] Z. Zhang, T.S. Sudarshan, Evolution of basal plane dislocations during 4H−SiC homoepitaxy, Appl. Phys. Lett. 87 (16) (2005) 1−3.

[201] H. Tsuchida, et al., Comparison of propagation and nucleation of basal plane dislocations in 4H-SiC(000-1) and (0001) epitaxy, Mater. Sci. Forum 527-529 (2006) 231−234.

[202] H. Tsuchida, et al., Investigation of basal plane dislocations in the 4H-SiC epilayers grown on {0001} substrates, Mater. Sci. Forum 483-485 (2005) 97−100.

[203] N. Hoshino, et al., Fast growth of n-type 4H-SiC bulk crystal by gas-source method, J. Cryst. Growth 478 (2017) 9−16.

[204] B. Pelissier, et al., Seed surface preparation for SiC sublimation growth, Materials Science Forum 338-342 (2000) 47−50.

[205] T. Kato, S.-I. Nishizawa, K. Arai, Dislocation constraint by etch back process of seed crystal in the SiC sublimation growth, J. Cryst. Growth 233 (1−2) (2001) 219−225.

[206] Y. Kitou, et al., Flux-controlled sublimation growth by an inner guide-tube, in: S. Yoshida, et al. (Eds.), Materials Science Forum 389-393, 2002, pp. 83−86.

[207] D. Nakamura, K. Shigetoh, Fabrication of large-sized TaC-coated carbon crucibles for the low-cost sublimation growth of large-diameter bulk SiC crystals, Jpn. J. Appl. Phys. 56 (8) (2017) 085504.

[208] D. Nakamura, A. Suzumura, K. Shigetoh, Sintered tantalum carbide coatings on graphite substrates: highly reliable protective coatings for bulk and epitaxial growth, Appl. Phys. Lett. 106 (8) (2015) 082−108.

[209] C. Zhu, et al., Influence of solution flow on step bunching in solution growth of SiC crystals, Cryst. Growth Des. 13 (8) (2013) 3691−3696.

[210] K. Ariyawong, et al., Analysis of Macrostep Formation during top seeded solution growth of 4H−SiC, Cryst. Growth Des. 16 (6) (2016) 3231−3236.

[211] B.M. Epelbaum, D. Hofmann, On the mechanisms of micropipe and macrodefect transformation in SiC during liquid phase treatment, J. Cryst. Growth 225 (1) (2001) 1−5.

[212] O. Filip, et al., Micropipe healing in SiC wafers by liquid-phase epitaxy in Si−Ge melts, J. Cryst. Growth 271 (1−2) (2004) 142−150.

[213] Y. Yamamoto, et al., Low-dislocation-density 4H-SiC crystal growth utilizing dislocation conversion during solution method Appl. Phys. Express 7 (6) (2014) 065501.

[214] S. Harada, et al., Different behavior of threading edge dislocation conversion during the solution growth of 4H-SiC depending on the burgers vector, Acta Mater. 81 (2014) 284−290.

[215] S. Harada, et al., Evolution of threading screw dislocation conversion during solution growth of 4H-SiC, APL Mater. 1 (2) (2013) 022109.

[216] N. Tsavdaris, et al., Macroscopic approach to the nucleation and propagation of foreign polytype inclusions during seeded sublimation growth of silicon carbide, Cryst. Growth Des. 15 (1) (2015) 156−163.

[217] A. Fissel, Artificially layered heteropolytypic structures based on SiC polytypes: molecular beam epitaxy, characterization and properties, Phys. Rep. 379 (3−4) (2003) 149−255.

[218] T. Shiramomo, et al., Study of the effect of doped impurities on polytype stability during PVT growth of SiC using 2D nucleation theory, J. Cryst. Growth 385 (2014) 95−99.

[219] T. Shiramomo, et al., Thermodynamical analysis of polytype stability during PVT growth of SiC using 2D nucleation theory, J. Cryst. Growth 352 (1) (2012) 177−180.

[220] K. Ariyawong, et al., A first step toward bridging silicon carbide crystal properties and physical chemistry of crystal growth, CrystEngComm 18 (12) (2016) 2119−2124.

[221] J. Su, et al., A niching genetic algorithm applied to optimize a SiC-bulk crystal growth system, J. Cryst. Growth 468 (2017) 914−918.

This page intentionally left blank

# III Arsenide

# 6

*Christiane Frank-Rotsch*[1], *Natasha Dropka*[1], *Peter Rotsch*[2]
[1]Leibniz Institute for Crystal Growth, Berlin, Germany; [2]OSA Opto light GmbH, Berlin, Germany

## 6.1 Introduction

The investigation of groups III and V compounds by Heinrich Welker was driven by the systematic search for semiconducting compounds. The target was to achieve advantages in comparison to the semiconducting elements of silicon and germanium. The III arsenides and III phosphides are semiconductors, crystallize in a zinc-blende structure, and form solid solutions without limitations [1]. Thus every composition of the solid solution of aluminum–gallium–indium (Al,Ga,In) arsenic–phosphorus (As,P) can be deposited in a zinc-blende structure and the lattice constant depends on the composition. The composition control allows variation in the energy gap between 2.45 eV (AlP) and 0.356 eV (InAs). Light/radiation-emitting devices require direct semiconductors. The transition between direct and indirect semiconductors is observed between 2.23 and 2.33 eV for the (Al,Ga,In)P solid solution lattice matched to a GaAs substrate [2], the widest direct energy gap in this solid solution system. The possible range for emitters with arsenide substrate based devices is 550–3800 nm. Most of the solid solutions show an electron carrier mobility higher than in silicon-based structures. Thus both electronic devices (such as high-mobility field-effect transistors and microwave integrated circuits) and optoelectronic devices (such as light-emitting diodes (LEDs), laser diodes, and photo diodes) can be realized.

The huge economic relevance of III arsenide-based devices is indicated by a market volume of US$ 1.7 billion for signage and channel letter LEDs [3], US$ 3 billion for semiconductor lasers without fiber optics [4], and US$ 5.2 billion for GaAs-based electronic devices [5] in 2012. The market growth is undamped, e.g., a global market of US$ 8 billion for GaAs-based electronic devices in 2017 [6]. This growth includes market changes, for example the replacement of the mobile phone by the smartphone and the change from GaAs-based IC for high-speed CPU to fast silicon-based processors, and the emergence of new applications, for example horticultural lighting (red and near-infrared LEDs based on GaAs) and vertical resonant cavity laser diode arrays. As a result there is massive activity in basic and applied research focusing on applications, devices, and materials needed.

Almost all recent active device structures are made with epitaxial layers, and these are grown by different technologies like vapor phase epitaxy (VPE), metalorganic chemical vapor deposition (MOCVD), molecular beam epitaxy (MBE), and liquid phase epitaxy. It is possible to match the lattice constant of compositions in the mixed crystal systems (Ga,Al)As, (Ga,Al,In)P, and (Ga,In) (As,P) to GaAs, making it the

**Single Crystals of Electronic Materials.** https://doi.org/10.1016/B978-0-08-102096-8.00006-9
Copyright © 2019 Elsevier Ltd. All rights reserved.

preferred substrate for epitaxial processes. The lattice match at epitaxial process temperature between the growing layer and the substrate avoids the generation of dislocations and other defects in the active device layer.

The existing literature about compound semiconductor devices is as huge as the economic relevance and cannot be reviewed within the scope of this chapter; it focuses on the important materials of GaAs, GaP, and InP and their applications [7,8]. One aim of this chapter is to derive the demands on substrate from the epitaxial process and device requirements, as well as to show processes and methods that can achieve these properties. Considerable progress in GaAs bulk growth over recent years is taken into account. It required massive support from numerical simulation, so this chapter includes the application of two-dimensional (2D) and three-dimensional (3D) simulations in the apparatus design and process parameters. Besides the bulk itself, the surface and mechanical substrate properties are of relevance for the epitaxial and device processes. To cover this, the preparation of the wafer and some aspects of wafer characterization are addressed with this chapter.

Furthermore, the III arsenides are an excellent demonstration of the ideas of Mendeleev's periodic system of elements, hence this chapter addresses all III arsenides and tries further to demonstrate relations between them in different aspects of their chemical, physical, and crystallographic behavior. This may assist the reader to understand the behavior of the solid solutions between the pure arsenides.

## 6.2 Comparison of properties

### *6.2.1 Physical properties*

Arsenide compounds are formed from the III main group elements and the V main group element As. Their position in the periodic system of elements is shown in Fig. 6.1. The III element Ga has not an own mineral. Ga is not enriced in an ore and behaves very similar to Al. It is a side product in the extraction of Al, zinc, and copper. The abundance of In is more than two orders of magnitude lower than that of Ga, and it is enriched in the electrolyte during the electrolytic refining of zinc. There is no mining for In. Thus Ga and In availability is limited, restricting their usage in general. The semiconducting properties of GaAs and InAs in combination with a high X-ray mass attenuation coefficient keeps them in mind for radiation detection purposes. Table 6.1 summarizes some properties of the important compounds for their physical, crystallographic, and chemical behavior and their applications. The data basis for GaAs is excellent and it is quite good for InAs and AlAs, though it is quite low for BAs and TlAs.

The band structure is usually well understood, and is important in the application of a semiconductor. When experimental values are absent the band structure can be calculated as for BAs and TlAs. The transition from direct to indirect semiconductor is observed at a composition of $(Al_{0.61}Ga_{0.39})As$ increasing the Al content [10], and at $(B_{0.5}In_{0.5})As$ increasing the B content [9] correspondingly. BAs, AlAs, and the system (B,Al)As are indirect semiconductors, and therefore photon-emitting devices cannot

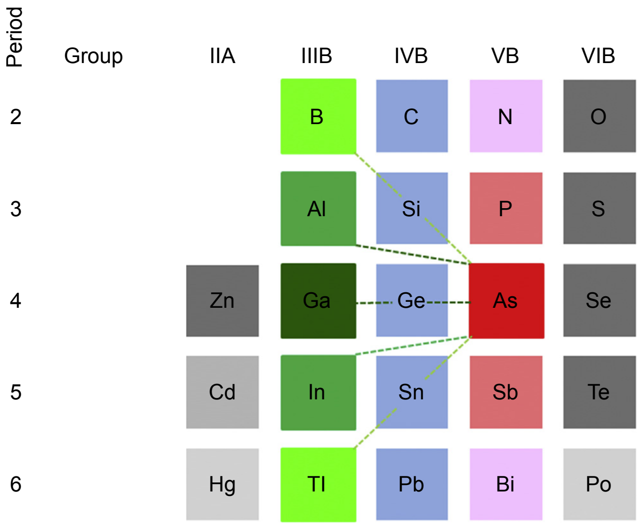

**Figure 6.1** Part of periodic table of elements regarding III arsenides.

be made using them. Electron mobility and hole mobility are summarized in detail by Adachi [38]. AlAs and BAs as indirect semiconductors have lower electron mobility, and the highest electron mobility is observed in InAs. Electron mobility is significant higher than hole mobility, and the theoretical mobility limits for pure, undoped GaAs are 8500 $cm^2/V \cdot s$ for electrons and 400 $cm^2/V \cdot s$ for holes [38]; consequently n-doping is the preferred choice for current-carrying layers in high-speed devices. Carrier mobility is usually measured by the Hall method and depends on impurity/doping level and intrinsic defect density caused by stoichiometry deviations, thus it is an important quality criterion for wafers and crystals.

In the arsenides the As—III bond is mainly covalent; the ionicity is 4.4% for BAs and increases to 35.7% for InAs. The heat of formation decreases with decreased covalence of the bonding as well as the melting temperature, thermal conductivity, and specific heat. For groups III—V the reduced covalence of bond leads to reductions in hardness, value of elastic constants, and critical resolved shear stress [33]. This is of importance for expected mechanical behavior and dislocation forming and multiplication. Stacking-fault energy decreases as a function of increased ionicity, as shown in Fig. 6.5 in reference [33], and with decreased stacking-fault energy the risk of twinning during crystal growth increases. The ionic part of the bond explains the good cleavability and brittle behavior at temperatures below 0.4 $T_m$ [K].

### 6.2.2 Crystallographic properties

All III arsenides crystallize under standard pressure in a zinc-blende structure with the space group $F\bar{4}3m$. The zinc-blende structure is very similar to the diamond structure of Si and Ge, but the lattice sites in the structure are alternatively occupied by As atoms

**Table 6.1** **Comparison of properties**

| **Property** | **BAs** | **AlAs** | **GaAs** | **InAs** | **TlAs** |
|---|---|---|---|---|---|
| **Type** | **Semiconductor indirect** | **Semiconductor indirect** | **Semiconductor direct** | **Semiconductor direct** | **Semiconductor/ Semimetal** |
| $E_g^{\Gamma}$ [eV] | 3.25 calculated [9] | 3.099 @ 0 K<br>3.00 @ 300 K [10] | 1.519 @ 0 K<br>1.42 @ 300 K [10] | 0.417 @ 0 K<br>0.35 @ 300 K [10] | <0.1 calculated [11] |
| $E_g^{X}$ [eV] | 1.63 [9] calculated | 2.24 @ 0 K<br>2.16 @ 300 K [10] | 1.981 @ 0 K<br>1.899 @ 300 K [10] | 1.433 @ 0 K<br>1.37 @ 300 K [10] | 3.5−4.0 calculated [11] |
| X-ray mass attenuation coefficient [g/cm$^{-2}$][a] | 0.539 g/cm$^2$ | 0.484 g/cm$^2$ | 0.560 g/cm$^2$ | 1.20 g/cm$^2$ | 4.10 g/cm$^2$ |
| Density (ρ) [g/cm$^3$] @ 300 K | 5.22 [12] | 3.730 (calculated)<br>3.598 (observed) [13] | 5.3176 [14] | 5.68 [15] | Unknown |
| Thermal expansion coefficient, linear (β) [K$^{-1}$] @ 300 K | Unknown | 5.66 10$^{-6}$ [16] | 5.73 10$^{-6}$ [15] | 4.52 10$^{-6}$ [17] | Unknown |
| Thermal conductivity (λ) [Wm$^{-1}$K$^{-1}$] | 200 observed<br>2000 expected @ 300 K [18] | 90 @ 300 K [19] | 55 @ 300 K [15]<br>17.8 @ $T_m$(s) [20] | 27 @ 300 K<br>8 @ 1000 K [21] | Unknown |
| Specific heat ($c_p$) [Jg$^{-1}$K$^{-1}$] | 0.408 [19] | 0.424 [19] | 0.327 [19] | 0.25 [17]<br>0.352 [19] | Unknown |
| Melting temperature ($T_m$) [K] | 2348 [18]<br>2300 [19] | 1740 ± 20 [22] | 1513 ± 2 [19] | 1210 [19] | 929 ± 300 [11] |
| CAS- No. | 12005-69-5 | 2281-42-1 | 1303-00-0 [23] | 1303-11-3 | 120006-09-6 [24] |

| | | | | | |
|---|---|---|---|---|---|
| Classification GHS[c] | Not available | H301, H331, H410 [13] | H350, H360 F, H372 [23] | H301, H331, H400, H410 [25] | At least similar to the elements Tl and As |
| Molar mass (M) [g/mol] | 85.73 | 101.91 | 144.64 | 189.74 | 279.3 |
| Abundance of III elements in relation to silicon[b] in earth's crust [26] | $3.5 \cdot 10^{-4}$ | $8.5 \cdot 10^{-2}$ | $4.8 \cdot 10^{-5}$ | $1.89 \cdot 10^{-7}$ | $1.92 \cdot 10^{-7}$ |
| Standard heat of formation ($\Delta H$) [kJ/mol] | Unknown | −148 [12]<br>−153 [19] | −87,7 ± 0.5 [27] | −60 ± 1 [27] | Unknown |
| Ionicity [19] | 0.044 | 0.274 | 0.31 | 0.357 | Unknown |
| Arsenic pressure at melting temperature ($p_{As}$)[bar] | Unknown | >2 bar [7] | 2 [28]<br>0.73 ± 0.04 [29] | 0.33 [30] | Unknown |
| Crystal structure | Zinc-blende | Zinc-blende | Zinc-blende | Zinc-blende | Zinc-blende |
| Group of symmetry | $T_d^2$ $F\bar{4}3m$[d] | $T_d^2$- $F\bar{4}3m$ | $T_d^2$- $F\bar{4}3m$ | $T_d^2$- $F\bar{4}3m$ | $T_d^2$- $F\bar{4}3m$ |
| Lattice constant ($a_0$) [nm] | 0.477 [31]<br>0.4783 [18] | 0.5661 [19] | 0.5653 [19] | 0.60583 [19] | 0.594−0.636 [11]<br>0.604 [32] |
| Critical resolved shear stress (CRSS) [kPa] | Unknown | Unknown | 1900 @ 873 K ($0.65 \cdot T_m$) [33]<br>$\sigma_{CRSS} = 22.72$ expected$^{(4334.0/T)}$ [34] | 700 @ 813 K ($0.65 \cdot T_m$) | Unknown |
| Elastic constants<br>$C_{11}$ [GPa]<br>$C_{12}$ [GPa]<br>$C_{13}$ [GPa] | 267−292<br>64−72<br>148−162 [35] | 113 ± 5.7%<br>55.5 ± 3.5%<br>57.5 ± 3.4% [36] | 114 ± 1<br>52 ± 1<br>57 ± 1 [37] | 91 ± 1<br>44 ± 1<br>39 ± 1 [37] | 88.5<br>44.1<br>44.1 [36] |

*Continued*

**Table 6.1** Continued

| **Property** | **BAs** | **AlAs** | **GaAs** | **InAs** | **TlAs** |
|---|---|---|---|---|---|
| **Type** | **Semiconductor indirect** | **Semiconductor indirect** | **Semiconductor direct** | **Semiconductor direct** | **Semiconductor/ Semimetal** |
| Microhardness [19] [GPa] | 19.0 | 4.7–5.0 | 7.0–7.5 | 3.74–3.8 | Unknown |
| Young's module (E) [Mbar] [36] | 2.623 | 0.766 | 0.941 | 0.610 | 0.592 |
| Poisson ratio [36] | 0.200 | 0.329 | 0.293 | 0.335 | 0.333 |
| Stacking-fault energy ($mJ/m^2$) | Unknown | Unknown | 55 ± 5 [20] | 30 ± 3 [33] | Unknown |

[a] Calculated acc [138]., Eq. (6.6) for 10 keV photons (X-ray).
[b] Silicon = 1, for comparison arsenic $6.6 \times 10^{-6}\%$.
[c] Globally Harmonized System of Classification, Labelling and Packaging of Chemicals (GHS).
[d] Group of symetry according to Schönflies or Hermann–Mauguin notation.

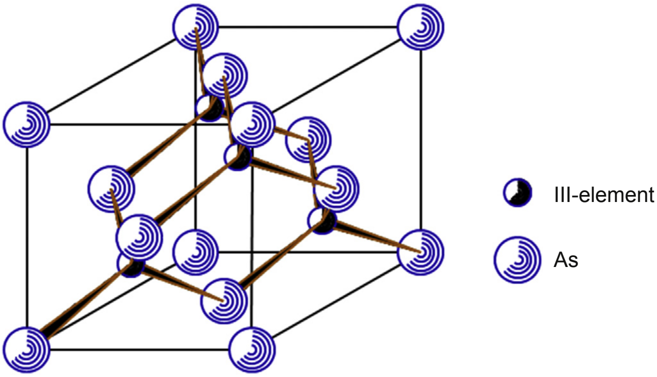

**Figure 6.2** Sketch of crystal structure of III arsenide (zinc-blende).

and atoms of III elements. Fig. 6.2 shows a model of a zinc-blende crystal structure in the face-centered cubic cell.

In this structure all atoms are fourfold tetrahedral coordinated, which means every III element is surrounded by four As atoms in the corners of the tetrahedron, as seen in Fig. 6.3. In Fig. 6.4 the position of an As tetrahedron is shown in correlation to the crystallographic directions in the structure.

The most important lattice planes are the 4 $\{111\}$ and $\{111\}$A planes, the 4 $\{\overline{111}\}$ and $\{111\}$B planes forming a tetrahedron crystal shape, the 12 $\{110\}$ planes forming a rhombic dodecahedron, and the 6 $\{100\}$ planes forming a hexahedron. Samples cut in $\{110\}$ or $\{100\}$ directions are not polar due to crystal symmetry, but the $\{111\}$ directions are polar. The $\{110\}$ plane is the cleavage plane, of importance for laser facets. The $(111)$ and $(\overline{111})$ planes have the strongest polarity and the lowest lattice plane

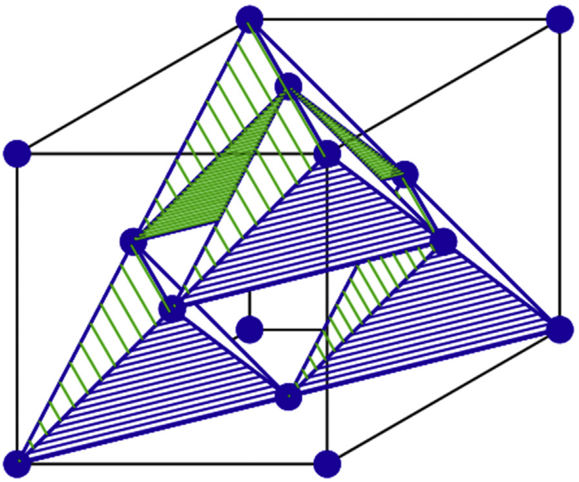

**Figure 6.3** Sketch of tetragonal arrangement of atoms in a zinc-blende crystal structure.

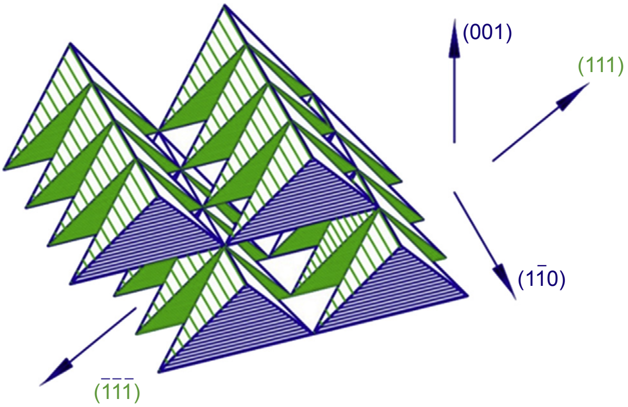

**Figure 6.4** Sketch of As tetrahedron with a III atom in the middle in correlation with crystallographic orientation.

distance. The most preferred plane is {100}. The perfect {100} plane consists of As and a III element in the ratio of 1:1, and the distances to the atom layer below and above are equal at $\frac{1}{4}a_0$. In [111]-direction the structure consists of double layers (III and As), with alternating short and long distances between the layers. The distance between the double layers in Fig 6.4 is $\sqrt{3}\ \frac{1}{4}a_0$. The distance between the As and III layers is $\frac{1}{4}a_0$, and between the As and III elements in the "double layer" there are three bonds. The fourth bond of each tetrahedron interconnects the double layers (see Figs. 6.2 and 6.4). The top layer of a $\{\overline{111}\}$ plane consists of III elements; in the reverse direction the top layer of a {111} plane consists of arsenic. This leads to the strong anisotropic behavior.

III arsenides grown from the melt do not have a perfect 1:1 stoichiometry, with a well-known case being GaAs [28,39]. The slight As enrichment in the crystal ($8 \times 10^{-5}$ mol%) depends on growth temperature and As partial pressure. The excess As forms As interstitials in the octahedron cavity. The thermodynamic stable maximum concentration of $I_{As}$ reduces with reduced temperature [39]. These interstitials can agglomerate to As precipitates, dependent on postgrowth annealing temperature and time. They also support the formation of the El2 complex, which is of importance in semiinsulating behavior. The nomenclature for point defects has been described [40], and beside the intrinsic defects there are point defects due to unintended residual contamination and doping.

The different types of dislocations are well-investigated one-dimensional defects. Usually the visualization of dislocations and the determination of their density are carried out by etching, e.g., with a KOH melt at 400°C on <100>-oriented wafers according to DIN 50454-1 [41]. Here atoms within the volume of tension near dislocations are faster dissolved. Etch pits are formed and their density can be counted using an optical microscope, giving the etch pit density (EPD). Besides KOH etching of GaAs to determine the EPD, the diluted Sirtl-like etchant with light (DSL) method is a well-established technique to analyze the s/l interface shape of grown crystals and defects, i.e., dislocations, precipitates, facets, and twins [42,43]. Usually the features of the etched surface are examined with an optical microscope using Normarski or differential interference contrast. The DSL etchant is applicable on nearly all crystal orientations and even on polycrystalline samples. The DSL method is applicable for GaAs samples based on the light-induced generation of electron−hole pairs in GaAs. As an alternative, an AB etchant [44] could be used for GaAs and InAs.

Dislocations are generated through plastic deformation when the mechanical stress [45] exceeds the elastic limit of the crystal. The Burgers vector is usually the $^1/_2$ $a_0$<110> vector, and the angle between the Burgers vector and the dislocation line defines the dislocation type. Typical angles are 0 degree "screw dislocations," 90 degree "edge dislocations," and 60 degree and 30 degree "mixed dislocations." The plane between the Burgers vector and the dislocation line is the glide plane, usually a {111} plane [46]. A special case is the "Hornstra IX dislocation," with a dislocation direction of <100>, a Burgers vector of a/2<110>, and a glide plane of {100} [47]. Dislocations can move by gliding (not leaving the glide plane), climbing (leaving the glide plane), interacting to form dislocation nodes, and other reactions [46]. In case of high point defect concentration with a thermodynamic supersaturation for screw dislocations, a "helix transformation" is possible due to climb processes. An example is shown in Fig. 6.5, where a low EPD−vertical gradient freeze (VGF)-grown (001)-oriented sample is shown after DSL etching. The 60 degrees dislocation is still straight, but the 0 degree dislocation is transformed to a helix with decorations.

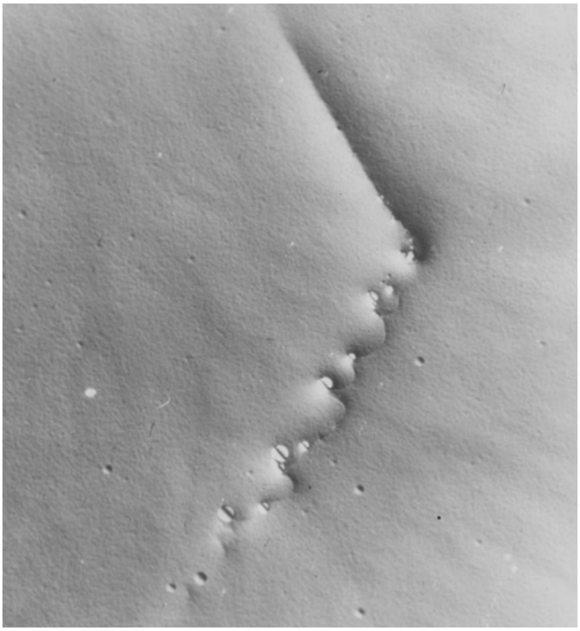

**Figure 6.5** DSL-etched dislocation structure with precipitate undoped VGF GaAs.

A further property is the dissociation of edge dislocations and mixed dislocations $\overrightarrow{b} = \frac{a}{2}[110]$ into partial Shockley dislocations $\overrightarrow{b} = \frac{a}{6}[112]$ with a stacking fault between the two partial dislocations. The stacking-fault energy determinates the distance between the two partial dislocations [33].

Twinning is observed during the crystal growth; the nucleation of twinning starts in VGF/vertical Bridgman (VB) growth processes at the crystal edge and is often correlated with fluctuations in the facet length at the As facet [48]. Twinning can also be initiated by plastic deformation, even at room temperature; in this case, very often twin lamellae are observed [49]. The most probable twinning plane is the {111} plane.

### 6.2.3 Chemical properties

The III arsenides can be considered as salts of $AsH_3$. Arsenic has the formal oxidation state of $-3$. With the transition from B to Tl as the III element, the iconicity increases. In the case of BAs the binding is 97.6% covalent with a nearly complete electron transition. A reduced covalent bond share in combination with a reduced standard heat of fusion leads to a tendency for reduced chemical stability and increased reaction velocity during etch processes.

The III arsenides are very often considered as dangerous due to the toxicity of the arsenic in the compound, even if they (like GaAs and InAs) are stable under normal conditions and in oxidant-free aqueous solutions. The solubility of the oxides at $pH = 7$ in water is very low [50]. In case of fire very toxic $As_2O_3$ can be formed in the smoke [23]. Grinding processes are the most critical among III arsenide manufacturing processes, which include cutting of crystals, thinning of wafers from processing thickness to final chip thickness, and dicing of wafers into chips. Depending on the grain size in the tool (diamond or SiC grains are typical abrasive materials), the GaAs dust achieves grain sizes down to several nanometers. Due to this a very large surface in relation to the volume ground is observed. The oxygen from the air oxidizes the surface and mainly trivalent As(III) is observed (85% As(III) versus 15% As(V)) [51]. The toxicity of GaAs is considerably higher than that of the InAs or phosphides investigated in this study [51]. Furthermore, the arsenic can react with $H_2O$ to form $AsH_3$ (arsine) during aqueous cooled grinding processes [52]. Thus the working conditions and waste treatment require careful design and management. Nevertheless, GaAs wafers and chips are not considered as harmful [52].

Besides synthesis from the pure elements (see Section 6.5.1), the III arsenides can be deposited from III melt or the gas phase [53]. The most popular among the physical methods is MBE, since other physical methods have to take into account the large vapor pressure difference between As (86.5 kPa @ 881 K [54]) and the III elements (Ga: 0.25 Pa @ 1250 K [55]). The low substrate temperature during deposition offers an advantage to achieve a low interdiffusion between the grown layers. However, only low growth rates are attainable and a high intrinsic defect density results from the low mobility of the adsorbed species on the surface.

Chemical vapor deposition or VPE summarizes the decomposition of gaseous species at the substrate surface. The arsenic source is either $AsH_3$ (hydride VPE) or $AsCl_3$

(chloride VPE), and the III source is $IIICl_3$. This technology has been very important for Ga(As,P) deposition. The substitution of the $IIICl_3$ by metalorganic III sources, for example $Al(CH_3)_3$, $Ga(CH_3)_3$, and $In(CH_3)_3$, leads to metalorganic vapor phase epitaxy (MOVPE), also known as organometallic vapor phase epitaxy or MOCVD. The gaseous compounds are decomposed on the hot substrate surface, similar to:

$$Ga(CH_3)_3 + AsH_3 \xrightarrow{\sim 700^\circ C} GaAs + 3CH_4 \tag{6.1}$$

The availability of metalorganic compounds for all III elements as well as for dopants and the opportunity to determine the composition of the growing layer comparably free by gas composition are the reasons why this process has become the major substrate load for III arsenides. MOVPE has been reviewed extensively, e.g., [56]. Thus the MOVPE process requirements determine the expectations of III arsenide substrates and their surfaces.

The deposition of III arsenides from a III melt by liquid phase epitaxy (see, e.g., [53,57,58]) is a close-to-equilibrium option for material growth. This technology has been established as the preferred choice for layers with a very low concentration of intrinsic defects (due to the close-to-equilibrium growth conditions), thick layers up to 200 μm thickness, and lowest available stoichiometric deviations. Optoelectronic devices are the main industrial applications. The principal problem of this epitaxy is that a wide range of mixed crystal compositions cannot be achieved due to distribution coefficient limitations.

In the case of chemical dissolution in liquids there are aqueous solutions and organic solutions, mainly methanol, both in combination with an oxidant. An example is shown here with $H_2O_2$ as oxidant, which forms an oxide layer according to:

$$2GaAs + 6H_2O_2 \rightarrow Ga_2O_3 + As_2O_3 + 6H_2O \tag{6.2}$$

The oxidation state of arsenic in the oxide layer is mainly $As^{3+}$, but part of the arsenic is found in the oxidation state $As^{5+}$ [51], as well as in the presence of other oxidants like oxygen from the air [59] or halogenates [60]. In alkaline aqueous solutions with excess oxidant the dissolution can formulated as follows:

$$Ga_2O_3 + 3H_2O + 2OH^- \rightarrow 2\left[Ga(OH)_4\right]^- \tag{6.3}$$

$$As_2O_3 + 2H_2O_2 + 2OH^- \rightarrow 2[AsO_4]^{3-} + 5H_2O \tag{6.4}$$

In acid aqueous solutions with excess oxidant the dissolution of the oxide layer is described as follows:

$$Ga_2O_3 + 6H^+ \rightarrow 2Ga^{3+} + 3H_2O \tag{6.5}$$

$$As_2O_3 + 2H_2O_2 + H_2O \rightarrow 2H_3AsO_4 \tag{6.6}$$

In both cases the final arsenic oxidation state is $As^{5+}$. The etch rates depend in aqueous solutions on pH: the highest etch rates are observed in the strong acid ($pH < 1$) or strong alkaline ranges ($pH > 11$) and are above 40 μm/min [60]. In pH ranging from 5 to 9 the solubility of the III compound is very low, e.g., $\log C_{Ga(OH)3} = -7.5$ @ $pH = 7.5$ and $\log C_{In(OH)3} = -9$ @ $pH = 7.0$. The solubility of As is $\log C_{AsO2-} = -1$ @ $pH = 6-9$ [50]. In this range a further complexing substance increases the reaction (dissolution) velocity considerably. Keppel [61] reports the application of $KHCO_3$ as a complexing substance, and the dissolution of the surface layer can be described as:

$$Ga_2O_3 + 4HCO_3^- \rightarrow 2Ga(CO_3)^- + 2OH^- + H_2O \tag{6.7}$$

$$As_2O_3 + 2OH^- \rightarrow 2AsO_2^- + H_2O \tag{6.8}$$

In the case of organic solutions a solution of halogens like bromine in methanol is reported. In this case bromides are formed:

$$GaAs + 3Br_2 \rightarrow GaBr_3 + AsBr_3 \tag{6.9}$$

and dissolved in the methanol [62], and high etch rates with polished surfaces are observed. The polishing processes are described in Chapter 6. A third possible reaction is decomposition without changing the oxidation state. This is seen during, e.g., grinding processes where the formation of arsine ($AsH_3$) is observed. In the case of AlAs this dissolution is found for high-concentrated hydrofluoric acid (>30%) and used for epitaxial wafer lift-off processes (thin-film LED production) according to:

$$AlAs + 3HF \rightarrow AsH_3 + AlF_3 \tag{6.10}$$

This reaction is similar for (Al,In)P but is not observed for GaAs and phosphides like (Al,Ga,In)P, and therefore there is a very high selectivity in etching [63,64].

The anisotropic behavior of the III arsenides leads to orientation-dependent etching behavior. Fig. 6.6 describes different grooves achieved with different systems. In general, a reaction-controlled etchant can lead to anisotropy (activation energy $E_A > 40$ kJ/mol), and diffusion-controlled etchants ($E_A < 20$ kJ/mol) tend to show isotropic grooves. Popular descriptions for the grooves in Fig. 6.6 are “dove-tail grooves” and “V-grooves.”

Under natural atmosphere the III As surface forms an oxide layer, as mentioned above. The composition and thickness depend on the final cleaning/oxide-removing steps like alkaline or acid etching. The natural oxide layer consists of III oxides, $As_2O_3$, and at the surface $As_2O_5$ or $GaAsO_4$, but also several impurity elements like carbonates, organic compounds, water, and metal ions [65]. After acid etching the oxide layer can have a thickness below 1 nm with a very low concentration of metal ions [66]. Irradiation with photons can increase the adsorption of carbon impurities in the layer at the III As and restrain the layer desorption in MBE oxide desorption [66].

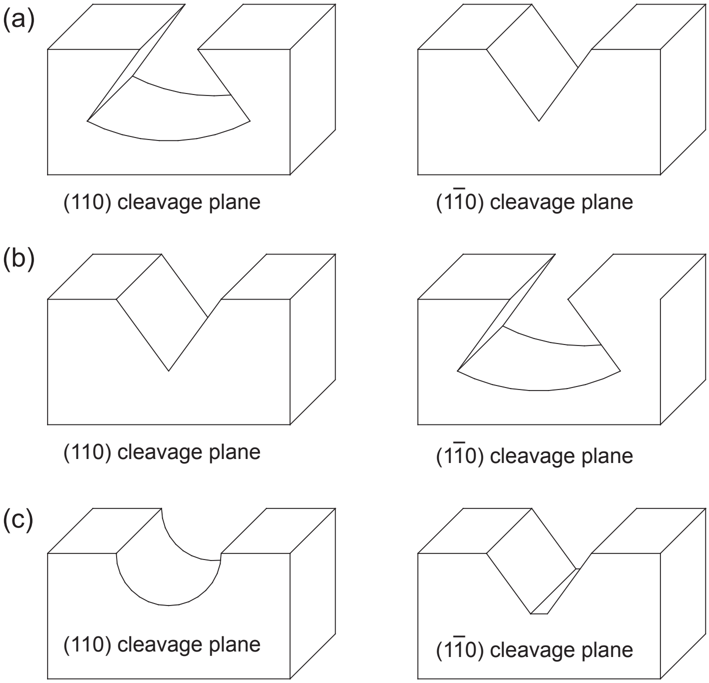
(a)
(110) cleavage plane
(1$\bar{1}$0) cleavage plane
(b)
(110) cleavage plane
(1$\bar{1}$0) cleavage plane
(c)
(110) cleavage plane
(1$\bar{1}$0) cleavage plane

**Figure 6.6** Etched groves in (001)-oriented GaAs samples, principal sketches: (a) 1 vol% $Br_2$ in methanol [60]; (b) 1 M $KHCO_3$, 1 M $H_2O_2$ in water [61]; (c) 0.25 M $KClO_3$, 7 M $H_2SO_4$ in water [60].

Gas-phase etching of III arsenides is applied for example for in-situ etching/ cleaning prior to gas-phase epitaxy processes or for "dry" etching processes during device production. An active cleaning process can also use an ion beam with for example Ar+ ions. This ion milling removes unspecific surface layers, but leaves the surface with damage requiring a further etching or annealing step [67].

In understanding gas-phase etching processes the very low vapor pressures of the oxides is of importance. The III halogenides like $IIICl_3$ or $IIIF_3$ have higher volatility and therefore active etching processes contain a chloride compound (or even pure chlorine) and no oxygen. The etch rate of an ICP plasma with a gas consisting of 15.1% Ar, 60.7% $Cl_2$ and 24.2% $O_2$ is 48 nm/min. A 33% Ar/67% $Cl_2$ plasma achieves an etch rate of 3300 nm/min [68]. In the case of chlorine as the reactive gas the summarized chemical reaction can be described as:

$$GaAs + 2Cl_2 \rightarrow GaCl + AsCl_3 \tag{6.11}$$

Compared to wet-etching processes, inductively coupled plasma etching processes are feasible and provide very low underetching of the resistant layers with very high aspect ratios and nearly perpendicular side walls [69].

## 6.3 Applications and availability

### 6.3.1 BAs

BAs is of some recent interest due to its predicted high thermal conductivity of 2000 $Wm^{-1}K^{-1}$. It is an indirect semiconductor and synthesis from the elements would require very high pressures, so a solid-phase reaction is used for synthesis along with a vapor transport reaction (iodine as transport gas) for purification and crystallization of up to 500 μm large crystals [18]. In this work the high thermal conductivity could not be confirmed; this is explained by a high concentration of As vacancies. Up to now BAs is not available in single crystalline form.

### 6.3.2 AlAs

Pure AlAs is used as source for experiments and to generate physical or other data. The high melting temperature (higher arsenic pressure), the aggressive Al in the melt on one side, and the fact that the compound is an indirect semiconductor on the other side limit its interest from an application point of view. AlAs corrodes under moisture, forms arsenic and aluminum hydroxides, and is not stable in standard device packages. Due to this, single crystalline material is not available. The mixed crystal system (Ga,Al)As is widely used for optoelectronic application LEDs [70], lasers [71], and spectral selective photodiodes [72,73]. Comparable thick layers up to 150 μm can be realized by liquid-phase epitaxy on GaAs substrates. After removal of the GaAs substrate these layers forms a free-standing (Ga,Al)As substrate, e.g., for high-efficiency LEDs in the range 650−880 nm [74]. The moisture and oxygen sensitivity of AlAs is also observed but attenuated in the (Ga,Al)As system and leads to limited durability of LEDs and lasers (see, e.g., [75]).

### 6.3.3 GaAs

The market size for GaAs wafers was US$350 million in 2012, consisting of 19,000 $m^2$ semiconducting and 24,000 $m^2$ semiinsulating wafers [76]. With this volume, GaAs is economically the most important compound semiconductor. Wafers between 2″ and 150 mm are available, with the focus on <001> orientation, and suppliers and online shops are easy to find. VGF technology has replaced the liquid encapsulation Czochralski (LEC) method as the most advanced growth technology. For major applications like high-brightness LED and RF devices there is a further shift from 100 mm toward 150 mm wafers. The capability to produce semiinsulating 200 mm wafers has been demonstrated, where the advantage of the VGF method in comparison to the LEC method is clearly visible. EPD is one order of magnitude lower, while similar electrical properties are achieved [77,78].

Semiconducting crystals (SC GaAs) are doped with Si (VGF technology) or Te (LEC technology) n-type conductivity (see Section 6.4.1.). Zinc is the preferred element for p-type conductivity. “Semiinsulating” high-resistive crystals (SI GaAs) can be grown applying a compensation mechanism with intrinsic defects, or in the past by Cr doping (see Section 6.4.1.). As discussed in the past, a low indium content in the crystal to reduce the dislocation density leads to inhomogeneous distribution of the lattice constant and is therefore not of major research or application interest. Besides this main market there is still considerable demand for smaller wafers used for older LED technologies (structures using liquid phase epitaxy) or low-volume applications, where established technologies remain present.

Trials to replace GaAs substrates by cheaper or easier-to-handle substrates like silicon represent an attractive research target due to their potential [79,80]. However, thanks to price reductions and diameters increasing on the GaAs side and technological progress leading to faster devices on the silicon-based device side, they have not been commercially successful [81].

Nearby all GaAs wafers are used as substrates in epitaxial growth process. An important exception is the application of GaAs:Cr for high-energy radiation detectors like X-rays and $\gamma$ rays [82], where thick, high resistive active layers up to 500 μm are required [83,84]. GaAs:Fe doping leads to a carrier concentration in the range $10^{12}$–$10^{14}$ $cm^{-3}$ and has been applied to produce $\gamma$-detector devices [85]. Direct implantation of n-doped channels in SI GaAs:Cr for high-speed electronics had been applied [86], but the conventional silicon technology now provides a better device performance so this method is no longer a focus of application.

### 6.3.4 InAs

The main applications of InAs are in active optoelectronic devices like photodiodes operating in the range above 1700 nm, where the cut-off wavelength is temperature dependent with 3300 nm @ −85°C up to 3800 nm @ 22°C [87], high-speed laser in the THz-range [88], and LEDs in the same wavelength range. This wavelength range is of special interest for detection of pollutants and toxic gases in air [89]. A further application is the usage for infrared optics like edge filters. There are both p-doped and n-doped 2″ and 3″ wafers with mainly (100) orientation, although <111>A and 111>B orientations are also available [90–92]. The crystals are grown by the LEC method. The EPD is in the range of $1.5 \cdot 10^4$ $cm^2$ for a 2″ wafer and $4 \cdot 10^4$ $cm^2$ for a 3″ wafer [90].

### 6.3.5 TlAs

TlAs has been investigated by the methods of theoretical physics [11,36], but any practical investigations since 1900 have not been widely published. In "Gmelin Kraut's Handbook of Inorganic Chemistry" [93] the compound is described as follows: "Weighted samples of both elements in molecular ratio 1:1 react during melting, the melt evaporates Arsenic vapor. The alloy is clear crystalline, the crystal faces does not react with air. The alloy is very soft and can be cut with knife, fresh surfaces are silver −white, exposed to air they tarnish soon brass yellow, later blue. Treatment with diluted $H_2SO_4$ develops $AsH_3$, simultaneously is observed the formation of dark powder." The verbal description explains the expected similarity to InAs as its nearest neighbor, from both chemical and physical points of view. The strong toxicity of the compound discourages either academic or application-driven interest, so the compound is not available and nor are applications reported.

## 6.4 Requirements for the substrate

The advanced development of GaAs allows the specification of very high demands on the wafer, in terms of both crystal perfection and wafer quality. The substrate characteristics achieved for this material and described below are determined by the application and the manufacturing process.

### 6.4.1 *Crystal defects, characterization, and requirements*

To avoid crystal defects and/or to control their distribution are the most important issues for crystal growers. Polycrystalline regions, e.g., arrays with strong dislocation bunching in the crystal or twins, mean that a crystal cannot be used for any application. Single crystal growth is the basic requirement for crystal quality; even twin lamellae are not acceptable. Facets in the crystal are not a major problem for the requirements of the application: typically the incorporation of impurities or dopants in facets is increased, but the facets exist in the used crystal region with a constant diameter and only a very small length at the edge, and are removed by diameter calibration, so the electrical homogeneity of the wafer is not disturbed. The region with enlarged facets is the conical part of the crystal and not used in applications. Facets with a constant length stabilize the crystal growth and reduce the probability of twinning.

Dislocation-free crystals are very difficult to achieve, even though there is some progress in the growth of (001) GaAs:Si. The reduction of dislocation densities and a homogeneous distribution are the main objectives in growing GaAs. State-of-the-art VGF growth of GaAs is characterized by an EPD below $100\,\text{cm}^{-2}$ for $4''$ Si-doped GaAs, with large areas almost dislocation free, and around $5 \cdot 10^3\,\text{cm}^{-2}$ for undoped 4 inch GaAs [20]. Other crystal growth techniques do not achieve these dislocation densities: in LEC growth the dislocation density is an order of magnitude larger. Dislocations can thread in the epitaxial layer [94] and limit reliability in devices with very high current densities, like laser diodes; due to this the lowest possible dislocation density is requested ("laser grade"). Thermal stress during crystal growth determines the EPD, but the control of stoichiometry and the type of doping are also important. Stoichiometry deviation leads to increased EPD [95]. Si doping leads to reduced EPD, but EPD in Zn-doped or Te-doped material is comparable to undoped crystals; Cr doping is often correlated to an increased EPD.

Typically, the dislocations show a cellular arrangement. In Fig. 6.7 a dislocation structure with the typical cellular pattern of undoped 4-inch GaAs is shown. The dislocation cells in GaAs have a globular shape with almost dislocation-free interiors and entangled cell walls. A lower EPD leads to larger cell sizes up to some millimeters and is observed down to dislocation densities below $500\,\text{cm}^{-2}$ [96]. The cell and dislocation cell wall formation is a process to reduce the dislocation length in the crystal, and occurs during crystal growth; the dislocations interact with other dislocations and point defects to form a meshwork. The sum of the Burgers vectors in the wall determines the tilt of the crystal matrix at both sides of the dislocation wall, but a tilt is not mandatory. Both dislocation nodes and creep processes lead to a pinned dislocation structure. The point defect controlled creep

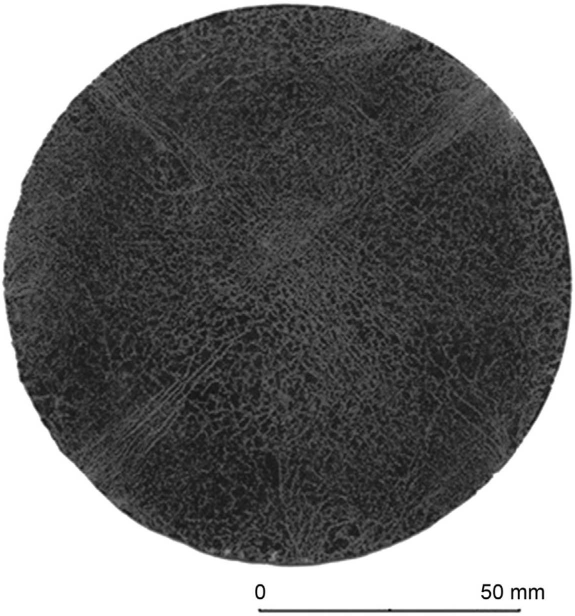

**Figure 6.7** 4 inch; undoped VGF <100>-oriented wafer with EPD $\sim 2.4 \cdot 10^3$ cm$^{-2}$ (U. Juda, IKZ Berlin).

processes become dominant at low thermal stress during growth, and the thermal history of the grown crystals has to be taken into account.

From dislocation pinning it follows that stress induced later cannot easy be reduced by dislocation movement. A high level of residual stress, e.g., detectable by photoelastic measurements [97], leads to an increased risk of wafer breakage or dislocation formation during subsequent high-temperature steps.

The dislocations in the cell walls of GaAs are decorated with precipitates: near the cell wall is an area which is nearly free of precipitates, and some precipitates are visible in the inner cells (see Fig. 6.8). The main precipitates in low-doped GaAs are As precipitates formed by agglomeration of arsenic interstitials during cooling of the crystal. The distribution and size of As precipitates are thus determined by the thermal history and stress of the crystal.

Apart from the analysis methods described above, there are a large number of other established investigation techniques for GaAs crystals and wafers, e.g., X-ray [98], photoluminescence [99], and infrared techniques [100]. For investigation of precipitates in GaAs crystals, laser scattering tomography [101] is a further powerful tool.

### 6.4.2 Electrical properties, characterization, and requirements

For vertical devices (with the back side used as the electrical contact), mainly optoelectronic devices, semiconducting arsenides are applied. In the case of integrated circuits, a low carrier concentration of the semiconductor insulates the single active device.

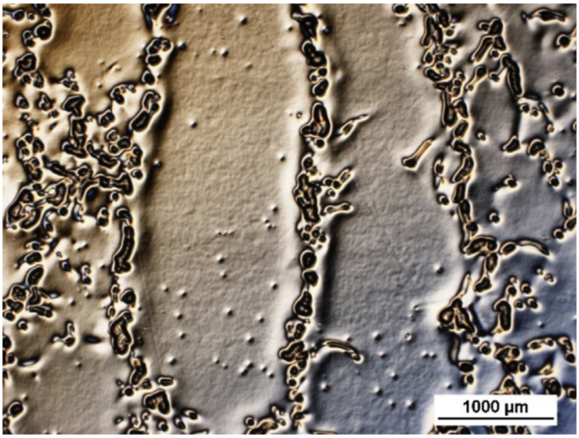

**Figure 6.8** Cellular arrangement of dislocation with precipitates: DSL-etched <110> oriented undoped GaAs VGF wafer (U. Juda, IKZ Berlin).

The electrical properties of semiconductors are primarily determined by the specification of the temperature-dependent values of the doping $N_A{}^* = N_A - N_D$, the degree of compensation $N_A/N_D$ or $N_D/N_A$ for n- or p-conducting material, the charge carrier concentration (n or p) and their mobilities $\mu_n$, $\mu_p$, and the lifetime of the minority charge carriers $\tau_n$, $\tau_p$. The charge carrier concentrations and mobilities are related to the relatively easily measurable variables of electrical conductivity and Hall constant RH. The electrical conductivity σ is defined [102] by the following equation:

$$\sigma = q\left(\mu_n \cdot n + \mu_p \cdot p\right) = \frac{1}{\rho} \tag{6.12}$$

with: $q = 1.6 \times 10^{-19}$ as (absolute value of elementary charge).

For the Hall constant:

$$R_H = r\frac{p \cdot \mu_p^2 - n \cdot \mu_n^2}{q\left(p \cdot \mu_p + n \cdot \mu_n\right)^2} \tag{6.13}$$

with: $r =$ correction factor $\approx 1-2$.

The determination of electrical conductivity is normally carried out by van der Pauw measurement [103], supplemented by Hall measurements [104]. The Hall effect enables the determination of charge carrier concentration for more than 10 orders of magnitude.

Both intended and unintended impurities in the semiconductor can have an energy level in the forbidden gap. Those with an energy level close to the valence or conducting band are called shallow impurities. They are easy to activate, and contribute to electrical conductivity. Typical impurities/dopants are Te (group VI element) on an arsenic site for n-type GaAs, and Zn on a III site or C on an As site for p-type GaAs. Si is amphoteric and can be a donor ($Si_{Ga}$) or an acceptor ($Si_{As}$).

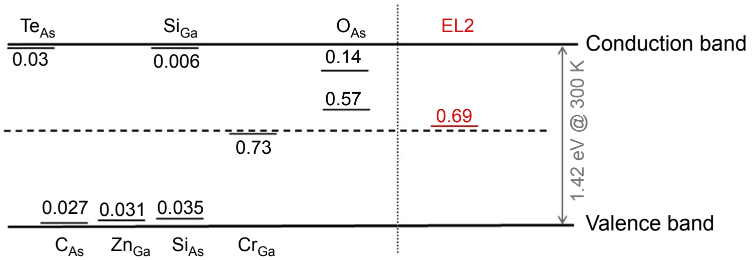

**Figure 6.9** Schematic overview of energy level of defects in the bandgap of GaAs [105].

In Fig. 6.9 the position of the energy level of the most important dopants is shown along with the energy level of the most important intrinsic defect, the midgap double donor EL2. The As antisite defect $As_{Ga}$ is known to be the source of the EL2 defect in GaAs [106]. The EL2 concentration can measured by near-infrared absorption measurements [107]. GaAs is very sensitive to the stoichiometry of the melt [108]. The EL2 concentration can be adjusted between $5 \times 10^{15}$ cm$^3$ and $8 \times 10^{15}$ cm$^3$ using As pressure control during VGF through a separately temperature-controlled As source [109]. Annealed, arsenic-rich LEC GaAs can achieve a higher EL2 concentration of $1.2 \times 10^{16}$ cm$^3$ [110].

To achieve stable semiinsulating behavior, which means GaAs with high electrical resistivity, the following mechanism is utilized.

There are both n- and p-type unintended impurities, like silicon or zinc. To compensate the donors a swallow acceptor is requested; the preferred one is carbon. Under this condition the deep-level EL2 defect can compensate the acceptor. The requirements for semiinsulating behavior can be described following the simplified compensation model [111]:

$$N_{EL2} > N_A - N_D > 0 \tag{6.14}$$

Thus GaAs for semiinsulating material has to be grown from As-rich melts. An impurity concentration below $5 \times 10^{14}$ cm$^{-3}$ is required, meaning only material of the highest purity can be used to achieve reproducible semiinsulating properties. Under these conditions the EL2 and carbon concentrations determine the carrier concentration in semiinsulating GaAs, and thus the electrical resistivity [112]. Another way to achieve high resistivity with less requirement for a low impurity level is Cr doping [86].

A further important extrinsic defect for the compensation of GaAs is $O_{As}$. This deep defect is sometimes discussed in correlation with the intrinsic EL3 defect [113]. Especially in $Ga_2O_3$-doped material this defect is relevant, and a "medium-resistivity material" with charge carrier concentration in the range of $10^{10}$–$10^{12}$ cm$^{-3}$ is achieved [114]. This material is used in special applications like detectors.

Semiconductive properties are achieved by swallow donors (Te, Si) and swallow acceptors (Zn). In commonly applied carrier concentration ranges ($10^{16}$ cm$^{-3}$–$10^{18}$ cm$^{-3}$) the concentration of the mobile carrier is in first approximation proportional to the chemical concentration ($n \approx N_D^*$ respectively $p \approx N_A^*$). If the chemical concentration exceeds the concentration being soluble in the lattice, the correlation between chemical concentration and mobile carrier concentration is no longer valid (see, e.g., [115]), and the higher chemical concentration leads to formation of agglomerated point defects. Semiconducting n-type VGF GaAs is mainly produced by adding silicon to the melt, with a carrier concentration in the range of $10^{17}$ $cm^{-3}$ … $10^{18}$ $cm^{-3}$. The initial Si concentration in the melt has to exceed the target concentration in the crystal by about one order of magnitude due to the small distribution coefficient of Si in GaAs $k_{eff} \approx 0.14$ [116]. Silicon shows amphoteric behavior. At low Si concentrations the carrier concentration increases linearly with the Si concentration and Si on Ga sites acts as shallow donors $Si_{Ga}$. At higher Si concentrations of about $5 \times 10^{18}$ $cm^{-3}$ Si also occupies As lattice sites, acting as shallow acceptor $Si_{As}$ [117]. Compensation of the charge carriers takes place, leading to reduction of the free carrier concentration. A part of the added Si will be dissolved in the $B_2O_3$ encapsulation during the growth process, and the B concentration can increase in the GaAs melt up to values higher than the Si concentration. Besides the isoelectronic defect $B_{Ga}$, acceptor defects $B_{As}$ and $B_{As}$-$Si_{Ga}$ are observed. The doping efficiency thus depends on the B concentration in the crystal. Investigations of Te-doped GaAs as still used for LEC GaAs [105] show a lower B concentration and thus a higher doping efficiency in the material [118]. The carrier mobility decreases with increased charge carrier concentration, especially with increased boron concentration in the crystal. To achieve optimal doping efficiency and defined specification for doped GaAs the crystal growth process has to be optimized, taking the influence of the dopant reaction with $B_2O_3$ into account [118].

### 6.4.3 Mechanical and surface specification of wafers, requirements and characterization

The requirements of device manufacturing determine the wafer specification; requirements include thickness of the wafer, diameter, edge forming, main wafer orientation, off orientation, primary/secondary flat/notch orientation, global and local flatness parameters, polishing, surface quality (haze, light point defects, and allowed scratch level), and surface contamination level.

The wafer thickness is defined depending on breakage probability and mechanical stability. It increases with diameter and is independent on the final device thickness, e.g., a 625 μm optoelectronic 4″ wafer is thinned down to 225 μm for a standard LED at the end of the process. Tight thickness tolerances below ±10 μm are requested to achieve a fast and reproducible lithographic reproduction. Calibrated wafer diameters (2″ … 200 mm) open the door to automatic wafer processing tools. In the case of manual wafer handling, irregular shapes may give cost advantages, since less wafer area is lost in calibration. The main orientation is (100), but other orientations like (110) or (111) are available. In particular, vapor-phase deposition processes like MOCVD require an off orientation to improve the layer quality, and so the wafer axis tilt (off orientation) and direction of tilt (often toward $\left(0\bar{1}1\right)$ or $\left(0\bar{1}\bar{1}\right)$) have to be specified.

The flats are parallel to the cleavage plane $\left(0\overline{1}1\right)$ or $\left(0\overline{11}\right)$, with the two options of SEMI EJ (Europe/Japan) or SEMI Am. In the case of SEMI Am the primary (longer) flat is perpendicular to the V-groove etching figure (a wet-etched trench with $H_2SO_4$-$H_2O_2$-$H_2O$, as shown in Fig. 6.6(a)). In the case of SEMI EJ the primary (longer) flat is perpendicular to the dove-tail groove etching figure (an etched trench using the same procedure). The alignment of the dicing streets parallel to the cleavage plane reduces kerf chipping during the dicing process (chip sawing). Notches are oriented to (010) and the cleavage plane is 45 degrees turned to this direction.

The main goals of mechanical wafer preparation and polishing are a flat surface, the lowest possible roughness, and the removal of layers damaged by previous mechanical grinding processes like wafer sawing and surface grinding. The flatness of a wafer is defined by global parameters like total thickness variation (TTV) and total integrated reading (TIR) with respect to contact or projection lithography. Typical TTV values below 5 μm and TIR values below 4 μm are standard [119]. An important aspect, the warp of a bare wafer, is mainly influenced by the subsequent steps. The probability of very low warp or a pure wafer can be massively increased by epitaxial layers. Local flatness parameters like local thickness variation (LTV) refer to a hypothetical exposition field of step and repeat lithography projections, and are thus not generally defined. Values below 1 μm per 20 × 20 mm field can be achieved. Surface interferometry with a reference plane is an option to measure all flatness parameters, clamping the wafer on a very flat vacuum chuck as reference allows measurement of global and local parameters like LTV and TTV. Release of the vacuum at the chuck allows measurement of the warp in the same arrangement (see example in [120]).

Arsenides are brittle at room temperature, and induced microcracks and local stress fields, often called subsurface damage, are stored in the surface layer. The thickness of this layer during wafer cutting by wire saw or inboard dicing is below 10 μm [121]. They form larger defect structures at temperatures of 350°C [122], which can downgrade the epitaxial layer quality. The polishing process removes these damaged layers. The possible remaining subsurface defects can be viewed destructively by wet chemical etching [123] or nondestructively by laser scattering [124]. They are visible after the initial steps ("buffer layer") of a subsequent epitaxial process by means of surface laser scattering [125].

The polishing quality is one of the main properties of a wafer for the initial steps of the epitaxial process. It is again characterized by global and local methods. The AFM measured roughness shall be $R_A < 0.15$ nm in an area of 1 × 1 μm for (100) GaAs [126]. For detailed wafer inspection differential interference contrast or Nomarski interference contrast, in combination with dark field illumination, are common technologies. Global inspection of wafers helps to make scratches, particles, and general haze visible, and can be carried out by scattered light analysis. The reference model is a latex sphere on a bare silicon wafer [127]; the amount of light scattered by this sphere defines the nominal particle size [125]. Anisotropic scattering behavior, etched pitches, or other deviations in optical properties of the particle have to be considered to understand the result of a scanning surface inspection system. A simpler but powerful method to characterize the surface is manual inspection below a narrow-beam white light spot [128]. The unspecific particle counts shall be $<25\ \mathrm{cm}^{-2}$ for a latex sphere size larger then 0.3 µm. Higher densities of particles increase the defect density in the epitaxial layer and can affect the initial growth steps.

The III arsenides form an oxide layer during mechanochemical polishing (the reaction product layer); its thickness depends on polishing conditions [126]. Even after removal of this layer by a subsequent etching step, the oxide layer is formed again at normal atmosphere [59]. This oxide layer thickness of a fresh polished wafer shall be in the range of 1−2 nm, measured by ellipsometry. The thickness increases depending on storage condition. This surface layer also contains residual contaminations, analyzed by time-of-flight (TOF) SIMS or TXRF. The contaminants include metal ions and organic compounds. A monolayer GaAs contains $1.28 \times 10^{15}$ atoms/cm$^2$. Metal ions can be detected on a bare GaAs wafer in a concentration down to $10^8$ atoms/cm$^2$ [65], and the analysis methods TOF-SIMS and TXRF are correlated between $1 \times 10^{10}$ cm$^{-2}$ and $4 \times 10^{13}$ cm$^{-2}$ for important metal contaminants like copper, iron, titanium, and nickel [129]. After final cleaning a "prime wafer" must have a remaining contamination of metal ions below $1 \times 10^{10}$ cm$^{-2}$ [66] and only organic compounds or oxides, which can desorbed during the initial processes.

Last but not least, adequate packaging has to maintain the achieved surface quality to protect against dust and moisture during transport before use. Direct usability in the growth process is often described as "ready to use," "epi-ready," or similar expressions.

## 6.5 Growth of GaAs crystals

### 6.5.1 Synthesis of feedstock

Presynthesized polycrystalline material is often used in single crystal growth techniques to simplify the process and reduce process costs. In VGF technology the use of polycrystalline material is mandatory to protect the seed. The highest purity of elements (e.g., Ga, As $\geq$ 6N) must be used. The main residual impurities in As and Ga are Si, S, Al, Na, Mg, and C. Their concentration in the starting materials must not exceed $\approx$0.1 ppm [130]. In preparation for synthesis, all other materials used should have the same purity and cleanliness as the starting materials. Special attention must be given to the removal of oxides, contaminants, and water from the materials during preparation, thus all equipment parts have to be etched and dried in vacuum before use.

The vapor pressure of arsenic at melting temperature over stoichiometric or lightly As- rich GaAs is in the range 1.5−2 bar [28]. GaAs can be synthesized in principle using the following techniques:

1. Low-pressure synthesis
2. High-pressure synthesis
3. Injection synthesis.

The low-pressure and high-pressure syntheses are of practical importance, and are described below more in detail. A detailed description of injection synthesis can be found in [7].

### 6.5.1.1 Low-pressure synthesis

Usually synthesis takes place in a three-zone furnace (see Fig. 6.10), which is located in a closed setup for safety reasons. The vapor pressure zone (lowest temperature) heats the arsenic source and defines the arsenic partial pressure in the ampoule. The main heater has a temperature above the melting temperature of the binary compound, and the after heater ensures that the excess arsenic always condenses at the arsenic source. The arsenic partial pressure must be high enough to avoid decomposition of the solid arsenide in the after-heater zone. The synthesis is done in a closed, at room temperature evacuated ampoule. The ampoule should be made from fused silica. Procedure (GaAs, Fig. 6.10):

1. Gallium is placed in a graphite, BN, or fused-silica boat in the ampoule. The arsenic is positioned at one end of the ampoule.
2. The furnace is heated to the initial profile; the boat with the gallium melt is positioned at the transition between main heater and after heater. The main heater is heated up to melting temperature.
3. The arsenic is heated in the vapor pressure zone to a temperature which ensures an adequate evaporation rate; this rate is determined by the consumption of arsenic in the reaction zone. This requires the increase of the temperature in the vapor pressure zone from initially about 500°C to about 780°C at the end of the synthesis. The gaseous As reacts with the Ga in the boat, which is held at melting temperature. Due to convection in the reaction zone, only an unsaturated GaAs melt can form.
4. The ampoule or furnace is transported with a rate of feed in the rage of 5−15 cm/h to move the boat into the after-heater zone. When the solubility limit of GaAs in Ga is exceeded as a result of the temperature reduction, the compound crystallizes at the cold end of the boat. By suitable parameter choices, the evaporation rate, transport, and consumption of the As in the Ga melt are the same and GaAs crystallizes as a single-phase product. A Ga phase (droplets) is included when the arsenic supply is too low or the ampoule rate of feed is too high. An excess supply of arsenic leads to holes in the GaAs and the risk of bursting the ampoule based on the increased As partial vapor pressure.
5. At the end of the process the boat has left the main zone and will contain the synthesis ingot. The synthesis should be controlled in such a manner that the arsenic in the source almost completely reacts with the Ga melt.

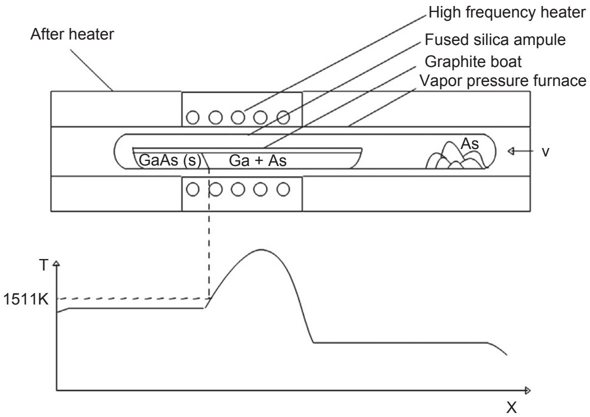

**Figure 6.10** Sketch of low-pressure synthesis equipment for GaAs.

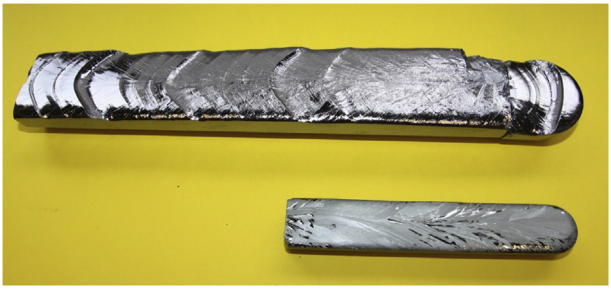

**Figure 6.11** Image of GaAs ingot with a shoulder width of 5 cm (top) and InAs ingot with a shoulder width of 2.5 cm (bottom). Both were synthesized by the low-pressure method at VEB Spurenmetalle Freiberg in 1988.

The achieved charge weight of the described low-pressure synthesis is about 3 kg. The process time is about one day. Yields of up to 95% can be achieved. The average crystallization rate of the polycrystalline GaAs is about 20–30 mm/h.

The low-pressure synthesis furnace shown in Fig. 6.10 has the following approximate dimensions:

- length of quartz glass ampoule ~100 cm
- length of graphite boat ~30 cm
- shoulder width of graphite boat ~ 5–6 cm.

The reaction of the arsenic with the fused silica is one disadvantage, as it leads to unintended Si pollution of the ingot; nearly all impurities from the raw material will be included in the ingot, and purification due to directed solidification is limited [131].

Low-pressure synthesis technology is used principally for all III arsenides except BAs, especially for smaller quantities. In the 1980s it was also used for the synthesis of InAs. Fig. 6.11 shows an image of a half GaAs low-pressure ingot and a half InAs ingot; both were produced in 1988.

### 6.5.1.2 High-pressure synthesis

The high-pressure synthesis of GaAs can be carried out in situ in a high-pressure LEC puller or ex situ in a separate process. The ex-situ process is technologically more relevant, because the polycrystalline GaAs material can be used for VGF growth. High-pressure synthesis is carried out in a pressure vessel, which is based in principle on an LEC puller without a pull rod, although clearly simplified.

High-pressure synthesis is carried out as follows.

1. Gallium and arsenic (≈0.1% As excess) with encapsulated $B_2O_3$ are charged in a pyrolytic boron nitride (pBN) crucible. The inert gas pressure in the reaction chamber is ≈40–50 bar in the "cold state" to avoid evaporation of the arsenic.
2. After the melting of $B_2O_3$ (400–500°C), As and Ga are encapsulated and separated from the gas atmosphere. The reaction between As and Ga starts at a temperature of about 800°C.

3. The reaction is exothermic. The melt heats up due to the fast reaction, and a pressure of about 70–80 bar is achieved during reaction. Therefore the reaction furnace must be a pressure vessel with the ability to withstand up to 100 bar. After 1–2 h the reaction is nearly finished, leaving the melt at equilibrium and homogenized.
4. The melt is cooled down and crystallized as a polycrystalline ingot with a growth direction from the bottom to the top of the melt.

The advantages of high-pressure synthesis are the higher quantities of polycrystalline material synthesized, meaning the process has greater productivity. Furthermore, the polycrystalline GaAs has a lower content of impurities (e.g., C and Si) than low-pressure synthesis material and a defined As/Ga ratio, so GaAs with an As excess can be synthesized. The boron oxide contributes to further purification of the melt, and the general impurity level is reduced [132,133]. A properly chosen crucible provides ingots in a form that can be used for the later growth process.

However, there some disadvantages:

- the high-pressure vessel should be specified for an operating pressure of 100 bar, which is associated with higher equipment costs
- the synthesis may not be interrupted, because this leads to uncontrolled solidification and eventual rupture of the crucible.

## 6.5.2 *Crystal growth techniques*

III arsenides can be grown by different methods from melt, taking into consideration the preservation of the stoichiometric composition of the melt. This can be done either by liquid encapsulation with, e.g., $B_2O_3$ of the melt, or by crystallization under equilibrium pressure of the arsenic in a closed system.

Initially III arsenides were grown by the horizontal Bridgman (HB) method and the LEC technique, but later vertical arrangements became more important. In the 1990s the LEC and HB methods were the main techniques to grow GaAs, but they lost importance because of the demand for higher structural perfection (e.g., lower EPD) with the switch from ion implant devices to epitaxial-grown applications (see Section 6.3).

Over the last 20 years the ratio between LEC and VGF wafers has changed completely: in 2015 the ratio between LEC and VGF techniques was 10:90 [20], wherein one has to differentiate between semiinsulating and doped GaAs. Production of semiinsulating GaAs is dominated by the VGF technique, but in doped GaAs for LEDs there is still some HB GaAs production [3,6].

Fig. 6.12 shows GaAs single crystal growth methods, and in Section 6.5.3 the modelling of LEC and VGF (Tamman-Stöber type) [134] are described explicit. In principle one can divide the growth methods into crucible methods (a–d) and the crucible-free LEC method (e). Bridgman methods in vertical and horizontal arrangement (Fig. 6.12(a) and (b)) have a moved furnace or a moved ampoule. The abbreviation "H" usually denotes "horizontal" methods and "V" vertical methods. A growth setup without mechanical movement but only a moving temperature field is called a gradient freeze mode (Fig. 6.12(c) and (d)).

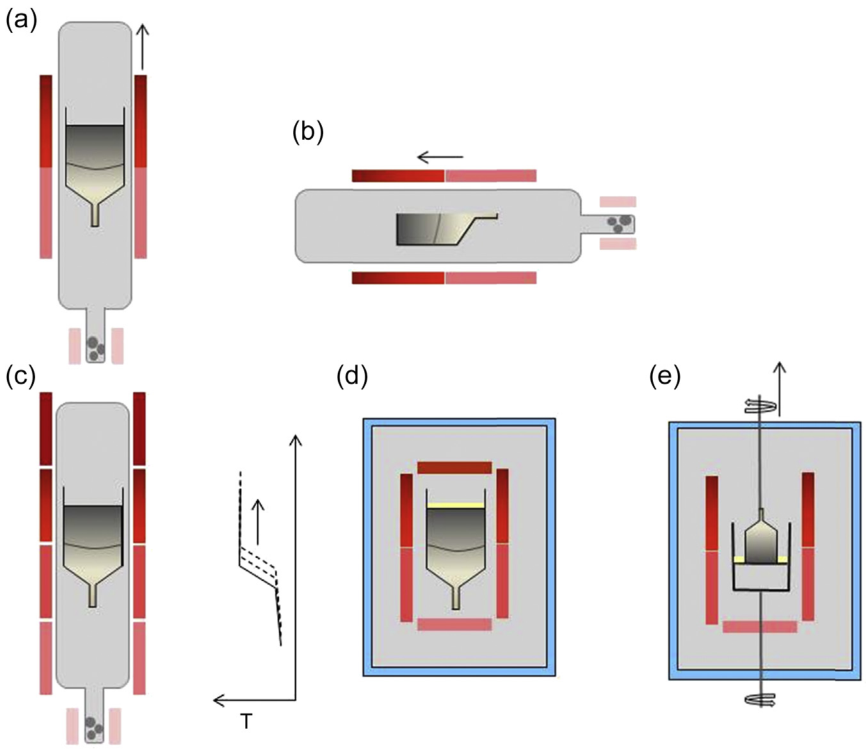

**Figure 6.12** Sketches of GaAs growth methods: (a) VB, (b) HB, (c) VGF (ampoule technique), (d) VGF (Tamman-Stöber method), (e) LEC.

### *6.5.2.1 Liquid encapsulation Czochralski*

LEC was for decades the main growth technique for GaAs and InAs, and was first described by Mullin in 1965 [135]. The basic principle has not changed since then; a sketch of the configuration is given in Fig. 6.12(e).

The melt is in a crucible, which is now usually made from pBN and covered with molten boric oxide ($B_2O_3$) as encapsulation to avoid the evaporation of arsenic. An inert gas pressure higher than the vapor pressure of the As exists in the growth chamber; nitrogen or argon can be used as the inert gas. The $B_2O_3$ has another important function: it influences the impurity level in the crystal depending on the water content [136].

During the growth process the crucible and crystal are rotated to minimize thermal inhomogeneities and influence the melt flow (e.g., to reduce thermal turbulence). Typical rotation rates are in the range of 2—30 rpm, depending on the crystal diameter and growth rate [7].

For LEC growth a seed is touched into the melt and then slowly, at a rate of 1—15 mm/h, pulled up. First the crystal diameter is increased by reducing the temperature of the heaters, and the conical part of the crystal is grown. When the desired diameter is reached, the cylindrical crystal part of the desired diameter is grown.

The diameter and growth rate are computer controlled, and the diameter is calculated by the signal of change of the weight of the grown crystal using load cells.

The advantages of the LEC method are a relatively high growth rate, a large initial weight up to 50 kg [137], no direct contact between crystal and crucible, avoiding mechanically induced stress, and easy control of the carbon concentration to enable adjustment of electrical resistivity. The main disadvantage is the high dislocation density (EPD) of the grown crystal based on the high axial thermal gradients (100−150 K/cm) in the crystal during the process. Furthermore, LEC-grown crystals have to be annealed to reduce the remaining residual stress. Typically the EPD is in the range of $0.5-1 \times 10^5$ $cm^{-2}$. There are several comprehensive reviews of the method in the literature [7,138].

To reduce the dislocation density a reduction of thermal gradients is necessary. This leads to an increase of the surface temperature of the grown crystals after leaving the boron oxide melt, and therefore to an evaporation of arsenic. This evaporation can lead to Ga droplets on the surface. The droplets induce stress in the crystal, so deformation twinning or dislocation multiplication occurs. To avoid this, different approaches such as fully encapsulated Czochralski and hot-wall Czochralski techniques have been investigated over the last few decades. Vapor-pressure-controlled Czochralski (VCz) is a powerful method to realize more homogeneous temperature fields with lower axial temperature gradients in the range of 15−35 K/cm. In the VCz technique an inner chamber is placed in the growth chamber; by controlling the As partial pressure in the inner chamber using a separately heated As source, dissociation on the crystal surface can be avoided. The achieved EPD is one order of magnitude lower than in LEC-grown crystals, but still nonhomogeneously distributed over the wafer at a factor of about 5−10 times larger than in VGF crystals. On an industrial scale the VCz technique has not caught on, mainly because the highly complex growth equipment entails higher investment costs and the lower axial temperature gradient reduces the growth rate. A detailed overview of the achieved results of VCz GaAs crystal growth is available [139].

The LEC technique is still used for some application areas of GaAs and InAs, as mentioned before, with diminishing importance. But there is literature describing further advancements in the LEC technique, such as its use in magnetic fields [140]. Opportunities to optimize the LEC process further are discussed in Section 6.5.3.

### 6.5.2.2 Vertical gradient freeze

The development of GaAs VGF was triggered by the successful experiments of Gault and coworkers in 1986 [141]. They demonstrated the growth of semiinsulating 2-inch GaAs with low EPD. In the following years an international boom in VGF process development began. Initially multizone VGF furnaces with up to 28 zones were built, though over the course of several years the equipment was simplified.

There are two different basic VGF techniques: one is based on an open design using a liquid encapsulation of the melt in a high-pressure furnace to avoid decomposition; the other is based on a closed ampoule with an arsenic atmosphere inside, with or without encapsulation [142] (see Fig. 6.12(c) and (d)). All VGF process versions have in common that pBN is currently used as the crucible material: pBN has the advantage that there is no Si contamination in the melt, and the thermal expansion [143] of the pBN allows cooling of GaAs to room temperature free of cracks. This is not possible when using $SiO_2$ crucibles and $B_2O_3$ [144]. A typical axial furnace gradient is in the range of 2−10 $Kcm^{-1}$ and the crystal growth rate is in the range of 1−3 $mmh^{-1}$. Typical temperature fields in the melt are shown in Fig. 6.24. The influence of the shape of the conical part of the crucible on the crystal quality was investigated [48] and verified among the different users of VGF techniques.

VGF growth using a sealed quartz ampoule with a separately controlled As reservoir enables precise adjustment of the melt composition by means of As temperature. It is shown [109] that the stoichiometric deviation in correlation to the As source temperature is in the range of 600−631°C, and the transition from Ga-rich to As-rich melt compositions occurs in this temperature range. While an As source temperature of 631°C leads to polycrystalline growth based on constitutional undercooling on the As side, a source temperature of 600°C leads to a polycrystalline growth based on the Ga-rich melt. A single crystal growth was possible only in the process window of an As source temperature of 607−620°C. In the case of an As source temperature ($T_{As}$) of 613°C the crystal tail region was faceted and like a mirror without particles (Fig. 6.13(b)), but by $T_{As} = 620°C$ the tail region of the crystal had facets and small crystallized "particles" of As-rich remaining melt (Fig. 6.13(a)). An As source temperature of 607°C leads to strong facets in the tail region with additional small columnar crystallites interspersed by Ga (Fig. 6.13(c)).

The electrical properties, especially the concentration of the EL2 defect, depend on the As source temperature [109].

A disadvantage of a VGF ampoule technique with heaters only at the side is a limitation of the diameter of the grown crystal, hence the Tamman-Stöber VGF technology has become more and more common with the increased diameter of GaAs crystals: today it is the state of the art for production of VGF GaAs with diameters of 4 and 6 inches, and has also been demonstrated for 8 inch crystals[20, 137, 145, 146].

The ampoule technique has also occasionally been used for 2-inch VB GaAs production [147]. The authors described in this paper the difficulties in managing

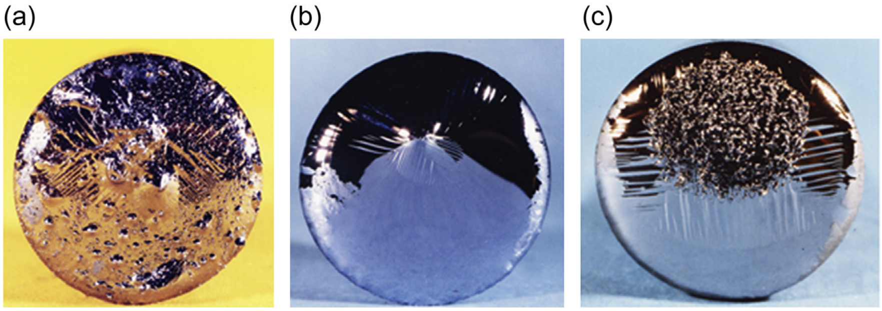

**Figure 6.13** Tail regions of GaAs single crystals (Ø = 40 mm) grown at different As source temperatures: (a) $T_{As} = 620°C$; (b) $T_{As} = 613°C$; (c) $T_{As} = 607°C$.

the As vapor pressure in the ampoule: a wrong adjustment of the As pressure led to strong deformation of the $SiO_2$ ampoule, resulting in an arrangement with five ampoules in parallel growth. In spite of these difficulties this technology must be kept in mind for basic research and for other arsenides such as InAs, if only a low number of crystals is required. The VGF ampoule technique has been used for InAs crystals in a research laboratory at the Mining Academy Freiberg [148].

As mentioned, the Tamman-Stöber-like VGF furnace is currently the state of the art for GaAs growth of large-diameter crystals. The basic idea is to realize an axial heat flow from the top of the setup by means of a top heater to the bottom part of the crystal. Normally a bottom heater is used to control the axial gradient and then the temperature is cooled down during crystal growth. The temperature field is distinguished by low radial gradients, which can be controlled by the side heaters. It is possible to grow GaAs crystals with very low EPD by this method based on low gradient and low thermal stress. The process can be controlled by temperature measured by thermocouples inside the furnace or direct by power control of the heaters. The control of impurities (and thereby the electrical properties) is handled in the same way as for the LEC technique by using $B_2O_3$ with different water content and controlling the gas atmosphere. As inert gas, Ar or $N_2$, is used. Fig. 6.14 shows an image of a 4-inch GaAs VGF single crystal grown at IKZ Berlin. The partial roughness of the crystal surface is due to the contact with the $B_2O_3$ and the crucible. The s/l interface shape in cross-section should be symmetric and nearly flat or slightly convex. This is the best condition to grow crystals with homogeneous radial distribution of dislocation and dopants, and leads to uniform electrical parameters and low residual stress.

The main challenge of this technique is as follows. The heat sink of this setup is the bottom region. The crystal has a lower thermal conductivity then the melt and the diameter is reduced in the seed range. At the s/l interface the heat of crystallization increases the tendency to form a concave interface shape. From a flat s/l interface follows very low radial gradients, so no thermal-driven melt flow is exited. A stable temperature gradient over the crystal and a stable melt flow are required to increase the crystal length, crystal homogeneity, and growth velocity.

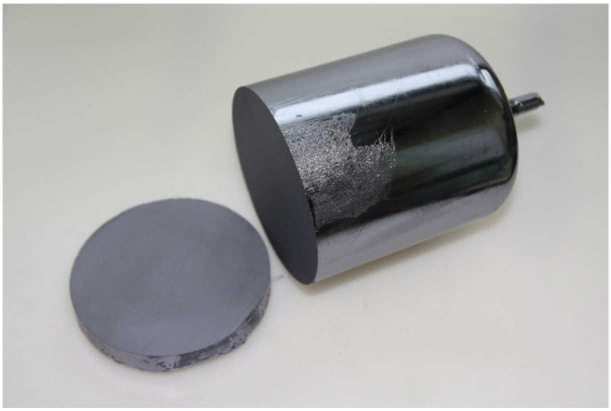

**Figure 6.14** 4" GaAs VGF single crystal grown at IKZ Berlin, initial weight = 7 kg.

At present there are different approaches to intensify the VGF process, which as discussed [149,150] include the use of a magnetic field to influence the melt flow. In Section 6.5.3.4 different approaches to the VGF process intensification are introduced more in detail. The simultaneous growth of multiple crucibles is of particular importance and achieves a significant increase in effectiveness of the VGF process. Further, the use of external fields like a magnetic field provides the option to optimize the VGF technique. The use of modeling is thereby indispensable; some examples are given in Section 6.5.3.4.

## *6.5.3 Modeling of transport phenomena*

Bulk crystal growth of binary compound semiconductors is inevitably coupled with a control of transport phenomena (i.e., momentum, heat, and mass transport during melting and solidification). Due to the high operating temperatures and pressures, the chemically aggressive environment, and strong contamination restrictions, experimental studies in situ and in operando are difficult, time-consuming, and expensive. Thus crystal growth modeling offers a faster and better alternative that provides excellent understanding/visualization of the physical processes, as well as a way to control them. Growth of crystals with a high quality (e.g., desired dopant distribution and flat s/l interface) and yield is feasible only if the furnace/hot zone is properly designed and the growth recipe is developed and optimized. Moreover, process improvement by utilization of external forces (e.g., Lorentz forces originated from static, traveling, and rotating magnetic fields), especially for suppressing flow turbulences, flattening the s/l interface, and reducing dopant nonuniformity, is feasible only if the external forces are properly selected. Again, the most efficient way to reach these goals is to use computer simulations. An extensive review of the progress of bulk crystal growth modeling and growth control is available [151].

Besides these general features, modeling of crystal growth of binary compound semiconductors has some peculiarities. For example, GaAs has a high latent heat and low heat conductivity that hampers latent heat removal from the growing interface and lowers growth rates (Table 6.2); thus the s/l interface shape easily becomes concave, causing thermal stress within a crystal and an occurrence of dislocations. The low critical shear stress induces high dislocation density under lower thermal stress and thus degrades the crystal quality. These facts explain why the accuracy requirements for simulations of temperature distribution are higher by bulk crystal growth of binary compounds than by other materials.

After general considerations that include balance equations, boundary conditions, characteristic dimensionless numbers, and common simulation software, this section discusses various modeling approaches and furnace design, as well as simulation results concerning geometry and process optimization, process intensification, s/l interface flattening, and melt stirring.

### *6.5.3.1 General considerations*

The governing differential equations of momentum, heat, mass, and charge transport in crystal growth are given in Table 6.3. These equations are written for one single phase.

## Table 6.2 GaAs physical properties [151,152]

| GaAs | | | |
|---|---|---|---|
| **Property** | **Unit** | **Melt** | **Solid** |
| $\lambda$ | $W/(m \cdot K)$ | 13.6 | 7.2 |
| h | $W/(m^2 \cdot K)$ | 350–1000 | 350–1000 |
| $\rho$ | $kg/m^3$ | 5710 | 5320 |
| Cp | $J/(kg \cdot K)$ | 434 | 424 |
| $\Delta H_{s,l}$ | J/kg | – | 7200 |
| $T_m$ | K | 1511 | 1511 |
| $\alpha$ | $m^2/s$ | $7.29 \cdot 10^{-6}$ | $2.9 \cdot 10^{-6}$ |
| $\nu$ | $m^2/s$ | $5 \cdot 10^{-7}$ | – |
| E | GPa | – | 1.1 |
| $\beta$ | $K^{-1}$ | – | $1.1 \cdot 10^{-5}$ |
| $\sigma_{el}$ | $\Omega^{-1}\,m^{-1}$ | $7.9 \cdot 10^5$ | 10 |

## Table 6.3 Governing equations for transport phenomena in crystal growth

| **Equation** | **Name of equation** |
|---|---|
| $\frac{\partial \rho}{\partial t} + \nabla(\rho \vec{u}) = 0$ | Continuity equation |
| $\rho \frac{\partial \vec{u}}{\partial t} + \vec{u}\nabla\vec{u} = \rho \vec{g} - \nabla P + \nu \nabla^2 \vec{u} + \vec{F}_L$<br>$\rho g = \rho_0(1 - \beta T_0)g$ | Navier–Stokes equation with Boussinesq approximation |
| $\rho C_P \left( \frac{\partial T}{\partial t} + \vec{u}\nabla T \right) = \lambda \nabla^2 T$ | Energy conservation equation |
| $\frac{\partial C}{\partial t} + \vec{u}\nabla C = D\nabla^2 C + R$ | Species conservation equation |
| $\nabla \times \vec{H} = \vec{j}$ | Ampère’s circuital law |
| $\nabla \times \vec{E} = -\frac{\partial \vec{B}}{\partial t}$ | Maxwell–Faraday equation |
| $\nabla \vec{B} = 0$ | Gauss’s law for magnetism |
| $\nabla \vec{E} = 0$ | Gauss’s law |
| $\vec{j} = \sigma_{el}\left(\vec{E} + \left(\vec{u} \times \vec{B}\right)\right) \approx \sigma_{el} \vec{E}$ | Ohm’s law |
| $\vec{B} = \mu \mu_0 \vec{H}$ | Magnetic field strength |
| $\vec{F}_L = \vec{j} \times \vec{B}$ | Lorentz force law |

Table 6.4 **Boundary conditions for balance equations given in Table 6.2**

| BC definition | Description; type | Transport equation | Boundary |
|---|---|---|---|
| $u = u_0$ | No slip; Dirichlet | Navier Stokes | Crucible/fluid (gas or melt) |
| $[u]_{x=0-} = [u]_{x=0+}$ | Free slip; Dirichlet | Navier Stokes | Melt/gas |
| $[\tau]_{x=0-} = [\tau]_{x=0+}$;<br>$\tau_l = \frac{d\gamma}{dT}\nabla T$ | Marangoni stress defined; Robin | Navier Stokes | Melt/gas |
| $T = T_0$ | Defined T; Dirichlet | Energy balance | Housing/cooling water |
| $q = q_0$ | Constant heat flux; Neumann | Energy balance | Gas/heater |
| $[q]_{x=0-} = [q]_{x=0+}$;<br>$\lambda_l \left[\frac{dT}{dx}\right]_l + r_{growth}\Delta H_{s,l}\,\varrho_s = \lambda_s \left[\frac{dT}{dx}\right]_s$ | Heat flux continuity; Neumann | Energy balance | Melt/crystal |
| $[T]_{x=0-} = [T]_{x=0+}$ | Same T on both sides; Dirichlet | Energy balance | Melt/crystal |
| $[q]_{x=0} = h\cdot(T-T_0)$ | Empirical flux defined; Robin | Energy balance | Housing/ambient gas |
| $[n]_{x=0} = k\cdot(c-c_0)$ | Empirical mass flux defined; Robin | Mass balance | |
| $c = c_0$ | Constant concentration; Dirichlet | Mass balance | Melt/crucible |
| $[c]_{x=0-} = k\cdot[c]_{x=0+}$<br>$c_s = k\cdot c_l$<br>$c_g\cdot R\cdot T = H_A\cdot c_l$ | Solute segregation and evaporation; Dirichlet | Mass balance | Melt/crystal; melt/gas |

Since the crystal growth system includes at least two phases (melt and crystal), but usually more (melt, crystal, gas, heaters, isolation, etc.), it is necessary to write a set of balance equations for each phase with corresponding material properties. For multicomponent systems, a species conservation equation should be written for each component separately.

Boundary conditions are given in Table 6.4. They can be defined in a common Dirichlet, Neumann, and Robin form. When using a Dirichlet boundary condition, one specifies the value of a variable (e.g., velocity, temperature, and concentration of species) at the boundary (e.g., $u = 0$ at the crucible wall; $T = 295$ K at a furnace outer wall; and $C_L = k \cdot C_S$ at the s/l interface). When using a Neumann boundary condition, one prescribes the flux of a variable at the boundary, e.g., $\partial u/\partial n = \text{const.}$ When using a mixed boundary condition, a function of the form $a \cdot u + \partial u/\partial n = \text{const.}$ is applied. Different types of boundary conditions can be used for different variables at the same boundary.

These governing equations and boundary conditions are written in Tables 6.3 and 6.4 in dimensional form. Sometimes equations are normalized, i.e., written in dimensionless form to facilitate the scaling up of obtained results to real growth processes and to assess the relative importance of terms in the model equations.

The fundamental approach to scaling up is achieved by applying a principle of similarity, which involves maintaining the dimensionless groups, characterizing the phenomena of interest, constant from the small scale to the commercial furnace. Characteristic dimensionless numbers for bulk crystal growth are given in Table 6.5.

The governing equations given in Table 6.3 cannot be solved analytically and must therefore be studied using computer-aided numerical simulations. There are many codes devoted to solving problems in transport phenomena, both general purpose and specialized for crystal growth. Nowadays the world market is dominated by commercial software, such as ANSYS (Fluent, CFX) and CD-adapco (Star-CCM+), but noncommercial Open Source OpenFOAM is also available. These software products are based on finite volume methods and are not particularly designed for crystal growth. There are also commercial software products focused on crystal growth from the melt, e.g., FEMAG [162], CapeSym [163], CrysVUn [164], Comsol [165], CGSim [166], PROCOM [167], STHAMAS [168], etc.

### 6.5.3.2 Modeling approach

To select a model of the crystal growth process from the diverse range available (e.g., axisymmetric versus 3D, steady versus transient, laminar versus turbulent, global (furnace) versus local (melt) etc.), it is necessary to weigh the complexity of the model with the difficulty involved in finding its solution. The more complex models can usually more accurately describe the real phenomena, but they are also more expensive (in time, money, and labor). The most feasible approach is to develop a model iteratively with continual refinement. To what extent the model simplifications are justified can be determined only by experimental verification. Detailed discussions of various numerical issues in bulk crystal growth in general and for case studies of silicon and cadmium zinc telluride growth are available [169].

#### 2D versus 3D

Whether a 2D or a 3D model will be adopted to offer better insights into the crystal growth depends on many parameters. The most important criteria for choosing between 2D and 3D models are the geometry of the furnace/melt, melt flow regime, computational costs, and desired accuracy. 3D models are complex to build and require long simulation times, which can lead to prohibitively high costs. 2D models can be successfully used as easy first approximations to predict flow patterns in rotational symmetric geometry like VGF and Cz furnaces. However, 2D model predictions

**Table 6.5** **Dimensionless numbers in bulk crystal growth of GaAs**

| Name | Symbol | Formula | Range | Critical value | Meaning |
|---|---|---|---|---|---|
| Grashof number | Gr | $Gr = g\cdot\beta\cdot\Delta T\cdot L^3/\nu^2$ | $10^7$–$10^8$ (Cz&LEC GaAs) [153–155] | $1.5 \times 10^8$ (LEC; GaAs) [156,157] | Ratio of buoyancy to viscous forces |
| Hartmann number | Ha | $Ha = B\cdot L\cdot(\sigma/\mu)^{1/2}$ | 0–50 (LEC&MF; GaAs) [158] | 15 (LEC&MF; GaAs) [158] | Ratio of electromagnetic force to viscous force |
| Nusselt number | Nu | $Nu = h\cdot L/\lambda$ | $>>1$ (VB; GaAs) [159] | | Ratio of convective to conductive heat transfer |
| Peclet number | $Pe = Re\cdot Pr$ | $Pe = u\cdot L/\alpha$ | 7.3 (VB; GaAs) [159]<br>$0$–$2\cdot 10^{-3}$ (HB; GaAs) [152] | | Ratio of advective to diffusive heat transfer |
| Prandtl number | Pr | $Pr = \nu/\alpha$ | 0.068 (Cz; GaAs) [153] | | Ratio of momentum diffusivity to thermal diffusivity |
| Rayleigh number | $Ra = Gr\cdot Pr$ | $Ra = g\cdot\beta\cdot\Delta T\cdot L^3/(\nu\cdot\alpha)$ | $10^6$–$10^8$ (LEC; GaAs) [137] $9.6\cdot 10^5$(VGF GaAs) [160] | $2\cdot 10^3$ (LEC; GaAs) [158]<br>$4\cdot 10^4$ (LEC&MF; GaAs) [158] | Ratio of buoyancy to diffusive heat transport |
| Reynolds number | Re | $Re = u\cdot L\cdot\rho/\mu$ | $10^3$–$10^4$ (LEC&VGF; GaAs) [150,154,156] | $1.6\cdot 10^4$ (LEC; $u = \omega\cdot D$) [156] | Ratio of inertial forces to viscous forces |
| Magnetic Reynolds number | $Re_m$ | $Re_m = u\cdot L\cdot\mu_0\cdot\sigma_{el}$ | $5\cdot 10^{-4}$ (VGF GaAs) [160] | | Ratio of magnetic advection to magnetic diffusion |
| Schmidt number | Sc | $Sc = \mu/(\rho\cdot D)$ | $>10^1$ [151,161] | | Ratio of momentum diffusivity and mass diffusivity |
| Marangoni number | Ma | $Ma = \frac{\partial\gamma}{\partial T}\,\frac{L\cdot\Delta T}{\mu\cdot\alpha}$ | $3\cdot 10^5$–$1\cdot 10^6$ (LEC; GaAs) [155] | | Ratio of surface tension forces to viscous forces |

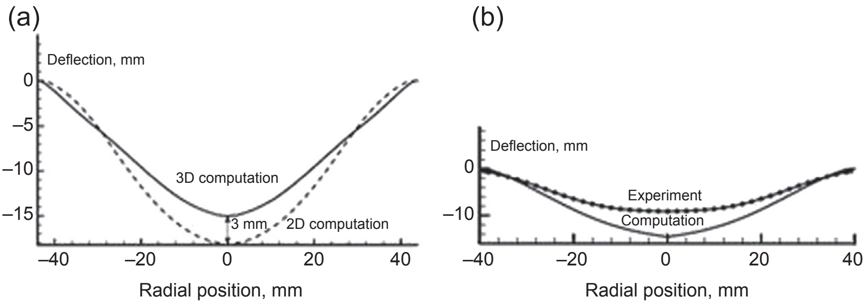

**Figure 6.15** Interface shape in VCz GaAs growth predicted by 2D and 3D simulations and verified by experiments [170].
E.V. Yakovlev, V.V. Kalaev, I.Y. Evstratov, C. Frank-Rotsch, M. Neubert, P. Rudolph, Global heat and mass transfer in vapor pressure controlled, J. Cryst. Growth 252 (2003) 26–36.

will only provide a good representation of real flows if the flow is in a laminar regime, since turbulence always has a 3D character. For example, VCz growth of GaAs was studied experimentally and by modeling [170]. In this study the melt flow was in the turbulence regime, resulting in much better predictions of interface geometry by 3D modeling than by conventional 2D modeling (Fig. 6.15).

Alternatives include a combined 2D/3D model: the 2D approximation can be used to study the processes in the furnace as a whole, and the 3D model should serve for the analysis of unsteady phenomena in the near-crystallization zone [170].

### Quasisteady state versus transient

The quasisteady state (QSS) assumption is used to simplify the simulations and reduce the number of variables when one part of the system reacts much more quickly (i.e., has a shorter characteristic timescale) than another part. Then only a snapshot of a process is considered; the geometry of the crystal, melt (i.e., s/l interface and free surface), and the boundary condition are considered fixed/constant in time. This assumption has been discussed in detail for Cz Si growth [171,172]. The QSS model failed to predict accurately the operating states when the crystal shape changed appreciably. However, this assumption is valid in, for example, describing Cz growth runs where crystal diameter control is successful.

Industrial 3″ VGF GaAs process using QSS 2D simulations were studied and the results compared with transient 2D simulations and experiments [164]. At a growth rate of 2.5 mm/h the VGF process can be considered as a sequence of quasisteady growth steps (see Fig. 6.16).

### Optimization by inverse modeling versus by artificial neural networks

Optimization of crystal growth processes is aimed at finding optimal heating and cooling profiles for the furnace. In the presence of magnetic fields, it is also necessary to optimize the magnetic parameters to certain growth processes. Up to now, two optimization approaches have been tested in crystal growth: inverse modeling and artificial neural networks (ANNs).

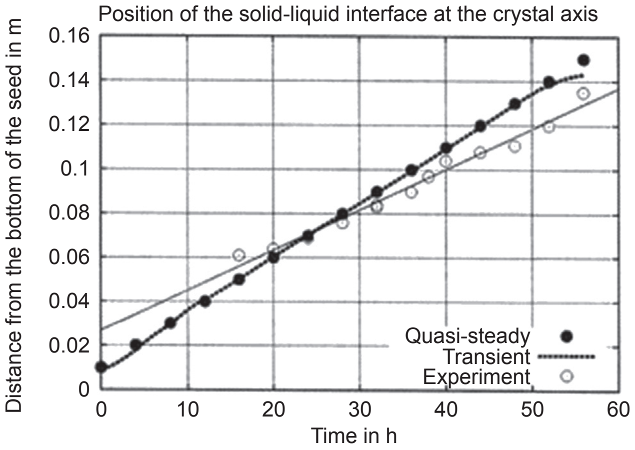

**Figure 6.16** Position of s/l interface in VGF GaAs growth simulated by QSS, by transient model, and by experiment [164].
R. Backofen, M. Kurz, G. Mueller, Process modeling of the industrial VGF growth process using the software package CrysVUN++, J. Cryst. Growth 211 (2000) 202–206.

By using inverse modeling, the power of heaters $p_i$ was adjusted to achieve a given temperature distribution at predefined control points in a growing crystal T → T $(p_1,\ldots,p_n)$. This approach is based on the well-known Newton method for solving nonlinear minimization problems. The algorithm is implemented in CrysVUN software for global thermal simulation of crystal growth processes. The efficiency of inverse modeling is demonstrated by applying it to an industrial 2D 3″ VGF GaAs QSS and transient growth with completely neglected convection in the melt and gas [173,174] (Fig. 6.17).

The strength of this approach is a low computational cost (short computation time). A drawback is a loss of accuracy by neglecting convection in gas and melt. That leads to significant error by pronounced radial T gradients and consequently strong buoyancy in upscaled crucibles (at present the standard is 6″), as well as by higher growth rates (at present the standard is 3–5 mm/h). A comparison with experiments showed an offset of around 20 K for the seeding position [175], which is around a 2% error. By small gradient T = 2 K/cm and short melts the position of the interface was 10 cm shifted, which is a significant error. Nevertheless, the shape of the interface was accurately predicted.

The second optimization approach was applied to magnetic-driven VGF GaAs and DS Si growth [176,177]. It is well known that the s/l interface shape and morphology can be influenced by the change of the flow pattern in the melt with traveling magnetic fields (TMFs). To assess the correlation between the growth and magnetic parameters that enables the optimization of magnetic parameters for interface flattening, static ANNs were proposed (Fig. 6.18(a)). ANN is a statistical method for quick pointwise prediction of unknown functions that can depend on a large number of variables. In two case studies, 2D CFD simulations provided required datasets of inputs $x_i$

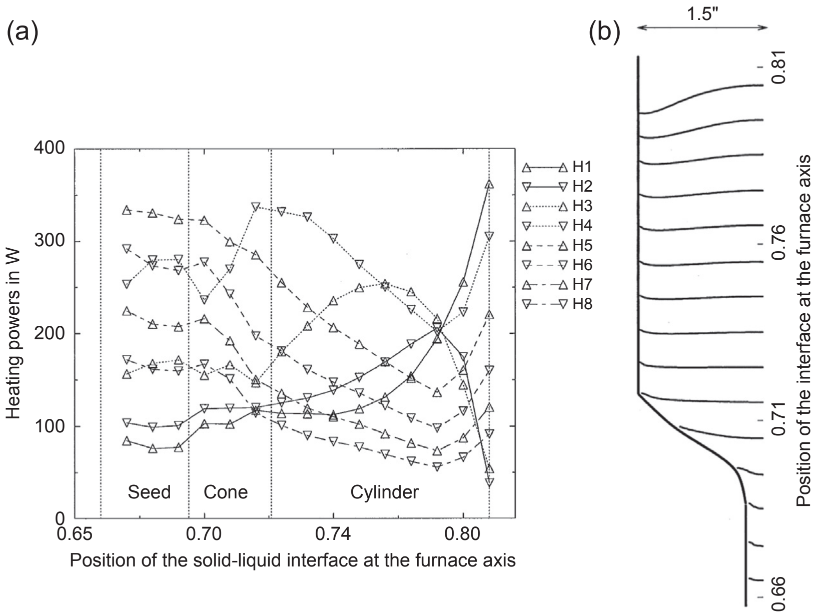

**Figure 6.17** Process optimization of industrial 2D 3″ VGF GaAs by inverse modeling [174]: (a) calculated heating powers in heaters H1−H8 versus position of the s/l interface,
(b) interface shapes during the growth for powers shown in (a).
M. Kurz, G. Müller, Control of thermal conditions during crystal growth by inverse modeling, J. Cryst. Growth 208 (2000) 341−349.

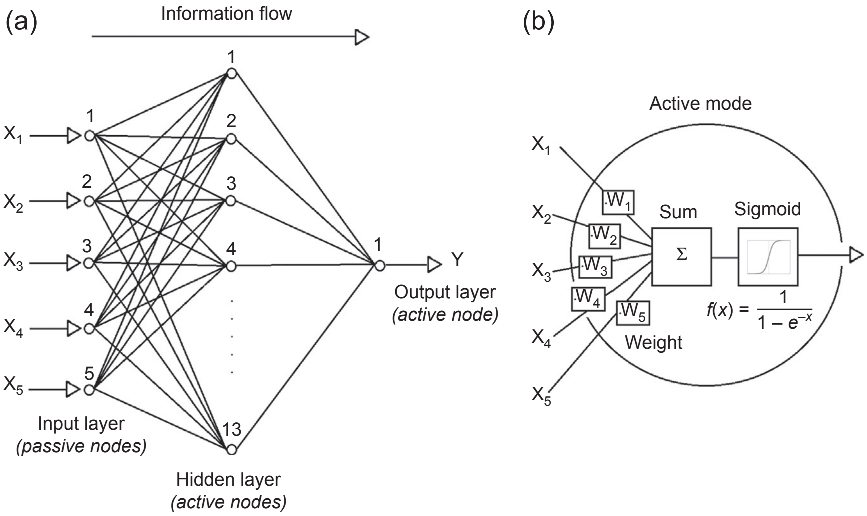
(a)
Information flow
$X_1$
$X_2$
$X_3$
$X_4$
$X_5$
1
2
3
4
5
1
2
3
4
13
1
Y
Input layer
(passive nodes)
Hidden layer
(active nodes)
Output layer
(active node)
(b)
Active mode
$X_1$
$X_2$
$X_3$
$X_4$
$X_5$
$W_1$
$W_2$
$W_3$
$W_4$
$W_5$
Sum
Σ
Sigmoid
$f(x) = \frac{1}{1 - e^{-x}}$
Weight

**Figure 6.18** Architecture and information flow in a static feed forward artificial neural network (a) and one of its node (b).

(frequency, phase shift, ac magnitude, and growth rate) and output y (s/l interface deflection) for derivation of ANN. To be able to use ANN it is first necessary to define the ANN architecture (i.e., the number of nodes, and the structure of their connections that represents information flow). Each node is a computational unit that receives inputs $x_i$, multiplies them by weights $w_i$, and then uses the sum of such weighted inputs as the argument for a sigmoidal function which yields the final outputs $y_i$ (Fig. 6.18(b)). By iteratively adjusting the weights of connections among nodes, one can obtain the targeted outputs $y_i$ for a specific combination of inputs $x_i$. More information about ANN modeling can be found in the literature [178].

In the VGF GaAs case study, the lowest mean square error was obtained for a static ANN architecture with 1 hidden layer and 13 nodes (Fig. 6.18(a)). The results showed that the flat interface can be obtained for various combinations of magnetic parameters if the initial deflection is slightly concave. In contrast, for very concave initial interface no combination of magnetic parameters can flatten the interface. Results are further discussed in Section 6.5.3.4.

Considering the rapid development of dynamic ANN (Fig. 6.19) as an effective method for forecasting time-series events, its application in bulk crystal growth can be expected soon. The most attractive feature of dynamic ANN is that it has memory. Its response at any given time depends not only on the current input but also on the history of the input sequence. Hence dynamic ANNs will be very useful to assess the complex relationships between a growth recipe from one side (i.e., inputs $x_i$)

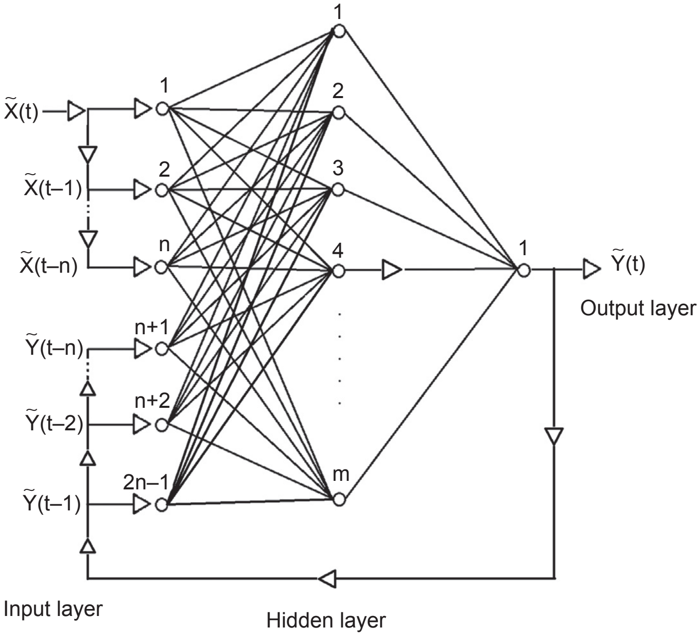

**Figure 6.19** Architecture and information flow in a dynamic recurrent artificial neural network with n time-step delays and m nodes in hidden layer.

and temperature at various control points in a furnace, position of s/l interface, and interface deflection from the other side (i.e., outputs $y_i$). This relationship can be further used to obtain the optimum values of input parameters or to automate and regulate the process.

The comparison of inverse modeling with the ANN method for crystal growth optimization shows the clear superiority of ANN due to its ability to correlate an unlimited number of variables, its ability to work in a stand-alone mode that enables numerous applications in the field of automation and process control, and its high accuracy in predictions. Nevertheless, the quality and number of the datasets used to construct the ANNs are a critical issue. In bulk crystal growth fields the amount and range of data required is nearly impossible to provide experimentally. Fortunately, 2D CFD modeling results verified by available experimental data can be a useful alternative.

### 6.5.3.3 Furnace design

There are presently two main techniques commercially used to grow single-crystalline binary compound semiconductors [112]: LEC and VGF. To limit the scope of this work we focus on the furnace design for these methods for the growth of GaAs. Typical furnace designs are shown in Fig. 6.20.

Common Cz growth of GaAs required complex equipment because of the high vapor pressure of As. Development of a liquid encapsulation technique with $B_2O_3$

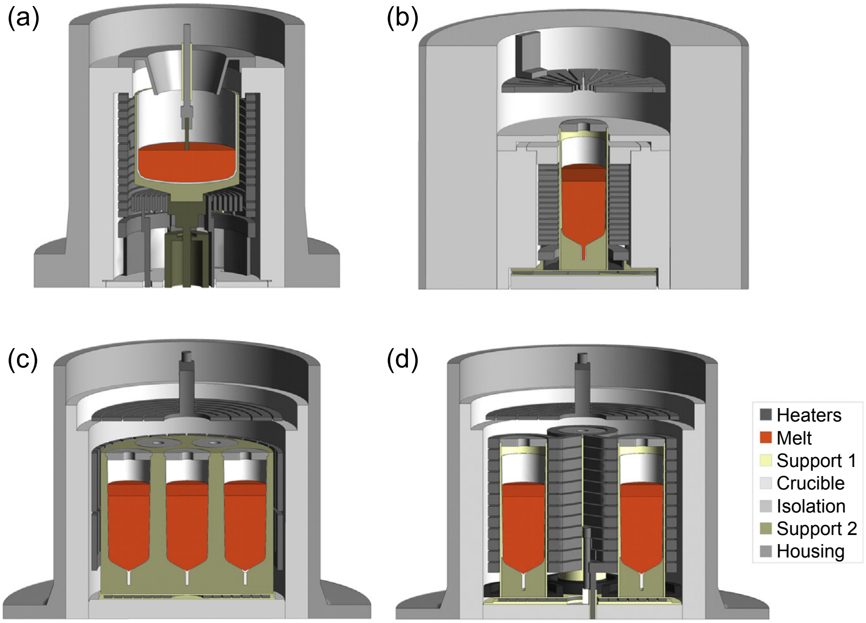

**Figure 6.20** Various furnace designs for (a) Cz growth, (b) TMF-driven VGF growth, (c) multicrucible VGF growth (inspired by [145]) and (d) multicrucible TMF-driven VGF growth (inspired by [150]).

allowed Cz GaAs growth in a commercial silicon crystal puller (Fig. 6.20(a)). GaAs is melted in a pBN rotating crucible surrounded by graphite heaters. A precisely oriented seed crystal mounted on a rod is dipped into the melt. The seed is slowly pulled upwards and rotated. By precisely controlling the temperature gradients and pulling and rotational rates, a cylindrical crystal is extracted from the melt.

In a VGF GaAs furnace (Fig. 6.20(b)), chunks of polycrystalline GaAs are placed in a pBN cylindrical crucible with a seed crystal on the bottom and covered with $B_2O_3$ encapsulant. The crucible is then exposed to an axial temperature gradient that enables first downward melting followed by upward crystal growth. Heat is generated by top, side, and bottom graphite heaters. Further information about the LEC and VGF techniques is given in Section 6.5.2.

Since the first success in growing GaAs by the VGF method in the 1980s [141], this process has reached industrial maturity. Nevertheless, the low productivity of the VGF process remains an issue. One way to enhance the productivity is increasing the number of crucibles. Designs proposed by Freiberger Compound Materials GmbH (FCM) consist of several crucibles arranged side by side with a common graphite heater surrounding them [145] (Fig. 6.20(c)). The s/l interface shape in each melt was solely determined by the cooling program.

In the past decade successful control of the melt flow pattern by magnetic fields boosted further development of VGF GaAs. Increasing the number of crucibles was combined with TMFs [150]. The authors proposed the multicrucible furnace design shown in Fig. 6.20(d). The furnace was equipped with an internal side KRIST*MAG* heater—magnet module with graphite heating coils positioned upon each other; each coil closely encircled four crucibles. Coils are supplied with a combination of DC and out-of-phase AC. Such a design allows the simultaneous generation of heat and TMFs in the melt.

### 6.5.3.4 Modeling examples

A number of examples from the literature and from our research are presented here to illustrate various challenges in the growth of binary compounds and the proposed solutions by numerical modeling that significantly contributed to the success of crystal growth. Typical applications of numerical modeling give a deeper understanding of the growth process and optimize the furnace design and operating parameters to grow high-quality crystals with a high yield. To reach these goals, s/l interface shape during growth has to be flat or slightly convex, melt must be well mixed, and a high crystal growth rate is needed.

#### Geometry optimization

The VGF growth of Si-doped GaAs crystals can be significantly improved by lowering the thermal stress in crystals by optimization of the crucible support design. In particular, the shaping of the cone region and choice of the crucible material can significantly improve the crystal quality [179]. The best results are obtained for a crucible support material with $\lambda = 3$ W/mK and a geometry with a gap of 1 mm between the crucible and the support (Fig. 6.21).

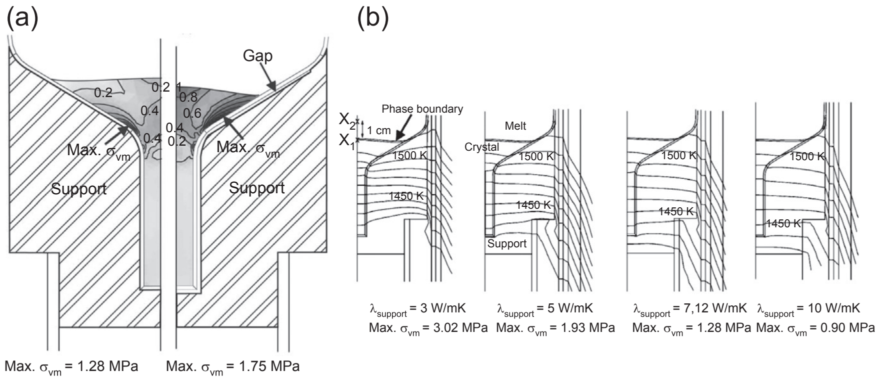
(a)
(b)
Gap
0.2
0.2
0.8
0.4
0.6
0.4
0.4
0.2
Max. $\sigma_{vm}$
Max. $\sigma_{vm}$
Support
Support
Max. $\sigma_{vm}$ = 1.28 MPa
Max. $\sigma_{vm}$ = 1.75 MPa
Phase boundary
$X_2$
$X_1$
1 cm
Melt
Crystal
1500 K
1450 K
Support
$\lambda_{support}$ = 3 W/mK
Max. $\sigma_{vm}$ = 3.02 MPa
$\lambda_{support}$ = 5 W/mK
Max. $\sigma_{vm}$ = 1.93 MPa
$\lambda_{support}$ = 7,12 W/mK
Max. $\sigma_{vm}$ = 1.28 MPa
$\lambda_{support}$ = 10 W/mK
Max. $\sigma_{vm}$ = 0.90 MPa

**Figure 6.21** (a) Von Mises stress and (b) temperature distribution in a crystal and a crucible support for various materials crucible support in VGF GaAs growth [179].
G. Müller, B. Birkmann, Optimization of VGF-growth of GaAs crystals by the aid of numerical modeling, J. Cryst. Growth 237–239 (2002) 1745–1751.

In liquid encapsulated vertical Bridgman crystal growth of GaAs, the ampoule shape, anisotropic properties of the ampoule, and ambient temperature distribution affect growth rate and interface shape [180]. For example, the response time on the growth rate is shorter for a conic-bottom ampoule but longer for a flat-bottom ampoule. However, due to the conic bottom, the former case takes longer for interface deflection to reach a steady state.

## Process optimization

Parameters for the process must be maintained in a narrow range to ensure performance consistency and robustness. The key process parameters are those that, when varied within the characterization range, have a significant impact on crystal growth. Definition of the key parameters strongly depends on the growth method.

For example, in VCz growth of GaAs, the crystal and crucible rotational rates are two of the main factors influencing the transport phenomena in the melt [170]. The heat and momentum transport in the melt are governed by interactions between buoyancy and rotation. An increase in the crystal and crucible rotation rates from 5 to 20 rpm by the growth of a 3-inch crystal caused a transition from a multivortex flow pattern governed mostly by natural convection to a rotationally dominated flow (Fig. 6.22).

In LEC growth of GaAs the argon gas pressure has a strong influence on the consumption of heater power. The s/l interface convexity and the maximum thermal stress (von Mises criterion) are found to increase with increasing gas pressure [181].

In VGF growth of GaAs the simulation showed that the low value of temperature gradients in GaAs enabled growth of high-quality crystals with an extremely low dislocation density. By optimizing the temperature–time program for the nine heaters it was possible to keep temperature gradients low in 3-inch GaAs ($\text{grad}T_l = 2$ K/cm; $\text{grad}T_s = 7$ K/cm) during the whole process [182].

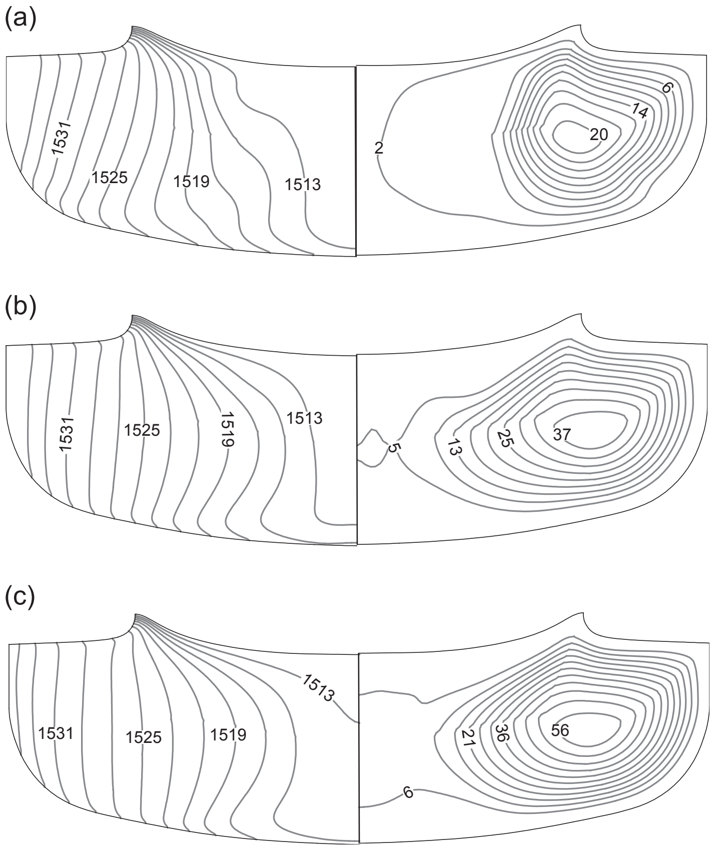

**Figure 6.22** Temperature and dimensionless effective viscosity for various crucible and crystal rotational rates (10−15−20 rpm) in vapor-pressure-controlled Czochralski growth of GaAs crystals [170].
E.V. Yakovlev, V.V. Kalaev, I.Y. Evstratov, C. Frank-Rotsch, M. Neubert, P. Rudolph, Global heat and mass transfer in vapor pressure controlled, J. Cryst. Growth 252 (2003) 26−36.

### Process intensification

The most common approach to increase yield is to intensify the process by scaling up and numbering up the crucibles [145,147,150], and by the use of external fields (e.g., magnetic fields, vibration, and ultrasound [160,183−185]).

The parallel growth of three to nine crystals using FCM multicrucible technology (Figs. 6.20(c) and 6.23(b)) improves the total energy efficiency by a factor of 2.9. The specific energy requirement of the growth process, correlated to the grown wafer surface, can be reduced from 0.2 to 0.05 kWh/cm$^2$ [186]. Besides high energy efficiency, this multicrucible furnace design has one significant drawback: asymmetric heating (i.e., a common heating coil surrounding all crucibles) causes a tilt in temperature distribution in each single melt (Fig. 6.23(a)) that may lead to inhomogeneous doping distributions across the wafers. A better proposed alternative is to use common heating coils that closely encircle each crucible [150](Fig. 6.20(d)).

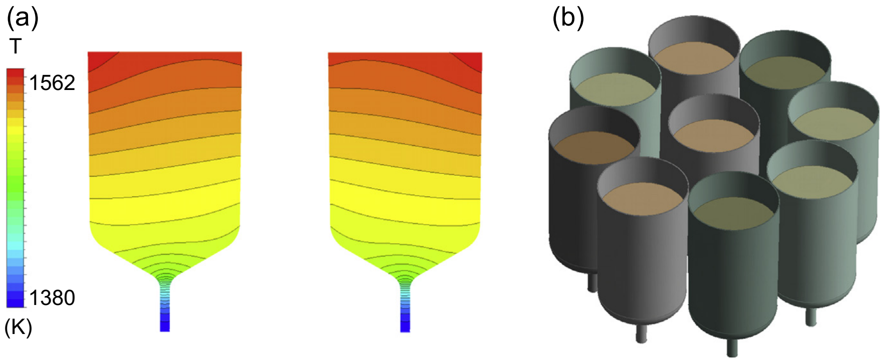

**Figure 6.23** Numbering up in VGF GaAs growth: (a) example of temperature distributions in two opposite GaAs melts/crystals in four-crucible setup, (b) nine-crucible setup.
Based on G. Hirn, BINE Information Service, 13 10 2015. Available: http://www.bine.info/fileadmin/content/Publikationen/Projekt-Infos/2015/Projekt_01-2015/ProjektInfo_0115_engl_internetx.pdf

Scaling up crystal growth processes can be performed with respect to the length and the size of ingots. For bulk crystal growth of Si GaAs, length and size scale-ups are very good by VCz, good by LEC, VGF, and VB, but poor by HB [187]. The influence of ingot length scale-up on the temperature distribution in 4 inch VGF GaAs growth has been studied [150]. The temperature distributions for loads of 7 and 9 kg GaAs are shown in Fig. 6.24. With the progress of the crystallization front (i.e., from left to right in the figure), melt and crystal axial temperature gradients decreased. Because the GaAs crystal has lower heat conductivity than the melt and because of the high latent heat, the heat accumulates in front of the growing s/l interface, promoting its concavity. If the comparison is performed at the same moment of crystallization, an increase in GaAs load will cause an increase in axial temperature gradients and a decrease in growth rate. An adjustment of the cooling program can counteract such a deceleration.

In the last decades numerous studies have been published on the influence of magnetic fields, i.e., Lorentz forces, on the improvement of the s/l interface shape, on melt stirring and growth acceleration for various materials, type of magnetic fields, and growth methods.

Magnetic fields have been gaining attention due to their ability to control the melt flow pattern without contact. In particular, downward TMFs generated in a KRIST*MAG* heater–magnet module [183] in the vicinity of the melt proved to be very efficient in improving the VGF GaAs growth process in various ways [150,160,176,185]. In buoyancy-driven flow without magnetic fields, characteristic temperature and velocity distributions in GaAs melt are shown in Fig. 6.25(a) and (b). The temperature distribution is sliced, the s/l interface shape is concave (Fig. 6.26(a)), and the melt flow pattern is toroidal. Introducing the downward TMF with Lorentz forces shown in Fig. 6.25(c), the melt flow distribution starts changing, particularly near the melt

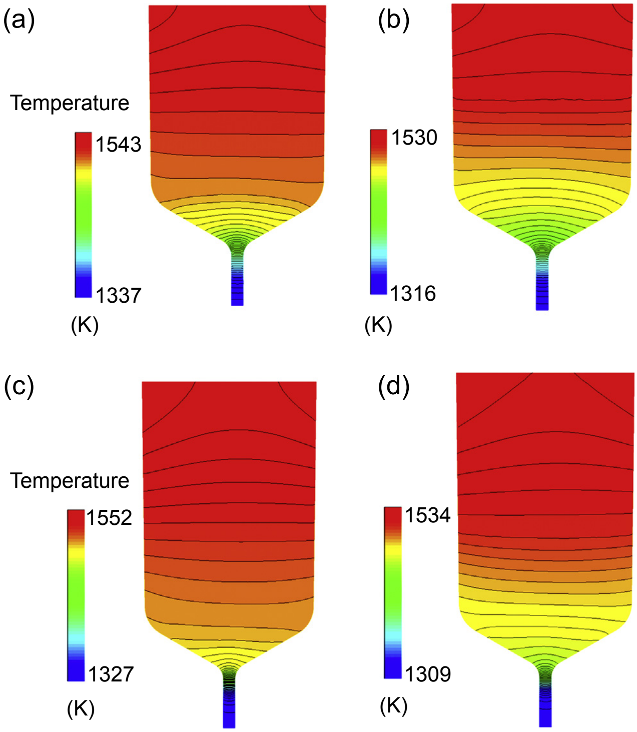

**Figure 6.24** Snapshots of the simulated temperature distributions in 7 and 9 kg of 4-inch VGF GaAs grown using the same cooling program [150].

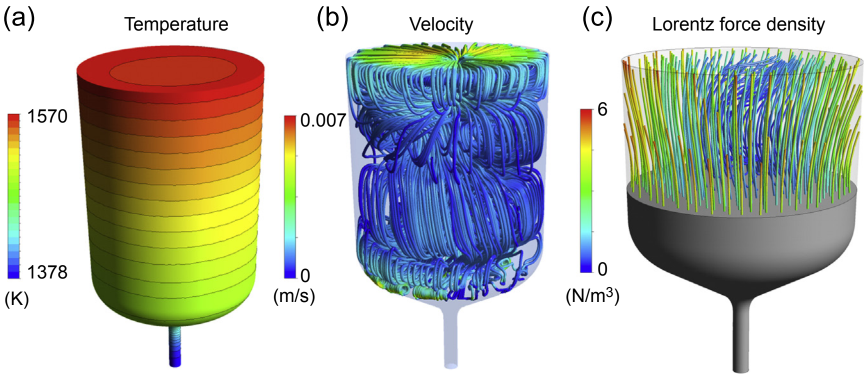
(a)
Temperature
1570
1378
(K)
(b)
Velocity
0.007
0
(m/s)
(c)
Lorentz force density
6
0
(N/m3)

**Figure 6.25** Showcase distributions in VGF GaAs growth: (a) temperature (contours), (b) velocity (streamlines), and (c) Lorentz force density (streamlines).

side rim. As a consequence, the interface shape starts flattening or becomes slightly convex (Fig. 6.26(b)). If the Lorentz forces are too strong relative to buoyancy forces, sliced temperature distribution in the melt may disappear and interface shape becomes too convex or even wavy (Fig. 6.26(c)).

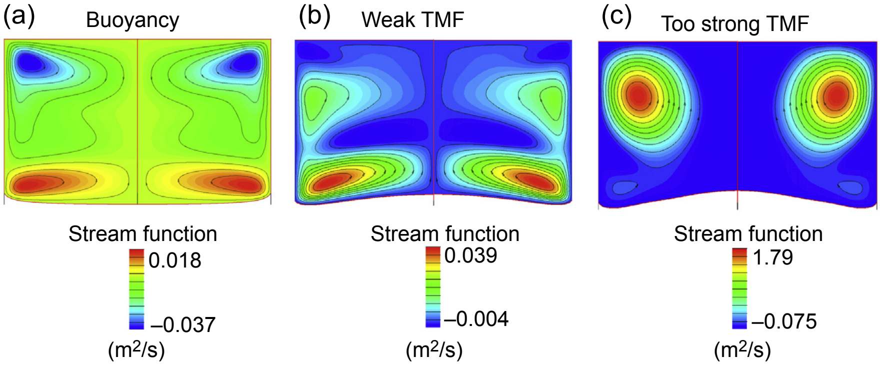

**Figure 6.26** Stream function in VGF GaAs melt: (a) buoyancy and (b) and (c) TMF-driven flows. Results are given for a vertical mid-plane.

The initial deflection of the s/l interface in a buoyancy regime strongly depends on the cooling program, i.e., the dynamic change of power distribution in heaters. The higher the growth rate, the stronger is the concavity of the interface (Fig. 6.27(a)). For success in magnetic stirring and interface shaping, proper adjustments of the TMF intensity and Lorentz force density distribution and direction are necessary. There are several approaches to predict the optimal magnetic parameters for interface flattening in VGF GaAs growth: by dimensionless numbers, and by a combination of ANNs and Gaussian process models. The first approach predicted the maximal improvement of the interface deflection for a combination of dimensionless numbers $F \cdot Gr^{-1}Ste^{-1} = 2.4\text{–}3.1$, as shown in Fig. 6.27(b) [185].

In the second approach ANN assessed the nonlinear dependences among the magnetic and growth parameters from one side and interface deflection from the other side, while Gaussian process offered the probability distribution of ANN predictions for the flat interface (Fig. 6.28, [176]).

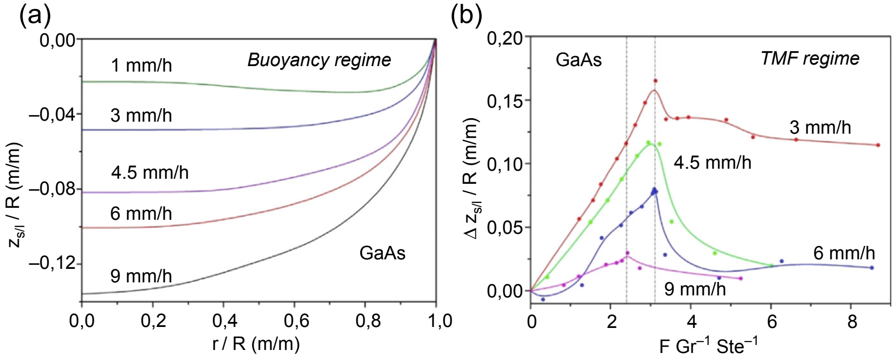

**Figure 6.27** (a) s/l interface shape for buoyancy-driven flows in VGF GaAs growth for various crystal growth rates; (b) relative interface deflection Δz/R as a function of: magnetic forcing F, Grashof Gr and Stefan Ste number. Crystal growth rate varied in the range of 1–9 mm/h [185] and the crystal radius was 2 inches.

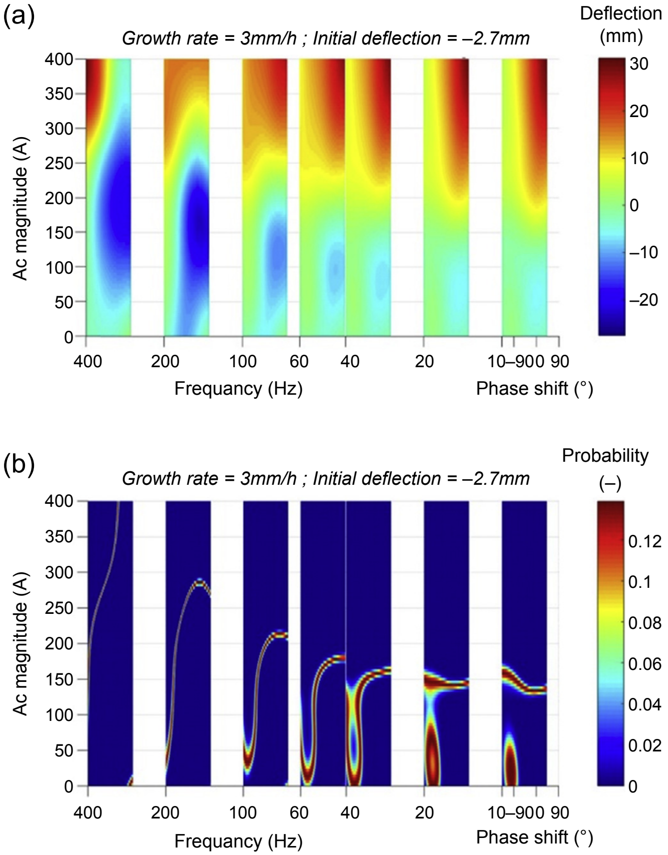

**Figure 6.28** Gaussian process results using ANN basic function for magnetic-driven VGF GaAs growth: (a) mean value of interface deflection Δ and (b) probability distribution for flat interface (deflection < 0.1 mm), as a function of frequency f, phase shift Δϕ, AC magnitude I for specified growth rate $r_{growth}$, and initial buoyancy deflection [176].

The beneficial effects of TMFs in crystal growth can be further improved if two or more TMFs are superimposed on each other. For example, by the superposition of two downward TMFs with frequencies $f_1 = 10$ Hz and $f_2 = 100$ Hz in VGF GaAs growth, the lower frequency with larger skin depth bent the interface up to the melt core, while the larger one had an increasing influence near the crystal edge [149]. The sole use of a low frequency may flatten the initially pronounced concave s/l interface, but with a risk of obtaining a W shape and high thermal stress in the crystal.

Despite the basic rotational symmetry of VGF and Cz furnaces, the asymmetric position of current supplies for the graphite heaters disturbs the azimuthal homogeneity of temperature, Lorentz force, and (if present) dopant concentration distributions. These graphite supplies behave as heat and magnetic field sinks that may provoke polycrystallinity, for example in VGF ingots. The risk may be particularly high if a strong TMF is needed to counteract the strong buoyancy forces in cases of high growth

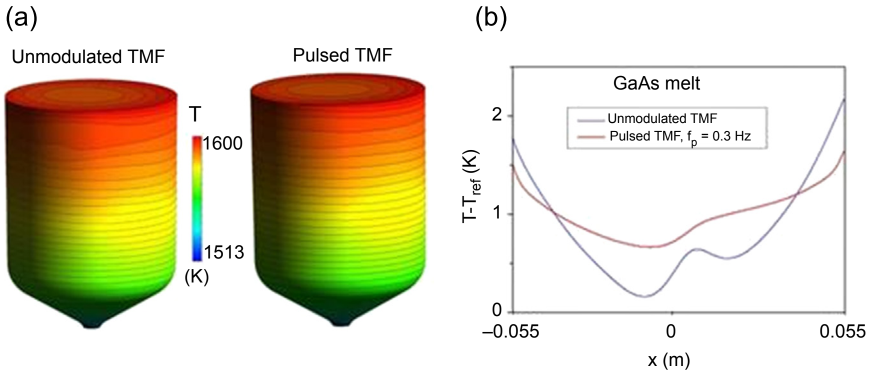

**Figure 6.29** Snapshot of temperature contours (a) and radial temperature profiles (b) in GaAs melt driven by unmodulated and pulsed TMFs with pulse frequency $f_p = .3$ Hz.

rates. The potential of AC magnitude pulsing for enhancement of temperature and Lorentz force density homogeneity in TMF-driven VGF GaAs growth was studied [160]. For sinusoidal AC magnitude modulation with pulse frequency $f_p = .3$ Hz, instability in temperature distribution can be completely suppressed. For higher pulsing frequencies, the melt inertia was too high to follow the fast magnetic pulsing and flow and temperature fields remained unaffected (Fig. 6.29).

### 6.5.3.5 *Conclusions of modeling*

We gave a short overview of transport phenomena characterizing bulk crystal growth of binary compounds, and some representative examples of numerical solutions. Numerical simulation of crystal growth is still a challenging task due to its multidisciplinary nature and the complex geometry of crystal growth furnaces. Its final goal is to relate furnace geometry, properties of construction materials, and process parameters to the process outputs: crystal yield, quality, and production costs. Obtained results should provide information on the velocity, temperature, and concentration fields in the system, thermal stress in the crystals, etc., which usually cannot be measured experimentally or only partially. The ultimate success of numerical modeling depends on the availability and quality of the material data over a wide range of temperatures. Thus numerical simulations are still not an alternative to experiments, but a supplement. Nevertheless, the recent advances in modeling research have had a great impact on process improvements, particularly due to better understanding of the physics behind them. Through numerical simulation and flow visualization, the interplay of transport processes and crystal quality can be better understood, which gives the foundation for the future growth of perfect crystals.

## 6.6 Wafer and sample preparation

The most developed preparation processes are used for GaAs; all technologies for wafer preparation therefore refer to this material. On other hand, requirements using a GaAs specimen are considerably higher than for other compound semiconductors (see Section 6.4). In general, the mechanical processing of the brittle materials is a grinding process, even if it is sometimes described as sawing. The grinding materials are more or less small grains of hard materials like diamond, boron carbide, or silicon carbide. The grains can be fixed in a matrix, typically a metal bond [188], or dispensed in slurry. Fixed grains, for example in surface grinders [189], have the advantage of a well-defined result. For labor safety reasons and to increase the process stability, the grinding process is cooled with an appropriate liquid consisting mostly of water.

The process of wafer production typically starts with a crystal characterization. After a visual inspection at least one sample wafer from the beginning and the end of the crystal are cut to measure the electrical properties (determination of carrier concentration and mobility by Hall measurement). Larger defects like twins, small-angle grain boundaries, and inclusions can be characterized by defect etching, which is also used for determination of EPD. Then the crystals are calibrated by diameter (circular grinding), followed by a careful crystal orientation by X-ray measurement with accuracy below 0.05 degrees.

The most advanced technology for cutting wafers, used for high-volume products, is multiwafer wire sawing. This method combines low cutting losses with high productivity and high wafer flatness. It is possible to cut a whole crystal at once [190]. A similar technology uses diamond wires for one cut, where cut widths down to 100 μm are possible [191,192]. The main steps from crystal to wafer are described in principle in the literature [193−195]. Mechanochemical polishing is one important step to achieve a high-quality surface. The principal approach is to form a thick, soft, reaction product layer consisting of oxides, and to remove the oxide layer by parallel polishing. Hence polishing abrasives of lower hardness then the bulk material and small grain size like colloidal $SiO_2$ can be used. This avoids scratches and subsurface damage in the bulk material and a flat, polished surface is achieved. One possible oxidant is sodium hypochlorite in alkaline solutions; in this case the chemical reaction can be summarized as:

$$2GaAs + 6\,Ocl^- + 3H_2O \rightarrow 2Ga(OH)_3 + As_2O_3 + 6Cl^- \tag{6.15}$$

forming the reaction product layer. During mechanical abrasion of the oxide layer the arsenic trioxide oxidizes to arsenic acid. At the end of the reaction the arsenic is five-valent due to the high redox potential of the chlorine [62, p. 111]. Correctly chosen parameter fields lead to high-quality (100), (111), and $(\overline{111})$ surfaces and reaction product layer thicknesses below 2 nm [126]. Double-sided polishing usually provides better flatness, especially the important local thickness variation, the wafer warp, and the total thickness variation. The final cleaning determines the surface properties. The packaging/storage after final cleaning must protect against moisture, oxygen, and light to avoid light-accelerated growth of an oxide layer. In the case of GaAs the final cleaning steps and packaging should have a quality that allows use of the wafer directly for the epitaxial process.

The surface properties can be changed by a subsequent wet chemical treatment with diluted HCl or other agents toward hydrophobic or hydrophilic characteristic [59] and cleaned by polishing wet etching to prepare for application steps like epitaxy or metallization [196]. Even for a "ready-for-epitaxy" prepared sample, the first step in an epitaxial process has to be a carefully chosen process to remove the natural oxide layer and reconstruct the surface, as described for an MBE [197] or an MOCVD process [198]. During the initial process step in MOCVD a thin, clean oxide layer can removed be $H_2$/$AsH_3$- annealing [199].

## Nomenclature for Chapter 6.5.3

| | |
|---|---|
| **B** | magnetic induction [T] |
| $\mathbf{C_p}$ | heat capacity [J/kg/K] |
| **C** | concentration [$mol/m^3$] |
| **D** | diffusion coefficient [$m^2/s$] |
| **d** | crucible diameter [m] |
| **E** | electrical field [V/m], Young's modulus [Pa] |
| $\mathbf{F_L}$ | Lorentz force density [$N/m^3$] |
| **f** | frequency of AC [Hz] |
| **g** | gravity acceleration [$m/s^2$] |
| **h** | coefficient of heat transfer [$W/(m^2 \cdot K)$] |
| **H** | magnetic field [A/m] |
| $\mathbf{H_A}$ | Henry's constant [$mol/(m^3 \cdot Pa)$] |
| $\mathbf{\Delta H_{s,l}}$ | latent heat [J/kg] |
| **I** | AC magnitude [A] |
| **j** | current density [$A/m^2$] |
| $\mathbf{k_d}$ | mass transfer coefficient [m/s] |
| **L** | characteristic dimension [m] |
| **n** | mass flux [$kg \cdot s^{-1} m^{-2}$] |
| **P** | pressure [Pa] |
| **p** | power [W] |
| **q** | heat flux [$W \cdot m^{-2}$] |
| **r** | rate [m/s], radial coordinate [m] |
| **R** | radius of crucible [m], reaction rate [$mol/(m^3 s)$], gas constant [J/(K mol)] |
| **t** | time [s] |
| **T** | temperature [K] |
| **u** | velocity [m/s] |
| $\mathbf{\Delta z}$ | interface deflection [m] |
| **x,y,z** | coordinate [m] |

## Greek symbols

| | |
|---|---|
| $\boldsymbol{\alpha}$ | thermal diffusivity [$m^2/s$] |
| $\boldsymbol{\beta}$ | thermal expansion coefficient [$K^{-1}$] |

| | |
|---|---|
| $\gamma$ | surface tension [N/m] |
| $\Delta$ | interface deflection [m] |
| $\Delta\phi$ | phase shift [°] |
| $\lambda$ | thermal conductivity [W/m· K] |
| $\mu$ | dynamic viscosity [Pa s], magnetic permeability [H/m] |
| $\nu$ | kinematic viscosity [$m^2/s$] |
| $\rho$ | density [$kg/m^3$] |
| $\sigma_{el}$ | electric conductivity [$AV^{-1}m^{-1}$] |
| $\tau$ | stress [Pa] |

## Subscripts

| | |
|---|---|
| **g** | gas |
| **l** | liquid |
| **m** | melting, magnetic |
| **s** | solid |

## References

[1] H. Welker, H. Weiss, Group III- group V compounds, Solid State Phys. 3 (1956) 1–78.

[2] E.F. Schubert, T. Gessmann, High-efficiency AlGaInP light-emitting diodes for solid-state, J. Appl. Phys. 95 (5) (2004) 2203–2216.

[3] T. Carli, February 13, 2013. Available: www.strategies-u.com http://www.ledsmagazine.com/ugc/2013/02/worldwide-led-component-market-grows-9-with-lighting-ranking-first-among-all-application-segments-ac.html. [Online].

[4] Semiconductor Today, July 21, 2015. Available: www.semiconductor-today.com http://www.semiconductor-today.com/news_items/2015/jul/transparency_210715.shtml. [Online].

[5] E. Higham, Compoundsemiconductor.net," Compound Semiconductor, October 5, 2015. Available: https://compoundsemiconductor.net/article/97973/The_GaAs_revolution. [Online].

[6] Xinxiang Shenzhou Crystal Science and Technology Development Co., Ltd, Shenzhou Crystal Technology Development Co.,Ltd., May 6, 2016. Available: http://www.xxszkj.com http://www.xxszkj.com/eng/productInfo.php?pid=24. [Online].

[7] P. Dutta, Bulk growth of crystals of III-V compound semiconductors, in: Comprehensive Semiconductor Science and Technology, Elsevier, Amsterdam, 2011, pp. 37–78.

[8] O. Oda, Compound Semiconductor Bulk Materials and Characterisations, World scientific publishing Co.Pte.Ltd, Singapore, 2007.

[9] N. Tayebi, K. Benkabou, F.Z. Aoumeur-Benkabou, Predict electronic and structural properties of BxIn1-xAs, Phys. B Condens. Matter 407 (2012) 2739–2743.

[10] I. Vurgaftman, R.J. Meyer, L.R. Ram-Mohan, Band parameters for III–V compound semiconductors and their alloys, J. Appl. Phys. 89 (2001) 5815–5875.

[11] L. Shi, L. Duan, L. Qin, Structural phase transition, electronic and elastic properties in TlX, Comput. Mater. Sci. 50 (1) (2010) 203–210.

[12] L.I. Berger, Semiconductor Materials, CRC Press, Boca Raton, 1997, p. 121.

[13] S. Adachi, GaAs and Related Materials: Bulk Semiconducting and Superlattice Properties, World Scientific, Singapore, 1994, p. 18.

[14] B. El-Kareh, Fundamentals of Semiconductor Processing Technology, New York: Springer Science, 1995, p. 31.

[15] IOFFE. www.ioffe.ru. Available: http://www.ioffe.ru/SVA/NSM/Semicond/InAs/basic.html. [Online].

[16] M. Ettenberg, R.J. Paff, Thermal expansion of AlAs, J. Appl. Phys. 41 (1970) 3926−3927.

[17] M.E. Levinštein, Handbook Series on Semiconductor Parameters, World Scientific, Singapore, 1996, 1, Si, Ge, C (Diamond), GaAs, GaP, GaSb, InAs, InP, InSb.

[18] B. Lv, Y. Lan, X. Wang, Q. Zhang, Y. Hu, A.J. Jacobs, D. Broido, G. Chen, Z. Ren, C.-W. Chu, "Experimental study of the proposed super-thermal-conductor: BAs", Appl. Phys. Lett. (2015), 074105-1-074105-4.

[19] S. Adachi, Properties of Group-IV, III-V and II-VI Semiconductors, Wiley, Hoboken, 2005.

[20] M. Jurisch, S. Eichler, M. Bruder, Vertical Bridgman growth of binary compound semiconductors, in: Handbook of Crystal Growth Vol. II, Elsevier, Amsterdam, 2015, pp. 332−372.

[21] R. Bowers, J. Bauerle, A. Cornish, InAs1-xPx as a thermoelectric material, J. Appl. Phys. 30 (1959) 1050−1054.

[22] K. Kischio, Über Aluminiumarsenid, Z. Anorg. Allg. Chem. 328 (1964) 187−193.

[23] German Social Accident Insurance (DGUV), Gestis Substance Data Base. Available: http://gestis-en.itrust.de/nxt/gateway.dll/gestis_en/000000.xml?f=templates$fn=default.htm$vid=gestiseng:sdbeng$3.0. [Online].

[24] U.S. National Libary of Medicine. https://chem.nlm.nih.gov. Available: https://chem.nlm.nih.gov/chemidplus/name/thallium%20arsenide%20(tlas). [Online].

[25] Thermo Fisher (Kandel) GmbH. www.alfa.com. Available: https://www.alfa.com/de/catalog/012932/. [Online].

[26] A. Cameron, Abundances of the elements in the solar system, Space Sci. Rev. 15 (1970) 121−146.

[27] K. Yanaguchi, Y. Takeda, K. Kameda, K. Itagaki, Measurement of heat of formation of GaP, InP, GaAs, InAs, GaSb and InSb, Mater. Trans. 35 (9) (1994) 596−602.

[28] H. Wenzl, A. Dahlen, A. Fattah, S. Petersen, K. Mika, D. Henkel, Phase relations in GaAs crystal growth, J. Cryst. Growth 109 (1991) 191−204.

[29] S. Hegewald, K. Hein, C. Frank, M. John, E. Buhrig, Investigation on the equilibrium vapour pressure, Cryst. Res. Technol. 29 (1994) 549−554.

[30] R.J. Malik, III-V Semiconductor Materials and Devices, Elsevier, Amsterdam, 1989.

[31] J.A. Perri, S. Laplaca, B. Post, New group III-group V compouns: BP and BAs, Acta Crystallogr. 11 (1958) 310.

[32] Y. Kajikawa, M. Kametani, N. Kobayashi, N. Nishimoto, Y. Yodo, Y. Kitano, Y. Ohtani, Effect of Tl content on the growth of TlGaAs films by low-temperature molecular-beam epitaxy, J. Appl. Phys. 93 (3) (2003) 1409−1416.

[33] H. Gottschalk, G. Patzer, H. Alexander, Stacking fault energy and ionicity of cubic III-V compounds, Phys. Status Solidi A 45 (1978) 207−216.

[34] G. Meduoye, D. Bacon, K. Evans, Computer modelling of temperature and stress distributions in LEC-Grown GaAs crystals, J. Cryst. Growth 108 (1991) 627−636.

[35] M. Ustundag, The first-principles study on physical properties and phase stability of Boron-V (BN, BP, BAs, BSb and BBi) compounds, Comput. Mater. Sci. (January 2014) 471−477.

[36] S. Wang, H. Ye, First-principles study of elastic phase stability of III-V compounds, Phys. Status Solidi B 240 (2003) 45−54.

[37] A. de Bernabe, C. Prieto, L. González, Y. González, A. Every, Elastic constants of InxGa1-xAs and InxGai-xP determined using surface acoustic waves, J. Phys. Condens. Matter 11 (1999) 323–327.

[38] S. Adachi, Handbook on Physical Properties of Semiconductors Vol2 III-v- Semiconductors, Kluwer academic publishers, Boston, 2004.

[39] N.F. Chen, H. He, Y. Wang, L. Lin, Stoichiometric defects in semi-insulating GaAs, J. Cryst. Growth 173 (3–4) (1997) 325–329.

[40] M. Kaminska, M. Skowronski, Imperfections in III-V-materials, in: Semiconductors and Semimetals vol. 38, London Press, Academic, 1993, pp. 59–85.

[41] DIN 50454-1, Prüfung von Materialien für die Halbleitertechnologie; Bestimmung von Versetzungen in Einkristallen von III-V-Verbindungshalbleitern mittels Ätztechnik; Galliumarsenid, Beuth, Berlin, 1991.

[42] J.L. Weyer, J. Van de Ven, Selective etching and photoetching of {100} Gallium arsenide in CrO3-HF aqueous solutions: I. Influence of composition on etching behaviour, J. Cryst. Growth 63 (1983) 285–291.

[43] J.L. Weyer, J. Van der Ven, Selective etching and photoetching of GaAs in CrO3-HF aqueous solutions: III. Interpretation of defect-related etch figures, J. Cryst. Growth 78 (1986) 191–217.

[44] M.S. Abrahams, C.J. Buiocchi, Etching of dislocations on the low-index faces of GaAs, J. Appl. Phys. 36 (9) (1965) 2855–2863.

[45] V.L. Indenbom, Ein Beitrag zur Entstehung von Spannungen, Krist. Tech. 14 (5) (1979) 493–507.

[46] H. Saka, Classical Theory of Cystal Dislocations, World scientific publishing Co. Pte.Ltd, Singapore, 2017.

[47] D. Holt, Defects in the sphalerite structure, J. Phys. Chem. Solids 23 (1962) 1353–1362.

[48] J. Amon, F. Dumke, G. Müller, Influence of the crucible shape on the formation of facets and twins in the growth of GaAs by the vertical gradient freeze technique, J. Cryst. Growth 187 (1998) 1–8.

[49] K. Wasmer, M. Parlinska-Wojtan, R. Gassilloud, C. Pouvreau, J. Tharian, J. Micher, Plastic deformation modes of gallium arsenide in nanoindentation and nanoscratching, Appl. Phys. Lett. 90 (2007) 031902, 1-3.

[50] M. Pourbaix, Atlas d'equilibres Electrochimies, Gouthier-Villars, Paris, 1963.

[51] W. Jiang, S. Lin, C.H. Chang, Z. Ji, B. Sun, X. Wang, R. Li, N. Pon, T. Xia, A.E. Nel, Implications of the differential toxicological effects of III-V ionic and particulate materials for hazard assessment of semiconductor slurries, ACS Nano 9 (12) (2015) 12011–12025.

[52] Freiberger Compound Materials, September 25, 2014. Available: http://www.freiberger.com http://www.freiberger.com/fileadmin/Download/GaAs_kompakt_Produktinfo_deu_Rev_K.pdf. [Online].

[53] H.G. Schneider, Halbleiterepitaxie, Geest & Portig, Leipzig, 1984, pp. 290–321.

[54] A. Lisak, K. Fitzner, Pressure Measurements of arsenic and arsenic trioxide over condensed phases, J. Phase Equil. 15 (2) (1994) 151–154.

[55] R. Speiser, H.J. Johnston, Vapor pressures of inorganic substances. IX. Gallium, J. Am. Chem. Soc. 75 (6) (1952) 1469–1470.

[56] G.B. Stringfellow, Organometallic Vapor-phase Epitaxy: Theory and Practice, Academic Press, San Diego, 1999.

[57] H.J. Scheel, Introduction to liquid phase epitaxy, in: Liquid Phase Epitaxy of Electronic, Optical and Optoelectronic Materials, Wiley & Sons, Chichester UK, 2007, pp. 1–19.

[58] A.W. Vere, Crystal Growth: Principles and Progress, Springer Science, New York, 1987, p. 71.

[59] A. Gocalinska, S. Rubini, E. Pelucchi, Native oxides formation and surface wettability of epitaxial III−V materials: the case of InP and GaAs, Appl. Surf. Sci. 383 (2016) 19−27.

[60] P. Rotsch, Thesis:Untersuchungen zur naßchemischen Ätzung von AiiBV- Verbindungen mit halogenoxidhaltigen Ätzmedien, Humboldt- Universität zu Berlin, Berlin, 1992.

[61] P. Keppel, Thesis:Ein Beitrag zur dreidimensionalen Strukturierung von AIIIBV- Halbleiteroberflächen, Humboldt- Universität zu Berlin, Berlin, 1986.

[62] H. Löwe, P. Keppel, D. Zach, C. Moritz, Halbleiterätzverfahren, Akademie- Verlag, Berlin, 1990.

[63] M. Englhard, B. Reuters, F. Michaelis, M. Behringer, P. Sundgren, C. Klemp, O. Skibitzki, T. Schroeder, A novel vacuum epitaxial lift-off (VELO) process for separation of hard GaAs substrate/carrier systems for a more green semiconductor LED production, Mater. Sci. Semicond. Process. 71 (2017) 389−395.

[64] C. Chen, K.T. Shiu, N. Li, S.J. Han, L. Shi, D.K. Sadana, Epitaxial lift-off process for gallium arsenide substrate reuse and flexible electronics, Nat. Commun. 4 (1577) (2013) 1−7.

[65] E. Niehuis, T. Heller, U. Jürgens, A. Benninghoven, Analysis of surface contaminants on gallium arsenide and silicon by high-resolution time-of-flight secondary ion mass spectrometry, J. Vac. Sci. Technol. B. Microelectron. Process. Phenomena 7 (1989) 512−516.

[66] F. Schröder, W. Storm, M. Altebockwinkel, L. Wiedmann, A. Benninghoven, Analysis of passivating oxide and surface contaminants on GaAs (100) by temperature dependent, J. Vac. Sci. Technol. B Microelectron. Nanometer Struct. Process. 10 (4) (1992) 1291−1296.

[67] S. Pearton, U. Chakrabarti, A. Perley, Ion milling damage in InP and GaAs, J. Appl. Phys. 68 (6) (1990) 2760−2768.

[68] K. Liu, X-m. Ren, Y-q. Huang, S-w. Ca, X-f. Duan, Q. Wang, C. Kang, J-s. Li, J-r. Fei, Inductively coupled plasma etching of GaAs in Cl2/Ar, Cl2/Ar/O2 chemistries with photoresist mask, Appl. Surf. Sci. 356 (2015) 776−779.

[69] Samco, Deep Etching of Compound Semiconductors, September 29, 2011. Available, https://www.samcointl.com/tech_notes/pdf/TechnicalReport_71.pdf. [Online].

[70] P. Chapper, M. Mauk, Liquid Phase Epitaxy of Electronic, Optical and Optoelectronic Materials, John Whiley & Sons Ltd, West Sussex, 2007, p. 410.

[71] Y. Mori, N. Watanabe, C.W. OPERATION OF AlxGa1-xAs/AlyGa1-yAs lasers grown by metalorganic C.V.D. in wavelength range 760−780 nm, Electron. Lett. 16 (8) (1980) 284−285.

[72] M. Humeniuk, H. Obernik, B. Kloth, Wellenlängenselektive pn-Übergangs-Photodiode, 12 04 2000. Germany Patent DE 10019089 C1.

[73] Jenoptik Polymer Systems GmbH, Roithner, December 07, 2015. Available, www.jenoptik.de, https://www.jenoptik.de/-/media/websitedocuments/optics/photodiodes-led/selective-photodiodes.pdf. [Online].

[74] H. Ishiguro, K. Sawa, S. Nagao, H. Yamanaka, S. Koike, High efficient GaAlAs light-emitting diodes of 660 nm with a double heterostructure on a GaAlAs substrate, Appl. Phys. Lett. 43 (1983) 1034.

[75] A. Knauer, H. Wenzel, G. Erbert, B. Sumpf, M. Weyers, Influence of oxygen in AlGaAs-based laser structures with Al-Free active region on device properties, J. Electron. Mater. 30 (11) (2001) 1421−1424.

[76] Yole Development, GaAs wafer market to exceed $650m by 2017, Semicond. Today Compd. Adv. Silicon 7 (3) (2012).

[77] A. Seidl, S. Eichler, T. Flade, M. Jurisch, A. Köhler, U. Kretzer, B. Weinert, 200mm GaAs crystal growth by the temperature gradient, J. Cryst. Growth 225 (2001) 561−565.

[78] J. Stenzenberger, T. Bünger, F. Börner, S. Eichler, T. Flade, R. Hammer, M. Jurisch, U. Kretzer, S. Teichert, B. Weinert, Growth and characterization of 200mm SI GaAs crystals, J. Cryst. Growth 250 (2003) 57−61.

[79] W.-C. Kuo, H.-C. Hsieh, W. Chih-Hung, H. Wen-Hsiang, C.-C. Lee, J.-Y. Chang, High quality GaAs epilayers grown on Si substrate using 100 nm Ge buffer layer, Int. J. Photoenergy (2016), 7218310.

[80] Y.B. Bolkhovityanov, O.P. Pchelyakov, GaAs epitaxy on Si substrates: modern status of research and engineering, Phys. Uspekhi 51 (5) (2008).

[81] M. La Pedus, P. Clarke, Motorola Closes GaAs-on-silicon Wafer Subsidiary, eetimes.com, January 1, 2003. Available: https://www.eetimes.com/document.asp?doc_id=1173746. [Online].

[82] D. Budnitsky, A. Thyazhev, V. Novikov, A. Zarubin, O. Tolbanov, M. Skakunov, E. Hamann, A. Fauler, M. Fiederle, H. Procz, H. Graafsma, S. Rybakov, Chromium-compensated GaAs detector material and sensors, in: 15th International Workshop on Radiation Imaging Detectors, Paris, 2013.

[83] M.C. Veale, S.A. Bell, D.D. Duarte, M.J. French, A. Schneider, P. Seller, M.D. Wilson, A.D. Lozinskaya, V.A. Novikov, O.P. Tolbanov, A. Tyazhev, A.N. Zarubin, Chromium compensated gallium arsenide detectors for X-ray and $\gamma$-ray spectroscopic imaging, Nucl. Instrum. Methods Phys. Res. Sect. A Accel. Spectrom. Detect. Assoc. Equip. 752 (2014) 6−14.

[84] E. Hamann, Thesis:Characterization of High Resistivity GaAs as Sensor Material for Photon Counting Semiconductor Pixel Detectors, Albert-Ludwigs-Universität Freiburg im Breisgau, Freiburg, 2013.

[85] T. Kobayashi, I. Kuru, Development of Gallium Arsenide Gamma Spectrometric Detector, International Atomic Energy Agency (IAEA-R−1393-F, Viena, 1975.

[86] Y.J. Park, T.H. Yeom, I.W. Park, S.H. Choh, S.K. Min, Compensation center of Cr3+ in GaAs codoped with Cr and In for obtaining a semi-insulating property, Solid State Commun. 101 (4) (1997) 219−223.

[87] Teledyne Judson. http://www.teledynejudson.com. Available: http://www.teledynejudson.com/prods/Pages/Indium-Arsenide-Detectors.aspx#. [Online].

[88] M. Brandstetter, M.A. Kainz, T. Zederbauer, M. Krall, S. Schönhuber, H. Detz, W. Schrenk, A.M. Andrews, G. Strasser, K. Unterrainer, InAs based terahertz quantum cascade lasers, Appl. Phys. Lett. 108 (2016) 0111091−0111094.

[89] A. Krier, Mid-infrared Semiconductor Optoelectronics, Springer Verlag London Ltd, London, 2006.

[90] Wafer technology Ltd. http://www.wafertech.co.uk/_downloads/Indium-Arsenide.pdf. [Online].

[91] XIAMEN, January 16, 2016. Available: www.powerwaywafer.com http://www.powerwaywafer.com/InAs-wafer.html. [Online].

[92] Semiconductor wafer inc. www.semiwafer.com. Available: http://www.semiwafer.com/inas%20wafer.html. [Online].

[93] C. Friedheim, F. Peters, Gmelin Kraut's Handbuch der anorgaischen Chemie Band IV Abteilung 1, Carl Winters Universitätsbuchhandlung, Heidelberg, 1910.

[94] G. Booker, J. Titchmarsh, J. Fletcher, D. Darby, M. Hockly, M. Al-jassim, Nature, origin and effect of dislocations in epitaxial semiconductor layers, J. Cryst. growth 45 (1974) 407−425.

[95] J.M. Parsey, Y. Nanishi, J. Lagowski, H.C. Gatos, Bridgman-type apparatus for the study of growth-property relationships: arsenic vapor pressure-GaAs property relationship, J. Electrochem. Soc. 129 (2) (1982) 388−393.

[96] C. Frank-Rotsch, U. Juda, F.M. Kiessling, P. Rudolph, Dislocation patterning during crystal growth of semiconductor compounds (GaAs), Mater. Sci. Technol. 21 (12) (2005) 1450−1454.

[97] H.D. Geiler, H. Karge, M. Wagner, S. Eichler, M. Jurisch, U. Kretzer, M. Scheffer-Czygan, Photoelastic characterization of residual stress in GaAs-wafers, Mater. Sci. Semicond. Process. 9 (2006) 345−350.

[98] B. Birkmann, J. Stenzenberger, M. Jurisch, J. Härtwig, V. Alex, G. Müller, Investigation of residual dislocations in VGF-grown Si-doped GaAs, J. Cryst. Growth 276 (2005) 335−346.

[99] M. Baeumler, M. Maier, N. Herres, T. Bünger, J. Stenzenberger, W. Jantz, 2K PL topography of silicon doped VGF GaAs wafers, Mater. Sci. Eng. B 91−92 (2002) 16−20.

[100] K. Sonnenberg, A. Altmann, Variation of free charge carrier concentration in doped GaAs studied by phase microscopy, Mater. Sci. Eng. B 28 (1−3) (1994) 481−484.

[101] T. Steinegger, M. Naumann, M. Jurisch, J. Donecker, Recipitate engineering in GaAs studied by laser scattering tomography, Mater. Sci. Eng. B 80 (2001) 215−219.

[102] H. Beneking, Halbleiter-Technologie: Eine Einführung in die Prozeßtechnik von Silizium und III-V-Verbindungen, Teubner Verlag, Stuttgart, 1991.

[103] L.J. van der Pauw, A method of measurement the resistivity and hall coefficient on lamellae of arbitrary shape, Philips Tech. Rev. 26 (1958/59) 220−224.

[104] E.H. Puthley, The Hall Effect and Semi-conductor Physics, Dover Publications, New York, 1960.

[105] U. Kretzer, Thesis:Punktdefekte und elektrische Kompensation in Galliumarsenid-Einkristallen, Technischen Universität Chemnitz, Chemnitz, 2006.

[106] D.J. Chadi, Arsenic-antisite defect in GaAs: multiplicity of charge and spin states, Phys. Rev. B 68 (2003) 93204 (1-4).

[107] W. Walukiewicz, J. Lagowski, H.C. Gatos, On the optical evaluation of the EL2 deep level concentration in semi-insulating GaAs, Appl. Phys. Lett. 43 (2) (1983) 192−194.

[108] L. Hrivnák, SEMI-insulating GaAs, Czech. J. Phys. B 34 (5) (1984) 436−444.

[109] C. Frank, K. Hein, C. Hannig, G. Gärtner, Growth of GaAs Crystals by VGF at different as source temperatures, Cryst. Res. Technol. 31 (1996) 753−761.

[110] T. Flade, M. Jurisch, A. Kleinwechter, A. Köhler, U. Kretzer, J. Prause, T. Reinhold, B. Weinert, State of the art 6A SI GaAs wafers made of conventionally grown LEC-crystals, J. Cryst. Growth 198/199 (1999) 336−342.

[111] G.M. Martin, J.P. Farges, G. Jacob, J.P. Hallais, G. Poiblaud, Compensation mechanisms in GaAs, J. Appl. Phys. 51 (1980) 2840−2852.

[112] M. Jurisch, F. Börner, T. Bünger, S. Eichler, T. Flade, U. Kretzer, A. Köhler, J. Stenzenberger, B. Weinert, LEC-and VGF-growth of SI GaAs single crystals - recent developments and current issues, J. Cryst. Growth 275 (2005) 283−291.

[113] M. Skowronski, Oxygen related point defects in GaAs, Mater. Sci. Forum 83−87 (1992) 377−388.

[114] C. Frank, Thesis: Züchtung undotierter VGF-GaAs-Kristalle unter besonderer Berücksichtigung der Einstellung halbisolierender Eigenschaften, TU Bergakademie, Freiberg, 1992.

[115] D. Hurle, Solubility and point defect dopant interactions in GaAs I tellurium doping, J. Phys. Chem. Solids 40 (8) (1979) 627−637.

[116] P.D. Greene, Growth of GaAs ingots with high free electron concentrations, J. Cryst. Growth 50 (3) (1980) 612−618.

[117] R. Newman, The lattice locations of silicon impurities in GaAs:effects due to stoichiometry, the Fermi energy, the solubility limit and DX behaviour, Semicond. Sci. Technol. 9 (1994) 1749−1762.

[118] U. Kretzer, F. Börner, T. Bünger, S. Eichler, Influence of boron on the point defect equilibrium in highly n-doped gallium arsenide single crystals, Phys. B Condens. Matter 401−402 (2007) 246−249.

[119] Freiberger Compound Materials, 150 Mm SI VGF, November 27, 2013. Available: http://www.freiberger.com/produkte/gaas-wafer/spezifikationen.html. [Online].

[120] Corning Tropel Corporation, Tropel® FlatMaster® MSP Wafer Surface Metrology System, October 28, 2013. Available: http://www.corning.com/media/worldwide/csm/documents/2FEBC293-D9FB-4C9C-9D6C-B7EBC2A8B916.pdf. [Online].

[121] D. Schneider, R. Hammer, M. Jurisch, "Non-destructive testing of damage layers in GaAs wafers by surface acoustic waves, Semicond. Sci. Technol. 14 (1999) 93−99.

[122] H. Höche, J. Schreiber, Anisotropic deformation behaviour of GaAs, Phys. Status Solidi A 86 (1984) 229−236.

[123] K. Sankaranarayanan, R. Sumathi, M. Udhayasa, New etchant to reveal the subsurface damage on polished gallium arsenide substrates, J. Cryst. Growth 178 (1997) 229−232.

[124] F. Orazio, Subsurface Damage Characterization Laboratory, University of Dayton, 2017. Available: https://www.udri.udayton.edu/EnergyTechnologiesAndMaterials/AdvancedHighTemperatureMaterials/Pages/SubsurfaceDamageCharacterizationLaboratory.aspx. [Online].

[125] KLA Tencor, Surfscan 6420- Unpatterned Surface Inspection System, February 2, 2005. Available: https://www.kla-tencor.com/Certified-Used-Equipment/surfscan6420.html. [Online].

[126] T. Ookawa, T. Nishiguchi, Improvement of pad life in mirror polishing for GaAs wafers, JSME Int. J. 1 (47) (2004) 98−104.

[127] VLSI Standards, Inc, Absolute Contamination, January 16, 2017. Available: http://www.vlsistandards.com/pdf/products/Contamination/ACS.pdf. [Online].

[128] H-Square Corporation, Photomask Handling, H-Square Corporation, 2017. Available: http://www.h-square.com/A_Photomask_Handling.html. [Online].

[129] I. Mowat, P. Lindley, L. McCaig, A correlation of TOF-SIMS and TXRF for the analysis of trace metal contamination on silicon and gallium arsenide, Appl. Surf. Sci. 203−204 (2003) 495−499.

[130] H. Immenroth, U. Lambert, E. Tomzig, Advanced arsenic purification and GaAs synthesis for improved reproducible growth of undoped semi-insulating GaAs, J. Cryst. Growth 142 (1994) 37−48.

[131] K. Hein, C. Frank, Theoretische Grundlagen und Anwendungen zur Einkristallzüchtung von Galliumarsenid, TU Bergakademie, Freiberg, 1993.

[132] E. Bourret, E. Merk, Effects of total liquid encapsulation on the characteristics of GaAs single crystals grown by the vertical gradient freeze technique, J. Cryst. Growth 110 (1991) 395−404.

[133] J. Korb, T. Flade, A. Köhler, T. Reinhold, B. Weinert, Carbon, oxygen, boron, hydrogen and nitrogen in the LEC growth of SI GaAs: a thermochemical approach, J. Cryst. Growth 198−199 (1999) 343−348.

[134] K.T. Wilke, J. Bohm, Kristallzüchtung, VEB Deutscher Verlag der Wissenschaften, Berlin, 1988.

[135] J.B. Mullin, B.W. Straughhan, W.S. Brickell, Liquid encapsulation techniques: the use of an inert liquid in suppressing dissociation during the melt-growth of InAs and GaAs crystals, J. Phys. Chem. Solids 26 (4) (1965) 782−784.

[136] J. Nihio, H. Fujita, Ambient gas constituents and segregation of carbon and boron in LEC GaAs single crystals: the role of water in boric oxide encapsulants, J. Cryst. Growth 134 (1993) 97−104.

[137] S. Eichler, F. Börner, T. Bünger, M. Jurisch, A. Köhler, U. Kretzer, M. Scheffer-Czygan, B. Weinert, T. Flade, Recent progress in GaAs growth technologies at Freiberger, in: Crystal Growth Technology: From Fundamentals and Simulation to Large-scale Production, Wiley-VCH Verlag GmbH & Co. KGaA, Weinheim, Germany, 2008, pp. 231−264.

[138] P. Rudolph, M. Jurisch, Bulk growth of GaAs an overview, J. Cryst. Growth 198/199 (1999) 325−335.

[139] M. Neubert, P. Rudolph, Growth of semi-insulating GaAs crystals in low temperature gradients by using the vapour pressure controlled Czochralski method, Prog. Cryst. Growth Char. Mater. (2001) 119−185.

[140] P. Rudolph, M. Czupalla, B. Lux, LEC growth of semi-insulating GaAs crystals in traveling magnetic field, J. Cryst. Growth 311 (2009) 4543−4548.

[141] W.A. Gault, E. Monberg, J.E. Clemans, A novel application of the vertical gradient freeze method to the growth of high quality III−V crystals, J. Cryst. Growth 74 (3) (1986) 491−506.

[142] C. Frank, K. Hein, Growth of semiinsulating GaAs crystals, Cryst. Res. Technol. 30 (1995) 897−909.

[143] A.W. Moore, Einsatz von pyrolytischem Bornitrid bei der Verarbeitung von Halbleiterwerkstoffen, in: Technische Keramische Werkstoffe, Deutscher Wirtschaftsdienst, Köln, 1991, 8.2.2.1 (1-22).

[144] R. Naeven, GaAs-Einkristallzucht mit totaler Flüssigeinkapselung im vertikalen Bridgman Verfahren (Dissertation RWTH, Aachen), 1993.

[145] S. Eichler, T. Bünger, M. Butter, R. Rühmann, M. Scheffer-Czygan, Arrangement and Method for Producing a Crystal from the Melt of a Raw Material and Monocrystal, 06 03 2013. Patent EP2106465 B1.

[146] M. Althaus, K. Sonnenberg, E. Küssel, R. Naeven, "Some new design features for vertical Bridgman furnaces and the investigation of small angle grain boundaries developed during VB growth of GaAs, J. Cryst. Growth 166 (1) (1996) 566−571.

[147] M. Jin, H. Shen, S. Fan, Q. He, J. Xu, Industrial growth and characterization of Si-doped GaAs crystal, Cryst. Res. Technol. 52 (6) (2017) 1700052 (1-7).

[148] G. Roewer, E. Buhrig, 50 Jahre Halbleitermaterialien in der Region Freiberg, in: Zeitschrift für Freunde und Förderer der TU Bergakademie Freiberg, 2007, pp. 49−62.

[149] C. Frank-Rotsch, N. Dropka, A. Glacki, U. Juda, VGF growth of GaAs utilizing heater-magnet module, J. Cryst. Growth 401 (2014) 702−707.

[150] N. Dropka, A. Glacki, C. Frank-Rotsch, GaAs-vertical gradient freeze process intensification, Cryst. Growth Des. 386 (2014) 146−153.

[151] C.W. Lan, Recent progress of crystal growth modeling and growth control, Chem. Eng. Sci. 59 (2004) 1437−1445.

[152] G. Young, Thermal stress analysis of crystal growth in a horizontal Bridgman furnace, J. Cryst. Growth 171 (1997) 361−372.

[153] A.S. Jordan, Estimated thermal diffusivity, Prandtl number and Grashof number of molten GaAs, InP, and GaSb, J. Cryst. Growth 71 (1985) 551−558.

[154] O. Klein, C. Lechner, P.E. Druet, P. Philip, J. Spreckels, C. Frank-Rotsch, F.M. Kießling, W. Miller, U. Rehse, P. Rudolph, Numerical simulation of Czochralski crystal growth under the influence of a traveling magnetic field generated by an internal heater-magnet module (HMM), J. Cryst. Growth 326 (1−2) (2008) 27−37.

[155] S.X. Chen, M. Li, Flow instability of buoyant-Marangoni convection in the LEC GaAs melt, Sci. China E Technol. Sci. 51 (2008) 397−406.

[156] V.I. Polezhaev, Modeling of technologically important hydrodynamics and heat/mass transfer processes during crystal growth, in: Crystal growth Technology, John Wiley & Sons, Weinheim, 2004, pp. 155−186.

[157] V.I. Polezhaev, Convective interaction and instabilities in GaAs Czochralski model, J. Cryst. Growth 230 (2001) 40−47.

[158] J.S. Walker, D. Henry, H. BenHadid, Magnetic stabilization of the buoyant convection in the liquid-encapsulated Czochralski process, J. Cryst. Growth 243 (2002) 108−116.

[159] J. Friedrich, Yield improvement and defect control in Bridgman-type crystal growth with the aid of thermal modeling, in: Crystal Growth Technology: From Fundamentals and Simulation to Large-scale Production, Wiley-VCH Verlag GmbH & Co, Weinheim, 2008, pp. 138−172.

[160] N. Dropka, C. Frank-Rotsch, Enhanced VGF-GaAs growth using pulsed unidirectional TMF, J. Cryst. Growth 386 (2014) 146−153.

[161] G. Müller, B. Fischer, Optimization of melt growth processes by experimental analysis and computer modeling, in: Advances in Crystal Growth Research, Elsevier, Amsterdam, 2001, pp. 167−190.

[162] Femag, Available: http://www.meca.ucl.ac.be/femag. [Online].

[163] CapeSym, Available: http://www.capesym.com/index.html. [Online].

[164] R. Backofen, M. Kurz, G. Mueller, Process modeling of the industrial VGF growth process using the software package CrysVUN++, J. Cryst. Growth 211 (2000) 202−206.

[165] Comsol, Available: https://www.comsol.com/. [Online].

[166] STR, Available: http://www.semitech.us/products/. [Online].

[167] Crosslight, Available: http://www.crosslight.com. [Online].

[168] M. Hainke, T. Jung, J. Friedrich, B. Fischer, M. Metzger, G. Müller, Equipment and process modelling of industrial crystal growth using the finite volume codes CrysVUn and Sthamas, in: Progress in Industrial Mathematics at ECMI 2000. Mathematics in Industry (The European Consortium for Mathematics in Industry) vol. 1, Springer, Berlin, Heidelberg, 2002, pp. 218−222.

[169] A. Yeckel, J.J. Derby, Computer modeling of bulk crystal growth, in: Bulk Crystal Growth of Electronic, Optical and Optoelectronic Materials, John Wiley & Sons, Weinheim, 2005, pp. 73−119.

[170] E.V. Yakovlev, V.V. Kalaev, I.Y. Evstratov, C. Frank-Rotsch, M. Neubert, P. Rudolph, Global heat and mass transfer in vapor pressure controlled, J. Cryst. Growth 252 (2003) 26−36.

[171] J.J. Derby, R.A. Brown, On the quasi-steady-state assumption in modeling Czochralski crystal growth, J. Cryst. Growth 87 (1988) 251−260.

[172] G. Müller, J. Friedrich, J. Cryst. Growth 266 (2004) 1−19.

[173] M. Metzger, Optimal control of crystal growth processes, J. Cryst. Growth 211 (2001) 210−216.

[174] M. Kurz, G. Müller, Control of thermal conditions during crystal growth by inverse modeling, J. Cryst. Growth 208 (2000) 341−349.

[175] B. Birkmann, M. Rasp, J. Stenzenberger, G. Müller, Growth of 3″ and 4″ gallium arsenide crystals by the vertical gradient freeze (VGF) method, J. Cryst. Growth 211 (1−4) (2000) 157−162. http://www.sciencedirect.com/science/journal/00220248.

[176] N. Dropka, M. Holena, C. Frank-Rotsch, TMF optimization in VGF crystal growth of GaAs by artificial neural networks and gaussian process models, in: Proceedings of XVIII International UIE-Congress on Electrotechnologies for Material Processing, 2017, pp. 203−208.

[177] N. Dropka, M. Holena, Optimization of magnetically driven directional solidification of silicon using artificial neural networks and Gaussian process models, J. Cryst. Growth 471 (2017) 53−61.

[178] R. Rojas, Neural Networks: A Systematic Introduction, Springer, Berlin, 1996.

[179] G. Müller, B. Birkmann, Optimization of VGF-growth of GaAs crystals by the aid of numerical modeling, J. Cryst. Growth 237−239 (2002) 1745−1751.

[180] C.W. Lan, C.C. Ting, Numerical investigation on the batch characteristics of liquid encapsulated vertical Bridgman crystal growth, J. Cryst. Growth 149 (1995) 175−186.

[181] J. Fainberg, H.J. Leister, G. Müller, Numerical simulation of the LEC-growth of GaAs crystals with account of high-pressure gas convection, J. Cryst. Growth 180 (1997) 517−523.

[182] J. Amon, P. Berwian, G. Müller, Computer-assisted growth of low-EPD GaAs with 3″ diameter by the vertical gradient-freeze technique, J. Cryst. Growth 198/199 (1999) 361−366.

[183] P. Rudolph, Travelling magnetic fields applied to bulk crystal growth from the melt: the step from basic research to industrial scale, J. Cryst. Growth 310 (2008) 1298−1306.

[184] G.N. Kozhemyakin, V.G. Kosushkin, S.Y. Kurochkin, Growth of Ga−As crystals pulled under the presence of ultrasonic vibrations, J. Cryst. Growth 121 (1992) 240−242.

[185] N. Dropka, C. Frank-Rotsch, Accelerated VGF-crystal growth of GaAs under traveling magnetic fields, J. Cryst. Growth 367 (2013) 1−7.

[186] G. Hirn, BINE Information Service, October 13, 2015. Available: http://www.bine.info/fileadmin/content/Publikationen/Projekt-Infos/2015/Projekt_01-2015/ProjektInfo_0115_engl_internetx.pdf. [Online].

[187] R. Szweda, Gallium Arsenide, Electronics Materials and Devices. A Strategic Study of Markets, Technologies and Companies Worldwide 1999−2004, Elsevier, Amsterdam, 2000.

[188] Advanced dicing technologies, Hub Blade Brochure_4web, 2014. Available: http://www.adt-co.com/ADT2014/userdata/SendFile.asp?DBID=1&LNGID=1&GID=1804. [Online].

[189] Disco High Tec, Automatic Surface Grinder DAG 810, April 26, 2016. Available: https://www.disco.co.jp/eg/products/catalog/pdf/dag810.pdf. [Online].

[190] R. Hammer, F. Bergner, T. Flade, M. Jurisch, A. Kleinwechter, Material-related fundamentals of cutting techniques for GaAs wafer manufacturing, Z. Metallkd 96 (7) (2005) 785−791.

[191] Diamond WireTec GmbH & Co.KG, Overview of Diamond Wire Saws. Available: https://www.diamondwiretec.com/wire-saws/overview. [Online].

[192] Well Diamantdrahtsägen GmbH, Produktübersicht Diamantdrahtsägen. Available: http://www.well-deutschland.de/produkte/. [Online].

[193] Freiberger Compound Materials GmbH, Freiberger Compound Materials- Technology. Available: http://www.freiberger.com/en/technology.html. [Online].

[194] Logitech ltd, Gallium Arsenide, July 9, 2015. Available: http://logitech.uk.com/wp-content/uploads/GaAs-Whitepaper-03.pdf. [Online].

[195] Rice University/OpenStax CNX, Formation of Silicon and Gallium Arsenide Wafers. Available: https://archive.cnx.org/contents/ecf00d82-a47a-47fd-8980-207a74c9f4a9@5/formation-of-silicon-and-gallium-arsenide-wafers#eip-367. [Online].

[196] D. Sadowska, A. Gladki, K. Mazur, E. Talik, Optimisation of the epi-ready semi-insulating GaAs wafer preparation procedure, Vacuum 72 (2004) 217−223.

[197] A. Guillén-Cervantes, Z. Rivera-Alvarez, M.M. López-López, E. López-Luna, I. Hernández-Calderón, GaAs surface oxide desorption by annealing in ultra high vacuum, Thin Solid Films 373 (2000) 159−163.

[198] D.A. Allwood, N.J. Mason, P.J. Walker, In situ characterisation of MOVPE by surface photoabsorption I. Substrate oxide desorption, J. Cryst. Growth 195 (1998) 163−167.

[199] M. Englhard, C. Klemp, M. Behringer, A. Rudolph, O. Skibitzki, P. Zaumseil, T. Schroeder, Characterization of reclaimed GaAs substrates and investigation of reuse for thin film InGaAlP LED epitaxial growth, J. Appl. Phys. 120 (2016) 045301.

# Indium phosphide

# 7

*David F. Bliss*[1], *Roberto Fornari*[2]
[1]United States Air Force Research Laboratory, Retired, MA, United States; [2]University of Parma, Parma, Italy

## 7.1 Applications and requirements of indium phosphide

Indium phosphide (InP), because of its physical and electrical properties, is especially suited for applications combining optoelectronics with high-speed electronics. The revolution in optical fiber telecommunications relies significantly on large-diameter substrates of InP because of these properties. Table 7.1 lists some of the important properties at room temperature that make InP an attractive substrate for optoelectronic devices:

Crystallizing in the sphalerite structure, InP has a lattice parameter coinciding with the ternary and quaternary alloys required for laser transmission through the 1.3 and 1.5 μm wavelength windows in optical fiber. For example, InP has become the substrate of choice for lattice-matched growth of ternary GaInAs, and InAlAs and quaternary GaInAsP and AlGaInAs. Heterostructure devices based on these and other alloys have also produced transistors with high operating speeds, low noise, low threshold voltage, and high reliability. As the industry moves to introduce optical devices with speeds in excess of 40 Gbits/s, there is a strong driving force for development of InP crystal growth.

Typical applications for InP photonic devices include lasers, photodetectors, avalanche photo diodes, optical modulators and amplifiers, waveguide-based devices, quantum photonic devices, and both optoelectronic and photonic integrated circuits, as well as new devices for optical communications, switching, networking, and signal processing.

Many optoelectronic applications operating at speeds of 40 Gbits/s and above require compatibility with InP-based optical devices. Thus InP-based high-electron mobility transistors offer a solution to low-noise operation at such speeds. Future generations of fiberoptic transmission systems such as passive optical networks and cloud data connectivity will require speeds of 80 Gbits/s and above, where InP heterojunction bipolar transistors have a commercial niche. As 6-inch diameter InP technology becomes available, these substrates have the capacity to meet the stringent requirements of 5G wireless technology.

The availability of such promising devices that operate at high frequencies and emit light at infrared wavelengths depends on the development of high-quality bulk crystals with uniform properties and homogeneous distribution of defects. The control over defects is in fact the means of exploiting all the useful electrical and optical properties

**Single Crystals of Electronic Materials.** https://doi.org/10.1016/B978-0-08-102096-8.00007-0
Copyright © 2019 Elsevier Ltd. All rights reserved.

**Table 7.1** **Room-temperature properties of InP**

| Crystal structure | | Sphalerite |
|---|---|---|
| Lattice constant | Å | 5.86 |
| Energy gap | eV | 1.35 |
| Density | g/cm$^3$ | 4.79 |
| Bulk modulus | dyn/cm$^2$ | $7.1 \times 10^{11}$ |
| Thermal conductivity | W/cm-°K | 0.68 |
| Thermal expansion coefficient | K$^{-1}$ | $4.6 \times 10^{-6}$ |
| Electron effective mass | $m_0$ | 0.078 |
| Electron mobility | cm$^2$/V-s | $\leq$5400 |
| Intrinsic resistivity | Ω-cm | 8.2 e 7 |

of semiconductors. This chapter covers the primary aspects of bulk InP crystal growth, defect control, and characterization of its electrical and photonic properties.

## 7.2 Thermodynamic properties and definition of suitable growth technologies

### 7.2.1 Properties of InP

The physical and thermal properties of InP give rise to advantages and limitations of specific crystal growth methods. InP is a brittle, gray-colored crystal semiconductor which must be grown from a high-purity melt. Due to its physical properties, the production of large-diameter InP boules places extreme demands on control of the crystal growth environment. Table 7.2 gives some of the important InP thermodynamic properties that must be considered in selecting a suitable growth method.

**Table 7.2** **High-temperature properties of InP, according to Jordan [1]**

| Melting temperature | °C | 1062 |
|---|---|---|
| Vapor pressure at MP | Atm | 27 |
| Thermal conductivity | W/cm-°K | 0.11 |
| Thermal expansion coefficient | °K$^{-1}$ | 6.8 e−6 |
| Thermal diffusivity | cm$^2$/s | 0.0624 |
| Critical resolved shear stress | Dyn/cm$^2$ | 0.0243 (undoped) |
| Shear modulus (1200°K) | GPa | 23.6 |
| Poisson ratio (111 @ 1200°K) | ν | 0.365 |

At the melting temperature of 1062°C, the equilibrium vapor pressure of phosphorus over InP is 27 atm. A pressure vessel operating at a minimum of 30 atm is required to perform controlled crystal growth. Because of this pressure dependence, two main issues arise: how to synthesize a stoichiometric InP compound, and how to contain the highly volatile melt. Early experiments on compound semiconductor crystal growth from volatile compounds in the 1960s focused on two possibilities: either the crystal must be grown in a completely sealed hot-wall ampoule [2] (vertical Bridgman (VB) or vertical gradient freeze (VGF) methods), or it can be pulled using a pressure-balancing technique with an encapsulating layer over the melt. For the latter, a breakthrough came in 1962 when Metz and a group at Westinghouse [3] developed the liquid-encapsulated Czochralski (LEC) method for growth of ZnSe. The LEC method was later adapted for growing InP using $B_2O_3$ as an encapsulant [4–6]. Meanwhile, work continued on vertical container growth at several locations [7,8].

The production of bulk InP crystals today is divided between two suitable crystal growth technologies: top-seeded crystal pulling with liquid encapsulation, and vertical growth in a container with bottom seeding. Various names for these techniques have arisen from each unique laboratory research effort. In general, the pulling method has been the most cost effective, but the crystals usually contain high dislocation densities because of the large thermal gradients and high level of strain imposed during growth. In contrast, vertical container growth offers a very low dislocation density because of its lower-stress environment, but there are yield problems due to twinning and interface breakdown. Two earlier reviews [9,10] compared the growth, characteristics, and applications of InP crystals grown by both techniques. This chapter focuses on the development of techniques to control crystal growth and methods to characterize the electrical and optical properties of InP crystals after growth and thermal treatment.

### 7.2.2 Challenges for crystal growth

Because of its unique thermodynamic properties, InP crystal growth faces several challenges, and three main defect types dominate the list: a tendency to form twins and twin lamellas; uncontrolled dislocation density; and nonuniform doping distribution. Controlling these yield-limiting defects is the key to developing a suitable growth technology. In addition, the design of any apparatus must include a method for synthesis of a stoichiometric compound.

#### 7.2.2.1 Twinning

Twins in InP are two regions in the crystal that are associated by a 180 degree rotation about the {111} lattice plane. In some cases, part of the crystal is bounded by two parallel twin planes called a twin lamella. Normally the {111} planes in InP have a stacking sequence of ABCABC... However, the formation of a twin is tied to a flaw in the stacking sequence so that the close-packed cubic structure is interrupted by a missing layer ABCBCA...This tendency to form twins is recognized to be directly proportional to ionicity and inversely proportional to the stacking fault energy [11]. Compared to all other III–V binary compound semiconductors, the probability of twin formation during growth of InP is quite high. Unfortunately, InP has the lowest stacking fault energy and the highest ionicity of all III−V semiconductors. The problem becomes more acute for growth from indium-rich melts, or for low axial temperature gradients. Although there are many possible causes of twinning during LEC growth of InP, some can be mitigated by engineering controls

1. Uncontrolled crystal shape in growing from a narrow seed to a full-diameter body can lead to a conical angle with a higher probability of twin formation. This angle is a function of the imposed thermal gradient and the crystal pulling rate. The first theoretical treatment of twinning in III−V compound semiconductors was offered by Hurle in 1995 [12]. He observed that there were certain conditions under which internal (111) edge facets could be anchored to the three-phase boundary (TPB) at the solid−liquid−encapsulant interface. The modified Hurle [13] model focuses on uncontrolled shape as the thermodynamic cause of twinning, where, by twinning, the system finds a lower energy state. The diagrams in Fig. 7.1 illustrate the model of twins being nucleated at {111} edge facets anchored to the TPB. For <100> seeded InP crystals, this condition is most likely to occur when the angle, ν, between the edge facet and the extension of the crystal surface falls in the range $31° < \nu < 112°$. The conical growth angle, α, where twinning is most likely is 74.2 degrees because a {115} external shoulder facet is converted to a lower-energy {111} shoulder facet. At a growth angle of 74 degrees, the $\{115\}_M$-$\{111\}_T$ transformation follows exactly the crystallographic orientation relationships of 180 degree rotation twins. In other words, if the external surface of the growing crystal becomes parallel to a {115} lattice plane, a twin with a lower-energy {111} shoulder facet would be likely to occur. On the other hand, the most favorable angle for conical growth is 35.3 degrees, where diagonal twin formation is minimized for <100>-oriented InP crystals. However, this angle allows the possibility of producing patch twins. At a growth angle of 35.3 degrees, the dominant {111} matrix facets typically appear on the crystal shoulders, and these facets are favored because of their low surface energy. Above the angle $\nu > 112$ degrees the crystal has a nearly flat top, and twins are less likely to form because edge facets do not appear to be attached to the TPB. Several methods of crystal shape control are discussed in the next section.
2. Many other possible causes of twinning have been suggested as alternatives to the above argument. One statistical study of twinning suggests that other factors outweigh the effect of facet-energy reduction [14]. Because LEC InP crystals are grown with the encapsulant surface exposed to high-pressure gas, temperature gradients in the liquid are steep (50−110°/cm). Uncontrolled oscillatory flows can cause severe thermal perturbations in

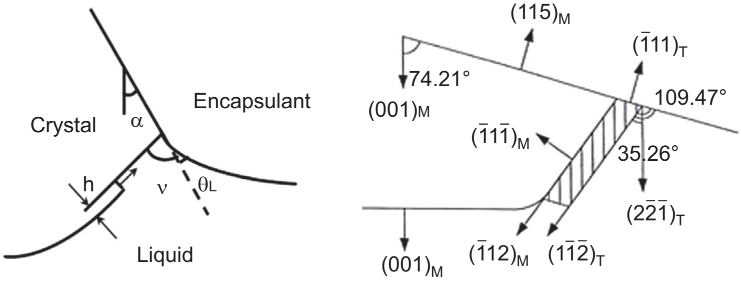

**Figure 7.1** Diagram showing solid−liquid−encapsulant TPB (left) and the most likely angle $\alpha = 74.2$ degrees for twin formation (right) [12,13].

the melt, resulting in rapid changes in the solid–melt interface shape. Other issues for VGF growth are the low temperature gradient, the sudden melt-back of the interface, and growth from In-rich melts. Various methods to control the fluid flow in the crystal growth environment have been proposed and are discussed in the next section.

### 7.2.2.2 Doping uniformity

A uniform distribution of desirable trace elements, or dopants, in the crystal depends on the configuration of the melt and the crystal growth apparatus. The concentration in the solid, $C_s$, varies with the liquid concentration, $C_l$, because of segregation effects, which can be controlled to some extent by controlling convection in the liquid. The model of Burton et al. [15] reveals the effect of melt convection on crystal growth. A diffusion boundary layer of thickness $\delta$ is assumed, beyond which the melt composition is maintained uniform by convection and inside which transport is by diffusion only. The boundary layer is thus confined by the characteristic melt velocity. After a steady state is reached, for an infinite liquid one can define an effective distribution coefficient, $k_{eff}$:

$$C_s/C_l = K_{eff} = K_0 \Big/ \left[K_0 + (1 - K_0)e^{-(R\delta/D)}\right] \tag{7.1}$$

where R is the growth rate and D is the diffusion coefficient for the solute in the melt, while $K_0$ represents the "true" distribution coefficient at the solid/liquid interface. This is a useful expression because it relates the composition of the growing crystal to convection conditions and the growth rate. It describes the dopant distribution provided that the thickness of the boundary layer is small compared to the extent of the crucible. For example, a higher growth rate or a thicker boundary layer produces a more uniform dopant distribution by driving the effective distribution coefficient toward unity. Thus a suitable growth technology must include design of an apparatus that affords control of convection in the melt.

### 7.2.2.3 Dislocation density

Dislocations are known to degrade the performance of certain photodiodes [16] and other devices, and a high density of dislocations may alter the mechanical properties of InP and contribute to point defects and impurity migration [17]. The primary cause of dislocation generation is slip due to thermal stress during crystal growth. Thermoelastic stress is the result of steep thermal gradients in the crystal growth system; typically, a high density of dislocations is a problem associated with pulled crystals and not with VGF or VB crystals. Densities of less than 500 $cm^{-2}$ are generally reported for VGF crystals, or less than can be counted using an optical microscope. Thermal gradients are in the order of 10–30°C/cm in the VGF process, which is very low compared to typical LEC growth at 130°C/cm or higher. For LEC growth, steep temperature gradients give stability to the crystal growth environment. Without such steep gradients, diameter control is more difficult, twinning probability is increased, and surface decomposition occurs as the crystal grows out of the encapsulant. Although many reliable InP-based lasers have been built on substrates with dislocation densities in excess of $10^4$ per $cm^2$, the demand for reduced dislocation density is increasing, as structural defects may limit the performance of advanced monolithic microwave integrated circuits and optoelectronic integrated circuits (OEICs) with very small linewidths. The larger the crystal diameter, the more dislocations are generated at the periphery of the boule due to tensile hoop stresses, and at the center due to compressive stresses. This has prompted research efforts to reduce the density of dislocations in InP with the help of modeling, and to redesign of the growth apparatus to reduce the axial temperature gradient and local thermal fluctuations.

## 7.3 Schematics for synthesis and crystal growth apparatus

### 7.3.1 InP synthesis

For successful large-scale commercialization of InP crystals, one primary requirement is a low-cost method to produce the InP compound. Efficient and rapid synthesis is necessary to maintain low-cost and high-quality InP material. However, compounding red phosphorus and indium in the crucible is impossible because of the vapor pressure of phosphorus. Pure red phosphorus has a vapor pressure of well over 100 atm at 1000°C [18] (Fig. 7.2), which would exceed the limits of normal pressure vessels. On the other hand, the phosphorus dissociation pressure over InP at the melting point of 1062°C is much lower (27 atm). For this reason it is possible to form the compound by transporting phosphorus vapor into the indium melt using a two-zone furnace.

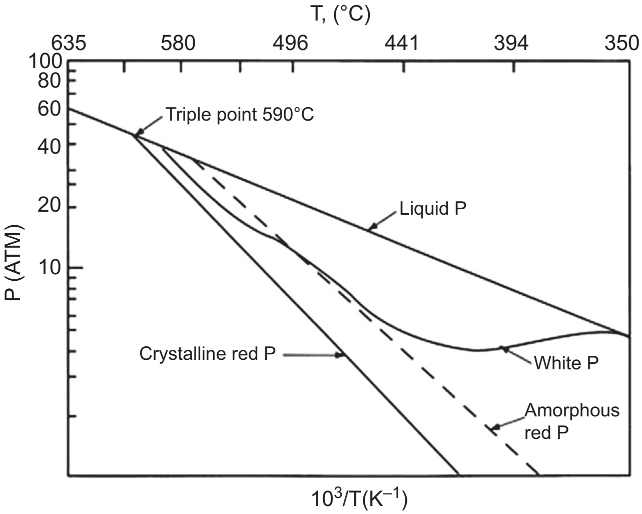

**Figure 7.2** Vapor pressure of phosphorus versus reciprocal temperature [5].

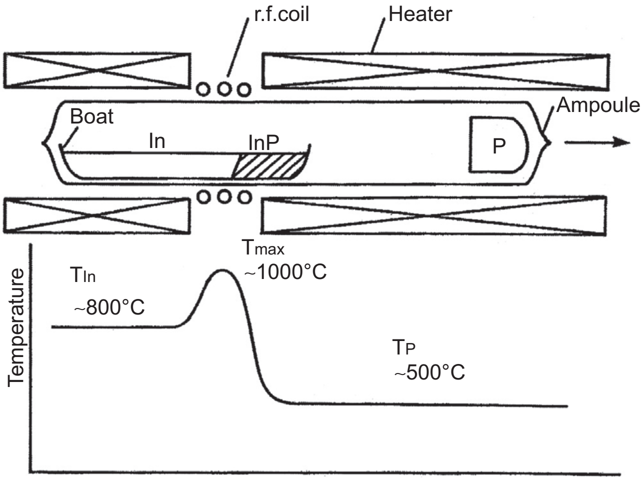

**Figure 7.3** Horizontal furnace for polycrystal InP synthesis. Here $T_p$ is the temperature in the phosphorus zone, $T_{max}$, that of the synthesis zone, and $T_{In}$, that of the indium melt zone [19].

The furnace is designed so that solid phosphorus can be held at ~550°C (see Fig. 7.3) in equilibrium with an InP melt at ~1100°C. The stoichiometry of the InP charge can then be controlled by controlling the temperature of the phosphorus. Synthesis is performed either in situ inside the crystal growth chamber or in another high-pressure chamber, in which case the polycrystal charge is removed and shaped to fit the growth crucible. An alternative method is to inject phosphorus vapor through an encapsulating layer of $B_2O_3$ directly into the molten indium, as shown in Fig. 7.4. A stoichiometric compound is produced quickly by this method.

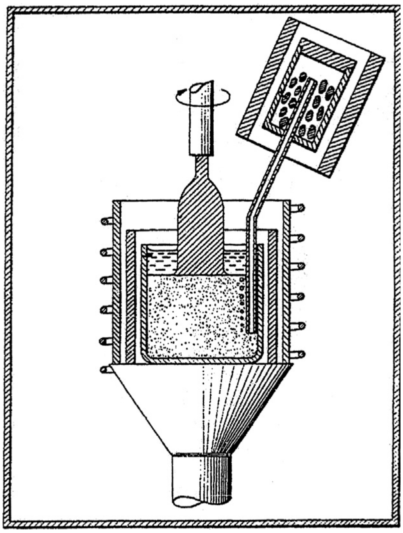

**Figure 7.4** Schematic of apparatus for in-situ injection technique for compounding InP (from 1974 UK patent application 1,353,917 from Fischer at RCA).

### 7.3.1.1 Polycrystal synthesis

The preferred method for polycrystal synthesis involves the use of a horizontal furnace apparatus, such as the schematic design shown in Fig. 7.3 [19]. Here a sealed silica ampoule is employed inside a high-pressure chamber with three heater zones: an indium melt zone, a synthesis zone, and a phosphorus vapor control zone. This method provides a high degree of flexibility for control of polycrystal purity and stoichiometry, but because of the time requirements and capital expenditure it has a large production cost. The flexibility of the horizontal system stems from the many variables which can be controlled. Three temperature zones and the ampoule transfer rate must be carefully optimized to achieve the reported polycrystal properties: no indium inclusions or intergranular precipitates; low residual impurity concentrations as determined by chemical analysis; and electron transport measurements indicating low free carrier concentration (less than 1 × 1015 $cm^{-3}$) and high 77 K mobility (greater than 40,000 $cm^2/v \cdot s$).

In the process to reduce contamination by silicon [19], which commonly dissolves from silica fixtures, the synthesis zone temperature is controlled no higher than 1100°C, just above the congruent melting temperature of InP. A lower temperature would be better as far as impurity contamination is concerned, but a reduced synthesis temperature reduces phosphorus content of the melt and may cause indium inclusions.

Ideally, the indium melt is saturated with phosphorus, and as it cools down InP solidifies out of the supersaturated solution at the liquidus line. One caveat is that the ampoule translation rate must be slower than the solidification rate, to prevent breakdown of the growth front and formation of indium inclusions or intergranular precipitates. These defects, easily seen by optical microscopy, obviously result in off-stoichiometric indium-rich melts. Indium inclusions can be reduced by raising the synthesis temperature and phosphorus pressure, by steepening the temperature gradient at the solidification front, or by reducing the ampoule translation rate. For example, using a synthesis temperature of 1000°C, as shown in Fig. 7.3, the maximum growth rate would be ~4 mm/h without indium inclusions. At this rate, synthesis time for a 4 kg InP polycrystal charge would be about 100 h.

The phosphorus zone temperature can be raised to increase the phosphorus content of the melt, but raising the phosphorus pressure requires balancing the chamber pressure as the phosphorus temperature approaches the triple point. The vapor pressures of the different condensed phases of phosphorus vary considerably and the sublimation rates are quite different, so it is not possible to rely upon phosphorus vapor pressure data as a function of temperature. For this reason, polycrystal synthesis is performed with a phosphorus temperature of ~500°C, corresponding to a pressure of about 20 atm using only the red phase.

### 7.3.1.2 Direct synthesis

The direct injection method is performed in a high-pressure crystal growth furnace prior to LEC growth. A schematic of the apparatus for in-situ injection and crystal growth is shown in Fig. 7.4. The main advantage of direct synthesis over horizontal Bridgman (HB) polysynthesis is the lower production cost. The time required to synthesize a 2 kg melt, including preparation and heating, is only about 3 h. Crystal purity is also a benefit of this technique, since the shorter synthesis time considerably reduces the diffusion of impurities from crucible. After the experimental work of Fischer [20] in the early 1970s, the concept of direct synthesis was turned into industrial practice by Antypas [21] and Hyder [22]. They reported a high-purity in-situ process using a silica ampoule injector, where crystal growth was initiated immediately after injection. They also reported slightly lower purity levels for a two-step process where a presynthesized polycrystal charge was used to grow a single crystal [23]. Other variations of the injection process have been proposed [24], but the question of reproducibility has lingered because it is difficult to automate such a rapid reaction.

A phosphorus injection system that also allows crystal growth in the same vessel [25] is shown in Fig. 7.5. The phosphorus-containing ampoule is raised or lowered independently of the shaft, the ampoule being designed around an annular-shaped tube. Phosphorus is injected through the encapsulant into the indium melt through a transfer tube when the injector is placed near the crucible. Red phosphorus is vaporized, and the increased pressure forces it down the transfer tube along with the inert gas $N_2$. A physical model [26] of the injection process shows that the $P_4$ pressure builds up slowly toward its equilibrium value in the injector while the melt absorbs phosphorus very rapidly, so the actual pressure inside the injector is significantly lower than the equilibrium pressure of phosphorus. When synthesis is complete, the injector is raised and crystal growth is initiated.

A revised in-situ synthesis and crystal growth process demonstrated the capability to synthesize P-rich polycrystalline charges of InP [27]. In this demonstration, the

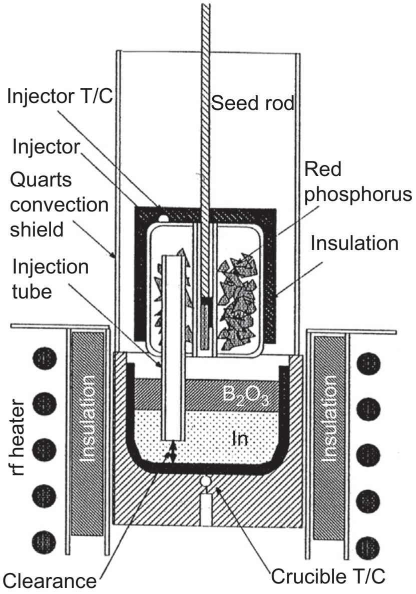

**Figure 7.5** Schematic of system for in-situ synthesis and crystal growth [9].

injector was heated by an independent resistance heater and the InP compound was then used to grow single crystal boules. The crystals grown from stoichiometric charges were of high purity without indium inclusions. Analysis of InP crystals grown from P-rich melts [28] showed the presence of a P-related defect as an electron trap with an activation energy of 0.4 eV. This defect may be analogous to the As-related deep-level EL2 in GaAs, but the InP defect had a minimal effect on electrical transport, which was still dominated by shallow donors. Another publication described a direct in-situ phosphorus injection process for LEC growth of 4-inch diameter <100> InP boules. For this process [29], stoichiometric crystals were grown with an etch pit density (EPD) of less than $5 \times 10^3\ \mathrm{cm}^{-2}$, but P-rich melts resulted in cluster defects that reduced the wafer uniformity.

### 7.3.2 Crystal growth apparatus

Technologies suitable for InP crystal growth fall into two general categories, crystal pulling methods (e.g., LEC) and vertical container methods (e.g., VGF), both with distinct assets and liabilities. LEC crystals are typically grown in the (100) orientation, convenient for slicing round wafers, while for VGF growth the preferred axis is (111), necessitating additional wafer processing. But top-seeded liquid encapsulated melts are thermally unstable, characterized by turbulent or oscillatory flows, whereas bottom-seeded container melts are more thermally stable, the melt Grashof number being several orders of magnitude lower. Optimization of each technique has led to a number of variants, but almost all have one aim in common: to reduce thermal gradients and control transient temperature fluctuations to achieve improved crystal quality. Crystal growth under low gradient conditions requires the utmost process control: reduction of turbulent fluid flows and elimination of mechanical perturbations. To accomplish the goal of process control, new levels of sophistication are added to the crystal growth hardware. Modifications aimed at twin-free growth of crystals include thermal baffles, vapor pressure control, optimized rotation conditions, stoichiometry control, magnetic field stabilization, and crystal shape control; all are active areas of research and development in crystal growth workshops.

## 7.4 Benefits of computer modeling

Thermal modeling by Jordan et al. [30] has contributed an estimate of physical and thermal parameters for InP, as well as a thermoelastic strain model based on the concept of “critical resolved shear stress” (CRSS). Völkl and Müller [31] developed a more sophisticated model for numerical simulation of dislocation formation in InP crystals. Their model takes into account the thermally activated nature of the plastic deformation process, i.e., the generation and multiplication of dislocations.

In the case of InP growth, the chamber pressure is very high, above 2.83 MPa, and the flow and heat transfer interaction among the recirculating gas, the encapsulant surface, and the crystal is extremely complex. To simulate the gas flow for a high-pressure LEC furnace, a multizone adaptive grid process model [32] was developed.

This simulation showed that high-pressure LEC growth conditions are greatly influenced by turbulent and oscillatory gas convection in the furnace. A multicellular flow pattern in the gas can change the melt/crystal interface shape and modify the temperature distribution in the encapsulant and the crystal [33]. The gas flow also enhances the heat transfer both from the encapsulant surface and the crystal (when it emerges out of the $B_2O_3$ layer).

Calculations by Zou et al. [34] demonstrate a strong correlation between the heat transfer and thermal stress generation in the crystal. The highest stress is introduced primarily by the distorted temperature field in the crystal when a sudden change of the cooling condition takes place, especially as the crystal first emerges from the encapsulant. There are two stress maxima at the periphery of the crystal, one just above the encapsulant layer and the other at the crystal–melt interface. The maximum stress spot near the gas–encapsulant interface is the most likely to propagate dislocations because the CRSS in this region is low due to a high crystal temperature. The large thermal stress is attributed to the radial temperature gradient in the crystal. For example, generation of slip bands on the edge of the crystal may be due to these large stresses. Since the temperature at the melt–solid interface is the highest anywhere in the crystal, the CRSS value will be lowest there, and hence the excess stress near the interface may be very high, leading to the generation of dislocations. Either one of the two high stress points (at the melt interface or at the three-way interface of crystal/gas/encapsulant) may be the main source of generation and multiplication of dislocations.

The stress variation predicted by Zou et al. as the crystal grows agrees with the observation of Volkl [35], who suggested that all the growing crystal passes through an almost unchanged high-stress zone. Volkl also found a maximum stress spot near the three-way interface of the crystal/gas/encapsulant using a simplified heat transfer model.

The high-pressure LEC model has also been used to study the effect of segregation [36]. As the crystal grows, more and more solute is rejected from the crystal/melt interface. This solute accumulates in the melt near the interface, and is transferred away from the interface region by both diffusion and convection. This is explained by the flow structure in the melt. The rotation of the crystal has a pumping effect on the melt, which brings the melt up from the bottom along the center line of the system. This flow of melt washes the solute away from the interface area as it turns outward radially. On the other hand, the melt flow induced by the buoyancy force brings the melt in the outer region inward from the crucible side wall. This opposing flow of the melt pushes the solute toward the central portion of the interface. As a result, depending on the strength of these two convective rolls, these two cells can meet close to the periphery of the crystal, and most of the solutes therefore accumulate in that area, showing the highest concentration along the melt/crystal interface. As the crystal grows, the solute concentration in the melt increases because of the solute rejection from the interface. Meanwhile, radial segregation also develops because of complex flow patterns in the melt. For all locations, the solute concentration keeps increasing as the crystal grows, with the largest rate of increase at the location where the two convection cells meet, especially during the early stages of growth.

In modeling studies of vertical container growth, the models have been very successful in simulating real conditions as they apply to practical applications. In one example the influence of rotating magnetic fields (RMFs) and traveling magnetic fields (TMFs) were studied by numerical simulations [37] of the growth of 2” InP crystals by VGF. Both types of magnetic field were investigated for a realistic VGF configuration with respect to bending the solid/liquid interface, resulting in thermoelastic stress and stability of the flow regime in the InP melt. The results of the simulations showed clearly that the use of TMFs offers a significant improvement with respect to the bending of the interface, as well as in reducing the thermoelastic stress in the growing InP crystal. The model did not show an equivalent benefit from the use of RMFs.

These simulations have shown interesting features of high-pressure growth and provide important insights into InP growth phenomena. They have also demonstrated that the thermal conditions and mechanisms for defects and dislocation generation and propagation in a high-pressure system are quite different to those in the lower-pressure GaAs LEC furnace.

## 7.5 Tailoring crystal properties via growth technology

### *7.5.1 Crystal pulling*

Liquid-encapsulated crystal pulling methods have historically been the most cost-effective means of producing high-quality InP single crystals. Commercial LEC producers have been supplying 2-inch InP wafers since the early 1980s. Improvements in process control have made wafers with higher purity and lower defect density available for advanced device processing. However, the trade-off to achieve these goals is in the increasingly complex hardware setup and higher costs for manufacturing. In the quest to reduce thermal gradients and control temperature fluctuations, hardware and software must be added to suppress convection in a normally chaotic fluid system. The low gradient raises an additional demand for vapor pressure control, since thermal decomposition of the growing crystal above the encapsulant becomes a yield-limiting factor.

#### *7.5.1.1 Vapor-controlled LEC*

Adapting LEC growth to reduce temperature gradients, vapor-pressure-controlled Czochralski (VCz) [38] and pressure-controlled LEC (PCLEC) [39,40] were developed to overcome the problem of crystal “bleeding” during growth in a low gradient. Both methods use $B_2O_3$ encapsulant with a hot-wall containment vessel, sealed to maintain a partial pressure of phosphorus over the encapsulated melt. The axial temperature gradient in the $B_2O_3$ is reduced from about 150 to 30°C/cm, so the temperature of the InP crystal just above the encapsulant is about 980°C. At such a high temperature the crystal will decompose or “bleed,” since the equilibrium vapor pressure of phosphorus $P_4$ over InP is about 1 atm. To prevent dissociation of InP, a vapor pressure of $P_4$ inside the hot-wall container is provided by an independently heated solid phosphorus reservoir. In the VCz method a liquid $B_2O_3$ seal is used to prevent leakage of phosphorus vapor from the hot-wall container, while for PCLEC a solid seal is used. Both methods have been successfully used to reduce the dislocation density of 2-inch Fe-doped wafers to the range of 2000–8000 $\text{cm}^{-2}$, and S-doped wafers below $10^3$ $\text{cm}^{-2}$.

### *7.5.1.2 Magnetic stabilization techniques*

The application of an external magnetic field during crystal growth was proposed in the 1960s [41,42] to eliminate solute striations caused by time-dependent convective flows. More recently there has been research interest in growth of InP crystals under applied magnetic fields [43,44]. In principle, there are two advantages which result from magnetic field growth: thermal fluctuations in the melt are reduced, stabilizing the microscopic growth rate; and at the melt–solid interface the diffusion boundary layer thickness $\delta$ is increased, causing a more uniform dopant distribution.

Impurity distribution in crystals is directly affected by the magnitude and direction of fluid flow in their melts. For conducting liquids like semiconductors and metals, fluid flows can be restricted by imposing a magnetic field in opposition to the fluid flow. The amount of restriction is given by the Lorentz force, $L$:

$$L = j \times B \tag{7.2}$$

where $j$ is the ionic current density vector and $B$ is the applied magnetic field. The net effect of imposing a magnetic field is an increase in the effective viscosity of the melt. This increased magnetic viscosity reduces the rate of fluid transport, thus increasing the momentum boundary layer thickness. Although it is not practical to produce a magnetic flux density large enough to eliminate all melt motion due to natural and forced convection, a strategy of controlling melt motion for dopant uniformity can be achieved with moderate magnetic fields. When crystal growth reaches a steady state, using Burton's analysis [15] we can define an effective distribution coefficient, $k_{\text{eff}}$. This useful concept expresses the effective distribution of dopants in a crystal as a function of convection conditions in the melt and the growth rate. For example, as $k_{\text{eff}}$ approaches a value of one, the dopant distribution in the crystal will be more uniform from beginning to end. And in the case of an applied magnetic field, the increased boundary layer thickness tends to bring the effective distribution coefficient toward unity. As a result, a more uniform incorporation of dopant in the crystal is achieved.

Magnetic Czochralski growth has been modeled by several authors [45,46] for LEC InP [47], and they have pointed to the significant enhancement of the effective segregation coefficient due to an axial magnetic field. Crystal growth of InP in an applied magnetic field has been explored by a number of laboratories. By applying an axial magnetic field of 1000 G, Miyairi [26] showed that thermal fluctuations are reduced from 9°C to less than 1°C and random, time-dependent striations disappeared. The suppression of compositional variations in the melt was considered to be a reason for the disappearance of dislocation clusters in the material. Ozawa [48] used a programmed reduction of applied magnetic field to achieve a homogeneity improvement in Fe-doped InP.

A variation of LEC growth called magnetic liquid-encapsulated Kyropoulos (MLEK) demonstrated growth with a magnetic field compared with normal LEC growth of InP [49]. In MLEK growth the crystal is grown initially without pulling the seed, in a characteristic flat-top shape. After the crystal has reached full diameter, the seed is slowly raised as the melt level drops, to pull a cylindrical (100) crystal. There are some important distinctions between MLEK growth and normal LEC InP growth. To compare the two methods, two tin-doped InP crystals were grown, one by LEC and the other by MLEK, both at similar rates from melts weighing about 1 kg with tin concentrations of $5 \times 10^{19}\ \text{cm}^{-3}$ The MLEK crystal was grown in an axial magnetic field of 2 kG, while the LEC crystal was grown without a magnetic field. The two processes were compared after growth by measuring the tin concentration of each crystal at several points representing equivalent fractions of growth. At each fraction of solid a sample was measured by glow discharge mass spectrometry (GDMS) to determine the tin concentration. To establish the effective distribution coefficient, $k_{\text{eff}}$, for each process, the concentration ratio, $C_s/C_l$, was determined from the first slice of each crystal. A comparison of the axial doping profiles for each crystal (Fig. 7.6) reveals a distribution coefficient for the MLEK process which is a factor of 2.5 times larger than that for LEC (that is, closer to unity). For MLEK the measured tin concentration starts higher and remains higher until the tail, where the nonmagnetic LEC exceeds the MLEK. A factor of two error bar is expected for GDMS measurements, which may explain the bump in the LEC data. The difference in $k_{\text{eff}}$ is an indication that magnetic fields increase the boundary layer thickness $\delta$ at the melt–solid interface. The possible use of axial magnetic fields as a practical method of growth control has great appeal.

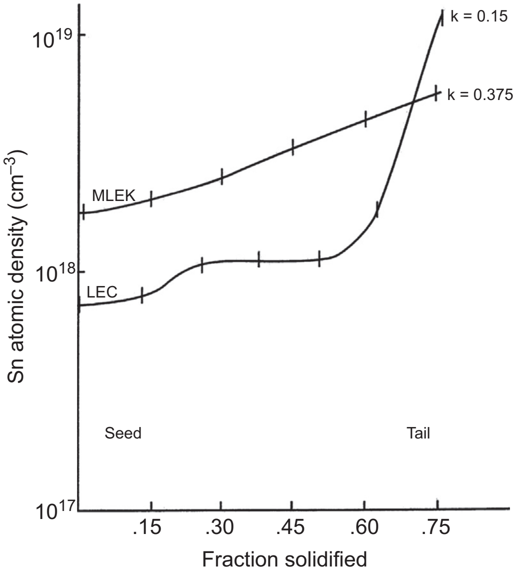

**Figure 7.6** Axial tin doping profile of LEC and MLEK crystals as determined by electron microprobe analysis [9].

### 7.5.2 Vertical container growth

Successful design of a low-temperature-gradient system for growth of InP crystals was first demonstrated in 1986 at AT&T [50]. They grew 2-inch InP single crystals by the VGF method using a two-zone heater system, one to control the phosphorus vapor pressure, and the other to provide a dynamic thermal gradient for crystal growth. The system is thermally stable, because the temperature gradient is aligned with the density gradient. Taking advantage of the system's thermal stability, they controlled the axial gradient between 8 and 40°C/cm during growth from a seed. The dislocation density of crystals grown by this technique measured less than 500 $\text{cm}^{-2}$, demonstrating the effect of crystal growth in a low thermal gradient. No encapsulating layer was needed; instead stoichiometry was maintained by holding the phosphorus reservoir at 550°C to control the vapor pressure at $\sim$27 atm. This temperature happens to be near the phase transformation point [51] between white and red phosphorus with different vapor pressures; hence the semitight seal was needed to avoid explosions.

Improvements on VGF growth [52] showed defect-free regions in the center of S-doped crystals, and dislocation densities less than 100 $\text{cm}^{-2}$ at the wafer edges. For iron-doped crystals [53] dislocation density is reported below 2000, and for undoped crystals below 1000 $\text{cm}^{-2}$. From the point of view of reduced dislocation density, the VGF technique offers an unprecedented capability for growth of low-defect InP material. However, the crystallographic orientation in the <111> growth direction, the frequent occurrence of twins and twin lamellas, and the nonuniform dopant distribution create an inherent yield problem. The AT&T patent was licensed to American Crystal Technology, Inc. for commercial production of VGF InP crystals. With further modifications [54], they are manufacturing InP wafers grown in the <100> direction. The dislocation density is comparable to that reported earlier for <111> growth, but few details are available concerning the growth process, as there has been no other publication of the results.

To overcome the yield problems of InP growth, a multizone furnace was designed and built to enable a high degree of thermal flexibility for control of temperature gradients [55]. Each segment of the multizone furnace, with typical spacing between elements of 1–2 cm, is cooled and heated separately, and the furnace is constructed of materials which resist phosphorus contamination. The greater flexibility of these furnaces over standard VGF means vastly more process variables to control the heat and mass transport during crystal growth. Software tools [31] simulating real-time growth conditions are available to predict the position and shape of the solid–liquid interface and to calculate the content of the boundary layer adjacent to the interface for each time segment of crystal growth. In fact, the investment in software, sensors, and controls is a significant part of the capital cost of these state-of-the-art furnaces.

Research on a related technique [56] has shown that twin-free <100> InP single crystals can be grown by liquid-encapsulated VB. This method utilizes translation of the charge through a fixed temperature gradient of about 23°C/cm; to avoid the problem of twinning in the cone section, a full-diameter seed is used, so the entire crystal grows in cylindrical shape. The use of $B_2O_3$ as an encapsulant eliminates the need for a separate phosphorus heater zone.

The dopant segregation problem is another dilemma for container growth, as illustrated in Fig. 7.7 from an article by Favier [57]. This theoretical model of transient behavior compares Czochralski growth with an infinite melt to Bridgman and zone-melting growth with finite melts. For most crystal growth configurations, an initial transition occurs as the normalized concentration, $C_S/C_O$, approaches steady state. For zone melting the ratio goes to unity, i.e., the effective distribution coefficient, $k_{eff} = 1$. However, for Bridgman growth where a finite volume of melt is contained with some degree of convection, an increase in dopant concentration begins after the starting transient and a steady state of constant composition cannot be achieved. For a finite melt volume any source of convection is a problem for the yield of usable material within the doping range. For VGF growth the vertical configuration prevents buoyancy-driven convection, but there are other forces such as surface tension and mechanical vibrations responsible for flows in the melt.

Some engineering solutions have been suggested to reduce the segregation effect in VGF growth. Müller [58] proposed a process which allows only axial heat flow through the melt. With only vertical temperature gradients, horizontal temperature and density gradients do not disturb the hydrostatic stability of the melt and a planar interface is maintained. A flat axial doping profile is generated in the crystal, similar to that calculated for pure diffusive transport. This process and other yield improvements are achieved by upscaling the whole crystal growth apparatus and increasing the process windows to allow for parameter variations. In reference [59] it was discussed how "defect engineering" relates to the whole crystal growth process as well as the cooling and annealing processes. Advanced defect control means on one hand a reduction of the number of deficient crystal defects, and on the other hand the formation of beneficial crystal defects with a uniform distribution and well-defined concentration in the whole crystal. These topics were illustrated by examples of modeling and experimental results of InP. Systems for defect control have also been modeled using applied magnetic fields to control dopant segregation in VGF InP crystal growth [60]. These examples involve state-of-the-art modeling of the most important melt growth techniques: crystal pulling (Czochralski methods) and VGF (Bridgman-type methods).

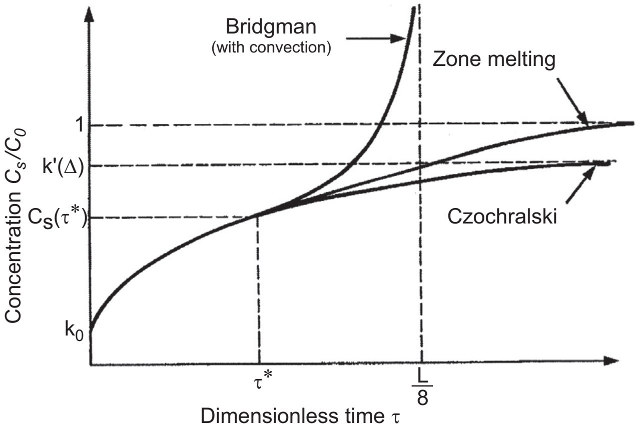

**Figure 7.7** Normalized concentration versus dimensionless time for directional solidification of finite melt volumes (Bridgman and zone melting) and for infinite volume (Czochralski) [57].

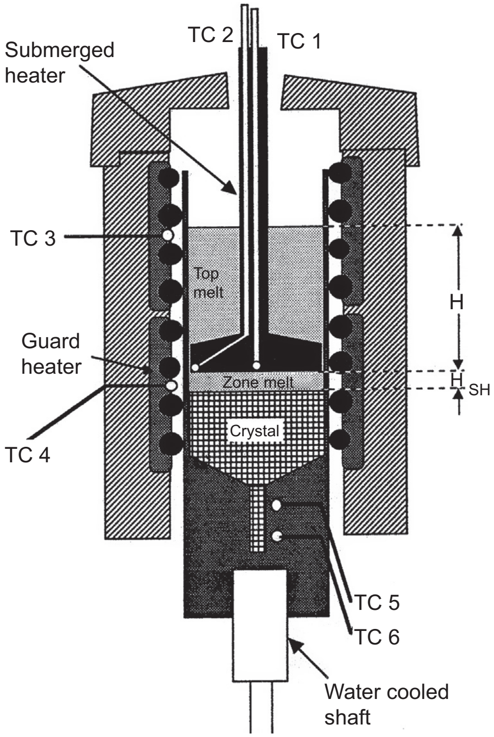

**Figure 7.8** Schematic of the submerged heater growth system [61].

Another approach is suggested by Ostrogorsky and Müller [61]. The submerged heater method (shown in Fig. 7.8) is a vertical growth method where the crystal is grown from a small zone in which melt and impurities are continuously replenished. One advantage of this system is that the submerged heater acts as a baffle to reduce destabilizing buoyancy forces in the melt. The other advantage of zone melting is that the concentration of impurities does not change with time. Although InP has not been grown by this method, Ge and InSb [62] crystals grown in this way show very uniform axial doping profiles, even for dopants with very small $k_{eff}$. Similar to the zone-leveling scheme of Pfann, this technique has promise for higher yield from vertical container growth [63].

## 7.6 Doping issues and reduction of defect density

### 7.6.1 Semiconducting InP

At room temperature InP has an intrinsic carrier concentration in the order of $n_i \approx 10^7\ \text{cm}^{-3}$, but because there are unintentional trace impurities like Si and S which are ionized at that temperature, the measured free carrier concentration is always above the intrinsic level. Typically, the free electron concentration measured in undoped InP is in the range of $10^{14}$–$10^{15}$ cm$^{-3}$. For conducting substrates the usual doping specification is substantially higher, in the range of $10^{18}$–$10^{19}$ cm$^{-3}$, hence the issue of compensation is not as important in the selection of conducting substrates as it is for semiinsulating material. However, the uniform distribution of dopants in the bulk material is key to qualifying the material for production.

The choice of dopant species influences the electrical properties. For example, InP crystals with n-type conductivity can be grown by adding shallow donors such as Sn, which substitutes for In, or S, which substitutes for P [64]. Either way, the free carrier concentration varies continuously with dopant concentration up to the limit of solid solubility for that donor species, unless a compensating acceptor impurity is present. As $n$ increases, or if the compensation ratio increases, the electron mobility, $\mu_n$, decreases due to ionized impurity scatter [65]. These mobility values fit closely for bulk material, but for epitaxial InP [66] material with a lower concentration of intrinsic defects, calculations of mobility data give higher values.

Bulk p-type InP is grown by adding group II elements such as Cd, Zn, Be, or Hg, which substitute for In. The range of resistivity for p-type doping is not as large as for n-type, because the mobility $\mu_p$ falls off rapidly with increased carrier concentration. The effect is even more pronounced at 77 K, where a partial freeze-out occurs due to the relatively deep level of acceptor impurities. For p-type InP with $p < 1 \times 10^{18}$ cm$^{-3}$, the free carrier concentration falls off by an order of magnitude between 300 and 77 K while the mobility increases, so the resistivity remains constant within a range of 25%.

Whether n-type or p-type, as-grown InP bulk crystals are usually nonuniform in resistivity over their length, as noted in the previous section. The dopant concentration $C_s$ incorporated in the growing crystal varies according to Eq. (7.1), depending on the effective distribution coefficient $k_{eff} = C_s/C_L$ for a variety of dopant species. The values of the effective distribution coefficients are tabulated in a monograph by Iseler [67]. Over a short time scale, the nonuniform distribution of dopants is revealed in striations, especially in LEC growth, where steep thermal gradients can induce natural thermal convection in the melt.

### 7.6.2 Semiinsulating bulk InP

A key requirement for fabrication of high-speed devices and OEICs is uniform substrate material that is electrically semiinsulating. Because of its 1.35 eV bandgap, semiinsulating wafers of InP are available with resistivity greater than $10^7$ Ω-cm. In contrast with GaAs, semiinsulating behavior in InP cannot be produced without the use of intentional dopants. As mentioned in the previous section, undoped (or unintentionally doped) InP is usually n-type conductive due to trace impurity donors. Furthermore, residual carbon in the starting material or from graphite heaters does not act as an acceptor but rather a weak donor in InP. Crystals grown from P-rich melts have shown an intrinsic defect level at $\approx 0.4$ eV, at relatively low concentration [28], but this energy level is too low to give semiinsulating properties. Among the different deep impurities tested, only iron gives an effective mid-gap acceptor level that leads to resistivity greater than $10^7$ Ω-cm. However, because of iron's diffusivity,

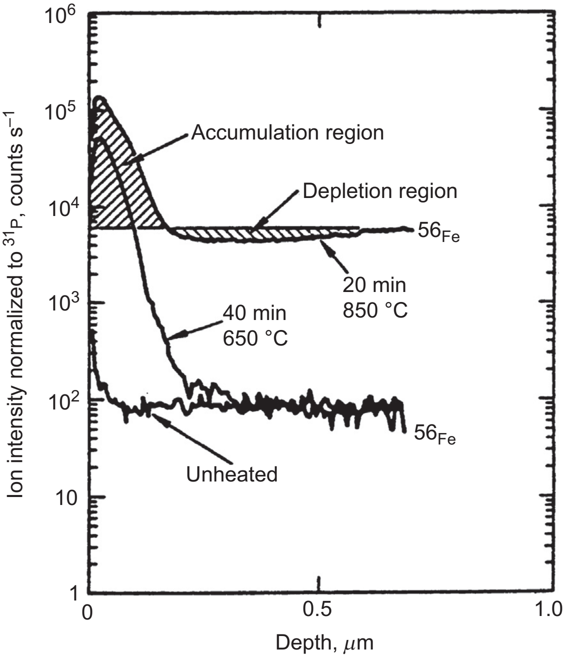

**Figure 7.9** Comparison of SIMS profiles for substrates heated at 650°C for 0, 20, and 40 min (different initial concentrations were used) [68].

its distribution must be controlled both during crystal growth and postgrowth during high-temperature processing. Redistribution of Fe during epitaxial growth is a problem which has been studied by several authors [68,69]. Fig. 7.9 illustrates the problem of iron redistribution for liquid-phase epitaxy. A comparison of Fe depth profiles before and after heat treatment, studied by secondary-ion mass spectroscopy (SIMS), shows that Fe accumulates near the surface of the substrate. The depth of the accumulation region for samples treated at 650°C ranged from 0.1 to 0.2 μm, as shown in Fig. 7.9. Note that the Fe profile seems to level off at a depth of 0.6 μm, indicating the transport of iron over a distance of many micrometers from the surface. Redistribution of Fe has two possible effects: first, an epitaxial layer deposited on the surface may become contaminated with iron, and second, strain in the epitaxial layer may cause the formation of slip lines. Both of these effects impact device performance and reliability. Iron has another significant drawback, namely a very low distribution coefficient in InP ($K_{eff}$ is about $1 \times 10^{-3}$), which gives rise to a pronounced segregation. This in turn limits the number of high-resistivity, high-quality wafers obtained from a single boule. When the molten Fe-doped charge is entirely pulled, only the first two-thirds of the ingot are suitable for device production, the tail being rich in iron phosphide precipitates and unusable. In any case, even in the usable part of the ingot the iron content differs from wafer to wafer, and along the diameter of each wafer following a U-shaped profile. To counter the negative segregation effects, two approaches were attempted: use of magnetic fields to increase the distribution coefficient artificially, and LEC growth with melt replenishing [70].

The relatively low yield and instability of Fe-doped InP has led many authors to seek alternatives to Fe doping. Chromium [71] behaves as a deep acceptor (0.35 eV from the conduction band) in n-type InP and, like Fe, it becomes $Cr^{2+}$ when ionized, resulting in resistivity of $10^3$—$10^5$ Ω-cm. In p-type material, however, Cr behaves as a deep donor and becomes $Cr^{4+}$ when ionized. Cobalt introduces an acceptor level located closer to the valence band than the Fe level, resulting in p-type material with low conductivity. Rhodium [72] is a deep acceptor which has a much lower diffusion coefficient than Fe, but until now no bulk semiinsulating material has been produced using Rh. Codoping with two elements has also been attempted [73]. The most promising combination seems to be a shallow acceptor (Hg or Cd) and a deep donor (Ti or Cr), which results in resistivity of $10^4$—$10^5$ Ω-cm and low mobility due to compensation. Although diffusion of Hg and Ti is very low compared to Fe, because the Ti level is less than 0.5 eV from the conduction band, the resistivity is not sufficiently high to support isolation and capacitance requirements for OEICs.

### 7.6.2.1 Compensation mechanism of InP:Fe

Understanding the compensation mechanism of iron in InP material was an early area of active research. Several questions concerning the compensation mechanism were not fully resolved. It was known that the Fe content necessary to fix resistivity in as-grown crystals at $10^7$ Ω-cm is much greater than the residual shallow donor concentration [74]. Mass spectrometric analysis showed that semiinsulating crystals required an Fe concentration to be about $1 \times 10^{16}$ $cm^{-3}$, whereas the total residual donor concentration (Si and S) was in the order of $10^{15}$ $cm^{-3}$. It was argued [75] that either Fe is not always on an active site, or there are some "intrinsic" shallow donors [74] which cannot be measured by chemical analysis. Some of these intrinsic donors were soon discovered to be related to hydrogen in bulk InP crystals [76].

When Fe is introduced in InP it substitutes for In and primarily adopts the neutral $Fe^{3+}$ oxidation state. However, some of the iron is compensated by shallow donors to form $Fe^{2+}$, and it was noted [77] that the ratio between the ionized and neutral concentrations, $Fe^{2+}/Fe^{3+}$, varies linearly with the free carrier concentration, $n$ (see Fig. 7.10). A linear dependence of $n$ on $Fe^{2+}/Fe^{3+}$ is expected, since both quantities are proportional to the exponential term in the Fermi distribution function, expressed as $[-E_F/(kT)]$ where $E_F$ = Fermi energy, $T$ is the absolute temperature, and $k$ = Boltzmann constant. The free carrier concentration can be expressed as:

$$n \cong N_c \exp\left[\left(-\frac{E_c - E_A}{kT}\right)\right] \frac{[Fe^{2+}]}{[Fe^{3+}]} \frac{g(Fe^{3+})}{g(Fe^{2+})} \tag{7.3}$$

where $N_c$ is the density of states in the conduction band and $g$ represents the degeneracies of the two iron defect states. The difference $E_c$—$E_A$ is simply the change in free energy associated with the transfer of an electron from the occupied iron acceptor level to the conduction band, known from deep level transient spectroscopy (DLTS)

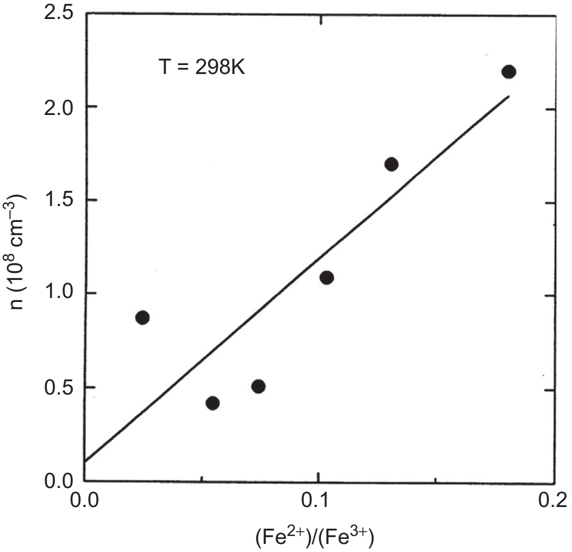

**Figure 7.10** Experimental data for semiinsulating InP crystals showing a linear dependence of free carrier concentration, *n*, with $Fe^{2+}/Fe^{3+}$ ratio between ionized and neutral iron concentrations. The solid line is the best fit to the data [77].

measurement to be 0.63 eV. This would be the case at absolute zero, with all the residual donors frozen, but for practical device performance at room temperature a temperature shift of the iron acceptor level is calculated. Using this analysis, the temperature shift is calculated to be different from the temperature shift of the bandgap. Fig. 7.11 shows the relative shift of the bandgap versus the deep defect level, indicating that the thermodynamic position of the $Fe^{2+}/Fe^{3+}$ level at room temperature is 0.49 eV below the conduction band. This is the energy that determines the carrier

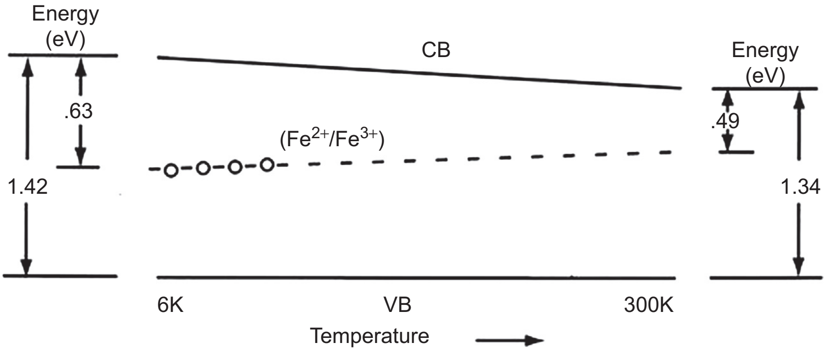

**Figure 7.11** Energy band diagram versus temperature for InP:Fe showing the shift in bandgap energy (slope $= -3.8 \times 10^{-4}$ eV/K) and the shift in the Fe acceptor ionization energy (slope $= 4.7 \times 10^{-4}$ eV/K).

concentration at room temperature. Taking, for example, an iron concentration twice as high as the residual donor concentration, $Fe^{2+}/Fe^{3+} = 1/2$, the room-temperature carrier concentration would be $n \approx 10^9\ cm^{-3}$, too high for electrical isolation. To meet the specification of semiinsulating InP a ratio of $Fe^{2+}/Fe^{3+} = 1/10$ would be required for a free carrier concentration of $n \approx 10^7$. In practice, for typical bulk growth of semiinsulating InP with residual donor concentrations of $1-3 \times 10^{15}\ cm^{-3}$, a minimum Fe doping level of $1-3 \times 10^{16}\ cm^{-3}$ is required. Hence a reduction in the residual donor concentration is needed if the goal of reduced iron concentration is to be achieved.

### *7.6.2.2 Annealing and the role of hydrogen*

In the 1990s several experiments [78,79] began to explore the possibility of annealing high-purity InP wafers with only a small amount of Fe to obtain semiinsulating material. The best results were obtained using very low $\sim 10^{15}\ cm^{-3}$ Fe content material, with a free carrier concentration of $n \approx 1-2 \times 10^{15}\ cm^{-3}$ as grown. Slices of this material were annealed at 900°C for 20−80 h under a partial pressure $P_P$ of a few atmospheres, and slowly cooled. After annealing, the wafers converted to high-quality semiinsulating material in these experiments. Furthermore, the purity of annealed InP wafers produced by this method is very high, with mobilities in excess of $4000\ cm^2/v\text{-}s$, proving that high resistance is not caused by recombination centers. The implication is that additional donors, not detected by impurity analysis were present in these samples; and under high-temperature conditions these “intrinsic” shallow donors were annealed out of the material. It was proposed [80] that hydrogen donors were indeed present in the as-grown material, thereby contributing to the ionized $Fe^{2+}$ concentration.

Studies of the absorption spectra of hydrogen in InP [81] have established the structure of the hydrogen-related complexes. The local vibrational mode (LVM) absorption at $2315.6\ cm^{-1}$ in LEC InP is due to the vibrational absorption of the PH stretching modes [82]. To determine the hydrogen symmetry in the lattice, crystals grown with deuterium as well as hydrogen doping were used [76] to investigate the hydrogen spectra in InP. The splitting caused by the presence of two different isotopes in the InP bulk material was helpful in determining hydrogen’s electronic behavior. The D−H spectra were consistent with the model of a defect with tetrahedral symmetry, and the authors proposed that the absorption is due to a fully passivated indium vacancy $[V_{In}(PH_4)]$. Further investigation [83] into the electrical properties of the hydrogen defect in InP showed that this defect has a characteristic donor behavior. A model of the $V_{In}H_4$ defect shown schematically in Fig. 7.12 illustrates the donor behavior, which arises from a tetrahedral formation of H around an indium vacancy.

The $V_{In}H_4$ defect disappears during annealing at ≈ 900°C under a phosphorus overpressure, as shown in Fig. 7.13. A comparison of Hall measurements before and after annealing of undoped bulk InP material shows the loss of the LVM absorption peak is accompanied by a reduction in free carrier concentration. This result is consistent with the other published results mentioned previously, where the electrical

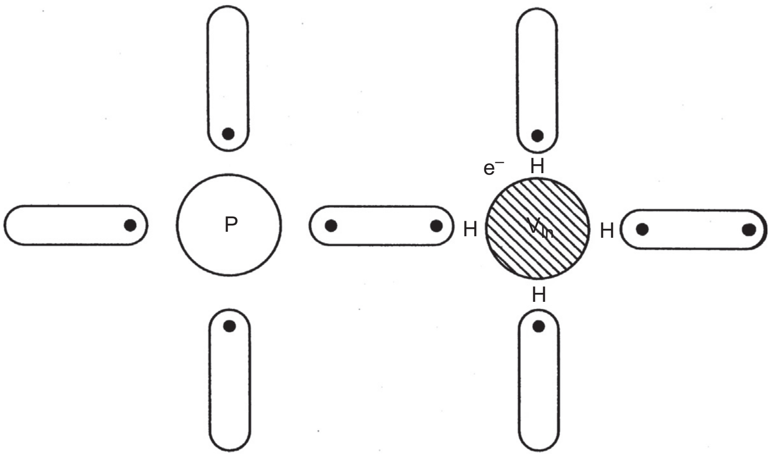

**Figure 7.12** Schematic of the $V_{In}H_4$ defect [76].

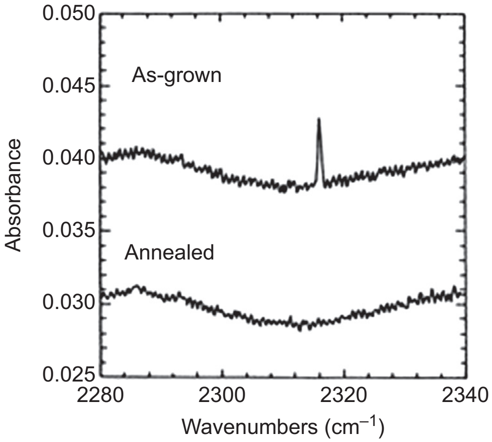

**Figure 7.13** Infrared absorption spectra in the range of the InP:H LVM line before and after annealing.
From F.X. Zach, E.E. Haller, D. Gabbe, G. Iseler, G.G. Bryant and D.F. Bliss, Electrical properties of the hydrogen defect in InP and the microscopic structure of the 2316 cm$^{-1}$ hydrogen related line, J. Electron. Mater. 25 (1996) 331–335.

activity of iron changes when "intrinsic" donors are reduced by annealing. The annealing cycle which occurs naturally during crystal growth also contributes to the electrical activity of Fe in as-grown InP [84]. In other words, the concentration of active iron in a given cross-section of the ingot depends on its thermal history and the concentration of In vacancies in that section. This observation led to the development of undoped semiinsulating InP wafers obtained by Fe diffusion [85]. In this new approach, nominally undoped InP crystals were grown and sliced into wafers.

The wafers were first cleaned with solvents and chemically etched before depositing a thin Fe layer on to both sides (via a chemical route). The samples were then sealed under vacuum in quartz ampoules and annealed at 900°C for 50 h. As the Fe diffusion coefficient was known to be in the $10^{-9}-10^{-10}$ $cm^2/s$ range, the selected annealing temperature and duration were amply sufficient to allow complete diffusion of the Fe atoms across the 0.5 mm thick wafers. The diffusion profile of iron in InP was indeed seen to be very flat, with the exception of a 20−30 μm thick surface layer adjacent to the Fe topping where the concentration increases very steeply. This Fe-rich zone could be completely removed by two-sided polishing, leaving a uniform Fe profile throughout the wafer thickness. SIMS measurements confirmed that the Fe distribution in these diffused wafers was more homogeneous, both radially and across the wafer section, than in standard LEC Fe-doped wafers. Furthermore, GDMS with a subppb detection limit showed that the Fe concentration in the Fe-diffused semiinsulating wafers was about one-third of that typical of LEC-grown semiinsulating InP. The Hall effect measurements performed according to the Van der Pauw method nevertheless showed that all wafers had become semiinsulating, with resistivity well above $10^7$ Ωcm and mobility in the range 3000−4000 $cm^2/Vs$.

The evident advantage of this postgrowth Fe doping is the higher throughput, as the problems arising from the strong Fe-segregation effects mentioned above can be avoided. In the diffusion method, the full batch of wafers from an undoped ingot can be processed under the same conditions: cleaning, Fe deposition, annealing, and polishing, with excellent results and maximum yield.

Some questions still persist, however, concerning the precise mechanism of thermal conversion. Does high-temperature treatment annihilate the $VH_4$ defect complex, or does it merely stimulate the diffusion to free surfaces? Likewise, if iron atoms are "electrically active" only on substitutional In sites, what happens to the InP crystal when iron diffusion occurs through an interstitial mechanism? After annealing, are some iron atoms quenched into inactive interstitial sites?

Another link to understanding the compensation mechanism is quantitative measurement of infrared absorption peaks related to the $Fe^{2+}$ intracenter. Two peaks associated with the $Fe^{2+}$ intracenter electronic transition are seen at 2830 $cm^{-1}$ and 2844 $cm^{-1}$. To distinguish between donor reduction and impurity compensation, the fourier transform infrared spectroscopy (FTIR) spectra of InP samples were measured before and after annealing [86]. To determine the activation behavior of iron, Fe-doped InP crystals were grown with total iron concentration ranging from $1 \times 10^{16}$ to $1 \times 10^{17}$ $cm^{-3}$ from seed to tail. The crystals were cut into rectangular $1 \times 1 \times 2$ cm polyhedra, and then annealed in quartz ampoules with sufficient phosphorus to provide an overpressure of 5 atm at 900°C, well above the equilibrium partial pressure of P over InP [87]. After being held at 900°C for 36 h the samples were cooled either slowly or rapidly to room temperature. Slow cooling was performed at a rate of less than 1°C per minute, whereas rapid cooling was in excess of 5°C per minute.

Optical absorption spectra in the range from 500 to 3500 $cm^{-1}$ were performed on the samples mounted in an exchange gas optical cryostat and cooled to temperatures between 6.5 and 12 K. For the slow-cooled samples, an increase in mobility after annealing was observed consistent with a $V_{In}H_4$ donor reduction. Measurements of the hydrogenated vacancy, $VH_4$, from the integrated absorption at 2316 $cm^{-1}$ showed virtually complete annihilation of the defect after annealing. In these same samples, the $Fe^{2+}$ absorption lines were measured before and after annealing. The reduction in the $Fe^{2+}$ concentration after annealing is directly proportional to the reduction of integrated absorption due to the hydrogen defect. The following quantitative calibration correlates the hydrogen—vacancy complex with the $Fe^{2+}$ absorbance (equivalent to the net donor concentration):

$$[V_{In}H_4] = 4.2 \times 10^{16}\left(cm^{-1}\right) \times Fe^{2+}\text{Absorbance}\left(cm^{-2}\right) \tag{7.4}$$

Further confirmation came from experiments on semiinsulating Fe-doped material, showing the role of hydrogen-related donors in controlling resistivity [88]. In this experiment, the $Fe^{2+}$ infrared absorption peak was measured quantitatively to determine the residual shallow donor concentration. For slow cooling, annealing reduces the $Fe^{2+}$ absorption peak without any increase in $Fe^{3+}$ by diffusion or other mechanisms.

For the rapidly cooled samples, the results are somewhat different. The annealing process is less efficient than for the slowly cooled sample. The change in $Fe^{2+}$ concentration is not as large, indicating that new compensating acceptors may have been introduced during cooling. Annihilation of $VH_4$ donors appears to be complete because of the total disappearance of the absorption peak at 2316 $cm^{-1}$. However, the mechanism of acceptors being quenched during cooling remains a possibility. If iron is trapped on interstitial sites, could this also contribute to the inefficiency of thermal conversion?

Two observations concerning the spectra of quenched samples may supply clues to the answer. First, a sharp peak, not shown here, is found at 2204 $cm^{-1}$. This peak has been identified [89] as an LVM belonging to $VH_2$, an intermediary in the breakup of the $VH_4$ defect. As the number of H atoms in the vacancy decreases, the P—H bonds lengthen and the frequency of the vibrational mode decreases. As each hydrogen atom is removed from the vacancy, an electron is removed from the highest occupied state. The resulting defects $V_{In}H_2$, $V_{In}H$, and $V_{In}$, have been identified as single, double, and triple acceptors, respectively, thereby compensating the residual donor concentration. The appearance of the $VH_2$ defect is likely contributing to the inefficient thermal conversion of quenched InP samples. These experimental results point to the important role of hydrogen in the compensation mechanism of Fe-doped InP, and especially in annealing undoped InP to generate semiinsulating material.

Second, an interesting feature in the infrared absorption spectrum of rapidly cooled samples is seen in Fig. 7.14. Before annealing, in the upper plot, two peaks associated with the $Fe^{2+}$ intracenter electronic transition are seen at 2830 and 2844 $cm^{-1}$. After annealing followed by rapid cooling, the integrated area of the two peaks is reduced, but not as much as for slowly cooled samples, and some new absorption lines emerge at 2864 $cm^{-1}$ and a possible triplet centered around 2877 $cm^{-1}$. The new peaks are

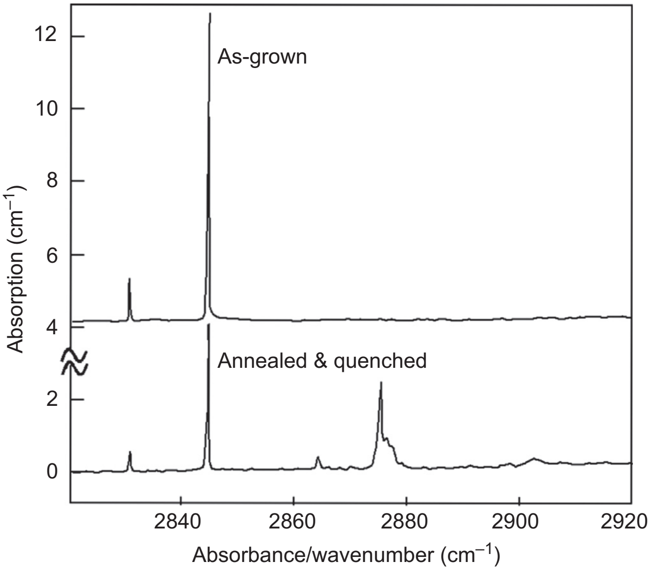

**Figure 7.14** Infrared absorption spectrum in the range of the Fe$^{2+}$ intracenter absorption before and after annealing [86].

not identified in the literature, and it is not certain if they are caused by electronic transitions or by local vibrational modes. However, because of their similar spacing and proximity to the well-known iron peaks, one could suspect an iron-related defect. Possibly a high temperature defect becomes quenched in the rapidly cooled samples. For example, if iron diffuses at high temperature by an interstitial mechanism, it is likely that rapid cooling could leave some iron atoms on inactive sites. Substitutional iron (Fe$^{3+}$) and a low Fe$^{2+}$/Fe$^{3+}$ ratio are both required for semiinsulating InP. If iron is trapped on interstitial sites, this will also contribute to the inefficiency of thermal conversion.

Other rationales have been offered to explain the conversion of undoped (or low Fe-doped) InP to semiinsulating material by annealing. In one case [90] the neutralization effect of hydrogen comes from the hydrogen passivation of donors. In addition, authors have argued the dissociation of hydrogen complexes during annealing induces new hydrogen-related acceptors in the bandgap. Another approach used a multistep annealing [91] to achieve virtually undoped semiinsulating InP with high mobility and excellent uniformity. Although the crystals were unintentionally doped, the data showed a trace level of iron in the material. A third method [92] has rendered a viable option for producing semiinsulating InP with significantly lower iron content than standard LEC or VGF material. By annealing low-Fe-content wafers at 900°C, the production yield of the crystal ingot is increased and the onset of Fe precipitates is delayed. Wafers cut from the conducting portion of the crystal can then be converted to semiinsulating material by annealing. Here the conversion was primarily due to annealing-related loss of shallow donors.

In summary, high-temperature annealing of InP can be used to improve semiinsulating crystal properties. Annealing not only reduces the hydrogen-related donor complexes, but also apparently causes Fe redistribution. Substitutional iron requires an indium vacancy to be electrically active, just as hydrogen becomes a donor only in the configuration $V_{In}H_4$. Thus the concentration of indium vacancies is critical to the annealing process. With this understanding, it is possible to lower the critical threshold concentration of Fe in semiinsulating InP.

## 7.7 New trends and future developments

Despite extensive research on methods to reduce the iron concentration in InP crystals, the commercial specification for semiinsulating InP finds Fe doping levels to be acceptable in the range of $1-6 \times 10^{16}$ $cm^{-3}$. Perhaps the cost of annealing individual wafers is too high, or the cost/benefit analysis is not yet established. However, in a recent study [93] epitaxial growth of layers on Fe-doped substrates has been compared with epigrowth on undoped semiinsulating material. This study showed some advantages for the use of undoped semi-insulating InP wafers. Tensile-strained InAlAs layers were grown by solid-source molecular beam epitaxy (MBE) on as-grown Fe-doped (SI) InP substrates and wafer-annealed undoped (SI) InP wafers. The InAlAs epilayers and InAlAs/InP type II heterostructures were compared to determine the difference between the two substrates. The data shows that the out-diffusion of Fe atoms in InP substrates may not take place at the relatively low temperature of MBE growth at 510°C. However, double-crystal X-ray diffraction measurements show that the lattice mismatch between the InAlAs layers and the two substrates is different, as a result of their different Fe concentrations. Furthermore, photoluminescence results indicate that the type II heterostructure grown on the wafer-annealed InP substrate exhibits better optical and interface properties than that grown on the as-grown Fe-doped substrate.

Commercial production of InP material today is focused on conformity to physical properties like flatness, bow, and defect density. These are the main issues of concern to wafer fabrication facilities. As long as the resistivity and mobility meet the specifications, there is no requirement to limit the total iron concentration. Much more important is the drive to grow InP crystals of larger diameter. At present, the state of the art is 100 mm diameter InP material. Since 2016, production is ongoing of 150 mm diameter InP wafers [94] using the VB technique. The schematic in Fig. 7.15 shows the use of a $B_2O_3$ encapsulating layer above the melt and a <100>-oriented seed placed at the bottom of a vertical boat. This method employs a temperature gradient of 5−20°C/cm near the solid−liquid interface. This allows the growth of 4-inch diameter InP crystals with an average EPD of 3700 $cm^{-2}$ and 6-inch wafers with average density of 4200 $cm^{-2}$, far lower than those grown by VCz or LEC methods. Such a low value exceeds the specified EPD for most InP wafer manufacturers. Although it is not an official association of semiconductor industries (SEMI) standard, the usual specification for 2−4 inch semiinsulating InP wafers is less than 5000 $cm^{-2}$ and for 6-inch wafers less than 10,000 $cm^{-2}$.

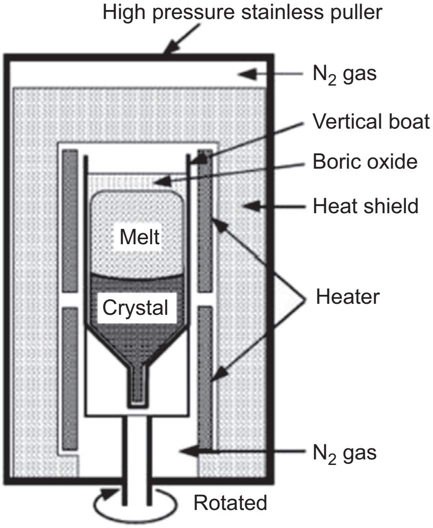

**Figure 7.15** Schematic for vertical Bridgman growth of 6-inch diameter InP crystals [94].

# References

[1] A.S. Jordan, Some thermal and mechanical properties of InP essential to crystal growth modeling, J. Cryst. Growth 71 (1985) 559−565.

[2] T. Harman, J. Jenco, W. Allred, H. Goering, “Preparation and some characteristics of single crystal indium phosphide, J. Electrochem. Soc. 105 (1958) 731.

[3] E. Metz, R. Miller, R. Mazelsky, A technique for pulling single crystals of volatile materials, J. Appl. Phys. 33 (1962) 2016−2017.

[4] J.B. Mullin, R. Heritage, C. Holiday, B. Straughan, Liquid encapsulation crystal pulling at high pressures, J. Cryst. Growth 3/4 (1968) 281−285.

[5] K. Bachmann, E. Buehler, The growth of InP crystals from the melt, J. Electron. Mater. 3 (1974) 279.

[6] R.L. Henry, E.M. Swiggard, InP growth and properties, J. Electron. Mater. 7 (1978) 647−657.

[7] W.A. Gault, E.M. Monberg, J.E. Clemans, A novel application of the vertical gradient freeze method to the growth of high-quality III-V crystals, J. Cryst. Growth 74 (1986) 491−506.

[8] G. Müller, D. Hoffmann, N. Schafer, Perspectives of the VGF growth process for the preparation of low-defect InP substrate crystals, in: Proc. 5th Int. Conf. InP and Related Materials, Paris, 1993, pp. 60−65.

[9] InP Bulk Crystal Growth and Characterization, D.F. Bliss (Chapter 5), in: O. Wada, H. Hasegawa (Eds.), InP-based Materials and Devices: Physics and Technology, John Wiley & Sons, NY, 1999, pp. 109−164.

[10] Indium Phosphide Crystal Growth I.R. Grant (Chapter 4), in: P. Capper (Ed.), Bulk Crystal Growth of Electronic, Optical, and Optoelectronic Materials, John Wiley & Sons, Chichester, UK, 2005.

[11] H. Gottschalk, G. Patzer, H. Alexander, Stacking fault energy and iconicity of cubic III-V compounds, Phys. Status Solidi A. 45 (1978) 207.

[12] D. Hurle, A mechanism for twin formation during Czochralski and encapsulated vertical Bridgman growth of III-V compound semiconductors, J. Cryst. Growth 147 (1995) 239−250.

[13] H. Chung, M. Dudley, D.J. Larson Jr., D.T.J. Hurle, D.F. Bliss, V. Prasad, The Mechanism of growth-twin formation in zincblende crystals: new insights from a study of magnetic liquid encapsulated Czochralski-grown InP single crystals, J. Cryst. Growth 187 (1998) 9−17.

[14] M. Neubert, A. Kwasniewski, R. Fornari, Analysis of twin formation in sphalerite-type semiconductors, J. Cryst. Growth 310 (2008) 5270−5277.

[15] J. Burton, R. Prim, W. Slichter, The distribution of solute in crystal grown from the melt: 1. Theoretical, J. Chem. Phys. 21 (1953) 1987−1991.

[16] E. Beam, H. Temkin, S. Mahajan, Influence of dislocation density on I-V characteristics of InP photodiodes, Semicond. Sci. Technol. 7 (1992) A229−A232.

[17] T. Lee, C. Burrus, Dark current and breakdown characteristics of dislocation-free InP photodiodes, Appl. Phys. Lett. 36 (1980) 587−589.

[18] J.R. van Wazer, Phosphorus and its Compounds, vol. 1, 1958, pp. 93−125. “Chemistry,” Interscience, NY.

[19] O. Oda, K. Katagiri, K. Shinohara, S. Katsura, Y. Takahashi, K. Kainosho, k. Kohiro, R. Hirano, InP crystal growth, substrate reparation and evaluation, in: R. K. Willardson, A. C. Beer (Eds.), Semiconductors and Semimetals, vol. 31, Academic Press, San Diego, CA, 1990. “Indium Phosphide: Crystal growth and Characterization”.

[20] A. Fischer, T. Pruss, Experiences with crystal growth using liquid encapsulation, in: Presented at American Association for Crystal Growth Conf., Gaithersburg, Md., 1969.

[21] G. Antypas, Synthesis of polycrystalline InP and single crystal growth, in: Proc. 2nd NATO Workshop on Materials Aspects of InP, Lancaster, England, 1983. No. 8.

[22] S. Hyder, G. Antypas, Synthesis and ‘in-situ’ LEC growth of (100) oriented InP single crystals, in: Proc. 3rd NATO Workshop on Materials Aspects of InP, Harwichport, Mass, 1986. No. 3.

[23] G. Antypas, Preparation of high puritybulk InP, Inst. Phys. Conf. Ser. 33b (1977) 55−59.

[24] J.-P. Farges, A method for the ‘in-situ’ synthesis and growth of InP in a Czochralski puller, J. Cryst. Growth 59 (1972) 665−668.

[25] D.F. Bliss, InP bulk crystal growth and characterization, in: O. Wada, H. Hasegawa (Eds.), InP-based Materials and Devices, John Wiley and Sons, NY, 1999.

[26] G. Iseler, A. Anselmo, D.F. Bliss, G. Bryant, R. Lancto, A model for rapid synthesis of large volume InP melts, in: Proc. 4th Int. Conf. InP and Related Materials, Schwabischgmund, Germany, 1996, pp. 50−52.

[27] W.M. Higgins, G.W. Iseler, D.F. Bliss, G. Bryant, V. Tassev, I. Jafri, R.M. Ware, D.J. Carlson, Improved phosphorus injection for bulk InP, J. Cryst. Growth 225 (2001) 225−230.

[28] D. Bliss, J. Adamski, W. Higgins, V. Prasad, F. Zach, Phosphorus-rich InP grown by a one-step in-situ MLEK crystal growth process, in: Proc. 5th Int. Conf. InP and Related Materials, 1993, pp. 66−88.

[29] X. Zhou, Y. Zhao, N. Sun, G. Yang, Y. Xu, T. Sun, Study on the perfection of in situ P-injection synthesis LEC-InP single crystals, J. Cryst. Growth 264 (1−3) (2004) 17−20.

[30] A.S. Jordan, op. cit.

[31] J. Völkl, G. Müller, A new model for the calculation of dislocation formation in semiconductor melt growth by taking into account the dynamics of plastic deformation, J. Cryst. Growth 97 (1989) 136−145.

[32] H. Zhang, V. Prasad, A multizone adaptive process model for low and high pressure crystal growth, J. Cryst. Growth 155 (1995) 47−65.

[33] H. Zhang, V. Prasad, D.F. Bliss, Modeling of high pressure, liquid-encapsulated Czochralski growth of InP crystals, J. Cryst. Growth 169 (1996) 250−260.

[34] Y.F. Zou, H. Zhang, V. Prasad, Dynamics of melt-crystal interface and coupled convection-stress predictions for Czochralski crystal growth processes, J. Cryst. Growth 166 (1996) 476−482.

[35] J. Volkl, Vol. 2b, Chap. 14, in: D.T.J. Hurle (Ed.), Handbook of Crystal Growth, North-Holland, 1994, p. 821.

[36] Y.F. Zou, G.-X. Wang, H. Zhang, V. Prasad, D.F. Bliss, Macro-segregation, dynamics of interface, and stresses in high pressure LEC grown crystals, J. Cryst. Growth 180 (1997) 524−533.

[37] P. Schwesig, M. Hainke, J. Friedrich, G. Mueller, Comparative numerical study of the effects of rotating and travelling magnetic fields on the interface shape and thermal stress in the VGF growth of InP crystals, J. Cryst. Growth 266 (1−3) (2004) 224−228.

[38] M. Tatsumi, T. Kawase, T. Araki, N. Yamabayashi, T. Iwasaki, Y. Miura, S. Murai, K. Tada, S. Akai, Growth of low-dislocation-density InP single crystals by the VCZ method, in: SPIE Proc. Vol. 1144, "Indium Phosphide and Related Materials, 1989, p. 18.

[39] M. Tatsumi, Y. Hoshokawa, T. Iwasaki, N. Toyoda, K. Fujita, Growth and characterization of III-V materials grown by vapor-pressure-controlled Czochralski method, Mater. Sci. Eng. B 28 (1994) 65−71.

[40] K. Kohiro, K. Kainosho, O. Oda, Growth of low dislocation density InP single crystals by the phosphorus vapor controlled LEC method, J. Electron. Mater. 20 (12) (1991) 1013.

[41] H. Chedzey, D. Hurle, Avoidance of growth striae in semiconductor and metal crystals grown by zone melting techniques, Nature 210 (1966) 933−934.

[42] H. Utech, M. Flemings, Elimination of solute banding in indium antimonide crystals by growth in a magnetic field, J. Appl. Phys. 37 (1966) 2021−2024.

[43] H. Miyairi, T. Inada, M. Iguchi, T. Fukuda, Growth and properties of InP single crystals grown by the magnetic field LEC technique, J. Cryst. Growth 79 (1986) 291−295.

[44] S. Bachowski, D.F. Bliss, B. Ahern, R.M. Hilton, Magnetically stabilized Kyropoulos and Czochralski growth of InP, in: Proc. 2nd Int. Conf. InP and Related Materials, Denver, Colo., 1990, pp. pp.30−34.

[45] T. Hicks, N. Riley, Boundary layers in magnetic Czochralski crystal growth, J. Cryst. Growth 96 (1989) 957−968.

[46] D. Hurle, R. Series, Effective distribution coefficient in magnetic Czochralski growth, J. Cryst. Growth 73 (1985) 1−9.

[47] J.L. Morton, N. Ma, D.F. Bliss, G.G. Bryant, Dopant segregation during liquid-encapsulated Czochralski crystal growth in a steady axial magnetic field, J. Cryst. Growth 242 (3/4) (2002) 471−485.

[48] S. Ozawa, T. Kimura, J. Kobayashi, T. Fukuda, Programmed magnetic field liquid encapsulated Czochralski crystal growth, Appl. Phys. Lett. 50 (1987) 329−331.

[49] D. Bliss, R. Hilton, J. Adamski, MLEK crystal growth of large diameter (100) indium phosphide, J. Cryst. Growth 128 (1993) 451−456.

[50] W.A. Gault et al., op. cit.

[51] W.L. Roth, T. DeWitt, A. Smith, Polymorphism of red phosphorus, J. Am. Chem. Soc. 69 (1947) 2881−2885.

[52] E. Monberg, W. Gault, F. Dominguez, F. Simchock, S.N.G. Chu, C.M. Stiles, The growth and characterization of large size, high-quality InP single crystals, J. Electrochem. Soc 135 (1988) 500−503.

[53] E. Monberg, Bridgman and related techniques, in: D.T.J. Hurle (Ed.), Handbook of Crystal Growth, vol. 2, North Holland, Amsterdam, 1994, pp. 53−97. Ch. 2.

[54] R. Tobin, M. Young, H. Helava, X. Hu, Vertical Gradient Freeze Growth of III-v Materials, 1997. Final report, Contract F33615-92-C-5921, USAF (WL/MLPO), Dayton, OH.

[55] G. Müller et al., op. cit.

[56] F. Matsumoto, Y. Okano, I. Yonenaga, K. Hoshikawa, T. Fukuda, Growth of twin-free <100> InP single crystals by the vertical liquid encapsulated Bridgman technique, J. Cryst. Growth 113 (1993) 348−350.

[57] J.J. Favier, Macrosegregation - I. Unified analysis during non-steady state solidification, Acta Mater. 29 (1981) 197−204.

[58] G. Müller, Crystal Growth from the Melt, Springer-Verlag, Berlin, 1988, pp. 57−60.

[59] G. Müller, J. Friedrich, Yield improvement and advanced defect control: driving forces for modeling of bulk crystal growth, J. Rare Earths (z1) (2006) 200−207.

[60] X. Wang, N. Ma, D. Bliss, G.W. Iseler, B. Becla, Comparing modified vertical gradient freezing with rotating magnetic fields or with steady magnetic and electric fields, J. Cryst. Growth 287 (2) (2006) 270−274.

[61] A. Ostrogorski, G. Müller, Normal and zone solidification using the submerged heater method, J. Cryst. Growth 137 (1994) 64−71.

[62] A. Ostrogorsky, H. Sell, S. Scharl, G. Müller, Convection and segregation during growth of Ge and InSb crystals by the submerged heater method, J. Cryst. Growth 128 (1993) 201−206.

[63] P. Gille, S. Scharl, G. Müller, A generalized description of solute distribution in melt growth by the submerged heater method, J. Cryst. Growth 148 (1995) 183−188.

[64] G.W. Iseler, Resistivity of bulk InP, in: J. Brice, S. Adachi (Eds.), Properties of InP, INSPEC, London, 1991, pp. 25−32.

[65] W. Walukiewicz, J. Lagowski, L. Jastrzebski, P. Rava, M. Lichtensteiger, C.H. Gatos, H.C. Gatos, Electron mobility and free-Carrier absorption in InP: determination of the compensation ratio, J. Appl. Phys. 51 (1980) 2659−2668.

[66] M. Benzaquen, K. Mazuruk, D. Walsh, A. Springthorpe, C. Miner, Determination of donor and acceptor impurity concentrations in n-InP and n-GaAs, J. Electron. Mater. 16 (1987) 111−117.

[67] G. Iseler, op.cit.

[68] D. Holmes, R. Wilson, P. Yu, Redistribution of Fe in InP during liquid phase epitaxy, J. Appl. Phys. 52 (1981) 3396−3399.

[69] R. Fornari, Influence of iron content on electrical characteristics and thermal stability of LEC indium phosphide, J. Electron. Mater. 20 (1991) 1043−1048.

[70] R. Fornari, M. Thirumavalavan, E. Gilioli, A. Sentiri, A. Zappettini, G. Mignoni, G. Zuccalli, Growth of semi-insulating InP with uniform axial Fe-doping by a double-crucible LEC technique, J. Cryst. Growth 179 (1997) 57−66.

[71] G. Iseler, Properties of InP doped with Fe,Cr, or Co, in: Inst. Phys. Conf. Ser., vol. 45, 1979, pp. 144−153. Chap. 2.

[72] A. Näser, A. Dadgar, M. Kuttler, R. Heitz, D. Bimberg, J. Hyeon, H. Schumann, Thermal stability of the midgap acceptor rhodium in indium phosphide, Appl. Phys. Lett. 67 (1995) 479−481.

[73] Y. Toudic, R. Coquille, M. Gauneau, G. Grandpierre, L. Marechal, B. Lambert, Growth of double doped semi-insulating InP single crystals, J. Cryst. Growth 83 (1987) 184−189.

[74] G. Hirt, D. Wolf, G. Müller, Quantitative study of the contribution of deep and shallow levels to the compensation mechanisms in annealed InP, J. Appl. Phys. 74 (1993) 5538−5545.

[75] R. Fornari, A. Brinciotti, E. Gombia, R. Mosca, A. Huber, C. Grattepain, Annealing-related compensation in bulk undoped InP, in: M. Godlewski (Ed.), Proc. 8th Conf. On Semi-insulating III-v Materials, Warsaw, World Scientific, 1994, pp. 283−286.

[76] F.X. Zach, E.E. Haller, D. Gabbe, G. Iseler, G.G. Bryant, D.F. Bliss, Electrical properties of the hydrogen defect in InP and the microscopic structure of the 2316 $cm^{-1}$ hydrogen related line, J. Electron. Mater. 25 (1996) 331−335.

[77] F.X. Zach, New insights into the compensation mechanism of Fe-doped InP, J. Appl. Phys. 75 (1994) 7894.

[78] R. Fornari, A. Brinciotti, E. Gombia, R. Mosca, A. Sentiri, Preparation and characterization of semi-insulating undoped indium phosphide, Mater. Sci. Eng. B 28 (1994) 95−100.

[79] D. Wolf, G. Hirt, G. Müller, Control of low Fe content in the preparation of semi-insulating InP by wafer annealing, J. Electron. Mater. 24 (1995) 93.

[80] F.X. Zach, op.cit.

[81] B. Pajot, J. Chevallier, A. Jalil, B. Rose, Spectroscopic evidence for hydrogen-phosphorus pairing in zinc-doped InP containing hydrogen, Semicond. Sci. Tecnhol. 4 (1989) 91−93.

[82] R. Darwich, B. Pajot, B. Rose, D. Robein, B. Theys, R. Rahbi, C. Porte, F. Gendron, Experimental study of the hydrogen complexes in indium phosphide, Phys. Rev. B 48 (1993) 48.

[83] C. Ewels, S. Oberg, R. Jones, B. Pajot, Briddon, Vacancy- and acceptor- H complexes in InP, Semicond. Sci. Technol. 11 (1996) 502−507.

[84] R. Fornari, On the electrical activity of Fe LEC indium phosphide, Semicond. Sci. Technol. 14 (1999) 246−250.

[85] R. Fornari, T. Görög, J. Jimenez, E. De la Puente, M. Avella, I. Grant, M. Brozel, M. Nicholis, Uniformity of semi-insulating InP wafers obtained by Fe diffusion, J. Appl. Phys. 88 (2000) 5225−5229.

[86] J. Wolk, G. Iseler, G. Bryant, E. Bourret-Courchesne, D. Bliss, Annealing behavior of the hydrogen-related defect in LEC indium phosphide, in: Proc. 9th Int. Conf. on InP and Related Materials, Hyannis, MA, 1997, pp. 408−411.

[87] R. Fornari, A. Brinciotti, A. Sentiri, T. Gorog, M. Curti, G. Zuccalli, Pressure of phosphorus in equilibrium with solid InP at different temperatures, J. Appl. Phys. 75 (1994) 2406.

[88] A. Zappettini, R. Fornari, R. Capelletti, Electrical and optical properties of semi-insulating InP obtained by wafer and ingot annealing, Mater. Sci. Eng. B 45 (1997) 147−151.

[89] C. Ewels, op cit.

[90] N. Sun, X. Wu, X. Wu, Y. Zhao, L. Cao, Q. Zhao, W. Guo, J. Zhang, K. Bi, T. Sun, Hydrogen neutralization effect in bulk N-type LEC InP materials, J. Cryst. Growth 225 (2−4) (May 2001) 244−248.

[91] M. Uchida, K. Kainosho, M. Ohta, O. Oda, Fabrication of undoped semi-insulating InP by multiple-step wafer annealing, J. Electron. Mater. 27 (1) (1998) 10−13.

[92] R. Fornari, A. Zappettini, E. Gombia, R. Mosca, K. Cherkaoui, G. Marrakchi, Conductivity conversion of lightly Fe-doped InP induced by thermal annealing: a method for semi-insulating material production, J. Appl. Phys. 81 (1997) 7604.

[93] H.W. Dong, Y.W. Zhao, Y.P. Zeng, J.H. Jiao, J.M. Li, L.Y. Lin, Influence of semi-insulating InP substrates on InAlAs epilayers grown by molecular beam epitaxy, J. Cryst. Growth 250 (3−4) (April 2003) 364−369.

[94] T. Morishita, K. Kounoike, S. Fujiwara, Y. Hagi, Y. Yabuhara, Crystal growth and Wafer Processing of 6-inch InP Substrate, Extended Abstract, 2016 (CS Mantech Conference).

# Cadmium telluride and cadmium zinc telluride

# 8

*Andrea Zappettini*
IMEM-CNR, Parma, Italy

## 8.1 Applications and requirements

Since the pioneering work of De Nobel [1], cadmium telluride (CdTe) crystals have gained more and more attention for their use in several applications:

- substrates for infrared (IR) imaging [2,3]
- room-temperature X-ray and gamma-ray detectors [3]
- electrooptic devices [4,5]
- solar cells [6].

Room-temperature bandgap and lattice parameters of CdTe were reported to be 1.5 eV and 6.484 Å respectively, and 2.2 eV and 6.1037 for zinc telluride (ZnTe) [7].

By alloying CdTe with ZnTe it is possible to change the two parameters continuously to meet the demands of different applications. For example, the development of spectroscopic gamma-ray detectors operating at room temperature requires the minimization of leakage current. This can be achieved by alloying CdTe and ZnTe to increase bandgap energy and thus intrinsic material resistivity. Usually, a cadmium zinc telluride (CdZnTe) alloy with a zinc concentration of around 10% is considered optimal for this application [8].

For substrates for IR imaging, the CdTe lattice parameter does not match that required for $Hg_yCd_{1-y}Te$ layers to be grown (usually with $y = 0.2$). This results in the formation of a high density of dislocations in the epitaxial layers. CdZnTe substrates with a zinc concentration of 4.2% allow perfect lattice matching with consequent dislocation reduction in the active layers [9].

As far as electrooptic modulators are concerned, alloying CdTe with zinc improves the device operation in the third telecommunication window [10], and improves the switch-off time of all-optical devices [11].

For all these reasons, exploitation of CdZnTe crystals has increased in recent years, and while older reviews discuss only CdTe crystals [1,3], more recent coverage addresses CdTe and CdZnTe crystals together [8,12,13].

Of course, material requirements change according to the specific application. For example, in substrates for IR devices the first requirement is the availability of large, single, twin-free wafers. Another issue is the precise control and uniformity of the zinc content [2], because this determines the lattice matching of the epitaxial layer. Generally, any structural defects, such as dislocations, inclusions, and precipitates, must be minimized to avoid the propagation of defects in the active layers [14].

**Single Crystals of Electronic Materials.** https://doi.org/10.1016/B978-0-08-102096-8.00008-2
Copyright © 2019 Elsevier Ltd. All rights reserved.

In particular, inclusions and precipitates are detrimental because they strongly reduce IR transmission [15]. Impurity concentration is also an issue, because fast-diffusive impurities can migrate to the active layers of the device during high-temperature processing.

For X-ray and gamma-ray detector applications, material requests are somewhat different. In general the material must show high room-temperature resistivity, which means control of background impurity concentration and optimal doping; high carrier mobility lifetime to allow charge drift without trapping, which can be achieved by a strong reduction of carrier traps; the material must deplete upon application of external bias, which is another property connected with the reduction of trap concentration; no inclusions, the most detrimental being those with diameter larger than 5 μ, due to their dramatic effects on detector spectroscopic performance [16]; and the material should be free from dislocations, subgrain boundaries, and twins that can locally steer the electric field and worsen charge collection.

As far as electrooptic modulators are concerned, the material is required to show high resistivity, because high electric fields must be applied, and low natural birefringence. As CdTe and CdZnTe are optically isotropic crystals, the zero-bias residual birefringence is due to the lack of homogeneity and extrinsic defects. Also, the material must be transparent at the working wavelength. Because the material has high resistivity, the free carrier contribution to optical absorption is negligible and the main contributions usually derive from inclusions/precipitates and intragap impurity electronic states.

CdTe is also employed as an absorbing layer in manufacturing solar cells. In this case the CdTe layer is just a few microns thick and is evaporated in situ, during the preparation of the solar cell. Starting material of 5N purity is usually enough for solar cell applications. It was shown [17,18] that mass transport in the case of vapor phase growth is strongly influenced by deviation of feed charge stoichiometry. Thus, starting material for solar cell applications require feed material with precise stoichiometry.

## 8.2 Thermodynamic properties and definition of suitable growth technologies

Figs. 8.1 and 8.2 respectively show the X—T and P—T projections of a CdTe phase diagram, as obtained by vapor pressure scanning [19]. The near-solidus region is shown on an enlarged scale, and the diagram also indicates the vapor composition (solid line, squares). At the maximum melting temperature (1092°C), both solid and liquid phases are rich in Te. This means that by starting from a nearly stoichiometric melt, the crystal will also be rich in Te. At melting point the total pressure is 1.36 atm [20] and the vapor is mostly composed of Cd. As a consequence, when a perfectly stoichiometric charge is heated up and melted, due to the formation of Cd vapors in the headspace a Te deviation in the melt is induced. For large Cd deviations the system can reach a pressure of almost 4 bars (see Fig. 8.2), which

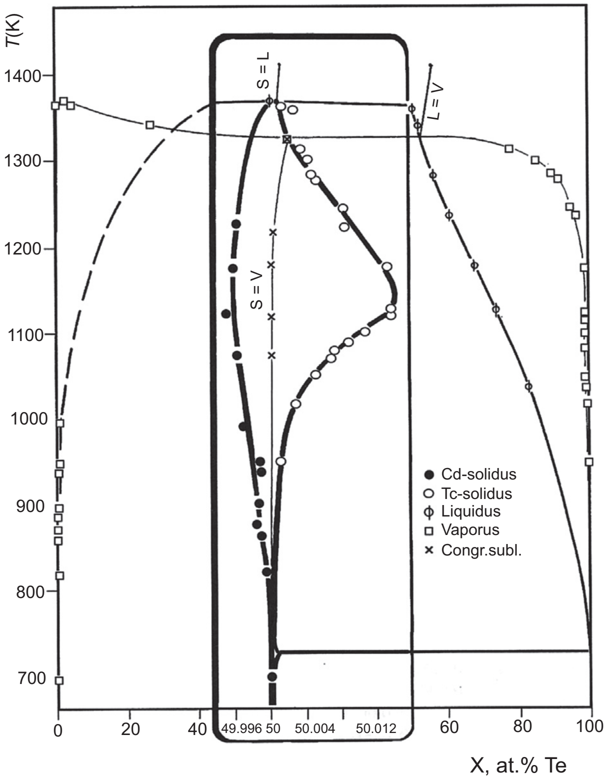

**Figure 8.1** T−X projection of the CdTe diagram. The near-solidus region is given on an enlarged scale.
From J.H. Greenberg, J. Cryst. Growth 161 (1996) 1.

can be dangerous for quartz ampoules. Also, the congruent evaporation curve is in the Te-rich side of the phase diagram. Because the congruent evaporation condition also corresponds to the minimum pressure for the system at that temperature, it is expected that crystals growing from the vapor phase in open or semiclosed systems are Te rich. Moreover, the solid composition along the congruent sublimation curve (S = V in Fig. 8.1) changes with temperature. Thus it is expected that during crystal cooling, if vapor pressure is not actively controlled, the composition of the crystal can change. Above 1051°C congruent sublimation is no longer possible.

Cd-solidus and Te-solidus curves in Fig. 8.1 define the existence region of the compound. The existence region is not symmetric at all, being much wider on the Te side than on the Cd side. The maximum solubility of Te in CdTe is as much as 50.014 mol% at 850°C. Similar results concerning tellurium solubility in solid CdTe were found by Fang and Brebrick [21], who determined partial pressure by means of optical density measurements.

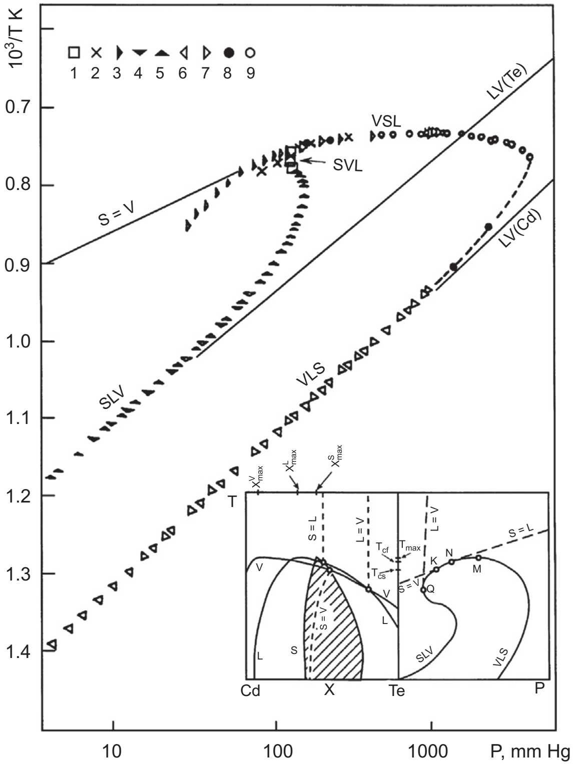

**Figure 8.2** P–T projection of the CdTe diagram. Initial composition (at % Te): (1) 50.031; (2) 50.03; (3) 50.02; (4) 50.04; (5) 52.84; (6) 49.70; (7) 41.90.
From J.H. Greenberg, J. Cryst. Growth 161 (1996) 1.

Another important point is that, according to Fig. 8.1, CdTe has noticeable solubility into Te, thus CdTe growth from a Te solution is feasible.

By alloying CdTe and ZnTe a solid solution is formed for any possible ZnTe molar fraction (Fig. 8.3) [22]. The pseudobinary section liquidus and solidus for the CdTe–ZnTe system are shown in Fig. 8.3. At any given temperature, the Zn concentration in the solid is higher than the Zn concentration in the liquid. At equilibrium condition the Zn distribution coefficient of Zn in CdTe is known to be 1.35 [24]. In the case of melt growth, because of kinematic effects the distribution coefficient is smaller, and close to 1.25 [25].

The existence region of CdZnTe has also been studied for different Zn concentrations (10%, 15%, 20%) [26,27]. Fig. 8.4 shows the T–X projection of CdZnTe. As in the case of CdTe, the homogeneity region is strongly asymmetric, being much wider on the Te side. Also the congruent sublimation line is in the Te-rich side and the maximum congruent evaporation temperature is much below the maximum melting temperature. It seems that the maximum solubility of Te in CdZnTe increases with zinc content.

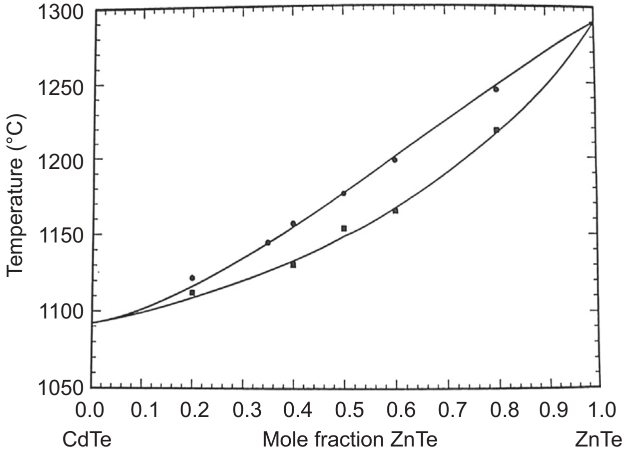

**Figure 8.3** Pseudobinary section liquidus and solidus for the CdTe−ZnTe system.
From T.C. Yu, R.F. Brebrick, Phase diagram of Cd/Zn/Te/Se compounds, in: Properties of Narrow Gap Cadmium-Based Compounds, INSPEC EMIS Datareviews Series No. 10 (1994) 414.

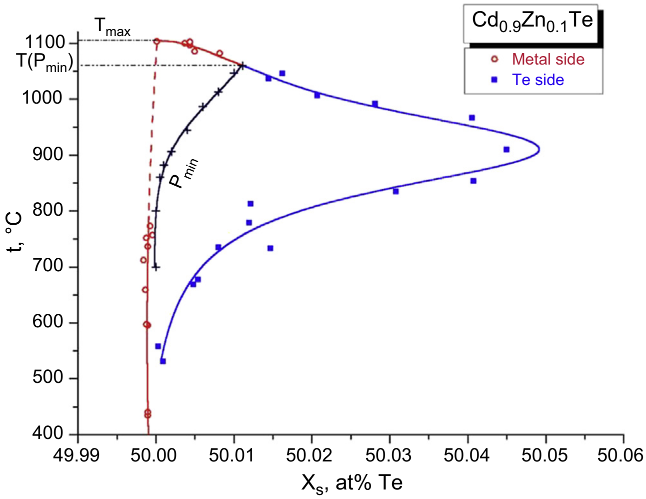

**Figure 8.4** T−X projection of $Cd_{0.1}Zn_{0.9}Te$ solidus.
From J.H. Greenberg, V.N. Guskov, J. Cryst. Growth 289 (2006) 552−558.

It is worth mentioning that pretransition phenomena near the melting point have been discovered in CdTe [28] and CdZnTe [29]. Due to the high ionicity of the Cd−Te bond, a high degree of association and preservation of spatial structuring within the molten state was found. This was demonstrated by differential thermal analysis measurements [28,29] and neutron scattering [30], and also explained by theoretical investigation [31]. These structures can be removed by superheating the melt (typically at least 40°C above the melting point) [32]. Without proper superheating, the melt complexes can greatly affect the nucleation and the twinning.

Another complication comes from the fact that the thermal conductivity of the solid is low in comparison with other semiconductors [33]. This slows down the latent heat removal, and, in general, the growth speed. The thermal conductivity of the melt is also very low, comparable with that of the solid (about 20 time less than that of silicon and 7 times less than that of GaAs) [33], so in general the heat transport in the melt phase is mainly dominated by convection rather than conduction.

Finally, the stacking fault energy is extremely low in CdTe, and hence the critical resolved shear stress, so the tendency to twinning and generation of dislocations is quite high.

## 8.3 Synthesis of the polycrystalline material

Impurity control is an important issue for most of the applications of CdTe and CdZnTe crystals. In most cases precise control of the feed material stoichiometry is also essential [17,18]. This is why it is generally very important to control the purity and the stoichiometry of the starting polycrystalline material strictly, even if the subject is rarely dealt with in dedicated papers [34]. Nowadays 7N Cd, Te, and Zn are available on the market and also 7N CdTe and CdZnTe polycrystalline material. Several techniques have been proposed for the synthesis of CdTe and CdZnTe polycrystalline material.

One of the most widely used techniques relies on synthesis from the liquid phase. In this case, Cd and Te are charged and sealed inside a quartz ampoule (eventually carbon coated) and the temperature is progressively raised according to a defined procedure [35–38]. This type of synthesis can be carried out in a horizontal or a vertical furnace. Generally, the reaction starts at low temperature (basically around the Te melting temperature). Usually only a fraction of the material reacts, leaving "bubbles" of unreacted material (pure Te and Cd). Once the temperature is further raised, due to the high vapor pressure of Cd or to the fast reaction of such bubbles the quartz ampoule may break. The use of a rocking furnace [35] or optimized temperature ramping can avoid such events.

To overcome these problems, a high-pressure synthesis method has been proposed [39], exploiting boron oxide as the encapsulant, and allowing the synthesis of large material batches in a short time. Recently, a similar high-pressure procedure has been carried out without the use of boron oxide, avoiding the possible contamination from boron [39].

Another possibility is the synthesis of the compound in a tellurium solution by the traveling heater method (THM) [40,41]. CdTe synthesis by THM is performed by vertically sweeping a Te-rich molten zone along a crucible charged with high-purity elements, as shown in Fig. 8.5.

The quartz tube is top-loaded with a certain amount of tellurium (referred to as the "molten zone tellurium"). The actual charges, composed of a near-stoichiometric ratio

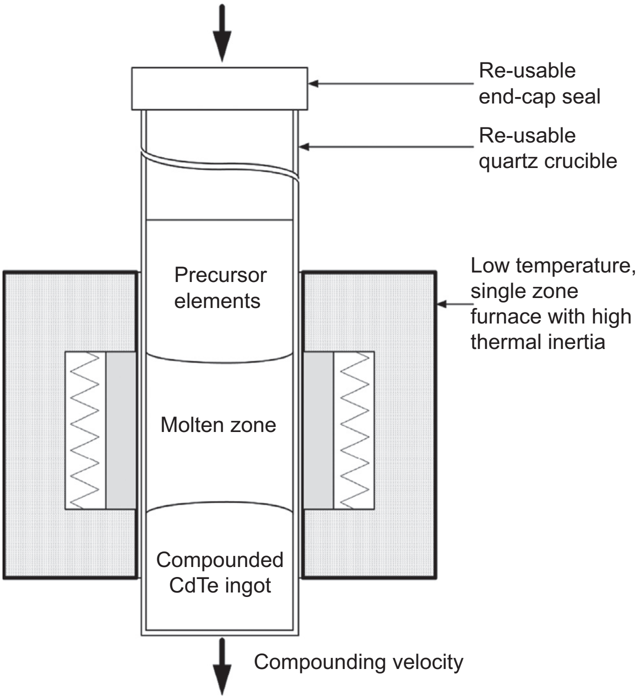
Re-usable
end-cap seal
Re-usable
quartz crucible
Precursor
elements
Low temperature,
single zone
furnace with high
thermal inertia
Molten zone
Compounded
CdTe ingot
Compounding velocity

**Figure 8.5** Scheme of the THM synthesis setup.
From N. Audet, B. Levicharsky, A. Zappettini, M. Zha, IEEE Trans. Nucl. Sci. 54 (2007) 782−785.

of tellurium and cadmium, are then loaded directly on top of the initial molten zone tellurium. The top ends of the crucibles are closed with stainless steel endcaps using standard o-ring seals. The charged crucibles are pumped down until a high vacuum level is reached, and then back filled with a partial pressure of a high-purity inert or reducing gas. The crucible is then inserted into the THM furnace, positioned so that the molten zone tellurium is located near the middle of the furnace. To initiate the synthesis process, the furnace temperature is slowly ramped up to the desired process temperature. After an appropriate delay for reaching equilibrium conditions, the crucible is lowered through the furnace at a steady rate.

The advantages of this system are manifold: the synthesis is carried out at a relatively low temperature, so impurity contamination is limited; the risk of explosions is reduced, because the synthesis is carried out in Te-rich conditions and part of the ampoule is always at a low temperature; in spite of the Te-rich conditions, the off-stoichiometry of the material is limited [41]; and the use of endcaps, made possible by the fact that the top extremity of the crucible is maintained at low temperature during the entire synthesis process, allows the repeated use of individual crucibles.

CdZnTe polycrystalline material was also synthesized by this method, and with an appropriate furnace design it was possible to growth crystals in situ after synthesis [42].

## 8.4 Description of up-to-date growth technologies/ processes

The basic thermodynamic properties discussed in the previous section indicate that several methods can be used to grow CdTe and CdZnTe crystals. In this section the most exploited and up-to-date growth technologies are described and reviewed.

### 8.4.1 Crystal growth from the melt

#### 8.4.1.1 Liquid-encapsulated Czochralski

The first attempts to grow CdTe crystals by the liquid-encapsulated Czochralski (LEC) method were unsuccessful [43–45], mainly due to the low thermal conductivity of CdTe and the decomposition of the crystal at high temperature during the pulling. More recently, attempts were made using large axial gradients (>400°C/cm) to overcome the low thermal conductivity of CdTe [46]. However, in this case crystals were characterized by a high incidence of twinning and polycrystallinity and large contamination by boron [47].

#### 8.4.1.2 Directional solidification

Bridgman is one of the most used directional solidification techniques for the growth of CdTe and CdZnTe crystals. The crystal is grown moving the molten charge in an optimized temperature gradient. Both vertical [48–51] and horizontal [52] configurations were tested. Quartz ampoules are generally used because of the possibility of soldering under vacuum or with a desired inert gas pressure, but graphitization of the ampoule walls is generally adopted for minimizing spurious nucleation at the ampoule walls [50].

Because of the necessity of superheating the molten charge, seeding is not possible. Thus fully single crystals cannot be obtained by Bridgman growth even if crystals with large single grains are reported [48,50–52].

As noted earlier, the maximum melting point is on the Te side of the phase diagram, so with standard Bridgman growth a Te-rich crystal is generally obtained. As shown in Fig. 8.1, the homogeneity region of CdTe is quite large at high temperature on the Te side. However, after growth, when the crystal is cooled, because of the retrograde shape of the solidus line, Te solubility in CdTe greatly reduces and Te precipitations takes place. This is why Bridgman-grown crystals are typically characterized by a large concentration of Te inclusions and precipitates [50].

To enhance mass and heat transport in the melt, an accelerated crucible rotation technique (ACRT) has been proposed for growing CdZnTe crystals [53]. Theoretical work shows controversial results on the real ability of ACRT to control the fluidodynamics of the system [54,55], and in any case it seems that the effect of ACRT depends on the system parameters [54]. Recent results showed that ACRT gives good results only by the proper choice of the acceleration/deceleration scheme and the growth parameters [56]. When this happens, Zn radial distribution can be improved and tellurium inclusion dimensions can be reduced [56].

Among the directional solidification techniques, the vertical gradient freeze (VGF) method must be mentioned. In this case the furnace has many heating zones, whose heating power is controlled (with a computer) to change the furnace temperature profile over time in such a way as to cause crystallization without the need to move the feed container. The major advantage of VGF over vertical Bridgman is the greater flexibility to control the thermal environment of the liquid phase, the crystal, and the crystal cooling. CdTe crystals of 25 mm diameter, with large single grains, were grown in a 24-zone furnace with an optimized temperature gradient of 8°C/cm [35]; 25 mm diameter CdZnTe crystals were grown in a furnace with five zones [57]. The temperature ramps of the heating zones were optimized to stabilize the thermal gradient at the growth interface. Using a different approach, 4-inches CdZnTe crystals were grown by VGF in such a way that the first crystallization started from the top of the melt [58]. It is difficult to obtain a convex interface during the growth of CdTe and CdZnTe crystals (discussed later). However, it was shown that using a highly thermal conductive pedestal for the crucible causes the growth interface to be convex [59], at least in the first part of the growth.

### 8.4.1.3 Vapor-pressure-controlled Bridgman growth

To overcome the presence of tellurium precipitates in the crystals, the use of an external Cd source for controlling cadmium vapor pressure during growth has been proposed. This was achieved in both vertical [60–63] and horizontal [36,37] Bridgman growth.

In the case of vertical Bridgman growth (Fig. 8.6(a)), the Cd source can be allocated in the lower [60] or upper part of the furnace [61–63]. The Cd vapors are in equilibrium with the CdTe melt, so the stoichiometry of the melt is controlled by the Cd reservoir temperature. Because vapor at the maximum melting point is mainly constituted by Cd, and the equilibrium vapor pressure was determined to be 1.36 atm [17], a higher vapor pressure (2.7 atm [60]) increases the concentration of Cd in the melt, and consequently reduces the crystal off-stoichiometry. As a result, crystals with a low concentration of Te inclusions/precipitates were obtained [14,60,61]. The control of Cd overpressure also affects the single crystal yield [2].

The control of Cd pressure was realized in a VGF furnace [33,58,64,65], with the advantage of better control of thermal gradients. High-resistivity crystals for gamma-ray detector applications of 92 mm diameter were grown by this technique with a low Te inclusion concentration [64]. Other authors report the growth of 88 and 115 mm diameter CdZnTe crystals (4% Zn) to be used as substrates for epitaxy [65]. The authors claimed to obtain reproducible growth of <111>-oriented single crystals, with low dislocation density and low concentration of inclusions, thanks to active Cd pressure control.

In the case of horizontal Bridgman growth (Fig. 8.6(b)), the vapors are in equilibrium with both the solid and the melt, so a three-phase equilibrium occurs [36,37,52,66] and a better control of crystal stoichiometry can, in principle, be

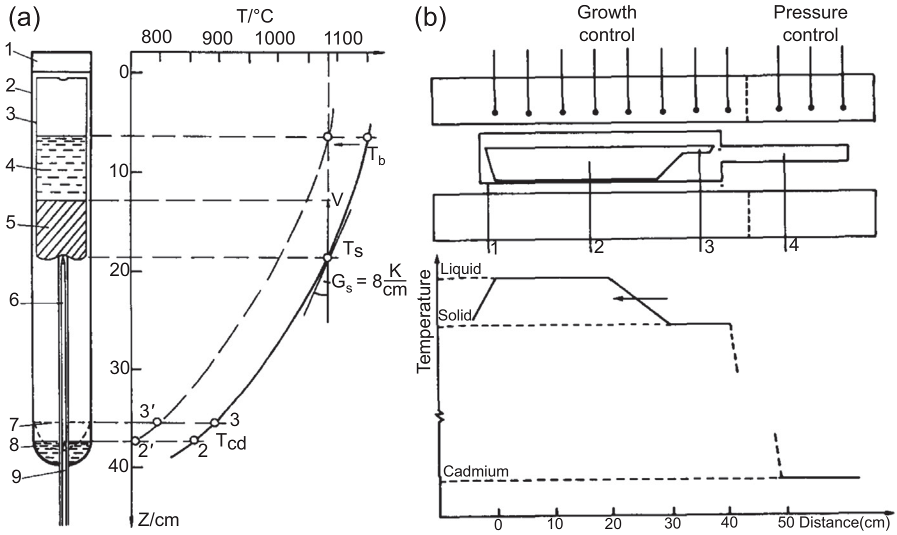

**Figure 8.6** Schemes for growing CdTe and CdZnTe crystals by vapor-pressure-controlled Bridgman method. (a) Vertical configuration: (1) plug, (2) silica container, (3) silica growth ampoule, (4) melt, (5) solid CdTe, (6) capillary, (7, 8) position of Cd source at two different temperatures, (9) thermocouple. (b) Horizontal configuration: (1) quartz ampoule, (2) boat, (3) seed, (4) cadmium reservoir.

(a) From P. Rudolph, U. Rinas, K. Jacobs, J. Cryst. Growth 138 (1994) 249–254. (b) From P. Cheuvart, U. El-Hanani, D. Schneider, R. Triboulet, J. Cryst. Growth 101 (1990) 270–274.

achieved [20]. However, with respect to vertical Bridgman, crystals do not have the advantageous cylindrical shape. Also, growth instabilities are expected as a consequence of the Marangoni convection due to the large contact area between vapors and melt [66]. The selected Cd overpressure was shown to influence the concentration of inclusions [52].

In general the vapor-pressure-control Bridgman method offers the possibility to reduce stoichiometry-related defects greatly, and it is thus largely used for the production of substrates for the realization of IR devices [2,14,67]. By increasing Cd pressure in the growth chamber, the material conductivity usually switches from p-type to n-type. More recently, thanks to In doping and control of postgrowth cooling procedures and the temperature of the Cd reservoir, high-resistivity crystals were obtained [63].

### 8.4.1.4 High-pressure Bridgman

The high-pressure Bridgman (HPB) method was proposed to avoid the use of quartz crucibles, and hence the unavoidable contamination of oxygen from silica [68]. The furnace used (Fig. 8.7) can withstand over 100 atm of internal pressure. High-purity elements are loaded in a high-purity graphite crucible, with a tight-fitting cap that reduces charge loss. After purging, the inert gas pressure of the furnace is increased up to 100 atm. After compounding, growth is carried out in the same crucible. Both CdTe

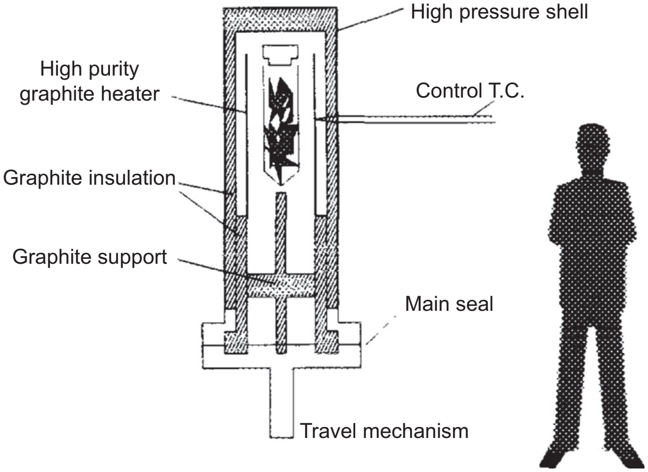

**Figure 8.7** Scheme of HPB apparatus.
From F.P. Doty, J.F. Butler, J.F. Schetzina, K.A. Bowers, J. Vac. Sci. Technol. B 10 (1992) 1418−1422.

[68] and CdZnTe crystals [69] were obtained. Because the crucible cap is not soldered, a residual charge loss of a few percent in weight occurs, with the loss being limited by the low diffusion length due to the high inert gas pressure. Because at the melting temperature the vapor is mainly composed of Cd, the crystal is expected to grow in Te-rich conditions: accordingly, Te inclusions were observed [70]. Even if it were possible to grow CdZnTe crystals with large Zn concentrations, the most promising properties were shown by crystals with low Zn concentrations (<20% [71]). An evolution of HPB considers the VGF technique to cause solidification without moving the ampoule by using a multizone furnace [72]. Because HPB does not require crucible soldering, it was possible to grow crystals of very large diameters, up to 140 mm [72].

### 8.4.1.5 Boron oxide encapsulated vertical Bridgman

The use of boron oxide is another way to avoid the technological problems related to the soldering of ampoules. Boron oxide is largely employed as encapsulant in the LEC technique to prevent material decomposition when growing III/V semiconductor crystals, and was also proposed in the case of the vertical Bridgman configuration to grow GaAs [73] and CdTe crystals [74−76]. The polycrystalline material is charged in a quartz ampoule with a boron oxide pellet on the top (see Fig. 8.8). When the temperature is raised, boron oxide softens before charge melting, and if an appropriate inert gas pressure is applied (usually 6 bars), charge decomposition is prevented. Then crystal growth goes on as in a standard vertical Bridgman furnace. One of the advantages of this method is that there is no free volume in the ampoule, so the charge stoichiometry is not modified by the incongruent sublimation of the material at the melting point. Moreover, it was demonstrated [77,78] that in the case of both 1-inch and 2-inch crystals, boron oxide fully encapsulates the growing crystal so

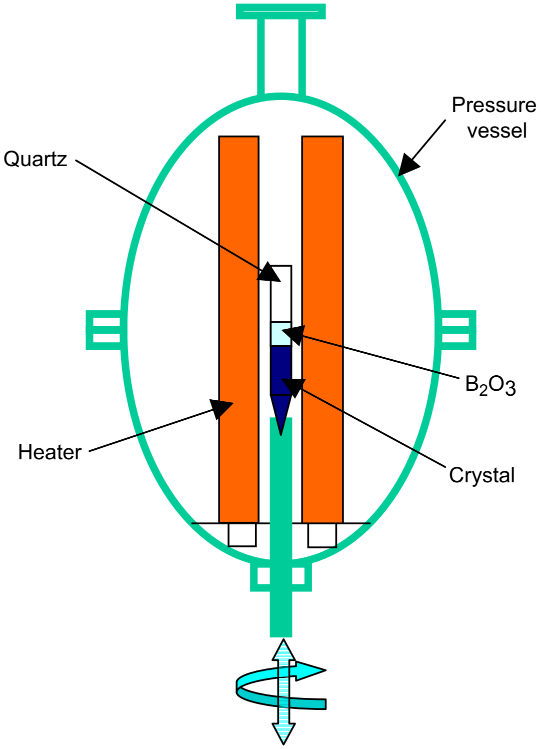

**Figure 8.8** Apparatus for boron oxide vertical Bridgman growth.
From M. Zha, A. Zappettini, F. Bissoli, L. Zanotti, V. Corregidor, E. Dieguez, J. Cryst. Growth 260 (2004) 291–297

direct contact with the crucible walls is prevented. As a consequence, low dislocation density was achieved [78,79], and the boron contamination appeared to be much lower that observed in LEC-grown crystals [79].

### 8.4.2 Vapor-phase growth

By means of physical vapor transport (PVT) it is possible to grow crystals at a temperature well below the melting point, thus in general it is possible to obtain crystals with a lower defect concentration than seen in melt-grown crystals. In particular, in the case of CdTe PVT is favored by the fact that, at temperatures well below the maximum congruent evaporation temperature, equilibrium vapor pressure reaches values (1–10 mbar) that allow a reasonable mass transport. Moreover, PVT looks particularly attractive for CdTe because it avoids the previously discussed seeding problems connected with melt growth.

The simplest way to grow CdTe crystals by vapor phase is to seal a CdTe charge in a quartz ampoule and vertically move it up an adequate thermal gradient [80]. Even without seeding, it is possible to obtain crystals with reasonable single grains.

However, vapor mass transport in closed ampoules was found to be greatly affected by total vapor pressure, and total vapor pressure was influenced by charge feed stoichiometry [17,18]. This is why the stoichiometry of the feed charge is particularly important in the case of vapor-phase growth, and heat treatments were proposed to approach the congruent evaporation composition [81,82]. Also, a method was demonstrated to characterize with high accuracy the off-stoichiometry of the feed charge [83,84]. Another issue that can change in a not-reproducible way the inner gas pressure in a growth ampoule is high-temperature degassing of quartz [85]. However, the method was quite flexible, so CdZnTe crystals [86] and doped CdTe crystals were grown [87]. In some cases seed was used to control the nucleation process [88]. A horizontal growth configuration was also proposed [89].

To avoid the problems linked to the use of a closed ampoule, semiclosed systems were proposed, similar to the well-known Markov method [90], in both horizontal [91] and vertical configurations [92]. The growth chamber has a high-temperature zone (where the feed charge and the seed are located) and a low-temperature zone that acts as a heat sink. The role of the latter is to reduce the overall pressure of the system by gettering impurities and condensing the stoichiometry excess component. In this way it was possible to achieve a higher transport rate, more reproducible growth conditions, and the reproducible growth of twin-free CdTe crystals [92].

A noticeable evolution of the semiclosed system is the multitube PVT system [93−97]. The growth system (Fig. 8.9) comprises three vertical furnaces connected by heated horizontal cross-members. Each cross-member incorporates a calibrated capillary flow restrictor to regulate the throughput. Vapor pressures on either side of

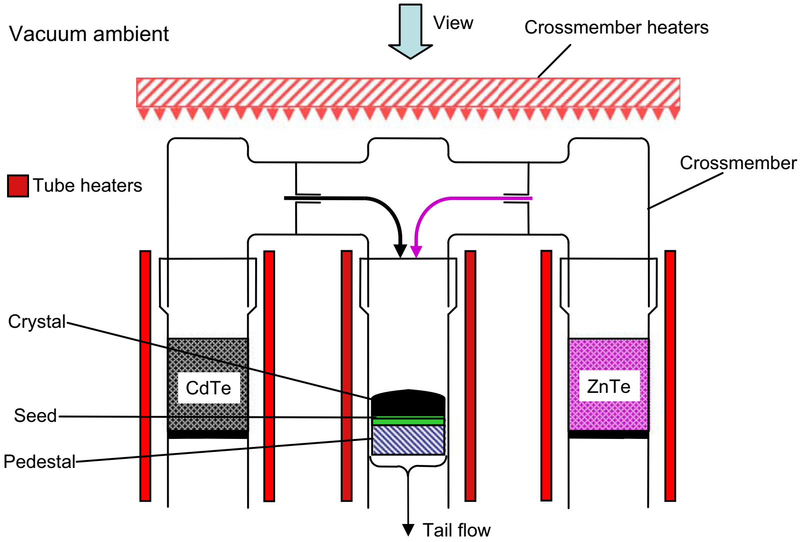

**Figure 8.9** The multitube PVT growth system.
From J.T. Mullins, B.J. Cantwell, A. Basu, Q. Jiang, A. Choubey, A.W. Brinkman, B.K. Tanner, J. Electron. Mater. 37 (2008) 1460−1464.

the capillary can be measured in situ by optical absorption. CdTe and ZnTe polycrystalline charges are in the external furnaces. In the central furnace the seed is on a pedestal that is smaller than the inner diameter of the furnace, so the lowest part of the furnace acts as a heat sink.

Adjusting source temperature, Cd and Zn fluxes can be independently controlled to obtain the desired material stoichiometry. With this technique 2" CdTe [94,95] and CdZnTe crystals [96,97] were grown using (211)B GaAs wafers as substrates.

Another interesting solution for the realization of large-area detectors is the MOVPE deposition of thick CdTe films on silicon substrates [98,99]. Recently, thick CdTe films have grown also by MBE at low temperature directly on the Medipix readout chip for demonstrating the chance to avoid postprocess bonding procedures in the realization of imaging X-ray detectors [100].

### 8.4.3 Traveling heater method

Growth from solution generally presents several advantages over melt growth. Because solution growth happens at a temperature lower than the melting point, lower contamination from the crucible and lower defect density is expected. Among the disadvantages is the possible contamination of the solvent, which can be avoided if one of the crystal components is used as the solvent.

This strategy has been extensively applied in growth of CdTe and CdZnTe crystals by the THM. Te is preferred as solvent due to the lower vapor pressure and because high-resistivity material with optimal carrier transport properties can be obtained by group III and group VII element doping when the crystal is grown under Te-rich conditions. However, the use of Cd as solvent has been exploited in the past [101,102] and recently reconsidered, with the aim of enhancing arsenic doping [103]. Polycrystalline CdTe or CdZnTe is charged in a quartz ampoule (Fig. 8.10 [104]). The seed in the lower zone is separated from the charge by a Te zone where the compound dissolves according to the solubility fixed by the phase diagram (Fig. 8.1). The ampoule is moved down with respect to the heater, so seed can grow while polycrystalline material is dissolved in the upper part. Because of the relatively low growth temperature (700−900°C) of the Te-rich conditions, and because most of the ampoule is outside the heater, the vapor pressure is low and the risks of explosions are avoided. Moreover, the Te zone efficiently getters background impurities [42]. This is the main reason why large-volume high-quality CdTe detectors were first obtained by using THM-grown crystals [105,106].

The previously mentioned difficulty of seeding that affects melt growth is less important in the case of solution growth, so seeding looks feasible for THM growth, in particular using <111>B-oriented seeds [107]. Because twinning is always a possibility, a misorientation of 5 degrees towards the nearest <110> direction was shown to optimize conditions in terms of single crystal yield [107]. The feed charge was a CdTe boule previously grown by Bridgman. CdTe single crystals with diameters of 50 mm [107], 75 mm [108], and 100 mm [109] were subsequently demonstrated. The growth rate could be increased from 5 to 15 mm/day without affecting crystal properties [110].

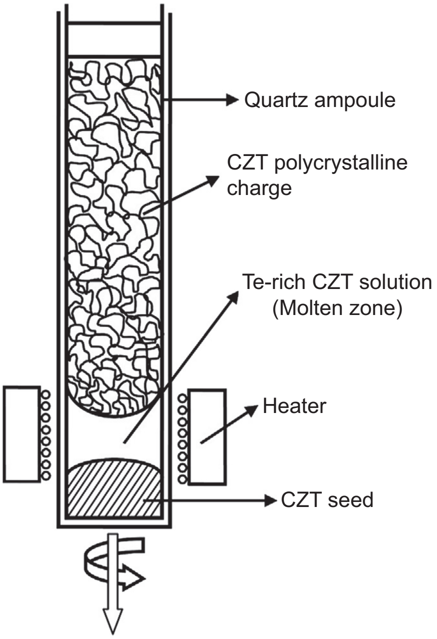
Quartz ampoule
CZT polycrystalline charge
Te-rich CZT solution (Molten zone)
Heater
CZT seed

**Figure 8.10** Schematic of THM technique.
From U.N. Roy, A. Burger, R.B. James, J. Cryst. Growth 379 (2013) 57–62.

CdZnTe crystals can also be grown by THM [42]. The reproducible growth of 50 mm diameter single CdZnTe crystals was demonstrated [111]. A <111>-oriented seed is preferred [112]. Thanks to the fact that only part of the overall feed charge is molten, uniform Zn distribution could be achieved. More recently, 75 mm diameter crystals were obtained [113].

For several reasons, the growth interface should be convex toward the crystal. A smooth convex interface was connected to the growth of large single grains and a reduction in the incorporation of Te inclusions [114]. The length of the molten zone is an important issue, affecting the shape of the growth interface. This is because strong convection dominates the molten region due to the large thermal gradient involved [42]. In the growth of 50 mm diameter CdTe a length of the melt region between 30 and 50 mm resulted in a convex interface [107]. The convection helps the mass transport in the molten zone, but to reduce diffusion boundary layers close to the crystal surface the ACRT was proposed [42], and has been proposed again very recently [115,116]. It was shown that using ACRT it is possible to change the interface from concave to flat or convex, depending on the ACRT parameters. Moreover, the use of ACRT significantly decreased the incorporation of Te inclusions.

The growth interface of CdZnTe crystals grown by THM under a static magnetic field of 3 T has also been investigated [117,118]. It was found that the microstructure of the interface improved, with a reduction of twinning and incorporation of Te. The effect was attributed to the damping of convection in the Te solution due to the Lorenz force.

## 8.5 Benefits of computer modeling

Computer modeling is gaining more and more importance in all fields of material science, and in particular in crystal growth. The development of more powerful computing systems now allows the simulation of complex systems. In crystal growth the system is complicated by the presence of different phases (at least one of them a fluid phase), separated by moving surfaces whose behavior should in general be a result of the modeling of temperature and concentration gradients, and external fields such as gravity, electric, or magnetic fields. In spite of the technical difficulties, the use of computer modeling for crystal growth can be extremely rewarding, because crystal growth is in many cases a slow process that requires much time and extensive use of an expensive furnace, pure raw materials, and costly crucibles and consumables. But although the development of a robust crystal growth technology requires the conduct of a large series of experiments, computer modeling can quickly guide scientists toward the best growth parameters and suggest the feasibility of novel and convenient growth techniques.

Modeling has been applied to the study of CdTe/CdZnTe directional solidification technology, in particular in the vertical Bridgman and VGF methods. Sen et al. [33] analyzed the heat transfer in 2-inches CdTe crystals. Pfeiffer and Mühlberg [49] considered the effects of latent heat, and predicted a concave growth interface. Kuppurao et al. [119] developed a finite element model accounting for heat transfer, melt convection, and solid/liquid interface shape. This model also showed the formation of a concave interface, especially for large growth rates (>1 mm/h). Pandy et al. [120] and Gasperino et al. [121] studied electrodynamic VGF furnace for the growth of CdZnTe. Derby et al. suggested the use of a dynamic bell-curve furnace profile to achieve a convex interface [122]. Aiming to improve homogeneity in the melt and decrease the incorporation of Te inclusions, the effects of ACRT have been studied for vertical Bridgman [54,55], HPB [123], and VGF [124,125] growth. Generally, the results of using ACRT are much more complicated than classical wisdom suggests, and the outcomes seem to be strongly dependent on the ACRT rotation circle that is adopted. In some cases ACRT can actually suppress mixing in the melt [54], increase concavity of the growth interface, or cause concentration striations [123]. This means that ACRT can be useful only if careful optimization of the process parameters (acceleration, frequency, etc.) is considered. On the other hand, the use of traveling magnetic fields that were beneficial for other semiconductors [126] seem not to be advantageous for CdZnTe [127].

Modeling studies have also been carried out on THM growth. The main issues related to this technology are the low growth rate, which is limited by the mass transport in the liquid phase, and the shape and instabilities of the growing interface. Chang et al. [128] considered a finite element steady-state model for analyzing the thermal field in THM growth of HgCdTe, assessing the effect of various factors on the interface shape. In a later work, thermal and solutal buoyancy were taken into account and the coupling of heat and mass transport was investigated [129], revealing the influence of the fluid flow on the solute distribution in the liquid zone. Dost et al. developed a model for THM growth of CdTe [130] which takes into account heat and mass transfer and fluid flow in the molten zone, and studies the conditions for achieving a flat growing interface. Stelian and Duffar [131] investigated the thermal field and melt convection in CdTe THM growth. A novel furnace configuration for growing large crystals with a flattened interface was proposed. More recently, Peterson et al. developed a more accurate model that also takes into account the local thermodynamic conditions at the dissolution interface [132,133]. The model presents a strong interplay among thermal, solutal, and flow effects that gives rise to complicated flow structures. In particular, the model shows the formation of particular flow structures, lee waves, that inhibit the removal of Te rejected at the growth interface, leading to constitutional supercooling at growth rates lower than expected. This is the phenomenon that severely limits the growth rate in THM.

The effects of vertically oriented static magnetic fields [134] and rotating magnetic fields (RMFs) under microgravity and terrestrial conditions [135−137] have been investigated by numerical modeling. The effects of RMFs seem to be negligible with respect to natural convection at 1 g (except for high field values around 50 mT) [135,136]. In contrast, in microgravity conditions, in the absence of natural convection, RMFs are effective, but not always beneficial for interface stability and dopant distribution [136,137]. Barz et al. have shown that the use of ACRT for the growth of CdTe by THM is effective to increase the mixing in the liquid zone and thus allows higher growth rates [138].

## 8.6 Postgrowth thermal treatments

It is well known that the properties of materials for electronics can be greatly improved by postgrowth thermal treatments carried out in a controlled atmosphere at temperatures well below the material melting point. The effects of thermal treatments on CdTe samples have been studied for a long time, as has the possibility of changing the conduction type on the basis of the type of vapors used during the annealing (Cd or Te) [1].

The main motivation for performing thermal treatments on CdTe and CdZnTe has been the elimination of Te inclusions. These inclusions are extremely detrimental no matter what material is used as a substrate for HgCdTe growth or for the realization of X-ray and gamma-ray detectors. In the first case, Te inclusions increase the absorption in the IR and can potentially limit the quality of the epitaxial layers [14]. In the second case they have dramatic effects on the spectral response of the gamma detectors [16]. It was also shown that the density of inclusions that can be tolerated by a device depend on their dimension, as the larger ones are the most detrimental [139]. Inclusions larger than 5 μ limit detector properties [16,139,140]. Moreover, Te inclusions are typically surrounded by a network of defects that locally reduce carrier lifetimes [141−143].

Thermal treatments are carried out in quartz ampoules sealed under vacuum, or with a certain pressure of inert gas. Also, it can be convenient to carry out the thermal treatment with a desired pressure of $Te_2$, Cd, or Zn vapor. In this case the ampoule is introduced in a two-zone furnace, with the sample to be treated at a higher temperature and a reservoir of the element to be evaporated in a second zone whose temperature is selected according to the Clausius Clapeyron relationship for the particular element.

Different methods have been proposed to characterize the concentrations of Te inclusions. For example, the off-stoichiometry determination that can be measured by the study of equilibrium vapor pressure of samples at high temperature [83,84] is directly linked to the overall Te inclusion concentration. However, all information on dimensions and distributions of the inclusions is lost. Inclusions can also be revealed by optical transmission in the near-IR. Te and Cd inclusions are actually opaque in the IR, in the transparent region of the material. A relation between the IR extinction spectra and inclusion density was found [15]. Dimensions and distribution of the inclusions can be studied by IR optical microscopy [144]. The determination of the inclusion concentration is complicated by the fact that at high magnification, the depth of the field is much lower than the sample thickness, so in a single photograph only a few inclusions appear really sharp. To overcome this problem, a set of photographs is taken at different focal planes, reconstructing all inclusions on a single focal plane [145]. A system for a complete three-dimensional reconstruction of inclusion distribution based on optical microscopy was recently proposed [139,146]; the system is able to detect inclusions with a diameter down to 1 μ [146].

Thermal treatments under Cd pressure are known to eliminate Te inclusions in a wide temperature range (550−900°C) [147−152], improving the quality of CdTe and CdZnTe substrates for IR applications [147]. In the case of CdZnTe crystals, treatment with a mixture of Cd and Zn powders was also considered [153,154]. According to the selected temperature and duration, the number and dimensions of Te inclusions can be reduced. However, several authors report that a small portion of the original inclusion cannot be removed [152,155,156]. This is attributed to the presence of voids that are sometimes observed in Te inclusions [148].

The disappearance of inclusions is generally attributed to the in-diffusion of Cd that reacts with the molten Te. CdTe and CdZnTe density is lower than Te density, so an expansion is expected. This fact, in connection with the different thermal expansion coefficients, is at the basis of the observed formation of defects during the process. As a consequence, star-like defects appear after annealing, replacing large Te inclusions [148−151,153]. These defects involve a much larger portion of the material and are constituted by a dislocation cluster. A treatment above 750°C increases the etch pit density (EPD) far from the inclusion region [148]. It was also found that annealing in Cd vapors causes the formation of stacking faults [154].

Crystals grown for detector applications usually show a very high resistivity ($>1E10\ \Omega \times cm$), which usually decreases by several orders of magnitude as a consequence of Cd vapor annealing.

To restore the high resistivity, and taking into consideration the CdTe point defect model [157], several authors propose second thermal treatments with a Te atmosphere [158–162]. The process has been demonstrated successfully at low temperatures (around 500°C). However, some authors report that at the end of the two-step process the detector properties of the material are not optimal [159,162]. Only in one case was an improvement of the detector properties registered, but it should be underlined that the final properties were not in any case at the state of the art [160].

In contrast, crystals grown under Cd-rich conditions exhibit Cd inclusions that can be eliminated by a thermal treatment in a Te atmosphere [155,158]. It was suggested that 700°C is the optimal temperature for this process [154].

It was also shown that inclusions can be moved inside the crystal by means of thermodiffusions. Inclusions move inside a temperature gradient toward the higher temperature by a mechanism of solution/dissolution. The higher solubility of CdTe/CdZnTe in Te at higher temperature causes the crystal to dissolve at the high-temperature side of the inclusion and to deposit at the low-temperature side [163]. This mechanism can be used to remove inclusions from substrates, and is effective in both Te [156] and Cd/Zn atmospheres [153,164]. In a few cases large Te inclusions break into two during the thermodiffusion, with the smaller piece not moving in the thermal gradient [156,164]. The interpretation of this phenomenon is that the liquid part of the inclusion actually moves, according to the described mechanism, while the void does not. Because of the difficulty of taking IR pictures in situ during the thermal treatments, the method for studying thermodiffusion relies on comparison of IR images taken before and after the annealing. A direct demonstration of thermodiffusion has been given using an IR laser to generate a thermal gradient locally close to the inclusions, while keeping the sample at room temperature under the scrutiny of an IR microscope [165].

Different crystal cooling procedures were proposed aiming to minimize inclusion density, thus preventing the need of postgrowth treatments. For CZT crystals grown by vertical Bridgman, the combined effects of stoichiometry and cooling rate were considered [166]. In a further study it was evidenced that a slow cooling rate (10°C/h) results in the formation of large inclusions, while a faster one (50–60°C/h) produces only small inclusions, but a larger concentration of point defects [167]. For CdTe crystals grown by THM, Fochuk et al. reached a different conclusion, suggesting that the best condition for limiting inclusion density as well as other structural defects was to cool down the crystal at a moderate rate (10°C/h) [168].

The heat treatment parameters for getting rid of both Cd and Te inclusions are clearly described in the literature, but it should be underlined that there is not yet a clear process (or a combination of processes) to produce a material that is free from inclusions and, at the same time, shows high resistivity and optimal transport characteristics for electrons and holes. This holds true in spite of the fact that it is sometimes claimed that high-quality material is obtained by an optimized thermal treatment [113,169], and that highly spectroscopic material with extremely reduced inclusion density is actually available on the market.

## 8.7 State of the art of CdTe and CdZnTe crystals

As described in the previous sections, many improvements have been made in recent years in the development of CdTe and CdZnTe crystals. Because crystal quality is driven by specific applications, it is appropriate to discuss the state of the art reached by the technology separately for the two main applications of CdTe and CdZnTe crystals.

### 8.7.1 X-ray and gamma-ray detector application

The first spectroscopic detectors were mainly made using CdTe:Cl crystals grown by THM [105], because of the gettering effect of the liquid Te zone. Since 1988, the technology for growing CdZnTe crystals by HPB was developed [68–72] and detectors with very good spectroscopic performances [70–72,170,171] and large dimensions (up to 6 $cm^3$ [172], with thickness up to 2.5 cm [173]) were realized, and mobility-lifetime product for electrons as high as $6 \times 10^{-2}$ $cm^3/V$ [172]. However, it should be noted that even if large CZT crystals are grown by HPB, the crystals are not reproducibly single [71,72]. So postgrowth selection of the part of the crystal useful for the production of high-quality detectors is necessary, with a consequent effect on the process yield.

Good-quality detectors were also demonstrated by other growth technologies, such as horizontal Bridgman [174], vertical Bridgman [51,175,176], boron oxide encapsulated vertical Bridgman [177], and multitube PVT [97].

However, in recent years THM-grown crystals seemed to be the most interesting for detector applications. CdTe crystals of 75 and 100 mm diameter can be reproducibly obtained by THM with optimal detector properties [108–110]. The crystals show a low inclusion density, probably because inclusions diffuse out of the growth interface due to the large temperature gradient during THM growth [144]. The mobility-lifetime product is reproducibly around $2-3 \times 10^{-3}$ $cm^{-2}/V$ for electrons and around $2-5 \times 10^{-4}$ $cm^{-2}/V$ for holes. CdZnTe crystals up 100 mm diameter can be reproducibly grown by THM [111–113] with a mobility-lifetime product larger than $1 \times 10^{-2}$ $cm^{-2}/V$ for electrons. Detectors with a volume of 6 $cm^3$, exhibiting very good spectral resolution, can be made [111–113,178,179].

Thus THM looks as the most interesting technology for the realization of both CdTe and CZT crystals for detector applications. The question of whether CdTe or CdZnTe is the best choice for detector applications has been the subject of previous studies [180–182]. CdTe is more homogeneous than CZT (there is not the problem of Zn distribution) and it shows a higher mobility-lifetime product for holes. However, CdTe suffers the problem of polarization: a decrease in the full energy pulse height and efficiency with time under irradiation [183]. CZT, on the other hand, has a higher resistivity (one order of magnitude) and a higher mobility-lifetime product for electrons, and does not show polarization effects, except for a high flux of radiation. To overcome the lower resistivity of CdTe, which may result in a larger leakage current of the detectors and thus worse spectral resolution, Schottky structures using at least one blocking contact have been proposed [184], with an extremely low leakage current. Unfortunately, it is difficult to realize Schottky structures for detectors exceeding 1−2 mm. For these reasons, CdTe seems to be more promising for applications at photon energy up to 100 keV (where large thickness is not an issue), especially for imaging applications where good homogeneity is required [185]. In contrast, the higher resistivity and mobility-lifetime product for electrons of CZT enable the realization of thicker detectors (up to 15 mm CZT detectors are commercially available) to detect photons at higher energy (up to 1.5 MeV [186]). The limitation of the poor mobility-lifetime product for holes is avoided by a correct choice of the contact geometry (coplanar grids, stripes, pixels) to ensure the realization of single carrier devices [105,180,187].

### 8.7.2 Substrates for IR devices

Vertical Bridgman with control of Cd overpressure proved to be an advantageous technology for the realization of substrates for IR devices [14] because it ensures low background impurity contamination, low inclusion concentration, good optical transmission in the IR (thanks to the control of the Cd pressure), good single crystal yield, and low EPD (around $5 \times 10^4$ cm$^{-2}$). Substrates as large as $4 \times 6$ cm$^2$ can be reproducibly grown by this technique [14]. However, the crystals are not fully single, so the substrates are selected from the obtained large single grains.

More recently, multizone VGF furnaces have been developed that allow better control of the thermal gradient at the interface during growth and better control of the temperature during crystal cooling [58,65]. Thanks to this technique, fully single crystals were obtained [65] with 80 and 115 mm diameters, <111> oriented, with EPD of $<5 \times 10^4$ cm$^2$. Cd pressure control was necessary to reduce the concentration of inclusions.

In recent years THM CZT crystals have been proposed as substrates for IR imaging applications [188,189]. The obtained substrates show a uniform Zn distribution, low EPD ($<3 \times 10^4$ cm$^{-2}$), and good IR transmission.

## 8.8 New trends and future developments

As shown in the previous sections, CdTe and CdZnTe growth techniques have seen huge development in recent years. However, some issues are still open, and some of the required developments are described below.

First of all, medical applications, and in particular computer tomography, require detectors operating at very high fluxes, exceeding $10^8$ photons s$^{-1}$ cm$^{-2}$. It was found that CZT-based detectors show a polarization effect under such high fluxes [190], which seems to be mainly linked to the low hole mobility-lifetime product [191]. Although recently CdZnTe detectors with relatively high hole mobility-lifetime product were reported, showing no polarization effect [179,192], it is not clear how to control the hole mobility-lifetime in CZT crystals.

A more general field of applications for detectors is X-ray imaging for nondestructive testing. Pixels detectors are made and usually directly bump bonded to Application-Specific Integrated Circuit (ASICs) to obtain maximum performance [185,193−196]. Despite the high efficiency shown by these detectors at high energies, however, the homogeneity of the detector response is not satisfactory: images acquired with no objects in the optical path (basically an evaluation of the detector homogeneity) shows dark spots and dark lines that are attributed respectively to the presence of inclusions and subgrain boundaries in the detector material [185,193]. Moreover, nonlinearity in the pixel response and the presence of polarization necessitate additional calibration procedures to obtain a reasonable flat-field image [194,195]. Also, characterization of the pixel detectors with collimated synchrotron radiation revealed that a nonuniform electric field in the detector causes variations in the counting and spectroscopic performances of individual pixels [196]. These studies demonstrate that X-ray imaging applications require better crystals with a lower concentration of extended defects, such as inclusions, dislocations, and small-angle grain boundaries, and also a homogeneous and controlled distribution of point defects.

Another important issue is the final cost of CdTe/CdZnTe crystals: this is not related to the cost of the raw material, but is related to the cost of the process and the low yield of good-quality material. Alternative technologies, mostly based on III−V semiconductors for substrates for IR imaging and on scintillators for gamma-ray detectors, show lower performance but extremely competitive prices. This means that along with improvements of the crystal quality, improvements in the overall yield of the growing process must be sought.

THM and VGF are today the growing techniques that produce the best-quality crystals. It was shown that some modifications, such as the introduction of ACRT, are very promising, but process parameters must in any case be carefully optimized. Also the vapor phase promises interesting results, especially for preparation of thick-film devices directly on the read-out electronics.

Another important issue is that because CdTe and CdZnTe crystals are gaining market share, an increasing gap is forming between the technology level acquired by private and public entities, with the difference that only the latter disclose technology details. Because the devices realized with CdTe and CdZnTe crystals are employed in fields that have so large impact on life of people, such as medicine, security, environmental control, it is important that also public research institutions keep on researching on this subject.

For all these reasons there is still room for improvement and a need for research efforts to grow larger, more perfect, cost-effective CdTe and CZT crystals.

## References

[1] D. De Nobel, Philips Res. Rep. 14 (4) (1959) 361−363. Abstract Number: A1960-02893.
[2] S.L. Price, H.L. Hettich, S. Sen, M.C. Currie, D.R. Rhiger, E.O. Mc Lean, J. Electron. Mater. 27 (1998) 564−572.

[3] K. Zanio, Semiconductors and Semimetals, Volume 13, “Cadmium Telluride”, Academic Press, 1978, pp. 164−185.
[4] J.E. Kiefer, T.A. Nussmeier, F.E. Goodwin, IEEE J. Quant. Electron. QE-8 (1972) 173−179.
[5] M. Ziari, W.H. Steier, Appl. Optic. 32 (1993) 5711−5723.
[6] N. Romeo, A. Bosio, R. Tedeschi, A. Romeo, V. Canevari, Sol. Energy Mater. Sol. Cells 58 (1999) 209−218.
[7] D.J. Williams, Densities and lattice parameters of CdTe, CdZnTe and CdTeSe, in: Properties of Narrow Gap Cadmium- Based Compounds, INSPEC EMIS Datareviews Series No. 10, 1994, pp. 399−401.
[8] T.E. Schlesinger, J.E. Toney, H. Yoon, E.Y. Lee, B.A. Brunett, L. Franks, R.B. James, Mater. Sci. Eng. 32 (2001) 103−189.
[9] M.J. Bevan, N.J. Doyle, D. Snyder, J. Cryst. Growth 102 (1990) 785−792.
[10] A. Milani, E. Bocchi, A. Zappettini, S.M. Pietralunga, M. Martinelli, J. Cryst. Growth 214 (2000) 913−917.
[11] A. Zappettini, L. Cerati, A. Milani, S.M. Pietralunga, M. Martinelli, J. Cryst. Growth 214 (2000) 866−869.
[12] R. Dieguez, in “Crystal Growth Technology”, Wiley, 2011, pp. 19−75, https://doi.org/10.1002/0470871687.ch17.
[13] R. Triboulet, CdTe and CdZnTe growth, in: CdTe and Related Compunds; Physics, Defects, Hetero- and Nano-structures, Crystal Growth, Sufaces and Applications, Part II: Crystal Growth, Surfaces and Applications, 2010, pp. 19−75.
[14] S. Sen, H.L. Hettich, D.R. Rhiger, S.L. Price, M.C. Currie, R.P. Ginn, E.O. Mc Lean, J. Electron. Mater. 28 (1999) 718−725.
[15] U. Becker, P. Rudolph, R. Boyn, M. Wienecke, I. Utke, Phys. Status Solidi A 120 (1990) 653−660.
[16] G.A. Carini, A.E. Bolotnikov, G.S. Camarda, G.W. Wright, R.B. James, Appl. Phys. Lett. 88 (2006) 143515.
[17] N. Yellin, S. Szapiro, J. Cryst. Growth 69 (1984) 555−560.
[18] N. Yellin, S. Szapiro, J. Cryst. Growth 73 (1985) 77−82.
[19] J.H. Greenberg, J. Cryst. Growth 161 (1996) 1.
[20] J.H. Greenberg, J. Cryst. Growth 197 (1999) 406−412.
[21] R. Fang, R.F. Brebrick, J. Phys. Chem. Solid. 57 (1996) 443−450.
[22] J.H. Greenberg, V.V. Guskov, A.S. Alikhantan, Cryst. Res. Technol. 38 (2003) 598−603.
[23] T.C. Yu, R.F. Brebrick, Phase diagram of Cd/Zn/Te/Se compounds, in: Properties of Narrow Gap Cadmium- Based Compounds, INSPEC EMIS Datareviews Series No. 10, 1994, p. 414.
[24] K. Mochizuki, K. Masumoto, K. Miyazaki, Mater. Lett. 6 (1988) 119.
[25] A. Zappettini, L. Marchini, M. Zha, G. Piacentini, N. Zambelli, G. Benassi, D. Calestani, CrystEngComm 15 (2013) 2227−2231.
[26] C.-H. Su, J. Cryst. Growth 281 (2005) 577−586.
[27] J.H. Greenberg, V.N. Guskov, J. Cryst. Growth 289 (2006) 552−558.
[28] L. Shcherbak, J. Cryst. Growth 197 (1999) 397−405.
[29] L. Shcherbak, O. Kopach, P. Fochuk, A. Kanak, A. Bolotnikov, R.B. James, Proc. SPIE 8142 (2011). Article No. 81421L.
[30] J.-P. Gaspard, J.-Y. Raty, R. Uolin, R. Bellissent, J. Noncryst. Solids 205−207 (1996) 75−78.
[31] V. Godlevsky, J. Derby, J. Chelikowsky, Phys. Rev. Lett. 81 (1998) 4959.
[32] P. Rudolph, H.J. Koh, N. Schäfer, T. Fukuda, J. Cryst. Growth 166 (1996) 578.

[33] S. Sen, W.H. Konkel, S.J. Tighe, L.G. Bland, S.R. Sharma, R.E. Taylor, J. Cryst. Growth 86 (1988) 111−117.

[34] R. Triboulet, J. Alloy. Comp. 371 (2004) 67−71.

[35] C.-H. Su, S.L. Lehoczky, B. Rahothamachar, M. Dudley, Mater. Sci. Eng. B 147 (2008) 35−42.

[36] S. Wen-Bin, Y. Mei-Yun, W. Wen-Hai, J. Cryst. Growth 86 (1988) 127−131.

[37] P. Cheuvart, U. El-Hanani, D. Schneider, R. Triboulet, J. Cryst. Grwoth 101 (1990) 270−274.

[38] Yu M. Ivanov, J. Cryst. Growth 194 (1998) 309−316.

[39] A. Zappettini, T. Görög, M. Zha, L. Zanotti, G. Zuccalli, C. Paorici, J. Cryst. Growth 214−215 (2000) 14.

[40] R. Triboulet, A. Heurtel, J. Rioux, J. Cryst. Growth 101 (1990) 131.

[41] N. Audet, B. Levicharsky, A. Zappettini, M. Zha, IEEE Trans. Nucl. Sci. 54 (2007) 782−785.

[42] A. El Mokri, R. Triboulet, A. Lusson, A. Tromson-Carli, G. Didier, J. Cryst. Growth 138 (1994) 168−174.

[43] G.S. Meiling, R. Leombruno, J. Cryst. Growth 3/4 (1968) 300.

[44] J. Vandekerkhof, in: P. Siffert, A. Cornet (Eds.), Proc. Intern. Symp. On Cadmium Telluride Material Gamma Ray Detectors, Strasbourg, 1971.

[45] J.B. Mullin, B.W. Straughan, Rev. Phys. Appl. 12 (1977) 105.

[46] H.M. Hobgood, B.W. Swanson, R.N. Thomas, J. Cryst. Growth 85 (1987) 510−520.

[47] G.W. Blackmore, S.J. Courtney, A. Royle, N. Shaw, A.W. Vere, J. Cryst. Growth 85 (1987) 335−340.

[48] L.G. Casagrande, D. Di Marzio, M.B. Lee, D.J. Larson Jr., J. Cryst. Growth 128 (1993) 576−581.

[49] M. Pfeiffer, M. Mühlberg, J. Cryst. Growth 118 (1992) 269−276.

[50] J.J. Kennedy, P.M. Amirtharaj, P.R. Boyd, S.B. Quadri, R.C. Dobbyn, G.G. Long, J. Cryst. Growth 86 (1988) 93−99.

[51] A. Zappettini, L. Marchini, M. Zha, G. Benassi, N. Zambelli, D. Calestani, L. Zanotti, E. Gombia, R. Mosca, M. Zanichelli, M. Pavesi, N. Auricchio, E. Caroli, IEEE Trans. Nucl. Sci. 58 (2011) 2352−2356.

[52] K.Y. Lay, D. Nichols, S. McDevitt, B.E. Dean, C.J. Johnson, J. Cryst. Growth 86 (1988) 118−126.

[53] E.O. Schulz-Dubois, J. Cryst. Growth 12 (1972) 81.

[54] A. Yeckel, J.J. Derby, J. Cryst. Growth 233 (2001) 599−608.

[55] X. Liu, W. Jie, Y. Zhou, J. Cryst. Growth 219 (2000) 22.

[56] A. Datta, S. Swain, Y. Cui, A. Burger, K. Lynn, J. Electron. Mater. 42 (2013) 3041−3053.

[57] J. Crocco, J. Franc, J. Zázvorka, P. Hlídek, E. Dieguez, V. Babentsov, M.V. Sochinski, R.B. James, IEEE Trans. Nucl. Sci. 59 (2012) 1516−1521.

[58] J. Franc, L. Sedivy, E. Belas, M. Bugár, J. Zázvorka, J. Perárek, S. Uxa, P. Höschl, R. Fesh, Cryst. Res. Technol. 4 (2013) 214−220.

[59] J. Crocco, I.-I. Bensalah, Q. Zheng, V. Carcelen, E. Dieguez, J. Cryst. Growth 360 (2012) 92−94.

[60] P. Rudolph, U. Rinas, K. Jacobs, J. Cryst. Growth 138 (1994) 249−254.

[61] H.L. Glass, A.J. Socha, C.L. Parfeniuk, D.W. Bakken, J. Cryst. Growth 184/185 (1998) 1035−1038.

[62] A. Muranevich, M. Roitberg, E. Finkman, J. Cryst. Grwoth 64 (1983) 285−290.

[63] C.-H. Su, S.L. Lehoczky, J. Cryst. Growth 319 (2011) 4−7.

[64] C. Szeles, S.E. Cameron, J.O. Ndap, W.C. Chalmers, IEEE Trans. Nucl. Sci. 49 (2002) 2535−2540.
[65] D. Brellier, E. Gout, G. Gaude, D. Pelenc, P. Ballet, T. Miguet, M.C. Manzato, J. Electron. Mater. 43 (2014) 2901−2907.
[66] P. Brunet, A. Katty, D. Schneider, A. Tromson-Carli, R. Triboulet, Mater. Sci. Eng. B 16 (1993) 44−47.
[67] M. Kestigian, A.B. Bollong, J.J. Derby, H.L. Glass, K. Harris, H.L. Hettich, P.K. Liao, P. Mitra, P.W. Norton, J. Electron. Mater. 28 (1999) 726−731.
[68] E. Raiskin, J.F. Butler, IEEE Trans. Nucl. Sci. 35 (1988) 81−84.
[69] F.P. Doty, J.F. Butler, J.F. Schetzina, K.A. Bowers, J. Vac. Sci. Technol. B 10 (1992) 1418−1422.
[70] C. Szeles, IEEE Trans. Nucl. Sci. 51 (2004) 1242−1249.
[71] N.N. Kolesnikov, A.A. Kolchin, D.L. Alov, Yu N. Ivanov, A.A. Chernov, M. Schieber, H. Hermon, R.B. James, M.S. Goorsky, H. Yoon, J. Toney, B. Brunett, T.E. Schlesinger, J. Cryst. Growth 174 (1997) 256−262.
[72] C. Szeles, S.E. Cameron, S.A. Soldner, J.-O. Ndap, M.D. Reed, J. Electron. Mater. 33 (2004) 742−751.
[73] G. Muller, P. Berwian, E. Buhrig, B. Weinert, GaAs substrates for high-power diode lasers, in: High-power Diode Lasers: Fundamentals, Technology, Applications, Book Series: Topics in Applied Physics, vol. 78, 2000, pp. 121−171.
[74] L. Carlsson, C.N. Ahlquist, J. Appl. Phys. 43 (1972) 2529−2536.
[75] M. Zha, T. Görög, A. Zappettini, F. Bissoli, L. Zanotti, C. Paorici, J. Cryst. Growth 234 (2002) 184−189.
[76] M. Zha, A. Zappettini, F. Bissoli, L. Zanotti, V. Corregidor, E. Dieguez, J. Cryst. Growth 260 (2004) 291−297.
[77] M. Zha, A. Zappettini, D. Calestani, L. Marchini, L. Zanotti, C. Paorici, J. Cryst. Growth 310 (2008) 2072−2075.
[78] A. Zappettini, M. Zha, M. Pavesi, L. Zanotti, J. Cryst. Growth 307 (2007) 283−288.
[79] A. Zappettini, M. Zha, L. Marchini, D. Calestani, R. Mosca, E. Gombia, L. Zanotti, M. Zanichelli, M. Pavesi, N. Auricchio, E. Caroli, IEEE Trans. Nucl. Sci. 56 (2009) 1743−1746.
[80] N. Yellin, D. Eger, A. Shachna, J. Cryst. Growth 60 (1982) 343.
[81] C.-H. Su, Yi-G. Sha, S.L. Lehoczky, H.-C. Liu, R. Fang, R.F. Brebrick, J. Cryst. Growth 183 (1998) 519−524.
[82] M. Zha, F. Bissoli, A. Zappettini, G. Zuccalli, L. Zanotti, C. Paorici, J. Cryst. Growth 237−239 (2002) 1720−1725.
[83] F. Bissoli, A. Zappettini, M. Zha, L. Zanotti, C. Paorici, J. Alloy. Comp. 371 (2004) 89.
[84] A. Zappettini, R. Waldner, F. Bissoli, M. Zha, L. Zanotti, C. Paorici, J. Cryst. Growth 275 (2005) e571−e575.
[85] W. Palosz, H. Wiedemeier, J. Cryst. Growth 131 (1993) 193−198.
[86] W. Palosz, M.A. George, E.E. Collins, K.-T. Chen, Y. Zhang, Z. Hu, A. Burger, J. Cryst. Growth 174 (1997) 733−739.
[87] R. Schwarz, W. Joerger, C. Eiche, M. Fiederle, K.W. Benz, J. Cryst. Growth 146 (1995) 92−97.
[88] M. Laasch, R. Schwarz, P. Rudolph, K.W. Benz, J. Cryst. Growth 141 (1994) 81−88.
[89] K. Chattopadhyay, S. Feth, H. Chen, A. Burger, C.-H. Su, J. Cryst. Growth 191 (1998) 377−385.
[90] E.V. Markov, A.A. Davydov, Nerg. Mater. 4 (1971) 575−581.

[91] J.L. Boone, G. Cantwell, W.C. Harsch, J.E. Thomas, B.A. Foreman, J. Cryst. Growth 139 (1994) 27−36.

[92] M. Laasch, T. Kunz, C. Eiche, M. Fiederle, W. Joerger, G. Kloess, K.W. Benz, J. Cryst. Growth 174 (1997) 696−707.

[93] J.T. Mullins, J. Carles, N.M. Aitken, A.W. Brinkman, J. Cryst. Growth 208 (2000) 211.

[94] J.T. Mullins, B.J. Cantwell, A. Basu, Q. Jiang, A. Choubey, A.W. Brinkman, J. Cryst. Growth 310 (2008) 2058−2061.

[95] B.J. Cantwell, A.W. Brinkman, A. Basu, J. Cryst. Growth 275 (2005) e543.

[96] J.T. Mullins, B.J. Cantwell, A. Basu, Q. Jiang, A. Choubey, A.W. Brinkman, B.K. Tanner, J. Electron. Mater. 37 (2008) 1460−1464.

[97] A. Choubey, P. Veeramani, A.T.G. Pym, J.T. Mullins, P.J. Sellin, A.W. Brinkman, I. Radley, A. Basu, B.K. Tanner, J. Cryst. Growth 352 (2012) 120−123.

[98] M. Niraula, K. Yasuda, A. Watanabe, Y. Kai, H. Ichihashi, W. Yamada, H. Oka, T. Yoneyama, H. Nakashima, T. Nakanishi, K. Matsumoto, D. Katoh, Y. Agata, IEEE Trans. Nucl. Sci. 56 (2009) 836−840.

[99] K. Yasuda, M. Niraula, M. Kojima, S. Kitagawa, S. Tsubota, T. Yamaguchi, J. Ozawa, Y. Agata, J. Electron. Mater. 46 (2017) 6704−6708.

[100] A. Vogt, S. Schutt, K. Frei, M. Fiederle, J. Cryst. Growth 477 (2017) 114−117.

[101] S.A. Medvedev, YuV. Klevkov, K.V. Kiseleva, N.N. Sentyurina, Izv. Akad. Nauk, Nearg. Mater 8 (1972) 1210−1213.

[102] R. Triboulet, R. Legros, A. Heurtel, B. Sieber, G. Didier, D. Imhoff, J. Cryst. Growth 72 (1985) 90−96.

[103] A. Nagaoka, K.-B.U.M. Han, S. Misra, T. Wilenski, T.D. Sparks, M.A. Scarpulla, J. Cryst. Growth 467 (2017) 6−11.

[104] U.N. Roy, A. Burger, R.B. James, J. Cryst. Growth 379 (2013) 57−62.

[105] P. Siffert, Nucl. Instrum. Methods 150 (1978) 1.

[106] M. Richter, P. Siffert, Nucl. Instrum. Methods Phys. Res. 322 (1992) 529−539.

[107] M. Funaki, T. Ozaki, K. Satoh, R. Ohno, Nucl. Instrum. Methods Phys. Res. 436 (1999) 120−126.

[108] H. Shiraki, M. Funaki, Y. Ando, S. Kominami, K. Amemiya, R. Ohno, Nuclear Science Symposium Conference Record, IEEE, 2007, https://doi.org/10.1109/NSSMIC.2007.4436506. NSS ’07.

[109] H. Shiraki, M. Funaki, Y. Ando, A. Tachibana, S. Kominami, R. Ohno, IEEE Trans. Nucl. Sci. 56 (2009) 1717−1723.

[110] H. Shiraki, M. Funaki, Y. Ando, S. Kominami, K. Amemiya, R. Ohno, IEEE Trans. Nucl. Sci. 57 (2010) 395−399.

[111] H. Chen, S.A. Awadalla, J. Mackenzie, R. Redden, G. Bindley, A.E. Bolotnikov, G.S. Camarda, G. Carini, R.B. James, IEEE Trans. Nucl. Sci. 54 (2007) 811−816.

[112] J. Mackenzie, F.J. Kumar, H. Chen, J. Electron. Mater. 42 (2013) 3129−3132.

[113] S.A. Awadalla, H. Chen, J. Mackenzie, P. Lu, K. Iniewski, P. Marthandam, R. Redden, G. Bindley, Z. He, F. Zhang, J. Appl. Phys. 105 (2009) 114910.

[114] U.N. Roy, S. Weiler, J. Stein, J. Cryst. Growth 312 (2010) 2840−2845.

[115] B. Zhou, W. Jie, T. Wang, Y. Xu, F. Yang, L. Yin, B. Zhang, R. Nan, J. Electron. Mater. 47 (2018) 1125−1130.

[116] B. Zhou, W. Jie, T. Wang, L. Yin, F. Yang, B. Zhang, S. Xi, J. Dong, J. Cryst. Growth 483 (2018) 281−284.

[117] Y. Wang, K. Kudo, Y. Inatomi, R. Ji, T. Motegi, J. Cryst. Growth 275 (2005) e1551−e1556.

[118] Y. Wang, K. Kudo, Y. Inatomi, R. Ji, T. Motegi, J. Cryst. Growth 284 (2005) 406−411.

[119] S. Kuppurao, S. Brandon, J.J. Derby, J. Cryst. Growth 155 (1995) 93−102.

[120] A. Pandy, A. Yeckel, M. Reed, C. Szeles, M. Hainke, G. Müller, J.J. Derby, J. Cryst. Growth 276 (2005) 133−147.

[121] D. Gasperino, M. Bliss, K. Jones, K. Lynn, J.J. Derby, J. Cryst. Growth 311 (2009) 2327−2335.

[122] N. Zhang, A. Yeckel, J.J. Derby, J. Cryst. Growth 355 (2012) 113−121.

[123] A. Yeckel, J.J. Derby, J. Cryst. Growth 209 (2000) 734−750.

[124] M.S. Divecha, J.J. Derby, J. Cryst. Growth 468 (2017) 630−634.

[125] M.S. Divecha, J.J. Derby, J. Cryst. Growth 480 (2017) 126−131.

[126] C. Frank-Rotsch, D. Jockel, M. Ziem, P. Rudolph, J. Cryst. Growth 310 (2008) 1505−1510.

[127] A. Jeckel, J.J. Derby, J. Cryst. Growth 364 (2013) 133−144.

[128] C. Chang, B. Baird, P. Liao, R. Chang, L. Colombo, J. Cryst. Growth 98 (1989) 595−609.

[129] Y. Apanovich, E. Ljumkis, J. Cryst. Growth 110 (1991) 839−854.

[130] S. Dost, Y. Liu, Compt. Rendus Mec. 335 (2007) 323−329.

[131] C. Stelian, T. Duffar, J. Cryst. Growth 400 (2014) 67−75.

[132] J.H. Peterson, A. Yeckel, J.J. Derby, J. Cryst. Growth (2016) 12−16.

[133] J.H. Peterson, M. Fiederle, J.J. Derby, J. Cryst. Growth 454 (2016) 45−58.

[134] Y. Liu, S. Dost, B. Lent, R.F. Redden, J. Cryst. Growth 254 (2003) 285−297.

[135] C.K. Ghaddar, C.K. Lee, S. Motakef, D.C. Gillies, J. Cryst. Growth 205 (1999) 97−111.

[136] C. Stelian, T. Duffar, J. Cryst. Growth 429 (2015) 19−26.

[137] Z. Li, J.H. Peterson, A. Yeckel, J.J. Derby, J. Cryst. Growth 452 (2016) 17−21.

[138] R.U. Barz, P. Sabhapathy, M. Salcudean, J. Cryst. Growth 180 (1997) 566−577.

[139] A.E. Bolotnikov, N.M. Abdul-Jabbar, O.S. Babalola, G.S. Camarda, Y. Cui, A.M. Hossain, E.M. Jackson, H.C. Jackson, J.A. James, K.T. Kohman, A.L. Luryi, R.B. James, IEEE Trans. Nucl. Sci. 55 (5) (2008) 2757−2764.

[140] L. Marchini, A. Zappettini, M. Zha, N. Zambelli, A. Bolotnikov, G. Camarda, R.B. James, IEEE Trans. Nucl. Sci. 59 (2012) 264−267.

[141] E.S. Elshazly, G. Tepper, Appl. Phys. Lett. 93 (2008) 042112.

[142] G. Yang, A.E. Bolotnikov, Y. Cui, G.S. Camarda, A. Hossain, K.H. Kim, R. Gui, R.B. James, Appl. Phys. Lett. 98 (2001) 261901.

[143] N. Zambelli, L. Marchini, G. Benassi, D. Calestani, A. Zappettini, IEEE Trans. Nucl. Sci. 59 (2012) 1526−1530.

[144] P. Rudolph, A. Engel, I. Schentke, A. Grochocki, J. Cryst. Growth 147 (1995) 297−304.

[145] R.J. Pieper, A. Korpel, Appl. Optic. 22 (1983) 1449−1453.

[146] N. Zambelli, L. Marchini, M. Zha, A. Zappettini, J. Cryst. Growth 318 (2011) 1167−1170.

[147] H.R. Vydyanath, J. Ellsworth, J.J. Kennedy, B. Dean, C.J. Johnson, G.T. Neugebauer, J. Sepich, P.K. Liao, J. Vac. Sci. Technol. B 10 (1992) 1476.

[148] F. Sheng, J. Yang, S. Sun, C. Zhou, H. Yu, J. Electron. Mater. 43 (2014) 2702−2708.

[149] G. Yang, A.E. Bolotnikov, P.M. Fochuk, O. Kopach, J. Franc, E. Belas, K.H. Kim, G.S. Camarda, A. Hossain, Y. Cui, A.L. Adams, A. Radja, R. Pinder, R.B. James, J. Cryst. Growth 379 (2013) 16−20.

[150] K.H. Kim, A.E. Bolotnikov, G.S. Camarda, J. Franc, P. Fochuk, R.B. James, J. Cryst. Growth 390 (2014) 1−4.

[151] O.O. Korovyanko, L.P. Shcherbak, I.Y. Nakonechnyi, Z.I. Zakharuk, P.M. Fochuk, A.E. Bolotnikov, R.B. James, J. Cryst. Growth 475 (2017) 26−32.

[152] P. Fochuk, R. Grill, O. Kopach, A.E. Bolotnikov, E. Belas, M. Bugar, G. Camarda, W. Chan, Y. Cui, A. Hossain, K.H. Kim, I. Nakonechnyi, O. Panchuk, G. Yang, R.B. James, IEEE Trans. Nucl. Sci. 59 (2012) 256−263.

[153] Y. Xu, N. Jia, Y. He, R. Guo, Y. Gua, W. Jie, CrystEngComm 17 (2015) 8639.

[154] P. Yu, W. Jie, Nucl. Instrum. Meth. Phys. Res. 737 (2014) 29−32.

[155] E. Belas, M. Bugar, R. Grill, P. Horodysky, R. Fesh, J. Franc, P. Moravec, Z. Matej, P. Höschl, J. Electron. Mater. 36 (2007) 1025−1030.

[156] K.H. Kim, J. Suh, A.E. Bolotnikov, P.M. Fochuk, O.V. Kopach, G.S. Camarda, Y. Cui, A. Hossain, G. Yang, J. Hong, R.B. James, J. Cryst. Growth 354 (2012) 62−66.

[157] R. Grill, J. Franc, P. Höschl, I. Turkevych, E. Belas, P. Moravec, IEEE Trans. Nucl. Sci. 52 (2005) 1925−1931.

[158] M. Bugar, E. Belas, R. Grill, J. Prochazka, S. Uxa, P. Hlidek, J. Franc, R. Fesh, P. Hoschl, IEEE Trans. Nucl. Sci. 58 (2011) 1942−1948.

[159] J. Franc, E. Belas, M. Bugar, P. Hlidek, R. Grill, G. Yang, A. Cavallini, B. Fraboni, A. Castaldini, S. Assali, JINST 7 (2012) C11001.

[160] P. Yu, W. Jie, CrystEngComm 15 (2013) 5045−5049.

[161] J. Franc, L. Sedivy, E. Belas, M. Bugar, J. Zazvorka, J. Pekarek, S. Uxa, P. Hoschl, R. Fesh, Cryst. Res. Technol. 48 (2013) 214−220.

[162] G. Piacentini, N. Zambelli, G. Benassi, D. Calestani, M. Pavesi, A. Zappettini, J. Cryst. Growth 415 (2015) 15−19.

[163] H.R. Vydyanath, J.A. Ellsworth, J.B. Parkinson, J. Kennedy, B. Dean, C.J. Johnson, G.T. Neugebauer, J. Sepich, P.-K. Liao, J. Electron. Mater. 22 (1993) 1073−1080.

[164] Y. He, W. Jie, T. Wang, Y. Xu, Y. Zhou, Y. Zaman, G. Zha, J. Cryst. Growth 402 (2014) 15−21.

[165] A. Zappettini, N. Zambelli, G. Benassi, D. Calestani, M. Pavesi, Appl. Phys. Lett. 104 (2014) 252105.

[166] S.K. Swain, K.A. Jones, A. Datta, K.G. Lynn, IEEE Trans. Nucl. Sci. 58 (2011) 2341−2345.

[167] X. Xing, J. Min, X. Liang, J. Zhang, L. Wang, L. Yang, Y. Ling, L. Duan, Y. Shen, J. Cryst. Growth 426 (2015) 270−275.

[168] P. Fochuk, Z. Zakharuk, Ye Nykonyuk, A. Rarenko, M. Kolesnik, A.E. Bolotnikov, G. Yang, R.B. James, IEEE Trans. Nucl. Sci. 63 (2016) 1839−1843.

[169] J. Mackenzie, H. Chen, S.A. Awadalla, P. Marthandam, R. Redden, G. Bindley, Z. He, D.R. Black, M. Duff, M. Amman, J.S. Lee, P.N. Luke, M. Groza, A. Burger, Mater. Res. Soc. Symp. Proc. 1164 (2009). Materials Research Society 1164-L10-04.

[170] C. Szeles, D. Bale, J. Grosholz, G.L. Smith, M. Blostein, J. Eger, Hard x-ray and gamma-ray detector physics and penetrating radiation systems VIII, in: Proceedings of SPIE, vol. 6319, 2006, p. 631909.

[171] C. Szeles, Phys. Status Solidi B 241 (2004) 783−790.

[172] H. Yang, F. Zhang, Y.F. Zhu, Z. He, IEEE Nuclear Science Symposium Conference Record (NSS/MIC), IEEE Nuclear Science Symposium Conference Record, 2010, pp. 3756−3758.

[173] A.E. Bolotnikov, K. Ackley, G.S. Camarda, Y. Cui, J.F. Eger, G. De Geronimo, C. Finfrock, J. Fried, A. Hossain, W. Lee, M. Prokesch, M. Petryk, J.L. Reiber, U. Roy, E. Vernon, G. Yang, R.B. James, IEEE Trans. Nucl. Sci. 62 (2015) 3193−3198.

[174] T.E. Schlesinger, B. Brunett, H. Yao, J.M. Vanscyoc, R.B. James, S.U. Egarievwe, K. Chattopadhyay, X.-Y. Ma, A. Burger, N. Giles, U. El-Hanany, A. Shahar, A. Tsigelmen, J. Electron. Mater. 28 (1999) 864−868.

[175] L. Li, F. Lu, C. Lee, M. Black, R.B. James, H.W. Yao, A. Burger, R. Olsen, L.J. Cirignano, D.R. Ouimette, Hard x-ray and gamma-ray detector physics vi, in: Proceedings of the Society of Photo-optical Instrumentation Engineers (SPIE), vol. 5540, 2004, pp. 181−185.
[176] M. Fiederle, A. Fatiler, A. Zwerger, IEEE Trans. Nucl. Sci. 54 (2007) 769−772.
[177] N. Auricchio, L. Marchini, E. Caroli, A. Zappettini, L. Abbene, V. Honkimaki, J. Appl. Phys. 110 (2011) 124502.
[178] Y.A. Boucher, J. Jaworski, W. Kaye, F. Zhang, Z. He, IEEE Trans. Nucl. Sci. 59 (2012) 3332−3338.
[179] M. Prokesch, S.A. Soldner, A.G. Sundaram, M.D. Reed, H. Li, J.F. Eger, J.L. Reiber, C.L. Shanor, C.L. Wray, A.J. Emerick, A.F. Peters, C.L. Jones, IEEE Trans. Nucl. Sci. 63 (2016) 1854−1859.
[180] Y. Eisen, A. Shor, J. Cryst. Growth 184/185 (1998) 1302−1312.
[181] P. Fourgeres, P. Siffert, M. Hageali, J.M. Koebel, R. Regal, Nucl. Instrum. Meth. Phys. Res. 428 (1999) 38−44.
[182] L. Verger, M. Boitel, M.C. Gentet, R. Hamelin, C. Mestais, F. Mongellaz, J. Rustique, G. Sanchez, Nucl. Instrum. Methods Phys. Res. 458 (2001) 297−309.
[183] H.L. Malm, M. Martini, M. Martini, IEEE Trans. Nucl. Sci. 21 (1974) 322−330.
[184] T. Takahashi, S. Watanabe, M. Kouda, G. Sato, Y. Okada, S. Kubo, Y. Kuroda, M. Onishi, R. Ohno, IEEE Trans. Nucl. Sci. 48 (2001) 287−291.
[185] T. Koenig, J. Schulze, M. Zuber, K. Rink, J. Butzer, E. Hamann, A. Cecilia, A. Zwerger, A. Fauler, M. Fiederle, U. Oelfke, Phys. Med. Biol. 57 (2012) 6743−6759.
[186] M. Streicher, Y. Zhu, F. Zhang, Y.A. Boucher, C.G. Wahl, H. Yang, Z. He, IEEE Nuclear Science Symposium and Medical Imaging Conference, NSS/MIC 201410 March 2016, 2014, 7431272.
[187] P.N. Luke, IEEE Trans. Nucl. Sci. 42 (1995) 207−213.
[188] J.P. Flint, B. Martinez, T.E.M. Betz, J. Mackenzie, F.J. Kumar, G. Bindley, in: Proc. of SPIE, vol. 9819, 2016, p. 981913.
[189] J.P. Flint, B. Martinez, T.E.M. Betz, J. Mackenzie, F.J. Kumar, L. Burgess, in: Proc. of SPIE, vol. 10177, 2017, p. 1017717.
[190] D.S. Bale, C. Szeles, Phys. Rev. B 77 (2008) 035205.
[191] M. Prokesch, D.S. Bale, C. Szeles, IEEE Trans. Nucl. Sci. 57 (2010) 2397−2399.
[192] B. Thomas, M.C. Veale, M.D. Wilson, P. Seller, A. Schneider, K. Iniewski, J. Inst. Met. 12 (2017) C12045.
[193] A. Cecilia, E. Hamann, C. Haas, D. Greiffenberg, A. Danilewsky, D. Haenscke, A. Fauler, A. Zwerger, G. Buth, P. Vagovic, T. Baumbach, M. Fiederle, J. Inst. Met. 6 (2011) P10016.
[194] V. Astromskas, E.N. Gimenez, A. Lohstroh, N. Tartoni, IEEE Trans. Nucl. Sci. 63 (2016) 252−258.
[195] J.S. Lee, D.-G. Kang, S.O. Jin, I. Kim, S.Y. Lee, Sensors 16 (2016) S1604518.
[196] M.C. Veale, S.J. Bell, D.D. Duarte, A. Schneider, P. Seller, M.D. Wilson, V. Kachkanov, K.J.S. Sawhney, Nucl. Instrum. Methods Phys. Res. A 729 (2013) 265−272.

This page intentionally left blank

# II sulfides and II selenides: growth, properties, and modern applications

# 9

*Nazar O. Kovalenko*[1,3], *Sergei V. Naydenov*[1], *Igor M. Pritula*[1], *Sergiy N. Galkin*[2]
[1]Institute of Single Crystals, Kharkiv, Ukraine; [2]Institute of Scintillation Materials, Kharkiv, Ukraine; [3]V.N. Karazin Kharkiv National University, Kharkiv, Ukraine

## 9.1 Introduction

In accordance with Plank's quantum law, every heated solid, including a semiconductor, emits thermal radiation in a thermodynamic equilibrium state. If this state is disturbed by, e.g., lighting, a strong electrical field, or irradiation (by X-rays, gamma–quanta, or fast particles), nonequilibrium charge carriers are generated in the semiconductor. Their recombination gives rise to light emission, i.e., luminescence. The world-famous Soviet physicist S.I. Vavilov [1] was the first to define this remarkable phenomenon: "Luminescence is the emission in excess with respect to equilibrium thermal emission of the given body; such an excessive emission has a finite duration essentially exceeding the period of light oscillations." In most cases, significant modern applications of II sulfides and II selenides (the so-called $A_2B_6$ chalcogenides) are bound up with their strong luminescence.

Luminescent properties of semiconductor $A_2B_6$ compounds are associated with the formation of structure and impurity defects in the crystal lattice. The former defects result from thermal disturbances of the ideal structure of the crystal matrix, and mainly take the form of vacancies, antisite defects, and ions or atoms located in interstitial sites of the crystal lattice. Luminescence caused by structure disturbances is called nonactivated (or self-activated) luminescence, since it does not require introduction of an activating impurity. Excitation of such a semiconductor followed by the formation of nonequilibrium electron–hole pairs may give rise to recombination radiation after direct recombination of an electron and a hole (exciton annihilation) located at the edges of the forbidden energy band, or as recombination of nonequilibrium carriers (electrons and holes) at recombination traps (structural defects) which act as luminescence centers. The characteristic spectral composition of self-activated luminescence of typical $A_2B_6$ compounds is presented in Table 9.1.

From the viewpoint of crystal structure perfection, chalcogenides are almost always imperfect, i.e., they contain point defects and impurity ions located at certain energy levels of the crystal. Impurity ions, both donors and acceptors, can participate in recombination processes and also generate defect levels in the forbidden energy band of the luminophore. Donors and acceptors can also form donor–acceptor complexes, and light emission may arise from nonequilibrium charge carriers that

**Single Crystals of Electronic Materials.** https://doi.org/10.1016/B978-0-08-102096-8.00009-4
Copyright © 2019 Elsevier Ltd. All rights reserved.

**Table 9.1** **Maximum self-activated luminescence of $A_2B_6$ compounds with different types of crystal lattice (hex −, cub −)**

| $A_2B_6$ compound | $\lambda_{max}$, nm | |
|---|---|---|
| | **At 300°K** | **At 77°K** |
| ZnS (hexagonal) | 460 | 470 |
| ZnS (cubic) | 450 | 460 |
| CdS (hexagonal) | 760 | 800 |
| ZnSe (cubic) | 605−640 | 500−624 |

recombine through such complexes. As a rule, luminescence of this type occurs in $A_2B_6$ compounds doped with different dopants. At low temperatures, or high densities of exciting radiation, there is a finite probability of "pure" exciton luminescence in these substances. However, that is more characteristic of pure single crystals with extremely low concentration of defects and impurities.

If $A_2B_6$ luminophores contain nonradiative deep traps, light emission quenching can result. The deep centers are caused by the presence of particular chemical impurities or defect centers in the luminophores. Hence for luminescence optimization it is important to ensure the highest chemical purity of raw materials, and effectively influence the structure of point defects by adding specific dopants and/or using various technological procedures to treat the crystals, including annealing in a gaseous medium, etc.

$A_2B_6$ compounds crystallize with the structure of zinc-blende, with cubic (sphalerite) or hexagonal (wurtzite) symmetry. The chemical bond has a mixed covalent−ionic character. In comparison with $A_3B_5$-type semiconductors, the ionic bond component of chalcogenides is more pronounced, due to a larger difference in electro-negativity of the elements that form the compound. For increasing atomic mass of anions while keeping the cation fixed, the forbidden band and the melting temperature of the compound decrease, as shown in Table 9.2. At the same time the charge carrier mobility rises. As the interatomic distances increase, the strength of chemical bonds decreases, for instance going from sulfides to selenides and then to tellurides.

## 9.2 Zinc sulfide: classical phosphor and new compositions

Among sulfide compounds, zinc sulfide (ZnS) is one of the most widely used materials [2]. It was applied as bright phosphor (powder) in detection screens in the classic experiments performed by Wilhelm Röntgen with X-rays and Ernest Rutherford with alpha particles.

ZnS is widely applied in electronics due to the width of its forbidden band (3.7 eV), which is suitable for many optical devices. Many methods were employed to obtain this material in the form of powder, films, or single crystals, and in combination with many

**Table 9.2** Physical properties of typical $A_2B_6$ compounds

| Substance | Density g/cm$^3$ | Melting temperature, °C | Lattice parameter, Å | Forbidden band width (300° K), eV | Debye temperature, °K | Dielectric constant ε, CGC units | |
|---|---|---|---|---|---|---|---|
| | | | | | | High-frequency (optical) | Low-frequency (static) |
| ZnS | 4.09 (s) | 1830 | 5.4093 | 3.67 | 315 | 8 | – |
| ZnSe | 5.26 (s) | 1515 | 5.6687 | 2.7 | 400 | 8.1 | 5.75 |
| CdS | 4.82 (w) | 1475 | 5.82 | 2.4 | 250 | 5.2 | 9.0 |
| CdSe | 5.81 (w) | 1239 | 6.05 | 1.8 | 230 | 9.7–10.7 | – |

*s*, sphalerite; *w*, wurtzite.

different impurities able to influence concentration and the nature of intrinsic point defects and thus tailor the properties of the luminophore (see, e.g., [3–5]).

As a rule, emission spectra of most phosphors are complex and consist of several elementary bands [2]. ZnS-based luminophores are no exception [5]. Each individual emission band of their luminescence spectra is ascribable to a certain type of emission center. ZnS luminophores ZnS:Ag, ZnS:Cu, and ZnS:(Cu, Mn) have been extensively investigated, and the bands of impurity centers are known to lie in the wavelength range of 430–650 nm [5]. Emission of manganese (Mn) ions in ZnS is started by energy transfer from copper (Cu) ions. This is confirmed by the fact that the intensity of scintillation in the band of Mn rises when Cu ions, at an optimum concentration of $(3–6) \times 10^{-3}\%$, are introduced into ZnS to play the role of coactivator [5]. Changes in the ratio of Cu to Mn concentrations modify the spectral characteristics of ZnS luminophores.

Nowadays much attention is being paid to studying the properties of mixed crystals of the $ZnS_xSe_{(1-x)}$ type. This is due to the existence of a continuous series of the solid solutions of concentrations changing within the whole range of compositions [6,7], the variety of methods for obtaining mixed crystals (such as solid-phase and gaseous-phase synthesis and melt growth), and the possibility to vary their optical and electric characteristics widely by changing the forbidden bandwidth from 2.7 eV for pure ZnSe to 3.7 eV for pure ZnS [7,8]. The compounds ZnS and ZnSe are used as a base to obtain mixed crystals. They have a sphalerite-type cubic structure under normal conditions and a wurtzite-type structure at temperatures higher than 1300°K, as well as at room temperature, if doped with elements which give rise to distortions of the lattice [7,8]. The optical, electrical, and structural properties of $ZnS_xSe_{(1-x)}$ crystals depending on their composition and growth conditions have been reported [9–14]. Studies of photo-, radio-, and cathodoluminescence in these crystals are available [13,14].

One of most important applications of ZnS-type compounds is the use of powder ZnS:Ag luminophore in detectors of alpha particles and neutrons [15–17]. This luminophore has very high scintillation efficiency, but is available usually as a polycrystalline powder. As a result, its use is limited to thin screens primarily meant for alpha-particle or neutron detection. The density of such screens must not exceed 25 mg/cm$^2$ due to the low transparency of thick screens to their own luminescence. It should be noted that ZnS:Ag crystals can be grown as single crystals and have a spectrometric resolution of several percentage points when detecting alpha particles (Fig. 9.1).

Usually a neutron detection layer consists of ZnS:Ag as a phosphor and $^6$LiF as a neutron converter for $^6$Li(n,$\alpha$)T reaction. The counting rate of ZnS:Ag for alpha particles is higher than that of other phosphors, and its lifetime is 200 ns. However, ZnS:Ag phosphor has a slow lifetime component of about 0.1 ms. ZnO:Zn, ZnO:Ga, and ZnSSe:Ag phosphor ceramic compounds without the slow lifetime component were obtained using an electric furnace or a Spark Plasma Sintering (SPS) apparatus [18]. Such compounds are suitable for neutron detectors under high counting rates. The detection efficiencies of these phosphors for thermal neutrons are listed in Table 9.3. The detection efficiency of ZnO:Zn (P15) was nearly equal to that of the standard ZnS:Ag/$^6$LiF detection layer. It was found that the short-lifetime phosphors ZnO:Zn (SPS) and ZnO:Ga had low (a few percentage points) detection efficiencies due to their short photon lifetime.

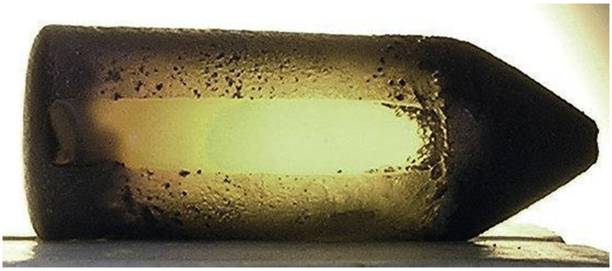

**Figure 9.1** ZnS:(Ag,Al) single crystal for alpha-particle spectrometry grown by the Bridgman method.

**Table 9.3 Detection efficiency and photon lifetime for phosphors irradiated by thermal neutrons. Experimental data is measured by a photon counting method [18] with an integration time of 4 ms**

| Phosphor | Detection efficiency (%) | Photon lifetime (ms) |
|---|---|---|
| ZnO:Zn (SPS) | 2.9 | 0.0044 |
| ZnO:Zn (P15) | 33.1 | 0.1894 |
| ZnO:Ga | 6.5 | 0.0069 |
| ZnSSe:Ag | 2.4 | 0.1460 |
| ZnS:Ag (BC704) | 36.0 | 0.2220 |

## 9.3 Zinc–selenide compounds: scintillation properties and crystal growth

Nowadays a new class of $A_2B_6$ scintillators based on semiconductor ZnSe compounds doped with isovalent impurities is of considerable interest. Isovalent doping of such crystals gives rise to the formation of associations of intrinsic defects which define their optical and luminescent properties. Table 9.4 presents the parameters of chalcogenide scintillators. As seen, although ZnSe(Al, O) has none of the drawbacks characteristic of other scintillators, its transparency to self-luminescence is low. It should be noted that CdS:Te scintillators have not found wide application due to insufficiently high light output, instability of the parameters of the crystal with time, and high toxicity of the material.

Investigations of the luminescent characteristics of ZnSe crystals at low temperatures were first reported in the 1960s. In particular, studies described edge luminescence observed as a large quantity of distinct lines in ZnSe photoluminescence spectra in the 4–77°K temperature range [19], as well as impurity defect emission in the form of wide bands in the region of longer wavelengths [20]. It is assumed that the edge luminescence bands are caused by recombination of free electrons

**Table 9.4** Scintillation characteristics of typical $A_2B_6$ crystals

| | ZnS(Cu) | CdS(Te) | ZnSe(Te) | ZnSe(Al, O) |
|---|---|---|---|---|
| Effective atomic number | 27 | 44 | 33 | 33 |
| Density, g/cm$^3$ | 4.1 | 4.8 | 5.28 | 5.26 |
| Emission maximum, $\lambda_{max}$, nm | 520 | 730 | 640 | 605 |
| Refraction index at $\lambda_{max}$ | 2.38 | 2.40 | 2.42 | 2.42 |
| Light output, % (as compared to CsI:Tl) | 130–150 | 40–60 | 110–140 | 100–130 |
| Absorption coefficient, cm$^{-1}$ | 0.10 | 0.06 | 0.20 | 0.20 |
| Decay time, μs | 0.1 | 0.3 | 30 | 6 |
| Afterglow (after 6/20 ms), % | 10 | 1.5/0.5 | 2/0.05 | 0.01/0.001 |

with holes located on acceptor centers [21]. At the same time, in the opinion of some authors [22] this luminescence is due to recombination on donor–acceptor pairs. Others attribute the centers of edge luminescence to isolated oxygen $O_{Se}$ centers and remote $O_{Se}$–$O_{Se}$ pairs [13].

At room temperature the luminescence spectrum of ZnSe is characterized by the presence of wide bands in the region of 590–650 nm (orange/red glow). This provides an important application of the material as an effective scintillator, since the given spectral region corresponds to the maximum spectral sensitivity of modern Si photodetectors.

The technology of preparation of doped scintillation ZnSe crystals is based on the well-known method of growing crystal from the melt [23,24] in vertical pressurized furnaces under inert gas (argon) pressure up to $5 \cdot 10^6$ Pa, using the Bridgman technique. For scintillation ZnSe crystals the growth rate is 2–5 mm/h, with temperatures in the melt zone of up to 1850 K; the crystals are grown in graphite crucibles. The grown crystals are annealed in Zn vapor for optimization of the kinetics and intensity of luminescence in the spectral region of 610–640 nm.

The technology developed at the Institute of Scintillation Materials (ISMA, Kharkov, Ukraine) allows repeated growth of several types of doped ZnSe crystals with a mass up to 1200 g and a diameter up to 50 mm (see Fig. 9.2). In particular, a technique was created for the production of ZnSe-based scintillators for X-ray scanners and alpha–beta detectors for security control setups at airports [25].

When crystals of $A_2B_6$ compounds are grown from the melt under pressure, deviations from the stoichiometry in the grown crystals may exceed 1%. As the growth is carried out in semipermeable graphite crucibles, the stoichiometry of the solid crystalline phase is affected by two independent processes: diffusion of the initial charge components through the crucible walls, and their evaporation. These processes lead to the formation of an ensemble of intrinsic point defects in the crystal structure. These defects are interstitial atoms of metal $M_I$ or chalcogen $M_X$, vacancies of $V_M$ or $V_X$

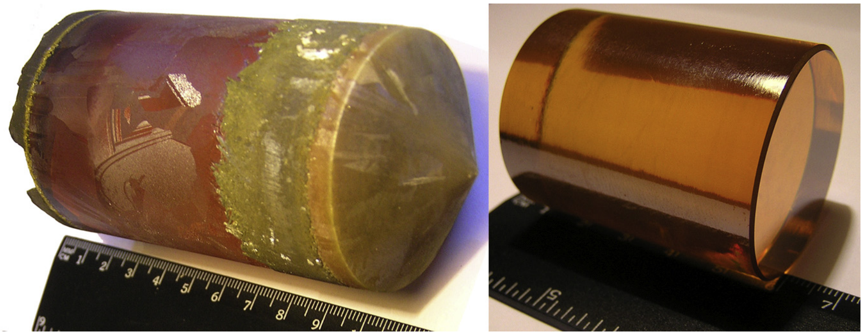

**Figure 9.2** Photos of as-grown ZnSe crystal and the scintillation element (ISMA, Kharkov, Ukraine).

types, antistructural defects $M_X$, $\text{Ч}_M$, and complexes of defects involving impurity atoms, thus each defect may exist in several charge states. The intrinsic point defects located in the vicinity of donor ions extend to several interatomic distances. In the process of crystallization the formation of vacancies is energetically more favorable, but when the diffusion processes are predominant, and either the melt or the crystal is in an atmosphere with an excess of one of the components, interstitial intrinsic point defects are mainly formed [25].

ZnSe-based crystals have wide practical application due to their unique characteristics, such as very high (up to 80,000 photon/MeV) light output that is 15%–20% higher than that of CsI(Tl) scintillators, low afterglow level (less than 0.01% after 6 ms), nonhygroscopicity, and high (up to $5 \times 10^6$ Gy) radiation stability. Their main applications include radiometry, spectrometry, and, especially, security and industrial radiography (see the next Section 9.4). For spectrometry, ZnSe(Te) scintillation detectors have an energy resolution of $R_\alpha = 3\%$ for detection of 5.15 MeV α-particles from a $^{239}$Pu source; $R_\gamma = 5.4\%$ for detection of 662 keV γ-rays from a $^{137}$Cs source; and $R_\beta = 3.7\%$ for detection of internal conversion electrons from a $^{207}$Bi source. ZnSe(Te) crystals also have a sufficiently large ratio of $\alpha/\beta \approx 3$ for light output from alpha and beta particles, respectively.

Several studies have been dedicated to the choice of the best-suited nuclide and crystal hosts to be applied as scintillating bolometers in neutrinoless double β-decay experiments (0νDBD) [26,27]. The use of enriched isotopes for the production of such crystals has been widely discussed. The LUCIFER project [28] was the first attempt to achieve a background-free condition in an 0νDBD experiment by using scintillation crystals grown from isotopically enriched materials, and Zn$^{82}$Se crystal was the first candidate for this experiment [29]. Obtaining scintillation crystals is more complex, since no scintillation material suitable for 0νDBD experiments has been produced on a large scale so far. It was therefore necessary to reconsider the entire process of the growth of Zn$^{82}$Se crystals to meet the specific requirements of low-background 0νDBD experiments. In this context a process of Zn$^{82}$Se crystal production was developed consisting of 18 technological stages. The most important stages are production of Zn and $^{82}$Se; synthesis of Zn$^{82}$Se powder and preparation of the

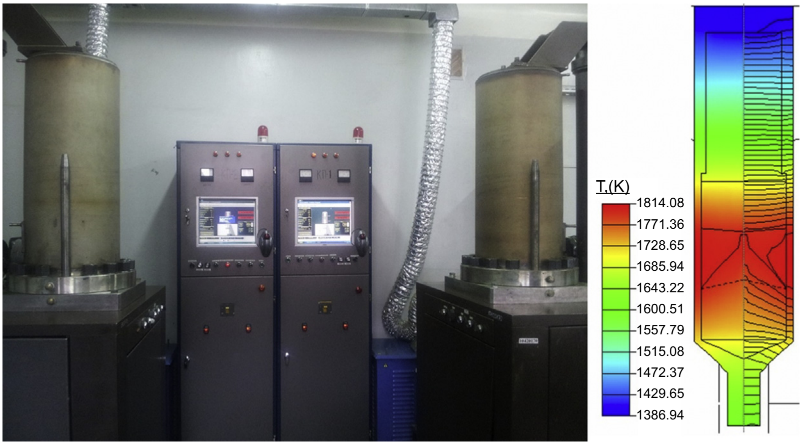

**Figure 9.3** Installation used for Zn$^{82}$Se crystal growth at ISMA (Kharkov, Ukraine). On the left there are two furnaces with the computer-controlled power supply system. Shown on the right is an example of the temperature profile in the crystal growth furnace (for 3.95 kW total power supply).

charge for crystal growth; Zn$^{82}$Se crystal growth; Zn$^{82}$Se crystal cutting, surface processing, and handling; cryogenic testing; and recovery and recycling of $^{82}$Se. The crystals were grown from the melt in graphite crucibles using the Bridgman technique (see Fig. 9.3). Charging the crucibles with Zn$^{82}$Se powder was done in a controlled atmosphere (ultrapure Ar, relative humidity $<1\%$) using a glove box and other equipment previously certified for radio purity (gloves, containers, plastic bags, jars, pestles, etc.). The crystal was grown in a vertical furnace kept in an argon atmosphere (up to 15 MPa). The furnace had two heaters giving a temperature gradient from 1540 to 1280°C at the initial charge melting phase and then a temperature of about 900°C in the thermalization zone. The liquid–solid interface gradient applied was 5 degrees/cm. The growth rate was typically 1 mm/h, with the accuracy of temperature control being ±3°C. The whole process of crystal growth was computer-aided using original software. Fig. 9.4 shows a typical Zn$^{82}$Se crystal ingot ready for mechanical processing (cutting, shaping, and polishing). Fig. 9.5 illustrates the transparency of an optically polished 50 mm long, 50 mm diameter Zn$^{82}$Se crystal produced in this work.

This project successfully grew high-purity Zn$^{82}$Se crystals to be used as scintillating bolometers in the search for 0νDBD of $^{82}$Se. To obtain crystals with excellent crystallographic characteristics, special methods and equipment were used at all stages of production. The grown crystals had a very good energy resolution with respect to phonon signals (with Full Width at Half Maximum (FWHM) in the order of 30 keV in the energy range of interest for 0νDBD of $^{82}$Se). The scintillation characteristics of the crystals are also promising: the light yield of typically 5 keV/MeV for β-particles or γ-ray and 10 keV/MeV for α-particles excitation will guarantee identification

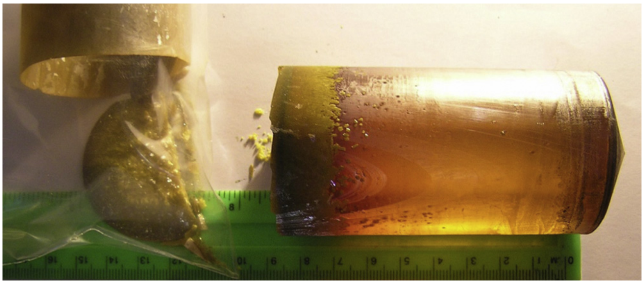

**Figure 9.4** Typical Zn$^{82}$Se crystal ingot grown by ISMA (Kharkov, Ukraine). On the left (in a plastic bag) is the evaporated material deposited inside the crucible on the upper part of the walls.

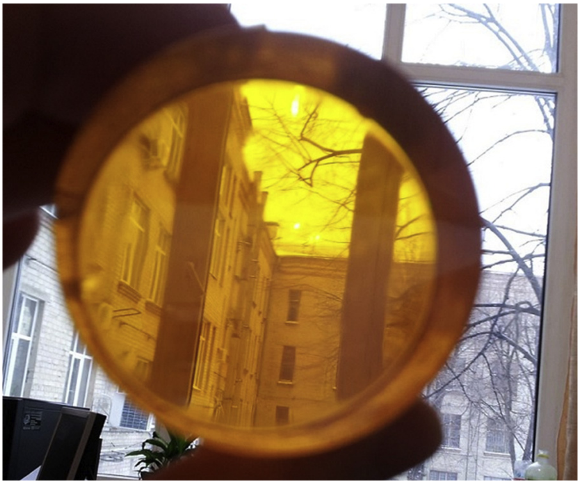

**Figure 9.5** Optically polished Zn$^{82}$Se crystals grown in ISMA (Kharkov, Ukraine).

of the nature of the interacting particles, thus contributing to achievement of a zero background level in the region of interest for double-beta decay investigation of $^{82}$Se. High-sensitivity measurements of radio-isotope concentrations in the raw materials, reactants, consumables, ancillaries, and intermediary products, and the application of very strict production and certification protocols led to a very low radio contamination level measured in the ready-to-use Zn$^{82}$Se crystals. A cryogenic test performed under the conditions similar to those foreseen for the 0νDBD experiment showed radioactive contamination of the crystals in the order of a few μBq/kg for the most critical isotopes. This is compatible with the challenging requirements of 0νDBD experiments [30].

Table 9.5 presents the detector baseline resolutions and light yield of scintillating bolometers built using the preliminary data obtained for the three Zn$^{82}$Se crystals [30].

**Table 9.5** **Energy resolutions and light yield of scintillating bolometers made from three $Zn^{82}Se$ crystals. Measurements were made for beta-, gamma-, and alpha-particle radiation**

| Sample no. | Baseline energy resolution, FWHM, keV | Energy resolution, FWHM, keV | Light yield (β or γ), keV/MeV | Light yield (α), keV/MeV |
|---|---|---|---|---|
| $Zn^{82}Se$-1 | 7.0 | 30.1 ± 1.7 | 5.2 | 14.1 |
| $Zn^{82}Se$-2 | 14.1 | 29.7 ± 1.4 | 3.3 | 9.1 |
| $Zn^{82}Se$-3 | 18.6 | 30.2 ± 1.7 | 4.6 | 13.7 |

## 9.4 Multi-energy radiography based on $A_2B_6$ scintillators for security and medical applications

In recent decades international terrorism, illegal transportation of prohibited substances and subjects, explosives, radioactive substances, and nuclear materials have become a severe menace around the world. In this context, increasing the efficiency of detection of such dangerous items and their reliable identification among nonhazardous subjects is a topical problem for up-to-date security inspection systems installed at airport terminals, railway stations, seaports, and other places/sites of mass public gathering. An advanced technology widely used for this is multienergy digital radiography (see [31—40] and references therein). This method is also applied in medical diagnostics (see, e.g., [41—46]) for effective identification and treatment of early stages of breast, prostate, and other kinds of cancer, osteoporosis, atherosclerosis, tuberculosis, and other widespread and dangerous diseases. Leading world manufacturers have developed two- and multienergy X-ray scanners designed for public safety [47—60] and medicine [51—53].

Traditional digital radiography allows effective differentiation of inorganic substances from organic ones [54]. This is due to the fact that radiation attenuation when X-raying an object is mainly due to a photo effect [55] for which the scattering cross-section is proportional to $Z_{eff}^4$, where $Z_{eff}$ is the effective atomic number of the material [36]. Thus radiography images of inorganic substances (with $Z_{eff} > 20$) are well distinguished from those of organic substances (with $Z_{eff} < 10$), e.g., the images of salt and sugar, or of bone and soft tissues, are essentially different, since the ratios of the signals registered for such objects ($(20/10)^4 \sim 16$) will differ by more than 10fold. However, traditional radiography is unable to differentiate an organic substance from another organic substance, e.g., to reveal a plastic explosive against a background of a plastic material or paper. Moreover, this method is insufficiently effective in distinguishing organic substances from lightweight metals and alloys (with $10 < Z_{eff} < 20$), and it cannot quantitatively identify the examined material on the base of its effective atomic number, density, and relative concentration of elements. These problems can be solved using multienergy radiography [33–36], which makes it possible to single out several different energy ranges from the continuous spectrum of the source examined using certain methods. Thus X-raying an object results in registration of not one but several radiographic signals corresponding to the specified ranges. Processing these multisignals allows reconstruction of not only the spatial structure but also the atomic parameter of the material under consideration.

A key point for creation of X-ray introscopes or tomographs is the choice of an effective scintillator most suitable for detection of penetrating radiation and high-quality representation of latent images of objects. The scintillator's physical parameters must satisfy the technical requirements of radiographic inspection systems; the basic characteristics are the following:

- *penetrating power* (with respect to steel and/or aluminum);
- *contrasting sensitivity and spatial resolution*;
- *absolute and relative detection sensitivity* (detectivity/detection ability);
- *number of channels* (the number of detectors or pixels) and *dynamic range*;
- *multienergy processing* and possibility of separate imaging of materials;
- *speed scanning and false alarm rate* (the number of false artifacts or events registered during a certain time interval).

The main physical parameters of scintillators are:

- *efficiency of registration* (or probability of absorption) of ionizing radiation depending on the effective atomic number and density of scintillators;
- *scintillation efficiency* or *light output* (scintillator brightness) expressed in absolute (number of photons per 1 MeV) or relative units;
- *time response* (characteristic scintillation decay time for fast and slow emission components) and *afterglow* (residual light output after emission of the main portion of scintillations);
- *spectral characteristics*, including wavelength of maximum of emission spectrum;
- *optical absorption* (the length of bulk absorption of optical photons);
- *energy resolution* for spectrometric applications;
- *radiation hardness* to high-dose and/or long-duration irradiation.

On the whole, detection efficiency of scintillators is proportional to their scintillation efficiency, or, rather, their technical light output. The brighter a scintillator is, the more contrasting and high-quality digital images are produced. The spatial resolution of the detectors depends on many factors, including the radiation energy and dose rate, peculiarities of the receiving–detecting circuit, and the material of the object examined (the role of scattered radiation). However, in most cases the use of scintillators with higher brightness and speed of response gives better results. Moreover, high spatial resolution requires high transparency of scintillators to their own radiation, i.e., low optical loss.

In digital radiography, relative detection sensitivity is the detector's ability to recognize small components of objects against the general background. Usually it is defined by the ratio ($\Delta d/d$) of the minimal registered change in the thickness of the object $\Delta d$ to this thickness $d$. In industrial radiography, technical diagnostics, and radiation defectoscopy, this parameter defines the minimal size of the defect detected. Taking into account exponential attenuation of the intensity of a narrow

X-ray beam $I(x) = I_0\exp(-\mu x)$ passing through a layer of a material whose thickness $x$ and linear attenuation coefficient are $x$ and $\mu$, respectively, *the static relative sensitivity* $(\Delta d/d)_0$ at X-ray examination of an immobile object is equal to

$$\left(\frac{\Delta d}{d}\right)_0 = \frac{\xi B}{\mu d}. \tag{9.1}$$

In this expression $\xi = \Delta V/\Delta I$ is the dimensionless coefficient of the transmission of digital contrast for the receiving—detecting circuit (where $\Delta V$ is the increment of the digital signal corresponding to the increment $\Delta I$ of the intensity of radiation transmitted through the examined object); and $B \geq 1$ is the building factor of accumulation of scattered radiation at irradiation of an object by spread of X-ray beams in real conditions. The parameter $\xi$ is determined experimentally, whereas $\mu$ and $B$ for concrete materials can be found in X-ray scattering databases. The sensitivity increases for scanning of objects with small thickness $d$ or low value of $\mu$ and weak radiation absorption (materials with not too highly effective atomic number and density). Sensitivity also increases with diminution of X-ray energy $E$ at which the linear coefficient decreases $\mu(E) \sim E^{-\gamma}$. Accumulation of scattered radiation (rise of factor $B$) in objects containing iron or other metals diminishes the detection sensitivity; it intensifies blurred of images and worsens recognition of radiographic images.

The considered expression does not take into account the time-dependent character of the formation of radiographic images. While detecting the radiation transmitted through an object, the scintillator at first emits photons, which are registered by the photoreceiver and then amplified and transformed into digital signals. The amplitude and time parameters of these signals depend on the scintillator kinetics, i.e., the time dependence of the intensity of the scintillation light arising at registration of ionizing radiation quanta. The representation of scintillation response in the form of the sum of several components with different decay times (for fast and slow components) is experimentally substantiated. When taking into account the decay kinetics, the expression for sensitivity is modified:

$$\left(\frac{\Delta d}{d}\right) = \frac{\xi B}{\mu d}\left[1 - \sum_i p_i \exp\left(-\frac{t}{\tau_i}\right)\right]^{-1}, \tag{9.2}$$

and summation is realized over all the partial components with the relative weight $p_i$ and the decay time $\tau_i$, thus $\sum_i p_i = 1$. The parameters $p_i$ and $\tau_i$ can be determined from experimental data obtained at irradiation of scintillators used in a scanning system without an investigated object.

The time of signal readout $t$ or registration of a variation (defect) $\Delta d$ against the background of an absorber with a thickness $d$ will be in the order of the time during which this defect is observed in the visual field of the detector. To assume for simplicity that the defect has the linear dimension $l$ in the direction perpendicular to the radiation and is moving at the constant velocity $u$, then the time of its observation is $t = l/u$. Hence the dynamic relative sensitivity of scanning of a moving object is expressed as

$$\left(\frac{\Delta d}{d}\right) = \frac{\xi B}{\mu d}\left[1 - \sum_i p_i \exp\left(-\frac{l}{u\tau_i}\right)\right]^{-1}. \tag{9.3}$$

The efficiency of the detector and the quality of the obtained images of an object will be better if the value of expression (9.3) is lower. A simple estimation of this expression gives the relation

$$\left(\frac{\Delta d}{d}\right) \leq \frac{\xi B}{\mu d}\,\frac{u\tau}{l}, \tag{9.4}$$

where $1/\tau \equiv \sum p_i/\tau_i$ is the mean average for inverse decay times of the scintillator. The time dependence of the scintillator decay curve can be presented as a combination of the fast $\tau_f$ and slow $\tau_s$ components with the weights $p_f$ and $p_s$, thus $p_f + p_s = 1$. Since $\tau_f \ll \tau_s$ and $p_s \ll 1$, $\tau \approx \tau_f/p_f \approx \tau_f\ (1 + p_s)$. The relative weight of the slow component is identified with the scintillator afterglow level $p_s \equiv p_A$. Then

$$\left(\frac{\Delta d}{d}\right) \leq \left(\frac{\xi B}{\mu d}\right)\left(\frac{u}{l}\right)\tau_f(1 + p_A). \tag{9.5}$$

As follows from the above formula, the sensitivity is better if the scintillator is faster, i.e., if the time $\tau_f$ is smaller and the afterglow $p_A$ is less. The value $p_A$ can be roughly estimated as $p_A \approx A\ (\tau_A/\tau)$, where $A$ is the level of afterglow after the characteristic time $\tau_A$ in the order of several milliseconds; $\tau$, the time of exponential decay of scintillations. For most inorganic scintillators (excluding very fast ones), $\tau$ is in the order of several microseconds, so

$$p_A \approx 10A(\%), \tag{9.6}$$

where the level of afterglow $A(\%)$ is expressed in as a percentage. Hence it is seen that the detection sensitivity is admissible, i.e., $p_A \ll 1$, only when $A \ll 0.1\%$.

If an electronic signal is registered with a finite discrimination time $\tau_D$ when the detector does not react to another quantum of radiation which has hit it, then expression (9.3) is to be complemented by the multiplier $[1 - \exp(l/u\tau_D)]^{-1}$ connected with the time delay in the operation of electronic devices. So the final estimation has the form

$$\left(\frac{\Delta d}{d}\right) \leq \left(\frac{\xi B}{\mu d}\right)\left(\frac{u}{l}\right)^2 \tau_D\tau_f(1 + p_A), \tag{9.7}$$

where $\tau_D$ is the discrimination (dead) time of the receiver. For raising the detector sensitivity, it is necessary either to decrease the rate of scanning $u$

(relative displacement of the object, radiation source, and/or the detector) or to diminish the detector's inertia and the discrimination time $\tau_D$, i.e., to increase the speed of response of the electronics used.

In radiography the controlled objects are arranged perpendicular to the incident radiation flux. Radiation registration is realized by the receiving−detecting circuit with the conversion efficiency $\eta_{eff}$, which depends on the type of the detector and the radiation energy $E$. If the latter remains unchanged after radiation has been passed through the substance, the output signal $V$ has the form

$$V(E) = \eta_{eff}(E)V_0(E)\exp[-\,\mu(E;Z,\rho)d], \tag{9.8}$$

where $V_0$ is the intensity of the source (the readings of the detector in background mode); $\mu$ is the coefficient of linear attenuation in the object; and $d$ is the thickness of the cross-section of the object at scanning. In the logarithmic scale and dimensionless units the signal is expressed in terms of the reflexes $R$:

$$R(E) = -\ln[V(E)/\eta_{eff}(E)V_0(E)]. \tag{9.9}$$

In a general case, the response of the detectors is described by the system of equations

$$R(E_i) = \sum_{j=1}^{P}\sum_{k=1}^{Q}\mu\left(E_i;Z_j,\rho_j\right)d_k; \quad i = 1,\ldots,M, \tag{9.10}$$

where $P$ and $Q$ are the numbers of simple elements (or components of a homogeneous mixture) and of the layers, respectively; and $M$ is the order of multienergy (the number of specified energy ranges). The solution of the problem inverse to Eq. (9.10) makes it possible to restore the physical parameters of the objects under control, such as their spatial thickness, atomic number $Z$, and density $\rho$. For unambiguous solution of the inverse problem the order of multienergy $M$ must satisfy the condition $M = P + Q$. The simplest case is two-energy radiography $M = 2$ for raying homogeneous ($P = 1$) and one-layer ($Q = 1$) objects.

In some cases control of materials may be reduced to reconstruction of the effective atomic number $Z_{eff}$ to an accuracy of 0.5 unit, if the corresponding parameter of different substances differs by less than several percentage points. In particular, it is possible to identify black steel with $Z_{eff} \approx 26$ or stainless steel with $Z_{eff} \approx 26.5$; chalk with $Z_{eff} \approx 17.4$ ($Ca_3(PO_4)_2$) or bone tissue (in medicine); sand with $Z_{eff} \approx 13.3$ ($SiO_2$); low-density aluminum alloys with $Z_{eff} \approx 11.7$ ($Al_2O_3$); glass with $Z_{eff} \approx 11.5$ ($Na_2SiO_3$); water with $Z_{eff} \approx 8$; soft biological tissue with $Z_{eff} \approx 7.8$; explosive with $Z_{eff} \approx 7.0-7.7$; plastic with $Z_{eff} \approx 5.9$, etc.

At energies ranging from several tens to several hundreds of keV, attenuation of radiation most often used in radiography is followed by photo-effect and Compton scattering (see e.g., [55]). Thus the coefficient of linear attenuation is expressed as

$$\mu(E;Z,\rho) = \left[\alpha(E)\sum_{k=1}^{M} a_k Z_k^4 + \beta(E)\sum_{k=1}^{M} a_k Z_k\right]\rho, \tag{9.11}$$

where $\alpha$ and $\beta$ are the energy dependences of the cross-sections of photo-effect and Compton scattering, respectively. In this case one can reconstruct $Z_{eff}$ [36]:

$$Z_{eff} = f\left(R_1/R_2; C_{ij}; Z_1^*, Z_2^*, \rho_1^*, \rho_2^*, d_1^*, d_2^*\right), \tag{9.12}$$

where the dependence $f(\ldots)$ is not presented explicitly. This expression contains the reflexes $R_{1,2}$ and the calibration data $C_{ij} = R\left(E_i; Z_j^*, \rho_j^*, d_j^*\right)$ of the measurements of two samples $j = 1{,}2$ of known chemical composition, density, and thickness. It should be emphasized that the reconstructed $Z_{eff}$ depends on the ratio of the reflexes $r = R_1/R_2$, i.e., on two readings of a two-energy detection system fixed simultaneously. Note that in traditional radiography $r \equiv 1$, as $R_1 \equiv R_2$ by definition, therefore in this case $Z_{eff}$ cannot be reconstructed in principle.

Formula (9.12) allows estimation of the relative sensitivity $S(Z) = (\Delta Z/Z)$ of the two-energy method of $Z_{eff}$ reconstruction. The expected threshold for $\Delta Z$ value satisfies the estimation

$$\left(\frac{\Delta Z}{Z}\right) \geq \left(\frac{1}{Z}\right)\left|r\frac{df}{dr}\right|\sum_{i=1}^{M} S_i, \tag{9.13}$$

where $S_i = |\Delta R_i/R_i|$ are the partial radiography sensitivities for which it may be supposed that $|\Delta R_i/R_i| \propto (\Delta\mu/\mu)_i \propto (\Delta d/d)_i$, since the same threshold increment of a digital signal $\Delta R \approx \Delta(\mu d)$ can be interpreted as the least change in the coefficient of linear attenuation $\Delta\mu$, or in the thickness of the material $\Delta d$. For the working (linear) section of the dynamical range of the detector $r(df/dr) \approx \Delta f \approx const$. Hence the relative detection sensitivity of two-energy radiography

$$S(Z) \approx \frac{const}{Z}\left[S_1(d) + S_2(d)\right], \tag{9.14}$$

where $S_i(d) = (\Delta d/d)_i$ are the earlier introduced partial detector sensitivities (see Eq. 9.7). If $S_1(d) \approx S_2(d)$ then $S(Z) = 2S(d)/Z$. Thus the accuracy of determination of the parameter $Z_{eff}$ depends on the sensitivity of the detector ($\Delta d/d$) and $Z_{eff}$ of the material itself. In particular, inorganic materials are identified much better than organic substances. It should be emphasized that the problem of identification of organic substances with $Z_{eff} \leq 10$ is especially topical. As follows from Eq. (9.14), accuracy $\Delta Z/Z \approx 1\%$ can be achieved when $(\Delta d/d) \approx 0.2$. For identification of small ($\sim$1 mm) inclusions this corresponds to a spatial resolution no worse than 2.5 line pairs/mm (characteristic of up-to-date introscopes and tomographs).

As a rule, in multienergy radiography the signals are registered by several combined (located one under the other) linear detector arrays for registration of "low"

(60−80 keV) and “high” (120−140 keV) energies. An example of this approach is the well-known sandwich design [32] of the detectors for two-energy radiography. Thus it is extremely important to provide energy separation at which every kind of “low-energy” or “high-energy” detector fully detects its own range of radiation and easily passes the radiation of other remaining ranges. For registration of “high” energies it is expedient to use alkali halide (CsI(Tl), $LaBr_3$(Ce), etc.) or oxide (CWO, BGO, LSO(Ce), etc.) scintillators with high $Z_{eff}$ and density and small radiation length. The scintillator meant for registration of “low” energies must transmit radiation of “high” energies, and must consequently possess a medium effective atomic number. At the same time, it must effectively register “low”-energy radiation and be an effective low-energy filter. Among all known scintillators of this type, ZnSe(Te) possesses the best parameters.

Table 9.6 contains comparative parameters of widespread modern scintillators. As is seen, due to their combination of characteristics, doped ZnSe crystals are most suitable for application in low-energy detector arrays of multienergy X-ray scanners.

For comparison, Figs. 9.6 and 9.7 present images of the same suitcase containing dangerous objects obtained by two-energy radiography with different scintillation detectors of “low”-energy radiation. The orange color of the palette corresponds to an organic substance, while the blue color points to an inorganic substance or a metal. The image obtained using an ZnSe(Te) crystal (Fig. 9.6) is characterized by a more precise identification of prohibited subjects (grenades containing an explosive and a pistol with a bullet in the charger), and better contrast and spatial resolution. The images obtained using CsI(Tl) crystal (Fig. 9.7) is distinguished by the presence of artifacts, obviously due to an excessive afterglow of CsI(Tl).

The use of bright ZnSe(Te) with a low afterglow level avoids (in agreement with the estimates in Eqs. 9.7 and 9.14) the appearance of different artifacts and essentially raises the detective ability of the method. Scintillators based on ZnSe compounds are applied in the best world safety inspection systems (see, e.g., [47]).

## 9.5 II selenides with metal dopants: laser applications and improved growth

In 1995 a group of scientists from the Livermore Laboratory reported the results of studying the generation properties of ZnSe crystals doped with $Cr^{2+}$ ions [56]. In 1996 the patent [57] was granted for the active medium on the base of $A_2B_6$ crystals doped with bivalent ions of transition metals $TM^{2+}$ (Ti, V, Cr, Mn, Fe, Co, Ni, and Cu). This gave rise to intense development of solid-state lasers on the base of $A_2B_6$: $TM^{2+}$. Lasers based on zinc and cadmium chalcogenides with wide-frequency tuning bands are recognized as a worthy analog of the well-known $Ti^{3+}$: $Al_2O_3$ material meant for the infrared (IR) spectral range [58]. The existing experimental samples of laser systems are able to work in various operation modes, such as continuous lasing [59−62], pulsed lasing with Q-switching, picosecond lasing with mode locking, and femtosecond with a wide pulse spectrum realized by means of the optical elements

**Table 9.6** Comparative parameters of inorganic scintillators used for digital X-ray radiography

| Scintillator | $Z_{eff}$ | Density, g/cm$^3$ | Light output, rel. % | Decay time, μs, fast/slow | Afterglow, in 6–10 ms, % | Wavelength emission maximum, nm | Absorption coefficient, cm$^{-1}$ | Radiation hardness, Gy |
|---|---|---|---|---|---|---|---|---|
| CsI(Tl) | 54 | 4.52 | 100 | $<1$ | $>1$ | 540 | 0.05 | $10^1$–$10^2$ |
| $CdWO_4$ | 66 | 7.9 | 40 | $>1$ | $<0.005$ | 480 | 0.02 | $10^6$ |
| CdS(Te) | 44 | 4.8 | 30 | 0.3/3 | $<0.5$ | 640/730 | 0.4 | $10^6$ |
| ZnSe(Te) | 33 | 5.42 | 120 | 3/30 | $<0.01$ | 610/640 | 0.1–0.3 | $10^6$–$10^7$ |

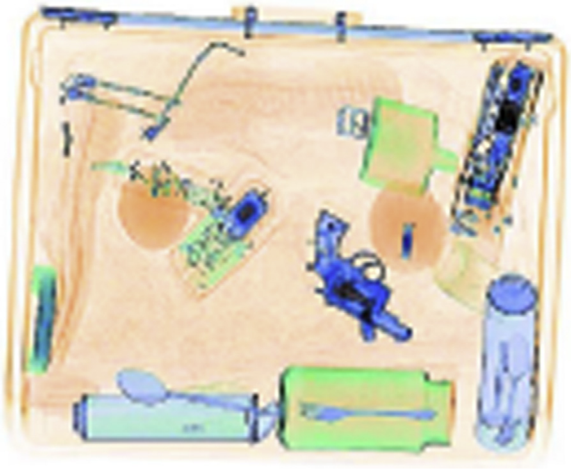

**Figure 9.6** Radiographic images obtained by means of low-energy detectors based on ZnSe(Te) crystals.

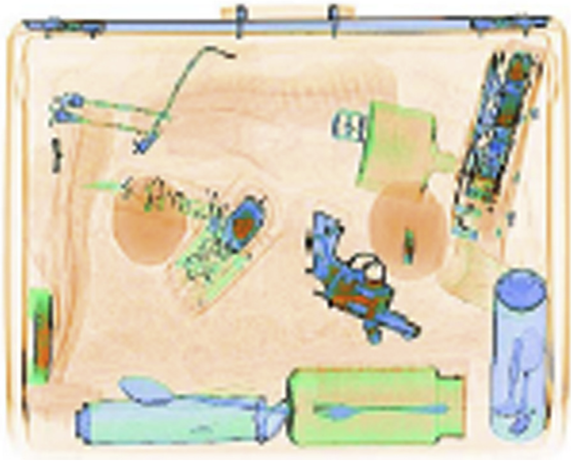

**Figure 9.7** Radiographic images obtained by means of low-energy detectors based on CsI(Tl) crystals.

SESAM (semiconductor saturable absorber mirror). The level of average power of these systems exceeded 10 W [63]. Further development of optical schemes for such lasers made it possible to create the systems' MOPA (master oscillator power amplifier) from optical amplifiers. Such systems are promising for creation of optical pulses with high levels of peak power. At present there are systems which generate optical pulses with a duration of 300 fs and a peak power of ~1 GW [64]. Low-volume production of tunable lasers on the base of polycrystalline ZnS and ZnSe doped with transition metals was started by IPG Photonics. Specialists from this organization created laser systems based on chalcogenides doped with chromium. The average power of these systems is higher than 100 W, which is a qualitative leap in the field of development of chalcogenide lasers [65]. Intense development is seen for active laser media based on ZnSe/ZnS:$Fe^{2+}$ meant for the 4–5 μm range [66].

The field of practical application of these laser systems gradually extends. A wide band of generation tuning allows creation of high-efficiency transmitters and amplifiers of wide-band signals for optical communication channels in the middle IR region. Generation of ultrashort femtosecond pulses is effective for creation of supercontinuum sources, i.e., superwide-band signals whose spectral width exceeds an octave. Chalcogenide lasers are also used for pumping of parametric generators [67]. The possibility of pumping frequency tuning by means of existing electronic methods not using mechanically mobile elements makes it possible to create parametric generators with an immovable nonlinear element and fast tuning of generation wavelength.

Femtosecond sources for Fourier-Transform Infra-Red (FTIR) spectrometry which replace conventional filament lamps shorten the time of measurements by several-orders. But most promising is the use of femtosecond generators for the creation of fast high-resolution spectrometers [68].

The working characteristics of laser sources, the frequency tuning bands, are defined by the physical properties of their crystal matrixes (Fig. 9.8).

A wide tuning band of so-called "vibronic" lasers is due to the peculiarities of the energy spectrum of the activator in the chalcogenide matrixes presented in Fig. 9.9. Such peculiarities give rise to the appearance of wide luminescence bands of the ZnSe matrix (2–3 μm for Cr ions and 4–5.5 μm Fe ions).

Binary $A_2B_6$ compounds extend potentialities of laser systems, since one can select the matrix most suitable for particular practical applications. However, the binary compounds have fixed parameters which can change to only a small extent under the influence of external factors. Another and more effective way to change the working characteristics is the use of substitution solid solutions whose physical properties essentially depend on the chemical composition, in the capacity of crystalline matrixes. At present there are known active media based on solid solutions of chalcogenides doped with transition metals. Their working characteristics are noticeably different

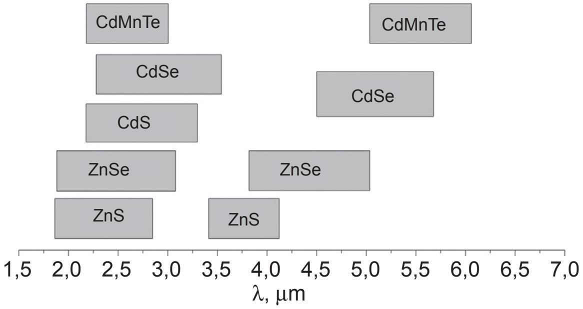

**Figure 9.8** Bands of emission wavelength tuning depending on the crystal matrix and type of activator: (left) with $Cr^{2+}$ions, (right) with $Fe^{2+}$ ions.

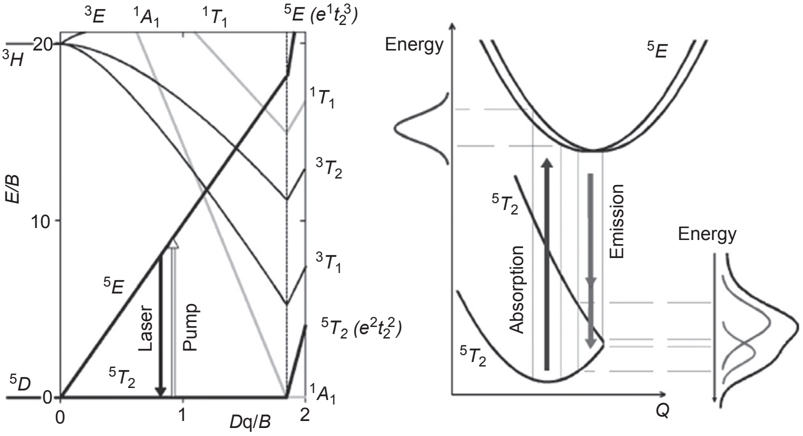

**Figure 9.9** Sugano–Tanabe diagram and Franck–Condon energy diagram of $Cr^{2+}$ ion in chalcogenide host [69].

from those of binary compounds [70–73]. Such prospects advance the task of finding and creating new substitution solid solutions that would allow expansion of the operational characteristics of the existing chalcogenide hosts.

The main technologies for the growth of bulk zinc and cadmium chalcogenide crystals are the Markov [74] or Physical Vapor Transport (PVT) method [75], Chemical Vapor Transport (CVT) [76], chemical vapor deposition (CVD) [77], and the Bridgman melt method and its modifications [78]. The PVT method, which is not based on chemical reactions, is most effective for the growth of single crystals with high structural perfection, a low level of dislocation density, and high purity that is due to the use of pure initial components. The method allows doping of the crystals during their growth. Its main drawback is a low (~0.03 mm/h) crystal growth rate [79]. The PVT method is applicable for obtaining chalcogenide crystals of both cubic (ZnS, ZnSe) and hexagonal (CdS, CdSe) structures.

The CVD method is based on a chemical reaction which results in the formation of chalcogenide vapors, followed by their precipitation on a substrate. This method was developed to meet the demand for high-quality optical materials for the middle IR spectral range. The main quality criterion for application in this range is a low absorption coefficient ($\alpha$) in the region of 10 μm. ZnSe crystals obtained by the CVD method are characterized by $\alpha \sim 10^{-4}\ \text{cm}^{-1}$ [80–82], close to the theoretical limit, while crystals grown from the melt have the absorption coefficient of $\alpha \sim 10^{-3}\ \text{cm}^{-1}$. The given method makes it possible to obtain crystals with a large area of $\sim 1\ \text{m}^2$, but a limited thickness, the latter being unimportant for optical elements. The main drawback of this method is the fact that the structure of the grown crystals is polycrystalline with a chaotic orientation of crystallites, the size of single-crystalline grains being of tens of micrometers. Thus the CVD method does not allow production of chalcogenide crystals with a hexagonal structure, e.g., CdS and CdSe.

The growth of chalcogenide crystals by the Bridgman method is realized under an excess pressure of inert gas (argon). The thermal unit of a growth furnace made exclusively from graphite consists of a bifilar heater with magnetic field compensation, and heat-insulating materials made from graphite and graphite felt. The crucible material may be either pyrolyzed graphite with a thickened inner surface or glassy carbon for reducing adhesion to the crystalline materials.

Such a furnace (Fig. 9.10) makes it possible to grow crystals of $A_2B_6$ compounds with melting temperatures up to 1900°C using graphite crucibles at an excess inert gas pressure up to 150 atm. The temperature of the growth process is limited by the operational characteristics of the heater material, as well as by the chemical aggressiveness of the melt and the raw material components.

Operation of the furnace is controlled by an automatic regulator at all growth stages. The time interval of the growth process is divided into several sections, and the heating or cooling rate can be programmed separately for each one. A more uniform distribution of the doping impurities is achieved by repeated passage of the crucible through the melting zone. However, the given method has certain drawbacks. In particular, crystal growth from the melt requires the use of high-pressure inert gas over the melt which promotes the formation of residual gas-saturated pores in the crystal bulk, thus giving rise to enhanced absorption and scattering of optical radiation.

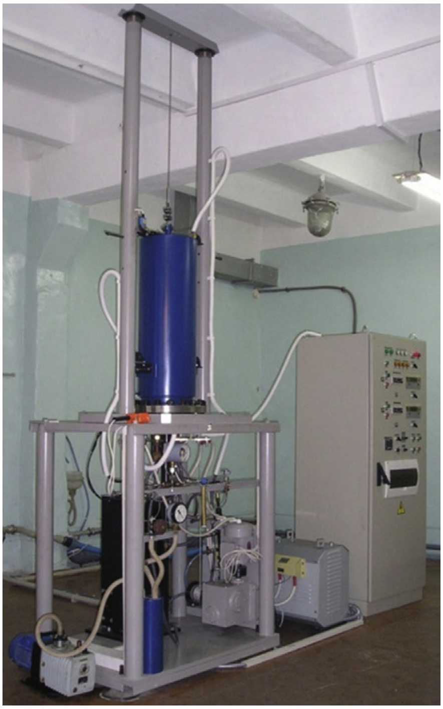

**Figure 9.10** Furnace for the growth of crystals of the chalcogenide series (from ZnS to CdTe) by the Bridgman method under excess pressure of inert gas.

Crystallization in the space limited by the crucible walls results in the formation of residual mechanical stresses in the crystal bulk and, as a consequence, in the appearance of anomalous birefringence uncharacteristic of crystals with isotropic crystalline structure. In ZnS and ZnSe crystals the high-temperature phase transition from the hexagonal "wurtzite" to the cubic "sphalerite" structure is not completed, leading to the appearance of crystal structure defects, the so-called twins. In ZnS crystals such defects cause the formation of uniform birefringence. However, it is possible to create technological conditions which will enable the growth of twin-free crystals [83]. Despite these drawbacks, the Bridgman method is the best technological procedure for the growth of large-bulk chalcogenide single crystals with different types of crystalline structure.

Doping of CVD-grown crystals with transition metals, aimed at obtaining new active media for IR lasers, is conventionally realized by the diffusion method [84]. The one-dimensional profile of the distribution of a doping impurity characteristic of the classical technique of thermal doping [85] is described by the function of "errors" $N(x,t) = N_0 \ \mathit{erfc}\left(x/2\sqrt{Dt}\right)$. Here $N(x, t)$ is the impurity distribution at point $x$ for the moment of time $t$; $N_0$ is the initial impurity distribution; and $D$ is the diffusion coefficient. Since the uniformity of the coefficient of amplification in active media is defined by the uniformity of the activator distribution, it is necessary to realize long-term annealing of the crystals in an inert medium. This gives rise to thermal etching of the surface and disturbance of the stoichiometry of the surface-adjacent layers. Upgrading the method of thermal doping by the addition of a coactivator made it possible to increase the effective diffusion coefficient of the main activator by more than an order [68]. This result reduces the duration of the technological procedure of diffusion doping by several fold, and achieves the desired uniformity of the activator distribution.

The growth of chalcogenide single crystals from the melt, e.g., by the Bridgman method, makes it possibie to dope the crystals in the process of crystallization. For this purpose the doping impurity is mixed with the raw material initially, or placed into the nose part of the crucible. The doping component distribution is defined by the segregation coefficient. For chromium in zinc sulfide and zinc selenide the segregation coefficient is less than 1. Fig. 9.11 presents the typical distribution of chromium when doping ZnSe crystals with the addition of metallic chromium in the nose part of the crucible. The technique of such doping in the process of crystal growth makes it possible to obtain large single crystalline blocks with uniform doping. In the process of doping the ions of transition metals occupy the sites of в $Zn^{2+}$ or $Cd^{2+}$ cations. The gradient of activator concentration is associated with the difference in the ionic radii of the doping impurities in the crystal lattice (Table 9.7). The distribution of iron along the ingot is more uniform, and this is connected with a lesser difference in the ionic radii of zinc and iron.

Despite intense development of film technologies used for practically all types of semiconductor materials, $A_2B_6$ group semiconductors are widespread in the modern world. Their classical use in IR optics is still popular, and new fields are emerging for their application in laser and scintillation engineering. This is explained by the wide variety of the physical and chemical properties of chalcogenide $A_2B_6$ group

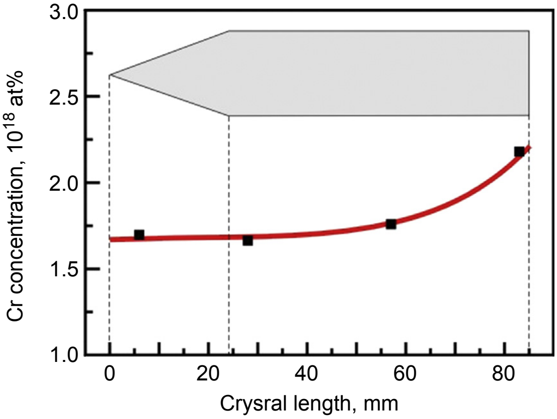

**Figure 9.11** Typical Cr distribution along the pulling direction for crystals grown by the Bridgman method (obtained in ZnSe crystal).

**Table 9.7 Ionic radii of ions in 2+ charge state in IV coordination [86]**

| Metal ion | $Zn^{2+}$ | $Cd^{2+}$ | $Cr^{2+}$ | $Fe^{2+}$ |
|---|---|---|---|---|
| R, Å | 0.74 | 0.92 | 0.87 | 0.77 |

crystals, as well as by a high throughput of pure and doped materials. Further investigations aimed at modifying the properties of crystalline materials of "II sulfides and II selenides" type, improving their working characteristics, and developing new optoelectronic devices, lasers, and radiation instruments on their base are being carried out around the world.

## References

[1] S.I. Vavilov, The Human Eye and the Sun: "Hot" and "cold" Light, first ed., Pergamon Press, Oxford, New York, 1965, p. 168.
[2] W.M. Yen, S. Shionoya, H. Yamamoto (Eds.), Phosphor Handbook, second ed., CRC press, Boca Raton, FL, USA, 1999.
[3] M. Bredol, H. Schulze Dieckhoff, Materials for powder-based AC-electroluminescence, Materials 3 (2) (2010) 1353–1374, https://doi.org/10.3390/ma3021353.
[4] M.J. Abdala, A. Godin, J.P. Noblanc, DC-electroluminescence mechanisms in ZnS devices, J. Lumin. 18/19 (2) (1979) 743–748.
[5] S. Ummartyotin, N. Bunnak, J. Juntaro, M. Sain, H. Manuspiya, Synthesis and luminescence properties of ZnS and metal (Mn, Cu)-doped-ZnS ceramic powder, Solid State Sci. 14 (3) (March 2012) 299–304, https://doi.org/10.1016/j.solidstatesciences.2011.12.005.
[6] G.J. Russel, J. Woods, Vapor growth and defect characterization of large crystals of ZnS and Zn(S, Se), J. Cryst. Growth 47 (1979) 647–653.

[7] K.L. Lewis, D.J. Cook, P.B. Roscoe, The structure and optical properties of polycrystalline $ZnS_xSe_{1-x}$ prepared by chemical vapor deposition, J. Cryst. Growth 56 (1982) 614−620.

[8] N.K. Morozova, V.A. Kuznetsov, Sul'fid Tsinka (Zinc Sulfide), Nauka, Moscow, 1987, p. 200.

[9] K. Kassali, N. Bouarissa, Composition and temperature dependence of electron band structure in $ZnS_xSe_{1-x}$, Mater. Chem. Phys. 76 (2002) 255−261.

[10] K. Mochizuki, Vapor growth and stoichiometry control of zink sulfo-selenide, J. Cryst. Growth 58 (1982) 87−94.

[11] V. Kumar, T.P. Sharma, Structural and optical properties of sintered $ZnS_xSe_{1-x}$ films, Opt. Mater. 10 (1998) 253−256.

[12] J.H. Song, E.D. Sim, K.S. Baek, S.K. Chang, Optical properties of $ZnS_xSe_{1-x}$ ($x<0.18$) random and ordered alloys grown by metalorganic atomic layer epitaxy, J. Cryst. Growth 214−215 (2000) 460−464.

[13] N.K. Morozova, D.A. Mideros, E.M. Gavrishuk, Self-Activated luminescence in ZnS-ZnSe system from positions of the band anticrossing model, in: Izvestija Vuzow (Russia), Fisika, vol. 10, 2006, pp. 166−169.

[14] K. Ohmori, M. Ohishi, T. Okuda, Edge emission in melt-grown $ZnSe_xS_{(1-x)}$, J. Appl. Phys. 49 (8) (August 1978) 4506−4508.

[15] M.M. Chiles, Low-level detector for alpha contamination monitor in continuously flowing process waste water, Nucl. Instrum. Methods 109 (1973) 541−546.

[16] ZnS(Ag) Product Data Sheets, Saint-gobain Crystals. www.detectors.saint-gobain.com/data/element/node.

[17] S.A. McElhaney, J.A. Ramsey, M.L. Bauer, M.M. Chiles, A more rugged ZnS(Ag) alpha scintillation detector, IEEE Trans. Nucl. Sci. 37 (1990) 868−872.

[18] N. Kubota, M. Katagiri, K. Kamijo, H. Nantoa, Evaluation of ZnS-family phosphors for neutron detectors using photon counting method, Nucl. Instrum. Meth. Phys. Res. 529 (2004) 321−324.

[19] P.J. Dean, J.L. Merz, Pair spectra and "edge emission" in zinc selenide, Phys. Rev. 3 (178) (1969) 1310−1318.

[20] V. Swaminathan, L.C. Greene, Pair spectra, edge emission and the shallow acceptors in melt-grown ZnSe, Phys. Rev. B 12 (14) (1976) 5351−5363.

[21] L.Y. Markovskii, I.A. Mironov, YuS. Ryzhkin, About photoluminescence of zinc selenide, Optic Spectrosc. 1 (27) (1969) 167−169.

[22] N.K. Morozova, V.A. Kuznetsov, V.D. Ryzhikov, et al., Zinc selenide. Obtaining and optical properties, Science (1992) 96. Moscow.

[23] M.P. Kulakov, A.V. Fadeev, About stoichiometry crystals ZnSe were growing from melting, Izv. AN USSR Ser. Inorg. Mater. 17 (1981) 1565−1570.

[24] V. Susdal, Y. Yepifanov, S. Strelnikov, O. Lalaiants, Y. Voronkin, S. Galkin, Device for Growth of Monocrystals of Group of AIIBVI, 2009. Patent of USA UA87944 (C2).

[25] V. Ryzhikov, B. Grinyov, S. Galkin, N. Starzhinskiy, I. Rybalka, ZnSe doped crystals, growing technology and luminescent characteristics, J. Cryst. Growth 364 (2013) 111−117.

[26] V.B. Mikhailik, H. Kraus, Performance of scintillation materials at cryogenic temperatures, Phys. Status Solidi B 247 (7) (2010) 1583−1599.

[27] F.A. Danevich, Development of crystal scintillators from enriched isotopes for double β decay experiments, IEEE Trans. Nucl. Sci. 59 (5) (October 2012) 2207.

[28] F. Ferroni, LUCIFER: a new technique for double beta decay, II Nuovo Cimento C 33 (5) (2010), https://doi.org/10.1393/ncc/i2011-10696-1.

[29] J.W. Beeman, F. Bellini, P. Benetti, L. Cardani, et al., Current status and future perspectives of the LUCIFER experiment, Adv. High Energy Phys. 2013 (2013) 15. Article ID: 237973.

[30] I. Dafinei, S. Nagorny, S. Pirro, L. Cardani, M. Clemenza, F. Ferroni, M. Laubenstein, S. Nisi, L. Pattavina, K. Schaeffner, M.L. di Vacri, A. Boyarintsev, I. Breslavskii, S. Galkin, A. Lalayants, I. Rybalka, V. Zvereva, M. Enculescu, Production of 82Se enriched Zinc Selenide (ZnSe) crystals for the study of neutrinoless double beta decay, J. Cryst. Growth 475 (2017) 158−170, https://doi.org/10.1016/j.jcrysgro.2017.06.013.

[31] J.J.H. Coumans, Dual energy X-ray diagnostics, Philips Tech. Rev. 42 (8−9) (1986) 274−285.

[32] R.M. Harrison, Digital radiography − a review of detector design, Nucl. Instrum. Methods A 310 (1991) 24−34, https://doi.org/10.1016/0168-9002(91)90995-3.

[33] S.V. Naydenov, V.D. Ryzhikov, Determination of chemical composition by the method of multi-energy radiography, Tech. Phys. Lett. 28 (5) (2002) 357−360, https://doi.org/10.1134/1.1482736.

[34] S.V. Naydenov, V.D. Ryzhikov, Multi-energy techniques for radiographic monitoring of chemical composition, Nucl. Instrum. Methods A 505 (2003) 556−558, https://doi.org/10.1016/S0168-9002(03)01146-X.

[35] S.V. Naydenov, V.D. Ryzhikov, C.F. Smith, Multi-energy approach in radiography and introscopy, Nucl. Instrum. Methods A 537 (2003) 462−466, https://doi.org/10.1016/j.nima.2004.08.065.

[36] S.V. Naydenov, V.D. Ryzhikov, C.F. Smith, Direct reconstruction of the effective atomic number of materials by the method of multi-energy radiography, Nucl. Instrum. Methods B 215 (2004) 552−560, https://doi.org/10.1016/j.nimb.2003.09.020.

[37] High accuracy x-ray dual-energy experiments and non-rotational tomography algorithm for explosives detection technique in luggage control, in: Proc. Int. Symp. on Digital Industrial Radiology and Computed Tomography (DIR 2007), June 25−27, 2007, Lyon, France, 2007, http://www.academia.edu/download/43682735/16.pdf.

[38] V. Rebuffel, M. Tartare, A. Brambilla, V. Moulin, L Verger, Multi-energy X-ray techniques for NDT: a new challenge, in: 11th European Conf. on Non-destructive Testing (ECNDT 2014), October 6−10, 2014, Prague, Czech Republic, 2014, http://www.ndt.net/search/docs.php3?showForm=off&id=16676.

[39] D. Kim, S. Lee, P.-H. Jeon, Experimental results of use of triple-energy X-ray beam with K-edge filter in multi-energy imaging, J. Instrum. 11 (2016) P04009, https://doi.org/10.1088/1748-0221/11/04/P04009.

[40] C. Paulus, V. Moulin, D. Perion, P. Radisson, L. Verger, Multi-energy x-ray detectors to improve air-cargo security, in: Proc. SPIE 10187, Anomaly Detection and Imaging with X-rays (ADIX) II, vol. 101870I, May 1, 2017, https://doi.org/10.1117/12.2262585.

[41] R.E. Alvarez, A. Macovski, Energy-selective reconstructions in X-ray computerized tomography, Phys. Med. Biol. 21 (1976) 733−744, https://doi.org/10.1088/0031-9155/21/5/002.

[42] C.H. McCollough, S. Leng, L. Yu, J.G. Fletcher, Dual- and multi-energy CT: principles, technical approaches, and clinical applications, Radiology 276 (3) (2015) 637−653, https://doi.org/10.1148/radiol.2015142631.

[43] J. Fornaro, S. Leschka, D. Hibbeln, A. Butler, et al., Dual- and multi-energy CT − approach to functional imaging, Insights Imag. 2 (2) (2011) 149−159, https://doi.org/10.1007/s13244-010-0057-0.

[44] N.P. Ghonge, Computed tomography in the 21st century: current status & future prospects, J. Int. Med. Sci. Acad. 26 (1) (2013) 35−42, http://medind.nic.in/jav/t13/i1/javt13i1p35.pdf.

[45] H. Bouchard, Energy Selective Computed Tomography: A Potential Revolution for Radiotherapy, National Physical Laboratory, UK, 2014, http://www.npl.co.uk/science-technology/radiation-dosimetry/energy-selective-computed-tomography-a-potential-revolution-for-radiotherapy.

[46] Wikipedia. Dual-energy X-ray Absorptiometry (DXA, DEXA), 2017, https://en.wikipedia.org/wiki/Dual-energy_X-ray_absorptiometry, https://en.wikibooks.org/wiki/Basic_Physics_of_Nuclear_Medicine/Dual-Energy_Absorptiometry.

[47] Heimann Systems Company, 2017. Germany, http://vww.heimainisystems.com.

[48] MultiX Company, X-ray Spectrometric Imaging, 2017. France, http://www.multixdetection.com/.

[49] Rapiscan Systems Company, USA, Rapiscan 632DV. Dual View Technology and a Heavy Duty Design for Pallet and Air Cargo X-ray Screening, 2017, 2017, http://www.rapiscan.com, http://www.rapiscansystems.com/en/products/bpi/productsrapiscan_632dv.

[50] L3 Security & Detection Systems Company, 2017. USA, http://www.sds.l-3com.com/.

[51] Siemens Healthcare. Dual Source CT Scanner (DSCT), 2017. Germany, http://www.healthcare.siemens.co.uk/computed-tomography/dual-source-ct.

[52] General Electric Healthcare, Spectral Imaging (GSI) Xtream Revolution CT, 2017. USA, http://www3.gehealthcare.com/en/products/categories/computed_tomography/revolution_ct.

[53] Philips Healthcare, IQon Spectral CT (SCT), EU, 2017, http://www.usa.philips.com/healthcare-product/HCNOCTN284/iqon-spectral-ct.

[54] Wikipedia. Digital Radiography, 2017, https://en.wikipedia.org/wiki/Digital_radiography.

[55] G.F. Knoll, Radiation Detection and Measurement, fourth ed., John Wiley & Sons, New York, 2010, https://phyusdb.files.wordpress.com/2013/03/radiationdetectionandmeasurementbyknoll.pdf.

[56] L.D. DeLoach, R.H. Page, G.D. Wilke, S.A. Payne, W.F. Krupke, Properties of transition metal-doped Zinc Chalcogenide crystals for tunable IR laser radiation, in: B. Chai, S. Payne (Eds.), Advanced Solid State Lasers, 1995. Vol. 24 of OSA Proceedings Series (Optical Society of America, 1995), Paper #LM4.

[57] W.F. Krupke, R.H. Page, DeLoach, D. Laura, S.A. Payne, Transition-metal Doped Sulfide, Selenide, and Telluride Laser Crystal and Lasers, 1996. U.S. Patent #5541948.

[58] D. Frédéric, B. Francois, G. Patrick, New laser crystals for the generation of ultrashort pulses, Comptes Rendus Phys. 8 (2007) 153−164, https://doi.org/10.1016/j.crhy.2006.04.004.

[59] G.J. Wagner, T.J. Carrig, R.H. Page, K.I. Schaffers, J.-O. Ndap, X. Ma, A. Burger, Continuous-wave broadly tunable $Cr^{2+}$:ZnSe laser, Optics Lett. 24 (1999) 19−21.

[60] A.O. Sennaroglu, C.R. Konca, Pollock, Continuous-wave power performance of a 2.47-um $Cr^{2+}$:ZnSe laser: experiment and modeling, IEEE J. Quant. Electron. 36 (10) (October 2000) 1199.

[61] I.T. Sorokina, E. Sorokin, S. Mirov, V. Fedorov, V. Badikov, V. Panyutin, A. Di Lieto, M. Tonelli, Continuous-wave tunable $Cr^{2+}$:ZnS laser, Appl. Phys. B 74 (6) (April 2002) 607−611.

[62] V.A. Akimov, V.I. Kozlovskii, Yu V. Korostelin, A.I. Landman, Yu P. Podmar'kov, Ya K. Skasyrsky, M.P. Frolov, Efficient cw lasing in a $Cr^{2+}$:CdSe crystal, Quant. Electron. 37 (11) (2007) 991−992.

[63] P.A. Berry, K.L. Schepler, High-power, widely-tunable $Cr^{2+}$:ZnSe master oscillator power amplifier systems, Optics Express 18 (14) (July 5, 2010) 15062.

[64] E. Slobodchikov, P.F. Moulton, 1-GW-peak-power, Cr:ZnSe laser, in: Laser Science to Photonic Applications, Report at Conf. CLEO-2011, Baltimore Convention Center, Baltimore, Maryland, USA, 2011.

[65] I. Moskalev, S. Mirov, M. Mirov, S. Vasilyev, V. Smolski, A. Zakrevskiy, V. Gapontsev, 140 W Cr:ZnSe laser system, Optics Express 24 (2016) 21090−21104.

[66] S. Vasilyev, I. Moskalev, M. Mirov, V. Smolski, D. Martyshkin, V. Fedorov, S. Mirov, V. Gapontsev, Progress in Cr and Fe doped ZnS/Se mid-IR CW and femtosecond lasers, in: Proc. SPIE 10193, Ultrafast Bandgap Photonics II, 101930U, May 8, 2017, https://doi.org/10.1117/12.2264209.

[67] P.S. Kuo, K.L. Vodopyanov, M.M. Fejer, Polarization-diverse parametric processes in Zincblende crystals, in: Conf. on Lasers Electro-optics, Baltimore, MD, USA, May 31−June 5, 2009, 2009.

[68] B. Bernhardt, E. Sorokin, P. Jacquet, R. Thon, T. Becher, I.T. Sorokina, N. Picque, T.W. Hansch, Mid-infrared dual-comb spectroscopy with 2.4 mkm $Cr^{2+}$:ZnSe femtosecond lasers, Appl. Phys. B 100 (2010) 3−8.

[69] I.T. Sorokina, Chapter “Broadband Mid-infrared Solid-state Lasers” in the Book “Mid-infrared Coherent Sources and Applications”, in: M. Ebrahim-zadeh, I.T. Sorokina (Eds.), Springer, 2008, pp. 225−260.

[70] M. Mond, D. Albrecht, E. Heumann, G. Huber, et al., 1.9-mm and 2.0-mm laser diode pumping of $Cr^{2+}$:ZnSe and $Cr^{2+}$:CdMnTe, Optic Lett. 27 (12) (June 15, 2002) 1034−1036.

[71] E.V. Sorokin, V.K. Komar, V.M. Puzikov, YuA. Zagoruiko, A.S. Gerasimenko, N.O. Kovalenko, A.K. Kapustnik, I.T. Sorokina, Spectroscopy and tunable continuous-wave operation of $Cr^{2+}:Zn_{1-x}Mg_xSe$ single crystal around 2.5 μm, Quant. Electron. 45 (4) (2015) 301−304.

[72] H. Jelínková, M.E. Doroshenko, M. Jelínek, J. Šulc, M. Němec, V.V. Osiko, N.O. Kovalenko, I.S. Terzin, Fe:CdMnTe active material spectroscopic properties and laser generation around 5 μm, in: Proc. SPIE 10082, Solid State Lasers XXVI: Technology and Devices, 100820F, February 24, 2017, https://doi.org/10.1117/12.2252317.

[73] H. Jelínková, M.E. Doroshenko, V.V. Osiko, M. Němec, J. Šulc, M. Jelínek, D. Vyhlídal, V. Kubecek, M. Čech, N.O. Kovalenko, A.S. Gerasimenko, Fe:ZnMnSe laser active material properties at room and cryogenic temperature, in: Proc. SPIE 9893, Laser Sources and Applications III, 98930A, May 9, 2016, https://doi.org/10.1117/12.2228844.

[74] E.V. Markov, A.A. Davydov, Growing oriented single crystals of CdS from the vapor phase, Neorg. Mater. 11 (1975) 1755.

[75] Y. Namikawa, ZnSe single crystals grown by vapor growth methods and their applications, SEI Tech. Rev. 72 (April 2011) 25−33.

[76] S. Fujiwara, Y. Namikawa, Y. Hirota, M. Irikura, K. Matsumoto, T. Kotani, Growth of ZnSe single crystal by CVT method with self-moving convection shield, J. Cryst. Growth 196 (1999) 83−87.

[77] J. McCloy, “International development of chemical vapor deposited zinc sulfide”, window and dome technologies and materials X, in: R.W. Tustison (Ed.), Proc. of SPIE, vol. 6545, 2007, p. 654503, https://doi.org/10.1117/12.717870.

[78] I. Kikuma, M. Matsuo, T. Komuro, Growth and properties of ZnSe crystals by a modified bridgman method, Jpn. J. Appl. Phys. 30 (1991) 2718.

[79] S. Fujiwara, T. Kotani, K. Matsumoto, T. Shirakawa, Crystal growth of ZnSe by PVT using a semi-open ampule, J. Cryst. Growth 169 (1996) 660−664.

[80] H.G. Lipson, Impurity absorption in CVD ZnSe, Appl. Optics 16 (1977) 2902−2908.

[81] A. Swanson, R. Donadio, R. Gentilman, J. Pappis, J. Connolly, P. Reagan, in: Proceedings of the Fifth Annual Conference on Infrared Laser Window Materials, 1975.

[82] unpublishedC.R. Andrews, C.L. Strecker (Eds.), Available on Request from Charles Strecker, Air Force Materials Laboratory, Wright-Patterson Air Force Base, Ohio, 1976, p. 1052, 45433.

[83] J.F. Wang, A. Omino, M. Isshikia, Bridgman growth of twin-free ZnSe single crystals, Mater. Sci. Eng. B. 83 (1−3) (June 21, 2001) 185−191.

[84] K.N. Firsov, E. M Gavrishchuk, V. B Ikonnikov, S. Yu Kazantsev, et al., CVD-grown $Fe^{2+}$:ZnSe polycrystals for laser applications, Astro Ltd Laser Phys. Lett. 14 (5) (March 30, 2017) 055805.

[85] R. Ghez, Diffusion Phenomena: Cases and Studies, Springer Science & Business Media, June 29, 2013, p. 316.

[86] R.D. Shannon, Revised effective ionic radii and systematic studies of interatomic distances in Halides and Chalcogenides, in: Central Research and Development Department, Experimental Station, E.I. Du Pont de Nemours and Company, Wilmington, Delaware 19898, USA, 1976, pp. 751−767. Published in Acta Crystallographica, A32.

# Diamond

# 10

*Hideaki Yamada*
National Institute of Advanced Industrial Science and Technology, Ikeda, Japan

## 10.1 Introduction

Diamond has several of the highest material constants among materials. Its mechanical, thermal, and electrical material constants are in most cases superior to those of other materials. These properties are summarized and compared with reference values of other materials in Table 10.1 [1–3].

Based on these superior material constants, many industrial applications of diamond have been seen, of which the best known and largest today is its use for mechanical tools [4]. It is reported that the next growing market will be the heat sink [5]. As shown in Table 10.1, for example, the thermal conductivity of GaN is similar or less than that of Si and much lower than that of SiC and diamond. Such low thermal conductivities limit the allowed power density for power devices. It has been reported that power consumption with a diamond heat sink might be two times higher than that with a heat sink made of SiC [6]. On the other hand, the high thermal conductivity and low dielectric constant of diamond attract interest in it as an optical window with high frequency and power. Polycrystalline diamond is adopted for window to introduce millimeter wave with several 10 GHz and several 10 kW class power [7].

National and international projects are currently ongoing aimed at realizing the industrial use of diamond as a power semiconductor material [8]. Each project develops the materials and devices: the material constants which relate to power device applications are summarized in Fig. 10.1, where they are compared to the respective constants of diamond. Based on these material constants, power devices with high blocking voltage, rapid response, and low resistivity, i.e., high power efficiency, and which can be relatively easily cooled down can be expected using diamond.

Recent development of devices made with diamond has revealed its potential, which is expected to be higher than that of other materials. Comparison between characteristics of Schottky barrier diodes (SBDs) made of diamond and SiC shows the more rapid response and higher blocking voltage of diamond than of SiC [9]. So far, in addition to SBDs [9–11], FETs, JFETs, MESFTEs, and PiN diodes with a blocking voltage of more than several hundred volts have been demonstrated [12–17]. Recently, MOSFETs used an inversion channel made of diamond [18].

Most of these awaited applications require large-size round substrates: at least 2-inch wafers are needed to keep manufacturing quality and cost within acceptable limits. Because it is impossible to obtain such wafers from nature, it is indispensable to establish ways to prepare it artificially. Currently, several companies produce single crystal diamond substrates [19–24].

**Single Crystals of Electronic Materials.** https://doi.org/10.1016/B978-0-08-102096-8.00010-0
Copyright © 2019 Elsevier Ltd. All rights reserved.

**Table 10.1** **Material constants of diamond compared with those of other materials**

| | Diamond | Reference materials | |
|---|---|---|---|
| Knoop hardness (GPa) | 60–120 | cBN | 34–73 |
| | | WC | <20 |
| | | $Al_2O_3$ | <20 |
| Density (g/cm$^3$) | 3.5 | Graphite | 2.1 |
| | | 4H–SiC | 3.2 |
| | | cBN | 3.2 |
| Thermal expansion coefficient ($10^{-6}$/°C) | 1.1 | Cu | 17.7 |
| | | cBN | 4.7 |
| | | Al | 18.0 |
| Thermal conductivity (W/cm°C) | $\lesssim$33 | 4H–SiC | 4.9 |
| | | Si | 1.6 |
| | | Cu | 4.0 |
| | | GaN | $\lesssim$2 |
| Reflective index | 2.4 | $ZrO_2$ | 2.4 |
| | | Sapphire | 1.8 |
| | | $SiO_2$ | 1.5 |
| Dielectric constant | 5.7 | Si | 11.8 |
| | | 4H–SiC | 9.7 |
| | | $SiO_2$ | 3.5 |
| Bandgap (eV) | 5.5 | Si | 1.1 |
| | | 4H–SiC | 3.3 |
| | | GaN | 3.4 |
| Breakdown field ($10^5$ V/cm) | 56 | Si | 2.5 |
| | | 4H–SiC | 30 |
| | | GaN | 40 |
| Mobility (electrons) (cm$^2$/Vs) | 4500 | Si | $\approx$1450 |
| | | 4H–SiC | 1000 |
| | | GaN | 1350 |
| Mobility (holes) (cm$^2$/Vs) | 3800 | Si | $\approx$480 |
| | | 4H–SiC | 115 |
| | | GaN | 370 |

## 10.2 Growth technologies for artificial diamond

Artificial diamond was first prepared by General Electric Company in the 1950s, using the high-pressure high-temperature (HPHT) method [25]. This method was popularized as a way to produce mechanical tools, powders, and gemstones in many countries. As it is well known, this method gives diamond in its stable phase. Bulk single crystal

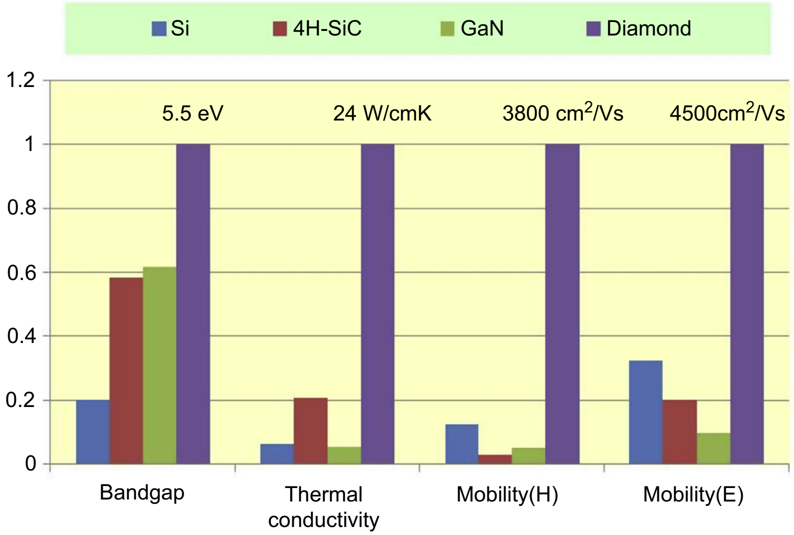

**Figure 10.1** Material constants from the view of wide bandgap materials.

diamond of almost 1 inch size can be synthesized using this method [26]. To realize this phase in a limited space, several types of apparatus were proposed; their size is typically over 3 m in height. As indicated (top right) in Fig. 10.2, a cell is installed inside the apparatus in which carbon sources and metal catalysts are encapsulated. More than 5 GPa pressure and 1000°C temperature are imposed on the cell simultaneously in various ways, as shown in the figure. Investment cost and usability largely depend on the types of anvils and system size.

By using this method it is reported that single crystal diamonds with very high purity and low dislocation density can be synthesized [27]. However, the method tends to grow blocky diamond but not plate-like crystal. For example, fabrication of wafers with 4–6 inch diameter using this method is considered to be not feasible in practice [28]. Another artificial way to growth diamond, plasma chemical vapor deposition (CVD), was demonstrated in the 1970s [29]; a schematic is given in Fig. 10.3. In the case of microwave plasma CVD (MWCVD), microwave is introduced into an evacuated region. The vacuum level is about 1–10 k Pa. Electrons respond to the introduced microwave and start elastic collisions with the source gas mixture. This causes a phase shift from the microwave oscillation and allows electrons to absorb the microwave power. Absorption of the microwave power causes the discharge by ionizing the source gas mixture.

Various radicals are generated by dissociation of the source gas mixture. Some of them react with the top surface of the substrate, whose temperature is kept around 800–1200°C. One widely accepted growth mechanism is dimer opening [30,31]. The diamond surface is terminated by hydrogen and reconstructed as dimer rows, confirmed by Scanning Tunneling Microscope (STM) measurement [32] as shown (bottom right) in Fig. 10.3, where turquoise and white spheres represent hydrogen

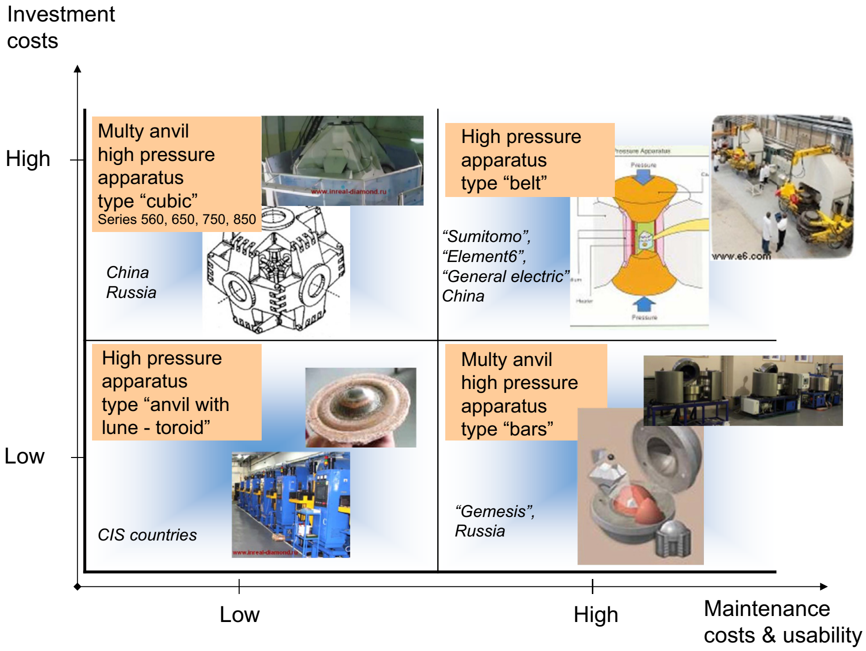
Investment costs
High
Low
Multy anvil high pressure apparatus type “cubic”
Series 560, 650, 750, 850
www.inreal-diamond.ru
China
Russia
High pressure apparatus type “belt”
“Sumitomo”, “Element6”, “General electric”, China
www.e6.com
High pressure apparatus type “anvil with lune - toroid”
www.inreal-diamond.ru
CIS countries
Multy anvil high pressure apparatus type “bars”
“Gemesis”, Russia
Low
High
Maintenance costs & usability

**Figure 10.2** State-of-the-art apparatus for high-pressure, high-temperature growth [26].

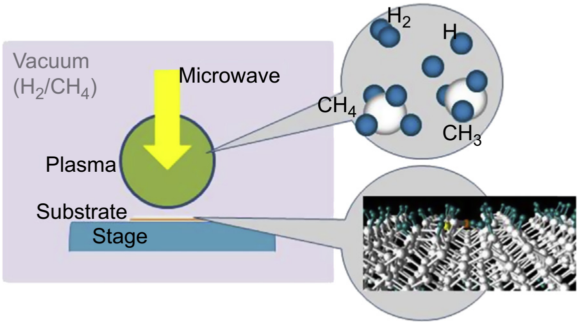
Vacuum
($H_2$/$CH_4$)
Microwave
Plasma
Substrate
Stage
$H_2$
H
$CH_4$
$CH_3$

**Figure 10.3** Schematic of microwave plasma chemical vapor deposition.

and carbon atoms. Atomic hydrogen abstracts surface hydrogen, and then methyl radical terminates this radical site. This methyl radical is incorporated into the surface by bridging the dimer. This is described again below based on numerical simulation.

At present, MWCVD is the most widely adopted method for growth of diamond films on planes and even raw stones. But the CVD method is not limited only to MWCVD; microwave is just an excitation source to dissociate the source gas mixture. Actually, the gas pressure in the case of microwave plasma for diamond growth is relatively higher than for usual processing plasma, thus the absorbed power of microwave is mostly consumed to increase the gas temperature up to 2000–3000°C. Then the source gas mixture is thermally dissociated. Thus it is known that other excitation sources could be adopted to grow diamond, such as hot filament (HF) [33], Direct Current (DC) plasma [34], arc jet [35], Inductively Coupled Plasma (ICP) plasma torch [36,37], millimeter-wave plasma [38], combustion flames [39], among the most popular.

The discharge region is typically filled with a large amount of hydrogen and a small amount (typically ≤10%) of methane. In addition to these species one may introduce oxygen and/or nitrogen. Oxygen is believed to improve the crystal quality [40]. Introduction of nitrogen enhances the growth rate and promotes selective growth into <100> directions [41−43]. The fractions of these species in the source gas mixture to allow diamond growth are summarized by the Bachmann diagram [44] (Fig. 10.4). The three sides of the triangle represent fractions of carbon, hydrogen, and oxygen with respect to other species. Bachmann and coauthors summarized several reports on trials of diamond growth in this diagram. They clearly showed that diamond growth is attained at the isosceles triangular region, colored in red in the middle of the triangle diagram.

The gas pressure is relatively high compared with that adopted in typical plasma CVDs. When the gas pressure is relatively high, such as 1−10 kPa, the absorbed microwave power is immediately transferred to increase the gas temperature. The source gas mixture is dissociated into radicals by inelastic collisions with electrons and thermal reactions among the mixtures. The threshhold gas temperature for these

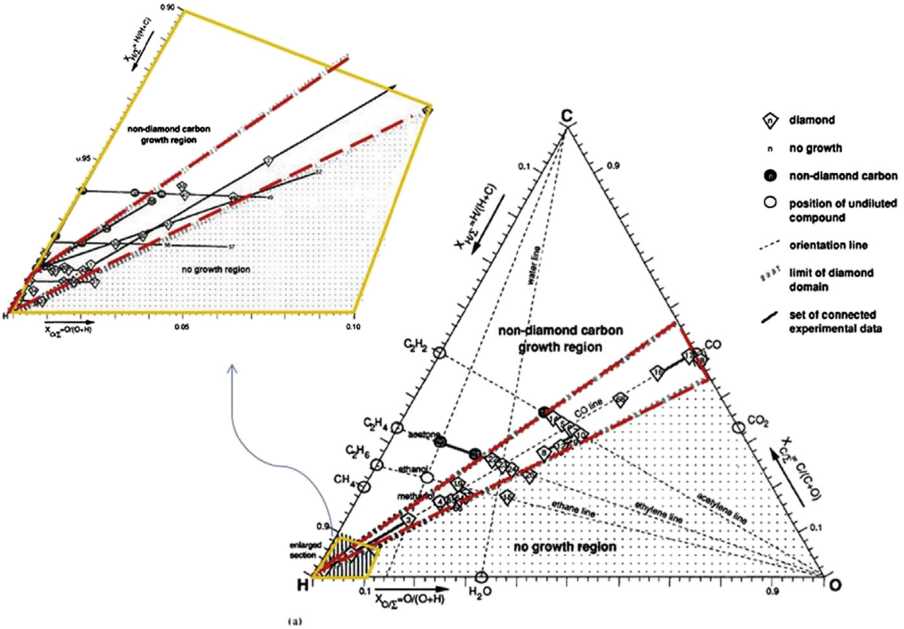
0.90
$X_{H/\Sigma}=H/(H+C)$
non-diamond carbon growth region
0.95
no growth region
H
$X_{O/\Sigma}=O/(O+H)$
0.05
0.10
C
0.1
0.9
water line
non-diamond carbon growth region
$C_2H_2$
$C_2H_4$
acetone
$C_2H_6$
ethanol
$CH_4$
methanol
CO line
CO
$CO_2$
$X_{C/\Sigma}=C/(C+O)$
ethane line
ethylene line
acetylene line
no growth region
enlarged section
0.9
0.1
H
0.1
$H_2O$
0.9
O
diamond
no growth
non-diamond carbon
position of undiluted compound
orientation line
limit of diamond domain
set of connected experimental data
(a)

**Figure 10.4** The Bachmann diagram. Each *dot* represents an experimental report with the number of the reference in [44]. *Diamond* growth was realized in the *triangular region* enclosed by a *red dashed line*.

dissociation processes is considered to be 2000°C; when the gas temperature is higher (lower) than this, thermal reactions among the mixtures (inelastic collisions with electrons) are dominant and generate radicals, for example atomic hydrogen [45]. The growth conditions which have been adopted for diamond growth are summarized in Fig. 10.5, where the gas pressure and imposed power are adopted as horizontal and vertical axes, respectively [29,34,36,43,46–54].

In almost all reports the deposition area is limited to 2–3 mm square. Some big circles and squares even for MWCVD used 915 MHz of microwave frequency, where typically 2.45 GHz is adopted. HF-CVD gives a relatively large deposition area with a low growth rate; for example, commercialized equipment allows a deposit over 300 mm in diameter [55]. In the first report from National Institute for Research in Inorganic Materials (NIRIM), Japan, the gas pressure was set to be several kPa with microwave power of less than 1 kW [29]. Because increased gas pressure limits the discharge area, which means enhancement of the power density under fixed-input microwave power, several trials with elevated gas pressure were reported [43,45,47–50]. The obtained growth rate is close to that obtained using the flame method [53]. One may adopt moderate gas pressure and introduce microwave power up to or over 10 kW to enlarge the deposition area [54,56]. In these cases, however, the growth

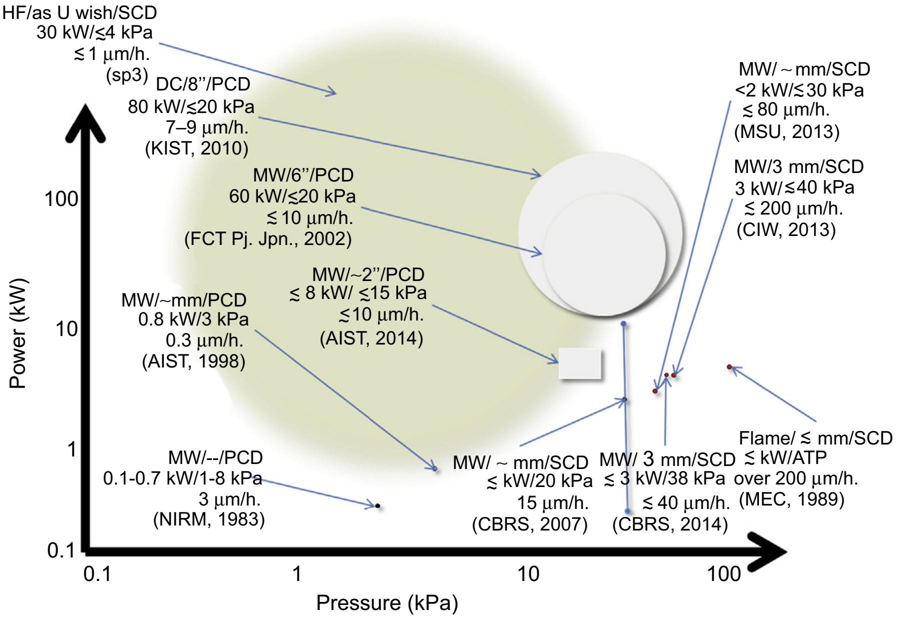

**Figure 10.5** Progress of diamond growth conditions [29,34,36,43,46–54]. *Dots and circles* represent the respective growth conditions where the areas of the *circles* correspond to the deposition area. MW, Flame, DC, and HF (hot filament) represent the respective excitation source to dissociate the source gas mixture for growth. Description of each *dot/circle* gives: the adopted excitation source/deposition area/singe or polycrystalline diamond/imposed power/adopted gas pressure/growth rate, with reporting institution and year in the bracket.

rate is still around 10 μm, because increasing the imposed power causes enlargement of the discharge area but not concentration of the power consumption near the top surface of the substrate. Therefore, local amount of the precursor production does not change so much only by increasing the imposed power.

After finding that MWCVD is a possible method to grow diamond, several commercial CVD equipment were proposed. Some of them are shown in Fig. 10.6 [55−60].

The color contours show distribution of electron number density at the region enclosed by the dashed line of the respective structure of the microwave plasma chamber configuration (second left). In each case, the microwave with the lowest transverse electric field mode is introduced from the rectangular waveguide. This is transferred to the cylindrical or ellipsoidal chamber, where the microwave mode is changed to a transverse magnetic field mode by a coaxial antenna set at the connection between the rectangular waveguide and the cylindrical chamber. Except for the case second from the left, they all have basically the same structure and their discharge regions are limited by dielectric windows or belljars. The case second from the left differs from the others in that the dielectric window, which is set at the bottom, is out of sight from the discharge region [61]. This allows relatively high microwave power introduction and reduces the possibility of the window breaking owing to concentration of the plasma at the window. All plasma distributions are hemispherical and similar to each other in these apparatuses [62], with the extent roughly limited by the wavelength. Thus technically the easiest way to enlarge the deposition area is to reduce the microwave frequency from 2.45 GHz−915 MHz [54,63,64]. On the other hand, the mean-free path of the radicals is typically several millimeters under the gas pressure for diamond growth [65]. This means that power consumption in the region beyond this length might not contribute to the growth. The typical size of the discharge region is around 50 mm diameter; thus almost 80% of the absorbed power is consumed as heat loss, and this power loss increases when the microwave frequency is reduced. This is an ongoing issue for current microwave plasma growth technology.

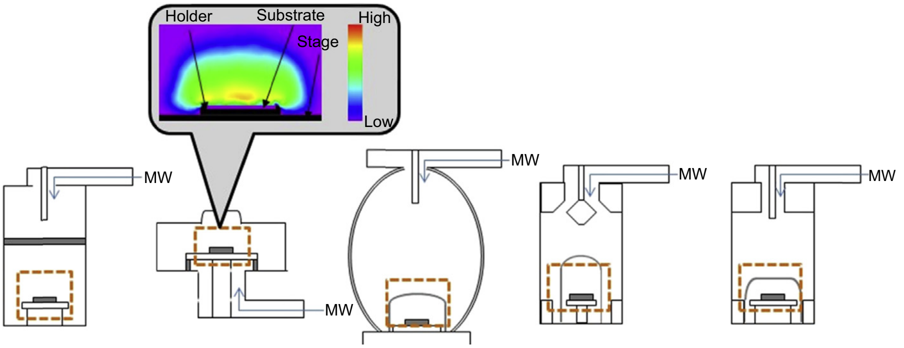

**Figure 10.6** Schematic of MWCVD apparatus. Plasma is generated in regions enclosed by the *dashed lines*, where *gray-colored squares* represent the substrates. Representative plasma distribution, which was numerically predicted, is also shown for the apparatus second left.

## 10.3 Promotion of predominant crystal surfaces via growth parameters

The growth condition of diamond is frequently characterized by the alpha parameter (Fig. 10.7), which is defined by the following equation [66]:

$$\alpha \equiv \frac{1}{\sqrt{3}} \frac{V_{100}}{V_{111}}$$

where $V_{001}$ and $V_{111}$ are the growth rate in the <001> and <111> directions. Depending on this parameter, the morphology of the resultant crystal is determined. Characterization of the growth condition was firstly done by Koidl [66] and further generalized [67].

Under conditions where $\alpha$ is high, growth in the <100> direction is enhanced and hence growth in the other direction is suppressed. As a result, {100} faces are diminished, as shown Fig. 10.7; right most. Recently, in addition to the $\alpha$ parameter, $\beta$ and $\gamma$ parameters were defined as the relative growth rate of $V_{001}$ against growth rates in <110> and <113> directions, respectively [67]. These parameters depend on several growth parameters, for example the substrate temperature and methane concentration in the source gas mixture. An example is shown in Fig. 10.8 [68]. Generally, increase of the methane concentration and decrease of the substrate temperature promotes enhancement of the $V_{001}$. In other words, to grow diamond layers on a <111>-directed single crystalline diamond substrate, one may choose a relatively low methane concentration and high substrate temperature.

It is noteworthy that this dependence of the $\alpha$ parameter also varies by changing the power density [68]. It is known that crystal quality and growth rate could be improved by increasing the power density [43,68–70]. As described below, this is considered to be due to the generation of large amounts of atomic hydrogen and hydrocarbon precursors by increasing the power density. This could be confirmed by simulation with simple chemistry [71].

## 10.4 Benefits of computer modeling

Plasma distribution under the microwave-excited discharge is not easy to predict without numerical simulation. This is because one may encounter unexpected

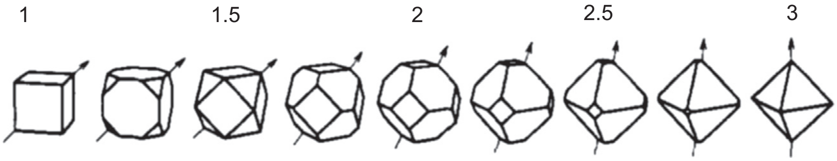

**Figure 10.7** Crystal shapes grown by various alpha parameters [65].

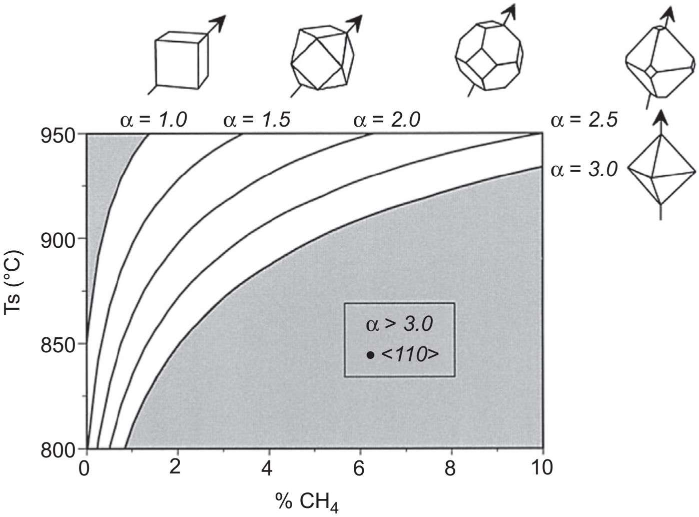

**Figure 10.8** Dependence of the alpha parameter on the substrate temperature and methane concentration in the source gas mixture, which are indicated by *vertical and horizontal axes* [68].

discharge even for minimal setup changes in the order of several millimeters. In addition, relatively high gas pressure makes it difficult to measure the plasma parameters experimentally because insertion of any probes inside the chamber disturbs the plasma and hinders the actual state of processing. Thus all experimental observations of the microwave plasma for diamond growth have so far been limited to optical methods, such as observations of the optical emission/absorption spectra [42,72–75], coherent antiStokes Raman scattering [76,77], cavity-ring-down spectroscopy [78], and so on. However, the available information from such observations is line-integrated values, and it is hard to understand, for example, spatial distributions of the radicals above the top surface of the substrate.

Many attempts to model the plasma for diamond deposition exactly have therefore been proposed at macroscopic scale [31,45,62,65,66,71,77–85] as well as atomic scale [30,85–97]. However, the relatively rigorous way to describe even the bulk plasma requires huge computational resources. For example, a full-kinetic model in which dynamics of electrons and each atom/molecule are described by the respective Boltzmann equations was conducted, but the calculation was performed in just one spatial point inside the chamber [80,81]. This much-simplified but time-resolved calculation showed that the dissociation dynamics happen within several milliseconds. Several fluid dynamics approaches were proposed [45,62,65,66,71,77–79]. Fig. 10.9 shows an example of a simulation conducted by a fluid dynamics model [97]. In this model the Maxwell equations, which are coupled with a simplified equation of electrons, are solved. It is noteworthy that the conservation equations of electrons could be reduced into only one differential equation [65,71] under appropriate assumptions which are acceptable for diamond growth. Such fluid-based simulation reveals that under typical growth conditions, such as gas pressure of 120 torr and input microwave power of 5 kW, the gas temperature is around 3000°C, which is much higher than the substrate temperature, 800−1000°C. Electron density is around $10^{17}$ $m^{-3}$, which is relatively higher than those obtained by other plasma sources. It is also shown that in this range of gas temperature and pressure the radicals are dissociated by thermal dissociation rather than inelastic collision with electrons [76]. This can be seen by comparisons of reaction probabilities among the species numerically. The source gas mixture is introduced from the top edge of the chamber wall. The gas follows the upwind above the substrate owing to the high gas temperature. Because of the importance of the thermal dissociations, atomic hydrogen (H) concentrates around the central region of the plasma. This is similar to those of the gas temperature and electron number density, which have the respective highest magnitudes in the same region. On the other hand, the concentration of the methyl radical ($CH_3$) has a shell-like structure, where its magnitude is relatively *low* at the central region of the plasma. This is because the recombination with H and dissociations of other hydrocarbon radicals, $CH_x$ ($x < 3$) are promoted there.

Even if fluid approximation is adopted for all constituent species, the computational resources needed are huge because there is a large variety of possible hydrocarbon species [76,84] even if one limits interest to neutral species [97−99]. Thus a phenomenological

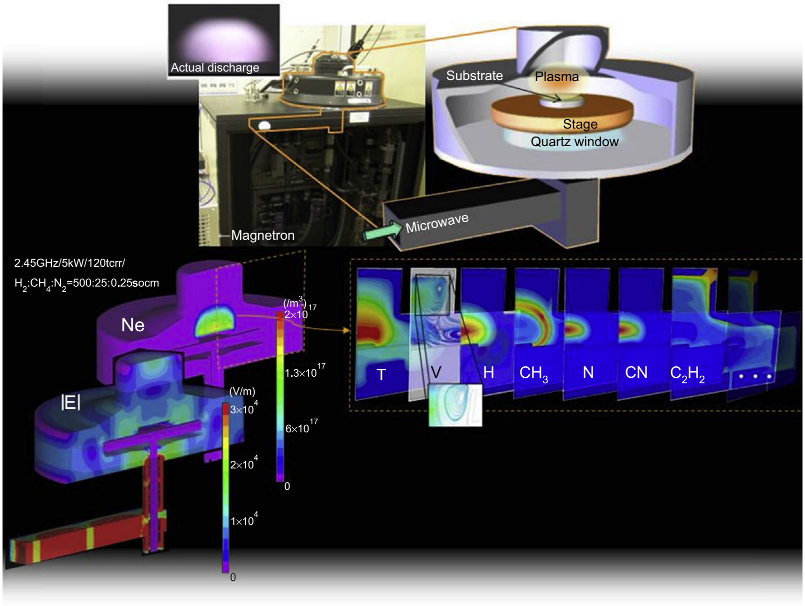

**Figure 10.9** An example of flowdynamic simulation [97] which was conducted for the configuration of AX6500 by SEKI Diamond Systems [57]. (Left top) the actual apparatus; (right top) a schematic of its interior. Contours and streamlines in the bottom are the calculated results. Ne and |**E**| indicate electron number density and local field strength, respectively. *T* and *V* are the gas temperature and flow. Contours of atoms and molecules are shown for a cross-section of the evacuated regions.

model was proposed by Füner et al. [63] for practical understanding of the discharge. In this model, the electron number density is assumed to be proportional to the local field strength if this field strength is larger than a threshhold value; see Fig 10.10(a). Thanks to this simple phenomenological assumption, we do not have to solve differential equation numerically in addition to the Maxwell equations. While this model cannot be applied to high-density plasma, where the skin effect becomes important and the peak positions of the local field strength and electron number density must be different, it is very useful to get an intuitive image and specify at least the region where the discharge starts with reduced computational resources. In addition to such predictions of the ignition region, dependence on the holder shape and configuration of the substrate can be studied to some extent [99].

In addition to simulation of the bulk plasma, atomic-scale simulations have been proposed to understand the growth mechanism and optimal dopant conditions [30,85–96]. By using the density-functional technique (DFT), the diamond growth mechanism has been studied [85] (Fig. 10.11).

In this case the model cluster with the reconstructed surface structure shown in Fig. 10.11(a) was adopted for computation. Dangling bonds of diamond surface are fully terminated by atomic hydrogen; the anchor layer is also terminated by atomic hydrogen to exclude artificial lone-pair electrons from the calculation domain. As shown in Fig. 10.11(b), the steric repulsion among the hydrogen atoms, $H_3$, $H_4$, and $H_5$, at the step edge causes energetic instability. This promotes extraction of these hydrogen atoms by desorption with hydrogen atoms from the gas phase. Then, at the generated radical site (Fig. 10.11(b) and (c)), methyl radical is adsorbed (Fig. 10.11(c)). This methyl radical is incorporated into the surface and generates the next diamond layer through breaking of the dimer bridge and reconstruction.

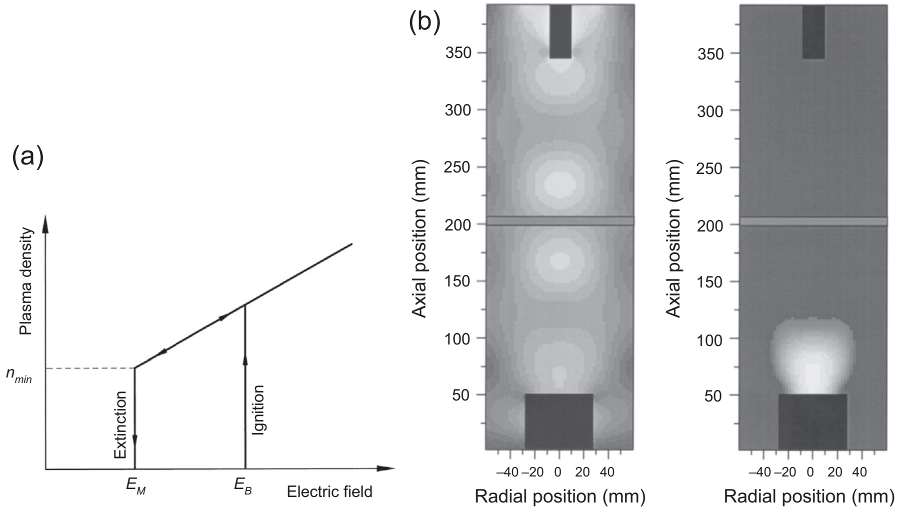

**Figure 10.10** (a) Ad hoc assumption of an example of phenomenological model, (b) examples of the calculated results for AX5200 type reactor; local field strength (left) and electro number density (right) [56,57,63].

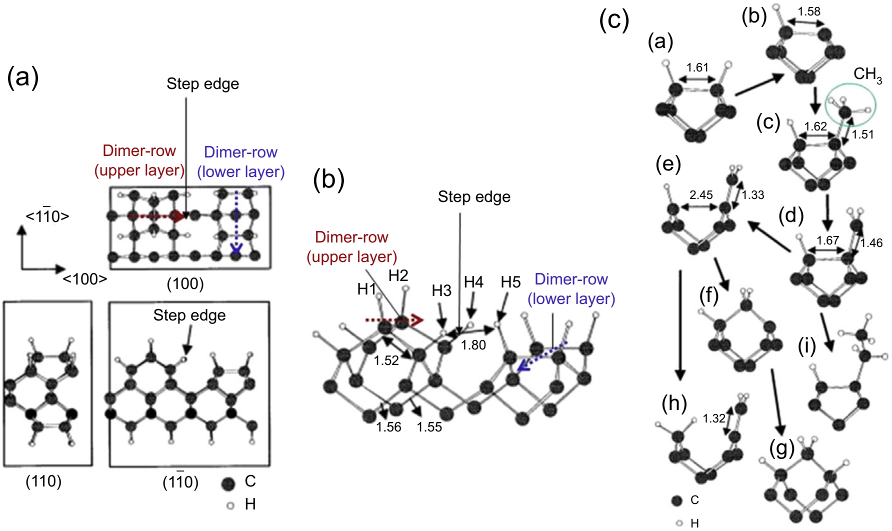

**Figure 10.11** (a) Model cluster to conduct DFT calculation, (b) stabilized structure of the cluster, (c) possible procedure of growth [85].

There are several possible species as precursors of diamond growth, but they have not been studied except for the methyl radical. Classical molecular dynamics simulation requires relatively small computational resources compared with the DFT calculations. Thus one may be able, for example, to calculate sticking coefficients of the radicals on to the diamond surfaces. Some results [95,96] show sticking coefficients of the hydrocarbon radicals on to {100} and {111} surfaces. As mentioned for bulk plasma simulation, $CH_3$ is one of the major radicals generated in the plasma phase, but its reactivity is relatively low. Actually, along with the increased number of lone-pair electrons, atomic carbon has almost 10 times higher sticking coefficients than $CH_3$ [95,96]. This result may arouse interest in which species are the most important precursors as a contributor for growth. Based on numerical simulation, concentration of carbon is almost 10 times lower than that of $CH_3$ [76,97]. In addition, horizontal distribution of $CH_3$ cannot explain the horizontal distribution, i.e., nonuniformity of the growth rate [79,100−102]. If one calculates the growth rate distribution based on the radical distribution, there may be a concave profile of the growth rate owing to the concave profile of $CH_3$ in the horizontal direction, while actually obtained growth rate distribution has a convex profile. In this respect, understanding of the growth mechanism is still not perfect. Especially, it is hard to find a model to predict uniformity of growth, which is one of the most important purposes of the modeling. As mentioned above, hydrocarbon radicals with lone-pair electrons and therefore reactivity rather higher than that of $CH_3$ may have key roles to play in this matter.

Nitrogen in the system has a remarkable effect on the growth. This has also been studied by atomic-scale simulation and several models have been proposed [90−93]. One may predict possible sites and bonding structure of the doped species. For example, it was shown that phosphorus is likely to generate a P-V structure rather than its substitution doped state [88]. Because P-V structures cause self-compensation, it was proposed that phosphorus should be doped with a rich hydrogen mix during growth. In addition to the p-type and n-type dopants, B and P respectively, which are presently widely adopted species, the possibilities of sulfur and its hydrogen complex were studied [89].

## 10.5 Issues in large-size wafer production

One of the difficult issues in diamond technology is to manufacture large-size wafers, due to their hardness. As mentioned, compared with the HPHT method, the deposition area can be enlarged relatively easily using CVD methods. However, the problem of enlarging the seed crystal is not so easy to resolve. The size of commercialized wafers is still several millimeters; typically 2–3 mm at present. Several approaches have been reported, as summarized in Table 10.2. The $\alpha$ parameter control is the optimization of the growth condition which allows enlargement of the top surface of the substrate during growth [66,69]. This, however, does not produce a higher growth rate, because growth rate enhancement in the <100> direction gives shrinking of the top surface, as mentioned [103]. Impurity introduction cannot be used to avoid this, so growth may have to continue for an extremely long time. For example, if growth in the <100> direction in the order of 1 μm/h is realized, 1 mm enlargement requires at least 1000 h of growth. In addition, growth in other directions requires even longer times. It is still not easy to avoid non-epitaxial growth and/or polycrystalline growth for such long times. To date, inch-size wafers have not been demonstrated by this method, and research has been directed toward hetero-epitaxial growth on foreign substrates, for example Si, Ir, MgO, SiC, and so on [104–108].

Recently Augsburg University demonstrated a hetero-epitaxial diamond wafer of almost 4 inch diameter [108], where substrates with yttria-stabilized zirconia coating are adopted. Although the dislocation density, $\approx 4 \times 10^{7}\ \mathrm{cm}^{-2}$, is still much higher than in monocrystalline diamond, $10^{4-6}\ \mathrm{cm}^{-2}$, this method could be used in particular applications.

**Table 10.2** **Approaches to enlarge seed crystals of diamond**

| Method | $\alpha$ parameter control | Hetero-epitaxial growth | Three-dimensional growth | Tiling |
|---|---|---|---|---|
| Quality | ◎ | ▲ | ○ | ○ |
| Speed | × | ○ | ◎ | ◎ |
| Institute | SEI<br>CNRS | Aoyama-gakuin University<br>Ausburg University | AIST<br>E6 | SEI, AIST<br>CNRS, NRL, MIT |

*AIST*, National Institute of Advanced Industrial Science and Technology, Japan; *CNRS*, National Center for Scientific Research, France; *MIT*, Massachusetts Institute of Technology, USA; *NRI*, Naval Research Laboratory; *SEI*, Sumitomo Electric Industry, Japan.

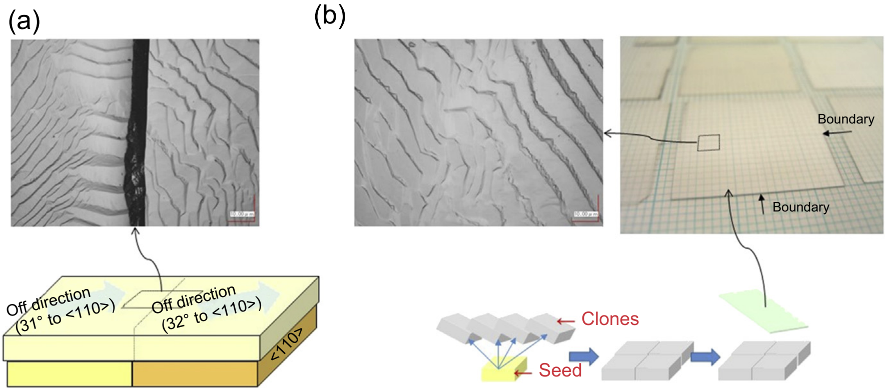

**Figure 10.12** Comparison between (a) conventional and (b) recently proposed tiling techniques ([50] and references therein).

Another possible method is the so-called three-dimensional growth. Because the diamond has a cubic structure, the growth surface (001) is in principle identical on all side surfaces, for example (010). Therefore, after growth in the [001] direction, one may grow diamond in the [010] direction. If one repeats such growth for the family of <001> directions, the seed crystal can be enlarged [103,109]. To date, a half-inch-size wafer has been realized by using this technique.

Tiling is more efficient way to obtain large-size wafers. Its underlying idea is that of connecting many seed crystals ([50] and references therein). While it is expected that many dislocations will form at the boundaries, one could fabricate devices not on but between the boundaries. A major issue of this approach is the difficulty in merging seeds of sufficient quality. Even with substrates with similar crystal properties, such as mismatching in off-angles and off-directions around 1°, one would have cracking and pinholes at the grain boundaries, as shown in Fig. 10.12(a) [50,70]. This problem was solved by the use of "clone" substrates, which are freestanding wafers made from one identical seed crystal [50,110]. In the case of Fig. 10.12(b), for example, one may prepare four clone substrates from one seed crystal. These are then connected with each other by overgrowing a CVD layer on them. The overgrown layer could be separated from the tiled cones by using the techniques described in the following section. As shown in Fig. 10.12(b), the morphology on the boundary is relatively smooth and almost invisible. One may use this tiled-clone substrate as a seed substrate and make copies [50,111,112]. The quality is sufficient to prepare freestanding wafers from these wafers. A 2-inch wafer was demonstrated by using this technique [110].

## 10.6 Doping

A bipolar transistor made of a natural p-type diamond was reported by Prins at the beginning of the 1980s [113]. In this case, the n-type region was prepared by implantation of carbon ions. A B-doped artificial diamond made by the HPHT method is already commercially available. However, as mentioned above, this method has practical limitations in the substrate size, and therefore techniques to prepare artificial p-type diamond under low pressure have been studied. One way is ion implantation of boron, where ion implantations with high substrate temperature and high energy (MeV) were reported [114–117]. To prepare p-type film and even freestanding wafers, the CVD method with boron doping has been studied [117–123], in which a B-containing impurity, such as $B_2H_6$ or $(CH_3)_3B$, is introduced into the source gas mixture forepitaxial growth. The highest level of mobility, around 1800 $cm^2/Vs$, was reported with a doping level of $2 \times 10^{14}\ cm^{-3}$ [118,121]. Soot formation is known to be a problem in preparing p-type layers with a high doping level to obtain low resistivity using MWPCVD. This limits growth itself, and possibly becomes an origin of nonepitaxial components. HF-CVD [122] could avoid this problem even with a high doping level: using this method, resistivity of 1 mΩcm was realized with a doping level of $1 \times 10^{21}\ cm^{-3}$.

Diamond with n-type conductivity has not been found in nature. At present, phosphorus is considered to be a candidate impurity to realize p-type diamond: phosphorus doping into the diamond could be realized by MWPCVD [124–126]. In this case, $PH_3$ is introduced into the source gas mixture for epitaxial growth. In an early report [124], a <111>-oriented substrate was utilized. Because it is not easy to prepare <111>-oriented substrates owing to difficulties in growing and processing (polishing) in this orientation, p-type films on the <100>-oriented substrate are desirable. It is still not easy to obtain <111>-oriented substrates rather than <100>-oriented substrates owing to the difficulty of preparation. Kato tried to obtain p-type layers on <100>-oriented substrates with a relatively high concentration of P in the gas phase [126]. The highest mobility reported was 570 $cm^2/Vs$ with $5 \times 10^{17}\ cm^{-3}$, which are still lower than those reported in the p-type diamond.

## 10.7 Processing techniques

Diamond is the hardest material in resisting static pressure, but features cleavage especially in the <111> direction. In spite of this, mechanical polishing is still used to planarize and polish substrate surfaces [127–129]. The typical mechanical polishing process, the so-called skife polishing, consists in loading the diamond substrate on a rotating iron plate on which diamond particles are dispersed. In addition to the possibility of cleavage during polishing, the major issue in mechanical polishing is damage beneath the polished surface [130,131]; one may have unknown defects center after the polishing, which can be confirmed by comparison of the luminescence profiles before and after polishing [131]. It is known that such subsurface damage enhances generation of dislocation from the interfaces [132]. Several techniques have been proposed to enhance polishing efficiency and accuracy with reduced damage, such as use of polishing plates with elevated temperature [133], silica-based polishing particles [134], chemical assistance [135], and ultraviolet assistance [136,137]. The finest processing is dressed photon-assisted surface treatment, which can clear away atomic-level bumps on the surface [138]. To planarize the as-grown surface, one may utilize plasma and/or ion beam etching [139,140]. Usually the etching rate is very low; several micrometers per hour or less. Ni-based processing can be used to achieve an efficient etching rate [105,141]. Carbon atoms diffuse into Ni, so one may coat the diamond surface and put it in an atmosphere where carbon atoms are evaluated. Then the top surface is etched by removing the diffused carbon atoms throughout the Ni layer with ambient hydrogen and hydroxyl radicals. Because this process can be conducted at atmospheric pressure, the etching rate is much higher than processes using plasmas; for example, 3 μm/min.

While other semiconductor materials are cut by diamond-wire sawing, it is not considered appropriate to slice diamond wafers from the seed crystals. Laser cutting is one of the common ways to prepare freestanding plates from the seed substrate. But this technique creates significant waste due to focusing the laser: the laser emitted from the source is focused on the processing point, which requires larger cutting loss for larger wafers. Laser cutting with a water-jet guide can avoid this drawback [142]. One can prepare freestanding wafers by using high-speed ion implantation [109,143−146]. Carbon atoms accelerated with very high potential, e.g., 1 MeV, are injected on to the top surface of the seed substrate. Then the graphitic layer is generated *beneath* the top surface, whereby its depth is determined by the injection energy at around 1−2 μm. This graphitic layer can be selectively etched to obtain the freestanding wafer. The waste of the seed substrate is only the implantation depth, and much smaller than using other methods. Another benefit of this technique is that the cryptographic characteristics are mirrored to the prepared freestanding wafers. This technique is utilized to obtain clone wafers for fabrication of inch-sized "tiled clones" [111].

## 10.8 New trends and future developments in the growth technique and applications

The current growth technique using plasma CVD is not greatly different with respect to those adopted decades ago. To enhance growth efficiency without increasing gas pressure and lowering microwave frequency, several trials have been proposed. For example, Ar addition is known to increase the growth rate [147,148]. The mechanism, however, is considered to be different from that of nitrogen. The thermal conductivity of Ar is almost 10 times lower than that of hydrogen. This reduces power dissipation from the discharge region to the outside, which results in increased gas temperature for a fixed imposed power. On the other hand, pulse mode discharge is also known to enhance the growth rate without scarifying the deposition area [149]. This technique enhances electron density by peak power above the average. This gives some reduction of the gas temperature without scarifying the growth rate and area. In addition to such trials optimizing the processing parameters, optimization of the structure of the apparatus has been proposed [150−152]. Most techniques have their origins in previous proposals [56−64]. Structures or concepts which give much higher power efficiency have not yet been proposed.

Among the recent applications of diamond, use of Nitrogen-Vacanvy (NV) center has become an hot topic [153−158]. This is because this defect center can maintain quantum information for a relatively long time even at room temperature [153]. In addition to the application to the quantum computing, several types of sensors with wide ranges of resolutions and sensitivity have been proposed [156−158].

## References

[1] S. Koizumi, C.E. Nebel, M. Nesladek (Eds.), Physics and Applications of CVD Daimond, Wiley-VCH Verlag GmbH & Co. KGaA, Weinheim, 2008.
[2] (Supervised by N. Fujimori, S. Shikata), Frontier of Diamond for Electronics Applications, CMC Publishing Co., Ltd., Tokyo, 2008 (in Japanese).
[3] M. Yoshikawa, K. Suzuki, N. Ohtake, S. Ohta, R. MUkai (Eds.), Comprehensive Bibliography of Diamond Technology, NGT Ltd., Tokyo, 2007 (in Japanese).
[4] Diamond, Industrial D.W. Olson, Minerals Yearbook, U.S. Geological Survey, 2012.
[5] Diamond Materials for Semiconductor Applications report, The Diamond Materials Market for Semiconductor Devices Will Surpass $43M, November 13, 2013. Milan Rosina, Yole Développement's.
[6] K. Hirama, Y. Taniyasu, M. Kasu, Appl. Phys. Lett. 98 (2011) 162112.
[7] K. Sakamoto, A. Kasugai, M. Tsuneoka, et al., Rev. Sci. Instrum. 70 (1999) 208.
[8] In the EU the Green Diamond project was started in 2010, with 13 universities and institutes participating. In the United States the ARPA-E project started in 2015 in Arizona State University and Michigan State University. In Japan, SIP (Cross-ministerial Strategic Innovation Promotion Program) was started in 2014.
[9] K. Kodama, T. Funaki, H. Umezawa, et al., IEICE Electron. Express 7 (2010) 1246.
[10] H. Umezawa, S. Shikata, T. Funaki, Appl. Phys. Express 6 (2013) 011302.
[11] S. Nicley, S. Zajac, R. Rechenberg, et al., Phys. Status Solidi A 212 (2015) 2410.
[12] A. Aleksov, M. Kubovic, N. Kaeb, et al., Diam. Relat. Mater. 12 (2003) 391.
[13] H. Kawarada, H. Tsuboi, T. Naruo, et al., Appl. Phys. Lett. 105 (2014) 013510.
[14] T. Iwasaki1, Y. Hoshino1, K. Tsuzuki, et al., Appl. Phys. Express 5 (2012) 091301.
[15] H. Umezawa, T. Matsumoto, S. Shikata, IEEE Electron Device Lett. 35 (2014) 1112.
[16] M. Dutta, F.A.M. Koeck, Wenwen Li, et al., IEEE Electron Device Lett. 38 (2017) 600.
[17] M. Suzuki, T. Sakai, T. Makino, et al., Phys. Status Solidi A 210 (2013) 2031.
[18] K. Matsumoto, H. Kato, K. Ogura, et al., Sci. Rep. 6 (2016) 31585.
[19] Sumitomo Electric Industries, Ltd., October 25, 2017. http://www.sumitool.com/en/products/diamond-cbn/.
[20] New Diamond Technology, October 25, 2017. http://ndtcompany.com/.
[21] Element Six, October 25, 2017. https://www.e6.com/en/Home.
[22] SCIO Diamond, October 25, 2017. http://sciodiamond.com/diamonds-for-industry/.
[23] IIa Technology, October 25, 2017. http://2atechnologies.com/.
[24] EDP Corp, October 26, 2017. http://www.d-edp.jp/en/.
[25] F.P. Bundy, H.T. Hall, H.M. Strong, et al., Nature 4471 (1955) 51.
[26] B. Deljanin, M. Alessandri, A. Peretti, et al., Contrib. Gemol. 15 (2015) 1.
[27] H. Sumiya, N. Toda, Y. Nishibayashi, et al., J. Cryst. Growth 178 (1997) 485.
[28] A. Katrusha, in: Invited Talk in 28th International Conference on Diamond and Carbon Materials, Gothenburg, Seden, September 6, 2017, 2017.
[29] M. Kamo, Y. Sato, S. Matsumoto, et al., J. Cryst. Growth 62 (1983) 642.
[30] B.J. Garrison, E.J. Dawnkaski, D. Srivastava, Science 255 (1992) 835.
[31] P.W. May, Y.A. Mankelevich, J. Phys. Chem. C 112 (2008) 12432.

[32] T. Tsuno, T. Imai, Y. Nishibayashi, et al., Jpn. J. Appl. Phys. 30 (1991) 1063.
[33] S. Matsumoto, Y. Sato, M. Kamo, et al., Jpn. J. Appl. Phys. 21 (1982) L183.
[34] K.-W. Chae, Y.-J. Baika, J.-K. Park, et al., Diam. Relat. Mater. 19 (2010) 1168.
[35] F.X. Lu, W.Z. Tang, T.B. Huanget, et al., Diam. Relat. Mater. 10 (2001) 1551.
[36] M. Kohzaki, K. Higuchi, S. Noda, et al., Electronic Journal - R&D Review of Toyota CRDL 29, 1994, p. 61 (in Japanese).
[37] Y. Haruta, K. Fujimoto, S. Horita, et al., J. Phys. Conf. Ser. 441 (2013) 012017.
[38] A.L. Vikharev, A.M. Gorbachev, A.V. Kozlov, et al., Diam. Relat. Mater. 17 (2008) 1055.
[39] M. Murayama, S. Kojima, K. Uchida, J. Appl. Phys. 69 (1989) 7924.
[40] T. Teraji, J. Appl. Phys. 118 (2015) 115304.
[41] C.-S. Yan, Y.K. Vohra, H.-K. Mao, et al., Proc. Natl. Acad. Sci. U.S.A. 99 (2002) 12523.
[42] A. Chayahara, Y. Mokuno, Y. Horino, et al., Diam. Relat. Mater. 13 (2004) 1954.
[43] J. Achard, F. Silva, A. Tallaire, X. Bonnin, et al., J. Phys. D Appl. Phys. 40 (2007) 6175.
[44] P.K. Bachmann, D. Leers, H. Lydtin, Diam. Relat. Mater. 1 (1991) 12.
[45] G. Lombardi, K. Hassouni, G.-D. Stancu, et al., J. Appl. Phys. 98 (2005) 053303.
[46] S. Ohmagari, H. Yamada, H. Umezawa, et al., Diam. Relat. Mater. 48 (2014) 19 and references therein.
[47] Q. Liang, C.Y. Chin, J. Lai, et al., Appl. Phys. Lett. 94 (2009) 024103.
[48] J. Lu, Y. Gu, T.A. Grotjohn, et al., Diam. Relat. Mater. 37 (2013) 17.
[49] Y. Mokuno, A. Chayahara, H. Yamada, Diam. Relat. Mater. 17 (2008) 415.
[50] H. Yamada, A. Chayahara, Y. Mokuno, et al., Appl. Phys. Express 3 (2010) 051301.
[51] N. Derkaoui, C. Rond, K. Hassouni, et al., J. Appl. Phys. 115 (2014) 233301.
[52] H. Watanabe, H. Kume, N. Mizuochi, et al., Diam. Relat. Mater. 15 (2006) 554.
[53] Y. Matsui, A. Yuuki, M. Sahara, et al., Jpn. J. Appl. Phys. 28 (1989) 1718.
[54] Y. Ando, Y. Yokota, T. Tachibana, et al., Diam. Relat. Mater. 11 (2002) 596.
[55] J.W. Zimmer, G. Chandler, T. Sharda, Thin Solid Films 516 (2008) 15.
[56] E. Sevillano, B. Williams, Diam. Films Technol. 8 (1998) 73.
[57] Seki Diamond Systems, October 28, 2017. http://sekidiamond.com/.
[58] Diamond Materials, October 28, 2017. http://www.diamond-materials.com/EN/company/deposition.htm.
[59] PLASSYS, October 28, 2017. https://plassys.com/diamond-coating/.
[60] Microwave Enterprises, October 28, 2017. http://www.mwe-ltd.com/cvd-products.asp?partno=dt%201800.
[61] US patent number 5501740 A.
[62] F. Silva, K. Hassouni, X. Bonnin, et al., J. Phys. Condens. Matter 21 (2009) 364202 and references therein.
[63] M. Füner, C. Wild, P. Koidl, Surf. Coat. Technol. 116−119 (1999) 853.
[64] J. Asmussen, T.A. Grotjohn, T. Schuelke, et al., Appl. Phys. Lett. 93 (2008) 031502.
[65] H. Yamada, A. Chayahara, Y. Mokuno, J. Appl. Phys. 101 (2007) 063302.
[66] C. Wild, P. Koidl, W. Müller-Sebert, et al., Diam. Relat. Mater. 2 (1993) 158.
[67] F. Silva, J. Achard, X. Bonnin, et al., Diam. Relat. Mater. 17 (2008) 1067.
[68] A. Gicquel, F. Silva, K. Hassouni, J. Electrochem. Soc. 147 (2000) 2218.
[69] T. Teraji, T. Ito, J. Cryst. Growth 271 (2004) 409.
[70] A. Tarraire, J. Achard, F. Silva, et al., Compt. Rendus Phys. 14 (2013) 169.
[71] H. Yamada, A. Chayahara, Y. Mokuno, et al., Jpn. J. Appl. Phys. 50 (2011) 01AB02 and references therein.
[72] J.C. Richley, M.W. Kelly, M.N.R. Ashfold, J. Phys. Chem. A 116 (2002) 9047.
[73] J. Ma, M.N.R. Ashfold, Y.A. Mankelevich, J. Appl. Phys. 105 (2009) 043302.

[74] S. Hamann, C.R. Rond, A.V. Pipa, et al., Plasma Sources Sci. Technol. 23 (2014) 045015.
[75] G. Shivkumar, S.S. Tholeti, M.A. Alrefae, et al., J. Appl. Phys. 119 (2016) 113301.
[76] G. Lombardi, H. Hassouni, F. Bénédic, et al., J. Appl. Phys. 96 (2004) 6739.
[77] H. Hassouni, T.A. Grotjohn, A. Gicquel, J. Appl. Phys. 86 (1999) 134.
[78] J. Ma, J.C. Richley, M.N.R. Ashfold, et al., J. Appl. Phys. 104 (2008) 103305.
[79] Y. Mankelevich, P.W. May, Diam. Relat. Mater. 17 (2008) 1021.
[80] E. Hyman, K. Tsang, D. Drobot, J. Vac. Sci. Technol. A 12 (1994) 1474.
[81] E. Hyman, K. Tsang, I. Lottati, et al., Surf. Coat. Technol. 49 (1991) 387.
[82] V.A. Koldanov, A.M. Gobachev, A.L. Vikharev, et al., Plasma Phys. Rep. 31 (2005) 1038.
[83] C. Rond, R. Salem, S. Hamann, et al., Plasma Sources Sci. Technol. 25 (2016) 025016.
[84] Y. Mankelevich, M.N.R. Ashfold, J. Ma, J. Appl. Phys. 104 (2008) 113304.
[85] H. Tamura, H. Zhou, Y. Hirano, et al., Phys. Rev. B 62 (2000) 16995.
[86] A. Cheesman, J.N. Harvey, M.N.R. Ashfold, J. Phys. Chem. A 112 (2008) 11436.
[87] D. Petrini, K. Larsson, J. Phys. Chem. C 112 (2008) 14367.
[88] T. Miyazaki, S. Ymasaki, Phys. B 376−377 (2006) 304.
[89] T. Miyazaki, H. Okushi, T. Uda, et al., Appl. Phys. Lett. 78 (2001) 3977.
[90] T.V. Regemorter, K. Larssson, Diam. Relat. Mater. 18 (2009) 1152.
[91] Z.M. Shah, A. Mainwood, Diam. Relat. Mater. 17 (2008) 1307.
[92] T. Frauenheim, G. Jungnickel, P. Sitch, et al., Diam. Relat. Mater. 7 (1998) 348.
[93] Z. Yiming, F. Larsson, K. Larsson, Theor. Chem. Acc. 133 (2014) 1432.
[94] S. Skokov, C.S. Carmer, B. Weiner, et al., Phys. Rev. B 49 (1994) 5662.
[95] M. Eckert, E. Neytz, A. Bogaerts, J. Phys. D Appl. Phys. 41 (2008) 032006.
[96] H. Yamada, A. Chayahara, Y. Mokouno, et al., Diam. Relat. Mater. 15 (2006) 522.
[97] H. Yamada, Jpn. J. Appl. Phys. 51 (2012) 090105.
[98] P. Bou, J.C. Boetner, L. Vandenbulcke, Jpn. J. Appl. Phys. 31 (1992) 1505.
[99] B. Shokri, M. Yaghmaee, A. Sarani, Plasma Process. Polym. 6 (2009) S450.
[100] H. Yamada, A. Chayahara, S. Ohmagari, et al., Diam. Relat. Mater. 63 (2016) 17.
[101] D.G. Goodwin, J. Appl. Phys. 74 (1993) 6888.
[102] Y.A. Mankelevich, A.T. Rakhimov, N.V. Suetin, Diam. Relat. Mater. 5 (1996) 888.
[103] Y. Mokuno, A. Chayahara, Y. Soda, et al., Diam. Relat. Mater. 15 (2006) 455.
[104] T. Aoyama, N. Amano, T. Goto, et al., Diam. Relat. Mater. 16 (2007) 594.
[105] H. Aida, S.-W. Kim, K. Ikejiri, et al., Diam. Relat. Mater. 75 (2017) 34.
[106] J. Yaita, T. Iwasaki, M. Natal, et al., Jpn. J. Appl. Phys. 54 (2015) 04DH13.
[107] M. Schreck, M. Mayr, O. Klein, et al., Phys. Status Solidi A 213 (2016) 2028.
[108] M. Schreck, S. Gsell, R. Brescia, et al., Sci. Rep. 7 (2017) 44462.
[109] Y. Mokuno, A. Chayahara, H. Yamada, et al., Diam. Relat. Mater. 18 (2009) 1258.
[110] H. Yamada, A. Chayahara, Y. Mokuno, et al., Appl. Phys. Lett. 104 (2014) 102110.
[111] H. Yamada, A. Chayahara, H. Umezawa, et al., Diam. Relat. Mater. 24 (2012) 29.
[112] H. Yamada, A. Chayahara, Y. Mokuno, et al., Diam. Relat. Mater. 33 (2013) 27.
[113] J.F. Prins, Appl. Phys. Lett. 41 (1982) 950.
[114] T. Vogel, J. Meijer, A. Zaitsev, Diam. Relat. Mater. 13 (2004) 1822.
[115] N. Tsubouchi, M. Ogura, H. Kato, et al., Appl. Phys. Lett. 89 (2006) 012101.
[116] L.H. Willems van Beveren, R. Liu, H. Bowers, K. Ganesan, et al., J. Appl. Phys. 119 (2016) 223902.
[117] R. Kalish, Carbon 37 (1999) 781 and references therein.
[118] H. Yamanaka, H. Watanabe, S. Masai, et al., Jpn. J. Appl. Phys. 37 (1998) L1129.
[119] N. Tokuda, H. Umezawa, T. Saito, et al., Diam. Relat. Mater. 16 (2007) 767.
[120] R. Issaoui, J. Achard, A. Tallaire, et al., Appl. Phys. Lett. 100 (2012) 122109.

[121] J. Barjon, E. Chikoidze, F. Jomard, et al., Phys. Status Solidi A 209 (2012) 1750.
[122] S. Ohmagari, K. Srimongkon, H. Yamada, et al., Diam. Relat. Mater. 58 (2015) 110.
[123] A. Tallaire, A. Valentin, V. Mille, et al., Diam. Relat. Mater. 66 (2016) 61.
[124] S. Koizumi, M. Kamo, Y. Sato, et al., Appl. Phys. Lett. 71 (1997) 1065.
[125] M. Katagiri, J. Isoya, S. Koizumi, et al., Appl. Phys. Lett. 85 (2004) 6365.
[126] H. Kato, T. Makino, S. Yamasaki, et al., J. Phys. D Appl. Phys. 40 (2007) 6189.
[127] E.H. Kraus, C.B. Slawson, J. Mineral. Soc. Am. 24 (1939) 661.
[128] T. Schuelke, T.A. Grotjohn, Diam. Relat. Mater. 32 (2013) 17.
[129] L. Zhou, S.T. Huang, L.F. Xu, Int. J. Refract. Metals Hard Mater. 29 (2011) 698.
[130] D. Araujo, E. Bustarret, A. Tajani, et al., Phys. Status Solidi A 207 (2010) 2023.
[131] P.-N. Volpe, P. Muret, F. Omnes, et al., Diam. Relat. Mater. 18 (2009) 1205.
[132] I. Friel, S.L. Clewes, H.K. Dhilon, et al., Diam. Relat. Mater. 18 (2009) 808.
[133] G. Bussone, T.A. Lafford, F. Masiello, et al., Phys. Status Solidi A 208 (2011) 2612.
[134] E.L.H. Thomas, S. Mandal, E.B. Brousseau, et al., Sci. Technol. Adv. Mater. 15 (2014) 035013.
[135] A. Kubota, S. Nagase, M. Touge, Diam. Relat. Mater. 70 (2016) 39.
[136] J. Watanabe, M. Touge, T. Sakamoto, Diam. Relat. Mater. 39 (2013) 14.
[137] H. Kato, S. Umezawa, Shikata, et al., Appl. Phys. Express 6 (2013) 0225506.
[138] T. Yatsui, W. Nomura, M. Naruse, et al., J. Phys. D Appl. Phys. 45 (2012) 475302.
[139] J. Widiez, M. Rabrot, S. Saada, et al., Solid State Electron. 54 (2010) 158.
[140] Y. Ando, Y. Nishibayashi, A. Sawabe, Diam. Relat. Mater. 13 (2004) 633.
[141] K. Nakanishi, H. Kuroshima, T. Matsumoto, Diam. Relat. Mater. 68 (2016) 127.
[142] T. Ikeda, K. Ozawa, M. Kutsuna, et al., Water Jet Guid. Laser 47 (2003) 3.
[143] M. Marchywka, P.E. Pehrsson, D.J. Vestyck Jr., et al., Appl. Phys. Lett. 63 (1993) 3521.
[144] N.R. Parikh, J.D. Hunn, E. McGucken, et al., Appl. Phys. Lett. 61 (1992) 3124.
[145] Y. Tzeng, J. Wei, J.T. Woo, et al., Appl. Phys. Lett. 63 (1993) 2216.
[146] V.S. Bormashov, S.A. Terentiev, S.G. Buga, et al., Diam. Relat. Mater. 75 (2017) 78.
[147] A. Tallaire, C. Rond, F. Bénédic, et al., Phys. Status Solidi A 208 (2011) 2028.
[148] A.P. Bolshakov, V.G. Ralchenko, V.Y. Yurov, et al., Diam. Relat. Mater. 62 (2016) 49.
[149] H. Yamada, A. Chayahara, Y. Mokuno, Appl. Phys. Lett. 109 (2016) 092102 and references therein.
[150] E. Pleuler, C. Wild, M. Füner, P. Koidl, Diam. Relat. Mater. 11 (2002) 467.
[151] K. An, S.W. Yu, X.J. Li, et al., Vacuum 117 (2015) 112.
[152] H. Yamada, A. Chayahara, Y. Mokuno, et al., Diam. Relat. Mater. 18 (2009) 117.
[153] V.M. Acosta, E. Bauch, M.P. Ledbetter, et al., Phys. Rev. B 80 (2009) 115202.
[154] P.C. Mauer, G. Kucsko, C. Latta, et al., Science 336 (2012) 1283.
[155] R. Schirhagl, K. Chang, M. Loretz, et al., Annu. Rev. Phys. Chem. 65 (2014) 83.
[156] T. Iwasaki, W. Natuki, K. Tahara, et al., ACS Nano 11 (2017) 1238.
[157] D. Le Sage, K. Arai, D.R. Glenn, et al., Nature 496 (2013) 486.
[158] J.R. Maze, P.L. Stanwix, J.S. Hodges, et al., Nature 455 (2008) 644.

## Further Reading

[1] R. Blumenthal, S.F. Webb, J. Vac. Sci. Technol. B 24 (2006) 643.
[2] H. Yamada, Y. Mokuno, A. Chayahara, et al., Diam. Relat. Mater. 16 (2007) 576.

# Gallium nitride

# 11

*Siddha Pimputkar*
Lehigh University, Bethlehem, PA, United States

## 11.1 Overview of applications

Gallium nitride (GaN) is a wide bandgap semiconductor that was first synthesized using hydride vapor phase epitaxy (HVPE) in 1969 by Maruska and Tietjen [1]. They determined it to be a direct bandgap semiconductor with a bandgap of 3.4 eV. But only when suitable metalorganic chemical vapor deposition (MOCVD) equipment was developed for GaN in 1991 by Nakamura [2,3] did the material realize its true potential. The ability to grow high-quality GaN on large-area foreign substrates ultimately allowed determination of the fundamental mechanism of p-type doping of GaN [4,5] and its reproducible growth. By combining the buffer-layer technology developed by Akasaki and Amano [6] and Nakamura [3] with the idea of double heterostructures, the first bright blue light-emitting diode (LED) was demonstrated using GaN and its ternary alloy with indium, $In_xGa_{1-x}N$ [7]. Development of the blue laser rapidly followed [8], and commercialization of blue and white LEDs was started in 1996 by Nichia Corporation. For their important contributions the researchers Akasaki, Amano, and Nakamura were awarded the Nobel Prize in Physics in 2014 for "the invention of efficient blue light-emitting diodes which has enabled bright and energy-saving white light sources".

While enabling the white LED has been arguably the most significant contribution GaN has made to society to date, due to significant energy savings compared to other white light sources [9], numerous other applications exist or are being developed. Addition of indium (In) to GaN narrows the energy bandgap, resulting in longer wavelength light, while adding aluminum (Al) to GaN results in a widening of the bandgap. Both of these alloys form solid solutions enabling a variety of devices. Fig. 11.1 depicts the bandgap variation of the three ternary alloy systems (AlGaN, InGan, and AlInN) for this system as a function of lattice parameter and compared to the traditional III−V system. All three ternary alloys possess a wurtzite crystal structure (see Fig. 11.2 for unit cell), which is thermodynamically the most stable phase at ambient conditions.

Using appropriate alloying within the III-Nitrides family, it is possible to span the entire ultraviolet (UV) visible light spectrum. Ongoing research is focused on developing high-efficiency UV LEDs and solid-state lasers to enable efficient disinfection of surface, water, and air, in addition to providing the means to cure resins [11]. For longer-wavelength applications, development of high-efficiency blue, green, and yellow LEDs and lasers for integration in displays is of interest. Due to the polar nature of

**Single Crystals of Electronic Materials.** https://doi.org/10.1016/B978-0-08-102096-8.00011-2
Copyright © 2019 Elsevier Ltd. All rights reserved.

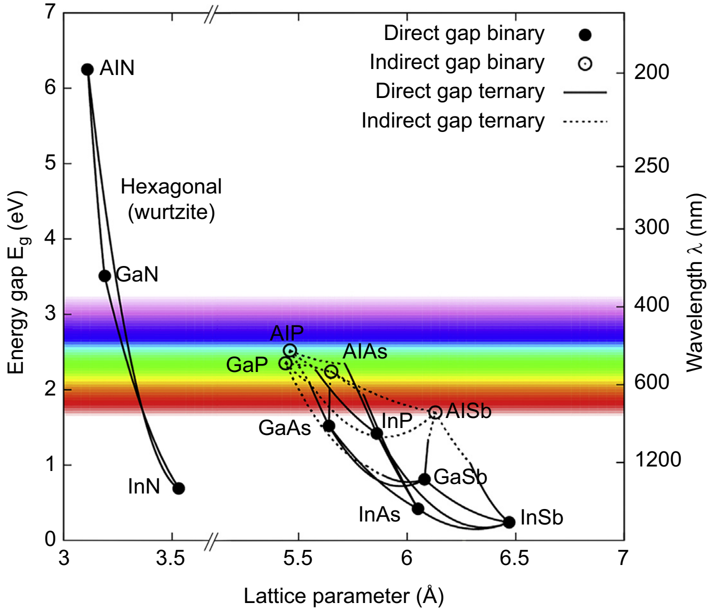

**Figure 11.1** Bandgap diagram of III nitrides and III−V with overlaid visible light colors versus their corresponding lattice parameters.
After M.A. Caro Bayo, Theory of Elasticity and Electric Polarization Effects in the Group-III Nitrides (PhD thesis), University College Cork, 2013.

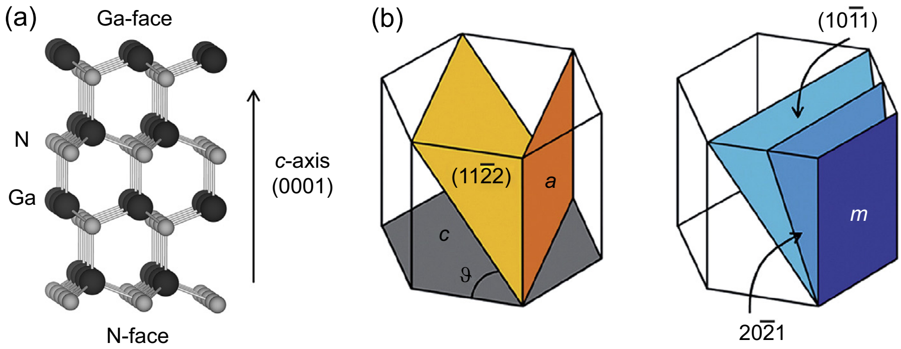

**Figure 11.2** (a) Ball-and-stick model of the wurtzite GaN crystal structure. Ga atoms are *larger darker spheres*, N atoms are *smaller lighter spheres*. The top crystal surface (0001) is referred to as the gallium face, while the (0001) is the nitrogen face. [15] (b) Schematic of conventional GaN unit cell with highlighted crystal planes showing the polar c-plane (gray), nonpolar a-plane and associated semipolar planes (orange) (left unit cell), and nonpolar m-plane and associated semipolar planes (blue) (right unit cell) [16].

wurtzite GaN and its alloys, it is further possible to develop emitters with 100% polarized light using nonpolar crystal orientations (e.g., m-plane) [12], potentially providing an efficient white light source for use with liquid crystal displays. Development of white LEDs and lasers permits efficient lighting of spaces, but also their integration in a wide variety of monitoring and communication equipment. For example, by modulating white light at a high frequency it is possible to use it as a wireless communication technology; this is known as Li-Fi or visible light communication [13,14].

Another major market for GaN devices is the power electronics sector (Fig. 11.3), in particular high-frequency and high-power transistors. GaN promises superior properties over silicon (Si) and silicon carbide (SiC), an indirect wide bandgap semiconductor. GaN and its alloys have a wide bandgap which leads to low intrinsic carrier concentrations, enabling high-temperature operations, attractive transport properties (high electron mobility of ~1300 $cm^2/V\,s$ and saturation velocity of ~$2.5 \times 10^7$ cm/s), a high critical breakdown electric field (~3.5 MV/cm, as compared to 0.3 MV/cm for Si), and high thermal conductivity. These properties permit the creation of smaller devices which consume less energy and can operate at higher frequencies [17]. Most GaN power electronic devices to date are oriented laterally, largely due to the lack of widely available large-area, high-quality bulk GaN substrates which would enable vertical device architectures. Vertical architectures are considered

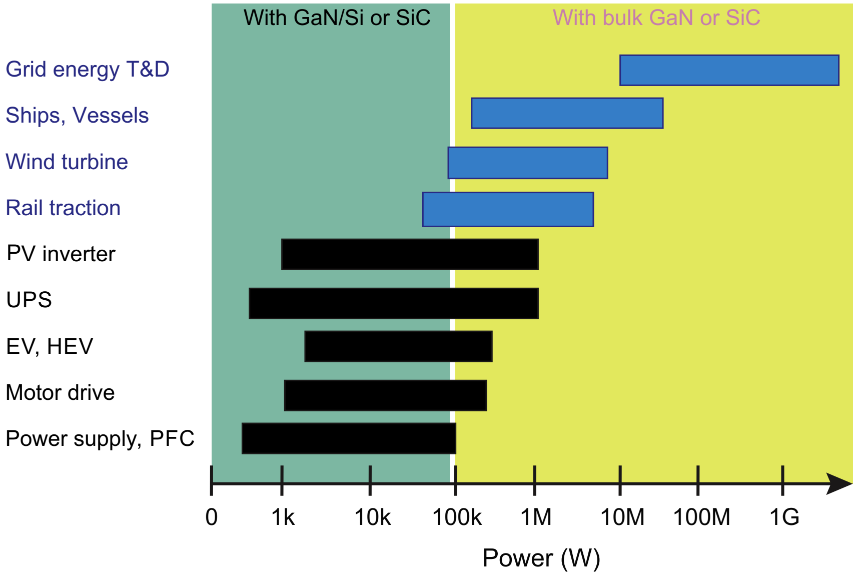

**Figure 11.3** Summary of potential power electronic markets for GaN. *EV/HEV*, electric and hybrid electric vehicle; *PFC*, power factor correction circuits; *PV*, photovoltaic; *T&D*, transmission and distribution; *UPS*, uninterruptible power supply.
Adapted from S. Chowdhury, U.K. Mishra, Lateral and vertical transistors using the AlGaN/GaN heterostructure, IEEE Trans. Electron Devices 60 (2013) 3060−3066, https://doi.org/10.1109/TED.2013.2277893.

superior to lateral devices owing to the ability to realize higher breakdown voltages by utilizing an arbitrarily thick electron drift layer, and are currently the norm for power applications operating at 600 V for Si and SiC devices.

A common need in lasers and power electronic devices is material with low concentrations of defects, in particular line defects ($< \sim 10^4\ \mathrm{cm}^{-2}$). Growth of GaN on foreign substrates (typically sapphire, Si, or SiC) leads to appreciable concentrations of the threading dislocations needed to accommodate the large lattice mismatch (16%, −17%, and 3.1% for GaN on sapphire, silicon, and silicon carbide, respectively). Typical concentrations range from $10^8$ to $10^{11}\ \mathrm{cm}^{-2}$. These dislocations are detrimental to device performance and lifetime, as they provide nonradiative recombination pathways and trap sites [19,20,21]. Growth of GaN on foreign substrates typically results in defective c-plane growth in which the polar axis is out of plane. To access nonpolar or semipolar orientations of GaN either to take advantage of different growth modes on these planes or to access intrinsic properties of GaN along nonpolar or semipolar orientations [15,22], it is necessary to grow on bulk GaN substrates along the desired orientation. Somewhat unexpectedly, high-brightness GaN-based LEDs can be created using heavily defective GaN materials grown on foreign substrates [23]. As such, the two main drivers for bulk GaN substrates today are the need for low dislocation concentration ($<10^4\ \mathrm{cm}^{-2}$) material enabling lattice-matched growth in arbitrary orientations for high-power and high-efficiency (opto-)electronic devices; and availability of large-area substrates to aid development of GaN-based power electronics. Of these two application areas, power electronics represents a significant untapped market with few alternatives to bulk GaN substrates, and as such will likely drive its development.

## 11.2 Single crystal growth technologies

GaN is not found in nature and is a purely man-made material. Due to its high covalency ($E_{\text{Ga-N bond}} \approx 9.12$ eV/atom), the decomposition pressure at the melting point is extremely high [24]. The melting temperature of GaN is currently thought to lie in the vicinity of $T_{\mathrm{melt}} \sim 4000$ K with an associated vapor pressure of $P_{\mathrm{melt}} \sim 12$ GPa [25]. For nitrogen pressures below $P_{\mathrm{melt}}$, GaN does not melt and yet can decompose into metallic gallium and nitrogen gas. At 1 atm nitrogen gas pressure, GaN is stable up to ~1200 K. Higher nitrogen pressures stabilize GaN to higher temperatures prior to decomposition [26]. Fig. 11.4(a) summarizes the current understanding of the decomposition curve of GaN, experimental data for the melting point of GaN, and the predicted melting temperature and associated pressure (see [25] for further details and discussion), while Fig. 11.4(b) provides a close-up of the lower temperature region for GaN decomposition. It is due to this fundamental behavior of GaN that standard techniques of bulk single crystal growth (such as the Bridgman, Czochralski, or Verneuil methods) cannot be readily applied to this material.

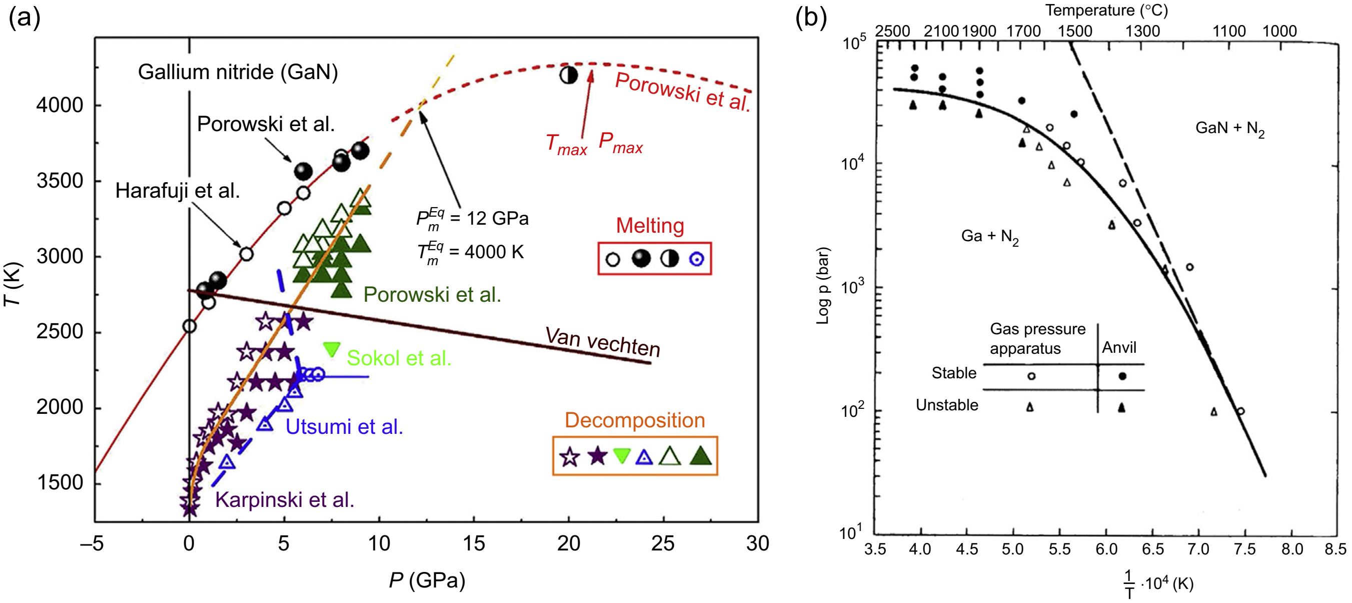

**Figure 11.4** (a) Pressure dependence of GaN melting and GaN P–T decomposition equilibrium curves [25] (references in figure: Utsumi et al. [27], van Vechten [24], Harafuji et al. [28], Karpinski et al. [26], Sokol et al. [29], and Porowski et al. [25]). (b) Equilibrium pressure of $N_2$ over GaN. *Dashed line* calculated from ideal gas [26].

Despite challenges related to the direct synthesis of solid GaN from molten GaN, a few methods have been developed which can grow bulk single crystal GaN under more moderate conditions.

- Vapor phase growth
  - HVPE
  - Hydride-free vapor phase epitaxy (HF-VPE)
- Flux growth
  - High-pressure nitrogen solution growth (HPNSG)
  - Sodium flux (Na flux)
  - Low-pressure solution growth
- Solution growth
  - Ammonothermal.

Vapor phase growth of GaN typically occurs at or below 1 atm pressure and temperatures up to ~1200 K using ammonia ($NH_3$) gas and gallium-containing compounds, such as gallium monochloride (GaCl) or gallium trichloride ($GaCl_3$) for HVPE growth. HF-VPE growth has also been explored for bulk growth of GaN. One method uses gallium oxide ($Ga_2O$) vapor as the gallium-containing compound [30,31], while another uses metallic gallium [32]. Both methods are still in the early stages of development and operate at similar, or slightly hotter ($T < 1600$ K), conditions to the HVPE method. A key advantage of the HF-VPE method is the lack of powder formation in the exhaust of the reactor upon cooling of the gases, which occurs in the HVPE method due to reactions between ammonia and hydrogen chloride resulting in condensation of solid ammonium chloride ($NH_4Cl$).

Flux growth of GaN utilizes a molten bath of flux material in which nitrogen gas dissolves. HPNSG utilizes a pure gallium melt in which nitrogen can dissolve and diffuse. Typical growth conditions are $T \approx 1800$ K and pressure of up to 2 GPa of nitrogen. Addition of sodium to the gallium melt, resulting in a Na–Ga melt, has been found to reduce both the required growth temperature and pressure while significantly enhancing the nitrogen solubility in the solution. Typical growth conditions are $T \approx 1100$ K and $P \approx 5$ MPa using nitrogen ($N_2$) gas. Addition of metals, such as Ge, Sn, Bi, Au, Ag, or mixtures thereof, to liquid Ga has led to low-pressure fluxes which have synthesized GaN if ammonia is used as the reactive nitrogen species. Typical growth temperatures for these systems lie at around 1100–1300 K, with ammonia-containing gas pressures of 1–2 atm.

The ammonothermal method for growth of GaN dissolves Ga into a supercritical ammonia solution containing additional mineralizers. Mineralizers act to enhance the solubility of Ga into the solution, which results in either a basic solution (utilizing alkali metals such as sodium or potassium as mineralizers) or and acidic solution (utilizing halogens such as fluorine and chlorine as mineralizers). To achieve appreciable solubility of GaN in solution and prevent decomposition of the solvent (ammonia), appreciable pressures (~100–300 MPa) are needed while maintaining elevated growth temperatures of ~800–1000 K.

Of all these techniques, the three major technologies that are being pursued on an industrial scale are the ammonothermal method, the Na-flux method, and HVPE growth of GaN [33]. The remainder of this chapter focuses on these three growth technologies. Additional information on these growth methods can be found in the literature for Na flux [34], ammonothermal [35,36], and HVPE [37,38].

# 11.3 Ammonothermal method

## 11.3.1 Fundamentals of the method

### 11.3.1.1 General

The ammonothermal method is a solvothermal bulk crystal growth technique which is analogous to the hydrothermal method used to grow single crystal quartz ($SiO_2$) on an industrial scale of ~3000 tons per year [39]. The ammonothermal system is well suited for growth of nitrides, as demonstrated by a wide variety of nitrides synthesized using this method [40]. For GaN growth the underlying process involves the dissolution of Ga (typically polycrystalline GaN or metallic Ga) into a supercritical ammonia solution, transport of the Ga-containing species to a different temperature zone, and its deposition on to a high-quality GaN seed crystal. The solubility of Ga is enhanced by adding additional materials, also known as mineralizers, to the solution, thereby forming higher concentrations of either amides $\left(NH_2^-\right)$ or ammoniums $\left(NH_4^+\right)$, resulting in basic or acidic chemistries respectively. Basic ammonothermal solutions are typically created using alkali metals, in particular sodium or potassium, and acidic ammonothermal solutions are created using halogens, typically fluorine and chlorine. Analysis of powders present in ammonothermal autoclaves postrun suggests Ga tends to form compounds with ammonia, such as $[Ga(NH_3)_{6-n}X_n]^{(3-n)+}$ ($n = 0, 1, 2, 4$; $X = F, Cl, Br, I$), for acidic solutions [41] and with amides, such as $[Ga(NH_2)_4]^-$, for basic solutions containing alkali metals [42,43].

### 11.3.1.2 Solubility

The solubility of Ga is dependent on the concentration of the mineralizer, the temperature, and the pressure of the solvent. Fig. 11.5(a) compares the solubility of GaN in supercritical basic and acidic ammonothermal environments as a function of temperature and, in the case of potassium amide ($KN_2$) mineralizer, pressure as well [44]. Generally, acidic ammonothermal solutions exhibit higher solubilities of Ga than basic ammonothermal conditions. Furthermore, acidic ammonothermal solutions exhibit normal solubility, although recent studies suggest that at higher temperatures the solubility begins to decrease with temperature, i.e., becomes it retrograde soluble [45,46]. Basic ammonothermal solutions exhibit retrograde solubility behavior, but a detailed study on the solubility of GaN in sodium containing supercritical ammonia solutions suggests minimal solubility changes as a function of temperature (see Fig. 11.4(b): orange round data points) [47]. Additional research is needed to understand comprehensively the solubility behavior of Ga

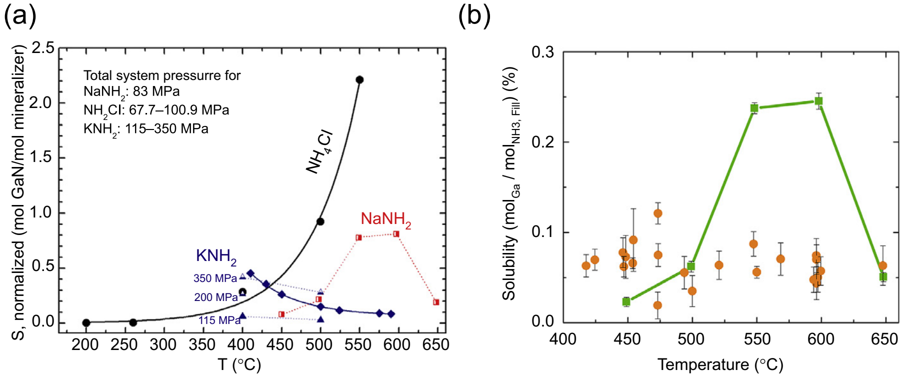

**Figure 11.5** (a) Comparision of solubility S of GaN under supercritical acidic and basic ammonothermal environments. (b) Comparision of two solubility studies for GaN in basic ammonothermal environments containing sodium. Orange round points are from a recent study [47]. Green square points are from [49].
(a) After D. Ehrentraut, T. Fukuda, Ammonothermal crystal growth of gallium nitride—a brief discussion of critical issues, J. Cryst. Growth. 312 (2010) 2514–2518, https://doi.org/10.1016/j.jcrysgro.2010.04.004.

in both acidic and basic ammonothermal systems. Novel in situ methods are being developed which will provide valuable insights [48].

### 11.3.1.3 Solvent

Supercritical ammonia is used as a solvent for Ga species and may also act as a nitrogen source. Ammonia readily decomposes at high temperature via the following reaction:

$$NH_3 \rightarrow 1/2\ N_2 + 3/2\ H_2$$

To achieve desirable solubilities, temperatures of >700 K are needed; and to prevent decomposition, appreciable pressures (>100 MPa) need to be maintained. Despite the important functions the solvent provides in growth, little is understood of its thermodynamic behavior or fluid properties at typical ammonothermal growth temperatures and pressures. Initial work has been performed on developing a new equation of state (EOS) which can be used to describe the individual gases ($N_2$, $H_2$, $NH_3$) at typical ammonothermal growth conditions ($T = 800-1000$ K, $P = 100-300$ MPa). Using this EOS, thermodynamic analysis permits determination of the equilibrium concentration of ammonia at these temperatures to within 1%–2% accuracy, as summarized in Fig. 11.6 [50]. While significant pressures are needed to prevent ammonia decomposition, appreciable concentrations can be retained for growth.

While it is encouraging that ammonia decomposition can be prevented at elevated temperatures and pressures, it is important to note that hydrogen diffusion through the pressure-retaining vessel can be appreciable if it is held at high temperature. This can lead to significant mass loss for small-scale pressure vessels (large surface-to-volume ratio). Hydrogen loss, in turn, results in continued decomposition

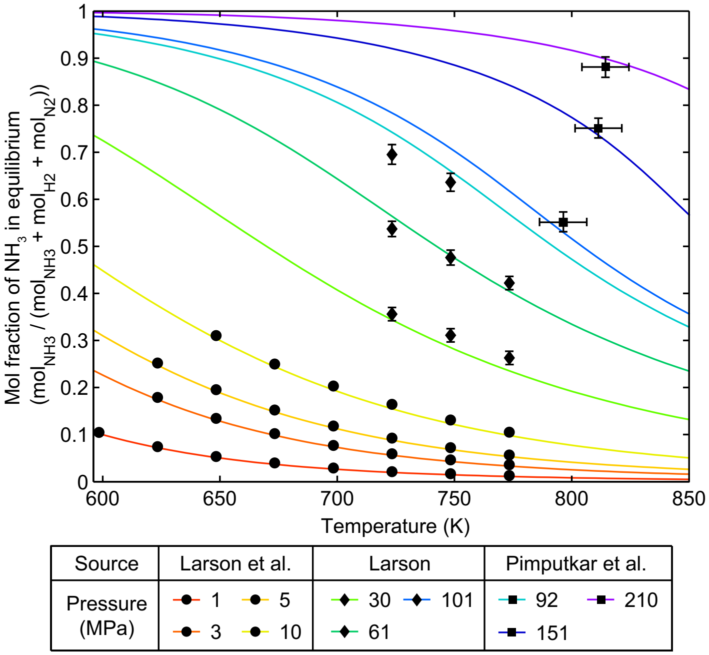

**Figure 11.6** Amount of ammonia decomposition at various temperatures and pressures expressed as mole fraction ammonia in the system. Points are experimentally measured points, while the lines represent the thermodynamically calculated equilibrium conditions.
After S. Pimputkar, S. Nakamura, Decomposition of supercritical ammonia and modeling of supercritical ammonia-nitrogen-hydrogen solutions with applicability towards ammonothermal conditions, J. Supercrit. Fluids 107 (2016) 17—30, https://doi.org/10.1016/j.supflu.2015.07.032.

of ammonia (via Le Chatelier's principle) until the pressure vessel is completely depleted of hydrogen and only contains nitrogen gas. It is possible to reduce significantly, if not prevent, hydrogen diffusion by using, for example, a silver liner or capsule [51].

### 11.3.1.4 Growth

Growth of crystals can be achieved by supersaturating the Ga-containing solution around one or more single crystal GaN seeds. Supersaturation can be achieved by changing the temperature of the solution toward a lower solubility region (see Fig. 11.5 and Fig. 11.7(b)). For basic ammonothermal solutions this is achieved by heating the solution (retrograde solubility), and for acidic solutions by lowering the temperature (normal solubility). The amount of supersaturation must be controlled. Large supersaturation will lead to spontaneous nucleation of GaN crystals on the internal surfaces of the autoclave and other components. These crystallites parasitically consume Ga from the solution, leading to a drop in the growth rate of the desired single crystal GaN boules.

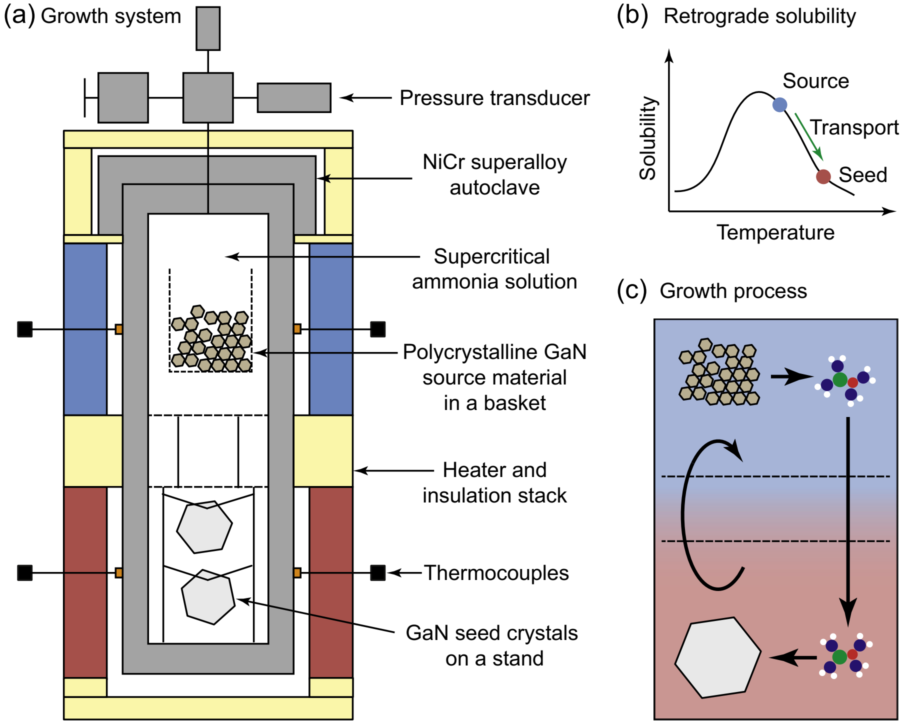
(a) Growth system
Pressure transducer
NiCr superalloy autoclave
Supercritical ammonia solution
Polycrystalline GaN source material in a basket
Heater and insulation stack
Thermocouples
GaN seed crystals on a stand
(b) Retrograde solubility
Solubility
Temperature
Source
Transport
Seed
(c) Growth process

**Figure 11.7** (a) Schematic of a typical externally heated autoclave used for ammonothermal growth of GaN. The depicted configuration is for basic ammonothermal growth utilizing retrograde solubility. For acidic ammonothermal growth the source and seed would be swapped, and for NiCr superalloy autoclaves a liner would be present. (b) Schematic solubility curve for retrograde solubility with indicated temperature choices for source and seed/growth zone. Mass transport occurs via fluid transport of dissolved species from the cold zone to the hotter zone. (c) Schematic of basic ammonothermal growth process entailing dissolution of GaN source material into solution as, for example, $Na[Ga(NH_2)_4]$, and transport through baffle plates to a higher temperature zone wherein the solution becomes supersaturated and GaN crystallizes on the provided GaN seed crystal. Buoyancy forces cause the hotter fluid to rise, leading to continuous mass transport from the source to the seed/growth zone [58].

To achieve continuous growth of single crystals, a Ga-containing source (typically polycrystalline GaN or metallic Ga) is placed in the higher solubility region. The higher temperature region is placed below the lower temperature region. For acidic growth this leads to the source material being placed below the GaN seeds, whereas for basic growth the opposite is the case. This configuration allows buoyancy forces to stir the solution naturally, causing continuous transport of Ga species from the source material to the seed crystals via movement of the solvent; see Fig. 11.7(b) and (c) for a schematic of this process for retrograde conditions.

This growth process has been implemented using two different system configurations, discussed below. Both systems permit the creation of a temperature gradient between two zones in an autoclave (source/seed) at elevated temperatures (>500°C) while retaining elevated pressures (>150 MPa) to prevent ammonia decomposition.

## 11.3.2 Growth systems

Irrespective of the implemented growth system, one common challenge exists for all ammonothermal methods. Ammonothermal solutions have the ability to dissolve metals beyond just Ga, and the high nitrogen activity leads to a strongly nitriding environment. As such, suitable materials need to be found which do not dissolve into the solution and are not negatively impacted by nitridation of their surfaces or subsurface layers. Generally speaking, basic ammonothermal chemistries are not exceptionally corrosive, but acidic ammonothermal solutions are. Corrosion studies have been performed to learn the feasibility of using a wide variety of engineering materials [52–55] or coatings [56] for acidic and basic solutions.

### 11.3.2.1 Externally heated autoclave

The traditional method for ammonothermal growth of GaN utilizes a standard autoclave design (Fig. 11.7(a)). The autoclave is externally heated using two or more heat sources (resistive heaters, gas flame, etc.). The upper heater zone is set to a lower temperature than the lower, leading to a temperature gradient within and along the autoclave. As the autoclave wall is hot and must retain the pressure, high-temperature, creep-resistant alloys need to be used. Nickel chromium (NiCr) superalloys, such as René 41 or Inconel 718 or 625, are a common choice, while TZM (titanium zirconium molybdenum, a molybdenum alloy) also shows great promise.

To control fluid motion properly between the upper and lower zones within the autoclave, baffle plates are used which have a fixed open-to-closed area. Proper design of these baffle plates leads to the maximum amount of fluid motion while retaining the temperature gradient and uniformity within the seed crystal zone.

While this growth system is relatively inexpensive, it has the drawback that advanced superalloys need to be used. The autoclave is ultimately limited in diameter by the largest size ingot available for the desired material, and the peak growth temperature is limited by creep. For Inconel 718, usable ingot diameters of at least 26 inches have been reported to date, while peak temperatures should be below ~650°C for safety reasons.

Use of this autoclave design for acidic ammonothermal growth of GaN requires the use of a precious metal liner if a NiCr superalloy autoclave is used. Platinum is commonly used. TZM autoclaves, on the other hand, do not require any liners, though they are still in the early stages of development [45]. Basic ammonothermal growth of GaN can be achieved in unlined NiCr superalloy autoclaves, though some transition metals dissolve into solution leading to impurities in the growing crystals. Silver or molybdenum capsules have been developed to prevent this from occurring [51,57].

### 11.3.2.2 Anvil-style pressure vessel

An alternative design of a growth system separates the pressure retention from the hermetically sealed volume containing the ammonia solution. This more sophisticated anvil-style pressure vessel builds on expertise gained in the high-pressure anvil systems used to grow diamond crystals. Adaption of such a system to the ammonothermal method permits growth temperatures of up to 1000°C [59] and pressures up to 2 GPa [60].

A schematic of this growth system is provided in Fig. 11.8. In general it follows the same setup as the traditional autoclave design, but it differs in using a hermetically sealable container which is ultimately in contact with ceramic blocks and transfers the pressure load to an external belt or other pressure-retaining mechanism. Use of ceramic blocks provides thermal insulation, thereby significantly reducing the temperature experienced by the external pressure-retaining material. As such, inexpensive and strong steels can be used.

This design the important advantage that it is relatively easy to scale to larger sizes and can operate at higher pressures (reduced ammonia decomposition) and temperatures (improved kinetics and solubility). A critical challenge with this design relates to the increased complexity and the need for tight tolerances of the various parts, along with the internal heater systems which are in close proximity to the hermetic container.

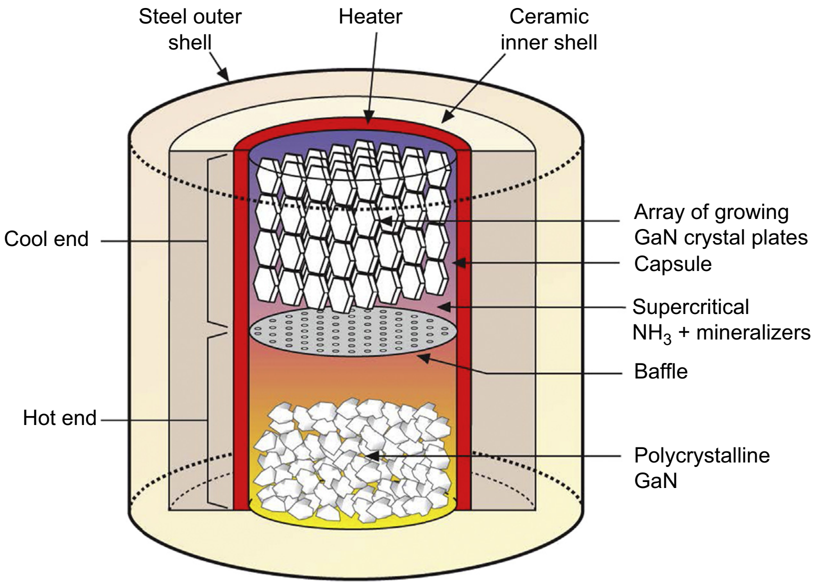

**Figure 11.8** Schematic of an internally heated high-pressure ammonothermal apparatus [59].

### 11.3.3 State-of-the-art crystals

The first reported growth of ammonothermal GaN occurred in 1995 [61]. Significant advances have led to demonstrations of thick 2-inch diameter boules for c-plane GaN using both the acidic [62] and basic [63] variants of this method, along with 1-inch [64] and 2-inch [65] m-plane boules using the basic and acidic methods, respectively. Semipolar orientations have also been demonstrated for basic ammonothermal GaN [66]. Ammono S.A. is currently the only commercial company selling ammonothermal GaN substrates. All bulk GaN boules are phase-pure wurtzite GaN. Fig. 11.9 summarizes a few bulk GaN boules grown using both the basic and acidic ammonothermal methods. GaN boules are typically terminated by (0001), $(000\bar{1})$, and $\{10\bar{1}0\}$ planes, while for acidic growth they may be terminated by $\{10\bar{1}\bar{1}\}$ planes instead of a large $(000\bar{1})$ plane.

Current ammonothermal boules typically have dislocation densities below $10^4\,\mathrm{cm}^{-2}$, with densities as low as $\sim 10^2\,\mathrm{cm}^{-2}$ being reported [67]. Synchrotron X-ray topography studies suggest that most of the threading dislocation defects are of a screw character [68]. Due to high concentrations of Ga vacancies, annealing of these high-quality crystals at high temperature can lead to formation of helical dislocations due to diffusion and interaction of these vacancies with the dislocations [69].

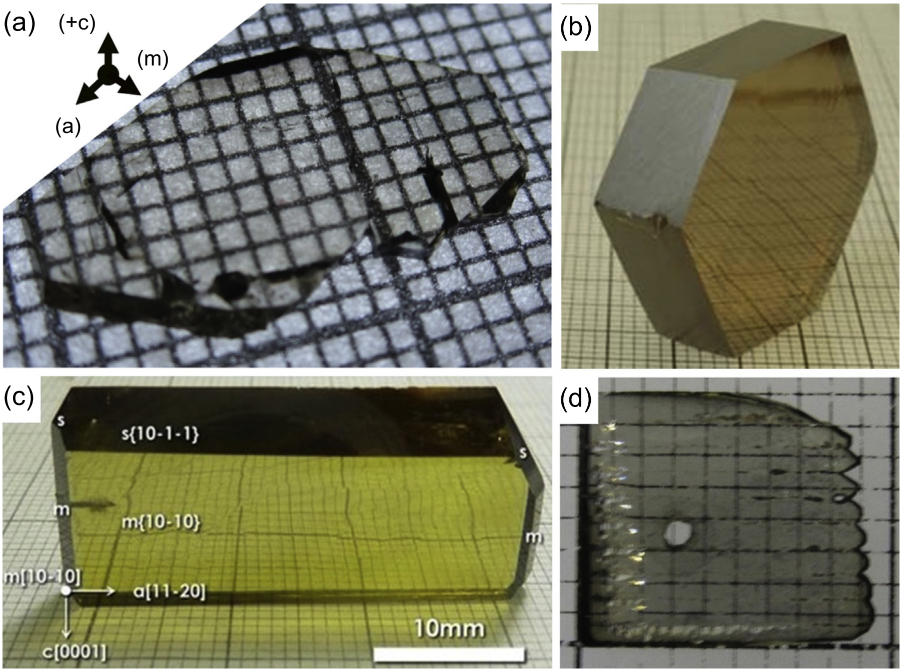

**Figure 11.9** Photographs of basic (a) and (b) and acidic (c) and (d) ammonothermal GaN crystals grown in (a) a silver capsule, (b) an unlined autoclave, (c) a lined Ni-based autoclave, and (d) an unlined TZM autoclave. All squares 1 × 1 mm. Further details are provided in [58].

The truly excellent crystal quality is also reflected in typical omega rocking curve (ω-XRC) full width at half maximum (FWHM) achieving 9–16 arcsecs for c-, a-, m-, and semipolar planes [67]. Lattice curvature for the c-plane has been reported to be >600 m [67], with the best crystals reporting >1 km [70]. This correlation can be explained given recent calculations relating threading dislocation concentrations and inclination with observed curvature in bulk GaN crystals [71].

## 11.3.4 Point defects

Visual inspection of GaN boules reveals coloration of the crystals, with basic ammonothermal crystals typically showing gray, yellow, or orange-brown coloration and acidic ammonothermal crystals being gray, yellow, or green. This coloration can be traced to point defects (impurities and Ga vacancies), while the graying of the crystal is due to phonon-assisted free carrier absorption and is present for all n-type doped GaN crystals regardless of growth method [72]. The green coloration of acidic crystals is not currently understood.

### 11.3.4.1 Impurities

Use of unlined NiCr superalloy autoclaves leads to incorporation of transition metals by dissolution of these elements from the autoclave walls. Common impurities for basic ammonothermal crystals include Fe and Mn, with concentrations typically in the low-$10^{17}$ to low-$10^{16}$ $cm^{-3}$ and low-$10^{18}$ to low-$10^{17}$ $cm^{-3}$, respectively. Ti, Co, Cr, and Ni are typically measured to be below the detection limit (DL) of SIMS (secondary ion mass spectrometry). Mn is thought to contribute to the distinct orange/brown coloration of basic ammonothermal crystals. Use of a silver or molybdenum capsule in NiCr superalloy autoclaves yields crystals with significantly improved purity, leading to a reduction of all transition metals below DL in most crystals.

Remaining impurities include O, H, Na, Al, Si, C, and Mg. Al, Si, and Mg are only found in basic ammonothermal crystals at levels below low-$10^{17}$ $cm^{-3}$. Their source is thought to be the source material used to grow those crystals (polycrystalline GaN wall deposits formed during HVPE growth of GaN) or the mineralizer material (sodium). Sodium is an impurity only found in basic ammonothermal crystals and is a direct result of using Na as a mineralizer material. Its incorporation is not yet understood, and large variations within a single boule have been found ($10^{16}$–$10^{19}$ $cm^{-3}$). Carbon is thought to be introduced via surface contamination, and as such improved cleaning processes should lead to its complete removal.

Hydrogen is a major impurity for both basic and acidic ammonothermal crystals and ranges between mid-$10^{17}$ and low-$10^{20}$ $cm^{-3}$. It is thought to be closely tied to the concentration of Ga vacancies ($V_{Ga}$) as they form the hydrogenated Ga vacancy complex $V_{Ga}$-$H_x$, where $x = 0, 1, 2, 3$. Reduction of these defects should lead to a reduction of H concentrations in the crystals. Hydrogen is not currently thought to impact negatively on use of these crystals as a substrate.

Oxygen contamination can be attributed to surface contamination of the various internal parts of the autoclave, along with bulk contamination of the source material.

Oxygen, which is an electron donor in GaN, is prevalent in the system and crystals typically contain low-$10^{19}$ $cm^{-3}$ of this impurity. If efforts are made to remove oxygen sources prior to a run, values as low as mid-$10^{17}$ $cm^{-3}$ have been reported. Oxygen getters have been explored to improve on the purity, though their effectiveness is currently not substantial.

Generally, oxygen negatively impacts observed crystal properties by increasing subbandgap optical absorption via phonon-assisted free carrier absorption [72], expands the lattice constant [73] leading to strain buildup and possible cracking of boules due to order-of-magnitude differences in oxygen incorporation based on the growth plane (e.g., c-plane versus lateral m-plane growth) [74], increases Ga vacancy concentrations via formation of $O\text{-}V_{Ga}\text{-}H_x$ complexes [75], and reduces thermal conductivity by up to 42% [76].

Fig. 11.10 provides an overview of the major remaining observed impurities in basic and acidic ammonothermal crystals, while Table 11.1 provides an overview of the remaining minor ($<10^{18}$ $cm^{-3}$) impurities that have been measured using SIMS.

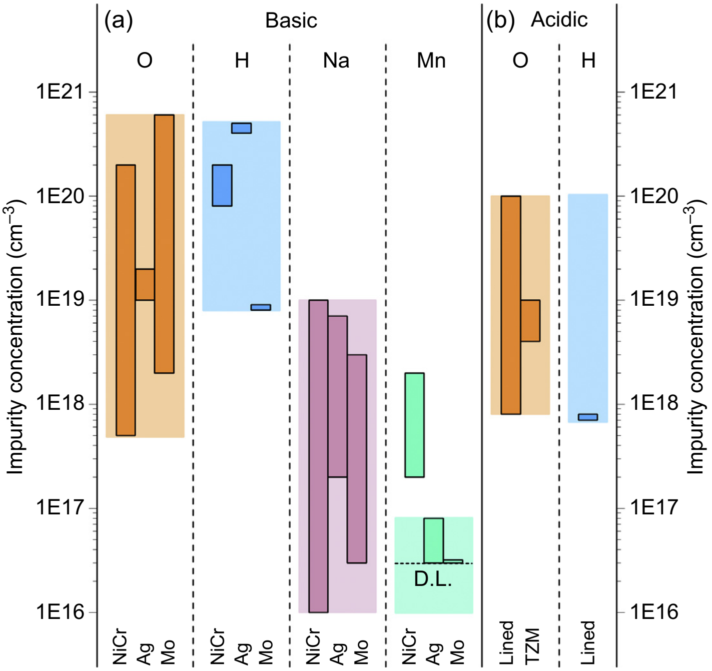

**Figure 11.10** Range of reported major impurity concentrations determined by SIMS in basic (H, O, Na, Mn) and acidic (H, O) ammonothermal GaN crystals. Light shaded backgrounds highlight the range of current typically observed values, while dark columns are from literature reports. Residual impurities are typically $<10^{18}$ $cm^{-3}$ and reported in Table 11.1. Reported impurities result from bulk GaN crystals grown in (a) basic ammonothermal chemistries in NiCr superalloy autoclaves without a liner (NiCr), within a silver capsule (Ag), and within a molybdenum capsule (Mo) and (b) acidic ammonothermal chemistries in a lined Ni-based alloy autoclave (lined) or a TZM autoclave (TZM) [58].

Table 11.1 **Impurity concentrations measured by SIMS in bulk GaN crystals not reported in Fig. 11.10. Crystals grown using the basic ammonothermal method in an NiCr autoclave (NiCr) with a silver capsule (Ag) or an Mo capsule (Mo), or using the acidic ammonothermal method in a lined Ni-based alloy autoclave (lined) or a TZM autoclave (TZM). Omitted elements were not reported on in recent literature [58]**

| | | **Impurity concentration ($cm^{-3}$)** | | |
|---|---|---|---|---|
| | | **~ Low-$10^{18}$** | **Low-$10^{17}$–high-$10^{16}$** | **Below DL** |
| Basic | NiCr | Al, Si | C, Mg, Fe, Mo | K, Li, Ti, Co, Cr, Ni |
| | Ag | | C, Mg, Fe, Mn, Al, Si | Mo |
| | Mo | | C, Mg, Si | Fe, Mn, Mo |
| Acidic | Lined | | | Transition metals, alkaline metals |
| | TZM | | C, Fe | Cr, Mo, Zr, Nb, Cl, Ti |

### 11.3.4.2 Gallium vacancies

Both basic and acidic ammonothermal crystals have significant concentrations ($>10^{18}$ $cm^{-3}$) of vacancy-related defects, orders of magnitude higher than those reported for HVPE GaN. (Hydrogenation) gallium vacancies form deep levels in the bandgap (resulting in yellow coloration of the crystals), causing nonradiative recombination, contributing to subbandgap optical absorption, and compensating n-type doping [75]. Their concentration has been measured using positron annihilation spectroscopy [77] and optical absorption measurements in the mid-infrared wavelength range.

Use of fast Fourier transform spectroscopy has recently led to a better understanding of the types of hydrogenation gallium vacancy present and their concentration [78]. Initial results suggest large concentrations ($\sim 10^{18}$ $cm^{-3}$) of $V_{Ga}$-$H_x$, for $x = 1, 2, 3$. The mechanism of their formation is unknown, but it is thought to be due to kinetics as these concentrations are in excess of what would be anticipated from thermodynamic considerations. Reduction of oxygen concentrations in acidic ammonothermal crystals has been shown to decrease the concentration of these defects, suggesting the presence of O-$V_{Ga}$-$H_x$ complexes [75].

### 11.3.4.3 Doping

Appreciable unintentional concentrations of oxygen within the crystals make it challenging to dope the crystal controllably. While n-type doping can be readily achieved, it is diffiult to achieve target concentrations repeatedly and uniformly. Semiinsulating

GaN can be grown by codoping with Fe or Mg, resulting in a resistivity of $\rho \sim 10^6-10^{12}$ Ω-cm. Magnesium-doped GaN has been grown using the basic method and has demonstrated p-type doping, with hole concentrations of $\sim 10^{18}$ cm$^{-3}$ and a resistivity of $\rho \sim 10^1-10^2$ Ω cm. The impact of doping on optical transparency, which is important for optoelectronic devices grown on these materials as substrates, has been discussed [79].

Additional doping of GaN crystals has been explored for transition metals such as Mn, Fe, Cr [80], and Er [81]. These studies were performed to investigate the possibility of introducing ferromagnetism into heavily doped GaN crystals and to introduce intra-4f shell transitions for highly luminescent optoelectronic devices, respectively.

## 11.3.5 Growth rate

Improvements to growth rates are desired, as they result in increased yield per growth run and as such lower-cost substrates. Generally, basic ammonothermal growth results in inferior growth rates as compared to acidic ammonothermal growth.

Basic ammonothermal growth exhibits a strong tendency for high c-plane growth rates and slow m-plane growth rates. Peak reported total growth rates in the c direction are up to ~350 μm/day for growth in silver capsule systems (see Fig. 11.11(a)), though the reason for this improved growth rate over unlined growths of ~150 μm/day is not understood [57]. M-plane growth rates are slow, typically <30 μm/day, resulting in significant challenges in laterally scaling the boule and achieving large c-plane area substrates. Growth rate improvements will need to be tied to a better understanding of the underlying chemistry and related growth kinetics.

Acidic ammonothermal growth exhibits high growth rates in all boule directions, in particular m-plane directions. There are reports of peak growth rates of up to

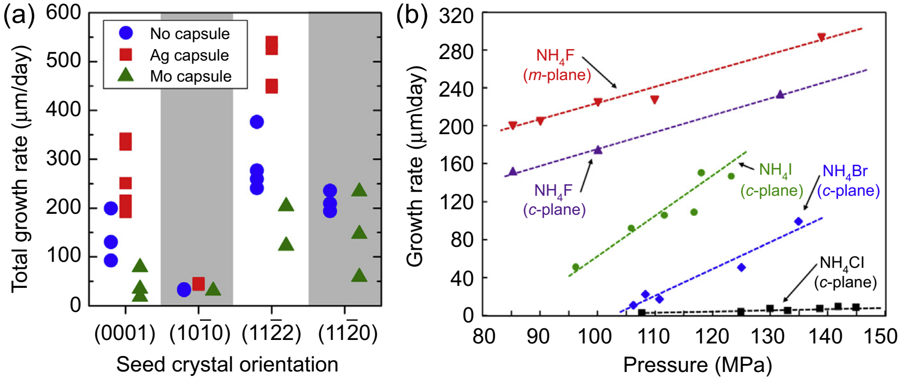

**Figure 11.11** (a) Total growth rates for basic ammonothermal GaN observed for different autoclave systems (unlined NiCr superalloy autoclave, silver capsule, and molybdenum capsule) and crystallographic growth plans [57]. (b) Effect of acidic mineralizer on growth rate of GaN for certain crystallographic planes [82].

almost 1 mm/day, though growth rates of ~700 μm/day are typical [62]. Based on existing literature, use of fluorine as a mineralizer provides a significant boost to overall growth rates (see Fig. 11.11(b)) and may relate to high solubility of Ga into these solutions [82].

### 11.3.6 Computer modeling

A few research groups are working on accurately modeling the environment inside the autoclave during ammonothermal growth. These models are primarily needed to improve our understanding of the fluid motion, temperature uniformity, and solute distribution within the autoclave, as it is exceedingly hard, although not impossible, to obtain in situ data during growth runs.

Initial reports on the modeling of ammonothermal systems suggest a high Grashof number, indicating a strongly three-dimensional flow (3D) pattern which is time dependent [83]. Additional work focused on investigating the effect of the baffle plates and porosity of the source material [84,85]. More involved thermodynamic-based simulations included mass-transport aspects, though their results significantly overestimated growth rates, suggesting kinetic limitations during growth [86]. Recent work provides a more comprehensive view on the ammonothermal process by including multiple aspects of growth: fluid flow, heat transfer, GaN metastable phase transport, dissolution and crystallization rates, and crystal formation [87,88].

Computer modeling promises to provide important insights into the specifics of the growth environment during growth, yet to date few experimental validations of these models have occurred. Currently, insufficient data is available for the thermodynamics, kinetics, and fundamental fluid properties to provide an accurate universal model for ammonothermal growth. Ongoing efforts are being made to improve our understanding of these fundamental aspects of growth and the supercritical solution. It is thought that computation modeling will play an increasingly important role for commercialization of this method by ensuring uniformity within and across multiple crystal boules while providing higher yields of large-area single crystal GaN boules.

### 11.3.7 Future developments

The ammonothermal method is considered the most promising route toward production of high-quality, large-area GaN substrates at low cost. As such, efforts are being made to understand the process further from both a fundamental growth perspective and a yield and uniformity standpoint.

To better our understanding of the underlying growth chemistry and growth kinetics, innovative in situ autoclaves have being designed which will provide novel insight into the process in the near future by interrogating the solution using optical (UV-vis, X-ray) methods and in situ probes, such as time-dependent temperature measurements during growth. Further investigations of the thermodynamics of the growth, building on existing work related to ammonia decomposition and found chemical compounds in these systems under ammonothermal conditions, will help provide a better fundamental understanding of this method.

Continuous improvements in uniformity and yield are expected through experimental and computational advances. Reduction of strain and cracking in boules [89] will further increase overall growth run yields. Due to the long growth times required to produce large-area seed crystals using the ammonothermal method, use of HVPE and Na-flux GaN as seeds for growth in ammonothermal systems will be explored to increase boule size rapidly [90].

Overall, it is expected that scaling of existing seeds and boules will be of lesser immediate importance compared to improving the existing process to produce inexpensive large-area c-plane substrate repeatedly and controllably for the market. Continued collaboration between academia and industry should result in these desired outcomes.

## 11.4 Na-flux method

### 11.4.1 Fundamentals of method

#### 11.4.1.1 General overview

The sodium-flux method is a high-temperature solution growth method which precipitates GaN from a molten sodium—gallium (Na—Ga) solution supersaturated in nitrogen due to a high nitrogen ($N_2$) pressure environment. The process was pioneered by Yamane and DiSalvo, and the first demonstrations of GaN growth occurred in 1997 [91]. The process was quickly adopted by Mori [92], and in the subsequent decades this method has been chiefly developed by these two groups. Of the bulk GaN growth methods presented, this method is arguably the least mature, though it holds great promise.

Current implementations of this method either place a seed crystal within a stagnant Na—Ga solution or a solution that is agitated by stirring, swinging, or dipping of the crystal. In all cases the solution is held at a constant temperature (typically 800—900°C) and growth is controlled by the nitrogen pressure (typically 3—5 MPa) and resulting supersaturation of nitrogen in solution.

Key challenges of this method include the diffusion of nitrogen through the molten metal melt, spontaneous nucleation of GaN crystals on the crucible and surface of the melt, changes in the ratio of Na:Ga in the melt as growth of GaN proceeds, and proper containment of the Na vapor while permitting a continuous replenishment of $N_2$ gas. Additional challenges include an incomplete thermodynamic understanding of the Na—Ga solution along with a lack of detailed understanding of the kinetics involved in the migration of the nitrogen gas into the solution and the incorporation of nitrogen into the growing crystal.

#### 11.4.1.2 Melt properties and solubility

The thermodynamics of the Na—Ga system has been studied by several groups, though experimental data only exists for temperatures $<650°C$. As such, there is some uncertainty as to the accuracy of the phase diagram of this system, and in particular the

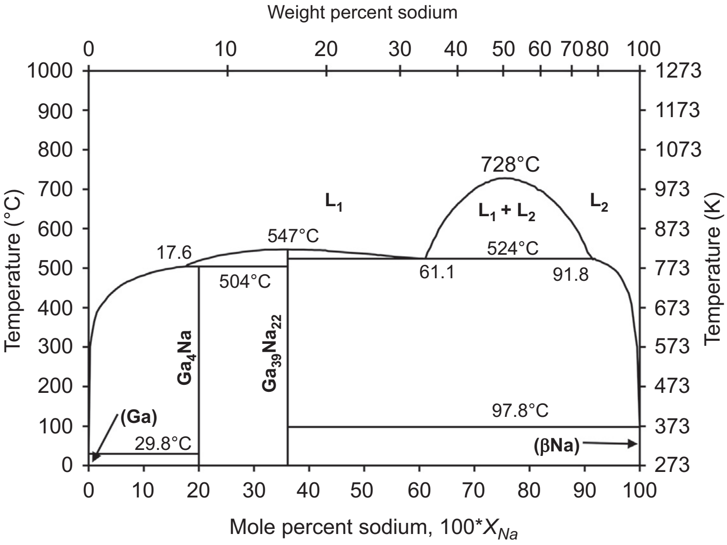

**Figure 11.12** Phase diagram of Na–Ga system. The two-phase liquid ($L_1 + L_2$) has not been experimentally verified [94].

possibility of a two-phase liquid region which has not been experimentally measured. Note that typical melt compositions of Na:Ga = 73:27 mol held at ~850°C used for growth of GaN place the growth solution in close proximity to this region, presenting an intriguing question as to whether a two-phase liquid plays a role in growth of GaN in this system. The most recent phase diagram [93] is shown in Fig. 11.12.

High nitrogen solubility is critical in achieving appreciable growth rates. Nitrogen is a poor solute in pure metal melts, such as Ga and Na, though certain compositions of a Na–Ga melt exhibit up to five orders of magnitude higher solubility of N (see Fig. 11.13(c)), effectively enabling growth of nitrides from solution. The solubility is found to increase with temperature (normal solubility, Fig. 11.13(a)) and increase with $N_2$ pressure (following Sievert's Law, Fig. 11.13(b)) [34].

The drastic increase in solubility is not fully understood, although two explanations have been put forward. The first proposes that sodium ionization leads to nitrogen reduction ($N^{3-}$ formation), which forms complexes with gallium in the melt (sodium does not readily nitride). The second builds on first-principle calculations with density functional theory and molecular dynamic simulations, suggesting sodium and gallium have a tendency to segregate, thereby creating voids in the liquid. Nitrogen can readily fill these voids and bond with gallium.

## *11.4.2 Growth systems*

Generally speaking, there are two types of systems available to perform growth of GaN using this method: one uses a pressure vessel and internal heating of the crucible, while the other externally heats the pressure vessel and indirectly heats the crucible.

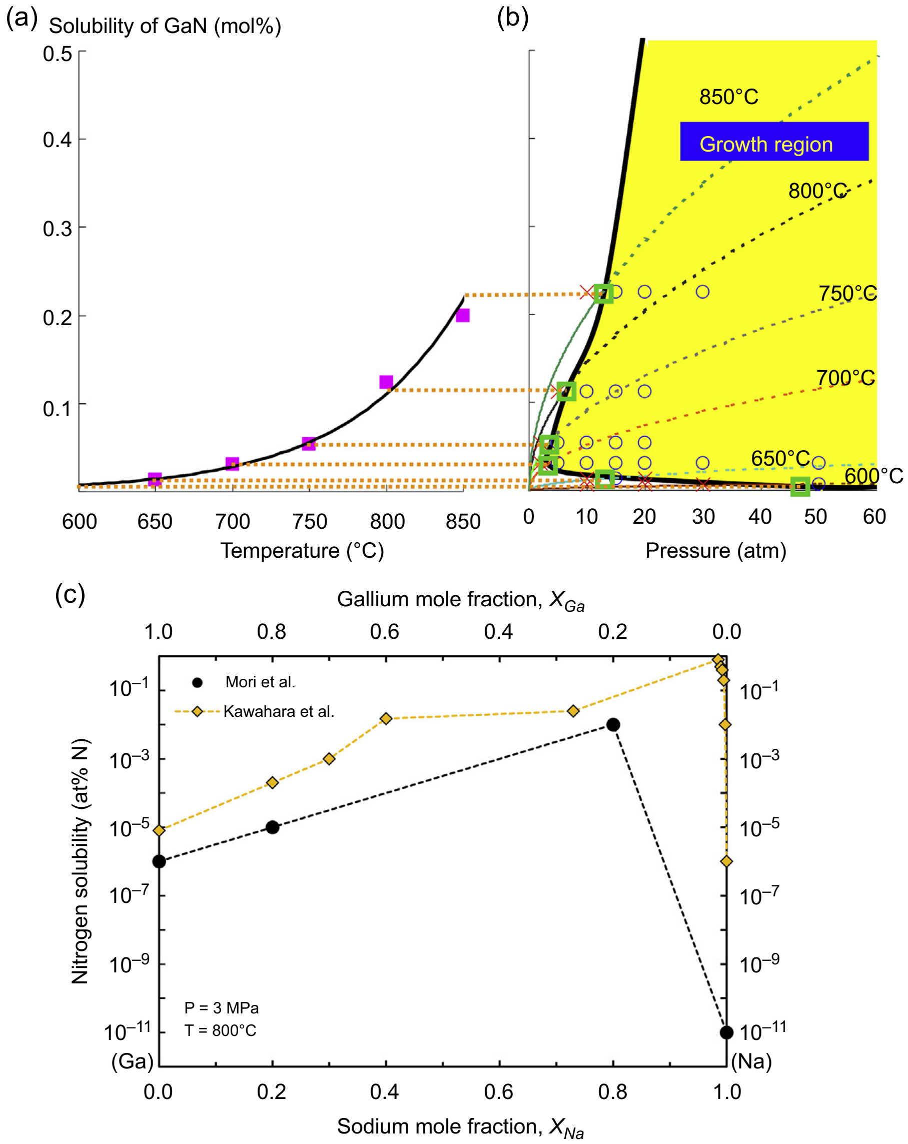

**Figure 11.13** Solubility of N in Na—Ga melt (73:27 mol) solution as a function of (a) temperature, (b) pressure [34], and (c) Na—Ga composition [94].

Important to both systems is the need to replenish consumed nitrogen gas during growth while retaining Na vapor within a well-defined volume to maintain the desired melt composition.

Use of a Na—Ga melt requires a crucible to hold the corrosive liquid. A wide variety of materials have been investigated, though no crucible material has yet been found that is completely inert and does not either mildly react with the Na or Ga in solution or dissolve into the Na—Ga solution. Currently, high-purity alumina or TZM are used, though both have a finite lifetime: sodium diffuses into the aluminas, forming presumably sodium aluminate, while molybdenum has finite solubility in the Na—Ga solution and as such slowly etches.

### *11.4.2.1 Externally heated systems*

Stainless steel is corrosion resistant to sodium vapor and so can be used as a pressure containment material. Simple laboratory-scale pressure vessels were created by using stainless steel tubes, placing an alumina crucible holding Na and Ga and a seed, if desired, in them, and using standard compression fittings to seal the ends and connect the crucible to a nitrogen gas tank. These tubes can operate at typical pressures of 3—5 MPa up to ~890°C, though they are single use. Fig. 11.14 provides a schematic overview of such a system, but omits the (resistive) heaters used to hold the crucible and pressure vessel under isothermal conditions.

While this method is suitable for laboratory-scale work, it is ill suited for large-scale implementation (i.e., commercialization) due to safety concerns over failure of the stainless steel due to high-temperature creep and corrosion. Nevertheless, this inexpensive system has been widely used in exploring this growth method.

### *11.4.2.2 Internally heated systems*

Integration of the heater into the pressure vessel increases system complexity, but it provides the means to integrate in situ monitoring capabilities. While electrical

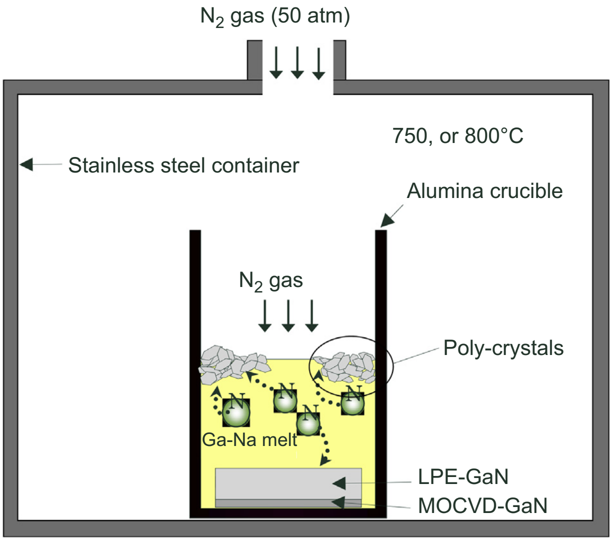

**Figure 11.14** Schematic of a typical system for GaN growth using the Na-flux method. External heaters heating the entire assembly have been omitted [34].

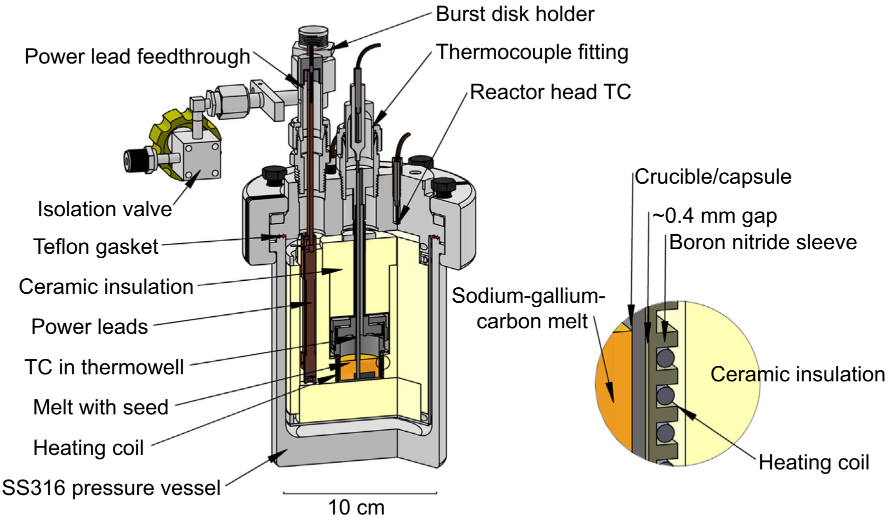
Burst disk holder
Power lead feedthrough
Thermocouple fitting
Reactor head TC
Isolation valve
Teflon gasket
Ceramic insulation
Power leads
TC in thermowell
Melt with seed
Heating coil
SS316 pressure vessel
10 cm
Crucible/capsule
~0.4 mm gap
Boron nitride sleeve
Sodium-gallium-carbon melt
Ceramic insulation
Heating coil

**Figure 11.15** Cutaway view of internally heated pressure vessel reactor system for sodium-flux growth of bulk GaN. Inset is a detail view of the heater area [95].

feedthroughs can be managed with some ease, containment of the sodium vapor is challenging. Various designs have been proposed to contain the Na vapor properly within a volume separated from the internal heater to prevent damage to the heaters. Use of ceramic crucibles typically leads to labyrinth-type seals due to challenges in machining parts after sintering, while use of TZM permits development of a gasket-sealed crucible which simultaneously acts as a capsule. A long, unheated condenser tube is attached to this sealed capsule, permitting condensation of Na vapor on the inner walls while allowing a continuous supply of $N_2$ to the growth system through the center. Fig. 11.15 depicts one possible implementation of such an internally heated system using a TZM crucible and a sodium reflux system [95].

One advantage of the system depicted in Fig. 11.15 is a direct line of sight to the melt, permitting in situ growth temperature measurements and instantaneous feedback on growth rates determined by either measuring the instantaneous mass consumption of $N_2$ gas using a mass flow controller or sealing the system and monitoring the pressure drop [96]. This system allows exploration of methods to replenish Ga in the melt during growth, enabling long-term growths. Internally heated systems can be used repeatedly for long growth runs, as ceramic thermal insulation considerably lowers the temperature inside the stainless steel pressure vessels (<200°C).

### 11.4.3 State-of-the-art crystals

GaN crystals grown using the Na-flux method typically come in two variations: single-point seeded or multipoint seeded, which ultimately coalesce to form a large single crystal. Either way, it is common to seed the growth with a GaN template, i.e., a thin, heteroepitaxial GaN layer deposited on a sapphire substrate using MOCVD. Mechanisms by which extended defects are significantly reduced are elaborated later. GaN templates are typically c-plane oriented, permitting growth of Na-flux GaN on the (0001) face. Self-nucleated crystals are less common, primarily because the method is less well suited to expand these crystals laterally to produce truly large-area crystals.

### *11.4.3.1 Self-nucleated and point-seed growth*

Self-nucleated crystals were first demonstrated in 1997 and were ~100 μm in size [91]. Within 3 years 3 mm size, transparent, colorless, n-type GaN crystals of high quality were reported, with ω-XRC FWHM of 25 arcsec for the (0004) peak and a mobility of 100 $\text{cm}^2/\text{V s}$ at room temperature [97].

Seeded growths were performed on unmasked 2-inch GaN templates, resulting in the demonstration of the first 3 mm thick, crack-free, 2-inch Na-flux GaN crystal in 2006 [98,99]. Similar results were demonstrated for 2-inch and 4-inch HVPE GaN seeds, though only of 0.75 mm thickness, in 2013 [100].

Small-seeded or point-seeded growth results in characteristic boule formation with m-plane, c-plane, and $\{10\overline{1}1\}$ plane termination. Point-seeded growths occur when a small opening is etched through an otherwise completely masked GaN template, yielding growth of GaN only from the small opening or, more commonly, by etching all the GaN from the template except for a small spot (the "point seed") [101]. These crystals have been grown to centimeter sizes (see Fig. 11.16(a)) and typically have very low dislocations (less than $10^3\ \text{cm}^{-2}$ in laterally grown regions). Despite darkening of some crystals, typical impurity concentrations were below the detection limit for Na, C, Si, and Al. O and Ca have been detected in the order of $10^{16}\ \text{cm}^{-3}$ indicating pure crystals can be grown using this technique. A relationship between a decrease in transparency and an increase in vacancy-type defects (such as a recently identified Ga vacancy coupled with an N vacancy) has been observed for small-seeded growths [102].

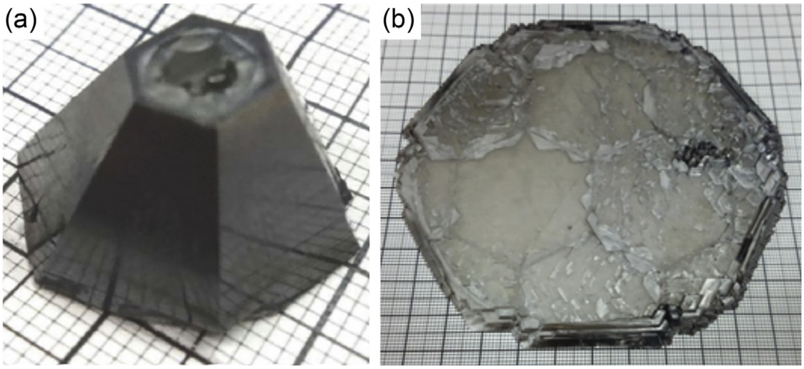

**Figure 11.16** (a) Large bulk pyramidal-shaped GaN crystal grown on a small GaN seed crystal [100]. (b) Image of an Na-flux grown GaN crystal on a 111 mm diameter tiled crystal with approximately 4 mm thickness [104]. One square corresponds to 1 × 1 mm.

Small-seeded or point-seeded growths typically result in different growth sections (usually separated into [0001], $<10\bar{1}1>$, and $<10\bar{1}0>$ sectors). Growth striations are visible in cathodoluminescence and sometimes optically (dark lines) in each of these zones. The [0001] sector is typically morphologically unstable, which results in skeletal growth, presumably due to the Berg effect. This process degrades the crystal quality and is undesired. As such, minimization of the c-sector growth is highly desired in this growth method.

Crystals are typically transparent or black, depending on the growth sector and addition melt modifications. Transparent crystals have an absorption coefficient of $\sim 0.1\ \mathrm{cm}^{-1}$ at 450 nm due to their high purity and quality. They generally exhibit strong near-band-edge emission under cathodoluminescence, emitting around 365 nm.

### *11.4.3.2 Multipoint-seed growth*

Due to the high crystal quality of laterally grown regions of point-seeded-grown crystals, a new technique ("coalescence growth") was proposed by periodically arranging small GaN point-seed crystals on a sapphire substrate. Upon growth and coalescence of these small crystals, a large single crystal can be achieved with surprisingly high crystal quality. If the point-seeded crystals are placed sufficiently close to each other and coalescence is achieved along the a direction, void-free, high-quality coalescence can be achieved; 2-inch, crack-free coalescence growth was achieved in 2014 using over 500 point seeds and demonstrated dislocation densities in the order of $10^2\ \mathrm{cm}^{-2}$ (both at and away from the coalescence boundary), a radius of lattice curvature of >100 m, highly oriented grains, and ω-XRC FWHM <30 arcsec for (0002) and <17 arcsec for $(10\bar{1}2)$ [103]. These remarkably low dislocation densities are largely due to a change in habit ($\{10\bar{1}1\}$ facets which can bend dislocations) in the early stages of growth, followed by planar (0001) growth upon coalescence. Further details are provided later.

Taking this approach on a larger scale, 2-inch GaN wafers can be used as "point seeds." These hexagonally shaped crystals with a-plane facets are tiled and fused together using the Na-flux method, creating a larger single crystal. This technique was used to demonstrate a 111 mm diameter crystal with 4 mm thickness in 2016 (see Fig. 11.16(b)) [104].

## *11.4.4 Melt modifications*

### *11.4.4.1 Growth rate and carbon additives*

A key challenge of Na-flux growth is the spontaneous parasitic nucleation of GaN on the crucible and gas interfaces with the melt (see Fig. 11.14). This limits the degree of supersaturation that can be achieved, and hence the growth rate. A major advance was made in 2008 when it was found that adding carbon (typically $\sim 0.5$ mol%) suppresses parasitic nucleation and thus widens the supersaturation window for growth [105]. Using carbon additives, growth rates as high as 80 μm/h (1.9 mm/day) along the $a$ axis (lateral growth) and 63 μm/h (1.5 mm/day) along the $c$ axis were achieved [106].

Interestingly, the delivery of carbon (carbon nanotube, active carbon, graphene, graphite, mesoporous carbon, or methane) has a marked impact on growth rate, with methane resulting in the highest reported growth rates due to minimal polycrystalline GaN formation at high driving forces [107]. Depending on the source of carbon, the habit of the crystal was found to change from prismatic to platelets, while ordered mesoporous carbon provided the highest growth rates and carbon nanotubes the lowest (50% lower) [108]. The purity of the carbon sources may have contributed to these changes.

First-principles molecular dynamics simulations of an Na—Ga melt with C additives suggests the mechanism for suppression of GaN nucleation is the high energy barrier for C—N dissociation in the melt (>3 eV). The cyanide compound has a lower barrier for dissociation on a kink site at the Na/GaN interface in the presence of excess Ga atoms (~1.0 eV), permitting incorporation into the crystal [109].

### 11.4.4.2 Effect of temperature, pressure, and melt composition

Generally speaking, the habit of a GaN crystal is terminated by $(000\bar{1})$, $\{10\bar{1}0\}$, $\{10\bar{1}1\}$, and (0001). Depending on the conditions within the melt, the $\{10\bar{1}1\}$ and (0001) facets appear or vanish, leading to a pyramidal or prismatic/platelet crystal habit. The amount of supersaturation of the flux is an important growth parameter that affects the growth habit, with low supersaturation typically exhibiting more defined inclined facets.

For growth of spontaneous nucleated polycrystalline GaN material on the wall of the crucible, a slightly different trend in morphology was observed: with increasing temperature and pressure, the GaN crystals transitioned from pyramidal to prismatic, and finally to thin platelets. A growth—time dependence was found, resulting in a change of the habit from pyramidal to prismatic, and ultimately platelets with growth times up to 50 h. After 50 h, high lateral growth rates perpendicular to the *c* axis led to large, thin platelets after 200 h [110]. In multipoint-seed configurations, GaN crystals grown at higher temperatures have a tendency to change from truncated pyramidal to pyramidal habits [111].

Increasing the ratio of Na to Ga was found to change the habit from prismatic to platelets and ultimately granules [112]. For multipoint-seeded growths, void-free coalescence is best achieved by growing at relatively low Ga compositions (~15 mol%), resulting in pyramidal terminated crystal columns [113].

### 11.4.4.3 Agitation of the melt

Due to low solubility of N in the Na—Ga melt, agitating the solution can rapidly homogenize the solution, thereby eliminating the typical diffusion gradient which is established in stagnant melts. This has the effect of reducing local supersaturation variations (thus reducing skeletal growth), providing uniform growth rates across large-area crystals, and increasing growth rates due to enhanced N arrival at the crystal growth front. Generally, crystals are rocked in a seesaw or swinging motion or rotated in a spinning action, thereby stirring the solution. Increasing the reversal frequency of the rotation or swinging increased growth rates and suppressed parasitic nucleation of GaN and skeletal growth. Furthermore, increasing the stirring rate flattens the habit of the crystal, minimizing the $\{10\overline{1}1\}$ facets of the prismatic crystals and leading to a larger c-plane area, which is advantageous during coalescence of multiple GaN grains [114].

A swinging motion resulted in flow velocity of the melt up to 2 cm/s—a 30 times increase from what would be expected without motion due to natural convective effects in the melt. The growth rate was found to increase from several μm/h to 30 μm/h. Using swing stirring, the position of the point seed within the crucible had little impact on its growth rate and crystal size, which is advantageous when applying the multipoint-seed growth method.

Stirring the solution via rotation also resulted in an increase in growth rate of crystals up to 46 μm/h (from ~13 μm/h in unstirred systems), though a greater positional dependence of the point seed within the crucible was found. Crystals grown close to the crucible wall tend to be larger than those in the center [115].

Given these benefits, considerable research has been performed on agitating the molten solution by swinging and/or rotating. Ultimately, the two consequences of these applications are the effective elimination of diffusion gradients and temporarily producing a thin melt layer above the crystal (with the bulk of the melt being temporarily distributed to a different location in the crucible), resulting in enhanced growth rates [116].

#### 11.4.4.4 Melt additives

Additions of metals to the Na–Ga melt can modify the habit of the crystal, along with its purity, optical transparency, and growth characteristics.

With regard to habit, Fe, Co, Ni, and Mn additives enhanced the growth of prismatic-shaped crystals. With an increasing amount of Sr in the melt, the GaN habit changed from pyramidal ($\{10\overline{1}1\}$ facets) to prismatic (exclusively m-plane termination) elongated along the <0001> direction [117]. While Fe, Co, Ni, and Cr were not incorporated into the crystal, Mn was (0.10–0.35 at%), leading to red or orange coloration and Curie-like paramagnetism [118]. Additions of Al accelerated nucleation of polycrystalline GaN. Grown polycrystals were highly transparent and Al was incorporated at levels below $3 \times 10^{16}\ \mathrm{cm}^{-3}$ [119].

Generally, the additions of Ca, Li, and Ca–Li enhanced the solubility of N in solution due to high binding energies of these elements with nitrogen. This enabled growth of GaN at either lower pressures (~50% lower) or higher temperatures (>900°C). Increasing the growth temperature was found to decrease impurity concentrations (such as Ca, Li, and O) while yielding very transparent crystals. Crystals tend to grow with a prismatic habit in Ca–Na fluxes, while Li–Na fluxes tend to produce platelets. Use of these additives reduced the surface roughness of the growing crystals [120,121].

Additions of Ba to the melt suppressed the formation of the voids within crystals which can be found in regular Na-flux growth on occasion. Furthermore, the crystallinity of crystals was greatly improved, including for growth on less common a-plane-oriented GaN templates. Ba is thought to incorporate at levels below $10^{15}$ cm$^{-3}$ [122].

## 11.4.5 Crystal properties

### 11.4.5.1 Dislocation reduction

One of the characteristics of GaN grown on GaN templates using the Na-flux method is the drastic reduction in dislocation density from $\sim 10^9$ cm$^{-2}$ in the GaN template to $10^3-10^6$ cm$^{-2}$. Detailed TEM (transmission electron microscopy) investigations have revealed that submicron-scale voids are formed at the interface between the MOCVD GaN layer and the Na-flux GaN. These voids preferentially form above dislocations with a c component, presumably in an initial etch-back period during which N is dissolved into the undersaturated solution and the spiral step of the c-component dislocation is readily etched. These voids largely prevented propagation of these types of defects.

A-type dislocations penetrate the interface, though to a large extent are bent and propagate parallel to the c plane. During the initial phases of growth there is only a small supersaturation, resulting in few nucleation sites, followed by 3D growth of nucleated GaN grains. During the 3D-growth phase, the grains develop with (0001) and inclined $\{10\overline{1}1\}$ facets. Partial lateral growth causes propagating dislocations to bend and propagate laterally as well (see Fig. 11.17) [123]. An additional result

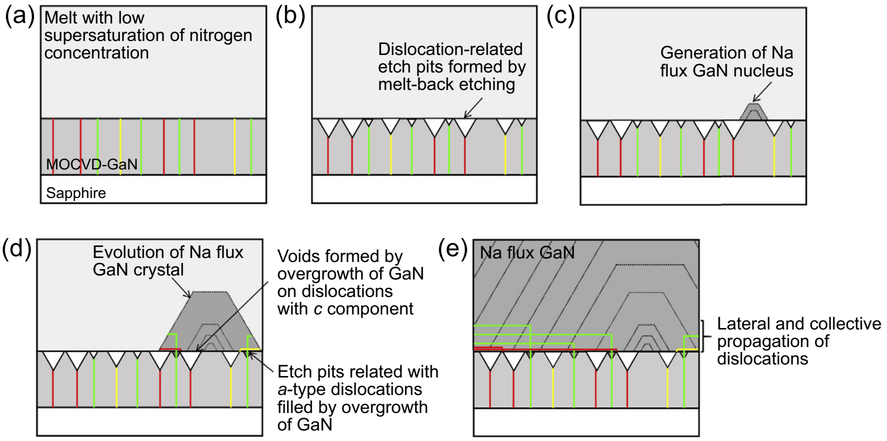
(a)
Melt with low supersaturation of nitrogen concentration
MOCVD-GaN
Sapphire
(b)
Dislocation-related etch pits formed by melt-back etching
(c)
Generation of Na flux GaN nucleus
(d)
Evolution of Na flux GaN crystal
Voids formed by overgrowth of GaN on dislocations with *c* component
Etch pits related with *a*-type dislocations filled by overgrowth of GaN
(e)
Na flux GaN
Lateral and collective propagation of dislocations

**Figure 11.17** Schematic model for, and dislocation behavior during, Na-flux GaN growth on MOCVD GaN. Formation of dislocation-related etch pits (a) before and (b) after melt-back etching, (c) generation of the Na-flux GaN nucleus on MOCVD GaN, (d) formation of voids by lateral growth of GaN crystal and lateral propagation of dislocations with c component in the Na-flux GaN crystal, and (e) lateral and collective propagation of all dislocation types by 3D growth of the Na-flux GaN crystal. Yellow, red, and green lines indicate c-, (a+c)-, and a-type dislocations, respectively [123].

of this dislocation behavior is the homogenization of the GaN crystal domain structure, leading to less misorientation between the nucleated grains [124].

While these description can be used for planar growth of GaN on planar seeds, point-seeded-grown crystals exhibit equally low threading dislocation, though significant variations are observed depending on initial seed crystal size. Investigations reveal that for small point seeds ($\sim 250\ \mu m$ in diameter) the c-oriented growth zone has a tendency to shrink laterally. This may occur by inward growth of inclined facets or macrobunching of steps from the outer edge of the crystal to the center due to hopper growth of the crystal. These facets or macrosteps have the ability to bend and guide dislocations toward the center of crystal where they annihilate or otherwise interact, resulting in a significant reduction in their density [125]. For larger-area point seeds, the lateral distance for the macrosteps to travel to coalesce is too great, preventing reduction of dislocations by the same amount and leading to crystals with typically $10^6\ cm^{-2}$ dislocations as opposed to $10^3\ cm^{-2}$.

### 11.4.5.2 Doping

GaN crystals grown using the Na-flux method are of high purity with no measured Na or C incorporation using SIMS. Controlled uniform doping of crystals can be challenging, though n-type doping is possible. Unintentionally doped crystals have oxygen as the dopant and an electron concentration of ~ mid-$10^{16}$ and mobility of $930\ cm^2/V\ s$. Germanium-doped n-type crystals result in mid-$10^{17}$ to mid-$10^{18}\ cm^{-3}$ concentrations with mobilities between 250 and $430\ cm^2/V\ s$. Zinc doping ($[Zn] = \sim 10^{19}\ cm^{-3}$) yields insulating crystals with a resistivity of $\sim 10^8\ \Omega$-cm. P-type GaN crystals have yet to be demonstrated [100].

Praseodymium-doped GaN was investigated as a possible phosphor. Growing GaN with 1.2 mol% Pr added to the melt resulted in crystals exhibiting a strong red emission at ~ 650 nm [126]. Europium-doped crystals were achieved up to a concentration of 0.15 at%, resulting in black crystals or transparent with <0.1 at%. Strong red emission (621 nm) occurred for the transparent material [127].

## 11.4.6 Future developments

The Na-flux method is a promising technique to produce high-quality and high-purity GaN. Substantial progress has been made toward achieving large-area crystals using novel approaches. Despite the important progress that has been made, much remains to be explored on a fundamental level, including the thermodynamics of the Na–Ga melt and the specifics of N behavior from the gas phase to incorporation into the crystal. Recent progress in developing novel autoclave designs which enable more in situ investigations [96] will help advance the field.

From a growth perspective, improvements to the growth systems will be needed to enable truly large, thick growth of GaN. A key limitation which has not really been overcome yet is the ability to grow large boules; resolving this problem would truly thrust this method to the forefront of bulk GaN growth methods to produce inexpensive GaN substrates. Additional research is needed to explore ways to enable continuous feeding of Ga to the Na–Ga flux without causing instabilities during growth. Even if this ambitious challenge cannot be achieved in the near future, this method is a promising route toward producing GaN seeds for other bulk GaN growth methods or, alternatively, an inexpensive way to produce polycrystalline GaN of high purity which can be used for ammonothermal growth of GaN. Either way, this technique will significantly impact the future of bulk GaN.

## 11.5 Hydride vapor phase epitaxy

The first demonstration of GaN growth achieved using the HVPE method was in 1968 by Maruska and Tietjen [1]. Since then it has grown to be a mature technique capable of producing large-area GaN boules of thicknesses up to ~1 cm and is currently the preferred industrial choice for bulk GaN substrates, which are commercially available primarily in c-plane orientations up to 6-inch in diameter with demonstrations existing up to 175 mm (~7 inch) diameters. Due to the maturity of the technique, this chapter focuses on recent developments; more in-depth discussion of the technique can be found in the literature [37,38].

### 11.5.1 Fundamentals of method

#### 11.5.1.1 General overview

The HVPE method is a vapor phase growth technique in which volatilized gallium species (in the form of gallium chlorides) react with ammonia gas to form GaN. Formation of gallium chlorides readily occurs by flowing hydrogen chloride (HCl) gas over a boat containing a gallium melt held at the optimal temperature (~800–900°C). At temperatures in excess of 600°C it is found that gallium monochloride (GaCl) is stable and present in appreciable concentrations in the gas phase (see Fig. 11.18(a)), thus the flow of group III metals to the crystal can be controlled by increasing or decreasing the HCl flow over the Ga boat. Upon entering the growth zone, typically held at 1000–1100°C, the driving force for growth is achieved by supersaturating the gas phase in GaCl. This can be achieved by introducing more GaCl than is thermodynamically stable under the prevailing conditions within the growth zone, or by modifying the gas environment by introducing an inert gas, such as helium (see Fig. 11.18(b)). Either way, it is found that the growth rate of GaN increases linearly with HCl flow rates (mass transport/diffusion limited growth), resulting in growth rates up to 100 μm/h (2.4 mm/day) [128]. Continuous improvements to equipment design and chemistries have led to demonstrations of crystal growth along the *c* axis at rates in excess of 1870 μm/h (44.9 mm/day) [129].

Sapphire is typically used as a substrate due to the availability of high-quality, large-area seeds commonly grown using the edge-defined film-fed growth, Czochralski, or Kyropoulos methods. Heteroepitaxial growth of GaN brings challenges related to lattice mismatch and thermal expansion coefficient mismatches, ultimately leading to increased threading dislocation concentrations, resultant lattice curvature, and in

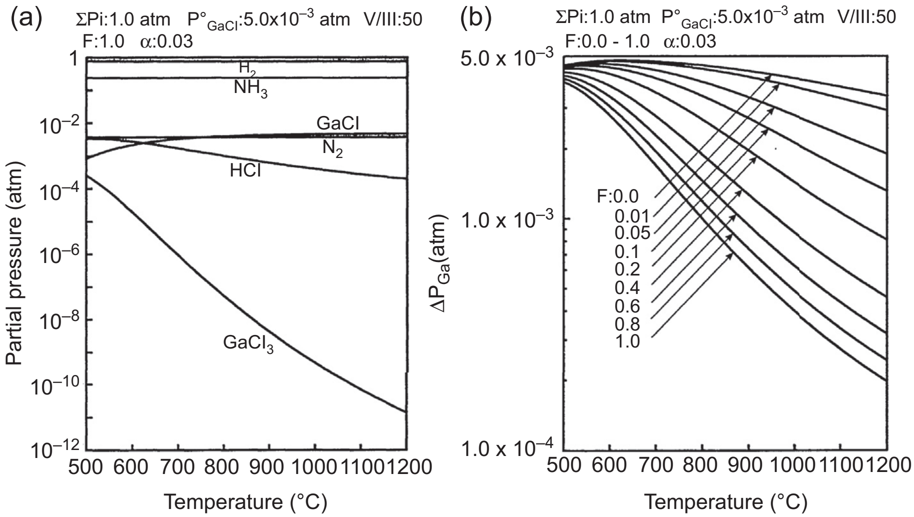

**Figure 11.18** (a) Equilibrium partial pressures of species in the growth zone as a function of temperature held at 1 atm, input partial pressure of GaCl: $5.0 \times 10^{-3}$ atm, V/III = 50 (III source is $NH_3$), assuming the mole fraction of decomposed ammonia is 0.03, and using $H_2$ carrier gas. (b) Driving force for growth of GaN as a function of growth temperature and mole fraction of hydrogen relative to inert gas atoms (=F) in the growth zone with otherwise identical conditions as in (a) [128].

extreme cases cracking of the boules. Nevertheless, it is still the preferred choice of substrate to date. Only recently, due to advancements in true bulk growth methods such as the ammonothermal and Na-flux methods, is it possible to explore growth of high-quality GaN on exceptionally high-quality substrates. This topic is discussed in later sections.

### *11.5.1.2 Gas thermodynamics of growth*

Due to the relatively mild growth conditions (1 atm, ~1000°C) and the availability of vast databases of thermodynamic properties of the various compounds present in the gas phase, a detailed thermodynamic analysis of the system can be achieved. This has led to comprehensive thermodynamic understanding of the process and the impact of multiple parameters on the thermodynamic driving forces, for example the impact of using an inert gas (such as helium) instead of hydrogen to increase the driving force for growth and hence the growth rate (Fig. 11.18(b)). Furthermore, investigations can be performed on growth of ternary III nitride alloys (addition of Al and/or In to the system) or use of alternative halides, such as Br or I [130].

While most commercial growth of GaN uses HVPE with GaCl as the Ga carrier, ongoing research is investigating the use of $GaCl_3$, formed by reacting $Cl_2$ with Ga and GaCl. This has the potential to solve the problem of ammonium chloride formation in the exhaust due to lack of HCl (see next subsection). Additionally, the thermodynamic driving force for growth of GaN is higher with $GaCl_3$ than with GaCl, enabling not only a higher growth rate but also growth at higher temperatures (demonstrations up to 1350°C exist), permitting higher-quality growth of GaN. Due to steric hindrance of the $GaCl_3$ molecule, growth in the $[000\bar{1}]$ direction is preferred, contrary to most HVPE-grown GaN material which uses [0001]. Overall, use of trichlorides opens new opportunities for growth of ternary alloys, such as thick InGaN layers [131], or in directions other than the traditional polar direction [132].

### 11.5.2 Growth systems

The HVPE technique typically uses a hot-wall reactor due to the low vapor pressure of the metal chlorides at low temperatures, thereby preventing condensation of these molecules on the unheated surfaces. Many modifications of HVPE reactor designs exist, though they can be summarized into two groups: horizontal- and vertical-flow reactor designs (see Fig. 11.19 for schematics). Generally at least two temperature zones are required in an HVPE reactor to grow binary nitrides: one source zone with the metal, and one crystallization zone with the seed crystal. More zones (permitting doping and/or alloying of the nitride) require additional heater zones with added flexibility and complexity. The system typically uses resistive heating, though RF heating is also popular. Gases are introduced in separated parallel quartz tubes or in a coaxial design for better fluid mixing prior to deposition. The substrate is typically flat or inclined in horizontal reactor design, and flat in vertical designs. In vertical designs the seed can be readily rotated to improve the uniformity of the grown film and also can be displaced vertically to ensure constant separation from the gas inlets, improving on the fluid dynamics for long-term growth. For both designs configurations exist wherein the substrate is mounted on the bottom or suspended from the top, thereby preventing solid particles from contaminating the growing crystal.

As mentioned previously, the growth of III nitrides is strongly thermodynamically driven, and as such homogeneous gas phase reactions and parasitic wall deposition are

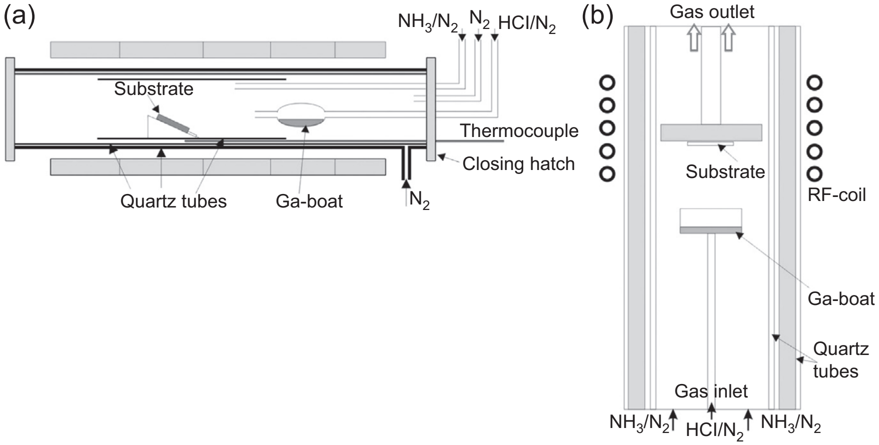

**Figure 11.19** Schematic drawings of (a) horizontal-flow and (b) vertical-flow configurations of HVPE reactors [37].

readily achieved. This is detrimental for long-term growth, as it depletes the gas phase sources and ultimately causes clogging or other negative effects due to excessive wall deposits of GaN. Additionally, due to the formation of ammonium chloride from the ammonia and chlorides remaining after the growth zone, the exhaust lines of the reactor have to accommodate continuous deposition of this compound in powder form as the gas cools below ~300°C. This ultimately limits the duration of a growth run from a system's standpoint due to maintenance and cleaning needs.

### 11.5.3 State-of-the-art crystals

The HVPE method is mature and has long been optimized to produce high-quality GaN boules. Typically, growth occurs on sapphire or GaAs-yielding large c-plane area boules, but more recently growth on arbitrarily oriented GaN substrates is being investigated. Numerous companies worldwide manufacture and sell bulk GaN substrates (for example, Sumitomo Electric Industries, Mitsubishi Chemical Corporation, Nanowin, Kyma, Furukawa Metals, Sino Nitride, and Saint-Gobain (Lumilog)).

#### 11.5.3.1 Foreign seeds

Heteroepitaxial growth of GaN has led to demonstrations of threading dislocation densities as low as mid-$10^{15}$ $cm^{-3}$. All impurities measured by SIMS, including Si, O, and C, are below detection limit (~< mid-$10^{15}$ $cm^{-3}$) when grown in a quartz-free system. Crystal boules with 4″ diameter have been achieved. Undoped material exhibits insulating behavior, while Si doping can be controlled over a wide range down to $1 \times 10^{14}$ $cm^{-3}$ with mobilities of over 1100 $cm^2/V\,s$ [133–135]. Growth thickness of GaN boules is limited primarily by system limitations, morphological breakdown of the surface, or cracking of the boules. Thicknesses up to ~1 cm have been achieved. Cross-cutting these boules yields high-quality semipolar and nonpolar substrates, largely for research purposes. Fig. 11.20(a) shows a 2-inch diameter GaN boule grown using the HVPE method.

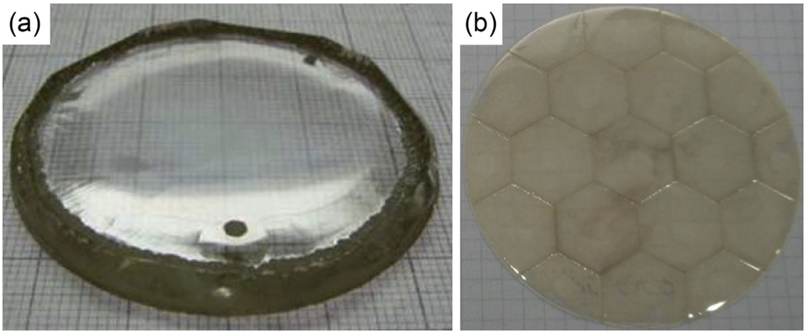

**Figure 11.20** (a) Freestanding bulk HVPE GaN crystal grown at 1010°C for 55 h with a thickness of 5.8 mm and diameter of 52 mm. [136], (b) As-grown 7″ (175 mm) HVPE GaN grown on tiled GaN substrates [133].

### 11.5.3.2 Native seeds

Growth on native (i.e., GaN) seeds yields higher-quality material, but necessitates the availability of such a substrate. Reuse of HVPE GaN substrates for additional growth runs is not common, presumably due to high curvature of the lattice planes ($R < 10$ m) leading to cracking in boules. A notable exception is the recent demonstration of a 7-inch substrate achieved by tiling 2-inch HVPE GaN substrates [104]. Recent advances in ammonothermal and Na-flux growth of GaN have opened the opportunity to explore HVPE growth of GaN on these high-structural-quality materials with large radii of curvature ($R >$ a few tens to 100 m).

Limited research has been done on HVPE growth of GaN on Na-flux seeds. One study suggests that differences in O concentrations between seed and grown crystals must be eliminated to maintain crystal quality of the seed. Varying incorporation of O in the Na-flux substrate due to the presence of inclined facets during multipoint-seeded growth leads to varying lattice parameters in the substrate. Growth of thick GaN layers on top of these layers introduces sufficient strain to give multiple cracks within the boule. HVPE growth of GaN on planar-grown Na-flux GaN, on the other hand, duplicated the seed crystal quality (dislocations: $10^3$–$10^5$ cm$^{-2}$) and yielded a higher radius of curvature material (>80 m) [137].

Ammonothermal GaN is currently commercially available, and its use as a substrate of HVPE growth of GaN is being researched. In brief, the high structural quality of the substrates is duplicated into the HVPE-grown material (ω-XRC FWHM of 22 arcsec and exciton peaks as narrow as 130 μeV [138]) while keeping the developed high level of control of uniformity and low impurity incorporation, yielding the highest overall quality of GaN crystals [139]. Growth on misoriented ammonothermal seeds in the $[10\bar{1}0]$ direction resulted in material with comparably low dislocations as the seed crystal: $\sim 5 \times 10^4$ cm$^{-2}$ [140].

Use of acidic ammonothermal GaN has also recently enabled the growth of 2-inch m-plane-oriented boules, which in turn could be processed as substrates for use in HVPE growth of m-plane-oriented GaN [141]. Growth in nonpolar directions is susceptible to the formation of basal-plane stacking faults (BSF), reducing crystal quality. It was recently found that basal-plane dislocations in the seed are a cause of BSF formation. Use of ammonothermal GaN with extremely low basal-plane dislocations as a seed for HVPE growth resulted in material with a dislocation density of $\sim 4 \times 10^4$ cm$^{-2}$, an average BSF density of 2.0 cm$^{-1}$, and a ω-XRC FWHM of 13 arcsec, demonstrating exceptionally high-quality m-plane substrate with a large area [65].

## 11.5.4 Point defects

### 11.5.4.1 Doping

HVPE GaN can be doped using a select few dopants. N-type doping is easily achieved, while p-type doping is more challenging. N-type doping has been achieved over a wide range (low-$10^{19}$ cm$^{-3}$ to mid-$10^{15}$ cm$^{-3}$) using Si doping (using dichlorosilane,

$H_2SiCl_2$, as the precursor) [142,143]. Ge is also a suitable dopant for n-type GaN, with the promise of achieving even higher n-type levels than Si [144–146]. Semiinsulating substrates with resistivity up to $10^{12}$ Ω-cm can be achieved by ultrahigh-purity growth in quartz-free reactors, or more easily through compensation doping of intrinsic n-type with Fe [147] or C [148]. Reports of p-type HVPE GaN are sparse, with publications reporting incorporation of Mg (p-type dopant) into HVPE GaN crystals [149] and p-type behavior for thick (3–7 μm) heteroepitaxial HVPE GaN films [150]. No reports of freestanding p-type HVPE GaN substrates exist to date.

### 11.5.4.2 Impurities

Common impurities in GaN grown using quartz-containing HVPE reactors include Si, C, O, and H, while for quartz-free HVPE reactors all impurities are below the SIMS detection limit. For planar c-plane growth, Si, C, O, and H concentrations are routinely below $10^{17}$ $cm^{-3}$, unless deliberately introduced. For GaN growth on inclined facets (such as $\{10\bar{1}1\}$) the O concentration increases drastically (by ~ 1000x) [151]. In certain HVPE growth systems contamination of the GaN boules with Mn can occur, which leads to orange coloration [152].

### 11.5.4.3 Ga vacancies

Ga vacancies ($V_{Ga}$) are found in HVPE GaN boules and can be relatively easily formed in heavily n-type doped material, especially with O as the dopant, due to a tendency to form $V_{Ga}$-O complexes. $V_{Ga}$ act as deep acceptors, thereby compensating n-type doping. Heavily oxygen-doped ($\sim 5 \times 10^{19}$ $cm^{-3}$) GaN is found to have Ga vacancies in excess of $1 \times 10^{18}$ $cm^{-3}$ while typical undoped GaN boules have in the order of $10^{15}$–$10^{17}$ $cm^{-3}$ [153].

## 11.5.5 Crystal properties

### 11.5.5.1 Optical, electronic, and structural properties

Overall, HVPE GaN can be grown with high purity, resulting in low-level background doping and, through optimization, reduced hole trap sites ($\sim 5 \times 10^{13}$ $cm^{-3}$ demonstrated) [154]. Uniform doping of the crystals with minimal biaxial strain can be achieved if ammonothermal GaN is used as a substrate [155]. Optically these crystals are transparent, unless heavily n-type doped which leads to a graying of the crystal due to phonon-assisted free carrier absorption [72]. Low-temperature photoluminescence reveals relatively weak defect-related bands; a yellow luminescence band commonly occurs, with a maximum at ~2.2 eV. HVPE GaN material has among the highest reported mobilities, at around 1100 $cm^2/V$ s, clearly highlighting the excellent quality of the material.

A major shortcoming of heteroepitaxial HVPE GaN is the introduction of large amounts of threading dislocations. While their concentration has been reduced to mid-$10^{15}$ $cm^{-2}$, they still negatively impact its properties. Increasing the thickness

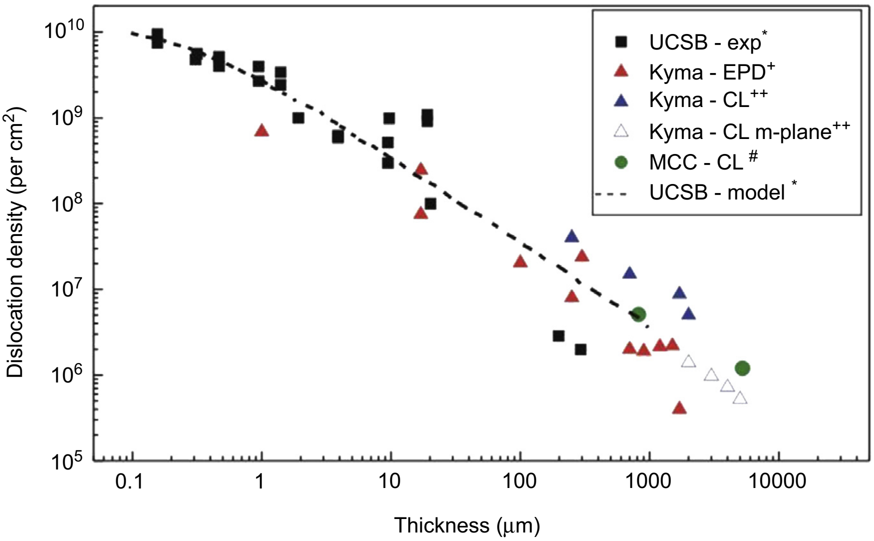

**Figure 11.21** Combined graph of experimental and theoretical predictions for dislocation density as a function of GaN layer thickness. Further details can be found in the literature [37].

of a crystal can lead to dislocation reduction due to annihilation or termination at the edge of the boule. Fig. 11.21 summarizes that even if truly thick (>1 cm) boules were grown using this method, it cannot readily achieve the low dislocation densities currently observed in ammonothermal or Na-flux GaN ($\sim 10^3$ cm$^{-2}$). As such, a transition to bulk GaN substrates is desired to provide material of higher structural quality. Ammonothermal GaN susbstrates have reproduced the excellent structural quality of HVPE growth, replicating the ω-XRC FWHM of 16 arcsec of the substrate [155].

### *11.5.5.2 Anisotropic growth*

Growth of thick GaN boules leads to both c-plane-oriented growth (desired) and lateral growth on inclined or nonpolar facets (undesired). The growth of inclined facets is common for HVPE (typically {10−11} planes), leading to a gradual reduction in diameter of the desired c-plane area. While this is detrimental, ongoing research is investigating methods to modify the inclined facet to a $\{10\bar{1}0\}$ plane by changing growth conditions (T, P, and gas composition). Nevertheless, lateral growth will always occur and is detrimental to achieving large boule thicknesses due to the preferential incorporation of impurities (mostly oxygen) on these planes, leading to impurity levels that are orders of magnitude higher. These impurities and associated electron concentrations lead to an increase of the lattice constants [73] (Fig. 11.22). Once a critical thickness is reached for the given seed crystal thickness, the built-up strain in the circumferential regions of the GaN boule introduces dislocations into the c-plane-oriented growth of the boule, leading to plastic deformation [156]. In some cases the boule may simply crack. Ultimately, this process prevents HVPE GaN

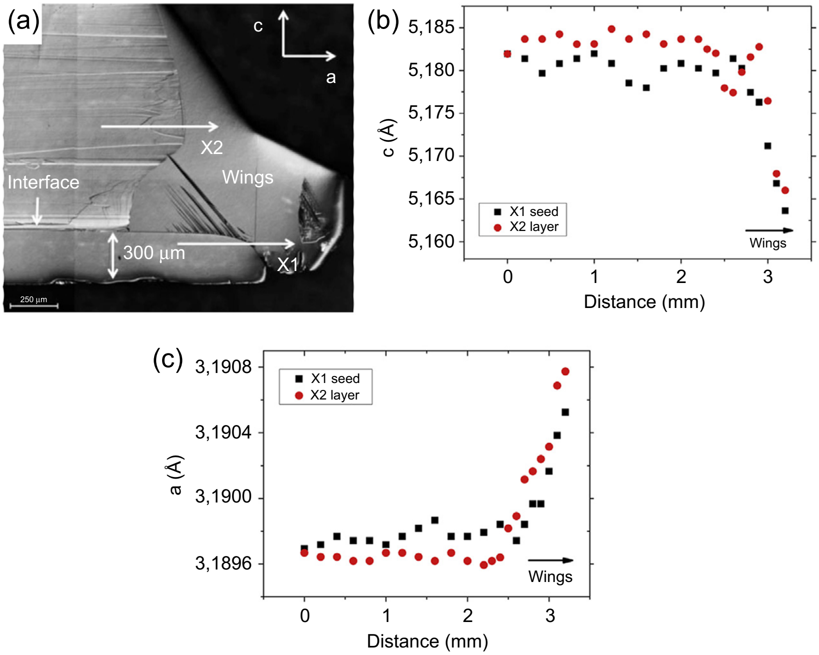

**Figure 11.22** (a) Images of m-plane cross-sections of the edge of HVPE GaN/ammonothermal GaN coupled with 1.5 mm thick HVPE layers grown on 300 µm thick Am−GaN seed. Scans parallel to the ammonothermal GaN/HVPE GaN interface through the seed toward the edge (*squares*) and through the HVPE GaN toward the edge (*circles*) with the distribution of (b) c-lattice constant, and (c) a-lattice constant [156].

from achieving truly thick boules, even if perfect seed crystals were used. As such, the HVPE method is considered to be a wafer-to-wafer method until a breakthrough on this front is achieved.

### 11.5.6 Computational contributions

Given the advanced maturity level of HVPE systems for growth of nitrides and III−V materials, commercial software packages, such as Hydride Epitaxial GaN Simulator (HEpiGANS) [157], can simulate growth of GaN and associated conditions within the HVPE reactor. These multiphysics simulation packages can model fluid motion, heat transfer by conduction, convection, and radiation, and species transport via convection, multicomponent diffusion, and thermodiffusion. Use of these models is particularly useful for optimizing gas velocities and patterns within the reactor, enabling good uniformity of growth conditions and impurity incorporation into the growing boule and reducing parasitic wall nucleation. Computational studies have found use, for example, in investigating scaling of the reactor design [158,159], hillock formation due to nonuniformity in deposition rates [160], and pit formation [161].

Atomic-scale simulations, such as density functional theory and molecular dynamics simulations, are also used to investigate various growth aspects near the growth front, such as hydrogen etching of GaN surfaces [162], formation energies of defects [163,164], and formation of inversion domain boundaries [165].

### 11.5.7 Future developments

Major advances in HVPE growth of GaN will most likely occur on two fronts. Scaling of boules and resulting GaN wafer sizes will be of great interest due to the ever-increasing demand for large-area substrates for power electronics. Given the demonstrated high quality of the material and associated control over various point defects, it is currently thought that HVPE will be a suitable substrate for vertical power electronic devices. The second front for advances includes furthering cross-pollination of GaN substrates from the ammonothermal or Na-flux method. Currently, growth from these two methods provides the highest-quality material available, though at a high cost. Use of HVPE to replicate and multiply the high structural quality while leveraging the greater control over purity, dopant incorporation, and uniformity may provide highly desired substrates at a sufficiently low cost point to permit pervasive use. Nevertheless, additional work is still needed to enable this on a commercial scale, with incorporation of ammonothermal substrates by industry being the most likely immediate advance. In the longer term, fabrication of large-area (>6 inch) GaN substrates by Na flux is anticipated, providing a route toward large-area growth of HVPE GaN (>6 inch).

Research to overcome the two major drawbacks of this method (parasitic nucleation and anisotropic growth) will continue. Elimination of ammonium chloride in the exhaust lines can be achieved through improved system designs or elimination of HCl from the gas stream. Should a breakthrough occur in reducing anisotropic incorporation of impurities on the c-plane versus inclined facets, increases in boule thicknesses can be envisioned, with the prospect of creating >1 cm thick boules. Even with today's limitations, HVPE remains the most viable method for inexpensive production of GaN with the desired material properties and low doping levels.

## References

[1] H.P. Maruska, J.J. Tieljen, The preparation and properties of vapor-deposited single-crystal-line Gan, Appl. Phys. Lett. 15 (1969) 327–329, https://doi.org/10.1063/1.1652845.

[2] S. Nakamura, Y. Harada, M. Seno, Novel metalorganic chemical vapor deposition system for GaN growth, Appl. Phys. Lett. 58 (1991) 2021–2023, https://doi.org/10.1063/1.105239.

[3] S. Nakamura, GaN growth using GaN buffer layer, Jpn. J. Appl. Phys. 30 (1991) L1705–L1707, https://doi.org/10.1143/JJAP.30.L1705.

[4] S. Nakamura, T. Mukai, M. Senoh, N. Iwasa, Thermal annealing effects on P-type Mg-doped GaN films, Jpn. J. Appl. Phys. 31 (1992) L139–L142, https://doi.org/10.1143/JJAP.31.L139.

[5] S. Nakamura, N. Iwasa, M. Senoh, T. Mukai, Hole compensation mechanism of P-type GaN films, Jpn. J. Appl. Phys. 31 (1992) 1258−1266, https://doi.org/10.1143/JJAP.31.1258.

[6] H. Amano, N. Sawaki, I. Akasaki, Y. Toyoda, Metalorganic vapor phase epitaxial growth of a high quality GaN film using an AlN buffer layer, Appl. Phys. Lett. 48 (1986) 353−355, https://doi.org/10.1063/1.96549.

[7] S. Nakamura, T. Mukai, M. Senoh, Candela-class high-brightness InGaN/AlGaN double-heterostructure blue-light-emitting diodes, Appl. Phys. Lett. 64 (1994) 1687−1689, https://doi.org/10.1063/1.111832.

[8] S. Nakamura, M. Senoh, S. Nagahama, N. Iwasa, T. Yamada, T. Matsushita, et al., Room-temperature continuous-wave operation of InGaN multi-quantum-well structure laser diodes, Appl. Phys. Lett. 69 (1996) 4056−4058, https://doi.org/10.1063/1.117816.

[9] S. Pimputkar, J.S. Speck, S.P. DenBaars, S. Nakamura, Prospects for LED lighting, Nat. Photon. 3 (2009) 180−182, https://doi.org/10.1038/nphoton.2009.32.

[10] M.A. Caro Bayo, Theory of Elasticity and Electric Polarization Effects in the Group-III Nitrides (Ph.D. thesis), University College Cork, 2013.

[11] M. Kneissl, J. Rass, III-nitride ultraviolet emitters, in: Spring Series in Materials Science, 2016, ISBN 9783319240985, https://doi.org/10.1007/978-3-319-24100-5.

[12] C.O. Holder, J.T. Leonard, R.M. Farrell, D.A. Cohen, B. Yonkee, J.S. Speck, et al., Nonpolar III-nitride vertical-cavity surface emitting lasers with a polarization ratio of 100% fabricated using photoelectrochemical etching, Appl. Phys. Lett. 105 (2014) 031111, https://doi.org/10.1063/1.4890864.

[13] P.H. Pathak, X. Feng, P. Hu, P. Mohapatra, Visible light communication, networking, and sensing: a survey, potential and challenges, IEEE Commun. Surv. Tutor. 17 (2015) 2047−2077, https://doi.org/10.1109/COMST.2015.2476474.

[14] S. Rajbhandari, J.J.D. McKendry, J. Herrnsdorf, H. Chun, G. Faulkner, H. Haas, et al., A review of gallium nitride LEDs for multi-gigabit-per-second visible light data communications, Semicond. Sci. Technol. 32 (2017) 023001, https://doi.org/10.1088/1361-6641/32/2/023001.

[15] J.S. Speck, S.F. Chichibu, Nonpolar and semipolar group III nitride-based materials, MRS Bull. 34 (2009) 304−312, https://doi.org/10.1557/mrs2009.91.

[16] M.T. Hardy, D.F. Feezell, S.P. DenBaars, S. Nakamura, Group III-nitride lasers: a materials perspective, Mater. Today 14 (2011) 408−415, https://doi.org/10.1016/S1369-7021(11)70185-7.

[17] Power GaN devices, in: M. Meneghini, G. Meneghesso, E. Zanoni (Eds.), Series: Power Electronics and Power Systems, Springer, 2017, ISBN 978-3-319-43197-0, https://doi.org/10.1007/978-3-319-43199-4.

[18] S. Chowdhury, U.K. Mishra, Lateral and vertical transistors using the AlGaN/GaN heterostructure, IEEE Trans. Electron Devices 60 (2013) 3060−3066, https://doi.org/10.1109/TED.2013.2277893.

[19] K. Motoki, Development of gallium nitride substrates, SEI Tech. Rev. 70 (2010) 28−35, http://global-sei.com/tr/staticFile/81/rakcat&DESTINATION=TLVL03_E&HAKKO_NO=70&TECHNICAL_CD=225.htm.

[20] E.C.H. Kyle, S.W. Kaun, P.G. Burke, F. Wu, Y.-R. Wu, J.S. Speck, High-electron-mobility GaN grown on free-standing GaN templates by ammonia-based molecular beam epitaxy, J. Appl. Phys. 115 (2014) 193702, https://doi.org/10.1063/1.4874735.

[21] S. Tomiya, T. Hino, S. Goto, M. Takeya, M. Ikeda, Dislocation related issues in the degradation of GaN-based laser diodes, IEEE J. Sel. Top. Quantum Electron. 10 (2004) 1277−1286, https://doi.org/10.1109/JSTQE.2004.837735.

[22] T. Melo, Y.-L. Hu, C. Weisbuch, M.C. Schmidt, A. David, B. Ellis, et al., Gain comparison in polar and nonpolar semipolar gallium-nitride-based laser diodes, Semicond. Sci. Technol. 27 (2012) 024015, https://doi.org/10.1088/0268-1242/27/2/024015.

[23] S.D. Lester, F.A. Ponce, M.G. Craford, D.A. Steigerwald, High dislocation densities in high efficiency GaN-based light-emitting diodes, Appl. Phys. Lett. 66 (1995) 1249−1251, https://doi.org/10.1063/1.113252.

[24] J.A. Van Vechten, Quantum dielectric theory of electronegativity in covalent systems. III. Pressure-temperature phase diagrams, heats of mixing, and distribution coefficients, Phys. Rev. B 7 (1973) 1479−1507, https://doi.org/10.1103/PhysRevB.7.1479.

[25] S. Porowski, B. Sadovyi, S. Gierlotka, S.J. Rzoska, I. Grzegory, I. Petrusha, et al., The challenge of decomposition and melting of gallium nitride under high pressure and high temperature, J. Phys. Chem. Solids 85 (2015) 138−143, https://doi.org/10.1016/j.jpcs.2015.05.006.

[26] J. Karpinski, J. Jun, S. Porowski, Equilibrium pressure of N2 over GaN and high pressure solution growth of GaN, J. Cryst. Growth 66 (1984) 1−10, https://doi.org/10.1016/0022-0248(84)90070-8.

[27] W. Utsumi, H. Saitoh, H. Kaneko, T. Watanuki, K. Aoki, O. Shimomura, Congruent melting of gallium nitride at 6 GPa and its application to single-crystal growth, Nat. Mater. 2 (2003) 735−738, https://doi.org/10.1038/nmat1003.

[28] K. Harafuji, T. Tsuchiya, K. Kawamura, Molecular dynamics simulation for evaluating melting point of wurtzite-type GaN crystal, J. Appl. Phys. 96 (2004) 2501−2512, https://doi.org/10.1063/1.1772878.

[29] A.G. Sokol, Y.N. Palyanov, N.V. Surovtsev, Incongruent melting of gallium nitride at 7.5 GPa, Diam. Relat. Mater. 16 (2007) 431−434, https://doi.org/10.1016/j.diamond.2006.08.018.

[30] D. Nakamura, T. Kimura, K. Horibuchi, Halogen-free vapor phase epitaxy for high-rate growth of GaN bulk crystals, Appl. Phys. Express 10 (2017) 045504, http://doi.org/10.7567/APEX.10.045504.

[31] M. Imade, H. Kishimoto, F. Kawamura, M. Yoshimura, Y. Kitaoka, T. Sasaki, et al., Vapor-phase epitaxy of high-crystallinity GaN films using Ga2O vapor and NH3, J. Cryst. Growth 312 (2010) 676−679, https://doi.org/10.1016/j.jcrysgro.2009.12.028.

[32] Y. Yamaguchi, Y. Taniyama, H. Takatsu, A. Kitamoto, M. Imade, M. Yoshimura, et al., Improvement of crystallinity of GaN layers grown using Ga2O vapor synthesized from liquid Ga and H2O vapor, Jpn. J. Appl. Phys. 55 (2016) 05FB04, http://doi.org/10.7567/JJAP.55.05FB04.

[33] D. Ehrentraut, E. Meissner, M. Bockowski (Eds.), Technology of Gallium Nitride Crystal Growth, first ed., Springer, 2010, http://doi.org/10.1007/978-3-642-04830-2.

[34] Y. Mori, M. Imade, M. Maruyama, M. Yoshimura, H. Yamane, F. Kawamura, et al., Growth of bulk nitrides from a Na flux, in: P. Rudolph (Ed.), Handbook of Crystal Growth − Bulk Crystal Growth, Elsevier, 2015, pp. 505−533, https://doi.org/10.1016/B978-0-444-63303-3.00013-4.

[35] D. Ehrentraut, M. Bockowski, High-pressure, high-temperature solution growth and ammonothermal synthesis of gallium nitride crystals, in: P. Rudolph (Ed.), Handbook of Crystal Growth − Bulk Crystal Growth, Elsevier, 2015, pp. 577−619, https://doi.org/10.1016/B978-0-444-63303-3.00015-8.

[36] M.J. Callahan, Q.-S. Chen, Hydrothermal and ammonothermal growth of ZnO and GaN, in: G. Dhanaraj, K. Byrappa, V. Prasad, M. Dudley (Eds.), Springer Handbook of Crystal Growth, Springer, 2010, pp. 655−689, https://doi.org/10.1007/978-3-540-74761-1_19.

[37] M. Bickermann, T. Paskova, Vapor transport growth of wide bandgap materials, in: P. Rudolph (Ed.), Handbook of Crystal Growth - Bulk Crystal Growth, Sixteen ed., Elsevier, 2015, pp. 621−669, https://doi.org/10.1016/B978-0-444-63303-3.00016-X.

[38] C. Hemmingsson, B. Monemar, Y. Kumagai, A. Koukitu, Growth of III-nitrides with halide vapor phase epitaxy (HVPE), in: G. Dhanaraj, K. Byrappa, V. Prasad, M. Dudley (Eds.), Springer Handbook of Crystal Growth, Springer, 2010, pp. 869−896, https://doi.org/10.1007/978-3-540-74761-1_26.

[39] K. Byrappa, M. Yoshimura, Handbook of Hydrothermal Technology, second ed., Elsevier, 2013, https://doi.org/10.1016/B978-0-12-375090-7.00011-6.

[40] T. Richter, R. Niewa, Chemistry of ammonothermal synthesis, Inorganics 2 (2014) 29−78, https://doi.org/10.3390/inorganics2010029.

[41] S. Zhang, F. Hintze, W. Schnick, R. Niewa, Intermediates in ammonothermal GaN crystal growth under ammonoacidic conditions, Eur. J. Inorg. Chem. 2013 (2013) 5387−5399, https://doi.org/10.1002/ejic.201300958.

[42] P. Molinie, R. Brec, J. Rouxel, P. Herpin, Structures des amidoaluminates alcalins MAl(NH2)4 (M = Na, K, Cs). Structure de l'amidogallate de sodium NaGa(NH2)4, Acta Crystallogr. B Struct. Crystallogr. Cryst. Chem. 29 (1973) 925−934, https://doi.org/10.1107/S0567740873003651.

[43] S. Zhang, N.S.A. Alt, E. Schlücker, R. Niewa, Novel alkali metal amidogallates as intermediates in ammonothermal GaN crystal growth, J. Cryst. Growth 403 (2014) 22−28, https://doi.org/10.1016/j.jcrysgro.2014.06.015.

[44] D. Ehrentraut, T. Fukuda, Ammonothermal crystal growth of gallium nitride − a brief discussion of critical issues, J. Cryst. Growth 312 (2010) 2514−2518, https://doi.org/10.1016/j.jcrysgro.2010.04.004.

[45] T.F. Malkowski, S. Pimputkar, J.S. Speck, S.P. DenBaars, S. Nakamura, Acidic ammonothermal growth of gallium nitride in a liner-free molybdenum alloy autoclave, J. Cryst. Growth 456 (2016) 21−26, https://doi.org/10.1016/j.jcrysgro.2016.07.045.

[46] K. Yoshida, K. Aoki, T. Fukuda, High-temperature acidic ammonothermal method for GaN crystal growth, J. Cryst. Growth 393 (2014) 93−97, https://doi.org/10.1016/j.jcrysgro.2013.09.010.

[47] S. Griffiths, S. Pimputkar, J.S. Speck, S. Nakamura, On the solubility of gallium nitride in supercritical ammonia−sodium solutions, J. Cryst. Growth 456 (2016) 5−14, https://doi.org/10.1016/j.jcrysgro.2016.08.041.

[48] S. Schimmel, M. Koch, P. Macher, A.C.L. Kimmel, T.G. Steigerwald, N.S.A. Alt, et al., Solubility and dissolution kinetics of GaN in supercritical ammonia in presence of ammonoacidic and ammonobasic mineralizers, J. Cryst. Growth 479 (2017) 59−66, https://doi.org/10.1016/j.jcrysgro.2017.09.027.

[49] T. Hashimoto, M. Saito, K. Fujito, F. Wu, J.S. Speck, S. Nakamura, Seeded growth of GaN by the basic ammonothermal method, J. Cryst. Growth 305 (2007) 311−316, https://doi.org/10.1016/j.jcrysgro.2007.04.009.

[50] S. Pimputkar, S. Nakamura, Decomposition of supercritical ammonia and modeling of supercritical ammonia-nitrogen-hydrogen solutions with applicability towards ammonothermal conditions, J. Supercrit. Fluids 107 (2016) 17−30, https://doi.org/10.1016/j.supflu.2015.07.032.

[51] S. Pimputkar, S. Kawabata, J.S. Speck, S. Nakamura, Improved growth rates and purity of basic ammonothermal GaN, J. Cryst. Growth 403 (2014) 7−17, https://doi.org/10.1016/j.jcrysgro.2014.06.017.

[52] S. Pimputkar, T.F. Malkowski, S. Griffiths, A. Espenlaub, S. Suihkonen, J.S. Speck, et al., Stability of materials in supercritical ammonia solutions, J. Supercrit. Fluids 110 (2016) 193−229, https://doi.org/10.1016/j.supflu.2015.10.020.

[53] B. Hertweck, T.G. Steigerwald, N.S.A. Alt, E. Schluecker, Different corrosion behaviour of autoclaves made of nickel base alloy 718 in ammonobasic and ammonoacidic environments, J. Supercrit. Fluids 95 (2014) 158−166, https://doi.org/10.1016/j.supflu.2014.08.006.

[54] S. Schimmel, U. Künecke, M. Meisel, B. Hertweck, T.G. Steigerwald, C. Nebel, et al., Chemical stability of carbon-based inorganic materials for in situ x-ray investigations of ammonothermal crystal growth of nitrides, J. Cryst. Growth 456 (2016) 33−42, https://doi.org/10.1016/j.jcrysgro.2016.08.067.

[55] B. Hertweck, S. Schimmel, T.G. Steigerwald, N.S.A. Alt, P.J. Wellmann, E. Schluecker, Ceramic liner technology for ammonoacidic synthesis, J. Supercrit. Fluids 99 (2015) 76−87, https://doi.org/10.1016/j.supflu.2015.01.017.

[56] B. Hertweck, T.G. Steigerwald, N.S.A. Alt, E. Schluecker, Applicability of metals as liner materials for ammonoacidic crystal growth, Chem. Eng. Technol. 37 (2014) 1835−1844, https://doi.org/10.1002/ceat.201400414.

[57] S. Pimputkar, J.S. Speck, S. Nakamura, Basic ammonothermal GaN growth in molybdenum capsules, J. Cryst. Growth 456 (2016) 15−20, https://doi.org/10.1016/j.jcrysgro.2016.07.034.

[58] S. Suihkonen, S. Pimputkar, S. Sintonen, F. Tuomisto, Defects in single crystalline ammonothermal gallium nitride, Adv. Electron. Mater. 3 (2017) 1600496, https://doi.org/10.1002/aelm.201600496.

[59] M.P. D'Evelyn, D. Ehrentraut, W. Jiang, D.S. Kamber, B.C. Downey, R.T. Pakalapati, et al., Ammonothermal bulk GaN substrates for power electronics, ECS Trans. 58 (2013) 287−294, https://doi.org/10.1149/05804.0287ecst.

[60] M.P. D'Evelyn, H.C. Hong, D.-S. Park, H. Lu, E. Kaminsky, R.R. Melkote, et al., Bulk GaN crystal growth by the high-pressure ammonothermal method, J. Cryst. Growth 300 (2007) 11−16, https://doi.org/10.1016/j.jcrysgro.2006.10.232.

[61] R.T. Dwiliński, A. Wysmolek, J.M. Baranowski, M. Kamińska, R.M. Doradziński, J. Garczyński, et al., GaN synthesis by ammonothermal method, Acta Phys Polonica A 88 (1995) 833−836, https://doi.org/10.1269/APhysPolA.88.833.

[62] D. Ehrentraut, R.T. Pakalapati, D.S. Kamber, W. Jiang, D.W. Pocius, B.C. Downey, et al., High quality, low cost ammonothermal bulk GaN substrates, Jpn. J. Appl. Phys. 52 (2013) 08JA01, https://doi.org/10.7567/JJAP.52.08JA01.

[63] R. DwilinÌ ski, R. DoradzinÌ ski, J. GarczynÌ ski, L.P. Sierzputowski, R. Kucharski, M. RudzinÌ ski, et al., Properties of truly bulk GaN monocrystals grown by ammonothermal method, Phys. Status Solidi C 6 (2009) 2661−2664, https://doi.org/10.1002/pssc.200982582.

[64] R.T. Dwiliński, R.M. Doradziński, J. Garczyński, L.P. Sierzputowski, R. Kucharski, M. Zając, et al., Ammonothermal GaN substrates: growth accomplishments and applications, Phys. Status Solidi. A 208 (2011) 1489−1493, https://doi.org/10.1002/pssa.201001196.

[65] Y. Tsukada, Y. Enatsu, S. Kubo, H. Ikeda, K. Kurihara, H. Matsumoto, et al., High-quality, 2-inch-diameter m-plane GaN substrates grown by hydride vapor phase epitaxy on acidic ammonothermal seeds, Jpn. J. Appl. Phys. 55 (2016) 05FC01, https://doi.org/10.7567/JJAP.55.05FC01.

[66] R. Kucharski, M. Zając, R.M. Doradziński, M. Rudziński, R. Kudrawiec, R.T. Dwiliński, Non-polar and semi-polar ammonothermal GaN substrates, Semicond. Sci. Technol 27 (2012) 024007, https://doi.org/10.1088/0268-1242/27/2/024007.

[67] N.A. Mahadik, S.B. Qadri, J.A. Freitas Jr., Structural inhomogeneities and impurity incorporation in growth of high-quality ammonothermal GaN substrates, Cryst. Growth Des. 15 (2015) 291−294, https://doi.org/10.1021/cg5013523.

[68] S. Sintonen, M. Rudziński, S. Suihkonen, H. Jussila, M. Knetzger, E. Meissner, et al., Synchrotron radiation x-ray topography and defect selective etching analysis of threading dislocations in GaN, J. Appl. Phys. 116 (2014) 083504, https://doi.org/10.1063/1.4893901.

[69] K. Horibuchi, S. Yamaguchi, Y. Kimoto, K. Nishikawa, T. Kachi, Formation of helical dislocations in ammonothermal GaN substrate by heat treatment, Semicond. Sci. Technol. 31 (2016) 034002, https://doi.org/10.1088/0268-1242/31/3/034002.

[70] R.T. Dwiliński, R.M. Doradziński, J. Garczyński, L.P. Sierzputowski, A. Puchalski, Y. Kanbara, et al., Bulk ammonothermal GaN, J. Cryst. Growth 311 (2009) 3015−3018, https://doi.org/10.1016/j.jcrysgro.2009.01.052.

[71] H.M. Foronda, A.E. Romanov, E.C. Young, C.A. Robertson, G.E. Beltz, J.S. Speck, Curvature and bow of bulk GaN substrates, J. Appl. Phys. 120 (2016) 035104, https://doi.org/10.1063/1.4959073.

[72] S. Pimputkar, S. Suihkonen, M. Imade, Y. Mori, J.S. Speck, S. Nakamura, Free electron concentration dependent sub-bandgap optical absorption characterization of bulk GaN crystals, J. Cryst. Growth 432 (2015) 49−53, https://doi.org/10.1016/j.jcrysgro.2015.09.016.

[73] M. Krysko, M. Sarzynski, J. Domagała, I. Grzegory, B. Łucznik, G. Kamler, et al., The influence of lattice parameter variation on microstructure of GaN single crystals, J. Alloy. Comp. 401 (2005) 261−264, https://doi.org/10.1016/j.jallcom.2004.10.077.

[74] S. Sintonen, P. Kivisaari, S. Pimputkar, S. Suihkonen, T. Schulz, J.S. Speck, et al., Incorporation and effects of impurities in different growth zones within basic ammonothermal GaN, J. Cryst. Growth 456 (2016) 43−50, https://doi.org/10.1016/j.jcrysgro.2016.08.040.

[75] W. Jiang, M. Nolan, D. Ehrentraut, M.P. D'Evelyn, Electrical and optical properties of gallium vacancy complexes in ammonothermal GaN, Appl. Phys. Express 10 (2017) 075506, https://doi.org/10.7567/APEX.10.075506.

[76] A. Jeżowski, O. Churiukova, J. Mucha, T. Suski, I.A. Obukhov, B.A. Danilchenko, Thermal conductivity of heavily doped bulk crystals GaN: O. Free carriers contribution, Mater. Res. Express 2 (2015) 085902, https://doi.org/10.1088/2053-1591/2/8/085902.

[77] F. Tuomisto, I. Makkonen, Defect identification in semiconductors with positron annihilation: experiment and theory, Rev. Mod. Phys. 85 (2013) 1583−1631, https://doi.org/10.1103/RevModPhys.85.1583.

[78] S. Suihkonen, S. Pimputkar, J.S. Speck, S. Nakamura, Infrared absorption of hydrogen-related defects in ammonothermal GaN, Appl. Phys. Lett. 108 (2016) 202105, https://doi.org/10.1063/1.4952388.

[79] R. Kucharski, Ł. Janicki, M. Zając, M. Welna, M. Motyka, C. Skierbiszewski, et al., Transparency of semi-insulating, n-type, and p-type ammonothermal GaN substrates in the near-infrared, mid-infrared, and THz spectral range, Crystals 7 (2017) 187. Page 26. 7, https://doi.org/10.3390/cryst7070187.

[80] M. Zając, J. Gosk, E. Grzanka, S. Stelmakh, M. Palczewska, A. Wysmołek, et al., Ammonothermal synthesis of GaN doped with transition metal ions (Mn, Fe, Cr), J Alloys Compd. 456 (2008) 324−338, https://doi.org/10.1016/j.jallcom.2007.02.046.

[81] B.T. Adekore, M.J. Callahan, L.O. Bouthilette, R. Dalmau, Z. Sitar, Synthesis of erbium-doped gallium nitride crystals by the ammonothermal route, J. Cryst. Growth 308 (2007) 71−79, https://doi.org/10.1016/j.jcrysgro.2007.07.058.

[82] Q. Bao, M. Saito, K. Hazu, K. Furusawa, Y. Kagamitani, R. Kayano, et al., Ammonothermal crystal growth of GaN using an NH 4F mineralizer, Crystal Growth and Design 13 (2013) 4158−4161, https://doi.org/10.1021/cg4007907.

[83] Q.-S. Chen, V. Prasad, W.R. Hu, Modeling of ammonothermal growth of nitrides, J. Cryst. Growth 258 (2003) 181−187, https://doi.org/10.1016/S0022-0248(03)01508-2.

[84] Q.-S. Chen, S. Pendurti, V. Prasad, Effects of baffle design on fluid flow and heat transfer in ammonothermal growth of nitrides, J. Cryst. Growth 266 (2004) 271−277, https://doi.org/10.1016/j.jcrysgro.2004.02.055.

[85] Y. Masuda, A. Suzuki, Y. Mikawa, Y. Kagamitani, T. Ishiguro, C. Yokoyama, et al., Numerical simulation of GaN single-crystal growth process in ammonothermal autoclave − effects of baffle shape, Int. J. Heat Mass Transf. 53 (2010) 940−943, https://doi.org/10.1016/j.ijheatmasstransfer.2009.11.027.

[86] S. Pendurti, Q.-S. Chen, V. Prasad, Modeling ammonothermal growth of GaN single crystals: the role of transport, J. Cryst. Growth 296 (2006) 150−158, https://doi.org/10.1016/j.jcrysgro.2006.07.034.

[87] J. Erlekampf, J. Seebeck, P. Savva, E. Meissner, J. Friedrich, N.S.A. Alt, et al., Numerical time-dependent 3D simulation of flow pattern and heat distribution in an ammonothermal system with various baffle shapes, J. Cryst. Growth 403 (2014) 96−104, https://doi.org/10.1016/j.jcrysgro.2014.06.007.

[88] I. Mirzaee, M. Charmchi, H. Sun, Heat, mass, and crystal growth of GaN in the ammonothermal process: a numerical study, Numer. Heat Transf. A Appl. 70 (2016) 460−491, https://doi.org/10.1080/10407782.2016.1173470.

[89] E.R. Letts, D. Key, T. Hashimoto, Reduction of crack density in ammonothermal bulk GaN growth, J. Cryst. Growth 456 (2016) 27−32, https://doi.org/10.1016/j.jcrysgro.2016.08.023.

[90] R. Kucharski, M. Zając, A. Puchalski, T. Sochacki, M. Bockowski, J.L. Weyher, et al., Ammonothermal growth of GaN crystals on HVPE-GaN seeds prepared with the use of ammonothermal substrates, J. Cryst. Growth 427 (2015) 1−6, https://doi.org/10.1016/j.jcrysgro.2015.06.019.

[91] H. Yamane, M. Shimada, S.J. Clarke, F.J. DiSalvo, Preparation of GaN single crystals using a Na flux, Chem. Mater. 9 (1997) 413−416, https://doi.org/10.1021/cm960494s.

[92] M. Yano, M. Okamoto, Y.K. Yap, M. Yoshimura, Y. Mori, T. Sasaki, Control of nucleation site and growth orientation of bulk GaN crystals, Jpn. J. Appl. Phys. 38 (1999) L1121−L1123, https://doi.org/10.1143/JJAP.38.L1121.

[93] H. Okamoto, Ga-Na (Gallium-Sodium), J. Phase Equilibria Diffus. 31 (2010) 206, https://doi.org/10.1007/s11669-010-9662-3.

[94] P. Von Dollen, Sodium Flux Growth of Bulk Gallium Nitride, Ph.D. Thesis, UCSB, 2016.

[95] P. Von Dollen, S. Pimputkar, M.A. Alreesh, H. Albrithen, S. Suihkonen, S. Nakamura, et al., A new system for sodium flux growth of bulk GaN. Part I: system development, J. Cryst. Growth 456 (2016) 58−66, https://doi.org/10.1016/j.jcrysgro.2016.07.044.

[96] P. Von Dollen, S. Pimputkar, M.A. Alreesh, S. Nakamura, J.S. Speck, A new system for sodium flux growth of bulk GaN. Part II: in situ investigation of growth processes, J. Cryst. Growth 456 (2016) 67−72, https://doi.org/10.1016/j.jcrysgro.2016.08.018.

[97] M. Aoki, H. Yamane, M. Shimada, T. Sekiguchi, T. Hanada, T. Yao, et al., Growth of GaN single crystals from a Na-Ga melt at 750 degrees C and 5 MPa of N-2, J. Cryst. Growth 218 (2000) 7−12, https://doi.org/10.1016/S0022-0248(00)00518-2.

[98] F. Kawamura, H. Umeda, M. Morishita, M. Kawahara, M. Yoshimura, Y. Mori, et al., Growth of a two-inch GaN single crystal substrate using the Na flux method, Jpn. J. Appl. Phys. 45 (2006) L1136−L1138, https://doi.org/10.1143/JJAP.45.L1136.

[99] T. Sasaki, Y. Mori, F. Kawamura, M. Yoshimura, Y. Kitaoka, New developments in crystal growth from solutions: oxides, proteins, and nitrides, J. Cryst. Growth 310 (2008) 1288−1297, https://doi.org/10.1016/j.jcrysgro.2007.11.228.

[100] Y. Mori, M. Imade, M. Maruyama, M. Yoshimura, Growth of GaN crystals by Na flux method, ECS J. Solid State Sci. Technol. 2 (2013) N3068−N3071, https://doi.org/10.1149/2.015308jss.

[101] M. Imade, K. Murakami, D. Matsuo, H. Imabayashi, H. Takazawa, Y. Todoroki, et al., Centimeter-sized bulk GaN single crystals grown by the Na-flux method with a necking technique, Cryst. Growth Des. 12 (2012) 3799−3805, https://doi.org/10.1021/cg300643r.

[102] A. Uedono, M. Imanishi, M. Imade, M. Yoshimura, S. Ishibashi, M. Sumiya, et al., Vacancy-type defects in bulk GaN grown by the Na-flux method probed using positron annihilation, J. Cryst. Growth 475 (2017) 261−265, https://doi.org/10.1016/j.jcrysgro.2017.06.027.

[103] M. Imade, M. Imanishi, Y. Todoroki, H. Imabayashi, D. Matsuo, K. Murakami, et al., Fabrication of low-curvature 2 in. GaN wafers by Na-flux coalescence growth technique, Appl. Phys. Express 7 (2014) 035503−035505, https://doi.org/10.7567/APEX.7.035503.

[104] T. Yoshida, M. Imanishi, T. Kitamura, K. Otaka, M. Imade, M. Shibata, et al., Development of GaN substrate with a large diameter and small orientation deviation, Phys. Status Solidi B 254 (2017) 1600671, https://doi.org/10.1002/pssb.201600671.

[105] F. Kawamura, M. Morishita, M. Tanpo, M. Imade, M. Yoshimura, Y. Kitaoka, et al., Effect of carbon additive on increases in the growth rate of 2in GaN single crystals in the Na flux method, J. Cryst. Growth 310 (2008) 3946−3949, https://doi.org/10.1016/j.jcrysgro.2008.06.008.

[106] M. Hayashi, M. Imanishi, T. Yamada, D. Matsuo, K. Murakami, M. Maruyama, et al., Enhancement of lateral growth of the GaN crystal with extremely low dislocation density during the Na-flux growth on a point seed, J. Cryst. Growth 468 (2017) 827−830, https://doi.org/10.1016/j.jcrysgro.2016.11.128.

[107] K. Murakami, S. Ogawa, M. Imanishi, M. Imade, M. Maruyama, M. Yoshimura, et al., Increase in the growth rate of GaN crystals by using gaseous methane in the Na flux method, Jpn. J. Appl. Phys. 56 (2017) 055502−055505, https://doi.org/10.7567/JJAP.56.055502.

[108] Z. Liu, G. Ren, L. Shi, X. Su, J. Wang, K. Xu, Effect of carbon types on the generation and morphology of GaN polycrystals grown using the Na flux method, CrystEngComm 17 (2015) 1030−1036, https://doi.org/10.1039/C4CE01899K.

[109] T. Kawamura, H. Imabayashi, M. Maruyama, M. Imade, M. Yoshimura, Y. Mori, et al., Mechanism for enhanced single-crystal GaN growth in the C-assisted Na-flux method, Appl. Phys. Express 9 (2015) 015601−015605, https://doi.org/10.7567/APEX.9.015601.

[110] F.J. DiSalvo, H. Yamane, M. Aoki, T. Yamada, M. Shimada, H. Goto, et al., Time dependence of the growth morphology of GaN single crystals prepared in a Na−Ga melt, Jpn. J. Appl. Phys. 44 (2005) 3157−3160, https://doi.org/10.1143/JJAP.44.3157.

[111] M. Honjo, M. Imanishi, H. Imabayashi, K. Nakamura, K. Murakami, D. Matsuo, et al., Habit control during growth on GaN point seed crystals by Na-flux method, Jpn. J. Appl. Phys. 56 (2017) 01AD01, https://doi.org/10.7567/JJAP.56.01AD01.

[112] H. Yamane, M. Shimada, T. Sekiguchi, F.J. DiSalvo, Morphology and characterization of GaN single crystals grown in a Na flux, J. Cryst. Growth 186 (1998) 8−12, https://doi.org/10.1016/S0022-0248(97)00480-6.

[113] M. Honjo, M. Imanishi, H. Imabayashi, K. Nakamura, K. Murakami, D. Matsuo, et al., Effect of flux composition ratio on the coalescence growth of GaN crystals by the Na-flux method, Opt. Mater. 65 (2017) 38−41, https://doi.org/10.1016/j.optmat.2016.09.017.

[114] K. Murakami, M. Imade, M. Imanishi, M. Honjo, H. Imabayashi, D. Matsuo, et al., Control of GaN crystal habit by solution stirring in the Na-flux method, Jpn. J. Appl. Phys. 56 (2017) 01AD05, https://doi.org/10.7567/JJAP.56.01AD05.

[115] K. Murakami, D. Matsuo, H. Imabayashi, H. Takazawa, Y. Todoroki, A. Kitamoto, et al., Effects of solution stirring on the growth of bulk GaN single crystals by Na flux method, Jpn. J. Appl. Phys. 52 (2013) 08JA03, https://doi.org/10.7567/JJAP.52.08JA03.

[116] F. Kawamura, M. Morishita, K. Omae, M. Yoshimura, Y. Mori, T. Sasaki, Novel liquid phase epitaxy (LPE) growth method for growing large GaN single crystals: introduction of the flux film coated-liquid phase epitaxy (FFC-LPE) method, Jpn. J. Appl. Phys. 42 (2003) L879−L881, https://doi.org/10.1143/JJAP.42.L879.

[117] T. Iwahashi, Y. Kitaoka, M. Kawahara, F. Kawamura, M. Yoshimura, Y. Mori, et al., Fabrication of a-plane GaN substrate using the Sr−Na flux liquid phase epitaxy technique, Jpn. J. Appl. Phys. 46 (2007) L103−L106, https://doi.org/10.1143/JJAP.46.L103.

[118] F.J. DiSalvo, M. Aoki, H. Yamane, M. Shimada, S. Sarayama, H. Iwata, Influence of 3d-transition-metal additives on single crystal growth of GaN by the Na flux method, Jpn. J. Appl. Phys. 42 (2003) 5445−5449, https://doi.org/10.1143/JJAP.42.5445.

[119] H. Imabayashi, K. Murakami, D. Matsuo, M. Honjo, M. Imanishi, M. Maruyama, et al., Effects of Al additives on growth of GaN polycrystals by the Na flux method, Opt. Mater. 65 (2017) 42−45, https://doi.org/10.1016/j.optmat.2016.09.030.

[120] Y. Konishi, K. Masumoto, K. Murakami, H. Imabayashi, H. Takazawa, Y. Todoroki, et al., Growth of prismatic GaN single crystals with high transparency on small GaN seed crystals by Ca−Li-Added Na flux method, Appl. Phys. Express 5 (2012) 025503, https://doi.org/10.1143/APEX.5.025503.

[121] M. Honjo, H. Imabayashi, H. Takazawa, Y. Todoroki, D. Matsuo, K. Murakami, et al., High-temperature growth of GaN single crystals using Li-added Na-flux method, Jpn. J. Appl. Phys. 51 (2012) 121002, https://doi.org/10.1143/JJAP.51.121002.

[122] K. Masumoto, T. Someno, K. Murakami, H. Imabayashi, H. Takazawa, Y. Todoroki, et al., The effects of Ba-Additive on growth of a-plane GaN single crystals using Na flux method, Jpn. J. Appl. Phys. 51 (2012) 0402031, https://doi.org/10.1143/JJAP.51.040203.

[123] S. Takeuchi, H. Asazu, M. Imanishi, Y. Nakamura, M. Imade, Y. Mori, et al., Dislocation confinement in the growth of Na flux GaN on metalorganic chemical vapor deposition-GaN, J. Appl. Phys. 118 (2015) 245306, https://doi.org/10.1063/1.4939159.

[124] S. Takeuchi, Y. Mizuta, M. Imanishi, M. Imade, Y. Mori, K. Sumitani, et al., Control of dislocation morphology and lattice distortion in Na-flux GaN crystals, J. Appl. Phys. 122 (2017) 105303−105307, https://doi.org/10.1063/1.4989647.

[125] M. Imanishi, Y. Todoroki, K. Murakami, D. Matsuo, H. Imabayashi, H. Takazawa, et al., Dramatic reduction of dislocations on a GaN point seed crystal by coalescence of bunched steps during Na-flux growth, J. Cryst. Growth 427 (2015) 87−93, https://doi.org/10.1016/j.jcrysgro.2015.07.001.

[126] E. Brown, U. Hommerich, T. Yamada, H. Yamane, J.M. Zavada, Spectroscopic characterization of Praseodymium doped Gallium Nitride powder prepared by a Na flux method, J. Alloy. Comp. 488 (2009) 628−631, https://doi.org/10.1016/j.jallcom.2008.11.029.

[127] T. Yamada, H. Nanbu, H. Yamane, K. Kohiro, Y. Tsuchida, Europium-doped gallium nitride prepared by Na flux method, Jpn. J. Appl. Phys. 45 (2006) L194−L196, https://doi.org/10.1143/JJAP.45.L194.

[128] A. Koukitu, S.-I. Hama, T. Taki, H. Seki, Thermodynamic analysis of hydride vapor phase epitaxy of GaN, Jpn. J. Appl. Phys. 37 (1998) 762−765, https://doi.org/10.1143/JJAP.37.762.

[129] T. Yoshida, Y. Oshima, K. Watanabe, T. Tsuchiya, T. Mishima, Ultrahigh-speed growth of GaN by hydride vapor phase epitaxy, Phys. Status Solidi C 8 (2011) 2110−2112, https://doi.org/10.1002/pssc.201000953.

[130] T. Hirasaki, K. Hanaoka, H. Murakami, Y. Kumagai, A. Koukitu, Thermodynamic analysis of InGaN-HVPE growth using group-III chlorides, bromides, and iodides, Phys. Status Solidi C 10 (2013) 413−416, https://doi.org/10.1002/pssc.201200695.

[131] T. Hirasaki, M. Eriksson, Q.T. Thieu, F. Karlsson, H. Murakami, Y. Kumagai, et al., Growth of thick and high crystalline quality InGaN layers on GaN (0001) substrate using tri-halide vapor phase epitaxy, J. Cryst. Growth 456 (2016) 145−150, https://doi.org/10.1016/j.jcrysgro.2016.08.019.

[132] K. Iso, K. Matsuda, N. Takekawa, K. Hikida, N. Hayashida, H. Murakami, et al., Thick nonpolar m-plane and semipolar 10-1-1 GaN on an ammonothermal seed by tri-halide vapor-phase epitaxy using GaCl3, J. Cryst. Growth 461 (2017) 25−29, https://doi.org/10.1016/j.jcrysgro.2017.01.005.

[133] H. Fujikura, T. Yoshida, M. Shibata, Y. Otoki, Recent progress of high-quality GaN substrates by HVPE method, in: J.-I. Chyi, H. Fujioka, H. Morkoc, Y. Nanishi, U.T. Schwarz, J.-I. Shim (Eds.), Spie Opto, SPIE, 2017, pp. 1010403−1010409, https://doi.org/10.1117/12.2257202.

[134] S. Goubara, T. Matsubara, K. Yukizane, N. Arita, S. Fujimoto, T. Ezaki, et al., Bulk GaN substrate with overall dislocation density on the order of 105/cm$^2$ fabricated by hydride vapor phase epitaxy, J. Cryst. Growth 478 (2017) 123−128, https://doi.org/10.1016/j.jcrysgro.2017.08.020.

[135] H. Fujikura, T. Konno, T. Yoshida, F. Horikiri, Hydride-vapor-phase epitaxial growth of highly pure GaN layers with smooth as-grown surfaces on freestanding GaN substrates, Jpn. J. Appl. Phys. 56 (2017) 085503−085510, https://doi.org/10.7567/JJAP.56.085503.

[136] K. Fujito, S. Kubo, H. Nagaoka, T. Mochizuki, H. Namita, S. Nagao, Bulk GaN crystals grown by HVPE, J. Cryst. Growth 311 (2009) 3011−3014, https://doi.org/10.1016/j.jcrysgro.2009.01.046.

[137] M. Imanishi, T. Yoshida, T. Kitamura, K. Murakami, M. Imade, M. Yoshimura, et al., Homoepitaxial hydride vapor phase epitaxy growth on GaN wafers manufactured by the Na-flux method, Cryst. Growth Des. 17 (2017) 3806−3811, https://doi.org/10.1021/acs.cgd.7b00388.

[138] T. Sochacki, Z. Bryan, M. Amilusik, M. Bobea, M. Fijalkowski, I. Bryan, et al., HVPE-GaN grown on MOCVD-GaN/sapphire template and ammonothermal GaN seeds

comparison of structural, optical, and electrical properties, J. Cryst. Growth 394 (2014) 55−60, https://doi.org/10.1016/j.jcrysgro.2014.02.020.
[139] M. Bockowski, M. Iwinska, M. Amilusik, M. Fijalkowski, B.L. Lucznik, T. Sochacki, Challenges and future perspectives in HVPE-GaN growth on ammonothermal GaN seeds, Semicond. Sci. Technol. 31 (2016) 093002, https://doi.org/10.1088/0268-1242/31/9/093002.
[140] T. Sochacki, M. Amilusik, B.L. Lucznik, M. Fijalkowski, J.L. Weyher, G. Nowak, et al., HVPE-GaN growth on misoriented ammonothermal GaN seeds, J. Cryst. Growth 403 (2014) 32−37, https://doi.org/10.1016/j.jcrysgro.2014.06.020.
[141] Y. Mikawa, T. Ishinabe, S. Kawabata, T. Mochizuki, A. Kojima, Y. Kagamitani, et al., Ammonothermal growth of polar and non-polar bulk GaN crystal, in: J.-I. Chyi, J.-I. Chyi, H. Fujioka, H. Morkoc (Eds.), SPIE Opto, SPIE, 2015, p. 936302, https://doi.org/10.1117/12.2078137.
[142] M. Iwinska, T. Sochacki, M. Amilusik, P. Kempisty, B.L. Lucznik, M. Fijalkowski, et al., Homoepitaxial growth of HVPE-GaN doped with Si, J. Cryst. Growth 456 (2016) 91−96, https://doi.org/10.1016/j.jcrysgro.2016.08.043.
[143] E. Richter, T. Stoica, U. Zeimer, C. Netzel, M. Weyers, G. Tränkle, Si doping of GaN in hydride vapor-phase epitaxy, J. Electron. Mater. 42 (2012) 820−825, https://doi.org/10.1007/s11664-012-2373-2.
[144] M. Iwinska, N. Takekawa, V.Y. Ivanov, M. Amilusik, P. Kruszewski, R. Piotrzkowski, et al., Crystal growth of HVPE-GaN doped with germanium, J. Cryst. Growth 480 (2017) 102−107, https://doi.org/10.1016/j.jcrysgro.2017.10.016.
[145] P. Hofmann, M. Krupinski, F. Habel, G. Leibiger, B. Weinert, S. Eichler, et al., Novel approach for n-type doping of HVPE gallium nitride with germanium, J. Cryst. Growth 450 (2016) 61−65, https://doi.org/10.1016/j.jcrysgro.2016.06.019.
[146] Y. Oshima, T. Yoshida, K. Watanabe, T. Mishima, Properties of Ge-doped, high-quality bulk GaN crystals fabricated by hydride vapor phase epitaxy, J. Cryst. Growth 312 (2010) 3569−3573, https://doi.org/10.1016/j.jcrysgro.2010.09.036.
[147] E. Richter, E. Gridneva, M. Weyers, G. Tränkle, Fe-doping in hydride vapor-phase epitaxy for semi-insulating gallium nitride, J. Cryst. Growth 456 (2016) 97−100, https://doi.org/10.1016/j.jcrysgro.2016.05.016.
[148] M. Iwinska, R. Piotrzkowski, E. Litwin-Staszewska, T. Sochacki, M. Amilusik, M. Fijalkowski, et al., Highly resistive C-doped hydride vapor phase epitaxy-GaN grown on ammonothermally crystallized GaN seeds, Appl. Phys. Express 10 (2017) 011003, https://doi.org/10.7567/APEX.10.011003.
[149] M.E. Zvanut, J. Dashdorj, J.A. Freitas Jr., E.R. Glaser, W.R. Willoughby, J.H. Leach, et al., Incorporation of Mg in free-standing HVPE GaN substrates, J. Electron. Mater. 45 (2016) 2692−2696, https://doi.org/10.1007/s11664-016-4413-9.
[150] A. Usikov, O. Kovalenkov, V. Soukhoveev, V. Ivantsov, A. Syrkin, V. Dmitriev, et al., Electrical and optical properties of thick highly doped p-type GaN layers grown by HVPE, Phys. Status Solidi C 5 (2008) 1829−1831, https://doi.org/10.1002/pssc.200778685.
[151] J.L. Weyher, T. Sochacki, M. Amilusik, M. Fijałkowski, B. Łucznik, R. Jakieła, et al., Photo-etching of HVPE-grown GaN Revealing extended non-homogeneities induced by periodic carrier gas exchange, J. Cryst. Growth 403 (2014) 77−82, https://doi.org/10.1016/j.jcrysgro.2014.06.009.
[152] F. Zimmermann, F.C. Beyer, G. Gärtner, C. Röder, N.T. Son, E. Janzén, et al., Origin of orange color in nominally undoped HVPE GaN crystals, Opt. Mater. 70 (2017) 127−130, https://doi.org/10.1016/j.optmat.2017.05.020.

[153] M.A. Reshchikov, A. Usikov, H. Helava, Y. Makarov, V. Prozheeva, I. Makkonen, et al., Evaluation of the concentration of point defects in GaN, Sci. Rep. 7 (2017) 9297, https://doi.org/10.1038/s41598-017-08570-1.

[154] A.Y. Polyakov, N.B. Smirnov, A.V. Govorkov, T.G. Yugova, H. Cox, A.S. Usikov, et al., Hydride vapor phase GaN films with reduced density of residual electrons and deep traps, J. Appl. Phys. 115 (2014) 183706−183707, https://doi.org/10.1063/1.4876061.

[155] J.A. Freitas Jr., J.C. Culbertson, N.A. Mahadik, T. Sochacki, M. Iwinska, M.S. Bockowski, HVPE GaN wafers with improved crystalline and electrical properties, J. Cryst. Growth 456 (2016) 113−120, https://doi.org/10.1016/j.jcrysgro.2016.06.052.

[156] J.Z. Domagala, J. Smalc-Koziorowska, M. Iwinska, T. Sochacki, M. Amilusik, B.L. Lucznik, et al., Influence of edge-grown HVPE GaN on the structural quality of c-plane oriented HVPE-GaN grown on ammonothermal GaN substrates, J. Cryst. Growth 456 (2016) 80−85, https://doi.org/10.1016/j.jcrysgro.2016.07.043.

[157] Semiconductor Technology Research Inc, http://www.str-soft.com/products/Virtual_Reactor/hepigans/.

[158] C.E.C. Dam, T. Bohnen, C.R. Kleijn, P.R. Hageman, P.K. Larsen, Scaling up a horizontal HVPE reactor, Surf. Coating. Technol. 201 (2007) 8878−8883, https://doi.org/10.1016/j.surfcoat.2007.04.009.

[159] X.-F. Han, M.-J. Hur, J.-H. Lee, Y.-J. Lee, C.-S. Oh, K.-W. Yi, Numerical simulation of the gallium nitride thin film layer grown on 6-inch wafer by commercial multi-wafer hydride vapor phase epitaxy, J. Cryst. Growth 406 (2014) 53−58, https://doi.org/10.1016/j.jcrysgro.2014.08.018.

[160] X.-F. Han, J.-H. Lee, Y.-J. Lee, J.-H. Song, K.-W. Yi, 3D numerical analysis of influence of the non-uniform deposition rate on the hillock density at HVPE-GaN surface, J. Cryst. Growth 474 (2017) 81−88, https://doi.org/10.1016/j.jcrysgro.2016.12.081.

[161] X.-F. Han, J.-H. Lee, Y.-J. Lee, J.-H. Song, K.-W. Yi, Numerical analysis on the origin of thickness unevenness and formation of pits at GaN thin film grown by HVPE, J. Cryst. Growth 450 (2016) 66−73, https://doi.org/10.1016/j.jcrysgro.2016.06.015.

[162] H. Suzuki, R. Togashi, H. Murakami, Y. Kumagai, A. Koukitu, Theoretical investigation on the decomposition process of GaN(0001) surface under a hydrogen atmosphere, J. Cryst. Growth 311 (2009) 3103−3105, https://doi.org/10.1016/j.jcrysgro.2009.01.096.

[163] C.G. Van de Walle, J. Neugebauer, First-principles calculations for defects and impurities: applications to III-nitrides, J. Appl. Phys. 95 (2004) 3851−3879, https://doi.org/10.1063/1.1682673.

[164] J.L. Lyons, C.G. Van de Walle, Computationally predicted energies and properties of defects in GaN, Npj Comput. Mater. 3 (2017) 180, https://doi.org/10.1038/s41524-017-0014-2.

[165] Y.N. Ahn, S.H. Lee, S.K. Lim, K.J. Woo, H. Kim, The role of inversion domain boundaries in fabricating crack-free GaN films on sapphire substrates by hydride vapor phase epitaxy, Mater. Sci. Eng. B 193 (2015) 105−111, https://doi.org/10.1016/j.mseb.2014.11.012.

This page intentionally left blank

# Growth of AlN and GaN crystals by sublimation

# 12

*E.N. Mokhov, A.A. Wolfson*
Ioffe Physical-Technical Institute of the Russian Academy of Sciences, St. Petersburg, Russia

## 12.1 Introduction

III nitride materials (AlN, GaN, InN, and their solid solutions) possess a unique combination of physical properties that guarantee demand for them in modern microelectronics and optoelectronics. Among these properties are wide bandgap, high saturated drift rate, high breakdown voltage, high thermal conductivity, remarkable chemical and thermal stability, etc. [1]. Due to these characteristics, nitrides are now considered as the most promising materials for fabrication of powerful high-frequency transistor structures capable of functioning at high temperatures and in hostile environments. Devices of this kind can be used in wireless communication systems, switching systems in the power industry, detectors for early detection of chemical or biological infection, etc. However, the greatest expectations in connection with development of nitride technologies relate to solid-state light sources, including shortwave light-emitting diodes (LEDs) and lasers of visible and ultraviolet (UV) ranges, and also basic UV elements of bright “white” LEDs [2]. One of the main applications of the AlN substrate is in the manufacture of powerful high-frequency transistors and photodetectors, including solar blind detectors capable of working at high temperatures and in harsh environments.

## 12.2 Methods of AlN and GaN bulk crystal growth

A considerable number of publications devoted to growth of bulk Al and Ga nitride crystals have resulted in excellent reviews [3–5]. A number of different growth methods are used, such as physical vapor transport (PVT), hydride vapor phase epitaxy (HVPE), high nitrogen pressure solution (HNPS) growth, ammonothermal growth, flux growth, and solution growth. These methods are discussed in detail in reviews [6,7], and short descriptions are given below.

The disadvantages of the majority of these methods are to a large extent caused by their rather low growth temperatures, at which formation of a large number of individual crystallization nuclei on the substrate surface is possible. Additionally, growth is carried out in the presence of chemical and active impurities, which can form inclusions as secondary phase and reduce the material quality. Under these conditions, coalescence of the nucleation centers in the chemosorbate layer does not end completely due to the low rate of surface diffusion. The sublimation growth method makes it possible to grow crystals without use of active foreign impurities on the surface.

**Single Crystals of Electronic Materials.** https://doi.org/10.1016/B978-0-08-102096-8.00012-4
Copyright © 2019 Elsevier Ltd. All rights reserved.

HVPE is to date the main growth method for GaN crystals, while bulk AlN crystals are mainly grown by sublimation (PVT).

The major issue in developing a new generation of nitride-based devices is the lack of native high-quality GaN and AlN wafers of the required sizes (>2 inch in diameter) [5,6]. Therefore substrates of other materials, such as SiC or sapphire, are often used for growth of bulk nitride crystals along with native crystals.

## 12.3 Goals of the present review

This chapter reviews the growth of Al- and Ga- nitrides on SiC seeds by the sublimation sandwich method (SSM) mainly carried out at the A. Ioffe Institute. We discuss the results of experimental investigations of sublimation growth of AlN and GaN crystals; for theoretical analysis the reader can refer to our earlier reviews [6–8]. Sublimation growth of AlN and GaN bulk crystals is difficult due to the strong binding energy of molecular nitrogen and the high chemical activity of vapor species. The reasons for acceleration of AlN crystal growth rate when silicon and carbon vapors are introduced into the growth system are discussed, and the recently developed technique of sublimation growth of AlN with simultaneous evaporation of the SiC seed is presented.

## 12.4 The sublimation sandwich method (SSM)

SSM is one of the modifications of PVT growth. In this method, first proposed in 1970 for growth of SiC crystals, the distance between the source and the seed maintains a ratio of 0.2 with respect to the linear sizes of the source[9]. The narrow gap in the sandwich cell promotes mass transfer from the source to the substrate by laminar streams, while the supersaturation remains almost constant over the whole surface of the growing crystal. Due to the relative isolation of the growth cell, the composition of the inner vapor is close to equilibrium, which promotes growth of crystals of homogeneous composition in a wide range of temperatures and pressures. For example, growth of single crystalline SiC by SSM is possible in the wide temperature range of 1600–2600°C, at various pressures of inert gas or in a vacuum. It is also possible to conduct growth simultaneously in several cells and to control the influence of temperature and supersaturation on kinetics and the growth mechanism.

The possibility of growth through evaporation across small gaps (and therefore low supersaturations) reduces the probability of formation of incoherent three-dimensional (3D) inclusions that negatively affect the structural perfection of the growing crystal [10]. At the same time, losses of crystallized material sharply decrease, which is especially important in growth of crystals with a certain isotope structure where rather expensive sources are used. In systems with several temperature zones SSM can be used for growth of both pure and doped crystals, with a concentration of impurities close to the solubility limit.

The growth rate in SSM significantly depends on the temperature, supersaturation, and vapor pressure as well as on the spacial gap between the source and the seed.

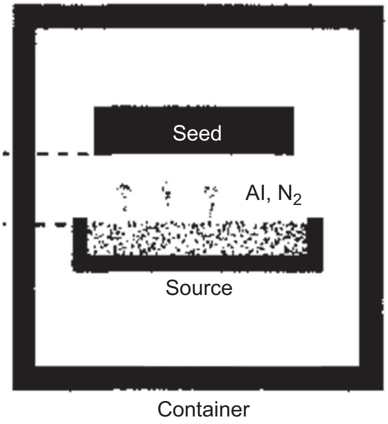

**Figure 12.1** Sketch of crucible for single crystal growth by the sublimation sandwich method.

If the mass-transfer mode is limited by diffusion at a minimal gap, a sharp intensification of vapors transfer from source to seed can be achieved. This allows growth of crystals at high rates without the use of a transporter, even in cases of low vapor pressure. SSM was originally used for growth of SiC crystals; further modifications of the method were suggested for growing GaN [11] and AlN [12] crystals. A schematic diagram of the cells used for SSM growth is shown in Fig. 12.1.

It should be noted that the source of vapors can be polycrystalline powder and, if necessary, single crystal powder, a solid ingot of the same material, or a mix of its components. So to grow GaN crystals GaN powder, metal gallium, and their mixture were used. What is more, SSM growth of crystals can be carried out with simultaneous evaporation of the seed. We initiated the growth of crystals and epitaxial layers of GaN and AlN in 1980. Today, the method of small-gap sublimation growth of nitrides is widely employed worldwide [3,13,14].

### 12.4.1 Sublimation growth of AlN bulk crystals

For growth of ingots, single crystal seeds of the same material are usually used. However, for nitrides considerable attention is paid to heteroepitaxial growth on alien seeds, mainly due to the lack of high-quality seeds of these materials with the desired cross-section of 2 inch or more. Expansion of crystals of smaller size up to the requested dimension is in principle possible, but it demands considerable efforts.

#### 12.4.1.1 Growth on AlN seeds

Spontaneously nucleated freestanding AlN needles, several millimeters long, were for the first time grown by Edgar [15] in 1976. The growth was carried out in a tungsten crucible at a temperature of about 2200°C. The grown crystals had very high structural perfection, but their practical use was limited by the small size of the crystals. Further attempts focused on increasing the crystal sizes. For this purpose, self-seeding deposits of AlN were made on nonoriented seeds (for example on a Ta disc surface), with subsequent selection and expansion of separate grains cut out from the polycrystalline deposit [16–18]. Growth was carried out at low supersaturation, which produced larger crystals, typically of millimeters in size. Very perfect AlN crystals, 15 mm in diameter and 15 mm high, were grown [17]. The full width at half maximum (FWHM) of the double crystal rocking curves decreased from 78 arcsec at the start of growth to 13 arcsec at growth end. At the same time, the crystals had low content of oxygen and carbon impurities (less than $1 \times 10^{19}\ \mathrm{cm}^{-3}$). AlN crystals of similar size and quality were grown by Hartmann et al. [19]. Unfortunately, by self-seeding, and subsequent freestanding growth it is difficult to grow high-quality crystals with a diameter of more than 2 inches. This is obviously connected with the low rate of lateral expansion of AlN crystals in comparison with the expansion rate of, for example, SiC crystals.

### 12.4.1.2 Growth on SiC seeds

Large AlN crystals are easier to grow on foreign seeds. Crystals with the same type of lattice and a low lattice and thermal mismatch must be used as seeds. Such crystals have to be stable and not degrade at the growth temperatures of nitrides. It is most desirable that the growth temperature of the seed crystals does not differ considerably from those of nitrides.

For these reasons, 4H or 6H SiC seeds are usually used. Such crystals, with dimensions of 10 × 10 mm, were obtained for the first time by Balkas [20] in 1997. In that work, growth was carried out by the sublimation method at the temperature of 1950–2150°C in graphite furnaces under nitrogen pressure of 0.5 atm. It was noted that high growth rates (up to 0.5 mm/h) are reached at high temperatures and with small gaps (about 4 mm) between the source and the seed. The color of crystals differed from transparent to dark blue, which was related to the influence of Si and C impurities. However, this conclusion concerning the influence of Si and C on the color of an AlN crystal was not confirmed in later works. So far 2-inch AlN crystals on SiC seeds have been produced [21,22].

In heteroepitaxial growth, especially in the course of cooling, high thermoelastic stress develops near the phase boundary, leading to formation of cracks and dislocations in the grown crystal. Data on the lattice parameters and thermal expansion coefficients (TECs) of Ga and Al nitrides compared with SiC, the most widely used seed material, are given in (Table 12.1).

Differences in lattice parameters, and especially in TEC values, cause tensions at the phase boundary of the seed and the growing crystal, leading to increased dislocation density and emergence of cracks. It is possible to reduce these tensions by heteroepitaxial growth in the following ways.

1. Increase the grown ingot length. By increasing the ingot length up to 10 mm or more it is possible to produce highly perfect crystals without cracks and with a low dislocation density, of about $5 \times 10^{4}\ \mathrm{cm}^{-2}$ [23]. X-ray measurements show that such crystals have FWHM of about 75–100 arcsec [24,25]. Furthermore, the increase of the ingot length leads to reduced content of Si and C impurities [26,27].

**Table 12.1** Lattice constants and thermal expansion coefficients

| Material | TECx $10^{-6}$ $K^{-1}$ | | Lattice constants | | Ref. |
|---|---|---|---|---|---|
| | **Δa/a** | **Δc/c** | **a** | **c** | |
| 6H SiC | 4.3 | 4.7 | 3.073 | 15.12 | [107] |
| AlN | 4.2 | 5.3 | 3.112 | 4.982 | [107] |
| GaN | 5.89 | 3.17 | 3.189 | 5.185 | [107] |

2. Use of buffer layers previously grown on the seed by other methods, for example HVPE [28].
3. Lift-off or removal of the substrate during growth or cooling of the crystal [29].

The techniques mentioned above certainly give a positive effect, but crystals grown on foreign seeds exhibit lower structural perfection in comparison to freestanding crystals. Moreover, the use of foreign seeds leads to contamination of the crystal by undesired impurities, and the content of silicon and carbon in thick crystals is at the level of 3%, which is more than 10 times higher than in growth on native seeds.

### *12.4.1.3 Issues in sublimation of bulk AlN crystals on SiC seeds*

#### Low nitrogen sticking coefficients

A large number of works, both theoretical [30–32] and experimental [33,34], are devoted to studying sublimation growth kinetics. It is often supposed that the equilibrium vapor over AlN consists only of atoms of metals and molecules of nitrogen ($N_2$), but this conclusion is not universally accepted. For example, according to one calculation [35] the equilibrium vapor over AlN also contains the species $Al_3N$, $Al_4N$, and $Al_2N$, which can participate in AlN mass transfer. In addition, in a real system containing impurities, for example atoms of oxygen or carbon, the probability of formation of various bonds with nitrogen atoms sharply increases. However, in this case a considerable portion of nitrogen exists in the form of $N_2$ molecules. Transfer of metal is problematic only for GaN, due to the low steam tension of Ga vapor at the growth temperature of this compound, which does not exceed 1200°C. In AlN growth temperatures of 1900–2300°C the steam tension of Al vapors is rather high and thus it is thought that the Al sticking coefficient is close to 1. In contrast, the sticking coefficient of the molecular nitrogen is very small, about $10^{-5}$–$10^{-6}$ at AlN growth temperatures [31,36].

Nitrogen molecules are extremely strong and their lifetime on the surface of the growing crystal is very short [32]. This causes low $N_2$ molecule condensation by sublimation growth. Low efficiency of nitrogen sticking is the reason why sublimation growth of nitrides (unlike SiC growth) is difficult to realize in an inert atmosphere. Nitride crystals are usually grown in a nitrogen-ambient atmosphere ($N_2$ or $NH_3$), with rather high partial pressures of nitrogen (considerably higher than the equilibrium pressure). In case of GaN sublimation, growth is possible only with introduction of active nitrogen ($NH_3$). A low nitrogen sticking coefficient widens the range of nitrogen pressures at which the growth rate is not diffusion limited but rather determined by superficial reactions. When the growth process is limited by diffusion in the gas phase [37], the following relation holds:

$$V_g \sim P^{-1} \tag{12.1}$$

where $V_g$ is growth rate and P is nitrogen pressure.

In contrast, a $V_g$ increase with pressure indicates that the surface molecular kinetic becomes the growth-limiting factor [31].

### High reactivity of vapors

The second problem arising in growth of nitrides is caused by the high chemical activity of metal vapors (especially Al vapors) in relation to the container material. This greatly limits the choice of materials for containers. A list of possible materials suitable for growth of AlN crystals is given in Table 12.2 [38,39].

The most popular are containers made of tungsten and tantalum carbide (TaC), but tungsten crucibles cannot be used for growth on SiC seeds as they form low-temperature eutectics with SiC vapors. It should be noted that TaC growth in clean conditions (in the absence of oxygen) provides the minimum chemical contamination of the growing crystal [40]. For comparison, AlN crystals grown in tungsten containers contain second-phase inclusions [41]. Chemical analysis has shown that precipitates

**Table 12.2** **Materials using for AlN bulk growth**

| N | Elements or compounds | T Boiling (°C) | Way of preparing | Advantages | Disadvantages |
|---|---|---|---|---|---|
| 1 | TaC | 3950 | Powder pressing and high-temperature annealing | High thermal stability | Brittleness |
| 2 | Ta | 2996 | Carbonization | High strength: may be used many times in growth processes | Long annealing time is necessary |
| 3 | W | 3410 | | Stable | Liquid eutectics with C and Si |
| 4 | BN | 3000 | | Stable | Diminishing growth rate |

contain tungsten as well as carbon and oxygen, and the presence of precipitates leads to increased dislocation density in the crystal. Thus growth of AlN on SiC seeds is preferably carried out in crucibles made of Ta or TaC. The design of these containers is described in earlier works [22,42].

We should note that Ta crucibles have been developed for growth of SiC crystals and then successfully applied for growth of AlN crystals. It is impossible to use Ta crucibles directly, because vapors of both Al and Si interact with Ta and form liquid eutectics. Therefore, prior to use, Ta crucibles are exposed to high-temperature annealing in a graphite environment. Annealing at 2300−2500°C for 50 h or more is effective in producing a reaction between Ta and carbon to form TaC. Containers prepared in this way have rather high stability. Since TaC is a very fragile material, to increase the durability of TaC crucibles, they are embedded in a dense graphite glass. Such binary crucibles have kept high tightness in the course of crystal growth at temperatures of 2000−2150°C for 500 h and more.

## Low AlN evaporation coefficients

It is known that sublimation of nitrides is a rather difficult process, and to correlate experimentally observed rates of evaporation with theoretical estimates it is necessary to introduce kinetic restrictions in the form of evaporation coefficients. Evaporation coefficients for nitrides are extremely low, and are in the limits of $10^{-3}$−$10^{-5}$ [43]. However, the real system contains impurities like oxygen and carbon, which can very significantly influence AlN mass transfer.

## The influence of residual oxygen

Nitrides of gallium and especially aluminum easily oxidize in air, so commercial powders of nitrides always contain a large amount of oxygen (about 10%). This percentage is unacceptable, as the presence of oxygen affects the quality of grown crystals negatively. Thus prior to growth the powder of nitrides to be used as a source is annealed for a long time in an atmosphere of pure nitrogen. In the process of powder recrystallization a considerable part of the oxygen is removed in form of volatile oxides. Thermal cleaning of the starting powder source takes many hours, but it is possible to reduce the oxygen content by an order of magnitude or more. Even higher purification can be reached by AlN powder resublimation onto an AlN polycrystalline substrate carried out in a clean tungsten container [42].

The sublimation rate of polycrystalline AlN of various origins was studied by placing the different powders in TaC containers intended for growth of AlN crystals and then heating at 1800−2300°C for 1−10 h. At a temperature of 1800°C the annealing is carried out in vacuum, and at higher temperatures in a nitrogen environment. The rate of evaporation is controlled by the change of weight and thickness of the initial crystal.

The evaporation rate of three types of polycrystalline AlN source:

1. Commercial AlN powder with high oxygen content.
2. Synthesized AlN powder previously annealed at a temperature of 2100°C.
3. Sublimated AlN deposited on to a nonoriented TaC substrate at a temperature of 2200°C.

**Table 12.3** **Evaporation rates of the different types of AlN samples ($T_e$ = 2050°C)**

| **Type of AlN samples** | **Commercial before annealing** | **Synthesized at temperature $T_a$ = 2100°C, 10 h** | **Sublimed AlN** | **Sublimed AlN** |
|---|---|---|---|---|
| Evaporation conditions | $T_e = 2050°C$<br>$P_{N2} = 1$ bar<br>Without SiC | $T_e = 2050°C$<br>$P_{N2} = 1$ bar<br>Without SiC | $T_e = 2050°C$<br>$P_{N2} = 1$ bar<br>Without SiC | $T_e = 2050°C$<br>$P_{N2} = 1$ bar<br>AlN + SiC |
| Ve, mg/h | 400 | 80 | 30 | 180 |

was studied and the results for the rate of evaporation of various types of sources are shown in Table 12.3.

It is clear that there is an essential difference in evaporation rates. AlN powders with increased oxygen content have the highest evaporation speed. In previously synthesized samples the evaporation rate significantly decreases, obviously explained by the reduction of the oxygen content in the annealed samples. We should note that the temperature increase and the time of the AlN source annealing lead to reduction of the evaporation rate. The sublimated AlN source, with the lowest oxygen content, has the lowest rate of evaporation. Thus the theoretical predictions that oxygen, being an AlN carrier, accelerates mass transfer are confirmed. According to theoretical models, mass transfer is carried out with participation of $Al_2O$ and AlO molecules and is especially effective at $T < 1850°C$ [6].

Further studies of AlN growth using sources with different content of oxygen have shown that the quality of the growing crystal gets worse with the increase of oxygen content in the source. Thus for AlN growth it is desirable to use the cleanest possible source. It is simpler to prepare this clean starting source by sublimation, because cleaning of oxygen in the course of annealing is not effective due to the considerable losses of material and time.

### The influence of silicon and carbon

The crystals obtained by growing AlN on SiC seeds always contain Si and C impurities at a level of 3%–6%. Their origin is probably the seed crystal. The high content of these impurities in the vapor phase necessitates studying their role in AlN mass transfer. To this extent, comparative experiments on the influence of Si and C on the processes of sublimation and condensation were carried out. In the first group of experiments, sublimation of AlN from clean containers and containers containing a certain amount of SiC was studied. These studies revealed an essential increase in the rate of AlN evaporation by SiC introduction (Table 12.3). Obviously, due to the increased AlN sublimation rate in the presence of SiC, the condensation rate also increased. As a result, identical growth rates were reached in the presence of SiC vapors at temperatures 150–200°C lower. The result correlates with reported data [3,6].

It was supposed that the higher mass transfer is caused by the presence in the sublimation zone of volatile compounds, AlN and $Si_2N$. To understand the increased speed of AlN evaporation in the presence of SiC, comparative experiments on evaporation of single crystal samples of AlN were carried out: bulk AlN crystals of different structural perfection with diameters of 15−50 mm were selected and placed in a TaC plate inside a closed TaC container. In this way a number of features of evaporation of such samples caused by the presence of SiC in the system were revealed.

As in the case of polycrystalline AlN, the rate of bulk AlN was higher if jointly evaporated with SiC. However, additional features of evaporation connected with crystal quality were revealed. With no SiC in the container, AlN samples evaporated almost isotropically, but with addition of SiC evaporation had a selective character, resulting in enhanced near-structural and morphological defects of the crystal. Deep pits were formed at these places, which quickly transformed into threading pores (Fig. 12.2).

It is difficult to explain the selective nature of evaporation as being due only to activation of the process of mass transfer by active agents in the gas phase. It is more correct to explain it by the presence of a liquid phase (specific surfactant) on the surface, leading to a sharp decrease in kinetic restrictions by sublimation evaporation. To get direct confirmation of the existence of a liquid phase on the surface of the evaporated crystal, experiments were made, in which the furnace was cooled down rapidly (Fig. 12.3).

The liquid phase is obviously formed on both evaporated and growth surfaces. It can exist on the surface in the form of a thin layer or as separate drops. Formation of a uniform thin layer is in general favorable for crystal growth, since coalescence of the generated nuclei is facilitated and thus their density decreases, promoting a layer-by-layer mechanism of growth.

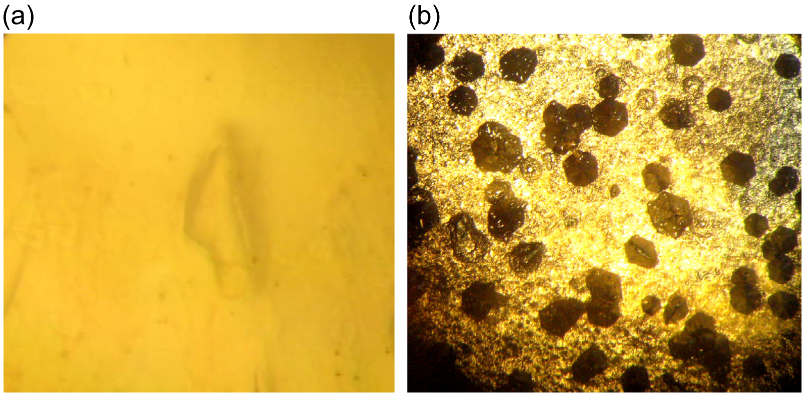

**Figure 12.2** Surface morphology of evaporated (0001) N face of AlN single crystals observed with optical microscopy. The samples were annealed in a closed TaC container without SiC (a) and with SiC (b). The temperature of annealing is 2010°C. $N_2$ pressure is 0.3 bar. Selective etching is observed due to presence of Si + C vapors.

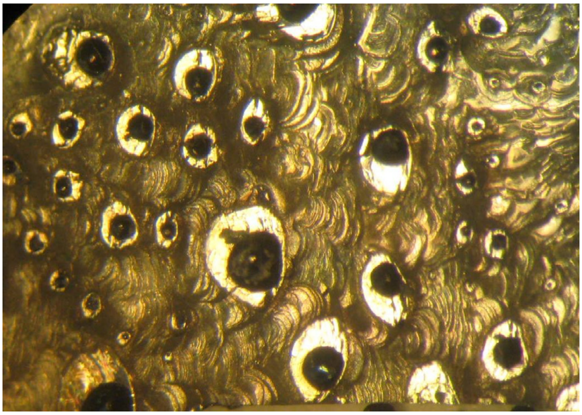

**Figure 12.3** Surface morphology of evaporated (0001) N face of AlN crystal after quick cooling observed with optical microscopy (photo). The AlN crystal was annealed in a closed TaC container simultaneously with SiC. The temperature of annealing is 2010°C. $N_2$ pressure is 1 bar. Spherical drops are observed on the surface of the AlN crystal.

The possibility of forming the liquid phase by annealing AlN with SiC was also tested [44,45], whereby the formation of the compounds $Al_2OCx$ and $Al_2OC \cdot 2AlN$ with a melting temperature in the range of 1950−2050°C was thought to take place. In the process of growth these compounds melt and promote an increased rate of sublimation and condensation (a mechanism of vapor−liquid−solid). However, emergence of big drops on the growth surface obviously leads to deterioration in the growth quality. These big drops result in evaporation and void formation underneath (the bigger the drop, the faster the evaporation). In this case, morphological and structural defects appear on the growth surface. The dependence of kinetic factors of sublimation on impurity concentration leads to an unstable sublimation process and variations in sublimation rate. It results in worse crystal quality.

### *12.4.1.4 Growth process of AlN crystals*

The AlN crystals were grown in a high-vacuum resistor furnace with a graphite heater [42,46]. A large number of viewing ports in the furnace enable reliable control of temperature and estimation of supersaturation in the working volume. A Ta container with a surface layer of TaC created by special annealing in contact with a carbon may be used, or a TaC container created by pressing TaC powder. The first type is faster to make, more stable, and more leak-tight, but in the process of service cracks appear and leakage arises. The second type does not react with Al vapor, but is more fragile and less leak-tight. Polycrystalline AlN powders obtained by sublimation of the synthesized AlN powder previously annealed at temperature of 2100°C were used as a vapor source. In the process of sublimation a considerable decrease of oxygen concentration in the source (10−30 times) was achieved.

Crack-free and micropipe-free 4H and 6H SiC wafers with low dislocation density ($1-4 \cdot 10^3$ $cm^{-2}$) were employed as seeds. The SiC crystals were polished and etched

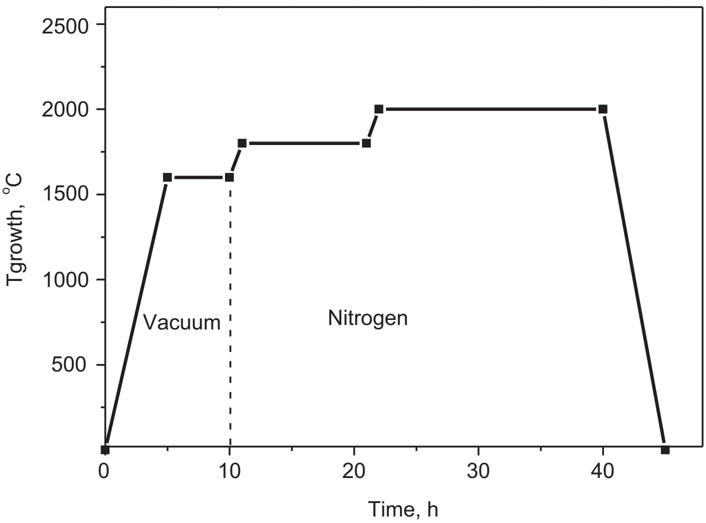

**Figure 12.4** Diagram of a typical process for the growth of AlN using the SiC evaporation method. During the first stage the source (polycrystalline AlN powder) is annealed in a vacuum at a temperature of 1650°C to reduce the addition of oxygen impurities. The main stages of growth are performed at 2000°C in a nitrogen atmosphere under a pressure of 0.3 bar.

in KOH melt. The growth was carried out on planes (0001) C or (0001) Si, with angles of off-orientation to the basal face of up to 3 degrees. The wafer orientation strongly influenced the growth kinetics and the quality of the grown crystal. The gap between the source and the substrate is typically 5—10 mm, while the source-to-seed temperature difference may change from 20 to 40° C.

A diagram of a typical process for the growth of AlN bulk crystals is shown in Fig. 12.4.

Prior to the start of growth, the growth chamber must be annealed in a high vacuum at a temperature over 1600°C, and after that for more than 10 h in an $N_2$ atmosphere at 1800°C. At this time $O_2$ evacuation and growth of a thin AlN buffer layer take place. The buffer layer reduces the tension in the interface and prevents SiC local dissociation at higher growth temperatures. The main stage of growth of AlN crystals is performed at temperatures of 1950—2120°C under nitrogen backpressure of 0.3—1 bar, and the growth rate increases from 0.05 to 0.2 mm/h.

## Optimization of the growth zone

The dependence of the growth rate of AlN on the temperature and temperature differences is reported in a number of works devoted to kinetics of sublimation mass transfer. However, this data is not sufficient to optimize the zone of crystal growth, as it is necessary to consider the kinetic factors limiting the process of mass transfer, depending on the growth conditions, the stability of the crucible, and the orientation of the growth surface.

The optimum growth zone was defined experimentally by the simultaneous use of several sandwich cells (usually four or five), located in a single container along the heater axis [47]. Each cell consists of a TaC crucible filled with AlN source and a substrate on which the AlN deposit is assessed. The growth temperature, the temperature difference between the AlN powder source and single crystal seed, and the ambient nitrogen pressure are varied to find the optimal growth conditions. The rates of evaporation and condensation of AlN and the mass transfer coefficient are defined considering the rate of the transferred substance from the source to the seed. The results of measurements are given in Fig. 12.5. The distribution of temperatures along the heater axis is also shown.

It is apparent that the growth rate does not change monotonically with the position of the cell. The maximum growth rate is observed in cell No. 2. A lower growth rate in the top cell is obviously explained by the lower temperature. However, in the lower cells (Nos 3 and 4) the temperature increases, and the condensation rate and transfer coefficient decrease. From this experimental data it is possible to conclude that the

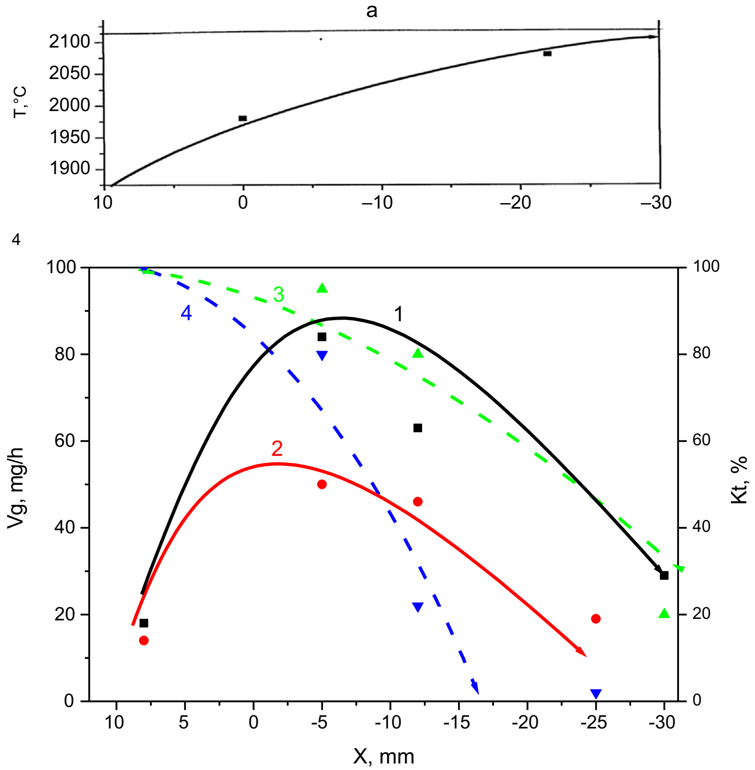

**Figure 12.5** Dependence of AlN growth rate (1,2) and source-to-seed mass-transfer coefficient (3,4) on the substrate's distance from the heater but at different nitrogen pressure ($P_{N2}$): 1 bar (1,3); 0.3 bar (2,4). Four growth cells are used. Axial temperature distribution in the heater is shown (a).

effective mass transfer of AlN requires not only a certain temperature but also a gradient of temperatures (i.e., supersaturation). If the gradient is below a certain limit the growth rate sharply decreases. Evidently, nitrogen sticking is more effective at high supersaturations. It is observed that when reducing the nitrogen pressure the zone of optimum growth moves toward bigger temperature differences. At very high temperature differences, the growth of AlN can be carried out at a low nitrogen pressure of $P < 0.1$ mmHg, and even in vacuum.

### Dependence of AlN growth rate on nitrogen pressure

The dependence of the growth rate on temperature, temperature gradient, and nitrogen pressure was investigated theoretically [30,31,37]. Great attention was paid to dependence on nitrogen pressure. The experiments show that it is possible to increase the growth rate by one order of magnitude only by decreasing nitrogen pressure [48,49]. The study also revealed that surface kinetic or diffusion-limited growth may take place [31,36]. In the case of diffusion-limited growth, nitrogen pressure reduction leads to increased growth rates (see Fig. 12.6).

However, at low $N_2$ pressures the growth rates are lower than the calculated rates [31]. As a rule, at close source-to-seed distance we have a wider growth window. For example, high-quality AlN crystals may be grown at lower nitrogen pressures than theoretically estimated [32], at pressures of 0.1—0.2 bar. Attempts at AlN growth at lower $N_2$ pressures or in inert gas media and vacuum were unsuccessful because of the poor crystal quality. An increase of pore density was observed at small supersaturations, probably because of the very low low nitrogen sticking coefficients ($K_N \sim 10^{-5}$ [31]).

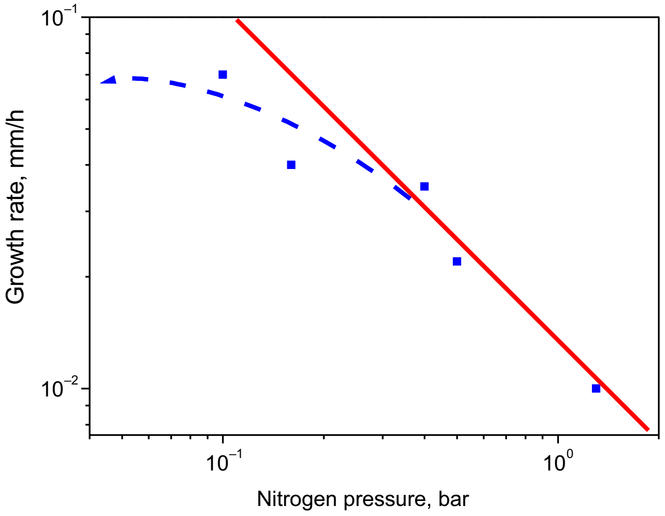

**Figure 12.6** Dependence of AlN growth rate on nitrogen pressure. Growth temperature Tg = 1960°C; ΔT/δ = 5 K/mm. Source-to-seed gap is 10 mm, ——— calculated curve [31] - – – – - experimental points (fitted by broken line).

The dependence of the growth rate on nitrogen pressure (Fig. 12.6) shows that it steadily increases as the pressure in the reactor decreases in a wide pressure interval of 0.02–1 bar. This suggests that the key role in the layer growth kinetics is played by the source-to-substrate diffusion of the components (Al, N), rather than by the adsorption–desorption processes on the source and substrate surface. The growth rate in argon is indeed much higher than in nitrogen when high pressures are used, and is nearly the same for lower pressures (0.02–0.05 bar).

### Dependence of AlN growth rate on source-to-seed distance

One of the most important parameters of the growth process is the clearance between the source and the substrate on to which the AlN layer is deposited. This quantity to a great extent determines which mechanism is dominant in the transport of source components to the substrate: diffusion, kinetic effects (i.e., absorption–desorption processes on the surface of the source and substrate) or their superposition, and finally the overall growth rate. Theoretically, the dependence of the layer growth rate on the key growth parameters (temperature, gas medium pressure, temperature gradient in the source–substrate clearance, and the size of the clearance itself) have been considered in detail [31,50]. However, there is no published experimental data for the effect of the source–substrate clearance on the AlN layer growth rate. When the diffusion model applies, the following formula is suitable to describe the growth rate as a function of the clearance $h$ [51]:

$$V_g = D_i \Delta P_i / RT_{ss} h, \text{ i.e.} V_g \sim 1/h \tag{12.2}$$

where $D_i$ is the diffusivity of the i-th component of the source, $\Delta P_i$ is the difference in the concentration of the i-th component on the surfaces of the source and the substrate, and $T_{ss}$ is the half sum of the temperatures on these surfaces.

In Fig. 12.7 the experimental dependences of the layer growth rate on the source–substrate distance are given for three nitrogen pressure values in the reactor: 1 bar (curve 1), 0.6 bar (curve 2), and 0.3 bar (curve 3).

Comparing these with theoretical data [31], it is argued that at large source-to-seed distances (>2–3 mm) they are diffusion limited, but at smaller distances, when we observe diminishing of $V_g$, it is necessary to take into account the kinetic factors. The same effect was observed in case of SiC sublimation [50].

### Substrate orientation

Bulk AlN crystals are usually grown on the (0001) Si face of the substrate. Such growth is assumed to be more perfect than growth at the (0001) C face. Actually, Si-face growth always results in formation of an Al polar surface but C-face growth results in formation of inversion domains [52,53]. So on the Si face a step-flow growth mode usually takes place and on the C face a spiral growth mode dominates [28]. C-face-grown crystals have broader X-ray diffraction rocking curves (FWHM), which indicate the presence of higher numbers of misfit dislocations. At the same time these crystals have lower concentrations of Si and C impurities as compared to crystals

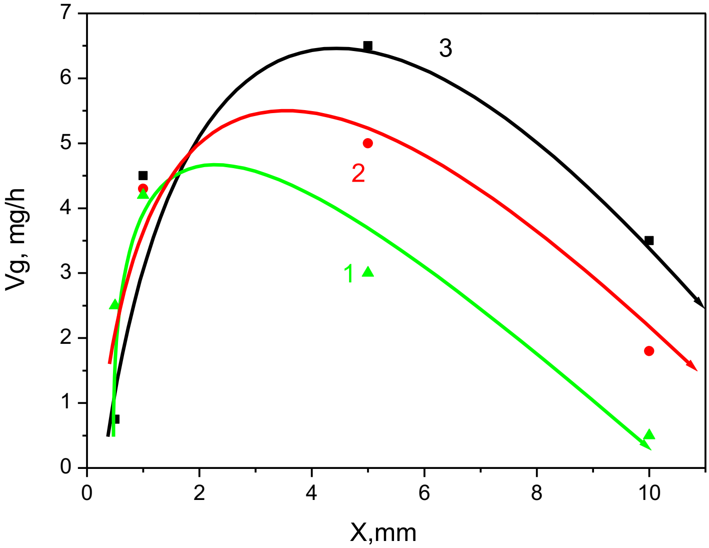

**Figure 12.7** Dependence of AlN growth rate on source-to-seed clearance at different nitrogen pressure ($P_{N2}$): 1—1 bar; 2—0.3 bar; 3—0.1 bar. Growth temperature is 2050°C.

deposited on the Si face. This is the result of the sharper phase SiC—AlN boundary for C-face growth. It is believed that for C-face step-by-step growth lower supersaturations are necessary. This is confirmed by results [54,55] where perfect layers were grown on the C face of SiC substrates.

## Characterization

AlN bulk crystal growth conditions are presented in Table 12.4, compared with the growth parameters for SiC crystals.

There are essential differences: high-quality AlN growth is possible only in $N_2$ at $P_{N2}$ higher than 0.1 atm; in contrast, SiC crystals can be grown in a vacuum or in inert gas.

The AlN growth window is relatively narrow. At temperatures higher than 2050°C SiC is decomposed (upper limit), and at temperatures below 1950°C the source sublimation rate is too low (lower limit). Additionally, the AlN growth rate strongly depends on temperature, due to the very high activation energy of AlN crystallization ($\Delta E$), which is ~ 645 kJ/mol. Thus small temperature fluctuations result in severe perturbations of the growth rate. The temperature difference between the source and the seed also affects the growth of AlN crystals. Unlike SiC, a higher temperature gradient is preferred for growth of AlN bulk crystals, as at small supersaturations the pore density increases.

The properties of AlN bulk crystals grown on SiC seeds have been described in ref. [55]. In optimal growth conditions the growth surface of AlN crystals is slightly convex, smooth, and covered by microsteps (Fig. 12.8). FWHM values are less than 180 arcsec and the dislocation density is less than $1 \times 10^{-5}$ cm$^{-2}$. The number of

**Table 12.4** **Relative properties of 2 inch AlN and SiC bulk crystals grown by sublimation on SiC seeds**

| Parameters | AlN | SiC | Metric method |
|---|---|---|---|
| Polytype | 2H | 6H, 4H, 15R, 3C | X-ray |
| Crack density ($cm^{-2}$) | $10^1$ | Low | Optical microscopy |
| Porous (micropipes) density ($cm^{-2}$) | $10^1$ | $10^1$ | Optical microscopy |
| Dislocation density ($cm^{-2}$) | $10^4$–$10^5$ | $10^3$ | Etch pit density |
| FWHM, arcsec | 70–300 | 40 | X-ray diffraction |
| Color | Yellow, amber, blue, green, depending on growth conditions | Green, blue, depending on concentration of impurities | Optical spectrum |
| Doping impurities | Si, C, O | N, Al, B | SIMS |
| Average reproducibility of high-quality crystal growth (%) | 62 | 94 | Optical microscopy, X-ray diffraction |

growth centers for layer growth is very small. Such surface morphology is typical of layer-by-layer growth. The same morphology is observed on the SiC as-grown surface.

At nonoptimal growth conditions, new 3D centers arise on the surface, in the shape of pyramids or cones. As a result, the smooth surface becomes uneven and rough, and the crystal quality becomes abruptly worse. Different factors lead to deterioration of the surface morphology; high oxygen contamination is one of them. At elevated oxygen concentration, an increase of Ta impurity was measured by SIMS (Secondary Ions Emission Mass Spectroscopy) in the AlN crystals.

Cracks are the most typical defects observed in AlN deposited on SiC seeds. Considerable tension arises near the crystal interface during cooling of the furnace, which leads to crystal bending and crack formation, mainly in AlN, despite small differences in lattice parameters and coefficients of thermal expansion. Some of these cracks extend into the AlN crystal over a distance of more than 2–3 mm. A layer with a high density of dislocations ($10^6$ $cm^{-2}$) forms near the interface, but the numbers of cracks, pores, and dislocations decrease rapidly with increased crystal thickness.

Various ways of reducing the crack density are described in the literature, but a radical decrease of crack density without deterioration of the crystal quality is reached

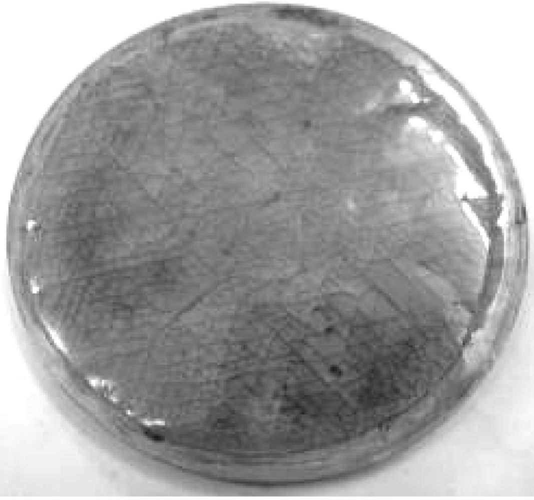

**Figure 12.8** Photograph of 2 inch AlN bulk crystal grown on SiC seeds.

only by separation of the SiC seeds before complete crystal cooling [56]. Such separation has been experimentally demonstrated, and AlN crystals usually do not contain cracks if the SiC seed is removed during the growth process.

Pores are defects specific to AlN bulk crystals grown by sublimation. Pores or micropipes in SiC and AlN crystals have a different nature: in SiC crystals they are initiated mainly by large screw dislocations; in AlN crystals pores appear during the growth process due to chemical etching of the growing surface by liquid drops [57].

X-ray microanalysis shows about 5% Si and 0.6% C in AlN crystals. The concentration of other impurities is less than 100 ppm. The impurity concentration rapidly drops during the subsequent growth of bulk AlN. The variation of the concentration of aluminum, nitrogen, carbon, silicon, and oxygen along the crystal thickness is shown in Fig. 12.9.

The resistivity of AlN crystals is generally lower than $10^5$ Ω cm. This value is much lower than the reference resistivity of undoped semiinsulating AlN ($10^{11}$−$1^3$ Ω cm). This result is attributed to the effect of the residual impurities (primarily Si) contained in AlN bulk crystals grown on SiC seeds.

Measurements of the UV transmittance spectra of wafers with a thickness in the 400 μm range have shown that most of the crystals have an average transmittance of 50%−60% and demonstrate a sharp cut-off between 250 and 320 nm.

After removal of the original SiC seed, the obtained crystals could be used as seeds for further growth of AlN ingots with lower impurity content. The obtained AlN crystals are of a quality suitable for manufacturing semiconductor devices, including the ultraviolet LEDs which are in demand in modern technology [2].

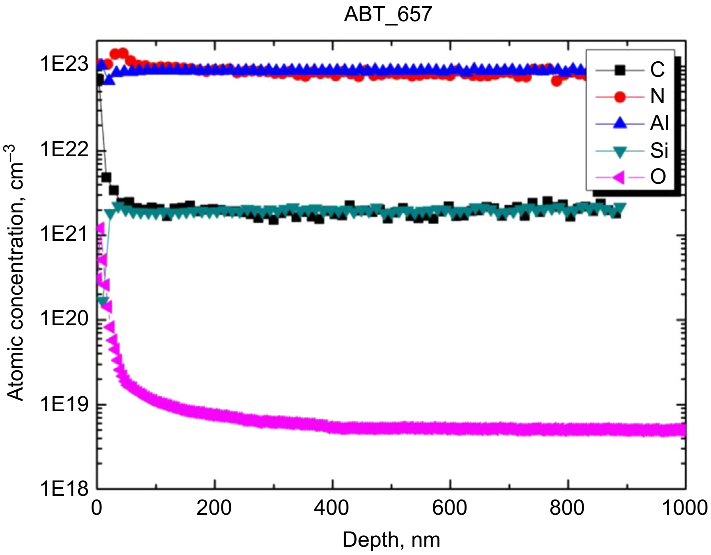

**Figure 12.9** Concentration of impurities measured by SIMS in AlN crystals grown on SiC seeds.

### 12.4.1.5 Freestanding single crystal AlN wafers grown by the SiC substrate evaporation method

In this method the seed material has a major impact on the crystal quality. First, the lattice mismatch between AlN and SiC generates dislocations at the AlN/SiC interface. Secondly, after cooling the PVT-grown boule can have cracks due to a large difference between the TECs of AlN and SiC. Cracked or defective AlN crystals are inappropriate for use in devices. The growth of high-structural-quality AlN crystals on SiC substrates becomes possible if the substrates are separated from crystals. There are four main approaches to fabricating a freestanding AlN layer.

1. Spontaneous separation upon cooling.
2. Gradual decomposition of SiC during high-temperature deposition of AlN.
3. Sublimation of the substrate during AlN film growth using the close-spaced sublimation method.
4. Evaporation of substrates coupled to the growth of thin ($\leq$2 mm) layers in one process.

AlN single crystals are grown on SiC in the temperature range of 1950−2050°C. Under these conditions, the equilibrium vapor pressure over a SiC substrate is almost three orders of magnitude lower than over an AlN layer [58], i.e., a very slow evaporation rate of SiC is achieved. Nevertheless, it was observed that in the presence of AlN vapor the evaporation rate of SiC depends on the vapor phase composition and temperature, and also on the structure, polarity, size, and thickness of the substrate. When SiC and AlN are heated together, the SiC evaporation rate significantly exceeds the rate in an inert atmosphere [59−64], which allows fabrication of crack-free freestanding AlN layers with 0.5−2 mm thickness and good crystalline quality.

AlN layer growth and SiC substrate evaporation can be performed in a closed tantalum carbide container. The SiC seed evaporates predominantly at the periphery, i.e., in the lateral direction, because the side evaporation rate is one order of magnitude greater than in the normal direction; hence the surface area of the substrate decreases drastically. A higher evaporation rate was also observed around structural defects such as dislocations, pores, and micropipes. The etch pits on the substrate surface change upon annealing: they are rapidly transformed into voids that can penetrate into the layer, making holes in it [63].

When investigating the influence of substrate polarity it is found that the evaporation rate for the carbon-terminated $(000\overline{1})$ faces of SiC (C-face SiC) is 1.5−2.0 times lower than that for the silicon-terminated (0001) faces (Si-face SiC). Thus it seems preferable to evaporate the Si face in the course of AlN layer growth. However, as the periphery of the Si-face SiC substrate evaporates much faster than the central part, the surface takes a convex shape while remaining mirror-like. In contrast, the surface of C-face SiC remains flat but not smooth, i.e., covered by macrosteps of different heights. The probability of formation of pits and pores is higher on the C face. They form predominantly at screw dislocation outcrops. Thus the presence of AlN vapor increases the evaporation rate of the SiC substrate. Due to the surface-dependent evaporation behavior, the central part of a large-area substrate evaporates at a rate of 3−6 μm/h, which is too low to remove the substrate completely during layer growth. The reason for this behavior is liquid phase formation on the surface of the substrate during AlN layer growth. This hypothesis is confirmed by the presence of droplets on an evaporating surface subjected to rapid cooling. The thickness of the liquid phase is determined, in particular, by the surface energy. Since the Si face has a higher surface energy than the C face [65], the Si face of the SiC substrate is better wetted and evaporates more uniformly. The most effective evaporation is obtained when the growth of AlN is performed on the C face of the SiC substrate; a mesa-shaped substrate is utilized to take advantage of a high lateral evaporation rate; and the seed−source clearance is minimized. Furthermore, grooves on the Si face of the substrate increase the evaporation rate by four or five times. The clearance between the source and the substrate is kept in the range of 1−5 mm, and the TaC lid is located at a distance of 2−8 mm above the evaporated surface.

The step flow is obtained in two stages: a very thin AlN layer is first grown at a low temperature (1800−1850°C), and then at the high-temperature stages (1950−2030°C) the layer thickness is increased up to 0.6−2.0 mm. At the same time, the substrate evaporates completely. The resulting morphology of AlN grown under these conditions is comparable to that of improved growth on off-oriented C-face SiC [19]. We emphasize the role of the low-temperature stage (1800−1850°C), during which the AlN layer grows on the substrate in the absence of evaporation. The first-to-grow layer protects the substrate and avoids the liquid phase, which would cause the appearance of etch pits and pores. This is a necessary precondition for further growth at higher temperatures.

Representative freestanding layers studied by X-ray rocking curves (ω scans) and longitudinal peak widths (2θ−ω) show that the rocking curves are broader for one layer (A) compared to another (B) (Fig. 12.10). Specimens A and B were grown for

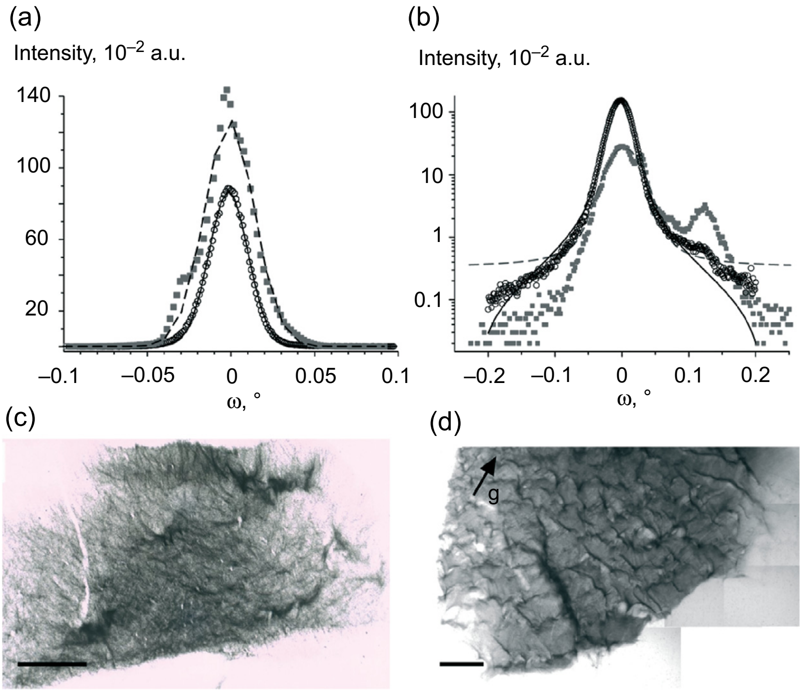

**Figure 12.10** X-ray diffraction peaks for both layer A (*solid squares*) and layer B (*open circles*), as well as the X-ray diffraction topographs of the same layers. (a) Linear scale plot of the triple crystal ω scans from the symmetric 0004 reflection. The curves are fitted using a Gaussian profile. (b) Log scale plot of the double crystal rocking curves from the asymmetric $10\bar{1}\bar{4}$ reflection in the grazing exit geometry; fitting to the Voigt function. (c) Transmission white-beam X-ray topograph recorded for layer B. (d) Topograph taken of layer A using monochromatic radiation. $g = 1\bar{2}1\bar{8}$. Principal photon energy of 20 keV. The films were Kodak SR-45 (c) and M-100 (d). Scale bars of 1 mm.

21 and 16 h with thicknesses of 1.5 and 0.6 mm, respectively. For these periods the substrates with initial thicknesses of 2.7 mm (A) and 0.15 mm (B) evaporated. Both samples were grown under $N_2$ atmosphere at a pressure of 1.01 bar and a temperature of 2100°C.

The symmetric 0004 triple crystal ω scans and asymmetric $10\bar{1}4$ double crystal rocking curves for layers A and B are shown in (Fig. 12.10(a) and (b)) [63]. One can see that the peak intensity of the 0004 reflection increases with the layer thickness (a); but the thicker layer A has a lower peak intensity of $10\bar{1}4$ reflection than layer B (b). The peak intensity, which is more sensitive to the structure than the integrated intensity, indicates that layer A is more defective than layer B. In addition, multiple peaks arise in the rocking curves from layer A, meaning that within layer A there is a distribution of tilted regions. The peak widths were determined by nonlinear least squares fits to the Gauss and Voigt functions. The central parts of the peaks were Gaussian, as is seen from the maxima on the linear scale, while the tails cannot be described by a Gaussian function;

they can be fitted by the Voigt function for both ω and 2θ−ω scan modes. The full width of half-height maximum (FWHM) for layers A and B is shown in Table 12.5, compared with the values from two other approaches: the fabrication of AlN free-standing films and the growth of AlN bulk crystals on SiC seeds [55,57].

For both layers fabricated by the two-step method, the widths of the 0002 ω-scan peaks are similar to the earlier reported widths of the double crystal rocking curves from bulk crystals; and these peaks are narrower than the peaks of the rocking curves from the bulk crystals grown on off-axis C-face SiC substrates.

In freestanding layers the 2θ−ω scan is very narrow compared to the ω scan. It means that the layers have lower strain and larger tilt distribution. In such cases, the above comparisons are appropriate because the rocking curves from the bulk crystals are dominated by the tilt distribution due to threading dislocations [25,53]. This low broadening of symmetric reflections is an index of a relatively low density of screw and mixed threading dislocations in the layers. Table 12.5 shows that for bulk crystals and freestanding films the peaks are broader for asymmetric reflections compared to symmetric reflections. This broadening is explained by the impact of edge threading dislocations on the width of the reflections.

The freestanding layer A shows an appreciable broadening in the asymmetric rocking curve measured in the double-axis mode: up to 187 arcsec. At the same time, the width of the triple crystal ω scan is 101 arcsec for the $10\bar{1}4$ reflection and 114 arcsec for the 0004 reflection. The important thing to note here is that a coplanar asymmetric reflection of $10\bar{1}4$ is less sensitive to edge dislocations than the reflections from planes with larger inclination. Nevertheless, there is reason to believe that the defect structures of layers A and B cause broadening in both symmetric and asymmetric rocking curves, rather than only significant broadening in the asymmetric reflection.

**Table 12.5** **Comparison of full widths at half-height maximum (FWHM) of rocking curves (ω scan) (arcsec) for AlN freestanding crystals grown by sublimation evaporation method (ANF layer) and AlN SiC and GaN/SiC templates of the different crystals thickness (mm)**

| | | **0002** | | **0004** | | **$10\bar{1}3$** | **$10\bar{1}4$** | | **$11\bar{2}4$** |
|---|---|---|---|---|---|---|---|---|---|
| Specimen | *t* | $W_\omega$ | $W_{2\theta-\omega}$ | $W_\omega$ | $W_{2\theta-\omega}$ | $W_\omega$ | $W_\omega$ | $W_{2\theta-\omega}$ | $W_\omega$ |
| AlN freestanding crystals | 0.6 | 116 | 18 | 96 | 38 | | 92 | 39 | |
| AlN/SiC | 1 | 250 | | | | 300 | | | |
| AlN/SiC | 8 | 110 | | | | 200 | | | |
| GaN/SiC | 6e-3 | 85 | | | | | | | 180 |

This broadening comes from regions that are tilted with respect to each other, i.e., from the subgrains, and from a random distribution of the dislocations. For quantitative assessment of the magnitudes of the average tilt angle $\tau$ and the average strain $\varepsilon$, a peak broadening analysis is carried out (the Williamson–Hall plot [66]).

The dislocation distribution is further analyzed in the crystal interior by X-ray topography using white radiation of photon energy 4–20 keV. Cracks that are not detected by optical inspection become easily visible in the topographs. Freestanding AlN layers were seen to be crack free within an area of 80 $\text{mm}^2$, which confirms a significant decrease in cracking compared to the thin layers on nonevaporated substrates. The dislocation images are observed as regions of intensified reflecting power (black). Other features of the topograph are the regions misoriented with respect to the main part of the crystal. Differently oriented regions give a white contrast. One can see that the dislocations do not lie in any specific direction but form piles. The individual dislocations are almost indiscernible, and can be seen only if their density is low enough to avoid overlapping of their projected images. In the transmission geometry, overlapping starts when the dislocation density reaches an upper limit of about $1.8 \times 10^4\ \text{cm}^{-2}$. The dislocations are randomly distributed.

The type B layer has broadening in the 000l rocking curves (100 arcsec) consistent with a screw or mixed threading dislocation density of $\sim 5 \times 10^5\ \text{cm}^{-2}$. Thus a reasonable mean density for this specimen would be $10^5$–$10^6\ \text{cm}^{-2}$. An example of a more defective crystal is shown in Fig. 12.10(d). This is a topograph of the freestanding layer A taken with the $\bar{1}2\bar{1}8$ reflection using a monochromatic synchrotron radiation beam.

The diffraction curve of the Ru/C multilayer monochromator with 100 bilayers and spacing $d = 40$ Å at 20 keV has a width of 48 arcsec. The specimen is a piece of crystalline plate with an area of 55 $\text{mm}^2$. The topograph shows a wavy contrast that can be generated by lattice curvature. There is good reason to believe that the wavy contrast arises from an imperfect material cut by the free surface of the specimen. We may suppose that such stress relief on the growing surface is produced by a marked increase in the dislocation density due to island nucleation at the early stages of growth. By advancing growth, the majority of the dislocations migrate to lie in or near the places where the growth islands coalesce to form the subgrain boundaries. Away from these boundaries, the topograph shows uniform contrast. However, the possibility that this uniformity is connected with the relatively poor spatial resolution in X-ray topographs cannot be ruled out.

From Table 12.5 it can also be noted that the peak width is inversely proportional to the domain size; hence it is directly proportional to the dislocation density. Therefore layer B has a lower dislocation density than layer A.

### Conclusion regarding preparation of freestanding AlN wafers

Using the substrate evaporation method, freestanding AlN layers have been grown on C-polar SiC substrates. The presence of AlN vapor significantly increases the rate of SiC evaporation compared to the sublimation rate in an inert atmosphere. SiC demonstrates a surface-selective evaporation behavior: the Si face evaporates more uniformly than the C face.

The free layers have greatly enhanced crystalline perfection compared to the layers sticking to substrates. They contain fewer cracks, but have lattice dislocations that strongly influence the values of the FWHM of the X-ray diffraction rocking curves.

From the triple crystal measurements it is concluded that broadening of the 0002 reflection is similar to that of a bulk AlN crystal. No evident broadening of the asymmetric $10\bar{1}4$ reflection compared to the 0004 symmetric reflection is detected, which is characteristic of structures with randomly distributed dislocations. For all the freestanding layers, the FWHMs were broader for the ω-scan peaks compared to the 2θ−ω-scan peaks, which means that the dislocations tend to form a mosaic structure. The key point for dislocation density reduction is to establish a step-flow growth. Once the growth on C-face SiC substrates is optimized, the freestanding layers show lower FWHM values and more uniform distribution of the dislocations because of the absence of boundaries between coalesced islands.

To facilitate the evaporation of SiC in the narrow process window for step-flow growth on the C face one can effectively take advantage of fast lateral evaporation**.** The yield of the evaporation process can be significantly improved by utilizing mesa-shaped substrates: the deep grooves in the back side (Si face) of the substrate increase the evaporation rate by up to four or five times.

## *12.4.2 Sublimation growth of GaN bulk crystals*

### *12.4.2.1 Introduction*

High-quality GaN substrates of appropriate size are necessary for optical and electrical devices. It is clear that the ideal and ultimate solution is GaN substrates sliced from bulk GaN crystals. Many groups around the world have been working on growing native substrate material for GaN-based devices in recent years. Development of various epitaxial techniques such as epitaxial lateral overgrowth reduced the extended defect density to mid-$10^7$ $cm^{-2}$, but high-performance devices require a defect density of $10^5$ $cm^{-2}$ or even lower. Therefore both conducting GaN, for mainly vertical junction devices such as lasers and LEDs, and high-resistivity material for devices such as high-power field-effect transistors need to be further developed. Several promising techniques to obtain GaN bulk crystals are presented in this section.

#### High nitrogen pressure solution growth

HNPS techniques [67−70] deal with very high pressures and temperatures (typically 1700°C and 20 kbar). Under these conditions, $N_2$ dissociates on the molten Ga surface and dissolves in Ga. Then GaN crystals grow from this solution due to the temperature gradient in the crucible containing the solution. HNPS growth results in GaN platelets up to 3 cm in diameter and with a thickness of about 100 μm, often with flat mirror-like faces. The quality of crystals is very high (colorless, dislocation density $2 \times 10^2$ $cm^{-2}$, FWHM of XRD rocking curves 20−30 arcsec). The main disadvantages of HNPS growth are the very complicated technology (because of the extreme growth conditions), and extremely low growth rates (near 1 μm/h).

## Ammonothermal methods

These methods [71,72] are based on the reaction of ammonia and Ga metal or polycrystalline GaN at pressures and temperatures which are not as high as for HNPS (typically close to 500°C and 1.5–5 kbar). The ammonia used as a polar solvent forms metastable products with the solute. Ammonothermal methods belong to the group of solvothermal growth techniques forming a separate class of technologies which can produce from nanosize to macrosize crystals under elevated pressure and temperature regimes. Solvothermal growth technology has the ability to operate near the thermodynamic equilibrium (the temperature gradient is zero at the crystal faces and very low in the growth zone). Thus it can ensure excellent crystallinity (FWHM up to 16 arcsec, dislocation density $\sim 10^3$ cm$^{-2}$, bending radius r $\sim$ 1000 m). Despite the very low growth rate (up to 0.1 mm per day [71]), a large amount of crystalline material can be obtained over a long process time. The process is easily scalable by simply increasing the size of the autoclave. The equipment needed is relatively simple, and although materials used for autoclave construction are expensive (NiCr, Pt), the maintenance cost is relatively low in the long term.

## Na-flux methods

These methods [73–84] deal with gaseous $N_2$ and Ga–Na-C melts at pressures and temperatures which are not so high as those for HNPS (650–870°C and 10–100 bar) owing to the addition of Na in the melt. Na acts as a catalyst for dissociation of N molecules. C (together with mechanical stirring) blocks formation of GaN polycrystals. $Na_3N$, Li, $Li_3N$, and $Ca_3N_2$ can also be used as parts of flux for flux-based growth methods [74,76,77]. The Na-flux technique leads to smaller GaN crystals, a few millimeters in size, compared to HNPS growth, but these high-quality single crystals (defect densities near $10^4$ cm$^{-2}$, FWHM of X-ray rocking curve of 50 arcsec) can be used as seeds for other growth methods. Seeded GaN growth from Na- flux is very promising [78–80], and progress in its industrial implementation has been shown recently [81,82]. Moreover, Li insertion in the melt at the final stage of growth dissolves the sapphire substrate before cooling starts [84]. This solves the problem of high thermal stress, and high-quality crack-free freestanding GaN crystals can be obtained. The seeded Na-flux method produces crystals of large size (diameter of up to 3 in) and good quality (up to $10^2$ cm$^{-2}$ dislocation density and FWHM near 100 arcsec). The growth rate is very low ($\sim$1 μm/h).

## Chloride hydride vapor phase epitaxy

The HVPE method [85–87] operates far from thermodynamical equilibrium (under high supersaturations), but it provides high growth rates (200–300 μm/h) and good-quality grown crystals. HVPE is presently the only industrial technology capable of supplying thick layers of relatively high optical and structural quality GaN [85] at reasonable growth rates, but with residual strain and extended defect concentration that might still be too high for optical and electronic devices. HVPE growth works via the reaction between ammonia and gallium chloride on foreign substrates (sapphire, GaAs, and SiC) at temperatures around 1100°C and normal ambient pressure. The foreign substrate is removed at the end of growth by lift-off techniques so that a large-diameter freestanding GaN wafer is finally obtained. The growth of 2 mm thick GaN single crystals on seeds grown by the high-pressure technique has been reported [85]. Moreover, 10 mm thick GaN boules and corresponding substrates up to 3 inch diameter can be obtained by this method.

The principal limitations of HVPE techniques are:

1. high concentration of dislocations (minimum ~$10^5$ $cm^{-2}$);
2. residual strain, cracks, and bending because of lattice mismatch and difference of thermal expansion coefficients;
3. use of aggressive gases such as HCl, $Cl_2$, and $H_2$.

### 12.4.2.2 *Bulk GaN crystal growth by SSM [88–90]*

In spite of the nearly equal binding energies in GaN and AlN crystal lattices, sublimation growth of GaN at near 2000°C (as normally used for AlN) is impossible because of disintegration of GaN. In a nitrogen atmosphere, GaN is stable at temperatures lower than 800°C. However, in an ammonia atmosphere GaN is stable at the temperatures of 900–1200°C, which makes the growth of GaN crystals possible even if these temperatures are considerably lower than the optimal temperature for GaN crystal growth. Multinucleation usually takes place in such conditions; as a result, the grown crystals contain grains and have a high dislocation density (near $10^8$ $cm^{-3}$). Higher growth temperatures may be utilized only by applying much higher pressures, up to several tens of kilobars. Hence $NH_3$ flow must accompany the GaN sublimation growth, but this is insufficient for Ga transport because of its very low vapor pressure ($10^{-7}$ bar) at growth temperatures of 1000–1200°C. Nevertheless, for small source–substrate gaps, Ga transport can be realized by an unusual blowout of liquid Ga drops. The drops form because of a "boiling" Ga surface layer in an ammonia atmosphere, as is discussed later.

Molecular nitrogen dominates in the vapor phase due to GaN decomposition. However, because of the extremely low chemical reactivity of $N_2$, GaN does not grow under these conditions, and an external flow of nitrogen-containing reactive species is required to initiate the growth process. The best choice in all respects is ammonia ($NH_3$). One study reports the first freestanding GaN crystals of considerable size grown in the vapor phase [91]. In this work, synthesized GaN powder was heated in a dry $NH_3$ flow at 1150–1200°C for 24 h. This resulted in growth of GaN needles with a size of 5 × 1 mm. The author concluded that growth of GaN occurs via sintering, although the contribution of the physical vapor transport seems to be important.

GaN was grown using ammonia passing over liquid gallium at 1000–1150°C in an open or partly closed quartz ampoule [92]. In the latter case, $NH_3$ was supplied to a boat with liquid Ga through a small orifice of 1 mm in diameter that provided a diffusion-limited growth condition. GaN was deposited on the walls of the ampoule in the form of whiskers, needles, platelets, etc. It was concluded that the GaN crystals had been grown from the vapor phase containing atomic gallium and ammonia [92]. In addition, it was shown that raising the growth temperature made it possible to increase the size of grown GaN crystals.

A detailed study of mechanisms of GaN crystallization due to reaction of Ga vapor with ammonia was carried out [93–95]. A wide temperature range of 825–1010°C and $NH_3$ pressure of 0.3–2.5 mbar were used for growth, and prismatic GaN crystals appeared in the reactor. The largest crystals (up to 2.5 mm long) were formed on SiC or GaN seeds. These crystals presented an electron concentration of $n \sim 10^{19}\ cm^{-3}$ with a mobility of 100 $cm^2/V \cdot s$.

Thus attempts to grow freestanding GaN crystals in a $Ga-NH_3$ system without a seed or substrate were not successful. At best, needles or platelets were obtained but their lateral size was of no practical use. A different scheme of growth process was proposed (see Fig. 12.1) SSM [88,89]. In this method, the source of Ga vapor and the substrate were separated by a clearance of several millimeters, forming a growth cell. This growth cell was placed in a temperature-gradient zone to initiate material transport from the source to the substrate. To introduce the reactive nitrogen into the growth cell an ammonia flow was provided. One of the advantages of this scheme was an ability to intensify mass transport in the growth cell due to a decrease of the clearance between the source and the substrate. This resulted in higher growth rates (up to 1 mm/h) and also in complete (with very small losses) transfer of the source material to the substrate. GaN crystals grown by SSM exhibited a high quality, comparable to that of GaN epilayers obtained by metalorganic vapor phase epitaxy (MOVPE) or molecular beam epitaxy (MBE). Advantages of this technique are the high growth rate, controlled by the evaporation temperature, the gas flow, the gap, and the temperature gradient in the gap; use of elemental sources; high yield of the growth components; high crystalline quality of the grown material; absence of surface-active agents in the vapor phase; and the possibility of doping the growing crystal by introducing suitable impurities in the source. For these reasons, SSM has become popular and is now being developed in several research centers [96,97].

## Experimental setup and results

GaN crystals are grown in a tubular quartz reactor with radio-frequency heating, schematically shown in Fig. 12.11.

The growth process is carried out in an ammonia flow of 0.3–0.7 L/min passing over and through the growth cell, which is placed on a graphite rod inside the reactor. The vertical configuration of the reactor is more suitable for longer process durations. Before growth the reactor is heated to 700°C and evacuated down to a pressure of less than $10^{-2}$ torr for 2 h and then purged by ammonia to remove residual gases (firstly oxygen). The substrate and the source of Ga form a "sandwich" through which the transport of the main growth species (Ga and $NH_3$) takes place. The growth cell is set within a temperature gradient, so a certain temperature difference $\Delta T$ (10–100°C) between the source and the substrate is imposed. This temperature difference serves as the driving force for Ga transport inside the growth cell and subsequent GaN crystallization on the substrate. Normally, the distance d between the source and the substrate (clearance) is in the range of 2–5 mm. Temperatures of the source and the substrate (near 1200°C) are controlled by W–Re thermocouples. GaN powder (grains of 0.1–2 mm), melted Ga, or a mixture of the two can be used

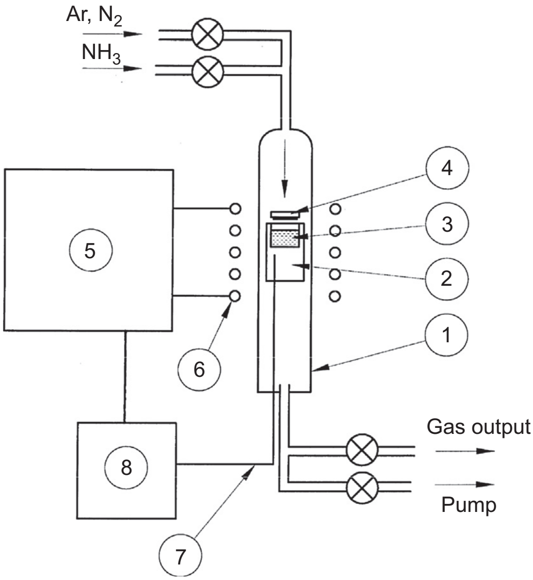

**Figure 12.11** Principle scheme of SSM apparatus. 1. Quartz tube reactor Ø50 mm, length 550 mm 2. Graphite heater. 3. Crucible filled with Ga–GaN powder mixture. 4. Substrate holder with attached substrate. 5. RF generator (440 khz, 8 kwt). 6. Inductor. 7. Thermocoupler. 8. Thermoregulator.

as a source. Experimentally, it was seen that the mixture is the most stable and most effective choice. If GaN powder is used a very fast decrease of evaporation takes place, whereas when pure Ga is used an excessive blowout of Ga drops takes place. However, a decrease of evaporation is also seen for the mixed source (Fig. 12.12).

To make the evaporation rate stable over a long time (1 day), a perforated tantalum lid is positioned on a source crucible. It is stated that the evaporation decrease is due to formation of a GaN crust on the source surface because of its reaction with backstreaming $NH_3$ [98,99]. To eliminate that effect two methods were proposed: additional blow of $N_2$ at the source surface, and placement of the white-hot filament near it. In both cases the evaporation rate was stabilized but the growth rates became very low—near 20 μ/h.

Both sapphire (10 × 10 to 25 × 25 mm$^2$) and 6H–SiC(0001) Lely crystals (about 10 × 10 mm$^2$), with Si and C faces, were used as substrates. SiC substrates are first etched in KOH melt at a temperature of 480°C to remove the lapping damaged and determine the polarity of the substrate, then boiled in a diluted solution of acetic acid, and finally rinsed in deionized water. Growth of GaN crystals is carried out at atmospheric pressure in the temperature range of 1000–1300°C. The temperature difference between the substrate and the source is normally between 10°C and 100°C. An inlet ammonia flow rate of 0.3–0.7 L/min is maintained during the growth process. GaN crystals with a thickness of 70–800 μm are grown in 5–120 min. Growth rate varies from 0.1 to 1.1 mm/h. The crystals of the best crystalline quality are obtained at temperatures of 1150–1230°C and growth rates of 0.2–0.4 mm/h. A photo of a typical GaN crystal grown by SSM is shown in Fig. 12.13.

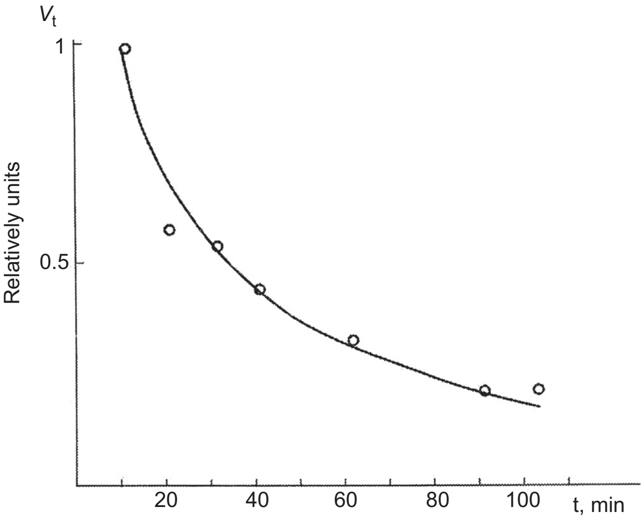

Figure 12.12 Typical dependence of GaN evaporation rate on growth process duration.

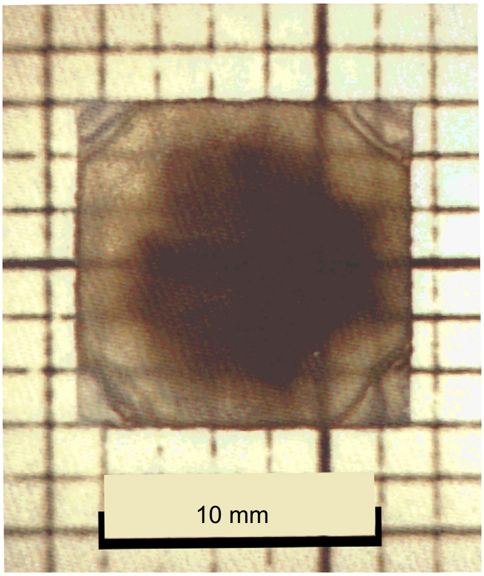

Figure 12.13 Photo of GaN crystal grown on sapphire substrate by SSM.

GaN layers obtained at higher temperatures (>1230°C) often contain Ga inclusions, which usually appeared near structural or morphological defects. Decreasing the growth temperature below 1150°C contributes to formation of voids. When temperatures are below 1050°C, GaN layers grown on SiC or sapphire substrates with no buffer layer are polycrystalline. In this case a large number of separated GaN crystals form, with platelet or prismatic morphology. Obviously, polycrystalline growth of GaN is caused by a high flux of Ga-containing molecules to the substrate. Growth of high-quality GaN layers, without a buffer template, is possible only at temperatures higher than 1100°C.

Another important factor affecting the quality of the growing crystal is the temperature difference between the source and the substrate ($\Delta T$). We find that at low $\Delta T$ (<2−5°C) there dominates the island growth featuring low density of the nuclei forming in the substrate's surface. This arises from the fact that the rate of Ga evaporation from the source becomes comparable with the rate of Ga evaporation from the growing surface. At the same time, at significant $\Delta T$ (>50°C) the possibility of Ga droplets on the growth surface increases sharply. The thickness of the crystal (Fig. 12.13) is 0.3 mm. The dark area in the center of the crystal is attributed to Ga droplets accumulated at the interface between sapphire and GaN. The appearance of these droplets at the initial stage of growth is related to a lower V/III ratio over the substrate from the periphery to the center. From the authors' experimental data it can be concluded that there is a certain growth region in coordinates $\Delta T$−T where single GaN crystals can be obtained, in particular within the interval T ~ 1000−1300°C and the interval $\Delta T$ ~ 2−80°C. Outside this region, growth is impeded by various factors.

The variation of GaN growth rate versus growth temperature is shown in Fig. 12.14. The growth rate increases with temperature only up to 1200°C; further temperature increase reduces the growth rate drastically because of thermal decomposition of GaN. This is evident from the appearance of metallic Ga inclusions on the surface of the GaN epitaxial layers.

Fig. 12.15 illustrates the dependence of the growth rate on the clearance of the sandwich cell. It is clear that the growth rate decreases with the increase of the source−substrate distance, and the highest rates are achieved at small clearances.

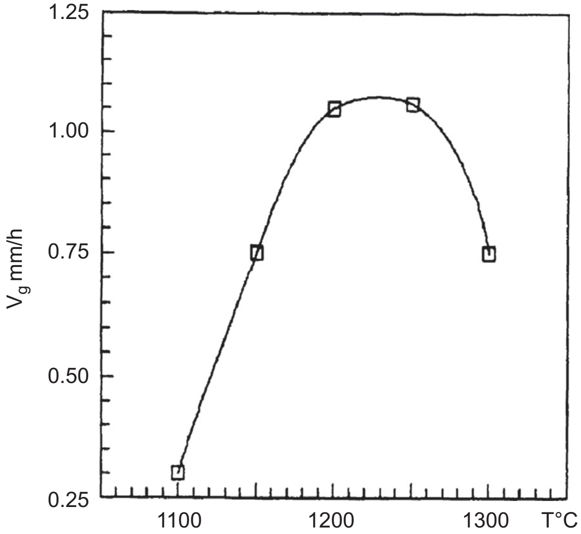

**Figure 12.14** Dependence of growth rate of GaN layers on temperature.

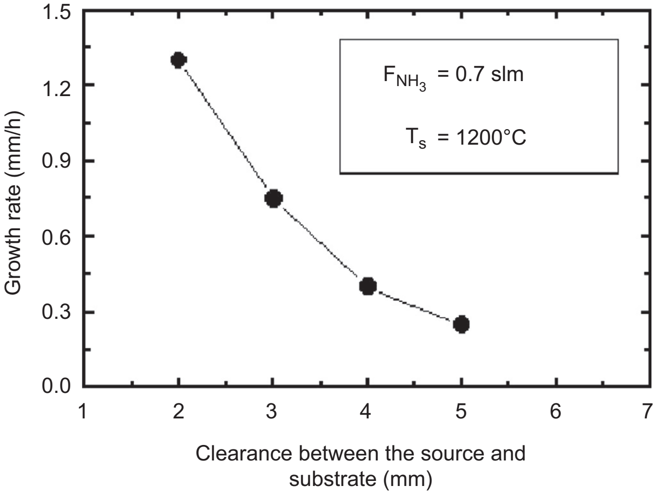

**Figure 12.15** Dependence of GaN growth rate on the distance between substrate and source.

However, below a critical distance the growth process becomes nonreproducible. Variation of the clearance influences the ammonia flux through the growth cell, and hence the growth rate. As a result, the dependence of the growth rate on the source-to-substrate gap has a complex, nonmonotonic pattern. At low ammonia flux (especially at high temperatures), a decrease of the GaN growth rate is observed, caused by the dissociative GaN decomposition. Reduction of the growth rate also occurs at high flux of ammonia due to the removal of Ga molecules from the sandwich cell.

GaN crystals have been found to contain several types of defects: cracks, second-phase inclusions, voids, and dislocations. Cracks, forming near the substrate/GaN interface, are the most typical defects. It is evident that the cracks are caused during cooling by the difference in TECs of the substrate material and the GaN layer. The second-phase inclusions come from free gallium, and are observed in the vicinity of voids and other morphological defects. The inclusions are caused by an active nitrogen deficiency near the growing surface, so a more intense ammonia flow into the growth cell and decrease of the growth temperature will help in eliminating such defects. Voids are the most characteristic defects in thick GaN layers. Their density strongly depends on the growth conditions and the state of the substrate surface. The void density usually rises with a growth temperature increase or an ammonia flow decrease. Voids formation is probably associated with a deficiency of active nitrogen.

The morphology of the GaN growth surface mainly depends on the substrate's orientation. Relatively smooth layers grow on the (0001) Si faces of SiC substrates (Fig. 12.16). Under the same conditions, GaN epilayers grown on (0001) C faces have a rough surface covered by hexagonal growth undulations. Probably the growth process on the carbon face involves 3D nucleation, while on the silicon face two-dimensional (2D) GaN nuclei form and then expand laterally. This growth

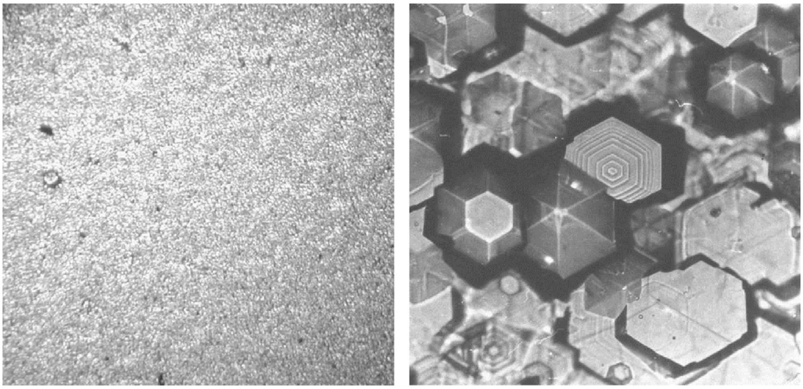

**Figure 12.16** Surface morphology of the GaN epitaxial layers grown on SiC substrates at the same conditions: left (0001)Si, right (0001)C.

mechanism may be interpreted as being due to the specific chemical bonding of silicon and carbon atoms, resulting in a higher surface energy of the (0001)Si face as compared to the (0001)C face.

**Transport of gallium from source to substrate** In this subsection we discuss the mechanisms controlling the process of GaN growth by SSM, and factors limiting the growth rate. The nature of an abnormally high Ga transport rate is also considered.

Comparison of theoretical and experimental data shows that the experimental growth rate systematically exceeds the calculated values at least by a factor of 10. This implies that the mechanism of Ga transport is different from that postulated in calculations [100]. Other evidence of the specific mechanism of Ga transport is provided in Fig. 12.15, where the dependence of the GaN growth rate on the clearance d between the source and the substrate is plotted. It is seen that the growth rate decreases more rapidly than 1/d, which is the expected dependence if one assumes that diffusion is the prevailing mechanism of transport.

To clarify this question, the Ga transport rate in the sandwich system was measured under various conditions: in an argon atmosphere at a pressure of 1 bar (resistive heating of the growth cell); in an ammonia atmosphere at a pressure of 1 bar (radio-frequency heating of the growth cell); and under low background pressure of $\sim 10^{-6}$ bar (resistive heating of the growth cell). In the first two cases the Ga transport between the source and the substrate is expected to occur via diffusion and convection, while in the latter case is should take a free-molecular character. Results of this study are summarized in Fig. 12.17.

It is apparent that all experimental points are confined within two calculated lines. One of the lines corresponds to pure diffusion of Ga from the source to the substrate, while the other describes free evaporation of Ga in a vacuum (actually this curve represents a physical limit for the evaporation rate). Both lines have nearly the same slope. In experiments, the gallium flux measured in an Ar atmosphere (under resistive heating of susceptor) corresponds exactly to the Ga transport by diffusion. At the same

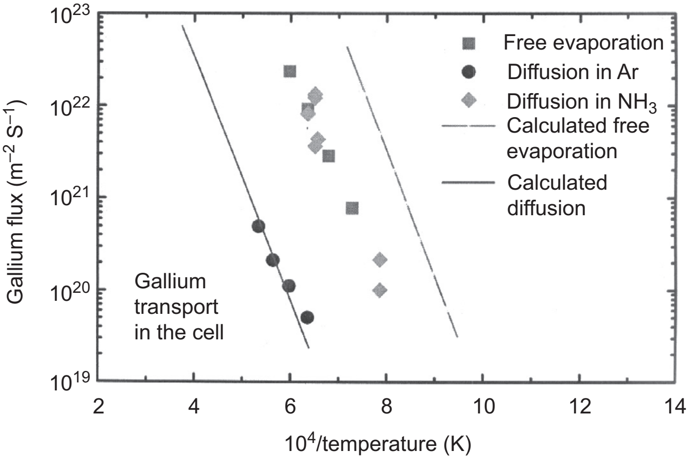

**Figure 12.17** Gallium flux from the source to the substrate calculated for different evaporation modes and measured experimentally.

time, experiments on free evaporation of Ga in a vacuum and the measurements carried out under actual growth conditions ($NH_3$ atmosphere) give nearly identical results, although a factor of 30 less than the calculated evaporation rate of Ga in a vacuum.

To understand the abnormally high rate of Ga transport between the source and the substrate using SSM in an $NH_3$ ambient, one must consider three effects: gas convection in the growth cell enhanced by hydrogen generation at the surface of the source due to $NH_3$ cracking; multiple channel desorption of Ga (via gaseous compounds with hydrogen and other possible species); and generation of Ga droplets at the surface of the source (specific "boiling" of the surface layer) followed by their transport to the substrate.

Actually, the effect of convection is accounted for while modeling the growth process but the model does not provide observable values of the growth rate. To estimate the effect of multiple channel desorption one must consider additional formation of GaH, $GaH_2$, and $GaH_3$ at the surface of the source, as well as of the adduct $Ga \cdot NH_3$. The contribution of these species into Ga desorption from the source was found to be negligible. The role of other gaseous species (probably formed during preparation of the source material) is excluded by experiments carried out with pure liquid gallium. Thus the first two reasons alone cannot explain the abnormally high rate of Ga transport observed experimentally, and the most probable origin of the high Ga transport rate is related to droplet generation. The nature of this effect is thought to come from the liquid Ga surface instability (specific boiling of the liquid Ga surface layer). In turn, this instability can be caused by different factors, such as an axial temperature gradient in the growth cell directed opposite to the gravity force, a lateral temperature gradient inducing Marangoni convection near the surface of the liquid, nucleation of GaN microcrystals near the walls of the growth cell resulting in formation of a foam-like material [98], etc. Due to the multiple possible mechanisms, the nature of the high gallium transport rate is not completely understood yet.

**Growth window for the sublimation sandwich technique** The above discussion of the GaN growth rate takes into account only limitations related to the rate of Ga transportation to the growth interface. Other factors can introduce additional limitations to the growth process, including formation of liquid Ga on the growth surface, failure of epitaxial growth resulting in polycrystal formation, surface morphology degradation, etc. Obviously, the relative impact of these factors depends on the chosen growth conditions.

As already mentioned, key parameters of the growth process are substrate temperature T and the temperature difference between the source and the substrate ΔT. In addition, the flow rate of ammonia can be easily varied, keeping constant pressure in the reactor. Analyzing a large number of experimental data it was found that there is a growth region in coordinates ΔT–T (ΔT ~ 2–80°C, T ~ 1000–1300°C) where single GaN crystals can be obtained. Outside this region, growth is impeded by various factors. The boundaries of the growth region are not clearly defined, and they indicate some transition zones rather than a sharp border corresponding to a drastic change in the growth mode. At high temperature and/or high ΔT, single crystal growth of GaN is impeded by the formation of liquid droplets on the surface. This results in morphology degradation, the appearance of Ga inclusions in the crystal, and enhanced defect concentration. It is interesting that the forerunner of this process is the formation of liquid Ga inclusions at the interface between the substrate and the grown GaN crystal (such inclusions are absent in the bulk of the crystal). The photo of the GaN crystal shown in Fig. 12.13 illustrates this situation. Ga droplets at the interface are found by inspection through transparent sapphire substrate by optical microscopy. The droplet formation can be suppressed by increasing the $NH_3$ flow in the growth cell. At a low substrate temperature, epitaxial growth of GaN fails as polycrystalline growth occurs. At low source–substrate ΔT, the gallium evaporation rate at the source becomes comparable to the gallium reevaporation rate at the growing surface and the growth rate decreases, which results in island nucleation. The epitaxial layer becomes irregular, and roughness of the surface gradually develops. If the substrate temperature is increased keeping ΔT low then liquid droplets start to form on the surface, and growth of single crystalline GaN fails again.

A similar growth window can be found for ammonia flows ($1.5 \cdot 10^{-2}$–$3.5 \cdot 10^{-2}$ L/cm$^2$ min). At low flow rates there is a deficit of $NH_3$ in the growth cell and consequently Ga droplets form. Increasing the ammonia flow rate initiates growth of numerous needles on the substrate. Growth of single GaN crystals takes place only within appropriate window parameters.

## Initial stage of GaN growth

An interesting feature of SST is that no special buffer layer is required to grow GaN crystals of good quality. To study the initial stage of growth, the color cathodoluminescence scanning electron microscopy (CCL-SEM) technique was applied [101]. This method is based on visualization of luminescence locally excited by an electron beam on the cleaved plane of the grown crystal. It is believed that the yellow emission band (~2.5 eV) in GaN is evidence of

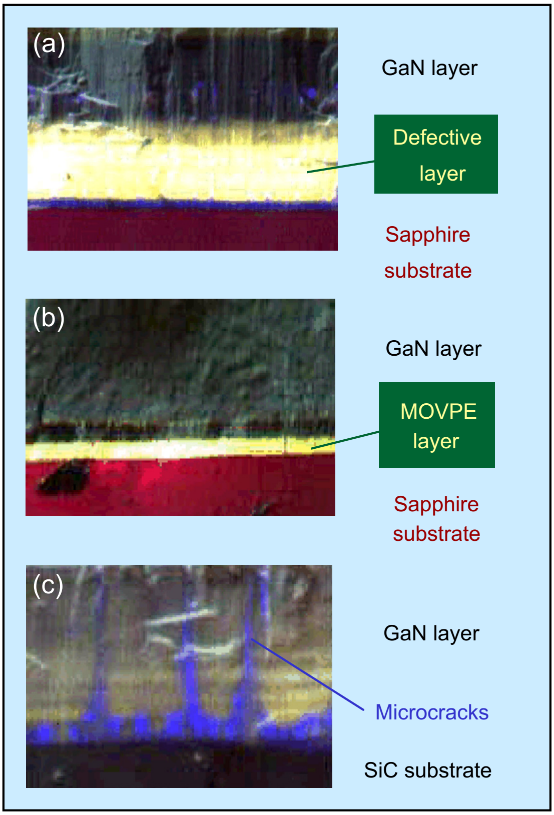

**Figure 12.18** Color CL images of GaN crystals grown (a) directly on sapphire substrate, (b) on MOVPE layer (~5 μm thick), and (c) on SiC(0001) Si-faced surface.

a defective material. On the other hand, luminescence of high-quality GaN lies in the UV spectral range, and is thus detected as a dark area in the cathodoluminescence (CL) image. This difference in color allows us to find the areas of material with higher (yellow) or lower (dark area) defect concentration.

Fig. 12.18(a) shows a micrograph of a CL image of a cross-section of a GaN crystal grown directly on sapphire. It is seen that the defective layer (~10–15 μm thick) with yellow luminescence appears at the initial stage of growth. Then a material of higher quality emitting in the UV spectral range follows (dark area in the micrograph). Notice the sharp change in material quality that is evident from the change of dominant emission wavelength. Further examination of the grown GaN crystal by X-ray shows that near the boundary between the high-defects and low-defects layers the density of threading dislocations decreases due to their bending.

Using a GaN buffer layer accelerates the formation of a good-quality crystal. Fig. 12.18(b) shows a CL image of a GaN crystal grown on a GaN layer (~3–5 μm thick) previously deposited by MOVPE on the sapphire substrate.

One can see that the GaN crystal formed by SSM is more perfect than the MOVPE buffer layer, which exhibits the yellow band emission.

Let us now compare the initial stages of GaN growth on sapphire and SiC substrates. Fig. 12.18(c) shows a CL image of GaN grown on Si-face SiC (0001). It is seen that no yellow luminescence is observed, even in the area adjacent to the substrate. A blue emission located at the crystal—substrate interface is revealed by CCL-SEM, which possibly originates from residual oxygen accumulated at the interface and then penetrated into the GaN crystal through microcracks, or the elastic strain related to the twin and inversion domains.

The use of the SiC $(000\bar{1})$ C surface for growth of GaN does not give good results: the morphology of the GaN surface degrades very quickly. Such differences in the quality of GaN crystal grown on Si and C faces can be understood considering that the face of SiC actually determines the polarity of the growing GaN crystal. Formation of Si—N bonds on the SiC (0001) Si face is thermodynamically favorable, as is formation of C—Ga bonds on the SiC $(000\bar{1})$ C face [100]. Since GaN grows in 2D mode via Ga—N bilayer lateral spreading, initially the Si face of the SiC surface provides the Ga-face surface of a grown GaN crystal. It is well known that this GaN surface tends to be smooth by any epitaxial techniques (MOVPE, MBE, HVPE) [102]. In contrast, N-face GaN is rough and exhibits 3D pyramidal features. In this respect, growth of GaN on sapphire gives an intermediate result (closer to that obtained on the SiC (0001) Si face) that is related to the different polarity of the grown GaN domains.

## Physical properties of GaN crystals grown by sublimation technique

**X-ray characterization** Crystallographic characterization of GaN crystals is carried out using double crystal and triple crystal X-ray diffractometry with $CuK_{\alpha1}$ and $MoK_{\alpha1}$ radiation. Both ω and θ—2θ scans are used for routine characterization of the material quality. To reveal in more detail the contribution of different factors to widening the diffraction curves, measurements in different configurations (symmetric Laue, and symmetric and asymmetric Bragg configurations) and for different reflexes ((0002), (0004), (1010), (2020), and (1124)) are carried out.

The FWHM of (0004) reflex, systematically measured in θ—2θ mode on a large number of GaN crystals grown on sapphire and 6H—SiC (0001) Si-face substrates, lies in the range of 6—9 arcmin and 2.5—6.5 arcmin, respectively. GaN crystals grown on 6H—SiC thus have a higher crystalline quality, which well correlates with the data of CCL-SEM and morphology examination.

A specific feature of the samples obtained by SSM is their strong bending related to the difference in the lattice constants and TECs of substrate and grown crystal. For example, the radius of bending of a 3 μm thick GaN MOVPE layer grown on sapphire is ~23 m. Further SST growth of 48 μm thick GaN on this template results in the value of the bending radius ~1 m (i.e., the crystal is highly strained upon cooling). Such a huge strain leads to breaking down of the GaN crystals during the growth process, and especially during sample cooling. Cracks occur predominantly in the substrate in the case of GaN growth on sapphire, and in the epitaxial GaN in the case of growth on 6H—SiC. Breakdown of the samples due to cracks becomes a serious problem for crystals of increased thickness and lateral size.

Using various scattering configurations and a number of diffraction reflexes reveals the contribution of different factors to the FWHM of the diffraction curve. Three main factors are considered: disorientation of the coherent scattering areas (blocks), size effect, and microdistortion of the crystalline lattice inside the blocks. It is found that the latter factor makes the dominant contribution to the width of the diffraction curve. The size effect is also remarkable. The block disorientation has a minor effect on the width of the diffraction curve for GaN layers grown by SST. Microdistortion of material inside the blocks is associated with dislocations of different types. By extracting components of microdistortion tensor from the X-ray measurements, the density of dislocations in the grown GaN crystals may be estimated. The upper limits for both screw and edge dislocation densities are found to be $(1-2)\cdot 10^{10}\ \mathrm{cm}^{-2}$. For comparison, MOVPE GaN layers grown on sapphire have upper limits for dislocation densities estimated to be $\sim 6\cdot 10^{8}\ \mathrm{cm}^{-2}$.

**Hall, photoluminescence, and Raman measurements** Hall measurements and infrared ($\lambda = 1-2\ \mu\mathrm{m}$) optical absorption give electron concentration in the range of $(2-6)\cdot 10^{17}\ \mathrm{cm}^{-3}$ and mobility between 30 and 80 $\mathrm{cm}^2/\mathrm{V}\bullet\mathrm{sec}$ in GaN grown by SSD. Such low mobility is typical for undoped GaN crystals where the electron concentration is controlled by native defects. All undoped GaN samples exhibit n-type conductivity.

Typical room-temperature photoluminescence (PL) of GaN grown on SiC (0001) (sample excitation by a He—Cd laser at $\lambda = 325$ nm) is shown in Fig. 12.19. Here the intensity of the visible (mainly yellow) emission band connected with impurities and defects is at least 10 times less than the intensity of the edge emission. The low-temperature (near 5 K) PL spectra of a GaN layer on an SiC substrate are shown in Figs. 12.20 and 12.21.

The low-temperature PL spectrum near the bandgap region is shown in Fig. 12.20: there are peaks at 3.47, 3.37, 3.31, and 3.26 eV, which are connected with different band—donor, band—acceptor, and donor—acceptor excitons and other impurity- or defect-connected transitions.

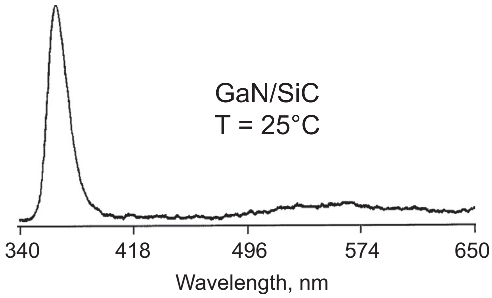

**Figure 12.19** Typical room-temperature emission spectrum of GaN grown on SiC(0001) Si-faced surface.

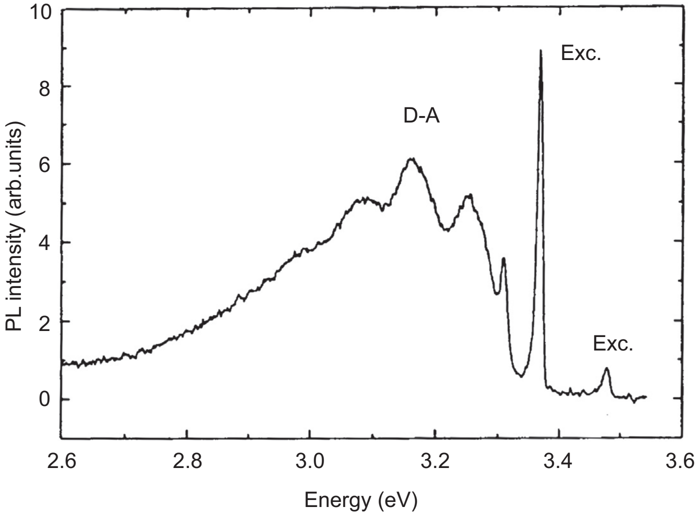

**Figure 12.20** Low temperature PL of GaN layer on SiC substrate in the bandgap region.

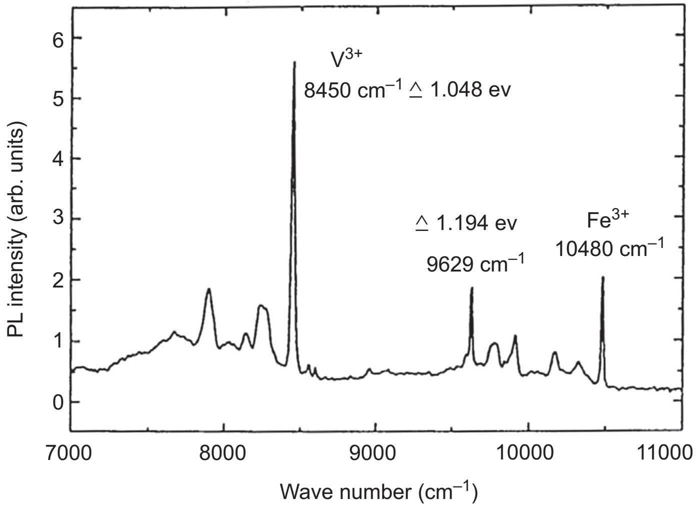

**Figure 12.21** Low temperature PL of GaN layer on SiC substrate in the infrared of V and Fe interval transitions. The line at 9629 cm$^{-1}$ is tentatively assigned to Cr.

Fig. 12.21 reports the low-temperature PL spectrum in the infrared region. Three prominent zero phonon lines (ZPL) are seen at 10,480, 9629, and 8450 cm$^{-1}$, followed by phonon replicas. The transition at 10,480 cm$^{-1}$ corresponds to the internal $^4T_1(G) - {}^6A_1(S)$ recombination of $Fe^{3+}$ on a Ga site. The ZPL at 9629 cm$^{-1}$ may be assigned to the $^3T_2(F) - {}^3A_2(F)$ transition of $Cr^{4+}$. The third line at 8450 cm$^{-1}$ is attributed to the well-known internal PL of $V^{3+}$ on a Ga site.

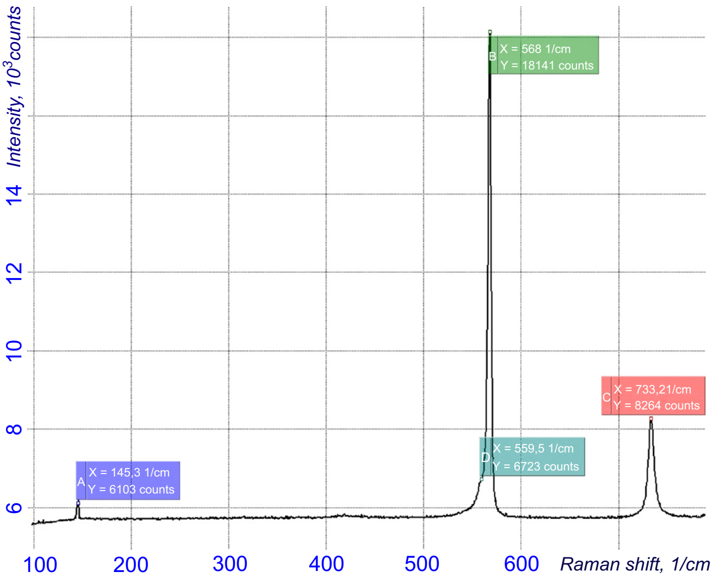

**Figure 12.22** Raman scattering of GaN layer grown by SST on SiC substrate.

It may be concluded that GaN layers grown by SSM have excellent crystalline and optical properties. The residual impurities in these thick layers are mainly assigned to Si and C contamination.

Raman spectra were recorded by confocal microscope in several points of the GaN sample using a laser excitation at 532 nm. Fig. 12.22 shows the TO mode 568 $cm^{-1}$ and LO mode 733 $cm^{-1}$ that confirm the high quality of the crystal, as stated in a previous work [103].

**Electron paramagnetic resonance study** GaN samples grown on 6H—SiC substrates, either undoped or with added Fe, Ni, or Mn impurities, were studied by electron paramagnetic resonance (EPR) using a conventional X-band (9.25 GHz) EPR spectrometer in the temperature range of 4—300 K. Corresponding traces of Fe, Ni, and Mn were found in these samples [104,105]. These observations confirm that doping the growing crystals may be achieved by adding an impurity to the evaporation source. Most probably, in their charge states of $Fe^{3+}$, $Ni^{3+}$, and $Mn^{2+}$ these impurities occupy Ga sites in the GaN crystalline lattice. Estimated impurity concentrations are $10^{17}$—$10^{18}$ $cm^{-3}$ for Fe and $10^{16}$—$10^{17}$ $cm^{-3}$ for Mn and Ni. The well-resolved lines in these EPR spectra indicate that the crystal quality was very high.

The energy level scheme of transition metals in GaN, as inferred from known levels in other III—V compounds via the Langer Heinrich rule, indicates that the acceptor levels of Mn and Ni are close to mid-gap [106]. Thus Mn and Ni seem to be more suitable impurities for preparation of semiinsulating GaN substrates than the previously proposed Fe and Cr.

### Conclusion about the SSM growth of GaN

The present status of SSM in growth of bulk GaN crystals has been outlined and discussed. It was shown that SSM gives a high growth rate (up to 1 mm/h) and provides good-quality GaN crystals. However, the crystalline quality ultimately depends on the substrate (the best results are obtained on 6H−SiC (0001) Si face) and chosen growth conditions. The experimentally observed high GaN growth rate is believed to originate from Ga droplets emitted from the boiling surface of the liquid Ga source at high temperature. A growth window can be determined in SSM considering two main growth parameters: substrate temperature, and temperature difference between the source and the substrate.

Modeling and experimental results show that there are some peculiarities in a sandwich growth cell: ammonia concentration in the gap is not uniform (higher near the edges), and after ammonia dissociation a bubble of $H_2$ can be formed in the center of the gap, so that nonuniformity of ammonia concentration increases. These facts would result in nonuniform growth, so to obtain uniform big crystals it is necessary to optimize the ammonia supply into the growth cell and simultaneously maintain a constant gap during the entire growth process. Novel technological solutions to this problem are to be implemented, for example special shields and nozzles for directing gas flow to the center of the growth cell, rotation and vibration of the substrate, and so on.

At high process temperatures the $NH_3$/Ga ratio in the growth cell influences the growth rate, but it also determines the density of defects in the grown crystals. Further investigation of the mechanisms of Ga transport in the sandwich system are necessary for better stabilization of Ga source operation, especially for long-duration growth processes.

It was also shown that the difference of TECs of the substrate and the growing layer are connected with the bending of GaN layers deposited on hetero-substrates and their possible cracking. This is a most serious problem, and hinders the scaling up of SSM crystals. The use of homoepitaxial seeds may be a suitable approach for producing larger GaN crystals.

## Acknowledgments

The authors acknowledge the help of Dr. T. Argunova, S. Nagalyuk, and O. Kazarova. E. N. Mokhov acknowledges the support of the Russian Science Foundation (grant RSF No. 16-42-01098).

## References

[1] H. Markoc, S. Strite, G.B. Gao, M.E. Lin, B. Sverdlov, M. Burns, Large-band-gap SiC, III-V-nitrides and II-VI-based semiconductor device technologies, J. Appl. Phys. 76 (3) (1994) 1363−1398.

[2] T.Y. Chemekova, O.V. Avdeev, S.S. Nagalyuk, E.N. Mokhov, K. Khelava, Y.N. Makarov, Aluminum nitride substrates for ultraviolet light-emitting diode structures, J. Surf. Investig. X-ray Synchrotron Neutron Tech. 5 (6) (December 2011) 1136−1139.

[3] C. Hartmann, A. Dittmar, J. Wollweber, M. Bickermann, Bulk AlN growth by physical vapor transport, Semicond. Sci. Technol. 29 (084002) (2014) 1−10.

[4] T.K. Hossain, J.V. Lindesay, M.G. Spenser, Growth and characterization of bulk nitride by physical vapor transport, Inside Internet (2005) 1−42.

[5] R. Dalmau, Z. Sitar, AlN bulk crystal growth by physical vapor transport, 24. Crystal Growth from Vapor. Part D, in: Springer Handbook of Crystal Growth, 2010, pp. 821−843.

[6] O.V. Avdeev, T.Y. Chemekova, E.N. Mokhov, S.S. Nagalyuk, H. Helava, M.G. Ramm, A.S. Segal, A.I. Zhmakin, Y.N. Makarov, Development of 2” AlN substrates using SiC seeds, Modern Aspects Bulk Cryst. Thin Film Prep. (2012) 213−262.

[7] O.V. Avdeev, T.Y. Chemekova, H. Helava, M.G. Ramm, Y.N. Makarov, E.N. Mokhov, S.S. Nagalyuk, A.S. Segal, Growth of bulk AlN crystals, Compr. Semicond. Sci. Technol. (2011) 282−301.

[8] O.V. Avdeev, T.Y. Chemekova, H. Helava, Y.N. Makarov, E.N. Mokhov, S.S. Nagalyuk, M.G. Ramm, A.S. Segal, A.I. Zhmakin, Copyright, in: P. Capper, P. Rudolpf (Eds.), Manufacturing of Bulk AlN Substrates. Crystal Growth Technology. Semiconductors and Dielectrics, WILEY-VCH Verlag GmbH & Co. KGaA, Weinheim, 2010, pp. 121−135.

[9] Y.A. Vodakov, E.N. Mokhov, Growth of Semiconductor SiC, Patent: USSR N 403275, 1970. Fr: No 2 264 589(1975); UK: No 1458445 (1977); FRG: No 24 09 005 (1977); USA No 414572 (1979).

[10] S.Y. Karpov, A.V. Kulik, I.A. Zhmakin, Y.N. Makarov, E.N. Mokhov, M.G. Ramm, M.S. Ramm, A.D. Roenkov, Y.A. Vodakov, Analysis of sublimation growth of bulk SiC crystals in tantalum container, J. Cryst. Growth 211 (2000) 147−151.

[11] Y.A. Vodakov, M.I. Karklina, E.N. Mokhov, A.D. Roenkov, Growth of GaN epitaxial layers on the sapphire and SiC substrates, Non Org. Mater 16 (2) (1980) 537−538 (in Russian).

[12] S.Y. Karpov, A.V. Kulik, M.S. Ramm, E.N. Mokhov, A.D. Roenkov, Y.A. Vodakov, Y.N. Makarov, AlN crystal growth by sublimation technique, Mater. Sci. Forum 353-356 (2001) 779−782. Trans. Tech. Publ. LTD, Switzerland Germany UK USA).

[13] T. Furusho, S. Oshima, S. Nishino, Crystal growth AlN by sublimation close space technique, Mater. Sci. Forum 389-393 (2002) 1449−1452.

[14] V. Noveski, R. Schlesser, S. Mahajan, S. Beaudoin, Z. Sitar, Mass transfer in AlN crystal growth at high temperatures, J. Cryst. Growth 264 (2004) 369−378.

[15] G.A. Slack, T.F. McNelly, Growth of high purity AlN, J. Cryst. Growth 34 (1976) 263−279.

[16] J.C. Rojo, et al., Report on the growth of bulk AlN and subsequent substrate preparation, J. Cryst. Growth 231 (2001) 317−321.

[17] Z.G. Herro, D. Zhuang, R. Schlesser, Z. Sitar, Growth of AlN single crystalline boules, J. Cryst. Growth 312 (2010) 2519−2521.

[18] H. Wu, R. Zheng, S. Meng, Y. Guo, Growth of AlN single crystals by modified PVT, Proc. of SPIE 7135 (2008), 71350H.

[19] C. Hartmann, M. Albrecht, J. Wollweber, J. Schuppang, U. Juda, C. Guguschev, S. Golka, A. Dittmar, R. Fornari, SiC seed polarity-dependent bulk AlN growth under the influence of residual oxygen, J. Cryst. Growth 344 (2012) 19−26.

[20] C.M. Balkas, Z. Sitar, et al., Sublimation growth and characterization of bulk AlN single crystals, J. Cryst. Growth 179 (1997) 363−370.

[21] T.Y. Chemekova, et al., Sublimation growth of 2 inch diameter bulk AlN crystals, Phys. Status. Solidi 5 (6) (2008) 1612−1614.

[22] Y.N. Makarov, O.V. Avdeev, I.S. Barash, D.S. Bazarevskiy, T.Y. Chemekova, E.N. Mokhov, S.S. Nagalyuk, A.D. Roenkov, A.S. Segal, Y.A. Vodakov, M.G. Ramm, S. Davis, G. Huminic, H. Helava, Experimental and theoretical analysis of sublimation growth of AlN bulk crystals, J. Cryst. Growth 310 (5) (2008) 881−886.

[23] I. Satoh, S. Arakawa, K. Tanizaki, M. Miyanaga, T. Sacurada, Y. Yamamoto, H. Nakanata, SEI Technical Review Number 71, 2010, pp. 78−82.

[24] R.R. Sumathi, P. Gille, Sublimation growth of c-plane AlN single crystals on SiC Substrates, Cryst. Res. Technol. 47 (3) (2012) 237−246.

[25] R.R. Sumathi, Bulk AlN single crystal growth on foreign substrate and preparation of free-standing native seeds, Cryst. Eng. Commun. 15 (2013) 2232−2240.

[26] R.R. Sumathi, R.U. Barz, T. Straubinger, P. Gille, Structural and surface topography analysis of AlN single crystals grown on 6H−SiC substrates, J. Cryst. Growth 360 (2012) 193−196.

[27] E.N. Mokhov, A.D. Roenkov, Y.A. Vodakov, S.Y. Karpov, M.S. Ramm, A.S. Segal, Y.N. Makarov, H. Helava, Growth of AlN bulk crystals by sublimation sandwich method, Mater. Sci. Forum 433-436 (2003) 979−982.

[28] Y. Shi, Z.Y. Xie, L.H. Liu, B. Liu, J.H. Edgar, M. Kuball, Influence of buffer layer and 6H-SiC substrate polarity on the nucleation of AlN grown by the sublimation sandwich technique, J. Cryst. Growth 233 (1/2) (2001) 177−186.

[29] G.R. Yazdi, M. Beckers, F. Giuliani, M. Syväjärvi, L. Hultman, R. Yakimova, Free-standing AlN single crystals enabled by self-organization of 2*H*-SiC pyramids on 4H-SiC substrates, Appl. Phys. Lett. 94 (2009) 082109.

[30] B. Wu, R. Ma, H. Zhang, M. Dudley, R. Schlesser, Z. Sitar, Growth kinetics and thermal stress in AlN bulk crystal growth, J. Cryst. Growth 253 (1−4) (2003) 326−339.

[31] S.G. Mueller, R.T. Bondokov, K.E. Morgan, G.A. Slack, S.B. Schujman, J. Grandusky, J.A. Smart, L.J. Schowalter, The progress of AlN bulk growth and epitaxy for electronic applications, Phys. Status Solidi A 206 (6) (2009) 1153−1159.

[32] A.S. Segal, S.Y. Karpov, Y.N. Makarov, E.N. Mokhov, A.D. Roenkov, M.G. Ramm, Y.A. Vodakov, On mechanisms of sublimation growth of AlN bulk crystals, J. Cryst. Growth 211 (1) (2000) 68−72.

[33] R. Yakimova, A. Kakanakova-Georgieva, G.R. Yazdi, G.K. Georgiev, M. Syvajarvi, Sublimation growth of AlN crystals: growth mode and structure evolution, J. Cryst. Growth 281 (1) (2005) 81−86.

[34] B. Gao, S. Nakano, K. Kakimoto, The impact of pressure and temperature on growth rate and layer uniformity in the sublimation growth of AlN crystals, J. Cryst. Growth 338 (2012) 69−74.

[35] Y. Li, D.W. Brenner, First principles prediction of the gas-phase precursors for AlN sublimation growth, Phys. Rev. Lett. 92 (2004) 75503.1−75503.4.

[36] A.S. Segal, A.N. Vorob'ev, S.Y. Karpov, Y.N. Makarov, E.N. Mokhov, M.G. Ramm, M.S. Ramm, A.D. Roenkov, Y.A. Vodakov, A.I. Zhmakin, Transport phenomena in sublimation growth of SiC bulk crystals, Mater. Sci. Eng. B 61-62 (1999) 40−43.

[37] A.S. Segal, A.N. Vorob'ev, S.Y. Karpov, E.N. Mokhov, M.G. Ramm, M.S. Ramm, A.D. Roenkov, Y.A. Vodakov, Y.N. Makarov, Growth of silicon carbide by sublimation sandwich method in the atmosphere of inert gas, J. Cryst. Growth 208 (1−4) (2000) 431−441.

[38] G.A. Slack, Growth of AlN single crystals, Mater. Res. Soc. Symp. Proc. 512 (1998) 35−40.

[39] R. Schlesser, R. Dalmau, D. Zhuang, R. Collazo, Z. Sitar, Crucible materials for growth of AlN crystals, J. Cryst. Growth 281 (1) (July 15, 2005) 75−80.

[40] Y.A. Vodakov, A.D. Roenkov, M.G. Ramm, E.N. Mokhov, Y.N. Makarov, Use of Ta − container for sublimation growth and doping of SiC bulk crystals and epitaxial layers, Phys. Status Solidi 202 (1) (1997) 177−200.

[41] F. Langhans, S. Kiefer, C. Hartmann, T. Markurt, T. Schulz, C. Guguschev, M. Naumann, S. Kollowa, A.D.J. Wollweber, M. Bickermann, Precipitates originating from tungsten crucible parts in AlN bulk crystals grown by the PVT method, Cryst. Res. Technol. 51 (2) (2016) 129−136, https://doi.org/10.1002/crat.201500201.

[42] H. Helava, S.J. Davis, M.G. Ramm, O.V. Avdeev, I.S. Barash, T.Y. Chemekova, E.N. Mokhov, S.S. Nagalyuk, A.D. Roenkov, A.S. Segal, Y.A. Vodakov, Y.N. Makarov, Growth of bulk aluminum nitride crystals, Phys. Status Solidi 4 (7) (2007) 2281−2284.

[43] Z.Y. Fan, N. Newman, Experimental determination of the rates of decomposition and cation desorption from AlN surfaces, Mater. Sci. Eng. B87 (2001) 244−248.

[44] P. Heimann, C. Pfeiffer, M. Bickermann, B.M.S. Nagata, A. Winnacker, Initial growth stage in PVT growth of AlN on SiC substrates: influence of $Al_2O_3$, Phys. Status Solidi C 4 (7) (2007) 2223−2226.

[45] P. Heimann, B.M. Epelbaum, M. Bickermann, S. Nagata, A. Winnacker, The initial growth stage in PVT growth of aluminum nitride, Phys. Status Solidi C 3 (6) (2006) 1575−1578.

[46] E.N. Mokhov, A.V. Avdeev, I.S. Barash, T.Y. Chemikova, A.D. Roenkov, S.Y. Karpov, A.S. Segal, A.A. Wolfson, Y.N. Makarov, M.G. Ramm, H. Helava, Sublimation Growth of AlN bulk crystals in Ta crucibles, J. Cryst. Growth 281 (1) (2005) 93−100.

[47] E. Mokhov, S. Smirnov, A. Segal, D. Bazarevskiy, Y. Makarov, M. Ramm, H. Helava, Experimental and theoretical analysis of sublimation growth of bulk AIN crystals, Mater. Res. Forum 457-460 (2004) 1545−1548.

[48] A.A. Wolfson, E.N. Mokhov, Dependence of the growth rate of an AlN layer on nitrogen pressure in a reactor for sublimation growth of AlN crystals, Semiconductors 44 (10) (2010) 1383−1385.

[49] E.N. Mokhov, A.A. Wolfson, H. Helava, Y. Makarov, Sublimation growth of AlN and GaN bulk crystals on SiC seeds, Mater. Res. Forum 740-742 (2013) 81−84.

[50] E.N. Mokhov, A.D. Roenkov, A.S. Segal, SiC sublimation growth at small spacing between source and seed, Mater. Res. Forum 740-742 (2013) 69−72.

[51] A.A. Wolfson, Dependence of the AlN layer growth rate on source−substrate clearance for the sublimation growth method, Semiconductors 48 (11) (2014) 1532−1534.

[52] R. Dalmau, R. Schlesser, Z. Sitar, Polarity and morphology in seeded growth of bulk A1N on SiC, Phys. Status Solidi C 2 (7) (2005) 2036−2039.

[53] R.R. Sumathi, P. Gille, Role of SiC substrate polarity on the growth and properties of bulk AlN single crystals, J. Mater. Sci. Mater. Electron. 25 (2014) 3733−3741.

[54] Z.G. Herro, D. Zhuang, R. Schlesser, R. Collazo, Z. Sitar, Seeded growth of AlN on N- and Al- polar <0001> seeds by physical vapor transport, J. Cryst. Growth 286 (2) (2006) 205−208.

[55] E. Mokhov, I. Izmaylova, O. Kazarova, A. Wolfson, S. Nagalyuk, D. Litvin, A. Vasiliev, H. Helava, Y. Makarov, Specific features of sublimation growth of bulk AlN crystals on SiC wafers, Phys. Status Solidi 10 (1) (2013) 201.

[56] A.A. Wolfson, Spontaneous department of AlN layer grown by sublimation method from 6H SiC substrate, Semiconductor 43 (6) (2009) 847−849.

[57] E.N. Mokhov, A.A. Wolfson, A.O. Avdeev, S.S. Nagalyuk, D.P. Litvin, A.V. Vasiliev, M.G. Ramm, H. Helava, Y. Makarov, Sublimation growth of bulk AlN crystals on SiC seeds, Mater. Res. Forum 740-742 (2013) 95−98.

[58] B.M. Epelbaum, M. Bickermann, S. Nagata, P. Heimann, O. Filip, A. Winnacker, Similarities and differences in sublimation growth of SiC and AlN, J. Cryst. Growth 305 (2) (2007) 317−325.

[59] T.S. Argunova, M.Y. Gutkin, J.H. Je, J.H. Lim, E.N. Mokhov, A.D. Roenkov, Structural transformation of lattice defects in free-spreading growth of bulk SiC crystals, CrystEngComm 16 (2014) 8917−8923, https://doi.org/10.1039/c4ce01515k. Advance Article.

[60] T.S. Argunova, M.Y. Gutkin, O.P. Kazarova, E.N. Mokhov, S.S. Nagalyuk, J.H. Je, Synchrotron x-ray study on crack prevention in AlN crystals grown on gradually decomposing SiC substrates, Mater. Sci. Forum 821-823 (2015) 1011−1014.

[61] T.S. Argunova, M.Y. Gutkin, K.D. Shcherbachev, E.N. Mokhov, Microstructure and strength of AlN−SiC interface studied by synchrotron X-rays. Interfaces and intergranular boundaries, J. Mater. Sci. 52 (8) (2017) 4244−4252.

[62] T.S. Argunova, M.Y. Gutkin, K.D. Shcherbachev, S.S. Nagalyuk, O.P. Kazarova, E.N. Mokhov, J.H. Je, Thermal and lattice misfit stress relaxation in growing AlN crystal with simultaneous evaporation of SiC substrate, Mater. Sci. Forum 897 (2017) 711−714.

[63] E.N. Mokhov, T.S. Argunova, J.H. Je, O.P. Kazarova, K.D. Shcherbachev, Free-standing single crystal AlN layers grown using the SiC substrate evaporation method, CrystEngComm 19 (2017) 3192.

[64] T.S. Argunova, M.Y. Gutkin, J.H. Je, A.E. Kalmykov, O.P. Kazarova, E.N. Mokhov, K.N. Mikaelyan, A.V. Myasoedov, L.M. Sorokin, K.D. Shcherbachev, Distribution of dislocations near the interface in AlN crystals grown on evaporated SiC substrates, Crystals 7 (163) (2017) 12.

[65] R.A. Stein, P. Lanig, S. Leibenzeder, Influence of surface energy on the growth of 6H and 4H SiC polytypes by sublimation, Mater. Sci. Eng. B 11 (1992) 69−71.

[66] M. Birkholz, Thin Film Analysis by X-ray Scattering, Wiley-VCH Verlag GmbH and Co. KGaA, Weinheim, 2006.

[67] S. Porowski, J. Jun, P. Perlin, I. Grzegory, H. Teissere, T. Suski, Prospects for high-pressure crystal growth of III-V nitrides, in: Inst. Phys. Conf. Ser., vol. 137, 1994, p. 369.

[68] S. Porowski, High pressure crystallization of III-V nitrides, Acta Phys. Polonica A 87 (2) (February 1995) 295−302.

[69] M. Leszczynski, I. Grzegory, H. Teisseyre, T. Suski, M. Bockowski, J. Jun, J.M. Baranowski, S. Porowski, J. Domagala, The microstructure of gallium nitride monocrystals grown at high pressure, J. Cryst. Growth 169 (2) (November 1996) 235−242.

[70] M. Bockowski, Bulk growth of gallium nitride: challenges and difficulties, Cryst. Res. Technol. 42 (12) (December 2007) 1162−1175.

[71] B. Wang, M.J. Callahan, Ammonothermal synthesis of III-nitride crystals, Cryst. Growth Des. 6 (6) (June 2006) 1227−1246.

[72] T. Fukuda, D. Ehrentraut, Prospects for the ammonothermal growth of large GaN crystal, J. Cryst. Growth 305 (2) (July 2007) 304−310.

[73] M. Aoki, H. Yamane, M. Shimada, S. Sarayama, F.J. DiSalvo, GaN single crystal growth using high-purity Na as a flux, J. Cryst. Growth 242 (1−2) (July 2002) 70−76.

[74] T. Iwahashi, F. Kawamura, M. Morishita, Y. Kai, M. Yoshimura, Y. Mori, T. Sasaki, Effects of ammonia gas on threshold pressure and seed growth for bulk GaN single crystals by Na flux method, J. Cryst. Growth 253 (1−4) (June 2003) 1−5.

[75] F. Kawamura, T. Iwahashi, M. Morishita, K. Omae, M. Yoshimura, Y. Mori, T. Sasaki, Growth of transparent, large size GaN single crystal with low dislocations using Ca-Na flux system, Pt. 2, Jpn. J. Appl. Phys. 42 (7A) (July 2003) L729−L731.

[76] M. Morishita, F. Kawamura, M. Kawahara, M. Yoshimura, Y. Mori, T. Sasaki, Promoted nitrogen dissolution due to the addition of Li or Ca to Ga-Na melt; some effects of additives on the growth of GaN single crystals using the sodium flux method, J. Cryst. Growth 284 (1−2) (October 2005) 91−99.

[77] J.K. Jian, G. Wang, C. Wang, W.X. Yuan, X.L. Chen, GaN single crystals grown under moderate nitrogen pressure by a new flux: $Ca_3N_2$, J. Cryst. Growth 291 (1) (May 2006) 72−76.

[78] T. Yamada, H. Yamane, H. Iwata, S. Sarayama, The process of GaN single crystal growth by the Na flux method with Na vapor, J. Cryst. Growth 286 (2) (January 2006) 494−497.

[79] F. Kawamura, H. Umeda, M. Kawahara, M. Yoshimura, Y. Mori, T. Sasaki, H. Okado, K. Arakawa, H. Mori, Drastic decrease in dislocations during liquid phase epitaxy growth of GaN single crystals using Na flux method without any artificial processes, Pt. 1, Jpn. J. Appl. Phys. 45 (4A) (April 2006) 2528−2530.

[80] T. Yamada, H. Yamane, Seeded growth of GaN single crystals by Na flux method using Na vapor, Jpn. J. Appl. Phys. 45 (33−36) (September 2006) L898−L900.

[81] F. Kawamura, H. Umeda, M. Morishita, M. Kawahara, M. Yoshimura, M. Mori, T. Sasaki, Y. Kitaoka, Growth of a two-inch GaN single crystal substrate using the Na flux method, Pt. 2, Jpn. J. Appl. Phys. 45 (43) (Oct. 2006) L1136−L1138.

[82] F. Kawamura, M. Imade, M. Yoshimura, Y. Mori, Y. Kitaoka, T. Sasaki, Growth of high-quality large GaN crystal by Na flux LPE method, in: Proc. Of SPIE, Gallium Nitride Materials and Devices IV, 2009, p. 7216. Paper OB-1-13.

[83] Y. Mori, M. Imade, K. Murakami, H. Takazawa, H. Imabayashi, Y. Todoroki, K. Kitamoto, M. Maruyama, M. Yoshimura, Y. Kitaoka, T. Sasaki, Growth of bulk GaN crystal by Na-flux method under various conditions, J. Cryst. Growth 350 (2012) 72−74.

[84] T. Yamada, M. Imanishi, K. Nakamura, K. Murakami, H. Imabayashi, D. Matsuo, M. Honjo, M. Maruyama, M. Imade, M. Yoshimura, Y. Mori, Crack-free GaN substrates grown by the Na-flux method with a sapphire dissolution technique, APEX 9 (2016), 071002.

[85] B. Feigelson, T. Paskova, Growth of bulk GaN crystals, in: Book Comprehensive Semiconductors Science and Technology, vol. 3, Elsevier B.V., 2011, pp. 232−281.

[86] I. Grzegory, B. Łucznik, M. Boćkowski, B. Pastuszka, M. Kryśko, G. Kamler, G. Nowak, S. Porowski, Growth of bulk GaN by HVPE on pressure grown seeds, Proc. SPIE 6121 (2006), 612107.

[87] A.D. Williams, T.D. Moustakas, Formation of large-area free-standing gallium nitride induced separation of GaN and sapphire, J. Cryst. Growth 300 (1) (2007) 37−41.

[88] Y.A. Vodakov, E.N. Mokhov, A.D. Roenkov, Method of Epitaxial Growth of Gallium Nitride, 1983. Patent of USSR No 1136501.

[89] Y.A. Vodakov, E.N. Mokhov, A.D. Roenkov, M.E. Boiko, P.G. Baranov, High rate GaN epitaxial growth by sublimation sandwich method, J. Cryst. Growth 183 (1/2) (1997) 10.

[90] P. Baranov, E. Mokhov, A. Ostroumov, M.G. Ramm, M.S. Ramm, V. Ratnikov, A. Roenkov, Y. Vodakov, A. Wolfson, G. Saparin, S. Karpov, D. Zimina, Y. Makarov, H. Juergensen, Current status of GaN crystal growth by sublimation sandwich technique, MRS Internet J. Nitride Semicond. Res. 3 (1998) 50.

[91] Z.A. Munir, A.W. Searcy, Activation energy for the sublimation of GalliuNitride, J. Chem. Phys. 42 (12) (1965) 4223.

[92] R.B. Zetterstrom, Synthesis and growth of single crystals of GaN, J. Mater. Sci. 5 (12) (1970) 1102.

[93] E. Ejder, Growth and morphology of GaN, J. Cryst. Growth 22 (1) (1974) 44.

[94] T. Matsumoto, M. Aoki, Temperature dependence of photoluminescence from GaN, Jpn. J. Appl. Phys. 13 (1974) 1804.

[95] D. Elwell, R.S. Feigelson, M.M. Simkins, W.A. Tiller, Crystal growth of GaN by the reaction between gallium and ammonia, J. Cryst. Growth 66 (1) (1984) 45.

[96] S. Fisher, C. Wetzel, W.L. Hansen, E.D. Bourett-Courchesne, Properties of GaN grown at high rates on sapphire and on 6H- SiC, Appl. Phys. Lett. 69 (18) (1996) 2716.

[97] S. Kurai, T. Abe, Y. Naoi, S. Sakai, Growth and characterization of thick GaN by sublimation method and homoepitaxial growth by metalorganic chemical vapor deposition, Jpn. J. Appl. Phys. 35 (3) (1996) 1637.

[98] Z. Sitar, R. Schlesser, Growth of Single Crystals and Fabrication of GaN AndAlN Wafers, Final Technical Report, 2006 03 17, March 2006.

[99] E. Berkman, R. Collazo, R. Schlesser, Z. Sitar, Growth of GaN from elemental gallium and ammonia via modified sandwich growth technique, MRS. 831 (January 2004). E11.38.

[100] S.S. Liu, D.A. Stevenson, Growth kinetics and catalytic effects in the vapor phase epitaxy of gallium nitride, J. Electrochem. Soc. 125 (7) (1978) 1161.

[101] G.V. Saparin, S.K. Obyden, M.V. Chukichev, S.I. Popov, Cathodoluminescent contrast of direct writing patterns in the scanning electron microscope, J. Lumin. 31/32 (1984) 684.

[102] C. Wetzel, D. Volm, B.K. Meyer, K. Pressel, S. Nilsson, E.N. Mokhov, P.G. Baranov, GaN on 6H-SiC − structural and optical properties, Mater. Res. Soc. Proc. 339 (1994) 453.

[103] V.Y. Davidov, Y.E. Kitaev, I.N. Goncharuk, A.N. Smirnov, J. Graul, O. Semchinova, D. Uffmann, M.B. Smirnov, A.P. Mirgorodsky, R.A. Evaristov, Phonon dispersion and Raman scattering in hexagonal GaN and AlN, Phys. Rev. B 58 (1998) 12899.

[104] P.G. Baranov, I.V. Ilyin, E.N. Mokhov, A.D. Roenkov, Identification of Mn and Ni trace impurities in GaN crystals by electron paramagnetic resonance, Inst. Phys. Conf. (1997) 985−988. Ser. No. 155, (Chapter 12).

[105] P.G. Baranov, I.V. Ilyin, E.N. Mokhov, Identification of iron transition group trace impurities in GaN bulk crystals by electron paramagnetic resonance, Solid State Commun. 101 (8) (1997) 611−615.

[106] J. Baur, M. Kunzer, K. Maier, U. Kaufmann, J. Schneider, Determination of the GaN/AlN band discontinuities via the (-/0-) acceptor level of iron, Mater. Sci. Eng. B 29 (1−3) (1995) 61.

[107] H.I. Helava, E.N. Mokhov, O.A. Avdeev, M.G. Ramm, D.P. Litvin, A.V. Vassiliev, A.D. Roenkov, S.S. Nagalyuk, Y.N. Makarov, Growth of low-defect SiC and AlN crystals in refractory metal crucibles, Mater. Res. Forum 740-742 (2013) 85−90.

# Further Reading

[1] E.N. Mokhov, A.A. Wolfson, O.P. Kazarova, Effect of a gas pressure in a reactor on the growth rate of AlN layer, Mater. Res. Forum 740-742 (2013) 107−110.

This page intentionally left blank

# Aluminum oxide

# 13

*Leonid Lytvynov*
Institute for Single Crystals of NASU, Kharkiv, Ukraine

## 13.1 Introduction

The term *sapphire* is widely used in the scientific and technical literature to identify the $\alpha$ phase of aluminum oxide ($Al_2O_3$) single crystals. However, the mineralogical name *leucosapphire* is more accurate, and the definition *single crystal of corundum* is also correct. The term *alumina* (*α-alumina*) is also sometimes used to denote sapphire, but it generally refers to raw material. More about definitions and trade names can be found in the literature [1].

For several millennia sapphire worked its way up from being a valuable decoration to being an indispensable material in most branches of engineering, especially hi-tech. Several industrial methods for growing sapphire were rapidly developed, and the volumes of grown sapphire ceased to be counted by carats and began to be counted by thousands of tons. Sapphire production does not pollute the environment. It is not classified as dangerous according to EC Directives. In the near future sapphire will join silicon and germanium to become one of the main strategic materials in electronics.

## 13.2 Growth methods

In principle, sapphire can be grown starting from gaseous, liquid, or solid nutrient phases. The choice of the most suitable method is based on the physical−chemical essence of the growth processes and the peculiarities of a particular method [2]. Sapphire for electronics is normally grown from its own melt by different methods, namely Verneuil, Czochralski (Cz), Kyropoulos (Ky), edge-defined film-fed growth (EFG) or classical Stepanov method (CS), the heat exchanger method (HEM) or controlled heat extraction system (CHES), the horizontal direct solidification method (HDSM) or horizontal direct solidification (HDS), and their modifications or, more rarely, by the vertical Bridgman (VB) method. Each of these methods has its own features, advantages, and drawbacks (growth zone environment, maximum achievable crystal size, temperature gradients at the crystallization front which define the level of stresses, fracture toughness, dislocation density, the presence of grain boundaries, etc.) [2]. The main criterion for the choice of a particular method is the quality of the crystal to be obtained; in other words, the functional parameters of the sapphire as well as the productivity of the given method and the cost of the grown crystal.

Due to space limitations, in this chapter we describe only the principles of the methods, which are shown schematically in Fig. 13.1A.

**Single Crystals of Electronic Materials.** https://doi.org/10.1016/B978-0-08-102096-8.00013-6
Copyright © 2019 Elsevier Ltd. All rights reserved.

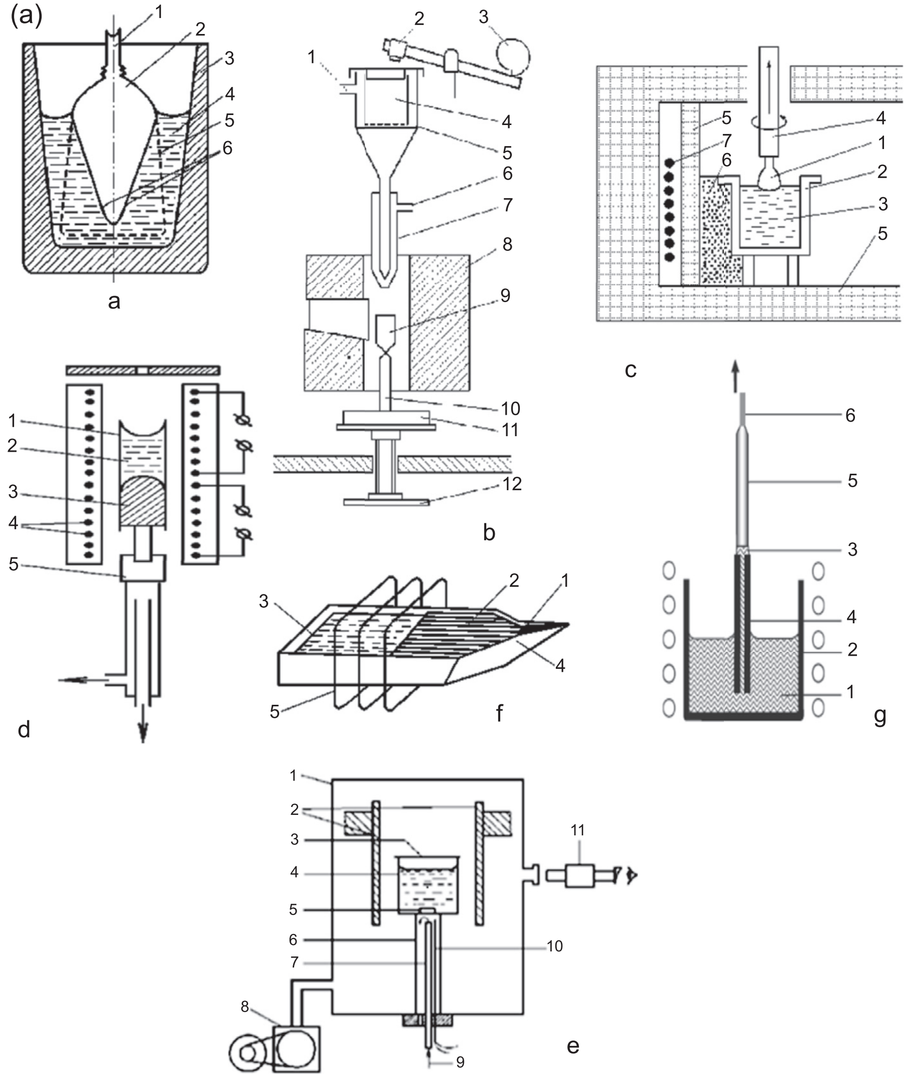

**Figure 13.1** (A) Methods for growing sapphire. (a) Ky: 1 seed, 2 growing crystal, 3 crucible, 4 melt, 5 final crystal, 6 crystallization front. (b) Verneuil: 1 oxygen connection, 2 hammer, 3 eccentric, 4 mesh capacity, 5 bunker, 6 hydrogen connection, 7 burner, 8 muffle, 9 crystal, 10 ceramics rod, 11−12 support. (c) CZ: 1 crystal, 2 crucible, 3 melt, 4 crystal holder, 5−6 insulation, 7 heater. (d) VB: 1 crucible, 2 melt, 3 crystal, 4 heater, 5 support. (e) HEM: 1 furnace shell, 2 heating element, 3 cover, 4 crucible, 5 seed, 6 heat exchanger, 7 tungsten tube, 8 vacuum pump, 9 helium, 10 thermocouple, 11 pyrometer. (f) HDS: 1 seed, 2 crystal, 3 melt, 4 boat, 5 heater. (g) EFG: 1 melt, 2 crucible, 3 film of melt, 4 capillary, 5 crystal, 6 seed. (B) Crystals grown by different methods. (a) EFG; (b) Verneuil; (c) CHES; (d) HDS; (e) Ky; (f) VB.

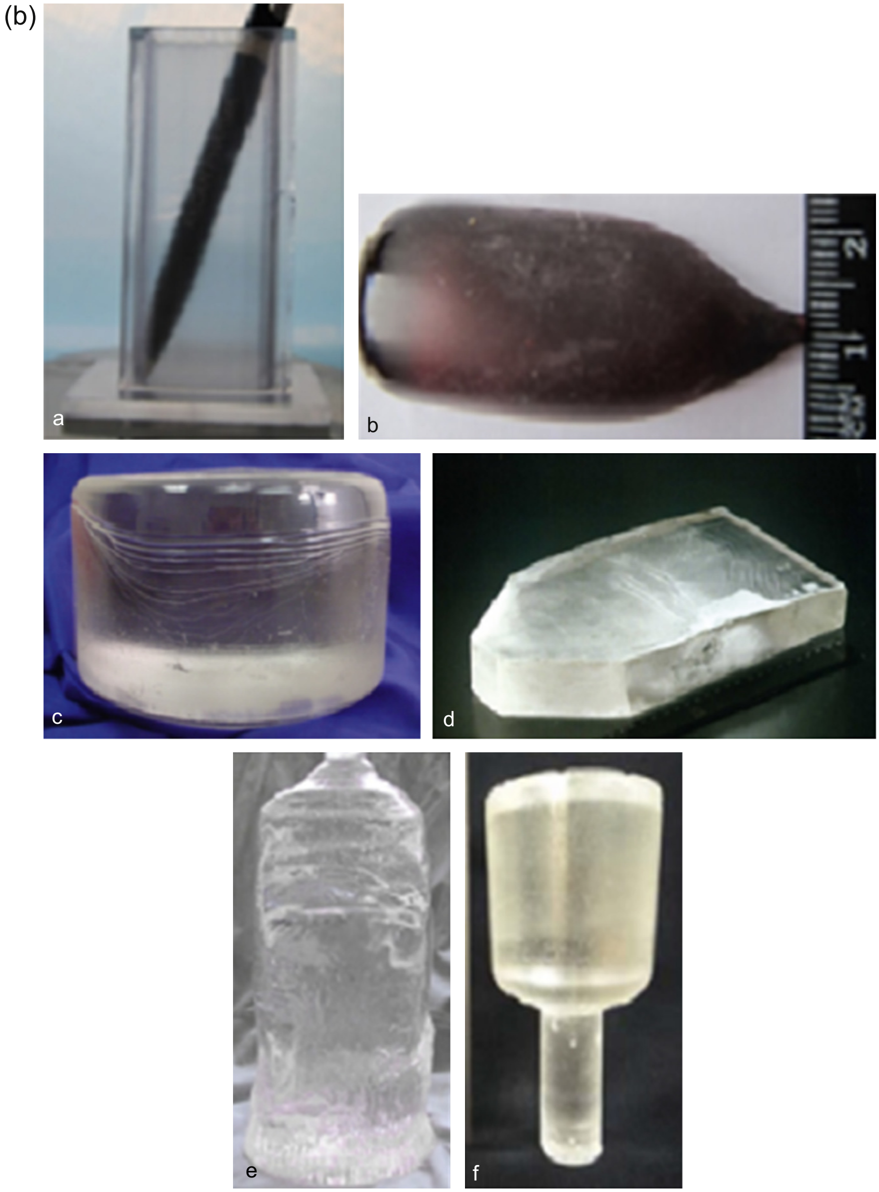

Figure 13.1 cont'd.

## 13.2.1 Concise description of methods

**EFG.** The method uses the idea of shaping by capillary action. A special die sets the profile of the growing crystal. During growth, the capillary system is fed to the die and through it to the pulled crystal. In this method the region and intensity of perturbations of the free liquid surface are limited (see Fig. 13.1A, g, p.3), and this leads to formation of a controlled shape. The dimensions and shape of the growing crystal are defined by:

- the shaper geometry;
- the pressure applied to the melt being introduced into the die;
- the shape of the seed (at the initial stage).

To obtain complicated profiles, a rod wetted with the melt may be used as a seed to lift the melt column above the die level.

**Verneuil**. The crystals are grown from dispersed fine powder of alumina which is fed through a flame of combustible gas on to a ceramic crystal holder. Flying through the flame, the raw material particles melt and hit the face of the crystal holder. The top of the formed cone melts and then grows until a preset diameter is obtained. The shouldering stage can be speeded up by preliminarily fixing the seed of the wanted size on the crystal holder.

**Cz**. In the Cz method crystals are gradually pulled from the melt by withdrawing an oriented seed. The melt temperature may be constant or may vary in a predetermined manner. The crystallization front during growth is above the surface of the melt. The high quality of the grown crystals, which to a considerable extent is caused by the absence of contact between the crystal and the crucible, makes this method popular for crystal production.

**HEM.** The method does not imply technological motion, as the driving force of crystallization is the change in the thermal field generated by the heater and the heat exchanger. Heat removal is realized by flowing pure gases, or their mixtures, with high thermal capacity, or by liquid coolants. Changes in the furnace temperature and the variation of the coolant flow passing through the heat exchanger create conditions for the independent control of temperature gradients in the solid and liquid phases.

**HDSM.** The raw material is placed in a molybdenum boat which moves horizontally at a velocity of 8−10 mm/h and passes through a rather narrow high-temperature zone. Due to segregation during solidification, impurities are pushed into the tail part of the crystal.

**Ky**. The essence of the method consists in the growth of crystals by a smooth, slow decrease of the melt temperature and heat removal through the crystal seed suspended from a cooled rod. The crystal grows inside the melt until it fully crystallizes. The crystallization front at growth varies from the initial conical shape (see Fig. 13.1A, a, p.2) to a cylinder-like shape (see Fig. 13.1A, a, p.5).

**VB**. The Bridgman technique implies vertical translation of either the crucible (in the case of a steady temperature gradient) or the heater which gives the temperature gradient. Crystal growth is realized under conditions of spontaneous nucleation (or with use of a seed) in a cylindrical container with a conical bottom.

Sapphire grown by the Verneuil method is not widely used in electronics because of the small diameter of the crystals. The method is described in detail in the literature [3].

Over the past 10 years the parameters of crystals grown by the Verneuil and Cz methods have changed slightly. At the same time, the size and weight of the crystals obtained by other methods have essentially increased. The most noticeable advances have been achieved for the Ky and EFG methods. In particular, in recent years thousands of growth installations have been set up.

The weight of crystals grown by the Ky method has increased by 10 times, from 30 to 300−400 kg, and production volume has grown from 5 to >1000 ton/year. The weight of a single crystal will reach 1000 kg by 2020. The growth of one crystal with a weight of 100, 200, or even 400 kg is more profitable than the growth of a corresponding quantity of smaller crystals. A crystal of 100 kg grows in ~18 days. Most of the crystals have perfect optical quality, although some inhomogeneity in volume is observed. The inhomogeneity is explained by the change in the shape of the crystallization front during the growth process. The method is well described in a book by the author of the adaptation of the Ky method for growing sapphire [4], and elsewhere in the literature [2,5]. The method of controlling the shape of the crystallization interface has also been described [6].

The volume of crystals produced by the Verneuil method has not changed with time, but the share of Verneuil crystals used as raw starting material for the Ky method has essentially increased.

Cz, Ky, HEM, and VB are methods of growing bulk crystals of cylindrical or near-cylindrical form. Crystals grown by HDSM have a thickness much smaller than their width and length [7]. Profiled crystals grown by EFG have almost the same shape as the final product [8,9]. Technologies for the simultaneous growth of numerous profiles (rods, ribbons, tubes) have been developed for improving productivity. The dimensions of plates produced by the EFG method have grown by several times. Such a tendency is expected to continue.

Technical and economic characteristics of the methods for growing sapphire, along with the typical structural characteristics of crystals, are compared in Tables 13.1−13.9.

Grain boundaries (blocks) are formed in the crystal when the dislocation density reaches a critical value. Table 13.2 shows the values of critical dislocation density determined on the plane (0001) in sapphire ingots grown by different methods.

Crystals grown by different methods differ in shape (Fig. 13.1B). The dimensions of a single crystal are given in Table 13.3.

Some parameters, e.g., the resistance of sapphire to high radiation doses, depend on the growth zone atmosphere and the container material more than on the method itself, when other growth conditions are kept equal (Table 13.4).

Optical-grade crystal mostly depends on temperature gradients in the growth zone and growth speed. The values of optical grades 1−6 are given in Table 13.5.

The C plane is the most closely packed. Since growth in the direction C(0001) is impeded, the preferential growth directions are R($1\bar{1}02$), M($10\bar{1}0$), and A($11\bar{2}0$). As a rule, sapphire is grown in these directions (Table 13.6). Crystals grow in these directions at a higher rate than in the C direction. When it is necessary to obtain C-oriented wafers or blocks, the seeds are oriented in such a way that the C plane goes out to the side surface of the crystal. Then the C pieces (substrates, windows, ingots) are cut out along the axis C, i.e., perpendicularly to the geometrical axis of the crystal. In this case, only part of the useful volume is used (Fig. 13.2). The share of this volume can be

**Table 13.1** Temperature gradient in the growth zone, dislocation density, and fracture toughness coefficient of sapphire grown by different methods

| Growth method | ΔT, degree/cm | Dislocation density, ρ, $cm^{-2}$ | Fracture toughness coefficient, $K_{1C}$, $MN \cdot m^{-3/2}$ |
|---|---|---|---|
| Verneuil | | | |
| Regular furnace | 200–250 | (2…8) × $10^5$ | 2.6…2.8 |
| Furnace with additional heater | ~80 | ~1 × $10^5$ | 2.9…3.1 |
| EFG | 50–55 | $10^4$…$10^5$ | 3…3.5 |
| Cz | 40 | $10^3$…$10^5$ | 3.8…4 |
| Ky | 25 | $10^2$…$10^3$ | 4…4.5 |
| HEM | 20 | $10^2$…$10^3$ | 4…4.5 |
| HDS | 40 | $10^3$ | 3.8…4 |

**Table 13.2** Critical density of dislocation in crystal

| Growth method | $\rho_{cr}$, $cm^{-2}$ |
|---|---|
| Verneuil | (2–4) × $10^5$ |
| EFG | (1–2) × $10^5$ |
| Cz | (5–7) × $10^4$ |
| HDS | (2–3) × $10^4$ |

somewhat increased by optimizing the way of cutting (drilling out cylinders with different diameters). Output of C ingots per Ky boule depends on the weight of the crystal (Table 13.7).

The productivity of the different methods and their prevalence are shown in Tables 13.8–13.9.

In reality, this comparative analysis of the potentialities of sapphire growth methods reflect the experience of the author. Other technologists may have different points of view regarding the relative importance of the listed growth methods.

**Table 13.3** Size of the rods ($D_r$, $L_r$) or cylinders and plates, mm

| | $D_r$ | | $L_r$ | | Cross-section for plate | | L for plate | |
|---|---|---|---|---|---|---|---|---|
| Growth method | Regular | Maximum | Regular | Maximum | Regular | Maximum | Regular | Maximum |
| Verneuil | 25–30 | 90 | 250 | 400 | – | – | – | – |
| VB | 76 | 150 | 250 | 400 | – | – | – | – |
| EFG | 25 | 50 | 500 | 1400 | 120 × 10 | 500 × 20 | 300 | 500 |
| Cz | 100 | 300 | 200 | 400 | – | – | – | – |
| Ky | 300 | 500 | 350 | 450 | – | – | – | – |
| HEM | 300 | 400 | 200 | 300 | – | – | – | – |
| CHES | 300 | 500 | 200 | 400 | – | – | – | – |
| HDS | – | – | – | – | 200 × 30 | 350 × 40 | 220 | 500 |
| LANCE[a] | – | – | – | – | 457 × 60 | 457 × 60 | 914 | 914 |

[a] LANCE (large-area net-shaped crystal extraction) is the development of the HDS technology by Rubicon Technology (United States) for growing the largest-area sapphire for windows.

**Table 13.4** Resistance of sapphire to big dose of radiation

| Growth method | Area in growth zone | Material of container | Resistance to radiation, ar. units |
|---|---|---|---|
| Verneuil | $H_2$–$O_2$ | No container | 1 |
| EFG | Vacuum | W | 0.7 |
| | Reducing | W | 0.9 |
| | Reducing | Mo | 0.8 |
| Cz | Vacuum | W | 0.7 |
| Ky | Vacuum | W | 0.7 |
| HEM | Vacuum, Ar | Mo | 0.7 |
| HDS | Vacuum | Mo | 0.6 |
| | Reducing | Mo | 0.8 |

**Table 13.5** Optical grade (%) of sapphire grown by different methods

| | Optical grade | | | | | |
|---|---|---|---|---|---|---|
| Growth method | 1 | 2 | 3 | 4 | 5 | 6 |
| Verneuil | – | – | 10 | 20 | 50 | 10 |
| EFG | – | – | 20 | 30 | 40 | 10 |
| Cz | – | 30 | 50 | 20 | – | – |
| Ky | 3 | 30 | 50 | 17 | – | – |
| HEM | 4 | 30 | 52 | 14 | – | – |
| HDS | – | 30 | 50 | 20 | 10 | – |

## 13.3 Properties

***Structure.*** Corundum crystals belong to the ditrigonal scalenohedral class of trigonal symmetry $D_{3d}^6 - R\bar{3}C(L_33L_23PC)$ with symmetry elements:

- mirror-turn axis of the sixth order (ternary inversion axis);
- three axes of the second order normal to it;
- three symmetry planes normal to the axes of the second order and intercrossing along the axis of the highest order;
- symmetry center.

There are seven simple forms (facets) in this class of symmetry. According to Bravais classification, they have the symbols pinacoid (0001), hexagonal prisms $\{10\bar{1}0\}$

## Table 13.6 Fraction of crystal volume effectively used for production of blocks which are parallel to R, M, A, and C planes, %

| Growth method | R | M | A | C |
|---|---|---|---|---|
| EFG | 70 | 75 | 80 | |
| Ky | 80 | 75 | 70 | ~50 for rectangular articles<br>15%–35% for cylindrical ingots for light-emitting diodes (LEDs) |
| VB | 80 | 80 | 80 | 80 |
| HDS | 80 | 75 | 70 | ~60 |
| HEM | 80 | 80 | 80 | 60 |
| CHES | 80 | 80 | 80 | 80 |

## Table 13.7 Theoretical length of Ky boule, mm

| | Weight of crystal, kg | | |
|---|---|---|---|
| **Diameter of ingot, inch/mm** | **28–30** | **75–80** | **120** |
| 2/50.8 | 1350 | 3500 | 5750 |
| 4/101.6 | 360 | 780 | 1900 |
| 6/152.4 | 145 | 470 | 630 |

## Table 13.8 Weight (P, kg) of crystal and productivity (G, g/h) of growth methods

| | P | | |
|---|---|---|---|
| **Growth method** | **Regular** | **Maximum** | **G** |
| Verneuil | 0.3 | 7 | 20–25 |
| EFG | 1 | 12 | 100–140 |
| Cz | 4 | 14 | 180–200 |
| Ky | 30, 60, 80, 200 | 400 | 230–350 |
| HEM | 40 | 84 | 200–250 |
| HDS | 5 | 19 | 200–250 |
| LANCE | 105 | 105 | 500 |

**Table 13.9 Growth methods applied to production of LED substrates in different countries**

| Growth methods | Countries |
|---|---|
| EFG | Japan, Korea, China |
| VB | Japan, Russia |
| Cz | Japan, France |
| Ky | United States, Russia, Korea, China, Taiwan, Poland |
| HEM | United States |
| CHES | China |

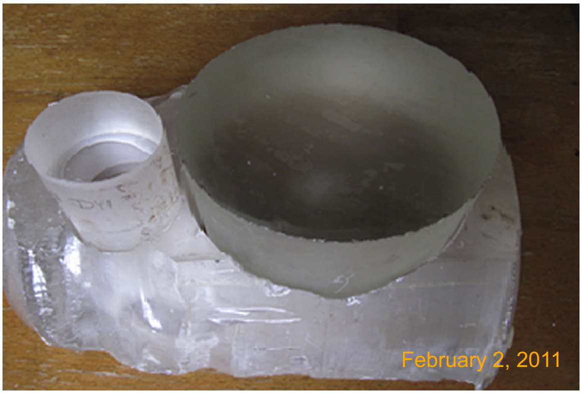

**Figure 13.2** Drilled C ingots from Ky crystal.

and $\{11\bar{2}0\}$, dihexagonal prism $\{hki0\}$, rhombohedron $\{h0\bar{h}l\}$, hexagonal bipyramid $\{hh2\bar{h}l\}$, and ditrigonal scalenohedron. Depending on its position with respect to the hexagonal crystallographic axes, the rhombohedron may be "positive" $\{10\bar{1}1\}$ or "negative" $\{01\bar{1}1\}$ [10].

For pure sapphire the lattice parameters at 295K are $a = 4.759213$ Å and $c = 12.991586$ Å. For $Al_2O_3$:Ti $a = 4.75950$ Å and $c = 12.99528$ Å. The lattice parameters increase with increasing temperature; $2Al^{3+} + 3O^{2+}$ occupy $19.9 \times 10^{-16}$ cm$^2$. Lattice energy is 3663−3708 (3708−theoretical) kcal/mol. Parameters characterizing sapphire lattice in more detail are available in the literature [2].

The mutual arrangement of the most frequently encountered crystallographic planes is shown in Fig. 13.3, while a model of sapphire structure is shown in Fig. 13.4.

The hexagonal lattice of sapphire is anisotropic. Fig. 13.5 clearly shows the difference in the crystallographic planes with respect to the density of atoms: atom density on the C plane is $1.3 \times 10^{15}$, on the A plane it is $1.6 \times 10^{14}$, and on the M plane it is $2.6 \times 10^{14}$ at/cm$^2$.

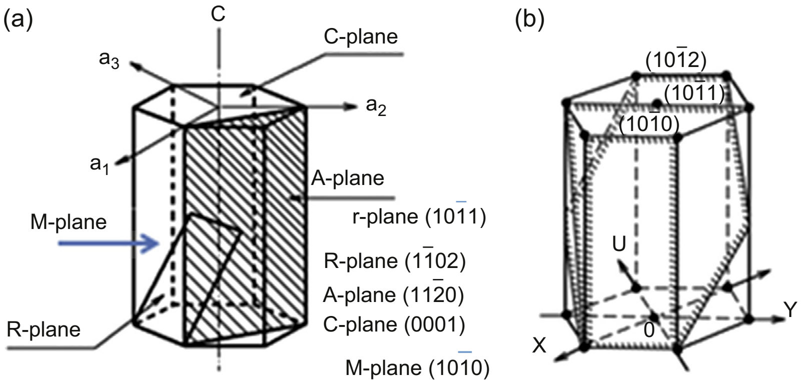
(a)
C
C-plane
a3
a2
a1
A-plane
M-plane
R-plane
r-plane (101̄1)
R-plane (11̄02)
A-plane (112̄0)
C-plane (0001)
M-plane (101̄0)
(b)
(101̄2)
(101̄1)
(101̄0)
U
Y
X
0

**Figure 13.3** (a) Frequently used crystallographic planes; (b) the position of the rhombohedron planes relative to the M plane.

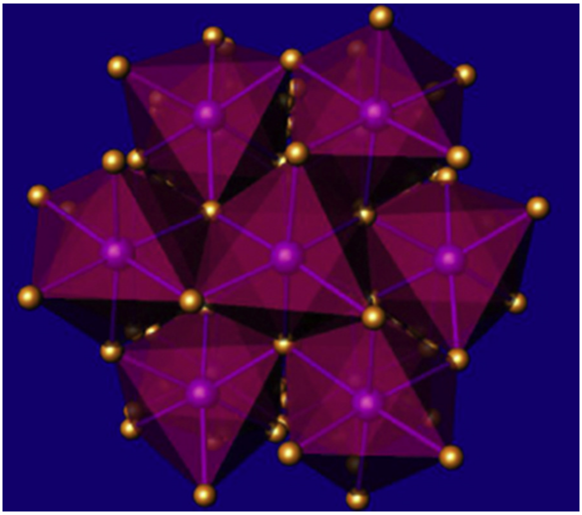

**Figure 13.4** Model of sapphire structure. The *purple and gold balls* represent aluminum and oxygen, respectively. The pink shadowing shows the octahedral coordination of aluminum.

The C plane (0001) is one of the most desirable for windows, substrates for electronic devices, and a number of other applications. The stability of the physical and chemical properties of the C plane is largely determined by the accuracy of its orientation. This plane has the highest reticular density of atoms (0.225 at/Å$^2$), the maximum number of free bonds (6.6), and the maximum fracture surface energy (FSE $>$40 J/m$^2$) compared to other planes of the crystal. At the same time, the chemical and corrosion resistance of the C plane is not the highest, and the resistance to extreme loads is lower than for the M and A planes [11].

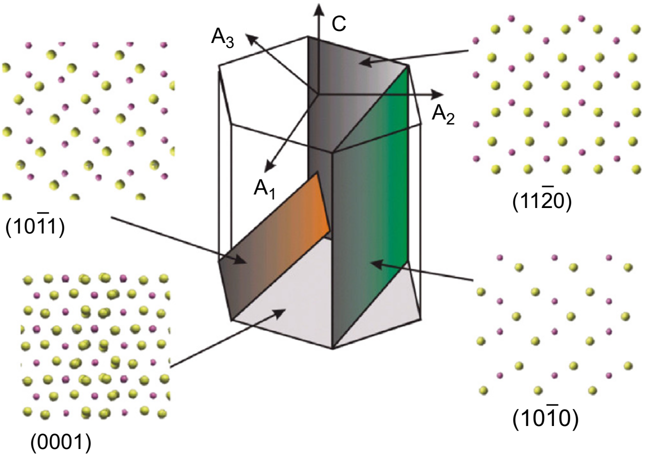

**Figure 13.5** Anisotropy of sapphire lattice.

**Table 13.10** **Exposure of sapphire to chemical and chemomechanical treatment, depending on the deviation of the surface from the C plane**

| Deviation from the C plane | Removal under chemomechanical polishing, μm/h | Removal under etching, μm/h |
|---|---|---|
| 1 min | 0.17 | 0.27 |
| 1° | 0.23 | 0.228 |
| 4° | 0.4 | 0.390 |

The wetting contact angle of the mechanically and chemomechanically polished surfaces increases with deviation from the C plane [12], which indicates that the surface energy decreases. A number of physical and chemical properties of the surface are associated with the value of the surface energy. The level of chemical exposure increases with increasing deviation from the C plane, especially upon chemomechanical treatment (Table 13.10) when the mechanisms of corrosion and chipping work at the same time.

The distance between the atomic layers of the basal plane is $d = 2.165$ Å. At a deviation of 4°, interlayer "gaps" appear with a width of $b = d/\sin 4° = 31.062$ Å. The width of such a gap is equivalent to nearly seven atoms on the C plane. This is one of the reasons for the reduced chemical and chemomechanical resistance of the surface with increasing off-orientation of the C plane. At a deviation of 4° for the A plane (the reticular density of the face is 0.119 at/Å$^2$), the width of the gap is equivalent to four atoms. The dependence of the change in the surface properties on the

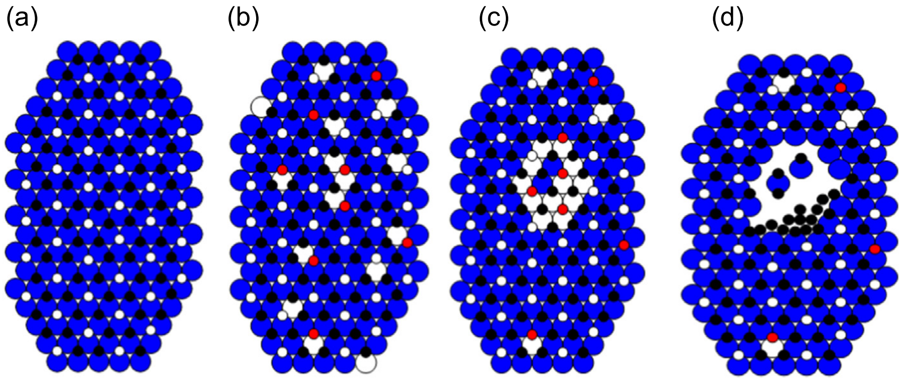

**Figure 13.6** Model of the formation of submicron inclusions in a sapphire lattice. (a) $Al_2O_3$ stoichiometric composition; (b–d) coalescence of excess aluminum and vacancies in a submicron in-phase inclusion 🔵 Oxygen of anionic sublattice; ● Aluminum of cationic sublattice; ◯ Vacancy of oxygen; ○ Octahedral emptiness; 🔴 Excess aluminum in an octahedral emptiness.

degree of deviation from the crystallographic planes characterized by a lower reticular density is much less pronounced.

The real structure of the crystal differs from the ideal stoichiometric lattice. The real structure includes anionic and cationic vacancies and interstitial atoms, which can interact, forming submicron in-phase inclusions. The process of excess Al and vacancies coalescing to form submicron inclusions is shown in Fig. 13.6.

Faceted foreign phase microinclusions have been found in sapphire grown in a carbon-containing medium. There are various viewpoints as to the nature and formation mechanism of those inclusions. One theory is that the inclusions are $AlO-Al_2O_3$ (Al–Al spinel) particles formed in the melt ahead of the crystallization front [13]. This phenomenon is due to the melt deviation from the stoichiometry caused by the high reducing chemical potential of the crystallization medium. The inclusions of 0.5–5 μm are gas bubbles captured by the crystal out of the melt that has lost overcooling resistance due to the reducing crystallization medium. In a carbon-containing medium the melt becomes depleted of oxygen; that is equivalent to increasing of content of aluminum ions in the melt. This is due to interaction of carbon oxide in the gas medium with oxygen arising due to thermal dissociation of $Al_2O_3$. Sapphire grown in those conditions can contain faceted inclusions of 2–17 μm size (Fig. 13.7). Such crystals are characterized by a high concentration of anionic vacancies ($\sim 2 \times 10^{17}$ $cm^{-3}$), as is indicated by optical absorption at 206, 225, and 268 nm. The submicrometer inclusions are formed along the (0001) planes and their distribution is characterized by an oriented striation that is not associated with the crystallization front shape. This indicates that the formation of the submicrometer inclusions occurs after growth, i.e., behind the crystallization front or directly at the front during the melt–crystal phase transition. It seems that it is just the excess anionic

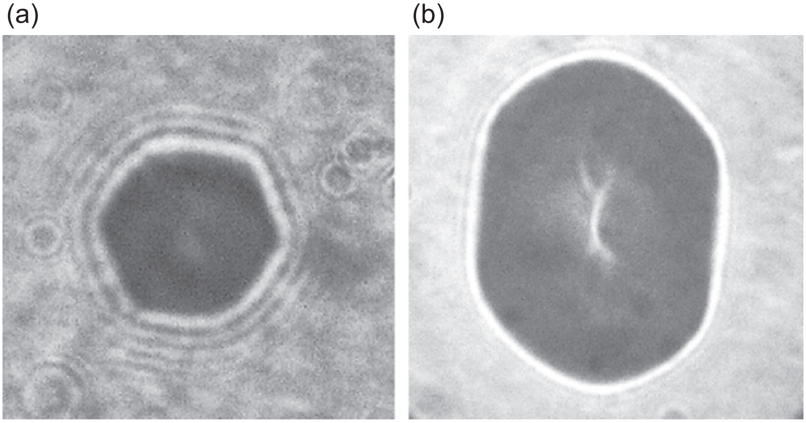

**Figure 13.7** Faceted (a) and partially faceted (b) inclusions of 17—40 μm size in sapphire grown in a carbon-containing atmosphere.

vacancies and aluminum ions that give rise to submicrometer-sized inclusions in the crystal. Due to coalescence of anionic vacancies, the submicrometer inclusions are formed in the crystal; the inclusions contain an excess of aluminum and its suboxides, which condense within submicrometer pores during cooling.

The structural perfection of the crystal is determined from the integral characteristic of the full width at half maximum (FWHM) of the X-ray diffraction rocking curve. The closer the FWHM to the theoretical (8.6″), the more perfect the lattice. For example, the FWHM experimental value in Fig. 13.8 is about 11 s, which characterizes a rather perfect crystal. The diffraction profile has only a sharp main peak and no big satellites.

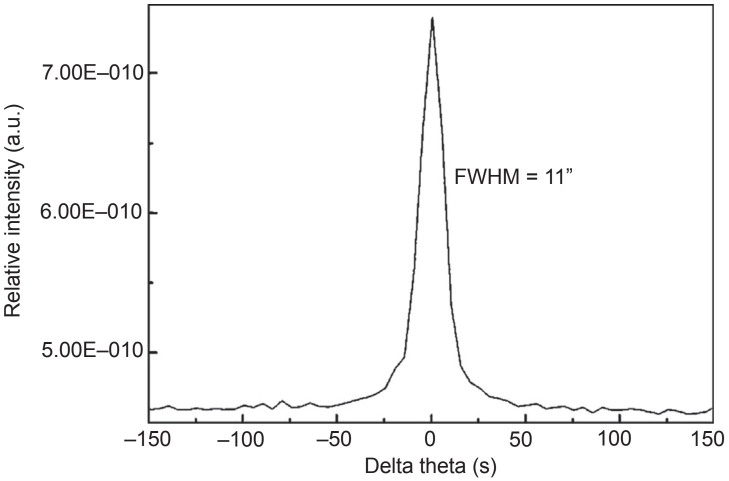

**Figure 13.8** The double crystal X-ray diffraction rocking *curve* in (0006) reflection.

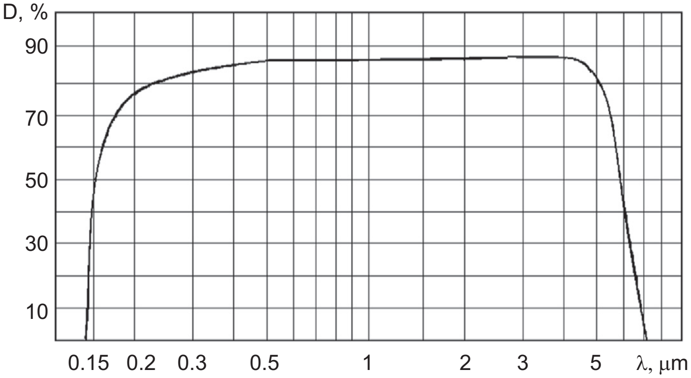

**Figure 13.9** Transmission curve of sapphire 1 mm thickness.

*Optical transmission.* As a rule, transmission in sapphire is described by the curve presented in Fig. 13.9, which was obtained from a pure, high-quality crystal.

In the ultraviolet (UV region), transmission of thin plates is essentially limited by the Fresnel loss. The presented values do not take into this loss account. Data on the transmission of pure perfect crystals in the UV region (UV grade) is presented in Fig. 13.10. Transmission in the UV region is increased by high-quality polishing of the surfaces (20/10 scratch—dig and better). Low-quality polishing may diminish the value of transmission by ~10%. The quality of the surface polishing is especially significant for $\lambda < 250$ µm. Under annealing in a carbon-containing atmosphere or in aluminum vapor, the sapphire reduction is accompanied by saturation of the crystal lattice with anionic vacancies. Crystals grown in a vacuum presented cationic stoichiometry violation, as shown by the broad optical absorption band at about 220 nm (Fig. 13.11a). The degree of cationic and anionic nonstoichiometry affects the absorption in the UV region [14]. Annealing in a medium with controlled redox potential at high temperatures can increase the transmission in the UV range (Fig. 13.11b).

In the infrared (IR) region of the spectrum, sapphire possesses high transmission at wavelengths ranging from 1.0 to 5.5 µm. In the 1.0—4.0 µm interval the value of

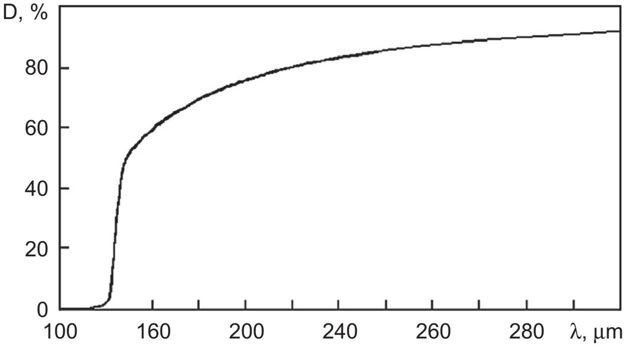

**Figure 13.10** Transmission of sapphire in UV region.

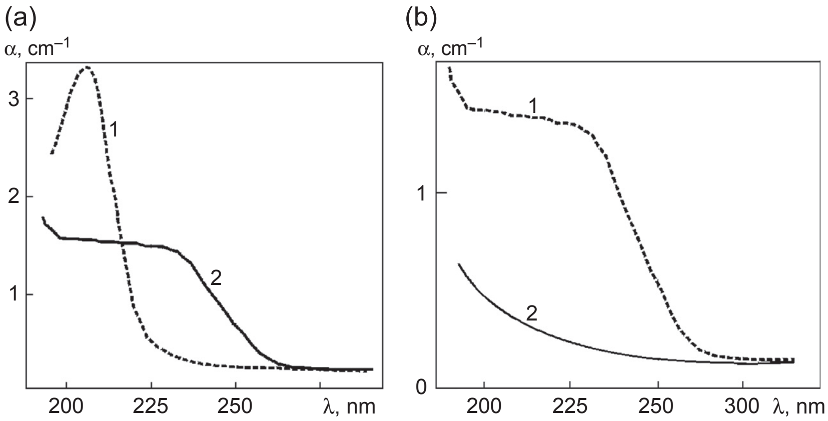

**Figure 13.11** (a) UV absorption spectrum typical of sapphire with violated stoichiometry. --------, anionic nonstoichiometry; ——, cationic nonstoichiometry. (b) UV absorption spectra of sapphire 2 mm thickness. (1) Before annealing. (2) After high-temperature annealing.

transmission is ~85%–86% (Fig. 13.9). Starting from $\lambda > 3$ μm the value of transmission decreases as the thickness of sample and the temperature grow (Fig. 13.12).

At $T < 80K$ the transmission of sapphire increases in the extreme IR region. Due to this effect, sapphire can be used in cold inner windows for IR measurements and in modern cryogenic systems.

As sapphire possesses high transmission and very low Fresnel loss, it can be applied in cases when other optical materials require antireflection coatings.

The presence of point defects and impurities gives rise to absorption at 204, 230, and 400 μm wavelengths. In real samples the value of transmission also depends on the medium in the growth chamber and even the equipment components used in

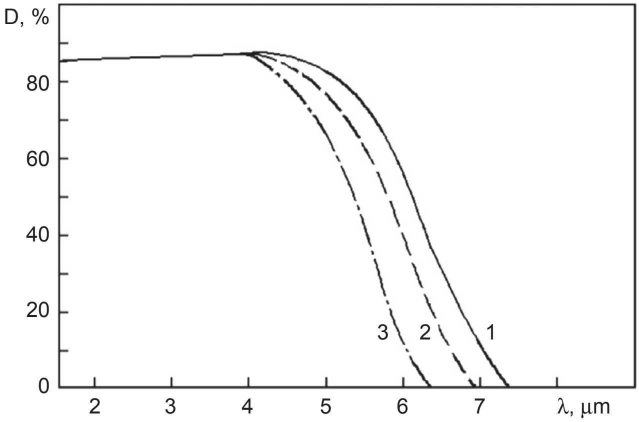

**Figure 13.12** Transmission of sapphire in IR region. Thickness: (1) 1 mm, 293K; (2) 1.5 mm, 293K; (3) 3.1 mm, 293K.

growth (for example, materials of the crucible and furniture of the growth zone). Spectral absorption curves for sapphire with single impurities or codoped are available [2] for chromium, vanadium, vanadium plus chromium, iron, iron plus chromium, titanium, iron plus titanium (blue sapphire), cobalt, cobalt plus chromium, nickel, and manganese.

The X and $\gamma$ irradiation of sapphire increases optical absorption; $n$ and $\gamma$ irradiation give rise to the formation of color centers and consequently to the appearance of absorption bands, which can be eliminated by high-temperature annealing. Reactor neutrons induce several absorption bands centered at 203, 229, 255, 300, 355, 450, and 572 nm. Most of these absorption bands are associated with electron-trapping oxygen vacancies produced by elastic collision with fast neutrons [15]. The absorption band at 300 nm is attributed to the contribution of both interstitial $Al^+$ ions and color centers [16]. The evolution of each absorption band is a function of fluence and annealing temperature.

Usually, sapphire is classified according to optical, technical, and mechanical grades, with reference to corresponding specifications.

*Optical grade*

1. No inclusions, lineage, twins, microbubbles, scattering centers.
2. No inclusions, lineage or twins, but microbubbles up to 10 μm are accepted.
3. No inclusions, lineage, or twins, but uniformly distributed bubbles no larger than 50 μm and no closer together than 500 μm are accepted.
4. No inclusions, lineage, or twins, but uniformly distributed bubbles no larger than 50 μm and no closer together than 500 μm as well as concentrations of bubbles with a diameter no larger than 200 μm and no closer together than 20 mm are accepted.

*Technical grade*

5. No inclusions, lineage, or twins but uniformly distributed bubbles no larger than 50 μm and no closer together than 500 μm as well as concentrations of bubbles with a diameter no larger than 500 μm and no closer together than 20 mm are permitted.
6. No inclusions, twins, or lineage with an angle of disorientation larger than 15 min, but individual bubbles and concentrated bubbles with a diameter no larger than 500 μm and no closer together than 15 mm are accepted.

*Mechanical grade*

7. Inclusions, lineage, twins, and concentrated bubbles with a diameter no larger than 200 μm are accepted.
8. All types of defects, other than cracks, are accepted

*Propagation of elastic waves* in sapphire was studied in connection with its use in antishock structures. A theoretical and experimental investigation of the process of wave propagation in sapphire rods with different crystallographic orientation and deformation in sapphire rods under longitudinal impact has been conducted. The general laws of propagation of waves in bodies are derived from three-dimensional equations of motion of an elastic medium obtained by analyzing wave equations. The problem of finding a wave velocity in an anisotropic medium is normally solved

**Table 13.11** **Theoretical and experimental values of strain wave velocities, m/s**

| Rod type (orientation) | Classical model | Rayleigh's model | Experiment |
|---|---|---|---|
| A | 10,409 | 10,407 | 10,419.0 |
| C | 10,761 | 10,760 | 10,751.6 |
| R | 9836 | 9834 | 10,134.0 |

by considering the motion of plane waves and reducing the problem to solving Christoffel's equation [17]. Such an approach reveals that three elastic waves could propagate (one quasilongitudinal and two quasitransverse) in an arbitrary direction in an anisotropic medium [18]. The experiment used sapphire rods with a diameter of 19 mm and length of 550 mm, grown by EFG. Table 13.11 shows that, for the rods considered, there is a slight difference between velocities obtained using the classical rod model, Rayleigh's rod model, and experimental data [19].

For the classical model, the wave velocity depends only on the physical—mechanical characteristics of a rod, whereas for Rayleigh's model it depends also on the geometric parameters of rods. The results of the theoretical analysis are in good agreement with experimental data.

It is seen from Fig. 13.13 that the value of the velocity of the strain wave depends on the crystallographic orientation of the rod.

*Thermal conductivity at low temperatures* was investigated in more detail in connection with the wide use of sapphire in cryogenic devices and systems [20]. At room temperature k(T) is considerably stronger than the classical $T^{-1}$ dependence. In all cases it is described by the function $T^{-1.6}$. In the vicinity of $T = 100K$ this dependence tends to $\approx T^{-3.6}$. At the lowest of the considered temperatures the curves

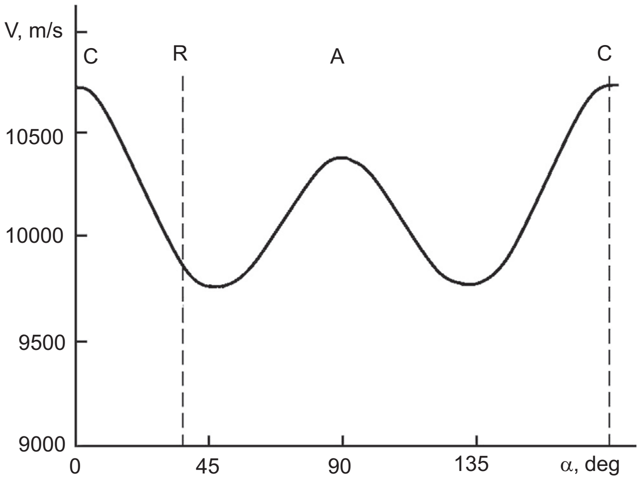

**Figure 13.13** Dependence of the wave velocity on the angle of rotation of the crystal axes.

start reaching the low-temperature maximum characteristic of single crystals. For sapphire this maximum is observed at a relatively high temperature of T ≈ 40K. However, all mentioned features are typical of crystals with a high melting temperature and, consequently, high characteristic Debye temperature (according to the calorimetric data, for $Al_2O_3$ $\Theta_D = 1000K$ at $T = 300K$).

At 300K the absolute values of thermal conductivity lie within the limits of the known literature data for sapphire. At 50K the value of thermal conductivity for the R direction is close to 10 kW/m·K, which suggests that the crystal has high chemical purity and structural perfection (Fig. 13.14). The thermal conductivity of sapphire is anisotropic in a wide temperature region. At 50K the value of thermal conductivities for the direction $<10\bar{1}2>$ is two times higher in comparison with that of the direction $<11\bar{2}0>$. For this pair of directions the anisotropy index was $\varepsilon > 0$ within the whole investigated temperature interval. Another situation is observed for the pair of directions $<10\bar{1}2>$ and $<0001>$. At the lowest of the studied temperatures the thermal conductivity along the direction $<10\bar{1}2>$ is essentially higher than that along $<0001>$. However, in the vicinity of $T = 110K$ the relation between the thermal conductivity values is reversed; with the rise in temperature the obtained k(T) values turn out to be the same. The thermal conductivity for the A direction is the lowest, at least in the 50−300K range.

The basic physical properties of sapphire are summarized in Table 13.12.

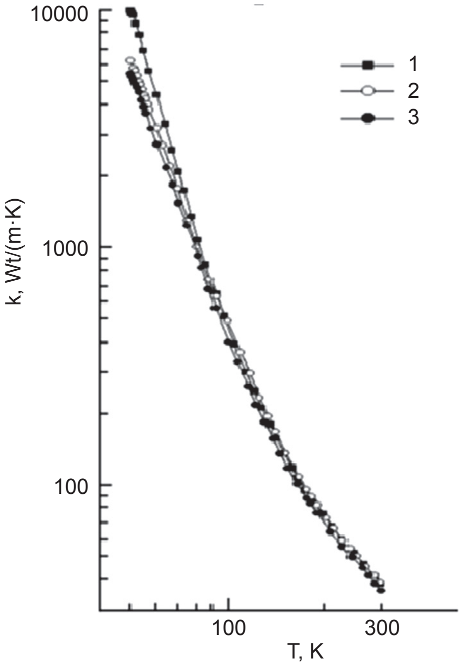

**Figure 13.14** The dependence k(T) for sapphire of different crystallographic orientation. 1.$<10\bar{1}2>$, 2. $<0001>$, 3. $<11\bar{2}0>$.

**Table 13.12** **Physical properties**

| | | |
|---|---|---|
| **Optical properties** | | |
| Optical transmission range, µm | 0.2−5.5 | |
| Refractive index @0.532 µm | $n_o = 1.7717$, $n_e = 1.76355$ | |
| Refractive index in partial transparency point | | |
| @5.75 µm | 1.556 at 297K, 1.628 at 2293K | |
| @6.00 µm | 1.540 at 297K, 1.600 at 2293K | |
| Reststrahlen peak, µm | 13.5 | |
| Birefrigence | 0.0087 @0.55 µm | |
| **Mechanical properties** | | |
| Density | 3.97−3.99 g/cm$^3$ | |
| Hardness | | |
| Mohs | 9 | |
| Knoop | ‖C 1525−1800 kg/mm$^2$ | ⊥C 1900−2100 kg/mm$^2$ |
| Vickers @9.8 N | ‖C 16−17 GPa | ⊥C 18−20 GPa |
| Young's modulus | 345−494 GPa | |
| Tensile strength | 400 MPa @298K | 275 MPa @770K |
| | 335 MPa @1000K | 345 MPa @1270K |
| Compressive strength | 2.0−2.9 GPa | |
| Flexural strength | ‖C 1.03 GPa | ⊥C 1.54 GPa |
| Shear modulus | ‖C 144 GPa | ⊥C 163 GPa |
| Rigidity modulus | 145−175 GPa | |
| Rupture modulus | 350−690 MPa | |
| Elasticity modulus | $3.6 \times 10^5$ N/mm$^2$ | |
| Poisson's ratio | 0.27−0.30 | |
| Elastic coefficient, GPa | $C_{11} = 497.6$, $C_{12} = 162.6$, $C_{13} = 117.2$, $C_{14} = 235$, $C_{33} = 498.1$, $C_{44} = 147.2$ | |
| Fracture toughness, MPa·m$^{1/2}$ | 2.5−4.5 | |
| Values of strain wave velocities (wave of deformation), m/s | ‖C 10751.6 | ⊥C 10419 |

**Table 13.12** **Continued**

| **Thermal characteristics** | | | |
|---|---|---|---|
| Melting point $T_m$ | 2323K (2050°C) | | |
| Softening point | 2070K | | |
| Increase in volume when heated to $T_m$, % | 6.3 | | |
| Thermal expansion coefficient ($\times 10^{-6} K^{-1}$) | 293–323K | ∥C 6.6 | ⊥C 5.5 |
| | 310–670K | ∥C 7.0 | ⊥C 7.7 |
| | 1270K | ∥C 9.03 | ⊥C 8.31 |
| Thermal conductivity, W/m·K | 30K | 10,000 | |
| | 298K | ∥C 32.5 | ⊥C 30.3 |
| | 670K | 12.56 | |
| | 1500K | 4 | |
| Specific heat, cal/g·K | 293K | | 0.181–0.167 |
| | 1273K | | 0.300 |
| **Electrical characteristics** | | | |
| Resistivity, Ω·cm | 293K ∥C | (1.2–2.9) $\times 10^{19}$ | ⊥C 5 × $10^{18}$ |
| | 573K | $10^{11}$ | |
| | 1770K | $10^{5}$ | |
| | 2270K | $10^{3}$ | |
| Dielectric constant | 293K | ∥C 11.53 | ⊥C 9.35 |
| | 570K | ∥C 12.07 | ⊥C 9.66 |
| | 970K | ∥C 13.18 | ⊥C 10.26 |
| | $10^2$–$10^3$ Hz | ∥C 10.55 | ⊥C 8.6 |
| Dielectric tangent loss at 293K | $10^2$ Hz | ∥C $10^{-3}$ | ⊥C $10^{-3}$ |
| | $10^3$ Hz | ∥C 2 × $10^{-4}$ | ⊥C 2 × $10^{-4}$ |
| | $10^{10}$ Hz | ∥C 8.6 × $10^{-5}$ | ⊥C 3.0 × $10^{-5}$ |
| Dielectric strength, V/m | 48 × $10^6$ | | |
| **Magnetic properties** | | | |
| Magnetic susceptibility | ∥C 0.21 × $10^{-6}$ | | ⊥C 0.25 × $10^{-6}$ |

*Radiation stability*: there is no change in transmission above 2.5 μm after exposure to $10^7$ rad, and no change in transmission below 0.3 μm after exposure to a total dose of $10^{12}$ proton/cm$^2$. Reactor $\gamma$-neutron irradiation of extra-pure sapphire samples results in the appearance of induced absorption bands with maxima at ~260 and 350 nm in the spectra at relatively low doses ($<10^{17}$ cm$^{-2}$). For increasing radiation flux, the inherent absorption edge shifts sharply up to the visible region of the spectrum. This is connected with the formation of point defects and the appearance of color centers. X-ray irradiation may change the color of the crystal. Lines of induced absorption are observed at 230, 400, 650 nm, and so on, depending on the content of controllable and noncontrollable impurities.

*Amorphous sapphire surfaces* are formed under irradiation at energy of approximately $3 \times 10^{23}$ keV/cm$^3$. The depth of the amorphous layer reaches 40−100 nm. The increased energy of the bombarding ions gives rise to radiation damage of the crystal lattice. Despite the fact that the depth reached by incorporated ion is quite large (in the order of 1000 Å), the crystal lattice distortions can be removed partially by annealing in oxygen at 870−1870K.

*Blisters* (gas-containing pores) are formed within the surface-adjacent irradiated layer with hydrogen ions, due to the bonds between vacancies and hydrogen. When the concentrations of hydrogen go above $10^{18}$ cm$^{-2}$, the blister density reaches its saturation. At certain critical values of hydrogen pressure in the pores, and upon heating, thermally activated desorption of hydrogen (blistering) is observed in sapphire. The resistance of the surface to blistering is high for the plane $(10\bar{1}0)$, average for the plane (0001), and low for the plane $(10\bar{1}2)$. This resistance depends on the interplanar distance but not on the density of the atoms. Oxygen ion bombardment of the surface may also lead to the formation of oxygen bubbles within the surface-adjacent layer and cause the appearance of excessive aluminum on the surface.

**Chemical properties**

| | |
|---|---|
| Molecular mass | 101.9612 |
| Electronegativeness | 2.58 |
| Dissociation energy of molecule, $D_{Al_2O_3}$ | 740 kcal/mol |
| Formation heat for $Al_2O_3$ molecule | 377 kcal |

The $Al_2O_3$ molecule has an essentially higher value of formation heat (377 kcal) in comparison with other oxides (e.g., 177 and 192 kcal for $Fe_2O_3$ and $SiO_2$, respectively); thus it is more difficult to reduce sapphire to the metal.

One of sapphire's features is its ability to operate in corrosive environments at high temperatures.

Sapphire possesses resistance to sulfur vapor up to ~1300K; to sodium and potassium up to 1100K (in Na melt its mass diminishes by 1% over 160 h at 1200K); to tin up to 2200K; in lead and bismuth up to 1300K; in caustic soda up to 1100K; in iodine

## Table 13.13 Corrosion resistance of sapphire surface depending on the type of treatment

| Type of treatment | Damaged layer depth, μm | Thickness (*h*) of layer removed at one etching action, μm |
|---|---|---|
| Natural facet (not treatment) | 0 | 0.72 |
| Polishing | 1–5 | 0.77 |
| Fine lapping | 20–30 | 0.96 |
| Rough lapping | >40 | 1.8 |

Sample grown by Ky method, (0001) plane.

and iodides up to 1300K; in hydrogen sulfide and $CO_2$ up to 1500K; in titanium tetrachloride up to 1300–1400K; and in mixed $H_3PO_4$:$H_2SO_4$ the dissolution rate for the C plane at 580K is 20 μm/h.

Constructional sapphire components work in Mg, Al, Cr, Co, Ni, Cs, Pb, Bi, and Zn melts and in their alloys, as well as in rare earth, cast iron, and steel melts. The crystals are resistant to hot water solutions as well as to melts of a number of compounds.

The role of water in the processes of hydrothermal dissolution of sapphire is investigated in connection with crystallization under hydrothermal conditions. Solubility of sapphire in pure water is very low, even at thermobaric parameters. Solubility of 8 mg of sapphire in 100 mL of water at 1070K and a pressure of 6 kbar is just 0.0035%.

Corrosion resistance depends on the type of surface treatment (Table 13.13) and the chemical reagents (Table 13.15). The resistance of the surface to aggressive media is influenced by defects in the surface-adjacent layer formed during mechanical treatment. The corrosion resistance of the surface was investigated by the method of layer-by-layer etching using 0.3 mL of condensed phosphoric acid spread on to the surface of the sample [21]. The rate of the chemical reaction is a function of the surface energy and the strength of the crystal lattice bond. It depends on the degree of destruction of the surface and the surface-adjacent layer. Mechanical treatment decreases the strength of the surface by more than two times (Table 13.13), depending on the degree of damage.

It is known that dislocations reaching the surface increase the rate of dissolution. However, at $\rho = 10^3 - 10^5$ cm$^{-2}$ this dependence is barely noticeable for a given crystallographic plane. The corrosion resistance depends more on the crystallographic features than on the dislocation density (Table 13.14). The C plane offers the lowest corrosion resistance. In the direction of the most densely packed row, the extraction work of atoms is the lowest and corrosion proceeds most rapidly. The second reason for the very low resistance of the basal plane arises from the plane grids, composed of aluminum and oxygen atoms. In the plane (0001) the flat grids consist of atoms O–Al–Al–O–Al–Al–O, and in the M plane: Al–O–Al–O. Thus the Al–Al pairs are available only in the basal planes. The bonding Al–Al is weaker than Al–O not only chemically but also mechanically. The grids $\{10\bar{1}0\}$ are electrostatically neutral.

**Table 13.14** **Dependence of sapphire surface chemical resistance on density of dislocation (ρ) and orientation**

| Growth method | ρ, $cm^{-2}$ | Plane | *h*, μm |
|---|---|---|---|
| Verneuil | $(1\ldots5) \times 10^5$ | C | 0.82 |
| Ky | $10^3$ | C | 0.77 |
| HDS | $5 \times 10^3$ | C | 0.83 |
| EFG | $10^5$ | C | 0.73 |
| | | M | 0.29 |
| | | A | 0.15 |

**Table 13.15** **Loss of sapphire mass (~7 $cm^2$ working surface) under the action of chemical reagents**

| Reagent | T, K | Time of action, hr | Loss of mass, % |
|---|---|---|---|
| **After boiling in water solution** | | | |
| $HNO_3$ (1:4.6) | 400 | 6.6 | 0.01 |
| $HNO_3$ (1:1) | 400 | 6.0 | 0.01 |
| KOH (70%) | 400 | 6.0 | 0.01 |
| $H_2SO_4$ (1:9) | 400 | 6.0 | 0.01 |
| HCl (1:1) | 400 | 6.0 | 0.01 |
| HF (1:1) | 400 | 6.0 | 0.01 |
| **After fusing** | | | |
| Lithium metaborate | 1300 | 1.0 | 93.4 |
| Lithium megaphosphate | 1300 | 1.0 | 7.2 |
| Potassium hydrosulfate | 1100 | 0.7 | 2.4 |
| Boron anhydrite | 1200 | 0.7 | 4.2 |
| $Na_2O_2$ + soda (1:5) | 900 | 0.25 | 0.5 |
| NaF | 1300 | 1.0 | 4.1 |
| $H_3PO_4$ | 699 | 1.0 | 0.2 |
| HCl | 1100 | 1.0 | 0.05 |
| LiF | 1200 | 1.0 | 0.4 |
| **After holding in melt** | | | |
| Copper | 1350 | 4.0 | 0.05 |
| Steel St3 | 1900 | 4.0 | 0.02 |
| Ni:Cr | 1500 | 4.0 | 0.01 |
| Carbon steel | 1900 | 4.0 | 0.13 |

The energy of the $Al_2O_3$ lattice is rather high (152 eV). The total contribution of $Al^{3+}$ to the potential energy of ions exceeds that of $O^{2-}$, but the contribution of the Van der Waals bonds of $O^{2-}$ (−1.3 eV) is much higher than the analogous energy of $Al^{3+}$ (−0.1 eV), which must facilitate the reaction of aluminum from Al—Al pairs.

However, mechanical treatment has the heaviest effect on the corrosion resistance of sapphire. Rough lapping lowers the resistance of the crystal surface by more than two times. Crystallographic factors also make a decisive contribution to the corrosion resistance. The resistance to aggressive media of different crystallographic planes may vary considerably.

*Wettability.* The usability of sapphire in electronics is defined by, among other factors, the wetting of its surface by liquid substances. Depending on the surface use, either maximum or minimum wetting may be required. Wetting was studied on pure sapphire crystallographic planes C, M, A, and R and for crystals doped with 0.1% Cr at the (0001) plane and with 0.05% Ti, by measuring the rest drop wetting angle with an optical microscope. This was done with distilled water, glycerin, and isotonic solution (0.9% NaCl) in air at 25°C. The wetting angle measurement error was 0.5%—1.3%. The wetting angles for the main crystallographic planes of sapphire are within the 63°—85° range (Table 13.16) in both a polar liquid (distilled water) and a nonpolar one (glycerin) [22]. It is clearly seen from the table that doping reduces the surface energy.

*Evaporation forms* of the crystals are similar to the dissolution forms. The mechanisms of evaporation and dissolution seem to be analogous: surface areas with elevated energy are first removed. In case of dissolution in a mother liquor medium, the growth and dissolution forms completely coincide. When the chemical composition of the medium is changed, the dissolution and evaporation forms may change, too. The surface morphology of a sapphire ball in hydrogen or in a carbon-containing medium is a combination of isolated hillocks [2]. The rate of Langmuir evaporation of the planes follows the order $(10\bar{1}0) > (\bar{2}110) > (0001)$. The evaporation morphologies of the planes $(10\bar{1}0)$ and $(\bar{2}110)$ correspond to the layer-by-layer mechanism; while the facet (0001) has a monolayer (normal) mechanism. The evaporation energy is 210 ± 20 kcal/mol.

## Table 13.16 Wetting angle of sapphire planes with water and glycerin, degree

| Sample orientation | Wetted by water | Wetted by glycerin |
|---|---|---|
| C | 84 | 73 |
| M | 78 | 70 |
| A | 74 | 70 |
| R | 79 | 67 |
| A:0.05Ti | 75 | 65 |
| C:0.1Cr | 73 | 63 |

## 13.4 Applications

Sapphire ($\alpha$-$Al_2O_3$) is a multifunctional crystal, given its unique combination of mechanical, optical, and radiation properties.

**Substrate (wafer).** Sapphire is hard, scratch-resistant, and chemically inert, with good thermal stability and a wide light transmission range. These characteristics make it an ideal material for a variety of applications, such as substrates for LEDs and laser diodes. Sapphire wafers are used for epitaxy of semiconductor films such as Si, gallium nitride (GaN), and AlGaN, and for making integrated circuits. C-plane sapphire substrates are used for growth of GaN and other III–V and II–VI compounds when manufacturing LEDs and for IR detector applications. R-plane sapphire $(1\bar{1}02)$, 57.6° to the C plane, is the preferred material for silicon-on-sapphire used in semiconductor, microwave, and pressure transducer applications. Substrates in the A plane $(11\bar{2}0)$ are applicable to high-speed superconductors.

Wafers can work at high temperatures, in aggressive ambient conditions, and under big mechanical loads, and can be obtained in large size. Thus they are used even in cases when the lattice parameters do not completely match the parameters of heteroepitaxial structures.

Sapphire substrates are used with different crystallographic orientations (Fig. 13.15). The crystallographic features of the C substrate are shown in Fig. 13.16. Silicon-on-sapphire device technology has a long history dating back to the 1960s. The substrate preparation for the structure of silicon-on-sapphire is shown in Fig. 13.17.

Sapphire blanks intended for the manufacture of substrates undergo several stages of quality control: inspection to detect any stress in the material, inspection to detect coloration, and inspection to detect any bubbles and cracks.

Substrates in the C plane are useful for IR detector applications; substrates in the A plane $(11\bar{2}0)$ are applicable to high-speed superconductors; and substrates in the R plane $(1\bar{1}02)$ are used for heteroepitaxial deposition of silicon for microelectronic integrated circuit applications.

Most of the produced sapphire (about 80%) is used to make substrates for LEDs. The market share of wafers with a diameter of 2″, previously dominant in the market, is constantly falling. Nowadays most wafers are produced with a diameter of 6″, with increasing demand for 8″ wafers. The microLED displays market is quickly being

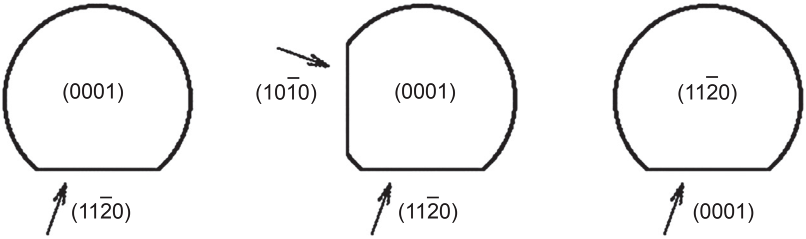

**Figure 13.15** Relative position of the basal and additional planes of substrates.

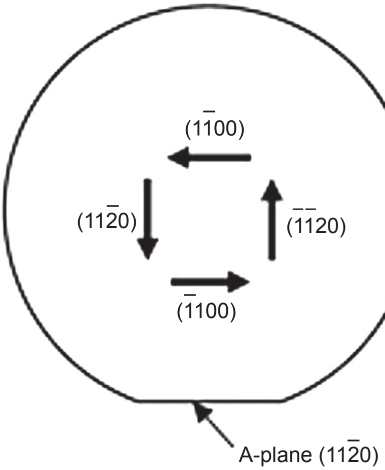
$(1\bar{1}00)$
$(11\bar{2}0)$
$(\bar{1}\bar{1}20)$
$(\bar{1}100)$
A-plane $(11\bar{2}0)$

**Figure 13.16** Crystallographic features of the C substrate.

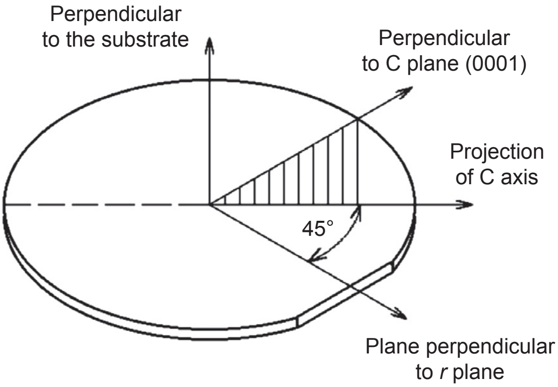
Perpendicular to the substrate
Perpendicular to C plane (0001)
Projection of C axis
45°
Plane perpendicular to *r* plane

**Figure 13.17** Scheme of substrate preparation for structure (100) Si film on *r* plane of sapphire.

developed, promising a potential revolution. MicroLEDs are used in smart watches, tablets, laptops, TVs, and monitors. The market for UV LEDs and IR LEDs is also expanding.

The sapphire wafer surface is prepared by a thermal cleaning in $H_2$ at 1150°C. The ultraclean sapphire wafers have only 20−50 particles of no more than 1 micron in size on their entire surface, so they are designated specifically for microLED production.

Patterned sapphire substrates (PSSs) are more effective than polished wafers. LEDs formed using dry-etched PSS wafers (or high-temperature wet etched) produce highly efficient, very bright light. The PSS reduces the dislocation density in the overgrown GaN layer and enhances the light extraction efficiency of the LED chip by scattering the light confined in the GaN layer, which is attributed to the critical angle between the GaN and the sapphire substrate. Periodically structured sapphire substrates are used to

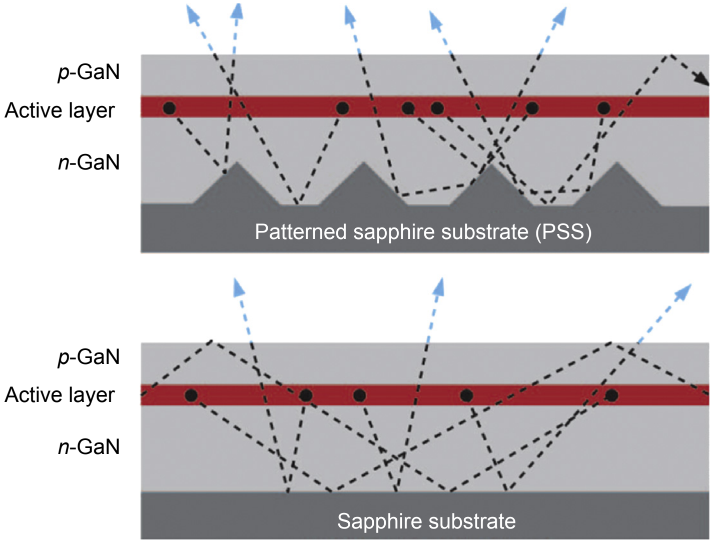

**Figure 13.18** Polished and patterned sapphire structures.

increase light output from the diodes (Fig. 13.18). In the PSS process structures such as cones, domes, or pyramids are etched into smooth sapphire wafers in the micron to nanometer range. The price trend for PSSs shows a tendency to rapid reduction.

Heterostructures of GaN/sapphire are widely applied in blue LEDs, despite the fact that the lattice mismatch runs about 13%, as are the related AlGaN/InGaN/GaN/(0001) sapphire heterostructures.

Typically the following orientation relations find application in optoelectronics:

(0001)A1N/(0001) sapphire
(0001)GaN/(0001) sapphire
$(11\bar{2}0)$A1N/$(10\bar{1}2)$ sapphire
$(11\bar{2}0)$GaN/$(10\bar{1}2)$ sapphire
$(11\bar{2}6)$A1N/$(10\bar{1}2)$ sapphire.

The UNIQUE project run by the Osram company and partners focused on the development of 260–280 nm emitters in the deep-UV spectrum. These are significantly shorter wavelengths than those realized before. These deep-UV LEDs are used for emerging applications in industrial disinfection and ecofriendly purification of water.

LEDs in the wavelength range 300–550 nm are realized with InGaN/GaN and are grown predominantly on sapphire substrates. After an LED structure is fabricated on the surface of the sapphire wafer, the wafer needs to be diced to separate the microdevices for encapsulation. The quality of the reflecting faces after dicing is critical for the fabrication of efficient and stable LEDs emitting light in the green–violet region. At Aston University (Birmingham) a technology known as “stealth dicing” was developed for dicing and scribing polished wafers 350 μm thick [23]. The technology uses a pulsed laser to damage a plane of material within the wafer, by exploiting multiphoton absorption instead of cutting through the wafer surface. The laser machining was performed using a Ti:sapphire laser system which generates 140 fs pulses at a 1 kHz repetition frequency and a center wavelength of 800 nm.

Among the promising trends in the use of sapphire substrates one should mention the technology of carbon nanotube growth on sapphire. This method is being developed at Northern California University. This new material seems to be promising for nanotransistors and sensors [24]. Researchers have found that single-walled carbon nanotubes spontaneously fall into useful patterns on A-plane sapphire surfaces. A sample of 6″ C-wafer specification is given in Table 13.17, and samples of silicon-on-sapphire parameters and parameters of sapphire substrates for Metal-Oxide Semiconductor (MOS), Complementary MOS (CMOS), and Microelectronic and Microelectromechanical System (MEMS) applications are given in Table 13.18.

**$Al_2O_3$:$Ti^{3+}$ scintillators.** *Sapphire-based scintillators* are promising for registration of $\alpha$ and $\gamma$ particles, as well as low-energy X-rays, owing to their excellent mechanical and optical characteristics [25,26]. In $Al_2O_3$:$Ti^{3+}$, $Me^{2+}$ creates shallow levels of charge capture (where Me is Mg or Ca, the bivalent coactivator). Holes formed at the capture of electrons by $Ti^{4+}$ ions settle on such levels, and this is followed by the recombination of electron–hole:

$$Mg^{2+} + h^{+} \rightarrow Mg^{3+} \underset{10\ \mu s}{\rightarrow} Mg^{2+} + h^{+}$$

**Table 13.17** Specification for 6″ C wafer

| Specification item | Unit | Target | Tolerance |
|---|---|---|---|
| 1. Surface orientation | C plane (0001) | | |
| 1.1. Off angle toward M axis | degree | 0.2 | ±0.05 |
| 1.2. Off angle toward A axis | degree | 0.00 | ±0.10 |
| 2. Diameter | mm | 150.0 | ±0.2 |
| 3. Thickness | mkm | 1300 | ±20 |
| 4. Flat orientation | A plane $(11\bar{2}0)$ | | |
| 4.1. Flat offset angle | degree | 0.00 | ±0.3 |
| 4.2. Flat length | mm | 50 | ±1 |
| 5. Front surface Ra | nm | ≤0.2 | |
| 6. Back surface Ra | mkm | 0.6–1.2 | |
| 7. Total Thickness Variation (TTV) | mkm | ≤0.15 | |
| 8. Life time value (LTV) | mkm | ≤0.10 | |
| 9. Bow | mkm | ≤0.20 | |

**Table 13.18** Silicon-on-sapphire parameters

| Parameter | |
|---|---|
| Sapphire substrate diameter, mm | 50.8 (±0.1), 76 (±0.5), 100 (±0.5) |
| Sapphire substrate orientation | $(10\bar{1}2)$ (±0.5°) |
| Sapphire substrate thickness, μm | 330–430, 450, 460 (±25) |
| Silicon layer orientation | (100) |
| Silicon thickness, μm | 330–430, 450, 460 (±25) |
| Silicon type | p (boron) |
| Silicon resistivity, Ohm/sq | 10–30 (±8%) |
| Sapphire backside finish | Ground |

The scintillator's light output decreases as the matrix stoichiometry is violated due to recombination of the charges on point defects. Thus the annealing medium potential needs to be maintained within the limits of $-20$ to $-150$ kJ/mol, depending on the content of $Ti^{3+}$.

*A combination of detecting materials* for the registration of mixed radiation of thermal neutrons and $\gamma$ rays can be used. A compositional material based on fine-crystalline $Al_2O_3$:$Ti^{3+}$ and LiF has been proposed for a long-wavelength scintillator [27].

Radiation-resistant *composite scintillators* based on grains of $Al_2O_3$:$Ti^{3+}$ were studied [28]. Experiments which are planned or being carried out at the new-generation high-luminosity particle and heavy-ion accelerators (such as the Large Hadron Collider (LHC) at CERN) require detectors and subdetectors (trackers, calorimeters, etc.) to be exposed to high-level radiation doses. There are plans for a gradual increase of the LHC luminosity by one order of the magnitude in the future. The maximum dose accumulated in the "critical" zones at the ultimate shutdown of the LHC is estimated as 30 Mrad [29].

In one study [28] the dielectric polydimethyl–siloxane gel Sylgard-184 was used as the base material for composite scintillators [30]. To obtain a composite scintillator a sapphire crystal was mechanically ground, and a set of sieves was used to select grains with the required sizes. The grains were then introduced into the dielectric gel. The optical transmittances $T$ were measured in the wavelength range from 300 to 700 nm. Figs. 13.19–13.22 demonstrate that composite scintillators based on $Al_2O_3$:$Ti^{3+}$ up to doses of 100 Mrad (dose rate was 0.23 Mrad/h) are radiation resistant. In the spectral band of their luminescence ($\lambda > 600$ nm), the $T$-values decrease less than two times. Fig. 13.22 shows that composite scintillators based on $Al_2O_3$:$Ti^{3+}$ single crystalline grains are radiation resistant up to a dose of 300 Mrad (dose rate 1500 Mrad/h), as proved by a reduction of transmittance by less than a factor of two within the luminescence spectral band ($> 600$ nm).

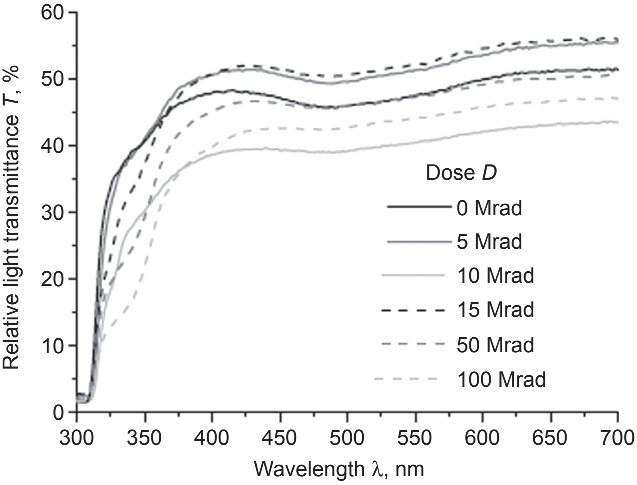

**Figure 13.19** Luminous transmittance *T* of a single-layer composite scintillator based on grains of an $Al_2O_3$:$Ti^{3+}$ single crystal (grain size is 0.3…0.5 mm). Dose rate was 0.23 Mrad/h.

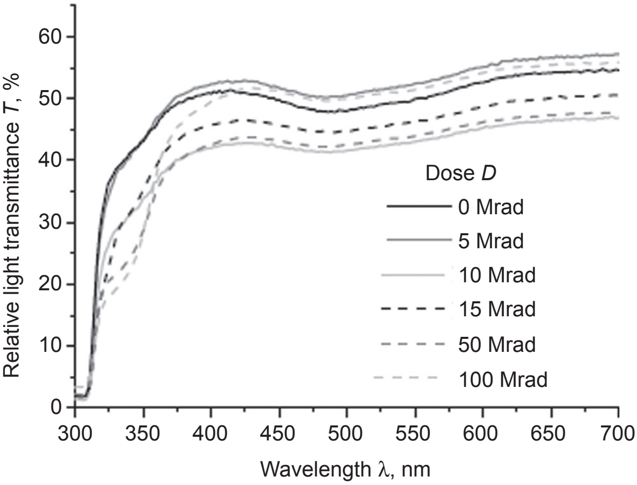

**Figure 13.20** Luminous transmittance *T* of a single-layer composite scintillator based on grains of an $Al_2O_3$:$Ti^{3+}$ single crystal (grain size is 0.5…1.0 mm). Dose rate was 0.23 Mrad/h.

Composite scintillators based on grains of $Al_2O_3$:$Ti^{3+}$ are radiation resistant at least up to $D = 100$ Mrad and $D = 300$ Mrad when the dose rate is 0.20 Mrad/h and 1500 Mrad/h, respectively. Transmittance decreases by less than a factor of two over the range of the luminescence of the scintillator, which indicates that these scintillators are radiation resistant.

**Thermoluminescent detectors (TLDs)** are made of sapphire with anionic nonstoichiometry. Sapphire-based structures have a number of advantages. Their sensitivity to

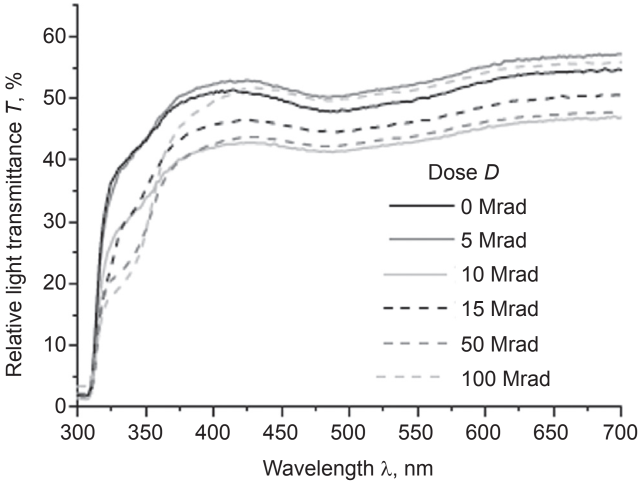

**Figure 13.21** Luminous transmittance *T* of a single-layer composite scintillator based on grains of an $Al_2O_3$:$Ti^{3+}$ single crystal (grain size is 1.5…2.0 mm). Dose rate was 0.23 Mrad/h.

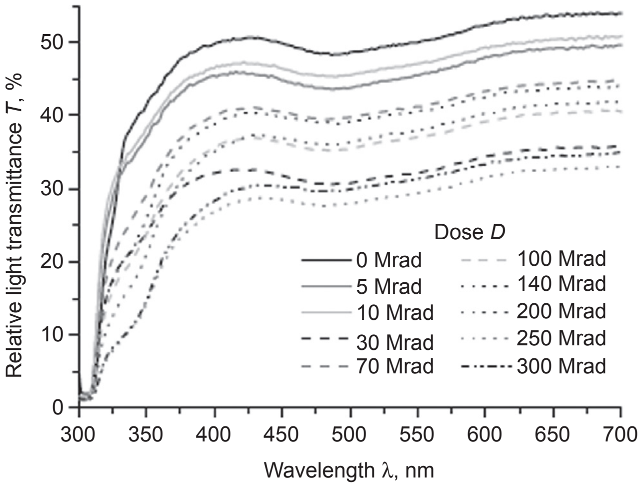

**Figure 13.22** Luminous transmittance *T* of a single-layer composite scintillator based on grains of an $Al_2O_3$:$Ti^{3+}$ single crystal (grain size is 0.3…0.5 mm). Dose rate was 1500 Mrad/h.

$\gamma$ radiation is an order of magnitude higher than that of LiF:Mg,Ti and allows registration of radiation doses on the level of 8 μGy. Their sensitivity is independent of the dose in $10^{-11}$–$10^{-2}$ Gy $s^{-1}$ range.

A technique for neutron dosimetry has been developed using fluorescent nuclear track detectors as a possible replacement for CR-39 plastic nuclear track detector technology. New aluminum oxide crystals containing aggregate oxygen vacancies, and doped with carbon and magnesium ($Al_2O_3$:C,Mg), are imaged using laser-scanning confocal fluorescence microscopy. $Al_2O_3$:C,Mg crystals have a greenish color due to a blue absorption band (435 nm) formed by a new type of aggregate defect consisting of two oxygen vacancies and charge compensated by two magnesium ions; these are $F_2^{+2}$ (2Mg) color centers. $F_2^{+2}$ (2Mg) centers efficiently capture the free electrons and undergo radiochromic transformation into a three-electron state, thus forming $F_2^{+}$ (2Mg) centers. If the $F_2^{+}$ (2Mg) center is optically stimulated into one of its excited states, the electron will relax back to its ground state with a 75 ns lifetime, emitting a photon at 750 nm [31].

Advancements in image processing allow better detection of fluorescence tracks. Dose dependences were obtained for four types of neutron converters. A comparison between enriched $^6$LiF (TLD-600) and LiF with natural abundance of $^6$Li (TLD-100) was also made. Dependence on the angle of incidence for fast neutrons was investigated and compared with simulations based on neutron-scattering theory. The reusability and rereadability of detectors were tested and confirmed to be satisfactory [32].

**Sapphire windows for withdrawal of energy.** One of the factors limiting the withdrawal of energy from devices is the secondary electron resonance discharge in vacuum proportional to the secondary electron emission coefficient. As seen from Table 13.19, sapphire compares favorably with other dielectrics in this regard.

**A fingerprint reader with a sapphire window sensor** is by far the most advanced biometric technology in use. Such technologies are rapidly spreading. Sapphire window sensors are not damaged and will serve for decades until contactless identification systems appear.

**Sapphire optical disks for long-term data storage**. One of the problems in data storage systems is finding long-life storage media. The materials currently used for disks have relatively short lives, while sapphire disks can maintain stability for centuries. It was calculated that the signal distortion introduced by thin sapphire with CD, DVD, and BD formats is not significant. The image quality through glass plate and sapphire plate with compensation is about the same [33].

**Interferometers based on sapphire**. *X-ray interferometers* of the Fabry–Perot type at first contained silicon crystals as X-ray grids. The next step in this direction may be the development of devices for synchrotron radiation. For this class of

**Table 13.19** **Secondary electron emission coefficient at a frequency of $10^9$–$10^{10}$ kHz**

| | Secondary electron emission coefficient | | |
|---|---|---|---|
| **Energy, keV** | **Sapphire** | **Ceramics** | **BeO** |
| 0.5 | 2.7 | 3.7–4.0 | 6.1 |
| 1 | 3.3 | | 5.7 |
| 2 | 2.8 | | 4.5 |

high-precision systems, grids (mirrors) made of dislocation-free sapphire are required. Small (d ~ 5–9 mm) in area, dislocation-free zones can be distinguished by selective etching of plates cut from Ky or HEM crystals.

*X-ray monochromators using sapphire* [34]. For X-ray diffractometers (Cu– $K_\alpha$ radiation), the sapphire planes $(10\bar{1}4)$ and $(03\bar{3}0)$ are used. High resolution is achieved with the plane $(14\bar{5}6)$, for which $2d = 1.660$ Å.

In recent years activities have been developed in the framework of international projects to study astrophysical gravitational waves and their sources. Projects such as LIGO (Laser Interferometer Gravitational-Wave Observatory), Advance LIGO 01, KAGRA, and VIRGO include underground vibration systems, cryocooler units, cryostats, and cryogenic payloads. In some of these projects two dual-recycled interferometers are used to measure the gravitational-wave strain at cryogenic temperature [35]. In LIGO two power-recycled Michelson interferometers with Fabry–Perot arm cavities at Richland, Washington and Baton Rouge, Louisiana, will operate simultaneously to reject false signals.

Silicon or sapphire is used to make the detector. Both silicon and sapphire have more desirable thermomechanical properties in the cryogenic regime and are thus very promising candidates for use in KAGRA. Silicon has a higher thermal conductivity than sapphire, but sapphire has the more immediate advantage of being optically transparent at 1064 nm. The most important part of wave detector is the mirror. A sapphire mirror suspended by sapphire fibers is used in the Japanese interferometric gravitational-wave detector (KAGRA). Heat absorbed in the sapphire mirror flows along fibers. Sapphire has the advantage of higher thermal conductivity near the operating temperature of 20K compared to the fused silica used in other gravitational-wave detectors, but there are some uncertain application properties such as hardness, optical absorption, and birefringence [36]. Massive mirrors made of sapphire of high structural perfection and homogeneity are suspended by delicate sapphire threads. The high conductivity at 20K (more 5000 W/m·K) of sapphire suspensions reduces thermal noise. Hydroxide–catalysis bonding is a precision technique used for jointing components in opto-mechanical systems, and has been implemented in the construction of quasimonolithic silica or sapphire suspensions in gravitational-wave detectors [37]. The Institute for Single Crystals has developed a way of connecting the suspension elements with its own melt [38]. These large international projects will be further expanded. Project LISA will build on the results of LIGO, and the European Space Agency announced ambitious plans to detect gravitational waves in space using laser interferometry, targeted for 2034. These giant optical systems, first used for the recent detection of gravitational waves by Earth-based laser interferometers, would be able to sense ripples in space–time of different frequencies generated by different types of cosmic events [39].

The overall detection limit of this kind of interferometer is limited by its noise.

**Luminophor screens** based on doped sapphire have been developed for accelerators. They are used for recording intense particle beam parameters in digital TV facilities [40]. In comparison with other materials, such screens have higher light output (Table 13.20). Their output is linear up to $2 \times 10^{14}$ proton/cm$^2$ and decreases

## Table 13.20 Characteristics of luminophor screens

| Screen material | Activator content, mass, % | Threshold sensitivity, prot./cm$^2$ | Light output, photon/prot.·s | Afterglow in 60 μs, % | Ultimate radiation resistance, prot./cm$^2$ |
|---|---|---|---|---|---|
| $Al_2O_3$:$Cr^{3+}$ single crystal | 0.066 | $1.7 \times 10^6$ | 440 | 8–10 | $10^{18}$–$10^{19}$ |
| | 0.08 | $2.0 \times 10^6$ | 377 | 2–4 | $10^{18}$–$10^{19}$ |
| | 1.16 | $2.8 \times 10^6$ | 263 | 50 | $10^{18}$–$10^{19}$ |
| $Al_2O_3$:Cr ceramics AF-995 | 0.1 | $4.5 \times 10^6$ | 159 | | $10^{18}$–$10^{19}$ |
| $Al_2O_3$:$Ti^{3+}$ single crystal | 0.011 | $1.9 \times 10^7$ | 39 | 1 | $10^{18}$–$10^{19}$ |
| | 0.047 | $2.7 \times 10^7$ | 27 | 1 | $10^{18}$–$10^{19}$ |
| ZnS | – | $3.0 \times 10^7$ | 8–16 | | $<10^{15}$ |
| BeO ceramics | – | $4.7 \times 10^8$ | 1.6 | | $>10^{18}$ |

Measured at the Institute of High-Energy Physics, Serpukhov, Russia, for a proton beam with 70 GeV energy, $10^{12}$–$10^{14}$ proton/cm$^2$ density, duration $10^{-6}$–0.4 s, 8 s period.

at Cr content <0.066 mass%. The highest light output was recorded for screens with a thickness of 1.5 mm made of $Al_2O_3$:$Cr^{3+}$ crystal in which the content of chromium was 0.066 mass%.

**$Al_2O_3$:$Cr^{3+}$-based luminescent pressure transducers.** The intensity of $Al_2O_3$:$Cr^{3+}$ luminescence is pressure dependent. At concentrations of chromium lower than 0.1 mass%, $Cr^{3+}$ luminescence is dominated by two strong lines (*R*1 and *R*2) of the isolated single $Cr^{3+}$ ions. If the concentrations are higher than 0.1 mass%, additional sharp lines appear (*N* lines) from the exchange-coupled pairs of $Cr^{3+}$–$Cr^{3+}$. With increasing $Cr^{3+}$ concentration, the *N*-line intensity increases with respect to that of *R* lines, thus reflecting the increasing probability of pair formation and the energy transfer from single ions to the pairs. Luminescent pressure transducers are used in the investigation of equilibrium thermophysical properties of high-temperature superconducting substances, as well as for the construction of phase diagrams. For this purpose, the studied material and a thin ruby plate are clamped between sapphire plates. Under the influence of electric current or laser heating on the investigated plate, a pressure of ~100 kbar arises over 1–2 ms. The pressure is measured from the shift in the ruby luminescence peak value. A pulse at $l = 532$ nm is applied to the ruby plate via a light guide and the sapphire plate. The luminescence signal is passed at $l = 700$ nm using the same light guide. The shift of the luminescence peak at this signal, equal to 0.5 nm, corresponds to an increase in pressure of 20 kbar. As an expendable transducer, high-quality ruby with a chromium content of 0.5%–0.7% is used.

$Al_2O_3$:$Cr^{3+}$-based pressure transducers are used for hydrostatic pressures in the order of 60 kbar. The sensor is shaped as a disk, with a diameter of 0.6 mm and a thickness of 0.1 mm, and contains $4 \times 10^{14}$ spins. The intensity of the $R1$ line is proportional to pressure.

**Titanium-doped sapphire** (Ti:sapphire, Ti:S) is one of the key active media of tunable lasers. This crystal is unique due to the fact that in addition to possessing a wideband amplification spectrum that allows pulses of femtosecond duration to be achieved, it has a large cross-section of induced emission. The merits of Ti:S include the possibility of tuning the radiation wavelength in a wide spectral range, high efficiency at room temperature, high radiation power, stability of generation parameters, and radiation strength. Moreover, Ti:S lasers can be pumped by gas, solid-state, and diode lasers, or by flashbulb, and work in pulsed and continuous regimes. One laser of this type can replace several lasers with fixed radiation wavelengths. Depending on the function to be performed by the crystals, the titanium content may vary from 0.02 to 0.3 mass%. Crystals are grown by Cz, HEM, Ky, and HDS methods in an inert or reducing gaseous medium [41].

The crystallization conditions of Ti:S are limited by the physical and chemical properties of the material. The Ti:S laser efficiency is determined by optical losses over the wavelength corresponding to the frequency generation, and is conditioned by the presence of $[Ti^{3+}–Ti^{4+}]$ color centers in the crystal. The optical properties of Ti:S depend on the type of point defects predominated in the crystal. The presence of activator–vacancy complexes of the type $[Ti^{4+} - V_{Al}]$, $[Ti^{3+} - (+2e^{-})]$, $[2Ti^{3+} - (+2e^{-})]$ and $[Ti^{4+} - Ti^{3+}]$ gives rise to optical absorption bands with maxima at 195, 268, 392, and 800 nm, respectively [42].

As revealed by electron microscopy, the parts of the crystal with submicron-size inclusions also contain 70…300 nm inclusions at a concentration of $(5–10) \times 10^{11}\,cm^{-3}$, in the form of chains located perpendicular to the crystallographic direction [0001]. In a first approximation, nonspherical particles may be presented as ellipsoids. Experimental estimations allow the conclusion that one axis of the ellipsoid is five times longer than the other, and this agrees with the natural faceting of corundum crystals. The appearance and distribution of submicron-size inclusions suggest their formation in the solid phase, or in the process of the melt–crystal phase transition. The main cause of the formation of such inclusions in Ti:S when grown in a carbon-containing environment is the excessive quantity of aluminum ions in the melt. Coalescence of excessive aluminum and Schottky defects gives rise to the formation of submicron-size inclusions which contain atoms of aluminum and its suboxides. Treatment of the melt with ultrasound at a frequency 350–400 kHz during crystallization decreases the efficiency of the capture of gaseous bubbles without influencing the crystal structure. The crystals grown by the Cz method in a carbon-containing ambient are characterized by high resistance to UV irradiation, absence of optical absorption at the generation wavelength, and an Figure-of-Merit (FOM) of 250–400. The laser damage thresholds in the bulk of the thermally treated crystal and on its surface reach 2.8 and 11 GW/$cm^2$, respectively [42].

The typical dimensions of laser elements are as follows.

- For flashbulb pumping: $d = 5-8$ mm, $l = 60-120$ mm.
- For laser pumping: $d = 4-30$ mm or rectangular cross-section, $l = 4-30$ mm.
- For powerful short-pulse lasers and laser-pumped amplifiers: $d = 80-110$ mm, $l \sim 30$ mm.

The tunable wavelengths covering a broad range from 700 to 1000 nm make Ti:S an excellent substitute for dye lasers in many applications.

**$Al_2O_3$:$Er^{3+}$ lasers** are of interest due to their emission at near 1.55 μm. This wavelength is safe for the eyes. The fabrication of low-loss $Al_2O_3$:$Er^{3+}$ waveguides enabled the realization of various integrated $Al_2O_3$:$Er^{3+}$ lasers on thermally oxidized silicon substrates.

## References

[1] L. Lytvynov, On the words used as names for ruby and sapphire, Funct. Mater. 18 (2) (2011) 274−277.

[2] E. Dobrovinskaya, L. Lytvynov, V. Pischik, Sapphire: Material, Manufacturing, Applications, Springer, 2009, p. 481.

[3] H. Scheel, L. Lytvynov, Flame-fusion (Verneuil) growth of oxides, in: Book of Lecture Notes. Third Intern. Workshop on Crystal Growth Technology. Switzerland, 2005, pp. 385−396.

[4] M. Musatov, Technique and Technology of Growth Sapphire by GOI Method. S-Peterbourg, 2013, p. 470 (in Russian).

[5] E. Dobrovinskaya, L. Lytvynov, V. Pischik, Sapphire in Science and Engineering, ISC, Kharkov, 2008, p. 380.

[6] I.V. Kryvonosov, L.A. Lytvynov, Optimization of Ky-crystallization process, Funct. Mater. 24 (1) (2017) 1−5.

[7] K.H.S. Bagdasarov, High Temperature Crystallization of the Melt, Fizmatlit, Moscow, 2004 (in Russian).

[8] L. Lytvynov, Growth of shaped high temperature oxides, in: Book of Lectures Notes. 1st Intern. School on Crystal Growth Tech. Swiss, 1998, pp. 712−720.

[9] V.A. Tatarchenko, Shaped crystal growth, in: G. Dhanaraj, K. Byrappa, V. Prasad, M. Dudley (Eds.), Springer Handbook of Crystal Growth, 2010, pp. 509−552.

[10] M.V. Klassen-Neklyudova, K.H.S. Bagdasarov (Eds.), Ruby & Sapphire: A Call, Nauka, Moscow, 1974 (in Russian).

[11] D. Galusek, L. Lytvynov, A. Kozhushko, A. Sinani, V. Sida, Light Weight and Transparent Armours, NATO Final Report, Grant NATO, Brussel, 2009.

[12] L.A. Lytvynov, A.N. Budnikov, Effect of deviations from the (0001) plane of sapphire on the surface properties, J. Surf. Investig. X Ray Synchrotron Neutron Tech. ISSN: 1027-4510 10 (1) (2016) 158−160. © Pleiades Publishing, Ltd.

[13] A.Y. Dan'ko, N.S. Sidelnikova, G.T. Adonkin, et al., Kristallografia 49 (2004) 294.

[14] S.D. Vishnevski, E.V. Kryvonosov, L.A. Lytvynov, Funct. Mater. 13 (2) (2006), 238−234.

[15] B.D. Evans, M. Stapelbroek, J. Nucl. Mater. 85−86 (1979) 497.

[16] M.J.P. Musgrave, The propagation of elastic waves in crystals and other anisotropic media, Rep. Prog. Phys. 22 (1) (1959) 74−96.

[17] F.I. Fedorov, Theory of Elastic Waves in Crystals, Nauka Publisher, Moscow, 1965.

[18] L.A. Lytvynov, A.N. Shupikov, S.V. Ugrimov, Investigating wave processes during strain of sapphire rods under low-velocity impact, in: V.M. Puzikov (Ed.), Crystal Materials for Optics and Electronics, NTK Inst. Monocrystals NAS Ukraine, Kharkov, 2012, pp. 305−329.

[19] P.A. Popov, V.D. Solomennik, P.V. Belyaev, L.A. Lytvynov, V.M. Puzikov, Thermal conductivity of pure and $Cr^{3+}$ and $Ti^{3+}$ doped $Al_2O_3$ crystals in 50-300 K temperature range, Funct. Mater. 18 (11) (2011) 476−483.

[20] M. Izerroukena, T. Benyahia, Nucl. Instrum. Methods Phys. Res. B 268 (2010) 2987−2990.

[21] L.A. Litvinov, T.V. Druzenko, V.G. Potapova, A.B. Blank, Crystallogr. Rep. 46 (2001) 347−349.

[22] A. Voloshin, L. Lytvynov, Wettability of sapphire, Funct. Mater. 13 (1) (2006) 66−68.

[23] A. Yadav, H.K. bashi, S. Kolpakov, et al., Stealth dicing of sapphire wafers with near infra-red femtosecond pulses, Appl. Phys. A 123 (2017) 369, https://doi.org/10.1007/s00339-017-0927-0.

[24] www.physorg.com/news3863.html.

[25] Y.A. Valbis, L.A. Litvinov, V.D. Ryzhikov, Patent USSR. 1410678, 1988.

[26] V.D. Ryzhikov, A.L. Litvinov, E.A. Danshin, et al., Materials for Electron Engineering Moscow, 2001, pp. 61−64 (in Russian).

[27] L.A. Litvinov, E.V. Krivonosov, V.D. Ryzhikov, et al., Voprosy atomnoi nauki i tekhniki. Ser.fizika rad. povrezhd. i rad. materialovedenie, Probl. Nucl. Sci. Eng. Phys. Radiat. Damage Radiat. Mater. Sci. 6 (82) (2002) 154−155 (in Russian).

[28] A.Y. Boyarintsev, N.Z. Galunov, L.A. Litvinov, et al., Radiation-resistant composite scintillators based on inorganic crystals GSO: Ce, GPS: Ce and $Al_2O_3$:Ti, Probl. At. Sci. Technol. ISSN: 1562-6016 N5 (105) (2016) 59−65. Series: Nuclear Physics Investigations (67).

[29] CMS Collaboration, Technical Proposal for the Upgrade of the CMS Detector through 2020, CERN-LHCC-2011-006, CMS-UG-TP-1, LHCC-P-004, CERN, Geneva, 2011.

[30] Sigma-Aldrich. 761036 Aldrich Sylgard-184. Available: http://www.sigmaaldrich.com/catalog/product/aldrich/761036.

[31] M.S. Akselrod, A.E. Akselrod, S.S. Orlov, et al., Fluorescent aluminum oxide crystals for volumetric optical data storage and imaging applications, J. Fluoresc. 13 (6) (2003) 503−511.

[32] G.J. Sykora, M. Salasky, M.S. Akselrod, Properties of novel fluorescent nuclear track detectors for use in passive neutron dosimetry, Radiat. Meas. 43 (2008) 1017−1023.

[33] V.V. Petrov, V.P. Seminozhenko, V.M. Puzikov, et al., Method of aberration compensation in sapphire optical disks for long term storage, Funct. Mater. 21 (1) (2014) 105−110.

[34] R. Belt, Synthetic corundum as x-ray monochromator, X Ray Spectr. 1 (2) (1972) 55−58.

[35] B.P. Abbott, R. Abbott, X. Last, Zhang, et al., Search for gravitational waves associated with gamma-ray bursts during the first advanced LIGO observing run and implications for the origin of GRB 150906B, Astrophys. J. 841 (2) (May 2017) 89.

[36] E. Hirose, D. Bajuk, G. Billingsley, et al., Sapphire mirror for the KAGRA gravitational wave detector, Phys. Rev. D 89 (6) (02/2014), https://doi.org/10.1103/PhysRevD.89.062003.

[37] R. Douglas, A.A. van Veggel, L. Cunningham, et al., Cryogenic and room temperature strength of sapphire jointed by hydroxide-catalysis bonding, Class. Quantum Gravity 31 (2014) 045001, https://doi.org/10.1088/0264-9381/31/4/045001 (10 pp).

[38] E.P. Andreev, L.A. Lytvynov, R. Safronov, Patent of Ukraine #105885, 2014.
[39] Optics.org, Laser Word of Photonic, special ed., June 21, 2017.
[40] S.D. Borovkov, V.S. Konevskii, L.A. Litvinov, et al., Screens for Beam Diagnostics, 1990. Preprint IFVE 90−34. (in Russian).
[41] E.V. Kryvonosov, S.V. Nizhankovski, L.A. Lytvynov, A.A. Bui, Optical and laser properties of Ti-sapphire grown in different methods in reducing medium, Funct. Mater. (2) (2012), 19.214−220.
[42] I.V. Kryvonosov, L.A. Lytvynov, Properties of Ti_sapphire as laser material, Crystallogr. Rep. ISSN: 1063-7745 57 (7) (2012) 94−100. © Pleiades Publishing, Inc.

This page intentionally left blank

# Gallium oxide

# 14

*Vladimir I. Nikolaev*[1,2], *Sergey I. Stepanov*[3],
*Alexey E. Romanov*[1,2], *Vladislav E. Bougrov*[1]
[1]ITMO University, St. Petersburg, Russia; [2]Ioffe Institute, St. Petersburg, Russia;
[3]Perfect Crystals LLC, St. Petersburg, Russia

## 14.1 Introduction

Gallium oxide ($Ga_2O_3$) belongs to the group III oxides and has the bandgap $E_g$ of about 4.8 eV and intermediate free carrier concentration of $\sim 10^{14} - 15 \times 10^{18}$ cm$^3$ (see Table 14.1). It is the widest bandgap (WBG) transparent semiconducting oxide. The very first report on gallium oxide came in 1871 when Dmitri Mendeleev theoretically predicted the existence of a new element, eka-aluminum, and related oxides [2]. In 1875 Lecoq de Boisbaudran experimentally isolated a new element, which he named gallium, and described properties of its compounds [3]. For a long time gallium oxide research was of purely academic interest, as the material did not have any technical applications, but recently the focus of research has begun to shift from a basic investigation of its properties toward the development of a technological background for various practical applications. Today it is evident that it is a material with great potential. Gallium oxide has been investigated and tested as a material for phosphors and electroluminescent devices, for chemical sensors and catalyzers, for transparent conductive coatings, and, of course, for high-voltage and power electronics. The latter require much higher material quality and purity, similar to those accepted in the semiconductor industry.

$Ga_2O_3$ is known to form several polymorphs (see Table 14.2), among which the β form is the only stable polymorph through the whole temperature range and up to the melting point (~1800°C at atmospheric pressure). All other polymorphs are metastable and transform into β-$Ga_2O_3$ at temperatures above 750–900°C [16,17]. Thus only β-$Ga_2O_3$ crystals can be produced by high-temperature processes such as crystallization from a melt.

## 14.2 Applications and requirements of a given crystalline material

Gallium oxide bulk crystals offer good prospects for various applications. However, this potential has yet to be realized, as the technology has not reached the commercial stage. The application chart shows the potential and current uses of devices based on single crystalline freestanding WBG semiconductors (Fig. 14.1). The main fields of WBG crystal applications are photodetectors (PDs), optoelectronics

**Single Crystals of Electronic Materials.** https://doi.org/10.1016/B978-0-08-102096-8.00014-8
Copyright © 2019 Elsevier Ltd. All rights reserved.

**Table 14.1** Electrical properties of group III oxides

| III-Group oxides | Band gap Eg (eV) | Electron concentration $N_e (cm^{-3})$ / Specific resistivity $\rho$ ($\Omega$ cm$^{-1}$) | Note |
|---|---|---|---|
| $Al_2O_3$ | ~8,5 | $\rho > 10^{14}$ | Insulator |
| $Ga_2O_3$ | ~5 | $N_e \sim 10^{14}$(undoped)–$10^{19}$(Sn, Si-doped) | Semiconductor, (TSO) |
| $In_2O_3$ | ~3 | $N_e \sim 10^{17}$(undoped) – $10^{21}$(Sn doped) | Good Conductor, (TCO) |
| $Tl_2O_3$ | 0,33 | $\rho \sim 10^{-4}$ [1] | Highly Conductive (like metal alloys) |

**Table 14.2** $Ga_2O_3$ polymorphs and their crystallographic parameters [4]

| Polymorph | Structure | Space group | Lattice parameters | Comment | Reference |
|---|---|---|---|---|---|
| α | Rhombohedral | $R\bar{3}c$ | $a$ = 4.9825 Å<br>c = 13.433 Å | Experimental | Marezio [5] |
| | | | $a$ = 5.059 Å<br>c = 13.618 Å | Calculated | Yoshioka [6] |
| | | | $a$ = 5.04 Å<br>c = 13.56 Å | Calculated | He [7] |
| β | Monoclinic | $C2/m$ | $a$ = 12.23 Å<br>$b$ = 3.04 Å<br>$c$ = 5.80 Å<br>β = 103.7° | Experimental | Kohn [8] |
| | | | $a$ = 12.27 Å<br>$b$ = 3.04 Å<br>$c$ = 5.80 Å<br>β = 103.7° | Calculated | He [9] |
| | | | $a$ = 12.214(3) Å<br>$b$ = 3.0371(9) Å<br>$c$ = 5.7981(9) Å<br>$\beta$ = 103.83(2)° | Experimental | Ahman [10] |
| γ | Cubic | $Fd\bar{3}m$ | $a$ = 8.238 Å | Experimental | Zinkevich [11] |
| | | | a = 8.30±0.005Å | Experimental | Arean [12] |
| δ | Body-centered cubic | $Ia\bar{3}$ | $a$ = 10.00 Å | Experimental | Roy [13] |
| | | | $a$ =9.401 Å | Calculated | Yoshioka [6] |
| k | Orthorhombic | $Pna2_1$ | $a$ = 5.120 Å<br>$b$ = 8.792 Å<br>$c$ = 9.410 Å | Calculated | Yoshioka [6] |
| | | | $a$ = 5.0557(1) Å<br>$b$ = 8.68842(9) Å<br>$c$ = 9.27585(6) Å | Experimental | Playford [14] |
| | | | $a$ = 5.0463(15) Å<br>$b$ = 8.7020(9) Å<br>$c$ = 9.2833(16) Å | Experimental | Cora [15] |
| ε | Hexagonal | $P6_3mc$ | $a$ = 2.9036(2) Å<br>$c$ = 9.2554(9) Å | Experimental | Playford [14] |
| | | | $a$ = 2.9081(7) Å<br>$c$ = 9.262(3) Å | Experimental | Cora [15] |

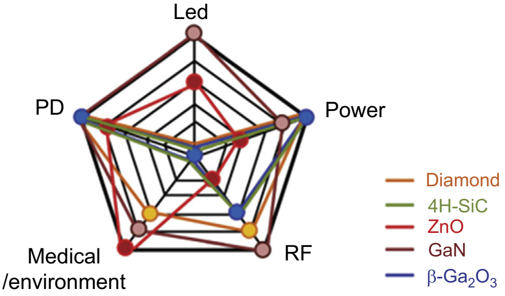

**Figure 14.1** Application chart of devices based on single crystalline freestanding β-$Ga_2O_3$ and other WBG semiconductors [18].

(light-emitting diodes (LEDs)), power electronics (power), radio-frequency (RF) devices, and medical equipment. Gallium oxide clearly outperforms other materials in power electronics, PDs, and RF applications up to 1 GHz frequency range.

### 14.2.1 High-power and high-voltage devices

Fig. 14.2 shows a power frequency diagram of the application space for various semiconductor materials. As can be seen, gallium oxide is the most effective for very high-power devices up to 1 GHz frequency, i.e., power electronics.

Table 14.3 compares the main characteristics of β-$Ga_2O_3$ and other semiconductor materials for high-power and high-voltage applications.

The bandgap of $Ga_2O_3$ is much larger than those of SiC and GaN. The critical breakdown electric field can be estimated from the bandgap using an empirical relationship [3]:

$$E_C = 1.73 \times 10^5 (E_g)^{2.5}. \tag{14.1}$$

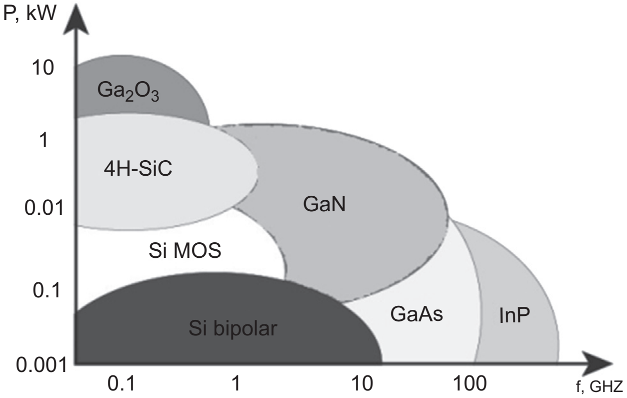

**Figure 14.2** Power frequency diagram of electronic application space for semiconductor materials, using data in the literature [19].

### Table 14.3 Physical properties at room temperature of semiconductor materials used in power electronics and normalized unipolar-related figures of merit (FOMs) (Johnson, Baliga, and Keyes). In the bandgap rows (i) and (d) denote an indirect and direct bandgap

| | Si | GaAs | 4H-SiC | GaN bulk | β-$Ga_2O_3$ | Diamond | Notes |
|---|---|---|---|---|---|---|---|
| **Bandgap $E_g$ [eV] (direct/indirect)** | 1.12<br>(i) | 1.42<br>(d) | 3.25<br>(i) | 3.4<br>(d) | **4.8-4.9**<br>**(d,i)** | 5.45<br>(i) | |
| **Dielectric constant, ε** | 11.8 | 12.9 | 9.7 | 9 | **10** | 5.5 | |
| **Breakdown field, $E_c$ [MV/cm]** | 0.3 | 0.4 | 2.5 | 3.3 | **8** | 10 | |
| **Electron mobility, μ [$cm^2$/V·s]** | 1500 | 8500 | 1000 | 1250 | **300** | 1000 | |
| **Hole mobility, μ [$cm^2$/V·s]** | 480 | 400 | 100 | 200 | **?** | 2000 | |
| **Set drift e⁻ velocity, $V_s$ [$10^7$ cm/s]** | 1 | 1 | 2 | 2.2 | **~2** | 2.7 | 1.8 <001> and <010>, 2.0 <010> |
| **Thermal conductivity, λ [W/cm·K]** | 1.5 | 0.5 | 4.9 | 2.3 | **0.23** | 22 | 0.13 <100>, 0.23 <010> |
| **Johnson = $E_c^2\ V_s^2/4\pi^2$** | 1 | 1.8 | 277.8 | 1089.0 | 2844.4 | 3064 | Switching delay |
| **Baliga = $\varepsilon \cdot \mu \cdot E_c^3$** | 1 | 14.7 | 317.1 | 846.0 | **3214.1** | 23017 | Resistive losses |
| **Combined = $\lambda \cdot \varepsilon \cdot \mu \cdot V_s \cdot E_c^2$** | 1 | 3.7 | 248.6 | 353.8 | **37.0** | | Combined power/frequency/ voltage |
| **Baliga high frequency = $\mu \cdot E_c^2$** | 1 | 10.1 | 46.3 | 100.8 | **142.2** | | Switching losses |
| **Keyes = $\lambda \cdot [(c \cdot V_s)/(4\pi \cdot \varepsilon)]^{1/2}$** | 1 | 0.3 | 3.6 | 1.8 | **0.2** | 215 | thermal capability for power density/speed |
| **Growth possible from melt (Cost-effective fabrication)** | Yes | Yes | No | No | Yes | No | |

*Green and red marks* show advantages and disadvantages of β-$Ga_2O_3$, respectively.

This results in a value of the critical field of over 8 MV/cm, which is three times larger than that of either SiC or GaN. The potential of a semiconductor material for high-power device applications can be estimated by the Baliga FOM [13], which describes the resistive losses of a unipolar device:

$$\text{Baliga FOM } \alpha\ \varepsilon\mu E_C^3. \tag{14.2}$$

The Baliga FOM is proportional to the cube of the breakdown field, but only linearly proportional to the electron mobility and dielectric constant. A Baliga FOM for β-$Ga_2O_3$ is therefore at least four times larger than those for SiC or GaN. Fig. 14.3 shows a theoretical limit of on-resistance versus breakdown voltage for $Ga_2O_3$ and other representative semiconductors. As can be seen, $Ga_2O_3$ is second only to diamond, and outperforms Si, GaN, and SiC. However, $Ga_2O_3$ has very poor thermal conductivity (10.9−27 W/mK) compared to Si (130 W/mK), GaN (~150−200 W/mK), and SiC (360−490 W/mK). This is clearly a drawback in terms of power device applications. A relatively low thermal conductivity (λ) of $Ga_2O_3$ creates self-heating effects that must be mitigated so it can be utilized in high-power devices.

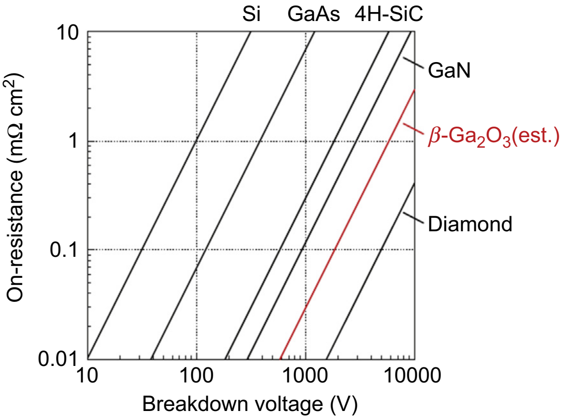

**Figure 14.3** Theoretical limit of on-resistance as a function of breakdown voltage for major power semiconductor materials and β-$Ga_2O_3$ [33].

Due to high values of the Baliga FOM and breakdown field, $Ga_2O_3$ is a promising candidate for the next generation of high-power devices, including Schottky barrier diodes (SBDs) and field-effect transistors (FETs).

### 14.2.1.1 Schottky barrier diodes

Breakdown voltage and on-resistance are the key parameters of a Schottky diode. These parameters are interrelated, i.e., increasing the thickness or decreasing the doping in the drift region increases the breakdown voltage but also increases the on-resistance, which is reflected in the following equation:

$$R_{on-sp(ideal)} = \frac{W_D}{q\mu_n N_D} = \frac{4(V_B)^2}{\varepsilon_S E_C^3 \mu_n}, \tag{14.3}$$

where $V_B$ is the breakdown voltage and $E_C$ is the critical field for avalanche breakdown in a particular semiconductor. The denominator in this equation is the Baliga FOM, which is exceptionally high in $Ga_2O_3$.

Bulk $Ga_2O_3$ substrates for SBDs offer a superior quality of epitaxial layers and the possibility of producing vertical Schottky diodes. Compared to lateral diodes grown on insulating substrates, vertical Schottky diodes on conducting substrates can deliver a higher power with full backside Ohmic electrodes. Sasaki et al. [24] were the first to report on fabrication of Schottky diodes on β-$Ga_2O_3$ substrates. The Schottky barrier height of the Pt/β-$Ga_2O_3$ interface was estimated as about 1.3−1.5 eV, which is comparable with those of Pt/SiC and Pt/GaN. The reverse breakdown voltage was up to 150V. This value was reasonably high, bearing in mind that the devices had a simple structure without passivation or edge termination (Table 14.4).

**Table 14.4** Examples of Schottky contacts to β-$Ga_2O_3$ (bulk, homoepitaxial, and epilayers) reported in the literature

| Substrate | | | | Schottky barrier | |
|---|---|---|---|---|---|
| **Growth [doping, $cm^{-3}$]** | **Orientation** | **Cleaning Method** | **Metal** | **Barrier height $\phi_B$ (eV)** | **Ideality factor $\eta$** |
| FZ single crystal ($10^{17}$ – $10^{18}$) [21] | (100) | Solvent, BOE | Au | 1.2 -~1.1 *(I-V)* | 1.8 – 1.1 |
| CZ single crystal (UID 0.6 – 8 × $10^{17}$) [22] | (100) | NR | Au | 0.98 *(I-V)*<br>1.01 ± 0.05 (PES) | 1.09 |
| CZ single crystal (UID 0.6 – 8 × $10^{17}$) [23] | (100) | Cleaved surface | Ni | 0.97 *(I-V)*<br>1.22 *(C-V)* | - |
| FZ single crystal (UID 3 - 5 × $10^{16}$) [24] | (010) | Solvent, HF, piranha | Pt | 1.46 – 1.47 (PES)<br>1.52 *(C-V)* | 1.04 – 1.06 |
| EFG single crystal (UID 1.1 × $10^{17}$) [25] | (010) | $BCl_3$ for ohmic contact | Ni | 1.49 *(I-V)*<br>1.55 *(C-V)*<br>1.55 (IPE) | 1.04 |
| 2 μm undoped homoepitaxial layer on n-type (~4.1 × $10^{18}$) [26] | (010) | NR | Ni | 0.95 – 1.01 *(I-V)* | 3.38 – 1.21 |
| EFG single crystal (2.8 × $10^{17}$) [27] | $(\bar{2}01)$ | Solvent, piranha, BOE | Ni | 1.08 *(I-V)*<br>1.12 *(C-V)* | 1.19 |
| EFG single crystal (~1.7 × $10^{17}$) [28] | $(\bar{2}01)$ | NR | Ni | 1.05 *(I-V)*<br>1.2 *(C-V)* | - |
| EFG single crystal (UID 1.2 × $10^{17}$) [29] | $(\bar{2}01)$ | NR | Ni | 1.25 *(I-V)*<br>1.18 *(C-V)* | 1.01 |
| EFG single crystal (3.9 × $10^{18}$) [30] | $(\bar{2}01)$ | NR | Ni | 0.9 *(I-V)*<br>1.49 *(C-V)* | 1.4 |
| PLD epi/ZnO/sapphire (1.6 × $10^{18}$) [31] | $(\bar{2}01)$ | NR | Cu | 0.92 *(I-V)* | 1.22 |
| HVPE homoepitaxial layer $n^-$ on $n^+$ EFG single crystals (1.2 × $10^{16}$) [32] | (001) | CMP, Solvent and acid. $BCl_3$ for ohmic contacts | Pt | 1.15 *(I-V)*<br>1.12 *(C-V)* | ~1 |

*CZ*, Czochralski method growth; *EFG*, edge-defined film-fed growth; *FZ* = floating zone growth, *HVPE*, halide vapor phase epitaxy; *IPE*, internal photoemission; *PES*, photoemission spectroscopy; *PLD*, plasma laser deposition; *UID*, unintentionally doped.

Based on data from Y. Yao, et al., Electrical behavior of β-$Ga_2O_3$ Schottky diodes with different Schottky metals, J. Vac. Sci. Technol. B Nanotechnol. Microelectron. Mater. Process. Meas. Phenom. 35 (3) (2017) 03D113.

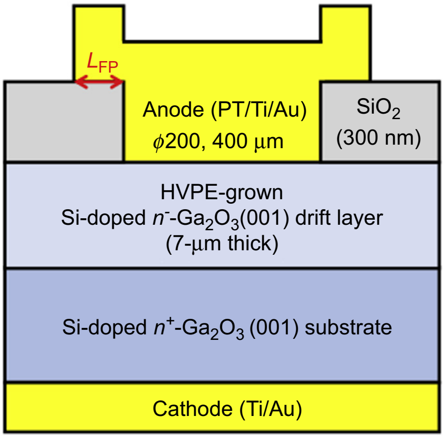
$L_{FP}$
Anode (PT/Ti/Au)
ϕ200, 400 μm
SiO2
(300 nm)
HVPE-grown
Si-doped n⁻-Ga2O3(001) drift layer
(7-μm thick)
Si-doped n⁺-Ga2O3 (001) substrate
Cathode (Ti/Au)

**Figure 14.4** A schematic cross-section of β-$Ga_2O_3$ field-plated SBD structure [34].

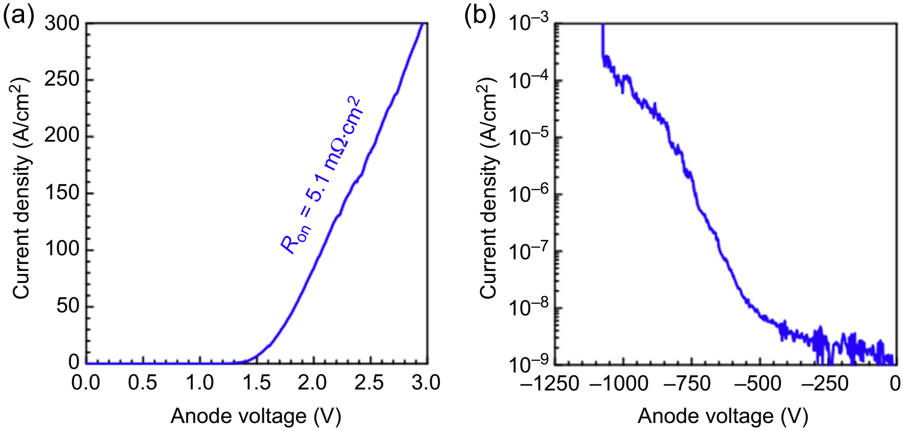

**Figure 14.5** (a) Forward and (b) reverse J—V characteristics of $Ga_2O_3$ field-plated SBD at room temperature [34].

The first demonstration of $Ga_2O_3$ SBDs with a $V_{br}$ of over 1 kV was recently reported [34]. A vertical field-plated SBD using a halide vapor phase epitaxy (HVPE) homoepitaxial drift layer with a record $V_{br}$ of 1076 V on bulk $Ga_2O_3$ was tested (Figs. 14.4 and 14.5) [34]. Excellent Schottky characteristics with near-unity η values of 1.03 ± 0.02 were obtained not only at room temperature but also at elevated temperatures up to 200°C.

### *14.2.1.2 Field-effect transistors*

The first β-$Ga_2O_3$ FET was fabricated by Matsuzaki et al. [35]. It had a top-gate metal—insulator semiconductor field-effect transistor (MISFET) structure, where gallium oxide films grown by pulsed laser deposition on a sapphire substrate had the role of the n-channel layer. The transistor operated under depression mode with a threshold voltage of 6.7 V and a saturation field-effect mobility of $5 \times 10^{-2}$ $cm^2V/s$. This small mobility might have been caused by the granular structures of the film surfaces and the difference in the crystal structure and gate structure.

Higashiwaki et al. [36] fabricated a metal—semiconductor field effect transistor (MESFET) with n-channel $Ga_2O_3$ on a single crystal β-$Ga_2O_3$ (010) substrate. An Sn-doped n-type $Ga_2O_3$ layer with a thickness of 300 nm was grown by molecular beam epitaxy (MBE) on an Mg-doped semiinsulating β-$Ga_2O_3$ (010) substrate fabricated by the floating zone (FZ) method. Ohmic contacts were formed using a reactive ion etching (RIE) treatment in $BCl_3$ and Ar plasma for 1 min, followed by evaporation of Ti(20 nm)/Au(230 nm) and a lift off. The RIE treatment significantly reduced the contact resistance. Schottky gates were fabricated by Pt(15 nm)/Ti(5 nm)/Au(250 nm) deposition and lift off. The breakdown voltage at the off state was as high as 257 V at $V_{GS} = -30$ V. The off-state drain leakage current was as small as 3 mA, and the on/off drain current ratio reached a high value of around 10,000.

Chabak et al. [37] reported Sn-doped $Ga_2O_3$ wrap-gate fin-array FETs (finFETs), which were formed by top-down $BCl_3$ plasma etching of an metal-organic vapour phase epitaxy (MOVPE) homoepitaxial layer on a native semiinsulating Mg-doped (100) β-$Ga_2O_3$ substrate. FinFETs, with a 20 nm $Al_2O_3$ gate dielectric and a 2 μm wrap-gate, demonstrate normally off operation with a threshold voltage between 0 and +1 V during high-voltage operation. The $I_{ON}/I_{OFF}$ ratio is greater than $10^5$ and is mainly limited by high on-resistance that can be significantly improved. A breakdown voltage exceeding 600 V at $V_{GS} = 0$ V off state was demonstrated, and represents the highest breakdown voltage measured without a field plate for β-$Ga_2O_3$ transistors, and the highest breakdown for any transistor technology utilizing nonplanar device channels.

A high pulsed current density β-$Ga_2O_3$ metal oxide field effect transistor (MOSFET) with a fixed channel thickness of 200 nm has been recently grown homoepitaxially on (010) Fe-doped semiinsulating substrate by MBE. A 20 nm thick gate dielectric layer of $HfO_2$ was deposited by plasma-enhanced atomic layer deposition. A pulsed current density of the device >450 mA/mm was achieved with the lowest sheet resistance and a gate length of 2 mμ [38].

### 14.2.2 Photodetectors on bulk β-$Ga_2O_3$

Deep-ultraviolet (DUV) PDs with WBG semiconductors are intensively studied because they can be used to control light power from any UV emitters, photolithography, biochemicals, and so on. In particular, PDs with solar-blind sensitivity and cut-off wavelength shorter than 280 nm have attracted a significant attention because they respond to DUV light only, even under sunlight or room light, and are also suitable for monitoring ozone holes and detecting flames. The majority of PD designs are based on polycrystalline β-$Ga_2O_3$ films grown on foreign substrates [39] and [40,41]. In contrast, Oshima et al. [42] reported on fabrication of DUV vertical-type PDs on bulk β-$Ga_2O_3$ substrates and demonstrated its solar-blind sensitivity with high photo current conversion efficiency. A vertical-type Schottky PD based on a (100)-oriented β-$Ga_2O_3$ substrate was fabricated by the simple processes of thermal annealing and vacuum evaporation. Undoped $Ga_2O_3$ substrates grown by the FZ method were used. The substrates exhibited n-type conductivity due to oxygen vacancies. The typical carrier concentration and mobility were $10^{17}-10^{18}$ $cm^3$ and 40−80 $cm^2/(V \cdot s)$, respectively. These relatively good electrical properties encouraged their application to vertical-type PDs. In this work, the substrate was cut along the (100) plane, and cut again to obtain an 8 × 8 × 0.4 $mm^3$ piece which was then polished chemically and mechanically. The PD exhibited a rectification ratio higher than $10^6$ at 3V, and showed DUV light detection at reverse bias. The spectral response shows solar-blind sensitivity with high photoresponsivities of 2.6−8.7 A/W at wavelengths of 200−260 nm [42].

### 14.2.3 β-$Ga_2O_3$ laser crystals

Mu et al. [43] successfully used a β-$Ga_2O_3$ crystal as a laser element. A passively Q-switched laser based on a gallium oxide saturable absorber (SA) was experimentally demonstrated. The $Cr^{4+}$-doped β-$Ga_2O_3$ crystal was grown by the edge-defined film-fed growth (EFG) method. The crystals have high thermal conductivity (16.2 W/m K) and favorable maximum phonon energy (767 $cm^{-1}$). The laser operates with a maximum average output power of 50 mW, a pulse repetition rate of 421.5 kHz, a pulse width of 235.2 ns, and a pulse energy of about 0.12 mJ. The authors predict that β-$Ga_2O_3$ should be a promising laser element crystal, not only used as SAs with Cr or Co transition-metal ions but also as laser crystals doped with Ti ions in the future.

### 14.2.4 Gallium oxide substrates for heteroepitaxy and homoepitaxy of III nitrides and $Ga_2O_3$ epilayers

β-$Ga_2O_3$ has good physical and chemical properties to be utilized as substrate material for various epitaxial semiconductor films. It may be a good substitute for nitride semiconductor substrates for III nitride epitaxy, bearing in mind that there is a problem with GaN bulk production. Shimamura et al. [44] were the first to demonstrate epitaxy of GaN structures on (100) β-$Ga_2O_3$ substrates. The metal-organic chemical vapour deposition (MOCVD) process was similar to that used for GaN growth on sapphire. In the same article the authors also reported on fabrication of GaN/InGaN blue LEDs with a vertical chip design on β-$Ga_2O_3$ substrates. GaN-based green LEDs on (100) $Ga_2O_3$ substrates have been reported [45]. Reduction of dislocation density in GaN and AlGaN MOCVD films grown on (100) $Ga_2O_3$ substrates was demonstrated by Ito et al. [46]. Growth on (100) β-$Ga_2O_3$ substrates is complicated by the cleavage nature of the (100) plane, which causes the striping of the epilayer and substrate. In contrast, growth on $(\bar{2}01)$ substrates is free of this problem. Muhammed [47] reported on MOCVD growth of wurtzite GaN on $(\bar{2}01)$ β-$Ga_2O_3$ substrates. The epitaxial relationships were defined as (010) β-$Ga_2O_3$ $\|(11\bar{2}0)$ GaN and $(\bar{2}01)$ β-$Ga_2O_3$ $\|(0001)$ GaN, leading to a lattice mismatch of ~4.7%. The GaN lattice parameters, determined by the Bond method, showed a slight compressive strain. Further work by Muhammed et al. [48] demonstrated the high structural and optical properties of MOCVD $In_xGa_{1-x}N$ epilayers ($0 \leq x \leq 23$) grown on conductive and transparent (201)-oriented β-$Ga_2O_3$ substrates using a low-temperature-conducting GaN buffer layer which enhances the quality and stability of the crystals compared to those grown on (100)-oriented β-$Ga_2O_3$. A low-temperature-grown GaN buffer layer is well known to decrease hillocks in the GaN epilayer surface and threading dislocation density. The epitaxial run has two additional temperature steps [48]. After changing the carrier gas from $N_2$ to $H_2$, the temperature of the substrate was increased to 1020°C to grow the Si-doped n-GaN epilayer (with a carrier density of $4 \times 10^{18}$ $cm^{-3}$ and a nominal thickness of ~1.75 μm). Then the temperature was further increased to 1100°C during the deposition of the remainder of the Si-doped GaN layer (of ~1.75 μm thickness). This two-step growth process was developed for GaN on sapphire, where it decreases the formation of epicracks by reducing dislocations between the GaN layers grown in the first and second steps, and was successfully used for GaN/$Ga_2O_3$ growth. The n-GaN layers grown on (201)-oriented β-$Ga_2O_3$ wafers with a GaN buffer have x-ray diffraction (XRD) rocking curves with full width at half maximum (FWHM) of 330 arcsec instead of 430 arcsec, as it was for the insulating AlN buffer.

Research groups at KOHA Co. and Tamura Corp, reported InGaN light blue emission peaking at 447 nm emitting diodes on $(\bar{2}01)$ β-$Ga_2O_3$ substrates [49]. The radiant flux for small-area chips of $300 \times 300$ $\mu m^2$ was 360 mW at 650 mA. Large area chips of $2 \times 2$ $mm^2$ provided a radiant flux of 4.82 W at 10 A. There are other articles devoted to different variants of epitaxial growth. MBE growth of GaN on (100) $Ga_2O_3$ substrates was reported by Villora et al. [50,51]. It was established that nitridation of $Ga_2O_3$ in ammonia is an important prerequisite for the growth of a wurtzite GaN layer. The latter alignment is energetically more favorable because a small rotation of the GaN lattice reduces the lattice mismatch from ~5% to 2.6%. Moreover, for this configuration the in-plane lattice expansion of both β-$Ga_2O_3$ and GaN is very similar, so the stress introduced to the epitaxial layer during the cooling process down to room temperature is minimal [49].

HVPE growth of GaN on β-$Ga_2O_3$ substrates was demonstrated by Nikolaev et al. [52]. $Ga_2O_3$ platelets with (100) orientation were produced by cleaving the β-$Ga_2O_3$ ingot. The surface of GaN layers is full of three-dimensional features such as faceted pyramids and pits. The FWHM of the X-ray rocking curve is 546 arcsec. The quality of GaN epitaxial films was somewhat inferior compared to that of GaN films grown on sapphire under optimized conditions, which can be attributed to nonoptimized growth conditions and defects in the β-$Ga_2O_3$ substrate.

Kachel et al. [53] published a study on GaN growth on (100) β-$Ga_2O_3$ substrates using a pseudo-HVPE technique. In this approach hot ammonia in contact with carbon at 1050°C forms HCN gas. The HCN reacts with gallium in the crucible at 1100°C to form GaCN; this is transported by nitrogen carrier gas flow to the substrate, where the reaction with $NH_3$ occurs and GaN is formed. First the substrate was annealed under $NH_3$ gas at 800−1000°C to form a thin GaN buffer layer on the substrate surface [54]. Then the temperature was increased to 1000−1200°C and thick GaN was grown. After cooling down to room temperature GaN layers self-separated from the $Ga_2O_3$ substrate, which was facilitated by the cleavage nature of β-$Ga_2O_3$. The estimated dislocation density of GaN on $Ga_2O_3$ substrates was in the range of $4.6 \times 10^9$ $cm^2$.

### 14.2.5 Gallium oxide membrane technology

Gallium oxide is a poor thermal conductor, which is a serious obstacle for high-power applications. Epitaxial growth on thin $Ga_2O_3$ membranes or substrate thinning after the growth can improve heat management in $Ga_2O_3$ devices. A similar approach is used in production of GaN LEDs on sapphire substrates, where wafers are thinned by mechanical grinding and polishing from ~400 μm down to 80–100 μm thickness. Alternatively, thin β-$Ga_2O_3$ films can be easily produced by mechanical exfoliation of bulk crystals along cleavage planes. These films can then be transferred and bonded to a suitable heat sink substrate. β-$Ga_2O_3$ has two strong cleavage planes parallel to the (100) and (001) planes. Out of the two, the (100) plane is the strongest. Exfoliated films exhibit an atomic flat surface which is ready for epitaxy without the complicated chemical mechanical polishing (CMP) process. Root mean square surface roughness values of as-exfoliated wafers are in the range of 0.043–0.1 nm [55]. From this perspective, β-$Ga_2O_3$ is potentially interesting for formation of ultrathin membranes and two-dimensional structures similar to those observed in graphene and $MoS_2$ [56,57].

Recently Schottky diodes have been successfully fabricated on (100) $Ga_2O_3$ substrates obtained by mechanical exfoliation [58]. The diodes showed good performances at room temperature, including rectification ratio of $10^{10}$ and an ideality factor (n) of 1.1.

Exfoliated substrates have also been tested for fabrication of PDs [55]. A simple metal–semiconductor–metal structure PD was fabricated directly on the as-obtained β-$Ga_2O_3$ flake. Exfoliated membranes offer many other opportunities; thin layers, so-called nanomembranes, are also available for device applications instead of epitaxial layers. Modern techniques allow attaching such nanomembranes to any place on a semiconductor device.

Hwang et al. [59] suggested a novel approach to the design of an FET using a fragment of mechanically exfoliated $Ga_2O_3$ nanomembranes. The nanomembranes were transferred on to a p+ silicon substrate covered with 285 nm of thermal oxide on the front surface. Although the described method has limited scalability because mechanical exfoliation can produce only small-area nanomembranes, the concept itself is rather attractive. It circumvents a problem of poor thermal conductivity of $Ga_2O_3$ by employing materials with high thermal conductivity as a host substrate for $Ga_2O_3$ nanomembranes. It was shown by Kim et al. [57] that β-$Ga_2O_3$ nanomembrane (nanobelt) FETs displayed an on/off ratio of approximately $10^4$ at room temperature and increased up to $10^7$ for operation at 250°C. The β-$Ga_2O_3$ nanobelt was processed into a back-gate FET via a conventional photolithography process consisting of metallization by electron beam evaporation and a lift-off process (Fig. 14.6).

Recently Zhou et al. [60] demonstrated high-performance depletion/enhancement-mode β-$Ga_2O_3$ on insulator (GOOI) FETs with record high drain currents ($I_D$) of

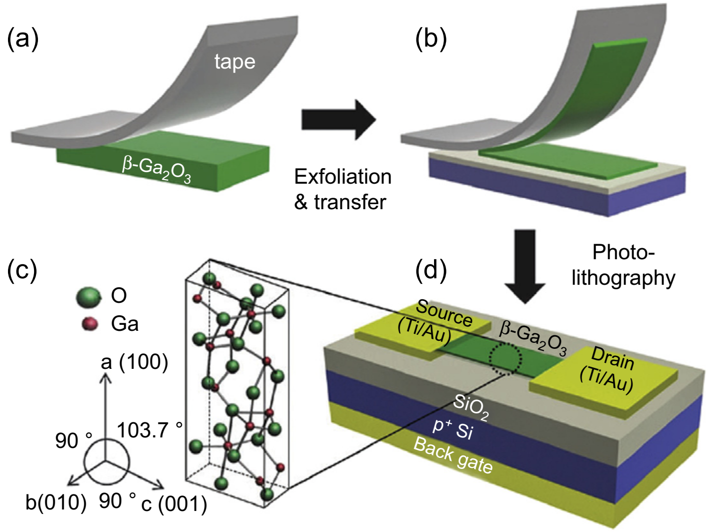

**Figure 14.6** A scheme of nanobelt FET fabrication; (a) exfoliation of a β-$Ga_2O_3$ microbelt by the scotch tape method, (b) transfer of the exfoliated b-$Ga_2O_3$ flake to the target substrate, (c) the atomic structure of β-$Ga_2O_3$, and (d) the fabricated β-$Ga_2O_3$ microbelt FET [57].

600/450 mA/mm, which are nearly one order of magnitude higher than any other reported $I_D$ values. A high on/off ratio of $10^{10}$, a low SS of 140 mV/dec, and a negligible transfer characteristic hysteresis reveal the high-quality interface between β-$Ga_2O_3$ and $SiO_2$. E-mode GOOI FET with LSD = 0.9 μm demonstrates a high $B_V = 185$ V and $E_{av} = 2$ MV/cm, showing the great promise of GOOI FETs for future power devices.

## 14.3 Thermodynamic properties and definition of suitable growth technologies

A thermodynamic study of the gallium−oxygen system was conducted by Zinkevich and Aldinger [61]. The thermodynamic properties of the liquid phase of α-, β-, γ-, and δ-$Ga_2O_3$ as well as solid $Ga_2O_3$ were assessed, and an optimized set of Gibbs energy functions were proposed. $Ga_2O_3$ has been proved experimentally to be almost stoichiometric (the atomic ratio of Ga:O is 2:3) at temperatures <1350°C and oxygen partial pressures >1 Pa; so a small amount of oxygen is sufficient to prevent evaporation completely [62]. A calculated phase diagram of the Ga−O system at 1 bar pressure is shown in Fig. 14.7. It shows four invariant equilibria in the Ga−O system: the congruent melting point of β-$Ga_2O_3$ at 2067 K (with enthalpy of 100,445 J $mol^{-1}$); disproportionation of gaseous $Ga_2O$ into gallium-rich liquid and β-$Ga_2O_3$ at 1599 K; and two gas-eutectic reactions (liquid β-$Ga_2O_3$ → $Ga_2O(g)$ at 2064 K and liquid β-$Ga_2O_3$ → $O_2(g)$ at 2057 K).

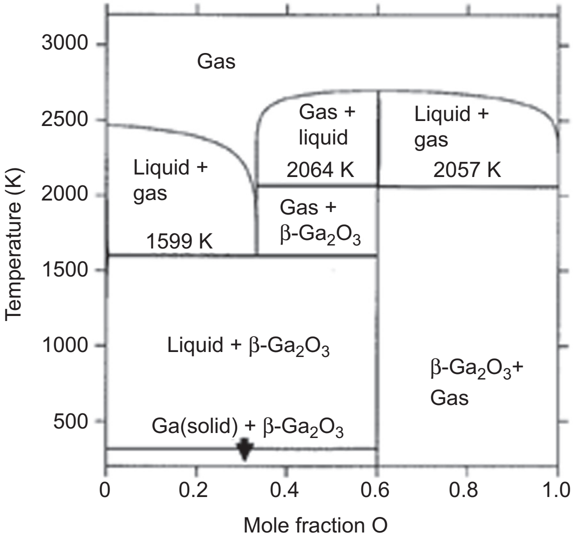

**Figure 14.7** Assessed Ga—O phase diagram at 1 bar pressure [61].

The vapor phase in the Ga—O system contains the species Ga, $Ga_2$, O, $O_2$, $O_3$, $Ga_2O$, and GaO. The GaO and $Ga_2O$ are thermodynamically unstable in the solid state. All attempts to produce solid GaO have failed. The $Ga_2O$ could be obtained only as an amorphous brown-colored substance using the reaction $Ga_2O_3 + 4Ga = 3Ga_2O$.

Thermal decomposition of $Ga_2O_3$ into volatile lower oxides crystals becomes noticeable at atmospheric pressure and temperatures above 1200°C when it is heated in an oxygen-deficient atmosphere. The following decomposition reactions take place:

$$\begin{aligned} &\mathrm{Ga_2O_3}(l) \rightarrow 2\mathrm{GaO}(g) + \frac{1}{2}\mathrm{O_2}(g) \\ &\mathrm{GaO}(g) \rightarrow \mathrm{Ga_2O}(g) + \frac{1}{2}\mathrm{O_2}(g) \qquad (14.4) \\ &\mathrm{Ga_2O}(g) \rightarrow 2\mathrm{Ga}(g) + \frac{1}{2}\mathrm{O_2}(g) \end{aligned}$$

The results of thermodynamic calculations [63] of partial pressures of volatile species of the $Ga_2O_3$ compound, oxygen provided by various atmospheres (Ar, Ar + $O_2$, Ar + $CO_2$), and pressures versus temperature are shown in Fig. 14.8.

Intensive evaporation causes some severe problems in growth processes. One is undesirable mass transport from hot to cold zones of the growth chamber. Another is that the formation of liquid gallium on metal parts of the growth zone leads at high temperature to their corrosion [64].

The range of suitable crucible materials which can withstand the high melting point and the corrosion attacks of the $Ga_2O_3$ melt and liquid Ga is rather limited. Under these

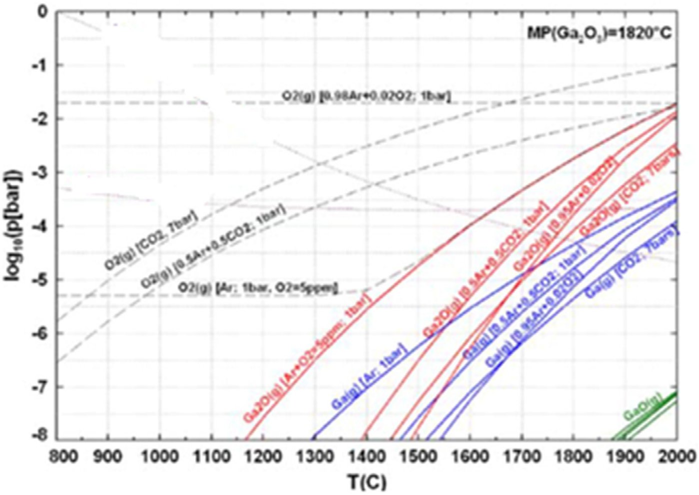

**Figure 14.8** Thermodynamic calculations (by FactSage software [63]) of partial pressures of volatile species of $Ga_2O_3$ compound versus temperature. *Solid lines* refer to volatile species of $Ga_2O_3$, *dashed lines* to oxygen provided by various atmospheres.

conditions, most refractory materials will be either oxidized or dissolved by the $Ga_2O_3$ melt. Noble metals with high melting temperature ≥2000°C are more suitable. Iridium crucibles are conventionally used, but good results were obtained in platinum–rhodium alloy crucibles [65,66]. The use of nonmetallic crucibles has been also reported [67].

Crucible-free techniques such as FZ growth [68–74] and the Verneuil method [75,76] have been used, especially in some earlier works on $Ga_2O_3$.

## 14.4 Schematics of adapted growth methods

### 14.4.1 Crystal-pulling methods

Crystal growth methods involving melt pulling are widely used in the semiconductor industry. Two of them, namely the Czochralski process (Cz) and the EFG method, are employed for the growth of gallium oxide crystals.

#### 14.4.1.1 Czochralski growth

The Cz method was suggested by Jan Czochralski in 1917. The basic idea is that a seed crystal is dipped into a melt and then a single crystal is slowly pulled out of the melt. A temperature gradient is created along the length of the crucible so that the temperature around the growing crystal is below the melting point. The crystal and the crucible are rotated in opposite directions to equalize radial distribution of temperatures. The main steps of β-$Ga_2O_3$ Cz runs are melting of the starting material; seeding; necking;

shouldering; and control of equal-diameter growth. The growth furnace for $Ga_2O_3$ includes an RF induction heater, alumina (zirconia) insulation ceramics, and an iridium crucible with an active iridium afterheater. $Ga_2O_3$ powder of 99.999% purity (5N) is used as a starting material. The growth atmosphere is a mix of Ar, $CO_2$, and $O_2$; pressure in the growth chamber is in the range of 1−7 bar. The growth and rotation rates are about 1−2 mm/h and 5−12 rpm, respectively [63]. The growth direction is chosen in such a way that cleavage planes (100) and (001) are parallel to the pulling axis [010].

### 14.4.1.2 The edge-defined film-fed growth technique

The EFG process is based on the idea of controlling and varying the shape of growing crystals by a shaper (or dies). The method was suggested by A.V. Stepanov [77] for metals, and the technology was later developed by H.E. LaBelle for industrial production of sapphire crystals [78]. A schematic drawing of this process for the growth of β-$Ga_2O_3$ crystals with a rectangular cross-section (ribbons) is shown in Figs. 14.9 and 14.10.

The main feature of this crystal-pulling method is that the melt goes up to the top of the die through the slit by capillary action. Crystal growth occurs on the top of the die. The crystal growth is initiated by placing a seed crystal in contact with the melt on the top surface of the die. After making contact with the seed, the crystal grows on the die top surface. The pulling rate of β-$Ga_2O_3$ crystals is about 10−15 mm/h. The growth direction and the principal surface are set to be the [010] direction and the (−201) plane of the β-$Ga_2O_3$ crystal, respectively. The grown β-$Ga_2O_3$ bulk crystal has the shape of a wide ribbon, which is well suited for cutting semiconductor substrates.

The source material for EFG is the same as for the Cz process, and it is placed in an iridium crucible. The shaper (die) is also made from iridium. For n-type doping of the

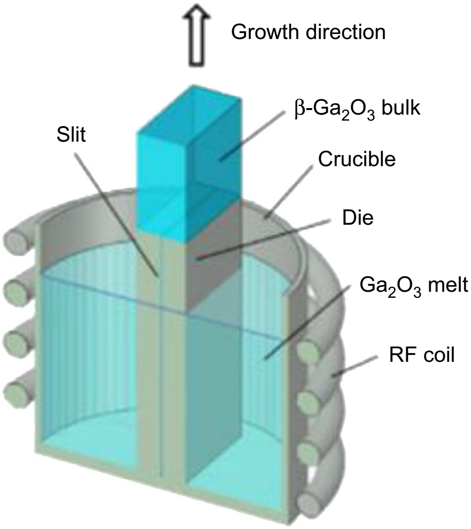

**Figure 14.9** Schematic drawing of EFG process for high-temperature oxide crystals [79].

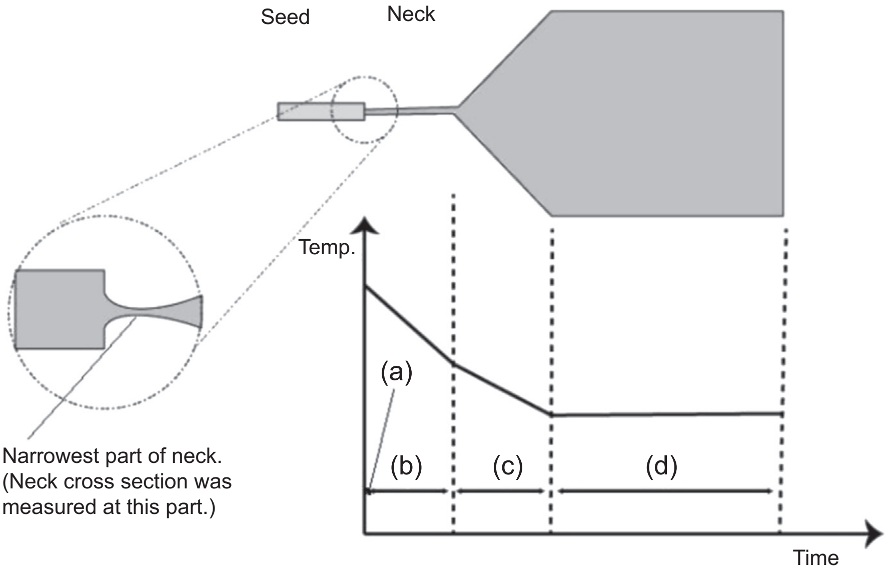

**Figure 14.10** Illustration of growth stages and typical temperature profiles: (a) seeding process, (b) necking process, (c) spreading process, and (d) main growth process.

crystals, tin dioxide ($SnO_2$) or silicon dioxide ($SiO_2$) powder is added to the $Ga_2O_3$ source. The growth runs at atmospheric pressure in a mixture of 98% nitrogen and 2% oxygen gas. The crystals are annealed in nitrogen ambient at 1450°C for 6 h to reduce residual stress in the crystal and achieve the full activation of donors before the substrate fabrication process [79].

### 14.4.2 Bridgman crystal growth

In this technique crystallization occurs inside a crucible which keeps moving via the temperature gradient in a furnace. There are some variants of the method. The process can be carried out in a horizontal or vertical orientation, and usually involves a rotating crucible. The single crystals can be obtained by this technique either with or without seed. A scheme of a vertical Bridgman (VB) growth setup with an RF induction heating furnace includes a work coil, heat shields, a heater, a crucible, a thermocouple, and a crucible shaft with a rotation and translation mechanism, as shown in Fig. 14.11.

The heat shields are constructed from zirconia and alumina ceramics. Similar to Cz and EFG techniques, noble metals are used in the construction of the hot zone. The heater and the crucible are made of Pt–Rh (70%–30%) alloy with a melting temperature above 2173 K. In contrast to iridium, this material has reasonable plasticity, which is needed for unloading the grown crystal from the crucible. Diagrams of the temperature distribution in the furnace and the growth processes are shown in Fig. 14.12. In the growth process, the feed material is melted and VB growth is carried out by raising (b-1) and lowering (b-2) the crucible through the temperature regions

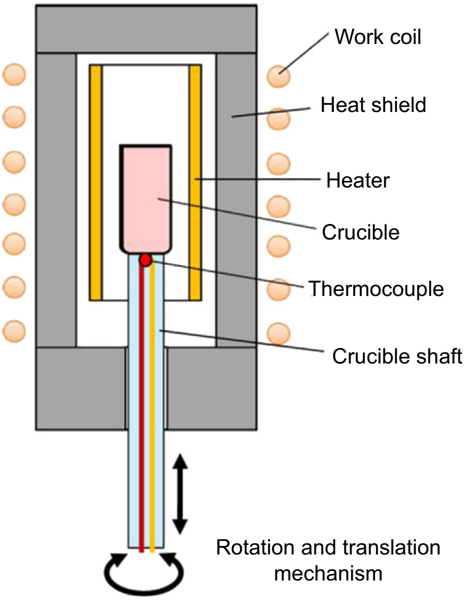
Work coil
Heat shield
Heater
Crucible
Thermocouple
Crucible shaft
Rotation and translation mechanism

**Figure 14.11** Schematic diagram of the VB growth furnace used for $Ga_2O_3$ growth [65].

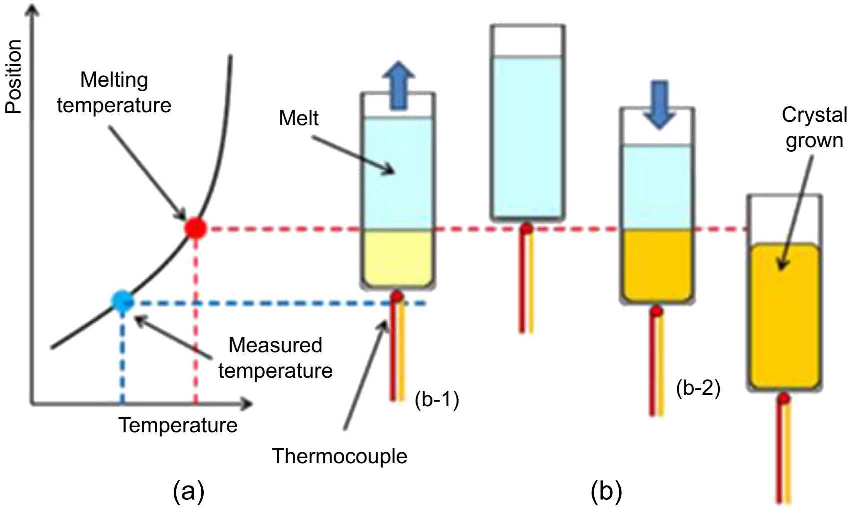
Position
Melting temperature
Measured temperature
Temperature
(a)
Melt
Thermocouple
(b-1)
(b-2)
Crystal grown
(b)

**Figure 14.12** Schematics of the temperature distribution in the furnace (a), and the growth processes (b) [65].

shown in Fig. 14.12(a) at a rate of ∼0.5 mm/h with a rotation of 3 rpm. The specifics of this method are that the operator cannot visually observe the melting and crystal growth processes, so it is imperative to control the temperature very precisely.

### 14.4.3 Floating zone method

The main feature of the FZ method is that no crucibles are used in it, and this is why a very low level of contamination of grown crystals by growth zone construction materials can be achieved. In the case of oxide crystals, due to their low conductivity lamps are used as a heater. A scheme of the process is shown in Fig. 14.13(a).

Firstly, $Ga_2O_3$ powder is pressed into rods by a cold isostatic press under a pressure of 70 MPa. Then the rods are sintered in a high-temperature furnace at 1500°C for 10 h in air. Crystal growth is carried out by an FZ technique using four halogen lamps. The sintered feed rods rotate at 15 rpm and the crystals are grown at a speed of 5−10 mm/h, under dry air flow with a rate of 0.2 $m^3/h$ [68]. A seed is used to control crystallization direction. After growth the crystals are annealed in the air at 1000°C for 72 h [80].

### 14.4.4 Verneuil method

Verneuil is also a noncrucible crystal growth technique. In this method a fine powder of a source material is placed into the flame of a downward-pointing oxyhydrogen torch. The powder melts in the flame and forms a small puddle of a liquid phase on a seed crystal. The crystal is slowly lowered down, allowing the base of the puddle to crystallize, while new melt is supplied by dropping powder through the flame. Long crystals with close to cylindrical shape are grown in this manner. The first

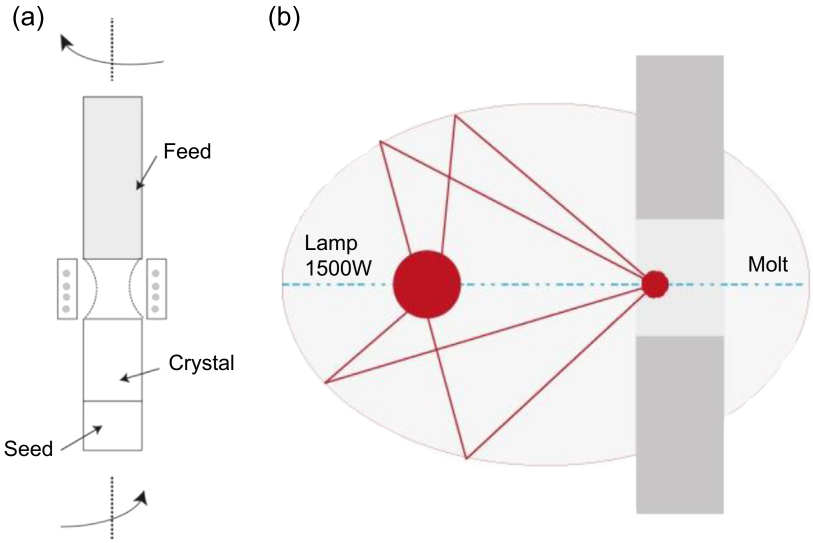

**Figure 14.13** Scheme of FZ method (a) and illustration of crystal melting by lamp (b) in FZ method.

Verneuil $Ga_2O_3$ crystals were grown in the 1960s by Chase [75]. The largest untwinned crystal fragment produced by this method had a cross-section of 2 by 8 mm and was 20 mm long. Verneuil crystals have high mechanical stresses, which are especially critical in the case of $Ga_2O_3$ because of the tendency to crack on cleavage. However, this method is viable to produce small $Ga_2O_3$ crystals for research purposes.

### 14.4.5 Crystallization from nonmetallic crucibles

Maslov et al. attempted to obtain $\beta$-$Ga_2O_3$ crystals from the melt in a nonmetallic crucible [67]. The crucible was made from a single crystal sapphire grown by the EFG method in the shape of a thick-wall test-tube. Gallium oxide powder was loaded into the crucible and it was slowly heated in the growth apparatus in an argon atmosphere at a pressure of 1 bar up to gallium oxide melting point. It was observed that the $Ga_2O_3$ melt was slowly dissolving the walls of the sapphire crucible and thus contaminating the melt with $Al_2O_3$. After heating of the $Ga_2O_3$−$Al_2O_3$ melt composition, up to 1 cm bulk single crystals and their druse were obtained in a process of free crystallization. Separate single crystals were cleaved easily. The Al content in grown crystals was in the range of 5−10 wt%, but the crystals had reasonably good optical and structural qualities very close to those of pure $\beta$-$Ga_2O_3$.

## 14.5 Description of up-to-date growth technologies/processes

### 14.5.1 Edge-defined film-fed growth technique

The EFG method is used for industrial production of many electronics and optics crystals. But it is interesting that, as a rule, it has never dominated among other available techniques. Only about 10% of sapphire crystals are grown by EFG. However, today this technique is becoming mainstream in the production of $Ga_2O_3$ substrates because only the EFG method is used to produce commercial $\beta$-$Ga_2O_3$ single crystals (Fig. 14.14). The process has been developed since the early 2000s and successfully realized for 2 inch diameter substrate production by Tamura [81]. The company demonstrates 4 and 6-inch $\beta$-$Ga_2O_3$ substrates.

$N_d$−$N_a$ in n-type doped crystals can be controlled in a certain range by changing the dopant content; for tin (Sn) the upper limit of $N_d$−$N_a$ is about $2 \times 10^{19}$ $cm^{-3}$.

The biggest obstacle to the development of larger crystals with single crystalline structure is the simultaneous growth of polycrystalline crystals [82]. In most cases, polycrystals are formed during the necking stage, thus detailed analyses of the seeding and necking processes are necessary. The growth parameters for the seeding and necking processes are systematically summarized in Figs. 14.15 and 14.16. When the seeding temperature is higher and the neck cross-section is smaller, the grown crystals were single crystalline. However, in the case of a lower seeding temperature and a larger neck cross-section, they were polycrystalline. The dotted line shown

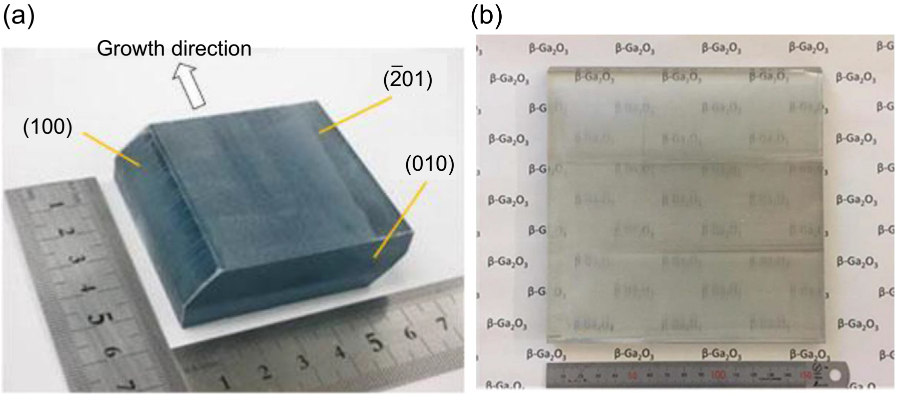

**Figure 14.14** Large EFG-grown β-$Ga_2O_3$ single crystals [79]. (a) The sample was cut perpendicularly to the growth direction [010] and shaped into a flat hexagonal prism. The principal plane is ($\bar{2}$01) and the cross-section was the (010) plane. The (100) planes which are cleavage planes appear as facets during growth; (b) 6″ × 6″ R&D-grade β-$Ga_2O_3$ plate [19].

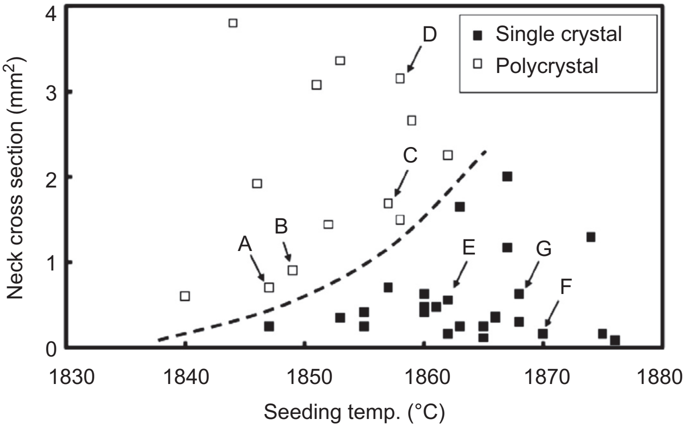

**Figure 14.15** Neck cross-sections of the grown crystals plotted as a function of seeding temperature. The ■ and □ marks indicate that the grown crystals are single crystalline and polycrystalline, respectively [82].

in Fig. 14.15 indicates the borderline between crystal types as a function of seeding temperature and neck cross-section. After the narrowing neck is formed, the temperature is reduced at a certain rate to grow the neck. The length of the neck of the grown crystals is plotted in Fig. 14.16 as a function of the temperature reduction rate during the necking process. The dotted line in the figure is a guide for reading the data, indicating the relationship between the temperature reduction rate and neck length. It was found that neck length depended on the reduction rate. A marked change in temperature during growth normally leads to degradation of the crystals, resulting in polycrystalline formation. However, when the parameters for the seeding condition and neck

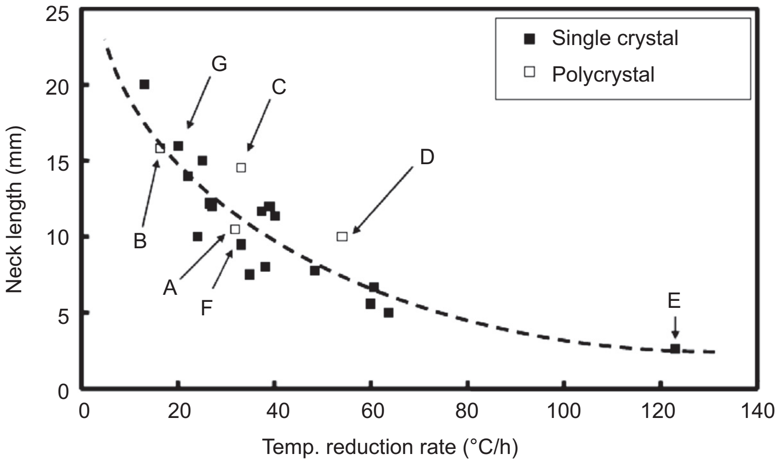

**Figure 14.16** Neck length of the grown crystals plotted as a function of temperature reduction rate during neck growth. The ■ and □ marks indicate that the grown crystals are single crystalline and polycrystalline, respectively [82].

cross-section satisfied the single crystalline region clarified in Fig. 14.15, single crystalline crystals were obtained even when the sample underwent a marked reduction in temperature during the necking process. In the case of sample E, for example, the grown crystal was single crystalline despite a temperature reduction of as much as 120 C/h. In contrast, samples A—D were polycrystalline crystals because of the unsatisfactory conditions of seeding temperature and neck cross-section, although the temperature reduction rate was sufficiently slow. A systematic study of growth parameters was carried out [82], indicating that the seeding temperature and neck cross-section were the most critical factors governing the crystalline type of EFG-grown crystals. The dislocations in the seed crystals propagate to the grown crystals. A narrower neck may thus prevent the propagation of dislocations. The seeding process may also affect the occurrence of new dislocations, and a higher seeding temperature may play an important role not only to suppress the occurrence of new dislocations but also to promote the reconstruction of the atomic arrangement.

The EFG method is quite flexible and can be used to produce both ribbon and cylinder-shape β-$Ga_2O_3$ crystals. A new approach to EFG β-$Ga_2O_3$ crystal growth has recently been suggested [83]. So-called columnar-shaped β-Ga2O3 crystal growth uses the main principles of the $Ga_2O_3$ EFG technique, i.e., an iridium crucible and die, RF heating furnace, and oxygen-containing atmosphere. A schematic diagram of the EFG run is shown in Fig. 14.17.

The shape of the die is a columnar with slits as used for growing $TiO_2$ single crystals [84]. The die has a diameter and a height of 20 and 40 mm, respectively. The growth direction is [010] orientation with a seed crystal. The atmosphere is 99.999% purity $CO_2$ gas at 1 atm and the flow rate is 1—2 L/min. The photographs in Fig. 14.17 Section (III) show the rod-shaped as-grown β-$Ga_2O_3$ ingots and the same crystals after 10 h annealing at 1500°C.

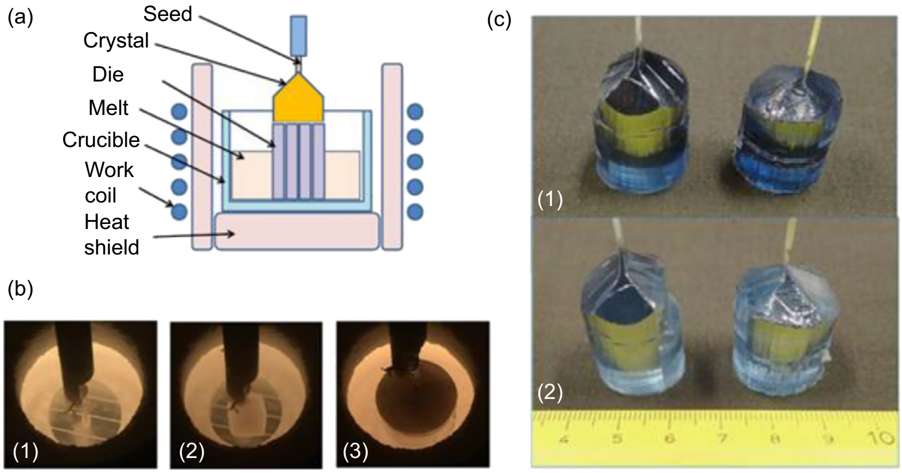

**Figure 14.17** EFG growth of cylinder crystals. (a) Schematic drawing of EFG runs. (b) Photos of growing crystal inside EFG furnace: (1) start of the growth process just after seeding, (2) the crystal size has expanded (3) main part of the growth run when the shape of crystals is controlled by the die. (c) EFG grown crystals (1) as-grown ingots, (2) after high-temperature annealing [83].

### 14.5.2 Czochralski growth

Scaling-up of bulk β-$Ga_2O_3$ single crystals by the Cz method was discussed by Galazka et al. [64]. The authors conclude that the decomposition of melt presents a serious problem for increasing the crystal size. For small crystals (i.e., crystal diameter $\leq$1 inch), even a small amount of oxygen (0.8−2.0 vol%) in the growth atmosphere is sufficient to minimize the decomposition. Thus small crystals of high structural quality could be relatively easily produced [64], because the amount of metallic Ga in the melt is very low and does not affect the growth process. The situation is quite different when a larger melt volume is used to grow crystals as large as 2−4 inches in diameter. The amount of metallic Ga in the melt is high enough to affect the quality of growing crystals and materials in the growth zone, where Ga reacts with Ir. This in turn leads to undesirable formation of eutectic or intermetallic phases with an iridium metal crucible.

The difference between 1, 2, 3, and 4 inch diameter crystals becomes clear with the results of the calculations shown in Fig. 14.18. The amount of metallic Ga in the melt increases dramatically when the crystal diameter (i.e., the melt volume) increases, and, in particular, at low oxygen concentrations (<5 vol%). For the growth of 1-inch diameter crystals a small amount of oxygen is sufficient to maintain the concentration of Ga in the melt below the critical level (shown as a horizontal dashed line). In contrast, growing 2-inch diameter crystals would require about 25 vol% of $O_2$, and in the case of 3-inch crystals it would be about 100 vol% of $O_2$. The growth of 4-inch

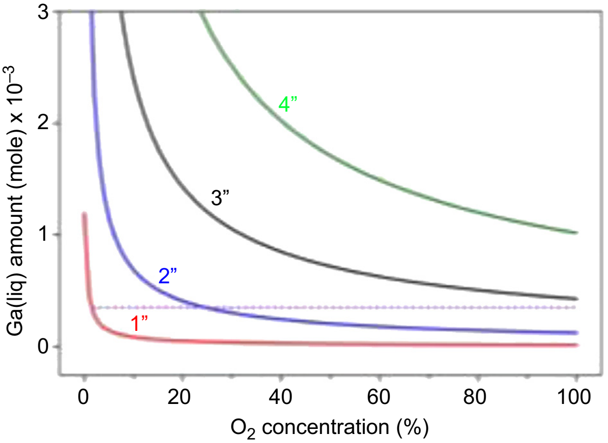

**Figure 14.18** The amount of metallic gallium formed in the $Ga_2O_3$ melt versus $O_2$ concentration in the growth atmosphere depending on crystal diameter (in inches). The dashed line in the inset corresponds to Ga(l) level, which is not harmful for the growth of a 1 inch diameter crystal [64].

diameter crystals is not feasible because Ga concentration in the melt is above the harmless level even when using pure oxygen as the growth atmosphere.

In theory, the absolute values of metallic Ga are not very high, because the calculations were made in a thermodynamic equilibrium (i.e., the whole melt volume has the same “access” to oxygen). In practice, the amount of Ga in the $Ga_2O_3$ melt will be much higher because oxygen in the growth atmosphere interacts with the exposed melt surface only and its penetration into the melt volume is limited. The hottest part of the crucible, where the decomposition is most advanced, is located just above the crucible bottom, i.e., far away from the melt surface. Metallic Ga produced in that region due to insufficient $O_2$ concentration in the melt volume may form eutectics with Ir despite the very high oxygen concentration above the melt surface.

It is not clear whether or not the Cz method is being used to grow 4-inch diameter crystals, but we can see intensive attempts to overcome the limitations of melt thermodynamics by a significant increase of the oxygen concentration. A serious problem is currently how to use such high oxygen concentrations in combination with Ir [64], when in the case of unprotected Ir crucibles typical Ir losses in growth runs for even 2-inch diameter crystals are between 5 and 8 wt% for high $O_2$ concentrations of 20−35 vol%. Galazka et al. [64] suggest decreasing Ir losses by variation of oxygen concentration in the atmosphere during the growth run. Oxygen concentration is changed according to the temperature in the growth chamber. The temperature range is divided into three regions: heating up the Ir crucible with the $Ga_2O_3$ starting material, melting, and growing a crystal (see Fig. 14.19).

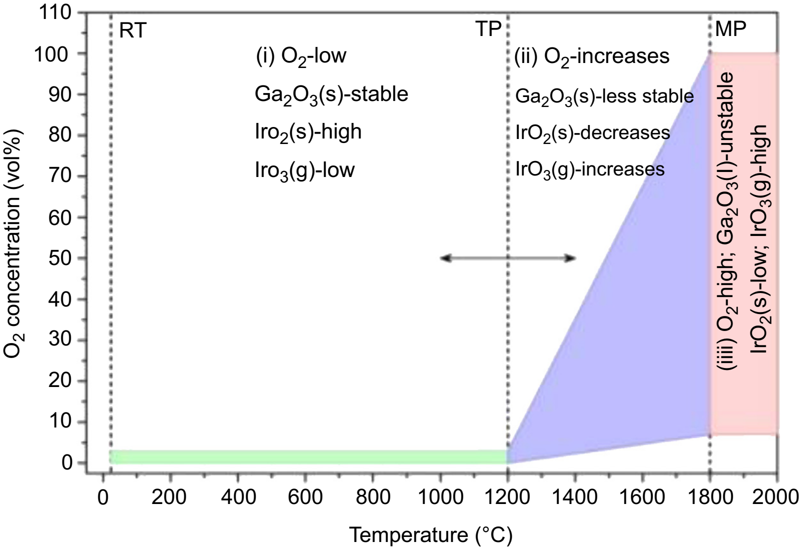

**Figure 14.19** Diagram of oxygen delivery to a growth furnace versus temperature for the growth of large-diameter β- $Ga_2O_3$ single crystals from an Ir crucible [64]. *MP*, melting point, *RT*, room temperature, *TP*, transition point.

The concentration of oxygen above the melt is different for the different stages of the growth cycle, and is varied as a function of temperature according to the following rules.

1. A low oxygen concentration is maintained between room temperature and a transition point (TP = 1000−1400°C, as an example TP = 1200°C in Fig. 14.19) to minimize or avoid the formation of $IrO_2$(s). It could be a few vol% or virtually no oxygen at all. Here the growth atmosphere may comprise a neutral gas (Ar, $N_2$) or an oxidizing gas (e.g., $CO_2$, Ar + $O_2$(low)/$CO_2$.
2. Between TP and melting point the oxygen concentration is increased from a low value to a high target value around the melting point of $Ga_2O_3$ (1800°C), In this region the $Ga_2O_3$ starting material becomes less stable and requires more oxygen, but on the other hand the formation of $IrO_2$(s) is minimized. It is not important how the oxygen concentration is increased, e.g., linearly, stepwise, parabolic, or in any other way. In this region the growth atmosphere typically consists of Ar + $O_2$, $N_2$+$O_2$, or $CO_2$ + $O_2$ and the increased $O_2$ concentration is achieved by changing the ratio of oxygen to the other gas.
3. An oxygen concentration of 5−100 vol% depending on the crystal diameter (or melt volume) is maintained. The final value can be reached just before melting, during melting, or just after melting of the $Ga_2O_3$ starting material. During crystal growth the oxygen concentration can be kept constant, or it can be decreased/increased to modify crystal properties. $Ga_2O_3$ in the liquid phase is much less stable compared with the solid phase, and $IrO_2$(s) formation is minimized while $IrO_3$(g) concentration is at a relatively high (but acceptable) level, which causes Ir losses by evaporation.

Following these rules it is possible [64] to obtain 2-inch diameter cylindrical crystals with a weight of up to 1 kg when oxygen concentration is varied between 8 and 35 vol%.

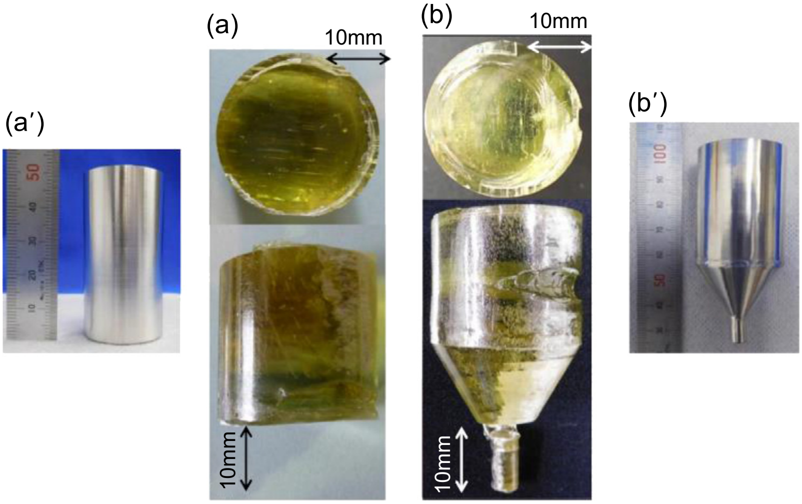

**Figure 14.20** β-$Ga_2O_3$ crystals grown by the VB method. Two views (a) of a crystal grown in the full-diameter crucible (a'), and two views (b) of a crystal grown in the conical crucible (b') [65].

### 14.5.3 Bridgman method

Hoshikawa et al. reported a successful growth run of β-$Ga_2O_3$ single crystals by the VB method without seeding in a full-diameter crucible, and in a conical crucible with a thin seed well [65]. The grown crystals were 25 mm in diameter and 25 mm long (Fig. 14.20). It is known that as a rule in the VB method it is very difficult to release the crystal seriously damaging to due to its adhesion to the crucible. It was found that β-$Ga_2O_3$ crystals did not adhere to Pt−Rh alloy crucibles with either vertical or conical walls. The crystals were released after growth by destructive peeling of the crucibles. The obtained crystals were very smooth and shiny.

Only the EFG, CZ, and VB techniques demonstrate the potential to produce large β-$Ga_2O_3$ bulk crystals. Expensive noble materials are used in all these methods, and they perform at the margin of material limits.

## 14.6 Tailoring of crystal properties via growth parameters

The main application of β-$Ga_2O_3$ single crystals is fabrication of substrates for epitaxial growth. The basic principles of substrate preparation are protected by patent by Tamura Co. [85]. It is claimed that the occurrence of cracks and latent scratches during surface polishing is reduced when the principal surface of the substrate is rotated 10−70 degrees about the [010] axis, or 100−150 degrees about the [010] axis, or 10−90 degrees about the [001] axis. Substrates with a crack density of less than 0.05 cracks/cm and no latent scratches can be produced.

In addition, rotation of the principal surface from 10 to 45 degrees, or from 135 to 150 degrees from the (100) plane about the [010] axis, or from 10 to 45 degrees from the (100) plane about the [001] axis increases the growth rate of the $Ga_2O_3$ crystal film, prevents the substrate from breaking during device manufacturing, and reduces the crack density on the principal surface (Figs. 14.21 and 14.22).

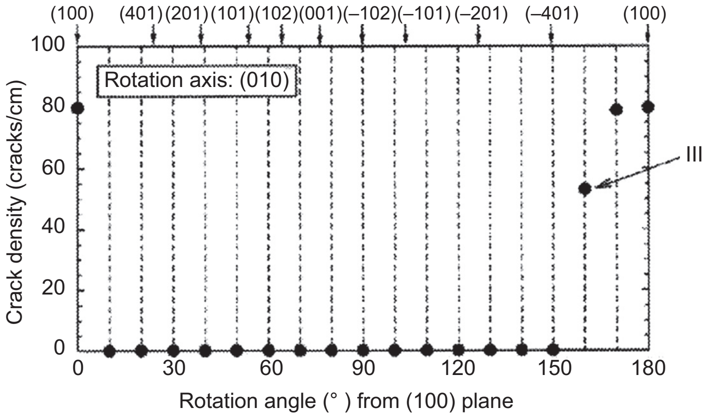

**Figure 14.21** The diagram illustrates the relation between the rotation angle of the principal surface of $Ga_2O_3$ single crystal substrate from the (100) plane about the [010] axis and the crack density on the principal surface [85].

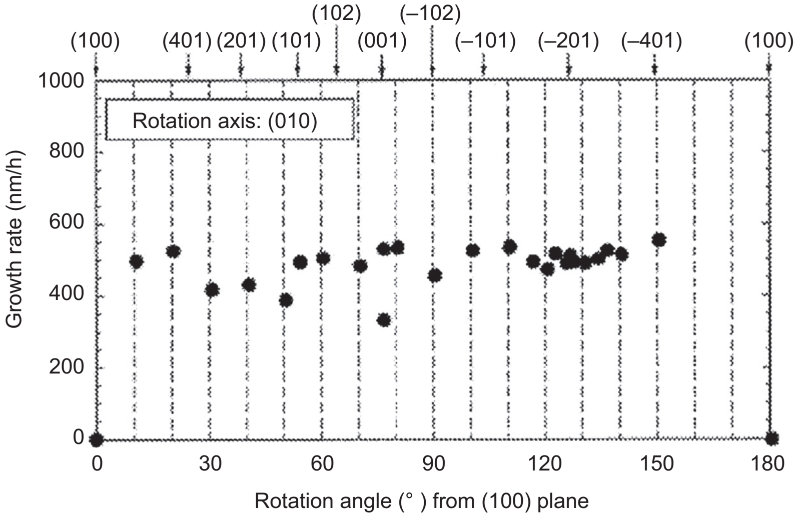

**Figure 14.22** The diagram illustrates the relation between the rotation angle of the principal surface of $Ga_2O_3$ single crystal substrate from the (100) plane when rotated about the [010] axis and the growth rate of an epitaxial film [85].

# 14.7 Doping issues and reduction of defect density

## 14.7.1 Conductivity control and doping

$\beta$-$Ga_2O_3$ is intrinsically an insulator, but conductive n-type crystals can also be produced. Conductivity of the $Ga_2O_3$ crystals can be controlled by changing the gas ambient or by doping. As reported by Uedaa and Hosono [72], the conductivity of $Ga_2O_3$ crystals can be controlled from $10^{-9}$ to 38 $\Omega^{-1}cm^{-1}$ by changing the oxygen content in the growth atmosphere. Highly insulating colorless crystals were synthesized in a pure $O_2$ atmosphere. The conductivity of the crystals increased as the oxygen content was decreased, but the growth was unstable under low $O_2$ conditions. The natural n-type is commonly attributed to oxygen vacancies which are ionized and form donors. The correlation between growth conditions and conductivity was observed by Galazka et al. [86] for $Ga_2O_3$ crystals produced by the Cz method. With increasing $CO_2$ partial pressure the color of the crystals changed from blue to colorless to gray. Transparent crystals had the lowest conductivity ($<1\ \Omega^{-1}cm^{-1}$). The blue coloration was the result of free carrier absorption, while the gray coloration could be due to possible carbon incorporation into the crystal lattice. An interesting observation is that the crystals grown under a higher oxygen partial pressure (7 bar of pure $CO_2$ overpressure) revealed higher donor concentration, which contradicts the results reported for the FZ method. Such behavior of $Ga_2O_3$ can be explained by a reducing action coming from the decomposition of $CO_2$ [63]. The increased conductivity of crystals grown under high $CO_2$ partial pressure can be also accounted for by carbon contamination.

Doping with other elements also affects the electrical conductivity and free electron concentration of $\beta$-$Ga_2O_3$ crystals. For example, group IV elements such as Si, Ge, and Sn substituting on the Ga site, or group VII elements such as Cl and F substituting on the O site, act as shallow donors [87]. Si and Ge prefer the tetrahedral coordination of the Ga(I) site, while Sn prefers the octahedral coordination of the Ga(II) site. F and Cl both prefer the threefold coordination of the O(I) site.

Highly conductive crystals were produced by the FZ method using $Ga_2O_3$ rods doped with 2–10 mol% of $SnO_2$. Even though the crystals were grown in an oxygen atmosphere, conductivity values of 0.96 $\Omega^{-1}cm^{-1}$ [72] and 56 $\Omega^{-1}cm^{-1}$ [71] have been reported. The incorporation efficiency was quite low, because a vast amount of the Sn atoms in the feed rods evaporated during the crystal growth. As reported by Ueda et al., growth using feed rods with 3 mol% of $SnO_2$ resulted in $Ga_2O_3$ single crystals with 0.05% of Sn atoms. The values given by Suzuki et al. are almost an order of magnitude lower. In their experiments residual elemental Sn was found to be about 32–45 ppm from a starting concentration in the feed rods of 2–10 mol%. Nevertheless, the quantity of remaining Sn atoms was still enough to provide a concentration of free electrons in the range of mid-$10^{18}$ $cm^{-3}$. Mobility was in the range 50–100 $cm^2/Vs$ [71]. $Ga_2O_3$ crystals doped with $SnO_2$ had a blue coloration [72].

Silicon is another potential donor impurity in $Ga_2O_3$. The relative difference between atomic radii of $Si^{4+}$ and $Ga^{3+}$ is approximately −40%. This is significant compared to relative atomic radii differences for $Ge^{4+}$ and $Sn^{4+}$, which are −16%

and +14%, respectively [50] [88]. From the point of view of atomic radius, $Ge^{4+}$ and $Sn^{4+}$ accommodate better than $Si^{4+}$ in the $Ga^{3+}$ cationic site. However, Si has higher potential as an n-type dopant for crystals grown from the melt, since it remains in the melt while Ge and Sn evaporate to a high extent [88]. Villora and coworkers [88] produced Si-doped $Ga_2O_3$ crystals by the FZ method. The feed rods were prepared by a sintering process from a mixture of $SiO_2$ and $Ga_2O_3$ powders, with the concentration of Si varying from 0 to 0.2 mol %. The resulting Si concentration in the $\beta$-$Ga_2O_3$ single crystals was in the range of $10^{16}$–$10^{18}$ $cm^{-3}$. As reported by a number of authors, magnesium doping results in insulating $\beta$-$Ga_2O_3$ crystals. Onuma et al. [89] grew Mg-doped $\beta$-$Ga_2O_3$ crystals by the FZ technique. The samples exhibited a semiinsulating behavior, and resistivity of $6 \times 10^{11}$ Ω cm was obtained with an Mg concentration of $4 \times 10^{18}$ $2 \times 10^{19}$ $cm^{-3}$. Galazka et al. [86] found that Cz-grown $\beta$-$Ga_2O_3$ crystals doped with Mg in a very low range of 6–28 wt ppm were insulating when grown at 100% of $CO_2$, indicating that Mg is a very efficient compensating acceptor. In addition, Mg doping was found to stabilize the growth and reduce the probability of the spiral formation. The equilibrium segregation coefficient of Mg across the liquid–solid interface during growth of $\beta$-$Ga_2O_3$ single crystals by the Cz method was estimated to be 0.10–0.12.

The possibility of p-type conductivity in $Ga_2O_3$ remains controversial. So far there are no reports of clear hole conduction in p-type $Ga_2O_3$. Liu et al. [90] claimed to have produced nitrogen-doped $Ga_2O_3$ nanowires with p-type conductivity, drawing the conclusion on p-type conductivity based solely on I–V measurements; no in-depth analysis of the carrier mobility and concentration was given. Theoretical modeling by Zhang and coworkers [91] revealed that nitrogen forms a shallow acceptor impurity level at the top of the valence band, with the Fermi level intersecting the impurity level.

According to other theoretical calculations [92], p-type conductivity in $\beta$-$Ga_2O_3$ is impossible because of strong self-localization of holes. This localization is due to the ionicity of metallic oxides. A positive hole, if it is successfully introduced by substitutional doping, for instance, localizes on a single oxygen atom and cannot migrate within the crystal lattice, even under an applied electric field [93]. Thus very low hole mobility in the order of $10^{-6}$ $cm^2/V \cdot s$ is expected at room temperature. Such a low value indicates that even if holes could be introduced in $Ga_2O_3$, no significant p-type conductivity can be achieved.

### 14.7.2 Defect density

Information about linear defects in the crystalline structure of gallium oxide is scarce. Selective chemical etching was employed for estimation of dislocation density. The crystals were etched in a hot $H_3PO_4$ acid solution to observe crystal defects and investigate the correlation between crystal defects and etch pits. The etching method was first reported by Oshima et al. [94]. At room temperature, $\beta$-$Ga_2O_3$ is practically insoluble in $H_3PO_4$ and $H_2SO_4$. Etching rates of several to several hundred nm/min are controlled by realistic etching temperatures of about 100–200°C. The density of dislocation pits in 2″ Tamura substrates is $10^3$–$10^4$ $cm^{-2}$.

The crystal defect distribution in EFG-grown crystals was investigated by reflection X-ray topography, transmission electron microscopy (TEM), and potassium hydroxide (KOH) etching [95]. Two types of defects in β-$Ga_2O_3$ were found: dislocations and nanopipes. TEM results indicate that dislocations are screw dislocations with Burgers vector parallel to [010]. The arrangement of etch pits indicates that most of them lie on (−201) and (001), which seem to be subgrain boundaries. Nanopipes are rod-like defects of 0.1 μm diameter and at least 15 μm length elongated along [010]. The results of electron diffraction patterns and elemental analyses reveal that nanopipes are hollow. No strain field was found around them [95].

Recently, TEM investigation of the defect structure in $(\mathrm{Al}_{\text{ч}}\mathrm{Ga}_{1-\text{ч}})_2\mathrm{O}_3$ with a monoclinic structure grown by HVPE on sapphire substrates has been performed [96], and various types of defects, including twins and stalking faults, have been detected and analyzed.

## 14.8 State-of-the-art of the material

The growth of high-quality β-$Ga_2O_3$ single crystals by the EFG technique is proved effective. In comparison with other materials like GaN, which need to be synthesized from the solution at high pressure or from the vapor phase, growth of β-$Ga_2O_3$ from the melt by the EFG technique is very advantageous. The crystals can be grown at high speed (10−30 mm/h), at atmospheric pressure, and to a desired industrial size up to 6 inch, since the EFG is a comparatively easily scalable technique. These facts favor in turn low production costs, thus price-competitive wafers for the production of LEDs, LDs, power and high-voltage devices, solar blind sensors, and other applications are feasible [49].

## 14.9 New trends and future developments

Researchers have demonstrated the great potential of an experimental transistor made of gallium oxide, which could bring new ultraefficient switches for applications such as the power grid, aircraft, and military equipment. Transistors and diodes operating at a voltage range of higher than 3 kV will probably become the main target for $Ga_2O_3$ power devices in future R&D [97]. However, $Ga_2O_3$ devices are not limited just to power device applications, and should also be developed for high-frequency and extreme-environment electronics. It is expected that $Ga_2O_3$ devices will compete with SiC Schottky and silicon laterally diffused metal oxide semiconductor (Si-LDMOS) for medium- and high-power applications. Compared with other WBG crystal growth technologies, it should be noted that β-$Ga_2O_3$ has high growth rates at normal pressure and thus today has advantages over GaN. Gallium oxide substrates are expected to become cheaper than SiC ones, but the future progress of $Ga_2O_3$ depends on how quickly its substrate cost decreases and its size increases. A roadmap for substrate scaling up of $Ga_2O_3$ and other WBG crystals is presented in Fig. 14.23.

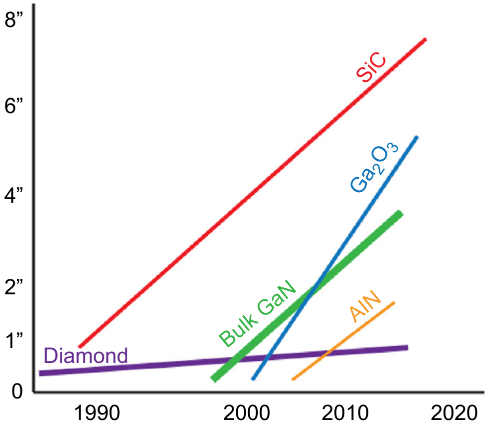

**Figure 14.23** Roadmap of WBG substrates (Yole Developpement 2016) [98].

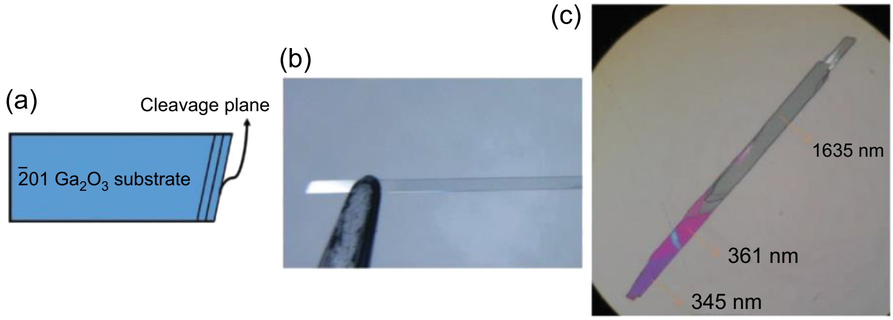

**Figure 14.24** Gallium oxide membrane fabrication and transferring. (a) Cross-section schematic showing the cleavage plane in the β-$Ga_2O_3$ substrate; (b) optical microscope images of the membrane extracted from the β-$Ga_2O_3$ substrate; (c) membrane transferred on to a Si wafer with the measured thickness of the membrane [18].

β-$Ga_2O_3$ thick crystalline layers (membranes) delaminated from their bulk crystal are also good for applications [18]. The membranes can be seen as a candidate for development of flexible high-performance electronic and optoelectronic devices. Transferring β-$Ga_2O_3$ membranes on to high-thermal-conductivity substrates could potentially circumvent the issue of poor thermal conductivity of bulk β-$Ga_2O_3$, which plagues the performance of gallium oxide power electronic devices (Fig. 14.24).

Mastro et al. recently formulated and listed the future needs and prospects of $Ga_2O_3$ [19]. The following directions for future research and development were outlined.

1. Better understanding of dopants and defects, lattice location of dopants, and native defects such as oxygen vacancies and their role in residual conductivity relative to extrinsic impurities such as hydrogen and silicon.
2. Continued development of high-quality bulk crystals of a large diameter.

3. Understanding the role of hydrogen in passivating/compensating acceptors or in enhancing incorporation of acceptors.
4. Establishing the sensitivity of $Ga_2O_3$ surfaces to adsorbed oxygen and water vapor.
5. Understanding radiation damage effects in β-$Ga_2O_3$ and related heterostructures.
6. Band offsets of candidate dielectrics for metal-oxide-semiconductor (MOS) devices, as well as process/patterning and contacting conditions.
7. Thermal management approaches for power devices.

This list can be extended. For example, linear defects in the $Ga_2O_3$ crystal structure require further in-depth study. Controllable n- and p-type doping to high levels ($>1 \times 10^{19}$ $cm^{-3}$) are essential for gallium oxide applications in high-voltage power electronics.

Breakthroughs in the aforementioned research topics will pave the way for the next generation of $Ga_2O_3$ semiconductor electronics.

# References

[1] A.B. Kehoe, D.O. Scanlon, G.W. Watson, Nature of the band gap of $Tl_2O_3$, Phys. Rev. B 83 (23) (2011) 233202.

[2] D. Mendeleev, The natural system of elements and its application to the indication of the properties of undiscovered elements, J. Russ. Chem. Soc. 3 (1871) 25−56.

[3] L. De Boisbaudran, On the chemical and spectroscopic characters of a new metal (gallium), Philos. Mag. J. Sci. 50 (1875) 414−416.

[4] S.I. Stepanov, et al., Gallium oxide: properties and applications − a review, Rev. Adv. Mater. Sci. 44 (1) (2016) 63−86.

[5] M. Marezio, J.P. Remeika, Bond lengths in the α-$Ga_2O_3$ structure and the high-pressure phase of $Ga_{2-x}$ $Fe_x$O3, J. Chem. Phys. 46 (5) (1967) 1862−1865.

[6] S. Yoshioka, et al., Structures and energetics of $Ga_2O_3$ polymorphs, J. Phys. Condens. Matter 19 (34) (2007) 346211.

[7] H. He, et al., First-principles study of the structural, electronic, and optical properties of $Ga_2O_3$ in its monoclinic and hexagonal phases, Phys. Rev. B 74 (2006) 195123.

[8] J.A. Kohn, G. Katz, J.D. Broder, Characterization of β-$Ga_2O_3$ and its alumina isomorph, θ-$Al_2O_3$, Am. Mineral. 42 (1956) 398−407.

[9] H. He, M.A. Blanco, R. Pandey, Electronic and thermodynamic properties of β-$Ga_2O_3$, Appl. Phys. Lett. 88 (26) (2006) 261904.

[10] J. Ahman, G. Svensson, J. Albertsson, A reinvestigation of [beta]-Gallium oxide, Acta Crystallogr. C C52 (1996) 1336−1338.

[11] M. Zinkevich, et al., Microstructural and thermodynamic study of γ-$Ga_2O_3$, Zeitschrift fuer Metallkunde/Mater. Res. Adv. Tech. 95 (9) (2004) 756.

[12] C.O. Arean, et al., Preparation and characterization of mesoporous γ-$Ga_2O_3$, Microporous Mesoporous Mater. 40 (1−3) (2000) 35−42.

[13] R. Roy, V.G. Hill, E.F. Osborn, Polymorphism of $Ga_2O_3$ and the system $Ga_2O_3$-$H_2O$, J. Am. Chem. Soc. 74 (3) (1952) 719−722.

[14] H.Y. Playford, et al., Structures of uncharacterised polymorphs of gallium oxide from total neutron diffraction, Chem. Eur. J. 19 (8) (2013) 2803−2813.

[15] I. Cora, et al., The real structure of ε-$Ga_2O_3$ and its relation to κ-phase, CrystEngComm 19 (2017) 1509−1516.

[16] S.-D. Lee, K. Akaiwa, S. Fujita, Thermal stability of single crystalline alpha gallium oxide films on sapphire substrates, Phys. Status Solidi C 10 (11) (2013) 1592−1595.

[17] R. Fornari, et al., Thermal stability of ε-$Ga_2O_3$ polymorph, Acta Mater. 140 (2017) 411−416.

[18] M. Kim, et al., Recent advances in free-standing single crystalline wide band-gap semiconductors and their applications: GaN, SiC, ZnO, β-$Ga_2O_3$, and diamond, J. Mater. Chem. C 5 (33) (2017) 8338−8354.

[19] M.A. Mastro, et al., Opportunities and future directions for $Ga_2O_3$, ECS J. Solid State Sci. Technol. 6 (5) (2017) P356−P359.

[20] Y. Yao, et al., Electrical behavior of β-$Ga_2O_3$ Schottky diodes with different Schottky metals, J. Vac. Sci. Technol. B Nanotechnol. Microelectron. Mater. Process. Meas. Phenom. 35 (3) (2017) 03D113.

[21] R. Suzuki, et al., Enhancement of responsivity in solar-blind β-$Ga_2O_3$ photodiodes with a Au Schottky contact fabricated on single crystal substrates by annealing, Appl. Phys. Lett. 94 (22) (2009) 222102.

[22] M. Mohamed, et al., Schottky barrier height of Au on the transparent semiconducting oxide β-$Ga_2O_3$, Appl. Phys. Lett. 101 (13) (2012) 132106.

[23] K. Irmscher, et al., Electrical properties of β-$Ga_2O_3$ single crystals grown by the Czochralski method, J. Appl. Phys. 110 (6) (2011) 063720.

[24] K. Sasaki, et al., $Ga_2O_3$ Schottky barrier diodes fabricated by using single-crystal β−$Ga_2O_3$ (010) substrates, IEEE Electron Device Lett. 34 (4) (2013) 493−495.

[25] Z. Zhang, et al., Deep level defects throughout the bandgap of (010) β-$Ga_2O_3$ detected by optically and thermally stimulated defect spectroscopy, Appl. Phys. Lett. 108 (5) (2016) 052105.

[26] S. Oh, G. Yang, J. Kim, Electrical characteristics of vertical Ni/β-$Ga_2O_3$ Schottky barrier diodes at high temperatures, ECS J. Solid State Sci. Technol. 6 (2) (2017) Q3022−Q3025.

[27] A. Jayawardena, A.C. Ahyi, S. Dhar, Analysis of temperature dependent forward characteristics of Ni/(-201) β-$Ga_2O_3$ Schottky diodes, Semicond. Sci. Technol. 31 (11) (2016) 115002.

[28] A.M. Armstrong, et al., Role of self-trapped holes in the photoconductive gain of β-gallium oxide Schottky diodes, J. Appl. Phys. 119 (10) (2016) 103102.

[29] Oishi, et al., High-mobility β-$Ga_2O_3$(-201) single crystals grown by edge-defined film-fed growth method and their Schottky barrier diodes with Ni contact, APEX 8 (3) (2015) 031101.

[30] T. Oishi, et al., Conduction mechanism in highly doped β-$Ga_2O_3$(-201) single crystals grown by edge-defined film-fed growth method and their Schottky barrier diodes, Jpn. J. Appl. Phys. 55 (3) (2016) 030305.

[31] D. Splith, et al., Determination of the mean and the homogeneous barrier height of Cu Schottky contacts on heteroepitaxial β-$Ga_2O_3$ thin films grown by pulsed laser deposition, Phys. Status Solidi A 211 (1) (2014) 40−47.

[32] M. Higashiwaki, et al., Temperature-dependent capacitance−voltage and current−voltage characteristics of Pt/Ga2O3 (001) Schottky barrier diodes fabricated on n—$Ga_2O_3$ drift layers grown by halide vapor phase epitaxy, Appl. Phys. Lett. 108 (13) (2016) 133503.

[33] K. Sasaki, et al., MBE grown $Ga_2O_3$ and its power device applications, J. Cryst. Growth 378 (2013) 591−595.

[34] K. Konishi, et al., 1-kV vertical Ga2O3 field-plated Schottky barrier diodes, Appl. Phys. Lett. 110 (10) (2017) 103506.

[35] K. Matsuzaki, et al., Growth, structure and carrier transport properties of $Ga_2O_3$ epitaxial film examined for transparent field-effect transistor, Thin Solid Films 496 (1) (2006) 37−41.

[36] M. Higashiwaki, et al., Gallium oxide ($Ga_2O_3$) metal-semiconductor field-effect transistors on single-crystal β-$Ga_2O_3$ (010) substrates, Appl. Phys. Lett. 100 (1) (2012) 013504.

[37] K.D. Chabak, et al., Enhancement-mode $Ga_2O_3$ wrap-gate fin field-effect transistors on native (100) β-$Ga_2O_3$ substrate with high breakdown voltage, Appl. Phys. Lett. 109 (21) (2016) 213501.

[38] N.A. Moser, et al., High pulsed current density b-$Ga_2O_3$ MOSFETs verified by an analytical model corrected for interface charge, Appl. Phys. Lett. 110 (14) (2017) 143505.

[39] Y. Kokubun, et al., Sol-gel prepared thin films for ultraviolet photodetectors, Appl. Phys. Lett. 90 (3) (2007) 031912.

[40] T.C. Wei, et al., See-through $Ga_2O_3$ solar-blind photodetectors for use in harsh environments, IEEE J. Sel. Top. Quant. Electron. 20 (6) (2014) 6809845.

[41] D. Patil-Chaudhari, et al., Solar blind photodetectors enabled by nanotextured β-$Ga_2O_3$ films grown via oxidation of GaAs substrates, IEEE Photonics J. 9 (2) (2017) 2300207.

[42] T. Oshima, et al., Vertical solar-blind deep-ultraviolet Schottky photodetectors based on β-$Ga_2O_3$ substrates, APEX 1 (1) (2008) 011202.

[43] W. Mu, et al., An extended application of β-Ga2O3 single crystals to the laser field: $Cr^{4+}$: β-$Ga_2O_3$ utilized as a new promising saturable absorber, R. Soc. Chem. 7 (2017) 21815−21819.

[44] K. Shimamura, et al., Epitaxial growth of GaN on (100) β-$Ga_2O_3$ substrates by metal-organic vapor phase epitaxy, Jpn. J. Appl. Phys. 44 (1) (2005) L7−L8.

[45] Z.L. Xie, et al., Demonstration of GaN/InGaN light emitting diodes on (100) β-$Ga_2O_3$ substrates by metalorganic chemical vapour deposition, Chin. Phys. Lett. 25 (6) (2008) 2185−2186.

[46] S. Ito, et al., Growth of GaN and AlGaN on (100) β-Ga2O3 substrates, Phys. Status Solidi C 9 (3−4) (2012) 519−522.

[47] M.M. Muhammed, et al., High optical and structural quality of GaN epilayers grown on (201) beta-$Ga_2O_3$, Appl. Phys. Lett. 105 (4) (2014) 042112.

[48] M.M. Muhammed, et al., High-quality III-nitride films on conductive, transparent (201)-oriented β-$Ga_2O_3$ using a GaN buffer layer, Sci. Rep. 6 (2016) 29747.

[49] E.G. Villora, et al., β-$Ga_2O_3$ and single-crystal phosphors for high-brightness white LEDs and LDs, and β-$Ga_2O_3$ potential for next generation of power devices, in: Proceedings of SPIE, vol. 8987, 2014, 89871U−12.

[50] E.G. Villora, et al., Molecular beam epitaxy of c-plane wurtzite GaN on nitridized a-plane β-$Ga_2O_3$, Thin Solid Films 500 (1−2) (2006) 209−213.

[51] E.G. Villora, et al., Epitaxial relationship between wurtzite GaN and β-$Ga_2O_3$, Appl. Phys. Lett. 90 (23) (2007) 234102.

[52] V.I. Nikolaev, et al., GaN growth on β-$Ga_2O_3$ substrates by HVPE, Mater. Phys. Mech. 22 (1) (2015) 59−63.

[53] K. Kachel, et al., A new approach to free-standing GaN using β-$Ga_2O_3$ as a substrate, CrystEngComm 14 (2012) 8536−8540.

[54] H.J. Lee, T.I. Shin, D.H. Yoon, Influence of NH3 gas for GaN epilayer on β-$Ga_2O_3$ substrate by nitridation, Surf. Coat. Technol. 202 (22−23) (2008) 5497−5500.

[55] W. Mu, et al., One-step exfoliation of ultra-smooth β-$Ga_2O_3$ wafers from bulk crystal for photodetectors, CrystEngComm 19 (2017) 5122−5127.

[56] X. Li, H. Zhu, Two-dimensional $MoS_2$: properties, preparation, and applications, J. Materiomics 1 (1) (2015) 33−44.

[57] J. Kim, Exfoliated b-$Ga_2O_3$ nano-belt field-effect transistors for air-stable high power and high temperature electronics, Phys. Chem. Chem. Phys. 18 (2016) 15760−15764.

[58] Q. He, et al., Schottky barrier diode based on β−$Ga_2O_3$ (100) single crystal substrate and its temperature-dependent electrical characteristics, Appl. Phys. Lett. 110 (9) (2017) 093503.

[59] W.S. Hwang, et al., High-voltage field effect transistors with wide-bandgap β-$Ga_2O_3$ nanomembranes, Appl. Phys. Lett. 104 (2014) 203111.

[60] H. Zhou, et al., High-performance depletion/enhancement-ode β-$Ga_2O_3$ on insulator (GOOI) field-effect transistors with record drain currents of 600/450 mA/mm, IEEE Electron Device Lett. 38 (1) (2017) 10−106.

[61] F. Aldinger, M. Zinkevich, Thermodynamic assessment of the gallium-oxygen system, J. Am. Ceram. Soc. 87 (4) (2004) 683−691.

[62] Y. Tomm, et al., Czochralski grown $Ga_2O_3$ crystals, J. Cryst. Growth 220 (4) (2000) 510−514.

[63] Z. Galazka, et al., Czochralski growth and characterization of β-$Ga_2O_3$ single crystals, Cryst. Res. Technol. 45 (12) (2010) 1229−1236.

[64] Z. Galazka, et al., Scaling-up of bulk β-$Ga_2O_3$ single crystals by the Czochralski method, ECS J. Solid State Sci. Technol. 6 (2) (2017) Q3007−Q3011.

[65] K. Hoshikawa, et al., Growth of β-$Ga_2O_3$ single crystals using vertical Bridgman method in ambient air, J. Cryst. Growth 447 (2016) 36−41.

[66] E. Ohba, et al., Defect characterization of β-$Ga_2O_3$ single crystals grown by vertical Bridgman method, Jpn. J. Appl. Phys. 55 (12) (2016) 1202BF.

[67] V.N. Maslov, et al., β-$Ga_2O_3$ crystal growing from its own melt, Tech. Phys. Lett. 40 (4) (2014) 303−305.

[68] J. Zhang, et al., Growth and spectral characterization of β-$Ga_2O_3$ single crystals, J. Phys. Chem. Solids 67 (12) (2006) 2448−2451.

[69] E.G. Villora, et al., Large-size β-$Ga_2O_3$ single crystals and wafers, J. Cryst. Growth 270 (3−4) (2004) 420−426.

[70] Y. Tomm, et al., Floating zone growth of b-$Ga_2O_3$: a new window material for optoelectronic device applications, Sol. Energy Mater. Sol. Cells 66 (1−4) (2001) 369−374.

[71] N. Suzuki, et al., Fabrication and characterization of transparent conductive Sn-doped β-$Ga_2O_3$ single crystal, Phys. Status Solidi C 4 (7) (2007) 2310−2313.

[72] N. Ueda, et al., Synthesis and control of conductivity of ultraviolet transmitting β-$Ga_2O_3$ single crystals, Appl. Phys. Lett. 70 (26) (1997) 3561.

[73] S. Ohira, et al., Characterization of transparent and conducting Sn-doped β-$Ga_2O_3$ single crystal after annealing, Thin Solid Films 516 (17) (2008) 5763−5767.

[74] H.A. Dabkowska, A.B. Dabkowski, Crystal growth of oxides by optical floating zone technique, in: G. Dhanaraj, K. Byrappa, V. Prasad, M. Dudley (Eds.), Springer Handbook of Crystal Growth, Springer, Berlin, Heidelberg, 2010, pp. 367−391.

[75] A. Chase, Growth of β-$Ga_2O_3$ by the Verneuil technique, J. Am. Chem. Soc. 47 (9) (1964) 470.

[76] M.R. Lorenz, J.F. Woods, R.J. Gambino, Some electrical properties of the semiconductor β-$Ga_2O_3$, J. Phys. Chem. Solids 28 (3) (1967) 403−404.

[77] A.V. Stepanov, New method of producing articles (sheets, tubes, rods, various sections, etc) directly from liquid metal, Sov. Phys. Tech. Phys. 4 (1959) 339−348.

[78] H.E. LaBelle, Growth of controlled profile crystals from the melt: Part II - edge-defined, film-fed growth (EFG), Mater. Res. Bull. 6 (7) (1971) 581−591.

[79] A. Kuramata, et al., High-quality β-$Ga_2O_3$ single crystals grown by edge-defined film-fed growth, Jpn. J. Appl. Phys. 55 (12) (2016) 1202A2.
[80] Z. JunGang, et al., Single crystal β-$Ga_2O_3$: Cr grown by floating zone technique and its optical properties, Sci. China E Technol. Sci. 50 (1) (2007) 1−6.
[81] http://www.tamura-ss.co.jp/en/products/gao/index.html.
[82] H. Aida, et al., Growth of β-$Ga_2O_3$ single crystals by the edge-defined, film fed growth method, Jpn. J. Appl. Phys. 47 (11) (2008) 8506−8509.
[83] T. Tanaka, K. Hoshikawa, Columnar-shaped β-$Ga_2O_3$ crystal growth by edge-defined, film-fed growth technique, in: IWGO 2017 International Workshop on Gallium Oxide and Related Materials, 2017, p. 62. Programme and Abstracts.
[84] K. Hoshikawa, T. Fukuda, H. Machida, Growth of $TiO_2$ single crystals using the edge-defined, film-fed growth technique, J. Cryst. Growth 137 (1994) 516−520.
[85] Ga2O3-Based Single Crystal Substrate Document Type and Number: United States. Patent Application 20170233892 Kind Code: A1.
[86] Z. Galazka, et al., On the bulk β-$Ga_2O_3$ single crystals grown by the Czochralski method, J. Cryst. Growth 404 (2014) 184−191.
[87] J.B. Varley, et al., Oxygen vacancies and donor impurities in β-$Ga_2O_3$, Appl. Phys. Lett. 97 (14) (2010) 142106.
[88] E.G. Villora, et al., Electrical conductivity and carrier concentration control in β-$Ga_2O_3$, Appl. Phys. Lett. 92 (20) (2008) 202120.
[89] T. Onuma, et al., Correlation between blue luminescence intensity and resistivity in β-$Ga_2O_3$ single crystals, Appl. Phys. Lett. 103 (2013) 041910.
[90] L.L. Liu, et al., Fabrication and characteristics of N-doped β-$Ga_2O_3$ nanowires, Appl. Phys. A 98 (4) (2010) 831−835.
[91] L. Zhang, et al., First-principles study on electronic structure and optical properties of N-doped P-type β-$Ga_2O_3$, Sci. China Phys. Mech. Astron. 55 (1) (2012) 19−24.
[92] J.B. Varley, et al., Role of self-trapping in luminescence and p-type conductivity of wide-band-gap oxides, Phys. Rev. B 85 (2012) 081109.
[93] H. Kawazoe, et al., Transparent p-type conducting oxides: design and fabrication of pn heterojunctions, MRS Bull. 25 (8) (2000) 28−36.
[94] T. Oshima, et al., Wet etching of β-$Ga_2O_3$ substrates, Jpn. J. Appl. Phys. 48 (4) (2009) 040208.
[95] K. Nakai, et al., Characterization of defects in β-$Ga_2O_3$ single crystal, Jpn. J. Appl. Phys. 54 (5) (2015) 051103.
[96] A.V. Kremleva, et al., Defects in thin epitaxial layers of $(AlxGa1\text{-}x)_2O_3$ grown on $Al_2O_3$ substrates, Mater. Phys. Mech. 32 (2) (2017) 178−185.
[97] M. Higashiwaki, et al., Recent progress in $Ga_2O_3$ power devices, Semicond. Sci. Technol. 31 (3) (2016) 034001.
[98] http://www.yole.fr/iso_upload/News/2016/PR_WBG_AlternativeTechnologies_YOLE_Jan2016.pdf.

This page intentionally left blank

# Indium oxide: $In_2O_3$

# 15

*Takahiro Nagata*
National Institute for Materials Science, Tsukuba, Japan

## 15.1 Introduction

The transparent semiconducting oxide (TSO) indium oxide ($In_2O_3$) is a wide-bandgap semiconducting material with a direct bandgap around 2.8−2.9 eV [1,2], although a recent study suggests a slightly indirect bandgap [3]. $In_2O_3$-based oxides are already used as transparent conducting oxides (TCOs). High tin (Sn)-doped $In_2O_3$ (ITO) shows a high electrical conductivity with transparency in the visible range. ITO films on glass can be easily fabricated at relatively low temperatures compared to other oxides such as $SnO_2$ or ZnO. ITO is drawing attention and has been widely used as transparent electrodes for flat-panel displays and solar cells. The current research in TCOs seeks superior properties of low resistivity and high mobility [4−7]. Consumer demand for enlarged display size and/or tandem-structure photovoltaics with sensitivity in a wide range of spectral regions of the sun is strongly accelerating this search.

In contrast to TCOs, unintentionally doped $In_2O_3$ has a gas-sensing ability due to a surface electron accumulation layer (SEAL) [8], but for applications such as Schottky diodes and field-effect transistors (FETs) the SEAL should be controlled. Some groups report the removal of the SEAL by an O-plasma or O-rich sputtering atmosphere [9−11]. The SEAL is observed not only in $In_2O_3$ but also in other wide-bandgap semiconducting oxides such as $SnO_2$ [12] and ZnO [13]. Many efforts have been undertaken to remove the SEAL from binary semiconductors such as ZnO, InN, and InAs by chemical and/or physical surface treatments [14,15], and the origins of the SEAL have been proposed to be metal adatoms, surface oxygen vacancies, and adsorbates [16,17].

Relating to the control of vacancies, electrical properties including the polarity of n-type or p-type conductivity and carrier density are investigated for various applications such as transparent transistors [18,19], optoelectronic devices [20,21], and spin-electronic devices [22]. For example, the FET requires a channel with high mobility and moderate carrier concentration, a Schottky contact or gate insulator as control gate, and low resistance source and drain regions.

For electronic device applications, most $In_2O_3$ films were grown on glass at low temperature with a polycrystalline and/or amorphous crystalline structure. However, to understand the potential and functions of the material, single crystals or epilayers are the model systems. This chapter focuses on $In_2O_3$ single crystalline, high-quality, thin film material only.

**Single Crystals of Electronic Materials.** https://doi.org/10.1016/B978-0-08-102096-8.00015-X
Copyright © 2019 Elsevier Ltd. All rights reserved.

# 15.2 Crystal growth

## 15.2.1 Thermodynamic properties and definition of usable growth methods

$In_2O_3$ is less stable than other wide bandgap oxides, such as ZnO and $Ga_2O_3$. Indium has long been known to form two oxides, $In_2O_3$ and $In_2O$ [23]; $In_2O$ is a gaseous oxide. Burns et al. investigated the vaporization of $In_2O_3$ by mass spectrometric study [24], suggesting that $In_2O \rightarrow In^+ + InO + e$ is energetically more favorable. In contrast, $In_2O_3$ (solid) → $In_2O_3$ (gas) would be independent of the partial oxygen pressure in the carrier gas, with the pressure measured by the transport method. Valderrama reported that In and $In_2O$ are the important species in the vapor phase, rather than the $In + In_2O_3$ mixture. The vapor pressure of $In_2O$ corresponds to the reaction $4In + In_2O_3 \rightarrow 3In_2O$ in the temperature range of 600−950°C [25]. This was confirmed by Nicholas, suggesting that no identification of the solid $In_2O$ and In-rich condition is easily from the oxygen vacancies in $In_2O_3$ [26].

In contrast, $In_2O_3$ has polymorph phases, a bixbyite-type structure, body-centered cubic (bcc-, space group $Ia\overline{3}$) shape with lattice parameter of $a = 10.117$ Å, and a corundum-type, rhombohedral (rh-, space group $R\overline{3}c$) polymorph with lattice parameters $a = 5.487$ Å, $c = 14.510$ Å structure [27−29], as shown in Fig. 15.1. The trivalent rare-earth sesquioxides tend to crystallize in the bcc-structure, and the transition metal sesquioxides assume the rh-structure. For $In_2O_3$, the structural relations between bixbyite and corundum have attracted significant attention. The high-pressure, high-temperature synthesis of corundum-type $In_2O_3$ was reported in the 1960s [30−32], meaning that corundum-type $In_2O_3$ is a metastable phase. Under normal conditions $In_2O_3$ crystallizes in a bixbyite-type structure.

In even the most stable bixbyite-type structure, $In_2O_3$ is less stable than other wide-bandgap oxides for single crystal growth. When dealing with the single crystal growth of metal oxides, the decomposition of both the melt and the crystalline phase should be suppressed at temperatures close to the melting point. However, the chemical instability of $In_2O_3$ causes decomposition and massive evaporation at elevated temperatures much below melting point. To understand these evaporation conditions, Galazka et al. reported thermodynamic calculations using Fact Sage software [33], as shown in Fig. 15.2 [34].

The reactions are set as follows:

$$In_2O_3(s) \leftrightarrows 2In(s, liq, g) + \frac{3}{2}O_2(g) \quad K_{eq}(MP) \approx 10^{-6}$$

$$In_2O_3(s) \leftrightarrows InO(g) + In(s, liq, g) + O_2(g) \quad K_{eq}(MP) \approx 10^{-12}$$

$$In(s, liq) \leftrightarrows In(g) \quad K_{eq}(MP) \approx 10^{0}$$

where (s) stands for solid, (liq) for liquid, (g) for gas, $K_{eq}$ for equilibrium constant, and MP for melting point. The results indicate that the decomposition of $In_2O_3$ will occur upon heating up, and the most volatile species will be In and $O_2$. To reduce $In_2O_3$

Bixbyite-type body centered cubic: $Ia\bar{3}$

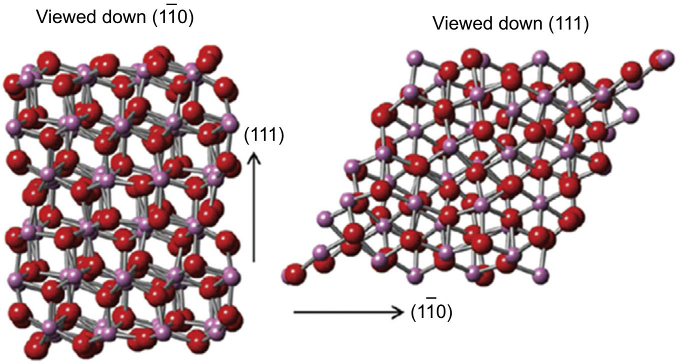

Corundum-type (rhombohedra: $R\bar{3}c$)

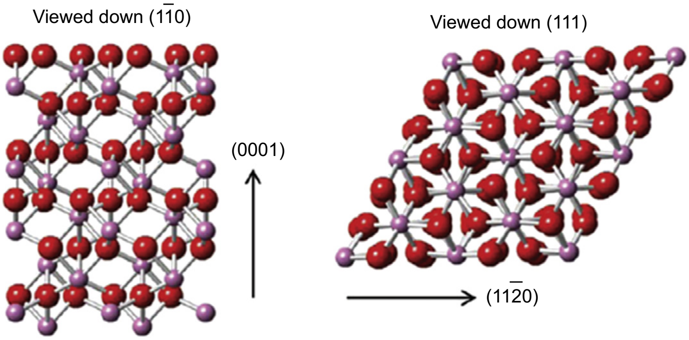

**Figure 15.1** Ball-and-stick representations of crystal structures of bcc-$In_2O_3$ (upper panels) and rh-$In_2O_3$ (lower panels). In atoms are pink and O atoms are dark red. The viewing directions and the in-plane orientation are indicated in the figure.
Reprinted with permission from K.H.L. Zhang, V.K. Lazarov, P.L. Galindo, F.E. Oropeza, D.J. Payne, H.H.-C.Lai, R.G. Egdell, Domain matching epitaxial growth of $In_2O_3$ thin films on α-$Al_2O_3$(0001), Cryst. Growth Des. 12 (2012) 1000−1007. Copyright (2012) by the American Chemical Society.

decomposition, high oxygen partial pressure is effective; this is achieved by changing the oxygen partial pressures provided by two different oxygen sources, ($O_2$ + Ar) and $CO_2$. $CO_2$ dynamically releases oxygen with increasing temperature, so oxygen partial pressure can be achieved by employing $CO_2$ at pressures above 100 bars. Nevertheless, even such high oxygen partial pressure is not sufficient to minimize $In_2O_3$ decomposition to the level needed for carrying out the typical Czochralski method and perhaps all other standard melt growth techniques.

### 15.2.2 Bulk single crystal growth

The thermodynamic calculations revealed that with conventional standard melt growth it is hard to obtain bulk single crystal $In_2O_3$. In contrast, for β-$Ga_2O_3$ three different

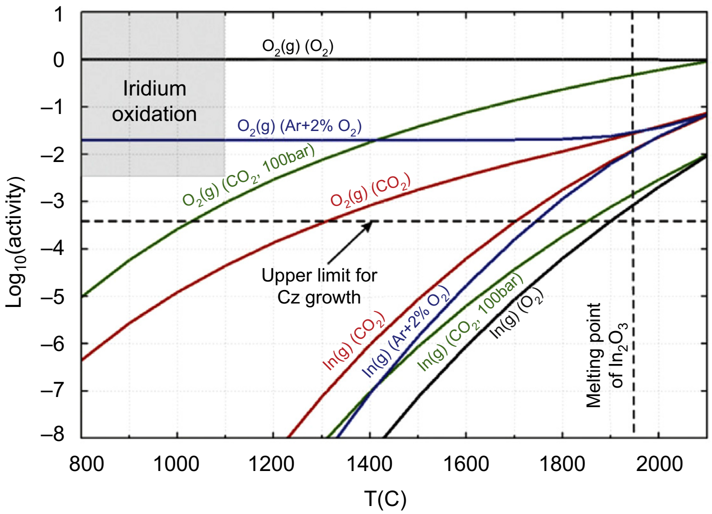

**Figure 15.2** Partial pressure of the most volatile component (In) during $In_2O_3$ decomposition versus oxygen partial pressure provided by two different oxygen sources, (Ar + $O_2$) and $CO_2$. Reprinted with permission from Z. Galazka, R. Uecker, K. Irmscher, D. Schulz, D. Klimm, M. Albrecht, M. Pietsch, S. Ganschow, A. Kwasniewski, R. Fornari, Melt growth, characterization and properties of bulk $In_2O_3$ single crystals, J. Cryst. Growth 362 (2013) 349−352. Copyright (2011) by Elsevier.

melt growth techniques can be used: Verneuil [35−37], optical floating zone [38−40], and the Czochralski method [41,42]. Instead of a melt growth technique, in early years the chemical vapor transport (CVT) method ([43,44]) was used for $In_2O_3$ bulk single crystals [45,46]. The advantage of CVT is the low growth temperature, below the melting temperature. Instead of vaporizing a solid directly at high temperatures, highly volatile chemicals are vaporized at much lower temperatures and react back the resulting gas mixture at a different temperature using the temperature dependence of the chamber. The reactions are easy to calculate by thermodynamic considerations. Scherer used pure powder of $In_2O_3$ and iodine and sulfur as the transport agents [47]. The chemical reaction is as follows:

$$2In_2O_3(s)+3I_2(s)+3S(s) \leftrightarrows 3InI(g)+InI_3(g)+3SO_2(g),$$

where (s) and (g) denote solid and gaseous, respectively. The forward reaction describes the formation of the constituents to the transport medium, and the backward reaction describes its decomposition into $In_2O_3$ single crystals and transport gases. By this technique, growth of $In_2O_3$ crystals with a typical size of $3 \times 3 \times 1\ mm^3$ has been demonstrated, as shown in Fig. 15.3(a) [48].

To obtain larger $In_2O_3$ crystals than those grown by CVT, Galazka et al. applied a new melt growth technique, levitation-assisted self-seeding crystal growth method (LASSCGM), to $In_2O_3$ [49]. LASSCGM involves electromagnetic levitation, which uses a radiofrequency coil surrounding a metal crucible. There are an oxide melt

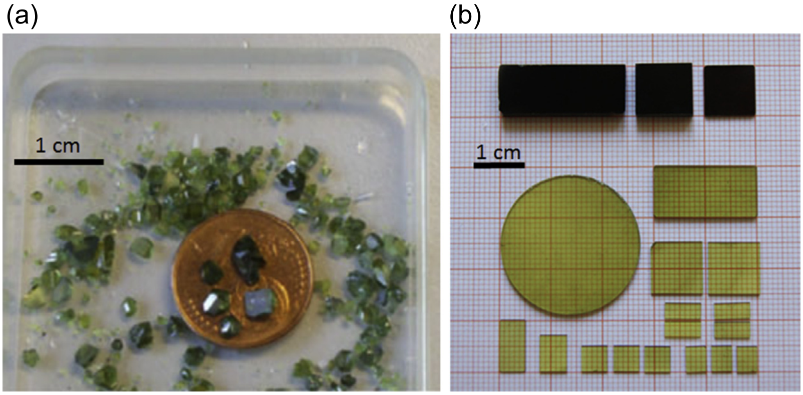

**Figure 15.3** Photograph of $In_2O_3$ bulk single crystal grown from (a) CVT and (b) melt (upper: as grown; bottom: annealed).
(a) Reprinted from D. Braun, V. Scherer, C. Janowitz, Z. Galazka, R. Fornari, R. Manzke, In-gap states of $In_2O_3$ single crystals investigated by scanning tunneling spectroscopy, Phys. Status Solidi A (2013) 1–7, copyright (2013), with permission from WILEY-VCH. (b) Reprinted from Z. Galazka, R. Uecker, K. Irmscher, D. Schulz, D. Klimm, M. Albrecht, M. Pietsch, S. Ganschow, A. Kwasniewski, R. Fornari, Melt growth, characterization and properties of bulk $In_2O_3$ single crystals, J. Cryst. Growth 362 (2013) 349–352, copyright (2011), with permission from Elsevier.

and a self-created seed inside the crucible. The levitation has two functions: it drags the melt away from the hottest region, where there is the highest probability of eutectic formation with the metal crucible, and it forms the thin seed necessary to obtain a single crystal. To function, the metal excess must be sufficient to turn the insulating charge into a conductive charge and speed up the melting via direct coupling of the charge material with the electromagnetic field generated by the radio frequency coil. When approaching the melting point, which is about 1950°C, the decomposition rate of $In_2O_3$ increases, inducing the In-rich conditions which enhance conduction. To keep these conditions, oxygen concentration is limited. Based on the thermodynamic calculation, $CO_2$ was used as an oxygen source to grow $In_2O_3$, and oxygen concentration was controlled at the level of several percentage points, typically 2%–6%. Growth of larger $In_2O_3$ crystals has been achieved, as shown in Fig. 15.3(b) [34]. The full width at half maximum value of the X-ray diffraction rocking curve of 222 peak on the (111) face of the $In_2O_3$ crystal was measured to be as low as 28 arcsec. As-grown crystals showed dark coloration with typical free electron concentrations of $1.8–3.1 \times 10^{18}$ $cm^{-3}$, and free electron mobility ranging from 135 to 170 $cm^2/Vs$. After annealing in a nonreducing atmosphere (neutral and oxidizing) for 5–120 h at temperatures between 700 and 1400°C, the electron concentrations were decreased by one order of magnitude. Typical free electron concentrations and free electron mobility were of $1.3–3.6 \times 10^{17}$ $cm^{-3}$ and 130–180 $cm^2/Vs$, respectively. The transmission electron microscope (TEM) observation on the (111) melt-grown $In_2O_3$ crystal revealed a defect-free and high-perfection crystal structure, as shown in Fig. 15.4(a). On this (111) melt-grown $In_2O_3$ crystal, Sadofev demonstrated the epitaxial growth of

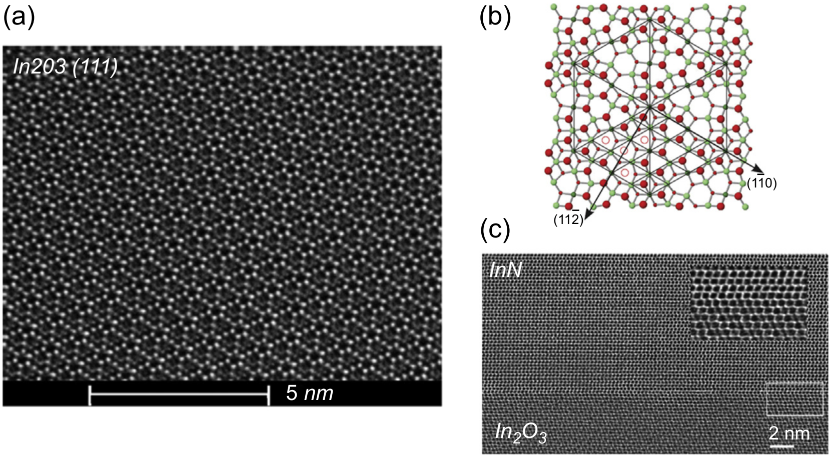

**Figure 15.4** (a) High-resolution (HR) TEM image of a melt-grown bulk $In_2O_3$ single crystal. (b) Top view of the (111) surface formed by a stoichiometric trilayer. *Thin solid lines* illustrate the 4:1 coincidence lattice of InN (0001) relative to $In_2O_3$ (111). (c) HR TEM image of the interface between InN and $In_2O_3$ substrates taken along the [11−20] direction of InN. The inset is a magnification of the image showing the regular structure of the interface.
(a) Reprinted from Z. Galazka, R. Uecker, K. Irmscher, D. Schulz, D. Klimm, M. Albrecht, M. Pietsch, S. Ganschow, A. Kwasniewski, R. Fornari, Melt growth, characterization and properties of bulk $In_2O_3$ single crystals, J. Cryst. Growth 362 (2013) 349−352, copyright (2013), with permission from Elsevier. (b) and (c) Reprinted from S. Sadofev, Y.J. Cho, O. Brandt, M. Ramsteiner, R. Calarco, H. Riechert, S.C. Erwin, Z. Galazka, M. Korytov, M. Albrecht, R. Uecker, R. Fornari, Growth of wurtzite InN on bulk $In_2O_3$(111) wafers, Appl. Phys. Lett. 101 (2012) 172102, copyright (2012), with permission from American Institute of Physics.

single-phase InN by plasma-assisted molecular beam epitaxy [50]. The InN/$In_2O_3$ orientation relationship was confirmed to be (0001) || (111) and [1100] || [112] with an effective mismatch of about 1%, as shown in Fig. 15.4(b). A cross-sectional TEM image indicated the smooth interface (Fig. 15.4(c)), suggesting that $In_2O_3$ has the potential to be a substrate for the growth of InN.

### 15.2.3 Epitaxial thin film growth

For practical electronic device applications, thin film technology is also important. Most undoped and doped $In_2O_3$ are grown in the form of amorphous or polycrystalline thin films or layers by techniques such as spray pyrolysis [51] and hydrolysis [52], sol−gel [53], sputtering [54], electron beam evaporation [55], pulsed laser deposition [56,57], molecular beam epitaxy (MBE) [18,58], metal organic chemical vapor deposition [59,60], and so on. While traditional applications such as TCOs and gas sensors can work with a low material quality, to move to advanced electronic devices such as a channel layer in the transistor, higher-mobility TCOs, high-material quality is mandatory in the film form. To this end, recent efforts on thin film growth by plasma-assisted MBE yielded high-quality material that allows the study of the intrinsic material physics [61,62].

An advantage of heteroepitaxial growth of $In_2O_3$ is controllability of crystal structure. During epitaxy a crystalline film is aligned to a crystalline substrate. On the cubic substrates, such as InAs, MgO, or $ZrO_2$:Y (YSZ), cubic $In_2O_3$ grows in a trivial cube-on-cube way. Cubic Y-stabilized $ZrO_2$ (YSZ) adopts the parent fluorite structure and provides an ideal substrate for growth of high-quality thin films of bcc-$In_2O_3$ due to a small mismatch of only 1.7%. $In_2O_3$ thin films with the highest reported electron mobilities of 226 $cm^2/Vs$ at room temperature and over 1200 $cm^2/Vs$ at 100 K have recently been grown on YSZ substrate by Bierwagen and Speck using oxygen plasma-assisted MBE [63]. In contrast, $\alpha$-$Al_2O_3$ (sapphire) has a rhombohedral crystal structure (space group $R\bar{a}c$) with lattice parameters $a = b = 4.759$ Å and $c = 12.991$ Å [64]. This material is widely used for epitaxial growth of ZnO and GaN [65,66], has an unusual epitaxial relationship with cubic $In_2O_3$, and forms rhombohedral epitaxial $In_2O_3$ films. However, be impeded by the large lattice mismatch (above 11%). Cubic $In_2O_3$ films could form on the $\alpha$-$Al_2O_3$ with a nontrivial epitaxial relation and domain structure. Vogt demonstrated the epitaxial growth of phase-pure cubic $In_2O_3$ (110) on r-plane sapphire ($01\bar{1}2$), and achieved a high concentration of Sn or Mg doping of over $10^{20}$ $cm^{-3}$ [67]. Zhang demonstrated the growth of phase-pure cubic $In_2O_3$ (111) with rotational domains on rhombohedral a-$Al_2O_3$ (0001) [29,61], and a mixture of cubic $In_2O_3$ (111) and rhombohedral $In_2O_3$ (00.01) on $\alpha$-$Al_2O_3$ (0001) (Fig. 15.5(a) and (b)). By combining a high-temperature nucleation layer and evolutionary structural selection of the rhombohedral phase during the growth process, Wang realized phase-pure rhombohedral $In_2O_3$ (0001) on $\alpha$-$Al_2O_3$ (0001) (Fig. 15.5(c)-(e)) [68]. Suzuki also demonstrated the growth of rhombohedral $In_2O_3$ on $\alpha$-$Al_2O_3$ by inserting an $\alpha$-$Fe_2O_3$ buffer layer, which has an intermediate lattice constant ($a = 5.0351$ Å [32]), between rhombohedral $In_2O_3$ and $\alpha$-$Al_2O_3$ [69]. Different crystal phases and their epitaxial relationship to the substrate lead to different crystal properties like electronic or heat transport properties.

## 15.3 Tailoring of crystal properties

### 15.3.1 Surface structure and accumulation layer

Using CVT-, melt-, and MBE-grown $In_2O_3$ crystals, several groups report the fundamental properties of $In_2O_3$. Braun et al. measured in-gap defect states of the cleaved {111} surface of $In_2O_3$ single crystals by scanning tunneling spectroscopy (STS) in the fundamental bandgap, as shown in Fig. 15.6 [48]. The crystal showed the clear dependence of the specific resistivity on the annealing time, suggesting the influence of oxygen treatment. Furthermore, besides the conduction band minimum (CBM) and the valence band maximum (VBM), gap states have been determined with high accuracy in the fundamental bandgap of $In_2O_3$ in the local density of states (LDOS) spectra by STS. Oxygen vacancies are major defects of $In_2O_3$, and defects of minor importance due to oxygen and indium atoms on interstitial lattice sites are identified by combining the density functional theory (DFT) calculations [70]. The defect states at approximately $-1$ and $-1.6$ eV are caused by oxygen vacancies ($V_O$s) and doubly occupied oxygen vacancies. The peak at $-1.78$ eV matches a defect level caused by

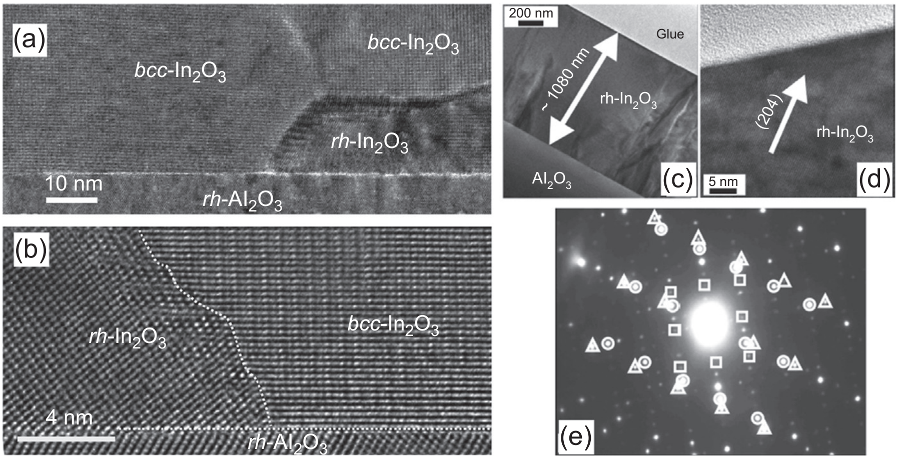

**Figure 15.5** (a) Large area TEM image of $In_2O_3$ layer on $Al_2O_3$ (0001). Rh-$In_2O_3$ inclusion close to the interface is surrounded by bcc-$In_2O_3$. (b) Expanded HR image shows contrasting structures of rh- and bcc- phases of $In_2O_3$. (c) Cross-sectional TEM image shows $In_2O_3/Al_2O_3$ interface. (d) HRTEM micrograph presents the rh-$In_2O_3$ structure near the surface area. (e) Selected area electron diffraction (SAED) pattern of $In_2O_3/Al_2O_3$ interface (*triangles*: $Al_2O_3$, *circles*: bcc-$In_2O_3$, and *squares*: rh-$In_2O_3$).
(a) and (b) Reprinted from K.H.L. Zhang, V.K. Lazarov, P.L. Galindo, F.E. Oropeza, D.J. Payne, H.H.-C. Lai, R.G. Egdell, Domain matching epitaxial growth of $In_2O_3$ thin films on α-$Al_2O_3$(0001), Cryst. Growth Des. 12 (2012) 1000−1007, copyright (2012), with permission from American Chemical Society. (c) and (d) Reprinted from C.Y. Wang, Y. Dai, J. Pezoldt, B. Lu, T. Kups, V. Cimalla, O. Ambacher, Phase stabilization and phonon properties of single crystalline rhombohedral indium oxide, Cryst. Growth Des. 8 (2008) 1257−1260, copyright (2008), with permission from American Chemical Society.

$V_O$s of lower occupation number. The gap state at −2.37 eV and that around −1.45 eV are probably caused by oxygen on interstitial sites. The states at −2.11 and −1.58 eV could be formed by indium atoms on interstitial sites. The shoulder peaks at approximately −0.01 and −2.78 eV correspond to the CBM and VBM, respectively. The fundamental bandgap of $In_2O_3$ from the LDOS spectra was determined as 2.78 ± 0.04 eV, which is consistent with the reported bandgap of CVT-grown $In_2O_3$ crystals obtained by high-resolution angular resolved photoelectron spectroscopy [47].

As mentioned in the introduction, for $In_2O_3$ the surface accumulation layer is a crucial issue, and may relate to the surface structure and defects. Nagata et al. reported the band diagrams of melt-grown $In_2O_3$ single crystals estimated from the results of surface-sensitive conventional soft X-ray photoelectron spectroscopy (SXPES: $h\nu = 1486.6$ eV) and bulk-sensitive hard X-ray photoelectron spectroscopy (HAXPES; $h\nu = 5.95$ keV) by combining the simulation of Poisson−Schrödinger solutions, as shown in Fig. 15.7(a) [71]. Within 5 nm of the surface there is a strong downward bending of the bands due to SEAL. At the surface the Fermi level is pinned strongly above the CBM by approximately 1.0 eV regardless of the oxygen annealing

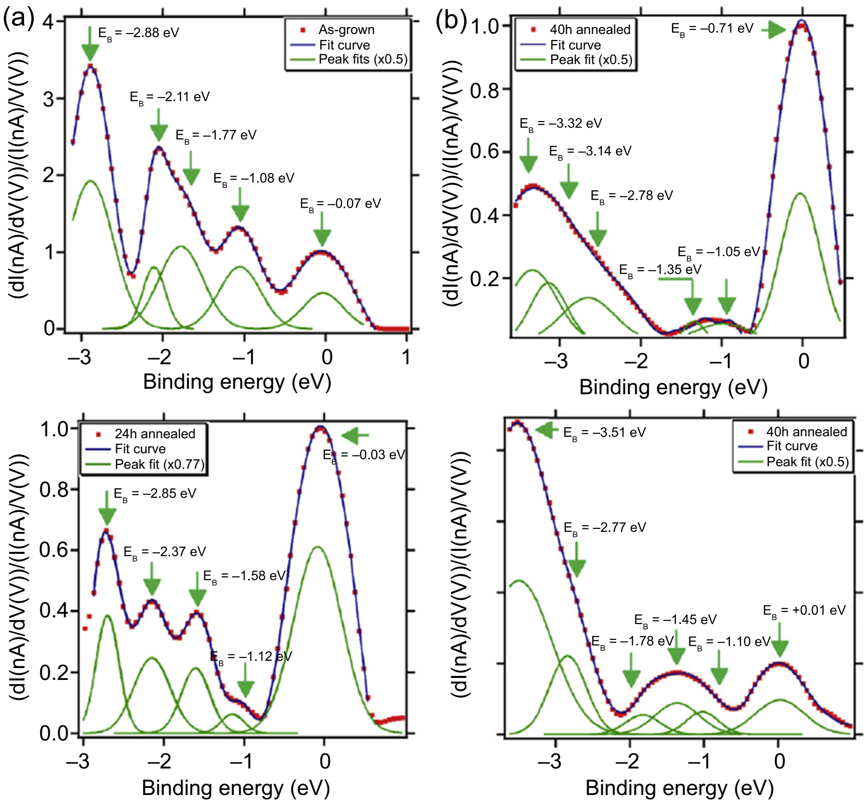

**Figure 15.6** (a) LDOS spectra against binding energy measured on as-grown CVT $In_2O_3$ crystals (top) and those annealed for 24 h in an oxygen flue (bottom) by means of STS. The binding energies of the LDOS maxima have been derived from a least-squares fit (*blue line*) by Gaussians (*green lines*) to the experimental curve (*red points*). (b) LDOS spectra against binding energy measured on $In_2O_3$ crystals grown from the melt. The STS spectra of two different charges are shown, but both have been annealed for 40 h in air. The binding energies of the LDOS maxima have been derived from a least-squares fit (*blue line*) by Gaussians (*green lines*) to the experimental curve (*red points*).
Reprinted with permission from D. Braun, V. Scherer, C. Janowitz, Z. Galazka, R. Fornari, R. Manzke, In-gap states of $In_2O_3$ single crystals investigated by scanning tunneling spectroscopy, Phys. Status Solidi A (2013) 1—7. Copyright (2013), with permission from WILEY-VCH.

conditions. At the Fermi level ($E_F$: binding energy = 0 eV) a weak but well-defined feature associated with conduction band states was observed, as shown in Fig. 15.7(b). Conduction band states originate from the electrons in the conduction band below the Fermi level, which is the region below 4 nm. In-gap states attributed to $V_O$s were observed as similar to the STS results. The bonding states relating to the $V_O$ were also confirmed at the In 3d and O 1s core spectra. However, Scherer et al. observed the absence of SEAL at the surface of the same melt-grown $In_2O_3$ (111) single crystal, cleaved and investigated in an ultrahigh vacuum condition

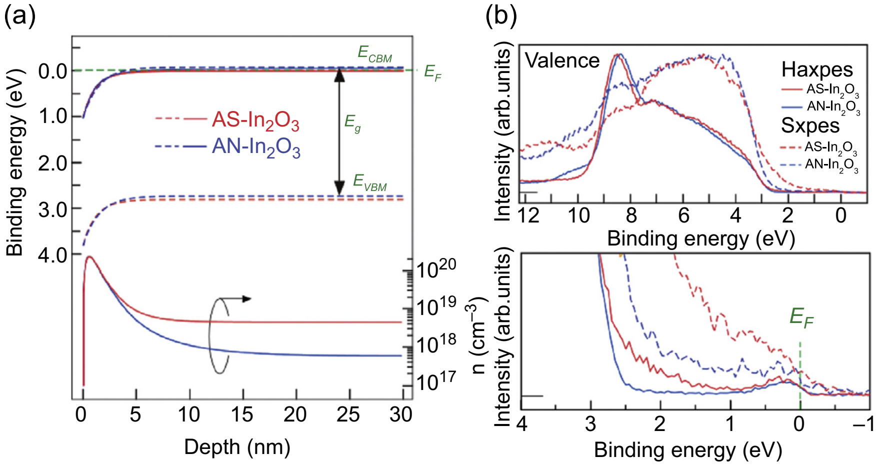

**Figure 15.7** (a) The dashed lines at the top show a schematic illustration of band diagrams from the surface (left) to the bulk (right) estimated by SXPES and HAXPES. $E_F$: Fermi level, $E_{CBM}$: conduction band minimum, $E_{VBM}$: VBM, and $E_g$: bandgap. The *solid lines* on the top and bottom sides show the diagram of the conduction band and the electron-concentration profile calculated using Poisson−Schrödinger solutions, respectively. (b) Valence band spectra for as grown (AS-) and annealed (AN-) $In_2O_3$ measured by HAXPES (*solid lines*) and SXPES (*dashed lines*). The Fermi level corresponds to 0 eV. The bottom panel is the magnified valence band spectra near $E_F$.

Reprinted with permission from T. Nagata, O. Bierwagen, Z. Galazka, M. Imura, S. Ueda, H. Yoshikawa, Y. Yamashita, T. Chikyow, Photoelectron spectroscopic study of electronic state and surface structure of $In_2O_3$ single crystals, Appl. Phys. Express 10 (2017) 011102. Copyright (2017) by the Japan Society of Applied Physics.

($\sim 10^{-9}$ Pa) [72]. Furthermore, in the film SEAL was observed regardless of the crystal orientation [2,11]. Considering both Scherer et al.'s result and HAXPES results, surface structure and adsorption should contribute to form the SEAL. Bierwagen demonstrated SEAL removal by an oxygen plasma treatment, and confirmed an electron depletion at the surface, the absence of the conduction band peak at the Fermi level, and a Schottky contact on an n-type semiconductor [63].

### *15.3.2 Optical properties*

There is still ambiguity in quantitative understanding of the fundamental optical absorption of $In_2O_3$. Many studies of optical absorption indicate an optical gap of about 3.5−3.8 eV [55,73,74]. Matino et al. showed a direct bandgap of 3.5 ± 0.1 eV and an indirect bandgap of 2.1 ± 0.2 eV of ITO by in-situ room temperature scanning tunneling microscopy observation after an annealing process in ultrahigh vacuum [75]. These results were based on an investigation of thin polycrystalline films. Irmscher pointed out that the steep increase of the absorption coefficient to above $10^5$ $cm^{-1}$ limits the ultraviolet transparency for wavelengths below 335 nm of even very thin (<<1 μm) $In_2O_3$ films. The shift of this absorption edge to higher energies with increased tin doping (up to $10^{21}$ $cm^{-3}$), which is applied to obtain high n-type conductivity of the layers, can be explained by the Burstein−Moss effect [3]. Weiher and Ley reported the onset of optical absorption at about 2.6 eV of a single crystalline sample grown from the vapor phase, in addition to the absorption at about 3.7 eV [77]. They suggested that for the indirect band structure, the CBM was at the Γ point of the Brillouin zone and the VBM was away from the Γ point by approximately 1 eV. The absorption edge at 3.7 eV and absorption onset at 2.6 eV were assigned as direct (allowed) transitions at the Γ point and indirect (forbidden) transitions between the VBM and the CBM, respectively. For melt-grown $In_2O_3$, Irmscher demonstrated the temperature dependence of optical absorption, and confirmed that the absorption onset at about 2.7 eV corresponded to intrinsic nature, as shown in Fig 15.8(a) [3,28,77]. This lowest-energy bandgap allows us to maintain high transparency at room temperature. The lowest-energy direct transition is dipole forbidden, while the onset of strong absorption due to dipole-allowed direct transitions is at about 3.8 eV [78]. In contrast, theoretical studies resulted in a direct gap at Γ, with two exceptions proposing the VBM away from the Γ but only 50 meV higher than that at the Γ point. A schematic of the band structure is shown in Fig. 15.8(b). By spectroscopic ellipsometry, Feneberg et al. confirmed that the onset of absorption due to dipole-allowed interband transitions was at 3.8 eV for a carrier concentration of below $10^{19}$ $cm^{-3}$ [79]. The onset of absorption shifted to higher absorption onset energies, with increasing electron densities explained by the interplay of Burstein−Moss shift and bandgap renormalization when taking the band nonparabolicity into account. Furthermore, analysis of the plasma frequencies showed that effective electron masses increased from a zero-density mass of $m^* = 0.18m_0$ to $0.4m_0$ at $n = 10^{21}$ $cm^{-3}$ (Fig. 15.8(c)), which is important in understanding the electrical and optical properties of $In_2O_3$.

## 15.4 Theoretical knowledge on $In_2O_3$

To understand the structural phase stability, electronic structure, and optical properties of $In_2O_3$, a first-principle calculation is beneficial. Fundamental understandings of the phase transitions of $In_2O_3$ relating to the electrical and optical properties are connected to its technological importance in many application fields.

First-principle calculations of $In_2O_3$ have been performed since the 1990s [80,81]. Several open questions still remain, such as the indirect and direct bandgap, and underestimation of the bandgap relating to the hybridization between In 4d and O 2p states. Albanesi et al.used a tight-binding method to calculate the band structure of $In_2O_3$, but did not include the In 4d orbitals in the valence [82]. A discrete variational Xα method and a linear combination of atomic orbitals including the In 4d electrons in the valence were reported, and an antibonding contribution near the top of the valence band and an indirect bandgap were observed [78]. DFT calculations by the linear muffin-tin orbital method also demonstrated indirect bandgap, with the VBM at the H point, and found a negative curvature of the valence band near the Γ point [80].

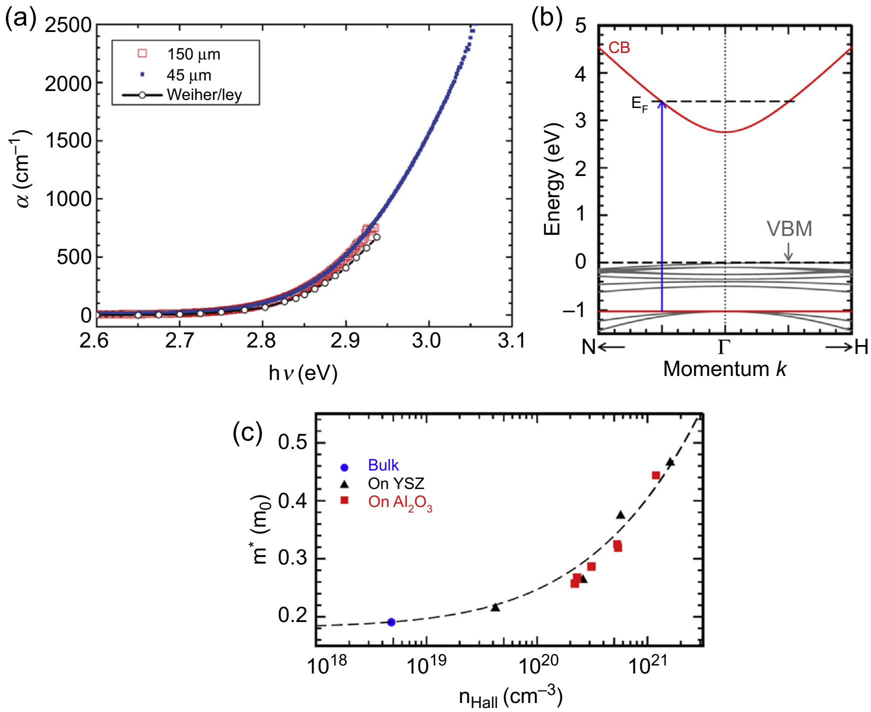

**Figure 15.8** (a) Absorption spectral dependence of the absorption coefficient ($\alpha$) of $In_2O_3$ at room temperature for two samples with thicknesses of 45 (*solid squares*) and 150 (*open squares*) μm. The data represented by a *black line* connecting open circles is taken from Weiher et al. [77]. (b) The band structure of bixbyite $In_2O_3$ is calculated by Fuchs and Bechstedt [28] in the vicinity of the Γ point of the Brillouin zone. The band structure is calculated to be indirect with the valence band maximum at $k \neq 0$ on the $-\Gamma$-$H$ line. The onset of strong absorption (represented by the vertical blue arrow for a selected Fermi energy $E_F$) originates from transitions from a lower valence band to the conduction band, with its minimum at $k = 0$. These bands are marked in red. Energy values, number, and masses of valence bands are chosen arbitrarily. (c) Determined effective electron masses (m*) of $In_2O_3$ as a function of free carrier density ($n_{\mathrm{Hall}}$). The different symbols represent samples grown on different substrates and a bulk crystal. The dashed curve is a nonparabolic model to describe the observed behavior.
(a) Reprinted from T. Minami, Present status of transparent conducting oxide thin-film development for Indium-Tin-Oxide (ITO) substitutes, Thin Solid Films 516 (2008) 5822−5828, copyright (2013), with permission from Wiley-VCH. (b) and (c) Reprinted from M. Feneberg, J. Nixdorf, C. Lidig, R. Goldhahn, Many-electron effects on the dielectric function of cubic $In_2O_3$: effective electron mass, band nonparabolicity, band gap renormalization, and Burstein-Moss shift, Phys. Rev. B 93 (2016) 045203, copyright (2016), with permission from American Physical Society.

However, these results indicated underestimation of the bandgap. Some authors mention that $In_2O_3$ the description of the metal d levels using the local density or generalized gradient approximation was partly incorrect [83−85]. The energetic position of the In 4d-derived orbitals affects the hybridization of In 4d levels with O 2s and

O 2p levels, affecting the structure near the VBM. In other In compounds, such as InP, the In 4d levels are known to split due to spin-orbit coupling by as much as 0.86 eV [86,87]. If a splitting of this magnitude occurs near the top of the valence band, an indirect band gap could result. Erhart employed the semiempirical local density approximation (LDA) + U and generalized gradient approximation (GGA) + U schemes [83] in the version by Dudarev [88], incorporating self-interaction corrections into the LDA and GGA functionals. The self-interaction parameter U−J was varied between 0 and 9 eV. The results obtained are consistent with available spectroscopic data [83,89−91], as shown in Fig. 15.9.

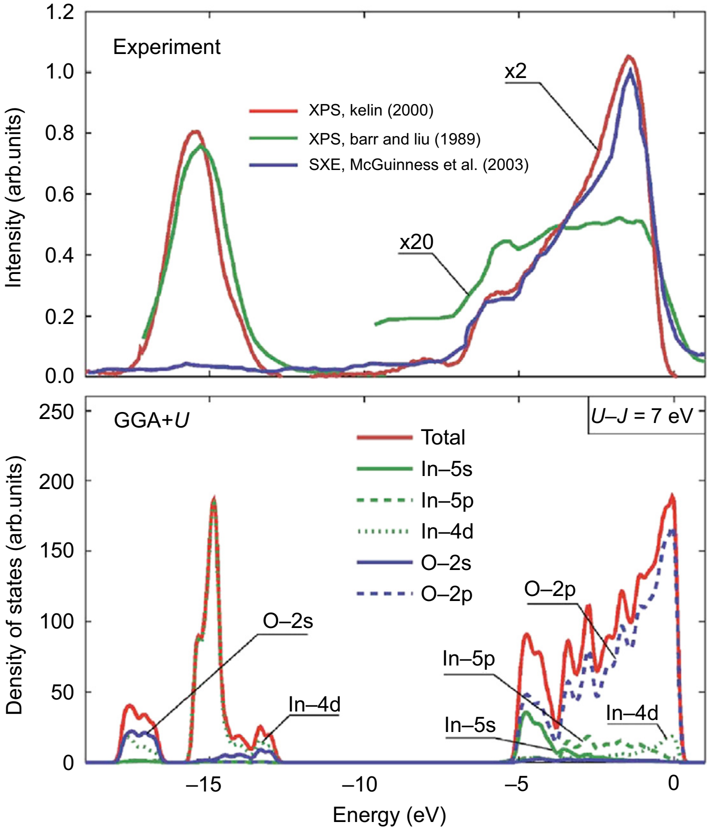

**Figure 15.9** Total and partial densities of states from GGA + *U* calculations using $\overline{U} - \overline{J} = 7$ eV. The results of X-ray photoelectron spectroscopy [94,95] and soft X-ray emission [96] spectroscopy measurements are shown for comparison. For better visualization the calculated density of states was broadened using a Gaussian filter with 0.1 eV and multiplied by a factor of five for energies larger than −8 eV.

Reprinted with permission from P. Erhart, A. Klein, R.G. Egdell, K. Albe, Band structure of indium oxide: indirect versus direct band gap, Phys. Rev. B, 75 (2007) 153205. Copyright (2007) by the American Physical Society.

The self-interaction in the 4*d* shell is corrected for by taking into account an empirical Coulomb interaction parameter *U*. Nevertheless, the energy gaps remain too small, as the excitation aspect is not included in the electronic structure calculation. The parameter *U* is found to influence the position of VBM in *k* space, and hence the relation between the direct and indirect bandgaps. Fuchs considers the influence of the actual crystallographic structure of $In_2O_3$ on the electronic bands. Concerning the crystallographic structure effect, Karazhanov et al. reported on structural phase stability, electronic structure, optical properties, and high-pressure behavior of $In_2O_3$; $In_2O_3$ was found to convert from bixbyite to corundum at a high pressure of around 3.8 GPa [27]. Calculations within local density and generalized gradient approximations indicated that the corundum-type $In_2O_3$ was an indirect bandgap semiconductor, while the bixbyite-type $In_2O_3$ was direct bandgap but remains within the framework of DFT−LDA and GGA. In contrast, Fuchs and Bechstedt studied the electronic structure on the basis of the hybrid HSE03 XC functional [28]. The structural phase stability is similar to the results found by Karazhanov. Both structures show similar electronic properties, especially densities of states. The bandgap of the bixbyite-type $In_2O_3$ is slightly indirect or direct. The calculated direct quasiparticle gaps of the bixbyite and corundum types amount to 3.1 and 3.3 eV, respectively. The lowest indirect gaps of the bixbyite and corundum types are 2.61 and 2.45 eV, respectively. Furthermore, the Burstein−Moss shift and Fermi level position and average effective mass as a function of the free electron density were calculated, and were similar to the experimental results (Fig. 15.8(a)). The corundum-type $In_2O_3$ is almost same as the bixbyite-type $In_2O_3$.

## 15.5 Doping issues and reduction of defect density

### 15.5.1 Unintentionally doped $In_2O_3$

The first principle suggested the origin donors in unintentionally doped $In_2O_3$ as $V_O$s and hydrogen. Ágoston et al. demonstrated the existence of doubly positive $\left(V_O^{2+}\right)$ and neutral $\left(V_O^0\right)$ defects in $In_2O_3$ by using the LDA and GGA functions, as shown in Fig. 15.10(a) [93]. The $V_O$ is a shallow donor with a low formation energy at reducing conditions, suggesting that abundant $V_O$s are the cause of the intrinsic n-type behavior. Furthermore, Tang et al. suggested that an indium interstitial ($In_i$) or a tin dopant (Sn: In−$V_O$) induces a shallow donor [94]. The coupling between these shallow donor levels and a deep donor level corresponding to a $V_O$ leads to a significant reduction in their formation energies, meaning the formation of defect pairs. Annealing in oxygen also decreased the electron concentrations of bulk single crystal or high-quality thin films [34]. In contrast, Limpijumnong et al. find that both interstitial hydrogen ($H_i$) and substitutional hydrogen ($H_O$) act as shallow donors by LDA + U calculations [95]. The anion antibonding sites are the preferred site for $H_i^+$ owing to the long In−O bond. The $H_i^+$ site is lower in energy than the other metastable sites. The H substitution on the O site is also exclusively a donor. Experimentally, Koida et al. demonstrated

H-doped $In_2O_3$ films by radiofrequency magnetron sputtering [96]. H composition controlled by varying water vapor pressure during the growth showed correlation with electrical properties [97]. The 1.9−6.3 at% H-contained films showed as high as 98−130 $cm^2/Vs$ at carrier concentration of $1.8 \times 10^{20}$ $cm^{-3}$. Furthermore, King et al. performed muon spin rotation measurements to investigate the electrical behavior of hydrogen in $In_2O_3$ [98]. By probing the electrical behavior of muonium in $In_2O_3$, a shallow-donor center was observed with an activation energy of 47.6 meV. Stavola et al. used infrared (IR) spectroscopy to investigate the properties of H in $In_2O_3$ single crystals [99]. The majority of the free-carrier absorption was produced by the interstitial H ($H_i$) defect only. The IR spectrum corresponding to the defect with H trapped by an oxygen vacancy ($H_O$) was not confirmed.

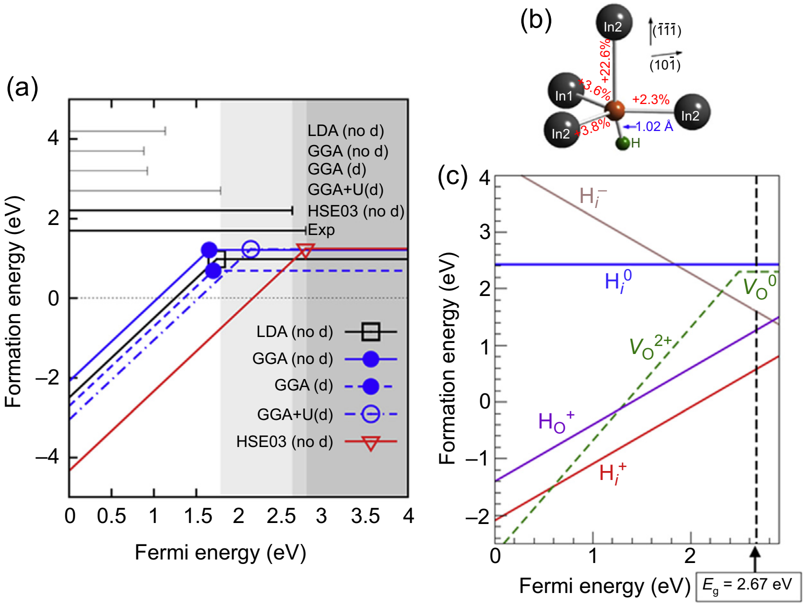

**Figure 15.10** (a) Formation energies of $V_O$s in $In_2O_3$ at reducing conditions. The lines with positive and zero slopes refer to $V_O^{2+}$ and $V_O^0$, respectively. $V_O^+$ is unstable. The horizontal bar on the top shows the calculated and experimental bandgaps. The LDA/GGA + U, HSE06/PBE0, and experimental bandgaps are denoted by shaded areas. (b) Schematic illustration of H defects in $In_2O_3$ ($H_i^+$ at the $AB_{O1}$ site). (c) Calculated formation energies of hydrogen defects and $V_O$s in $In_2O_3$ as a function of Fermi energy.

(a) Reprinted from P. Ágoston, K. Albe, R.M. Nieminen, M.J. Puska, Intrinsic n-type behavior in transparent conducting oxides: a comparative hybrid-functional study of $In_2O_3$, $SnO_2$, and ZnO, Phys. Rev. Lett. 103 (2009) 245501, copyright (2009), with permission from the American Physical Society. (b) and (c) Reprinted from S. Limpijumnong, P. Reunchan, A. Janotti, C.G. Van de Walle, Hydrogen doping in indium oxide: an ab initio study, Phys. Rev. B 80 (2009) 193202, copyright (2009), with permission from the American Physical Society.

### 15.5.2 Intentionally doped $In_2O_3$

For n-type doping, Sn has been regarded as the only useful dopant for $In_2O_3$, which is supported by the first-principle calculation. There is much experiment research using the various n-type dopants. High-mobility and near-IR-transparent $In_2O_3$ thin films have been reported for several doping metals, such as Mo [100,101], Ti [6], W [102], and Zr [103], which showed high carrier mobility of around 80 $cm^2$/Vs with carrier density larger than $10^{20}\,cm^{-3}$. However, both the best doping elements and the origins of high mobility are still unclear. The electrical properties of polycrystalline film grown on glass at a low temperature depend on the growth method and/or conditions. There are many reasons for electron carrier generation, such as $V_O$s, interstitial metals, and extrinsic dopants. These mechanisms occur simultaneously. To simplify the effects of various dopants on the electrical properties, single crystals or epilayers are beneficial. Bierwagen made a systematic investigation of Sn doping in the epitaxial $In_2O_3$ films grown by plasma-assisted MBE with small numbers of intrinsic donors [104]. The electron concentration increased and resistivity decreased with increasing Sn concentration, as shown in Fig. 15.11(a). These properties were improved by post-deposition annealing in a vacuum to remove compensating acceptors such as oxygen interstitials.

For p-type doping, unintentional p-type conductivity has not been observed in single crystalline $In_2O_3$, as acceptor-like intrinsic point defects like indium vacancy $V_{In}$ and oxygen interstitial $O_i$ can act as compensating centers. Ágoston et al. also suggested that the low formation energies predicted by hybrid-functional calculations are low for the oxygen-rich growing conditions [93]. The $V_O$ formation energies even become negative for the electron chemical potential near the VBM, indicating that p-type doping is impossible for these materials close to the thermodynamic equilibrium. However, acceptor doping gives a chance of obtaining high-quality p-type $In_2O_3$ or semiinsulating material. Weiher demonstrated one order of magnitude lower room-temperature conductivity of a Zn-doped sample compared to unintentionally doped samples using bulk single crystals [105], and the same qualitative effect was shown by de Wit with Ca-doped polycrystalline bulk samples [106]. Bierwagen prepared highly Mg-doped MBE-grown $In_2O_3$ and found the dopant concentration dependence of the resistivity after annealing in oxygen [107], as shown in Fig. 15.11(b). The highest Mg-doped sample, with a dopant concentration of $6 \times 10^{20}\,cm^{-3}$, showed a semiinsulating property with a film resistivity of above $10^5$ cm, although p-type conductivity was not observed. Other authors investigated the compensating vacancy defects ($V_{In}$, $V_O$) by positron annihilation spectroscopy in Sn-donor and Mg-acceptor doped $In_2O_3$ thin films [108]. In both types of oxygen-annealed films, acceptor type $V_{In}$ was detected. The concentration of the $V_{In}$ in the Sn-donor-doped sample was higher than that in Mg-acceptor-doped samples, suggesting that the interstitial oxygen $O_i$ may be the main compensating acceptor. However, isolated $V_O$ was not observed. The reason for the overcompensation of the Mg by the donor is still unclear.

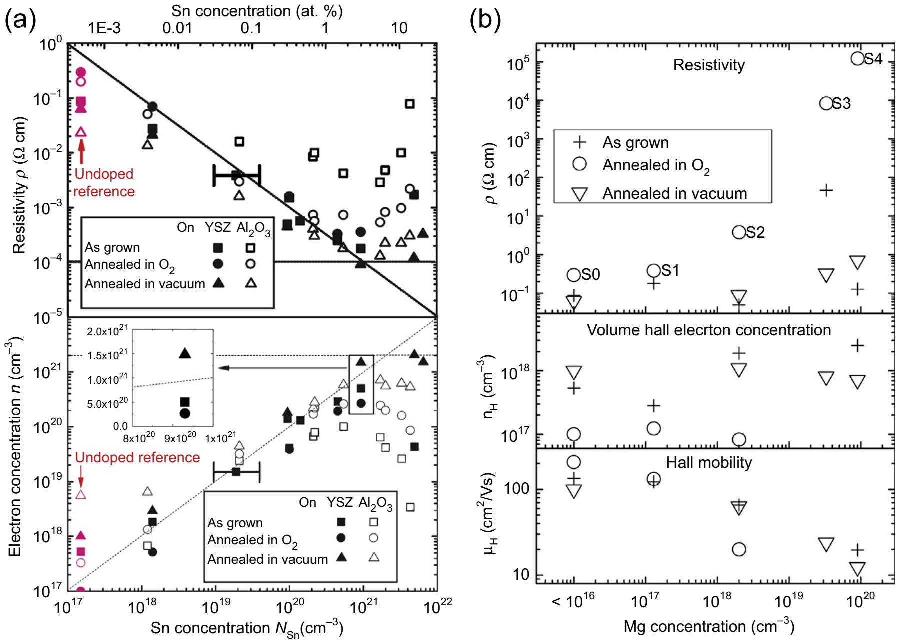

**Figure 15.11** Volume Hall electron concentration ($n$) and resistivity ($\rho$) as function of Sn-concentration ($N_{Sn}$) for as-grown and postgrowth-treated samples (annealed in oxygen, annealed in vacuum). The colored data points at the lowest Sn concentration correspond to an undoped reference film. The inset highlights the substantial impact of postgrowth annealing on electron concentration for extremely high Sn concentrations. The diagonal dashed line corresponds to $n = N_{Sn}$; the horizontal line denotes our empirical electron concentration (*dashed line*) and resistivity (*solid line*) limits. The horizontal error bar indicates the uncertainty of the secondary ion mass spectrometry (SIMS) measurement. (b) Film resistivity $\rho$, Hall electron concentration ($n_H$), and Hall mobility ($\mu_H$) of Mg-doped films as a function of Mg concentration and annealing conditions. The data points at an Mg concentration of $<10^{16}\text{cm}^{-3}$ were taken with the unintentionally doped reference sample. For samples with resistivity above 10 Ωcm only the resistivity could be reliably determined and no Hall data is given.
(a) Reprinted from O. Bierwagen, J.S. Speck, Plasma-assisted molecular beam epitaxy of Sn-doped $In_2O_3$: Sn incorporation, structural changes, doping limits, and compensation, Phys. Status Solidi A, 211 (2014) 48−53, copyright (2013), with permission from WILEY-VCH. (b) Reprinted from O. Bierwagen, J.S. Speck, Mg acceptor doping of $In_2O_3$ and overcompensation by oxygen vacancies, Appl. Phys. Lett. 101 (2012) 102107, copyright (2012), with permission from American Institute of Physics.

## 15.6 Summary

In earlier years $In_2O_3$-based oxides drew attention as TCOs for transparent electrodes in their amorphous or polycrystalline thin film form, with a lack of understanding of their intrinsic physical properties. After 2000 the progress of single crystal and epitaxial growth technologies has accelerated research concerning the intrinsic physical properties of $In_2O_3$ by combining the modern first-principle calculation and high-resolution analysis technologies. The indirect bandgap is approximately 2.7 eV; the effective electron mass is around $0.2m_0$; the high-quality epitaxial film achieved high Hall mobilities of over 200 $cm^2/Vs$; and the high concentration of n-type doping has been demonstrated below a resistivity of $10^{-4}$ Ωcm. Although there are still some open issues, such as p-type doping, SEAL formation, and the actual origin of intrinsic donors (either as $V_O$s or hydrogen vacancies), the new knowledge is useful for electronic device applications. For use of $In_2O_3$ in advanced electronic device applications, key technologies are the doping for spintronics [22], nanostructured crystal growth, and alloying. Single crystalline nanostructured $In_2O_3$ has been reported [109]. In other compound semiconductor materials high-quality single nanocrystals have been applied to field-effect transistors and optical devices with a high affinity to Si-based nanoelectronic devices [110,111]. Concerning alloying, $Ga_2O_3$ has recently attracted attention as a potential material for power devices [112], but there are issues such as carrier control, bandgap engineering, and crystal structure control. To overcome these issues, an Al–I–$GaO_x$ system should have the same potential for physical property control as the Al–In–GaN system.

## References

[1] J.E. Medvedeva, C.L. Hettiarachchi, Tuning the properties of complex transparent conducting oxides: role of crystal symmetry, chemical composition, and carrier generation, Phys. Rev. B 81 (2010) 125116J.

[2] P.D.C. King, T.D. Veal, F. Fuchs, ChY. Wang, D.J. Payne, A. Bourlange, H. Zhang, G.R. Bell, V. Cimalla, O. Ambacher, R.G. Egdell, F. Bechstedt, C.F. McConville, Band gap, electronic structure, and surface electron accumulation of cubic and rhombohedral $In_2O_3$, Phys. Rev. B 79 (2009) 205211.

[3] K. Irmscher, M. Naumann, M. Pietsch, Z. Galazka, R. Uecker, T. Schulz, R. Schewski, M. Albrecht, R. Fornari, On the nature and temperature dependence of the fundamental band gap of $In_2O_3$, Phys. Status Solidi A 211 (2014) 54.

[4] T. Minami, Present status of transparent conducting oxide thin-film development for Indium-Tin-Oxide (ITO) substitutes, Thin Solid Films 516 (2008) 5822–5828.

[5] Y. Meng, X. Yang, H. Chen, J. Shen, Y. Jiang, Z. Zhang, Z. Hua, A new transparent conductive thin film $In_2O_3$:Mo, Thin Solid Films 394 (2001) 219.

[6] M.F.A.M. van Hest, M.S. Dabney, J.D. Perkins, D.S. Ginley, M.P. Taylor, Titanium-doped indium oxide: a high-mobility transparent conductor, Appl. Phys. Lett. 87 (2005) 032111.

[7] H. Ohta, M. Orita, M. Hirano, H. Tanji, H. Kawazoe, H. Hosono, Highly electrically conductive indium–tin–oxide thin films epitaxially grown on yttria-stabilized zirconia (100) by pulsed-laser deposition, Appl. Phys. Lett. 76 (2000) 2740.

[8] J. Rombach, A. Papadogianni, M. Mischo, V. Cimalla, L. Kirste, O. Ambacher, T. Berthold, S. Krischok, M. Himmerlich, S. Selve, O. Bierwagen, The role of surface electron accumulation and bulk doping for gas-sensing explored with single-crystalline $In_2O_3$ thin films (2016), Sens. Actuators B Chem. 236 (2016) 909–916.

[9] H. von Wenckstern, D. Splith, F. Schmidt, M. Grundmann, O. Bierwagen, J.S. Speck, Schottky contacts to $In_2O_3$, APL Mater. 2 (2014) 046104.

[10] H. von Wenckstern, D. Splith, S. Lanzinger, F. Schmidt, S. Müller, P. Schlupp, R. Karsthof, M. Grundmann, pn-Heterojunction Diodes with n-Type $In_2O_3$, Adv. Electron. Mater. 1 (2015) 1400026.

[11] O. Bierwagen, J.S. Speck, T. Nagata, T. Chikyow, Y. Yamashita, H. Yoshikawa, K. Kobayashi, Depletion of the $In_2O_3$ (001) and (111) surface electron accumulation by an oxygen plasma surface treatment, Appl. Phys. Lett. 98 (2011) 172101.

[12] T. Nagata, O. Bierwagen, M.E. White, M.-Y. Tsai, Y. Yamashita, H. Yoshikawa, N. Ohashi, K. Kobayashi, T. Chikyow, J.S. Speck, XPS study of Sb-/In-doping and surface pinning effects on the Fermi level in $SnO_2$(101) thin films, Appl. Phys. Lett. 98 (2011) 232107.

[13] M.W. Allen, C.H. Swartz, T.H. Myers, T.D. Veal, C.F. McConville, S.M. Durbin, Bulk transport measurements in ZnO: the effect of surface electron layers, Phys. Rev. B 81 (2010) 075211.

[14] R. Schifano, E.V. Monakhov, U. Grossner, B.G. Svensson, Electrical characteristics of palladium Schottky contacts to hydrogen peroxide treated hydrothermally grown ZnO, Appl. Phys. Lett. 91 (2007) 193507.

[15] L.R. Bailey, T.D. Veal, C.E. Kendrick, S.M. Durbin, C.F. McConville, Sulfur passivation of InN surface electron accumulation, Appl. Phys. Lett. 95 (2009) 192111.

[16] K.H.L. Zhang, R.G. Egdell, F. Offi, S. Iacobucci, L. Petaccia, S. Gorovikov, P.D.C. King, Microscopic origin of electron accumulation in $In_2O_3$, Phys. Rev. Lett. 110 (2013) 056803.

[17] M. Nazarzahdemoafi, F. Titze, S. Machulik, C. Janowitz, Z. Galazka, R. Manzke, M. Mulazzi, Comparative study of the electronic structures of the in and Sn/$In_2O_3$(111) interfaces, Phys. Rev. B 93 (2016) 081303 (R).

[18] K. Nomura, H. Ohta, K. Ueda, T. Kamiya, M. Hirano, H. Hosono, Thin-film transistor fabricated in single-crystalline transparent oxide semiconductor, Science 300 (2003) 1269.

[19] Y.H. Hwang, J.H. Jeon, K.J. Seo, B.S. Bae, Solution-processed, high performance aluminum indium oxide thin-film transistors fabricated at low temperature, Electrochem. Solid State Lett. 12 (2009) H336.

[20] P.K. Nayak, J.V. Pinto, G. Goncalves, R. Martins, E. Fortunato, Environmental, optical, and electrical stability study of solution-processed zinc—tin—oxide thin-film transistors, J. Disp. Technol. 7 (2011) 640.

[21] H. Yanagi, T. Hase, S. Ibuki, K. Ueda, H. Hosono, Bipolarity in electrical conduction of transparent oxide semiconductor $CuInO_2$ with delafossite structure, Appl. Phys. Lett. 78 (2001) 1583.

[22] J. Philip, A. Punnoose, B.I. Kim, K.M. Reddy, S. Layne, J.O. Holmes, B. Satpati, P.R. Leclair, T.S. Santos, J.S. Moodera, Carrier-controlled ferromagnetism in transparent oxide semiconductors, Nat. Mater. 5 (2006) 298.

[23] L. Brewer, Thermodynamic properties of the oxides and their vaporization processes, Chem. Rev. 52 (1953) 1.

[24] R.P. Burns, G. Demaria, J. Drowart, M.G. Inghram, Mass spectrometric investigation of the vaporization of $In_2O_3$, J. Chem. Phys. 38 (1963) 1035.

[25] J.-N. Valderrama, K.T. Jacob, Vapor pressure and dissociation energy of ($In_2O$), Thermochim. Acta 21 (1977) 215—224.

[26] N.M. Lakin, G. van den Hoek, I.R. Beattie, J.M. Brown, The identification of $In_2O$ in the gas phase by high resolution electronic spectroscopy, J. Chem. Phys. 107 (1997) 4439.

[27] M. Marezio, Refinement of the crystal structure of $In_2O_3$ at two wavelengths, Acta Crystallogr. 20 (1966) 723.

[28] F. Fuchs, F. Bechstedt, Indium-oxide polymorphs from first principles: quasiparticle electronic states, Phys. Rev. B 77 (2008) 155107.

[29] K.H.L. Zhang, V.K. Lazarov, P.L. Galindo, F.E. Oropeza, D.J. Payne, H.H.-C. Lai, R.G. Egdell, Domain matching epitaxial growth of $In_2O_3$ thin films on $\alpha$-$Al_2O_3$(0001), Cryst. Growth Des. 12 (2012) 1000−1007.

[30] R.D. Shannon, New high pressure phases having the corundum structure, Solid State Commun. 4 (1966) 629.

[31] A.F. Reid, A.E. Ringwood, High-pressure scandium oxide and its place in the molar volume relationships of dense structures of $M_2X_3$ and $ABX_3$ type, J. Geophys. Res. 74 (1969) 3238.

[32] C.T. Prewitt, R.D. Shannon, D.B. Rogers, A.W. Sleight, C rare earth oxide-corundum transition and crystal chemistry of oxides having the corundum structure, Inorg. Chem. 8 (1969) 1985.

[33] http://www.crct.polymtl.ca/factsage/index_m.php.

[34] Z. Galazka, R. Uecker, K. Irmscher, D. Schulz, D. Klimm, M. Albrecht, M. Pietsch, S. Ganschow, A. Kwasniewski, R. Fornari, Melt growth, characterization and properties of bulk $In_2O_3$ single crystals, J. Cryst. Growth 362 (2013) 349−352.

[35] A.B. Chase, Growth of $\beta$-$Ga_2$, $O_3$ by the Verneuil technique, J. Am. Ceram. Soc. 47 (1964) 470.

[36] M.R. Lorenz, J.F. Woods, R.J. Gambino, Some electrical properties of the semiconductor $\beta$ $Ga_2O_3$, J. Phys. Chem. Solids 28 (1967) 403.

[37] T. Harwig, J. Schoonman, Electrical properties of $\beta$-$Ga_2O_3$ single crystals. II, J. Solid State Chem. 23 (1978) 205.

[38] N. Ueda, H. Hosono, R. Waseda, H. Kawazoe, Synthesis and control of conductivity of ultraviolet transmitting $\beta$-$Ga_2O_3$ single crystals, Appl. Phys. Lett. 70 (1997) 3561.

[39] Y. Tomm, J.M. Ko, A. Yoshikawa, T. Fukuda, Floating zone growth of $\beta$-$Ga_2O_3$: a new window material for optoelectronic device applications, Sol. Energy Mater. Sol. Cells 66 (2001) 369.

[40] E.G. Villora, K. Shimamura, Y. Yoshikawa, K. Aoki, N. Ichinose, Large-size $\beta$-$Ga_2O_3$ single crystals and wafers, J. Cryst. Growth 270 (2004) 420.

[41] Y. Tomm, P. Reiche, D. Klimm, T. Fukuda, Czochralski grown $Ga_2O_3$ crystals, J. Cryst. Growth 220 (2000) 510.

[42] Z. Galazka, R. Uecker, K. Irmscher, M. Albrecht, D. Klimm, M. Pietsch, M. Brutzam, R. Bertram, S. Ganschow, R. Fornari, Czochralski growth and characterization of $\beta$-$Ga_2O_3$ single crystals, Cryst. Res. Technol. 45 (2010) 1229.

[43] R. Nitsche, Crystal chemistry, growth and properties of multi-cation chalcogenides, J. Phys. Colloq. 36 (1975) C3−C9.

[44] H. Schäfer, Nachweis und anwendung von gaskomplexen beim chemischen transport, Z. Anorg. Allg. Chem. 403 (1974) 116.

[45] J.J.H.W. De Wit, Preparation of $In_2O_3$ single-crystals via chemical transport reaction, J. Cryst. Growth 12 (1972) 183.

[46] M. Jozefowicz, W. Piekarczyk, Preparation of $In_2O_3$ single crystals by chemical vapour transport method, Mater. Res. Bull. 22 (1987) 775.

[47] V. Scherer, C. Janowitz, A. Krapf, H. Dwelk, D. Braun, R. Manzke, Transport and angular resolved photoemission measurements of the electronic properties of $In_2O_3$ bulk single crystals, Appl. Phys. Lett. 100 (2012) 212108.

[48] D. Braun, V. Scherer, C. Janowitz, Z. Galazka, R. Fornari, R. Manzke, In-gap states of $In_2O_3$ single crystals investigated by scanning tunneling spectroscopy, Phys. Status Solidi A (2013) 1−7.

[49] Z. Galazka, R. Uecker, R. Fornari, A novel crystal growth technique from the melt: levitation-Assisted Self-Seeding Crystal Growth Method, J. Cryst. Growth 388 (2014) 61−69.

[50] S. Sadofev, Y.J. Cho, O. Brandt, M. Ramsteiner, R. Calarco, H. Riechert, S.C. Erwin, K. Galazka, M. Korytov, M. Albrecht, R. Uecker, R. Fornari, Growth of wurtzite InN on bulk $In_2O_3$(111) wafers, Appl. Phys. Lett. 101 (2012) 172102.

[51] J.J. Prince, S. Ramamurthy, B. Subramanian, C. Sanjeeviraja, M. Jayachandranc, Spray pyrolysis growth and material properties of $In_2O_3$ films, J. Cryst. Growth 240 (2002) 142−151.

[52] T. Yan, X. Wang, J. Long, H. Lin, R. Yuan, W. Dai, Z. Li, X. Fu, Controlled preparation of $In_2$O3, InOOH and $In(OH)_3$ via a one-pot aqueous solvothermal route, N. J. Chem. 32 (2008) 1843−1846.

[53] A. Gurlo, M. Ivanovskaya, A. Pfau, U. Weimar, W. Göpel, Sol-gel prepared In2O3 thin films, Thin Solid Films 307 (1997) 288−293.

[54] H.K. Müller, Electrical and optical properties of sputtered $In_2O_3$ films, Phys. Status Solidi 27 (1968) 723.

[55] I. Hamberg, C.G. Granqvist, Evaporated Sn-doped $In_2O_3$ films: basic optical properties and applications to energy-efficient windows, J. Appl. Phys. 60 (1986) R123.

[56] E.J. Tarsa, J.H. English, J.S. Speck, Pulsed laser deposition of oriented $In_2O_3$ on (001) InAs, MgO, and yttria-stabilized zirconia, Appl. Phys. Lett. 62 (1993) 2332.

[57] H. Ohta, M. Orita, M. Hirano, H. Hosono, Surface morphology and crystal quality of low resistive indium tin oxide grown on yittria-stabilized zirconia, J. Appl. Phys. 91 (2002) 3547.

[58] N. Taga, M. Maekawa, Y. Shigesato, I. Yasui, M. Kamei, T.E. Haynes, Deposition of heteroepitaxial $In_2O_3$ thin films by molecular beam epitaxy, Jpn. J. Appl. Phys. 37 (1998) 6524−6529.

[59] C.Y. Wang, V. Cimalla, H. Romanus, T. Kups, G. Ecke, T. Stauden, M. Ali, V. Lebedev, J. Pezoldt, O. Ambacher, Phase selective growth and properties of rhombohedral and cubic indium oxide, Appl. Phys. Lett. 89 (2006) 011904.

[60] F. Yang, J. Ma, X.J. Feng, L.Y. Kong, Structural and photoluminescence properties of single-crystalline $In_2O_3$ films grown by metal organic vapor deposition, J. Cryst. Growth 310 (2008) 4054−4057.

[61] Z. Mei, Y. Wang, X. Du, Z. Zeng, M. Ying, H. Zheng, J. Jia, Q. Xue, Z. Zhang, Growth of $In_2O_3$ single-crystalline film on sapphire (0001) substrate by molecular beam epitaxy, J. Cryst. Growth 289 (2006) 686.

[62] E.H. Morales, Y. He, M. Vinnichenko, B. Delley, U. Diebold, Surface structure of Sn-doped $In_2O_3$ (111) thin films by STM, N. J. Phys. 10 (2008) 125030.

[63] O. Bierwagen, J.S. Speck, High electron mobility $In_2O_3$ (001) and (111) thin films with nondegenerate electron concentration, Appl. Phys. Lett. 97 (2010) 072103.

[64] W.E. Lee, K.P.D. Lagerlof, Structural and electron diffraction data for sapphire ($\alpha$-$Al_2O_3$), J. Electron. Microsc. Tech. 2 (1985) 247−258.

[65] Y.F. Chen, H.J. Ko, S.K. Hong, T. Yao, Layer-by-layer growth of ZnO epilayer on $Al_2O_3$(0001) by using a MgO buffer layer, Appl. Phys. Lett. 76 (2000) 559.

[66] S. Strite, H. Morkoc, GaN, AlN, and InN: a review, J. Vac. Sci. Technol. B 10 (1992) 1237.

[67] P. Vogt, A. Trampert, M. Ramsteiner, O. Bierwagen, Domain matching epitaxy of cubic $In_2O_3$ on r-plane sapphire, Phys. Status Solidi A 212 (2015) 1433−1439.

[68] C.Y. Wang, Y. Dai, J. Pezoldt, B. Lu, Th Kups, V. Cimalla, O. Ambacher, Phase stabilization and phonon properties of single crystalline rhombohedral indium oxide, Cryst. Growth Des. 8 (2008) 1257−1260.

[69] N. Suzuki, K. Kaneko, S. Fujita, Growth of corundum-structured $In_2O_3$ thin films on sapphire substrates with $Fe_2O_3$ buffer layers, J. Cryst. Growth 364 (2013) 30−33.

[70] P. Ágoston, P. Erhart, A. Klein, K. Albe, Geometry, electronic structure and thermodynamic stability of intrinsic point defects in indium oxide, J. Phys. Condens. Matter 21 (2009) 455801.

[71] T. Nagata, O. Bierwagen, Z. Galazka, M. Imura, S. Ueda, H. Yoshikawa, Y. Yamashita, T. Chikyow, Photoelectron spectroscopic study of electronic state and surface structure of $In_2O_3$ single crystals, Appl. Phys. Express 10 (2017) 011102.

[72] V. Scherer, C. Janowitz, Z. Galazka, M. Nazarzadehmoafi, R. Manzke, Polaron character of the near-$E_F$ band of cleaved $In_2O_3(111)$ single crystals, Europhys. Lett. 113 (2016) 26003.

[73] Z.M. Jarzebski, Preparation and physical properties of transparent conducting oxide films, Phys. Status Solidi A 71 (1982) 13.

[74] J. Szczyrbowski, A. Dietrich, H. Hoffmann, Optical and electrical properties of RF-sputtered indium−tin oxide films, Phys. Status Solidi A 78 (1983) 243.

[75] F. Matino, L. Persano, V. Arima, D. Pisignano, R.I.R. Blyth, R. Cingolani, R. Rinaldi, Electronic structure of indium-tin-oxide films fabricated by reactive electron-beam deposition, Phys. Rev. B 72 (2005) 085437.

[76] I. Hamberg, C.G. Granqvist, K.-F. Berggren, B.E. Sernelius, L. Engström, Band-gap widening in heavily Sn-doped $In_2O_3$, Phys. Rev. B 30 (1984) 3240.

[77] R.L. Weiher, R.P. Ley, Optical properties of indium oxide, J. Appl. Phys. 37 (1966) 299.

[78] A. Walsh, J.L.F. Da Silva, S.-H. Wei, C. Körber, A. Klein, L.F.J. Piper, A. DeMasi, K.E. Smith, G. Panaccione, P. Torelli, D.J. Payne, A. Bourlange, R.G. Egdell, Nature of the band gap of $In_2O_3$ revealed by first-principles calculations and X-ray spectroscopy, Phys. Rev. Lett. 100 (2008) 167402.

[79] M. Feneberg, J. Nixdorf, C. Lidig, R. Goldhahn, Many-electron effects on the dielectric function of cubic $In_2O_3$: effective electron mass, band nonparabolicity, band gap renormalization, and Burstein-Moss shift, Phys. Rev. B 93 (2016) 045203.

[80] H. Odaka, S. Iwata, N. Taga, S. Ohnishi, Y. Kaneta, Y. Shigesato, Study on electronic structure and optoelectronic properties of indium oxide by first-principles calculations, Part 1, Jpn. J. Appl. Phys. 36 (1997) 5551.

[81] I. Tanaka, M. Mizuno, H. Adachi, Electronic structure of indium oxide using cluster calculations, Phys. Rev. B 56 (1997) 3536.

[82] E.A. Albanesi, S.J. Sferco, I. Lefebvre, G. Allan, M. Lannoo, Electronic structure of crystalline InP oxides, Solid State Commun. 86 (1993) 27−31.

[83] P. Erhart, A. Klein, R.G. Egdell, K. Albe, Band structure of indium oxide: indirect versus direct band gap, Phys. Rev. B 75 (2007) 153205.

[84] D. Vogel, P. Krüger, J. Pollmann, Self-interaction and relaxation-corrected pseudopotentials for II-VI semiconductors, Phys. Rev. B 54 (1996) 5495.

[85] V.I. Anisimov, J. Zaanen, O.K. Andersen, Band theory and Mott insulators: Hubbard U instead of Stoner I, Phys. Rev. B 44 (1991) 943.

[86] R.A. Pollak, S. Kowalczyk, L. Ley, D.A. Shirley, Evolution of core states from energy bands in the 4d5s5p region from Pd to Xe, Phys. Rev. Lett. 29 (1972) 274.

[87] T. Kendelewicz, P.H. Mahowald, K.A. Bertness, C.E. McCants, I. Lindau, W.E. Spice, Surface shifts in the In 4d and P 2p core-level spectra of InP(110), Phys. Rev. B 36 (1987) 6543.

[88] S.L. Dudarev, G.A. Botton, S.Y. Savrasov, C.J. Humphreys, A.P. Sutton, Electron-energy-loss spectra and the structural stability of nickel oxide: an LSDA+U study, Phys. Rev. B 57 (1998) 1505.

[89] A. Klein, Electronic properties of $In_2O_3$ surfaces, Appl. Phys. Lett. 77 (2000) 2009.

[90] T.L. Barr, Y.L. Liu, An x-ray photoelectron spectroscopy study of the valence band structure of indium oxides, J. Phys. Chem. Solids 50 (1989) 657−664.

[91] C. McGuinness, C.B. Stagarescu, P.J. Ryan, J.E. Downes, D. Fu, K.E. Smith, R.G. Egdell, Influence of shallow core-level hybridization on the electronic structure of post-transition-metal oxides studied using soft X-ray emission and absorption, Phys. Rev. B 68 (2003) 165104.

[92] S.Z. Karazhanov, P. Ravindran, P. Vajeeston, A. Ulyashin, T.G. Finstad, H. Fjellvåg, Phase stability, electronic structure, and optical properties of indium oxide polytypes, Phys. Rev. B 76 (2007) 075129.

[93] P. Ágoston, K. Albe, R.M. Nieminen, M.J. Puska, Intrinsic *n*-type behavior in transparent conducting oxides: a comparative hybrid-functional study of $In_2O_3$, $SnO_2$, and ZnO, Phys. Rev. Lett. 103 (2009) 245501.

[94] L.-M. Tang, L.-L. Wang, D. Wang, J.-Z. Liu, K.-Q. Chen, Donor-donor binding in $In_2O_3$: engineering shallow donor levels, J. Appl. Phys. 107 (2010) 083704.

[95] S. Limpijumnong, P. Reunchan, A. Janotti, C.G. Van de Walle, Hydrogen doping in indium oxide: an ab initio study, Phys. Rev. B 80 (2009) 193202.

[96] T. Koida, H. Fujiwara, M. Kondo, Hydrogen-doped $In_2O_3$ as high-mobility transparent conductive oxide, Jpn. J. Appl. Phys. 46 (2007) L685.

[97] T. Koida, H. Fujiwara, M. Kondo, Structural and electrical properties of hydrogen-doped $In_2O_3$ films fabricated by solid-phase crystallization, J. Noncryst. Solids 354 (2008) 2805−2808.

[98] P.D.C. King, R.L. Lichti, Y.G. Celebi, J.M. Gil, R.C. Vilao, H.V. Alberto, J.P. Duarte, D.J. Payne, R.G. Egdell, I. McKenzie, C.F. McConville, S.F.J. Cox, T.D. Veal, Shallow donor state of hydrogen in $In_2O_3$ and $SnO_2$: implications for conductivity in transparent conducting oxides, Phys. Rev. B 80 (2009) 081201 (R).

[99] M. Stavola, F. Bekisli, W. Yin, K. Smithe, W.B. Fowler, L.A. Boatner, Contrasting the experimental properties of hydrogen in $SnO_2$, $In_2O_3$, and $TiO_2$, J. Appl. Phys. 115 (2014) 012001.

[100] Y. Meng, X. Yang, H. Chen, J. Shen, Y. Jiang, Z. Zhang, Z. Hua, Molybdenum-doped indium oxide transparent conductive thin films, J. Vac. Sci. Technol. A 20 (2002) 288−290.

[101] A.E. Delahoy, S.Y. Guo, Transparent and semitransparent conducting film deposition by reactive-environment, hollow cathode sputtering, J. Vac. Sci. Technol. A 23 (2005) 1215−1220.

[102] P.F. Newhouse, C.-H. Park, D.A. Keszler, J. Tate, P.S. Nyholm, High electron mobility W-doped $In_2O_3$ thin films by pulsed laser deposition, Appl. Phys. Lett. 87 (2005) 112108.

[103] T. Koida, M. Kondo, High-mobility transparent conductive Zr-doped $In_2O_3$, Appl. Phys. Lett. 89 (2006) 082104.

[104] O. Bierwagen, J.S. Speck, Plasma-assisted molecular beam epitaxy of Sn-doped $In_2O_3$: Sn incorporation, structural changes, doping limits, and compensation, Phys. Status Solidi A 211 (2014) 48−53.

[105] R.L. Weiher, Electrical properties of single crystals of indium oxide, J. Appl. Phys. 33 (1926) 2834.

[106] J.H.W. de Wit, The high temperature behavior of $In_2O_3$, J. Solid State Chem. 13 (1975) 192−200.

[107] O. Bierwagen, J.S. Speck, Mg acceptor doping of $In_2O_3$ and overcompensation by oxygen vacancies, Appl. Phys. Lett. 101 (2012) 102107.

[108] E. Korhonen, F. Tuomisto, O. Bierwagen, J.S. Speck, Z. Galazka, Compensating vacancy defects in Sn- and Mg-doped $In_2O_3$, Phys. Rev. B 90 (2014) 245307.

[109] Y. Hao, G. Meng, C. Ye, L. Zhang, Controlled synthesis of $In_2O_3$ octahedrons and nanowires, Cryst. Growth Des. 5 (2005) 1617−1621.

[110] K. Tomioka, M. Yoshimura, T. Fukui, A III-V nanowire channel on silicon for high-performance vertical transistors, Nature 488 (2012) 189−192.

[111] S. Maeda, K. Tomioka, S. Hara, J. Motohisa, Fabrication and characterization of InP nanowire light-emitting diodes, Jpn. J. Appl. Phys. 51 (2012) 02BN03.

[112] M. Higashiwaki, K. Sasaki, A. Kuramata, T. Masui, S. Yamakoshi, Gallium oxide ($Ga_2O_3$) metal-semiconductor field-effect transistors on single-crystal $\beta$ -$Ga_2O_3$ (010) substrates, Appl. Phys. Lett. 100 (2012) 013504.

# Preparation, properties and electronic structure of $SnO_2$

# 16

*Karsten Henkel*[1], *Jörg Haeberle*[1], *Klaus Müller*[1], *Christoph Janowitz*[2], *Dieter Schmeißer*[1]
[1]BTU Cottbus-Senftenberg, Cottbus, Germany; [2]Humboldt-Universität zu Berlin, Berlin, Germany

## 16.1 Introduction

Tin oxide ($SnO_2$) belongs to the transparent conducting oxide (TCO) family. In this chapter we first summarize its general properties, such as the optical and electrical data. We discuss the growth techniques used for single crystals and also for preparation of the thin films which are the basis for device applications such as transparent electrodes, electronic devices, and sensors. We discuss the specific properties in the context of intrinsic electronic defect states, and focus in particular on the high conductivity, the high carrier mobility, and the ability to form p-type conductivity.

Most of the characteristic physical properties of $SnO_2$ are reviewed in Section 16.2. These include its optical and electric data, its electronic structure, and its possible application as an (opto)electronic material. We summarize the relevant crystallographic data and growth properties of $SnO_2$ single crystals and deposition techniques for amorphous $SnO_x$ (a-$SnO_x$) thin films. In Section 16.3 we describe spectroscopic results concerning the stoichiometry and X-ray absorption data. Subsequently, we focus in Section 16.4 on the signature of intrinsic electronic defects derived from spectroscopic data in the valence regime. These defects are attributed to be the basis of the fundamental physical properties needed for the TCO applications. In Section 16.5 we discuss the electronic band scheme, the optical and electronic properties, and n-type and p-type doping in terms of coexisting quasimetallic and ionic bonds. We use a model based on an experimentally derived energy diagram to explain the optical data, such as "optical gap," cathodoluminescence (CL), and the spectral width of the TCO window. In Section 16.5 we also discuss the differences between crystalline $SnO_2$ and a-$SnO_x$ thin films with regard to the data and model. Table 16.2 summarizes the most important characteristic values of $SnO_2$ and compares them to other TCO single crystal data.

## 16.2 Basic properties, crystal growth, and thin film deposition

The physical properties of $SnO_2$ single crystals and their different surface orientations are well studied and documented [1]. In this section we discuss applications and requirements of $SnO_2$ as an electronic material.

**Single Crystals of Electronic Materials.** https://doi.org/10.1016/B978-0-08-102096-8.00016-1
Copyright © 2019 Elsevier Ltd. All rights reserved.

## 16.2.1 Applications and electronic, electric, and optical properties

### 16.2.1.1 Applications

Thin films of $SnO_x$ are polycrystalline wide-bandgap semiconductors which are highly attractive for their use in TCO electrodes or as active channel material in thin film transistors (TFTs) for flexible displays, solar cells, and organic light-emitting diodes [2,3]. Such applications are particularly in focus due to $SnO_x$'s high electrical conductivity, charge carrier mobility, and transparency in the visible optical regime. In the fast-growing research field of perovskite solar cells, $SnO_2$ is investigated as a replacement for the $TiO_2$ electron selective layer due to favorable band alignment between $SnO_2$ and the typically used active perovskite layers [4]. $SnO_2$ thin films are the most studied materials for gas-sensing applications [5,6]. Metal-oxide semiconductor sensors based on $SnO_x$ are now produced industrially [7]. $SnO_2$ is also attractive for applications in lithium-ion batteries [8] and as a thermoelectric material [9], to name just a few uses.

For a-$SnO_x$ the ease of doping enables the preparation of films with varying doping concentrations between $10^{17}$ and $10^{20}$ $cm^{-3}$, i.e., between intrinsic and degenerately doped, depending on the particular application of the films. Such films exhibit weak, metallic-like, temperature-dependent conductivities with low activation energies with values up to about 100 meV [10]. The corresponding transport mechanisms are discussed in terms of shallow donors by H doping [11], or are attributed to scattering at the grain-boundary depletion layers [10]. The former is widely accepted for single crystalline samples, while the latter is considered as a general feature of polycrystalline semiconductors [10].

It is worth noting that $SnO_2$ has a similar band structure to $In_2O_3$. Due to the similar electronic configuration of $Sn^{4+}$ and $In^{3+}$ ($4d^{10}$), $SnO_2$ is also seen as an attractive candidate to replace $In_2O_3$ in the indium–gallium–zinc–oxide (IGZO [12]) system for low-cost and Earth-abundant TCO materials [13,14]. Hence the isostructural tin–gallium–zinc–oxide (SGZO) materials should share these advantages of high carrier mobility and optical transparency. High carrier mobility (24.6 $cm^2/Vs$) and good TFT performance were reported for SGZO active materials where only small amounts of gallium (<5%) and tin (<2%) were used [14].

### 16.2.1.2 Optical properties

$SnO_2$ has an optical gap of about 3.6 eV at the $\Gamma$-point [15]. This gap is also called fundamental gap, and is dipole forbidden [16,17]. In ellipsometric studies, absorption onsets at 4.28 and 5.42 eV corresponding to electric field polarization perpendicular and parallel to the optical axis are reported [16]. A quasiparticle gap of 3.65 eV has been calculated [17]. As an element of the TCOs, its transparency has a high value of 80% starting at the fundamental absorption of 343 nm up to wavelengths of around 2000 nm. The main luminescence signal appears around 350 nm [18].

For $SnO_2$, changes of the general optical gap value of 3.6 eV are reported when induced by doping, thermal, or other process treatments [9,19–21]. The mechanisms quoted include bandgap narrowing (decrease), alloying (decrease), and quantum confinement (increase, nanoparticles) [19,20].

### 16.2.1.3 Electrical properties and doping

High charge carrier concentrations in the range of $10^{18}$-$10^{21}$ $cm^{-3}$ and high charge carrier mobilities of 80–200 $cm^2/Vs$ have been achieved for $SnO_2$ single crystals as well as for thin amorphous $SnO_x$ layers, where generally higher mobilities were observed for the singe crystals [2,18,22,23].

For rutile $SnO_2$ static dielectric constants of 12 and 7 perpendicular and parallel to the tetragonal c-axis were calculated [24], while in early experiments corresponding values of about 14 and 9, respectively, were found [25].

Generally, $SnO_2$ (like the other TCOs) is predominantly n-type. As a basis for this property, either the ease of forming oxygen vacancies or cation interstitials is discussed [26] or, alternatively, hydrogen interaction with acceptor impurities is favored [11,27,28]. A typical n-type dopant is antimony [29]; ambipolar transport is also reported [21]. Hence there is a major research interest in fabricating p-type $SnO_2$, and its realization would open many new perspectives in applications [30]. Thus the use of acceptor dopants such as gallium, aluminum, indium, or nitrogen is investigated, where the oxygen atoms in the $SnO_2$ matrix are replaced by the respective acceptor atoms [21,31]. However, instability of N-doped $SnO_2$ is still an issue to be overcome [21].

Recently, dual acceptor codoping was suggested to improve the stability of N dopants in $SnO_2$. Researchers have demonstrated that a regulation of the polarity of conduction and carrier concentration can be achieved by GaN doping connected with proper thermal treatment [21]. These authors observed the transition of $n \rightarrow p \rightarrow n$, which was mainly attributed to N–O substitutions ($n \rightarrow p$) in GaN:$SnO_2$ films and their decomposition at higher temperatures ($p \rightarrow n$).

### 16.2.1.4 Electronic structure

The electronic structure of $SnO_2$ is discussed in detail in various papers [1,15,24]. In the band structure the highest occupied valence states consist of oxygen 2p states mixed with some Sn p states. The lowest unoccupied valence states form a band of empty Sn 5s states which has a broad and highly dispersive minimum at $\Gamma$, resulting in a small effective mass of about 0.3 $m_0$, high conductivity and mobility, and weak optical absorption [15,24].

In the context of this chapter, we develop an alternative model of the electronic structure which enables a better description of the available data and the optical and transport properties of $SnO_2$ and a-$SnO_x$. It is described in Section 16.5, and is based on the observation of intrinsic defects introduced in Section 16.4. The model implies that the valence electrons in $SnO_2$ are localized and cause an inhomogeneous charge distribution with spatial separated domains of quasimetallic and ionic bonding behavior. Many properties of the $SnO_2$ system can be described consistently with these experimental findings, unlike some of the above-listed models and explanations.

For example, it allows a consistent description of the optical transitions, doping behavior, stability of n-type or p-type conductivity, and more. This makes it a basis for a better understanding of the physical properties that are behind the numerous applications of $SnO_2$ systems.

Recently, we employed resonant photoelectron spectroscopy (resPES) on single crystals of $SnO_2$ [32,33]. We also discussed other TCO materials such as $In_2O_3$ [34,35], $Ga_2O_3$ [35–37], and ZnO [33,35], as well as the thin films of $SnO_x$ [32,33], ZnO [33,38], and IGZO [33,35]. We observed the existence of charge transfer (CT) bands, excitons (E), and polaronic (P) defects in all the investigated material systems, indicating a very similar mechanism for defect formation. Also, a combined participator–spectator Auger decay was commonly observed in these materials and discussed in connection to the intrinsic defect states. We generalized these close relations in the electronic structure in terms of the spatial and electronic localization of the intrinsic defect states, as all materials show similar physical behavior such as high optical transparency and n-type conductivity with high mobility [37]. In addition, these systems are easy to mix and easy to dope, while the other characteristic parameters stay unchanged.

### 16.2.2 Crystallographic properties

$SnO_2$ crystallizes in the tetragonal rutile structure with $P4_2/mnm$ space group and lattice constants of $a_0 = b_0 = 4.7374$ Å, $c_0 = 3.1864$ Å [39,40]. Each unit cell contains two formula units of $SnO_2$. The tin cation is octahedrally coordinated and forms chains along the c-axis, where each Sn atom is surrounded by a distorted octahedron of O atoms [39] in this configuration. Hence each oxygen atom is surrounded by three tin atoms approximately at the corners of a triangle [40].

$SnO_2$ and $In_2O_3$ have some common properties: both have high carrier concentrations, high mobilities, and spectral similarities in the X-ray absorption spectroscopy (XAS) data (see Section 16.3.2). The indium cations of $In_2O_3$ are also octahedrally coordinated, but (compared to $SnO_2$) these are in two nonequivalent sites. According to stoichiometry, the oxygen atoms in the $In_2O_3$ structure are coordinated by four metal atoms. The crystal structure of indium oxide is cubic and a bixbyite type, also known as a C-type rare-earth sesqui-oxide with the space group of Ia3. Each cell with $a_0 = 10.117$ Å contains 32 indium atoms and 48 oxygen atoms [41].

In the SGZO material compound only the spinel-type oxides $ZnGa_2O_4$, $SnZn_2O_4$, and their solid solution exist besides the binary oxides in the Sn–Ga–Zn–O system at 1250°C [40].

### 16.2.3 Crystal growth and thin film preparation

#### 16.2.3.1 Growth of single crystals

The growth of $SnO_2$ single crystals started more than 25 years ago (a short review is available [18]). $SnO_2$ appears at elevated temperatures to be much more unstable than other TCOs (such as $In_2O_3$, ZnO, or $Ga_2O_3$), showing a rapid decomposition even under very high oxygen pressures. It was reported that stoichiometric $SnO_2$ does not melt up to 2100°C, as crystals could not be grown from the melt [18]. The preferred methods to grow these crystals in bulk are solution growth (flux top-seeded solution growth) and growth via the gas phase (sublimation, chemical vapor deposition (CVD), and chemical vapor transport (CVT)). Growth of large single crystals of 1-inch diameter by physical vapor transport has also been described [18]. In that work, $SnO_2$ crystals grown under oxygen-rich conditions are electrical insulators, while those grown under SnO-rich conditions are n-type semiconductors with free electron concentrations of $3 \times 10^{17}-2 \times 10^{18}$ $cm^{-3}$ and electron mobilities between 125 and 200 $cm^2/Vs$.

The $SnO_2$ single crystals used in our study were grown by the CVT method [42]. CVT is another promising method for obtaining single crystals with extremely high melting points. Several transport agents had been applied previously [42–45] for CVT growth. The first promising results were obtained with sulphur, iodine, and chlorine agents [46], and these were successfully extended [47].

By using a four-zone furnace tilted by 5 degrees, we achieved single crystals of very high quality with front face dimensions up to 3 mm × 3 mm. We obtained single crystals with a yellow/brown color, although some crystals were uncolored. All single crystals were free of impurity phases as characterized by X-ray diffraction [32]. They show n-type conductivity with values of $1 \times 10^{18}$ $cm^{-3}$ for the free carrier concentration, according to Hall measurements.

### 16.2.3.2 $SnO_x$ thin film deposition

$SnO_x$ thin films have been prepared by various techniques, such as spray pyrolysis, sol–gel method, thermal evaporation, ac–dc magnetron sputtering, pulsed-laser deposition, CVD, and atomic layer deposition (ALD) [5,22,48]. Recently, for $SnO_x$ layers prepared by ALD, resistivities lower than $10^{-3}$ Ωcm, and transparencies of higher than 80% have been reported, fulfilling the desired requirements for TCOs in the aforementioned applications [2,22]. Thus a refractive index up to 2.05, carrier concentrations in the range of $10^{20}-10^{21}$ $cm^{-3}$, and mobilities up to 80 $cm^2/Vs$ could be achieved.

The $SnO_x$ films (5 nm in thickness) investigated here are prepared in Lisbon, and their electrical properties have been characterized in detail [23]. The $SnO_x$ films have p-type conductivity with a carrier concentration around $10^{18}$ $cm^{-3}$, an optical gap of 2.8 eV, and an average transmittance of about 85% (400–2000 nm). An annealing procedure gives an increase in mobility (up to values of 4.8 $cm^2/Vs$) [23].

The preparation of $SnO_x$ by ALD and possible applications were recently reviewed [49]. Metal–organic precursors are seen to have considerable advantages to reduce the process temperature and increase the growth rate and film purity [49]. The desired application might regulate the choice of reactant. For example, the tetrakis(methylamino) tin metallic precursor in combination with hydrogen peroxide delivers high growth rates [2,49]. The usage of $H_2O$ allows process temperatures below 100°C [49], which is attractive for thermally sensitive devices such as perovskite solar cells or organic light-emitting diodes. Ozone as a reactant delivers the highest conductivity so far [22,49], which is very important for TCO applications. To achieve polycrystalline films, process temperatures in the range of 250–300°C are required [49]. The precursors Sn(tbba) and Sn(dmamp)$_2$ showed the potential to decrease significantly the temperature required for the formation of crystalline films down to 120–130°C [49].

## 16.3 Photoelectron spectroscopy of SnO$_2$

This section discusses PES characterization of SnO$_2$ single crystals grown by CVT. The experiments reported here used a colorless SnO$_2$ single crystal. Its preparation is described in Section 16.2.3. The SnO$_2$ (100) surface is prepared by cleavage in ultra-high vacuum (UHV).

The PES data are measured at the U49/2-PGM2 at Bessy II in Berlin [50]. We apply the methods of PES, resPES, and XAS. Constant initial state (CIS) data are taken at a fixed binding energy of the electron energy analyzer. The partial integrated yield (pIY) represents the integration over all resPES spectra divided by the number of spectra. Angle-resolved photoelectron spectroscopy (ARPES) measurements are performed at the beamline BEST [51] at the Helmholtz-Zentrum Berlin (HZB).

A standard characterization of materials occurs via the X-ray PES (XPS) core-level data (Section 16.3.1). The XAS data is usually considered as a tool for characterizing the unoccupied states of the electronic structure (Section 16.3.2). The combination of such data enables the determination of the partial density of states (pDOS) of the valence states, discussed in Section 16.4.1. Dispersions in the band structure in the valence band (VB) region are discussed on the basis of ARPES data in Section 16.3.3.

### 16.3.1 *XPS data of the Sn3d and O1s core levels*

For SnO$_2$ we recorded the Sn-derived Sn3d and Sn4d core levels as well as the O1s core level, as shown in Figs. 16.1 and 16.2. Together with the valence band spectra (Fig. 16.1(b)), these data are reproduced by many groups [1,52] and show the good quality of the single crystals by its narrow line shape.

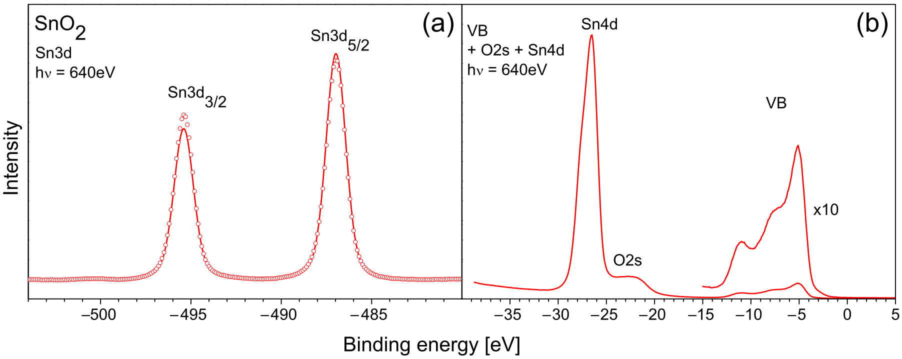

**Figure 16.1** Photoemission data of the SnO$_2$ single crystal, recorded at an excitation energy of 640 eV: (a) Sn3d core-level data; (b) spectra of the valence regime.

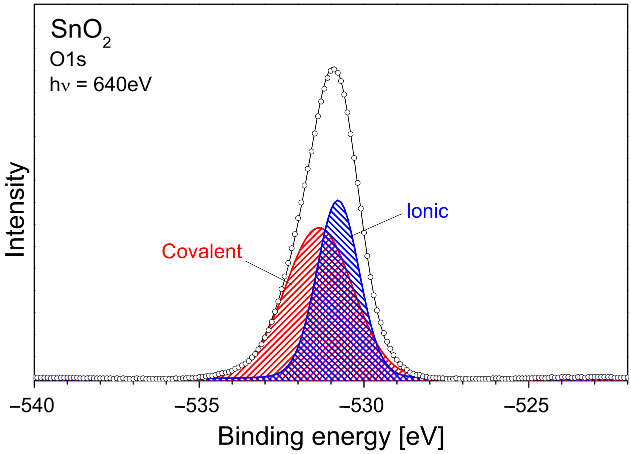

**Figure 16.2** O1s core-level data for $SnO_2$ (100) recorded at an excitation energy of 640 eV. The data are decomposed to show the ionic (blue curve) and the covalent (red) contributions.

In Fig. 16.1 we show the XPS core level data of Sn3d (Fig. 16.1(a)) as well as the valence regime with the Sn4d, O2s, and the O2p derived valence band emissions (Fig. 16.1(b)).

Here, we focus on information about the elemental compositions which can be determined from the XPS core-level intensities [32]. We find an excellent agreement with the expected stoichiometric values (Table 16.1), and argue that these crystals have a very low number of oxygen vacancies. The oxygen-to-metal intensity ratio of $SnO_2$ is given in comparison to other single crystals in Table 16.1. It shows that the method works well for single crystal materials in general.

The O1s core level shows two contributions, as evident from the peak decomposition shown in Fig. 16.2. One signal is at 530.8 eV (blue curve), and the second one appears at higher binding energy separated by 0.6 eV (red curve). In fact, in all TCO oxides there are two contributions in the O1s core levels. Their intensities and energy separation vary from system to system, but the relative intensities can be used to determine the particular ionicity value [53]. This gives the first evidence for coexisting

**Table 16.1** **Elemental composition of several TCO single crystals**

| Material | XPS O:M ratio[a] | Stoichiometric value |
|---|---|---|
| $SnO_2$ | 2.1 | 2.0 |
| $In_2O_3$ | 1.5 | 1.5 |
| $Ga_2O_3$ | 1.6 | 1.5 |
| ZnO | 1.1 | 1.0 |

[a] M stands for Sn, In, Ga, and Zn, respectively.

covalent and ionic contributions, as indicated in Fig. 16.2 and discussed in Section 16.4.3. In Fig. 16.2 the intensities (areas) of these two contributions are comparable, and this corresponds to a contribution of 45% of the covalent shoulder (red curve) in the total O1s intensity of $SnO_2$. From these intensities we deduce an ionicity phase angle of 65.6 degrees and a value of 0.83 for the ionicity factor (see Section 16.4.3).

### *16.3.2 X-ray absorption data: the O1s edge*

In our previous studies we focused on the XAS data of the O1s absorption edge, as the valence states mostly originate from the O2p states. We found evidence of multiatomic Auger processes, which are indicative of charge localization and polarization effects occurring between the valence states when an extra electron (caused by resonant excitation from the O1s core level) is added to the valence states. We identified 3-hole (3 h) and 4-hole (4 h) processes, which are interpreted as when the extra electron is screened by the occupied valence states or by electrons in a partially filled upper valence band, respectively [54].

Fig. 16.3 shows the XAS (in terms of the pIY) data at the O1s absorption edge of $SnO_2$ (red curve) and an a-$SnO_x$ film (blue curve). The O1s data of both samples are very similar, but that of the single crystalline $SnO_2$ is more structured. Both start at about 1 eV below the Fermi energy ($E_F$) and show a broad (5 eV) absorption band. In these data we marked the position of the Fermi energy for the O1s thresholds. Such XAS data are well established in the literature [55,56]. In our resPES data we prefer to use the pIY data as this enables a quantitative comparison to the valence band spectra.

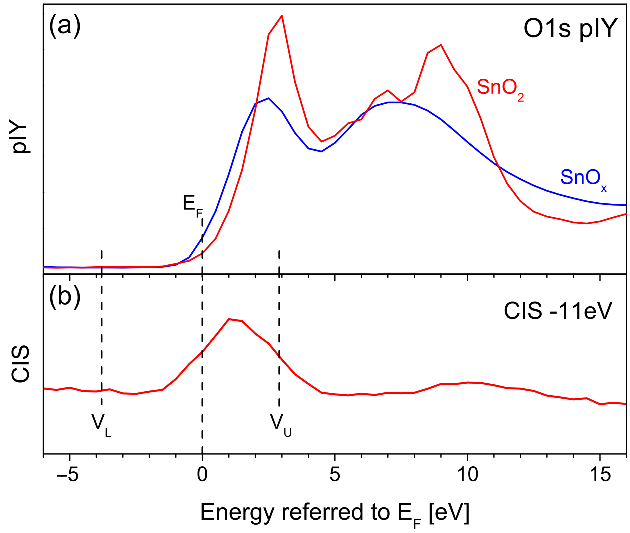

**Figure 16.3** (a) The XAS pIY data at the O1s edge for $SnO_2$ (red) and a-$SnO_x$ (blue). (b) CIS spectrum (−11 eV) which is characteristic for the CT defect states and the determination of the $V_U$ position. The width (FWHM) of the CT defect band $\Delta W_{CT}$ is given in Table 16.2.

**Table 16.2** Energetic and electrical values of several investigated TCO single crystals

| Material | $f_i$ | $I_{Pol}$ (%) | $\Delta E_{pol}$ (eV) | $\Delta W_{CT}$ (eV) | $\Delta V_{CT}$ (ev) | $E_{total}$ (eV) | $E_{opt}$ (eV) | N ($cm^{-3}$) | μ ($cm^2/Vs$) | References |
|---|---|---|---|---|---|---|---|---|---|---|
| $SnO_2$ | 0.83 | 25 | ~9 | 3.5 | 6.7 | 7.34 | 3.5 | $(0.3-2) \times 10^{18}$ | 125–230 | [18] |
| $In_2O_3$ | 0.72 | 13 | ~9 | 3.3 | 5.3 | 6.24 | 2.8 | $(1-4) \times 10^{18}$ | 140–180 | [65] |
| $Ga_2O_3$ | 0.90 | 19 | ~8 | 2.8 | 8.2 | 8.66 | 4.8 | $(0.04-2) \times 10^{18}$ | 80–150 | [66] |
| ZnO | 0.81 | 7 | ~8 | 3.6 | 7.4 | 8.23 | >3.1 | $2 \times 10^{17}$ | 200 | [67] |
| $TiO_2$ | 0.86 | 24 | ~8 | 1.7 | 4.2 | 4.53 | 3.0–3.5 | $10^{16}-10^{20}$ | 4–20 | [68–74] |

$I_{Pol}$ is the intensity of the polaron dip, $\Delta W_{CT}$ the width of the charge transfer band, $E_{total}$, $E_{opt}$ are the total (electronic) and optical energy gaps, n and μ are carrier concentration and mobility. All energy values are in eV. The $E_{opt}$, n, and μ values are taken from the literature ([18,65–74])

For $SnO_2$ we identified that the first broad band is mainly caused by the existence of multiple Auger decays with a 4h final state (4h Auger, [32]), which indicates that the upper valence states must have some partial filling. This is directly confirmed by the shape of the CIS (−11 eV) spectrum shown in Fig. 16.3(b). This CIS curve probes just the onset of the 4h Auger decays and we notice that these decays occur in an energy range of about 3 eV above $E_F$ (i.e. between 0 and 3 eV in the depicted energy axis). We use the width of this CIS curve ($\Delta W_{CT} = 3.5$ eV) to separate the localized CT states from the common band-like valence states (marked as $V_U$ in Fig. 16.3). Thus the width of the energy separation of the ionic states ($\Delta V_{CT}$) can be determined: it amounts to 6.7 eV for the $SnO_2$ single crystal where the maximum of the lower ionic valence band ($V_L$) appears at −3.8 eV (see Fig. 16.5(b) and Section 16.4.1). Here we use the term electronic gap ($\Delta V_{CT}$) in the sense of electronic excitations, not to be confused with the often-used terms "bandgap" from DFT calculations or the "optical gap." A further discussion is given in Section 16.5.

### 16.3.3 ARPES data

The ARPES measurements are taken with an energy resolution of 30 meV in normal emission of the in-situ cleaved (100) surface corresponding to the ΓZ line of the bulk Brillouin zone (Fig. 16.4(b)). Individual spectra are recorded between photon energies of 23 and 35 eV at a temperature of 30 K. Cleaving with the "knife and anvil" technique, we obtain flat (100) surfaces and curved (101) surfaces. The (100) surfaces used for ARPES in this chapter show no reconstruction. The dispersion of bulk bands perpendicular to the surface ($k_\perp$ reciprocal vector, $E_{kin}$ kinetic energy, $\varphi$ detection

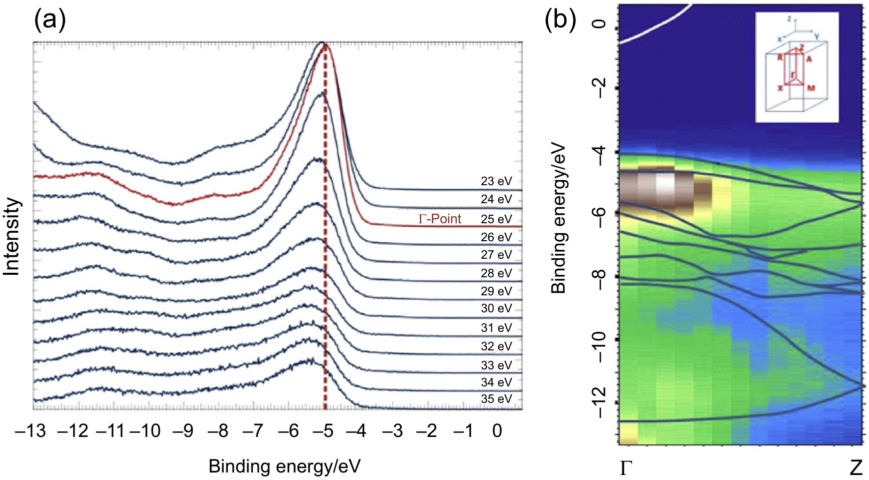

**Figure 16.4** (a) Normal emission spectra of $SnO_2$ (100) prepared by cleavage in vacuum. The red broken line is a guide showing the dispersion of states away from the Γ-point at 25 eV photon energy. (b) Intensity plot of the experimental band structure in ΓZ direction derived from (a). The theoretical band structure [57] is added and indicated by blue and white lines for the filled and unoccupied states, respectively.

angle) can then be determined by the formula $k_\perp = \frac{1}{\hbar}\sqrt{2m(E_{kin}\cos^2\varphi + V_0)}$ for reasonable values for the inner potential $V_0$. The position of the Fermi energy is separately determined from evaporated gold.

The spectra obtained from our $SnO_2$ (100) surfaces represent the intrinsic electronic structure free of reconstructions and surface states due to cleavage in UHV. In Fig. 16.4(a) a set of spectra recorded in normal emission, i.e., along the ΓZ line, for various photon energies is depicted. The Γ-point occurs at a photon energy of 25 eV (red spectrum) and shows the lowest observed binding energy values. The maximum intensity of the leading peak is 5 eV and it corresponds well to the first strong maximum of the VB data in Fig. 16.1(b). This peak disperses by 0.5 eV symmetric to the Γ-point (i.e., hole-like). A second group of bands with a highest binding energy of 11.5 eV shows an opposite dispersion. The spectrum at the Γ-point (photon energy of 25 eV) gives the highest occupied states at a binding energy of about 4 eV. This onset corresponds to the value of $V_L$ in Fig. 16.5. Directly at the Fermi energy for $SnO_2$ (100), no additional weak emission was observed, unlike for $In_2O_3$ [58]; rather, the gap region up to the Fermi energy is found free of states.

All spectra are displayed in an intensity plot in Fig. 16.4(b) where a theoretical band structure [57] is added. The white electron-like band at the top of the figure represents the dispersion of the $V_U$ band. The hole-like dispersion of the $V_L$ band (blue lines) and the electron-like dispersion of the states at 11.5 eV binding energy are evident, and agree well with the experimental dispersions.

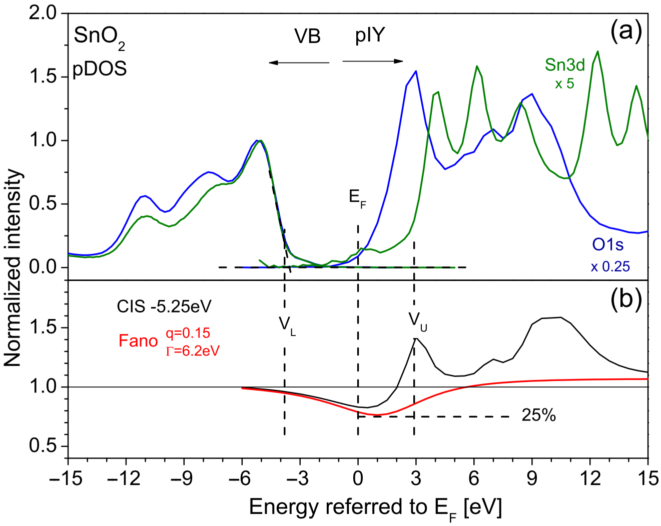

**Figure 16.5** (a) pDOS of a $SnO_2$ (100) single crystal, where the O1s- and Sn3d-derived data is shown in blue and green, respectively. The pIY data is depicted on the right-hand side, and selected corresponding VB spectra taken with photon energy of 526 eV (O1s) and 480 eV (Sn3d) on the left-hand side. (b) Fano analysis (red curve) of the CIS (−5.25 eV) spectrum (black curve). The difference between the experimental and the Fano curves represents transitions from O2p/Sn4d valence states into the empty valence states.

Spectra in normal emission for the ΓZ (100) direction obtained on sputter-annealed $SnO_2$ have also been reported [59]. Their spectrum at 26 eV for a stoichiometric sample resembles our spectrum, although these authors did not observe any dispersion perpendicular to the surface, from which they concluded the existence of two-dimensional, nondispersing surface states. The different surface preparation techniques may explain this discrepancy. Resonant photoemission at the Sn4d ⇒ Sn5p edge showed that for reduced (oxygen-deficient) surfaces at binding energies of about 2 eV, Sn5s states occur [59]. The authors also showed that the surface electronic structure clearly depends on the crystallographic face. Surface states forming at different binding energies could be detected by theory and experiment. For all three reduced (oxygen-deficient) (110), (100), and (101) surfaces, Sn-derived states (Sn5s) were found. The band structure of SnO [60] or SnO-like surfaces [59] also showed a strong peak at 2 eV binding energy, which is possibly of similar origin to that of our $SnO_x$ surfaces (see Section 16.5.3 and Fig. 16.7).

To summarize, we have characterized UHV cleaved $SnO_2$ single crystals grown by CVT. We deduce from the core-level data stoichiometric intensities. The ARPES data shows no surface states or surface reconstructions. This allows one to study the bulk properties of $SnO_2$ using resPES. The observed defect absorption bands in O2p XAS and Sn3d XAS data reflect intrinsic properties of the material, and are the basis for the next section dealing with intrinsic defect states.

## 16.4 pDOS and intrinsic electronic defects

Here we introduce the individual intrinsic defect states based on the experimental X-ray absorption features deduced from resPES data at the O1s edge, and describe their properties in detail. Based on the existence of intrinsic electronic defects such as polarons, excitons, and charge transfer defects, we establish a model for the electronic structure of $SnO_2$ in Section 16.5.

We show that the intrinsic electronic defects determine the doping mechanisms of $SnO_2$ and the charge carrier concentrations, and we compare their influence in the properties of the crystalline and amorphous films. Finally, we develop a novel understanding to discuss the stability of p-type and n-type conductivity based on the intrinsic defects.

### *16.4.1 pDOS*

The pDOS of the $SnO_2$ single crystal is derived by combining the VB spectra and the XAS pIY curves from the resPES data. This enables a quantitative comparison as the data are taken in the same run. To obtain the pDOS the individual data in the valence regime are combined on a common energy scale, as shown in Fig. 16.5. The pIY data are shifted by the values of the binding energies of the Sn3d and the O1s core levels, respectively, into a common diagram. This is also the basis for the scheme of energy levels discussed in Section 16.5.1.

Fig. 16.5(a) represents the occupied and empty valence states and their relative onset with respect to the Fermi energy. The pDOS is governed by the O2p-derived states distributed into the lower and upper band of valence states, as in most TCO systems. Please note that the relative intensities of the unoccupied O2p states are downscaled by a factor of 0.25. Taking the ratio of the oxygen-derived pDOS intensities in the upper and lower bands we obtain a value of 0.55; this value can be used to determine the ionicity phase angle (see Section 16.4.3). It should be mentioned that such quantitative analyses are possible only by this resPES data analysis, as both the VB spectra and the pIY curves are derived within the same scan. The maximum of the lower ionic valence band appears at −3.8 eV, and the O1s pIY data (blue curve in Fig. 16.5(a)) starts below $E_F$. This indicates that there are defect states related to the empty O2p states. The pIY curve of the Sn-derived states (green curve in Fig. 16.5(a)) has its main onset about 3 eV above $E_F$; in most TCO systems the XAS data of the metal anion reflect that excitonic states are formed and located around the Fermi energy. Evidently, in single crystalline $SnO_2$ this is not the case, as discussed in Section 16.5.3.

### 16.4.2 Description and derivation of the defect states

Intrinsic defect states are probed by resPES, as the resonantly excited photoelectron acts as a spy to observe the charge carrier dynamics in the valence regime. It monitors the collective interaction of charge carriers in the lower and upper valence bands. In particular, it reflects polarization and self-trapping effects.

In a simplified picture, it may be understood that intrinsic defects are formed when electrons in the lower band are excited into electronic levels within the gap and become stabilized by the polarization of the remaining charge carriers. The resulting states are localized because of the Coulomb interaction between the transferred electron and the ligand hole, which causes the energy separation $\Delta V_{CT}$ between the $V_L$ and $V_U$ bands. These localized defect states become observable by Auger processes following resonant excitation. The photoexcited electron probes the electronic interactions in the valence regime during its lifetime in the intermediate state as a consequence of the Kramers−Heisenberg scenario [61]. Such interactions are in particular caused by polarization, lattice relaxations, and redistributions in the local charge distributions.

Depending on the relative strengths of the covalent and the Coulomb interaction, i.e., the localization of the intrinsic defects, we distinguish weakly localized, covalent polarons (~10 lattice constants), intermediate localized excitonic states (one single ionic shell), and highly localized charge transfer states (a single metal−oxygen bond). The aforementioned values in brackets give an estimate about the spatial extension of the individual defect states. The localization process involves three mechanisms which hitherto have not been considered in detail.

First, there are polaronic states which become stabilized by structural relaxations. Polaronic defect states are deduced from the Fano profile of the VB states. The polaronic localization can be rationalized as a fluctuating charge density wave which leads to a charge separation between electron and hole polarons, witnessed by the Fano profile [62] of the VB resPES data. In Fig. 16.5(b) we show the results of a Fano analysis of the CIS spectrum taken at −5.25 eV initial state energy. The Fano profile (red curve) is for a q-parameter of 0.15 and a $\Gamma$ value of 6.2 eV. The former, with its $q \approx 0$ shape, causes the dip in the resonance profile of the VB states (CIS spectrum at −5.25 eV in Fig. 16.5(b)). From the Fano analysis we determine its intensity of 25%, and this value quantifies the amount of the polaronic states. The $\Gamma$ value describes the interaction between the localized indirect ($O2p^5$) and the delocalized direct ($O2p^6$) photoemission processes. It indicates in which energy regime the formation of polarons is feasible. The polaron band starts at about 2 eV below the upper limit of $V_L$ and extends over the gap to about 4 eV above the Fermi energy.

The second localized defect state is attributed to a charge−transfer reaction from O2p states into Sn4d levels. Such transitions become evident in the CIS data taken at the onset of the Auger processes at an initial state energy of −11 eV (Fig. 16.3(b)). Evidently, the onset of the Auger processes arises from states within a band of 3.5 eV width ($\Delta W_{CT}$), and starts about 1 eV below the Fermi energy.

The formation of CT states involves a hole state in the O2p states (ligand) and the missing electron being transferred into an empty metal state. These ligand-to-metal CT states cause right at the resonance energy the combined Auger processes, leading to a 4 h final state [63]. These cause some deviations from the normal oxygen-KLL Auger and appear at slightly higher kinetic energies. The CIS (−11.0 eV) spectrum (Fig. 16.3(b)) is the feature which characterizes their onset and the energy regime in which the 4 h Auger processes contribute to the resonance profile. The maximum of such 4 h processes appears about 1.5 eV above $E_F$.

From the width of these CT contributions we deduce that the regular Auger process starts about 3 eV above $E_F$. Consequently, the upper rim of this CIS spectrum is used to define the lowest energy position of the band-like unoccupied states in the $V_U$ band. This energy value separates the localized states from the extended valence states; its distance from the $V_L$ band documents the electronic gap $\Delta V_{CT}$.

The third localized defect state, namely the excitonic defect, appears in the X-ray absorption data recorded at the Sn3d edge; these are included in Fig. 16.5(a) for $SnO_2$ (green curve). The excitonic level appears right at the Fermi energy and shows up as a very weak feature. In contrast, in a-$SnO_x$ thin films this feature dominates (see Fig. 16.7). These remarkable differences are discussed in Section 16.5.3. Excitons have a localization length of a few bond lengths, and are in between the highly delocalized polarons and the highly localized CT defects. Energetically, this is reflected in their position around the Fermi energy. It also means that considerable lattice relaxation must occur to stabilize such electronic defects.

To summarize the defect story, the three types of defect states (P, E, CT) coexist and contribute to the electronic structure of $SnO_2$. In particular, they cause a phase separation into covalent and ionic regimes. The ratio of such phases is determined by the ionicity factor $f_i$ (see next subsection).

### *16.4.3 Ionicity factor to determine the abundance of ionic and covalent defect contributions*

The introduction of ionicity brings a novel parameter in the discussion of the electronic and transport properties of $SnO_2$ and the TCOs. A general method to determine the ionicity factors of oxides is suggested based on three experimental routes [53] which use the relative abundances of the covalent and the ionic contributions. In a complex plane these values define a phase angle [64].

For the $SnO_2$ we demonstrate this by using the two signals in the O1s core level (Fig. 16.2). The fraction of the ionic contribution in the total intensity ($O_{ion}/O_{total}$) is 0.55, and with $\cot\varphi = 1 - O_{ion}/O_{total}$ this corresponds to an ionicity phase angle of 65.7 degrees. It should be mentioned that the ionicity phase angle φ can be determined also from the relative intensities of the $V_L$ and $V_U$ bands in the O1s pDOS data (Fig. 16.5 and Section 16.4.1, consider the scaling factors given there) as well as by the ratio of the covalent width of the CT band ($\Delta W_{CT}$, see Fig. 16.3) and the electronic energy separation $\Delta V_{CT}$ [53]. For $SnO_2$, all three methods come up with a very similar value of around 65 degrees.

These experimental results can be used to obtain the ionicity factor $f_i = \sin^2\varphi$, and for $SnO_2$ a value of $f_i = 0.83$ is deduced. For $SnO_2$ the high value of $f_i$ indicates that the majority of the Sn—O bonds are ionic and 17% of the bonds are covalent. For a series of TCO crystals we found that the three experimental routes come to similar results. Some of the obtained ionicity values are listed in Table 16.2.

Furthermore, $f_i = E^2_{ion}/E^2_{total}$ relates the ionic energy to the total energy. The $E_{ion}$ term corresponds to the split of the valence states to obtain the lower ($V_L$) and the upper ($V_U$) bands of valence states. The $E_{ion}$ value is experimentally derived via the $\Delta V_{CT}$ in our data (Fig. 16.5(a)), and is 6.7 eV for $SnO_2$. For the Sn—O bonds in $SnO_2$ a value of $E_{total} = 7.34$ eV is determined. It is close to the interaction energy Γ which we used in the Fano profile to fit the data of the polaronic CIS curve in Fig. 16.5(b). This comparison shows that the polaronic bandwidth is comparable to or even larger than the ionic contributions, and thereby underlines the significance of the intrinsic electronic defect states within the electronic structure.

As mentioned above, the ionicity value of $SnO_2$ is 0.83: close to the value of ZnO (0.81), higher than that of $In_2O_3$ (0.72), and in the middle of the total range, which varies between 0.7 and 0.92 (see Table 16.2). The ionicity, i.e., the coexistence of intrinsic defects and their relative abundance, gives a consistent picture for a series of oxides of the TCO family, as shown in Table 16.2. This is true for the absolute values of the $f_i$ factors as well as for the close correspondence of the as-determined $E_{total}$ values and the widths of the polaronic bands.

The ionicity factor gives essential evidence for coexisting covalent and ionic contributions in the electronic structure. The intrinsic electronic defects (P, E, CT) discussed above cause an inhomogeneous charge distribution. This suggests that the commonly used picture of homogeneous charges in valence and conduction band is questionable. Instead, in Section 16.5, we give a novel concept to describe the optical and transport properties of $SnO_2$ and a-$SnO_x$ which considers the ionicity in detail.

## 16.5 Electronic energy diagram

In the electronic structure of the $SnO_2$ system we include the intrinsic electronic defect states and the ionicity. The energy diagram is derived from our pDOS analysis (Figs. 16.3 and 16.5), and we use it to explain some of the optical data, such as "optical gap," CL, and spectral width of the TCO window in the visible range. We discuss the differences between the single crystalline $SnO_2$ and the amorphous $SnO_x$ samples in the context of the model. Finally, we address the ambipolar nature of the charge carriers and the related p-type and n-type conductivities. A similar model has been discussed for $Ga_2O_3$ [37].

### 16.5.1 *Model of electronic structure and band scheme*

In the energy diagram in Fig. 16.6 we collect and summarize all our data about the energetics within the valence regime. The vacuum level ($E_{vac}$) is used as a reference, and the ionization potential (IP, 7.9 eV; this value is in good agreement with a series of experimental data [3]) and electron affinity (EA, 1.2 eV) values are shown to give the positions of the lower ($V_L$) and the upper ($V_U$) Sn—O bands. In the ionic subsystem the two bands of valence states are split by 6.7 eV (=$E_{ion}$) symmetrically around the $E_i$ value (4.5 eV below $E_{vac}$). They are attributed to the mixed atomic wave functions with strong intermixing and hybridization of Sn5s, Sn5p, Sn4d, and O2p, O2s states which are based on both, the covalent mixing of Sn5s and Sn4d states, and the ionic interaction between the O2p and Sn4d states. In the covalent subsystem the polaronic band has a width of about 9 eV, and the position of $E_F$ is 3.8 eV above the IP, according to the data shown in Fig. 16.1. Note that, concerning the optical excitation energies, $\Delta E_p$ (green arrow in Fig. 16.6) is smaller than $\Delta E_n$ (blue arrow) based on the experimental data. This indicates a p-type scenario and is discussed in Section 16.5.4.

We added the defect levels as determined from the resPES-derived pDOS data in Figs. 16.3 and 16.5. The O2p pDOS indicates the CT band appears about 1 eV below $E_F$ and extends up to the $V_U$ band; from the full width at half maximum (FWHM) of

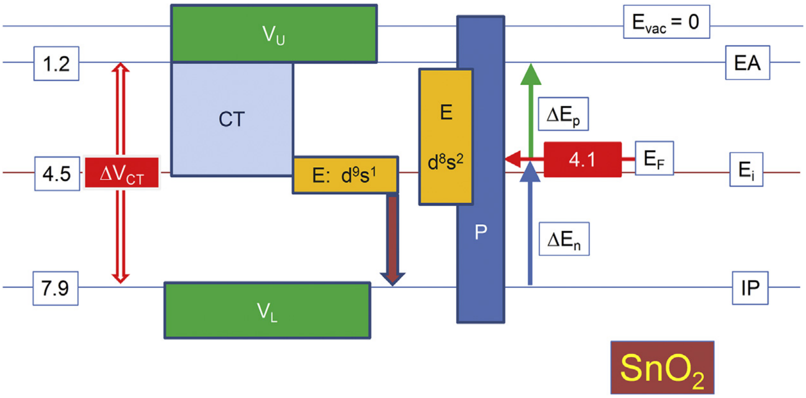

**Figure 16.6** Electronic energy scheme with the polaronic band (P, blue), the upper and lower valence states ($V_U$, $V_L$, green), and the defect levels of the CT (light blue) and the excitons (orange). The orange boxes depict the positions of the excitonic levels for $SnO_2$ and a-$SnO_x$, respectively. The open red arrow marks the ionic energy $\Delta V_{CT}$, and the position of $E_i$ is indicated by the thin red line and that of $E_F$ by a horizontal red arrow. The blue and green arrows mark the excitation energies $\Delta E_n$ and $\Delta E_p$, respectively.

the CIS curve we derive a width of about 3.5 eV. The Sn pDOS (orange vertical bar, $d^8s^2$) for $SnO_2$ which hybridizes with the polaronic band has a width of about 4 eV (see below). For a-$SnO_x$, the Sn pDOS (orange horizontal bar, $4d^95s^1$) indicates an excitonic level which is positioned around the $E_F$ level and is included in the same plot for comparison.

The diagram displays the separation of the ionic valence states (left-hand side) from the covalent polaronic band (blue vertical P band). This is a direct consequence of the ionicity, which implies that the covalent domains and the ionic contributions are electronically decoupled. They are also spatially separated to form covalent and ionic domains [37]. The minimum domain size must be in the order of one unit cell, at least. With our experiments we cannot give further details on the size or morphology of these domains.

The covalent carriers obey Fermi statistics as a result of the quasimetallic behavior of the states within the polaronic band. Accordingly, the Fermi energy varies by doping and regulates the population of the polaronic band. In contrast, in the ionic subsystem the ionic gap $\Delta V_{CT}$ ($=E_{ion}$) is determined by the strength of the Coulomb interaction of the CT dipoles between the neighboring oxygen and metal atoms only. Consequently, the values of $\Delta V_{CT}$ and the position of the upper ($V_U$) and lower ($V_L$) bands of valence states remain fixed in energy even when changes in the Fermi energy (by doping) occur.

### 16.5.2 Intrinsic defects and optical data

To understand the optical data of the $SnO_2$ systems [18] we learn from the energy scheme that the optical gap is caused by the transitions from the lower Sn—O band ($V_L$) into the Fermi energy, i.e., from the ionic level into the metallic states of the covalent systems. Consequently, the optical transitions must occur at the boundary between the spatially separated ionic and covalent regimes. This is another consequence of the fact that the polaronic covalent states and the ionic CT states are electronically and spatially decoupled.

In Fig. 16.6 the optical transitions have an activation energy of $\Delta E_n = (V_L - E_F)$ and are indicated by the blue arrow. Excitations from $E_F$ into the upper Sn—O band ($V_U$) are also possible (green arrow) and can be considered as optical transitions, too. They differ from the former in that they create holes in the covalent polaron band. Their excitation energy is $\Delta E_p = (E_F - V_U)$. In addition, such transitions can occur into the defect states (E and CT) with lower excitation energies. However, these appear only with a lower transition probability due to the localization of the defect states. Their excitation energies correspond to the infrared (IR) absorption and they limit the transparency of the $SnO_2$ in the IR wavelength region. Together, the two optical transitions $\Delta E_n$ and $\Delta E_p$ define the so-called TCO window (as introduced in Section 16.2.1) by absorption in the ultraviolet (UV, blue arrow) and IR (green arrow) regimes.

Furthermore, the CL data [18] can be explained in this diagram as well. The CL data shows a typical emission signal at around 350 nm (3.5 eV), which corresponds to transitions out of the Sn-derived excitonic band E into the $V_L$ band (lower Sn—O band, amber arrow in Fig. 16.6). Consistent with this explanation is the width of the CL signal, which is about 0.9 eV as only the lower states in the excitonic Sn band can contribute to the CL signal.

It should be mentioned that the diagram in Fig. 16.6 also explains the spread of experimental data concerning the value of the optical gap (see Section 16.2 and Table 16.2). Changes in the position of the Fermi energy occur upon doping by experimentally induced dopants (H, OH, etc). These cause shifts of $E_F$ which are different for individual samples and reflect in the optical excitation energies accordingly.

### 16.5.3 Comparison of the defects in $SnO_2$ crystals and thin a-$SnO_x$ films

In the electronic structure of a-$SnO_x$ we find there is only a change of the excitonic defect level. All other features remain unchanged when compared to the single crystalline $SnO_2$.

In Fig. 16.7 we display the XAS pIY data taken at the Sn3d absorption edge together with the respective VB spectra. We compare the corresponding pDOS data of the $SnO_2$ single crystal (red curves) and the a-$SnO_x$ thin film (blue curves). The valence band data are very similar. The pIY spectrum of the $SnO_2$ (100) exhibits its typical shape, namely the low intensity within the first 3 eV above $E_F$. This is an already mentioned characteristic property of $SnO_2$ and $In_2O_3$ single crystals [33]. We discussed the missing of any absorption signal recently in terms of a configuration interaction (CI) model in which the $Sn4d^8 5s^2$ configuration with its filled 5s band is able to hybridize with the quasimetallic polaron band. Such electronic configuration allows no electronic transition from the Sn3d levels into the 5s states as these are filled [32,35]. This is shown in Fig. 16.6 by the vertical orange box which overlaps with the polaron band.

The Sn3d XAS pIY data of the amorphous $SnO_x$ film (Fig. 16.7, blue curve) differs from that of the single crystalline sample, as right at $E_F$ there appears a sharp absorption band. In our explanation the amorphous state stabilizes the $Sn4d^9 5s^1$ configuration

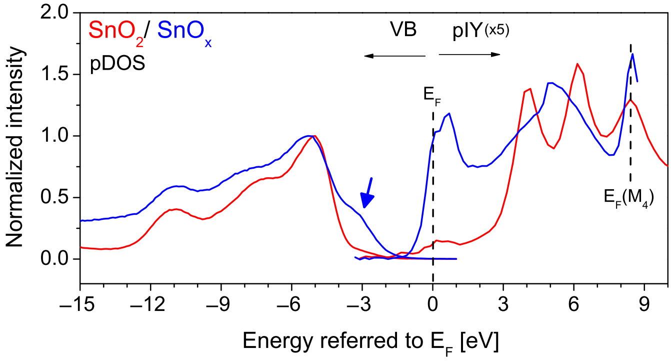

**Figure 16.7** Comparison of pDOS data of an $SnO_2$ single crystal (red) and that of an a-$SnO_x$ thin film (blue) taken at the Sn3d edge. The selected valence band spectra were recorded with 482.7 eV ($SnO_2$) and 480 eV ($SnO_x$). See Fig. 16.5 for further details.

(horizontal orange box in Fig. 16.6). In the Sn3d pIY data it enables an excitonic final state starting from the Sn3d levels, independently of whether the resonant excitation fills the partially filled 4d or 5s states and both resulting final states have an ionic configuration. As a result, it is part of the ionic moiety and hybridization with the polaronic band is no longer possible. Such localized intrinsic $4d^9L(5s5p)^2$ states are further confirmed by the analysis of the corresponding MNN Auger profiles at the Sn3d absorption edge [32].

Another characteristic difference occurs in the valence band data of the a-$SnO_x$ sample. It shows up in the shoulder at −3 eV (blue arrow), which is absent in the $SnO_2$ data, and is explained in the next subsection.

For a-$SnO_x$ the open d-shell $4d^95s^1$ configuration allows the admixture of the Sn5p states to the Sn5s states, which leads to the formation of 5s5p hybridized states. Such contributions appear only in the localized CT states ($4d^9L(5s5p)^1$) and not in the corresponding $4d^9L5s^25p^0$ configuration of the extended bands in the crystalline sample. The contribution of the Sn5s electronic states becomes significant, as they are able to hybridize with the Sn5p states and form Sn5s5p hybridized states. These are thought to cause the giant differences in the Sn3d absorption data between the a-$SnO_x$ and the $SnO_2$ samples due to the preferential $4d^9L5s^15p^1$ contribution, which enhances the localization of the amorphous $SnO_x$. In contrast, in the crystalline $SnO_2$ the lowest electronic excitations occur via the $4d^9L5s^2$ states, which form extended states enabling high mobility of the electrons in Sn- and In-based systems.

In Fig. 16.6 we show the two situations of the excitonic band. The $4d^85s^2$ configuration in crystalline $SnO_2$ hybridizes easily with the polaronic covalent band and becomes integrated in the polaronic band (the right-hand vertical orange band in Fig. 16.6). The $4d^9L5s^15p^1$ configuration is characteristic in amorphous $SnO_x$ and forms an excitonic level (the left-hand horizontal situation in Fig. 16.6).

### 16.5.4 P-type and n-type: ambipolar nature of the charge carriers in $SnO_2$

Concerning the transport properties, we have to consider the type and number of available charge carriers and their mobilities. Starting with the latter, in single crystals higher electron mobilities are observed (see Section 16.2.1). This is consistent with the filled and hybridized $Sn4d^85s^2$ configuration, while in a-$SnO_x$ thin films the excitonic localization of the $4d^9L5s^15p^1$ configuration limits the mobility.

The carrier concentration is only determined by the number of electrons in the polaron band. This explains why a carrier concentration of around $10^{18}$ $cm^{-3}$ is comparable in amorphous and crystalline samples [18,23], as there is no significant change in the position of the energy levels in the two situations in Fig. 16.6.

Furthermore, the experimentally determined optical excitation energy of 2.8 eV (see Section 16.2.3 [23]) is in perfect agreement with the value of $\Delta E_p = 3.0$ eV (green arrow in Fig. 16.6).

In general, the total number of intrinsic charges in the polaron band can be determined via the plasmon energy $\hbar\omega_P$, which considers all available valence electrons per atom. This number can be derived from the density of the material, the crystal structure (shape of the unit cell), and the resulting number of nearest neighbors. For $SnO_2$ a density of valence electrons of $3.3 \times 10^{23}$ $cm^{-3}$ and a corresponding plasmon frequency of $\hbar\omega_P = 21.4$ eV [75] are derived. This means that in our $SnO_2$ crystal only a small fraction of these intrinsic charges contribute to the free charge carrier concentration, based on the experimentally determined carrier densities of around $10^{18}$ $cm^{-3}$ (see Section 16.2.3 [32]). These values differ by more than five orders of magnitude of the charge density given by the plasmon frequency. We attribute the intrinsic carriers to be stabilized as self-trapped polaronic states, and only these charged states may contribute to the transport properties. The major part of the polaronic states is neutral (uncharged): among 1000 polaronic precursors (corresponding to a neutral polaronic site) only a single one leads to a stable charge trapping [76]. This comparison also explains the ease of external doping by ionizing the self-trapped polarons with external charges, as the polaronic band of valence states can be filled up to the value indicated by $\hbar\omega_P$ without further structural rearrangements. For an undoped system we expect (according to our model) the Fermi energy to be found at the $E_i$ level.

The analysis of the energy diagram in Fig. 16.6 shows that the excitation energies for $\Delta E_n$ and $\Delta E_p$ are comparable, in particular when the difference between $E_F$ and $E_i$ becomes negligible. This suggests the coexistence of p-type and n-type charge carriers and an ambipolar conductivity behavior in $SnO_2$.

However, thermally excited carriers are very unlikely due to the high values of these excitation energies. The reference levels of the polaronic ($E_F$) and the ionic ($E_i$) subsystems need to be shifted significantly against each other to change that situation. This can be achieved by a shift of the Fermi energy within the polaronic continuous band. In our model it is important to understand that only the band-like quasimetallic polaronic states are involved when the number of carriers is changed, and the energy separation between $E_F$ and the $V_U$, $V_L$ states will vary accordingly. As a result, both n-type and p-type conductivity can be achieved depending on whether $E_F$ has been shifted down or up with respect to $E_i$. The p-type conductivity is favored when $E_F$ is shifted upward in energy (with respect to $E_{Vac}$). Then electronic excitations from $E_F$ into the upper $V_U$ band become possible and enhance the hole concentration in the polaronic band. This mechanism for the stabilization of either p-type or n-type charge carriers in the polaronic band is not caused by external dopants; rather, in the context of the electronic scheme of Fig. 16.6, the ambipolar character is a consequence of the intrinsic electronic properties.

Another way to shift $E_i$ versus $E_F$ proceeds via local dipole momenta. A local dipole shifts only the ionic subsystem (relative to $E_{vac}$) and leaves the covalent moiety (i.e., the position of $E_F$) unchanged. Such local dipole momenta can be created by vacancies. Of particular importance is the oxygen vacancy $V_o^{\cdot}$ dipole, which shifts the ionic $V_U$, $V_L$ levels upward (i.e., towards $E_{vac}$) with respect to the $E_F$ of the quasimetallic band ($E_i < E_F$). It thus stabilizes the n-type channel without significant changes in the carrier densities or the electronic gap. In consequence, understoichiometric preparation conditions which prefer the formation of oxygen vacancies $V_o^{\cdot}$ will always end in n-type modification.

In contrast, p-type conductivity is favored by the formation of $V'_{Sn}$ vacancies which shift the ionic moiety downwards (with respect to $E_{vac}$) in energy ($E_i > E_F$). For p-type applications it is a good idea to anneal the oxygen vacancies in an oxygen atmosphere and/or to keep the devices in air. This ensures that the number of $V^{\cdot}_{o}$ vacancies becomes smaller than that of $V'_{Sn}$ vacancies. To enhance the p-type stability, negatively charged vacancies have to be implemented. The formation of $V'_{Sn}$ will be less probable, and more complex vacancy—interstitial combinations will be more effective. This was proposed recently in terms of dual acceptor codoping [21]; see Section 16.2.1). Generally, a single dipole momentum (per unit cell) can shift the ionic levels by 1 eV. In contrast, a change of $\Delta E_F = 0.1$ eV requires an increase of the carrier densities of several orders of magnitude.

Dipole momenta can be monitored by shifts in the IP of the core levels involved. Preparation-induced variations in the positions of the Sn3d and/or O1s core levels are most probably caused by the presence of vacancies and their associated dipole momenta. The same is true for changes in the FWHM of the XPS signals and the often-observed presence of shoulders or satellite features. In the valence band data in Fig. 16.7, particularly in the spectrum of the a-$SnO_x$ sample, the shoulder marked by the blue arrow is attributed to such a satellite process (see Section 16.3.3). Here the potential energy of the dipole is taken up by an emitted photoelectron and appears with a higher kinetic energy. Interpretation of such shifted core levels in terms of surface band bending is most probably erroneous.

In conclusion, in the transport properties we distinguish intrinsic polaronic charge carriers, thermally activated carriers, and potential induced charge carriers. The intrinsic carrier density is determined by the carriers in the polaronic bands. They cause the metallic-like activation energies in temperature dependent conductivity studies (see Section 16.2.1). Thermally activated carriers are unlikely due to the high excitation energies. Another mechanism comes into play, as local dipole momenta can shift the ionic levels with respect to the quasimetallic covalent moiety. Depending on the dipole orientation, they may favor either n-type or p-type conductivity. Such dipoles are influenced by oxygen vacancies or Sn vacancies, respectively.

To enhance the mobility, one should avoid the formation of the $4d^9L5s^15p^1$ exciton and reduce the ability of forming 5s—5p hybridization. Instead, the band-like $5s^25p^0$ configuration should be favored. Hitherto, however, there has been a general assumption that the unoccupied states are primarily s-like and modifications in the electronic structure are mostly attributed to the occupied states instead.

We like to emphasize that an ability for p-type conduction is an intrinsic property of a-$SnO_x$ and $SnO_2$.

Our model explains the general failure in the search for shallow acceptors in the TCOs (see e.g., [11,77]), as it is based on intrinsic electronic parameters only and there is no need for shallow acceptors. Furthermore, the stability of the electronic properties explains why these systems are easy to mix and easy to dope, as the other characteristic parameters stay unchanged in essential.

## 16.6 Summary

The resPES data of $SnO_2$ unravel the significance of intrinsic electronic defects. They are caused by polarization, lattice relaxations, and CT processes. In a novel interpretation of the electronic and optical properties, they give evidence that $SnO_2$ is not a conventional semiconductor: it does not have a homogeneous charge distribution and has no thermally activated carrier concentration. It rather is a prototype system of an inhomogeneous, mixed-ionic-covalent semiconductor in which polarization, relaxation, and self-trapping phenomena cause the stabilization of electronic intrinsic defects. We identify such defects and describe many of the fascinating properties of the $SnO_2$ and a-$SnO_x$ systems with this approach. These include the most significant properties of $SnO_2$: the optical and electronic gaps, the ionicity factor, the carrier density, and the mobility.

In Table 16.2 we summarize some of the specific values of $SnO_2$ single crystals and compare them to other TCO materials. This characteristic data are derived from our novel data analysis described in this chapter. Included are the data for the iconicity factor $f_i$, the intensity dip ($I_{Pol}$), and the width ($\Delta E_{Pol}$) of the polaronic band, the width of the CT band ($\Delta W_{CT}$), the width of the ionic band ($\Delta V_{CT}$), and the total energy width ($E_{total}$).

In addition, some data from the literature are given for the charge carrier concentration (n), the mobility (μ), and the optical gap ($E_{opt}$). The value of the latter depends strongly on the method applied. This is exemplarily given for $TiO_2$, where optical gaps in the range of 3.0−3.5 eV were found by ultraviolett-visible spectroscopy (UV−VIS), diffuse reflectance, or ellipsometry techniques [72−74]. In accordance with our model presented in this chapter, the optical gap is caused by transitions from the lower ionic metal−oxygen band ($V_L$) into the metallic states of the covalent systems (at $E_F$) occurring at the boundary between the spatially separated ionic and covalent regimes (see Section 16.5.2).

## Acknowledgments

The $SnO_2$ single crystals were provided by Valentina Scherer, Alica Krapf, and Stephan Machulik (Humboldt University Berlin). The a-$SnO_x$ samples were fabricated and made available by Pedro Barquinha and Elvira Fortunato (New University of Lisbon). Discussions with Zbigniew Galazka (Leibniz Institute for Crystal Growth) and Götz Seibold are acknowledged. The authors would like to acknowledge the technical assistance of Guido Beuckert and thank the Bessy II staff for their support during beam-times. This work was in part financially supported by German Research Foundation (DFG) within the project SCHM 745/31-1.

## References

[1] M. Batzill, U. Diebold, The surface and materials science of tin oxide, Prog. Surf. Sci. 79 (2−4) (2005) 47−154.

[2] D-won Choi, W.J. Maeng, J.-S. Park, The conducting tin oxide thin films deposited via atomic layer deposition using Tetrakis-dimethylamino tin and peroxide for transparent flexible electronics, Appl. Surf. Sci. 313 (2014) 585−595.

[3] M. Grundmann, F. Klüpfel, R. Karsthof, P. Schlupp, F.-L. Schein, D. Splith, C. Yang, S. Bitter, H. von Wenckstern, Oxide bipolar electronics: materials, devices and circuits, J. Phys. D Appl. Phys. 49 (2016), 213001.

[4] J.P. Correa Baena, L. Steier, W. Tress, M. Saliba, S. Neutzner, T. Matsui, F. Giordano, T.J. Jacobsson, A.R.S. Kandada, S.M. Zakeeruddin, A. Petrozza, A. Abate, M.K. Nazeeruddin, M. Grätzel, A. Hagfeldt, Highly efficient planar perovskite solar cells through band alignment engineering, Energy Environ. Sci. 8 (2015) 2928−2934.

[5] W. Göpel, K.D. Schierbaum, $SnO_2$ sensors: current status and future prospects, Sensors Actuators B 26−27 (1995) 1−12.

[6] A. Oprea, E. Moretton, N. Bârsan, W.J. Becker, J. Wöllenstein, U. Weimar, Conduction model of thin films based on conductance and Hall effect measurements, J. Appl. Phys. 100 (2006), 033716.

[7] N. Taguchi, Gas detecting Device, 1971. U.S. Patent No. 3,631,436.

[8] Q. Tian, Y. Tian, Z. Zhang, L. Yang, S-ichi Hirano, Facile synthesis of ultrasmall tin oxide nanoparticles embedded in carbon as high-performance anode for lithium-ion batteries, J. Power Sources 269 (2014) 479−485.

[9] S.-H. Lee, J.-M. Choi, J.-H. Lim, J. Park, J.-S. Park, A study on the thermoelectric properties of ALD-grown aluminum-doped tin oxide with respect to nanostructure modulations, Ceram. Int. 44 (2018) 1978−1983.

[10] M.W.J. Prins, K.-O. Grosse-Holz, J.F.M. Cillessen, L.F. Feiner, Grain-boundary-limited transport in semiconducting SnO thin films: model and experiments, J. Appl. Phys. 83 (1998) 888−893.

[11] A.K. Singh, A. Janotti, M. Scheffler, C.G. van de Walle, Sources of electrical conductivity in $SnO_2$, Phys. Rev. Lett. 101 (2008), 055502.

[12] K. Nomura, H. Ohta, A. Takagi, T. Kamiya, M. Hirano, H. Hosono, Room-temperature fabrication of transparent flexible thin-film transistors using amorphous oxide semiconductors, Nature 432 (2004) 488−492.

[13] E.M.C. Fortunato, L.M.N. Pereira, P.M.C. Barquinha, A.M. Botelho do Rego, G. Gonçalves, A. Vilà, J.R. Morante, R.F.P. Martins, High mobility indium free amorphous oxide thin film transistors, Appl. Phys. Lett. 92 (2008), 222103.

[14] N. Nguyen, B. McCall, R. Alston, W. Collis, S. Iyer, The effect of annealing temperature on the stability of gallium tin zinc oxide thin film transistors, Semicond. Sci. Technol. 30 (2015), 105004.

[15] B. Falabretti, J. Robertson, Electronic structures and doping of $SnO_2$, $CuAlO_2$, and $CuInO_2$, J. Appl. Phys. 102 (2007), 123703.

[16] M. Feneberg, C. Lidig, K. Lange, R. Goldhahn, M.D. Neumann, N. Esser, O. Bierwagen, M.E. White, M.Y. Tsai, J.S. Speck, Ordinary and extraordinary dielectric functions of rutile $SnO_2$ up to 20 eV, Appl. Phys. Lett. 104 (2014), 231106.

[17] A. Schleife, J.B. Varley, F. Fuchs, C. Rödl, F. Bechstedt, P. Rinke, A. Janotti, C.G. Van de Walle, Tin dioxide from first principles: quasiparticle electronic states and optical properties, Phys. Rev. B 83 (2011), 035116.

[18] Z. Galazka, R. Uecker, D. Klimm, K. Irmscher, M. Pietsch, R. Schewski, M. Albrecht, A. Kwasniewski, S. Ganschow, D. Schulz, C. Guguschev, R. Bertram, M. Bickermann, R. Fornari, Growth, characterization, and properties of bulk $SnO_2$ single crystals, Phys. Status Solidi A 211 (2014) 66−73 (and references therein).

[19] H.S. So, J.-W. Park, D.H. Jung, K.H. Ko, H. Lee, Optical properties of amorphous and crystalline Sb-doped $SnO_2$ thin films studied with spectroscopic ellipsometry: optical gap energy and effective mass, J. Appl. Phys. 118 (2015), 085303.

[20] M.P. Subramaniam, G. Arunachalam, R. Kandasamy, P. Veluswamy, I. Hiroya, Effect of pH and annealing temperature on the properties of tin oxide nanoparticles prepared by sol−gel method, J. Mater. Sci. Mater. Electron. 29 (2018) 658−666.

[21] Y. Zhou, W. Xu, S. Lv, C. Yin, J. Li, B. Zhu, Y. Liu, C. He, GaN co-doping and annealing on the optoelectronic properties of $SnO_2$ thin films, J. Alloy. Comp. 732 (2018) 555−560.

[22] D.-W. Choi, J.-S. Park, Highly conductive $SnO_2$ thin films deposited by atomic layer deposition using tetrakis-dimethyl-amine-tin precursor and ozone reactant, Surf. Coat. Technol. 259 (2014) 238−243.

[23] E. Fortunato, R. Barros, P. Barquinha, V. Figueiredo, S.-H.K. Park, C.-S. Hwang, R. Martins, Transparent p-type $SnO_x$ thin film transistors produced by reactive rf magnetron sputtering followed by low temperature annealing, Appl. Phys. Lett. 97 (2010), 052105.

[24] M. Dou, C. Persson, Comparative study of rutile and anatase $SnO_2$ and $TiO_2$: band-edge structures, dielectric functions, and polaron effects, J. Appl. Phys. 113 (2013), 083703.

[25] H.J. van Daal, The static dielectric constant of $SnO_2$, J. Appl. Phys. 39 (1968) 4467−4469.

[26] S. Lany, A. Zunger, Dopability, intrinsic conductivity, and nonstoichiometry of transparent conducting oxides, Phys. Rev. Lett. 98 (2007), 045501.

[27] W.M.H. Oo, S. Tabatabaei, M.D. McClusky, J.B. Varley, A. Janotti, C.G. Van de Walle, Hydrogen donors in $SnO_2$ studied by infrared spectroscopy and first-principles calculations, Phys. Rev. B 82 (2010), 193201.

[28] J.B. Varley, A. Janotti, A.K. Singh, C.G. Van de Walle, Hydrogen interactions with acceptor impurities in $SnO_2$: first-principles calculations, Phys. Rev. B 79 (2009), 245206.

[29] E. Shanthi, V. Dutta, A. Banerjee, K.L. Chopra, Electrical and optical properties of undoped and antimony-doped tin oxide films, J. Appl. Phys. 51 (1980) 6243−6251.

[30] D.O. Scanlon, G.W. Watson, On the possibilty of p-type $SnO_2$, J. Mater. Chem. 22 (2012) 25236−25245.

[31] S. Pan, S. Wang, Y. Zhang, Y. Luo, F. Kong, S. Xu, J. Xu, G. Li, p-type conduction in nitrogen doped $SnO_2$ films grown by thermal processing of tin nitride films, Appl. Phys. A Mater. Sci. Process. 109 (2012) 267−271.

[32] J. Haeberle, S. Machulik, C. Janowitz, R. Manzke, D. Gaspar, P. Barquinha, D. Schmeißer, Gap states in the Electronic Structure of $SnO_2$ single crystals and amorphous $SnO_x$ thin films, J. Appl. Phys. 120 (2016), 105101.

[33] D. Schmeißer, J. Haeberle, Intrinsic localized gap states in IGZO and its parent single crystalline TCOs, Thin Solid Films 603 (2016) 206−211.

[34] J. Haeberle, M. Richter, Z. Galazka, C. Janowitz, D. Schmeißer, Resonant photoemission at the O1s threshold to characterize $In_2O_3$ single crystals, Thin Solid Films 555 (2014) 53−56.

[35] J. Haeberle, S. Brizzi, D. Gaspar, P. Barquinha, Z. Galazka, D. Schulz, D. Schmeißer, A spectroscopic comparison of IGZO thin films and the parent $In_2O_3$, $Ga_2O_3$, and ZnO single crystals, Mater. Res. Express 3 (2016), 106302.

[36] M. Michling, D. Schmeißer, Resonant Photoemission at the O1s threshold to characterize $\beta$-$Ga_2O_3$ single crystals, in: IOP Conference Series: Materials Science and Engineering, vol. 34, 2012, 012002.

[37] D. Schmeißer, K. Henkel, Intrinsic electronic defects and multiple-atom processes in the oxidic semiconductor $Ga_2O_3$, J. Appl. Phys. 123 (2018), 161596.

[38] D. Schmeißer, J. Haeberle, P. Barquinha, D. Gaspar, L. Pereira, R. Martins, E. Fortunato, Electronic structure of amorphous ZnO films, Phys. Status Solidi C 11 (2014) 1476−1480.

[39] A.A. Bolzan, C. Fong, B.J. Kennedy, C.J. Howard, Structural studies of rutile-type metal dioxides, Acta Crystallogr. B 53 (1997) 373−380.

[40] G.B. Palmer, K.R. Poeppelmeier, Phase relations, transparency and conductivity in $Ga_2O_3$-$SnO_2$-ZnO, Solid State Sci. 4 (2002) 317−322.

[41] G.B. González, Investigating the defect structures in transparent conducting oxides using X-ray and neutron scattering techniques, Materials 5 (2012) 818−850.

[42] K. Matsumoto, S. Kaneko, K. Takagi, Crystal-growth of $SnO_2$ by chemical-transport method, J. Cryst. Growth 40 (1977) 291−297.

[43] R. Nitsche, Crystal growth by chemical transport reactions. 4. New results on growth of binary ternary and mixed-crystal chalcogenides, J. Phys. Chem. Solid. (1967) 215.

[44] B.I. Nolang, M.W. Richardson, Transport flux function - new method for predicting rate of chemical-transport in closed systems - theoretical study of systems and experimental conditions for chemical-transport of $SnO_2$, J. Cryst. Growth 34 (1976) 205−214.

[45] A. Toshev, P. Peshev, Preparation of $SnO_2$ single crystals by chemical transport using $Cl_2$ and $CCl_4$ as transporting agents, Mater. Res. Bull. 23 (1988) 1045−1051.

[46] G. Behr, G. Krabbes, J. Werner, P. Dordor, J.-P. Doumerc, Crystal growth and electrical properties of Sb-doped $SnO_2$ single crystals, Phys. Status Solidi A 118 (1990) K91−K94.

[47] G.R. Patzke, M. Binnewies, U. Nigge, H.-D. Wiemhöfer, Chemical transport of solid solutions. 8. Transport phenomena and ionic conductivity in the $In_2O_3/SnO_2$ system, Z. Anorg. Allg. Chem. 626 (2000) 2340−2346.

[48] R. Ertuğrul, A. Tataroğlu, Influence of temperature and frequency on dielectric permittivity and ac conductivity of Au/$SnO_2$/n-Si (MOS) structures, Chin. Phys. Lett. 29 (2012), 077304.

[49] D.V. Nazarov, N.P. Bobrysheva, O.M. Osmolovskaya, M.G. Osmolovsky, V.M. Smirnov, Atomic layer deposition of tin oxide: a review, Rev. Adv. Mater. Sci. 40 (2015) 262−275.

[50] D. Schmeißer, P. Hoffmann, G. Beuckert, Electronic properties of the interface formed by $Pr_2O_3$ growth on Si(001), Si(111) and SiC(0001) surfaces, in: E. Zschech, C. Whelan, T. Mikolajick (Eds.), Materials for Information Technology, Devices, Interconnects and Packaging, Series: Engineering Materials and Processes, Spinger, London, 2005, pp. 449−460.

[51] C. Janowitz, T. Zandt, L. Dudy, R. Manzke, G. Reichardt, A new UV and VUV beamline for angular resolved photoemission with high resolution and at low energy, Nucl. Instrum. Methods Phys. Res. A 693 (2012) 160−165.

[52] J.-M. Themlin, M. Chtaib, L. Henrard, P. Lambin, J. Darville, J.-M. Gilles, Characterization of tin oxides by x-ray-photoemission spectroscopy, Phys. Rev. B 46 (1992) 2460−2466.

[53] D. Schmeißer, C. Janowitz, Ionicity of ZnO − a key system for transparent conductive oxides, Europhys. Lett., 2018 (submitted).

[54] D. Schmeißer, J. Haeberle, M. Richter, P. Brazda, Spin state and satellite structures of ε-$Fe_2O_3$ as determined by resonant photoelectron spectroscopy, Nucl. Instrum. Methods Phys. Res. B 364 (2015) 127−131.

[55] C.X. Kronawitter, M. Kapilashrami, J.R. Bakke, S.F. Bent, C.-H. Chuang, W.-F. Pong, J. Guo, L. Vayssieres, S.S. Mao, $TiO_2$-$SnO_2$:F interfacial electronic structure investigated by soft x-ray absorption spectroscopy, Phys. Rev. B 85 (2012), 125109.

[56] A. Lussier, J. Dvorak, Y.U. Idzerda, S.B. Ogale, S.R. Shinde, R.J. Choudary, T. Venkatesan, Comparative x-ray absorption spectroscopy study of Co-doped $SnO_2$ and $TiO_2$, J. Appl. Phys. 95 (2004) 7190−7191.

[57] M.A. Mäki-Jaskari, T.T. Rantala, Band structure and optical parameters of the $SnO_2$(110) surface, Phys. Rev. B 64 (2001), 075407.

[58] V. Scherer, C. Janowitz, A. Krapf, H. Dwelk, D. Braun, R. Manzke, Transport and angular resolved photoemission measurements of the electronic properties of $In_2O_3$ bulk single crystals, Appl. Phys. Lett. 100 (2012), 212108.

[59] M. Batzill, K. Katsiev, J.M. Burst, U. Diebold, A.M. Chaka, B. Delley, Gas-phase-dependent properties of $SnO_2$ (110), (100), and (101) single-crystal surfaces: structure, composition, and electronic properties, Phys. Rev. B 72 (2005), 165414.

[60] V.M. Jiménez, G. Lassaletta, A. Fernández, J.P. Espinós, F. Yubero, A.R. González-Elipe, L. Soriano, J.M. Sanz, D.A. Papaconstantopoulos, Resonant photoemission characterization of SnO, Phys. Rev. B 60 (1999) 11171−11179.

[61] P. Glatzel, M. Sikora, M. Fernandez-Garcia, Resonant X-ray spectroscopy to study K absorption pre-edges in 3d transition metal compounds, Eur. Phys. J. Spec. Top. 169 (2009) 207−214.

[62] U. Fano, Effects of configuration interaction on intensities and phase shifts, Phys. Rev. 124 (1961) 1866−1878.

[63] M. Richter, U. Starke, D. Schmeißer, Multiple Auger processes in graphene, J. Electron. Spectrosc. Relat. Phenom. 192 (2014) 1−6.

[64] J.C. Phillips, Ionicity of the chemical bond in crystals, Rev. Modern Phys. 42 (1970) 317−356.

[65] Z. Galazka, K. Irmscher, M. Pietsch, T. Schulz, R. Uecker, D. Klimm, R. Fornari, Effect of heat treatment on properties of melt-grown bulk $In_2O_3$ single crystals, CrystEngComm 15 (2013) 2220−2226.

[66] Z. Galazka, K. Irmscher, R. Uecker, R. Bertram, M. Pietsch, A. Kwasniewski, M. Naumann, T. Schulz, R. Schewski, D. Klimm, M. Bickermann, On the bulk $\beta$-$Ga_2O_3$ single crystals grown by the Czochralski method, J. Cryst. Growth 404 (2014) 184−191.

[67] D. Klimm, S. Ganschow, D. Schulz, R. Fornari, The growth of ZnO crystals from the melt, J. Cryst. Growth 310 (2008) 3009−3013.

[68] C. Das, M. Richter, M. Tallarida, D. Schmeißer, Electronic properties of atomic layer deposited films, anatase and rutile $TiO_2$ studied by resonant photoemission spectroscopy, J. Phys. D Appl. Phys. 49 (2016), 275304.

[69] M.C.K. Sellers, E.G. Seebauer, Measurement method for Carrier concentration in $TiO_2$ via the Mott-Schottky approach, Thin Solid Films 519 (2011) 2103−2110.

[70] H. Tang, K. Prasad, R. Sanjinès, P.E. Schmid, F. Lévy, Electrical and optical properties of $TiO_2$ anatase thin films, J. Appl. Phys. 75 (1994) 2042−2047.

[71] L. Forro, O. Chauvet, D. Emin, L. Zuppiroli, H. Berger, F. Lévy, High mobility n-type charge carriers in large single crystals of anatase ($TiO_2$), J. Appl. Phys. 75 (1994) 633−635.

[72] K. Nagaveni, M.S. Hegde, N. Ravishankar, G.N. Subbanna, G. Madras, Synthesis and structure of nanocrystalline $TiO_2$ with lower band gap showing high photocatalytic activity, Langmuir 20 (2004) 2900−2907.

[73] A.B. Murphy, Band-gap determination from diffuse reflectance measurements of semiconductor films, and application to photoelectrochemical water-splitting, Sol. Energy Mater. Sol. Cell. 91 (2007) 1326−1337.

[74] G.E. Jellison Jr., L.A. Boatner, D. Budai John, B. Jeong, D.P. Norton, Spectroscopic ellipsometry of thin film and bulk anatase ($TiO_2$), J. Appl. Phys. 93 (2003) 9537−9541.

[75] J.A. Bittencourt, Fundamentals of Plasma Physics, Springer, New York, 2004.

[76] O.A. Dicks, A.L. Shluger, Theoretical modeling of charge trapping in crystalline and amorphous $Al_2O_3$, J. Phys. Condens. Matter 29 (2017), 314005.

[77] A. Kyrtsos, M. Matsubara, E. Bellotti, On the feasibility of p-type $Ga_2O_3$, Appl. Phys. Lett. 112 (2018), 032108.

# Index

*Note:* 'Page numbers followed by "f" indicate figures and "t" indicate tables.'

**A**

$A_2B_6$ compounds
  luminescence of, 304t
  physical properties of, 305t
  scintillation characteristics of, 308t
  scintillators, 312–318
Absorption edge, 95f
AlAs, 194
Alkaline texture morphology, 63f
Aluminum nitride (AlN) crystals
  bulk crystal growth, 401–402
  characterization, 415–417
  evaporation rates, 408t
  full widths at half-maximum (FWHM), 421t
  growth on
    AlN seeds, 403–404
    SiC seeds, 404–405
  growth process of, 410–417
  growth rate
    on nitrogen pressure, 413–414
    on source-to-seed distance, 414
  high reactivity of vapors, 406–407
  impurities measured by SIMS, 418f
  influence of
    residual oxygen, 407–408
    silicon and carbon, 408–410
  low AlN evaporation coefficients, 407
  low nitrogen sticking coefficients, 405–406
  materials, 406t
  optimization of growth zone, 411–413
  preparation of freestanding AlN wafers, 422–423
  relative properties of, 416t
  SiC substrate evaporation method, 418–423
  sublimation growth of, 403–423
  substrate orientation, 414–415
  thermal expansion coefficients, 405t
  X-ray diffraction, 420f
Aluminum oxide ($Al_2O_3$)
  applications, 472–483
  concise description of methods, 449–452
  $Er^{3+}$ lasers, 483
  growth methods, 447–452
  interferometers, 479–480
  luminescent pressure transducers, 481–482
  luminophor screens, 480–481
  properties, 454–471, 466t–467t
  sapphire optical disks, 479
  sapphire window sensor, 479
  sapphire window withdrawal, 479
  substrate (wafer), 472
  temperature gradient, 452t
  thermoluminescent detectors (TLDs), 477–478
  $Ti^{3+}$ scintillators, 475–476
  titanium-doped sapphire, 482
  Verneuil method, 450
Ammonothermal method
  bulk crystal growth, 357
  computer modeling, 368
  fundamentals method
    crystals growth, 359–361
    solubility, 357–358
    solvent, 358–359
  gallium nitride (GaN) crystals, 424
  growth rate, 367–368
  growth systems
    anvil-style pressure vessel, 362
    externally heated autoclave, 361
  point defects
    doping, 366–367
    gallium vacancies, 366
    impurities, 364–365
  Angle-resolved photoelectron spectroscopy (ARPES), 556–558

Anvil-style pressure vessel, 362
Argon consumption, 67−68
ARPES. *See* Angle-resolved photoelectron spectroscopy (ARPES)
Arsenide III
  AlAs, 194
  applications, 194−195
  availability, 194−195
  BAs, 194
  characterization, 196−202
  chemical properties, 190−193
  crystal defects, 196−197
  crystal structure of, 187f
  crystallographic properties, 183−190
  electrical properties, 197−200
  growth of GaAs crystals, 202−227
  InAs, 195
  mechanical and surface specification of wafers, 200−202
  physical properties, 182−183
  substrate requirements for, 196−202
  TlAs, 195
Artificial diamond, 332−337
Artificial neural networks (ANNs), 215−219
Axial distribution, 37f

**B**

Bachmann diagram, 335f
Band structure, of Ge, 92f
BAs, 194
β-$Ga_2O_3$ laser crystals, 495
Binary phase diagram, 131−132
Boltzmann equations, 339−340
Boron oxide, 283−284
Bridgman crystal growth
  chalcogenide series, 323f
  gallium oxide ($Ga_2O_3$), 502−504, 511
  germanium (Ge), 97−98
  vapor-pressure-controlled, 281−282
  zinc selenide, 307f
Bulk crystal growth
  aluminum nitride (AlN) crystals, 401−402
  ammonothermal method, 357
  gallium nitride (GaN) crystals, 401−402
  indium oxide ($In_2O_3$), 525−528
  silicon carbide (SiC), 134−139
Bulk microdefects (BMDs), 23

**C**

Cadmium telluride (CdTe)
  applications and requirements, 273−274
  benefits of computer modeling, 288−289
  boron oxide encapsulated vertical Bridgman, 283−284
  CdZnTe crystals, 292−293
  crystal growth from melt, 280−284
  directional solidification (DS), 280−281
  electrooptics, 273
  gamma-rays, 292−293
  high-pressure Bridgman (HPB) method, 282−283
  infrared imaging, 273
  IR devices, substrates for, 293
  liquid-encapsulated Cz, 280
  postgrowth thermal treatments, 289−291
  solar cells, 274
  synthesis of polycrystalline material, 278−279
  technologies/processes, 280−287
  thermodynamic properties, 274−278
  traveling heater method, 286−287
  vapor-phase growth, 284−286
  vapor-pressure-controlled Bridgman growth, 281−282
  X-ray and gamma-ray detector application, 292−293
Cadmium zinc telluride (CdZnTe), 292−293
Carbon additives, 375−376
CCz. *See* continuous Cz (CCz)
CF-PVT. *See* Continuous feed PVT (CF-PVT)
Chemical polishing, 97t
Chemical vapor deposition (CVD)
  grown polysilicon chucks, 17f
  polysilicon surface, 29f
Chloride HVPE, 424−425
Christoffel's equation, 463−464
Codoping, ML silicon, 80−81
Computer modeling
  ammonothermal method, 368
  cadmium telluride (CdTe), 288−289
  diamond, 338−343
  indium phosphide (InP), 250−252
  silicon carbide (SiC), 143−147
  silicon single crystals, 36

Concise description of methods
  Cz method, 450
  HDSM, 450
  HEM, 450
  Kyropoulos (Ky), 450
  Verneuil method, 450
  vertical Bridgman (VB) method, 450
Constitutional supercooling
  cells and grains, 49f
  critical concentration and velocity in, 110
  model of, 47f
  nucleation of dislocations, 48f
  silicon single crystals, 47f
Continuous Cz (CCz), 44–45, 69–70
Continuous feed PVT (CF-PVT), 137
Corrosion resistance, 469t
Cryogenic test, 310–311
Crystal defects
  arsenide III, 196–197
  description and derivation of $SnO_2$, 559–560
  energy level of, 199f
  intrinsic electronic, 558–561, 563–564
  ionic and covalent, 560–561
  optical data, 563–564
Crystal growth
  ammonothermal method, 359–361
  cadmium telluride (CdTe), 280–284
  dislocation-free. *See* Dislocation-free crystal growth
  germanium (Ge) crystals, 97–102
  indium oxide ($In_2O_3$), 524–529
  InP
    apparatus, 250
    dislocation density, 245–246
    doping uniformity, 245
    twinning, 243–245
  by SSM, 425–439
  techniques in GaAs, 205–210
  tin oxide ($SnO_2$), 547–552
Crystal-originated particles (COPs), 30, 111
Crystal pulling methods
  indium phosphide (InP), 252–254
  gallium oxide ($Ga_2O_3$), 500–502
Czochralski (Cz) method
  argon consumption, 67–68
  coated crucible, 69
  concise description of methods, 450
  continuous Cz (CCz), 69–70
  dislocation-free crystal growth, 101–102
  gallium oxide ($Ga_2O_3$), 500–501, 508–510
  Ge crystals growth, 98–100
  graphite degradation, 67–68
  hot-zone designs, 64
  liquid encapsulation, 206–207
  method, 57–58, 63–71
  multiple charges, 68–69
  power consumption, 65–66
  process steps, 26f
  pulling rate, 65–66
  quality improvement, 70–71
  silicon growth, 58f, 70f

**D**

Dash necking technique, 35–36, 101
Density-functional technique (DFT), 342f
Density functional theory, 370
Diamond
  alpha parameters, 338f–339f
  Bachmann diagram, 335f
  bandgap materials, 333f
  benefits of computer modeling, 338–343
  crystal surfaces via growth parameters, 338
  DFT calculation, 342f
  doping, 344–345
  growth, artificial, 332–337
  growth technique and applications, 346–347
  high-temperature growth, 334f
  large-size wafer production, 343–344
  material constants of, 332t
  microwave plasma chemical vapor deposition, 334f
  MWCVD apparatus, 337f
  processing techniques, 345–346
  seed crystals of, 343t
Digital X-ray radiography, 319t
Direct synthesis, 248–250
Directional solidification (DS)
  cadmium telluride (CdTe), 280–281
  different technologies, 72f
  method, 71–81
  technology and their dimensions, 61t
Dislocation-free crystal growth
  dash necking, 101
  new Cz method, 101–102
  seeding, 100–101

Dislocation-free crystal growth (*Continued*)
  temperature distribution, 103f
  Dopant concentration, 37f
Doping
  diamond, 344–345
  gallium oxide ($Ga_2O_3$), 513–515
  indium oxide ($In_2O_3$), 536–538
  indium phosphide (InP), 257–267
  silicon carbide (SiC), 147–164
  silicon single crystals, 36–41
  tin oxide ($SnO_2$), 549

**E**

Edge-defined film-fed growth (EFG), 501–502, 501f, 505–507
Electron paramagnetic resonance (EPR), 438
Electronic energy diagram, 561–567
Electronic materials, 1
Electrooptics, 273
Epitaxial thin film growth, 528–529
Equation of state (EOS), 358
$Er^{3+}$ lasers, 483
Etch pit density (EPD) mappings, 73–74
Externally heated autoclave, 361

**F**

Feedstock synthesis, 202–205
Fermi level, 532f
Field-effect transistors (FETs), 493–494
Floating zone (FZ) method
  gallium oxide ($Ga_2O_3$), 504
  silicon growth, 58f
Flow pattern defects (FPDs), 30
Fourier transform spectroscopy, 366
Franck–Condon energy diagram, 322f
Full widths at half-maximum (FWHM), 421t
Furnace design, 219–220

**G**

Gallium arsenide (GaAs) crystal
  arsenide III, 194–195
  growth techniques, 205–210, 206f
  high-pressure synthesis, 204–205
  liquid encapsulation Czochralski, 206–207
  low-pressure synthesis, 203–204
  modeling approach, 213–219
  modeling of transport phenomena, 210–227
  synthesis of feedstock, 202–205
  vertical gradient freeze, 207–210
  wafer and sample preparation, 227–229
Gallium nitride (GaN) crystals
  ammonothermal methods, 357–369, 424
  of applications, 351–354
  ball-and-stick model of, 352f
  bandgap diagram of, 352f
  bulk crystal growth, 401–402
  chloride hydride vapor phase epitaxy, 424–425
  crystal growth by SSM, 425–439
  electron paramagnetic resonance (EPR), 438
  evaporation rate on, 428f
  experimental setup and results, 426–433
  Hall measurements, 436–438
  high nitrogen pressure solution growth, 423
  HVPE, 380–388
  impurity, 366t
  initial stage of, 433–435
  MOCVD, 378f
  Na-flux methods, 369–380, 424
  photoluminescence, 436–438
  physical properties of, 435–438
  pressure dependence of, 355f
  Raman measurements, 436–438
  single crystal growth, 354–357
  solubility of, 358f
  SSD growth of, 439
  SSM, 402–439, 403f, 428f
  sublimation growth of, 423–439
  X-ray characterization, 435–436
Gallium oxide ($Ga_2O_3$)
  applications and requirements of, 487–498
  Bridgman crystal growth, 502–504, 511
  conductivity control and doping, 513–514
  crystal-pulling methods, 500–502
  crystallization from nonmetallic crucibles, 505
  crystallographic parameters, 488t
  Czochralski (Cz) growth, 500–501, 508–510
  defect density, 514–515
  definition, 498–500
  doping issues and reduction of defect density, 513–515
  edge-defined film-fed growth (EFG), 501–502, 501f, 505–507

  electrical properties of, 488t
  epilayers, 495–497
  field-effect transistors (FETs), 493–494
  floating zone (FZ) method, 504
  β-$Ga_2O_3$ laser crystals, 495
  heteroepitaxy and homoepitaxy III nitrides, 495–497
  high-power and high-voltage devices, 489–494
  light-emitting diodes (LEDs), 487–489
  membrane technology, 497–498
  nanobelt FET fabrication, 498f
  photodetectors, on bulk β-$Ga_2O_3$, 494–495
  radio-frequency (RF) devices, 487–489
  Schottky barrier diodes (SBDs), 491–493, 493f
  tailoring crystal properties via growth parameters, 511–512
  thermodynamic properties, 498–500
  Verneuil method, 504–505
Gamma-ray detector application, 292–293
Gas phase stoichiometry, 142–143
Gas thermodynamics, 381–382
Geometry optimization, 220–221
Germanium (Ge) crystals
  absorption edge for, 95f
  applications of, 91t, 119–121
  band structure for, 92f
  basic properties, 89–93, 91t–92t
  Bridgman growth, 97–98
  chemical polishing, 97t
  constitutional supercooling, 110
  crystal growth, 97–102
  Cz growth, 98–100
  dislocation-free crystal growth. *See* Dislocation-free crystal growth
  for electronics and photonics, 120
  flow chart of, 96f
  GeSi and GeSn, 120–121
  growth-related phenomena, 103–110
  impurity segregation, 94t
  for infrared optics, 119
  interface instabilities, 108–110
  material preparation, 96–97
  native point defects, 110–114
  oxygen donors, 114
  periphery facets, 103–105
  physical properties, 98t
  polyethylene terephthalates (PETs), 89
  for radiation detection, 119
  resonance method, 95f
  segregation, 105–108
  striations, 108
  structural defects, 110–119
  X-ray topographic observations, 108–110
GeSi, 120–121
GeSn, 120–121
Gettering, ML silicon, 80–81
Granular polysilicon beads, 46f
Graphite degradation, 67–68
Gulliver–Scheil expression, 14

**H**

Habit line collapse
  crystal terminated due, 19f
  LCM elevation map of, 21f
  location of, 20f
  orientation crystals, 18f
  SEM of, 21f
Hall measurements, 436–438
Hard X-ray photoelectron spectroscopy (HAXPES), 530–532
H-CVD. *See* Halide chemical vapor deposition (H-CVD)
Heat exchanger method (HEM), 7, 450
Heterojunction (HIT) solar cells, 63–64
Hertz–Knudsen equation, 133
High nitrogen pressure solution growth, 423
High-performance (HP) mc-Si, 57–58
High-power applications, 489–494
High-pressure Bridgman (HPB) method, 282–283
High-pressure synthesis, GaAs, 204–205
High-rate continuous process, 167
High-temperature chemical vapor deposition (HTCVD), 135
High-voltage devices, $Ga_2O_3$, 489–494
Horizontal direct solidification method (HDSM), 450
Hot-zone designs, Cz, 64
HTCVD. *See* High-temperature chemical vapor deposition (HTCVD)
HVPE. *See* Hydride vapor phase epitaxy (HVPE)

Hydride vapor phase epitaxy (HVPE), 424–425
  computational contributions, 387–388
  crystals
    anisotropic growth, 386–387
    electronic properties, 385–386
    foreign seeds, 383
    native seeds, 384
    optical properties, 385–386
    structural properties, 385–386
  fundamentals method, 380–382
  gas thermodynamics of growth, 381–382
  growth systems, 382–383
  point defects
    doping, 384–385
    Ga vacancies, 385
    impurities, 385
  reactors, 382f

**I**

Impurity segregation, 94t
InAs, 195
Indium oxide ($In_2O_3$)
  bulk single crystal growth, 525–528
  crystal growth, 524–529
  definition, 524–525
  doping issues and reduction of defect, 536–538
  epitaxial thin film growth, 528–529
  Fermi level, 532f
  intentionally doped, 538
  LDOS, 531f
  melt growth, 524–525
  optical properties, 532–533
  surface structure and accumulation layer, 529–532
  tailoring of crystal properties, 529–533
  TEM, 528f
  thermodynamic properties, 524–525
  unintentionally doped, 536–537
Indium phosphide (InP)
  annealing and hydrogen, 262–267
  applications and requirements of, 241–242
  benefits of computer modeling, 250–252
  for crystal growth, 243–246, 250
  crystal pulling, 252–254
  direct synthesis, 248–250
  doping issues and reduction of defect density, 257–267
  *vs.* Fe, 260–262
  high-temperature properties of, 242t
  magnetic stabilization techniques, 253–254
  phosphorus *vs.* reciprocal temperature, 246f
  polycrystal synthesis, 248
  semiconducting InP, 257–258
  semiinsulating bulk InP, 258–267
  synthesis and apparatus, 246–250
  tailoring crystal properties via growth technology, 252–257
  technologies growth, 242–246
  thermodynamic properties, 242–246
  vapor-controlled LEC, 252–253
  vertical container growth, 255–257
  vertical gradient freeze (VGF), 243
Infrared imaging, 273
Infrared optics, 119
Infrared (IR) spectroscopy, 536–537
Inorganic scintillators, 319t
Intentionally doped $In_2O_3$, 538
Interface concavity, 65
Interface instability, 108–110
Interferometers, 479–480
Intrinsic defects, $SnO_2$, 558–561, 563–564

**K**

Kyropoulos (Ky), 450

**L**

Langmuir isotherm type equation, 149
Laser-scattering tomography defects (LSTDs), 30
Large dislocation loops (LDLs), 30
Light-emitting diodes (LEDs), 487–489
Light point defects (LPDs), 30
Light reduceddegradation (LID), 58–59
Liquid-encapsulated Cz, 206–207, 280
Low-pressure synthesis, GaAs, 203–204
Low temperature gradient (LTG), 101–102
Luminescence
  of $A_2B_6$ compounds, 304t
  selenides II, 303
Luminescent pressure transducers, 481–482
Luminophor screens, 480–481

**M**

Magnetic Cz (MCz), 71
Magnetic liquid-encapsulated Kyropoulos (MLEK), 254
Magnetic stabilization techniques, 253–254
Markov method, 285
Maxwell equations, 339–341
mc-Si. *See* Multicrystalline silicon (mc-Si)
Melt growth, $In_2O_3$, 524–525
Meniscus-controlled growth, 140–141
Metalorganic chemical vapor deposition (MOCVD), 378f
Metalorganic vapor phase epitaxy (MOVPE), 190–191
Microwave plasma chemical vapor deposition, 334f, 337f
Minority-carrier lifetime, 70–71
MOCVD. *See* Metalorganic chemical vapor deposition (MOCVD)
Modeling approach
  furnace design, 219–220
  geometry optimization, 220–221
  optimization by inverse modeling *vs.* ANNs, 215–219
  process intensification, 222–227
  process optimization, 221
  QSS *vs.* transient, 215
  2D *vs.* 3D, 213–215
Modified-Lely method, 130, 134–135
Modified PVT (M-PVT), 137
Mono-like (ML) silicon, 75–81
  codoping and gettering, 80–81
  defect formation, 77–80
  nucleation from the crucible wall, 75–76
  seed cost, 76
Mono-like-multi (MLM), 7
Moore's law, 8
M-PVT. *See* Modified PVT (M-PVT)
Multicrystalline silicon (mc-Si)
  high-performance (HP), 57–58
  wafer, 63f
Multienergy radiography, 312–318

**N**

Na-flux method
  crystals
    dislocation reduction, 378–379
    doping, 379
    multipoint-seed growth, 375
    point-seed growth, 374–375
    self-nucleated, 374–375
  fundamentals method
    melt properties, 369–370
    solubility, 369–370
  gallium nitride (GaN) crystals, 424
  growth systems
    externally heated systems, 372
    internally heated systems, 372–373
  melt modifications
    agitation of melt, 376–377
    carbon additives, 375–376
    growth rate, 375–376
    melt additives, 377–378
    melt composition, effect of, 376
    pressure, effect of, 376
    temperature, effect of, 376
Nanobelt FET fabrication, 498f
Native point defects, 110–114
Nucleation, of dislocations, 48f

**O**

Open hot zone type, 31f
Optical data, $SnO_2$, 563–564
Optical properties, $In_2O_3$, 532–533
Optimization by inverse modeling, 215–219
Organometallic vapor phase epitaxy, 190–191
Orientation crystal, 22f
Quantum well action (QWA) mechanism, 151
Oxidation-induced stacking-fault ring (OISF ring), 71
Oxygen donors, 114
Oxygen precipitate, 25f

**P**

Partial density of states (pDOS), 558–559
pDOS. *See* Partial density of states (pDOS)
Phosphor, 304–306
Photodetectors, on bulk $\beta$-$Ga_2O_3$, 494–495
Photoelectric effect, 93
Photoelectron spectroscopy, 552–558
Photoluminescence (PL), 436–438
Photon counting method, 307t
Photovoltaics (PV), 57–58, 62f
Physical vapor transport (PVT), 130
Pfann's method, 96–97
Plank's quantum law, 303

Point defects
  ammonothermal method
    doping, 366–367
    Ga vacancies, 366
    impurities, 364–365
  HVPE
    doping, 384–385
    Ga vacancies, 385
    impurities, 385
Polycrystal synthesis, 248
Polycrystalline material, synthesis of, 278–279
Polyethylene terephthalates (PETs), 89
Polytypism, 133
Positron annihilation spectroscopy, 366
Postgrowth thermal treatments, 289–291
Power consumption
  effect of molybdenum, 66f
  and pulling rate, 65–66
Process chemistry, 168–169
Process intensification, 222–227
Process optimization, 221
P-type and n-type, $SnO_2$, 565–567

**Q**

Quantum well action (QWA), 145
Quasimono silicon, 7
Quasistationary state, 145
Quasisteady state (QSS), 215

**R**

Radiation detection, Ge, 119
Radio-frequency (RF) devices, 487–489
Radio frequency (RF) induction heating system, 99–100
Raman measurements, 436–438
Repeated *a*-face (RAF), 158
Resonance method, 95f
Resonant photoelectron spectroscopy (resPES), 550

**S**

Sapphire
  aluminum oxide ($Al_2O_3$). *See* Aluminum oxide ($Al_2O_3$)
  anisotropy of, 458f
  chemical properties, 468t
  chemical treatment, 458t
  chemomechanical treatment, 458t
  corrosion resistance of, 454t, 469t
  growing methods for, 448f
  optical disks, 479
  physical properties of, 466t–467t
  polished and patterned structures, 457f, 474f
  titanium-doped, 482
  transmission of, 461f
  wetting angle of, 471t
  window sensor, 479
  windows withdrawal, 479
Scanning tunneling spectroscopy (STS), 527f
Schottky barrier diodes (SBDs), 491–493, 493f
Seeded sublimation process, 134–135
Segregation, Ge crystals, 105–108
Selenides II
  laser applications and improved growth, 318–325
  luminescence, 303
Semiconducting InP, 257–258
Semiinsulating bulk InP, 258–267
Silicon carbide (SiC)
  applications of, 129–131
  benefits of computer modeling, 143–147
  binary phase diagram, 131–132
  bulk growth methods, 134–139
  CF-PVT, 137
  doping issues and reduction of defect density, 147–164
  evaporation method, 411f
  extended defects, 152t
  H-CVD, 135–137
  high-rate continuous process, 167
  HTCVD, 135
  materials requirements, 129–131
  M-PVT, 137
  polytypism, 133
  process chemistry, 168–169
  seeded sublimation process, 134–135, 143t, 404–405
  SiC material, 164–167
  substrate evaporation method, 418–423
  synchrotron transmission X-ray topograph, 157f–158f
  tailoring crystal properties via growth parameters, 139–143
  and technologies growth, 131–133
  thermodynamic properties, 131–133
  top-seeded solution growth (TSSG), 137–138, 138f
  ultimate-quality crystals, 167–168

  vapor phase description, 132–133
Silicon single crystals
  applications and requirements of, 8–14
  benefits of computer modeling, 36
  cells and grains, 49f
  constitutional supercooling. *See* Constitutional supercooling
  CVD-grown polysilicon chucks, 17f
  CVD polysilicon surface, 29f
  dopant concentration axial distribution, 37f
  doping issues and reduction of defect density, 36–41
  granular polysilicon beads, 46f
  growth processes, 7f, 30–35
  habit line collapse. *See* Habit line collapse
  material, 41–43
  mono-like-multi (MLM), 7
  nucleation, of dislocations, 48f
  open hot zone type, 31f
  orientation crystal, 22f
  oxygen precipitate, 25f
  property specifications, 10
  quasimono, 7
  resistivity, 37f
  schematics of growth methods, 25–30
  shape and purpose, 23f
  solar cells, 12f
  tailoring crystal properties via growth parameters, 35–36
  technologies growth, 30–35
  thermal donors (TDs), 23
  thermodynamic properties, 14–25
Single crystal growth
  gallium nitride (GaN), 354–357
  of tin oxide ($SnO_2$), 550–551
Skife polishing, 345–346
$SnO_x$ thin film, 551–552
Soft Xray photoelectron spectroscopy (SXPES), 530–532
Solar cells, 12f, 274
Solar silicon
  alkaline texture morphology, 63f
  Cz method, 57–58, 63–71
  different growth methods for, 59t
  DS method, 71–81
  floating-zone silicon growth, 58f
  interface concavity, 65
  mc-Si wafer, 63f
  minority-carrier lifetime, 70–71
  ML silicon, 75–81
  mono-like (ML) silicon. *See* Mono-like (ML) silicon
  multicrystalline silicon (mc-Si). *See* multicrystalline silicon (mc-Si)
  power consumption. *See* Power consumption
  value chain of PVs, 62f
SSD, 439
SSM. *See* Sublimation sandwich method (SSM)
Sublimation sandwich method (SSM)
  crystal growth by, 425–439
  gallium nitride (GaN) crystals, 402–439, 403f
  technique, 428f
Substrate orientation, 414–415
Sugano–Tanabe diagram, 322f
Surface electron accumulation layer (SEAL), 523
Synchrotron transmission X-ray topograph, 157f–158f

**T**

Tailoring crystal properties
  indium oxide ($In_2O_3$), 529–533
  indium phosphide (InP), 252–257
  gallium oxide ($Ga_2O_3$), 511–512
  silicon carbide (SiC), 139–143
  silicon single crystals, 35–36
Temperature distribution
  dislocation-free crystal growth, 103f
  Ge crystal growth, 103f
Thermal donors (TDs), 23
Thermal double donors (TDDs), 114
Thermal expansion coefficients, 405t
Thermal neutrons, 307t
Thermal radiation, 64
Thermodynamic equilibrium, 108
Thermodynamic properties
  cadmium telluride (CdTe), 274–278
  gallium oxide ($Ga_2O_3$), 498–500
  indium oxide ($In_2O_3$), 524–525
  indium phosphide (InP), 242–246
  nitride semiconductors, 1
  silicon carbide (SiC), 131–133
  silicon single crystals, 14–25
Thermoluminescent detectors (TLDs), 477–478
Thin a-$SnO_x$ films, 564–565
Thin film deposition, $SnO_2$, 547–552

$Ti^{3+}$ scintillators, 475–476
Tin oxide ($SnO_2$)
  applications, 548
  ARPES, 556–558
  band scheme, 562–563
  basic properties, 547–552
  crystal growth, 547–552
  crystallographic properties, 550
  description and derivation of defect states, 559–560
  electrical properties and doping, 549
  electronic energy diagram, 561–567
  electronic structure, 547, 549–550, 562–563
  intrinsic defects and optical data, 563–564
  intrinsic electronic defects, 558–561
  ionic and covalent defect, 560–561
  optical properties, 548–549
  pDOS, 558–559
  photoelectron spectroscopy of, 552–558
  p-type and n-type, 565–567
  resonant photoelectron spectroscopy (resPES), 550
  single crystals, growth of, 550–551
  Sn3d and O1s core levels, 552–554
  $SnO_x$ thin film, 551–552
  thin film deposition, 547–552
  transparent conducting oxide (TCO), 547
  *vs.* thin a-$SnO_x$ films, 564–565
  X-ray absorption data, 554–556
Titanium-doped sapphire, 482
TlAs, 195
Top-seeded solution growth (TSSG), 137–138, 138f, 140–141
Transient, 215
Transmission electron microscopy (TEM), 528f
Transparent conducting oxide (TCO), 547
Traveling heater method, 286–287
Twinning effects, InP, 243–245

**U**

Ultimate-quality crystals, 167–168
Unintentionally doped $In_2O_3$, 536–537

**V**

Valence band, 5–6
Vapor-controlled LEC, 252–253
Vapor phase, SiC, 132–133
Vapor-phase growth, 284–286
Vapor-pressure-controlled Bridgman growth, 281–282
Verneuil method, 450
  gallium oxide ($Ga_2O_3$), 504–505
Vertical Bridgman (VB) method
  concise description of methods, 450
Vertical container growth, 255–257
Vertical gradient freeze (VGF), 207–210, 243

**W**

Wafers
  large-size wafer production, 343–344
  mechanical and surface specification of, 200–202
  and sample preparation, 227–229
Wavelength dispersive X-ray (WDX) spectroscopy, 105–107
Wetting angle, 471t

**X**

X-ray absorption data, 554–556
X-ray characterization, GaN crystals, 435–436
X-ray detector application, 292–293
X-ray diffraction, 420f
X-ray topographic observations, 108–110

**Z**

Zinc selenide (ZnSe)
  Bridgman method, 307f
  compounds, 307–311
  digital X-ray radiography, 319t
  emission wavelength, 321f
  energy resolutions and light yield, 312t
  low-energy detectors, 320f
  properties and crystal growth, 307–311
  scintillation element, 309f
  security and medical applications, 312–318
Zinc sulfide (ZnS)
  $A_2B_6$ scintillators, 312–318
  classical phosphor and new compositions, 304–306
  compounds, 304
  multienergy radiography, 312–318
Zinc telluride (ZnTe), 273